Advanced Polymer Composite Materials

Processing, Modeling, Properties and Applications

Edited by
Giorgio Luciano, Paola Stagnaro and Maurizio Vignolo

MDPI

Advanced Polymer Composite Materials: Processing, Modeling, Properties and Applications

Advanced Polymer Composite Materials: Processing, Modeling, Properties and Applications

Editors

Giorgio Luciano
Paola Stagnaro
Maurizio Vignolo

MDPI

Editors

Giorgio Luciano
SCITEC
National Research Council of
Italy
Genova
Italy

Paola Stagnaro
SCITEC
National Research Council of
Italy
Genova
Italy

Maurizio Vignolo
SCITEC
Natinal Research Council of
Italy
Genova
Italy

This is a reprint of articles from the Special Issue published online in the open access journal *Polymers* (ISSN 2073-4360) (available at: www.mdpi.com/journal/polymers/special_issues/ advanced_polymer_composite_materials).

For citation purposes, cite each article independently as indicated on the article page online and as indicated below:

LastName, A.A.; LastName, B.B.; LastName, C.C. Article Title. *Journal Name* **Year**, *Volume Number*, Page Range.

Contents

About the Editors

Giorgio Luciano

Giorgio Luciano graduated with a Degree in Chemistry from the University of Genoa in 1999 (experimental thesis in physical chemistry). In 2002, he started a PhD (awarded in 2005) on the corrosion of metals. During his Ph.D. studies, he spent a period of time at the Academy of Fine Arts Vienna and the TU Wien. In 2005–2006, he was awarded the postdoc research grant UniGe (interactions between wood and metals). In 2006, he completed a postdoc multivariate analysis and design of an experiment applied to sensors (UniGe). In 2007–2008, he completed a postdoc at Matforsk Nofina (Oslo) prototyping algorithms for data analysis. In October 2009 he started working at CNR-ISMAR. In 2012 he became a CNR researcher. In 2014 he started to work at the Institute for the Research of macromolecules (ISMAC). Currently, he works on the characterization of materials (by means of several analytical techniques), chemometric techniques and thermodynamics.

Paola Stagnaro

Paola Stagnaro obtained her Degree in Chemistry, Magna cum Laude, in 1989 and her Ph.D. in Chemical Sciences in 1993. She obtained her PhD in 1995–1997 from the University of Genoa. Since 1998, she has been a researcher at CNR (IMAG until 2001, ISMAC until Sep. 2019, and now SCITEC). Since March 2008, she has been responsible for the Institute Genoa Section. From 2009 to 2016, she was a member of the Council of ISMAC, and from 2011 to 2016 she was on the Executive Committee of the Italian Association of Science and Technology of Macromolecules (AIM). Her experience abroad includes: May–June 1997 and April–May 1999, Polytechnic of Grenoble; October 2005, University of Manchester; and July 2007 and October 2012, Changchun Institute of Applied Chemistry.

Maurizio Vignolo

Maurizio Vignolo obtained his Master's Degree in Chemistry in 2000, and his Ph.D. in Material Sciences and technology in 2006. Since 2001, his research activity has been performed within research projects supported by national and international institutions or industries, and has been mainly focused on the development and study of innovative materials endowed with properties specific for superconductive applications, such as cables for the power distribution of electrical energy and energy storage. Since August 2020, he has been with the SCITEC Institute of National Research Council of Italy, where he now works in polymer material science.

Preface to "Advanced Polymer Composite Materials: Processing, Modeling, Properties and Applications"

The use of composite materials is ubiquitous in every field of human activities, including in the agricultural, industrial, environmental, biomedical and transport sectors. After a pandemic with the simultaneous unfolding of an energy and climatic crisis, we now realize how necessary it is to carry out studies on composite materials based on polymers to positively affect our current society and, in particular, future generations.

To this aim, in the present selection of scientific articles we have given visibility to worthy contributions on a wide variety of topics, highlighting how essential plastic-based composite materials and their derivatives are in our daily lives. The articles in this Special Issue were wide-ranging and devoted to the properties and characterization of composites for biological applications and, more generally, for the development of the chemical–physical properties of these materials.

Giorgio Luciano, Paola Stagnaro, and Maurizio Vignolo
Editors

Article

Study of Microwave-Active Composite Materials to Improve the Polyethylene Rotomolding Process

Giorgio Luciano *, Maurizio Vignolo, Elisabetta Brunengo, Roberto Utzeri and Paola Stagnaro

Istituto di Scienze e Tecnologie Chimiche "Giulio Natta"—SCITEC, National Research Council of Italy, Via de Marini 6, 16149 Genova, Italy
* Correspondence: giorgio.luciano@cnr.it

Abstract: The present paper reports on the formulation and characterization of composite coating materials susceptible to microwave (MW) heating to investigate their application in making the rotomolding process (RM) more energy efficient. SiC, Fe_2SiO_4, Fe_2O_3, TiO_2 and $BaTiO_3$ and a methyl phenyl silicone resin (MPS) were employed for their formulations. Experimental results showed that the coatings with a ratio of 2:1 w/w of inorganic/MPS are the most MW-susceptible materials. To test the coatings in working mimicking conditions, they were applied to molds, and polyethylene samples were manufactured by MW-assisted laboratory uni-axial RM and then characterized by calorimetry, infrared spectroscopy and tensile tests. The results obtained suggest that the coatings developed can be successfully applied to convert molds employed for classical RM process to MW-assisted RM processes.

Keywords: rotomolding; microwave heating; microwave-active materials; polyethylene processing

1. Introduction

World is implementing sustainable manufacturing and the consequence of effective utilization of resources is increasing productivity. Among the several ways of improving resource effectiveness is avoiding use of resources in the first place and reducing its footprint is paramount [1]. Plastic industry is an energy-intensive one requiring a high volume of electric power for thermal energy where energy use accounts for 5–10% of total production cost [2].

Among the plastic processing methods, rotational molding, also known as rotomolding (RM), is a casting and molding technique useful to produce hollow plastic items of medium to large size [3–5] and involves manufacturing in food and agriculture sector, industrial application, automotive, containers, consumer items and toys. RM is a relatively small part of the plastics industry practiced by approximately 2500 companies around the world. It consumes approximately 0.7% of the total volume of the world production of plastics [6–9] and references therein. To enhance the energy performance of the RM process, the setup required for heating the molds represents a key factor.

In the present paper we focused on enhancing the performance of the process by heating via microwave (MW) irradiation in alternative to using gas or electric ovens. For this aim, we formulated composite materials based on MW-susceptible inorganic compounds (MWSIC) and a methyl phenyl silicone resin to modify conventional RM molds.

In MW heating, also known as dielectric heating, we have a direct transfer of energy (which travels at the speed of light). Consequently, a large amount of power can be saved as well as process times and operational space, considering the physical phenomena involved in the thermal conduction, which is inversely proportional to the square of the distance in the between of the energy source and material to be mold [10].

MW heating is obtained by irradiating active materials in the microwave energy range (10^{-3} kJ/mol), which is too low of a value for chemical bonds cleavage, but it is sufficient

to heat or melt the material by conversion of electromagnetic energy of MW into thermal energy (vibrational motions of chemical bonds). For this reason, the involved materials need to have permanent dipoles (dielectric material) to work well.

In this study, attention was focused on the investigation of MW-active coating materials to be adopted to make the molds suitable for MW heating and thus make it possible to manufacture objects in polyethylene (PE), which is not a dielectrically active material.

Several formulations based on MWSIC were tested in terms of their response to MW irradiation. Measurements of electric power absorbed by selected composite formulations during the imposed microwave cycle were performed and compared to the power needed for corresponding resistive irradiation. PE samples were prepared by MW-assisted uni-axial rotomolding in a lab oven and their properties compared to those of commercial or differently prepared samples.

2. Materials and Methods

2.1. Materials

Five different MWSIC materials in powder form, namely, silicon carbide (SiC), iron (II) silicate (Fe_2SiO_4), iron (III) oxide (Fe_2O_3), titanium (IV) oxide (TiO_2), barium titanate (IV) ($BaTiO_3$), were tested. Furthermore, it was studied also the effect of different grain size: 35 μm (Fine) and 70 μm (Coarse) for SiC (SCF and SCC, respectively) and 35 μm (Fine) and 500 μm (Coarse) for Fe_2SiO_4 (ISF and ISC) (see Table 1).

Table 1. List of MW-susceptible inorganic compounds (MWSIC) investigated in this work.

MWSIC Formula	Labeled As	Description
SiC	SCF	Silicon carbide 35 μm grain size
SiC	SCC	Silicon carbide 70 μm grain size
Fe_2SiO_4	ISF	Iron silicate 35 μm grain size
Fe_2SiO_4	ISC	Iron silicate 500 μm grain size
Fe_2O_3	IO	Iron oxide powder < 5 μm, ≥99%
TiO_2	TO	Titanium oxide ≥ 99%
$BaTiO_3$	BTO	Barium titanate powder < 3 μm, ≥99%

Except for ISF and ISC kindly supplied by Slide S.r.l. (Italy), all other inorganic materials were purchased from Sigma-Aldrich (now Merck). Grain size of each substance was obtained from the corresponding label on the commercial container.

To select the most effective materials, that are most capable of efficiently absorbing the MW irradiation heat transfer measures were performed on pelletized samples (discs of 1.2 mm diameter and 0.5 mm thickness) prepared by mixing each MWSIC powder typology with a high-temperature-resistant methyl phenyl silicone resin (MPS). The resin used for the pellet formulation was a commercial two-component silicone elastomer resin (BLUESIL ESA 7252 A&B Italy), fast curable at r.t. and endowed with outstanding flame resistance and good thermal conductivity. The MWSIC powder:MPS resin ratio used was 2:1 (*w/w*).

To gather more information about the materials which can be used as molds, different cylindrical containers were coated with the MW-active composite materials. Aluminum (AL, 50 g), stainless steel (SS, 70 g) and glass (GL, 170 g) containers were tested.

A commercial PE grade (Plastene R210, Poliplast S.p.A. Italy, kindly supplied by Slide S.r.l.) in form of powder (mean dimension 410 μm), was employed for the tests in lab. Plastene R210 has melt flow index (ISO 1133, 190 °C, 2.46 kg) 6.25 g/10 min and density 0.936 g/cm^3 (ISO 1183).

For de-molding of PE objects TECNOSIL 21 (SOL TECNO S.r.l., Italy), a technical silicone oil employed in industrial production, was used as detaching agent.

For comparison purposes, two other polyethylene types, namely, Riblene and Kartell jar, were tested by mechanical tensile tests, DSC and ATR-FTIR.

2.2. Methods

For the MW-assisted RM process we used a mold coated with MW-susceptible material while in the conventional RM process the mold was uncoated.

A MW oven SAMSUNG M/O 20LT GE71A of 20 L in volume as internal space, operating at 2.45 GHz frequency and at 750 W in power consumption, also equipped with a grill (1100 W in power consumption), was used in heating cycles both with the microwave and the resistance irradiation, for comparison purpose.

To have more information about electric energy saving, the same process parameters (rpm, time, PE powder amount and mold) were adopted to simulate a PE molding using MW irradiation or the resistance of the oven (grill). In each process the absorbed electric current (I) was measured, as well as the voltage value (V) by a digital multimeter (Power-meter GBC KDM-360CTF), respectively, connected to the circuit in series as a galvanometer or in parallel mode as a voltmeter.

The heat transfer measurements were performed positioning each composite pellet on the center of a Teflon plate fixed to the motor axis of the MW oven; the heating cycle was tested at 750 W power both for 5 and 1.5 min.

After the MW irradiation, each pellet was immediately quenched into 20 g of demineralized water at room temperature contained in a plastic Petri with a stirring bar under movement. A Hg thermometer (± 0.5 °C in sensibility) was adopted for the temperature measurements.

The composite pellets were rapidly transferred from MW oven to water using high-temperature-resistant and low-thermal-conductivity plastic tweezers.

Microwave-active ISC powder was then chosen as the most suitable to prepare the coatings to be adhered to the molds using the same weight ratio (2:1 powder:resin) previously used for the testing pellets (in this case, 60 g ISC:30 g MPS).

The molding process of PE was tested by performing MW heating cycle of 300 W for 13 min, with a uni-axial rotational movement on the mold axis and a speed of 2 rpm. This speed, as well as the rotation of the mold even during the cooling phase, was possible by replacing the original oven motor (6 rpm). Such a low rotational speed was useful to have sufficient contact time between PE powder and the hot mold internal surface and thus improve the heat exchange.

For each test, 15 g of PE powder were utilized.

Uni-axial tensile measurements on produced PE objects and reference PE counterparts were performed with a Shimadzu ASG-X 10 kN universal machine operating at r.t. on 5 dog-bone specimens (for each PE type) prepared in shape and dimension as requested by ISO 527 (1–5) using a dog-bone shaped mold or a die cut from a previously die-cast PE plate.

To obtain the dog-bone test specimens from uni-axial RM process assisted by MW, a cylinder of PE was prepared from Plastene powder by applying a MW cycle of 10 min at a power energy of 750 W, and a cooling time of about 30 min at a speed of 6–8 °C/min was adopted.

As a first term of comparison, a PE plate was prepared from the same Plastene powder using a Colling press (Laboratory Platen Type P200 bar) and applying the following thermal cycle: heating up to 300 °C, heating rate 10 °C/min, 10 min isothermal at 100 bar, cooling rate at 10 °C/min to room temperature. As a second term of comparison, a commercial PE item, namely, a Kartell PE jar (1000 mL), was employed.

FTIR spectra of PE samples (commercial and rotomolded) were recorded using a Perkin Elmer FTIR Spectrum Two™ spectrophotometer. FTIR spectra were acquired in attenuated total reflection (ATR) mode in the range of 4000–400 cm^{-1}.

Calorimetric analysis was performed with a DSC Mettler 821^e instrument on specimens of 10 mg (cut from the manufactured samples) applying a heating–cooling–heating cycle in the range 100–240 °C under N_2 and at a scan rate of 10 °C/min (EN ISO 11357-1-3).

The morphology and elemental analysis of different MW-active coating formulations were performed by scanning electron microscope (SEM) equipped with a probe for energy-dispersive X-ray analysis (EDX); in detail, it is a HITACHI TM3000 benchtop SEM (15 kV).

3. Results and Discussion

The main objective of the present study is to prove the easiness of the conversion of the molds employed in a standard oven to the new coated ones for the MW-assisted RM process. For this purpose, we tested (by heat transfer measurements) the ISC/resin (2:1 ratio) composites on molds made of different materials.

Silicone elastomer resin was chosen due to the working temperature conditions ranging from ambient temperature to 400 °C. It is well established that silicon resins over a wide range of temperatures and they also acknowledged for their fire resistance properties. Moreover, the elastomeric nature of MPS leads to good adherence of the coatings to the molds.

The MWSIC materials of this study were chosen for their dielectric constant (relative permittivity ε_R) and dissipation factor values acquired from the literature and reported in Table 2 for room temperature [8–21] and considering negligible the change in value for frequencies higher than 100 MHz [15].

Table 2. Literature dielectric data of the MW-susceptible inorganic compounds investigated as suitable materials for molds coating in MW-assisted RM and of other reference materials.

Material	Measure at	Dielectric Constant (k')	Dielectric Loss (k'')	Loss Tangent (k''/k')
Fe_2SiO_4 [15,16]	25 °C, 10 GHz	5.77	0.01 **	0.0018
SiC [12]	25 °C, 3–10 GHz	10–60	0.01–36 **	0.001–0.58
TiO_2 [11–14]	20/25 °C, 4 GHz	80–170	0.008–0.017 **	0.0001
Fe_2O_3 [17]	20/25 °C, 3 GHz	6–50	1–4	0.2–0.6
$BaTiO_3$ [21]	30 °C, 1 MHz	2200	150	0.068 **
H_2O [12]	20 °C, 0.1/2.5 GHz	78.1/80.1	3.6	0.016/0.123
SiO_2 [12,20]	25 °C, 8.5 GHz	3.5–4	0.0008 **	0.0002
Na_2SiO_3 [16,17]	25 °C, 8.5 GHz	5.84	0.041 **	0.0070
PE [12,20]	25 °C, 2.5 GHz	2.444	0.002 **	0.0010 (2.6 *)
PVC [12,20]	30 °C, 0.01/2.5 GHz	3/2.666	0.018/0.04	0.001/0.013
PTFE [22]	25 °C, 8.5 GHz	2.058	0.0022 **	0.00108
Silicon RTV 521	23 °C, 8.5 GHz	3.31	0.085 **	0.0257

* Van der Graaff irradiated sample; ** valued by Equation (5).

Dielectric constant k' (and permittivity) and dissipation (loss) factor are related by Equation (1).

$$k* = k' - jk'' \tag{1}$$

In addition,

$$k' = \varepsilon'/\varepsilon_0 \tag{2}$$

and

$$k'' = \varepsilon''/\varepsilon_0 \tag{3}$$

where the terms ε' and ε'' represent, respectively, the real and imaginary part of complex permittivity $\varepsilon*$ and ε_0 is the vacuum permittivity.

Because k' can be related to the material capability to storage electrical energy and k'' represents its capability to dissipate electrical energy, we can define the ability of a material to convert the microwave radiation into heat as the tangential loss ratio:

$$\tan \delta = \varepsilon'' / \varepsilon' \tag{4}$$

Reference materials used in the experiment and the relative parameters for water, PVC, glass, and PTFE are reported in Table 2.

Because the literature data referred to different measurement parameters, such as temperature, frequency, shape, size and so on, heat transfer measurements were here performed in order to establish the response of the chosen compounds in the laboratory environment.

The values of heat exchanged Q of compounds pelletized with the silicone resin were calculated using Equation (5) and are reported in Table 3.

Table 3. Transferred heat calculated with Equation (5).

MW-Active Compound	Q [J] in Cycle at: 750 W, t = 5 min	Q [J] in Cycle at: 750 W, t = 1.5 min
ISC	1000	125
ISF	700	84
SCC	505	63
SCF	500	65
TO	170	75
IO	330	117
BTO	170	84
IO:BTO (1:1)	167	84

The amount of heat (Q) was estimated by Equation (5)

$$Q = m \cdot c \cdot (\Delta T) \; [J] \tag{5}$$

where ΔT is the difference between the temperature value of the water before and after immersion of the pellet, m correspond to the mass of water and c is its specific heat value ($4.18 \; J \cdot g^{-1} \cdot K^{-1}$). Irradiation time was checked using a precision chronometer.

The results indicate the higher response (expressed as exchanged heat between the material and water used as reference) was obtained by ISC/F samples, followed by SCC/F and IO. The role of the graininess in the response was evaluated both for iron silicate and silicon carbide. In the first case, a difference of 30% in the particles dimension caused a 30% difference in exchanged heat. For the silicon carbide, no effect was found due to the graininess (fine or grain silicon carbide gave identical results).

Among the main objectives of the project one of the most important was the easiness of the conversion of the molds employed in a standard oven to the new coated ones for the MW-assisted RM process. For this purpose, we tested (by heat transfer measurements) the ISC/MPS (2:1 ratio) composites on different materials used for the molds, namely, aluminum, stainless steel and glass (here labeled AL, SS and GL, respectively).

Absorbed power (P_{abs}) was calculated in W units with Equation (6), where V is the voltage and I the electric current, converted into W per hour (Wh) to have a direct comparison, considering the impulse time for MW irradiation and the continuous power adsorption for the resistance irradiation.

$$P_{abs} = V \times I \; [W] \tag{6}$$

In Tables 4 and 5, the resultant absorbed power values are reported.

Table 4. Absorbed power calculations with Equation (6) for the MW irradiation @ 300 W (t < 300 s).

Mold Material (Time)	Absorbed Current [A]	Grid Voltage [V]	Time [s]	Absorbed Power [Wh]
AL (780 s)	5.60	225	286	100
SS (780 s)	5.40	224	286	96
GL (780 s)	5.70	226	286	102

Table 5. Absorbed power calculations with Equation (6) for the resistance irradiation (780 and 960 s).

Mold Material (Time)	Absorbed Current [A]	Grid Voltage [V]	Time [s]	Absorbed Power [Wh]
AL (780 s)	4.00	226	780	196
SS (780 s)	4.01	224	780	195
GL (780 s)	4.01	225	960	241
GL (960 s)	4.03	223	780	195

All three molds, coated with different materials (AL, SS and GL), reached a maximum temperature of 160 °C under MW and 125 °C when employed under a resistance regime.

The results highlighted that by employing a MW regime, there is the possibility of melting PE and reaching the target temperature for effective RM laboratory processing (as shown in Figure 1).

Figure 1. The PE products of molding tests and respective molds (in the between): a, c and e from the MW heating of coated AL, GL and SS molds, respectively; b, d, and f from the resistance heating the corresponding molds.

Analogous results were obtained for the other materials employed. In all cases, MW-assisted RM ensured a more homogeneous heating of the mold with consequent formation of objects, while the heterogeneous heating obtained by resistance irradiation led to RM-manufactured objects severely failed (missing parts, high surface roughness and residual non-melted raw powder material).

In Table 6, the weights of each PE product in the respective irradiation regime are reported to sustain previous affirmations.

Table 6. Weight values of PE products obtained with both MW and Resistive method.

	MW Process	Resistive Process
Material mold	Weight [g]	Weight [g]
SS	14.4 (e)	13.3 (f)
GL	15.0 (c)	8.2 (d)
AL	15.0 (a)	8.2 (b)

Reported in Figure 2 are the setups used to study the influence of the geometry of the microwave apparatus on the rotomolding process.

(**a**)   (**b**)   (**c**)
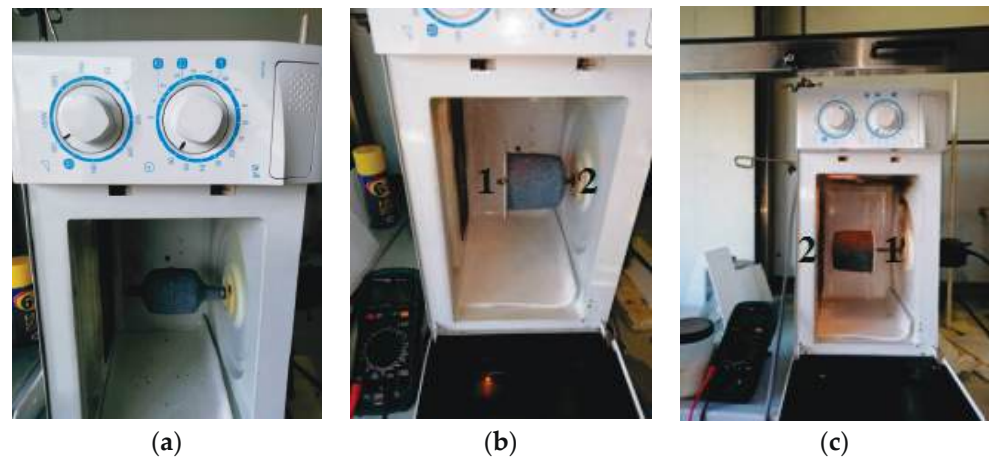
Figure 2. Different materials and configurations of molds: (**a**) AL, (**b**) GL and (**c**) SS in different configurations: white PTFE cap (labeled as 1) on the left side or on the right, respectively. The side of the MW-active material is labeled as 2.

Special care should indeed be employed to find the best focus position in the microwave oven in relation to the geometry of the mold, this to avoid unwanted reflection of the waves as they can cause a failure in the manufacturing process (Figure 3).
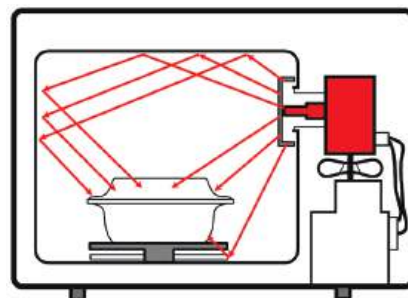
Figure 3. Sketch of MW propagation (as red rays) inside the oven. The direction is indicated by red arrows.

Considering the magnetron (i.e., the MW generator) position, we always needed to ensure that the maximum of the reflected radiation could be absorbed by the active material of the mold, as reported in [23,24], while also ensuring the maximum heat exchange in order to ensure the repeatability of the experiments.

The graph in Figure 4 shows the r.t. stress–strain curves obtained by uni-axial tensile measurements corresponding to the most representative samples of the various PE tested. Table 7 summarizes the ensuing tensile data relating to the average values and standard deviation of five specimens for each type of PE investigated.
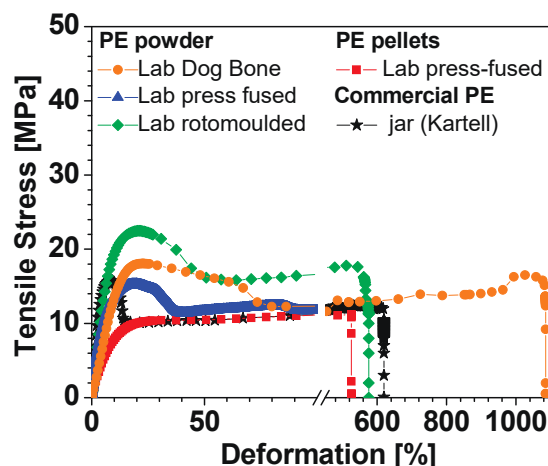
Figure 4. Representative stress–strain curves of several PE dog-bone specimens obtained from different processes: cut from commercial PE jar (Kartell 1000 mL), black star; cut from lab press-fused Plastene powder, blue triangle; cut from lab press-fused Riblene pellets, red square; lab press-fused Plastene powder into dog-bone mold, orange circle; cut from lab MW-rotomolded Plastene powder, green diamond.

Looking at Figure 4 and Table 7, a very similar behavior can be observed for all the samples. In particular, for the value of strength as well as for the elongation one, both referred at the break. The elongation at the break is more affected by the presence of defects in the structure [25,26], and then some samples break at ε_b values less than 200% and others resist until 1100%. The lab MW-rotomolded sample (green diamond) shows a very similar behavior to that of the commercial PE of the Kartell jar (black star). Without going into the details of the results obtained with tensile measurements, as it is beyond the scope of this work, it is possible to conclude that the microwave-assisted rotational molding process, although not yet studied and optimized in detail, proves to be competitive with the classic molding techniques.

Table 7. Data from r.t. uni-axial tensile measurements. # denotes the commercial sample is considered as produced by classic molding process, i.e., not using microwave-assisted rotomolding.

Sample/Preparation Process	Tensile Modulus [MPa]	Tensile Strength at Break [Mpa]	Elongation at Break [%]
Riblene (LDPE) [23]	120–550	32–60	450–810
Commercial PE/#	489 ± 115	12.5 ± 1.6	435 ± 178
Press-fused pellets	116 ± 12	11.6 ± 1.3	520 ± 217
Press-fused powder	291 ± 23	8.5 ± 2.6	160 ± 80
Lab Dog Bone	190 ± 35	16. ± 3.4	1100 ± 491
Lab MW-rotomolded	287 ± 78	21.7 ± 3.2	320 ± 201

FTIR techniques, as reported by Almond et al. [27], can be used to spot the degradation of the polymer highlighting the presence of groups derived from oxidation (such as carbonyl and hydroxyl groups). In our case, the MW-assisted rotomolding process did not degrade the PE material, as shown (Figure 5) by the absence of the abovementioned groups in the ATR-FTIR spectrum and by its substantial overlapping to that of the commercial PE sample. The only differences, visible between 900 and 1300 cm^{-1}, are ascribed to the peaks of surface-adhered silicone oil used as de-molding agent [28].
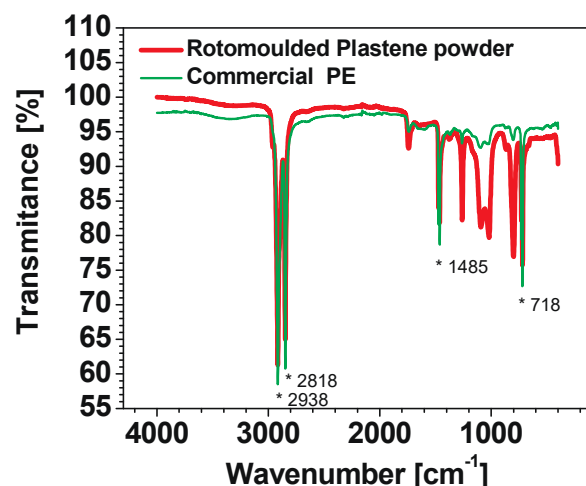
Figure 5. ATR-FTIR spectra of MW-rotomolded (red curve) and commercial (green curve) PE samples. The characteristic PE absorbance bands are located at 2914, 2847, 1470, and 718 cm^{-1} and marked with *.

Figure 6 show the thermograms resulting from DSC analysis. The canonical peak of PE melting in the interval between (100–135 °C during the I and II heating) is recognized for all the samples in the exam. An analogous observation can be performed for the crystallization peak (centered around 110 °C). No other peaks are present. The values of enthalpy of fusion are comparable (around 150 J/g), again suggesting that no degradation occurred during processing. The high crystallinity degree (X_c 50–52% taking 293 J g^{-1} as the fusion enthalpy value of a perfect polyethylene crystal) [29,30] of Plastene grade does not permit us to detect the transformation of the amorphous phase from rigid glass and viscous liquid phase (Tg = −80 °C) [30,31].
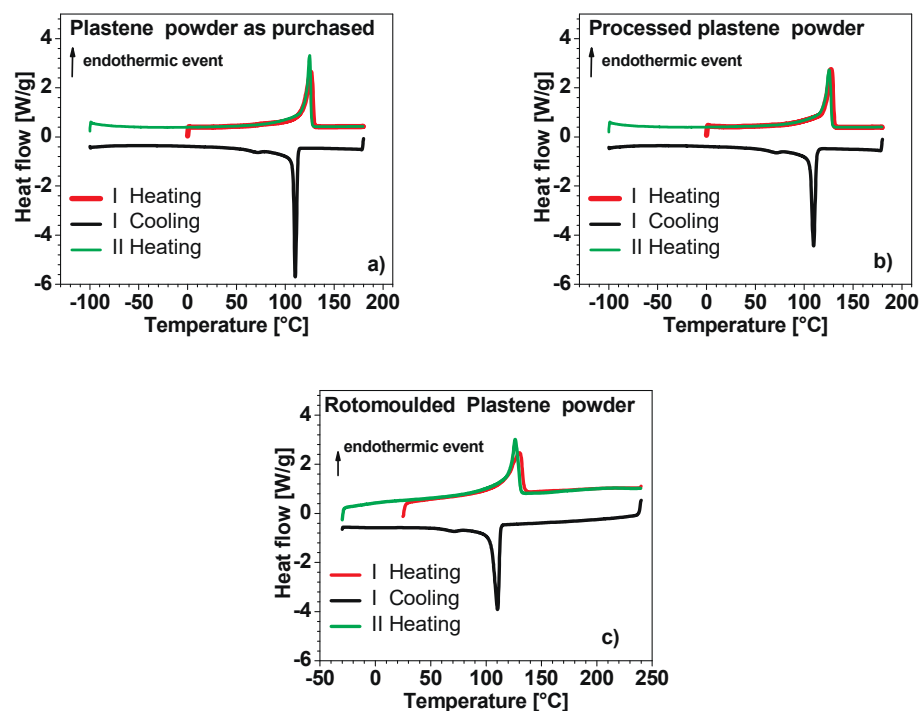
Figure 6. Differential scanning calorimetry graphs relatively to: (**a**) Plastene powder as purchased, (**b**) Plastene after press-fusion and (**c**) MW-rotomolded Plastene.

Furthermore, in order to have more information on the different MW-active coating materials used to cover aluminum, stainless steel and glass molds, each coating material was analyzed by SEM-EDX analysis. In Figure 7, the SEM images of the different MW-active coatings are reported: (a) IO (iron oxide), (b) ISF (iron silicate), (c) TO (titanium oxide) and (d) SCF (silicon carbide). Among the four materials, the iron silicate-based one appears to have a more inhomogeneous surface.
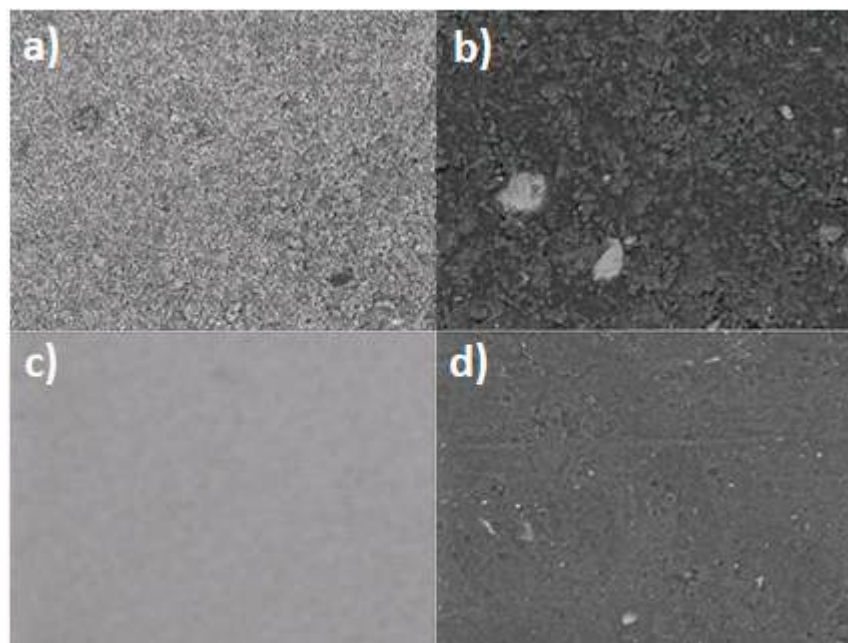
Figure 7. SEM images of the dispersion into the silicone resin of (**a**) Fe_2O_3, (**b**) Fe_2SiO_4, (**c**) TiO_2 and (**d**) SiC.

In Figure 8, the images corresponding to the EDX analysis of the four samples are reported. These confirm the homogeneous dispersion of the powders and their composition. Only the significative elements are reported for each formulation following this order: Fe_2O_3, Fe_2SiO_4, TiO_2 and SiC. The formulations are, respectively,

- Fe in (a), (e), (i) and (o);
- Si in (b), f), (l) and (p);
- Ti in (c), (g), (m) and (q);
- O in (d), (h), (n) and (r).

From EDX images, we can conclude that Si and O are present, as expected, in all the examined composite materials. Ti is obviously present only in (m), while Fe is present in (a) and (e).

Since the melting temperature range of PE is around 130 °C, we checked the chemical stability in air of the MW-active coating materials dispersed into the resin matrix in the range temperature between 0 °C and 300 °C (at the heating and cooling rate of 10 °C/min) by DSC. All the materials did not show any critical issue.
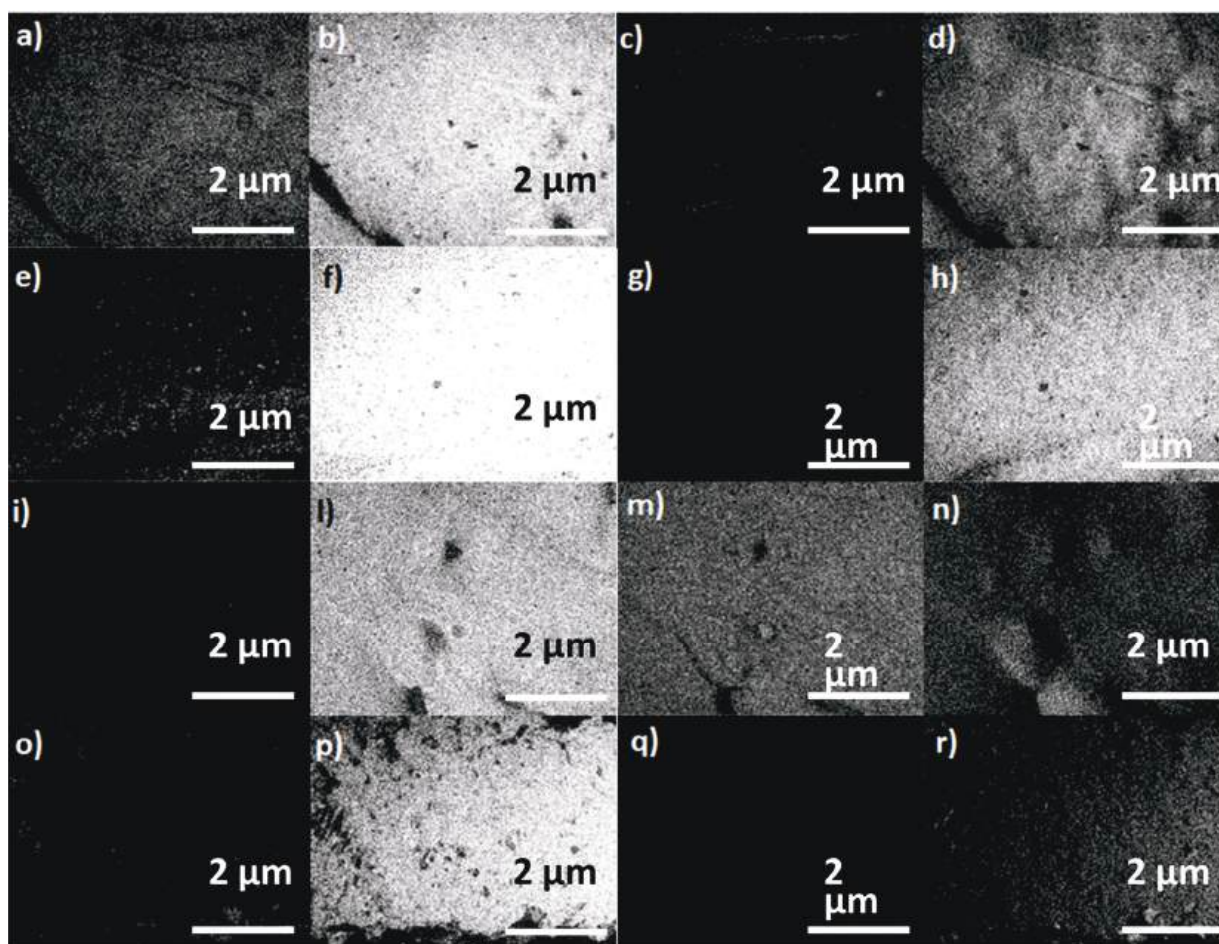
Figure 8. Elemental EDX analysis on the four different MW-active materials dispersed into silicone resin matrix: (**a**) Fe, (**b**) Si, (**c**) Ti, (**d**) O into Fe_2O_3, (**e**) Fe, (**f**) Si, (**g**) Ti and (**h**) O into Fe_2SiO_4, (**i**) Fe, (**l**) Si, (**m**) Ti and (**n**) O into TiO_2, (**o**) Fe, (**p**) Si, (**q**) Ti and (**r**) O in to SiC.

4. Conclusions

The focus of this article was the formulation of composite materials responsive to microwave heating as coatings for molds used in the classical rotomolding process to convert it to a microwave-assisted rotomolding technique, thus making the process more efficient.

For this purpose, we used formulates based on a methyl phenyl silicone resin and different inorganic susceptible powders.

The elastomeric material was confirmed to be highly resistant to heat and did not present any degradation during the processes.

The best MW-susceptible inorganic compound used results to be Fe_2SiO_4, followed by SiC and Fe_2O_3, regardless of the material used for the mold (stainless steel, aluminum and glass were tested).

The chemical nature of the composites prepared ensure that in the presence of damage, the composite material can be easily removed or repaired with subsequent additions of new material.

The measurements of the absorbed power reported showed that dielectric heating saves time and energy if compared to the conventional electric resistance heating process.

The results of the tensile test performed according to ISO 527 (1–5) showed the efficiency of the innovative MW-assisted RM process of PE powder, because the performances are comparable to those shown by the commercial PE jar (Kartell) obtained with a classic molding process.

Finally, it should be considered that the MW-RM process is not limited to PE plastic but can be adapted to any plastic or its composite whose molecules do not have a dielectric moment.

References

1. Dornfeld, D.A. Moving towards green and sustainable manufacturing. *Int. J. Precis. Eng. Manuf.-Green Tech.* **2014**, *1*, 63–66. [CrossRef]
2. Khripko, D.; Schlüter, B.A.; Rommel, B.; Rosano, M.; Hesselback, J. Energy demand and efficiency measures in polymer processing: Comparison between temperate and Mediterranean operating plants. *Int. J. Energy Environ. Eng.* **2016**, *7*, 225–233. [CrossRef]
3. Defonseka, C. *Processing Systems for Polymers*; Chapter 8; De Gruyter: Berlin, Germany, 2020; Volume 2020, pp. 65–94.
4. Stampi rotazionali—Tecnomodel. Available online: https://www.tecnomodel.com/stampi-rotazionali/ (accessed on 12 October 2022).
5. RotoDesign | Tecnologia-Processo. Available online: http://www.rotodesign.it/tecnologia-processo.html (accessed on 12 October 2022).
6. Crawford, R.J. Recent advances in the manufacture of plastic products by rotomolding. *J. Mater. Process. Technol.* **1996**, *56*, 263–271. [CrossRef]
7. Ogila, K.O.; Shao, M.; Yang, W.; Tan, J. Rotational molding: A review of the models and materials. *Express Polym. Lett.* **2017**, *11*, 778–798. [CrossRef]
8. Vignali, A.; Iannace, S.; Falcone, G.; Utzeri, R.; Stagnaro, P.; Bertini, F. Lightweight Poly(ε-Caprolactone) Composites with Surface Modified Hollow Glass Microspheres for Use in Rotational Molding: Thermal, Rheological and Mechanical Properties. *Polymers* **2019**, *11*, 624. [CrossRef] [PubMed]
9. Stagnaro, P.; Utzeri, R.; Vignali, A.; Falcone, G.; Iannace, S.; Bertini, F. Lightweight polyethylene-hollow glass microspheres composites for rotational molding technology. *J. App. Polym. Sci.* **2021**, *138*, 49766. [CrossRef]
10. Wypych, A.; Bobowska, I.; Tracz, M.; Opasinska, A.; Kadlubowski, S.; Krzywania-Kaliszewska, A.; Grobelny, J.; Wojciechowski, P. Dielectric Properties and Characterisation of Titanium Dioxide Obtained by Different Chemistry Methods. *J. Nanomater.* **2014**, *2014*, 124814. [CrossRef]
11. Wang, S.T.; Sun, J.; Yu, Y.; Li, Q.J.; Tong, L.; Guo, Y.M.; Wang, C.C. A Facile Method to Increase Dielectric Properties of Rutile TiO$_2$. *Ceram. Int.* **2018**. [CrossRef]
12. Hu, W.; Liu, Y.; Withers, R.L.; Frankcombe, T.J.; Norén, L.; Snashall, A.; Kitchin, M.; Smith, P.; Gong, B.; Chen, H.; et al. Electron-pinned defect-dipoles for high-performance colossal permittivity materials. *Nat. Mater.* **2013**, *12*, 821–826. [CrossRef]
13. Available online: https://www.microwaves101.com/encyclopedias/silicon-carbide (accessed on 17 October 2022).
14. Sabisky, E.S.; Gerritsen, H.J. Measurements of Dielectric Constant of Rutile (TiO$_2$) at Microwave Frequencies between 4.2° and 300 °K. *J. Appl. Phys.* **1962**, *33*, 1450. [CrossRef]
15. Silaghi, M.A. *Chapter 1. Dielectric Material*; IntechOpen: London, UK, 2012. [CrossRef]
16. Chakraborty, S. Frequency-dependent dielectric properties of sodium silicate. *Mod. Phys. Lett. B* **2018**, *32*, 185041. [CrossRef]
17. Chakraborty, S.; Basu, A.; Haldar, S. Effect of doping on dielectric loss of sodium silicate ceramic. *Adv. Sci. Lett.* **2016**, *22*, 21. [CrossRef]

18. Mascia, F.; Fratton, F. Compounds and Compositions for Susceptor Materials. 2011. Available online: https://patents.google.com/patent/WO2011095883A2/en (accessed on 17 October 2022).

19. Obarski, G.E. *Wavelength Measurement System for Optical Fiber Communications*; Technical Note NIST-Gov; National Institute of Standards and Technology: Gaithersburg, MD, USA, 1990.

20. Lunt, R.A.; Jackson, A.J.; Walsh, A. Dielectric response of Fe_2O_3 crystals and thin films. *Chem. Phys. Lett.* **2013**, *586*, 67–69. [CrossRef]

21. Brunengo, E.; Conzatti, L.; Schizzi, I.; Buscaglia, M.T.; Canu, G.; Curecheriu, L.; Costa, C.; Castellano, M.; Mitoseriu, L.; Stagnaro, P.; et al. Improved dielectric properties of poly(vinylidene fluoride)–$BaTiO_3$ composites by solvent-free processing. *J. Appl. Polym. Sci.* **2021**, *138*, 50049. [CrossRef]

22. Opyd, B.; Granat, K.; Nowak, D. Determination of electrical properties of materials used in microwave heating of foundry molds and cores. *Metalurgija* **2015**, *54*, 347–349.

23. Mello, P.A.; Barin, J.S.; Guarnieri, R.A. Chapter 2—Microwave Heating. In *Microwave-Assisted Sample Preparation for Trace Element Analysis*; Elsevier: Amsterdam, The Netherlands, 2014; pp. 59–75.

24. Kamol, S.; Limsuwan, P.; Onreabroy, W. Three-dimensional standing waves in a microwave oven. *Am. J. Phys.* **2010**, *78*, 492–495. [CrossRef]

25. Mejia, E.; Cherupurakal, N.; Mourad, A.-H.I.; Al Hassanieh, S.; Rabia, M. Effect of Processing Techniques on the Microstructure and Mechanical Performance of High-Density Polyethylene. *Polymers* **2021**, *13*, 3346. [CrossRef]

26. Osswald, T.A.; Menges, G. Failure and Damage of Polymers. In *Materials Science of Polymers for Engineers*; Carl Hanser Verlag: Munich, Germany, 2012; pp. 423–487. [CrossRef]

27. Almond, J.; Sugumaar, P.; Wenzel, M.N.; Hill, G.; Wallis, C. Determination of the carbonyl index of polyethylene and polypropylene using specified area under band methodology with ATR-FTIR spectroscopy. *e-Polymers* **2020**, *20*, 369–381. [CrossRef]

28. Chamerski, K.; Lesniak, M.; Sitarz, M.; Stopa, M.; Filipecki, J. An Investigation of the Effect of Silicone Oil on Polymer Intraocular Lenses by Means of PALS, FT-IR and Raman Spectroscopies. *Spectrochim. Acta Part A Mol. Biomol. Spectrosc.* **2016**, *167*, 96–100. [CrossRef]

29. Wunderlich, B. *Thermal Analysis of Polymeric Materials*; Springer: Berlin/Heidelberg, Germany, 2005.

30. Sadrabadi, T.E.; Zebarjad, S.M.; Khaki, J.V.; Sahebian, S. On the dependence of avrami indexes of MDPE on milling time. *Polym. Plast. Technol. Eng.* **2010**, *49*, 1284–1288. [CrossRef]

31. Wu, S.; Zhang, X.; Sun, Y.; Yang, H.; Lin, B.; Han, X.; Chen, P. Study on the influence of crosslinking density and free polysiloxan chain length on oxygen permeability and hydrophilicity of multicomponent silicone hydrogels. *Colloid Polym. Sci.* **2021**, *299*, 1327–1335. [CrossRef]

Article

Rheological Properties of Non-Adhesive Embolizing Compounds—The Key to Fine-Tuning Embolization Process-Modeling in Endovascular Surgery

Iuliia Kuianova [1] , Alexander Chupakhin [1], Alexey Besov [1], Anton Gorbatykh [2], Dmitry Kislitsin [2], Kirill Orlov [2] and Daniil Parshin [1,*]

[1] Lavrentyev Institute of Hydrodynamics SB RAS, 630090 Novosibirsk, Russia
[2] Meshalkin National Medical Research Center, 630055 Novosibirsk, Russia
* Correspondence: danilo.skiman@gmail.com

Abstract: The study of polymers' rheological properties is of paramount importance both for the problems of their industrial production as well as for their practical application. Two polymers used for embolization of arteriovenous malformations (AVMs) are studied in this work: Onyx-18® and Squid-12®. Viscosity curve tests and computational fluid dynamics (CFD) were used to uncover viscosity law as a function of shear rate as well as behavior of the polymers in catheter or pathological tissue models. The property of thermal activation of viscosity was demonstrated, namely, the law of dependence of viscosity on temperature in the range from 20 °C to 37 °C was established. A zone of viscosity nonmonotonicity was identified, and a physical interpretation of the dependence of the embolic polymers' viscosity on the shear rate was given on the basis of Cisco's model. The obtained empirical constants will be useful for researchers based on the CFD of AVMs. A description of the process of temperature activation of the embolic polymers' viscosity is important for understanding the mechanics of the embolization process by practicing surgeons as well as for producing new prospective embolic agents.

Keywords: embolic agent; rheology; hemodynamics; arteriovenous malformation (AVM); CFD

1. Introduction

In modern vascular surgery, more and more preference is given to minimally-invasive interventions that are less traumatic for the patient [1]. One direction for such operations is that the embolization of cancer, arteriovenous malformations (AVMs), fistulas, etc. Depending on the type of pathology, its localization, stage and other medical aspects, embolization polymers differ, respectively, as adhesive and non-adhesive. Adhesive polymers are adhesives based on cyanoacrylate and are designed to cause occlusion, i.e., sealing of, relatively large vessels (fistulas). In contrast, non-adhesive composites are aimed at occluding relatively small vessels (racemose components of the anomaly). The main pathologies for which such polymers are used are tumors and arteriovenous malformations (AVMs). The issues involved in choosing the optimal technique and embolization protocol are actively discussed in the literature. First of all, this is the choice of parameters for the optimality of this process: determining the embolization access—arterial or venous [2], and determining the sequence of using certain composites during embolization in the presence of both the racemose and fistula components of the AVM [3]. The main problems in this case are determining the volume of polymer required for embolization [4], the optimal law of its administration, as well as the function of its consumption depending on time. In fact, these are the only parameters that the surgeon controls after choosing one or the other embolic polymer. This is a very important task of practical medicine; therefore, a large number of medical works are devoted to the discussion of these issues [5,6].

To solve such problems, in recent years, along with experimentation, mathematical modeling has been increasingly used [7–9], as well as some trials of promising embolisates [10].

Non-adhesive polymers and polymers based on microspheres are of greatest interest for the study of rheological properties [11]. A feature of non-adhesive drugs is that they do not stick to the vascular wall during precipitation; thus, they have an increased ability to spread in the vascular bed, better filling the blood vessels of pathological formations, and the possibility of a longer and more controlled administration. On the other hand, these substances have an increased tendency to migrate into those vessels of the body where they are undesirable and may be accompanied by clinical complications. This is especially evident in the treatment of high-flow arteriovenous shunts [12,13]. The penetration of such drugs into the venous bed can cause vein thrombosis [14,15] and deterioration of lung tissue perfusion, which can have a negative effect on the whole organism. For adhesive polymers, most of which are based on cyanoacrylate derivatives, the number of possible complications is significantly less and mainly relate to complications associated with catheterization [16]. However, the scope of such polymers is usually large arteries, tumors, and fistulas.

Despite the presence of a number of studies on the chemical and rheological characteristics of the considered embolisates [10,11,17], it is worth noting a rather weak connection in such works with the formulation of medical problems [18], as well as problems from the field of computational modeling [19]. In the works reviewed, little attention is paid to the different temperature ranges and different ranges of shear rates at which embolisates are operated. These seemingly purely medical problems are, in fact, of a fundamental nature and can be solved only with an integrated approach that combines the study of the rheological properties of embolic polymers, as non-Newtonian media, and the study of the laws of motion of such media along with a geometrically complex, branched network of channels of various sizes. Rheological properties of the embolic polymer can vary depending on network geometry. Moreover, it turns out that it is necessary to take into account the detailed thermodynamics of this process, which, unlike the classical problems of hydrodynamics, cannot be considered isothermal.

If, for solving problems of hemodynamics in large vessels, the generally accepted gold standard is the use of Newtonian fluid models, then for solving problems of embolization of a small branched network of vessels with a caliber of up to 1 mm, such an assumption is unacceptable. Non-Newtonian properties begin to manifest themselves significantly in the course of such polymers and play a decisive role. Some information about penetration depth score, the dependence of pressure in a catheter with respect to volume flow rate of the embolic agent, length of reflux and others is known [17,20]. In addition, the rheology of such polymers is complicated by the presence of a contrast media [21,22], which significantly affects the sedimentation of polymers in the vasculature with respect to the origin of the contrasting agent. Figure 1 shows varieties of iodine radiopaque contrast agents (top—nephrotropic, low osmolar iohexol [23]; bottom—iocarmic acid [24]). Since an iodine-containing contrast agent is capable of causing anaphylactic shock, tantalum-containing analogues have been developed. Figure 2 shows the synthesis process of carboxybetaine zwitterionic-tantalum oxide nanoparticles (CZ-TaO NPs) which includes three stages: saline condensation, end-group hydrolysis and purification. In this regard, a number of questions arise considering the rheology of the flow of embolization polymers depending on shear rate and temperature. The last factor is fundamental, since the syringe with the embolic polymer is located in the operating room outside the patient's body, at a temperature of 20–25 °C degrees, and the filling of the anomaly node with the embolic polymer occurs inside the patient's body and is carried out at a body temperature of 37 °C degrees.
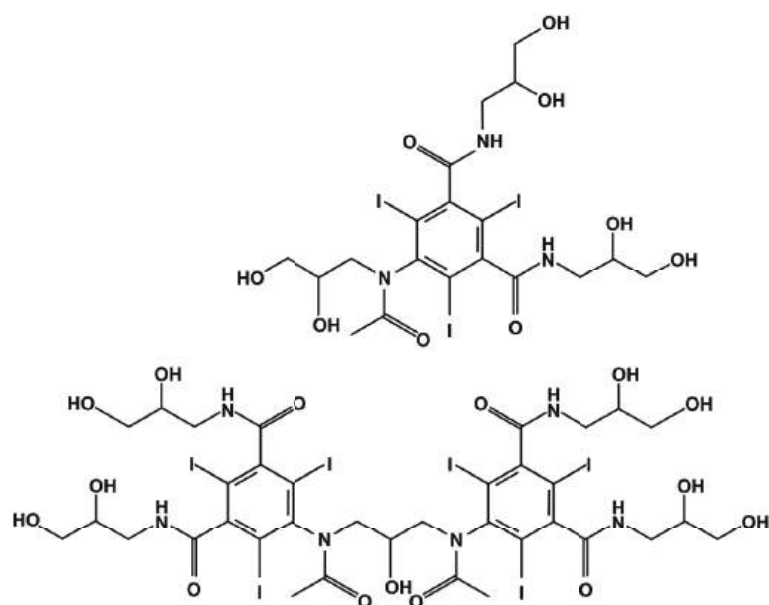
Figure 1. Structures of iodine-containing radiopaque substances.
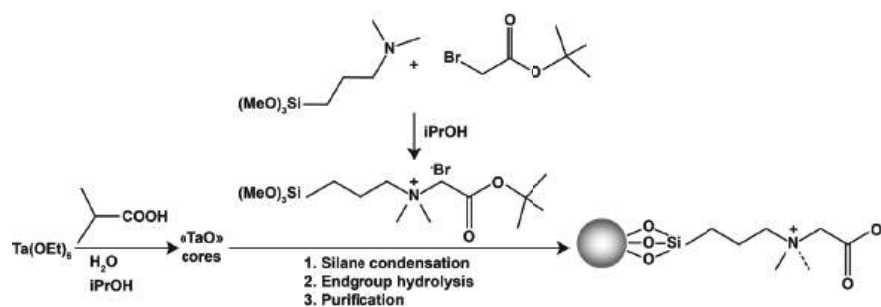
Figure 2. One of the mechanisms for creating tantalum powder for preparing a suspension consisting of an embolizing polymer and powder [17,22].

In this paper, an experimental approach to the study of the rheological properties of embolization materials used in clinical practice was considered. To highlight shear rate values that correspond to the physiological state of a human body, a numerical model of AVM embolization with non-adhesive embolization polymers was verified based on rheological test data. In addition to their fundamental importance to the understanding flow mechanics, rheometry data can become the basis for constructing a phenomenological model of the viscosity of such polymers. Therefore, specific parameters are proposed for models of pseudoplastic and dilatant fluids that study the viscosity of embolic polymers both under laboratory (T = 20 °C) and surgical (T = 37 °C) conditions.

2. Materials and Methods

2.1. Materials

The embolic polymer material provided by the clinical partner of the research was studied. The material consists of irretrievable remnants of endovascular interventions. Approximately 0.5 mL of material was used for each of the tests. Since the manufacturer's official instructions recommend shaking the embolic polymer vial for at least 15 min, this necessary procedure was performed before the test. Onyx® and Squid® are gelling solutions that are composed of PVA co-polymers in dimethyl sulphoxide (DMSO) with tantalum (see Figure 3). An ethylene vinyl alcohol co-polymer (48 mol/L of ethylene and 52 mol/L vinyl alcohol) was dissolved in DMSO (see Figure 4). Micronized tantalum powder was suspended in the liquid polymer/DMSO mixture to provide fluoroscopic visualization [25]. As can be seen from the experimental data (see Figure 5), the rheological

properties of the considered polymers during their regular agitation and their refusal to agitate significantly change, not only quantitatively (which is typical for both polymers at shear rates exceeding $10 \, \text{s}^{-1}$), but also qualitatively, which is most typical for the Onyx-18® polymer at shear rates less than $1 \, \text{s}^{-1}$. In the course of the experiments, the same polymer was used for the Onyx/Squid suspensions with mixed and not-mixed tantalum. In the first case, the bottle was agitated for 15 min; this way, a uniform distribution of the radiopaque contrast agent in the polymer was achieved. However, in the second case, agitation was not used. As a result, a transparent component of the embolic polymer, presented by a solution of vinyl alcohol in DMSO, remained in the test area. Due to this limitation, a number of long-term tests (such as frequency, requiring approximately 40 min to vary the spectrum of physiologically adequate particles) were not performed which would have been of interest for a detailed understanding of polymer rheology.
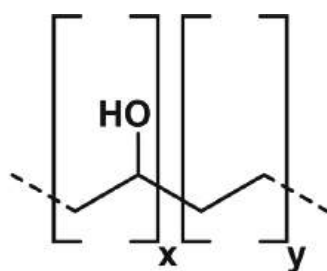
Figure 3. Schematic chemical formula of an ONYX-type embolic polymer [26].
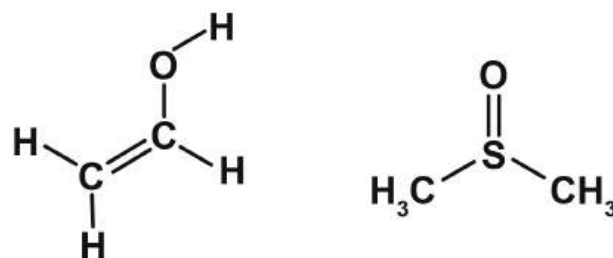
Figure 4. The structure of vinyl alcohol (**left**); the structure of DMSO (**right**).
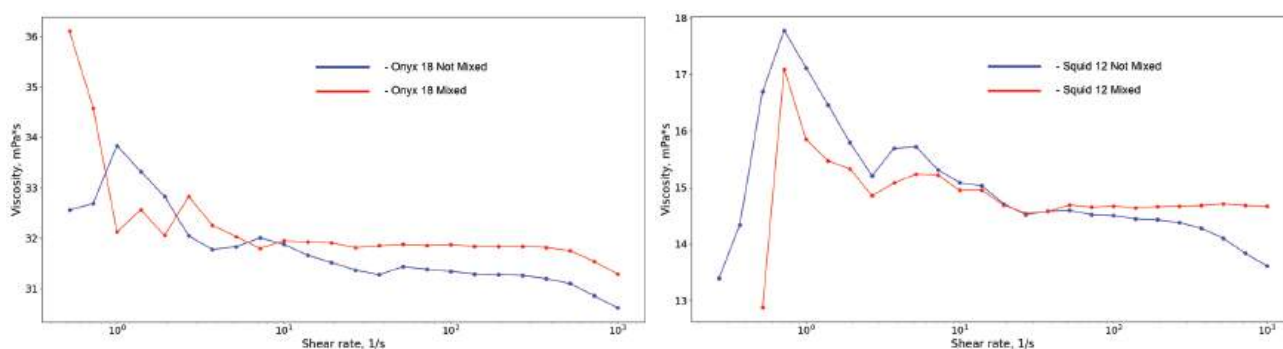
Figure 5. Experimental data of the viscosity dependence on shear rate of Onyx® (**left**) and Squid® (**right**) mixed and not mixed with tanthalum powder.

2.2. Experimental Protocol

The rheological properties of the embolization compositions were studied on an Anton Paar MCR302 rheometer (Austria) using the CP50-1 Cone-Plane measuring system (see Figure 6) with a diameter of 50 mm, minimum clearance of 0.1 mm and an angle of 1°. A P-PTD200 Peltier heating system and an H-PTD200 Peltier active housing, designed to minimize temperature gradients in the samples and prevent their evaporation during the measurement process, were used. The specified accessories provide maintenance of the set

temperature with an accuracy of 0.01 °C. Testing was carried out using viscosity curve tests of the rheometer software (RheoCompass 1.30.1164 Release). In the process of testing the studied samples, the dependence of effective viscosity of the embolization compositions on the shear rate at given temperatures (laboratory T = 20 °C and surgical T = 37 °C) was determined.
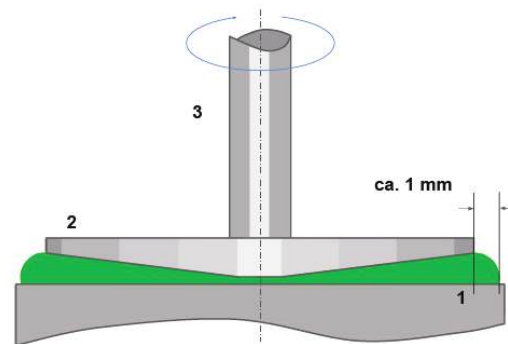
Figure 6. Illustrative scheme for testing using a cone-plane system [27]: 1: base of the measuring system; 2: device of the measuring system (in this case, the cone-plane); 3: shaft leading to the gas bearing of the measuring system.

2.3. Numerical Simulations

Numerical modeling of the embolization polymers' flow through the canal network (see Figure 7) was performed using the ANSYS 2020R2 software package (CFX, license LIH SB RAS). Since the time interval of the embolization effect (the process from the beginning of the introduction of a polymer-based drug to the achievement of the desired clinical effect) is from 20 to 40 min, it is reasonable to model it as a stationary course of the embolic polymer. At the first stage, this model includes a flow in a long, thin tube simulating a catheter through which the embolic polymer is delivered to the circulatory system; the flow in the network is first though diverging, branching vessels and, finally, in vessels that again converge into one vessel.
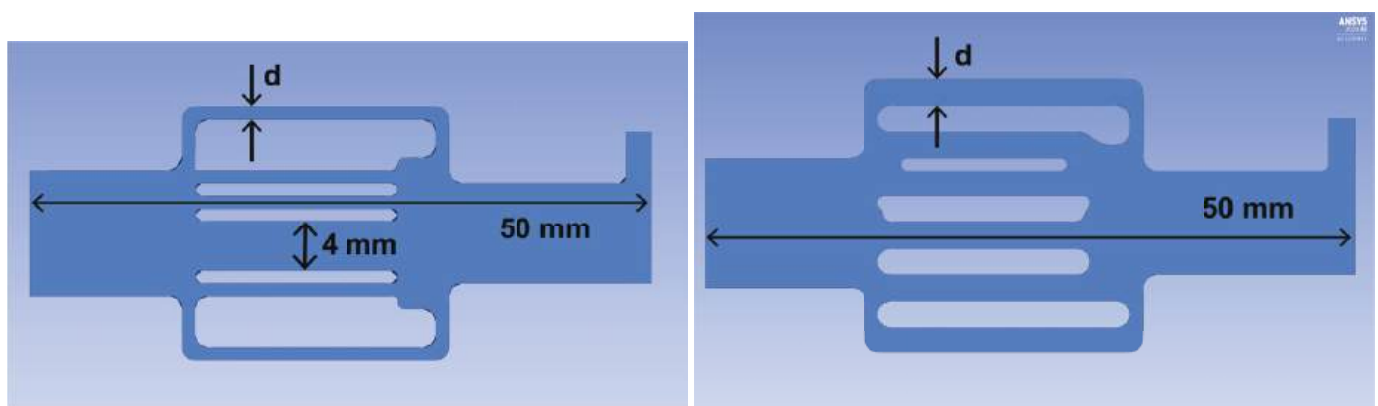
Figure 7. Geometry used for numerical calculations: AVM without fistula (**left**) with varying vessel diameter $d \in (0.5, 2)$ mm, AVM with fistula (**right**) 4 mm in diameter and varying vessel diameter $d \in (0.5, 2)$ mm.

The catheter wall is considered to be a thin material, but having a non-zero thickness of 0.2 mm. The condition on the fluid wall has type–interface (to take into account heat flux) with no slip velocity condition. At the outlet from the fluid flow region, the condition of zero pressure was set.

The Navier–Stokes equation system for the flow of a viscous, incompressible fluid was used as the governing equation. Considering that $m_\alpha = (\rho u_i \Delta n_i)_\alpha$ is the mass flow through the surface of the volume element, Navier–Stokes equations can be written in discrete form for solving the problem using the finite element method [28]:

$$\begin{cases} \sum_\alpha m_\alpha (\mathbf{u}_j)_\alpha - \sum_\alpha (\rho \mu \frac{\partial \mathbf{u}_i}{\partial x_j} \Delta n_i)_\alpha = - \sum_\alpha (p \Delta n_j)_\alpha \\ \sum_\alpha m_\alpha = 0, \end{cases} \tag{1}$$

where ρ—density, μ—dynamic viscosity, u—flow rate and n—normal vector to the computational domain.

Temperature effects can be neglected for the case of a convergent–divergent channel, since these flow stages occur at body temperature. On the contrary, when liquid flows through a conductor, there is a transition between the flow.

To use the obtained dependence of the polymers' viscosity on the shear rate in the polymer flow calculations in the AVM model configuration, it was necessary to approximate the experimental data. For this purpose, the viscosity graphs were divided into three different segments; on each segment, the function approximation was performed linearly Figure 8. The temperature of the polymer was assumed to be constant, equal to 37 °C. Thus, the temperature transition from laboratory conditions (20–25 °C) to physiological ones was not considered in this simulation option.
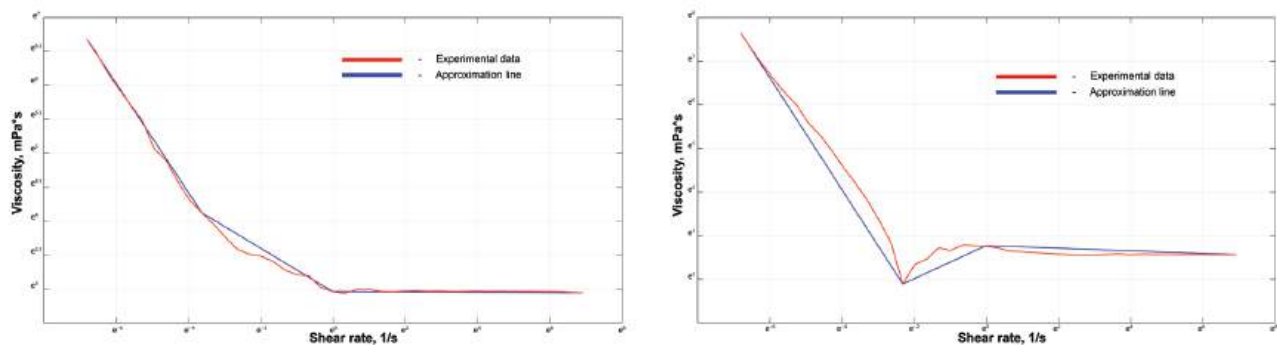
Figure 8. Experimental data of Onyx® (**left**) and Squid® (**right**) viscosity dependence on shear rate and the piecewise linear approximation that was used for numerical simulations (logarithmic scale).

The next stage of modeling was the implementation of a numerical calculation of the embolic polymer flow in the catheter using settings similar to the operating room. It was assumed that the catheter consists of two parts—an outer one, which is located outside the patient's body, and an inner one, which runs from the puncture site in the femoral artery to the AVM nidus. The simulation was performed for the second (internal) segment. A volume flow rate of about 0.6 mL/min was used for conditions at the inlet in this part of the catheter. A catheter with an inner diameter of 1 mm was considered, and the temperature of the supplied embolization polymer was 20 °C.

Since the polymer supply process can be considered quasi-stationary and the catheter diameter does not change, the shear rate can also be considered unchanged. Therefore, the viscosity of such a polymer must be considered as a function of temperature only at a shear rate of approximately $10\,\mathrm{s}^{-1}$ (Figure 9).
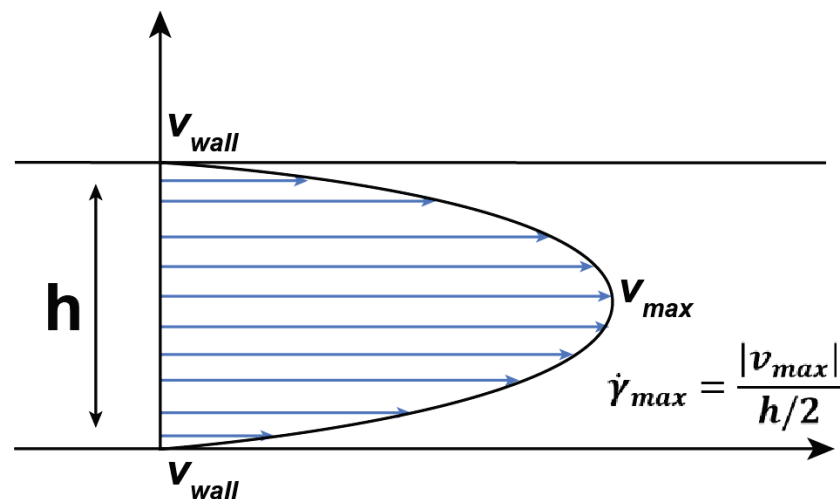
Figure 9. Poiseuille profile of the fluid flow and approximate shear rate.

At the liquid boundary (contact zone with the stent), the condition for maintaining the heat flux was set [29]:

$$Q = - \iint_A \dot{q}'' \, dA, \tag{2}$$

where

$$\dot{q}'' = -k\Delta T \tag{3}$$

T—heat flux, k—coefficient of thermal conductivity, and A—heat transfer area. Since more than 90% of the polymer solution is DMSO, the known thermal constants of this substance were used [30]: $k = 0.2 \, \text{w} \cdot \text{m}^{-1} \cdot \text{K}^{-1}$ and the specific heat coefficient $c = 0.47 \, \text{cal/g/C}$.

3. Results

3.1. Experimental Results

For the purposes of this work, rheological tests were carried out in the cone-plane system (Figure 6). The tests were carried out for two models of embolic polymers that are currently used in clinical practice for AVM embolization.

Similar flow regimes (bleaching 20 °C and separately 37 °C) were implemented in two different regions—at the injection site of the embolization polymer into the catheter (corresponding to 20 °C) and in the AVM nidus (corresponding to 37 °C). However, in the area of the catheter penetration into the femoral artery, a temperature transition was considered. Therefore, it was useful to study the behavior of embolic polymers in the temperature range of 20–37 °C:

In a numerical analysis of the flow of viscous liquids at a temperature of 37 °C, which have a rheology similar to the tested samples of ONYX-18® and SQUID-12® (see Table 1, Figure 10), it turned out that the maximum pressure for ONYX-18® -like liquid significantly exceeds the maximum pressure for SQUID-12® -like liquid in the presence of a fistula, which is easily explained by the need of using more viscous polymers in the presence of large vessels in the AVM nidus.
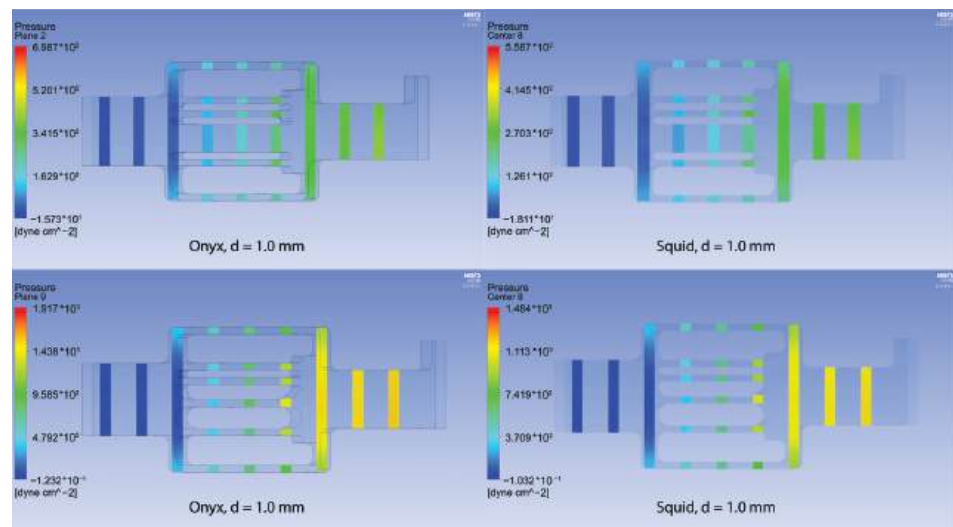
Figure 10. Pressure for the configurations with Onyx® (**left column**) and Squid® (**right column**) with fistula (**above**) and without it (**below**).

At the same time, the maximum shear stresses for both polymers remain comparable (see Figure 11). From essential considerations, it may be assumed that the zone of embolic polymer applicability is determined by the local pressure peak, which is achieved for the Onyx flow at d = 1.5, and for the Squid flow at d = 1.75 (see Figure 12). In their instructions, manufacturers indicate the necessity of preventing embolic polymers from entering the venous compartment of circulation only due to the possibility of its thrombosis [31,32]. At the same time, it is seen that a rational approach to selecting embolic polymers, based on the diameter of the vessels of the racimous compartment, is also associated with hydrodynamic factors—excessive pressure can lead to rupture of the AVM. In the absence of large vessels in the AVM nidus, the values of the pressure maxima for both polymers almost completely coincide, and the shear stresses differ only when a certain threshold value of the diameter of small vessels (1–1.2 mm) is exceeded. In addition, it can be seen from the experimental data (Figure 13, Table 2), that the velocity in the racimous part of the AVM decreases significantly and the maximum flow velocity increases for both polymers due to fistula presents.
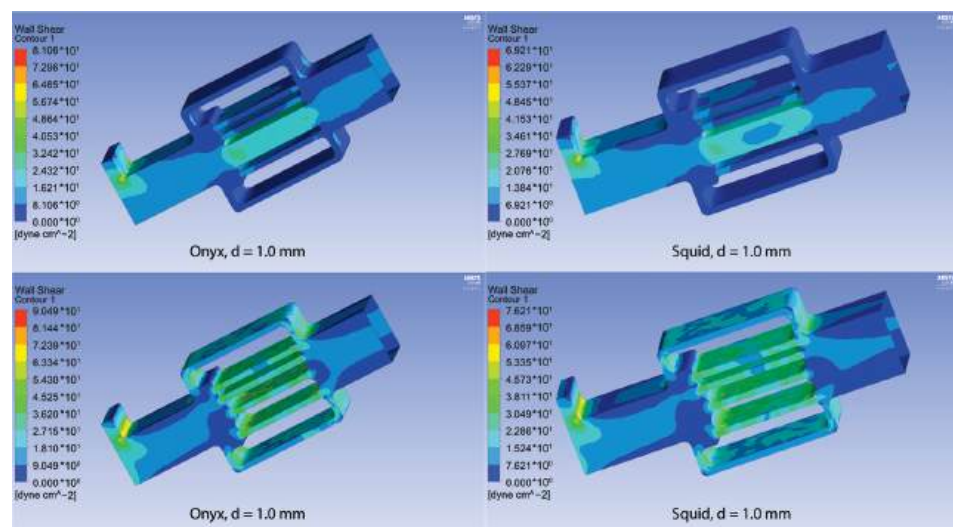
Figure 11. WSS for the configurations with Onyx® (**left column**) and Squid® (**right column**) with fistula (**above**) and without it (**below**).
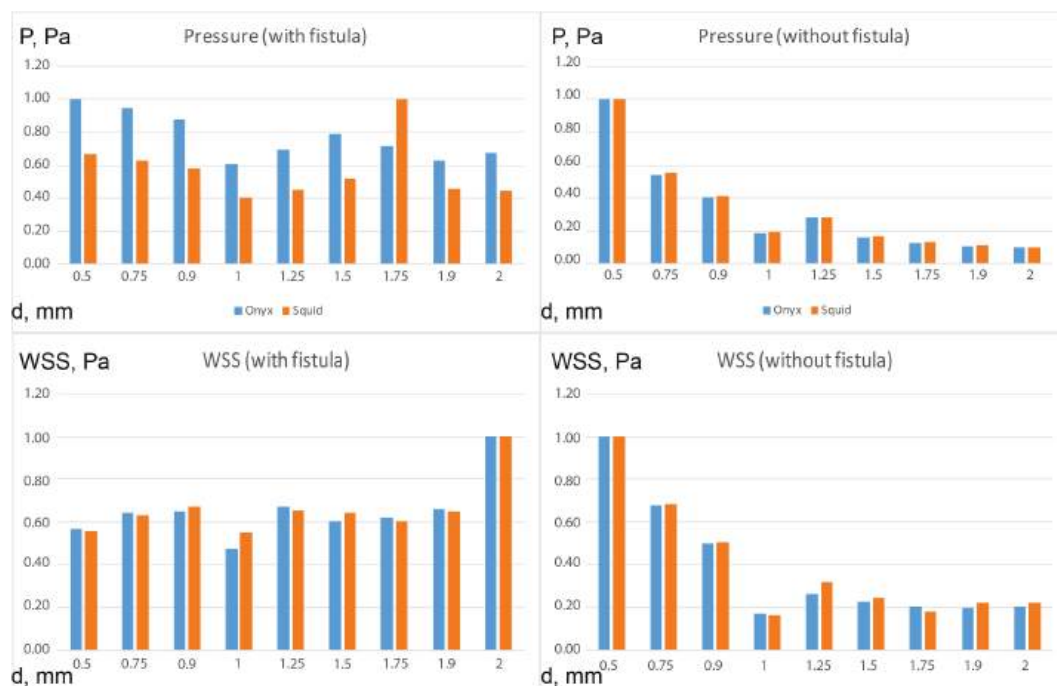
Figure 12. Pressure and WSS results of numerical calculations in the configuration with and without fistula for all considered vessel radii.
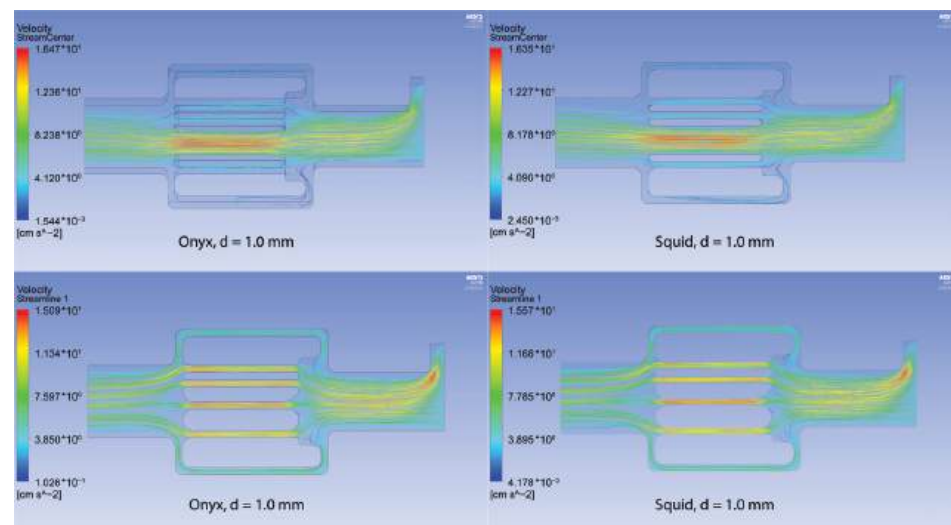
Figure 13. Velocity streamlines for the configurations with Onyx® (**left column**) and Squid® (**right column**) with fistula (**above**) and without it (**below**).

Table 1. Pressure and WSS results of numerical calculations in the configuration with and without fistula.

Diameter of the Vessel Racimous Part, mm	Fistula	Maximum Pressure in Racimous Part, Pa		Maximum WSS in Racimous Part, dyne/cm^2	
		Onyx-18 ®	Squid-12 ®	Onyx-18 ®	Squid-12 ®
0.5	−	7665.17	5588.45	441.79	329.42
0.75	−	4148.71	3083.56	298.36	225.19
0.9	−	3076.53	2290.17	220.04	166.06

Table 1. *Cont.*

Diameter of the Vessel Racimous Part, mm	Fistula	Maximum Pressure in Racimous Part, Pa		Maximum WSS in Racimous Part, dyne/cm²	
		Onyx-18 ®	Squid-12 ®	Onyx-18 ®	Squid-12 ®
1	−	1432.47	1083.3	74.77	54.32
1.25	−	2146.94	1590.51	115.62	105.26
1.5	−	1246.53	938.47	100.59	80.44
1.75	−	970.86	735.596	89.33	59.29
1.9	−	813.85	617.49	87.04	72.96
2	−	743.36	565.05	89.49	73.23
0.5	+	560.99	432.79	29.61	24.05
0.75	+	529.44	406.56	33.53	27.20
0.9	+	492.31	376.38	33.80	28.91
1	+	340.15	261.82	24.83	23.65
1.25	+	389.53	294.17	34.85	28.13
1.5	+	443.49	338.72	31.43	27.85
1.75	+	400.98	649.34	32.13	26.01
1.9	+	351.55	295.15	34.19	28.08
2	+	378.34	288.94	52.07	43.20

Table 2. Velocity and shear rate results of numerical calculations in the configuration with and without fistula.

	Onyx-18®			Squid-12®		
d = 1 mm	Max Velocity	Min Velocity	Shear Rate	Max Velocity	Min Velocity	Shear Rate
Fistula	0.15	1647.78	29.62	0.24	1635.40	30.83
Without fistula	0.25	1548.08	45.23	0.41	1556.58	46.60

3.2. Governing Equations for Viscosity

It can be seen from Figure 14 that at both body and laboratory temperatures (37 °C and 20 °C, respectively), the embolic polymers tend to behave like a pseudoplastic liquid with a non-zero flow limit. One of the simplest models of power–law dependence of viscosity on shear rate is the Ostwald–de Waele model. Its generalization of the spatial case of flow gives the following expression for the dependence of viscosity on shear rate [33]:

$$\mu_{eff} = kU^{n-1}, \tag{4}$$

where k—fluid consistency index, U—shear rate, and n—degree of non-Newtonian behavior of a material.

However, the obvious disadvantage of such models is the behavior of viscosity at very large ($U \gg 1$) or, conversely, very small ($U \ll 1$) shear rates. Cisco's rheological model overcomes this shortcoming [34]:

$$\mu_{eff} = \mu_0 + kU^{n-1} \tag{5}$$

where as μ_0, the value of viscosity to which the experimental data tend to stay at high shear rates must be chosen.

From these types of experimental graphs (see Figure 14) and an understanding of the different shear rates for the flow in the catheter and in the rational part of the malformation, it is seen that the interesting shear rate ranges are 10–100 and 0.1–10 s^{-1}. For the first interval, an almost constant value of viscosity is observed. For the second range of

shear rates, the viscosity changes, as in a pseudoplastic fluid, increasing with decreasing shear rates.
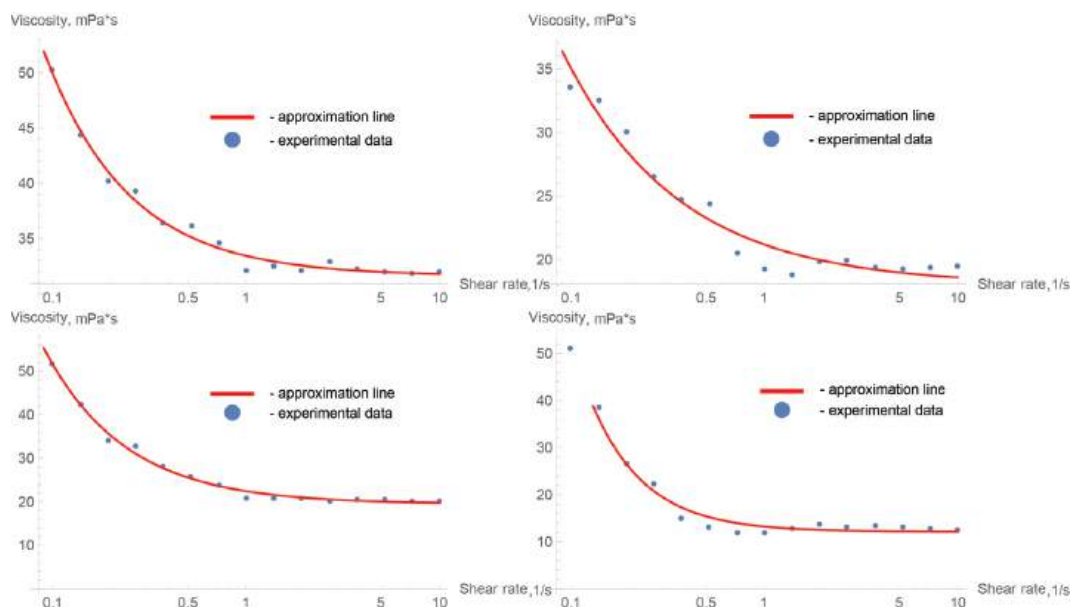
Figure 14. Approximation of experimental data of viscosity dependence on shear rate by Cisco's model (CM) for the Onyx-18® embolic polymer (**top**) and the Squid-12® embolic polymer (**bottom**); for laboratory temperature $T = 20$ °C (**left**) and for physiological conditions $T = 37$ °C (**right**).

This law is well approximated by the CM, and the approximation was made in the Wolfram Mathematica package (license of LIH SB RAS). The values of the empirical constants are given in Table 3.

Table 3. Values of empirical constants of the CM for the studied embolic polymers at laboratory (20 °C) and physiological (37 °C) temperatures.

Embolic Polymer	$T = 20$ °C			$T = 37$ °C		
	μ_0	k	n	μ_0	k	n
Onyx-18®	31.6187	1.80968	-0.004368	18.0138	3.17306	0.271126
Squid-12®	19.4711	2.9736	-0.03329	12.1248	1.10875	-0.5586

3.3. Understanding of Viscosity Activation Process

The selected model approximates the experimental data quite well (see Figure 14) for the selected interval; however, when it is considered over a larger interval, its approximating ability drops significantly, so it is not recommended to use this model in the shear rate range >10 s^{-1}. Indeed, the mechanism of viscosity for this non-Newtonian fluid at such values of shear rate is completely different, and the viscosity can be conditionally considered constant, although it depends significantly on temperature. Consequently, two interesting remarks can be made through analyzing the obtained experimental data.

First of all, a zone of nonmonotonic dependence of viscosity on shear rate at a value of the latter of about 1 s^{-1} can be noticed (see Figure 15). Moreover, it is seen that this nonmonotonicity is most noticeable precisely at physiological temperatures. This zone of nonmonotonicity can be given the following description. The fact is that the studied preparations are used to embolize a network of small vessels; however, between reaching this small network and leaving the microcatheter, the polymers, within a very short time, are in the vessel of a larger one or, in the case of inserting the tip of the microcatheter into the AVM nidus (which often has aneurysmal dilatations), of a significantly larger diameter, which causes the shear rate of the polymer to move through the region of nonmonotonicity

and, as a consequence, a significant decrease in viscosity (about 30%). This, together with the understanding of the presence of vortex formation in the AVM nidus, gives confidence in a more uniform distribution of the polymer from the AVM nidus into the network of small vessels.
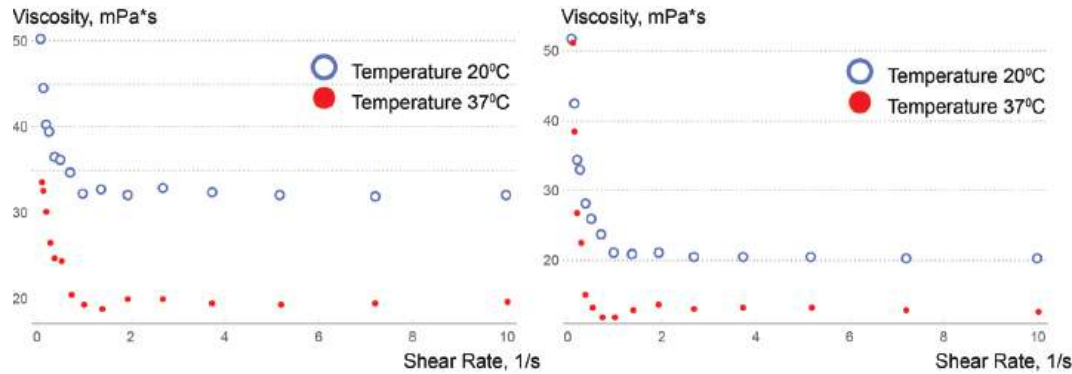
Figure 15. Comparison of experimental data on viscosity versus shear rate for Onyx-18® (**left**) and Squid-12® (**right**) embolic polymers.

Secondly, it gives an understanding that insufficiently heated polymer should not be delivered to the AVM nidus, since its high viscosity can prevent uniform distribution among the network of small vessels exiting the AVM nidus. From Figure 15, it is seen that the Squid-12® polymer is especially sensitive to this. In cases where the embolic polymer is used in neurosurgical operations, the length of the catheter from the site of catheter insertion (usually the femoral artery) to the site of embolic polymer injection is at least 1 m and, according to our numerical simulation (see Figure 16), the embolic polymer has time to warm up in the microcatheter before entering the blood. However, with other approaches and/or operations with infants, where the distance from the site of catheter insertion to the site of injection of the embolic polymer can be measured by only centimeters, one should take into account the fact that the embolic polymer may not completely warm up when it enters the bloodstream, which may affect the uniformity of filling small AVM vessels.
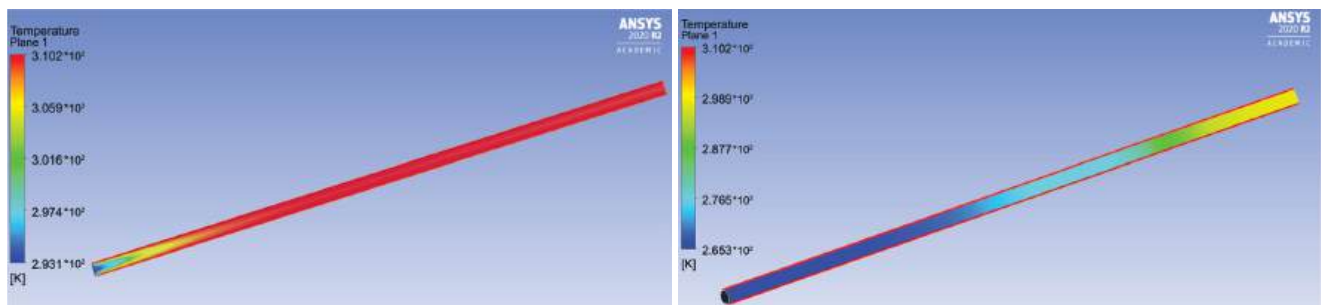
Figure 16. Temperature distribution in the catheter with a non-Newtonian (**left**) and Newtonian (**right**) model of Squid-12® viscosity.

Thirdly, understanding the process of changing the viscosity of the embolic polymer during an operation (see Figure 17) allows us to conclude that the embolization procedure needs to be improved. The fact is that according to the scheme in Figure 17, there is always a bolus of cold embolic polymer, which has a sufficiently high viscosity, between the surgeon and the patient. In our opinion, if you warm up as much of the catheter as possible between the patient and the syringe, then the control of the embolization process should become more accurate, and many different complications should be avoided [35,36].
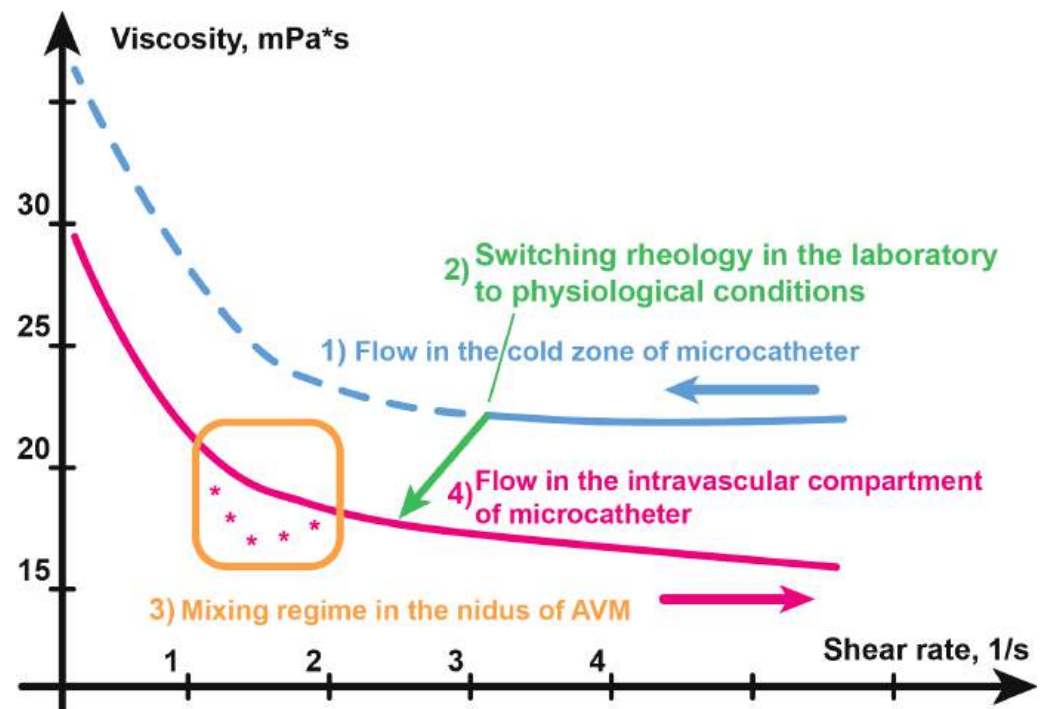
Figure 17. Viscosity change mechanism during embolization.

4. Discussion

From the point of view of fundamental hydrodynamics of complex media, this is the problem in describing the motion of a non-Newtonian fluid. The flow of a viscous fluid in a channel can occur in different modes, depending on the geometric dimensions of the channel and the rheological properties of the fluid. The task of embolization is multiparametric, and the optimal mode depends on several parameters: the cross section of the channel, the rate of its introduction and the rheology of the embolization polymer. The solution of this problem is intended to present a protocol to implement a process of filling with a polymer a geometrically complex, branched network of degenerate vessels of an arteriovenous malformation or tumor, subject to certain conditions that are dictated by the physiology of the blood circulation and the local anatomy of the vessels. In the task of embolizing an anomaly such as an arteriovenous malformation, the characteristic diameter of small vessels in the AVM is about 0.2–1 mm, and the Reynolds number in such channels for blood flow is small, which ensures the laminar nature of the blood flow [33]:

$$Re = \frac{\rho u L}{\mu},$$

where ρ—density, u—flow rate, L—hydraulic diameter, and μ—dynamic viscosity.

The Reynolds number for embolic flow is of the same order at the AVM nidus and will be of a completely different order for catheter flow. Indeed, to proceed from the size of the catheter 6 Fr and the volume of embolization of 0.6 mL/min, then the speed of material in the catheter will be about 3 mm/s. This means that the magnitude of the shear rate, according to Figure 9, is about 10 s^{-1}. Taking into account the results of numerical calculations (for example, for an AVM with a vessel diameter of the racimous part of 0.5 mm), the following values of the Reynolds number for the embolic polymers in the AVM and in the catheter will be

$$Re_{squid_{20}} = 0.44, Re_{squid_{37}} = 0.58, Re_{avm} = 4.8,$$

where $Re_{squid_{20}}$ is the Reynolds number of the SQUID-12$^\circledR$ embolisate in the cold part of the catheter ($T = 20\,^\circ$C), $Re_{squid_{37}}$ is the Reynolds number in the heated part of the catheter ($T = 37\,^\circ$C), and Re_{avm} is the Reynolds number for SQUID-12$^\circledR$ in the AVM nidus.

Thus, the task of determining the rheology of a polymer is key for its selection and the development of an optimal embolization scenario. This problem can be solved only with an integrated approach, using both experimental approaches to study the rheological properties of polymers, and mathematical and computer modeling to describe the embolization process. Qualitative assessments of the quantities of interest, the shape of the AVM vessels as round, and using the Darcy–Weisbach (DW) and Poiseuille formulas, can be proposed [37,38]:

$$h_{mp} = \lambda \frac{l}{d} \frac{c^2}{2g}, \tag{6}$$

$$\delta p = \frac{32 \mu l c}{d^2}, \tag{7}$$

where h_{mp}—head losses, δp—pressure drop, λ—Darcy friction factor, l—tube length, c—flow rate, d—tube diameter, g—local acceleration, and μ—dynamic viscosity.

The first is to calculate the pressure loss in the pipe during the flow of fluid. The second is to evaluate the pressure drop at the inlet and outlet, which is proportional to the viscosity of the fluid and inversely proportional to the square of the pipe diameter. The embolization process in the first approximation can be considered as quasi-stationary, since the polymer supply rate is rather low (see above). Therefore, at a constant pressure drop, which is provided by the surgeon by adjusting the polymer supply through the conductor, and the constancy of other system parameters (tube lengths and viscosity) in the DW formula, AVM vessels with a relatively large cross section will be filled first of all.

This will lead to a decrease in the effective area of the AVM vessels, and hence to an increase in the resistance of this node. To fill smaller AVM vessels, one must either increase the pressure drop or decrease the viscosity of the polymer. Its viscosity, in turn, depends on both the diameter of the vessel and the feed rate, in addition to, as it has been seen in the course of rheometric tests, temperature. It is different for the conditions of the operating room (the outer part of the catheter through which the embolic polymer is injected) and the circulatory zone, and also changes under the influence of heating of the catheter inside the body.

Given the complexity of the embolization procedure and preparation for it [31,32], the operating surgeon faces a challenge regarding the amount and method of administration of the material. The documentation of both studied preparations describes only borderline cases in which the administration of the embolization polymer should be stopped or, conversely, preparation begun for the start of embolization. Manufacturers do not give direct advice or protocols that would unambiguously regulate the embolization procedure of the company precisely because, as discussed above, the rheology of the polymer, the geometry of the flow area and the type of polymer are closely related, which makes it impossible to recommend one or the other protocol at the instruction level. It should be noted that attempts to develop such protocols as well as optimal embolization scenarios have been made in recent years.

The problem under consideration has several fundamentally difficult moments. Firstly, modern hydrodynamics does not have a complete solution to the problem of the flow of even a viscous Newtonian fluid through a bifurcation, or a branching of channels. For a stationary flow, there is only one law of conservation of mass, which does not require knowledge of the properties of the fluid and channel walls. In this case, the only mechanism of energy dissipation is viscous dissipation and vortex formation, which immediately complicates the flow structure, generating secondary flows. The fundamental question about the energy (structure) of such a flow, about the energy loss of the flow during the passage of the tee, is the key to controlling the fluid flow.

Orlowski et al. calculated the flow and observed the results of a numerical calculation of embolization of a two-dimensional cavity [19]; however, the authors did not draw any conclusions about the optimality of the injection process, since the optimal parameters were not introduced and the calculations were not compared with any clinical data. The flow area is a model and, again, does not map to a clinically significant area. The authors of this work used the power law of the dependence of viscosity on the shear modulus. In general, this correctly reflects the nature of rheological relationships. However, this approach is too simplistic, since, as seen from the test results, the coefficients in the rheological models describing them have different values for different polymers.

The first attempts at modelling the embolization process, in which pathological vessels overlap and further flow into a healthy vascular bed occurs, were based on Darcy's law and the Maag formula [39]. Branched network-type AVM models have been described by Golovin et al. [40]. Furher, the concept of considering AVM nidus embolization as a model of two-component filtration, in which the displaced component was blood and the displacing component was embolization material, which is a Newtonian fluid, was formulated and implemented by Cherevko et al. [41]. Such a simplification is essential, but it allowed the authors to solve the problem of optimal control of both single-stage (total) embolization and multi-stage embolization, when subtotal embolization is performed at all stages except the last one [42]. The use of rheological relations (Table 3) with a known set of constants for the two tested polymers will make it possible to more accurately formulate the law of optimal embolization.

In some papers, the clinical aspects of the use of both embolic polymers were evaluated in detail, and their brief chemical characteristics were given [43,44]. A review of the chemical properties of both the aforementioned embolic polymers and promising embolization hydrogels was carried out [26]. The study of their rheological properties is also an important task for the development of correct recommended protocols.

It should be noted that there are a number of aspects in the study that require further study. Further studies would make it possible to more accurately determine the laws of dependence of the rheology of embolization polymers on temperature. So far, this study has been carried out for a small temperature range. One of the explanations for this limitation is the difficulty in supplying these polymers for laboratory research, since the circulation of such polymers in the Russian Federation is allowed only through medical institutions. In medical institutions, these polymers are strictly accounted for and consumed exclusively for endovascular operations, so such substances can only get into the research laboratory as a "waste of operational activities". This leads to the fact that the collection of the amount of polymers necessary for all rheological tests took quite a long time. It should be noted that rheological tests of the Phil polymer have also been carried out, but at the moment enough "waste" of this polymer to carry out the entire line of tests has not been collected. Another limitation in our work is the assumption of a model AVM configuration for numerical calculation.

However, a number of authors [2,41] have worked with this kind of model configuration, which reflects the main patterns of fluid flow in a complex network of vessels. Many authors have tried to get a visualization of the flow of embolic polymer inside the AVM nidus [9,19], but so far this activity is associated with significant difficulties. In our opinion, the ultimate goal of modeling is not to reveal the picture of the flow of embolic polymers, but to obtain more general results; such an approach would help to build a model for the optimal selection of an embolization polymer for a particular clinical case and the optimal method for its administration.

5. Conclusions

In the framework of this study, rheological measurement tests of two non-adhesive polymers (Onyx-18® and Squid-12®) used in medicine for AVM embolization were performed. The analysis of the results of these tests showed a significant dependence of the viscosity not only on the shear modulus but also on the temperature. In the course

of numerical simulation of model embolization of a branched network of vessels, different behavior of these embolic polymers for fistula and racimous network models was demonstrated, which confirms the need to use embolic polymers of different viscosities for embolization of these AVM parts. Of particular interest is the physical interpretation of the law of dependence of the viscosity of embolic polymers and the mechanism of thermal and shear activation in the AVM nidus. The found non-monotonicity of the dependence of viscosity on shear rate gives a new idea of the non-randomness of this effect and, in general, the viscosity activation algorithm with a change in the viscosity of the embolic polymer opens up a qualitative understanding of the effects that arise during embolization. In addition, this understanding suggests ways to solve problems such as difficult pumping of embolic polymer through a small microcatheter, as well as performing operations on infants by controlling the temperature in the outer (outside the body) part of the catheter. The presented coefficients of the Cisco model will allow numerical hemodynamic specialists to perform calculations in the case of a simultaneous change in shear rate and temperature.

Abbreviations

The following abbreviations are used in this manuscript:

AVM	Arteriovenous malformation
CM	Cisco's model
DMSO	Dimethyl sulfoxide
DW formula	Darcy–Weisbach formula
WSS	Wall shear stress

References

1. Jiang, Y.; Zhang, Y.; Lu, Z.; Wang, X.; Bai, S.; Chen, Y.; Mao, J.; Liu, G. Liquid embolic agents for interventional embolization. *Chem. Phys. Mater.* **2022**, *1*, 39–50. [CrossRef]
2. Lv, X.; Li, Y.; Jiang, C. Percutaneous Transvenous Embolization of Intracranial Dural Arteriovenous Fistulas with Detachable Coils and/or in Combination with Onyx. In *Arteriovenous Fistulas—Diagnosis and Management*; Tjoumakaris, S., Ed.; IntechOpen: London, UK, 2013.
3. Oliveri, F.; Bonsignore, C.; Musumeci, I.; Murabito, P.; Scollo, S.; Rosa, V.L.; Terminella, A.; Cusumano, G.; Sofia, V.; Astuto, M. Arteriovenous Malformation Pulmonary (AVM) in a Post-Cesarean Woman: Intensive Care and Urgent Surgery Operation. *Eur. J. Mol. Clin. Med.* **2018**, *5*, 46–50. [CrossRef]
4. Baharvahdat, H.; Blanc, R.; Termechi, R.; Pistocchi, S.; Bartolini, B.; Redjem, H.; Piotin, M. Hemorrhagic complications after endovascular treatment of cerebral arteriovenous malformations. *Am. J. Neuroradiol.* **2014**, *35*, 978–983. [CrossRef]
5. Fennell, V.S.; Martirosyan, N.L.; Atwal, G.S.; Kalani, M.Y.S.; Ponce, F.A.; Lemole, G.M., Jr.; Dumont, T.M.; Spetzler, R.F. Hemodynamics Associated With Intracerebral Arteriovenous Malformations: The Effects of Treatment Modalities. *J. Neurosurg.* **2018**, *83*, 611–621. [CrossRef] [PubMed]

6. Ondra, S.L.; Troupp, H.; George, E.D.; Schwab, K. The natural history of symptomatic arteriovenous malformations of the brain: A 24-year follow-up assessment. *J. Neurosurg.* **1990**, *73*, 387–391. [CrossRef] [PubMed]

7. Papapanayotou, C.J.; Cherruault, Y.; De La Rochefoucauld, B. A mathematical model of the circle of Willis in the presence of an arteriovenous anomaly. *Comput. Math. Appl.* **1990**, *20*, 199–206. [CrossRef]

8. Guglielmi, G. Analysis of the hemodynamic characteristics of brain arteriovenous malformations using electrical models. *J. Neurosurg.* **2008**, *63*, 1–11.

9. Smith, F.T.; Jones, M.A. AVM modelling by multi-branching tube flow: Large flow rates and dual solutions. *Math. Med. Biol. Bf.* **2003**, *20*, 183–204. [CrossRef] [PubMed]

10. Lord, J.; Britton, H.; Spain, S.G.; Lewis, A.L. Advancements in the development on new liquid embolic agents for use in therapeutic embolisation. *J. Mater. Chem.* **2020**, *8*, 8207–8218. [CrossRef]

11. Yang, X.; Wang, S.; Zhang, X.; Ye, C.; Wang, S.; An, X. Development of PVA-based microsphere as a potential embolization agent. *Biomat. Adv.* **2022**, *135*, 112677. [CrossRef]

12. Okada, H.; Hashimoto, T.; Tanaka, Y.; Sakamoto, H.; Kohno, M. Embolization of Skull Base Meningiomas with Embosphere Microspheres: Factors Predicting Treatment Response and Evaluation of Complications. *World Neurosurg.* **2022**, *162*, e178–e186. [CrossRef]

13. Akinduro, O.O.; Mbabuike, N.; ReFaey, K.; Yoon, J.W.; Clifton, W.E.; Brown, B.; Wharen, R.E.; Quinones-Hinojosa, A.; Tawk, R.G. Microsphere Embolization of Hypervascular Posterior Fossa Tumors. *World Neurosurg.* **2018**, *109*, 182–187. [CrossRef] [PubMed]

14. Yeom, Y.K.; Shin, J.H. Complications of Portal Vein Embolization: Evaluation on Cross-Sectional Imaging. *Korean J. Radiol.* **2015**, *16*, 1079–1085. [CrossRef] [PubMed]

15. Gavrilov, S.G.; Mishakina, N.Y.; Efremova, O.I.; Kirsanov, K.V. Complications and Adverse Events of Gonadal Vein Embolization with Coils. *J. Pers. Med.* **2022**, *12*, 1933. [CrossRef] [PubMed]

16. Niimi, Y.; Berenstein, A.; Setton, A. Complications and Their Management during NBCA Embolization of Craniospinal Lesions. *Interv. Neuroradiol.* **2003**, *15*, 157–164. [CrossRef]

17. Kilani, M.S.; Zehtabi, F.; Lerouge, S.; Soulez, G.; Bartoli, J.M.; Vidal, V.; Badran, M.F. New Alcohol and Onyx Mixture for Embolization: Feasibility and Proof of Concept in Both In Vitro and In Vivo Models. *Cardiovasc. Intervent. Radiol.* **2017**, *40*, 735–743. [CrossRef]

18. Elliott, J.P., Jr.; Hageman, J.H.; Szilagyi, E.; Ramakrishnan, V.; Bravo, J.J.; Smith, R.F. Arterial embolization: Problems of source, multiplicity, recurrence, and delayed treatment. *Surgery* **1980**, *88*, 833–845.

19. Orlowski, P.; Summers, P.; Noble, J.A.; Byrne, J.; Ventikos, Y. Computational modelling for the embolization of brain arteriovenous malformations. *Med. Eng. Phys.* **2012**, *34*, 873–881. [CrossRef]

20. Siekmann, R. Basics and Principles in the Application of Onyx LD Liquid Embolic System in the Endovascular Treatment of Cerebral Arteriovenous Malformations. *Interv. Neuroradiol.* **2005**, *5*, 131–140. [CrossRef]

21. FitzGerald, P.F.; Butts, M.D.; Roberts, J.C.; Colborn, R.E.; Torres, A.S.; Lee, B.D.; Yeh, B.M.; Bonitatibus, P.J., Jr. A proposed CT contrast agent using carboxybetaine zwitterionic tantalum oxide nanoparticles: Imaging, biological, and physicochemical performance. *Invest. Radiol.* **2016**, *51*, 786–796. [CrossRef]

22. Khokhlov, A.L.; Kabanov, A.V.; Kozlova, O.G. X-ray contrast media: Focus on safety. *Med. Vis.* **2018**, *5*, 94–105. [CrossRef]

23. GE Healthcare. *Omnipaque (Iohexol) Injection*; Product label; DailyMed: Bethesda, MD, USA, 2006.

24. Van Dellen, J.R.; Lipschitz, R. Meglumine iocarmate (Dimer-X) ventriculography. *Clin. Radiol.* **1973**, *24*, 449–452. [CrossRef] [PubMed]

25. Loffroy, R.; Guiu, B.; Cercueil, J.P.; Krausé, D. Endovascular Therapeutic Embolisation: An Overview of Occluding Agents and their Effects on Embolised Tissues. *Curr. Vasc. Pharmacol.* **2009**, *7*, 250–263. [CrossRef] [PubMed]

26. Piacentino, F.; Fontana, F.; Curti, M.; Macchi, E.; Coppola, A.; Ossola, C.; Giorgianni, A.; Marra, P.; Mosconi, C.; Ierardi, A.M.; et al. Non-Adhesive Liquid Embolic Agents in Extra-Cranial District: State of the Art and Review of the Literature. *J. Clin. Med.* **2021**, *10*, 4841. [CrossRef]

27. Anton Paar GmbH. *Instruction Manual. MCR Series. Modular Compact Rheometer. MCR 102/MCR 302. SmartPave 102. MCR 502 S*; Anton Paar GmbH: Graz, Austria, 2018; p. 51.

28. Lozovskiy, A.; Olshanskii, M.A.; Vassilevski, Y.V. A finite element scheme for the numerical solution of the Navier–Stokes/Biot coupled problem. *Rus. J. Numer. Anal. Math. Model.* **2022**, *37*, 159–174. [CrossRef]

29. Favre-Marinet, M.; Tardu, S. *Convective Heat Transfer*; ISTE Ltd.: London, UK, 2009; pp. 1–7.

30. Zhou, J.C.; Che, Y.Y.; Wu, K.J.; Shen, J.; He, C.H. Thermal Conductivity of DMSO + C2H5OH, DMSO + H2O, and DMSO + C2H5OH + H2O Mixtures at T = (278.15 to 338.15) K. *J. Chem. Eng. Data* **2013**, *58*, 663–670. [CrossRef]

31. ONYX Patent and Methodology Information. Available online: https://www.accessdata.fda.gov/cdrh_docs/pdf3/P030004c.pdf (accessed on 1 January 2020).

32. SQUID Methodology and Patent Information. Available online: https://www.debene.com/productos/balt/media/docs/balt_squid_brochure.pdf (accessed on 1 January 2020).

33. Saramito, P. *Complex Fluids. Modeling and Algorithms*; Springer: Berlin, Germany, 2016; pp. 49–56, 64–65.

34. Matvienko, O.V. Investigation of the stabilized flow of pseudoplastic liquid, described by the Sisco model, in the cylindrical tube. *Tomsk. St. Univers. J. Math. Mech.* **2018**, *55*, 99–112. [CrossRef]

35. Lenton, J.; Kessel, D.; Watkinson, A.F. Embolization of renal angiomyolipoma: Immediate complications and long-term outcomes. *Clin. Radiol.* **2008**, *63*, 864–870. [CrossRef]

36. Rose, S.C.; Kikolski, S.G.; Chomas, J.E. Downstream hepatic arterial blood pressure changes caused by deployment of the surefire antireflux expandable tip. *Cardiovasc. Intervent. Radiol.* **2013**, *36*, 1262–1269. [CrossRef]

37. Chaudhry, M.H. *Applied Hydraulic Transients*, 3rd ed.; Springer: New York, NY, USA, 2013; pp. 48–49.

38. Batchelor, G.K. *An Introduction to Fluid Dynamics*; Cambridge University Press: Cambridge, UK, 2000; pp. 180–181.

39. Lv, X.; Wu, Z.; Li, Y. Arteriovenous malformation in the brain: A theoretical study explaining the behavior of liquid embolic agents during endovascular treatment. *J. Neuroradiol.* **2013**, *26*, 661–668. [CrossRef]

40. Golovin, S.; Khe, A.; Gadylshina, K. Hydraulic model of cerebral arteriovenous malformations. *J. Fluid Mech.* **2016**, *797*, 110–129. [CrossRef]

41. Cherevko, A.A.; Gologush, T.S.; Petrenko, I.A.; Ostapenko, V.V.; Panarin, V.A. Modelling of the arteriovenous malformation embolization optimal scenario. *R. Soc. Open Sci.* **2020**, *7*, 191992. [CrossRef] [PubMed]

42. Sharifullina, T.; Cherevko, A.; Ostapenko, V. Optimal control problem arising in mathematical modeling of cerebral vascular pathology embolization. *Sci. Rep.* **2022**, *12*, 1302. [CrossRef] [PubMed]

43. Vollherbst, D.F.; Chapot, R.; Bendszus, M.; Möhlenbruch, M.A. Glue, Onyx, Squid or PHIL? Liquid Embolic Agents for the Embolization of Cerebral Arteriovenous Malformations and Dural Arteriovenous Fistulas. *Clin. Neuroradiol.* **2022**, *32*, 25–38. [CrossRef]

44. Venturini, M.; Lanza, C.; Marra, P.; Colarieti, A.; Panzeri, M.; Augello, L.; Gusmini, S.; Salvioni, M.; De Cobelli, F.; Del Maschio, A. Transcatheter embolization with Squid, combined with other embolic agents or alone, in different abdominal diseases: A single-center experience in 30 patients. *CVIR Endovasc.* **2019**, *2*, 8. [CrossRef]

Article

Squeezing Mechanical Analysis and Model Establishment of the Viscoelastic Rubber-Strip-Feeding Process of the Cold-Feed Rubber Extruder

Yanchang Liu, Yiren Pan *, Xuehua Hu and Fang Yu

College of Electromechanical Engineering, Qingdao University of Science and Technology, Qingdao 266061, China
* Correspondence: pyr@qust.edu.cn; Tel.: +86-135-8934-5827

Abstract: In the process of rubber extrusion, the feed structure directly affects the extrusion quality, extrusion uniformity, screw lateral force, and feed power consumption. Until now, the feed structure was mainly based on empirical designs, and there was no theoretical model for the optimal design of a feed structure. This paper focused on the squeezing mechanical analysis and model establishment of the feeding process in which viscoelastic rubber strips are passed through feed-wedge clearance in cold-feed extruders. The screw flight rotation squeezing process was simplified into a disc rotation squeezing process; the instantaneous squeezing velocity $\dot{h}(t)$ in the disc rotation squeezing model was derived according to feed wedge clearance geometry and the disc rotating speed. By transforming rotation squeezing into differential slab squeezing, mathematical expressions of the velocity distribution, pressure distribution, total squeezing force, and power consumption in the feeding process were derived in a rectangular coordinate system under isothermal and quasi-steady assumptions and certain boundary conditions by using balance equations and a Newtonian viscous constitutive relation. Theoretical calculations and experimental values showed the same trend. Through comparison, it was found that the power consumption (P3) caused by sliding friction is about 200–900 W according to theoretical calculations, while the experimental test results show it to be about 300–700 W. Additionally, the difference between theoretical pressure value and the experimental pressure value can be controlled within 5–15%. This could reflect the main factors that affect the feeding process, so could be used for analyses of actual feeding problems, and to contribute to rough quantitative descriptions of the feeding process, finite element simulation, and the optimization of the feeding structure.

Keywords: squeezing mechanical analysis; rubber strip cold-feed process; viscoelastic rubber strip

1. Introduction

The extrusion process is an important step in rubber processing, and the vast majority of rubber compounds are extruded at least once during the molding process [1]. The feeding process has a significant impact on extrusion quality [2,3], extrusion stability, the side force applied to screw, and extruder power consumption. In modern research and applications, in order to realize a uniform feed rate in rubber extruders, rubber strip feeding has been used in either rarely used hot-feed extruders or widely used cold-feed extruders. Because rubber has relatively strong adhesiveness at room temperature in a highly elastic state, the cost of the granulation process will increase if a rubber extruder is fed granulated material. A large number of separating agents can be added to prevent the adhesion phenomenon of rubber granulates, resulting in changes in the formulation properties [4]. For a cold-feed extruder fed with a rubber strip form, regardless of whether a free-feeding structure or the widely used forced-feeding structure with a feed roll is used, the feed wedge clearance is always designed at the feed port. Figure 1a shows the common feeding model (feed roll structure) of a cold-feed rubber extruder. The feed wedge clearance is formed between the screw flight crest and the undercut groove on the inner wall of the feed barrel. The feed

wedge clearance is a key structure when feeding the rubber strip into the screw channel: the rubber strip is gradually squeezed (compressed) and thinned when the rotating screw flight drags the rubber strip through the feed wedge clearance. At the same time, the screw flight is more deeply embedded into the rubber strip (Figure 1b). When the rubber strip approaches the minimum wedge gap (the design gap between the outer diameter of the screw and the inner wall of the feed barrel), it is longitudinally broken off [5], thus entering the channels at both sides of the screw flight and completing the feeding process of the rubber strip. In a combined structure of a feed roll/screw system and the feed wedge clearance, the feed roll only increases the pushing force [6] when feeding the rubber strip or creating an additional pressure build-up [7]. Therefore, when using rubber extruders, the rubber strip is dragged through the feed wedge clearance and broken off longitudinally at the end of the feed wedge clearance; this is the key to successfully carrying out rubber strip feeding. In the vicinity of the minimum wedge gap, the thin strip easily causes longitudinal break-off under the axial thrust action of the screw flight. Since rubber is essentially a viscoelastic liquid at room temperature [8], a special kind of squeezing (compression) flow occurs in the feed wedge clearance. The feed wedge clearance geometry is a nonlinear wedge region with a narrow width (the width of the screw flight). The squeezing force is generated by dynamic viscous pressurization in the nonlinear wedge region through the rotation drag motion of the screw flight, and rubber flows in the nonlinear wedge region occur only in the directions towards both sides of the screw flight, because the minimum wedge gap is very small, and can be neglected for rubber compounds with very high viscosity.

(a)   **(b)**
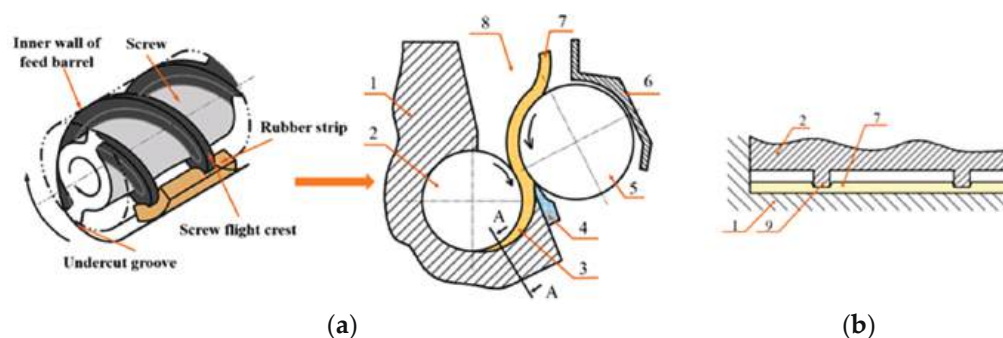
Figure 1. (**a**) Feed wedge clearance; (**b**) A-A section view; Feeding model of a cold-feed rubber extruder. (1) Feed barrel; (2) screw; (3) feed wedge clearance; (4) scraper; (5) feed roll; (6) feed door; (7) rubber strip; (8) feed opening; (9) screw flight.

The history of rubber extruders dates back more than 140 years, to the invention of hot-feed extruders in 1879. The continuous development of feeding technology is mainly reflected in the improvements to the feeding structure [9–13] and the control of feeding uniformity [4,14–16]. However, there has been little research into the feeding theory of rubber extruders, especially cold-feed extruders. The existing research on the theory of the rubber-strip feeding process has either analyzed the mechanical conditions of rubber strips being drawn into the feed wedge clearance [6], or used a disc rotation squeezing model device to carry out experimental research on the strip feeding process [5]. Since the study by Jianbin Li did not consider the contribution of the flight flanks to the additional drag effect [6], it reached the incorrect conclusion that the feeding mechanical condition of the friction coefficient μ_s between the flight crest and the rubber strip was greater than the friction coefficient μ_b between the barrel inner wall and rubber strip. Other experimental results in the studies of Yanchang Liu [5] included single-peak pressure distribution and the obvious power consumption when the rubber strip passed through the model clearance. To date, little theory of the rubber strip feeding process exists, which makes the feeding theory for rubber extruders lag far behind engineering practice. The side force applied to the screw and the feed power consumption have not been calculated theoretically, and the feed structure and technology have not been improved or innovated by theoretical guidance.

In order to establish a feeding process theory of cold-feed rubber extruders, the squeezing flow dynamics during this process must be analyzed. However, most studies of squeezing flow deal with the pure squeezing flow of viscoelastic materials [17–28], or viscoelastic materials [29–40], or non-Newtonian liquids with a squeezing–extrusion combined flow [41] between two parallel plates; very little research has considered the squeezing flow between two non-parallel plates. The squeezing and sliding flow of Oldroyd-B fluid was examined by N. Phan-Thien [42] in a wedge geometry of semi-wedge angle $a(t)$ with a wedge apex, using a numerical method. In this wedge, the flat plane boundaries of the wedge were closing at a rate $\dot{a}(t)$ and were sliding along the direction perpendicular to the two-dimensional wedge with a constant velocity. However, there was no consideration of the squeezing flow of non-Newtonian liquids in a nonlinear wedge region, in which the lubrication approximation was not valid due to large wedge angle or slip boundary condition. The squeezing flow in feed wedge clearance belongs to the latter category, because the rubber strip slides along the cylinder wall in the feeding process. Therefore, in this study, we attempted to analyze the dynamics of squeezing flow caused by the drag action of the screw flights in the nonlinear wedge region under sliding boundary conditions. In order to obtain an approximate analytical solution of the motion equation which reflects the basic characteristics of the squeezing flow, under some assumptions (Newton material, isothermal quasi-steady flow), the physical model was simplified (disc rotation squeezing model) and the motion transformation (differential slab squeezing flow) was applied. To verify the accuracy of the theoretical model, a comparison between the theoretical calculations and the experimental data was carried out. The theoretical model that was established could provide guidance and suggestions for the design and optimization of actual feed structures.

2. Physical Model and Squeezing Velocity

In this section, a physical model of feeding process is established and the calculation formula of squeezing velocity in the feed wedge clearance is obtained by analyzing the relationship between the rotation angle and the wedge gap.

2.1. Physical Model

At the feed port, the basic screw configuration of the cold feed extruder is a single screw section with double-flighted design. When rubber strips pass through the feed wedge clearance, the screw flight crest will always contact and squeeze the rubber strip. If expanded along the outer diameter of the screw, the contact traces between the screw flight crest and the rubber strip are two inclined narrow strips (the black areas in Figure 2). In Figure 2, β is the helical angle and w is the axial width of the flight. To describe the behavior of the feeding process, the geometry of the helix feed wedge clearance is simplified, and then motion transformation is applied, as discussed in Section 3.1. As the rubber strip passes through the feed wedge clearance, the effective flight compression path is perpendicular to the screw axis. Therefore, each feed's screw flight can be simplified to a disc (helical angle $\beta = 0°$), and the diameter and width of the disc are screw diameter D and screw flight axial width w, respectively. An effective feed wedge clearance is formed between the disc and the undercut groove on the inner wall of the feed barrel. In this way, a disc rotation squeezing model is built with a disc and a barrel (Figure 3). Because the two screw flights have the same geometry, one was chosen for mathematical description.

For all general specifications of cold-feed extruders, a standardized design of the feed wedge clearance has been achieved. In Figure 3, $a = 0.03 - 0.04D$, $b = 0.06 - 0.08D$, $R = 0.5D$, $R_1 \approx 0.5D$, H is the start position or maximum value of the wedge gap (on the extended line of O and O_1, that is $H = \overline{ss'}$), $h_{\min}$ is the end position or minimum value of the wedge gap (the typical value is $0.0045R$), and θ_0 is the center angle of the circular arc of the outer diameter of the disc in the whole range of the feed wedge clearance. For example, for a cold-feed extruder with $D = 65$ mm, $a = 2$ mm, $b = 5$ mm, $R = R_1 = 32.5$ mm, $H = 5.4$ mm, $h_{\min} = 0.146$ mm, and $\theta_0 = 85° \approx 1.483$ rad.
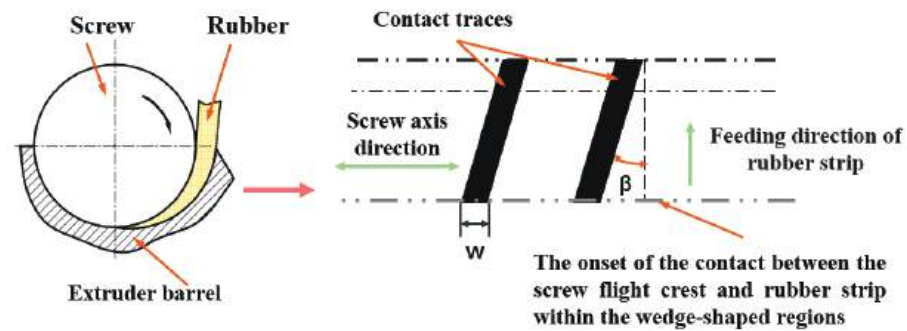
Figure 2. Expanded view of the contact trace between the screw flight crest and the rubber strip.
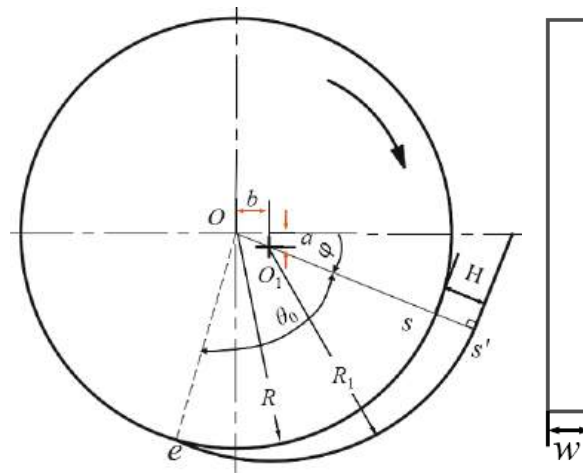
Figure 3. Disc rotation squeezing model.

2.2. Squeezing Velocity

An analysis of squeezing flow needs to determine either the squeezing force or the squeezing velocity. In the disc rotation squeezing model, the squeezing force is unknown, and the squeezing velocity can be derived according to the geometry of the feed wedge clearance and the disc speed. Figure 4 shows the relationship between the gap $h(\theta)$ and the angle θ.

If the initial thickness of the fed rubber strip is equal to the maximum value H of the wedge gap, the position of the line segment ss can be set as the initial point at which the rubber strip enters into the wedge clearance. When the disc rotates through an angle θ (rad) from time $t = 0$ to t(s), the strip is squeezed (compressed) from thickness H to $h(\theta)$ (Figure 4). The mathematical relationship between $h(\theta)$ and θ is

$$h(\theta) = (\overline{Om} + \overline{mn}) - R = c\cos\theta + \sqrt{R_1^2 - (c\sin\theta)^2} - R \tag{1}$$

where $c = \overline{OO_1} = \sqrt{a^2 + b^2}$.

By expanding the term with the root sign on the right side of Equation (1) into a power series,

$$\sqrt{R_1^2 - (c\sin\theta)^2} = R_1\left[1 - \frac{1}{2}\frac{(c\sin\theta)^2}{R_1{}^2} + \ldots\right] \tag{2}$$

By ignoring the terms greater than the quadratic term of the power series on the right side of Equation (2) and substituting it into Equation (1) and considering $R \approx R_1$, one obtains

$$h(\theta) = c\cos\theta - \frac{c^2}{2R_1}\sin^2\theta \tag{3}$$

If the rotating speed of the disc is N rpm, then $\theta = \pi Nt/30$. Substituting the expression of θ into Equation (3) gives

$$h(\theta) = c\cos\left(\frac{\pi Nt}{30}\right) - \frac{c^2}{2R_1}\sin^2\left(\frac{\pi Nt}{30}\right) \tag{4}$$

By differentiating both sides of Equation (4), one can obtain the instantaneous squeezing velocity $\dot{h}(t)$,

$$\dot{h}(t) = -\frac{\pi Nc}{30}\left[\sin\left(\frac{\pi N}{30}t\right) + \frac{c}{2R_1}\sin\left(\frac{\pi N}{15}t\right)\right] \tag{5}$$

where "$-$" indicates squeezing (compression). From Equation (5), $\dot{h}$ is directly related to the geometric parameters of the feed wedge gap clearance (c and R_1) and the operating parameters (N and t).
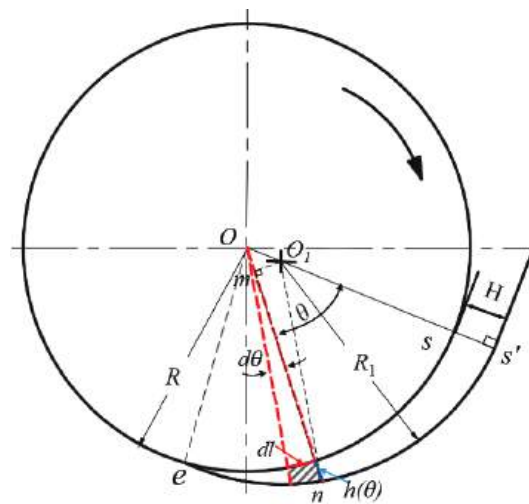
Figure 4. Relationship between the gap $h(\theta)$ and the angle θ.

To study the change in instantaneous squeezing velocity, according to Equation (5), MATLAB software was used to calculate and draw $\dot{h} - t$ curves at different disc speeds (N = 30, 45 and 60 rpm) for the disc rotation squeezing model of D = 65 mm ($c = \sqrt{2^2 + 5^2} \approx$ 5.39 mm, R_1 = 32.5 mm). Figure 5 shows that the $\dot{h} - t$ curve is approximately composed of two parts: a constant acceleration squeeze in the early stage and a constant velocity squeeze in the later stage. The former accounts for most of the whole rotational squeezing process, and the latter accounts for a small part. Setting t_0 and t_t to represent the time used during the whole rotational squeezing process and the transition time from the constant acceleration squeeze to the constant velocity squeeze, respectively, t_0 can be calculated according to the formula $t_0 = 30\theta_0/\pi N$, and t_t can be measured from the asymptotic transition part of the $\dot{h} - t$ curve in Figure 5. When N = 30, 45, and 60 rpm, t_0 is 0.47, 0.31, and 0.24 s, t_t is 0.39, 0.27, and 0.21 s, and t_t/ t_0 is 0.83, 0.87, and 0.875, respectively. Figure 5 also shows that the squeezing velocity increases faster with increasing disc speed. Similar results can be obtained by using the same method to calculate other disc rotation squeezing models with different diameters (D = 90, 120, 150, 200, and 250 mm).
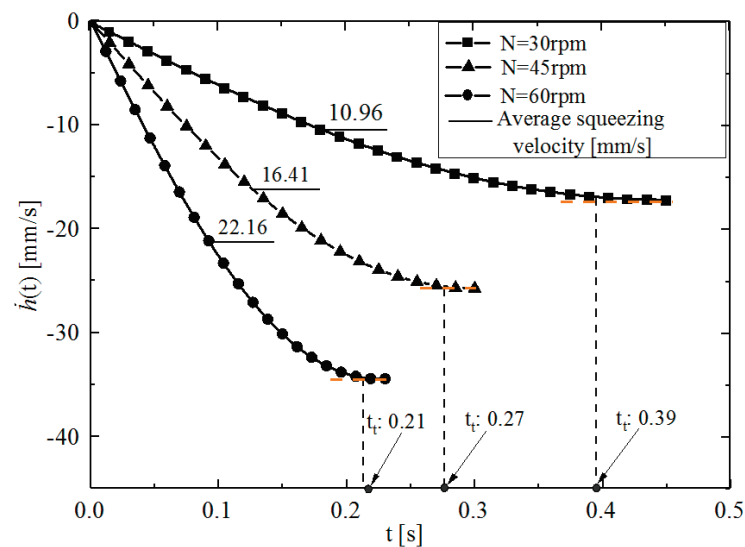
Figure 5. $\dot{h} - t$ curves in the disc rotation squeezing model with $D = 65$ mm at different disc speeds.

The above analysis shows that, for a given disk rotating squeezing model and disc rotating speed, the instantaneous squeezing velocity $\dot{h}(t)$ changes rapidly for most of the time taken for the whole squeezing process. This presents difficulties when analyzing the squeezing flow. To simplify the theoretical analysis, the average squeezing velocity $(-V)$ was introduced, where '$-$' also represents the squeezing direction, $V = |-V|$. According to N, H, and θ_0, it is easy to calculate V.

$$V = |-V| = \left| -\frac{H}{t_0} \right| = \left| -\frac{\pi NH}{30\theta_0} \right| = \frac{\pi NH}{30\theta_0} \tag{6}$$

Equation (6) shows that, for a given disc rotation squeezing model, the average squeezing velocity V is only proportional to N. For example, for the disc rotation squeezing model with $D = 65$ mm, the average squeezing velocities calculated by Equation (6) at $N = 30$, 45, and 60 rpm are -11.4, -17.1, and -22.8 mms^{-1}, respectively. For the disc rotation squeezing models for other general specifications of cold-feed extruders, when the rotational speed $N = 30$ rpm, the average velocities calculated by Equations (5) and (6) in the whole feed wedge gap are $V_{(5)}$ and $V_{(6)}$, respectively. The range of $[(V_{(5)} - V_{(6)})/V_{(5)}] \times 100\%$ is approximately $-0.51 \sim 1.30\%$, which strongly indicates that the simplified Equation (5) has a very high level of accuracy.

3. Mathematical Model

The disc rotation squeezing model established in Section 2 was further simplified into a differential slab squeezing model. According to the balance equations, mathematical formulas including velocity, pressure distribution, total squeezing force, and power consumption in the wedge clearance were obtained.

3.1. Kinematic Exchange

During the actual feeding process, the rubber strip that is adhered to the screw flight rotates with the rotational screw flight and slides along the barrel surface. Therefore, in the disc rotation squeezing model, the disc drags the rubber strip to rotate through an angle θ (rad) within time t, and the rubber strip is squeezed (compressed) from the initial thickness H to the thickness $h(t)$. This process can be regarded as one in which a "differential slab" of arc length Δl (Figure 4) squeezes the strip in parallel from the initial thickness H to the thickness $h(t)$ within time t at the squeezing velocity generated by the disc rotation. The squeezing flow obtained from the kinematic exchange is called the differential slab squeezing flow, which is shown in Figure 6. Since screw flight is always embedded into

the rubber strip during the feeding process, this flow belongs to a constant area squeezing flow [43].
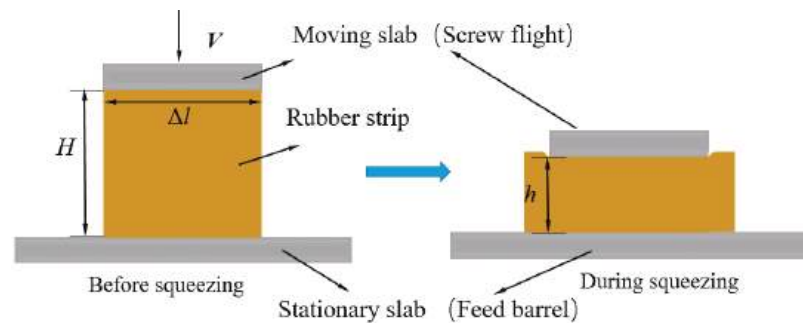
Figure 6. Differential slab squeezing flow.

3.2. Velocity and Pressure Distributions

The theoretical analysis used the rectangular coordinate system shown in Figure 7. First, the following assumptions about the differential slab squeezing flow were made to solve the balance equations for the analytic solutions of the velocity and pressure distributions:
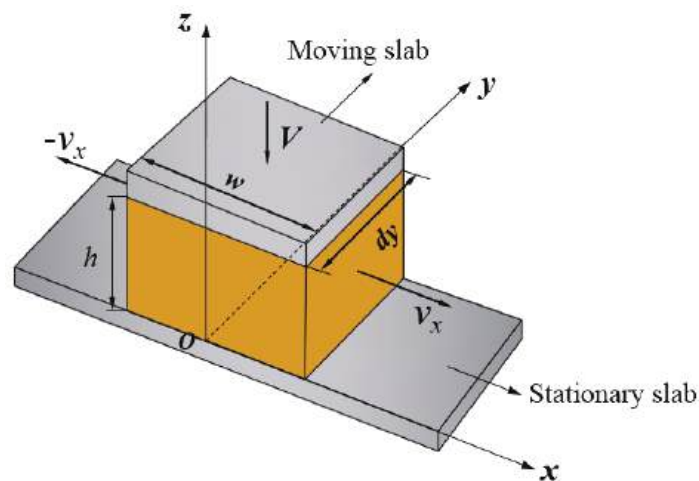
Figure 7. The rectangular coordinate systems used in the theoretical analysis, $dy = \Delta l$.

(i) The flow of the rubber compound is isothermal, has a quasi-steady state [42,44], and is laminar. In the quasi-steady state, locally and instantaneously, the squeezing flow may be regarded as a steady flow between fixed parallel plates [45].

(ii) The inertia, gravity, and normal stress terms in the momentum equation can be ignored.

(iii) The rubber compound is a noncompressible Newtonian liquid.

To simplify the analysis of the parallel plate squeezing flow, the component of momentum in the direction parallel to the plates (here, it is the x-component of momentum) is usually assumed to be the most important, and the component of momentum in the direction normal to the plates (here, it is the z-component of momentum) is not used [45]; that is, the component of velocity v_z normal to the plates is neglected [46].

Because the minimum value h_{min} of the feed wedge gap is very small ($h_{min} \approx 0$) and there is an additional pressure build-up created by the feed roll/screw system in the upstream position of the maximum wedge gap, the component of velocity v_y in the direction of the differential dimension (y-direction) can be assumed to be zero in the differential slab squeezing flow. In other words, the rubber compound can only be squeezed out along the directions on both sides of the disc (or flight) (x-direction) during the feeding process. This

is an important boundary condition for the disc rotation squeezing model or the differential slab squeezing flow.

Based on the above assumptions and analyses, and considering the isotropic pressure and the component of velocity to be constant at the differential dimension *dy,* the equations of momentum can be reduced to a one-dimensional form as follows:

$$\eta \frac{\partial^2 v_x}{\partial z^2} = \frac{\partial p}{\partial x} \tag{7}$$

where v_x is the *x*-component of velocity and *p* is isotropic pressure.

Because the rubber strip slides along the barrel surface during the feeding process, it is assumed that there is no slippage at the moving slab (screw flight crest) and at the stationary slab of the *x*-direction, that is, the boundary condition $z = 0$, $v_x = 0$ and $z = h$, $v_x = 0$. Integrating Equation (7) twice with respect to *z* and applying the boundary conditions can derive Equation (8):

$$v_x = \frac{1}{2\eta} \frac{\partial p}{\partial x} (z^2 - hz) \tag{8}$$

This v_x velocity distribution must satisfy the following overall continuity relationship:

$$V x dy = \int_0^h v_x dy dz \tag{9}$$

By substituting Equation (9) into Equation (8) and considering *dy* as a constant value:

$$\frac{\partial p}{\partial x} = -\frac{12\eta V}{h^3} x \tag{10}$$

Usually, the screw channel at the feed port is not fully filled with rubber [5]. Therefore, it can be assumed that the pressure on both sides of the disc (screw flight) is atmospheric pressure, that is, $x = \pm w/2$, $p = 0$. Under this boundary condition, integrating Equation (10) can obtain:

$$p = \frac{3\eta V w^2}{2h^3} - \frac{6\eta V}{h^3} x^2 \tag{11}$$

Equation (11) shows that the pressure distribution *p* in the model wedge *p* is related to *V*, *w*, *h*, *x*, and η, and the effects of *h*, *x*, and *w* on *p* are particularly significant. For a given disc rotation squeezing model, when the disc rotating speed *N* is constant, *p* is only related to *x* at any squeezing thickness *h*, showing the parabolic distribution shown in Figure 8. Figure 8 shows that, for an arbitrary *h*, the maximum pressure p_{max} can be obtained at $x = 0$.
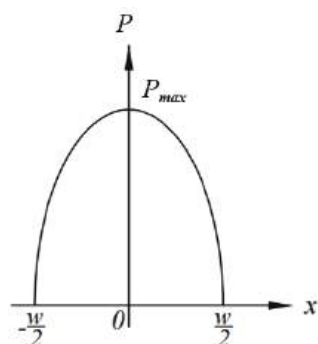
Figure 8. Relationship between *p* and *x*.

According to Equation (11), it is easy to calculate the average pressure $\bar{p}$ along *w* in Figure 8:

$$\bar{p} = \frac{\int_{-\frac{w}{2}}^{\frac{w}{2}} \left(\frac{3\eta V w^2}{2h^3} - \frac{6\eta V x^2}{h^3} \right) dx dy}{w dy} = \frac{\eta V w^2}{h^3} \tag{12}$$

Equation (12) shows that, for a given disc rotation squeezing model and rubber compound, when the disc rotation speed is constant, $\overline{p}$ is inversely proportional to the cubic power h, proportional to the quadratic power w, and proportional to η. As h decreases, $\overline{p}$ increases rapidly, and when $h \to 0$, $\overline{p} \to \infty$. However, p or $\overline{p}$ is always a finite value because h has a minimum design value h_{min} (at $\theta = \theta_0$). In addition, Liu Y. C. and Yu F [3] used a disc rotation squeezing model device with D = 65 mm and found that the rubber strip would be longitudinally broken off at a position of approximately h = 1 mm before the design value of the minimum wedge gap h_{min}(=0.16 mm). h_b and θ_b are set as the wedge gap value and the corresponding center angle when the rubber strip is longitudinally broken off, respectively. For the disc rotation squeezing model with D = 65 mm and h_b = 1 mm, the θ_b = 73° can be obtained by calculating or drawing, but the regularity of h_b and θ_b needs further experimental research.

A combination of Equations (8) and (10) obtains:

$$v_x = -\frac{6Vx}{h^3}(z^2 - hz) \tag{13}$$

From Equation (13), v_x depends on V, h, x, and z. When V, h, and x are fixed, the relationship between v_x and z shows a parabolic curve, and shear flow occurs along the z-direction. When V, h, and z are fixed, v_x is proportional to x and produces elongational flow in the x direction. When V, x, and z are fixed, v_x is inversely proportional to the cubic power of h; that is, when h decreases, v_x increases rapidly.

3.3. Total Squeezing Force

The total squeezing force refers to the resultant force of the pressures exerted on the rubber strip in the radial direction of the disc (screw) within the whole feed wedge clearance. In the design of a rubber extruder, for example, the total squeezing pressure is used to calculate the elastic flex deformation of the screw caused by the side force, because excessive flex deformation will cause scraping between the screw and the barrel.

The total squeezing force F can be deduced from the disc rotation squeezing model. The method for calculating F is as follows: first, the coordinate system $y'Oz'$ shown in Figure 9 was established, and the force dF acting on the area element $wdl(= wRd\theta)$ at position θ in the radial direction of the disc was decomposed into $dF_{y'}$ and $dF_{z'}$ components, as shown in the enlarged view. Second, the magnitudes of the $F_{y'}$ and $F_{z'}$ components of the total squeezing force F were calculated by integral, that is, $F_{y'} = \sum \left| dF_{y'} \right|$ and $F_{z'} = \sum |dF_{z'}|$. Finally, the magnitude and tangential direction angle of the total squeezing force F were calculated, that is, $F = \sqrt{F_{y'}^2 + F_{z'}^2}$ and $\tan \psi = F_{z'}/F_{y'}$. $\varphi + \arctan\psi$ is the angle between the direction of the total squeezing force and the horizontal line.

As mentioned in Equation (7), the pressure in the model wedge is isotropic. Therefore, the pressure in the radial direction in Figure 9 is equal to the pressures calculated by Equations (11) and (12). To simplify the calculation, the average pressure $\overline{p}$ was used. Hence:

$$dFy' = \overline{p}wR\cos\theta d\theta \tag{14}$$

$$dFz' = \overline{p}wR\sin\theta d\theta \tag{15}$$

Putting Equation (12) into Equations (14) and (15) and integrating them obtains:

$$Fy' = \int_0^{\theta_b} \overline{p}w\cos\theta Rd\theta = -\frac{\eta\pi NHw^3R}{30\theta_0 c^3}k_1 \tag{16}$$

$$Fz' = \int_0^{\theta_b} \overline{p}w\sin\theta Rd\theta = -\frac{\eta\pi NHw^3R}{60\theta_0 c^3}k_2 \tag{17}$$

where $k_1 = \tan\theta_b$, $k_2 = \left[\left(1 - \frac{\theta_b^2}{2} + \frac{\theta_b^4}{4!}\right)^{-2} - 1\right]$.
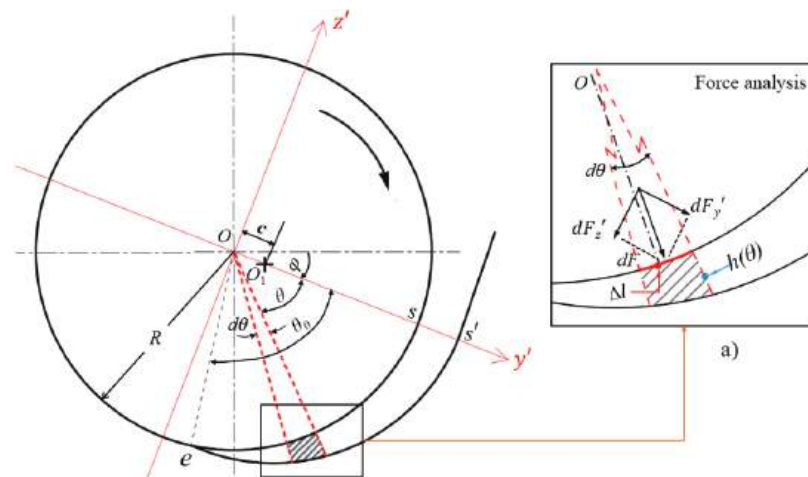
Figure 9. Force analysis of the disc during squeezing; (**a**) enlarged drawing of the force analysis.

Substituting Equations (16) and (17) into the above expressions of F and $\tan \psi$, respectively, can obtain:

$$F = \sqrt{(Fy')^2 + (Fz')^2} = \frac{\eta \pi N H w^3 R}{60 \theta_0 c^3} \sqrt{4k_1{}^2 + k_2{}^2} \tag{18}$$

$$\tan(\psi) = \frac{Fz'}{Fy'} = \frac{k_1}{2k_2} \tag{19}$$

For each given model wedge, φ is known; therefore, according to Equation (19), the angle $\varphi + \arctan\psi$ between the direction of the total squeezing force and the horizontal line can be obtained.

3.4. Power Consumption

When the rubber strip passes through the model wedge, the power consumption comes from the following three parts:

(i) The increase in kinetic energy when the rubber compound is squeezed out from both sides of the disc (screw flight);

(ii) Viscous dissipation in squeezing flow;

(iii) Friction loss of the rubber strip sliding along the barrel.

(1) Power consumption P_1 caused by an increase in kinetic energy

As h decreases, v_x shows a rapid increasing trend (Equation (13)), which increases the kinetic energy of the rubber in the extrusion direction (x direction); the kinetic energy reaches its maximum at the edges at both sides of the disc (screw flight). In Figure 7, the volumetric flow rate in the direction of $+x$ or $-x$ caused by the moving slab squeezing downwards is $Vxdy$ (V is the average squeezing velocity, which is shown in Equation (6)). Therefore, the average extrusion velocity $\overline{v}_x$ at the x position is:

$$\overline{v}_x = \frac{Vxdy}{hdy} = \frac{Vx}{h} \tag{20}$$

If the flow between the approaching slabs is regarded as potential flow, the average velocity $\overline{v}_x$ in the x direction is a function of x, not h [16]. The average velocity of the rubber extruded from the edges of the slabs ($x = \pm w/2$) is $\overline{v}_{w/2} = Vw/2h$ (only the magnitude of the velocity considered). Therefore, the rate of work performed on a moving slab with dy length elements is equal to the rate of change of the kinetic energy of rubber dP_1.

$$dP_1 = \frac{d}{dt}\left(\frac{1}{2} m \overline{v}_{\frac{w}{2}}{}^2\right) = \frac{V^2 w^2}{8h^2} \frac{dm}{dt} \tag{21}$$

where dm/dt is the mass flow rate of the extruded rubber, which is equal to $2hdy(Vw/2h)\rho$, and ρ is the density of rubber, so Equation (21) becomes:

$$dP_1 = \frac{\rho V^3 w^3}{8h^2} dy \tag{22}$$

According to Figure 2, considering $dy = Rd\theta$ and integrating Equation (22) along the whole wedge gap yields P_1:

$$P_1 = \int_0^{\theta_b} \frac{\rho V^3 w^3}{8h^2} Rd\theta \tag{23}$$

Considering the expression of $h(\theta)$ (Equation (3)) will make the integral operation of Equation (23) very complex. Therefore, the simple arithmetic mean $H/2$ of $h(\theta)$ was used to replace $h(\theta)$ to obtain the simple approximate solution of P_1:

$$P_1 = \frac{R\theta_b \rho V^3 w^3}{2H^2} \tag{24}$$

(2) Power consumption P_2 caused by viscous dissipation.

The velocity gradient of v_x in the z direction (Equation (13)) will cause viscous heat generation. Therefore, the shear rate $\dot{\gamma}$ can be obtained by differentiating Equation (13) with respect to z:

$$\dot{\gamma} = \frac{\partial v_x}{\partial z} = -\frac{6Vx}{h^3}(2z - h) \tag{25}$$

From Equation (25): 1) at $x = 0$, $\dot{\gamma} = 0$; 2) at $x = \pm w/2$ and $z = 0$ or h, the absolute value of the $\dot{\gamma}$ can take the maximum, $|\dot{\gamma}|_{\max} = 3Vw/h^2$. To simplify the calculation, the corresponding shear rate at $h = H/2$ can be taken as the average shear rate $\bar{\dot{\gamma}}$ in the whole squeezing flow process: that is, $\bar{\dot{\gamma}} = 12Vw/H^2$. Therefore, the rate of viscous dissipation of rubber compound per unit volume is:

$$\eta \bar{\dot{\gamma}}^2 = \frac{144\eta V^2 w^2}{H^4} \tag{26}$$

If the volume of the whole model wedge is V_w and the very small volume remaining after the longitudinal break-off of rubber strip is ignored, the power consumption P_2 caused by viscous dissipation is:

$$P_2 = \frac{144\eta V^2 w^2 V w}{H^4} \tag{27}$$

Through the geometric relationship in Figure 3, V_w can be obtained:

$$V_w = \frac{w(\alpha R_1^2 - \theta_b R^2 + Rc\sin\theta_b)}{2} \tag{28}$$

(3) Power consumption P_3 caused by sliding friction.

During the sliding process of rubber strips dragged by the disc (screw flight) along the barrel, the shape of the rubber strip is bent, and the local pressure is continuously changed. As shown in Figure 10, for a rubber element at position θ, setting $\angle OnO_1 = \beta$, according to the cosine theorem:

$$\cos\beta = \frac{(R + h)^2 + R_1^2 - c^2}{2(R + h)R_1} \tag{29}$$
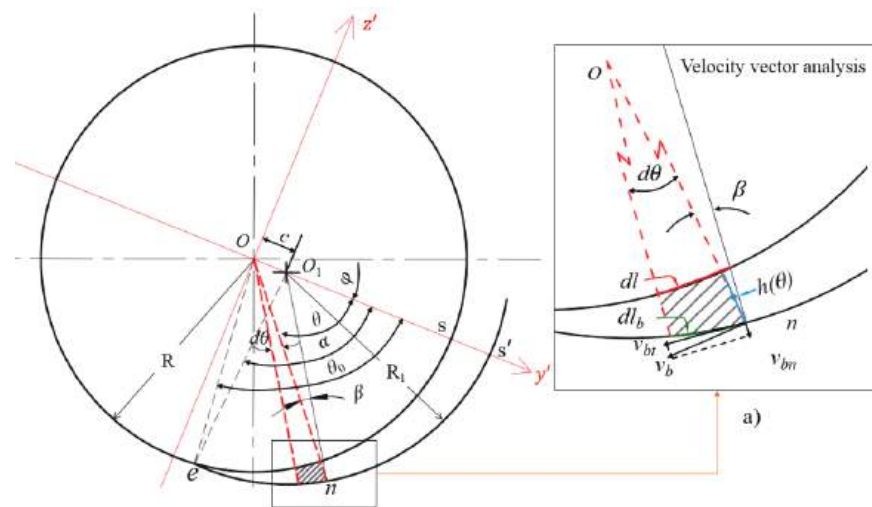
Figure 10. Velocity vector analysis of the rubber strip during squeezing; (**a**) enlarged drawing of velocity vector analysis.

Equation (29) shows that, in the feeding process, the value of β will change with h or θ. Since the center and radius of the cylinder arc $\widehat{e\,s'}$ are O_1 and R_1, respectively, the tangential velocity v_{bt} of the rubber element sliding along the cylinder at position θ is:

$$v_{bt} = v_b \cos \beta = \frac{\pi N (R + h)}{30} \cos \beta \tag{30}$$

Obviously, v_{bt} changes with h or θ.

Assuming that the total squeezing force F (Equation (18)) is evenly distributed on arc $\widehat{e\,s'}$, and the sliding friction coefficient f between the rubber strip and the barrel is a constant, the friction force dF_f generated by the barrel on the rubber element at position θ is:

$$dF_f = f \frac{F}{\alpha R_1} (R + h) d\theta \tag{31}$$

where $\alpha = \angle e O_1 s'$ for a given model wedge gap and α is a known constant.

From Equations (30) and (31), the friction power dP_3 generated by the barrel to the rubber element at position θ can be obtained:

$$dP_3 = dF_f v_{bt} = \frac{\pi N F f}{30 \alpha R_1} (R + h)^2 \cos \beta d\theta \tag{32}$$

The power consumption P_3 caused by sliding friction in the whole feeding wedge is:

$$P_3 = \frac{f \pi N F \int_0^{\theta_b} (R + h)^2 \cos \beta d\theta}{30 \alpha R_1} \tag{33}$$

To simplify the integral operation of Equation (33), the average value $\overline{\beta}$ of β is used, that is, $\overline{\beta} = \angle O e O_1 / 2$. For a given model wedge gap, $\angle O e O_1$ is known, and $\overline{\beta}$ and $\cos \overline{\beta}$ are known constants. For example, for the disk rotating squeezing model with $D = 65$ mm, $\angle O e O_1 \approx 9.5°$, $\overline{\beta} = 4.75°$, and $\cos \overline{\beta} \approx 0.9966$. So Equation (34) becomes

$$P_3 = \frac{f \pi N F \cos \overline{\beta} k_3}{30 \alpha R_1} \tag{34}$$

where

$$k_3 = \int_0^{\theta_b} (R + h)^2 d\theta = R^2\theta_b + 2R\left[c \sin\theta_b - \frac{c^2}{2R}\left(\frac{1}{2}\theta_b - \frac{1}{4}\sin 2\theta_b\right)\right]$$
$$+ \left[c^2 * \left(\frac{1}{2}\theta_b + \frac{1}{4}\sin 2\theta_b\right) - \frac{c^3}{3R_1}\sin^3\theta_b + \frac{c^4}{4R_1{}^2}\left(\frac{\sin 4\theta_b}{32} - \frac{\sin 2\theta_b}{4} + \frac{3\theta_b}{8}\right)\right]$$

By combining Equations (24), (27) and (34), the power consumption *P* in the process of the rubber strip passing through the model wedge gap is obtained:

$$P = P_1 + P_2 + P_3 \tag{35}$$

That is:

$$P = \frac{R\theta_b\rho V^3 w^3}{2H^2} + \frac{144\eta V^2 w^3}{H^4}Vw + \frac{f\pi NF \cos\bar{\beta}k_3}{30\alpha R_1} \tag{36}$$

It should be noted that the above mathematical expressions of total squeezing force and power consumption only consider a single disc. However, for an actual cold feed extruder, there are usually at least double-threaded flights at the feed port, and the calculation of the total squeezing pressure and the power consumption needs to multiply the above expressions by the number of flights.

The theoretical analysis model of the feeding process of cold-feed rubber extruders has important guiding significance for analyzing feeding problems and optimizing and innovating feeding structures: (1) the side force applied to the screw and the feeding power consumption can be roughly calculated without a feed roll, which provides basic calculation parameters for rubber extruder design and overcomes the pure experience of feed structure design. (2) The width of the screw flight at the feed screw segment should be as narrow as possible, because the total squeezing force and power consumption are proportional to the third power of the width of the screw flight. However, a screw width that is too narrow can reduce the drag-in force of the screw flight crest so that the rubber strip cannot be dragged through the feed wedge clearance. For a screw flight with a narrower width, shallow grooves can be opened on the top or the side of the screw flight to increase friction drag action, or else the screw flight can be interrupted to increase "penetration" drag action. The latter is often used in the feed screw segment of modern cold-feed extruders. (3) Under the condition of the same feed wedge clearance length, the maximum value (*H*) in the feed wedge clearance should be as large as possible, because the total squeezing force and the power consumption are proportional to the reciprocal of the power of *H*. In other words, a thicker rubber strip should be used for feeding. Therefore, the improvement direction of the structure of the feed wedge clearance was to increase the eccentricity values *a* and *b* and select the appropriate eccentric arc radius *R*. This design can shorten the feeding time and improve the feeding efficiency. (4) Because the power consumption mainly depends on the frictional resistance of the barrel to the rubber strip (see Section 5), the inner wall of the barrel should have a lower friction coefficient at the feed port; that is, the inner wall of the barrel should be smoother than it has been in previous designs. (5) If the feed wedge clearance, feed screw flight, and feed barrel are fully optimized, the effect of feed roll can be reduced or even rendered unnecessary, and the feeding power consumption can be further decreased.

4. Materials and Methods

4.1. Experiment and Materials

The pressure and power data obtained by using the disc rotation squeezing model device (Figure 11) were chosen. Test device: this model device comprises disc 2 driven by motor 1, semicylinder 4 with an eccentric undercut groove on the inner surface, pressure sensor 5, and a control system (which is not shown in the figure). The top surface of the disc, and the inner wall of the groove under the semicylindrical feed wedge clearance 6 and 7, using feeding rubber strips. The disc and drive device are supported by bracket 3. The DJYZ-10 cylindrical pressure sensors were installed in the upper (U), middle (M), and lower

(L) positions of the semicylinder, and were used to measure the pressures of the rubber strip through the feed wedge clearance. The pressure sensor had a measurement range of 0–500 kg and a nonlinearity of 0.3–0.5%. The pressure and power data were automatically calculated, recorded, and stored by upper computer software. The disc speed was changed by a variable frequency speed-regulating motor. The temperature of the laboratory was set at 23 ± 2 °C. The geometric parameters of the model device are shown in Table 1.
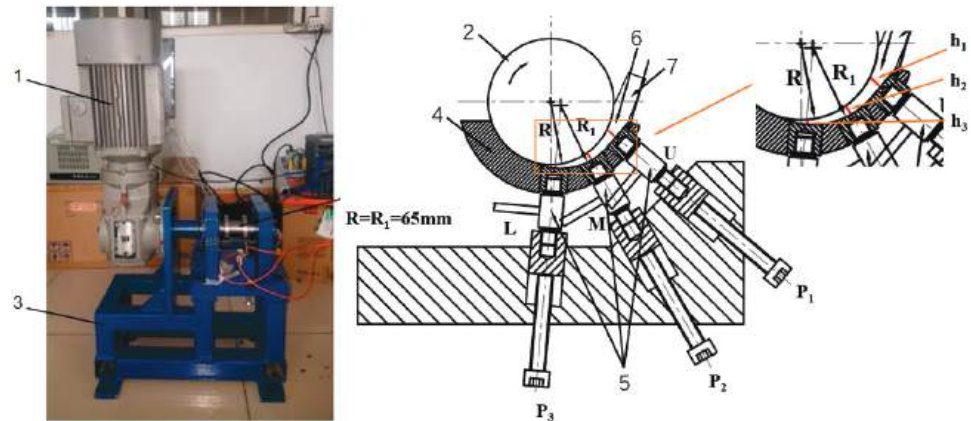
Figure 11. Disc rotation squeezing model device. (1) Motor; (2) disc; (3) bracket; (4) semicylinder; (5) pressure sensor; (6) feed wedge clearance; (7) rubber strip.

Table 1. Geometric parameters of the model device used in this experiment.

D (mm)	w (mm)	R (mm)	R_1 (mm)	a (mm)	b (mm)	H (mm)	θ_0 (°)
65	10	32.5	32.5	2	5	5.4	85

Test materials: truck radial tire compound, ruck tire inner liner compound (TTI) ((51 ML1 + 4 (100 °C); the Mooney viscosity of the rubber obtained by testing at 100 °C is 51), truck tire sidewall compound (TTS) (55 ML1 + 4 (100 °C)), and truck tire tread compound (TTT) (65 ML1 + 4 (100 °C)), provided by Shandong Anchi Tire Co., Ltd. The size of the feeding rubber strip was approximately 5.4 (thick) × 65 (width) × 100 (length) mm.

Test method: rotation squeezing tests were carried out at room temperature using the above three kinds of rubber compounds to measure the pressure distribution and power consumption of the feed wedge clearance under different disc speeds (30, 45, and 60 rpm).

4.2. Measurements of Viscosity and the Sliding Friction Coefficient

The shear viscosity and sliding friction coefficient of the above three compounds at room temperature are two physical parameters required by the theoretical model. These two parameters must be measured.

(1)   Viscosity

Due to the high viscosity of the rubber compound, it was necessary to use a parallel plate plastometer to measure the shear viscosity. The model of parallel plate plastometer used is the MZ-4014. The measurement was made at 23 ± 2 °C. The measurement principle is that, under a given temperature, for a squeezing flow with constant volume, the shear viscosity η can be calculated with the following formula using applied load F_N, load time t, measured sample heights of h_0 and h before and after the load F_N, and measured sample volume V_r [47]:

$$\frac{F_N t}{3\eta V_r} = \left(\frac{1}{h} - \frac{1}{h_0}\right) + \frac{V_r}{8\pi}\left(\frac{1}{h^4} - \frac{1}{h_0^4}\right) \tag{37}$$

The sample was a cylindrical sample with a diameter of 16 mm and a thickness of 3 mm. The applied load was 49 N, and the applied load time was 60 s. For the above three rubber compounds, the shear viscosity values obtained by calculation are shown in Table 2.

Table 2. Viscosity values of different rubber compounds at room temperature.

Rubber Compound	TTI	TTS	TTT
Viscosity (MPa·s)	0.24	0.22	0.21

Since the temperature changes from 23 °C to 50 °C during the experiment in previous studies, the viscosity corresponding to the temperature change can calculate according to the theoretical formula.

(2) Sliding friction coefficient

The sliding friction coefficient of the rubber compounds at room temperature was measured by Anton Paar TRB^3, and the measurement was made at 23 ± 2 °C. To obtain the approximate value of the sliding friction coefficient between the rubber strip and the inner wall of the barrel, the measured linear speed was made close to the linear speed of the disc rotation squeezing model, and the unit area pressure applied to the test metal element close to the average pressure in the disc rotation squeezing model. The test metal element material is Q235-A. The values of the sliding friction coefficient obtained by measurement are shown in Table 3.

Table 3. Sliding friction coefficients of different rubber compounds at room temperature.

Rubber Compound	TTI	TTS	TTT
Sliding friction coefficient *	1.0 ± 0.015	0.9 ± 0.01	1.0 ± 0.021

* Average approximation at different disc speeds (30, 45, and 60 rpm) in a disc rotation squeezing model with D = 65 mm.

5. Results and Discussion

(1) Pressure distribution

In Section 2.2, according to Equation (6), the average squeezing velocity V of the model device in Table 1 at N = 30, 45, and 60 rpm was -11.4, -17.1, and -22.8 mm·s^{-1}, respectively. In Figure 11, the $h_1(= H)$, h_2, and h_3 of the design wedge gap at the different positions of the pressure sensor installed in the upper (U), middle (M), and lower (L) sections were 5.4, 4.7, and 2.6 mm, respectively.

The w value in Table 1, the η value of different rubber compounds in Table 2, the V value at different disc speeds, and the h value at different positions were substituted into Equation (12) ($\overline{p} = \eta V w^2 / h^3$) to obtain the pressure distributions of different rubber compounds at different disc speeds. Figure 12 shows the pressure distribution of TTI, TTS, and TTT at N = 30 rpm. Figure 13 shows the pressure changes of TTI, TTS, and TTT in the position of $h_2 = 4.7$ mm at different disc speeds.

Figure 12 shows that, under a given disc speed, for different kinds of rubber strips, both theoretical prediction and experimental data had approximate pressure distribution curves, and the increase in pressure with the decrease in h in the region of large h was much slower than that in the region of small h, because $\overline{p}$ was proportional to the reciprocal of the third power of h (Equation (12)). However, except for the start position of squeezing $h_1(= H)$, the difference between the theoretical predicted pressure and the experimental value is 0.5–2 Mpa. This is the result of two main factors: average squeezing velocity V and viscosity η. In the initial stage of squeezing, V is greater than the instantaneous squeezing velocity $\dot{h}$ (Figure 5), and the theoretical pressure obtained using Equation (12) is higher than the test data. In the middle and end stages of squeezing, V is less than $\dot{h}$ (Figure 5), and there are also obvious shear thinning and viscous heat generation effects. Although

the pressure in the last two stages was calculated by using V, which was smaller than $\dot{h}$, the original viscosity data were larger, and the viscosity decrease caused by shear thinning and viscous heat generation was not considered; therefore, the theoretical prediction pressure was higher than that attained in the experimental data.

(a) TTI **(b)** TTS **(c)** TTT
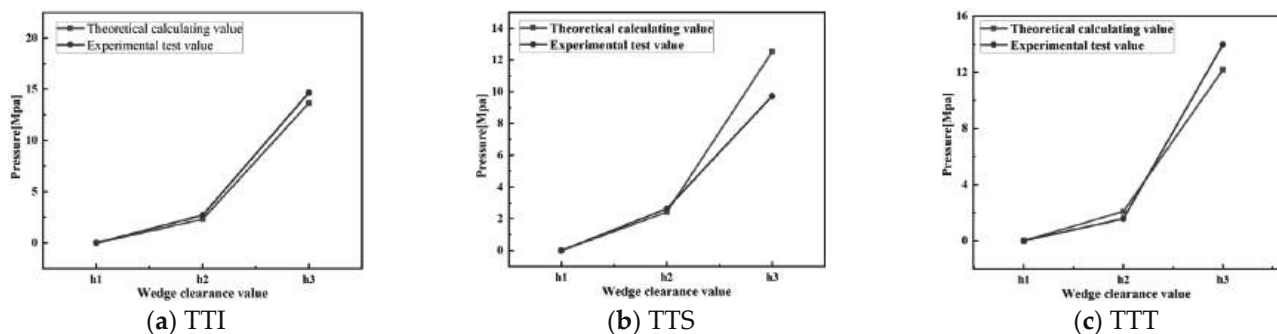
Figure 12. Comparison of calculated and experimental pressure distributions for TTI, TTS, and TTT at 30 rpm of the disc.

(a) TTI **(b)** TTS **(c)** TTT
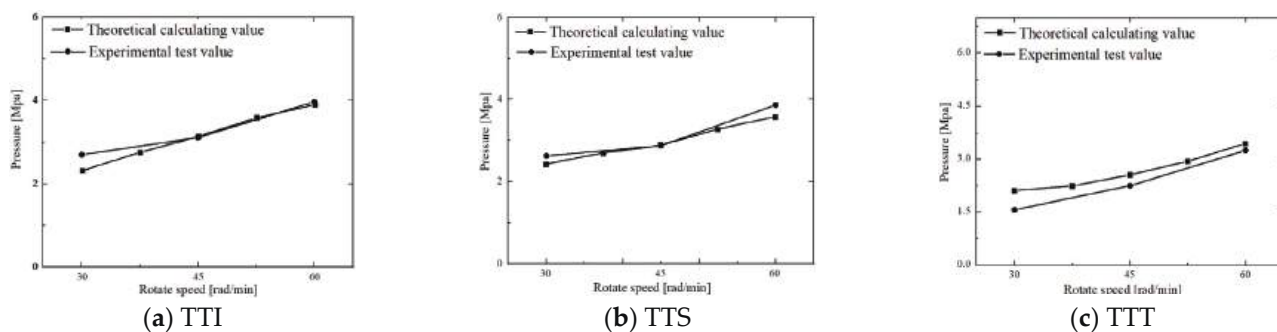
Figure 13. Comparison of calculated and experimental pressure changes of h2 = 4.7 mm for TTI, TTS, and TTT at different disc speeds.

Figure 13 shows that both pressures obtained by theoretical calculation and experimental measurement increase almost linearly with increasing disc speed; the reason for this phenomenon is that $\overline{p}$ is proportional to the disc speed (Equations (6) and (13)). Additionally, the difference between theoretical pressure and the experimental value is about 0.05–0.52 Mpa. However, Figure 13 also shows that the theoretical value was greater than the experimental data, and the difference increased significantly with increasing N. This is because the position of $h_2 = 4.7$ mm occurs in the middle stage of squeezing. With the increase in disc speed N, the effects of shear thinning and viscous heat generation caused by the increase in shear rate (Equation (27)) increase. It has been reported in the literature [3] that the temperature of the squeezed TTI rubber compound is approximately 27 °C higher than room temperature when the disc rotation squeezing model test for TTI strips was carried out under $N = 60$ rpm without cooling the disc and the semicylinder.

(2)   Power consumption

The density of the rubber compound is approximately 1.5×10^3 kg·m^{-3}. The relevant parameter values were substituted into Equation (37) to obtain the power consumptions of P1, P2, and P3 for the TTI, TTS, and TTT at different disc speeds. The range of P1 is 1.8×10^{-6}~1.5×10^{-5} W, P2 is 2.5~13 W, and P3 is 200~900 W. Compared with P3, P1 and P2 were small and negligible. In other words, during the feeding process, the power consumption of the strip through the feed wedge clearance mainly comes from the sliding friction of the strip along the barrel. This conclusion is of great significance for the feed structure design of a cold-feed extruder.

Figure 14 shows the comparison of the calculated power (P3) and experimental power for TTI, TTS, and TTT at different disc speeds.
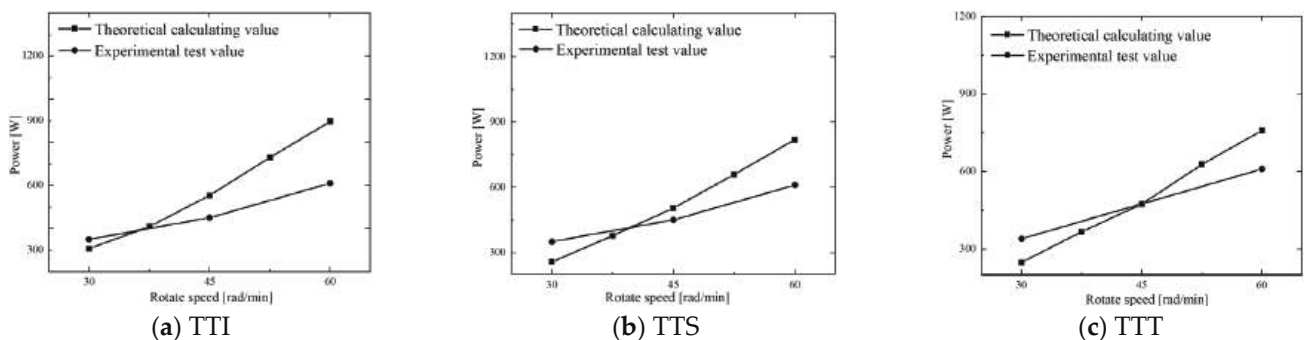
Figure 14. Comparison of calculated and experimental power consumptions for TTI, TTS, and TTT at different disc speeds.

Figure 14 shows that the power consumption obtained by theoretical calculation and by experimental measurement increased linearly with increasing disc speed, and the former increased faster than the latter. The difference between the theoretical predicted pressure and the experimental value is about 40–200 W. Moreover, from the data comparison, it was found that the theoretical value is almost greater than the experimental value. This is mainly because the large viscosity data were used for the calculation of the total squeezing force without considering the significant decrease in viscosity caused by shear thinning and viscous heat generation, especially in the middle and end stages of the feeding process at a high disc speeds. In other words, during the test, with the increase in disc speed, the decrease in rubber viscosity would make the squeezing force small, eventually resulting in a decrease in power consumption. However, in the theoretical calculation, a constant and high value of rubber viscosity was used, so the theoretical value of the power consumption was greater than its experimental value.

However, in the actual feeding process of the cold feed extruder, due to the cooling of the screw and the feed barrel, the temperature rise in the rubber compound in the feed wedge clearance would be greatly limited. The effect of the decrease in viscosity caused by the temperature rise would be smaller, and the viscosity decrease mainly arises due to the contribution of shear thinning. This would increase the measured values of the pressure and power consumption, and lessen the difference between the theoretical prediction and the experimental data.

Therefore, for the feeding process of a cold feeding rubber extruder, the piecewise change in the squeezing velocity, shear thinning, viscous heat generation, and heat transfer must be considered if we are to develop a more accurate mathematical model. Since the Deborah number of the rubber compound passing through the feed wedge clearance at a high screw speed is probably large, feeding analysis theory should also consider the elastic response of the rubber compound [23,44,48].

6. Conclusions

This paper offered a theoretical analysis of the feeding process of rubber strips passing through a feed wedge clearance in a cold-feed extruder. First, by simplifying the screw flight rotation squeezing process into a disc rotation squeezing process, the instantaneous squeezing velocity $\dot{h}(t)$ in the disc rotation squeezing model was derived according to the feed wedge clearance geometry and the disc rotating speed. The $h - t$ curve comprised two general parts: a constant acceleration squeeze in the early stage and a constant velocity squeeze in the later stage. To simplify the theoretical analysis, the squeezing process of the whole feed wedge clearance was regarded as constant velocity squeezing, and the average squeezing velocity V was used to replace the instantaneous squeezing velocity $\dot{h}$. Second, by transforming rotation squeezing into differential slab squeezing, mathematical

expressions of the velocity distribution, pressure distribution, total squeezing force, and power consumption in the process of the rubber strip passing through the model wedge were derived; this analysis utilized the rectangular coordinate system under isothermal and quasi-steady assumptions and certain boundary conditions by using balance equations and the Newtonian viscous constitutive relation. Third, the shear viscosity and sliding friction coefficient of three kinds of rubber compounds were measured at room temperature and under conditions close to the actual feeding process by using a parallel plate plastometer and a CSM Anton Paar TRB[3]. The measured shear viscosity and sliding friction coefficient were substituted into the theoretical formulas to compare the theoretical prediction with previous experimental data. The comparison of pressure distribution and power consumption showed that the established theoretical model of the feeding process of cold-feed rubber extruders was not very accurate, on a quantitative level; however, it might reflect the main factors that affect the feeding process, and can reveal the main trends in feeding behavior. It was also noted that the piecewise change of the squeezing velocity, shear thinning, viscous heat generation, and heat transfer must be considered in a more accurate mathematical model, and the elastic response of the rubber compound should also be considered at a high screw speeds.

References

1. Schöppner, V.; Schadomsky, M.; Hopmann, C.; Lemke, F. Investigations of the mixing behaviour of pin-type rubber extruders. *AIP Conf. Proc.* **2016**, *1713*, 130003-1–130003-5. [CrossRef]
2. Lewandowski, A.; Wilczyński, K. Modeling of Twin Screw Extrusion of Polymeric Materials. *Polymers* **2022**, *2*, 274. [CrossRef] [PubMed]
3. Francis, P.J.J.; Joseph, R.; George, K.E. Significance of Feeding Rate in the Extrusion of Filled and Gum IIR Vulcanizates. *Int. J. Polym. Mater. Polym. Biomater.* **1997**, *38*, 65–78. [CrossRef]
4. Water, H. Schiesser and Zürich, Apparatus for Automatic Uniform Drawing-in of Elastomeric Material into Worm Extruders. U.S. Patent 4,286,882, 1 September 1981.
5. Yanchang, L.; Fang, Y.; Chong, M.; Zhenglin, H.; Guangyi, L. Feeding Behaviour of Cold-Feed Rubber Extruders. *Polym. Mater. Sci. Eng.* **2020**, *36*, 103–108.
6. Jianbin, L.; Liangwei, F.; Jinbo, Z.; Shejun, D. Study on the Conveying Capacity of Feed Section of Rubber Cold Feeding extruder. *Rubber/Plast. Technol. Equip.* **1984**, *4*, 13–21.
7. Limper, A.; Schramm, D. Process Description for the Extrusion of Rubber Compounds-Development and Evaluation of a Screw Design Software. *Macromol. Mater. Eng.* **2002**, *287*, 824–835. [CrossRef]
8. Alan, N. *Gent, Engineering with Rubber*, 3rd ed.; Hanser Publishers: Munich, Germany, 2012; p. 18. [CrossRef]
9. Raymond, L.C. Extruder for Elastomeric Material. U.S. Patent 4,718,770, 12 January 1988.
10. Gerd, C.L. Method of Maintaining the Force of a Stripper Blade on an Extruder Feed Roller Constant and an Apparatus therefor. U.S. Patent 5,068,069, 26 November 1991.
11. Baiyuan, L.; Yanchang, L.; Penzhen, L.; Dianrui, Z. Study on the influence of feeding method on extrusion process of rubber cold feeding extruder. *Rubber Technol. Equip.* **1999**, *25*, 1–6.
12. John, L.R. Leakage-free Feed Roll Assembly for an Extruder Machine. U.S. Patent 7, 160, 099B2, 7 February 2007.
13. Thomas, J.O. Extruder Feed Section with Pivotable Feed Roll Assembly. U.S. Patent 8, 496, 463B2, 30 July 2013.
14. Brand, W. Apparatus to Control Feed of Material to an Extruder. U.S. Patent 3,785,527, 15 January 1974.
15. Ernest, S. Ulm, Feed Control Mechanism. U.S. Patent 3,858,857, 7 January 1975.
16. Anders, D. Method of and Apparatus for the Controlled Feeding of Quantity of Material into the Intake Opeening of an Extruder for Processing Rubber or Plastics Material. U.S. Patent 4,247,272, 27 October 1981.
17. Winther, G.; Almdal, K.; Kramer, O. Determination of polymer melt viscosity by squeezing flow with constant plate velocity. *J. Non-Newtonian Fluid Mech.* **1991**, *39*, 119–136. [CrossRef]

18. Tashtoush, B.; Tahat, M.; Probert, D. Heat transfers and radial flows via a visous fluid squeezed between two parallel disks. *Appl. Energy* **2001**, *68*, 275–288. [CrossRef]

19. Debbaut, B. Non-isothermal and viscoelastic effects in the squeeze flow between infinite plates. *J. Non-Newton. Fluid Mech.* **2001**, *98*, 15–31. [CrossRef]

20. Phan-Thien, N.; Tanner, R. Lubrication squeeze-film theory for the oldroyd-b fluid. *J. Non-Newton. Fluid Mech.* **1984**, *14*, 327–335. [CrossRef]

21. Phan-Thien, N.; Dudek, J.; Boger, D.; Tirtaatmadja, V. Squeeze film flow of ideal elastic liquids. *J. Non-Newton. Fluid Mech.* **1985**, *18*, 227–254. [CrossRef]

22. Gartling, D.K.; Phan-Thien, N. A numerical simulation of a plastic fluid in a parallel-plate plastometer. *J. Non-Newton. Fluid Mech.* **1984**, *14*, 347–360. [CrossRef]

23. Phan-Thien, N.; Sugeng, F.; Tanner, R. The squeeze-film flow of a viscoelastic fluid. *J. Non-Newt. Fluid Mech.* **1987**, *24*, 97–119. [CrossRef]

24. Lee, S.; Denn, M.; Crochet, M.; Metzner, A.; Riggins, G. Compressive flow between parallel disks: II. oscillatory behavior of viscoelastic materials under a constant load. *J. Non-Newton. Fluid Mech.* **1984**, *14*, 301–325. [CrossRef]

25. Lipscomb, G.; Denn, M. Flow of bingham fluids in complex geometries. *J. Non-Newton. Fluid Mech.* **1984**, *14*, 337–346. [CrossRef]

26. Kompani, M.; Venerus, D.C. Equibiaxial extensional flow of polymer melts via lubricated squeezing flow. I. Experimental analysis. *Rheol. Acta* **2000**, *39*, 444–451. [CrossRef]

27. Venerus, D.C.; Kompani, M.; Bernstein, B. Equibiaxial extensional flow of polymer melts via lubricated squeezing flow. II. Flow modeling. *Rheol. Acta* **2000**, *39*, 574–582. [CrossRef]

28. Jackson, J.D. A study of squeezing flow. *Flow Turbul. Combust.* **1963**, *11*, 148–152. [CrossRef]

29. Smyrnaios, D.; Tsamopoulos, J. Squeeze flow of Bingham plastics. *J. Non-Newton. Fluid Mech.* **2001**, *100*, 165–189. [CrossRef]

30. Alexandrou, A.N.; Florides, G.C.; Georgiou, G.C. Squeeze Flow of Semi-Solid Slurries. *Solid State Phenom.* **2012**, *193*, 103–115. [CrossRef]

31. Muravleva, L. Squeeze plane flow of viscoplastic Bingham material. *J. Non-Newton. Fluid Mech.* **2015**, *220*, 148–161. [CrossRef]

32. Muravleva, L. Axisymmetric squeeze flow of a viscoplastic Bingham medium. *J. Non-Newton. Fluid Mech.* **2017**, *249*, 97–120. [CrossRef]

33. Muravleva, L. Squeeze flow of Bingham, Casson and Herschel-Bulkley fluids with yield slip at the wall by accelerated augmented Lagrangian method. *J. Non-Newton. Fluid Mech.* **2020**, *282*, 104320. [CrossRef]

34. Fusi, L.; Farina, A.; Rosso, F. Planar squeeze flow of a bingham fluid. *J. Non-Newton. Fluid Mech.* **2015**, *225*, 1–9. [CrossRef]

35. Fusi, L.; Farina, A.; Rosso, F. Squeeze flow of a Bingham-type fluid with elastic core. *Int. J. Non-Newton. Fluid Mech.* **2016**, *78*, 59–65. [CrossRef]

36. Sherwood, J.; Durban, D. Squeeze flow of a power-law viscoplastic solid. *J. Non-Newton. Fluid Mech.* **1996**, *62*, 35–54. [CrossRef]

37. Sherwood, J.; Durban, D. Squeeze-flow of a Herschel–Bulkley fluid. *J. Non-Newton. Fluid Mech.* **1998**, *77*, 115–121. [CrossRef]

38. Adams, M.; Aydin, I.; Briscoe, B.; Sinha, S. A finite element analysis of the squeeze flow of an elasto-viscoplastic paste material. *J. Non-Newton. Fluid Mech.* **1997**, *71*, 41–57. [CrossRef]

39. Lawal, A.; Kalyon, D.M. Squeezing flow of viscoplastic fluids subject to wall slip. *Polym. Eng. Sci.* **1998**, *38*, 1793–1804. [CrossRef]

40. Muravleva, L. Axisymmetric squeeze flow of a Casson medium. *J. Non-Newton. Fluid Mech.* **2019**, *267*, 35–50. [CrossRef]

41. Kaushik, P.; Mondal, P.K.; Chakraborty, S. Flow dynamics of a viscoelastic fluid squeezed and extruded between two parallel plates. *J. Non-Newton. Fluid Mech.* **2016**, *227*, 56–64. [CrossRef]

42. Phan-Thien, N. Sliding and squeezing flow of a viscoelastic fluid in a wedge. *Math. Und. Phys.* **1990**, *41*, 431–440. [CrossRef]

43. Oliver, D.R. The influence of fluid inertia, viscosity and extra stress on the load bearing capacity of a squeeze film of oil. *Appl. Sci. Res.* **1979**, *35*, 217–235. [CrossRef]

44. Engmann, J.; Servais, C.; Burbidge, A.S. Squeeze flow theory and applications to rheometry: A review. *J. Non-Newton. Fluid Mech.* **2005**, *132*, 1–27. [CrossRef]

45. McClelland, M.A.; Finlayson, B.A. Squeezing flow of elastic liquids. *J. Non-Newton. Fluid Mech.* **1983**, *13*, 181–201. [CrossRef]

46. Dienes, G.J.; Klemm, H.F. Theory and Application of the Parallel Plate Plastometer. *J. Appl. Phys.* **1946**, *17*, 458–471. [CrossRef]

47. Gent, A.N. Theory of the parallel plate viscometer. *Br. J. Appl. Phys.* **1960**, *11*, 85–87. [CrossRef]

48. Grimm, R.J. Squeezing flows of polymeric liquids. *AIChE J.* **1978**, *24*, 427–439. [CrossRef]

In Situ Thermoset Cure Sensing: A Review of Correlation Methods

Molly Hall [ID]**, Xuesen Zeng *, Tristan Shelley** [ID] **and Peter Schubel**

Centre for Future Materials, University of Southern Queensland, Toowoomba, QLD 4350, Australia; molly.hall@usq.edu.au (M.H.); tristan.shelley@usq.edu.au (T.S.); peter.schubel@usq.edu.au (P.S.)
* Correspondence: xuesen.zeng@usq.edu.au

Abstract: Thermoset polymer composites have increased in use across multiple industries, with recent applications consisting of high-complexity and large-scale parts. As applications expand, the emphasis on accurate process-monitoring techniques has increased, with a variety of in situ cure-monitoring sensors being investigated by various research teams. To date, a wide range of data analysis techniques have been used to correlate data collected from thermocouple, dielectric, ultrasonic, and fibre-optic sensors to information on the material cure state. The methods used in existing publications have not been explicitly differentiated between, nor have they been directly compared. This paper provides a critical review of the different data collection and cure state correlation methods for these sensor types. The review includes details of the relevant sensor configurations and governing equations, material combinations, data verification techniques, identified potential research gaps, and areas of improvement. A wide range of both qualitative and quantitative analysis methods are discussed for each sensing technology. Critical analysis is provided on the capability and limitations of these methods to directly identify cure state information for the materials under investigation. This paper aims to provide the reader with sufficient background on available analysis techniques to assist in selecting the most appropriate method for the application.

Keywords: composite manufacturing; thermosetting polymers; cure behaviour; process monitoring; in situ cure monitoring; sensors

1. Introduction

Advanced thermoset polymer composites are implemented in a variety of industries, such as in civil [1,2] and energy [3–5] and in recreational and naval marine applications [6–10] as well as in performance automobiles [11,12] and in aerospace applications [13–15]. The adoption of thermoset materials has increased in recent years due to the tailorability of part properties and wide variety of manufacturing techniques and achievable geometries. Thermosets can be formed as unreinforced plastics or reinforced composites via injection and compression moulding [16] and resin infusion [17] or using automated laydown techniques [18]. The parts must then go through a cure cycle, commonly under elevated temperature and/or pressure conditions, such as in an as autoclave or oven [19,20]. Recently, research on fibre-reinforced polymer (FRP) composites has trended towards the development of high-quality parts that are up to tens of metres long [21] and more than 2 cm thick [22], with emphasis on optimising the processing conditions when making these complex parts [23].

Composite parts are susceptible to a variety of quality issues, such as fibre displacements, voids and porosity, geometric deformations, and inconsistent chemical reactions or polymerisations [24]. These final-part variations are frequently a result of manufacturing uncertainty stemming from either variation in the raw materials or in the processing conditions and environment [25]. In advanced composite applications, it is a critical quality objective to achieve a specified resin cure state, as the completion of the polymer conversion

process is directly linked to the mechanical performance of the final product [26]. To capture the effects of this variability, it becomes necessary to monitor the cure process for each individual part.

The final cure state of a thermoset part is typically evaluated using either a quantifiable degree of cure, specified as a percentage of the chemical reaction that has been completed, or by reaching a threshold value for the glass transition temperature (T_g) [27,28]. The degree of reaction or polymerisation can be analysed off-line, where testing is conducted externally to the manufacturing process, or in-line, where a sensor is integrated directly into the manufacturing process and captures live data [29]. The advantages of the in-line or in situ monitoring of composite processing are the ability to monitor the process in real time [30] and the potential to actively control the process as it occurs [31,32]. Further, some major limitations of off-line cure evaluation are that it may require destructive testing, cannot perfectly replicate the process conditions during part of the cure, and cannot be used to update the process conditions in real time.

This paper will briefly review the established off-line cure-monitoring techniques such as Dynamic Scanning Calorimetry (DSC), Dynamic Mechanical Analysis (DMA), and Dynamic Rheometry. A deeper evaluation of direct sensing technologies for in-line curing is then presented, specifically of thermocouple, dielectric, ultrasonic, and fibre-optic sensors. Extensive reviews have been completed regarding the capabilities and limitations of these sensors for composite process and cure monitoring [33,34]; however, a critical review of the correlation methods of these techniques has not been carried out to date. Each type of sensor monitors different parameters, and data analysis must be conducted to convert these parameters into information pertaining to the material cure state, with an example of the data flow and analysis procedure being shown in Figure 1. In this paper, a critical review of correlation processes for four in-line sensing technologies is presented. Special focus has been placed on the specific sensor type and material configuration, the results of the correlation analysis, and how the analysis has been verified for accuracy. The technologies are then evaluated for how effectively they monitor composite cure processes and how appropriate they may be for high-performance applications.
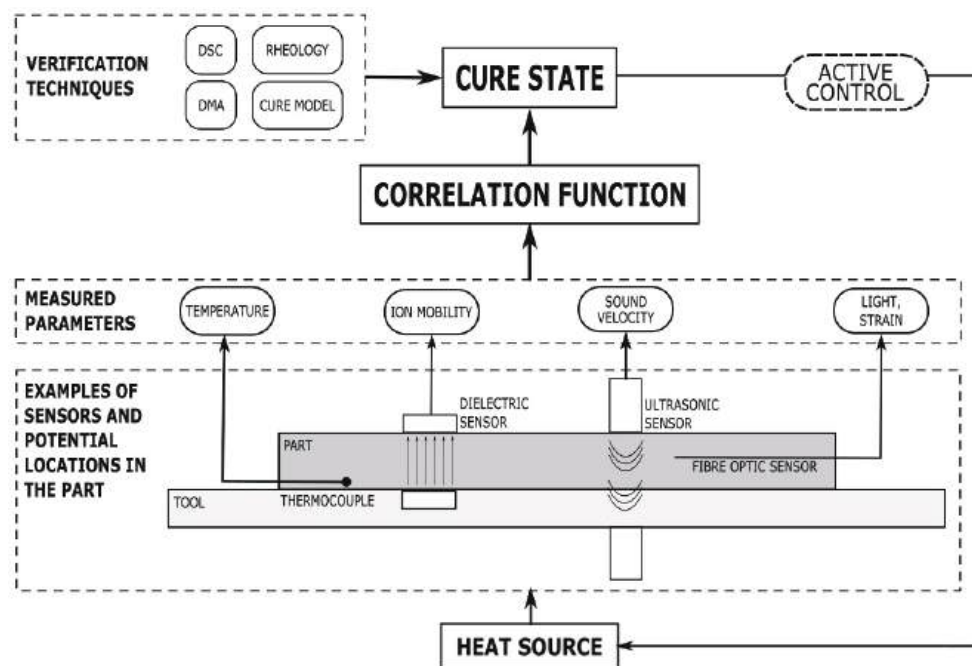
Figure 1. An overview of types of cure sensors, their placement, measured parameters, and verification techniques. The data flow process for an active control system is also proposed, with the sensors being correlated to cure state information during live processing, which can subsequently be used to actively alter the processing conditions.

2. Off-Line Cure Analysis

Off-line cure analysis techniques are frequently used to characterise new material systems or as a quality control evaluation of an existing cured part. Material characterisation enables researchers to build a model of the material that can then be used in process simulations. For example, a research team characterised Hexcel RTM6 using DSC [35] and rheometric [36] analysis to develop a kinetic and a chemosviscosity model of the tested epoxy. Three common off-line analysis techniques are discussed here, including their governing equations and identification principles for cure state information. Other analysis techniques, such as Fourier Transform Infrared (FTIR) [37] and Raman spectroscopy [38], are used for polymer analysis; these will not be discussed further.

2.1. Dynamic Scanning Calorimetry (DSC)

DSC measures heat flow in a sample when it is subjected to isothermal or non-isothermal temperature conditions. By integrating the peak of the heat flow (H) versus the time curve and dividing it by the total heat of reaction (H_R), we can calculate the degree of cure (α), as shown in Equation (1).

$$\alpha = \frac{\int_0^t H dt}{H_R} \tag{1}$$

There is an extensive amount of literature on the use of DSC to characterise cure reactions [39–42], and the procedure for kinetic parameter determination is detailed in standards such as ASTM E 2070, which contains methods for kinetic parameters by differential scanning calorimetry using isothermal methods [43]. DSC can also be used to measure thermoset cure reactions [44] and to calculate the degree of cure of an existing cured part. The residual heat of reaction can be measured for a cured sample, which allows for the calculation of the actual degree of cure of the part based on a known total heat of reaction for the material. DSC analysis is used to validate the results of new sensing technologies and will be mentioned throughout this paper as one of the main verification techniques.

2.2. Dynamic Mechanical Analysis (DMA)

The DMA of composite parts utilises a dual cantilever beam configuration in which a sample is oscillated at a set frequency through a set temperature range. The elastic modulus is evaluated throughout the test; specifically, the storage modulus (E') component, the loss modulus component (E''), and the *tanδ*, which is calculated as the ratio of the loss to the storage moduli, are considered. The main output of a DMA test is the T_g, which is calculated as the midpoint of the drop in the storage modulus. ASTM D 7028, which provides methods for T_g determination in Polymer Matrix Composites via DMA [45] details the process for the calculation of T_g by identifying the intersection of the tangent lines around the drop in E', as shown in Figure 2.
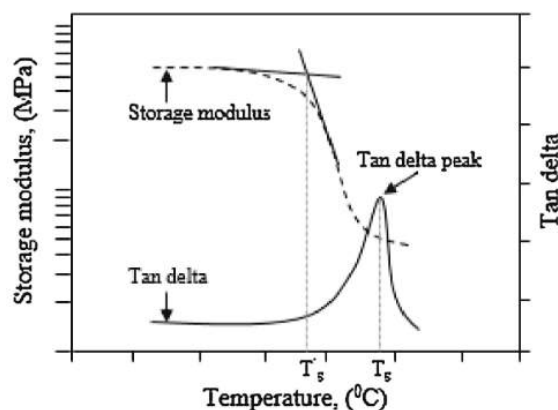
Figure 2. Graphic of the calculation of T_g using an E' modulus curve (**left-hand axis**) and *tanδ* curve (**right-hand axis**) from a DMA test. Reprinted with permission from Ref. [46]. 2016, Elsevier.

DMA has been used to identify the cure state of many materials, such as phenolics [47] and epoxies [48]. Such as with DSC, DMA testing is used throughout this paper to verify the T_g calculations of the in-line sensing techniques.

2.3. Dynamic Rheometry

The dynamic rheometry of thermoset composites typically occurs in a parallel-plate oscillating configuration, with the purposes of monitoring the change in the shear modulus under a set temperature range. Like DMA, rheometric testing evaluates the shear storage modulus (G'), the loss modulus (G''), and $tan\delta$, which is once again the ratio of loss to the storage moduli. From these values, the complex viscosity (η^*) can be calculated by Equation (2) using the complex modulus (G^*) and oscillating frequency (ω):

$$\eta^* = \frac{G^*}{\omega} \tag{2}$$

While this does not specifically relate to the final cure state of a thermoset polymer, resin viscosity can be a critical parameter during processing.

Regarding the cure state, the gel point can be defined in multiple ways in accordance with the rules of ASTM D 7750, which contains methods for evaluating cure behaviour of thermosetting resins [49], an example of which is displayed in Figure 3. Depending on the interactions of fibre and resin, the gel point can be defined as the intersection of G' and G'', the peak of G'', the peak of $tan\delta$, a sudden rapid increase in G', or a sudden drop in $tan\delta$.
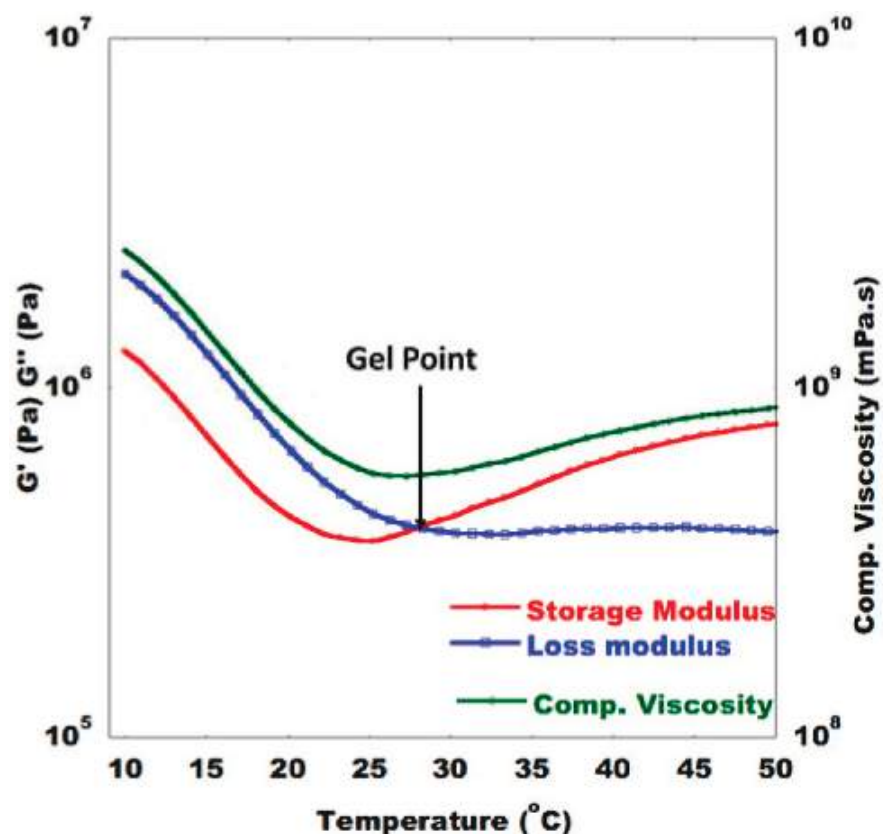
Figure 3. Example of how gel time can be determined by identifying where G' and G'' cross. Reprinted with permission from Ref. [50]. 2019, Elsevier.

The main challenge of rheometric cure monitoring is that during the crosslinking and solidification process, the viscosity trends towards infinite, so later step cure stages cannot be monitored. Despite this, rheometry has been used to evaluate viscosity and

cure progression for several thermoset polymers [42,51] and is also used as a verification technique for the sensors discussed in this paper.

3. In-Line Cure Monitoring Sensor Correlations

3.1. Thermocouple Sensors

3.1.1. Sensor Background and Governing Equations

There are a variety of sensors that are capable of monitoring the thermal properties of composite cure processing, including thermocouples (TCs), infrared thermographers (IRT) [52], heat flux sensors [22], and resistance temperature detectors (RTDs) [53]. While this paper specifically focuses on thermocouples, alternative temperature sensors have been reviewed [29], including details on their functionality, capabilities, and limitations.

Temperature is one of the most common parameters to measure during composite processing, as the time–temperature–transformation relationship of thermosetting polymers is well established [54], and most thermoset resins are cured under the application of a specific heating cycle [55]. Temperature monitoring of both the environmental conditions, for example, the oven or autoclave air temperature, and the material of choice is extremely important. Most composite processes include an air TC to account for environmental uncertainty, such as the natural fluctuations in the equipment over time. Additionally, the actual temperature experienced by the part is critical for cure monitoring, as many thermoset polymers tend to experience exothermic events, or a temperature increases due to the release of heat energy during the chemical reaction. Material uncertainties such as slight variations in the raw material; the initial degree of cure; and the material age, storage conditions, and resin content can all impact the likelihood and peak temperature of an exotherm [25]. For this reason, simply monitoring the equipment temperature may not be sufficient to identify and predict the exact temperature profile that the part is experiencing. Thermocouples are commonly placed in one or more representative locations: in the part, on or in the tool, and in the air, to monitor the environmental conditions. These locations and an overview of the parameter's monitoring process is shown in Figure 4.
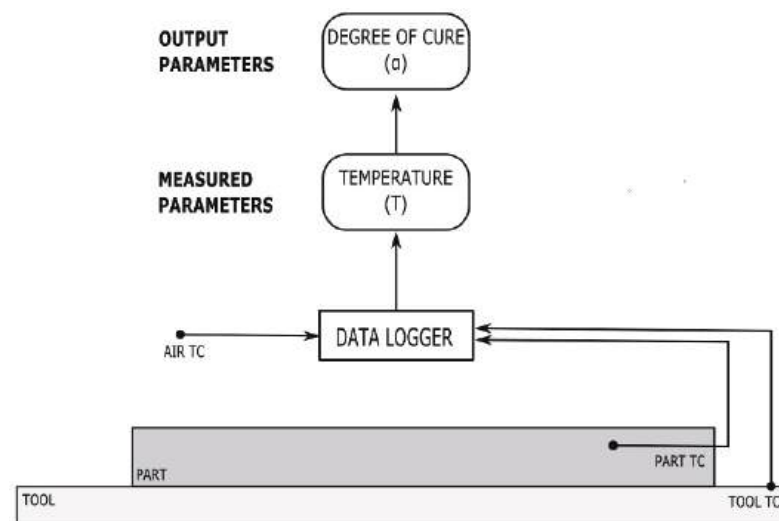
Figure 4. An overview of thermocouple placements and the data collection process flow.

Thermocouples comprise two different metal wires with known Seebeck voltages, which are welded or twisted into a junction at one end and separated at the other. The monitoring temperature (T_m) at the welded junction can be calculated using Equation (3) using the Seebeck coefficient (S), measured voltage (V), and reference temperature at the open junction (T_r).

$$T_m = \frac{V}{S} + T_r \qquad (3)$$

This equation is used to reliably calculate the temperature being experienced by the material in question. Using this temperature profile, the material properties can then be predicted according to the methods detailed in the following section.

3.1.2. Correlation Functions

An overwhelming amount of literature exists on the use of thermocouples and temperature devices to monitor the progression of thermoset cure. For example, TCs and IRTs have been used to monitor temperature distributions and exotherms of carbon fibre–epoxy composites and other polymers [56,57] and to monitor part cure as a method to validate simulation results [22]. Thermocouples are used to monitor processing and part temperatures in most composite cure studies, including in almost every paper mentioned in this review, due to their fundamental nature.

The most reliable method of directly correlating the measured temperature to the material degree of cure (α) is by evaluating the thermo-kinetic model of the material, which roughly follows the formula in Equation (4):

$$\frac{d\alpha}{dt} = K(T)f(\alpha) \tag{4}$$

in which $\frac{d\alpha}{dt}$ indicates the change in the degree of cure with respect to time, the component $K(T)$ represents the temperature dependency component, and $f(\alpha)$ represents the reaction model component. $K(T)$ follows an Arrhenius dependence and can be calculated using Equation (5) using the pre-exponential factor (A), activation energy (E), universal gas constant (R), and the temperature:

$$K(T) = Ae^{\frac{-E}{RT}} \tag{5}$$

The reaction model component, $f(\alpha)$, is specific to the material in question. Many reaction models have been proposed, with a comprehensive overview published by Yousefi et al. [44]. Examples include a simple nth-order rate equation [58], the autocatalytic model [59], or model-free kinetic analysis [60]. While some models can be broadly applied to material classes such as epoxies or polyesters, it is also best to conduct a kinetic analysis of each specific material component to increase the accuracy of the results.

In practice, the temperature profile of a composite part can be verified against the kinetic model or against a simulation that incorporates the kinetic model [61]. Once the temperature profile is verified to produce an acceptable degree of cure, it is typical to simply verify that the temperature parameters are met for each process cycle. For applications that may not have the capacity, need, or interest in completing such a process verification, it is common to follow the manufacturers' recommended cure cycle as found in the technical data sheet for most commercial thermosets or for composite materials, such as for Solvay Cycom® 5320-1 Prepreg [62]. The material manufacturer typically specifies one or more recommended cure cycles that will ensure that the part reaches a fully cured state. In this case, a temperature reading is taken from a representative location that is either in or on the part, on the tool, or elsewhere in the oven. The main verification method for quality control is to check the temperature as a function of time compared to the recommended cure cycle requirements, as shown in Figure 5, rather than to calculate a specific degree of cure for each individual part. This quality control step ensures that the cured material meets the minimum threshold for mechanical performance, as the required engineering properties can only be met in fully cured parts [63]. It should be noted that the definition of "fully cured" varies based on the specific material and application.
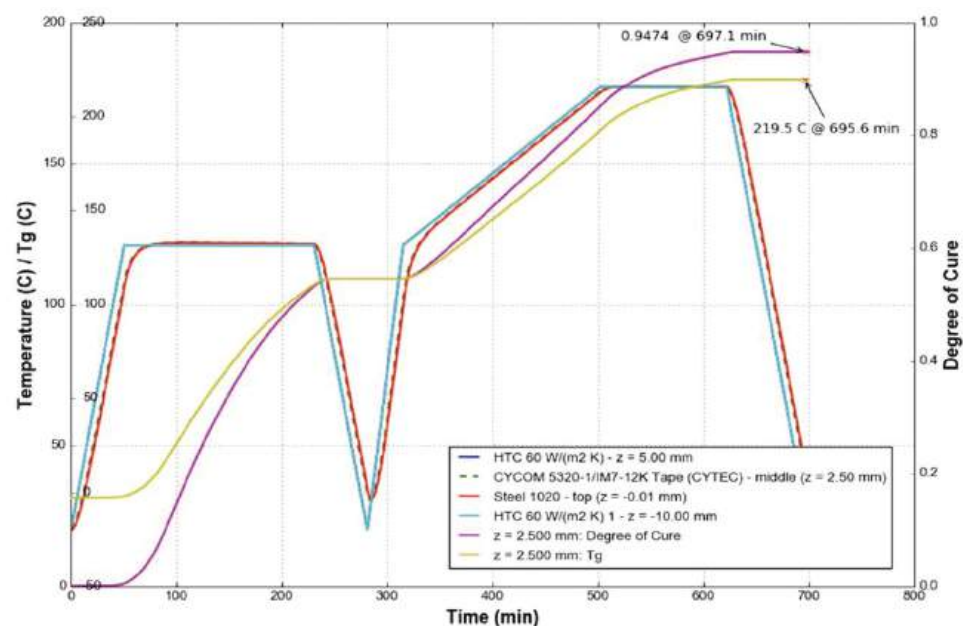
Figure 5. An example of the manufacturer's recommended cure cycle for Cycom® 5320-1 Prepreg and it's resultant predicted final properties (degree of cure and T_g).

3.1.3. Summary and Future Work

Thermocouples are the most common and widely used sensing technology for composite curing and process monitoring. They monitor not only the cure state, which is measured as the degree of cure, but are also able to monitor other critical process events such as temperature overshoots caused by exothermic events. Additionally, they are frequently required to be used in coordination with other sensing devices, such as those detailed in the below sections, to normalise for temperature effects [64,65] or as a supplemental monitoring technique for data collection. Thermocouples have also been used to monitor resin filling for infusion processes [66] and are commonly used to monitor temperature applications during process optimisation activities [23,67,68]. A major challenge of thermocouples is that to directly measure the material state, they must be embedded into the part, and some applications (such as those which require specific surface finishes) are unable to accept embedded sensors.

3.2. Dielectric Sensors

3.2.1. Sensor Background and Governing Equations

In recent decades, dielectric sensors have been investigated as a new method of in situ cure monitoring for thermoset composite materials due to their versatility and range of available configurations, both when purchased off the shelf and when custom-designed. The three most common types of dielectric sensors are parallel-plate, interdigital, and tool-mounted. Each of these has benefits and limitations, which have been discussed in depth elsewhere [33,34]. For example, parallel-plate dielectrics can detect through-thickness measurements that would otherwise require interdigital sensors to be embedded throughout the thickness of a part. Interdigital and tool-mounted sensors only take measurements of the surface that they are directly in contact with; however, interdigital sensors are commonly used invasively, making them less optimal for industries with stringent quality requirements.

Dielectric sensors work on the principle of monitoring dipole and ion movement within a material under a time-varying electric field (*E*). The alignment and relaxation of the charged particles within the sample are monitored by the sensor in the form of a capacitive (*C*) and resistive (*R*) response [69]. These values are used to calculate the dielectric parameters to be referenced throughout this paper. Thermoset curing can be

evaluated using these parameters due to the time-, temperature-, and frequency-dependent response of the dielectric sensor. The dielectric sensor captures the change in ion mobility, which directly relates to the cure state of the material as it crosslinks. It should be noted that some of the variable representations in this paper may differ from the cited sources to maintain the consistency of the variable meanings used in the following governing equations and correlations.

Permittivity (ε') is calculated in Equation (6) using capacitance, electrode spacing (L), the electrode area (A), and the permittivity of free space ($\varepsilon_0 = 8.854 \times 10^{-12}$ F/m), as derived from [70]:

$$\varepsilon' = \frac{CL}{\varepsilon_0 A} \tag{6}$$

Dielectric loss (ε'') is calculated in Equation (7) using resistance, the electrical excitation frequency (ω), electrode spacing and area, and the permittivity of free space, as derived from [70]:

$$\varepsilon'' = \frac{L}{R\omega A\varepsilon_0} \tag{7}$$

Impedance (Z) is calculated in Equation (8) with the resistance, excitation frequency, and conductance, with j as the imaginary component [71]:

$$Z = \frac{1}{\frac{1}{R} + j\omega C} \tag{8}$$

Ion conductivity (σ), which is related to the inverse relationship of ion viscosity and frequency-independent resistivity (ρ), is calculated in Equation (9) using resistance, electrode spacing, and electrode area [71]:

$$\rho = \frac{1}{\sigma} = \frac{RA}{L} \tag{9}$$

The dissipation factor (D), also known as *tanδ*, can be calculated in Equation (10) using the permittivity and dielectric loss or the resistance, capacitance, and excitation frequency [72]:

$$D = \tan\delta = \frac{\varepsilon''}{\varepsilon'} = \frac{1}{\omega RC} \tag{10}$$

While the dielectric response provides a great deal of information, it does not directly relate to information about the cure state of a thermoset polymer. A correlation function is needed to relate the dielectric properties to the state of the chemical reaction, specifically the degree of cure and glass transition temperature. The data may be interpreted qualitatively by evaluating artefacts from a graph or quantitatively by deriving equations. The data must also be corroborated using techniques that are currently known to provide insight into the cure state of a thermoset polymer: typically thermochemical or rheometric testing. Examples of these methods are provided in the following section, with an overview shown in Figure 6.

3.2.2. Correlation Functions

There are many methods for correlating dielectric signals with the degree of chemical reaction that has occurred in the resin or composite. Common methods and their variants will be discussed in this section, including the correlation functions and the supplemental testing techniques.

Dielectric Loss Correlation

Fournier et al. [73] used a dielectric loss correlation through their work evaluating neat epoxy resin using parallel-plate dielectric sensors. The dielectric loss factor (ε''), which can be calculated from Equation (7), was used to predict vitrification by identifying the time of maximum loss for each experimental frequency. Dielectric loss correlations have

also been used to identify the gel point and have been verified through comparison to rheology data [74]. Using neat RTM6 epoxy monitored by a tool-mounted dielectric sensor, the glass transition temperature was determined as the local maximum of the dielectric loss graph. Additionally, the crossover point between the permittivity and dielectric loss can be demonstrated to indicate the gel point. This has been correlated to rheology test data and specifically to the crossover point of the storage modulus and the loss modulus, G' and G'', as seen in Figure 7.
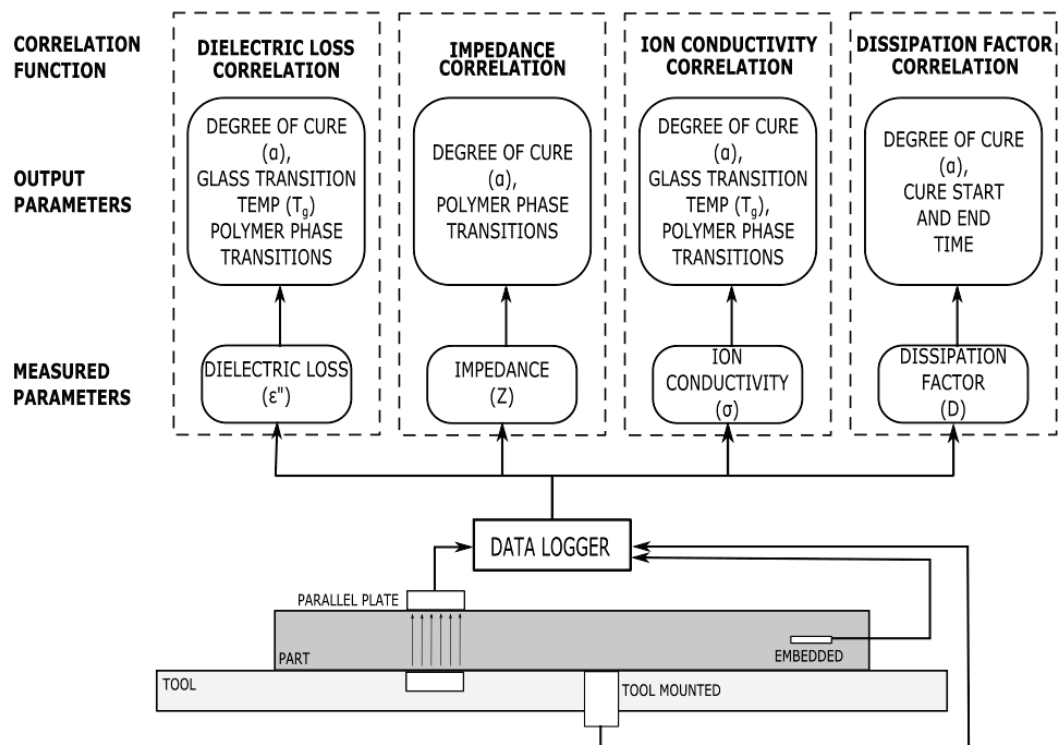
Figure 6. An overview of dielectric sensor correlation methods, including a visual depiction of the types of dielectric sensor, the parameters they measure, and how the parameters are converted into cure information.
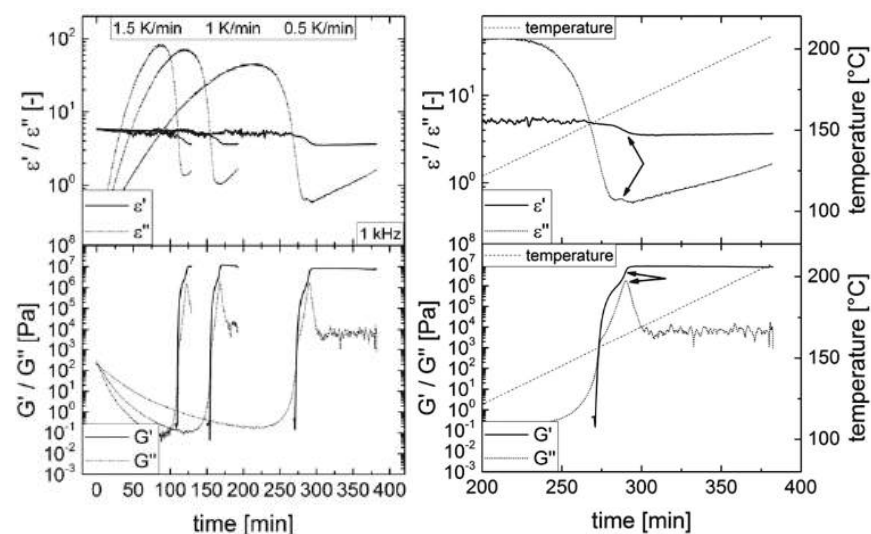
Figure 7. Comparison of dielectric loss to rheological storage and loss as a method to identify T_g (as identified by arrows in the right-hand image). Reprinted with permission from Ref. [74] 2018, John Wiley and Sons.

From a quantitative perspective, Hardis et al. proposed an equation for the degree of cure based on the progression of dielectric loss during the cure of an epoxy monitored with parallel-plate dielectrics [75]. The equation for degree of cure (α) with respect to time is stated in Equation (11):

$$\alpha(t) = \frac{\log \varepsilon_0'' - \log \varepsilon_t''}{\log \varepsilon_0'' - \log \varepsilon_\infty''} \tag{11}$$

where the subscripts ε'' represent the dielectric loss at start of cure (ε_0''), at time t (ε_t''), and at cure completion (ε_∞''). The degree of cure generated from this equation aligned well with degree of cure measurements determined from DSC and Raman spectroscopy.

Impedance Correlation

Mijovic et al. used an impedance correlation to calculate the resistivity of a sample based on the monitored impedance signal (Z) calculated in Equation (8). Impedance was used to calculate resistivity (ρ), and then boundary conditions were evaluated to derive Equation (12) for the degree of cure [71,76]:

$$\frac{\alpha}{\alpha_m} = \frac{\log \rho - \log \rho_o}{\log \rho_m - \log \rho_o} \tag{12}$$

in which α_m represents the maximum degree of cure, and ρ_0 and ρ_∞ represent the initial and maximum values of resistivity. The cure progression of neat epoxies was evaluated using this function, and graphs of the degree of cure versus time were compared successfully to those produced by HPLC and FTIR analysis, as shown in Figure 8. Further, the vitrification point was identified at the onset of the second step on the graph showing imaginary impedance (Z'') versus time, and this point was successfully correlated to the storage modulus (G'') peak from the corresponding rheological data.
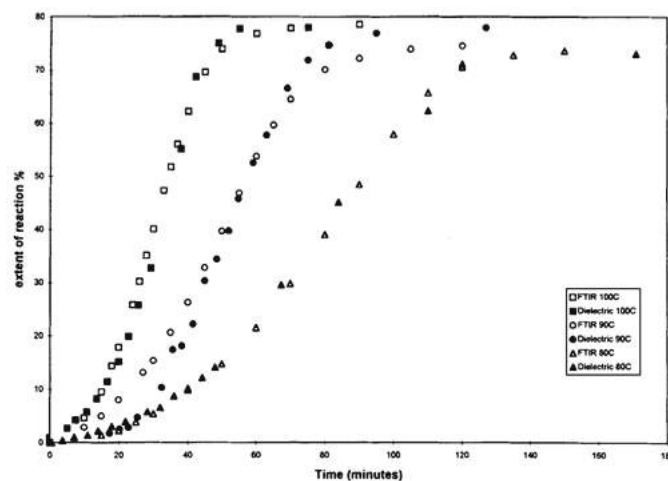
Figure 8. Comparison of degree of cure between dielectric and FTIR analysis represented as the extent of reaction (%) versus time (minutes), with curves indicated at various temperatures. Reprinted with permission from Ref. [76] 2003, John Wiley and Sons.

This method has recently been used for determining the vitrification point of an RTM6 epoxy reinforced with carbon fibre [77,78]. In this method, the imaginary impedance (Z''), a component of Equation (8), is evaluated across multiple frequencies to eliminate the impact of the constant phase element, the second term of Equation (13):

$$Z'' = \frac{\omega C R^2}{1 + \omega^2 C^2 R^2} + \frac{2}{(A_e \omega)^n} \tag{13}$$

in which A_e and n are coefficients of the constant phase element. The first term of Equation (13) provides Z_m'', or the material impedance, and a plot such as the one in Figure 9 has been overlaid on a graph of degree of cure derived from the material cure model. This qualitative comparison shows similar trends between the term Z_m'' and the degree of cure. Furthermore, the second step or shoulder region on the graph of Z_m'' versus time indicates the vitrification point. Studies by this research group were conducted using both a customized woven sensor for the cure monitoring and a lineal sensor for the flow monitoring of the resin infusion process. Interestingly, the lineal sensor configuration was also able to produce a cure signal that was reasonably similar to that produced by the cure sensor [78].
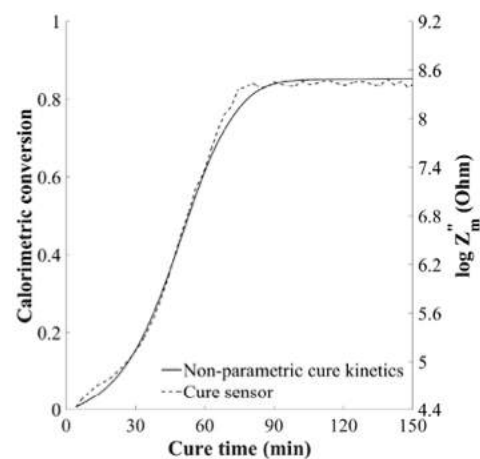
Figure 9. Comparison between Z_m'' and degree of cure generated from cure kinetics model [77].

Similarly, evaluating the frequency spectra of the imaginary impedance has been used to draw a direct correlation to the degree of cure [79]. By applying linear regression to the graph of degree of cure versus $\log(Z''_{max})$ at temperature T, the c coefficients in Equation (14) can be determined:

$$\log Z''_{max} = (c_{11} + c_{12}T)\alpha + c_2 \tag{14}$$

This equation was used to successfully model an isothermal cure cycle of RTM6 epoxy using an interdigitated dielectric sensor and a degree of cure prediction from the cure kinetics model. Figure 10 shows a comparison of this model to the experimental data of Z''. Furthermore, a non-isothermal cure was shown to fit the model quite closely, although with slightly more errors in the progression of the model.
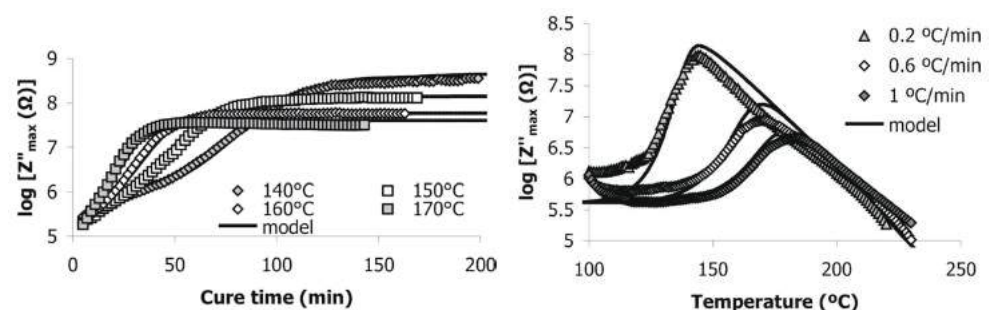
Figure 10. Comparison of experimental values of Z'' with the proposed model for Z'' for an isothermal cure (**left**) and a non-isothermal cure (**right**). Reprinted with permission from Ref. [79] 2005, Elsevier.

Ion Conductivity Correlation

Ion conductivity correlations have been used the most frequently due to the connection of ion conductivity, and therefore ion viscosity, to the bulk polymer viscosity. In this section,

various approaches are used based on whether the ion conductivity or ion viscosity, which is also known as the polymer resistivity (ρ), are being monitored.

Starting with ion conductivity, McIlhagger et al. determined the T_g of an epoxy matrix reinforced by both glass and carbon fibres using signals generated from parallel-plate dielectric sensors [53,80]. The derivative of the log of the ionic conductivity, known as the DLIC, approaches zero as the sample approaches full cure. This cure point has been compared to DMA and DSC results in addition to being verified by tension and flexure mechanical performance tests to identify the peak of material performance, which occurs at full cure [80]. Additional critical points have been determined using a plot of the ionic conductivity. The maximum conductivity occurs at the point of minimum resin viscosity, which can be a critical point for out-of-autoclave and resin infusion processing, and as seen in Figure 11, the minimum point of DLIC indicates the onset of gelation [53]. McIlhagger et al. determined the minimum viscosity, gel point, and point of full cure with the data corroborated using DMA and DSC testing [53].
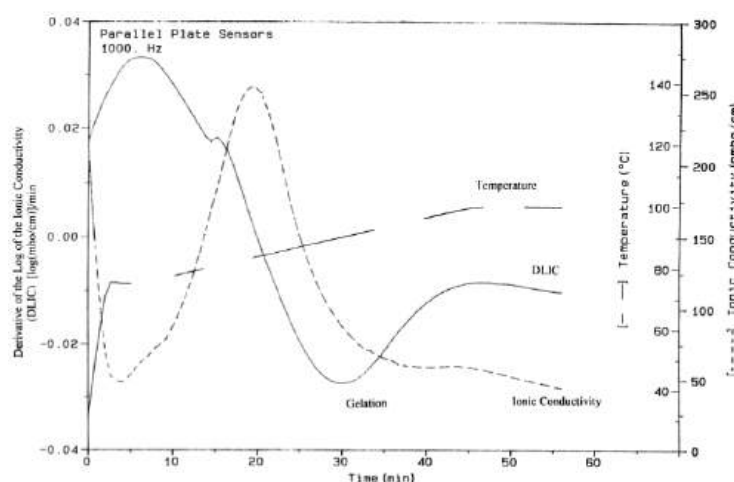
Figure 11. Gel point indicated on a DLIC curve. Reprinted with permission from Ref. [53] 2000, Elsevier.

This correlation method has also been employed elsewhere, specifically in assigning the maximum value of ionic conductivity to the point of minimum polymer viscosity, the inflection point of the LIC after the peak viscosity relating to the onset of gel, and the maximum of dielectric loss corresponding to the onset of vitrification [56,81,82].

Yang et al. proposed Equation (15) as a method to calculate the T_g of an epoxy resin using a miniature interdigital sensor to monitor ionic conductivity:

$$T_g = \frac{\log G_0(T) - \log G(t)}{\log G_0(T) - \log G_\infty(T)} T_{g\infty}(T) \tag{15}$$

where $G_0(T)$ and $G_\infty(T)$ are the temperature-dependent initial and final conductance, $G(t)$ is the time-dependent conductance, and $T_{g\infty}(T)$ is the T_g calculation based on a cure kinetics model [83]. Through this in situ calculation of T_g and use of the DiBenedetto equation, the degree of cure can be calculated as in Equation (16):

$$\alpha = \frac{T_g - T_{g0}}{T_g - \lambda T_g - T_{g0} + \lambda T_{g\infty}} \tag{16}$$

which uses the T_g values calculated from Equation (15) and λ, which is a ratio of the heat capacities as calculated during cure kinetics characterisation. This prediction has indicated a consistent trend, however an error of approximately 5–10% exists when compared with DSC.

Ion viscosity correlations are related to ion conductivity through the inverse relationship $\rho = 1/\sigma$ and is then correlated to polymer viscosity values through Equation (17):

$$\rho = \frac{6\pi\eta r}{q^2 n} \tag{17}$$

which uses polymer viscosity (η), ion particle size (r), ion charge (q), and ion concentration (n) [84]. As the ion viscosity thus has a direct relationship to polymer matrix viscosity, it is possible to understand key information regarding thermoset cure based on our knowledge of viscosity progression.

Boll et al. evaluated a carbon fibre/epoxy composite using a miniature embedded dielectric sensor by estimating that cure completion occurs when ρ reaches a plateau [84]. The cure state was then verified by completing a DSC evaluation of the cured part and by determining the degree of cure from the residual enthalpy. This method was also used by Moghaddam et al. when evaluating the effectiveness of their micro interdigitated sensor compared to current commercial sensors [85].

For a glass–epoxy prepreg monitored with a surface-mounted interdigitated electrode, Park established that the log of the ion viscosity had a linear relation to the cure temperature [86]. This enabled the calculation of Equation (18) for the degree of cure through a derivation of the DiBenedetto equation:

$$\frac{\log\rho - \log\rho_0}{\log\rho_\infty - \log\rho_0} = \frac{T_g - T_{g0}}{T_{g\infty} - T_{g0}} = \frac{\lambda\alpha}{1 - (1 - \lambda)\alpha} \tag{18}$$

in which the subscript 0 indicates the initial condition, and ∞ indicates the fully cured condition. A comparison of the degree of cure calculated from Equation (18) to that derived from DSC and FTIR analysis is shown in Figure 12, with the DEA results being comparable to those of the other methods.
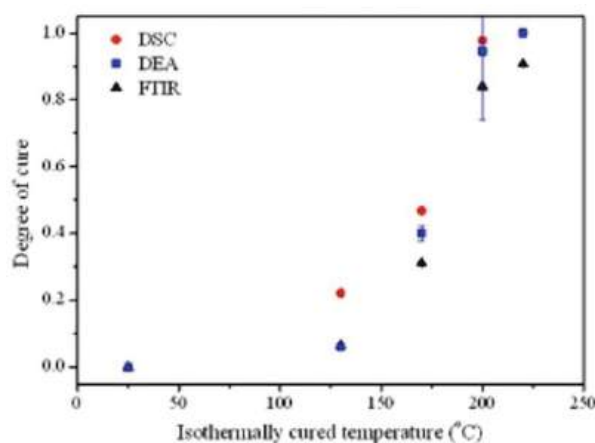
Figure 12. Comparison of degree of cure calculated from dielectric-monitored ion viscosity compared to DSC and FTIR analysis. Reprinted with permission from Ref. [86] 2017, John Wiley and Sons.

A similar equation for degree of cure was calculated from the ion viscosities in accordance with Equation (19):

$$\alpha = \frac{\log\rho - \log\rho_{min}}{\log\rho_{max} - \log\rho_{min}} \tag{19}$$

in which the subscripts indicate the minimum and maximum ion viscosities measured during the cure. Franieck et al. evaluated Equation (19) for a silica-filled epoxy in which cure was monitored using a tool-mounted monotrode dielectric sensor [87]. The results from this analysis were compared to the degree of cure calculated from DSC, with limited success. While the DEA and DSC graphs follow similar trends, the DEA results are limited by the onset of vitrification, where the DSC results appear to better capture conversion

during the diffusion-controlled period of cure. Figure 13 shows the differences in the results, with the DEA-calculated cure index operating on a shorter time scale than the DSC results.
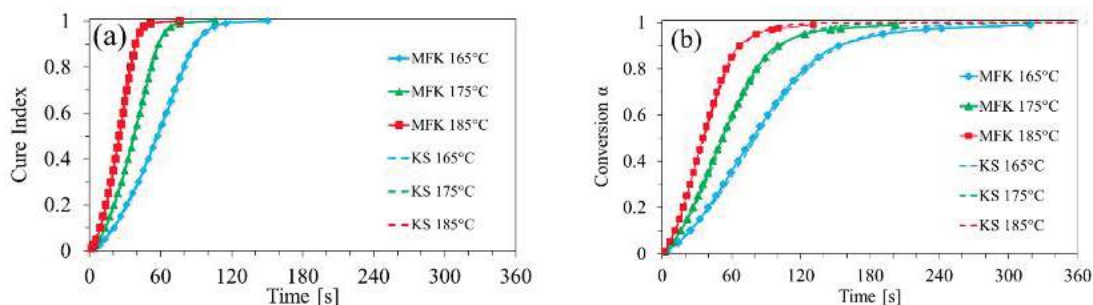
Figure 13. Comparison between cure index derived from DEA (**a**) and conversion derived from DSC (**b**) [87].

Interestingly, Franieck et al. did not limit their investigation into dielectric cure monitoring and instead used the dielectric results to develop a kinetic model. The focus of this paper was to compare both the model-free and model-based kinetic equations derived from dielectric analysis with those derived from DSC results. In this they determined that the dielectric kinetic model aligned with the experimental data; however, as stated previously, the dielectric model and DSC model showed differences around the vitrification point.

Dissipation Factor Correlation

Kim and Lee used a dissipation factor correlation, in which the dissipation factor was normalised for temperature effects, and an equation for the degree of cure was derived [64,88]. An interdigital dielectric sensor was used to monitor the resistance (*R*) and capacitance (*C*) of polyester–fibreglass and epoxy–fibreglass composites. The resistance and capacitance were used to calculate the dissipation factor following Equation (10). As the dissipation factor is a function of both the temperature and degree of cure of the matrix, the elimination of the temperature component will allow for the degree of cure to be calculated. The degree of cure determined from *D* was compared to that of DSC and demonstrated fair accuracy up to a cure level of approximately 70%, as seen in Figure 14.
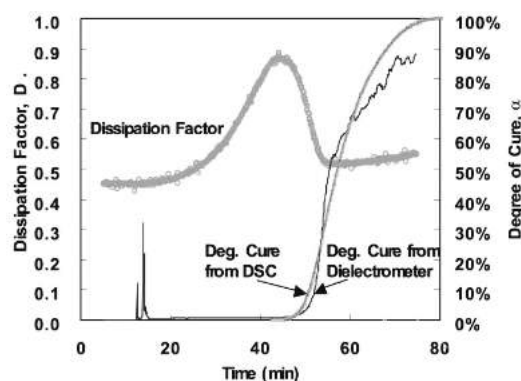
Figure 14. Comparison of degree of cure between dielectric testing and DSC. Reprinted with permission from Ref. [64] 2002, Elsevier.

Using the same method of eliminating the temperature effects, Equation (20) was derived to determine the degree of cure:

$$\alpha = -\frac{1}{s} \log\left[\left(\frac{\log D - \log D_o}{q(T - T_o)} \right) - \frac{p}{q} \right] \qquad (20)$$

in which the material parameters D_o, T_o, p, q, and s can be determined experimentally by following the procedure stated in [88].

Another method for evaluating the dissipation factor was calculated from an interdigital dielectric sensor reading and then used to determine the start and end points of cure for a carbon–epoxy composite [89]. The derivative of the dissipation factor was taken with respect to time, enabling the cure start time to be identified as the maximum of dD/dt, and the cure end time to be identified as $dD/dt = 0$.

3.2.3. Summary and Future Work

Dielectric analysis shows much promise for the in-line cure monitoring of thermoset composites. There are many methods of correlating dielectric data to material transitions, such as the gel and vitrification points, and physical properties, such as T_g and the degree of cure. Currently, a major gap in our understanding of dielectric cure analysis is which of these methods is the most accurate, and whether these methods are consistent with one another. The implementation of each technique may be dependent on the fidelity and specificity of data needed for the application, but up until now, the methods have not been compared to ensure if they can be used agonistically or not.

Aside from the capability of the technology to successfully monitor cure, there is other work to be carried out to successfully implement the technology into a production environment. For example, embedded sensors must not impact the integrity of the surrounding part [56]. One strategy is to use extremely small sensors to minimise the performance impact [84,85]. It has also been noted that a tool-mounted sensor can impact the heat transfer through a composite part depending on the tool's material, which can potentially cause a gradient in the degree of cure [90]. Finally, there are a number of opportunities for dielectric sensors to be used for the flow monitoring of resin-infused composite parts in addition to cure monitoring. A great deal of research has been carried out to show that dielectrics can successfully capture resin arrival during an infusion process [77,78,91]. This suggests that a dielectric sensor could be used to characterise multiple process steps with a single device.

3.3. Ultrasonic Sensors

3.3.1. Sensor Background and Governing Equations

Ultrasonic sensor technology is commonly used for the non-destructive inspection of composite part quality and has only recently been viewed as a potential method of monitoring the cure reaction of a thermoset polymer. The main principle of ultrasonic sensor cure monitoring is that as ultrasonic waves are transmitted through the material, the propagation behaviour of these waves is impacted by the progression of the chemical reaction [92,93]. As the polymer continues to react, the density and elastic behaviour change and thus impact the velocity and attenuation of the sound waves. Multiple wave propagation models have been proposed to understand the polymer cure state [94]. All ultrasonic devices function under these principles; however, there are multiple types of transducer and receiver configurations, which are depicted in Figure 15.

The different sensor types each produce an ultrasonic wave with a measured velocity (v) and attenuation (a) characteristics, the governing equations for which are provided below. It should be noted that in literature, attenuation is commonly represented as alpha (α); however, here, it will be indicated by (a) to differentiate it from the definition of the degree of cure being used throughout this paper.

Longitudinal velocity (c_L) is calculated in Equation (21) using the elastic modulus (E), velocity, and density (ρ) [33]:

$$c_L = \sqrt{\frac{E(1-v)}{\rho(1+v)(1-2v)}}$$
(21)
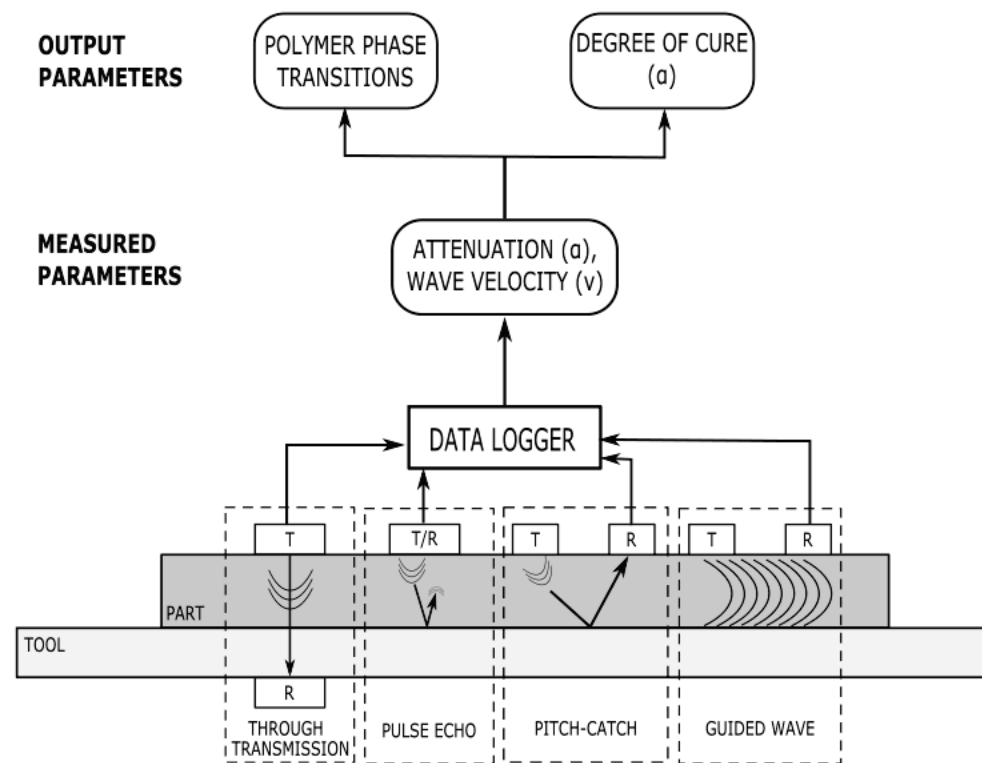
Figure 15. Types of ultrasonic sensors indicating how the ultrasonic waves propagate with the transmitters and receivers. The measurable parameters are linked with the cure parameters.

The shear velocity (c_s) is calculated in Equation (22) using the elastic modulus, density, and velocity [33]:

$$c_S = \sqrt{\frac{E}{2\rho(1+v)}} \tag{22}$$

Attenuation is calculated in Equation (23) using the ratio of the amplitude of the incident wave (A) to the change of amplitude from the incident (ΔA) [33]:

$$a = -\frac{A}{\pi\Delta A} \tag{23}$$

The longitudinal storage modulus (L') is calculated in Equation (24) using the density, longitudinal velocity, attenuation, and wavelength (λ) [95]:

$$L' = \frac{\rho c_L^2 \left(1 - \left(\frac{a\lambda}{2\pi}\right)^2\right)}{\left(1 + \left(\frac{a\lambda}{2\pi}\right)^2\right)^2} \tag{24}$$

The longitudinal bulk modulus (L'') is calculated in Equation (25) using density, longitudinal velocity, attenuation, and wavelength [95]:

$$L'' = \frac{\rho c_L^2 \left(\frac{a\lambda}{2\pi}\right)}{\left(1 + \left(\frac{a\lambda}{2\pi}\right)^2\right)^2} \tag{25}$$

The loss factor, or *tanδ*, is calculated as the ratio of the longitudinal storage and bulk moduli in Equation (26) [96]:

$$\tan\delta = \frac{L'}{L''} \tag{26}$$

Like dielectric cure monitoring, the parameters listed in the governing equations in this section do not correlate directly to information on material state or properties. The following section provides an overview of the correlation functions and analysis techniques that have been demonstrated in the literature to date.

3.3.2. Correlation Functions

Data taken from ultrasonic sensors are commonly interpreted qualitatively, with graphic artefacts indicating polymer phase transitions that appear very similar to a DMA curve. Some varieties of ultrasonic monitoring have been referred to as ultrasonic dynamic mechanical analysis [97]. The sound waves cause molecular movement, which becomes restricted as the material becomes cross-linked. The following section is a summary of the methods that have been used in literature and includes information on the type of ultrasonic transducers and what parameters can be monitored with them.

One of the more comprehensive methods for isolating phase transitions was suggested by Lionetto et al. [97] and has been used to evaluate a polyester resin with through transmission ultrasonic monitoring. In this method, the features of the velocity versus time curve are separated into three segments:

1. Velocity is constant when the resin is liquid, but the reaction is still slow;
2. At the gel point, the velocity begins to increase, and the reaction progresses rapidly;
3. The velocity reaches a plateau at the vitrification point, indicating the slowdown of the reaction.

The distinction between these phases is shown in Figure 16, with the vertical lines indicating the approximate gel point and vitrification point.
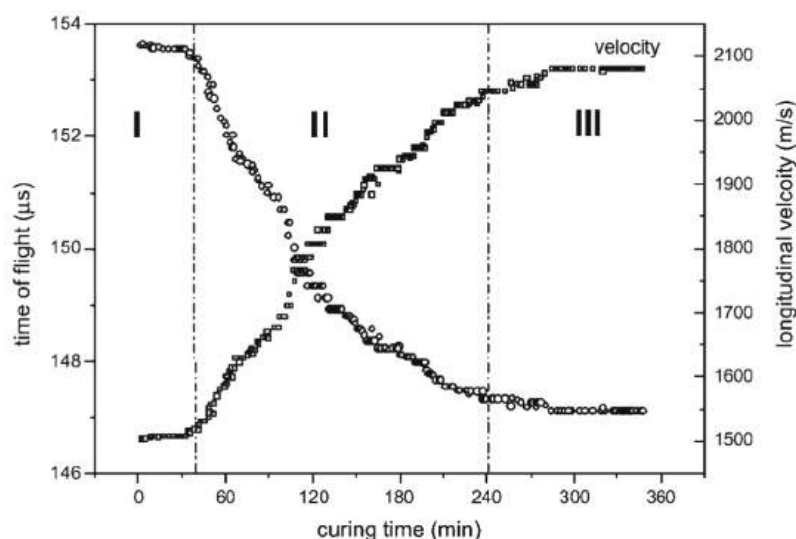
Figure 16. Representation of the three phases of thermoset cure based on the changes in sound velocity. Reprinted with permission from Ref. [98] 2007, John Wiley and Sons.

This method of evaluating cure was also applied to the one-sided air-coupled ultrasound monitoring of polyesters [98,99] and was verified by rheological testing. This viscoelastic interpretation of phase change has also been used for the cure monitoring of epoxies using fibre-optic ultrasound sensors [100].

Ghodhbani et al. [101] used a similar method to identify the different stages of the reaction; however, this was achieved by identifying the key features of the evolution of

the complex's c_{33} viscoelastic coefficient throughout the curing process, with c_{33} being calculated by the following equation, Equation (27):

$$c_{33} = \rho c_L^2 \left(1 + j\frac{2a_L v_L}{\omega}\right) \tag{27}$$

in which ρ is the density, and a_L and v_L are the longitudinal attenuation and velocity. Once c_{33} can be plotted with time, the tangent method can be applied to isolate the three phases of cure:

1.   The liquid viscous stage;
2.   The glass transition stage;
3.   The saturation solid stage.

The transition points of t_{gel} and $t_{saturation}$ are indicated in Figure 17. It should be further noted that the vitrification point can be assigned to the peak of the mechanical loss (δ_m), which also roughly correlates to the inflection point of c_{33}.
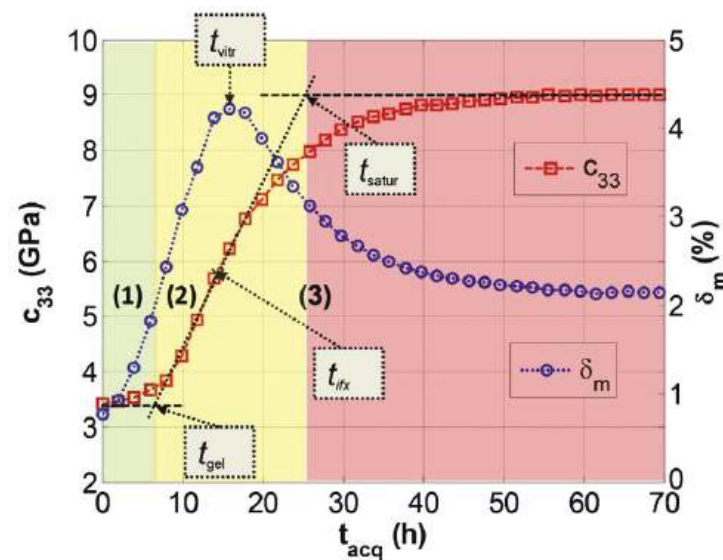
Figure 17. Different stages of the cure reaction based on a tangent evaluation of the complex viscoelastic coefficient, c_{33}. Reprinted with permission from Ref. [101] 2016, Elsevier.

Furthermore, Ghodhbani et al. proposed a degree-of-cure model based on a Weibull distribution model of c_{33}. The equation for the degree of cure is indicated by Equation (28):

$$\alpha(t) = \frac{c_{33}(t) - c_{33,0}}{c_{33,\infty} - c_{33,0}} \tag{28}$$

in which the 0 and ∞ subscripts for c_{33} indicate the initial and maximum values. This model compared to the Kamal chemical reaction model well.

Schmachtenberg et al. measured the sound velocity during the infusion and cure of epoxy-reinforced fibreglass and compared it to the degree of cure calculated off-line using the DSC measurements [102]. The inflection point of the sound velocity curve was correlated to approximately 65% conversion, as shown in Figure 18.

Hudson and Yuan [103] evaluated the cure of epoxy-reinforced carbon fibres using guided-wave ultrasonic monitoring. Specifically, the group velocity of the guided waves was evaluated to determine the correlation to the cure points identified by the Convergent Raven cure simulation program.
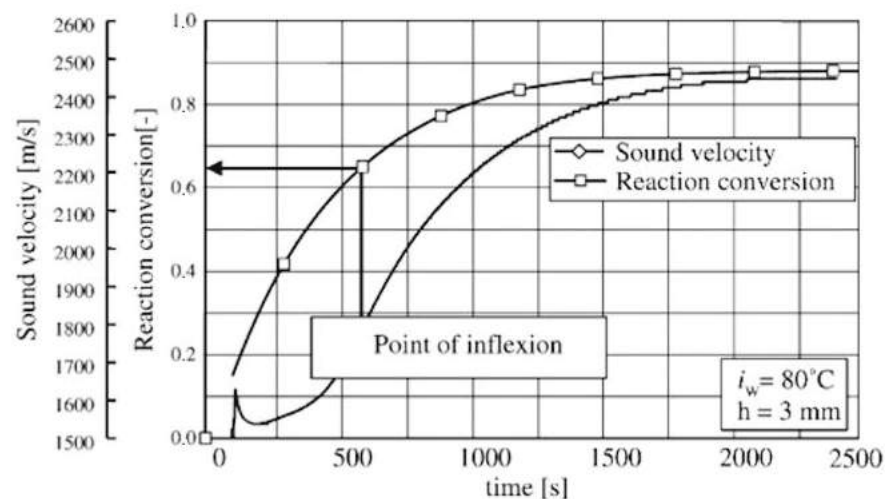
Figure 18. Comparison of degree of cure to the sound velocity of an epoxy-reinforced composite. Reprinted with permission from Ref. [102] 2005, Elsevier.

Samet et al. [104] used attenuation to correlate to material viscosity, which was demonstrated for silicone oils. While the pulse echo configuration was not used with thermoset polymers, the equation for attenuation was shown to correlate to material viscosity, which could be used to monitor the viscosity state of a curing polymer in the future. Finding the peak attenuation has also been used to correlate to the point of vitrification for the through-transmission ultrasonic evaluation of epoxies [105] and polyesters [106].

Maffezzoli et al. [96] used a pulse echo ultrasonic transducer for the process monitoring of a thin sheet of epoxy using the longitudinal velocity and attenuation to calculate the storage and bulk moduli. The loss factor, or *tanδ*, calculated from Equation (26) was then graphed, with the peak value indicating the glass transition.

3.3.3. Summary and Future Work

Ultrasonic cure monitoring may have the potential to identify cure transitions; however, this may not be sufficient for high-performance composite applications. Quality assurance requirements in the aerospace industry, for example, commonly depend on reaching a specific threshold of the degree of cure or T_g, and a statement on phase transitions may be insufficient for implementation. However, ultrasonics have also been demonstrated to potentially be capable of evaluating lingering chemical reactions where dielectrics cannot [107]. In a study comparing ultrasonics, dielectrics, and nuclear magnetic resonance, the ultrasonic sensor continued to detect a response after the vitrification point of the resin where dielectric monitoring showed no activity. This could potentially indicate that ultrasonics are more sensitive, particularly in late-stage chemical reactions.

For non-destructive inspection, ultrasonics have also been demonstrated to be useful in other areas of in-process composite inspection. Scholle and Sinapius [108] demonstrated the use of ultrasonics for the cure monitoring of pultrusion processing. Multiple research groups have demonstrated that ultrasonics can successfully detect the flow front and impregnation [102,109] in addition to monitoring the thickness changes [110,111] that occur during resin infusion processing. Ultrasonics have been embedded directly into rheometric plates to collect simultaneous rheology and ultrasonic data [112]. Finally, evaluations have been conducted to capture the mechanical performance impact of embedded sensors [113]. While many ultrasonic sensors are external to the part, it is critical to understand their functional impact when they are used internally.

3.4. Fibre-Optic Sensors

3.4.1. Sensor Background and Governing Equations

Fibre-optic sensors have gained attention for their use in monitoring residual strain during the thermoset cure process [89,114] and for their capabilities for structural health-monitoring in marine [115,116] and energy (wind turbine) [117] applications. The strain-monitoring capability of fibre-optic sensors has been shown to indicate phase changes during cure [81], and its potential for in situ cure monitoring has been reviewed in [117]. The two main types of optical fibres, those that detect optical properties and those that detect mechanical properties, have been reviewed in [33,34]. An overview of the types of sensing technology and their correlation techniques is show in Figure 19.
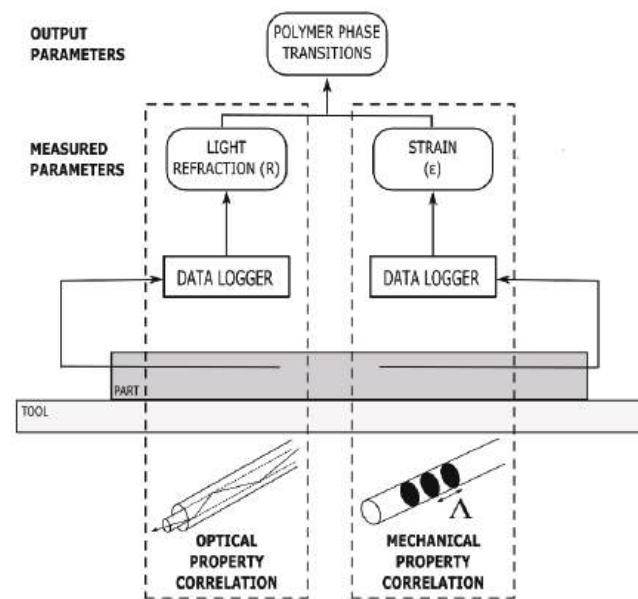
Figure 19. An overview of optical fibre sensing technologies, including their correlation techniques.

Optical fibre refractometers (OFR) utilise a cladded core fibre, in which an open portion of the core is in contact with the composite matrix material. The loss of the incident light signal is monitored based on the reflection coefficient (R_0) calculated using Fresnel's Law in Equation (29), in which n_1 and n_2, which are the refractive indices of the core and cladding, respectively:

$$R_0 = \left(\frac{n_1 - n_2}{n_1 + n_2} \right)^2 \tag{29}$$

The refractive index (*n*) of the material under inspection can then be related to its density (ρ) using the Lorentz–Lorenz Law in Equation (30), in which R_M is the molar refractivity, and *M* is the molar mass of the material:

$$\frac{n^2 - 1}{n^2 + 1} = \frac{R_M}{M} \rho \tag{30}$$

Optical fibre interferometers (OFI), most commonly Fabry–Pérot fibres, monitor the strain imparted to the fibre by identifying the shift in the light wavelength along a series of reflective microsurfaces on the core of the fibre. The most common type of Fabry–Pérot OFI is a fibre Bragg grating (FBG) optical fibre. Under applied strain, the distance (Λ) between these grating changes, which then causes a shift in the Bragg wavelength (λ_B). The initial Bragg wavelength is calculated via Equation (31) using the grating distance and the effective index of the fibre (n_0) [81]:

$$\lambda_B = 2n_o \Lambda \tag{31}$$

The shift in the Bragg wavelength ($\Delta\lambda_B$) can then be calculated by Equation (32) using the initial Bragg wavelength, the strain-optic coefficient (p_e), the change in strain ($\Delta\varepsilon$), the coefficient of thermal expansion (α_{CTE}), the thermo-optic coefficient (ξ), and the change in temperature (ΔT) [118]:

$$\Delta\lambda_B = \lambda_B(1 - p_e)\Delta\varepsilon + \lambda_B(\alpha_{CTE} + \xi)\Delta T \tag{32}$$

Equation (32) is divided into a strain-induced component of the Bragg wavelength shift and a thermal component. The decoupling of these components is an important part of interpreting the wavelength shift, as detailed in the following section, which discusses the correlation techniques for both optical property monitoring and strain monitoring.

3.4.2. Correlation Functions

Optical Property Correlations

Fibres that monitor optical properties such as light intensity or output have been correlated to key cure events. An optical fibre with a section of cladding removed was used to monitor the cure of a bismaleimide (BMI)–carbon fibre prepreg by monitoring the attenuation of the change in light intensity [119]. In this study, the minimum attenuation was attributed to the minimum resin viscosity, the increase was attributed to the crosslinking process, and the final plateau was correlated to the end of the cure reaction, each step of which has been correlated to a numerical model.

A second study [66] used this method to evaluate the reflected light intensity of optical fibre sensors during the cure of a resin-infused carbon fibre–epoxy composite. During the infusion process, it was noted that a sharp drop in the sensor signal corresponded to resin arrival. Regarding cure, the rapid increase in the light intensity was attributed to a solidification and density increase during crosslinking, and the subsequent plateau was correlated to the end of the reaction.

A third study [120] also used this method to evaluate the refractive index of a tilted fibre Bragg grating (TFBG) optical fibre to monitor a UV-cured epoxy. In this case, an initial dip in the refractive index was attributed to the temperature response due to the exothermic reaction of the epoxy. The signal increase and plateau were then attributed to the onset of the reaction and cure completion, respectively. Similarly, an optical fibre was used to monitor the power output due to light signal changes during the cure of an epoxy resin, with the plateau of the power signal indicating the gel point [121]. The gel point was confirmed with rheology measurements.

An alternate method was used to evaluate the reflected light intensity of an FBG sensor during the cure of a graphite–epoxy prepreg [122]. In this study, the rapid increase in the reflected light intensity was also attributed to the viscosity increase due to gel and the solidification of the matrix around the fibre. However, it was noted that as the material continued to crosslink, the increase in peak intensity slows down. It was further suggested that the T_g can be identified as the point where the slope of the best-fit lines for peak intensity changes. In this case, the T_g determination of 95 °C agreed with the material specifications.

Mechanical Property Correlations

Optical fibres can also be used to monitor strain measurements using a variety of methods. The most common interpretation of the cure events follows a similar trend to the interpretation of light signals:

1. An initial dip is observed in the signal due to an increase in temperature, as the resin is still liquid and not transmitting strain to the fibre;
2. An increase in the strain measurement is observed due to the crosslinking reaction;
3. The measurement plateaus at cure completion once the matrix has frozen the fibre into place.

Multiple research groups have identified that the strain signal plateaus once the resin forms a solid matrix. An extrinsic Fabry–Pérot interferometer (EFPI) and a FBG sensor were used to identify that the strain signals level off during the vitrification phase when monitoring cure in a carbon fibre–epoxy laminate [123]. Additionally, FBG has been used to monitor a 3D braided preform infused with epoxy in which the Bragg wavelength shift was observed to plateau as the epoxy solidified [124].

An evaluation of epoxy cure with two varieties of optical fibres, a Fresnel optical fibre and an FBG, correlated with the results of both light and strain monitoring strategies, with a comparison of the results in Figure 20 [125]. The signal of the optical fibre was evaluated using the three-phase evaluation detailed in the previous section, whereas the Bragg wavelength identified the peak value as the onset of gel and the plateau of the signal, indicating cure completion.
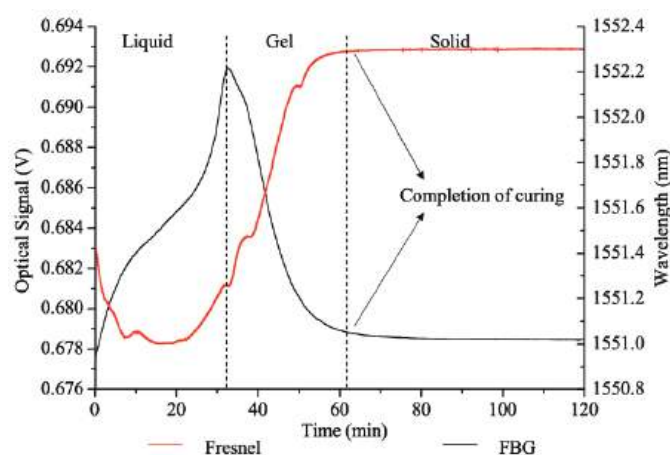
Figure 20. Comparison of cure behaviour for a Fresnel optical fibre sensor signal and the Bragg wavelength from an FBG signal [125].

A dual-period fibre Bragg grating and long-period grating (LPG) were used to monitor RTM6 epoxy cure by isolating the thermal and strain components of the Bragg wavelength shift [65]. By using two sets of gratings superimposed on the same fibre, it becomes possible to decouple the temperature and strain components. During a composite cure, there are two phases: an initial temperature ramp, at which point the resin is liquid and there is no measurable strain, and an isothermal hold, during which there is no temperature change. Using such a fibre can identify the Bragg wavelength shift as being dependent solely on the temperature component during the ramp and solely on the strain component during the dwell. Using this rationale, a 100 $\mu\epsilon$ drop in strain was observed during an isothermal cure hold. The onset of this strain drop was identified as the onset of gel, and the end point of the strain drop was correlated to the end of cure. This was compared to dielectric sensor measurements collected on the same sample, which were analysed using the ion viscosity correlation, similar to the methodology used in [56] but using ion viscosity measurements.

3.4.3. Summary and Future Work

Like ultrasonic sensors, at this time, fibre optics may not have the necessary quantitative output required for high-performance composite applications. While the signals can identify phase transitions in the matrix, a specific evaluation of the degree of cure is lacking. Further, it has been established that fibre-optic sensors are quite delicate and that both the embedding and the cure process have the potential to cause bending and constriction, which may negatively impact signal quality [126].

Aside from this, optical fibres show promise for residual stress measurement [122] and structural health monitoring compared to strain gauge measurement and are sensitive to changes in resin flow and mould closing during infusion processes [124]. Optical fibres can also be used to identify resin arrival and flow events during infusion processing [66,127],

commonly by monitoring changes in the light signals as the length of the fibre becomes wetted by the resin [121].

Finally, it is possible to monitor the crystallisation process of thermoplastic polymer by evaluating the residual strain. The processing mechanism for thermoplastic polymers is fundamentally different from the cure processing of thermosetting polymers, as they do not undergo a chemical reaction. For these materials, the sensor monitors the progression of crystallization rather than the progression of cure reaction. The Bragg wavelength shift of an FBG sensor was used to evaluate the crystallisation process for a fibreglass–polypropylene composite and successfully identified the key crystallisation points shown in Figure 21. These results were successfully compared to DSC.
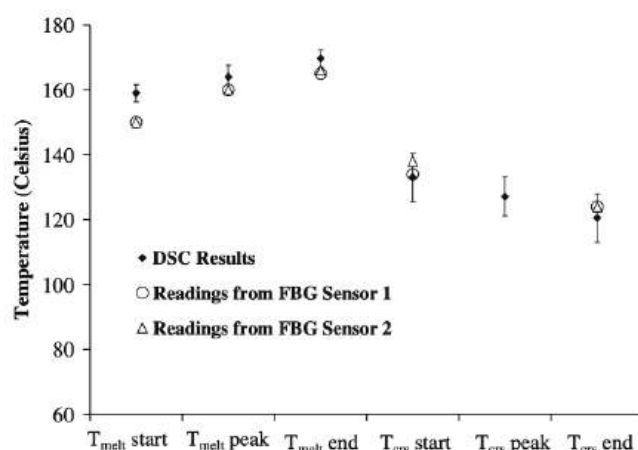
Figure 21. Identification of crystallisation features of a polypropylene composite using an FBG sensor compared to DSC results. Reprinted with permission from Ref. [128] 2005, Elsevier.

4. Conclusions

A critical review of the correlation methods for different in-line composite cure-sensing technologies has been presented. Thermocouple cure monitoring can be reliably correlated to a degree of cure using DSC evaluation or kinetic modelling. Dielectric analysis can produce a wide variety of cure state information, as there are many correlation methods that can be applied to the different monitored parameters. Ultrasonics and fibre optics are commonly used to correlate to the specific phase transitions of the polymer rather than a quantitative measurement of cure state. While the benefits and drawbacks of implementing each type of sensor have been evaluated elsewhere, this paper asserts that it is critical to select a sensor and correlation method to achieve the required fidelity during cure monitoring for the specific application. Providing a qualitative determination of cure ending, such as fibre-optic sensors, may be appropriate for some applications. Whereas an application which requires a degree of cure or T_g with a specific value may benefit from thermocouple or dielectric sensing.

There are multiple areas of potential improvement for in situ cure-sensing technology. The availability of non-invasive sensors and sensors that do not require a permanent installation would increase the ease of implementation. The development of a quantitative measure of cure for sensors, such as ultrasonics, would enable their use in a wider range of applications. A comparison of the different correlation methods for each sensor type would identify the most accurate method for evaluating cure progress, including whether the methods are applicable across multiple materials and multiple cure cycles. Finally, a robust evaluation of the correlation methods across repeated process cycles would indicate if the precision was sufficient to capture manufacturing variations. Future work in these areas would improve the fidelity of data collection and enable new sensing technologies to be readily and confidently adopted.

References

1. Alajarmeh, O.; Zeng, X.; Aravinthan, T.; Shelley, T.; Alhawamdeh, M.; Mohammed, A.; Nicol, L.; Vedernikov, A.; Safonov, A.; Schubel, P. Compressive behaviour of hollow box pultruded FRP columns with continuous-wound fibres. *Thin-Walled Struct.* **2021**, *168*, 108300. [CrossRef]

2. Alhawamdeh, M.; Alajarmeh, O.; Aravinthan, T.; Shelley, T.; Schubel, P.; Mohammed, A.; Zeng, X. Review on local buckling of hollow box FRP profiles in civil structural applications. *Polymers* **2021**, *13*, 4159. [CrossRef] [PubMed]

3. Brøndsted, P.; Lilholt, H.; Lystrup, A. Composite materials for wind power turbine blades. *Annu. Rev. Mater. Res.* **2005**, *35*, 505–538. [CrossRef]

4. Marsh, G. Composites—Prime enabler for wind energy. *Reinf. Plast.* **2003**, *74*, 29–45.

5. Mishnaevsky, L.; Branner, K.; Petersen, H.N.; Beauson, J.; McGugan, M.; Sørensen, B.F. Materials for wind turbine blades: An overview. *Materials* **2017**, *10*, 1285. [CrossRef]

6. Weaver, A. Composites drive VT diversification. *Reinf. Plast.* **1997**, *41*, 28–31.

7. Kim, S.-Y.; Shim, C.S.; Sturtevant, C.; Kim, D.; Song, H.C. Mechanical properties and production quality of hand-layup and vacuum infusion processed hybrid composite materials for GFRP marine structures. *Int. J. Nav. Archit. Ocean Eng.* **2014**, *6*, 723–736. [CrossRef]

8. Mouritz, A.P.; Gellert, E.; Burchill, P.; Challis, K. Review of advanced composite structures for naval ships and submarines. *Compos. Struct.* **2001**, *53*, 21–42. [CrossRef]

9. Hayman, B.; Echtermeyer, A.; McGeorge, D. Use of Fibre Composites in Naval Ships. 2001. Available online: https://www.researchgate.net/profile/Brian-Hayman/publication/242181832_USE_OF_FIBRE_COMPOSITES_IN_NAVAL_SHIPS/links/02e7e52a0c9c912c31000000/USE-OF-FIBRE-COMPOSITES-IN-NAVAL-SHIPS.pdf (accessed on 1 June 2022).

10. Kim, D.D.-W.; Hennigan, D.J.; Beavers, K.D. Effect of fabrication processes on mechanical properties of glass fiber reinforced polymer composites for 49 meter (160 foot) recreational yachts. *Int. J. Nav. Archit. Ocean Eng.* **2010**, *2*, 45–56. [CrossRef]

11. Feraboli, P.; Masini, A. Development of carbon/epoxy structural components for a high performance vehicle. *Compos. Part B Eng.* **2004**, *35*, 323–330. [CrossRef]

12. Feraboli, P.; Masini, A.; Taraborrelli, L.; Pivetti, A. Integrated development of CFRP structures for a topless high performance vehicle. *Compos. Struct.* **2007**, *78*, 495–506. [CrossRef]

13. Barile, C.; Casavola, C. Mechanical characterization of carbon fiber reinforced plastics specimens for aerospace applications. *Polym. Compos.* **2018**, *40*, 716–722. [CrossRef]

14. Rocha, H.; Semprimoschnig, C.; Nunes, J.P. Sensors for process and structural health monitoring of aerospace composites: A review. *Eng. Struct.* **2021**, *237*, 112231. [CrossRef]

15. Mouton, S.; Teissandier, D.; Sébastian, P.; Nadeau, J.P. Manufacturing requirements in design: The RTM process in aeronautics. *Compos. Part A Appl. Sci. Manuf.* **2010**, *41*, 125–130. [CrossRef]

16. Rajak, D.K.; Pagar, D.D.; Menezes, P.L.; Linul, E. Fiber-reinforced polymer composites: Manufacturing, properties, and applications. *Polymers* **2019**, *11*, 1667. [CrossRef] [PubMed]

17. Hindersmann, A. Confusion about infusion: An overview of infusion processes. *Compos. Part A Appl. Sci. Manuf.* **2019**, *126*, 105583. [CrossRef]

18. Frketic, J.; Dickens, T.; Ramakrishnan, S. Automated manufacturing and processing of fiber-reinforced polymer (FRP) composites: An additive review of contemporary and modern techniques for advanced materials manufacturing. *Addit. Manuf.* **2017**, *14*, 69–86. [CrossRef]

19. Park, S.Y.; Choi, C.H.; Choi, W.J.; Hwang, S.S. A comparison of the properties of carbon fiber epoxy composites produced by non-autoclave with vacuum bag only prepreg and autoclave process. *Appl. Compos. Mater.* **2018**, *26*, 187–204. [CrossRef]

20. Nele, L.; Caggiano, A.; Teti, R. Autoclave cycle optimization for high performance composite parts manufacturing. *Procedia CIRP* **2016**, *57*, 241–246. [CrossRef]

21. Summerscales, J.; Searle, T. Low-pressure (vacuum infusion) techniques for moulding large composite structures. *Proc. Inst. Mech. Eng. Part L J. Mater. Des. Appl.* **2005**, *219*, 45–58. [CrossRef]

22. Michaud, D.J.; Beris, A.N.; Dhurjati, P.S. Thick-sectioned RTM composite manufacturing: Part I—In situ cure model parameter identification and sensing. *J. Compos. Mater.* **2002**, *36*, 1175–1200. [CrossRef]

23. Tifkitsis, K.I.; Skordos, A.A. Stochastic multi-objective optimisation of composites manufacturing process. In Proceedings of the Thematic Conference on Uncertainty Quantification in Computational Sciences and Engineering, Rhodes Island, Greece, 15–17 June 2017; pp. 690–705.

24. Konstantopoulos, S.; Hueber, C.; Antoniadis, I.; Summerscales, J.; Schledjewski, R. Liquid composite molding reproducibility in real-world production of fiber reinforced polymeric composites: A review of challenges and solutions. *Adv. Manuf. Polym. Compos. Sci.* **2019**, *5*, 85–99. [CrossRef]

25. Mesogitis, T.S.; Skordos, A.A.; Long, A.C. Uncertainty in the manufacturing of fibrous thermosetting composites: A review. *Compos. Part A Appl. Sci. Manuf.* **2014**, *57*, 67–75. [CrossRef]

26. Ersoy, N.; Garstka, T.; Potter, K.; Wisnom, M.R.; Porter, D.; Clegg, M.; Stringer, G. Development of the properties of a carbon fibre reinforced thermosetting composite through cure. *Compos. Part A Appl. Sci. Manuf.* **2010**, *41*, 401–409. [CrossRef]

27. Ogale, A.; Potluri, P.; Rittenschober, B.; Beier, U.; Schlimbach, J. Out-of-autoclave curing of composites for high temperature aerospace applications. In Proceedings of the SAMPE, Seattle, WA, USA, 2–5 June 2014.

28. Boey, F.Y.C.; Lee, T.H.; Sullivan, P.L. High-pressure autoclave curing for a thermoset composite: Effect on the glass transition temperature. *J. Mater. Sci.* **1994**, *29*, 5985–5989. [CrossRef]

29. Fonseca, G.E.; Dubé, M.A.; Penlidis, A. A critical overview of sensors for monitoring polymerizations. *Macromol. React. Eng.* **2009**, *3*, 327–373. [CrossRef]

30. Tifkitsis, K.I.; Skordos, A.A. Integration of stochastic process simulation and real time process monitoring of LCM. In Proceedings of the SAMPE, Southampton, UK, 11–13 September 2018.

31. Buczek, M.B. Self-directed process control system for epoxy matrix composites. In Proceedings of the SAMPE, Anaheim, CA, USA, 8–11 May 1995.

32. Dunkersa, J.P.; Flynna, K.M.; Parnasa, R.S.; Sourlas, D.D. Model-assisted feedback control for liquid composite molding. *Compos. Part A Appl. Sci. Manuf.* **2002**, *33*, 841–854. [CrossRef]

33. Konstantopoulos, S.; Fauster, E.; Schledjewski, R. Monitoring the production of FRP composites: A review of in-line sensing methods. *Express Polym. Lett.* **2014**, *8*, 823–840. [CrossRef]

34. Torres, M. Parameters' monitoring and in-situ instrumentation for resin transfer moulding: A review. *Compos. Part A Appl. Sci. Manuf.* **2019**, *124*, 105500. [CrossRef]

35. Karkanas, P.I.; Partridge, I.K. Cure modeling and monitoring of epoxy/amine resin systems. I. Cure kinetics modeling. *J. Appl. Polym. Sci.* **2000**, *77*, 1419–1431. [CrossRef]

36. Karkanas, P.I.; Partridge, I.K. Cure modeling and monitoring of epoxy/amine resin systems. II. Network formation and chemoviscosity modeling. *J. Appl. Polym. Sci.* **2000**, *77*, 2178–2188. [CrossRef]

37. Nikolic, G.; Zlatkovic, S.; Cakic, M.; Cakic, S.; Lacnjevac, C.; Rajic, Z. Fast Fourier transform IR characterization of epoxy GY systems crosslinked with aliphatic and cycloaliphatic EH polyamine adducts. *Sensors* **2010**, *10*, 684–696. [CrossRef] [PubMed]

38. Merad, L.; Cochez, M.; Margueron, S.; Jauchem, F.; Ferriol, M.; Benyoucef, B.; Bourson, P. In-situ monitoring of the curing of epoxy resins by Raman spectroscopy. *Polym. Test.* **2009**, *28*, 42–45. [CrossRef]

39. Kamal, M.R.; Sourour, S. Kinetics and thermal characterization of thermoset cure. *Polym. Eng. Sci.* **1973**, *13*, 59–64. [CrossRef]

40. Kissinger, H.E. Reaction kinetics in differential thermal analysis. *Anal. Chem.* **1957**, *29*, 1702–1706. [CrossRef]

41. Sbirrazzuoli, N.; Vyazovkin, S. Learning about epoxy cure mechanisms from isoconversional analysis of DSC data. *Thermochim. Acta* **2002**, *388*, 289–298. [CrossRef]

42. Sbirrazzuoli, N.; Vyazovkin, S.; Mititelu, A.; Sladic, C.; Vincent, L. A study of epoxy-amine cure kinetics by combining iso-conversional analysis with temperature modulated dsc and dynamic rheometry. *Macromol. Chem. Phys.* **2003**, *204*, 1815–1821. [CrossRef]

43. *ASTM E2070-13(2018)*; Standard Test Methods for Kinetic Parameters by Differential Scanning Calorimetry Using Isothermal Methods. ASTM International: West Conshohocken, PA, USA, 2018.

44. Yousefi, A.; Lafleur, P.G.; Gauvin, R. Kinetic studies of thermoset cure reactions: A review. *Polym. Compos.* **1997**, *18*, 157–168. [CrossRef]

45. *ASTM D7028-07(2015)*; Standard Test Method for Glass Transition Temperature (DMA Tg) of Polymer Matrix Composites by Dynamic Mechanical Analysis (DMA). ASTM International: West Conshohocken, PA, USA, 2015.

46. Ferdous, W.; Manalo, A.; Aravinthan, T.; Van Erp, G. Properties of epoxy polymer concrete matrix: Effect of resin-to-filler ratio and determination of optimal mix for composite railway sleepers. *Constr. Build. Mater.* **2016**, *124*, 287–300. [CrossRef]

47. Stark, W.; Goering, H.; Michel, U.; Bayerl, H. Online monitoring of thermoset post-curing by dynamic mechanical thermal analysis DMTA. *Polym. Test.* **2009**, *28*, 561–566. [CrossRef]

48. Kister, G.; Dossi, E. Cure monitoring of CFRP composites by dynamic mechanical analyser. *Polym. Test.* **2015**, *47*, 71–78. [CrossRef]

49. *ASTM D7750-12(2017)*; Standard Test Method for Cure Behavior of Thermosetting Resins by Dynamic Mechanical Procedures using an Encapsulated Specimen Rheometer. ASTM International: West Conshohocken, PA, USA, 2017.

50. Mphahlele, K.; Ray, S.S.; Kolesnikov, A. Cure kinetics, morphology development, and rheology of a high-performance carbon-fiber-reinforced epoxy composite. *Compos. Part B Eng.* **2019**, *176*, 107300. [CrossRef]

51. Strobel, M.E.; Kracalik, M.; Hild, S. In-situ monitoring of the curing of a Bisphenol-A epoxy resin by raman-spectroscopy and rheology. *Mater. Sci. Forum* **2019**, *955*, 92–97. [CrossRef]

52. Pineda, U.; Montés, N.; Domenech, L.; Sánchez, F. On-line measurement of the resin infusion flow variables using artificial vision technologies. *Int. J. Mater. Form.* **2010**, *3*, 711–714. [CrossRef]

53. McIlhagger, A.; Brown, D.; Hill, B. The development of a dielectric system for the on-line cure monitoring of the resin transfer moulding process. *Compos. Part A Appl. Sci. Manuf.* **2000**, *31*, 1373–1381. [CrossRef]

54. Aronhime, M.T.; Gillham, J.K. Time-temperature-transformation (TTT) cure diagram of thermosetting polymeric systems. In *Epoxy Resins and Composites III*; Springer: Berlin/Heidelberg, Germany, 1986; Volume 78, pp. 83–113. [CrossRef]

55. Guo, Z.; Du, S.; Zhang, B. Temperature field of thick thermoset composite laminates during cure process. *Compos. Sci. Technol.* **2005**, *65*, 517–523. [CrossRef]

56. Maistros, G.M.; Partridge, I.K. Monitoring autoclave cure in commercial carbon fibre/epoxy composites. *Compos. Part B Eng.* **1998**, *29*, 245–250. [CrossRef]

57. Konstantopoulos, S.; Tonejc, M.; Maier, A.; Schledjewski, R. Exploiting temperature measurements for cure monitoring of FRP composites—Applications with thermocouples and infrared thermography. *J. Reinf. Plast. Compos.* **2015**, *34*, 1015–1026. [CrossRef]

58. Dollimore, D. *Thermal Characterization of Polymeric Materials*; Turi, E.A., Ed.; Academic Press: New York, NY, USA; London, UK, 1981; p. 972.

59. Sourour, S.; Kamal, M.R. Differential scanning calorimetry of epoxy cure: Isothermal cure kinetics. *Thermochim. Acta* **1976**, *14*, 41–59. [CrossRef]

60. Vyazovkin, S.; Sbirrazzuoli, N. Isoconversional kinetic analysis of thermally stimulated processes in polymers. *Macromol. Rapid Commun.* **2006**, *27*, 1515–1532. [CrossRef]

61. Pantelelis, N.; Vrouvakis, T.; Spentzas, K. Cure cycle design for composite materials using computer simulation and optimisation tools. *Forsch. Ing.* **2003**, *67*, 254–262. [CrossRef]

62. *Technical Data Sheet CYCOM(R) 5320-1 Prepreg*; Solvay Composite Materials; Solvay: Brussels, Belgium, 2017.

63. Bruk, D. Implementation Methodology, Validation, and Augmentation of a Cure Kinetic Model for Carbon Fiber/CYCOM 5320-1, FM309-1, and FM300-2. Ph.D. Thesis, Washington University in St. Louis, St. Louis, MO, USA, 2021.

64. Kim, H.G.; Lee, D.G. Dielectric cure monitoring for glass/polyester prepreg composites. *Compos. Struct.* **2002**, *57*, 91–99. [CrossRef]

65. Marin, E.; Robert, L.; Triollet, S.; Ouerdane, Y. Liquid resin infusion process monitoring with superimposed fibre Bragg grating sensor. *Polym. Test.* **2012**, *31*, 1045–1052. [CrossRef]

66. Wang, P.; Molimard, J.; Drapier, S.; Vautrin, A.; Minni, J.C. Monitoring the resin infusion manufacturing process under industrial environment using distributed sensors. *J. Compos. Mater.* **2011**, *46*, 691–706. [CrossRef]

67. Shevtsov, S.; Zhilyaev, I.; Soloviev, A.; Parinov, I.; Dubrov, V. Optimization of the composite cure process on the basis of thermo-kinetic model. *Adv. Mater. Res.* **2012**, *569*, 185–192. [CrossRef]

68. Aleksendrić, D.; Carlone, P.; Ćirović, V. Optimization of the temperature-time curve for the curing process of thermoset matrix composites. *Appl. Compos. Mater.* **2016**, *23*, 1047–1063. [CrossRef]

69. Chaloupka, A. Development of a Dielectric Sensor for the Real-Time In-Mold Characterization of Carbon Fiber Reinforced Thermosets. Ph.D. Thesis, University of Augsburg, Augsburg, Germany, 2018.

70. Day, D.R.; Lewis, T.J.; Lee, H.L.; Senturia, S.D. The role of boundary layer capacitance at blocking electrodes in the interpretation of dielectric cure data in adhesives. *J. Adhes.* **1985**, *18*, 73–90. [CrossRef]

71. Mijovic, J.; Yee, C.F.W. Use of Complex Impedance To Monitor the Progress of Reactions in Epoxy/Amine Model Systems. *Macromolecules* **1994**, *27*, 7287–7293. [CrossRef]

72. Kim, J.-S.; Lee, D.G. On-line cure monitoring and viscosity measurement of carbon fiber epoxy composite materials. *J. Mater. Process. Technol.* **1993**, *37*, 405–416. [CrossRef]

73. Fournier, J.; Williams, G.; Duch, C.; Aldridge, G.A. Changes in molecular dynamics during bulk polymerization of an epoxide−amine system as studied by dielectric relaxation spectroscopy. *Macromolecules* **1996**, *29*, 7097–7107. [CrossRef]

74. Chaloupka, A.; Pflock, T.; Horny, R.; Rudolph, N.; Horn, S.R. Dielectric and rheological study of the molecular dynamics during the cure of an epoxy resin. *J. Polym. Sci. Part B Polym. Phys.* **2018**, *56*, 907–913. [CrossRef]

75. Hardis, R.; Jessop, J.L.P.; Peters, F.E.; Kessler, M.R. Cure kinetics characterization and monitoring of an epoxy resin using DSC, Raman spectroscopy, and DEA. *Compos. Part A Appl. Sci. Manuf.* **2013**, *49*, 100–108. [CrossRef]

76. Mijović, J.; Andjelic, S.; Fitz, B.; Zurawsky, W.; Mondragon, I.; Bellucci, F.; Nicolais, L. Impedance spectroscopy of reactive polymers. 3. Correlations between dielectric, spectroscopic, and rheological properties during cure of a trifunctional epoxy resin. *J. Polym. Sci. Part B Polym. Phys.* **1996**, *34*, 379–388. [CrossRef]

77. Tifkitsis, K.I.; Skordos, A.A. A novel dielectric sensor for process monitoring of carbon fibre composites manufacture. *Compos. Part A Appl. Sci. Manuf.* **2019**, *123*, 180–189. [CrossRef]

78. Mesogitis, T.S.; Maistros, G.M.; Asareh, M.; Lira, C.; Skordos, A.A. Optimisation of an in-process lineal dielectric sensor for liquid moulding of carbon fibre composites. *Compos. Part A Appl. Sci. Manuf.* **2021**, *140*, 106190. [CrossRef]

79. Kazilas, M.C.; Partridge, I.K. Exploring equivalence of information from dielectric and calorimetric measurements of thermoset cure—a model for the relationship between curing temperature, degree of cure and electrical impedance. *Polymer* **2005**, *46*, 5868–5878. [CrossRef]

80. Abraham, D.; McIlhagger, R. Glass fibre epoxy composite cure monitoring using parallel plate dielectric analysis in comparison with thermal and mechanical testing techniques. *Compos. Part A* **1998**, *29*, 811–819. [CrossRef]

81. O'Dwyer, M.J.; Maistros, G.M.; James, S.W.; Tatam, R.P.; Partridge, I.K. Relating the state of cure to the real-time internal strain development in a curing composite using in-fibre Bragg gratings and dielectric sensors. *Meas. Sci. Technol.* **1998**, *9*, 1153–1158. [CrossRef]

82. Kim, D.; Centea, T.; Nutt, S.R. In-situ cure monitoring of an out-of-autoclave prepreg: Effects of out-time on viscosity, gelation and vitrification. *Compos. Sci. Technol.* **2014**, *102*, 132–138. [CrossRef]

83. Yang, Y.; Plovie, B.; Chiesura, G.; Vervust, T.; Daelemans, L.; Mogosanu, D.-E.; Wuytens, P.; De Clerck, K.; Vanfleteren, J. Fully integrated flexible dielectric monitoring sensor system for real-time in situ prediction of the degree of cure and glass transition temperature of an epoxy resin. *IEEE Trans. Instrum. Meas.* **2021**, *70*, 6004809. [CrossRef]

84. Boll, D.; Schubert, K.; Brauner, C.; Lang, W. Miniaturized flexible interdigital sensor for in situ dielectric cure monitoring of composite materials. *IEEE Sens. J.* **2014**, *14*, 2193–2197. [CrossRef]

85. Kahali Moghaddam, M.; Breede, A.; Chaloupka, A.; Bödecker, A.; Habben, C.; Meyer, E.-M.; Brauner, C.; Lang, W. Design, fabrication and embedding of microscale interdigital sensors for real-time cure monitoring during composite manufacturing. *Sens. Actuators A Phys.* **2016**, *243*, 123–133. [CrossRef]

86. Park, H. Dielectric cure determination of a thermosetting epoxy composite prepreg. *J. Appl. Polym. Sci.* **2017**, *134*. [CrossRef]

87. Franieck, E.; Fleischmann, M.; Hölck, O.; Kutuzova, L.; Kandelbauer, A. Cure kinetics modeling of a high glass transition temperature epoxy molding compound (EMC) based on inline dielectric analysis. *Polymers* **2021**, *13*, 1734. [CrossRef]

88. Lee, D.G.; Kim, H.G. Non-isothermal in situ dielectric cure monitoring for thermosetting matrix composites. *J. Compos. Mater.* **2007**, *38*, 977–993. [CrossRef]

89. Kim, S.S.; Murayama, H.; Kageyama, K.; Uzawa, K.; Kanai, M. Study on the curing process for carbon/epoxy composites to reduce thermal residual stress. *Compos. Part A Appl. Sci. Manuf.* **2012**, *43*, 1197–1202. [CrossRef]

90. Skordos, A.A.; Partridge, I.K. Effects of tool-embedded dielectric sensors on heat transfer phenomena during composite cure. *Polym. Compos.* **2007**, *28*, 139–152. [CrossRef]

91. Breede, A.; Moghaddam, M.K.; Brauner, C.; Herrmann, A.S.; Lang, W. Online process monitoring and control by dielectric sensors for a composite main spar for wind turbine blades. In Proceedings of the 20th International Conference on Composite Materials, Copenhagen, Denmark, 19–24 July 2015.

92. Lionetto, F.; Maffezzoli, A. Monitoring the cure state of thermosetting resins by ultrasound. *Materials* **2013**, *6*, 3783–3804. [CrossRef]

93. Tuloup, C.; Harizi, W.; Aboura, Z.; Meyer, Y.; Khellil, K.; Lachat, R. On the use of in-situ piezoelectric sensors for the manufacturing and structural health monitoring of polymer-matrix composites: A literature review. *Compos. Struct.* **2019**, *215*, 127–149. [CrossRef]

94. Challis, R.E.; Blarel, F.; Unwin, M.E.; Paul, J.; Guo, X. Models of ultrasonic wave propagation in epoxy materials. *IEEE Trans. Ultrason. Ferroelectr. Freq. Control* **2009**, *56*, 1225–1237. [CrossRef] [PubMed]

95. Perepechko, I. *Acoustic Methods Of Investigating Polymers*; Mir Publishers: Moscow, Russia, 1975.

96. Maffezzoli, A.; Quarta, E.; Luprano, V.A.M.; Montagna, G.; Nicolais, L. Cure monitoring of epoxy matrices for composites by ultrasonic wave propagation. *J. Appl. Polym. Sci.* **1999**, *73*, 1969–1977. [CrossRef]

97. Lionetto, F.; Montagna, F.; Maffezzoli, A. Ultrasonic dynamic mechanical analysis of polymers. *Appl. Rheol.* **2005**, *15*, 326–335. [CrossRef]

98. Lionetto, F.; Tarzia, A.; Coluccia, M.; Maffezzoli, A. Air-coupled ultrasonic cure monitoring of unsaturated polyester resins. *Macromol. Symp.* **2007**, *247*, 50–58. [CrossRef]

99. Lionetto, F.; Tarzia, A.; Maffezzoli, A. Air-coupled ultrasound: A novel technique for monitoring the curing of thermosetting matrices. *IEEE Trans. Ultrason. Ferroelectr. Freq. Control* **2007**, *54*, 1437–1444. [CrossRef] [PubMed]

100. Dorighi, J.; Krishnaswamy, S.; Achenbach, J.D. A fiber optic ultrasound sensor for monitoring the cure of epoxy. In *Review of Progress in Quantitative Nondestructive Evaluation*; Springer: Boston, MA, USA, 1998; pp. 657–664.

101. Ghodhbani, N.; Maréchal, P.; Duflo, H. Ultrasound monitoring of the cure kinetics of an epoxy resin: Identification, frequency and temperature dependence. *Polym. Test.* **2016**, *56*, 156–166. [CrossRef]

102. Schmachtenberg, E.; Schulte zur Heide, J.; Töpker, J. Application of ultrasonics for the process control of Resin Transfer Moulding (RTM). *Polym. Test.* **2005**, *24*, 330–338. [CrossRef]

103. Hudson, T.B.; Yuan, F.G. Automated in-process cure monitoring of composite laminates using a guided wave-based system with high-temperature piezoelectric transducers. *J. Nondestruct. Eval. Diagn. Progn. Eng. Syst.* **2018**, *1*, 021008. [CrossRef]

104. Samet, N.; Maréchal, P.; Duflo, H. Ultrasonic characterization of a fluid layer using a broadband transducer. *Ultrasonics* **2012**, *52*, 427–434. [CrossRef]

105. Pindinelli, C.; Montagna, G.; Luprano, V.A.M.; Maffezzoli, A. Network development during epoxy curing: Experimental ultrasonic data and theoretical predictions. *Macromol. Symp.* **2002**, *180*, 73–88. [CrossRef]

106. Lionetto, F.; Rizzo, R.; Luprano, V.A.M.; Maffezzoli, A. Phase transformations during the cure of unsaturated polyester resins. *Mater. Sci. Eng. A* **2004**, *370*, 284–287. [CrossRef]

107. Challis, R.E.; Unwin, M.E.; Chadwick, D.L.; Freemantle, R.J.; Partridge, I.K.; Dare, D.J.; Karkanas, P.I. Following network formation in an epoxy/amine system by ultrasound, dielectric, and nuclear magnetic resonance measurements: A comparative study. *J. Appl. Polym. Sci.* **2003**, *88*, 1665–1675. [CrossRef]

108. Scholle, P.; Sinapius, M. Pulse ultrasonic cure monitoring of the pultrusion process. *Sensors* **2018**, *18*, 3332. [CrossRef] [PubMed]

109. Tuloup, C.; Harizi, W.; Aboura, Z.; Meyer, Y.; Ade, B.; Khellil, K. Detection of the key steps during Liquid Resin Infusion manufacturing of a polymer-matrix composite using an in-situ piezoelectric sensor. *Mater. Today Commun.* **2020**, *24*, 101077. [CrossRef]

110. Liebers, N.; Buggisch, M.; Kleineberg, M.; Wiedemann, M. Autoclave infusion of aerospace ribs based on process monitoring and control by ultrasound sensors. In Proceedings of the 20th International Conference on Composite Materials, Copenhagen, Denmark, 20–24 July 2015.

111. Liebers, N.; Bertling, D. Ultrasonic resin flow and cure monitoring. In Proceedings of the Conference on Flow Processing in Composite Materials, Luleå, Sweden, 30 May–1 June 2018.

112. Liebers, N.; Raddatz, F.; Schadow, F. Effective and flexible ultrasound sensors for cure monitoring for industrial composite production. In Proceedings of the Deutscher Luft- und Raumfahrtkongress, Berlin, Germany, 10–12 September 2012.

113. Lin, M.; Chang, F.-K. The manufacture of composite structures with a built-in network of piezoceramics. *Compos. Sci. Technol.* **2002**, *62*, 919–939. [CrossRef]

114. Khoun, L.; de Oliveira, R.; Michaud, V.; Hubert, P. Investigation of process-induced strains development by fibre Bragg grating sensors in resin transfer moulded composites. *Compos. Part A Appl. Sci. Manuf.* **2011**, *42*, 274–282. [CrossRef]

115. Murawski, L.; Opoka, S.; Majewska, K.; Mieloszyk, M.; Ostachowicz, W.; Weintrit, A. Investigations of marine safety improvements by structural health monitoring systems. *Int. J. Mar. Navig. Saf. Sea Transp.* **2012**, *6*, 223–229.

116. Min, R.; Liu, Z.; Pereira, L.; Yang, C.; Sui, Q.; Marques, C. Optical fiber sensing for marine environment and marine structural health monitoring: A review. *Opt. Laser Technol.* **2021**, *140*, 107082. [CrossRef]

117. Schubel, P.J.; Crossley, R.J.; Boateng, E.K.G.; Hutchinson, J.R. Review of structural health and cure monitoring techniques for large wind turbine blades. *Renew. Energy* **2013**, *51*, 113–123. [CrossRef]

118. Rao, Y.-J. In-fibre Bragg grating sensors. *Meas. Sci. Technol.* **1997**, *8*, 355–375. [CrossRef]

119. Li, C.; Cao, M.; Wang, R.; Wang, Z.; Qiao, Y.; Wan, L.; Tian, Q.; Liu, H.; Zhang, D.; Liang, T.; et al. Fiber-optic composite cure sensor: Monitoring the curing process of composite material based on intensity modulation. *Compos. Sci. Technol.* **2003**, *63*, 1749–1758. [CrossRef]

120. Buggy, S.J.; Chehura, E.; James, S.W.; Tatam, R.P. Optical fibre grating refractometers for resin cure monitoring. *J. Opt. A Pure Appl. Opt.* **2007**, *9*, S60–S65. [CrossRef]

121. Lekakou, C.; Cook, S.; Deng, Y.; Ang, T.W.; Reed, G.T. Optical fibre sensor for monitoring flow and resin curing in composites manufacturing. *Compos. Part A Appl. Sci. Manuf.* **2006**, *37*, 934–938. [CrossRef]

122. Tsai, L.; Cheng, T.-C.; Lin, C.-L.; Chiang, C.-C. Application of the embedded optical fiber Bragg grating sensors in curing monitoring of Gr/epoxy laminated composites. In *Smart Sensor Phenomena, Technology, Networks, and Systems 2009*; SPIE: Washington, DC, USA, 2009; pp. 57–64.

123. Leng, J.S.; Asundi, A. Real-time cure monitoring of smart composite materials using extrinsic Fabry-Perot interferometer and fiber Bragg grating sensors. *Smart Mater. Struct.* **2002**, *11*, 249–255. [CrossRef]

124. Jung, K.; Kang, T.J. Cure monitoring and internal strain measurement of 3-D hybrid braided composites using fiber bragg grating sensor. *J. Compos. Mater.* **2007**, *41*, 1499–1519. [CrossRef]

125. Sampath, U.; Kim, H.; Kim, D.G.; Kim, Y.C.; Song, M. In-Situ cure monitoring of wind turbine blades by using fiber Bragg grating sensors and fresnel reflection measurement. *Sensors* **2015**, *15*, 18229–18238. [CrossRef]

126. Yeager, M.; Todd, M.; Gregory, W.; Key, C. Assessment of embedded fiber Bragg gratings for structural health monitoring of composites. *Struct. Health Monit.* **2016**, *16*, 262–275. [CrossRef]

127. Gupta, N.; Sundaram, R. Fiber optic sensors for monitoring flow in vacuum enhanced resin infusion technology (VERITy) process. *Compos. Part A Appl. Sci. Manuf.* **2009**, *40*, 1065–1070. [CrossRef]

128. Kuang, K.S.C.; Zhang, L.; Cantwell, W.J.; Bennion, I. Process monitoring of aluminum-foam sandwich structures based on thermoplastic fibre–metal laminates using fibre Bragg gratings. *Compos. Sci. Technol.* **2005**, *65*, 669–676. [CrossRef]

Article

Research on the Mechanical Properties and Stretch Forming Simulation of Triaxial Geogrid with Different Pre-Punched Hole Diameters

Xinbo Ren ![ORCID], Xinhai Zhao *, Chao Zheng, Libin Song, Ji Liu and Zhiyuan Si

Key Laboratory for Liquid-Solid Structural Evolution and Processing of Materials, Ministry of Education, School of Materials Science & Engineering, Shandong University, 17923 Jingshi Road, Jinan 250061, China; 17853143923@163.com (X.R.); zhengchao@sdu.edu.cn (C.Z.); derby@sdu.edu.cn (L.S.); liuji9707@163.com (J.L.); 18860870173@163.com (Z.S.)

* Correspondence: xhzhao@sdu.edu.cn

Abstract: In this paper, the tensile behavior of industrial polypropylene triaxial geogrid with different pre-punched hole diameters was studied by experiment and numerical analysis. The industrial polypropylene sheets with different diameters of circular holes were stretched at elevated temperature and then the tensile properties of triaxial geogrids at room temperature were evaluated. It was found that the pre-punched hole diameter of triaxial geogrid had a very close relationship with the mechanical properties. With the increase of the pre-punched hole diameter, the tensile strength of triaxial geogrid shows a trend of first increasing and then decreasing. Combined with numerical simulation, the optimal pre-punched hole diameter can be accurately obtained, and the distribution law of the width, thickness, stress, and strain of triaxial geogrid can be obtained. Under the condition of a stretching ratio of 3 and node spacing of 3 mm, it was found that the mechanical properties of industrial polypropylene triaxial geogrid was the best when the pre-punched hole diameter was 2.6 mm.

Keywords: triaxial geogrid; mechanical properties; numerical simulation; stretching process

1. Introduction

High-strength geogrid is a very important geosynthetic material, which is increasingly used in the construction of steep slopes and in the reinforcement of bridge abutments [1]. The geogrid reinforced structure has strong bearing capacity, small deformation, and can maintain good mechanical properties for decades [2]. At present, the most widely used geogrid is plastic geogrid. Plastic geogrid is a polymer mesh with a certain pore structure obtained by stretching. The traditional plastic geogrids conclude uniaxial geogrids and biaxial geogrids. With the continuous improvement of engineering requirements, new multi-axial geogrids have been developed and put on the market. One of the most widely used multi-axial geogrids is triaxial geogrid.

Triaxial geogrid is a new type of geogrid invented by Tensar [3]. Its forming process mainly includes sheet pre-punching, longitudinal, and transverse stretching at high temperature, cutting, and winding, etc. Its basic unit is generally an equilateral triangle, and its structure is shown in Figure 1. Taking the longitudinal stretching direction as the 90° direction, traxial geogrid is generally provided with ribs in the directions of 30°, 90°, and 150°. The 90° bars are called the longitudinal bars, and the others are named diagonal bars. Bars consist of nodes, ribs and transition areas. The nodes are basically not deformed during the forming process, while the ribs are the part mainly involved in the deformation, and the transition area connects the ribs and nodes.
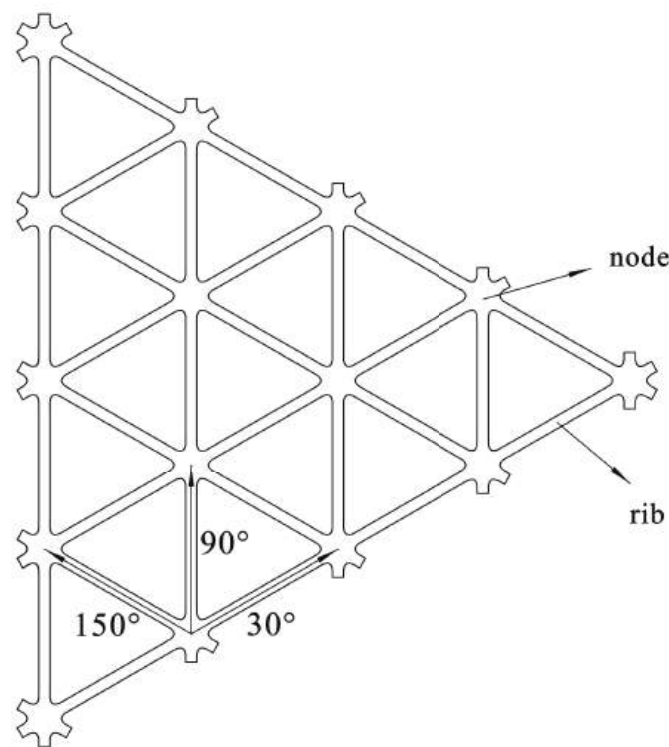
Figure 1. Basic structure of triaxial geogrid.

Compared with a biaxial geogrid with ribs only at 0° and 90°, a triaxial geogrid has higher tensile strength in more directions. Through experiments, Dong et al. [4] found that the geogrid with triangular holes had a more stable structure and could bear more uniform tensile force in all directions, and used FLAC software to respond to the geogrid with rectangular and triangular holes under uniaxial tensile loads in different directions. The triangular hole geogrid was found to have a more uniform tensile strength and strength distribution than the rectangular hole geogrid. Zhang et al. [5] monitored the internal displacement along the length of the geogrid by burying the triaxial geogrid specimen in the compacted sand and conducting multiple pull-out tests. The research results showed that triaxial geogrid had more uniform tensile strength in each loading direction than the biaxial geogrid. Arulrajah et al. [6] found that the higher stiffness triaxial geogrid attained higher interface shear strength properties than that of the lower stiffness biaxial geogrid.

Triaxial geogrid can form an interlocking block with the soil and stone to improve the friction between the grid and the foundation soil, thereby improving the mechanical properties of the substrate. Das et al. [7] effectively increased the CBR (California Bearing Ratio) strength by reinforcing triaxial geogrid for rigid pavement. The California bearing ratio increased by 15% and 39% in the soaked condition when the Tx160 and Tx170 geogrids were interfaced in the sample, respectively. Ma et al. [8] used geogrid to reinforce the filling body in cut-and-fill sections, analyzed the force of the geogrid, established a tensile force calculation model, and obtained the theoretical calculation formula of the geogrid tensile force. Triaxial geogrid reinforcement was found to be more economical and effective in reducing differential settlement and lateral displacement of cut-and-fill embankments.

Therefore, triaxial geogrid is a new type of high-performance geosynthetic material with good application prospects. To improve the mechanical properties of triaxial geogrid, it is necessary to optimize the geogrid material, the process parameters of the pre-punched sheet, and the stretching process parameters.

The materials for producing a geogrid are generally high-density polyethylene (HDPE), industrial polypropylene (PP), and polyethylene terephthalate (PET). Among them, the material for producing triaxial geogrid is generally selected as industrial PP. In the industry, new PP materials and recycled materials are commonly mixed in a ratio of 2:1 as the basic

material for the production of geogrids, which can reduce production costs on the premise of ensuring the stretching properties of PP [9]. Adding about 2% carbon black can inhibit the photoaging of the geogrid [10]. In addition, an appropriate amount of plasticizers and antioxidants should be added [11].

According to structure classification, PP can be divided into isotactic, syndiotactic, and atactic types [12]. Isotactic PP with high crystallinity is the main raw material for the production of various plastic products including geogrids. Isotactic PP contains two parts: a crystalline region and an amorphous region. The stretching process also includes the deformation of the first deformed amorphous region and the later deformed crystalline region [13]. Therefore, when plastic deformation occurs, PP tends to deform unevenly, resulting in "necking" [14].

Reinforcing materials can be added to polypropylene to improve certain properties. For example, experiments show that infusing PP with nanofibers increases the tensile modulus and yield strength, but decreases the ductility [15]. A modification method of the geogrid material is to add an appropriate amount of antioxidants to improve the service life of the geogrid. The antioxidants are effective to prevent polymer oxidation reaction in time [16], and the reaction rate of antioxidant depletion increased with temperature according to the Arrhenius equation, whereas the rate increased exponentially with oxygen pressure [17].

The process parameters of the pre-punched sheet determine the structure of the geogrid after stretching and have an important impact on the mechanical properties of the geogrid. Through stretch forming tests at elevated temperature and tensile fracture tests at room temperature, Zheng et al. [18] discovered the influence of the diameter of the circular pre-punching hole on the mechanical properties of the uniaxial geogrid. The transverse distance between circular pre-punched holes played important roles on the deformation and tensile fracture behavior of geogrids, and the too-small hole diameter limited the deformation of the rib and junction, resulting in forming failure of the geogrid. Ren et al. [19] found that under the condition of meeting the forming requirements, the smaller the diameter-to-distance ratio is beneficial to improve the tensile strength, nominal elongation, and performance utilization factor of the biaxial geogrid. When the longitudinal spacing is 1% larger than the transverse spacing, the material performance utilization factor is maximized.

The stretching process parameters, including stretching temperature, stretching speed, and stretching ratio, have a great effect on the tensile reinforcement of the geogrid [20]. The tensile temperature will affect the rheological properties of the material and the stress-strain distribution during the tensile process. Generally, the tensile temperature of industrial PP geogrids is 383–413 K. The experimental results show that the tensile stress-strain response of PP strongly depends on the applied strain rate and test temperature [21]. Generally speaking, decreasing the stretching speed and increasing the stretching temperature have the same effect on the stress-strain response [22]. The stretching ratio determines the size and shape of the geogrid. When the stretching ratio is too large, the ribs will be broken. On the contrary, if the stretching ratio is too small, it will lead to insufficient stretching and poor mechanical properties. Generally, the stretching ratio of multi-axial geogrid is about 3. In addition, the gap between punch and die will affect the accuracy of punching, thereby indirectly affecting the mechanical properties of the geogrid.

The stretching process at high temperature is the key to affect the performance of the geogrid. The geogrid tensile forming can be simulated and the forming results can be predicted by using Abaqus CAE software. This method is of great significance for obtaining the best pre-punching scheme for geogrids. At present, the numerical analysis of geogrid stretch forming is mainly limited to uniaxial and biaxial geogrids, and there are few simulations for triaxial or multi-axial geogrids. Caton-Rose et al. [23] used the elastic model of solid polymer with large deformation to predict the final shape of PP geogrids, verifying the feasibility of Abaqus simulation of uniaxial geogrids stretching process. Zheng et al. [18] studied the deformation behavior of isotactic PP in the manufacture of uniaxial geogrid by

experimental and numerical methods. The effect of pre-punched holes on the mechanical properties of the uniaxial geogrid was obtained through the tensile test. It was found that the lateral spacing of holes had a great influence on the forming performance and fracture behavior of the grid. Ren et al. [19] optimized the basic tensile simulation element of biaxial geogrid, established a "biaxial tensile model" and used Abaqus software to simulate the biaxial geogrid tensile forming process, which could obtain accurate results of the forming regulation.

Therefore, combined with the above research, the authors speculate that the diameter of the pre-punched hole will have a very important impact on the mechanical properties of triaxial geogrid. Through the forming and tensile failure test combined with the numerical simulation of tensile forming, the authors will study the mechanical properties of triaxial geogrid with different diameters of the pre-punched holes, obtain the relationship between the mechanical properties of the triaxial geogrid and the diameter of the pre-punched holes, and further obtain the optimal pre-punched diameter of a triaxial geogrid. This research is of great help to improve the application value of a triaxial geogrid.

2. Stretch Forming and Tensile Fracture Tests of Triaxial Geogrid

In this chapter, the effect of pre-punched hole diameter on the mechanical properties of a triaxial geogrid will be studied through experiments. Firstly, the process parameters of pre-punched sheet and stretching will be designed. Then, the stretching forming test will be carried out, and the forming properties of a geogrid with different pre-punched holes will be compared. Finally, the mechanical properties of triaxial geogrid after forming will be tested at room temperature, and the mechanical properties of the geogrid will be compared.

2.1. Experimental Design

In this section, the process parameters of pre-punched sheet and stretching are designed, and the mechanical property parameters of the tensile fracture test are defined.

2.1.1. Design of the Process Parameters of the Pre-Punched Sheet and Stretching

The industrial PP sheets used in this paper were provided by Feicheng Lianyi Engineering Plastics Co., Ltd., Taian, Shandong, China, and the thickness of the sheets was 4 mm. Because the round punch is simple to process and easy to debug and maintain, in this paper, the pre-punched holes of the industrial PP triaxial geogrid are all circular.

The first step is to punch the industrial PP sheet. In order to ensure that the triaxial geogrid sheet after high temperature stretching has enough uniform deformation area, the pre-punched sheet should be large enough. In this test, the pre-punched sheet is square, with a length and width of 150 mm, leaving a clamping area of 25 mm on each side, as shown in Figure 2a. The process parameters of the pre-punched structure are shown in Figure 2b. The diameter of the circular pre-punched hole (D) is a variable, taking the values 2.0, 2.5, 3.0, 3.5, and 4.0, and the unit of it is mm.

Then, stretch forming tests are performed on the pre-punched sheets. The optimal temperature and stretching speed of using industrial PP material to produce the geogrid are 393 K and 100 mm/min through experiments [22]. The pre-punched sheets are stretched longitudinally at high temperature. The holding time at elevated temperature is 5 min, the stretching temperature is 393 K, and the stretching speed is 100 mm/min. Subsequently, the pre-punched sheets are stretched transversely under the same process parameters.

Compared with biaxial geogrid, the pre-punched structure of multi-axial geogrid is more complicated, and the general stretching ratio should be lower. In this test, the stretching ratio of the triaxial geogrid is 3, and the distance between adjacent nodes is 30 mm. The stretching process parameters are shown in Table 1.
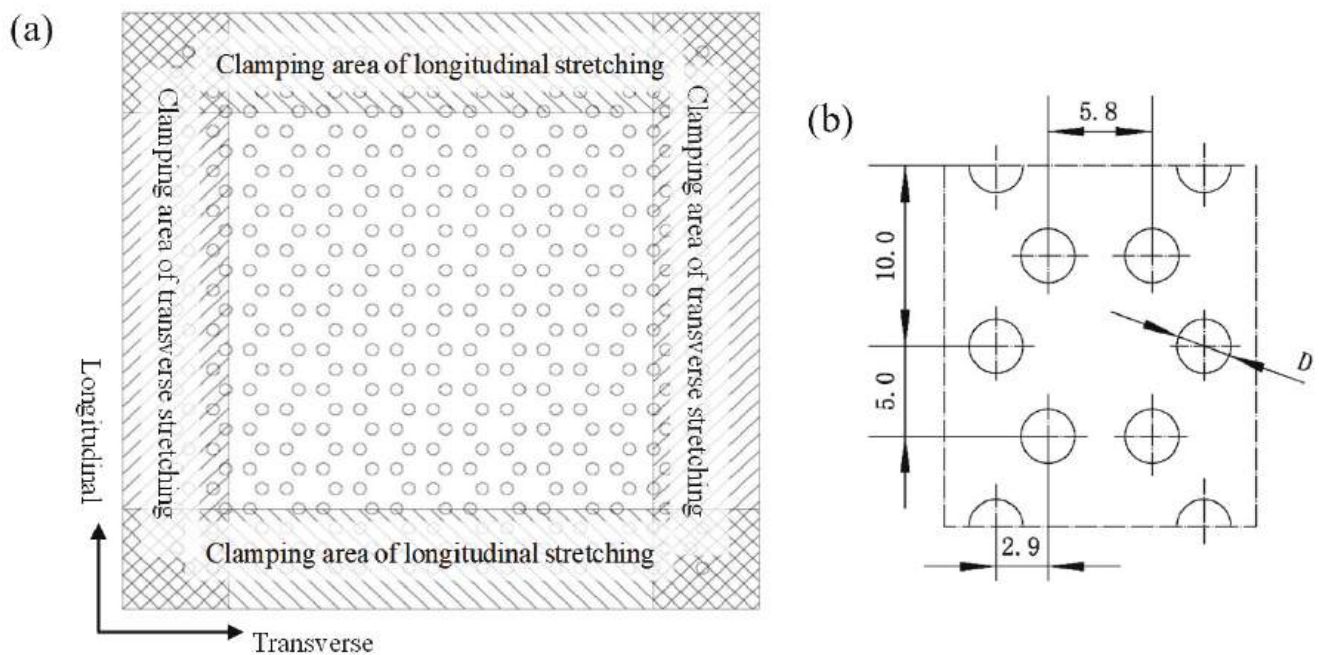
Figure 2. Pre-punched sheet of a triaxial geogrid. (**a**) Clamping area of pre-punched sheet, (**b**) process parameter diagram of the structure of the pre-punched sheet.

Table 1. Process parameter of stretching.

Parameter	Set Value
Material	Industrial PP
Stretching Ratio	3.0
Stretching Temperature	393 K
High Temperature Holding Time	5 min
Stretching Speed	100 mm/min
Thickness of Plates	4.0 mm

2.1.2. Mechanical Properties Index of the Tensile Fracture Test

The mechanical properties and product naming rules of uniaxial and biaxial geogrids are specified in Chinese national standard GB/T 17689-2008 [24] and American national standard ASTM D6637 [25]. The color of plastic geogrids should be uniformly black; the appearance should be free of damage or cracks, the mesh size and shape should be uniform, and the carbon black content should not be less than 2%. The relevant mechanical performance indicators include tensile strength, nominal tensile strength, nominal elongation, and creep, etc. The single-rib method or the multi-rib method can be used to test the mechanical properties of the geogrid.

Compared with uniaxial and biaxial stretched geogrids, multi-axial geogrids currently lack the corresponding relationship between relevant product specifications and specific parameters. According to the characteristics of the multi-axial geogrid, tensile strength and elongation at break are selected as the mechanical performance indicators of the multi-axial geogrid. Furthermore, the concept of multi-axial average tensile strength is proposed by the authors.

The multi-axial geogrid was sampled by the single-rib method at room temperature, and the samples were subjected to room temperature tensile fracture test by electronic universal testing machine. The part with nodes and ribs evenly distributed and flat was selected as sample. The length of the sample should include at least two basic elements, and the effective length should not be less than 100 mm. The sampling method is shown in Figure 3.
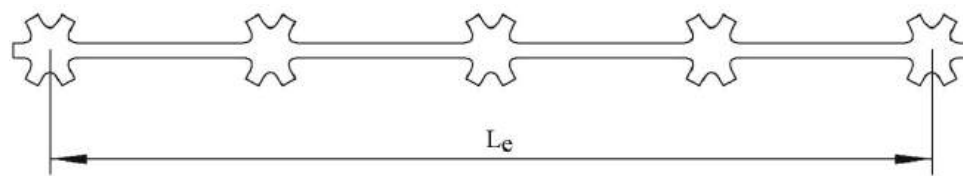
Figure 3. Sampling method for the tensile test at room temperature.

In Figure 3, L_e is the effective length of the sampling, which represents the distance between the center positions of the nodes at both ends of the sampling. In this test, L_e should be greater than 100 mm. During the clamping process, it should be ensured that the clamps clamp the node parts at both ends of the sample, and make sure that the tensile direction is parallel to the holding direction of the sample.

The tensile strength, elongation at break and multi-axial average tensile strength of the samples were obtained through the tensile fracture test at room temperature. The definitions and calculation methods are as follows.

(1) Tensile strength is one of the most important indicators to evaluate the performance of a geogrid, and its calculation method is shown in Equation (1).

$$F = \frac{fN}{nL_e} \tag{1}$$

F is the tensile strength, which unit is kN/m. f is the tensile force value of the sample, and the unit is kN. N is the number of ribs in the direction of the sample to be measured. n is the number of ribs in the non-measured direction. n is no less than 2 in multi-rib method, and equals to 1 in single-rib method. L_e is the effective width of the sample in the direction to be measured, in m.

(2) The elongation at break represents the ductility of the geogrid under tension, and its calculation method is shown in Equation (2).

$$\delta = \frac{\Delta G}{G_0} \tag{2}$$

Geogrids with large elongation at break are prone to node offset under the action of tensile force, which changes the appearance of the product and leads to failure. Therefore, the elongation at break should not be too large. In Equation (2), δ represents the elongation at break of the geogrid; ΔG represents the displacement of the fixture along the tensile direction when it breaks in mm; G_0 represents the distance between the fixtures under the pre-tension state.

(3) The multi-axial average tensile strength can be used to compare the average tensile strength of the multi-axial geogrid in all directions, and then measure the comprehensive mechanical properties of the multi-axial geogrid. The calculation method is shown in Equation (3).

$$\bar{F} = \frac{\sum_{i=1}^{s} F_i}{s} \tag{3}$$

If a basic unit of a geogrid contains ribs, the tensile strength in the direction of each rib $F_1, F_2, F_3, \ldots, F_s$ needs to be obtained first, and then the average of the tensile strength of all ribs is calculated.

2.2. Stretch Forming Tests of Triaxial Geogrid

Stretch forming tests were performed on the pre-punched sheets shown in Figure 2 according to the process parameters in Table 1. Figure 4 shows the uniformly deformed part of the center of the triaxial geogrid with different pre-punched hole diameters.
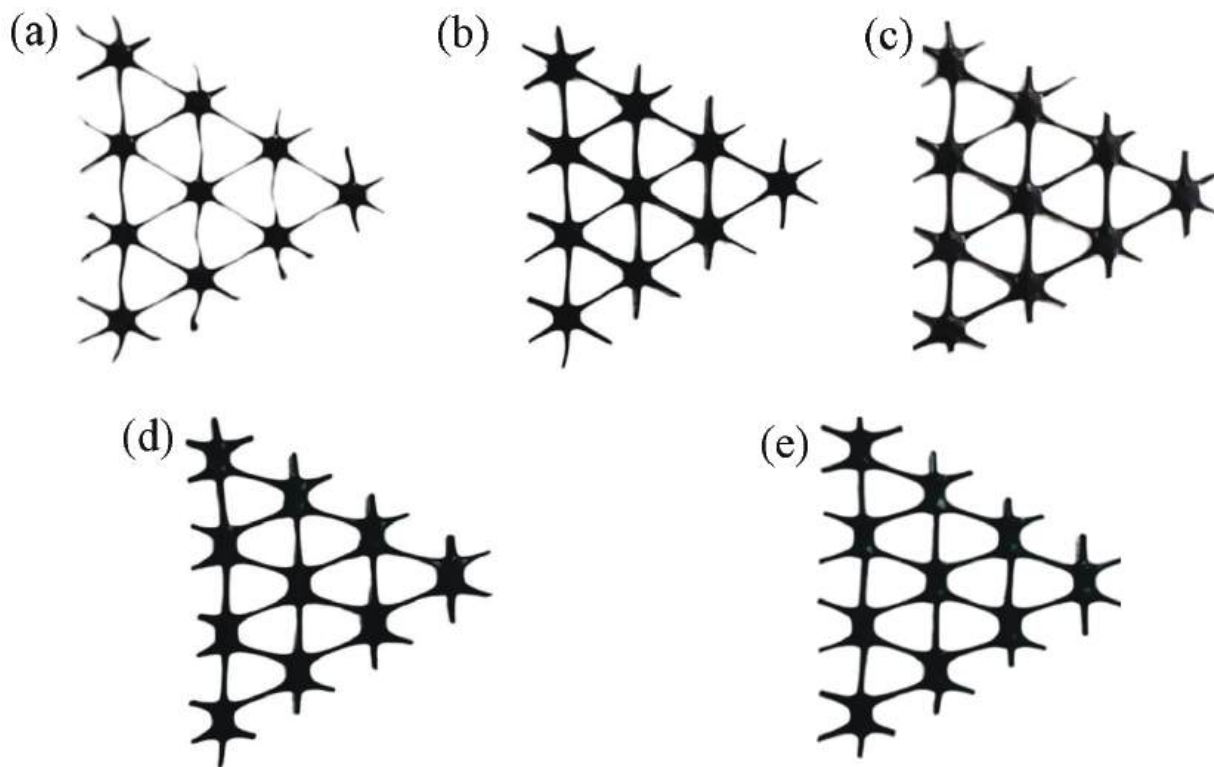
Figure 4. Circular pre-punched industrial PP triaxial geogrid with different diameters. (**a**) D = 4.0 mm, (**b**) D = 3.5 mm, (**c**) D = 3.0 mm, (**d**) D = 2.5 mm, (**e**) D = 2.5 mm.

As shown in Figure 4, the rib width of the triaxial geogrid gradually decreases and the nodes gradually become smaller with the increase of the diameter of the pre-punched hole. When D = 4.0 mm, the longitudinal ribs are bending, while this will not happen when D is less than 4.0 mm. We measure the width and thickness of the ribs for triaxial geogrids with different pre-punched holes after stretch forming, as shown in Figure 5.
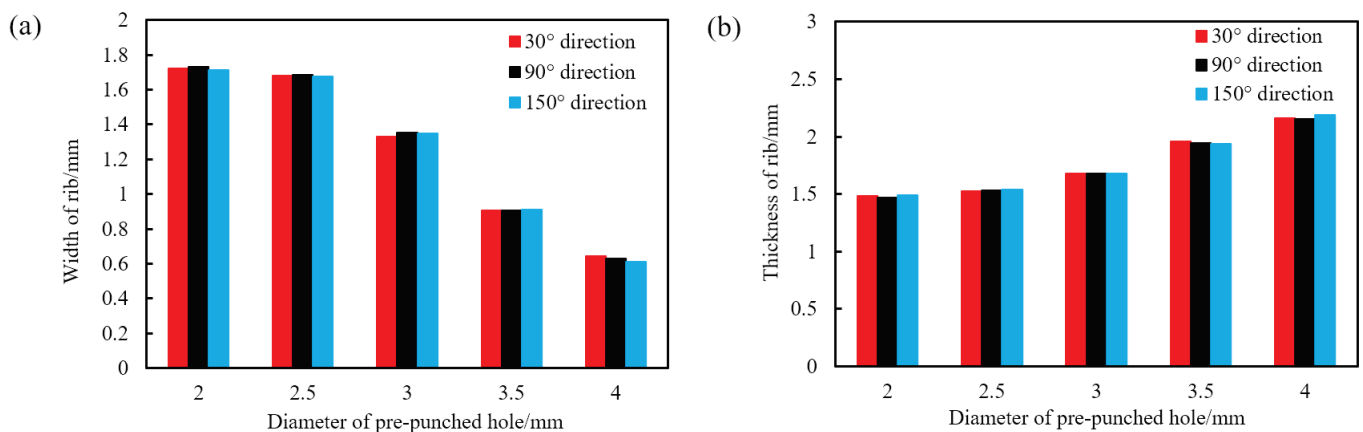
Figure 5. Rib width and thickness of an industrial PP triaxial geogrid with different pre-punched holes. (**a**) Width, (**b**) thickness.

As shown in Figure 5, with the increase of the diameter of the pre-punched holes, the width of the triaxial geogrid rib gradually decreases, and the thickness gradually increases. The width and thickness of the rib are closest to each other when D = 2.5 mm. When D is not less than 3.0 mm, the width is less than the thickness. When D = 2.0 mm or 2.5 mm, the width is greater than the thickness. When D = 4.0 mm, 3.5 mm, or 3.0 mm, the middle part of the node of the triaxial geogrid is convex, and the thickness gradually

decreases in all directions. When D = 2.0 mm, plastic deformation occurs in the central area of the node, resulting in a depression, and the thickness of the part near the rib is larger. When D = 2.5 mm, there are two kinds of nodes at the same time.

The above-mentioned nodes can be divided into two categories, namely, concave nodes in the middle and convex nodes in the middle, as shown in Figure 6. It was observed that in the process of high temperature stretching, the first deformation region was dominated by the concave nodes in the middle, and the post deformation region was dominated by the convex nodes in the middle.
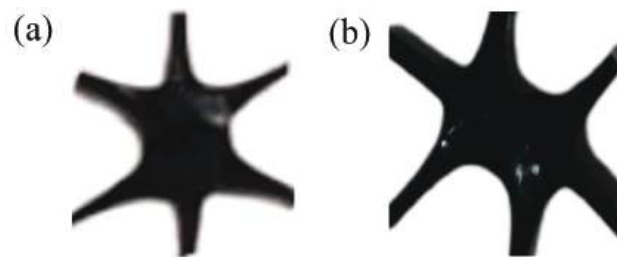
Figure 6. Nodes of different shapes. (**a**) Convex nodes in the middle, (**b**) concave nodes in the middle.

The reason for the generation of concave nodes in the middle is that during the longitudinal stretching process, due to the small size of the pre-punched holes and the large width of the longitudinal ribs, necking is difficult to occur, so the phenomenon of necking of nodes may occur. Therefore, convex nodes in the middle will be created. Due to the deformation of the nodes, the ribs in the 30° direction under the conditions of D = 2.5 mm and D = 2.0 mm are not on the same line, but the ribs remain parallel, and the ribs in the 150° direction show the same change.

2.3. Tensile Fracture Tests at Room Temperature of Triaxial Geogrid

In the tensile fracture test at room temperature, the triaxial geogrids obtained after stretch forming were sampled to obtain samples with straight ribs and evenly distributed nodes. The length of the samples was not less than 100 mm. Then the mechanical properties were tested using an electronic universal testing machine, and the tensile strength, elongation at break and multi-directional average tensile strength were obtained. Selection of samples and clamping method are shown in Figure 7.
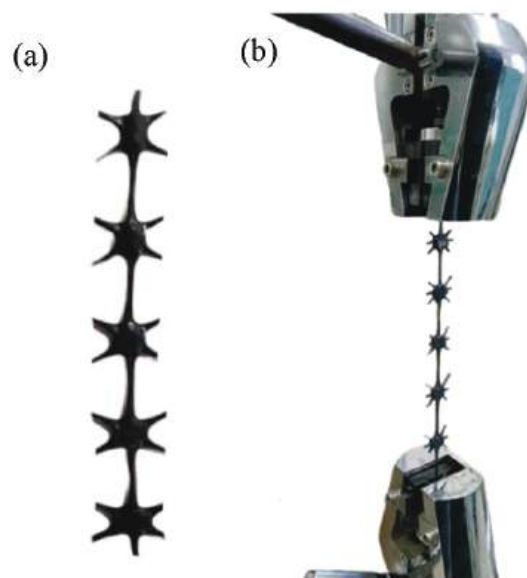
Figure 7. Test method for the mechanical properties of single rib method. (**a**) Selection of samples, (**b**) clamping method.

In this test, we take 20% of the distance between the clamps as the tensile speed per minute [24]. At least four experimental data of each group were taken for analysis. The relationship between the mechanical properties and the diameter of the pre-punched holes of the triaxial geogrid is shown in Figure 8.
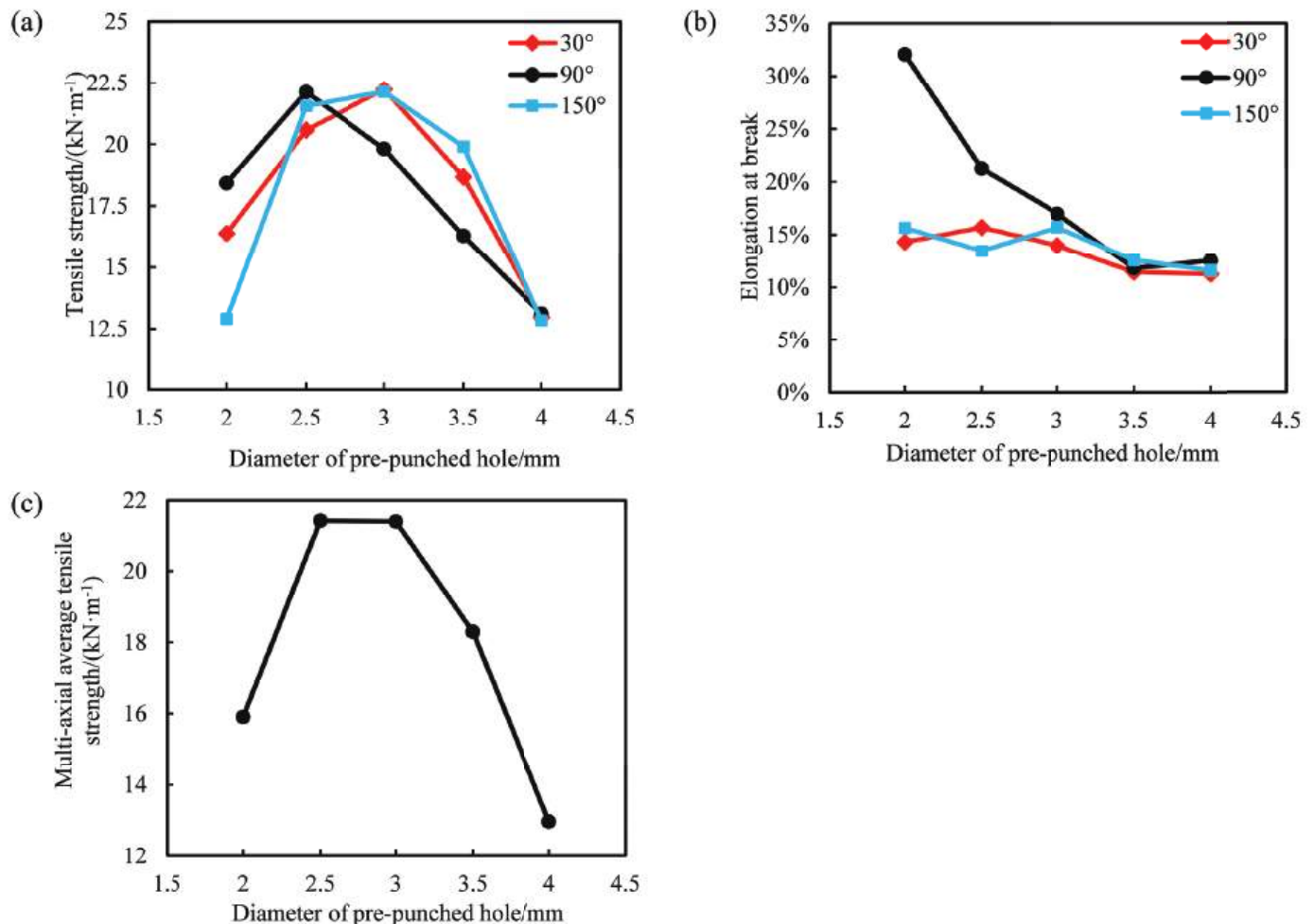
Figure 8. The relationship between the mechanical properties and the diameter of the pre-punched holes of triaxial geogrid. (**a**) Tensile strength, (**b**) elongation at break, (**c**) multi-axial average tensile strength.

It can be seen from Figure 8a that with the increase of the diameter of the pre-punched hole, the tensile strength in each direction increases first and then decreases. The tensile strength in the 30° and 150° directions reaches the maximum when D = 3.0 mm, while the tensile strength in the 90° direction takes the maximum value when D = 2.5 mm. The tensile strength in all directions showed a trend of first increasing and then decreasing. When D = 4.0 mm, the tensile strength in all directions was low. The main reasons for the above phenomenon are as follows.

(1) When D = 2.0 mm, the plastic deformation of the node occurs during the tensile process, the integrity of the node is damaged, the tensile strength of the node is low, and the fracture occurs at the node during the tensile fracture test, resulting in a lower tensile strength of the spline under this condition.

(2) When D = 2.5 mm, the phenomenon of plastic deformation of the node occurs, but due to the low degree, and the large width and thickness of the rib, the tensile strength of ribs in each direction is high.

(3) When D = 3.0 mm, the joint structure is complete, no plastic deformation occurs, and the overall tensile strength is high.

(4) When D = 3.5 mm or 4.0 mm, because the pre-punched hole is too large, there is less material to form the rib during the stretch forming process, leading to the small width of the rib after forming. In addition, the ribs are partly bent with a pre-punched diameter of 4.0 mm. Therefore, the tensile strength in all directions is low under this condition.

It can be seen from Figure 8b that the elongation at break in the 90° direction of the triaxial geogrid shows a decreasing trend with the increase of the diameter of the pre-punched hole. The elongation at break in the 30° and 150° directions has little relationship with the diameter of the pre-punched hole, and the elongation at break is generally 10% to 15%. This is because when D equals to 2.0 mm or 2.5 mm, the nodes undergo plastic deformation along the 90° direction during longitudinal stretching, and the middle of the nodes is concave during this process. In the process of breaking at room temperature, the concave nodes continued to thin and were completely pulled apart, and some splines appeared fractured in the node, which greatly increased the fracture elongation. When D = 3.0 mm, 3.5 mm or 4.0 mm, the elongation at break of the rib in the three directions is basically equal. During the room temperature tensile fracture test, the fracture area is the transition zone or rib.

It can be seen from Figure 8c that with the increase of the diameter of the pre-punched hole, the multi-axial average tensile strength of triaxial geogrid first increases and then decreases; when D = 2.5 or 3.0 mm, the multi-directional average tensile strength of triaxial geogrid reaches the maximum value, which is about 21 kN·m^{-1}.

In order to keep the shape of the geogrid stable under load, the elongation at break of plastic tensile geogrid should not be too large [24]. Compared with triaxial geogrid with D = 2.5 mm, the elongation at break is lower when D = 3.0 mm, so the comprehensive performance of triaxial geogrid under this condition is better. Due to the large sampling interval, the maximum value of the multi-axial average tensile strength is located in the sampling interval of (2.5 mm, 3.0 mm). Therefore, when D is in the range of 2.5 mm to 3.0 mm, the comprehensive mechanical properties of industrial PP triaxial geogrid are the best.

Therefore, when the stretching ratio is 3 and the distance between each node is 30 mm, the optimal pre-punched diameter of industrial PP triaxial geogrid is between 2.5 and 3.0 mm.

According to the experiments on biaxial geogrids of the same material by Ren et al. [19], the maximum tensile strength of biaxial geogrids is 23 kN·m^{-1}, which is slightly larger than the triaxial geogrid. However, the triaxial geogrid can carry loads in more directions, and has a stable structure and an obvious interlocking effect with soil and stone, so it has better application prospects.

In this chapter, stretch forming tests at elevated temperature and tensile fracture tests at room temperature were carried out on the triaxial geogrid with different pre-punched hole diameters, and the triaxial geogrid was analyzed from four angles: tensile strength, elongation at break, multi-axial average tensile strength, and comparison with the biaxial geogrid. The relationship between the mechanical performance of triaxial geogrid and the diameter of the pre-punched hole was analyzed. Meanwhile, the optimal range of the pre-punched diameter of the triaxial geogrid was obtained, and the reasons were analyzed.

3. Simulation Research on the Forming of Triaxial Geogrid

In Section 2, the authors studied the mechanical properties of the industrial PP triaxial geogrid by means of experiments. However, it is difficult to study the concrete forming process of the triaxial geogrid and the distribution law of stress and strain by means of experiments. In addition, the maximum value of the multi-axial average tensile strength obtained from the test is in the range of 2.5 mm to 3.0 mm. However, due to the large sampling interval, the specific value cannot be obtained. By means of numerical simulation analysis, the maximum point can be obtained simply and quickly without experiments, saving a lot of time and material resources. In this chapter, the Abaqus software is used to simulate and analyze the heat transfer and tensile forming process of triaxial geogrid,

and the thickness, width, stress and strain distribution of the triaxial geogrid with different pre-punched diameters are obtained.

3.1. Establishment of Triaxial Geogrid Constitutive Model

Algorithms in Abaqus CAE include the explicit algorithm and implicit algorithm. Compared with the implicit algorithm, the explicit algorithm is more suitable for dynamic analysis, as there is no need for equilibrium iteration, and the calculation speed is faster [26–28]. Therefore, the explicit algorithm is suitable for the numerical simulation analysis of geogrid stretch forming.

The material models in Abaqus CAE conclude linear elasticity, elasto-plasticity, hyperelasticity, hypoelasticity, hyperelastic foam, viscoelasticity, etc. [29]. Among them, linear elasticity is the simplest material model in Abaqus CAE, which can define isotropic, orthotropic, anisotropic, and other material behaviors, and is suitable for small elastic strains. The elasto-plasticity model must meet the small deformation conditions, that is, the displacement of each point inside the object is much smaller than the original size of the object. The hyperelasticity model can be used to describe an almost incompressible model, which is suitable for large deformations, especially large volume changes, and the mechanism of permanent deformation is added (hyperelasticity with permanent set), which can numerically analyze the stretching process of polymers in various glassy or superelastic states. The Marlow constitutive model in the hyperelastic model can accurately fit the stress-strain curve with a yield point, and accurately simulate the yield-necking-hardening process of glassy polymers.

The Marlow constitutive model uses strain potential energy to describe the stress-strain relationship of hyperelastic materials. The strain potential energy defines the stored strain energy per unit volume of a material as a function of the strain at that point. The strain potential energy function of the material in the Marlow model can be expressed as Equation (4).

$$U = U_{dev}(\overline{I_1}) + U_{vol}(J_{el}) \tag{4}$$

In Equation (4), U is the unit strain potential energy, U_{dev} is the stress-strain potential energy, U_{vol} is the volumetric strain potential energy, J_{el} is the elastic volume ratio, and $\overline{I_1}$ is the first-order deviatoric strain invariant, which can be expressed by Equation (5).

$$\overline{I_1} = \overline{\lambda_1}^2 + \overline{\lambda_2}^2 + \overline{\lambda_3}^2 \tag{5}$$

In Equation (5), $\overline{\lambda_i} = J^{-1/3}\lambda_i$, J is the total volume change rate and $\overline{\lambda_i}$ is the draw ratio in the main direction. In Equation (4), the stress part energy is determined by the uniaxial, biaxial, or planar test data, and the volume part energy is determined by the volume test data [19].

Therefore, it is necessary to carry out tensile tests on industrial PP materials, obtain stress-strain curves and import them into Abaqus software, in order to simulate the tensile forming process of triaxial geogrids.

According to Chinese national standard GB/T 1040.2-2006 [30], considering the limitation of the test equipment travel, it is advisable to use the 5A standard sample to sample industrial PP, as shown in Figure 9.

In Figure 9, L_0 is the gauge length of the 5A spline, L_1 is the length of the narrow parallel part, L_2 represents the total length of the 5A spline, and L is the initial distance between the fixtures. b_0 represents the width of the narrow part, and b_2 is the length of the spline end. r_1 and r_2 represent the small and large radii of the transition zone of the end and parallel sections respectively.

Industrial PP sheets were sampled and tested at high temperature. The tensile rate was set at 100 mm/min and the stretching ratio was set at 8 times, and the nominal stress-strain curves of the material were obtained at 373 K, 383 K, 393 K, 403 K, and 413 K, as shown in Figure 10a.
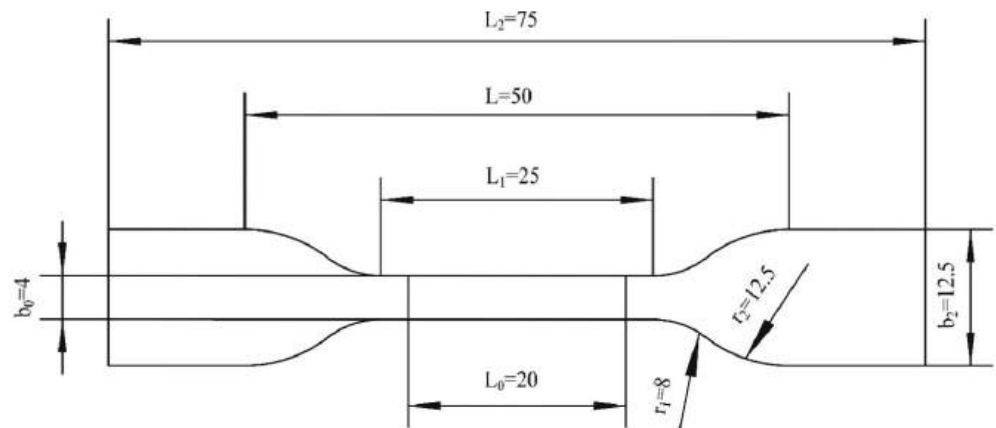
Figure 9. Schematic diagram of 5A standard sample.

Abaqus CAE obtains the material strain potential energy function through the material stress-strain data using the least squares method [29]. The simulation assumes that industrial PP is an isotropic material, and the stress-strain data is obtained through uniaxial tensile tests and imported into the analysis. In this numerical simulation, the 383–403 K stress-strain curve of industrial PP is used for fitting, as shown in Figure 10b.
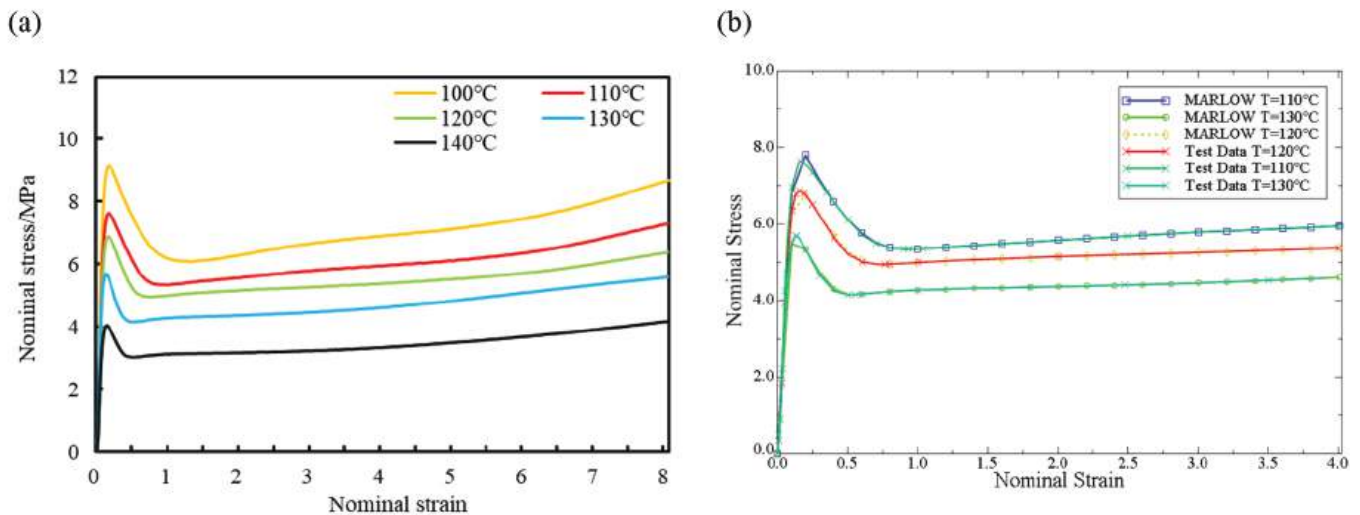
Figure 10. Nominal stress-strain curves of industrial PP. (**a**) Experimental value, (**b**) Fitting of the Marlow curve.

It can be seen from Figure 10a that under various temperature conditions in the range of 373–413 K, the nominal stress increases with increasing nominal strain before the yield point and first increases and then decreases after yielding. With the increase of temperature, the yield stress of industrial PP gradually decreased, the corresponding yield strength showed a slightly decreasing trend, and the elastic modulus also decreased gradually with the increase of temperature. Under the same nominal strain condition, the higher the temperature, the lower the nominal stress of the industrial PP material. The polymer has good tensile properties at high temperature, and remain unbroken under the condition of a larger stretching ratio.

It can be seen from Figure 10b that in the elastic section, there is a small deviation between the fitting of the Marlow curve and the experimental value. After reaching the yield point, the fitting of the Marlow curve is basically consistent with the experimental value. Since the stretching process is mainly the deformation of the plastic section, the deformation can basically be completely retained after removing the external force. The Marlow curve

can better describe the stress-strain behavior of industrial PP during the stretching process at 383–403 K, so in the numerical simulation part, the Marlow constitutive model is selected.

The method of appropriately reducing the size of the model can improve the simulation speed due to the symmetry of pre-punched plate [31]. For the triaxial geogrid, the selection of the basic simulation element from the pre-punched sheet is shown in the shaded area in Figure 11.
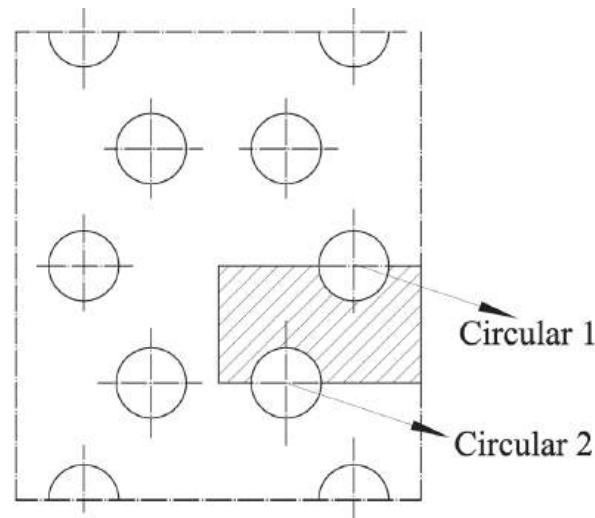
Figure 11. Simulation unit of triaxial geogrid.

The triaxial geogrid simulation unit has a length of 8.7 mm, a width of 5 mm, and a thickness of 4 mm. In Figure 11, the distance between the center of Circular 1 and the right boundary of the simulation unit is 2.9 mm, and the distance between the center of Circular 2 and the left boundary of the simulation unit is 2.9 mm. Once the basic elements of the simulation are set up, heat transfer simulations, and biaxial stretching simulations can be performed.

We model the basic simulation unit and name the loading surface as shown in Figure 12.
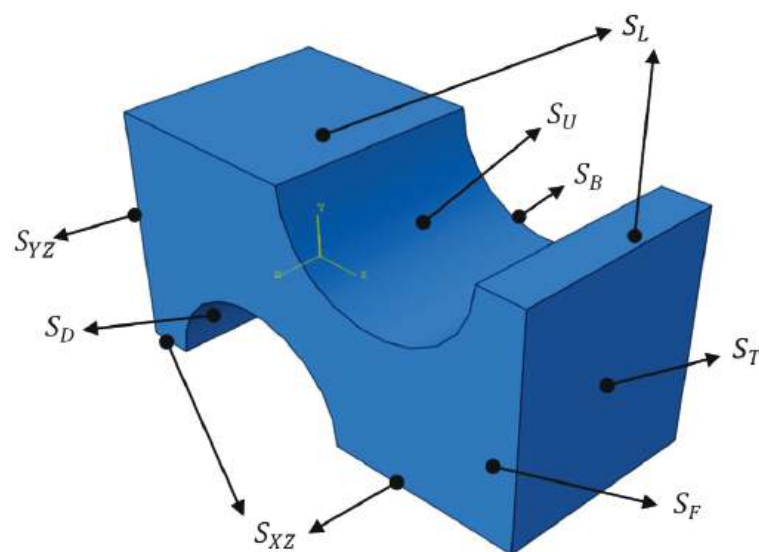
Figure 12. Loading surface and symmetry plane of the basic simulation unit

In Figure 12, S_U and S_D are the punching surfaces. S_F and S_B are the front and behind surfaces. S_{YZ} and S_{XZ} are the symmetry planes of the model along the XZ surface

and the YZ surface. S_L and S_T are the loading surfaces of longitudinal stretching and transverse stretching.

3.2. Heat Transfer Simulation of Industrial PP Triaxial Geogrid

Before the industrial PP triaxial geogrid is stretched longitudinally, the pre-punched sheet needs to be heated at a certain temperature. In this section, the heat transfer simulation of the heating process of industrial PP triaxial geogrid pre-punched sheets with different pre-punched diameters is carried out, and the relationship between the temperature distribution during the heating process and the diameter of the pre-punched holes is obtained.

The heat transfer process includes step Initial for describe initial conditions and Step-1 for describing the heat transfer process. In Initial, we set the model to be mirror-symmetrical along S_{YZ} and S_{XZ}, and inherit the boundary conditions into Step-1. In Step-1, we set the interaction conditions to simulate the heat transfer between the model and the hot air in the oven, and S_F, S_B, S_U, and S_D are the heat transfer surfaces. In this numerical simulation, the thermal conductivity of industrial PP is set to 0.24 [32], the temperature before heat preservation is 293 K, the target temperature is 393 K, and the high temperature holding time is 5 min.

The mesh type is set to the eight-node linear heat transfer hexahedron element DC3D8, and the mesh size is about 0.15 mm. We create a new task and submit it for analysis [33–35].

Taking the triaxial geogrid with a pre-punched hole diameter of 3.5 mm as an example, the heat transfer results and the setting of the path are shown in Figure 13.
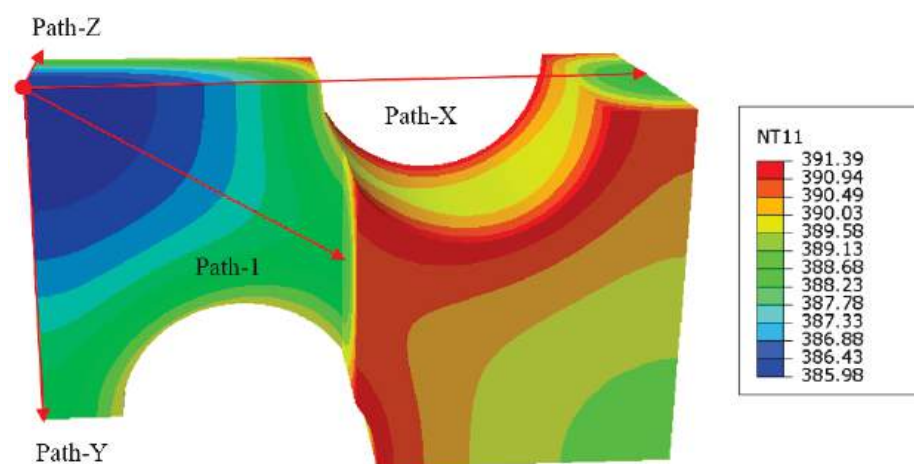
Figure 13. Heat transfer results and path specification of triaxial geogrid with a pre-punched diameter of 3.5 mm.

It can be seen from Figure 13 that after the heat transfer, the temperature at different positions is different. The temperature in the area close to the heat transfer surfaces is higher, and this part is easy to deform first in the stretching process, thereby forming ribs. The core material is far away from the heat transfer surface, the heat transfer is insufficient, and the temperature is lower after the heat transfer, which makes it easy to form nodes in the subsequent stretching process. The temperature at the junction of the circular pre-punched holes and the surface of the sheet is the highest after heat transfer, up to 391 K, and the lowest temperature of the core material is 386 K.

Heat transfer simulations were performed on triaxial geogrids with different pre-punched diameters, and the temperatures along Path-X, Path-Y, Path-Z, and Path-1 were calculated, as shown in Figure 14.

It can be seen from Figure 14a that the pre-punched holes will be passed along Path-X. Before Path-X passed the pre-punched hole, the temperature gradually increases along Path-X, and, after Path-X passed the pre-punched hole, the temperature gradually decreases.

For samples with the same pre-punched diameter, the temperature after Path-X passed the pre-punched hole is slightly higher than that before Path-X passed the hole.

It can be seen from Figure 14b that the temperature of each sample along Path-Y gradually increases, and the temperature difference at the end of Path-Y with different pre-punched diameters is greater than the temperature difference at the starting point of Path-Y.
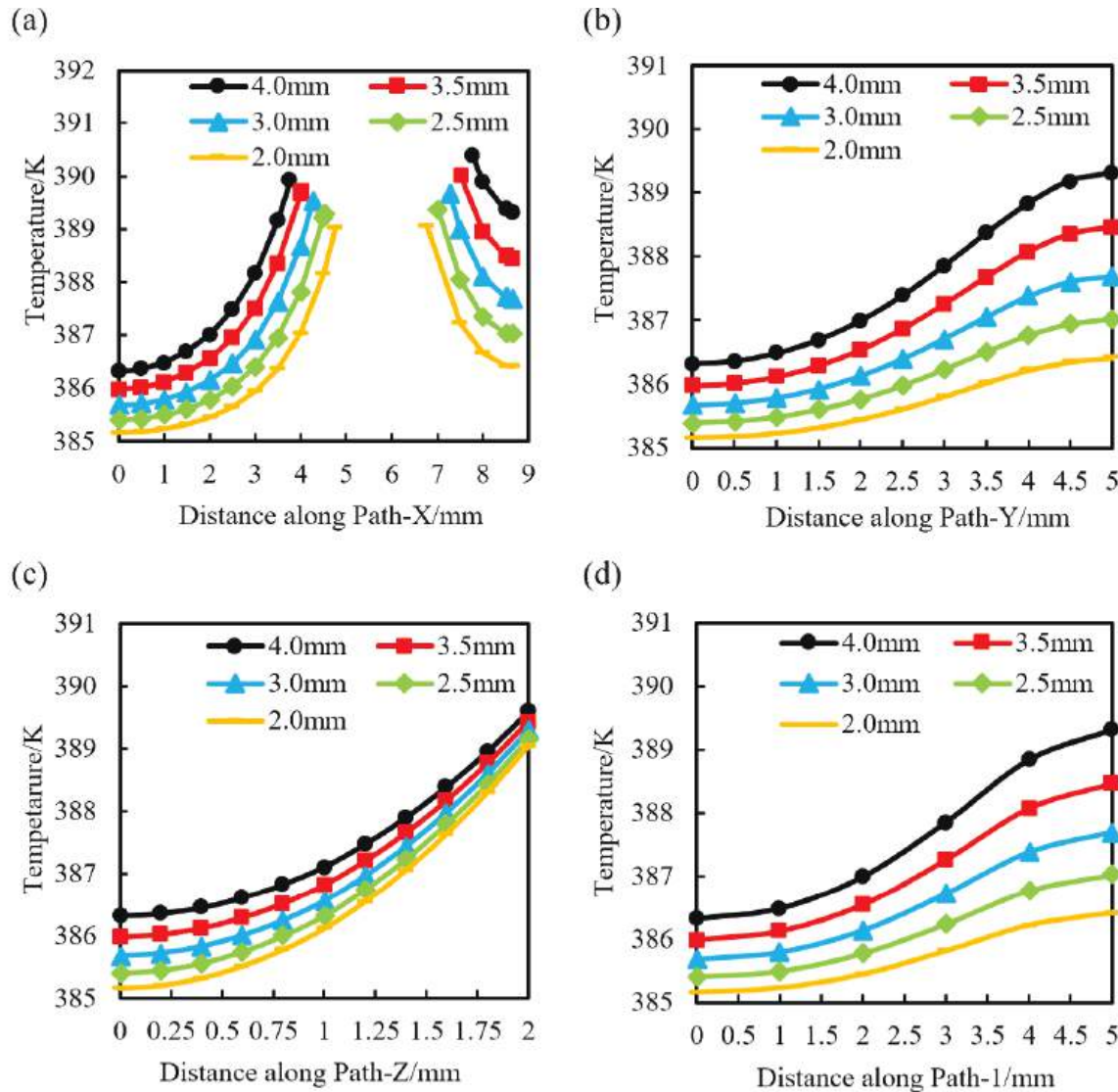
Figure 14. Temperature distribution of triaxial geogrid with a different pre-punched diameter along each path. (**a**) Path-X, (**b**) Path-Y, (**c**) Path-Z, (**d**) Path-1.

It can be seen from Figure 14c that the temperature of each sample along Path-Z gradually increases, and the temperature difference at the end of Path-Z for samples with different pre-punched diameters is smaller than the temperature difference at the starting point of Path-Z.

It can be seen from Figure 14d that the temperature distribution law of the sample along Path-1 direction is basically consistent with that along Path-Y, showing a trend of increasing temperature along Path-1. Furthermore, the temperature difference at the end of Path-1 is greater than that at the beginning.

Therefore, Figure 14 shows that with the increase of the diameter of the pre-punched hole, the temperature of the same position on each path increases continuously, indicating that the larger the pre-punched hole is, the better the heat transfer effect is. At the same time,

the temperature of each part is different under the same pre-punched condition, indicating that the subsequent stretching process is carried out under a certain temperature gradient, and an appropriate temperature gradient is beneficial to the forming of the geogrid.

3.3. Simulation of Stretch Forming of Industrial PP Triaxial Geogrid

In this section, stretch forming simulation of the geogrid will be performed. The stretching process of the triaxial geogrid includes longitudinal stretching and transverse stretching in turn.

In the Initial analysis step, we set the heat transfer simulation result file to a predefined field. We set the "Dynamic, Temperature-Displacement, Explicit" analysis step, Step-1, to represent longitudinal stretching, and Step-2 to represent transverse stretching.

In step Initial, we set the model to be mirror-symmetrical along S_{XZ} and S_{YZ}, and inherit the boundary conditions in the Step-1 and Step-2 analysis steps. In Step-1, a load is applied to S_L so that S_L is displaced by 10 mm in the direction of longitudinal stretching, and the model is constrained to be mirror-symmetrical along S_T. In Step-2, the boundary condition set in Step-1 is modified to "inactive", and a load is applied to S_T, so that S_T is displaced 17.3 mm in the direction of transverse stretching, and the model is constrained to be mirror-symmetrical along the S_L. This ensures that the longitudinal and transverse stretch ratios are both 3.

After the loads and boundary conditions are set, the model needs to be meshed. In this numerical analysis, the eight-node thermally coupled hexahedral element C3D8T is used. The mesh size is 0.15 mm, which is consistent with the heat transfer step. After meshing the model, we create a new job and submit it for analysis.

3.3.1. Shape Analysis of Stretch Forming

Taking the industrial PP triaxial geogrid with a diameter of 3.5 mm as an example, the simulated stretch forming process is shown in Figure 15.
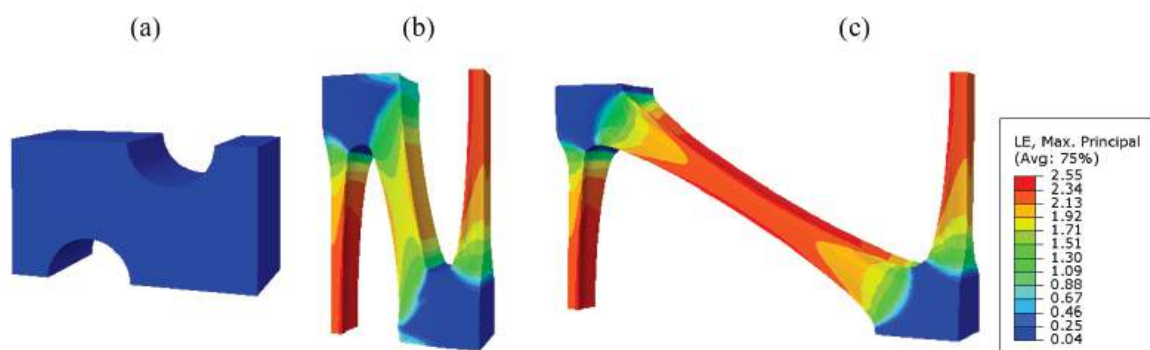
Figure 15. Strain cloud map of the triaxial geogrid stretch forming simulation. (**a**) Before longitudinal stretching, (**b**) after longitudinal stretching, (**c**) after transverse stretching.

As shown in Figure 15, the node is basically not deformed during the stretching process, and the main deformation area is the rib. During the longitudinal stretching process, the deformation degree of the 90° bars is greater than that of the diagonal bars. During the longitudinal stretching process, the transition zone is basically formed. The transverse stretching process is mainly the stretching process in which the diagonal ribs are deformed in the transverse direction.

In addition, it was found that during the stretching process, the 90° rib shrinks inwards in both the width and thickness directions, and the rib is thin in the middle and thick on both sides. This is because during the stretching process, the rib is subjected to inward compressive stress, and the edge and corner areas are prone to stress concentration and are not easily deformed, so the shape is thin in the middle and thick on both sides. During transverse stretching, the 90° rib will decrease in thickness and increase in width.

Furthermore, after longitudinal stretching, the cross-sectional area of the 90° rib is smaller than before stretching. This is due to the fact that uniaxial stretching and equal biaxial compression are equivalent for a nearly incompressible material such as industrial polypropylene. During longitudinal tension, the cross-sectional area of the 90° rib is continuously reduced.

The cross-section of the triaxial geogrid after transverse stretching is taken along the axis of symmetry in the thickness direction, as shown in Figure 16.
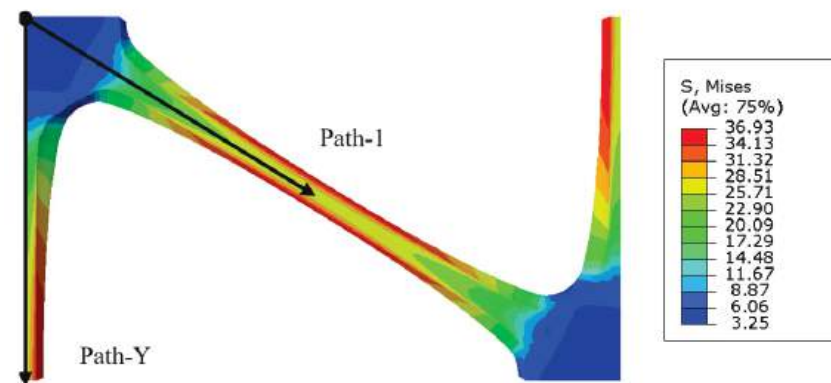
Figure 16. Cross section of the thick symmetry axis and path definition of triaxial geogrid.

It can be seen from Figure 16 that the maximum stress and strain of a triaxial geogrid after stretching appears on the surface of the rib. Paths are defined along the longitudinal and diagonal directions, named Path-Y and Path-1. Due to the symmetry of the sample, in order to shorten the analysis time, the starting point is selected as the center of the node, and the end point is selected as the center of the longitudinal and diagonal ribs.

Along the Path-Y path shown in Figure 16, we collect and compare the width and thickness of the 90° rib before and after transverse stretching, as shown in Figure 17.
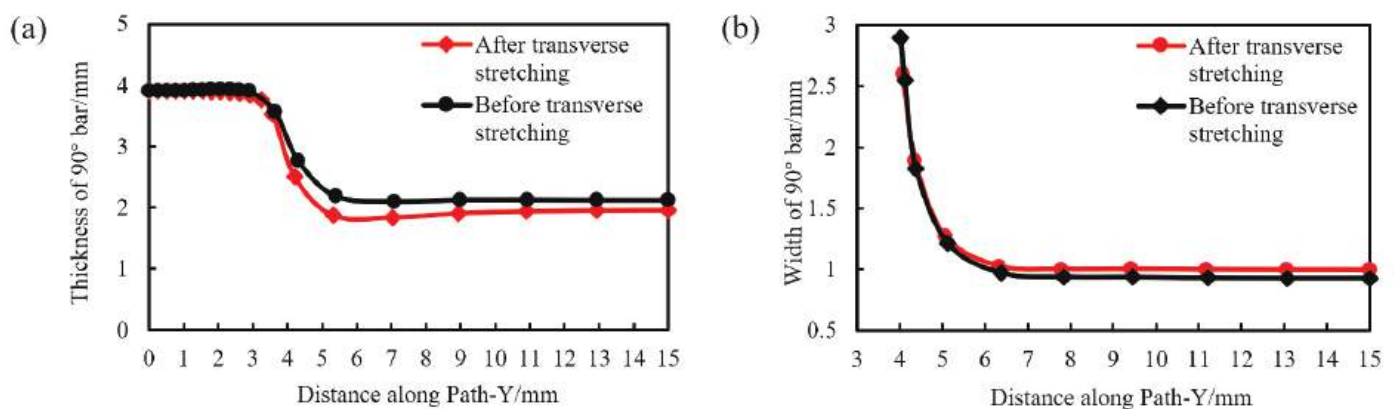
Figure 17. Thickness and width of the 90° rib before and after transverse stretching. (**a**) Thickness, (**b**) width.

As shown in Figure 17a, the thickness of the node before and after transverse stretching is basically unchanged, and the thickness of the transition zone and rib is slightly reduced. From Figure 17b, it can be seen that the width of the 90° rib has increased slightly. This is because the transverse tension is applied to the geogrid plate during the transverse stretching, and the material that has formed the longitudinal ribs is slightly deformed in the transverse direction.

By comparing the simulation results with the test data, the deviation can be calculated and the accuracy of the simulation method can be verified. The comparison between the simulation results of tensile forming and the test data is shown in Table 2.

Table 2. Comparison of tensile forming simulation results with experimental data.

Items for Comparison	Simulation Results	Test Results	Deviation
Thickness of the node	3.91 mm	4.02 mm	−2.74%
Width of the node	5.82 mm	5.69 mm	+2.28%
Thickness of longitudinal rib	1.95 mm	1.94 mm	+0.52%
Width of longitudinal rib	0.99 mm	0.91 mm	+8.79%

It can be seen from Table 2 that the simulation results are basically consistent with the test, and the deviation is controlled within 10%. Therefore, the simulation method can be applied to the stretch forming analysis of the triaxial geogrids.

Using this simulation method, the stretch process of triaxial geogrids with pre-punched diameters of 2.0 mm, 2.5 mm, 3.0 mm, and 4.0 mm were simulated. The stretching results are symmetrical along the X axis and the Y axis, and the obtained results are shown in Figure 18.
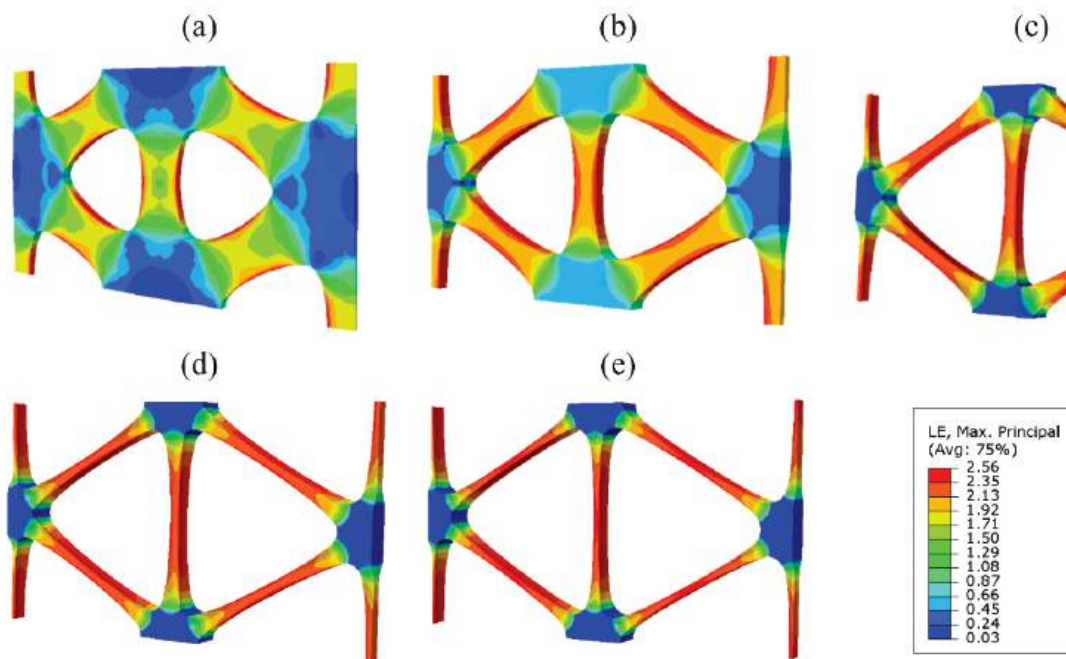
Figure 18. Simulation result of triaxial geogrid with different pre-punched diameters. (**a**) D = 2.0 mm, (**b**) D = 2.5 mm, (**c**) D = 3.0 mm, (**d**) D = 3.5 mm, (**e**) D = 4.0 mm.

It can be seen from Figure 18 that when D = 2.0 mm, the nodes are completely destroyed during the stretching process, and regular-shaped nodes cannot be formed. When D = 2.5 mm, the nodes are partially destroyed, and the maximum thickness of the grid appears at the edge of the nodes. When D is no less than 3.0 mm, a regular and complete triaxial geogrid can be formed.

According to the analysis in Figure 8, the tensile strength of triaxial geogrid increases first and then decreases with the increase of the diameter of the pre-punched hole. When D is greater than 2.5 mm and less than 3 mm, the tensile strength of triaxial geogrid must have a maximum value; and when the tensile strength takes the maximum value, the nodes are not damaged after forming. The minimum pre-punched diameter of triaxial geogrid with complete and regular nodes can be obtained quickly and accurately by finite element simulation.

For the pre-punched hole diameter D located in (2.5, 3.0) interval, with 0.1 mm as an interval, the numerical simulation of stretch forming was carried out with the same simulation method and process parameters from 2.6 mm to 2.9 mm. It was found that each sample could form a triaxial geogrid with regular node shape and complete structure after stretching. The simulation result for D = 2.6 mm is shown in Figure 19.
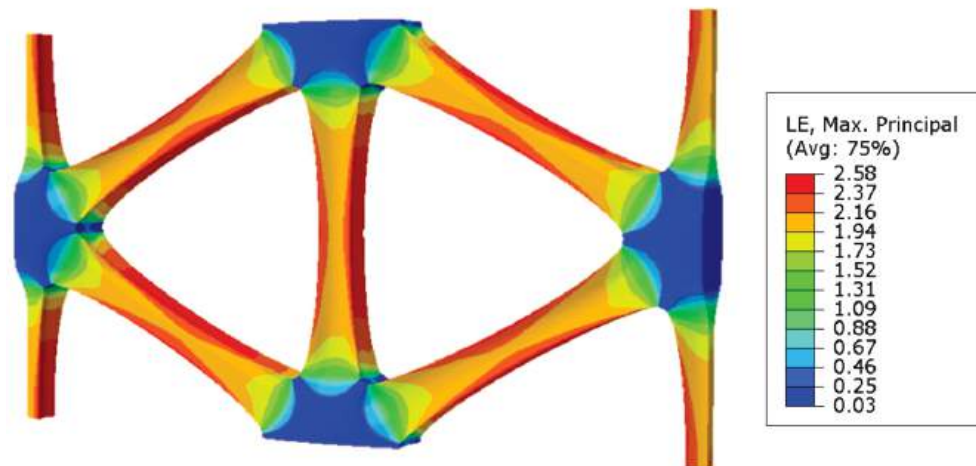
Figure 19. Simulation result of a triaxial geogrid with a pre-punched diameter of 2.6 mm.

It can be seen from Figure 19 that under the test parameters, the nodes are not damaged after forming, and the minimum diameter D of the pre-punched hole is 2.6 mm. It can be further speculated that when D = 2.6 mm, the tensile strength of the triaxial geogrid can reach the maximum value.

When D = 2.0 mm, the node is completely destroyed and does not have the complete structure of the geogrid. When D = 2.5 mm, the morphology of the node in the pre-stretched area and the post-stretched area are different, therefore, data sampling for a geogrid with 2.5 mm pre-punched hole is not representative. Therefore, in this part, data sampling and analysis are mainly carried out respectively on the simulation results of stretch forming with pre-punched diameters of 2.6 mm, 3.0 mm, 3.5 mm, and 4.0 mm.

The thickness and width of industrial PP triaxial geogrids with different pre-punched diameters were measured along Path-Y and Path-1, shown in Figure 16. The distribution of the width and thickness of the 90° and diagonal bars when D = 2.6 mm, 3.0 mm, 3.5 mm, and 4.0 mm were obtained, which is shown in Figure 20.

Figure 20a,b represent the thickness and width distribution of the 90° bar along the Path-Y. Figure 20c,d represent the thickness and width distribution of the diagonal bar along the Path-1.

It can be seen from Figure 20a,b that on the premise that the nodes are not damaged, the thickness and width of the samples with the same pre-punched hole diameter show a decreasing trend along Path-Y. It can be seen from Figure 20a that the thickness of the nodes and ribs changes to a small extent, and the thickness of the transition zone changes drastically along Path-Y. It can be seen from Figure 20b that the width of the transition region varies greatly, and the width of the rib varies less. With the increase of the pre-punched hole diameter, the thickness of the node decreases slightly. The thickness of each sample in the transition zone is basically the same, while the width in the transition zone decreases significantly. The thickness of the rib increases, while the width of the rib decreases significantly.

When D is less than 3.0 mm, due to the large hole spacing before forming, more materials are involved in the stretching process, and the width of the rib after forming is relatively large; and the material in the central area of the rib shrinks greatly along the

thickness direction, the degree of deformation in the thickness direction is large, so the width of the rib is greater than the thickness.

From Figure 20c,d, the variation rule of the width and thickness of the diagonal bar with the diameter of the pre-punched hole is the same as that of the 90° bar. Under the above conditions, when D = 2.6 mm, the thickness of the diagonal rib is the smallest and the width is the largest. When D = 4.0 mm, the thickness of the diagonal rib is the largest and the width is the smallest. The width and thickness of the diagonal bars with the same D are basically the same as those of the longitudinal bars. Therefore, when D is not less than 2.6 mm, the tensile strength and elongation at break of the longitudinal bars and the diagonal bars are basically the same and the mechanical performance is more balanced.
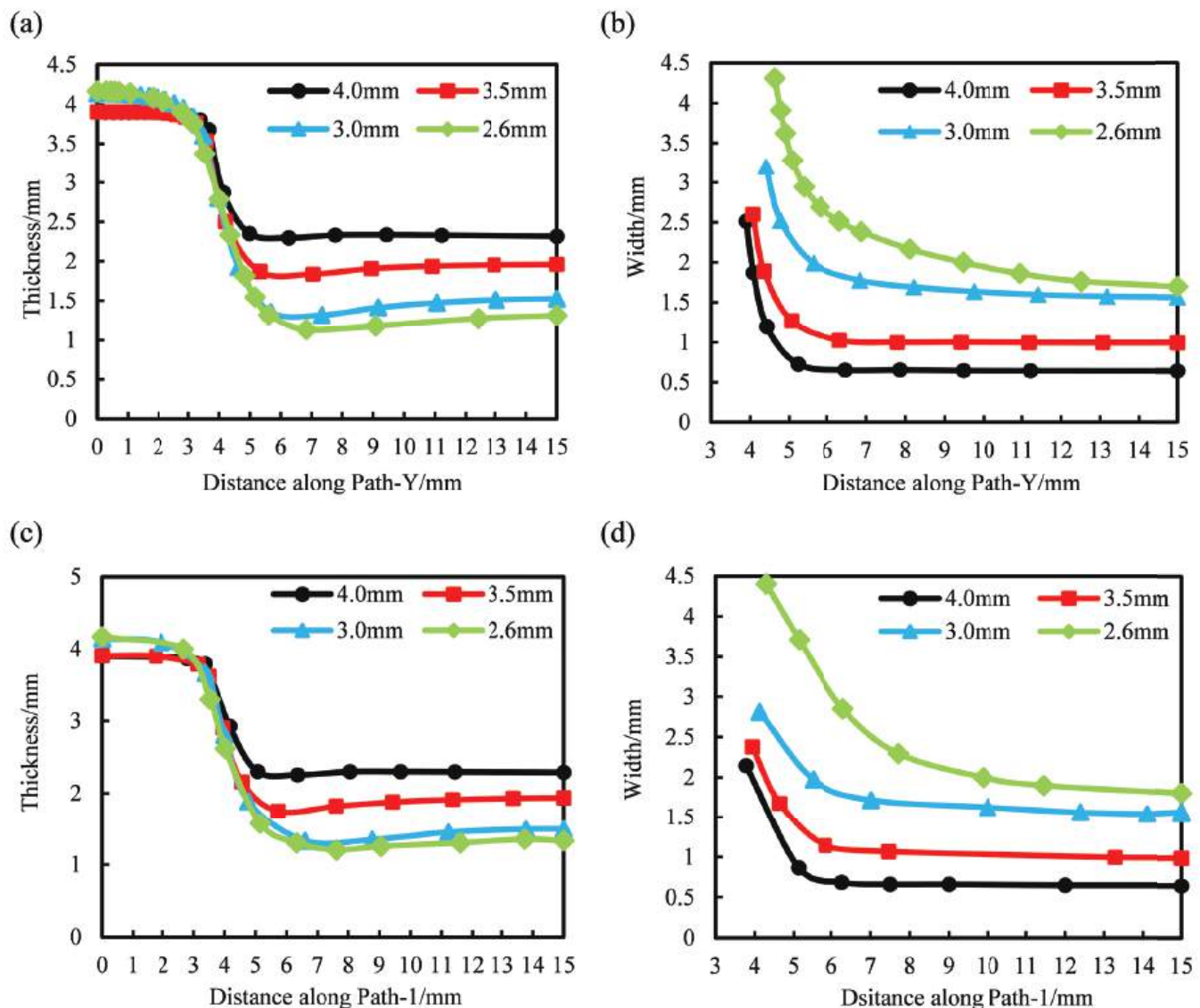
Figure 20. Variation of thickness and width of 90° bar along Path-Y and diagonal bar along Path-1. (**a**) Thickness of 90° bar along Path-Y, (**b**) width of 90° bar along Path-Y, (**c**) thickness of diagonal bar along Path-1, (**d**) width of diagonal bar along Path-1.

3.3.2. Stress and Strain Analysis of Stretch Forming

The stress and strain of the stretch forming process were analyzed by Abaqus CAE, and the distribution law of the stress and strain was obtained. This section will analyze the distribution of stress and strain after the triaxial geogrid is stretched from two aspects: the

distribution law of stress and strain along each path and the change law of stress and strain at special points.

Along Path-Y, starting from the starting point, data are collected at equal intervals. The data interval is 0.5 mm, and the values of stress and a logarithmic strain of 90° bar at each point are measured. The specific distribution law is shown in Figure 21a,b. In the same way, the distribution law of the stress and strain of the diagonal bar is measured along Path-1, as shown in Figure 21c,d.

It can be seen from Figure 21a that the internal stress of the node decreases with the increase of the diameter of the pre-punched hole, and the internal stress of the longitudinal rib increases with the increase of the diameter of the pre-punched hole. When D = 4.0 mm, the stress of longitudinal rib can reach 10 times that of the node. When D = 2.6 mm, the stress of longitudinal rib is 6 times that of the node, and the internal stress distribution is more uniform in this condition, so the tensile strength is higher in the room temperature tensile pulling off test.

It can be seen from Figure 21b that the strain distribution law is basically consistent with the stress distribution. The strain in the node region is small, and basically no deformation occurs during the stretching process. With the increase of the diameter of the pre-punched hole, the logarithmic strain of the node gradually decreases. The longitudinal rib has a large strain and is mainly involved in the deformation during the stretching process; and with the increase of the diameter of the pre-punched hole, the logarithmic strain of the longitudinal rib increases gradually.

The reason for the above phenomenon is that with the increase of the diameter of the pre-punched hole, the material participating in the deform of the rib decreases, and the rib can easily form stress concentration during the stretching process. However, when the diameter of the pre-punched hole is small, there are more materials involved in forming the rib, and the tensile force on the node increases during the stretching process, and the strain value of the node is large.

Figure 21c,d shows that the stress-strain distribution along Path-1 is basically the same as that of the 90° bar. It can be seen from Figure 21c that the diagonal bars are mainly involved in the deformation during the transverse stretching process, in which the node stress is small, and the rib stress is large. The internal stress of the diagonal rib can reach 6–10 times the internal stress of the node. It can be seen from Figure 21d that when D = 2.6 mm or 3.0 mm, the central strain of the diagonal rib is basically equal.
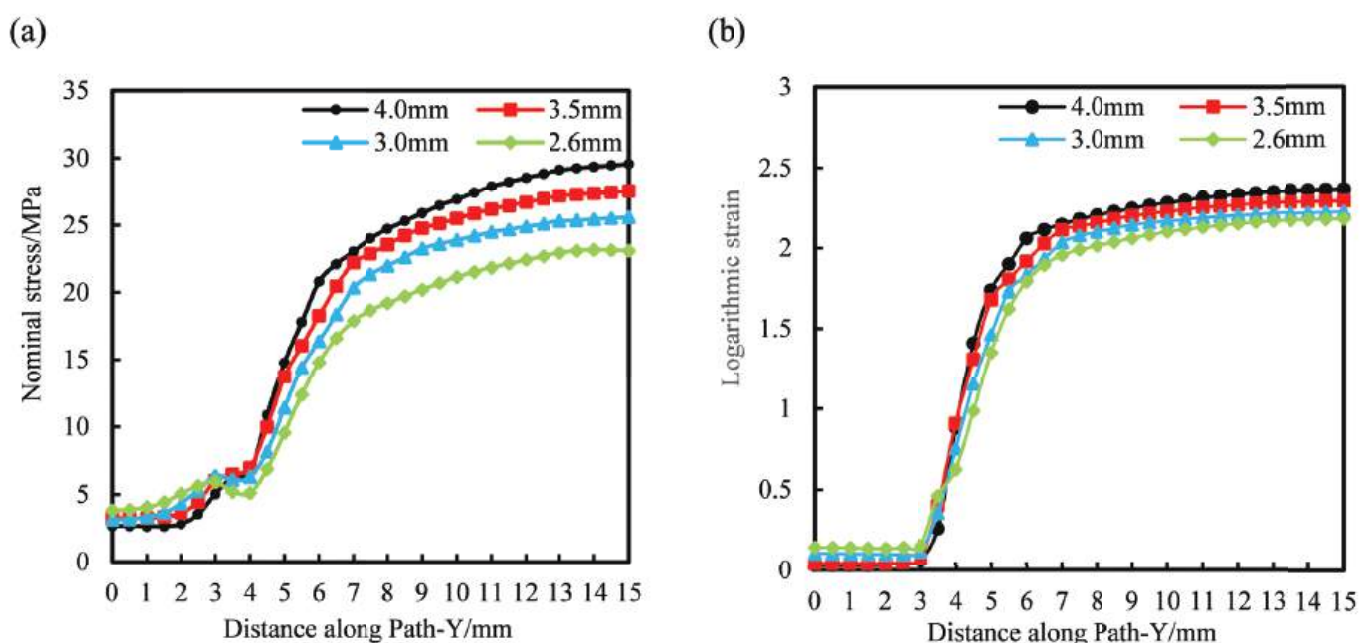
Figure 21. *Cont.*
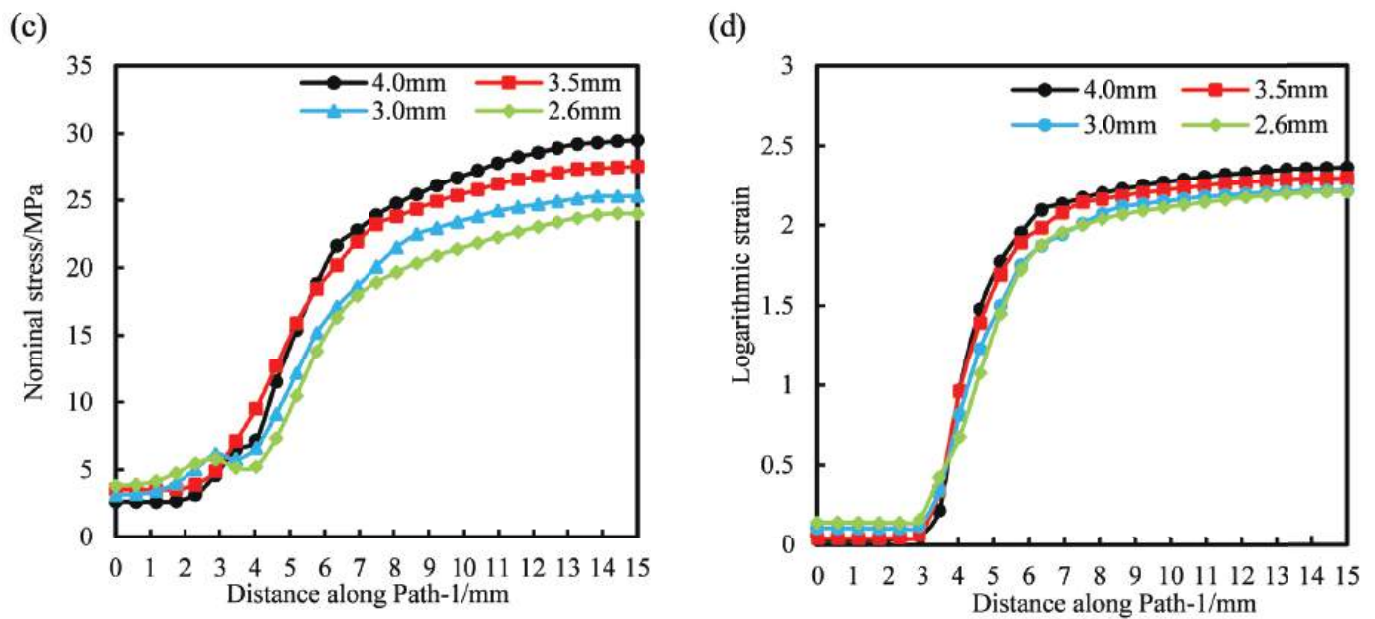
Figure 21. Variation law of stress and strain along Path-Y and Path-1 with the diameter of the pre-punched hole. (**a**) Nominal stress of 90° bar along Path-Y, (**b**) logarithmic strain of 90° bar along Path-Y, (**c**) nominal stress of the diagonal bar along Path-1, (**d**) logarithmic strain of the diagonal bar along Path-1.

The internal stress and strain distribution of industrial PP triaxial geogrid can be measured along Path-Y and Path-1, but, as shown in Figure 15, the maximum stress and strain of triaxial geogrid appears on the surface of the rib. Therefore, it is necessary to select special points and measure their stress-strain values to obtain the overall stress-strain distribution law of triaxial geogrid. The surface center points, internal center points and edge center points of nodes, longitudinal ribs, and diagonal ribs are selected as representative points, which are shown in Figure 22.
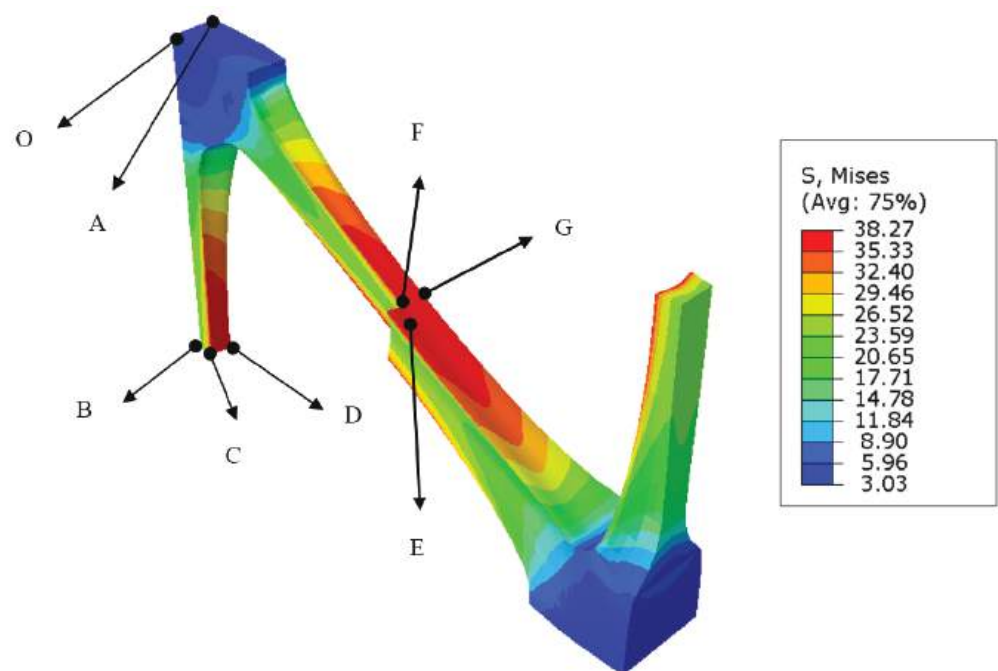
Figure 22. Stress-strain point position.

In Figure 22, point O can represent the center of the node, point A represents the surface of the node. Point B is the inner center point of the longitudinal rib, point C represents the surface of the longitudinal rib, and point D represents the edge of the longitudinal rib. Point E represents the center point inside the diagonal rib, point F represents the surface of the diagonal rib, and point G represents the edge of the diagonal rib. We use σ to indicate stress, ϵ to indicate strain. We add a superscript after σ and ϵ, U indicates after longitudinal stretching, and B indicates after transverse stretching. We add a subscript after σ and ϵ, and the subscript indicates the selected points on the triaxial geogrid. For example, σ_O^U represents the stress at point O after the longitudinal stretching is completed.

Table 3 shows the stress obtained at different positions of triaxial geogrid under the condition of different pre-punched hole diameters after longitudinal stretching.

Table 3. Stress at different positions of triaxial geogrid after longitudinal stretching. (MPa).

D	σ_O^U	σ_A^U	σ_B^U	σ_C^U	σ_D^U	σ_E^U	σ_F^U	σ_G^U
4.0 mm	2.27	2.39	29.38	36.51	35.89	18.65	22.26	21.86
3.5 mm	2.82	3.04	27.29	36.65	35.67	17.85	22.73	22.14
3.0 mm	4.37	4.92	25.57	37.59	36.77	16.16	21.91	21.45
2.6 mm	5.14	5.73	23.06	38.20	38.81	15.55	22.31	22.01

Table 4 shows the stress obtained at different positions of triaxial geogrid under the condition of different pre-punched hole diameters after transverse stretching.

Table 4. Stress at different positions of triaxial geogrid after transverse stretching. (MPa).

D	σ_O^B	σ_A^B	σ_B^B	σ_C^B	σ_D^B	σ_E^B	σ_F^B	σ_G^B
4.0 mm	2.66	3.22	29.57	36.74	36.05	29.52	36.65	35.79
3.5 mm	3.26	3.87	27.55	36.95	35.89	27.51	37.02	35.86
3.0 mm	3.14	4.01	25.58	37.50	36.49	25.31	37.43	36.19
2.6 mm	3.82	4.61	23.08	38.22	38.08	24.00	38.48	35.56

Table 5 shows the strain collected at special points of triaxial geogrid under different pre-punched hole diameters after longitudinal stretching.

Table 5. Logarithmic strain at different positions of triaxial geogrid after longitudinal stretching.

D	ϵ_O^U	ϵ_A^U	ϵ_B^U	ϵ_C^U	ϵ_D^U	ϵ_E^U	ϵ_F^U	ϵ_G^U
4.0 mm	0.034	0.033	2.359	2.534	2.517	1.944	2.105	2.090
3.5 mm	0.040	0.039	2.287	2.528	2.502	1.894	2.118	2.097
3.0 mm	0.071	0.076	2.224	2.542	2.521	1.776	2.083	2.058
2.6 mm	0.102	0.133	2.182	2.631	2.633	1.694	2.124	2.123

Table 6 shows the strain collected at special points of triaxial geogrid under different pre-punched hole diameters after transverse stretching.

Table 6. Logarithmic strain at different positions of triaxial geogrid after transverse stretching.

D	ϵ_O^B	ϵ_A^B	ϵ_B^B	ϵ_C^B	ϵ_D^B	ϵ_E^B	ϵ_F^B	ϵ_G^B
4.0 mm	0.028	0.032	2.365	2.540	2.521	2.359	2.542	2.523
3.5 mm	0.040	0.047	2.297	2.537	2.509	2.293	2.544	2.519
3.0 mm	0.104	0.129	2.227	2.542	2.515	2.218	2.549	2.518
2.6 mm	0.141	0.180	2.184	2.634	2.609	2.211	2.628	2.554

Combined with the data in Tables 3–6, it can be found that, compared with before the transverse stretching, the changes of each point after the transverse stretching of triaxial

geogrid are as follows: the stress at points O and A will increase, and the stresses at points B, E, F, and G will increase. The stress and strain at point C will increase, and the strain at point C will increase. As the diameter of the pre-punched hole increases, the strain at point O in triaxial geogrid after biaxial stretching will increase, the stress at point C will increase, the stress and strain values of A and F will increase, and the stress and strain at points B and E will decrease.

Therefore, transverse stretching will increase the stress value of the node, the inner center of the longitudinal rib, and each point of the diagonal rib. Moreover, transverse stretching will increase the strain value of the center and surface of the longitudinal rib and each point of the diagonal rib. When the diameter of the pre-punched hole increases, the stress on the node surface and longitudinal rib/diagonal rib surface of polypropylene triaxial geogrid will increase, and the stress at the center of longitudinal rib/diagonal rib will decrease; the strain on the center and surface of the node and the surface of the diagonal rib will increase, and the strain at the center of the longitudinal rib/diagonal rib will decrease.

4. Conclusions

In this paper, the relationship between the mechanical properties of industrial polypropylene triaxial geogrid and the diameters of pre-punched holes is studied by experiments combined with numerical simulation analysis, and the thickness, width, stress and strain distribution of triaxial geogrids with different diameters are obtained. The innovation of the paper is reflected in the analysis of pre-punched holes on the mechanical properties of triaxial geogrid through experiments and the application of finite element simulation to the forming process of triaxial geogrid. Furthermore, the feasibility of finite element simulation in the design of multi-axial geogrid is verified. The main conclusions are as follows.

1. When the diameter of the pre-punched hole is small, the node of triaxial geogrid will appear concave in the middle, the integrity of the node will be damaged, and fractures at the node will occur in the room temperature tensile test. When the diameter of the pre-punched hole is larger, the node will appear convex in the middle, and fractures in the transition zone often occur in the tensile fracture test at room temperature. The width of the triaxial geogrid rib decreases as the diameter of the pre-punched hole increases.

2. The tensile fracture tests at room temperature were carried out on the industrial polypropylene triaxial geogrid with a node center spacing of 30 mm, and it was found that the tensile strength increased first and then decreased with the increase of the diameter of the pre-punched holes, and the maximum point interval of the average tensile strength was obtained. Combined with numerical simulation analysis, it was obtained that when the pre-punched hole diameter is 2.6 mm, the comprehensive mechanical properties were the best. The fracture elongation of the rib in the 90° direction showed an overall decreasing trend with the increase of the diameter of the pre-punched hole, and the appearance of this phenomenon is related to the node concave in the middle.

3. The stress-strain curve at 373–413 K was obtained through the high-temperature tensile test of the 5A industrial polypropylene spline. After fitting in Abaqus, it was found that the Marlow constitutive model was applicable.

4. Through numerical simulation analysis of industrial polypropylene preheating process with different pre-punched hole diameters, it was found that a larger pre-punched hole was beneficial to heat transfer, so the heating was more sufficient. In addition, it was found that the temperature of each part was different under the same pre-punched condition, indicating that the subsequent stretching process was formed under a certain temperature gradient.

5. Through the simulation analysis of the industrial polypropylene stretching process, it was found that the transverse stretching had a certain influence on the geogrid after longitudinal stretching. In addition, the diameter of the pre-punched holes affected the shape of the nodes and ribs after forming, as well as the distribution of stress and strain.

The research is of great help to analyze the forming process of a triaxial geogrid, and is of great significance for regulating the mechanical properties of a triaxial geogrid. Therefore, it can promote the application of triaxial geogrid and the design of a new multi-axial geogrid.

Author Contributions: Conceptualization, X.Z. and L.S.; data curation, X.R., J.L. and Z.S.; investigation, X.Z.; supervision, L.S.; validation, X.Z. and L.S.; visualization, X.R. and C.Z.; writing—original draft, X.R. and X.Z.; writing–review and editing, X.R. All authors have read and agreed to the published version of the manuscript.

Institutional Review Board Statement: Not applicable.

Informed Consent Statement: Not applicable.

Data Availability Statement: The data used to support the findings of this study are available from the corresponding author upon request.

Conflicts of Interest: The authors declare that there are no known financial conflict of interest that may affect the reporting of this article.

References

1. Ziegler, M. Application of geogrid reinforced constructions: History, recent and future developments. *Procedia Eng.* **2017**, *172*, 42–51. [CrossRef]
2. Koda, E.; Kiersnowska, A.; Kawalec, J.; Osiński, P. Landfill slope stability improvement incorporating reinforcements in reclamation process applying observational method. *Appl. Sci.* **2020**, *10*, 1572. [CrossRef]
3. Chen, J.F.; Gu, Z.A.; Rajesh, S.; Yu, S.B. Pullout Behavior of triaxial geogrid embedded in a transparent soil. *Int. J. Geomech.* **2021**, *21*, 04021003. [CrossRef]
4. Dong, Y.L.; Han, J.; Bai, X.H. Numerical analysis of tensile behavior of geogrids with rectangular and triangular apertures. *Geotext. Geomembr.* **2011**, *29*, 83–91. [CrossRef]
5. Zhang, J.; Cao, W.Z.; Zhou, Y.J. Mechanical Behavior of Triaxial Geogrid Used for Reinforced Soil Structures. *Adv. Civ. Eng.* **2021**, *2021*, 5598987. [CrossRef]
6. Arulrajah, A.; Rahman, M.A.; Piratheepan, J.; Bo, M.; Imteaz, M. Evaluation of interface shear strength properties of geogrid-reinforced construction and demolition materials using a modified large-scale direct shear testing apparatus. *J. Mater. Civ. Eng.* **2014**, *26*, 974–982. [CrossRef]
7. Das, S.; Choudhury, M. Effectiveness of Triaxial Geogrid Reinforcement for the Improvement of CBR Strength of Natural Lateritic Gravel Soil for Rigid Pavements. *World J. Civ. Eng. Constr. Technol.* **2015**, *2*, 51–56.
8. Ma, Q.; Zheng, J.J.; Zhang, J. Study on the Cut-and-Fill Roadbed Reinforced by Triaxial Geogrid. In *Advanced Materials Research*; Trans Tech Publications Ltd.: Bäch, Switzerland, 2011; Volume 163, pp. 4612–4617.
9. Aurrekoetxea, J.; Sarrionandia, M.; Urrutibeascoa, I.; Maspoch, M.L. Effects of recycling on the microstructure and the mechanical properties of isotactic polypropylene. *J. Mater. Sci.* **2001**, *36*, 2607–2613. [CrossRef]
10. Haillant, O.; Lemaire, J. Natural and artificial photo-aging of non-stabilized and pigmented, hindered-amine stabilized propylene–ethylene copolymers. *Polym. Degrad. Stab.* **2006**, *91*, 2748–2760. [CrossRef]
11. Biale, G.; La Nasa, J.; Mattonai, M.; Corti, A.; Vinciguerra, V.; Castelvetro, V.; Modugno, F. A systematic study on the degradation products generated from artificially aged microplastics. *Polymers* **2021**, *13*, 1997. [CrossRef]
12. Suzuki, S.; Nakamura, Y.; Hasan, A.; Liu, B.; Terano, M.; Nakatani, H. Dependence of tacticity distribution in thermal oxidative degradation of polypropylene. *Polym. Bull.* **2005**, *54*, 311–319. [CrossRef]
13. Lin, Y.; Li, X.; Meng, L.; Chen, X.; Lv, F.; Zhang, Q.; Zhang, R.; Li, L. Structural evolution of hard-elastic isotactic polypropylene film during uniaxial tensile deformation: The effect of temperature. *Macromolecules* **2018**, *51*, 2690–2705. [CrossRef]
14. Rizzo, G.; Spadaro, G. Necking behavior of low-density polyethylene-isotactic polypropylene blends: A morphological investigation. *Polym. Eng. Sci.* **1984**, *24*, 264–267. [CrossRef]
15. Ingram, J.; Zhou, Y.; Jeelani, S.; Lacy, T.; Horstemeyer, M.F. Effect of strain rate on tensile behavior of polypropylene and carbon nanofiber filled polypropylene. *Mater. Sci. Eng. A* **2008**, *489*, 99–106. [CrossRef]
16. Kiersnowska, A.; Fabianowski, W.; Koda, E. The influence of the accelerated aging conditions on the properties of polyolefin geogrids used for landfill slope reinforcement. *Polymers* **2020**, *12*, 1874. [CrossRef] [PubMed]

17. Li, M.; Hsuan, Y.G. Temperature and pressure effects on the degradation of polypropylene tape yarns—Depletion of antioxidants. *Geotext. Geomembr.* **2004**, *22*, 511–530. [CrossRef]

18. Zheng, C.; Liu, J.; Fan, J.; Luan, Y.; Song, L. Research on deformation behavior of isotactic polypropylene in uniaxial geogrid manufacture. *Mater. Des.* **2016**, *91*, 1–10. [CrossRef]

19. Ren, X.; Zhao, X.; Zheng, C.; Song, L.; Yang, X.; Liu, Z. Research on mechanical performance of industrial polypropylene biaxial geogrid. *Polym. Test.* **2021**, *99*, 107214. [CrossRef]

20. Zhang J.-R.; Xia, L.; Lu, Z.-A. Material properties and tensile behaviors of polypropylene geogrid and geonet for reinforcement of soil structures. *J. Wuhan Univ. Technol. Mater. Sci. Ed.* **2002**, *17*, 83–86.

21. Jiang, B.; Cao, L.; Zhu, F. Dynamic tensile behavior of polypropylene with temperature effect. *Compos. Part B Eng.* **2018**, *152*, 300–304. [CrossRef]

22. Song, L.B.; Zheng, C.; Wang, Z.; Liu, J.; Fan, J.N.; Luan, Y.G. High-temperature Tensile Characteristics of Polypropylene for Plastic Geogrid. *Phys. Test. Chem. Anal.* **2015**, *51*, 688–692.

23. Caton-Rose, P.; Sweeney, J.; Collins, T.; Coates, P. Finite element simulation of geogrid manufacture using large deformation elastic formulation. *Plast. Rubber Compos.* **2000**, *29*, 51–58. [CrossRef]

24. *GB/T17689*; Geosynthetics-Plastic Geogrids. Standards Press of China: Beijing, China, 2008.

25. *ASTM D6637-11*; Standard Test Method for Determining Tensile Properties of Geogrids by the Single or Multi-Rib Tensile Method. American Society for Testing and Materials: West Conshohocken, PA, USA, 2015.

26. Nasrollah Barati, A.H.; Etemadi Haghighi, A.A.; Haghighi, S.; Maghsoudpour, A. Free and Forced Vibration Analysis of Shape Memory Alloy Annular Circular Plate in Contact with Bounded Fluid. *Iran. J. Sci. Technol. Trans. Mech. Eng.* **2022**, 1–16. [CrossRef]

27. Zhang, Y.; Sun, L.; Li, L.; Xiao, H.; Wang, Y. An efficient numerical method to analyze low-velocity impact response of carbon fiber reinforced thermoplastic laminates. *Polym. Compos.* **2020**, *41*, 2673–2686. [CrossRef]

28. Malekzadeh, P.; Dehbozorgi, M. Low velocity impact analysis of functionally graded carbon nanotubes reinforced composite skew plates. *Compos. Struct.* **2016**, *140*, 728–748. [CrossRef]

29. Simulia, D.C.S ABAQUS 6.11 Analysis User's Manual. Abaqus 6.11 Documentation. 2011. p. 22. Available online: https://www.google.com/url?sa=t&rct=j&q=&esrc=s&source=web&cd=&ved=2ahUKEwjexPrYs8D4AhVWRvEDHRk2 BpYQFnoECAcQAQ&url=http%3A%2F%2F130.149.89.49%3A2080%2Fv6.11%2Fpdf_books%2FANALYSIS_2.pdf&usg= AOvVaw2vb066sOl6lnkvhyRsDEWY (accessed on 1 May 2022)

30. *GB/T 1040.2-2006*; Plastics—Determination of Tensile Properties—Part 2: Test Conditions for Moulding and Extrusion Plastics. National Standard of the People's Republic of China: Beijing, China, 2006.

31. Gartner III, T.E.; Jayaraman, A. Modeling and simulations of polymers: A roadmap. *Macromolecules* **2019**, *52*, 755–786. [CrossRef]

32. Ganguli, S.; Roy, A.K.; Anderson, D.P. Improved thermal conductivity for chemically functionalized exfoliated graphite/epoxy composites. *Carbon* **2008**, *46*, 806–817. [CrossRef]

33. Li, W.; Li, Y.; Shang, J.; Chen, Y.; Zu, J. *Research on the Durability of Composite Pile Made of Ultra-High-Performance and Common Concrete: Finite Element Analysis*; IOP Conference Series: Earth and Environmental Science; IOP Publishing: Bristol, UK, 2021; Volume 719, p. 022072.

34. Wu, Y.; Li, J. Temperature and stress of RC T-beam under different heating curves. *J. Build. Eng.* **2022**, *46*, 103620. [CrossRef]

35. Ma, Z.; Lu, W.; Mäkeläinen, P.; Outinen, J. Prediction of Joint Temperatures in Shot-Nailed Cold-Formed Steel Sheeting with Finite Element Modelling. In Proceedings of the 21th International Specialty Conference on Cold-Formed Steel Structures, St. Louis, MI, USA, 24–25 October 2012; Department of Civil, Architectural & Environmental Engineering, Missouri University of Science and Technology: Rolla, MI, USA, 2012; pp. 599–609.

A Design of Experiments (DoE) Approach to Optimize Cryogel Manufacturing for Tissue Engineering Applications

Duarte Nuno Carvalho [1,2] , **Cristiana Gonçalves** [1,2,*] , **Joaquim Miguel Oliveira** [1,2] , **David S. Williams** [3] , **Andrew Mearns-Spragg** [3] , **Rui L. Reis** [1,2] and **Tiago H. Silva** [1,2]

1. 3B's Research Group, I3B's—Research Institute on Biomaterials, Biodegradables and Biomimetics of University of Minho, Headquarters of the European Institute of Excellence on Tissue Engineering and Regenerative Medicine, AvePark, Barco, 4805-017 Guimarães, Portugal; duarte.carvalho@i3bs.uminho.pt (D.N.C.); miguel.oliveira@i3bs.uminho.pt (J.M.O.); rgreis@i3bs.uminho.pt (R.L.R.); tiago.silva@i3bs.uminho.pt (T.H.S.)
2. ICVS/3B's—P.T. Government Associate Laboratory, Braga, 4805-017 Guimarães, Portugal
3. Jellagen Limited, Unit G6, Capital Business Park, Parkway, St. Mellons, Cardiff CF3 2PY, UK; david.williams@jellagen.co.uk (D.S.W.); andrew@jellagen.co.uk (A.M.-S.)
* Correspondence: cristianammg@gmail.com; Tel.: +351-253-510-931; Fax: +351-253-510-909

Abstract: Marine origin polymers represent a sustainable and natural alternative to mammal counterparts regarding the biomedical application due to their similarities with proteins and polysaccharides present in extracellular matrix (ECM) in humans and can reduce the risks associated with zoonosis and overcoming social- and religious-related constraints. In particular, collagen-based biomaterials have been widely explored in tissue engineering scaffolding applications, where cryogels are of particular interest as low temperature avoids protein denaturation. However, little is known about the influence of the parameters regarding their behavior, i.e., how they can influence each other toward improving their physical and chemical properties. Factorial design of experiments (DoE) and response surface methodology (RSM) emerge as tools to overcome these difficulties, which are statistical tools to find the most influential parameter and optimize processes. In this work, we hypothesized that a design of experiments (DoE) model would be able to support the optimization of the collagen-chitosan-fucoidan cryogel manufacturing. Therefore, the parameters temperature (A), collagen concentration (B), and fucoidan concentration (C) were carefully considered to be applied to the Box–Behnken design (three factors and three levels). Data obtained on rheological oscillatory measurements, as well as on the evaluation of antioxidant concentration and adenosine triphosphate (ATP) concentration, showed that fucoidan concentration could significantly influence collagen-chitosan-fucoidan cryogel formation, creating a stable internal polymeric network promoted by ionic crosslinking bonds. Additionally, the effect of temperature significantly contributed to rheological oscillatory properties. Overall, the condition that allowed us to have better results, from an optimization point of view according to the DoE, were the gels produced at −80 °C and composed of 5% of collagen, 3% of chitosan, and 10% fucoidan. Therefore, the proposed DoE model was considered suitable for predicting the best parameter combinations needed to develop these cryogels.

Keywords: marine biomaterials; marine origin biopolymers; factorial design; optimization; cryo-environment; cartilage tissue

1. Introduction

Despite the advances of modern medicine, there is still a severe difficulty in finding adequate donors of tissues and organs to meet the vast patient needs. Due to innumerable limitations, the scientific community has focused more on other alternatives, such as tissue engineering (TE). This approach can create adequate temporary (bio)material scaffolds to promote the regeneration of human tissues without altering the original anatomical and physiological function [1,2]. To perform this demand, (bio)materials should meet some

basic requirements such as matching to the native extracellular matrix (ECM), providing a favorable microenvironment to preserve the normal phenotype of cells and their metabolisms; being degradable; and above all, being safe for the patient [3].

In general, these structures can be prepared using a multicombination of two principal approaches: (1) the methodology or procedure to develop the biomaterials such as ionic chemical gelation, (bio)inks for 3D printers, cryo-environments, and freeze-drying, among others [4], and (2) the materials (e.g., polysaccharides, proteins, or polyesthers) and their origin that can be derived from natural resources, such as plant, mammal, and marine sources or synthetic and semi-synthetic materials [5]. In this sense, the methodology, reagents, and bioactive compounds make possible the creation of diverse and unique biomaterial scaffolds with distinct forms, sizes, and properties.

In the biomaterials group, it is possible to produce different types of scaffolds, such as cryogels that can be obtained from frozen polymeric solutions stimulated by polymerizable precursors that react in temperatures below zero and form an intricated network [6], having as a principal advantage a simple and faster methodology in relation to other procedures. During this process, the interconnected pore network is formed by ice crystals, highly influenced by the freezing temperature, which reflects on time until ice crystal formation: generally, the larger the temperature drop, the faster the freezing time, and smaller the ice crystals [7]. These polymeric solutions can be obtained from natural sources such as the marine environment, from which they can be extracted in a sustainable form, including different bioactive compounds such as collagen, chitosan, and fucoidan [8]. There is a deep concern of the use of materials of mammal origin due to the risks associated with infections (such as bovine spongiform encephalopathy (BSE)), immunogenicity, and rejection for ethical reasons in motivating research on the use of these marine resources [9,10]. Moreover, these marine compounds have been widely reported for their similarities with proteins and polysaccharides (e.g., collagen, hyaluronic acids, and chondroitin sulfates) present in human ECM, supporting a biomimetic approach of biomaterial development mimicking the composition with the native ECM [11].

In the development of biomaterials, each variable (method, origin material, and concentration, among others) can be defined as a different parameter that, individually or grouped, influence the material characteristics, behavior, properties, and consequently, its final application. However, the interaction between different parameters is complex since it depends not only on direct variables but also on indirect multivariable, such as surrounding temperature, moisture variations, and handling procedures [12], as shown in Figure 1. In the case of cryogels, the temperature (below zero), the chosen sources, the initial polymeric concentration, and their basic structural properties (e.g., the type of ionic charge available) are crucial for forming these types of biomaterials [13]. The selection of the most relevant parameters and the values promising improved performance should be made with caution, envisaging the final application or approach. Therefore, it is crucial to prudently reflect on the parameters to be considered, and for instance, construct a schematic representation of their role and interactions that may affect the final result.

At the moment, much research has been reported on the impact of specific parameters (i.e., the individual effect of each factor), such as the temperature [14] or pH [15], on the development of cryogels. However, little is known about the interactions of the chosen parameters with the biomaterial behavior, i.e., how they can influence each other toward improving their physical and chemical properties, given that it is difficult to instinctively recognize and predict the interactions between several factors. To achieve this quest, factorial design of experiments (DoE) and response surface methodology (RSM) are known as statistical tools to identify the most influential parameter and optimize production processes [16,17]. In brief, this method usually uses linear regression and analysis of variance (ANOVA) mathematical models to extrapolate and predict the interaction of the parameters, their interrelationship, and the optimal point [18]. DoE and RSM have been extensively applied in many areas, which includes the optimization of heterologous protein expression [19], bioactive extraction methods [20,21], and scaffold production, namely,

electrospun materials [22], membranes [23], and hydrogels [24], among others. However, to the best of our knowledge, there are no reports in the literature on the optimization of biomaterial systems based on cryo-environments envisaging biomedical approaches.
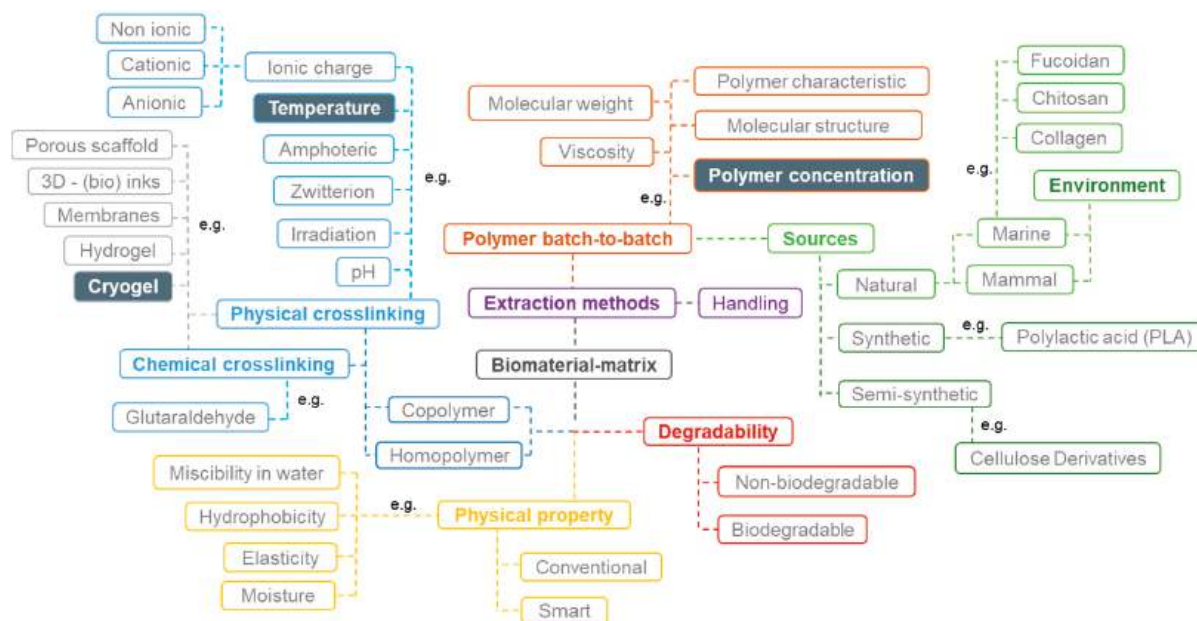
Figure 1. Schematic representation of a direct and indirect variable network. The main variables were: source type (green); polymer batch-to-batch (brown); biomaterial physical properties (yellow); degradability (red); lab experiments and handling (purple); crosslinking type (blue), and biomaterial type (grey).

In summary, in this work, the DoE method was applied to find the optimal values for pre-defined parameters (1) temperature, (2) collagen concentration, and (3) fucoidan concentration) which significantly influence the physico-chemical properties of cryogels developed with jellyfish collagen, chitosan, and fucoidan, and their behavior in contact with cells, being decisive for tissue engineering purposes. A three-level full factorial design for three factors ($n = 27$), Box–Behnken design, was applied. This resulted in a large dataset that reveals the importance of statistical parameter studies for a better understanding of the biomaterial behavior and process optimization.

2. Materials and Methods

2.1. Materials

Collagen from Jellyfish *Rhizostoma pulmo* (jCOL) was provided by Jellagen Pty Ltd. (Cardiff, UK). Fucoidan obtained from brown algae *Fucus vesiculosus* (aFUC) was supplied by Marinova (Maritech Fucoidan, FVF2011527 Marinova, Australia). In addition, chitosan was extracted from squid pens obtained from giant squids *Dosidicus gigas* (sCHT), with a deacetylation degree (DD) of 81.8%, and a molecular weight (M_w) of 334 kDa. According to the PCT patent WO/2019/064231 [25], the raw material was converted into chitosan using a deproteinization and deacetylation method with one single alkaline process under a nitrogen (N_2) atmosphere at 75 °C for 2 h.

2.2. Marine Cryogel Preparation

Firstly, the collagen and chitosan were dissolved in ammonium acetate (0.15 M NH_4OAc/0.2 M AcOH) (pH 4.5). Then, fucoidan was dissolved in a different container with ultrapure water (Milli-Q). Table 1 lists the initial solution concentration of each polymer and respective cryogel formulations. Finally, the marine solutions were gently mixed using an Ultra-Turrax® T18 overhead Blended, IKA Works Inc., Wilmington, NC, USA) in lower rotations to create a homogenous solution (and to avoid bubbles).

Table 1. Cryogel composition prepared by blending three marine origin biopolymers using different temperatures below zero to promote the gelation (ratio of each biopolymer in original solution and their distribution percentage after biomaterial formation).

Hydrogel Abbreviationratio 1:1:1 (100%)	% of Polymer in the Original Solution			Freezing Temperature
	Collagen	**Chitosan**	**Fucoidan**	
C_1 (T °C)	3; (27.27)	3; (27.27)	5; (45.46)	
C_2 (T °C)	3; (18.75)	3; (18.75)	10; (62.5)	
C_3 (T °C)	3; (14.29)	3; (14.29)	15; (71.42)	
C_4 (T °C)	5; (38.46)	3; (23.08)	5; (38.46)	−20 °C −80 °C −196 °C (liquid nitrogen)
C_5 (T °C)	5; (27.78)	3; (16.67)	10; (55.55)	
C_6 (T °C)	5; (21.74)	3; (13.04)	15; (65.22)	
C_7 (T °C)	7; (46.67)	3; (20)	5; (33.33)	
C_8 (T °C)	7; (35)	3; (15)	10; (50)	
C_9 (T °C)	7; (28)	3; (12)	15; (60)	

% w/v of polymer in the original solution; (% w/w of the total polymer mass in each cryogel formation). (T °C) is the respective freezing temperature.

To form the cryogels, the natural crosslinking between the biopolymers (by electrostatic interactions) was performed in a cryo-environment process, where the mixed solutions were placed overnight in temperatures below zero (−20 °C, −80 °C, and −196 °C) and then transferred for a few hours to the fridge (4 °C). To neutralize the pH, the cryogels were placed several times into a D-MEM solution (cell culture medium) with the intention of not compromising the viability of the cells by the presence of acidic material. The entire cryogel production procedure is demonstrated in Figure 2.
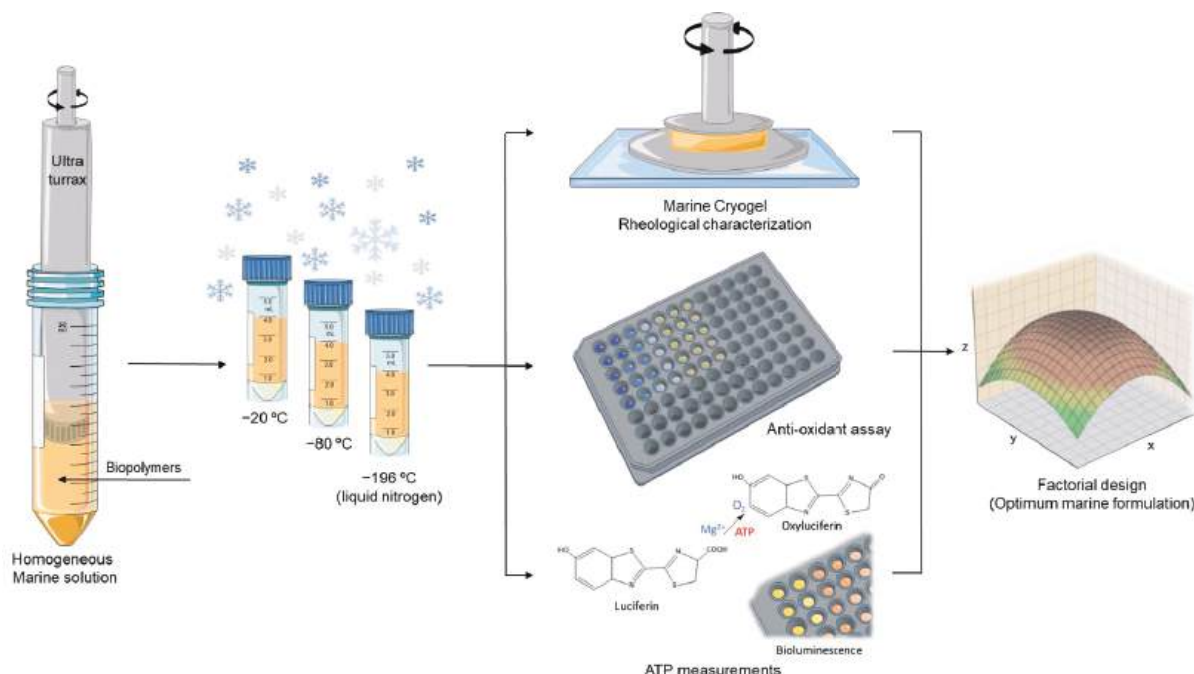
Figure 2. Schematic representation of the marine cryogel formation procedure comprising homogenization and freezing at different temperatures and then its characterization, aiming for a factorial design to extrapolate the optimum marine cryogel formulation according to the obtained results from rheology, anti-oxidants activity, and ATP measurements.

2.3. Rheological Measurements

The rheological oscillatory properties were assessed using a Kinexus pro+ rheometer and rSpace software (Malvern Instruments, Worcestershire, UK) for the data acquisition. The equipment has a top measurement geometry (8 mm in diameter) and a bottom plate pedestal, both with stainless steel (316 grade). The experiments were performed to investigate the cryogel viscoelastic properties through their mechanical spectra (frequency sweep curves) using a range of 0.1 Hz to 10 Hz at 25 °C, with the value of strain (1%) obtained from the Linear viscoelastic region (LVER). The LVER strain value was firstly determined through a strain sweep test (0.01–10%) using a constant frequency (1 Hz) at room temperature (25 °C). The oscillation experiments could be performed within this linear range without damaging the sample structure.

Additionally, some structural parameters, such as the average mesh size (ξ/nm) and the crosslinking density (n_e/(mol/m^3)) of the cryogels, could be calculated using the data obtained from the rheological oscillatory experiments [26]. Regarding this, ξ/nm was defined as the distance between the crosslinking points that can be established by the rubber elastic theory (RET), Equation (1):

$$\xi/\text{nm} = \sqrt[3]{\frac{RT}{G' \, N_A}} \times 10^9 \tag{1}$$

where G' is the storage modulus, N_A is the Avogadro constant (6.022×10^{23}), R is a value of gas constant (8.314 J/K mol), and T is the temperature in Kelvin (25 °C = 298.15 K) [27]. The values obtained with these units were in meters and then converted to nanometers.

The n_e/(mol/m^3) is nominated by the number of elastically active connection points in the network per unit of volume, calculated by RET, Equation (2):

$$n_e = \frac{G_e}{RT} \tag{2}$$

where G_e is the plateau value of storage modulus measured by the frequency sweep test [28].

2.4. Antioxidant Assay

Antioxidant analysis was performed using a straightforward method to measure the amounts of phenolic compounds [29]. The quantification of total phenolic contents was performed according to the traditional Folin–Ciocalteu reactive methodology, a well-known method (Folin–Ciocalteu index) [30,31]. This reaction involves oxidation, in an alkaline solution, of phenols by the yellow Folin–Ciocalteu reagent (a mixture of phosphomolybdate ($H_3PMo_{12}O_{40}$) and phosphotungstate ($H_3PW_{12}O_{40}$)), and the colorimetric measurement of the resultant combination of blue oxides, molybdenum, and tungsten, is proportional to the total phenolic compounds. In brief, 1 mg/mL of each marine cryogel condition was mixed with deionized (DI) water, the Folin–Ciocalteu reagent, and 15% sodium carbonate (Na_2CO_3). The microplate with the final mixtures was immediately placed in a 50 °C oven and removed after 10 min. After establishing at room temperature, the absorbance was read at 740 nm using a microplate reader (Synergy HT, Bio-Tek Instruments, Winooski, VT, USA). Caffeic acid was used as a standard to establish the calibration curve.

2.5. ATP Measurements

Intracellular adenosine triphosphate (ATP) levels were quantified to indicate viability and possible cell proliferation. CellTiter-Glo luminescent assay (Promega, Madison, WI, USA) was used for this analysis [32]. Firstly, the chondrocyte-like cell lines (ATDC5) were cultured on top of each marine cryogel inside a 96-well plate (3×10^4 cells/well) with Dulbecco's modified Eagle's medium-low glucose (DMEM, Sigma-Aldrich, Burlington, MA, USA) supplemented with 10% fetal bovine serum (Alfagene, Waltham, MA, USA) and 1% antibiotic–antimycotic solution (Gibco, Cambridge, UK) for 24 h. After that, at each time

point (24, 48, and 72 h), the reagent CellTiter-Glo was added in a 1:1 ratio (e.g., add 100 μL reagent to 100 μL of medium-containing cells) and incubated at room temperature for 30 min to allow the cellular lysis. The phosphorescence luminescence at 450–600 nm was then read using a fluorescence spectrometer with the capacity to execute phosphorescence experiments (JASCO FP-8500, Hachioji, Tokyo, Japan).

2.6. Statistics

Data analysis was performed using the OriginLab Pro 2019b program to analyze the rheological oscillatory behavior. Complementary statistical analysis of rheology, antioxidant activity (by phenolic groups), and ATP quantification results were performed by ANOVA followed by Tukey's post hoc test, using GraphPad Prism 8.0.1 (GraphPad Software, Inc., La Jolla, CA, USA). Differences between the groups with a confidence level of 95% ($p < 0.05$) were considered statistically significant. All results are presented as mean ± standard deviation.

Response surface methodology (RSM) is an empirical statistical modeling procedure used for multiple regression analysis applying quantitative data acquired from adequately designed experiments to solve multivariate equations simultaneously [33]. A 3^3 Box–Benkhen experimental design was applied in this research to optimize hydrogel formulation and study the influence of 3 parameters with 3 levels on the structure's performance, resulting in 27 experiments. Each parameter, an independent variable, was coded at 3 levels between −1 (low level), 0 (middle point), and +1 (high level). Coding of the variables was achieved by using Equation (3) [33]:

$$x_i = \frac{X_i - X_{cp}}{\Delta X_i}, \quad i = 1, 2, 3, 4, \ldots k \tag{3}$$

For an independent value, x_i is its dimensionless value; X_i its actual value; and X_{cp} is its real value at the center point. Moreover, ΔX_i is the step change of the actual value corresponding to a unit variation for the dimensionless value of the variable i.

The carefully considered parameters were temperature (x_1), collagen concentration (x_2), and fucoidan concentration (x_3) (Table 2). The structure's performance was measured by their rheological behavior, antioxidant potential, and cellular behavior (ATP quantification). Table 2 lists the process parameters (factors x_1, x_2, and x_3) and levels for hydrogel fabrication, with the coded (−1, 0, and 1) and actual values.

Table 2. Coded levels and the variables of the 3^3 Box–Behnken factorial design.

Variable	Factors	Level		
	x	−1	0	1
Temperature (°C)	x_1	−20	−80	−196
[collagen] (% *w/v*)	x_2	3	5	7
[fucoidan] (% *w/v*)	x_3	5	10	15

The design included the dependent variables (G′/Pa and Antiox/(μg/mL^{-1}), and ATP/RLU) was solved separately and used to find the optimal conditions by fitting a polynomial model, which gave the response as a function of relevant variables using RSM (Statistica, 12, Stat-Ease Inc., Minneapolis, MN, USA, 2014). The regression model of the present experimental Box–Behnken design system is described by Equation (4), to evaluate the effect of each independent factor on the response [34].

$$Y = \beta_0 + \beta_1 x_1 + \beta_2 x_2 + \beta_3 x_3 + \beta_{12} x_1 x_2 + \beta_{13} x_1 x_3 + \beta_{23} x_2 x_3 + \beta_{11} x_1^2 + \beta_{22} x_2^2 + \beta_{33} x_3^2 \tag{4}$$

Y corresponds to the predicted response; for instance, for the G′/Pa; x_1, x_2, and x_3 are the coded levels of the independent factors (temperature and concentration of collagen and fucoidan). The coefficients of the regression are β_0 for the intercept term; β_1, β_2, and β_3 the

linear coefficients; β_{12}, β_{13}, and β_{23} the interaction coefficients; and β_{11}, β_{22}, and β_{33} the quadratic coefficients.

3. Results and Discussion

3.1. Rheology Oscillatory Behavior

The rheological oscillatory experiments in distinct marine cryogel compositions were performed to understand their mechanical properties. This analysis consisted of measuring the elasticity modulus (G′), the viscosity modulus (G″), and the phase angle (δ/°) obtained from G″/G′ (or damping factor, tan δ) to evaluate the resistance to shear stress within a frequency range and performed at 25 °C. The obtained results and the respective statistical analysis are shown in Figure 3, with G′ and δ being barely independent of frequency (between 0.1 and 10 Hz) for all the analyzed cryogels. Moreover, the composition of the cryogels influenced the rheological behavior, as illustrated by the variability of G′ shown in Figure 3j).

When G′ > G″ and the tan δ < 1, the sample behavior tended to have a solid gel character (strong gel), which reflects the connectivity of the polymeric network [35,36]. The obtained oscillatory rheological experiments for the different cryogels (Figure 3a–i) exhibited exactly this behavior (viscoelastic character), thus revealing the presence of physical interactions between the polymers and resulting in cohesive matrices [26]. It is possible to quantify how strong these bonds are by determination of the distance between crosslink (i.e., average of mesh size) (ξ/nm) and the crosslinking density (n_e/(mol/m^3)) using the well-known rubber elastic theory (RET) and some rheological parameters such as the storage modulus (G′) value that can also be designated as G_e [27,37].

According to G_e results obtained at the plateau between 1–$10\ f$/Hz, it is clear that the cryo-environment temperatures and the ratio of the polymers directly influenced the rheological properties of the biomaterials due to differences in the internal network. Figure 3j shows an overview of all tested biomaterials and reveals that the temperature that provided a higher viscoelastic character was −80 °C, followed by −20 °C. In comparison, the formulations submitted to liquid nitrogen (−196 °C) resulted in lower internal network formation. This lower bond formation capacity may be related to the fast-freezing environment of the polymer solution, quickly hampering polymer mobility, which does not provide enough time for the material to organize properly, namely, to interact with the other biopolymers (through electrostatic attraction, among others), resulting in a less cohesive structure. Actually, the internal polymeric network structure in each formulation is promoted between the positively charged groups present on collagen and chitosan samples (i.e., protonated amines) and the negatively charged groups present on fucoidan (i.e., ester sulfates and eventually, carboxylate groups) [38]. In this regard, a cohesive structure is not only promoted by the appropriate cryo-environment procedure but also highly depends on greater or lesser availability of the positive and negative charges that are present in each formulation. Within each processing temperature, the formulations that demonstrated better rheological properties were C_5 and C_4, followed by C_7 and C_8. This phenomenon was mostly observed in formulations that contained higher collagen concentrations (i.e., C_5, C_7, and C_8) when calculating the total polymer mass in each cryogel formation. Fucoidan also has a vital function on biomaterial formation through electrostatic interactions, dependent on fucoidan concentration [39]. However, our rheological results demonstrated that despite the relevance of the presence of fucoidan, an extra concentration could respond negatively in the formation of bonds, which consequently would be reflected in rheological properties [40,41]. Thus, a balance between collagen and fucoidan amounts is required to create structures with significant stability.

Figure 3k shows a correlation between the G_e values with the calculated ξ and n_e/(mol/m^3). In general, the cryogels with better rheological properties (i.e., C_5 and C_4 at −80 and −20 °C) had the lowest mesh size (varied from 3.71 ± 0.17 nm to 4.44 ± 0.21 nm) and a crosslinking density that were proximal to the G_e values (followed the same trend), which confirmed excellent stability on these formulations compared to other samples, in

which ζ varied from 5.79 ± 0.18 nm to 8.46 ± 0.37 nm. This behavior is in accordance with the literature since it is expected to exist proportionally between the rheological parameters and the stiffness behavior of the biomaterials.
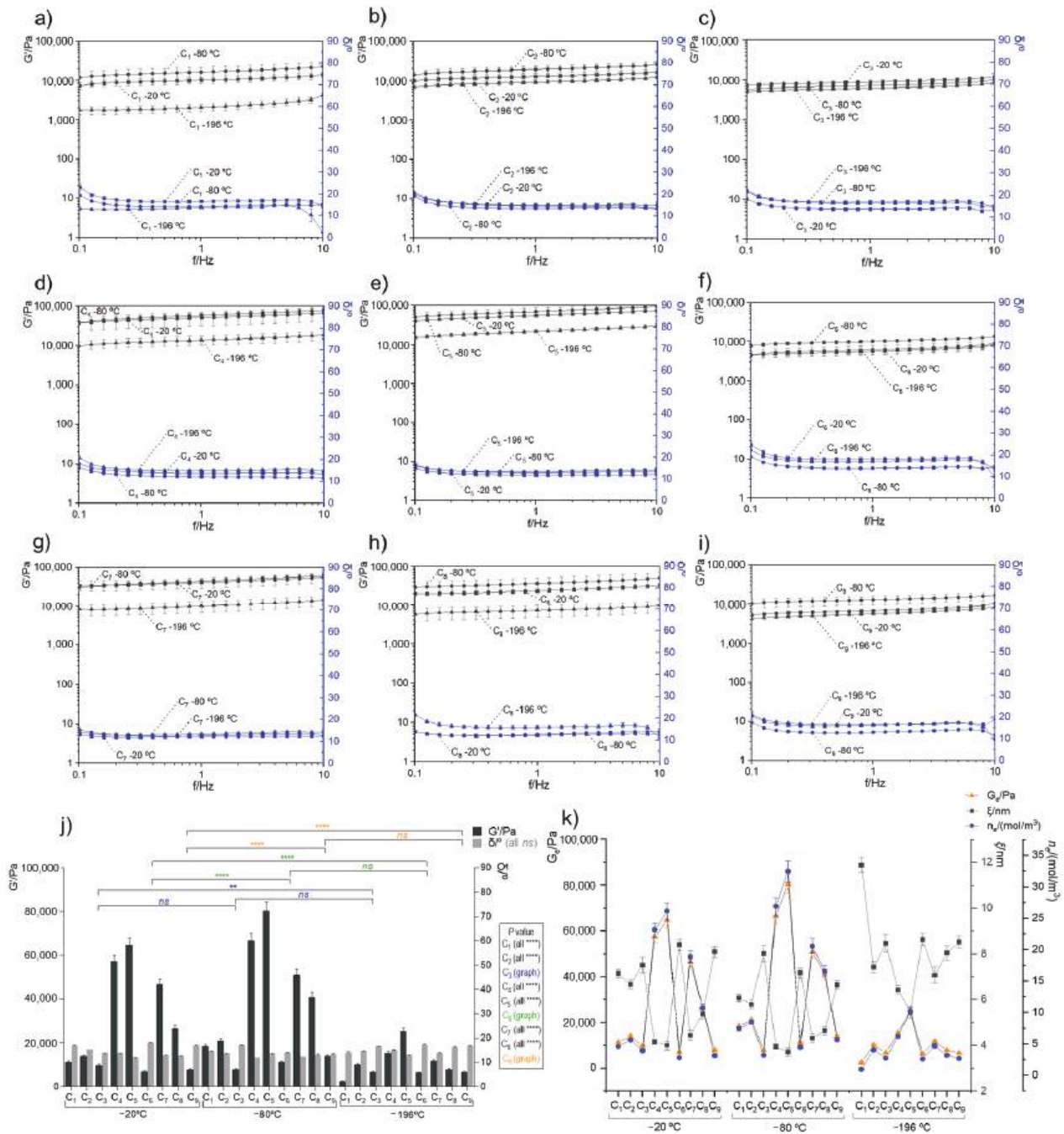
Figure 3. Oscillatory rheological behavior of different marine origin cryogels (**a–i**) corresponded to the developed cryogels C_1 to C_9, respectively, produced at -20, -80, and -196 °C. Data show the mean of three values from independent experiments and the standard error for G'/Pa (black lines) and the phase angle $\delta/°$ (blue lines). (**j**) Comparison of each marine cryogel as a function of G'/Pa and the $\delta/°$, with the average stable zone between 0.5 to 5 Hz. All differences between samples were statistically significant **** $p < 0.0001$ except those represented with the symbols of ** ($p < 0.01$) and *ns* (not significant). (**k**) Comparative analysis of the storage modulus at the plateau (G_e/Pa), mesh size (ζ/nm), and the crosslinking density ($n_e/mol/m^3$) of the developed marine cryogels.

3.2. Antioxidant Activities

Marine sources have been widely studied for their biological properties, attributed to different compounds and metabolites that are produced to protect the living being when exposed to harsh environmental conditions, such as abiotic and biotic factors, light intensity, salinity, and ultraviolet radiation, among others [42]. In the case of brown seaweeds, there are two major bioactive components—sulfated polysaccharides (SPs), namely, fucoidan, and polyphenol compounds—that have been classified as having a significant antioxidant activity [43]. Some authors defend the importance of the presence of phenolic compounds in commercial fucoidan samples due to the fact that the phenols are the main contributors to the antioxidant activities compared with fucoidan, which together can increase the biological properties without bringing negative consequences [44]. In particular, it was reported by Murray et al. [45] that the extracts of *Fucus vesiculosus* commercialized by Marinova (Australia), used in the present study, can contain up to 28% of polyphenols.

The Folin–Ciocalteu (F–C) method was used as a straightforward method to compare the samples regarding the polyphenolic antioxidant activity, also being indirectly interrelated with the amounts of fucoidan present on cryogel samples. This approach is equivalent to the work by Palanisamy et al. [46], where they concluded that the antioxidant activity can be correlated with the concentration of fucoidan. Briefly, this method is based on a reaction of electron transfer that involves a mixture of phosphomolybdate and phosphotungstate to determine the antioxidant activity. Thus, this methodology measures the reductive capacity of the antioxidants, being widely applied to determine these contents in plant-derived food, as well as in other biological samples, such as fucoidan [42,47]. Other antioxidant assays could have been used, such as DPPH (2,2-diphenyl-1-picryl-hydrazyl-hydrate), ORAC (oxygen radical absorbance capacity), and ABTS (2,2'-Azinobis-(3-Ethylbenzthiazolin-6-Sulfonic Acid), but the outcome would be the total antioxidant capacity, and it would not be possible to distinguish between the activities promoted by the polyphenols and fucoidan [48,49].

The obtained results of the total concentration of phenolic groups on the developed marine cryogels, depicted in Figure 4, showed a growth trend within each group of three samples (i.e., C_1 to C_3, C_4 to C_6, and C_7 to C_9), with similar values between those groups. These results were in good agreement with amount of fucoidan in the biomaterial formulation (Table 1). The compositions that contained a lower concentration of fucoidan (i.e., C_1, C_4, and C_7) showed lower antioxidant activity, while those that had a higher concentration (i.e., C_3, C_6, and C_9) had, in the same way, higher antioxidant functional activity.
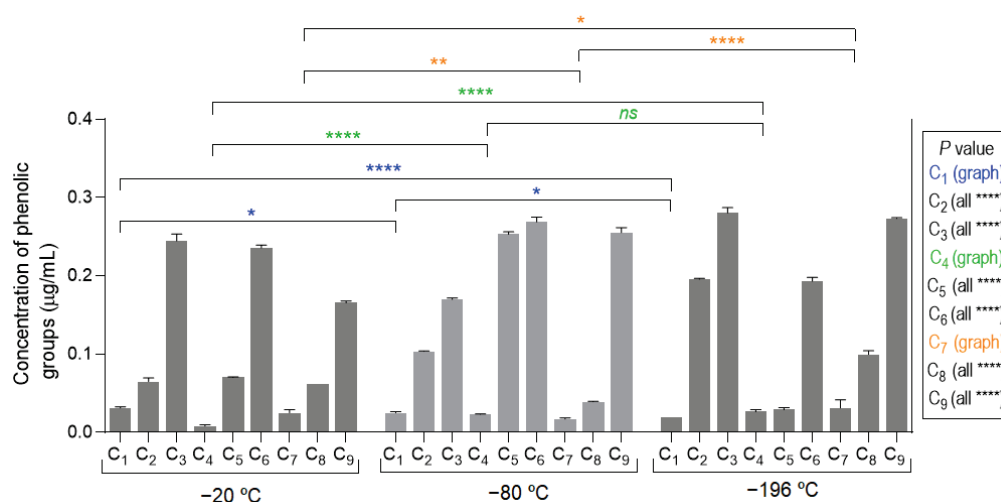
Figure 4. Assessment of antioxidant activity of marine origin cryogels (C_1 to C_9, produced at -20, -80, and -196 °C) by the quantification of phenolic groups. All samples (comparing the different temperatures) showed statistical significance of **** $p < 0.0001$ except those represented with the symbols of * ($p < 0.05$), ** ($p < 0.01$), and *ns* (not significant).

3.3. ATP Activity

Adenosine triphosphate (ATP), also called molecular unity of energy currency, is an intracellular nucleotide that provides energy for many metabolic processes in every living cell and is produced by ATP synthase [50]. Nowadays, ATPs can be measured using a (bio)luminescence or phosphorescence assay (similar emission light) [51]. During the chemical reaction, the enzyme luciferase has the ability to release energy in the form of light (luminescence) on the presence of its substrate luciferin, Mg^{2+} and ATP [52]. It is described in the literature that there exists a linear relationship between the amount of ATP present in samples and the amount of light produced, which is a direct indicator of cellular metabolic activity [53]. The amounts of ATP present in cells cultured on the developed marine cryogels are shown in Figure 5.
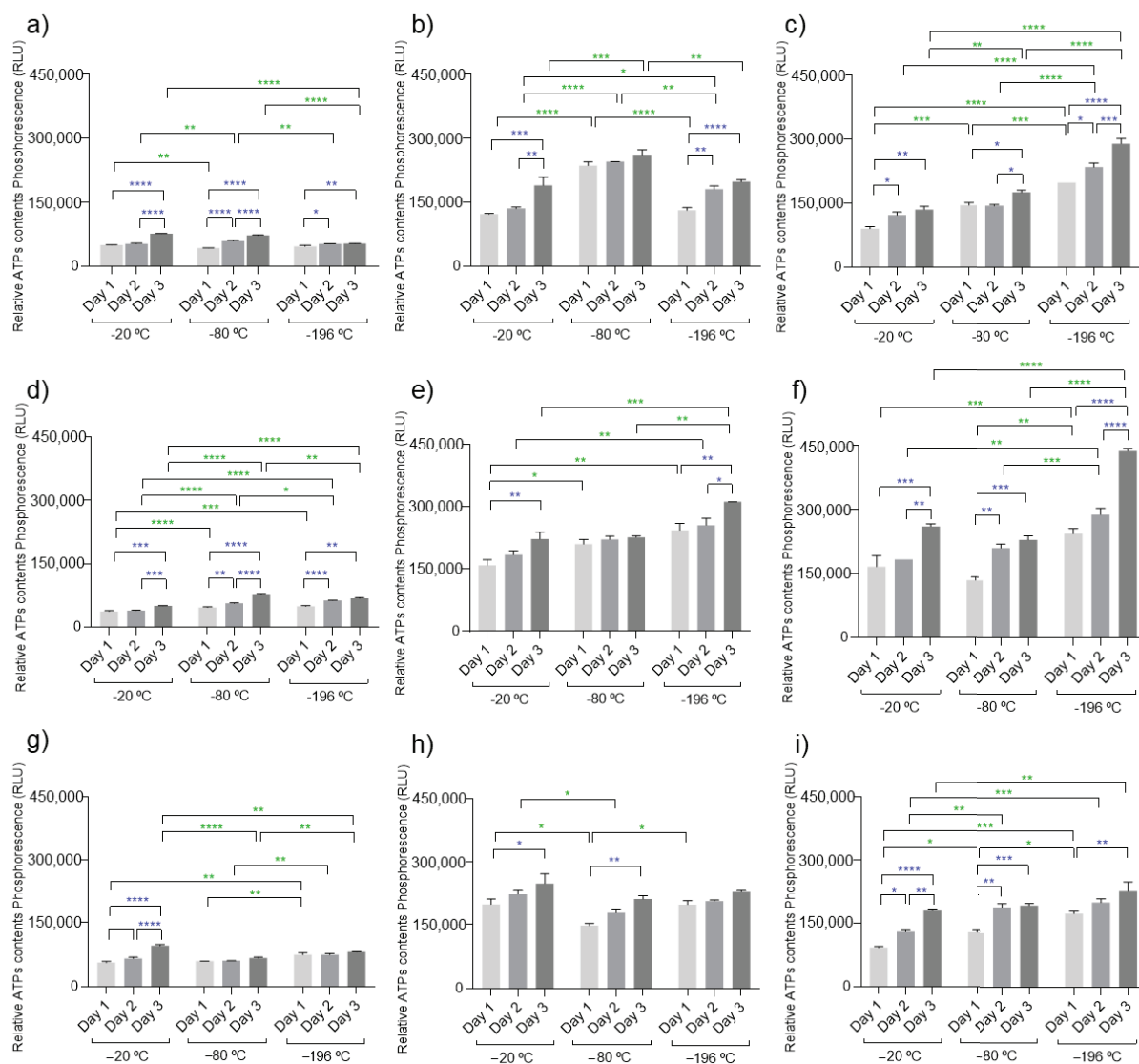
Figure 5. ATP cell measurements using ATDC5 cells in direct contact with all developed marine cryogels C_1 to C_9 ((**a–i**), respectively) at −20, −80, and −196 °C. There was a direct relationship between the measured phosphorescence and the concentration of ATP. The samples showed statistical significance of * ($p < 0.05$), ** ($p < 0.01$), *** ($p < 0.001$), **** $p < 0.0001$, or were not significant (not represented). The symbols of statistical analysis noticeable by blue color correspond to the comparison between each condition in relation to the time points while the symbols expressed by green color represent the comparison between the different temperatures of each marine condition.

The amounts of ATP were quantified on chondrocyte-like cells (ATDC5) cultured in direct contact with the developed cryogels during three time points (24, 48, and 72 h) as a measure of cellular metabolic activity. In general, the results demonstrated that these marine biomaterials do not compromise the metabolic activity of cells, since during the experiments, an increase in ATP content was observed, which is a good indicator of cell viability when encapsulated on the biomaterial. Typically, in favorable conditions, the energy expenditures by cells during the first hours are dedicated especially to cell adhesion, while the rest of the time is devoted to normal cell functionalities such as cell proliferation. Cell adhesion is essential for survival and communication (cell-to-cell) since it allows stimulation of important signals for cell migration, the cell cycle, proliferation, and taking the example of stem cells, for their differentiation [54]. Our data also showed that these cell types have a preference for biomaterials with a higher concentration of polymers on their formulations. This behavior was observed when comparing to the formulations C_1, C_4, and C_7 (lower concentration of fucoidan) to the other formulations, and showed the same tendency in all temperatures used. The concentration of collagen in the biomaterial did not show a significant influence on ATP quantification, suggesting that the presence of fucoidan was more impactful for the short time that the cultures were evaluated. The processing temperature did not significantly influence the cellular behavior, as no pattern could be identified on the variation in ATP content from cells cultured in each biomaterial formulation processed at different temperatures. This was certainly influenced by the short time that the cell cultures were studied, as hydrogels with a more compacted structure (as the hydrogels resulting from biomaterials processed with liquid nitrogen) are expected to hamper cell proliferation, and experiments with more extended culture periods might show some temperature influence. Nevertheless, under the studied conditions, the amount of fucoidan in biomaterial composition seems to be the determining factor for the cellular outcome.

4. Factorial Design

Box–Behnken designs (BBD) are a practical response surface design (RSD), such as the central composite design, that provides data based on experiment variables and overall experimental error. These designs possess excellent symmetry and rotatability, with minimal experimental runs [55]. The systematic optimization of the structure's performance was performed with the help of the BBD matrix, indicating 27 experimental trials, and the response data for characterization of those structures are represented in Table 3. This table was obtained primarily to perform the experiment concerning the considered factors and levels. Then, after performing the 27 experiments required, it was completed with the response data to analyze the response surface design.

Table 3. Experimental runs for Box–Behnken with 3^3 factorial design. Coded levels and the variable factors are shown. For response data, the information of rheology and antioxidant activity showing the average of three independent experiments and the information data of ATPs is relative to the average of three independent experiments of timepoint day three.

Run	Coded Level			Factors			Response Data		
	x_1	x_2	x_3	Temp (°C)	[jCOL]	[aFUC]	Rheological (G′)	Antiox (µg/mL)	ATPs (RLU)
1	−1	−1	−1			5	1.13×10^4	3.14×10^{-2}	7.67×10^4
2	−1	−1	0		3	10	139×10^4	6.51×10^{-2}	1.90×10^5
3	−1	−1	1			15	9.73×10^3	2.45×10^{-1}	1.35×10^5
4	−1	0	−1			5	5.73×10^5	8.22×10^{-3}	5.00×10^4
5	−1	0	0	−20	5	10	6.46×10^4	7.04×10^{-2}	2.22×10^5
6	−1	0	1			15	6.96×10^3	2.36×10^{-1}	2.61×10^5
7	−1	1	−1			5	4.67×10^4	2.51×10^{-2}	9.62×10^4
8	−1	1	0		7	10	2.67×10^4	6.19×10^{-2}	2.49×10^5
9	−1	1	1			15	7.78×10^3	1.66×10^{-1}	1.79×10^5

Table 3. *Cont.*

| Run | Coded Level | | | Temp (°C) | Factors [jCOL] | [aFUC] | Response Data Rheological (G′) | Antiox (µg/mL) | ATPs (RLU) |
	x_1	x_2	x_3						
10	0	−1	−1			5	1.84×10^4	2.51×10^{-2}	7.26×10^4
11	0	−1	0		3	10	2.11×10^4	1.04×10^{-1}	2.61×10^5
12	0	−1	1			15	7.97×10^3	1.70×10^{-1}	1.75×10^5
13	0	0	−1			5	6.66×10^4	2.30×10^{-2}	7.79×10^4
14	0	0	0	−80	5	10	8.04×10^4	2.53×10^{-1}	2.27×10^5
15	0	0	1			15	1.11×10^4	2.69×10^{-1}	2.30×10^5
16	0	1	−1			5	5.09×10^4	1.72×10^{-2}	6.75×10^4
17	0	1	0		7	10	4.10×10^4	3.93×10^{-2}	2.11×10^5
18	0	1	1			15	1.40×10^4	2.55×10^{-1}	1.93×10^5
19	1	−1	−1			5	2.46×10^3	1.93×10^{-2}	5.36×10^4
20	1	−1	0		3	10	1.01×10^4	1.96×10^{-1}	1.99×10^5
21	1	−1	1			15	6.78×10^3	2.81×10^{-1}	2.89×10^5
22	1	0	−1			5	1.54×10^4	2.67×10^{-2}	6.82×10^4
23	1	0	0	−196	5	10	2.53×10^4	2.92×10^{-2}	3.12×10^5
24	1	0	1			15	6.41×10^3	1.93×10^{-1}	4.38×10^5
25	1	1	−1			5	1.16×10^4	3.14×10^{-2}	8.14×10^4
26	1	1	0		7	10	7.91×10^3	9.99×10^{-2}	2.30×10^5
27	1	1	1			15	6.66×10^3	2.73×10^{-1}	2.27×10^5

The response surface analysis was performed for all the response variables based on the selected model. The statistical and correlation analysis of the model's response was performed with 3D response surface plots, histogram of distribution, Pareto plots, and analysis of variance (ANOVA). Figure 6 illustrates the 3D response surface plots for the studied responses. To draw the 3D surfaces, the ATPs (RLU) chosen were those from the 72 h, since this 3rd timepoint is when the normal metabolic function of the cells occurs (cellular proliferation), while during the 1st or 2nd timepoints, the cells are using energy for cell adhesion in the polymeric structure.

Nine response surface plots were generated to exhibit the effect of the three factors on the responses: G′ (Pa) (Figure 6a), antioxidant concentration (µg/mL) (Figure 6b), and ATPs (RLU) (Figure 6c). The quadratic models showed different forms for each response surface: "mound-shaped" maximum (a_1, a_2, a_3, b_1, and c_3), saddle point (c_1 and c_2), and rising ridge (b_2 and b_3) [56], with the optimum point able to be effortlessly observed on the first type since the region of optimum response was located inside the experimental region. Concerning the rheological behavior (Figure 6a), the optimum value was predicted to be inside the experimental region in the 3 surfaces, the optimum value (G′ of 6.47×10^4 Pa) being indicated for a temperature of −126 °C and a concentration of collagen and fucoidan of 5.3 mg/mL and 7.7 mg/mL (Table 4). Unfortunately, the optimum temperature could not be implemented in the laboratory environment, limited to −80 or −196 °C (liquid nitrogen) due to equipment limitations. However, according to the DoE results, the formulation that mostly resembled these values was the formulation C_5 at −80 °C, which comprised the percentage (*w/v*) of each polymer in the original solution, i.e., 5% collagen, 3% chitosan, and 10% fucoidan followed by C_4 at −80 °C. These results are consistent with our previous work [8], since we also found a trend for the formulation that comprised a similar polymeric concentration. Regarding the results obtained for the concentration of the antioxidants (µg/mL), the optimum value was not completely inside the experimental region surface. Thus, an optimum value (0.13 µg/mL) was predicted for a temperature of −54 °C, and 3.5 mg/mL of collagen concentration. No optimum value of fucoidan concentration for antioxidant concentration was found since the surfaces with the independent variable were from the type rising ridge [56]. Finally, the independent variable of ATP had the optimum value (ATP of 2.56×10^5 RLU) indicated for a temperature of −145 °C and a concentration of collagen and fucoidan of 5.1 mg/mL and 12.5 mg/mL, respectively (Table 4). It was impossible to achieve a formulation exhibiting the best values for all the properties being assessed (rheological behavior, antioxidant activity, and

ATP quantification) and compromises or priorities needed to be established, depending on the final application. In any case, according to the obtained analysis, the formulations that mostly resembled the obtained DoE values were the samples C_5 and C_6 at -196 and -80 °C.
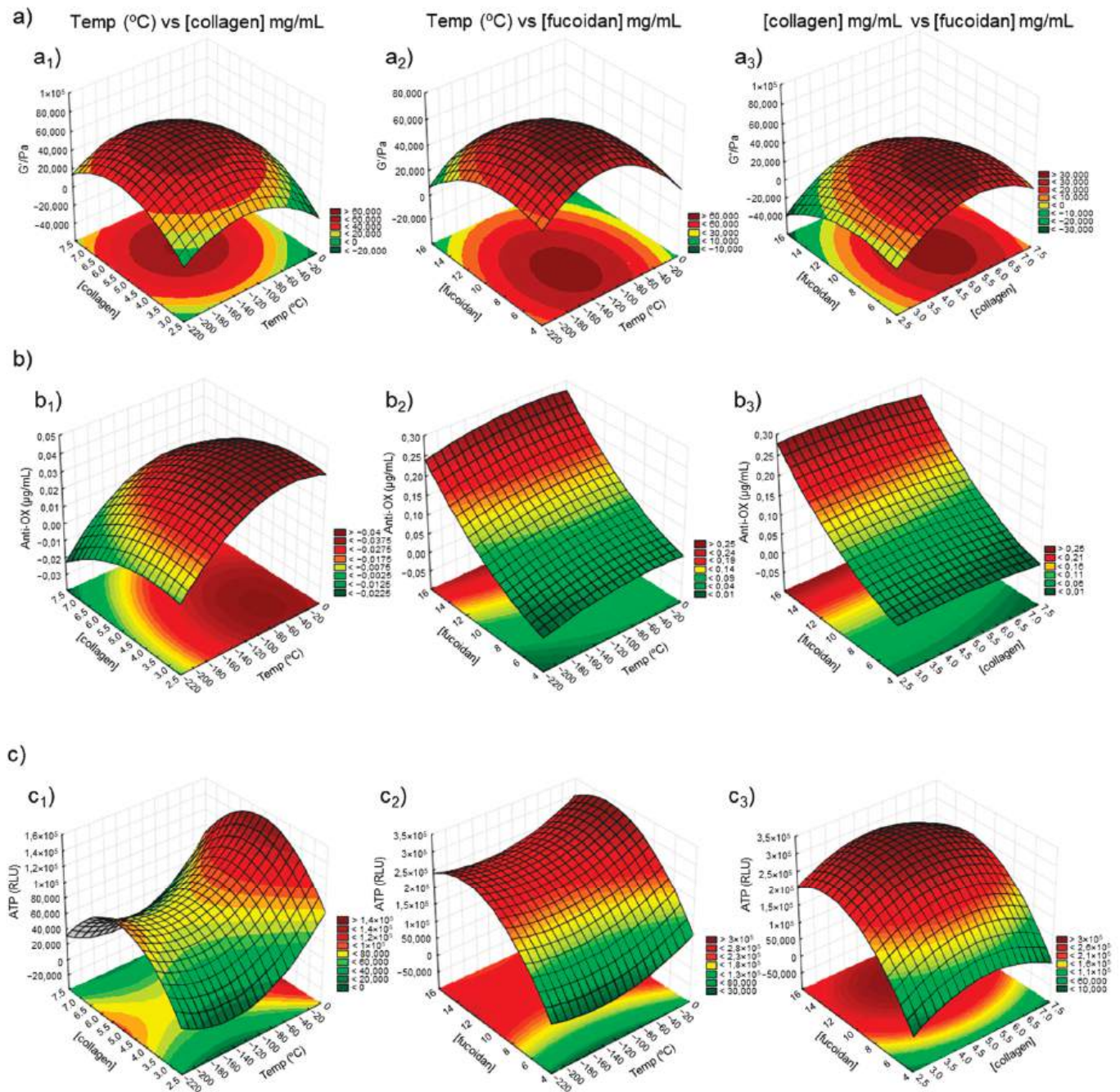
Figure 6. Factorial surface response of (**a**) rheological data (G′/Pa), (**b**) antioxidant activity (μg/mL), and (**c**) ATP (RLU) measurements on marine origin cryogels. The images of (**a₁**, **b₁**, and **c₁**) demonstrate the correlation between the temperature (°C) vs. concentration of collagen ([collagen]); (**a₂**, **b₂**, and **c₂**) represent the correlation between the temperature in relation to the concentration of fucoidan ([fucoidan]) while the images of (**a₃**, **b₃**, and **c₃**) show the correlation between the concentration of collagen vs. the concentration of fucoidan.

Table 4. Optimum conditions determined by surface factorial design and the predicted value according to the optimum values.

Response	Factors	Optimum Values	Predicted Value
G′/Pa	Temp (°C) [collagen] mg/mL [fucoidan] mg/mL	−126 5.3 7.7	6.47×10^4
Anti-oxidants (µg/mL)	Temp (°C) [collagen] mg/mL [fucoidan] mg/mL	−54 3.5 NF	0.13
ATPs (RLU)	Temp (°C) [collagen] mg/mL [fucoidan] mg/mL	−145 5.1 12.5	2.56×10^5

NF: not found or extrapolated.

At this point, it is essential to mention that when working with natural materials, many mathematical tools and models fail or are not completed, which is probably why they are rarely applied. This happens for numerous known reasons, such as reproducibility problems, the impossibility of repeating an optimal point, or the high material sensitivity. Contrary to what happens in other areas of more exact science where a wide range of options are available, even in this situation, limitations regarding available equipment can be an obstacle. Still, applying these tools is an enabling option to redirect the research work to better performing conditions, even when the experimental conditions do not allow one to achieve the final purpose of obtaining a full and irrefutable optimum point.

The experimental design also enabled us to build for each group of response data: a histogram of distribution, Pareto plot, and the correlation between what was observed and the predicted values (Figure 6). The histogram of distribution, showing frequency distributions, assesses normality (bell-shaped and symmetric about the mean). The Pareto chart shows a t-statistical test for each effect, where each bar represents the standardized effect, compared to a t-critical value (vertical line). Thus, it renders a method that detects the factor and interaction effects that are most important to the process or design optimization [57]. A plot of observed values (measurements) and predicted values (DoE regression) was also drawn. The blue diagonal line marks the best-case scenario where measurement and prediction ideally resemble each other [57].

A better quality of the experimental design was perceived for the data with rheological properties (Figure 7a) when observing the reached plots globally. The histogram of distribution for those data (Figure 7a1) showed a distribution near normality, while the others were slightly distant from it (Figure 7b1,c1). The Pareto chart also displays the statistically relevant effect of each factor on the response, and it is a helpful method to observe the results. The dotted line on the Pareto charts represents the t-critical value, and the effects on its right are significant [58]. Given the proximity of all variables, it is possible to state that the studied independent variables were significant to the process. The concentration of fucoidan followed by the concentration of collagen were the most significant. The correlation between what was observed and the predicted values makes it possible to state that the DoE regression function provided an acceptable approximation to reality in the investigated area. The regression was used to find the predictive equation, i.e., the quadratic model in coded units, for rheological data (Equation (5)), antioxidant activity (Equation (6)), and ATPs (Equation (7)).

$$Y = -14.6 \times 10^3 - 0.7 \times 10^3 x_1 + 52.2 \times 10^3 x_2 + 7.7 \times 10^3 x_3 - 3 x_1^2 - 4.9 \times 10^3 x_2^2 - 0.5 \times 10^3 \beta_{22} x_3^2 \quad (5)$$

$$Y = -10.6 \times 10^{-3} - 0.1 \times 10^{-3} x_1 + 11 \times 10^{-3} x_2 + 0.5 \times 10^{-3} x_3 - 1 \times 10^{-6} x_1^2 - 1.6 \times 10^{-3} x_2^2 + 1 \times 10^{-3} x_3^2 \quad (6)$$

$$Y = -0.4 \times 10^6 + 1.1 \times 10^3 x_1 + 80.1 \times 10^3 x_2 + 0.1 \times 10^6 x_3 + 4 x_1^2 - 10.9 \times 10^3 x_3^2 - 3.2 \times 10^3 x_2^2 \quad (7)$$

where, Y corresponds to the predicted response, and x_1, x_2, and x_3 are the coded levels of the independent factors (temperature and concentration of collagen and fucoidan).
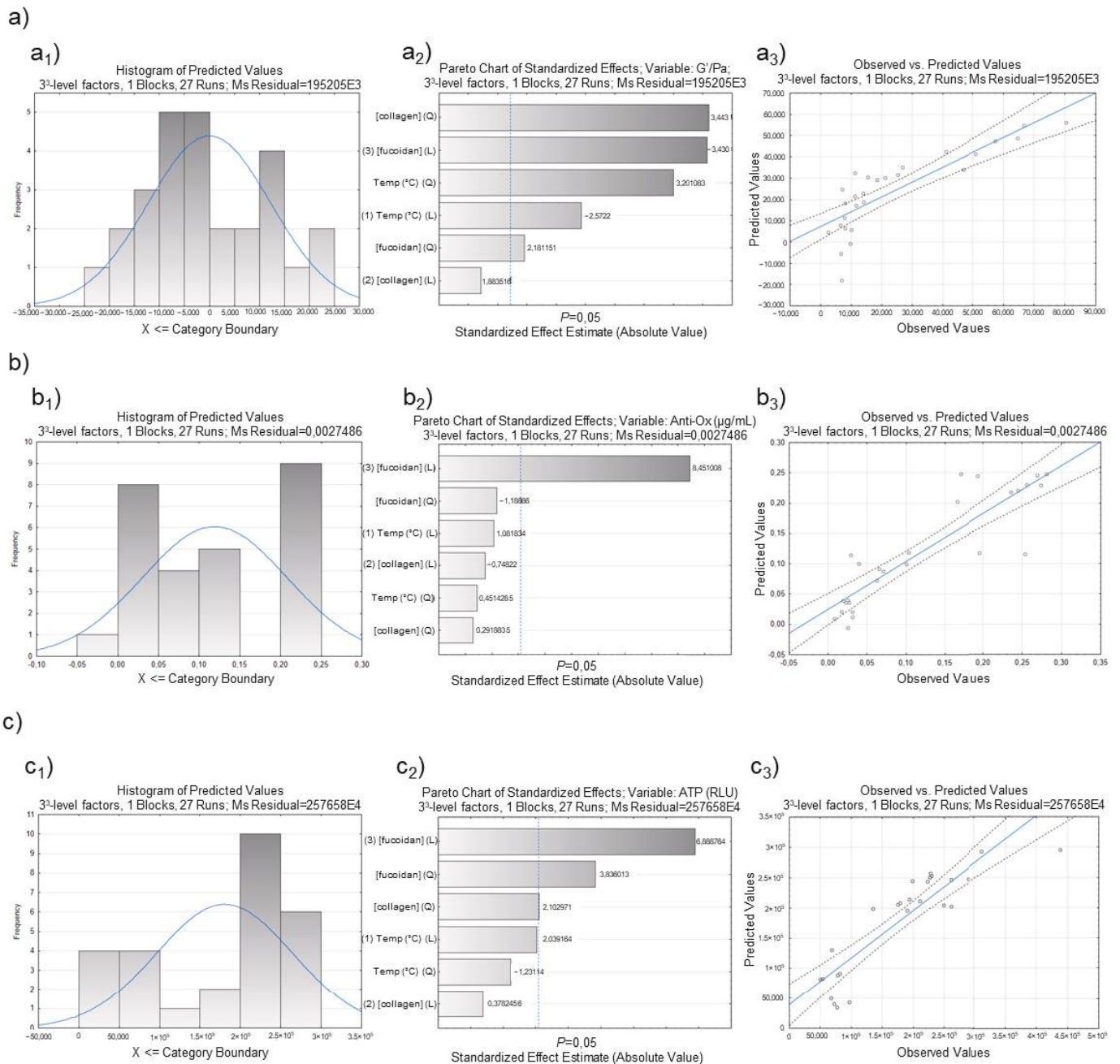
Figure 7. Factorial response of (**a**) rheological data (G′/Pa), (**b**) antioxidant activity (µg/mL), and (**c**) ATP (RLU) measurements on marine origin cryogels. The images (**a₁**, **b₁**, and **c₁**) demonstrate the histogram of distribution; (**a₂**, **b₂**, and **c₂**) represent the Pareto charts of standardized effects of the factorial design, while the images of (**a₃**, **b₃**, and **c₃**) show the Box–Behnken design plot for predicted versus actual values for each response variable.

The predictive equation, describing the polynomial model for the experimental response, was validated by analysis of variance (ANOVA) as shown in Table 5.

Table 5. Analysis of variance (ANOVA) for the fitted quadratic polynomial model for optimization of cryogel manufacturing.

Variable of G′/Pa					
Factor	Sum of Squares (SS)	df	Mean Square (MS)	*F*-Value	*p*-Value
(1) [fucoidan] (L)	2.29×10^9	1	2.29×10^9	11.766	0.002
[fucoidan] (Q)	9.28×10^8	1	9.28×10^8	4.757	0.041
(2) [collagen] (L)	6.92×10^8	1	6.92×10^8	3.547	0.074
[collagen] (Q)	2.31×10^9	1	2.31×10^9	11.855	0.002
(3) Temp (°C) (L)	1.29×10^9	1	1.29×10^9	6.616	0.018
Temp (°C) (Q)	2.00×10^9	1	2.00×10^9	10.246	0.004
Error	3.90×10^9	20	1.95×10^8		
Total SS	1.29×10^{10}	26			
$R^2 = 0.69$; adj $R^2 = 0.61$; MS = 195×10^3					
Variable of Anti-oxidant (µg/mL)					
Factor	Sum of squares (SS)	df	Mean square (MS)	*F*-value	*p*-value
(1) Temp (°C) (L)	0.003	1	0.003	1.170	0.292
Temp (°C) (Q)	0.000	1	0.000	0.203	0.656
(2) [collagen] (L)	0.001	1	0.001	0.560	0.462
[collagen] (Q)	0.000	1	0.000	0.085	0.773
(3) [fucoidan] (L)	0.196	1	0.196	71.419	0.000
[fucoidan] (Q)	0.003	1	0.003	1.412	0.248
Error	0.054	20	0.002		
Total SS	0.261	26			
$R^2 = 0.78$; adj $R^2 = 0.72$; MS = 0.00					
Variable of ATPs (RLU)					
Factor	Sum of squares (SS)	df	Mean square (MS)	*F*-value	*p*-value
(1) Temp (°C) (L)	1.07×10^{10}	1	1.07×10^{10}	4.158	0.054
Temp (°C) (Q)	3.90×10^9	1	3.90×10^9	1.515	0.232
(2) [collagen] (L)	3.68×10^8	1	3.68×10^8	0.143	0.709
[collagen] (Q)	1.13×10^{10}	1	1.13×10^{10}	4.422	0.048
(3) [fucoidan] (L)	1.22×10^{11}	1	1.22×10^{11}	47.455	0.000
[fucoidan] (Q)	3.79×10^{10}	1	3.79×10^{10}	14.715	0.001
Error	5.15×10^{10}	20	2.57×10^9		
Total SS	2.36×10^{11}	26			
$R^2 = 0.78$; adj $R^2 = 0.71$; MS = 257×10^4					

R^2: regression goodness of fit. df: degrees of freedom. L: linear. Q: quadratic.

According to the ANOVA results (Table 5), the quadratic model, including linear interactions, fitted acceptably to the experimental data giving coefficients of determination (R^2) ranging from 0.69 to 0.78. The coefficient of determination (R^2) indicates if the predictive equations adequately describe the experimental values [59]. Globally, the obtained R^2 values were not as close to one as desired. Nevertheless, natural products usually have such an impact on results. Additionally, their use regularly leads to difficulties of reproducibility (batch-to-batch variability) [60], processing, homogeneity, and the biological complexity of the molecules.

The regression coefficients and the interaction between independent factors can be considered statistically significant for *p*-values lower than 0.05, with a 95% confidence interval [61]. Thus, according to the ANOVA results (Table 5) and the Pareto chart (Figure 7a$_2$,b$_2$,c$_2$), fucoidan concentration's linear and quadratic terms were the factors that most affected the performance of the structures. Furthermore, as expected in the rheological properties, the temperature factor was more critical than in the other two parameters chosen due to how temperature can directly influence the internal structural network of the biomaterials, making them more cohesive or weaker. The rheological properties are usually temperature-dependent for these kinds of samples [62].

In this way, the best conditions regarding the rheological properties were C_5 $-80\,°C$ followed by C_4 $-80\,°C$, whereas concerning the antioxidant activity, they were C_2 $-80\,°C$ and C_3 $-80\,°C$, and in the quantification of ATPs, they were C_5 $-80\,°C$, C_6 $-80\,°C$, C_5 $-196\,°C$, and C_6 $-196\,°C$. Globally, the most recurred formulation was C_5 at a temperature of $-80\,°C$, being herein considered as the best formulation among the ones addressed. However, as mentioned above, it must be stressed that it is impossible to determine a formulation exhibiting the best values for all the assessed parameters, and choices must be made. In that case, a validation of the determined conditions to obtain the best of each of the parameters should be made, which would lead to an optimization process with respect to the selected parameter. [59]. As abovementioned, it was not possible to do those validations particularly due to limitations on freezing equipment (only determined values were possible, which did not include the value determined as the optimum to maximize the value of each of the different parameters), but that was not the goal of the present work. Being aware of the practical limitations of the application of the model to this experiment, we aimed to present it as a useful tool to give us a correct direction regarding the conditions that most influence each parameter toward the design of better-performing formulations.

5. Conclusions

The factorial design of experiments (DoE) model is an effective statistical experimental tool for identifying the most significant parameter(s) and demonstrating each parameter's effects according to their interactions. The present experimental work focused on identifying the better-performing biomaterial according to a carefully chosen set of parameters, such as the concentration of the polymers (collagen and fucoidan) and the cryo-environment temperature, which promoted the ionic crosslinking between the polymer-charged groups on the cryogels. Data on rheological oscillatory measurements, antioxidant activity, and adenosine triphosphate (ATP) concentration as a measure of cell metabolic activity showed that fucoidan concentration was the parameter that most significantly influenced cryogel formation, while the temperature was the variable that most influenced the rheological properties. The biomaterial that better fit the conditions determined by the DoE was the formulation C_5 at $-80\,°C$, which comprised the percentage (w/v) of each polymer in the original solution, i.e., 5% collagen, 3% chitosan, and 10% fucoidan. Moreover, depending on the final approach, the DoE provided a valuable indication of expected behavior of certain formulations within the limits of the model, avoiding unnecessary and excessive characterizations and waste of products, thus being a valuable tool for improved biomaterial design.

References

1. Zhang, Y.; Zhou, D.; Chen, J.; Zhang, X.; Li, X.; Zhao, W.; Xu, T. Biomaterials Based on Marine Resources for 3D Bioprinting Applications. *Mar. Drugs* **2019**, *17*, 555. [CrossRef] [PubMed]
2. Lalzawmliana, V.; Anand, A.; Mukherjee, P.; Chaudhuri, S.; Kundu, B.; Nandi, S.K.; Thakur, N.L. Marine organisms as a source of natural matrix for bone tissue engineering. *Ceram. Int.* **2018**, *45*, 1469–1481. [CrossRef]
3. Sumayya, A.S.; Kurup, G.M.; G, M.K.; A S, S. Marine macromolecules cross-linked hydrogel scaffolds as physiochemically and biologically favorable entities for tissue engineering applications. *J. Biomater. Sci. Polym. Ed.* **2017**, *28*, 807–825. [CrossRef] [PubMed]
4. Dhandayuthapani, B.; Yoshida, Y.; Maekawa, T.; Kumar, D.S. Polymeric Scaffolds in Tissue Engineering Application: A Review. *Int. J. Polym. Sci.* **2011**, *2011*, 290602. [CrossRef]
5. Ha, T.L.B.; Quan, T.M.; Vu, D.N.; Si, D.M. Naturally derived biomaterials: Preparation and application. In *Regenerative Medicine and Tissue Engineering*; IntechOpen: London, UK, 2013. [CrossRef]
6. Bakhshpour, M.; Idil, N.; Perçin, I.; Denizli, A. Biomedical Applications of Polymeric Cryogels. *Appl. Sci.* **2019**, *9*, 553. [CrossRef]
7. Kutlusoy, T.; Oktay, B.; Apohan, N.K.; Süleymanoğlu, M.; Kuruca, S.E. Chitosan-co-Hyaluronic acid porous cryogels and their application in tissue engineering. *Int. J. Biol. Macromol.* **2017**, *103*, 366–378. [CrossRef]
8. Carvalho, D.N.; López-Cebral, R.; Sousa, R.O.; Alves, A.L.; Reys, L.L.; Silva, S.S.; Oliveira, J.M.; Reis, R.L.; Silva, T.H. Marine collagen-chitosan-fucoidan cryogels as cell-laden biocomposites envisaging tissue engineering. *Biomed. Mater.* **2020**, *15*, 055030. [CrossRef]
9. Iswariya, S.; Velswamy, P.; Uma, T.S. Isolation and Characterization of Biocompatible Collagen from the Skin of Puffer Fish (*Lagocephalus inermis*). *J. Polym. Environ.* **2017**, *26*, 2086–2095. [CrossRef]
10. Lim, Y.-S.; Ok, Y.-J.; Hwang, S.-Y.; Kwak, J.-Y.; Yoon, S. Marine Collagen as A Promising Biomaterial for Biomedical Applications. *Mar. Drugs* **2019**, *17*, 467. [CrossRef]
11. Zhang, L.; Hu, J.; Athanasiou, K.A. The Role of Tissue Engineering in Articular Cartilage Repair and Regeneration. *Crit. Rev. Biomed. Eng.* **2009**, *37*, 1–57. [CrossRef]
12. Almouemen, N.; Kelly, H.M.; O'Leary, C. Tissue Engineering: Understanding the Role of Biomaterials and Biophysical Forces on Cell Functionality through Computational and Structural Biotechnology Analytical Methods. *Comput. Struct. Biotechnol. J.* **2019**, *17*, 591–598. [CrossRef] [PubMed]
13. Hixon, K.R.; Lu, T.; Sell, S.A. A comprehensive review of cryogels and their roles in tissue engineering applications. *Acta Biomater.* **2017**, *62*, 29–41. [CrossRef] [PubMed]
14. Reys, L.; Silva, S.; Pirraco, R.; Marques, A.; Mano, J.; da Silva, T.H.; Reis, R.L. Influence of freezing temperature and deacetylation degree on the performance of freeze-dried chitosan scaffolds towards cartilage tissue engineering. *Eur. Polym. J.* **2017**, *95*, 232–240. [CrossRef]
15. Shah, R.; Saha, N.; Saha, P. Influence of temperature, pH and simulated biological solutions on swelling and structural properties of biomineralized (CaCO$_3$) PVP-CMC hydrogel. *Prog. Biomater.* **2015**, *4*, 123–136. [CrossRef] [PubMed]
16. Myers, R.H.; Montgomery, D.C.; Anderson-Cook, C.M. *Response Surface Methodology: Process and Product Optimization Using Designed Experiments*, 2nd ed.; John Wiley & Sons: Hoboken, NJ, USA, 2012; ISBN 9781118916025.
17. Dean, A.M.; Voss, D.T. *Design and Analysis of Experiments*; Springer: New York, NY, USA, 1999; Volume 1, pp. 1–742.
18. Fisher, R.A. The arrangement of field experiments. *J. Minist. Agric. Great Br.* **1926**, *33*, 503–513.
19. Gutierrez-Gonzalez, M.; Farías, C.; Tello, S.; Pérez-Etcheverry, D.; Romero, A.; Zúñiga, R.; Ribeiro, C.H.; Lorenzo-Ferreiro, C.; Molina, M.C. Optimization of culture conditions for the expression of three different insoluble proteins in Escherichia coli. *Sci. Rep.* **2019**, *9*, 16850–16861. [CrossRef]
20. Blanco, M.; Vázquez, J.A.; Pérez-Martín, R.I.; Sotelo, C.G. Collagen Extraction Optimization from the Skin of the Small-Spotted Catshark (*S. canicula*) by Response Surface Methodology. *Mar. Drugs* **2019**, *17*, 40. [CrossRef]
21. Kiew, P.L.; Mat Don, M. Screening of significant factors in collagen extraction from hybrid *Clarias* sp. using astatistical tool. *Int. Food Res. J.* **2013**, *20*, 1913–1920.
22. Ruiter, F.A.; Alexander, C.; Rose, F.R.A.J.; Segal, J.I. A design of experiments approach to identify the influencing parameters that determine poly-D,L-lactic acid (PDLLA) electrospun scaffold morphologies. *Biomed. Mater.* **2017**, *12*, 055009. [CrossRef]
23. Gadomska-Gajadhur, A.; Kruk, A.; Wierzchowski, K.; Ruśkowski, P.; Pilarek, M. Design of experiments-based strategy for development and optimization of polylactide membranes preparation by wet inversion phase method. *Polym. Adv. Technol.* **2021**, *32*, 3028. [CrossRef]
24. Lam, J.; Carmichael, S.T.; Lowry, W.E.; Segura, T. Hydrogel design of experiments methodology to optimize hydrogel for iPSC-NPC culture. *Adv. Healthc. Mater.* **2015**, *4*, 534–539. [CrossRef] [PubMed]
25. López-Cebral, R.; Quinteros Lopes Henriquez da Silva, T.J.; Antunes Correia de Oliveira, J.M.; Novoa Carballal, R.; Gonçalves dos Reis, R.L. High Molecular Weight Chitosan, Process for Obtaining and Uses Thereof. US Patent US20200262937A1, 11 November 2019.

26. Karvinen, J.; Ihalainen, T.O.; Calejo, M.T.; Jönkkäri, I.; Kellomäki, M. Characterization of the microstructure of hydrazone crosslinked polysaccharide-based hydrogels through rheological and diffusion studies. *Mater. Sci. Eng. C* **2019**, *94*, 1056–1066. [CrossRef] [PubMed]

27. Welzel, P.B.; Prokoph, S.; Zieris, A.; Grimmer, M.; Zschoche, S.; Freudenberg, U.; Werner, C. Modulating Biofunctional starPEG Heparin Hydrogels by Varying Size and Ratio of the Constituents. *Polymers* **2011**, *3*, 602–620. [CrossRef]

28. Suriano, R.; Griffini, G.; Chiari, M.; Levi, M.; Turri, S. Rheological and mechanical behavior of polyacrylamide hydrogels chemically crosslinked with allyl agarose for two-dimensional gel electrophoresis. *J. Mech. Behav. Biomed. Mater.* **2014**, *30*, 339–346. [CrossRef] [PubMed]

29. Munteanu, I.G.; Apetrei, C. Analytical Methods Used in Determining Antioxidant Activity: A Review. *Int. J. Mol. Sci.* **2021**, *22*, 3380–3410. [CrossRef]

30. Singleton, V.L.; Rossi, J.A. Colorimetry of total phenolics with phosphomolybdic-phosphotungstic acid reagents. *Am. J. Enol. Vitic.* **1965**, *16*, 144–158.

31. Slinkard, K.; Singleton, V.L. Total phenol analysis: Automation and comparison with manual methods. *Am. J. Enol. Vitic.* **1977**, *28*, 49–55.

32. Rimann, M.; Laternser, S.; Gvozdenovic, A.; Muff, R.; Fuchs, B.; Kelm, J.M.; Graf-Hausner, U. An in vitro osteosarcoma 3D microtissue model for drug development. *J. Biotechnol.* **2014**, *189*, 129–135. [CrossRef]

33. Maran, J.P.; Manikandan, S. Response surface modeling and optimization of process parameters for aqueous extraction of pigments from prickly pear (*Opuntia ficus-indica*) fruit. *Dye. Pigment.* **2012**, *95*, 465–472. [CrossRef]

34. Palanikumar, K.; Davim, J.P. Electrical discharge machining: Study on machining characteristics of WC/Co composites. *Mach. Mach. Tools* **2013**, 135–168. [CrossRef]

35. Gloria, A.; Borzacchiello, A.; Causa, F.; Ambrosio, L. Rheological Characterization of Hyaluronic Acid Derivatives as Injectable Materials Toward Nucleus Pulposus Regeneration. *J. Biomater. Appl.* **2012**, *26*, 745–759. [CrossRef] [PubMed]

36. Zuidema, J.M.; Rivet, C.J.; Gilbert, R.J.; Morrison, F.A. A protocol for rheological characterization of hydrogels for tissue engineering strategies. *J. Biomed. Mater. Res. Part B Appl. Biomater.* **2014**, *102*, 1063–1073. [CrossRef] [PubMed]

37. Slaughter, B.V.; Khurshid, S.S.; Fisher, O.Z.; Khademhosseini, A.; Peppas, N.A. Hydrogels in Regenerative Medicine. *Adv. Mater.* **2009**, *21*, 3307–3329. [CrossRef] [PubMed]

38. Carvalho, D.N.; Goncalves, C.; Oliveira, J.M.; Williams, D.S.; Mearns-Spragg, A.; Reis, R.L.; Silva, T.H. Innovative methodology for marine collagen–chitosan–fucoidan hydrogels production, tailoring rheological properties towards biomedical application. *Green Chem.* **2021**, *23*, 7016–7029. [CrossRef]

39. Citkowska, A.; Szekalska, M.; Winnicka, K. Possibilities of Fucoidan Utilization in the Development of Pharmaceutical Dosage Forms. *Mar. Drugs* **2019**, *17*, 458. [CrossRef]

40. Horinaka, J.-I.; Kimura, A.; Takigawa, T. Rheological properties of concentrated solutions of fucoidan in water and in an ionic liquid. *Polymer* **2020**, *211*, 123090. [CrossRef]

41. Hentati, F.; Pierre, G.; Ursu, A.V.; Vial, C.; Delattre, C.; Abdelkafi, S.; Michaud, P. Rheological investigations of water-soluble polysaccharides from the Tunisian brown seaweed Cystoseira compressa. *Food Hydrocoll.* **2020**, *103*, 105631. [CrossRef]

42. Kordjavi, M.; Etemadian, Y.; Shabanpour, B.; Pourashouri, P. Chemical composition antioxidant and antimicrobial activities of fucoidan extracted from two species of brown seaweeds (*Sargassum ilicifolium* and *Sargassum angustifolium*) around Qeshm Island. *Iran. J. Fisheires Sci.* **2018**, *18*, 457–475.

43. Cheung, B.; Kwan, M.; Chan, R.; Sea, M.; Woo, J. Potential of Asian natural products for health in aging. *Mol. Basis Nutr. Aging* **2016**, 659–676.

44. Cikoš, A.-M.; Jokić, S.; Šubarić, D.; Jerković, I. Overview on the Application of Modern Methods for the Extraction of Bioactive Compounds from Marine Macroalgae. *Mar. Drugs* **2018**, *16*, 348. [CrossRef]

45. Murray, M.; Dordevic, A.L.; Ryan, L.; Bonham, M.P. The Impact of a Single Dose of a Polyphenol-Rich Seaweed Extract on Postprandial Glycaemic Control in Healthy Adults: A Randomised Cross-Over Trial. *Nutrients* **2018**, *10*, 270. [CrossRef] [PubMed]

46. Palanisamy, S.; Vinosha, M.; Marudhupandi, T.; Rajasekar, P.; Prabhu, N.M. In vitro antioxidant and antibacterial activity of sulfated polysaccharides isolated from Spatoglossum asperum. *Carbohydr. Polym.* **2017**, *170*, 296–304. [CrossRef] [PubMed]

47. Lamuela-Raventós, R.M. Folin–Ciocalteu method for the measurement of total phenolic content and antioxidant capacity. *Meas. Antioxid. Act. Capacit. Recent Trends Appl.* **2018**, 107–115.

48. Prior, R.L.; Wu, X.; Schaich, K. Standardized Methods for the Determination of Antioxidant Capacity and Phenolics in Foods and Dietary Supplements. *J. Agric. Food Chem.* **2005**, *53*, 4290–4302. [CrossRef]

49. Cotas, J.; Leandro, A.; Monteiro, P.; Pacheco, D.; Figueirinha, A.; Gonçalves, A.M.M.; Da Silva, G.J.; Pereira, L. Seaweed Phenolics: From Extraction to Applications. *Mar. Drugs* **2020**, *18*, 384. [CrossRef]

50. Zimmerman, J.J.; Saint André-von Arnim, A.; McLaughlin, J. Cellular respiration. *Pediatric Crit. Care* **2011**, 1059–1072.

51. Campbell, A.K. Darwin shines light on the evolution of bioluminescence. *Luminescence* **2012**, *27*, 447–449. [CrossRef]

52. Conti, E.; Franks, N.P.; Brick, P. Crystal structure of firefly luciferase throws light on a superfamily of adenylate-forming enzymes. *Structure* **1996**, *4*, 287–298. [CrossRef]

53. Casem, M.L. Cell metabolism, in Case Studies. *Cell Biol.* **2016**, 263–281. [CrossRef]

54. Khalili, A.A.; Ahmad, M.R. A Review of Cell Adhesion Studies for Biomedical and Biological Applications. *Int. J. Mol. Sci.* **2015**, *16*, 18149–18184. [CrossRef]

55. Beg, S.; Akhter, S. Box–Behnken Designs and Their Applications in Pharmaceutical Product Development. *Des. Exp. Pharm. Prod. Dev.* **2021**, 77–85. [CrossRef]

56. Mason, R.L.; Gunst, R.F.; Hess, J.L. Designs and analyses for fitting response surfaces. In *Statistical Design and Analysis of Experiments: With Applications to Engineering and Science*, 2nd ed.; John Wiley & Sons, Inc.: Hoboken, NJ, USA, 2003; pp. 568–606.

57. Sabela, M.I.; Suvardhan, K.; Bathinapatla, A.; Krishna, B. A Box-Behnken Design and Response Surface Approach for the Simultaneous Determination of Chromium (III) and (VI) Using Catalytic Differential Pulse Polarography. *Int. J. Electrochem. Sci.* **2004**, *2*, 140–146.

58. Cristóvão, R.O.; Gonçalvesa, C.; Botelhoa, C.M.; Martinsab, R.J.E.; Boaventura, R.A.R. Chemical oxidation of fish canning wastewater by Fenton's reagent. *J. Environ. Chem. Eng.* **2014**, *2*, 2372–2376. [CrossRef]

59. Tayeb, A.M.; Tony, M.A.; Mansour, S.A. Application of Box–Behnken factorial design for parameters optimization of basic dye removal using nano-hematite photo-Fenton tool. *Appl. Water Sci.* **2018**, *8*, 138. [CrossRef]

60. Abbott, R.D.; Kaplan, D.L. Engineering Biomaterials for Enhanced Tissue Regeneration. *Curr. Stem Cell Rep.* **2016**, *2*, 140–146. [CrossRef]

61. Satman, I.; Omer, B.; Tutuncu, Y.; Kalaca, S.; Gedik, S.; Dinccag, N.; Karsidag, K.; Genc, S.; Telci, A.; Canbaz, B.; et al. Twelve-year trends in the prevalence and risk factors of diabetes and prediabetes in Turkish adults. *Eur. J. Epidemiol.* **2016**, *28*, 169–180. [CrossRef]

62. Vlierberghe, S.V.; Dubluel, P.; Schachet, E. Effect of cryogenic treatment on the rheological properties of gelatin hydrogels. *J. Bioact. Compat. Polym.* **2010**, *25*, 1–24. [CrossRef]

Article

Effect of Organoclay Addition on Rheological, Thermal, and Mechanical Properties of Nitrile Rubber/Phenolic Resin Blend

Sara Shafiee [1], Leila Bazli [1], Mohammad Karrabi [1], Mir Hamid Reza Ghoreishy [1] and Milad Bazli [2,3,*]

1   Rubber Group, Processing Department, Iran Polymer and Petrochemical Institute, Tehran 1497713115, Iran;
     s.shafiee@ippi.ac.ir (S.S.); leilabazli64@gmail.com (L.B.); m.karabi@ippi.ac.ir (M.K.);
     m.h.r.ghoreishy@ippi.ac.ir (M.H.R.G.)
2   College of Engineering, IT and Environment, Charles Darwin University, Darwin 0801, Australia
3   School of Mechanical and Mining Engineering, The University of Queensland, Brisbane 4000, Australia
*   Correspondence: milad.bazli@cdu.edu.au or m.bazli@uq.edu.au

Abstract: In this study, the effects of NBR polarity and organoclay addition on the curing, rheological, mechanical, and thermal properties of an NBR/phenolic resin blend were investigated. The samples were prepared using a two-roll mill. The results showed that rheological and tensile properties improved due to the good distribution of nanoparticles, as well as the good compatibility of nitrile butadiene rubber with phenolic resin. The addition of 1.5 phr of nanoparticles to blends containing 33% and 45% acrylonitrile increased the curing torque difference by approximately 12% and 28%, respectively. In addition, the scorch time and curing time decreased in nanocomposites. Adding nanoparticles also increased the viscosity. The addition of phenolic resins and nanoparticles has a similar trend in modulus changes, and both of these factors increase the stiffness and, consequently, the elastic and viscous modulus of the specimens. Adding 1.5 phr of organoclay increased the tensile strength of the blends by around 8% and 13% in the samples with low and high content of acrylonitrile, respectively. Increasing the temperature of the tensile test led to a reduction in the tensile properties of the samples. Tensile strength, elongation at break, modulus, and hardness of the samples increased with increasing organoclay content. In addition, with increasing nanoparticle concentration, the samples underwent lower deterioration in tensile strength and Young's modulus at different temperatures compared to the blends. In the samples containing 1.5 phr of organoclay, the thermal decomposition temperatures were enhanced by around 24 and 27 °C for low and high acrylonitrile content.

Keywords: nitrile butadiene rubber; phenolic resin; rheology; nanoparticles; organoclay; thermal stability; mechanical properties

1. Introduction

Layered silicates or clays, among different nanofillers, occupy a leadership place in polymeric nanocomposites because of their moderate cost and commercial availability [1]. A tactoid or layered silicate consists of several single layers with regular gaps between them called galleries. These layers are held together by electrostatic forces [2,3]. Efficient polymer/clay nanocomposites are obtained when the silicate layers are separated into single layers and dispersed uniformly in the polymeric matrix. This dispersion condition, referred to as the exfoliated state, is optimal for a nanocomposite since it results in the highest improvement in physico-mechanical properties [4–6]. However, achieving the exfoliated morphology is arduous and the intercalated morphology is mostly obtained. In this case, the polymer chains enter the spaces between the layers (galleries), resulting in gallery expansion. To increase their interlayer spacing, a thermodynamic affinity for polymer chains and consequent enhancement of their dispersion in polymer matrices, organically modified clay, referred to as organoclay (OC), have been used. With the use of OC, both the exfoliated and intercalated morphologies are frequently achieved [7,8].

A mixture of phenolic resin and synthetic rubber has been used as a binder for friction materials of train vehicles' frictional braking systems [9,10]. Through the use of such blends, one can create a polymeric binder having the qualities of both a hard thermosetting resin and flexible rubber. Nevertheless, broad use of this combination as a friction material binder is limited by the rubber phase's inferior temperature stability when compared to phenolic resin [11–13].

Nitrile butadiene rubber (NBR) is a polar rubber that is exceptionally resistant to oil absorption because of the nitrile content. The amount of acrylonitrile in the nitrile rubber can be changed to alter its polarity and a variety of qualities. The lower the nitrile percentage, the better the low-temperature flexibility, while the higher the nitrile level, the better the resistance to aromatic hydrocarbons. Its compatibility with certain compounding ingredients can be influenced by its polarity [14]. Nevertheless, similar to other elastomers, it is not stable at high temperatures. When exposed to a high temperature and pressure flame, a strong char coating cannot be formed by the elastomer. This can be handled through the use of char-producing or flame-retardant compounds. According to Maamori et al. [15], using phenolic resin in conjunction with carbon black increased the thermal characteristics of nitrile rubber because of its high strength [16]. The polarity of the phenolic resin network results from the hydroxyl group's existence on the benzene ring. NBR and phenolic resin are both organic compounds with polar natures that are miscible with one another. Thus, an NBR/phenolic resin blend without the incorporation of any filler improves the composite's thermal properties and ablation resistance [15,17]. Mirabedini et al. reported that, by the addition of phenolic resin into NBR, the viscoelastic behavior of the compounds becomes more elastic and less viscous. Moreover, by increasing the phenolic resin content, crosslink density increased [17]. Nawaz et al. also demonstrated the reduced ablation rate and enhanced thermal stability with the addition of this resin to NBR [10]. Owing to the low cost of this blend, large quantities of its composite can be manufactured and it can be used in industries as a thermal insulator or flame retardant for high-temperature applications. For example, the addition of alumina nanoparticles was also reported to enhance the thermal stability of the blend [18]. Therefore, the addition of phenolic resin and nanoparticles such as OC to NBR can enhance its mechanical properties and thermal stability in order to obtain flexible materials with desirable mechanical performance.

Overall, there are limited studies considering the evaluation of the NBR rubber/phenolic resin systems, especially the impact of nanoparticle addition on the rheological, thermal, and mechanical properties of this system. The purpose of this study was the improvement of the viscoelastic and mechanical properties of this blend at high temperatures using OC nanoparticles. The influence of NBR polarity (low and high nitrile content) on the properties of the nanocomposites was also investigated. The nanoparticles were added to NBR/phenolic resin and the rheological, curing, morphological, dynamic mechanical, and thermal stability properties were investigated. The mechanical properties of the nanocomposites were also studied at 50 and 75 °C.

2. Materials and Methods

2.1. Materials and Preparation of the Samples

Table 1 lists the materials used to prepare the nanocomposites. Drying of the nanoparticles was performed in a 90 °C oven for 2 h before mixing. Commercially available NBR with two different amounts of acrylonitrile content, i.e., 33% and 45%, was used for the preparation of the samples. To improve the compounding of NBR with additives and fillers, the rubber was softened on a Polymix 200 L two-roll mill (Schwabenthan Co., Berlin, Germany) at 40 °C. The friction ratio of the two-roll mill was 1.6 and the rotation speed was 15 rpm. Then, at appropriate intervals, other components such as organo-modified montmorillonite (OMMT), activators, and antioxidants were added to the mixture and blended. At 80 °C, the powder Novolac was blended with the compound. At the end of the process, vulcanizing chemicals were introduced to the compound while it was still at 40 °C. It took 20 min to complete the full mixing process of the compound. The samples were vulcanized in

a hydraulic press at a pressure of 150 kg/cm² and 160 °C under controlled conditions. According to previous studies, a very small mass fraction of clay was required for the improvement of properties such as filler dispersion, the thermal degradation, stiffness, and strength of phenolic resin and NBR [19,20]. The OMMT content varied from 0 to 1.5 phr in this study. Table 2 contains information on the coding and composition of the samples.

Table 1. Materials used for the preparation of the samples.

Material	Supplier	Function
NBR (N 3345 and N 4560)	Polimeri Europa, Milan, Italy	Rubber base
Phenolic resin, Novolac	Moheb Co., Qom, Iran	Plastic phase
Organoclay (OMMT); No: 682640	Sigma-Aldrich, Oakville, ON, Canada	Reinforcement
S	Rangineh Pars, Babol, Iran	Curing agent
n-cyclohexyl -2- benzothiazole sulfenamide (CBS)	Vulkacit CZ, China	Accelerator
Mercaptobenzothiazole (MBT)	Bayer, Leverkusen, Germany	Accelerator
ZnO	Rangineh Pars, Babol, Iran	Activator
Stearic acid (SA)	Unichema International, Selangor, Malaysia	Dispersion agent for ZnO
4010 NA	Bayer, Leverkusen, Germany	Antioxidant

Table 2. Composition and coding of the samples.

Sample	NBR33	NBR45	Novolac (phr)	OMMT (phr)	4010NA (phr)	ZnO (phr)	SA (phr)	S (phr)	CBS (phr)	MBT (phr)
N33	100	0	0	0	1.5	4	2	1.5	0.8	0.7
N45	0	100	0	0	1.5	4	2	1.5	0.8	0.7
N33P	100	0	30	0	1.5	4	2	1.5	0.8	0.7
N45P	0	100	30	0	1.5	4	2	1.5	0.8	0.7
N33P-0.5	100	0	30	0.5	1.5	4	2	1.5	0.8	0.7
N33P-1	100	0	30	1	1.5	4	2	1.5	0.8	0.7
N33P-1.5	100	0	30	1.5	1.5	4	2	1.5	0.8	0.7
N45P-0.5	0	100	30	0.5	1.5	4	2	1.5	0.8	0.7
N45P-1	0	100	30	1	1.5	4	2	1.5	0.8	0.7
N45P-1.5	0	100	30	1.5	1.5	4	2	1.5	0.8	0.7

2.2. XRD Analysis

The structure of nanocomposites was investigated using X-ray diffraction analysis. Nanocomposites containing OMMT nanoparticles were analyzed by a Siemens D5000 X-ray spectrometer equipped with a Cu-kα radiation source, operated at a wavelength (λ) of 1.54 A°, a current of 30 mA, and a 40 kV working voltage. The measurements were carried out at room temperature within $2\theta = 0–2°$ with a step size of 0.02 °/s. Bragg's equation ($n\lambda = 2d \sin \theta$) was used to determine the distance between interplanar spacing.

2.3. Microstructural Study

Field emission scanning electron microscopy (FESEM) was utilized to examine the phase dispersion in NBR and the microstructure of the nanocomposites. The cross-sections of the samples that were obtained by fracturing in liquid nitrogen were examined before and after etching. By immersing the prepared samples in methanol for 72 h, the phenolic phase was extracted from the fracture surfaces. An oven was used to dry the resin-free samples before being coated with gold. Finally, the phase morphology was determined using FESEM (Tescan, MIRA3-XMU, Kohoutovice, Czech Republic) at a 30 kV voltage.

2.4. Rheology Measurements

To study the rheological behavior of the nanocomposites, a rubber processing analyzer (RPA 2000, Alpha Technologies Co., London, UK) was used. Prior to the curing procedure,

frequency sweep tests were conducted at 50 °C, between 0.05 and 30 Hz, with a 7% strain (linear viscoelastic region). The curing test was conducted at a temperature of 160 °C, with a strain of 7% and a frequency of 2 Hz.

2.5. DMTA Analysis

Dynamic mechanical thermal analysis (DMTA) is used to test the mechanical properties of a polymer nanocomposite when the temperature is continuously changing. The results can be used as a technique to determine the glass transition temperature (Tg) as well as the crystallization of polymers. The dynamic–mechanical evaluation of the nanocomposites (5 cm × 1 cm × 2 mm) was performed using a Triton Tritic 2000 DMTA device from −100 to 100 °C and at a frequency of 1 Hz (as per ASTM E1640) in an air environment. The heating rate was 5 °C/min and the samples underwent three-point bending.

2.6. TGA Analysis

Thermogravimetric analysis (TGA) (Pyris, Perkin Elmer, Llantrisant, UK) was utilized to determine the degradation and heat stability of the nanocomposites. Approximately 5 mg of the sample was thermogravimetrically analyzed in a nitrogen environment (flow rate = 60 cm^3 min^{-1}) at temperatures ranging from 25 to 800 °C, at a heating rate of 10 °C/min.

2.7. Mechanical Properties

To determine the tensile properties, a tensile instrument (STM-5, Santam, Tehran, Iran) equipped with a heating chamber was employed. The experiment followed the ASTM D412 standard. The evaluation of the samples was carried out at three temperatures of 50, 25, and 75 °C, at a speed of 500 mm/min. Additionally, each sample was tested three times to determine the average values of tensile strength, modulus, as well as elongation at break.

The hardness of the samples was determined using Zwick 3100 shore hardness testers from Germany based on ASTM D-2240. The samples were approximately 4 mm thick, and the value of hardness was determined after 3 s. For each sample, three measurements were taken and the average was reported.

3. Results and Discussion

3.1. Curing Properties

Table 3 shows the curing properties that were obtained from measuring the changes in torque with time at 160 °C. As the results demonstrate, with the increase in the amount of acrylonitrile in NBR rubber, the vulcanization torque and scorch time in the rubber and blend samples increased. In the N45 sample, the percentage of butadiene groups decreased, which reduced the sites available for crosslinking. On the other hand, due to the higher polarity of the acrylonitrile groups, they formed the rigid part of the NBR rubber, resulting in an increase in the torque value. The structures of the polymers are presented in Figure 1. In the N33P and N45P samples, a reduction in the scorching time occurred because the resin helped vulcanization and thereby the formation of sulfur bridges. Because the resin contained phenol and formaldehyde groups, it helped in the formation of a complex between the activator and its vulcanizing agents and reduced the scorch time. Nevertheless, an increase in the vulcanization time in N33P and N45P compared to N33 and N45 could be associated with the resin's interference in the reaction of sulfur bridges with each other and, therefore, the crosslink formation. Moreover, the enhancement of vulcanization torque in the blends—in particular, N45P compared to N33 and N45—could be the result of the hardening effect of the phenolic phase.

Table 3. Cure parameters of the samples.

Sample	Scorch Time (min)	Cure Time (min)	$M_H - M_L$ (dN·m)	Cure Rate (dN·m/min)
N33	2.7	6.5	11.9	0.9
N33P	2.4	6.8	13.6	0.9
N33P-0.5	2.3	6.8	14.0	1.0
N33P-1	2.1	6.3	14.5	1.0
N33P-1.5	1.7	5.8	15.5	1.1
N45	3.8	7.2	12.2	0.8
N45P	3.6	10.2	15.8	1.2
N45P-0.5	3.5	10.1	16.9	1.2
N45P-1	3.4	10.0	17.6	1.3
N45P-1.5	3.2	9.8	20.3	1.4
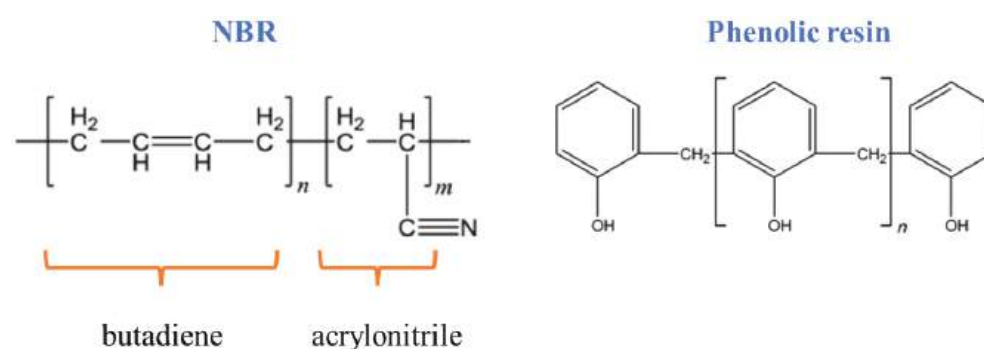
Figure 1. Chemical structure of NBR and phenolic resin.

A significant increase in the torque difference was observed by adding the phenolic resin, which could be the consequence of the thermosetting behavior of the phenolic resin during the vulcanization of the rubber at high temperatures. The results of the vulcanization rate show that the rate of vulcanization is related to the percentage of acrylonitrile. There were more butadiene groups in N33 compared to N45; therefore, more active sites were provided to form sulfur bridges, crosslinks were formed in a shorter time, and the curing speed increased. However, in blends—in particular, in the N45P sample—there existed a higher interaction between the rubber chains and phenolic phase, and on the other hand, due to the increase in polarity caused by the acrylonitrile groups, the attraction among rubber chains increased and crosslinks were formed more quickly. Therefore, the rubbers showed a lower curing rate compared to the blends.

With increasing the clay nanoparticle content, the torque increased because the mobility of polymer chains and crosslinks was decreased in the presence of nanoparticles so that, by adding 1.5 phr OMMT to N33P, the enhancement of the torque difference ranged from 13.6 dN m to 15.5 dN·m. Furthermore, a reduction in the scorch and cure times was observed in nanocomposites owing to the presence of ammonium groups on the surfaces of the OMMT nanoparticles, which accelerates crosslinking [21]. Similar to the rubber and blends, N45-containing nanocomposites showed larger scorch and cure times, resulting from lower butadiene groups. In all samples, the difference in vulcanization torque was increased by the addition of nanoparticles. The amount of reinforcement and the acrylonitrile percentage in the NBR phase are the two key parameters that change the torque difference so that, by increasing the acrylonitrile percentage and the nanoparticles, the final vulcanization torque increases. The chain mobility is reduced and the torque after the completion of the vulcanization increases due to good interaction between the particles and nitrile rubber/phenolic resin blend. In all samples, the cure rate increases when increasing the content of nanoparticles. The heat transfer to the nanocomposite is improved by an increment in the density of solid nanoparticles, increasing the cure rate.

3.2. XRD Analysis

The most important parameter that affects the rheological, mechanical, as well as physical properties of polymer-based nanocomposites is the dispersion of nanoparticles in the polymeric matrices and the ability of the polymeric chains to intercalate the galleries. Hence, in order to determine the intercalation and the increase in the galleries, tests such as XRD could be beneficial for obtaining the dispersion state and distances between layers of OMMT. In this study, Bragg's law was used to obtain the distance between layers. The XRD patterns of OMMT and the nanocomposites containing 1.5 phr of OMMT are shown in Figure 2. The OMMT powder presents a characteristic peak in $2\theta = 0.3$, which corresponds to a d-spacing of 239.7 nm. As shown in the figure, the addition of 1.5 phr of OMMT to the blends containing 33% and 45% acrylonitrile reduced the 2θ to 0.2 and 0.19, respectively. Increasing the distance between the layers indicates the entry of polymer chains into the OMMT galleries, especially in the N45P-1.5 sample. Better interaction of the matrix containing a higher percentage of acrylonitrile, and thereby a higher degree of polarity, with the polar surface of the nanoparticles, resulted in the better dispersion of nanoparticles in the matrix. Figure 3 schematically shows the intercalation of NBR chains in OMMT galleries. Nitrile groups can interact with the polar surfaces of clay layers or polar groups of aliphatic modifiers.
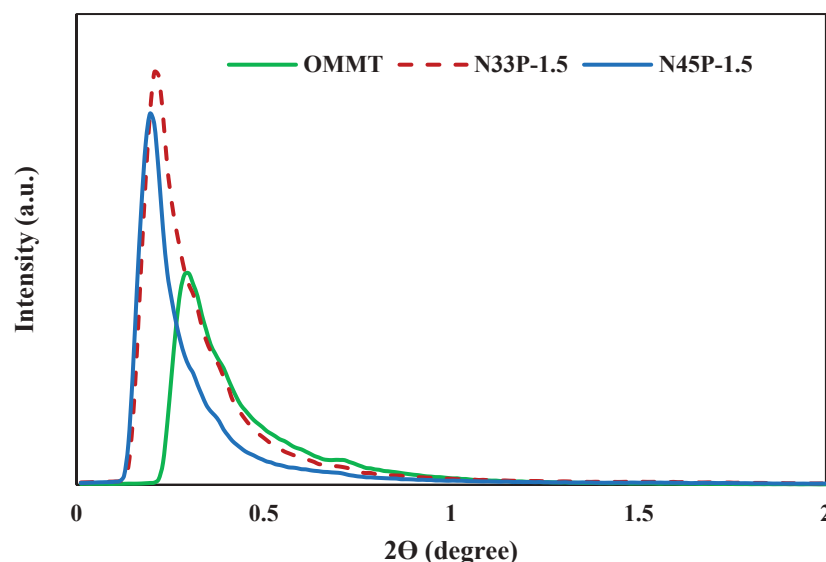
Figure 2. X-ray diffraction patterns of OMMT, N33P-1.5, and N45P-1.5.
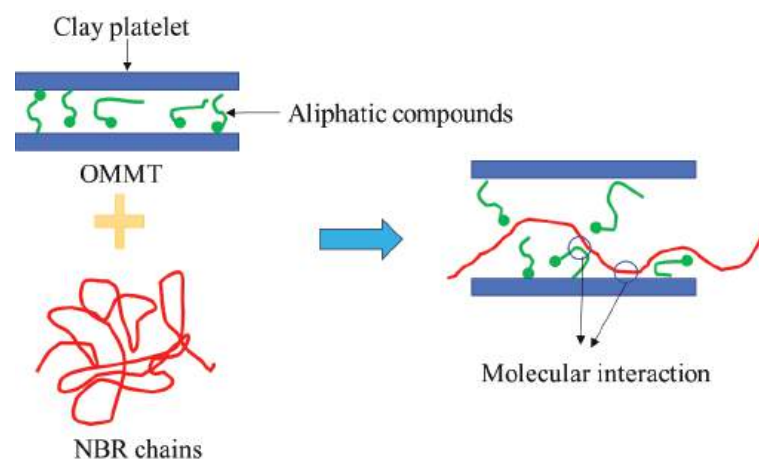
Figure 3. Schematic illustration of the intercalation of NBR chains in OMMT galleries.

3.3. Rheology

Figure 4a,b show the complex viscosity (■*), which is obtained from real and imaginary parts, vs. the frequency changes before the vulcanization process. According to the results, the viscosity increases with the percentage of acrylonitrile. This is because the segments containing acrylonitrile groups along the rubber chains have higher stiffness. In the blends, the complex viscosities were higher than those of the rubber samples due to enhanced crosslinks in the presence of the phenolic phase. The higher density of the crosslinks increases the force required for the deformation of the blend specimens, increasing the viscosity in the frequency sweep test. At higher frequencies, the entanglements between the chains open, and the viscosity is reduced significantly as the shear rate increases simultaneously [22,23].
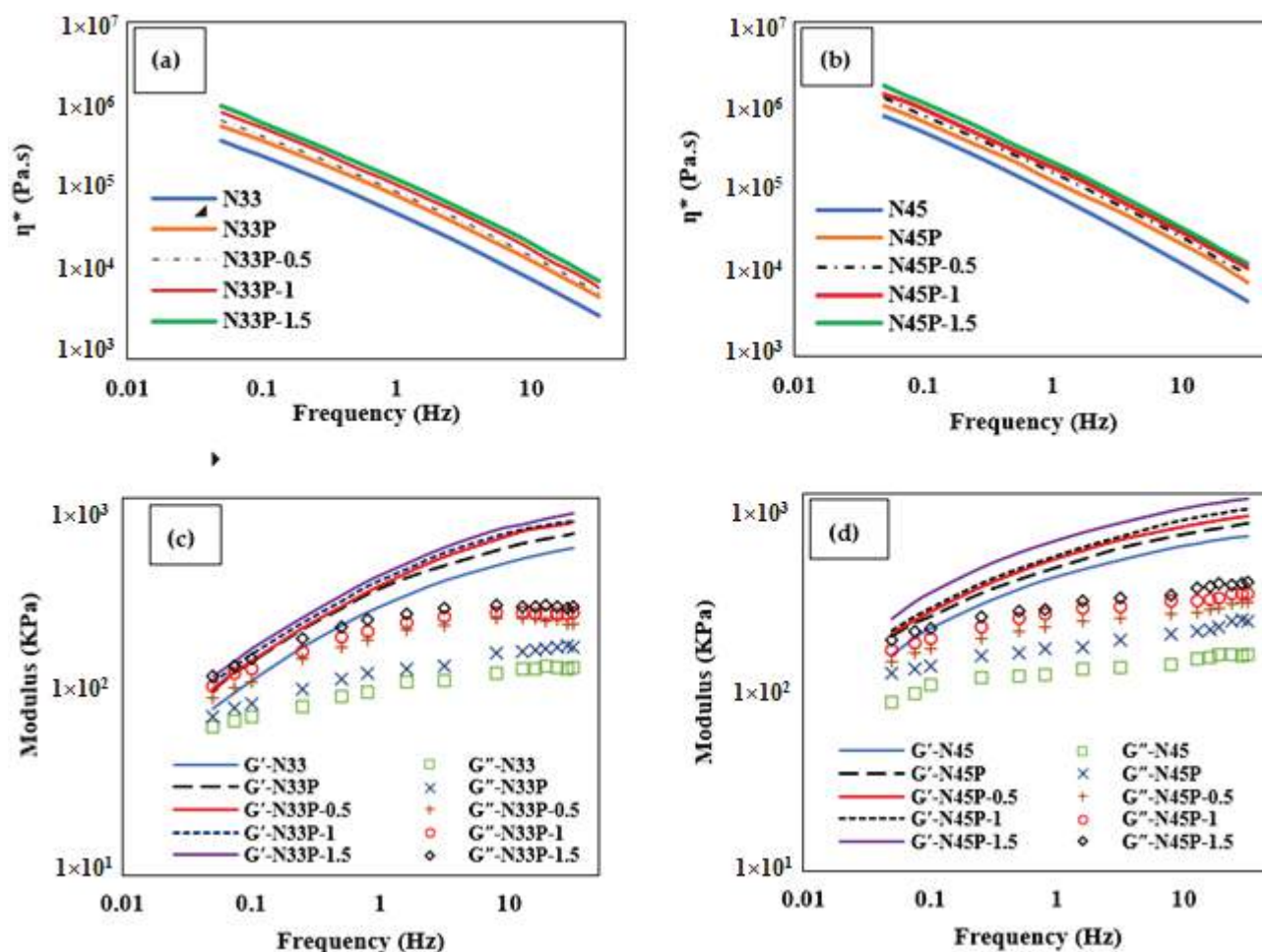
Figure 4. (**a**,**b**) Complex viscosity (■*) vs. the frequency changes; (**c**,**d**) Variations in the storage modulus (G′) and the loss modulus (G″) with frequency at 50 °C between 0.05 and 30 Hz with 7% strain.

As shown in Figure 4a,b, ■* increases when increasing the content of nanoparticles because of the interaction enhancement between the OMMT nanoparticles and the matrix. At higher frequencies, the shear rate increases, leading to the disentanglement of the chains, weakening of matrix/nanoparticle interactions, and a significant decrease in the complex viscosity. In N33P and N45P samples, when the amount of OMMT nanoparticles increases to 1.5 phr, the viscosity increases by around 55% and 60%, respectively. The higher viscosity of the samples with higher acrylonitrile content results from the polar nature of OMMT nanoparticles.

Figure 4c,d depict the variations in the storage modulus (G') and the loss modulus (G'') with frequency. As seen, both the storage and loss moduli increase with increasing frequency. The elastic behavior is higher at high frequencies. Moreover, the G' and G'' are higher in N45P compared to N33P. Higher G'' in samples with a higher percentage of acrylonitrile can be related to the viscous movements of the chains and a decrease in the flexibility of these samples. As a result of phenolic resin addition, G' increases due to the increase in stiffness resulting from its thermosetting behavior, and on the other hand, the reduction in its reversibility has increased the loss modulus. As the content of nanoparticles increases, the storage modulus increases, especially at lower frequencies, indicating stronger interactions between the matrix and the nanoparticles, as well as network formation and the semi-solid behavior of the nanocomposites. On the other hand, increasing G'' with the increase in the content of nanoparticles could be associated with viscous motions, particularly at higher frequencies. The viscous motions include breaking chains, weakening the matrix/nanoparticle interactions, as well as destroying the network of the nanoparticles.

3.4. Microstructure

To study the OMMT distribution, the FESEM analysis was used for the samples containing 1.5 phr nanoparticles before and after etching (Figure 5). As shown in the figure, good dispersion of the phenolic phase in the NBR phase is observed, which shows that the two polymers are highly compatible with each other. Nanocomposites that have a higher acrylonitrile percentage have more finely dispersed phase particles. In other words, higher polarity has caused a better interaction with the phenolic phase, resulting in improved compatibility. The presence of nanoparticles is shown with arrows in the figure. It is clear that OMMT nanoparticles are well dispersed in the matrix, which can lead to the production of nanocomposites with enhanced final properties. After etching, the elimination of the phenolic phase caused the formation of some pores, the size of which varied in different samples. Smaller pores are observed in N45P compared to N33P because of the better compatibility between the phenolic phase and N45 rubber. The incorporation of OMMT nanoparticles has improved the compatibility between the two phases and made the dispersed phase finer. Moreover, the tendency of clay nanoparticles to the phenolic phase (proximity of nanoclay to pores) is due to the polarity of OMMT particles.

3.5. Mechanical Properties

In Table 4 and Figure 6, the results of the tensile test at 25, 50, and 75 °C are reported. As shown, the use of N45 results in better tensile properties. However, the mechanical properties of the samples are weakened significantly by increasing the temperature. Moreover, the mechanical properties change from rubber to pseudo-plastic due to the phenolic resin addition, leading to the enhancement of the tensile strength and modulus, and a reduction in elongation at break. The tensile strength of blend specimens at the three temperatures is much higher than those of rubbers. In addition, the elongation of rubber samples is higher compared to blend samples due to the greater flexibility and elasticity of rubber. Furthermore, the use of NBR with a higher percentage of acrylonitrile and the addition of phenolic resin increased the stiffness and resistance of the sample to tensile force, which led to an increase in modulus.
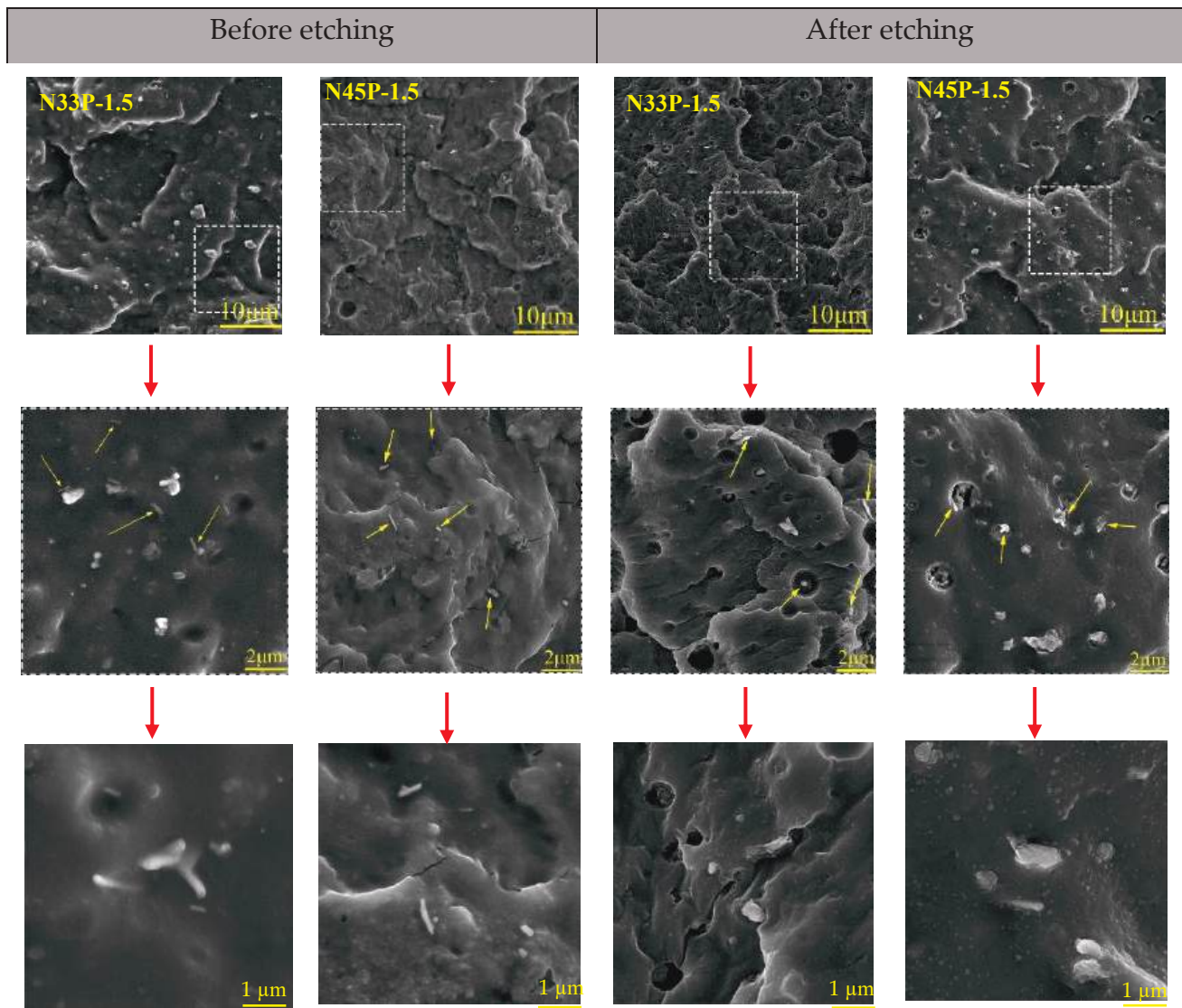
Figure 5. Microstructure of the blends and nanocomposites before and after etching in different magnifications.

Table 4. Mechanical properties of the samples at 25, 50, and 75 °C.

Sample	Strength (MPa)			Elongation (%)			Modulus (MPa)		
	25 °C	50 °C	75 °C	25 °C	50 °C	75 °C	25 °C	50 °C	75 °C
N33	3.54 ± 0.32	1.61 ± 0.24	1.30 ± 0.14	627 ± 22	243 ± 12	162 ± 4	0.97 ± 0.10	0.95 ± 0.08	0.92 ± 0.04
N33P	8.60 ± 0.30	2.87 ± 0.14	1.97 ± 0.18	420 ± 8	193 ± 3	111 ± 4	2.48 ± 0.20	1.73 ± 0.11	1.47 ± 0.18
N33P-0.5	9.26 ± 0.18	3.26 ± 0.20	2.21 ± 0.20	401 ± 6	188 ± 3	114 ± 4	3.58 ± 0.25	2.13 ± 0.18	2.06 ± 0.14
N33P-1	9.64 ± 0.15	3.34 ± 0.15	2.43 ± 0.11	379 ± 10	181 ± 4	109 ± 6	4.05 ± 0.18	2.35 ± 0.14	2.21 ± 0.09
N33P-1.5	9.31 ± 0.25	3.42 ± 0.15	2.55 ± 0.12	345 ± 7	158 ± 3	87 ± 3	4.91 ± 0.36	2.38 ± 0.20	2.36 ± 0.21
N45	7.43 ± 0.61	2.26 ± 0.32	1.59 ± 0.14	773 ± 32	293 ± 18	178 ± 7	1.28 ± 0.18	2.38 ± 0.14	2.36 ± 0.09
N45P	12.68 ± 0.39	5.82 ± 0.24	3.50 ± 0.17	432 ± 4	217 ± 2	134 ± 4	5.92 ± 0.35	3.92 ± 0.15	3.27 ± 0.14
N45P-0.5	13.29 ± 0.35	6.06 ± 0.20	3.96 ± 0.15	430 ± 6	210 ± 3	149 ± 7	6.56 ± 0.25	4.31 ± 0.12	3.44 ± 0.11
N45P-1	14.07 ± 0.35	6.29 ± 0.20	4.11 ± 0.10	401 ± 8	207 ± 4	137 ± 4	6.62 ± 0.14	4.45 ± 0.16	3.75 ± 0.08
N45P-1.5	14.39 ± 0.25	6.26 ± 0.15	4.25 ± 0.20	383 ± 7	181 ± 2	125 ± 6	7.19 ± 0.28	4.66 ± 0.24	3.90 ± 0.18
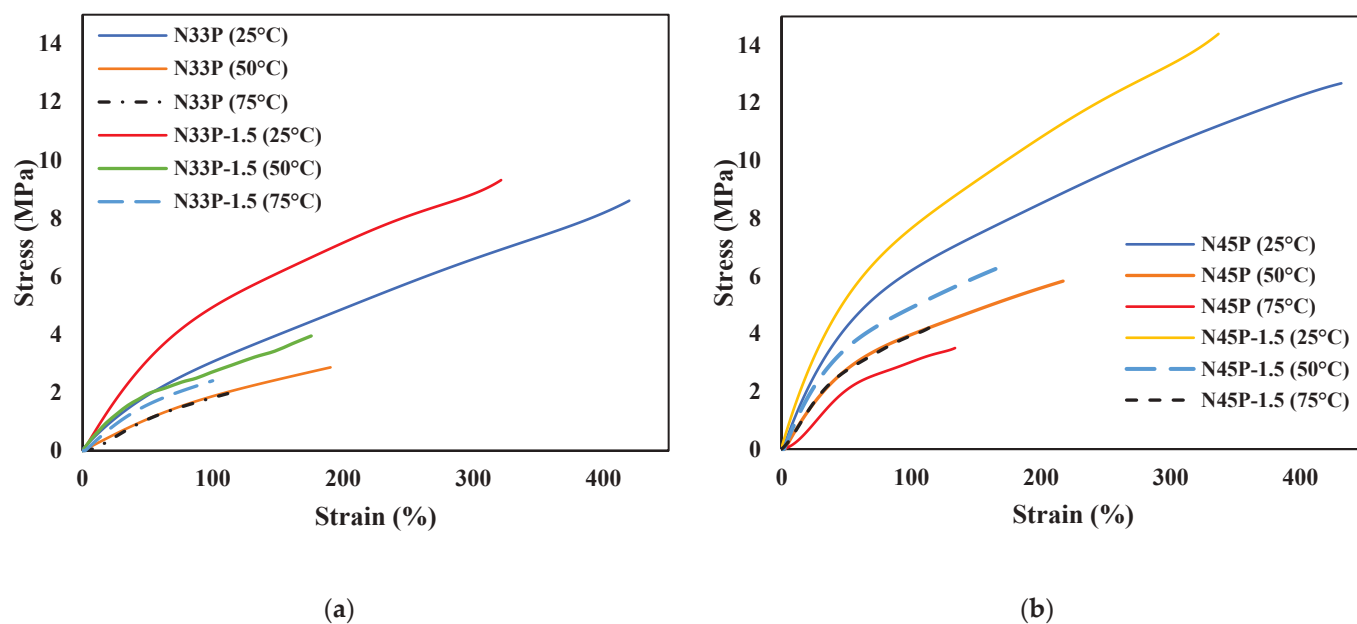
Figure 6. Stress–strain curves at 25, 50, and 75 °C for (**a**) N33P and N33P-1.5; (**b**) N45P and N45P-1.5.

Various factors affect the mechanical properties of nanocomposites, including the microstructure, mixing conditions, the interaction between polymer and filler, and filler content. According to the results, the addition of OMMT improves the mechanical properties at different temperatures, while the mechanical properties are deteriorated by increasing the temperature. When the temperature of the sample increases, the distance between rubber chains increases; hence, the interaction of the chains with the nanoparticles is weakened; therefore, the stress is not transferred properly. Thus, the samples have little resistance to the applied tensile force and the nanocomposites break at lower applied forces. One of the objectives of this study was to add nanoparticles to alleviate a significant reduction in the mechanical properties with increasing temperature. Another factor that is observed is that, with increasing temperature, the decrease in tensile properties is more tangible for samples containing N45, which is due to its higher plastic properties in comparison with the samples containing N33. The difference between the glass transition temperature of the phenolic phase and the test temperature is much less than that of the NBR phase; therefore, the samples containing phenolic resin or samples containing N45 are more sensitive to the temperature change.

Increasing the concentration of nanoparticles positively affects the mechanical properties of the samples and significantly reduces the effect of the temperature increase on the tensile parameters. The improvement in mechanical properties by the addition of nanoparticles has also been reported by other researchers [24–26]. At a certain temperature, with increasing nanoparticle concentration, tensile properties such as strength, elongation at break, and modulus increase. However, with higher content of nanoparticles, the elongation at break, which is an indicator of the chain movement ability, is reduced due to the planar morphology of OMMT, thus leading to the restriction of the movement and elongation of the polymer chains. According to the FESM images (Figure 5), nanoparticles were relatively well dispersed in both samples containing N33 and N45, and the effective interaction of polymer chains was achieved at the interface of nanolayers. Therefore, transferring the applied stress from the matrix to the reinforcement occurs well, resulting in an increase in the tensile strength. The addition of nanoparticles to both NBR blends with different acrylonitrile percentages increases the modulus of the samples. In other words, nanoparticles with plate morphology have a need for higher stress to deform the samples, and the modulus enhances with increasing nanoparticles. Due to the higher polarity, N45-containing samples show higher interaction with the phenolic phase; thus, they have better mechanical properties.

The results of the hardness test are shown in Figure 7. As the figure shows, the stiffness of the rubber has been increased by the addition of phenolics to the NBR due to the increased crosslinking. On the other hand, the hardness increases with the addition of OMMT to the nitrile rubber/phenolic resin blend. Previous reports also showed the hardness increase upon increasing the proportion of nanoparticles [27]. The more difficult penetration of the test indenter into samples containing N45 is due to the higher Mooney viscosity of these samples.
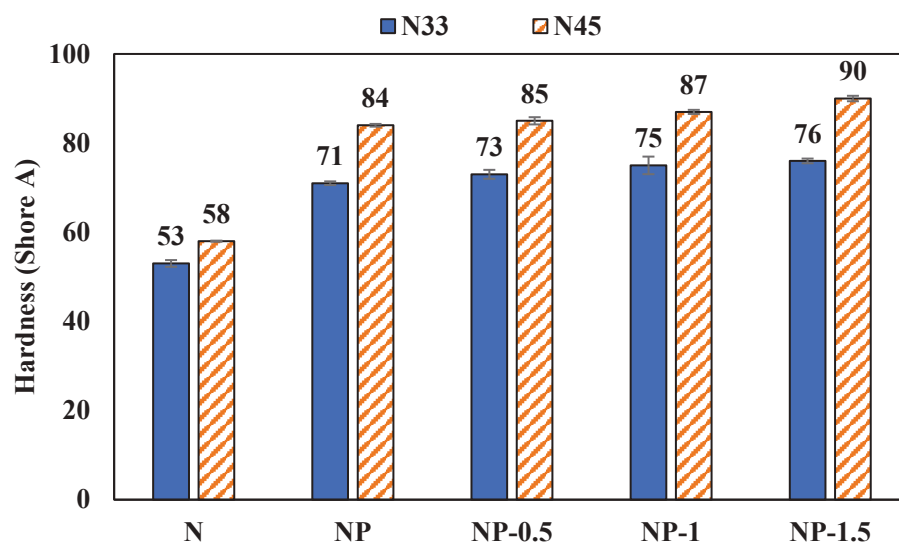
Figure 7. Hardness results of the samples.

3.6. DMTA Analysis

To evaluate the dynamic–mechanical properties of nanocomposites containing 1.5 phr OMMT, the DMTA test was used. Figure 8a shows the storage modulus variation in the temperature range of −100 to 100 °C, and the changes in tan δ (G″/G′) are shown in Figure 8b. According to the results, the blends and nanocomposites have a characteristic peak of Tg, showing the very good compatibility of these two phases, which was also observed in the FESEM images of the samples. Samples containing N45 have a Tg peak at higher temperatures, so N33P and N45P blends have Tg of 6.7 and 19.1 °C, respectively. Increasing the percentage of acrylonitrile in NBR increases the glass transition temperature. In the presence of the polar groups of acrylonitrile, the interaction among polymer chains increases; hence, a higher temperature is needed to make chains move, and therefore Tg increases. On the other hand, increasing the percentage of acrylonitrile has increased G′. The increment in hydrogen bonds in the presence of higher acrylonitrile groups and thereby higher polarity is considered the reason for the increase in G′ [28].

In the case of nanocomposites, the results show that the addition of nanoparticles to the blends increases the loss factor and shifts Tg to higher temperatures. The reason could be the increase in interfacial interactions between the matrix and the nanoparticle. The enhancement in the interactions results in the restriction of the mobility of the polymer chains and the increase in Tg [29]. The increase in the tan δ is also ascribed to the increase in filler/filler interactions [30]. Changes in storage modulus with temperature also indicate an increase with the addition of nanoparticles due to the OMMT plate morphology and their high hardness. Moreover, OMMT nanoparticles were more effective on N45-containing samples due to their polar characteristic. Adding 1.5 phr of OMMT increases the G′ of N33P and N45P by 15% and 18%, respectively.
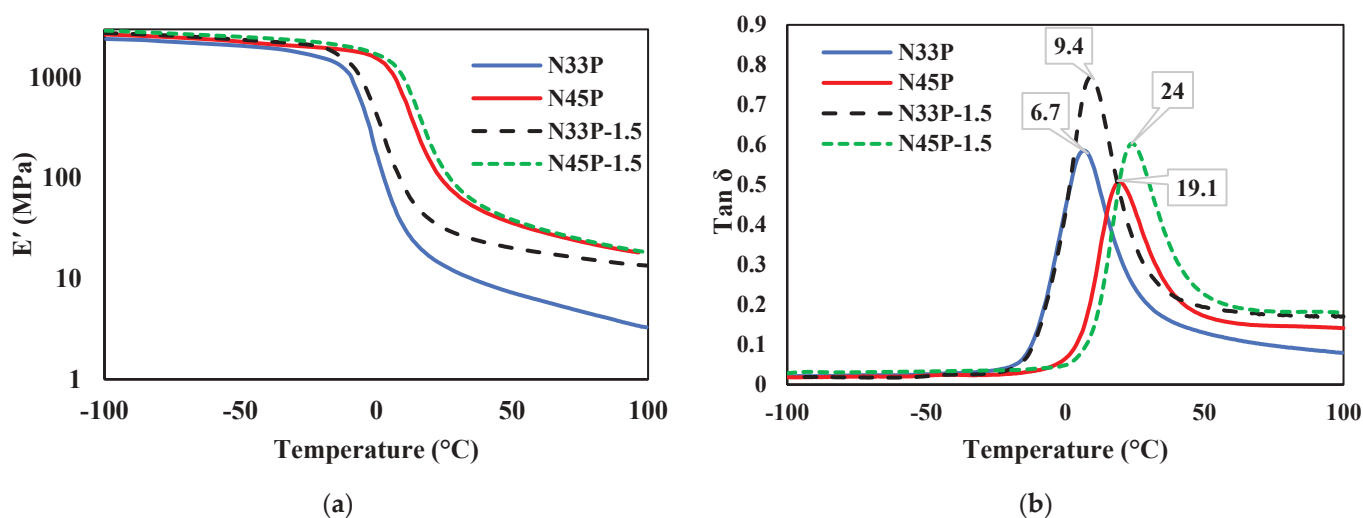
Figure 8. DMTA analysis results of the samples from −100 to 100 °C, at a frequency of 1, in an air environment; the heating rate was 5 °C/min; (**a**) storage modulus; (**b**) loss factor.

3.7. TGA

TGA analysis of selected samples, its first derivative, and the decomposition temperature and char residue are given in Figure 9 and Table 5, respectively. According to the figure, all samples show thermal degradation in the temperature range of 300–400 °C because of the breakage of phenolic and NBR chains. N45P has higher thermal stability than does N33P, which is probably due to polar acrylonitrile groups, which cause higher interactions between the polymer phases, leading to their destruction at higher temperatures [31]. By adding OMMT to the blends, degradation occurs at higher temperatures so that the addition of 1.5 phr of OMMT to N33P and N45P increases the thermal degradation temperature by approximately 23.4 and 27.1 °C, respectively. Moreover, by the addition of OMMT nanoparticles, the rate of thermal decomposition is reduced. The reason is that nanoparticles play the role of a physical barrier against the diffusion of small gas molecules upon thermal degradation. When the distribution of nanoparticles is better, the thermal stability of the nanocomposite is higher. Similar results are observed in the exothermic peaks shown in the derivative curve. Additionally, in the presence of nanoparticles, the char residue of nanocomposites has increased [1,32].
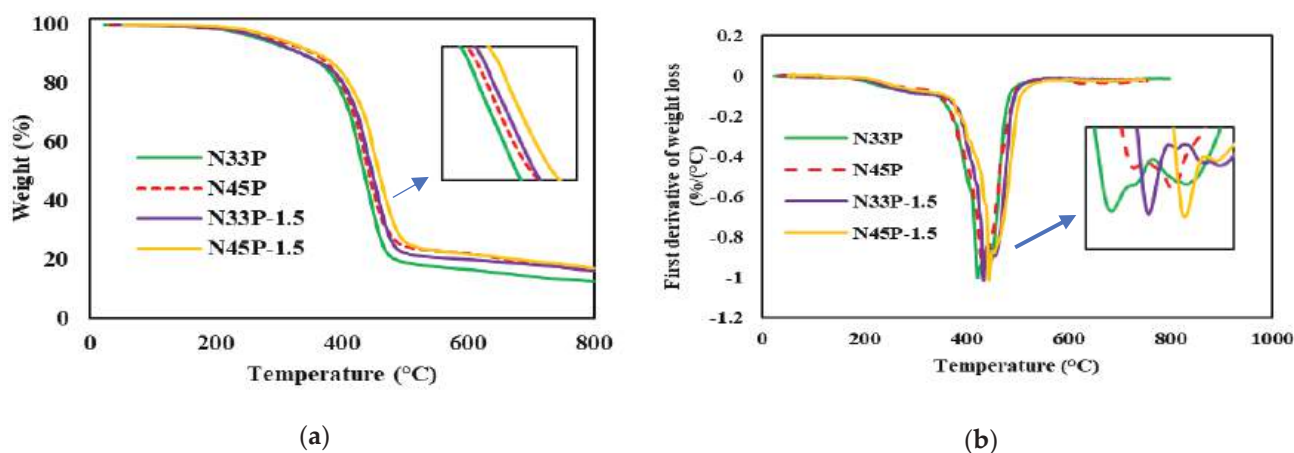
Figure 9. TGA analysis of the blends and nanocomposites conducted from 25 to 800 °C at a heating rate of 10 °C/min; (**a**) weight vs. temperature; (**b**) its first derivative.

Table 5. Thermal decomposition properties of the blends and nanoparticles.

Sample	Decomposition (Onset) Temperature (°C)	Peak Temperature (°C)	Char Residue (wt%)
N33P	373.8	422.8	12.3
N45P	380.3	431.4	15.8
N33P-1.5	397.2	434.9	16
N45P-1.5	407.4	444.7	17.1

4. Conclusions

In this study, the effects of NBR polarity and OMMT addition on the rheological properties, mechanical performance at high temperatures, and thermal stability of NBR/phenolic resin blends were investigated. The XRD patterns showed that by adding nanoparticles, the distance between the galleries increased. By adding the phenolic resin, the scorch time was reduced and vulcanization time increased. In nanocomposite samples, with an increase in the amount of OMMT nanoparticles, both the scorch and vulcanization times decreased. The final torque and the cure rate of the samples were enhanced by increasing the nanoparticles' percentage. By the addition of phenolic resins and nanoparticles, the storage and loss modulus increased. The complex viscosity also exhibited a similar trend upon increasing the content of nanoparticles. The tensile test at ambient temperature indicated that the phenolic resin addition changed the mechanical behavior from rubber to pseudo-plastic. Moreover, the addition of nanoparticles significantly reduced the thermally induced degradation of mechanical properties. The incorporation of the nanoparticles led to an increase in the loss factor and also the glass transition temperature. Decomposition and the char residue in the TGA test increased when adding nanoparticles in N33P and N45P. This study provides an insight into the formulation and design of composite materials based on NBR/phenolic resin with high mechanical performance and thermal stability for applications in which high mechanical properties and flexibility are required.

Author Contributions: S.S.: Writing—original draft preparation, writing—review and editing, methodology, investigation, formal analysis, software, and resources. L.B.: Writing—review and editing, formal analysis, software, methodology, investigation, and resources. M.K.: Writing—review and editing, formal analysis, software, methodology, investigation, resources and supervision. M.H.R.G.: Writing—review and editing, formal analysis, software, methodology, investigation, resources and supervision. M.B.: Writing—review and editing, supervision, and resources. All authors have read and agreed to the published version of the manuscript.

Institutional Review Board Statement: Not applicable.

Informed Consent Statement: Not applicable.

Data Availability Statement: Not applicable.

Conflicts of Interest: The authors declare no conflict of interest.

References

1. Mittal, V. Polymer layered silicate nanocomposites: A review. *Materials* **2009**, *2*, 992–1057. [CrossRef]
2. Abuchenari, A.; Hardani, K.; Abazari, S.; Naghdi, F.; Ahmady Keleshteri, M.; Jamavari, A.; Modarresi Chahardehi, A. Clay-reinforced nanocomposites for the slow release of chemical fertilizers and water retention. *J. Compos. Compd.* **2020**, *2*, 85–91. [CrossRef]
3. Bazli, L.; Eskandarinezhad, S.; Kakur, N.; Ramachandran, V.; Bacigalupe, A.; Mansilla, M.; Escobar, M. Electrical properties of polymer blend composites based on Silicone rubber/EPDM/clay for high voltage insulators. *J. Compos. Compd.* **2021**, *3*, 18–24. [CrossRef]
4. Bazli, L.; Khavandi, A.; Boutorabi, M.A.; Karrabi, M. Correlation between viscoelastic behavior and morphology of nanocomposites based on SR/EPDM blends compatibilized by maleic anhydride. *Polymer* **2017**, *113*, 156–166. [CrossRef]

5.   Rafiee, R.; Shahzadi, R. Predicting mechanical properties of nanoclay/polymer composites using stochastic approach. *Compos. Part B Eng.* **2018**, *152*, 31–42. [CrossRef]

6.   Eskandarinezhad, S.; Yusuf, M. An overview of materials, processing, and applications for wearable electronics. *J. Compos. Compd.* **2021**, *3*, 275–290. [CrossRef]

7.   Bazli, L.; Khavandi, A.; Boutorabi, M.A.; Karrabi, M. Morphology and viscoelastic behavior of silicone rubber/EPDM/Cloisite 15A nanocomposites based on Maxwell model. *Iran. Polym. J.* **2016**, *25*, 907–918. [CrossRef]

8.   Zhou, C.; Liu, T.; Liu, J.; Lu, X.; Shi, Y.; Zhou, S.; Xin, Z. Polybenzoxazine/organoclay composite coatings with intercalated structure: Relationship between solubility parameters and corrosion protection performance. *Prog. Org. Coat.* **2018**, *115*, 188–194. [CrossRef]

9.   Arsada, R.; Surojo, E.; Ariawan, D.; Muhayat, N.; Raharjo, W. Effect of NBR (Nitrile Butadiene Rubber) on flexural strength of composite friction brake. In Proceedings of the 2nd Nommensen International Conference on Technology and Engineering, Medan, Indonesia, 19–20 July 2018; p. 012057.

10.   Nawaz, R.; Rashid, N.; Ali, Z.; Khan, A.U.; Nazir, M.S.; Ul-Haq, N. 7Effects on Thermal and Ablative Properties of Phenolic Resin (Novolac) Blended Acrylonitrile Butadiene Rubber. *Fibers Polym.* **2018**, *19*, 1318–1326. [CrossRef]

11.   Song, M.; Yue, X.; Wang, X.; Huang, M.; Ma, M.; Pan, W.; Qin, Q. Improved high-temperature damping performance of nitrile-butadiene rubber/phenolic resin composites by introducing different hindered amine molecules. *e-Polymers* **2020**, *20*, 482–490. [CrossRef]

12.   Bijwe, J. NBR-modified resin in fade and recovery module in non-asbestos organic (NAO) friction materials. *Tribol. Lett.* **2007**, *27*, 189–196.

13.   Shojaei, A.; Faghihi, M. Analysis of structure—Properties relationship in nitrile-butadiene rubber/phenolic resin/organoclay ternary nanocomposites using simple model system. *Polym. Adv. Technol.* **2010**, *21*, 356–364. [CrossRef]

14.   Chandrasekaran, V.C. CHAPTER 6—Rubbers, Chemicals and Compounding for 'O' Rings and Seals. In *Rubber Seals for Fluid and Hydraulic Systems*; Chandrasekaran, V.C., Ed.; William Andrew Publishing: Oxford, UK, 2010; pp. 57–69. [CrossRef]

15.   Adachi, T.; Kataoka, T.; Higuchi, M. Predicting impact shear strength of phenolic resin adhesive blended with nitrile rubber. *Int. J. Adhes. Adhes.* **2015**, *56*, 53–60. [CrossRef]

16.   Al-Maamori, M.H.; Al-Zubaidi, A.A.-A.; Subeh, A.A. Effect of novolac on mechanical and physical properties of nitrile rubber (NBR). *Int. J. Mater. Sci. Appl.* **2015**, *4*, 43–47. [CrossRef]

17.   Mirabedini, A.S.; Karrabi, M.; Ghasemi, I. Viscoelastic behavior of NBR/phenolic compounds. *Iran. Polym. J.* **2013**, *22*, 25–32. [CrossRef]

18.   Faghihi, M.; Shojaei, A. Properties of alumina nanoparticle-filled nitrile-butadiene-rubber/phenolic-resin blend prepared by melt mixing. *Polym. Compos.* **2009**, *30*, 1290–1298. [CrossRef]

19.   Pappas, J.; Patel, K.; Nauman, E. Structure and properties of phenolic resin/nanoclay composites synthesized by in situ polymerization. *J. Appl. Polym. Sci.* **2005**, *95*, 1169–1174. [CrossRef]

20.   De Sousa, F.D.; Mantovani, G.L.; Scuracchio, C.H. Mechanical properties and morphology of NBR with different clays. *Polym. Test.* **2011**, *30*, 819–825. [CrossRef]

21.   Choi, D.; Kader, M.A.; Cho, B.H.; Huh, Y.I.; Nah, C. Vulcanization kinetics of nitrile rubber/layered clay nanocomposites. *J. Appl. Polym. Sci.* **2005**, *98*, 1688–1696. [CrossRef]

22.   Razavi-Nouri, M.; Karami, M.; Naderi, G. Rheological behavior and morphology of acrylonitrile-butadiene rubber/poly (ethylene-co-vinyl acetate) blends filled by various organoclay contents. *Appl. Clay Sci.* **2017**, *145*, 1–10. [CrossRef]

23.   Bazli, L.; Bagherian, M.H.; Karrabi, M.; Abbassi-Sourki, F.; Azizi, H. Effect of starch ratio and compatibilization on the viscoelastic behavior of POE/starch blends. *J. Appl. Polym. Sci.* **2020**, *137*, 48877. [CrossRef]

24.   Mensah, B.; Kim, S.; Arepalli, S.; Nah, C. A study of graphene oxide-reinforced rubber nanocomposite. *J. Appl. Polym. Sci.* **2014**, *131*, 40640. [CrossRef]

25.   Paran, S.; Naderi, G.; Ghoreishy, M. Mechanical properties development of high-ACN nitrile-butadiene rubber/organoclay nanocomposites. *Plast. Rubber Compos.* **2016**, *45*, 389–397. [CrossRef]

26.   Bazli, L.; Barghamadi, M.; Shafiee, S.; Karrabi, M.; Ghoreishy, M.H.R. Investigation of rheological, mechanical, and thermal properties of nanocomposites based on nitrile rubber-phenolic resin reinforced with nanographene. *J. Appl. Polym. Sci.* **2021**, *138*, 50906. [CrossRef]

27.   Jayaraj, S.; Egodage, S.; Walpalage, S. Incorporation of nanoclay into field latex to develop nanoclay filled dry rubber compounds. *J. Natl. Sci. Found. Sri Lanka* **2017**, *45*, 121–132. [CrossRef]

28.   Sadhu, S.; Bhowmick, A.K. Effect of nanoclay on the dynamic mechanical properties of styrene butadiene and acrylonitrile butadiene rubber vulcanizates. *Rubber Chem. Technol.* **2005**, *78*, 321–335. [CrossRef]

29.   Nigam, V.; Setua, D.; Mathur, G. Hybrid filler system for nitrile rubber vulcanizates. *J. Mater. Sci.* **2001**, *36*, 43–47. [CrossRef]

30.   Roland, C. Interpenetrating Polymer Networks (IPN Q1): Structure and Mechanical Behavior. In *Encyclopedia of Polymeric Nanomaterials*; Springer: Berlin/Heidelberg, Germany, 2013.

31.   Kumar, S.R.; Asseref, P.; Dhanasekaran, J.; Mohan, S.K. A new approach with prepregs for reinforcing nitrile rubber with phenolic and benzoxazine resins. *Rsc. Adv.* **2014**, *4*, 12526–12533. [CrossRef]

32.   Sengupta, R.; Chakraborty, S.; Bandyopadhyay, S.A.; Dasgupta, S.; Mukhopadhyay, R.; Auddy, K.; Deuri, A. A short review on rubber/clay nanocomposites with emphasis on mechanical properties. *Polym. Eng. Sci.* **2007**, *47*, 1956–1974. [CrossRef]

Article

A Low-Cost Filament Winding Technology for University Laboratories and Startups

Artem Andrianov [1],*[ID]**, Erika Kamada Tomita** [1]**, Carlos Alberto Gurgel Veras** [2][ID] **and Bruno Telles** [1]

1 Aerospace Engineering Course, University of Brasilia, Área Especial de Indústria Projeção A, Setor Leste (Gama), Brasília 72444-240, Brazil; erika.kamadat@gmail.com (E.K.T.); bruno@telles.com.br (B.T.)
2 Mechanical Engineering Department, Campus Universitário Darcy Ribeiro, University of Brasilia, Brasília 70970-900, Brazil; gurgel@unb.br
* Correspondence: andrianov@aerospace.unb.br; Tel.: +55-61-982344735

Abstract: This paper systematically explains the methodology and results of empirical work on the development of a low-cost filament winding technology for manufacturing axisymmetric polymer composite structures with a high length-to-diameter ratio, such as tubes, motor casings, and pressure vessels. The principal objective was to examine the experiences and most optimal practices in the development of computer-controlled equipment and auxiliary tooling for the wet filament-winding process. To preclude expensive commercial software for the automated control of a winding machine, analytical equations were derived for the winding trajectory of a four-axis filament-winding machine. The feasibility of the proposed equations was successfully validated by laying the fiber along the geodesic path marked on the surface of a cylindrical mandrel with hemispherical ends. Moreover, the carbon/epoxy cylindrical casings with hemispherical ends and port openings of the same diameter were wound to determine the thickness distribution in the hemispherical dome. The fiber volume ratio in the wound composite parts was evaluated using an optical technique.

Keywords: filament winding; winding trajectory; composite casing; polymer composite

1. Introduction

Filament winding technology has been deployed extensively in the aerospace industry since the early 1940s [1] and has persistently garnered interest from the scientific community. Data from Google Scholar, published in an insightful review on the automated manufacturing and processing of fiber-reinforced polymer composites, revealed the presence of a markedly high number of papers concerned with filament winding even in recent times [2]. However, the acquisition of composite structures with a unique shape of revolution and dimensions by university laboratories or startups requires sizeable investments. Under these conditions, small companies typically seek alternative solutions. University teams, however, can potentially benefit from sponsorship by equipment manufacturers, as demonstrated in the case of the production of filament-wound rocket fuselages [3]. Another tenable solution is the development of in-house low-cost equipment for filament winding [4].

A multitude of reports have highlighted the practicability of in-house laboratory equipment for assessing new filament winding techniques and for the experimental fabrication of advanced composite materials. Reference [5] presents a five-axis filament winding machine (FWM), including a numerical control unit and liner. It is suggested in [6] to increase the fiber volume ratio and decrease the void volume ratio of the composite casing. An environmentally friendly FWM, without any discernible loss of quality was devised by the separation of the resin components with their controllable feeding initially to a conventional static-mixer and subsequently to a custom-designed resin impregnation unit [7,8]. In the study reported in [9], the development of a controller using the B-spline interpolation technique entailed the construction of a three-axis FWM. A succinct description of the filament

winding hardware that features precision guidance of the carbon nanotube-based material is given in [10]. A "spiral-winder" was developed for the manufacturing cylindrical laminated veneer lumber in [11]. The majority of the said research had a narrow purview with their focus on specific scientific problems and engineering solutions related to filament winding technology, and only a few details were presented regarding the cost-effective design of the filament winder, its control system, and winding technique.

The volume ratio and decrease in the void volume ratio of the composite casing were recorded. An environmentally friendly FWM, without any discernible loss of quality was devised by the separation of the resin components with their controllable feeding initially to a conventional static-mixer and subsequently to a custom-designed resin impregnation unit [7,8]. In the study reported in [9], the development of a controller using B-spline interpolation technique entailed the construction of a three-axis FWM. A succinct description of the filament winding hardware that features precision guidance of the carbon nanotube-based material is given in [10]. A "spiral-winder" was developed for the manufacturing cylindrical laminated veneer lumber in [11]. The majority of the said research works had a narrow purview with their focus on specific scientific problems and engineering solutions related to filament winding technology, and only a few details were presented regarding the cost-effective design of the filament winder, its control system, and winding technique.

The methodology and results of one of the first attempts to design a low-cost computer-operated wet filament winding system for manufacturing cylindrical and conical parts or a combination of components are delineated in [12]. The associated system is accompanied by a software written in the AUTOLISP parametric programming language for the visualization of the winding patterns. Another innovative lathe-type machine based on a wet winding method is presented in [13]. The cost of the system is low because of the implementation of a rigid automation: the control system is not controlled by a computer, but is rather based on relays, limit switches, a timer, and a counter. Similar low-cost design solutions have been presented, which are based on a speed control of two DC [14] or AC motors [15]. An ingenious small-scale FWM has also been developed for educational purposes [16]. This machine generates helical winding patterns with angles ranging from 40 degrees to 80 degrees. The mandrel is driven by a cheap AC motor with a relatively constant speed. The translational motion of the carriage with delivery eye is provided by a stepper motor, which is more sophisticated in terms of control. All of the mentioned systems have only two controllable axes that apply known limitations on a variety of wound parts.

An example of modernization of a two-axis winder by adding two more controllable axes is systematically detailed in [17]. In fact, one axis is adjusted manually (the distance between delivery eye and mandrill) and the other axes are driven by three DC motors with the same number of controllers. An efficacious low-cost solution is presented in [18], wherein a three-axis filament winder is equipped with one AC motor for the mandrel rotation and two AC servo-motors for the translation of the carriage. Servo-motors are controlled by the LabView software. A three-axis portable FWM was developed with an extensive use of the standard accessories for fabrication of hobby and laboratory machines, such as OpenBuilds V-Slot aluminum profile and other parts (bearings, fixtures, pulleys, belts, etc.) [19]. All the three axes of the winder are driven by stepper motors and controlled by the microcontroller Arduino Uno and drive the expansion board computer numeric control (CNC) Shield. Universal G-Code Sender software is used to send commands from the computer to the winder in [20]. More recently, winders were equipped with mobile software for wireless control [21]. The winding performance was assessed as satisfactory in accordance with the criteria of the angle deviations and accuracy of the distance between two adjacent helical roving positions in [22]. In addition, tubular structures have been manufactured with the use of commercial software for generation of winding trajectory [23]. Notwithstanding the low-cost design philosophy deemed critical in the aforementioned projects, the validation of the final product has been demonstrated for the structural components with a non-sophisticated shape, such as tubes.

A methodical description of a three-axis filament winder with an original technical solution for the third degree of freedom (DOF) is given in the references [24,25]. Fibers are consolidated by a twisting of the tow to form a bar of a circular cross-section. The twisting can be performed by a rotation of the delivery carriage. Nevertheless, the developed equipment only allows for the manufacturing of wrapped tow reinforced trusses. A meticulous description of small-scale equipment with four DOF that combines the filament winding with automated fiber placement is provided in reference [26]. A noteworthy advantage of the contemporary technology is the likelihood of manufacturing components with concave surfaces. However, the validation was fulfilled only with numerical simulations and not by manufacturing the test specimen, the former being less complex and arduous than the latter.

At present, there exist several commercial programs for generating the filament winding trajectories that use the mandrel's shape as the initial data [27]. As stated in [28], a more intricate approach for path generation is currently under investigation to enhance the quality of the final product. The approach considers the alteration in the mandrel's shape due to an uneven thickness distribution of the ply from previous winding. Acquisition of the commercial software for path generation increases the final cost of the technology, and the latter approach requires the application of expensive equipment.

Another way to make the technology more cost-effective is the development of analytical solutions to determine the winding trajectories performed by components of the FWM [29]. Depending on the shape of the mandrel, the fibers are laid along geodesic or non-geodesic trajectories. In accordance with reference [30], which contains analytical solutions for the winding paths of the parameterized shells of revolution, geodesic trajectories provide the most stable and economical technique for filament-wound structures.

An efficacious, viable solution for the smooth winding motion is delineated in [29]. However, it is applicable only for two-axis FWMs. An analytical solution for four- and five-axis machines is described in the form of the coordinates for the feed-eye trajectory and the mandrel rotation [5,31]. Nevertheless, the solution in reference [5] only provides satisfactory results for the spherical dome when the distance from the delivery eye to the surface of the mandrel is zero. A generic kinematic model of the machine movements to create a particular filament-wound product, on a particular machine configuration, is discussed in reference [32]. The mathematical approach adopted for the derivation of the executive expressions in [31,32] demands tremendous effort or skill from an FWM operator.

The primary objective of this work was to design low-cost computer-controlled equipment for the filament winding of small-size axisymmetric aerospace structures, such as tubes, casings, and pressure vessels. The secondary objective of the work was to obtain simple and comprehensive analytical equations for the delivery eye trajectory by referring only to analytic geometry. The derived equations were used for the winding of a cylindrical casing with hemispherical domes, whose polar openings are of the same diameter.

The validation of the suggested low-cost winding technology was conducted by manufacturing small-scale composite casings to evaluate the thickness and fiber volume ratio of helical plies. The dimensions of the designed casing are close to the size of the test motor of a hybrid propellant decelerator [33].

2. Materials and Methods

2.1. Constituents of the Composite Material

Carbon fiber, being the most difficult fiber to manage [1], has been used in this study in the filament-winding process to appraise the capability of the proposed system under demanding situations. Continuous carbon fiber tows based on polyacrylonitrile Teijin Carbon HTS45 E23 12K (Table 1) and epoxy resins of different grades produced by Huntsman (Table 2) were used for manufacturing the casing on the developed winding machine.

Table 1. Properties of the carbon fiber tow [1].

Parameter	Minimal	Nominal	Maximal
ρ_f, tex	720	800	880
ρ, g/cm^3	1.77	1.80	1.83
F_{1f}, MPa	4050	4500	4950
E_{1f}, GPa	228	240	252

[1] as affirmed by local supplier Texiglass.

Table 2. Cure schedules for three types of resin-impregnated tows.

Designation	Resin Composition	Initial Viscosity at 25 °C [1], mPa·s	Cure Schedule
LY1564	Araldite LY1564/XB3473	1000–1200	30 min at 130 °C + 12 h at 160 °C
LY5052	Araldite LY5052/Aradur TM5052	600–700 (to 1500 after 56–60 min)	24 h at 25 °C + 15 h at 60 °C

[1] manufacturer's data.

The fiber volume ratio was determined using an optical technique based on an image analysis of micrographs of transverse cross sections of the coupons. The fiber volume ratio was calculated as a ratio of the area of the fiber cross sections to the total area within the frame of the micrograph. The thresholding tool of the open-source software ImageJ 1.53e was used to determine the area of fiber cross sections on the 8-bit micrograph with a magnification of 400×.

2.2. Calculation of the Winding Parameters

The winding parameters for the casing with hemispherical domes were calculated in accordance with the methodology and the recommendations delineated in [34,35]. The geodesic trajectory is feasible for the cylindrical pressure vessel with hemispherical domes of the radius R_c and polar openings of the equal radius r_p (Figure 1).

The winding angle for the cylinder β_c was calculated by equation:

$$\beta_c = \arcsin \frac{r_p}{R_c} \tag{1}$$

Along the length of the cylinder L_c, the mandrel has to rotate with a turn-around angle Φ_c computed as follows:

$$\Phi_c = \frac{L_c \tan \beta_c}{R_c} \tag{2}$$

The winding angle at any point on the surface of the hemispherical dome β_s can be defined as a function of the z-coordinate as:

$$\beta_s(z) = \arcsin \sqrt{\frac{R_c^2 - z_p^2}{R_c^2 - z^2}} \tag{3}$$

In addition, the turn-around angle on the hemispherical dome Φ_s can be defined as a function of the z-coordinate as well:

$$\Phi_s(z) = \int_0^z \frac{1}{R_c^2 - z^2} \sqrt{\frac{R_c^2 - z_p^2}{z_p^2 - z^2}} dz \tag{4}$$
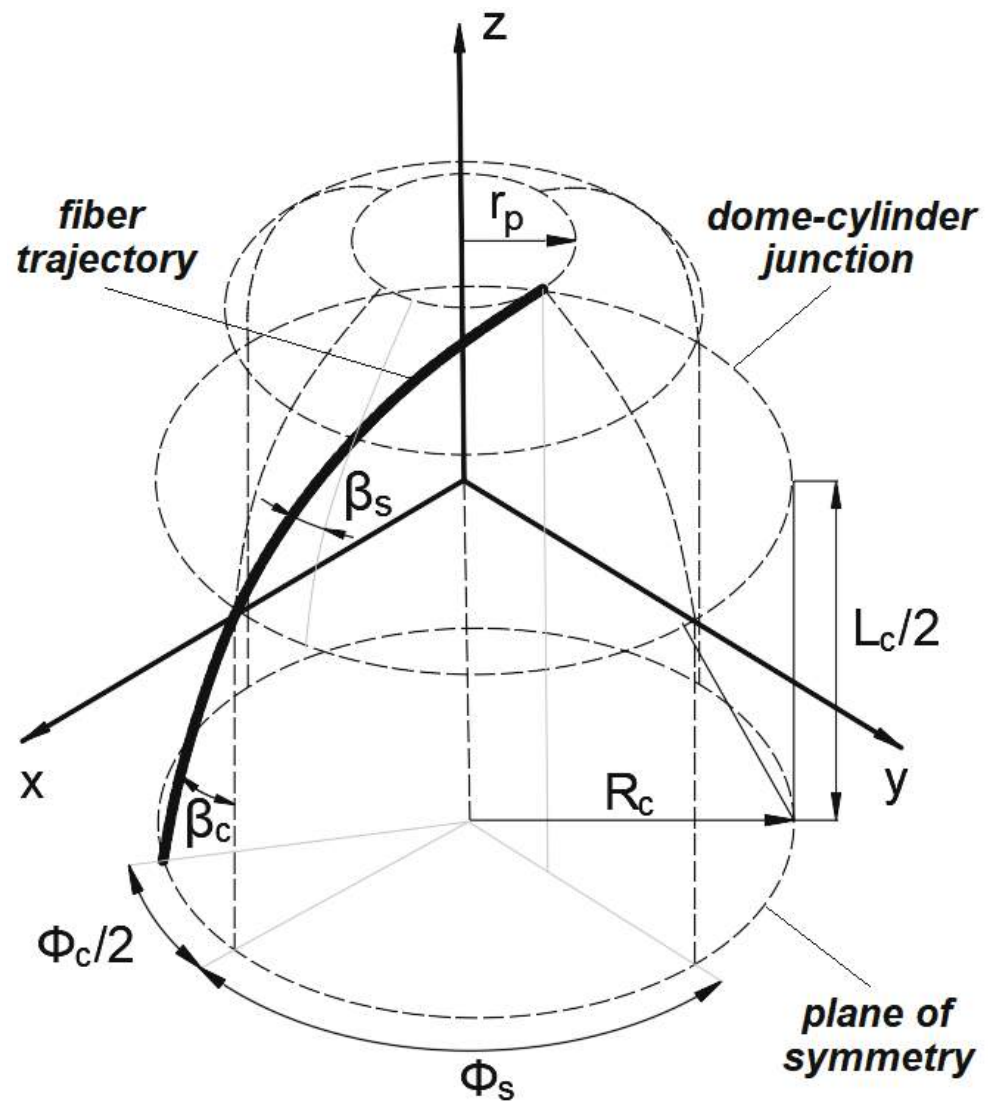
Figure 1. The definition of the winding parameters for a geodesic trajectory.

To lay the fiber along one side of the hemispherical surface, the mandrel ought to rotate by a turn-around angle equal to Φ_s, given as:

$$\Phi_s = \int_0^{z_p} \frac{1}{R_c^2 - z^2} \sqrt{\frac{R_c^2 - z_p^2}{z_p^2 - z^2}} \, dz = \frac{\pi}{2} \tag{5}$$

The turn-around angle for one winding cycle Φ_1 can be computed as:

$$\Phi_1 = 2\Phi_c + 4\Phi_s \tag{6}$$

The fiber crosses any latitude of the mandrel twice every winding cycle. For the obtained value Φ_1 not a multiple of 2π (360°), the tow after one winding cycle returns to the same latitude from which it started its trajectory but does not coincide with the starting point. The angular pitch of winding Φ_p^* is defined as an angle measured in the direction of the mandrel rotation between the starting and final points of one winding cycle and can be described mathematically as:

$$\Phi_p^* = \Phi_1 - 2\pi \cdot integer\left(\frac{\Phi_1}{2\pi}\right) \tag{7}$$

The angular pitch must be increased to the closest angle, which is a multiple of 360°

$$\Phi_p = \begin{cases} 60°, \, 72°, \, 90°, \, 120°, \, 180° \ when \ 60° \le \Phi_p^* < 180° \\ 240°, \, 270°, \, 288°, \, 300°, \, 360° \ when \ \Phi_p^* > 180° \end{cases}$$

The difference between the accepted and calculated angular pitch, Φ_f, distributed uniformly between two flanges of the mandrel, can be given as:

$$\Phi_f = \frac{\Phi_p - \Phi_p^*}{2} \tag{8}$$

At an angular pitch of less than or equal to 180°, the tow returns to the same starting point after $2\pi/\Phi_p$ winding cycles. Thus, to cover the entire surface of the mandrel with fibers, the mandrel must rotate every $2\pi/\Phi_p$ winding cycles by an angle corresponding to the width of the tow given as follows:

$$\Phi_w = \frac{b}{R_c \cos \beta_c} \tag{9}$$

2.3. Validation of the Analytical Solutions for the Winding Trajectory

The efficiency of the analytical solution for the kinematic motion of the FWM was ascertained by laying the synthetic strip along the geodesic path marked on the surface of a cylindrical mandrel with hemispherical domes. The mandrel with continuous grooves along geodesic path is printed with polylactide filament (Figure 2). The coordinates of the geodesic path were calculated by equations from the previous subsection. The G-code for controlling the four axes of the FWM was compiled manually after the discretization of the derived analytical solutions.

Figure 2. The mandrel with imprinted geodesic path.

2.4. Manufacturing and Characterization of the Casing

The casing is wound over two types of mandrel with the same geometry (R_c = 60 mm, r_p = 21 mm, and L_c = 160 mm). The mandrel for the cold-curing epoxy composition LY5052 is made from polyethylene terephthalate glycolmodified (PETG) filament by 3D printing. Water-soluble mandrel from sand/polyvinyl alcohol composition [35] was used for the heat-curing epoxy resin LY1564. The sand components of the mandrel (Figure 3) were molded together with aluminum bushings in low-cost silicon molds. After solidification in an electric oven, these were mounted on a threaded shaft (Figure 4) with other components of the mandrel, namely heat insulators and flanges. The sand mandrel was washed out with hot water after manufacturing and curing the casing.

Figure 3. Solidified sand components kit for manufacturing a soluble mandrel.
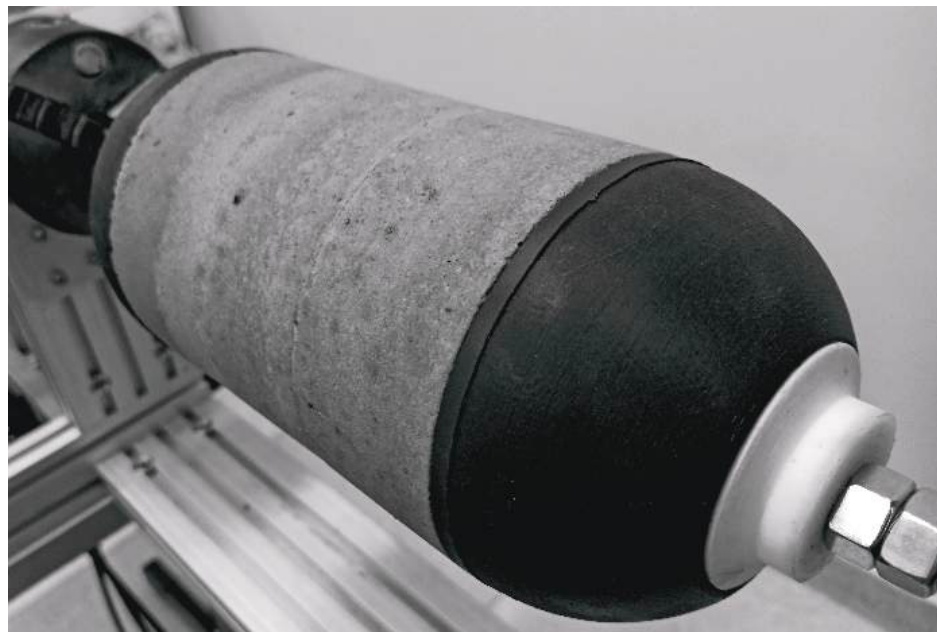
Figure 4. The sand mandrel assembled on a threaded shaft with flanges and heat insulators.

The average velocity of the winding was 65 mm/s and the winding pitch was 4 mm.

The thickness distribution for the spherical dome of the casing was evaluated by a so-called flat solution, suitable for a reliable and adequate approximation of real thickness distribution [1]. The thickness at the portion of the dome adjacent to the polar openings t_{do} is constant and can be defined as:

$$t_{do} = \frac{R_c t_c \cos\beta_s}{\sqrt{b\cos\left(\beta_c + \frac{b}{R_c}\right)\left[2r_p + b\cos\left(\beta_c + \frac{b}{R_c}\right)\right]}} \tag{10}$$

For the rest of the dome, the thickness t_d is a function of the z-coordinate:

$$t_d(z) \ = \frac{R_c r_p \cos\beta_s}{\sqrt{R_c^2 - r_p^2 - z^2}} \tag{11}$$

The predicted thicknesses were compared with the real ones measured on segments milled from the spherical dome of the wound casings. The measurements of the thickness were performed using a Mitutoyo digital caliper (resolution 0.01 mm) with thin jaws to avoid a distortion of the measured value due to the curvatures of the segments.

3. Results and Discussion

3.1. Design of the Filament Winder

3.1.1. Design Concept

The vast variety of equipment and techniques applied to the filament-winding process necessitates a comprehensive analysis of the technology to justify the design configuration [36]. The common filament-wound structures used in aerospace programs are tanks, pressure vessels, motor casings, struts, and booms [37]. Thus, the selected design concept must be adapted to design the shells of revolution, preferably with a high length-to-diameter ratio and appropriate for laboratory applications or a single-unit production.

In a previously conducted study [38], all filament winders were divided into two groups, namely conventional and robotic, based on the type of the equipment. The former has a minimum required DOF, i.e., it is optimized for specific applications [36]. The application of an industrial robot is the typical characteristic of a robotic filament winding complex [39]. Technical and economical comparisons of the filament winders depend on a multitude of factors, with the most prominent being the size of the product being manufactured, configuration of the equipment, and the level of automation. In general, conventional FWM can accommodate mandrels with a high length-to-diameter ratio and robotic FWM are more adapted for small components with complex shapes [38]. However, the working envelope of robotic systems can be extended using additional linear axis. Despite the high market demand and competitiveness, which are among the principal merits of the conventional technology, the substitution of the rigid automation of the conventional winders with flexible automation typical for the robotic cells discernibly enhances the product value and market prospects [40,41]. However, robotic systems may require skilled personnel and increased maintenance costs. Apparently, the conventional equipment is more rational for the custom-made production of the components with a relatively simple axisymmetric shape and high length-to-diameter ratio.

Notwithstanding the heterogeneity in the layouts of the conventional filament winding equipment mentioned in the references [42,43], there are three archetypal basic configurations [44]: a lathe-type (helical) winder, a racetrack (in-plane or polar) winder, and a tumble winder. The racetrack (polar or in-plane) winders are effective for winding angles close to zero, but the length-to-diameter ratios of the wound parts are delimited to 1.8–2.0 to obviate the fiber slippage [43]. The tumble winder is efficient for the low-cost and high-speed manufacturing of spherical or "Dutch cheese"-shaped shells of revolution, but is not appropriate for winding hoop layers on cylindrical surfaces [45]. The configuration of a tumble winder suggested in reference [39] is capable of manufacturing long structures,

but imposes demanding requirements on the rigidity of the mandrel holding structure. The lathe-type winders are the most prevalent and conventional machines with some limitations in the range of extremely small winding angles. Other disadvantages of the lathe-type machines include high delivery eye translations and accelerations in comparison with the racetrack or tumble winders. However, none of these drawbacks preclude the extensive use of the lathe-type configuration for manufacturing the axisymmetric aerospace structures mentioned above. Another cogent reason that renders a conventional lathe-type machine more appropriate for the applications presented here is the correlation of its cost with the number of DOF [36]. The sufficient number of DOF for the filament winder is determined by a number of independent parameters that describe the relative orientation between delivery eye and mandrel [39]. The greater the number of DOF the winder has, the more intricate the wound part and the control system are anticipated to be [46]. By the adoption of the conventional methods of linear algebra, it was shown that FWM must have at least six DOF [39]. However, for tow-winding, the sufficient number of DOF is four, as the twisting of the tow is of less importance. For the axisymmetric mandrel, some of the independent parameters might be constant. For instance, the distance between the surface of the mandrel and delivery tool might be constant for the helical tow-winding around the cylindrical mandrel. Thus, the number of sufficient DOF decreases to two. Components that are more complex than a cylinder can be wound with only two DOF [29]. It is worth noting that a low number of DOF requires a more elaborate calculation of the delivery eye trajectory and speed [31]. An additional DOF eliminates unrealistic translations in the winder components [32]. Consequently, the configuration with four DOF was selected for the filament winder under consideration.

From the three impregnation methods described in [47], only wet/dry winding has a widespread application for aerospace components. For occasional non-batch applications, the wet winding method is more advantageous when compared with the dry method for the following reasons [47,48]: (1) enhanced variety of fiber/resin combinations; (2) lower probability of fiber damage; (3) longer shelf life for resins, while prepregs must be stored in a freezer for a limited period; (4) room temperature cure; and (5) lower cost. Moreover, the wet winding equipment can be easily readjusted for prepreg winding.

The latter is considered available and straightforward from two roving impregnation systems, a dip-type and a drum-type bath system [49]. Notwithstanding the poor control over the fiber volume ratio that leads to an excess of resin, the drum-type bath systems have a wide application in industry. A doctor blade device may adjust the required resin-film thickness on the drum, restricting the amount of resin that can enter the polymer composite. Thus, the proposed low-cost technology for the irregular or laboratory production of the polymer composite shells of revolution with a high length-to-diameter ratio is based on a lathe-type filament winder with four DOF and a proper bath-type resin impregnation system. This low-cost concept is predicated on the extensive use of standard aluminum and steel profiles for the structural frames, off-the-shelf mechanical and electronic components, 3D-printed parts, obsolete personal computer and cheap software for the control system, and manual generation of the control codes supported by analytical equations. In addition, there are no complex adaptive tensioning systems. The pretension is provided by a simple tensioning mechanism, such as rotating scissor bars with manual adjustment [50]. The variation in fiber tension can be minimized by the appropriate feed-eye trajectory [31].

3.1.2. Description of the Filament Winder

The system for the filament winding comprises the main units formed by the winder, the stationary creel, and the operator's workplace (Figure 5). The stationary creel is a carbon steel shelf that holds a maximum of four fiber packages on a cardboard tube. The operator's workplace is a desk equipped with a monitor, a keyboard, and a mouse. The winder was installed on a carbon steel stand holding cabinets for the control system, protected from resin leakage by a silicone layer.
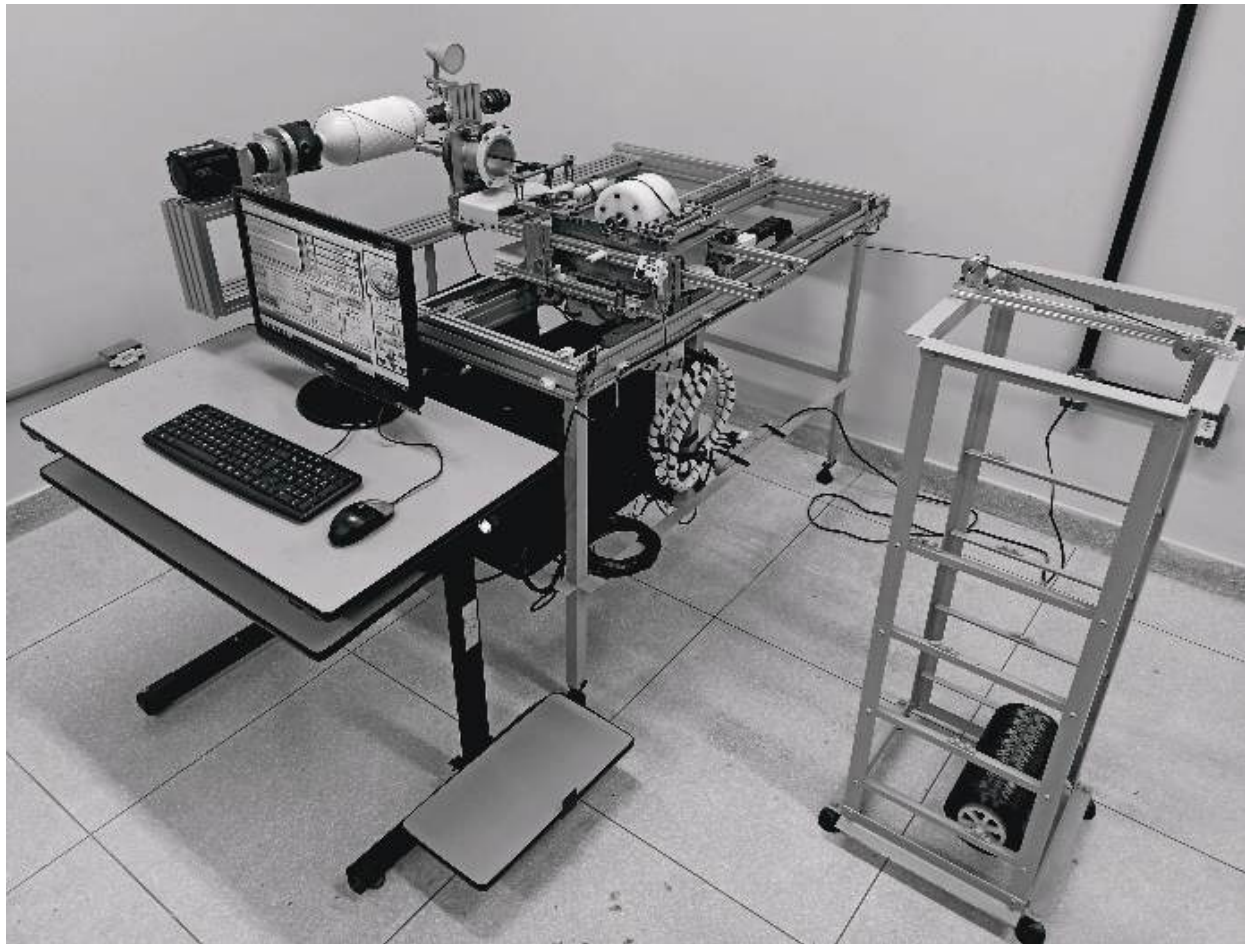
Figure 5. The devised low-cost filament winding system.

There are four fully controlled axes in the filament winder (Figure 6): X is the rotation of the mandrel, Y is the linear translation of the carriage along the mandrel's axis, Z is the linear translation of the delivery eye across the mandrel's axis and A is the eye-rotation axis. A stepper motor with a frame size established by the National Electrical Manufacturers Association (NEMA) is the primary source of torque for all controllable axes. The torque from the stepper motors to the executive mechanisms is transferred through the timing belt drive (axes Y, Z, and A).

The planetary drives with reductions of 1:10 and 1:5 are installed between the stepper motor and the timing belt of axes X and Y, respectively.

The winder consists of two primary assembly units: a frame and a carriage. The frame is made from a V-slot aluminum profile and holds the stepper motors of axes X and Y (Figure 7). The tailstock is equipped with both a rotating center and drill chuck to provide a variety of clamping methods. A pair of linear guides with slide blocks for installation of the carriage is also included.
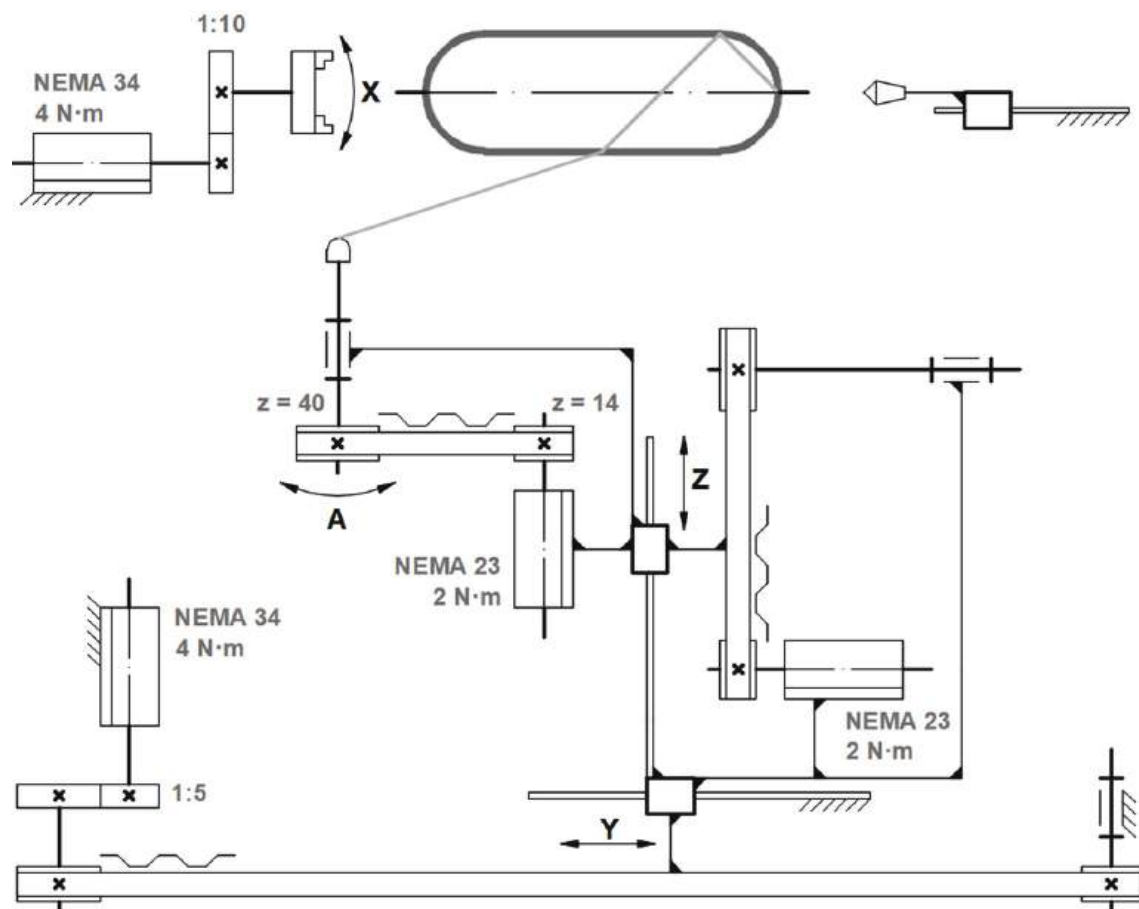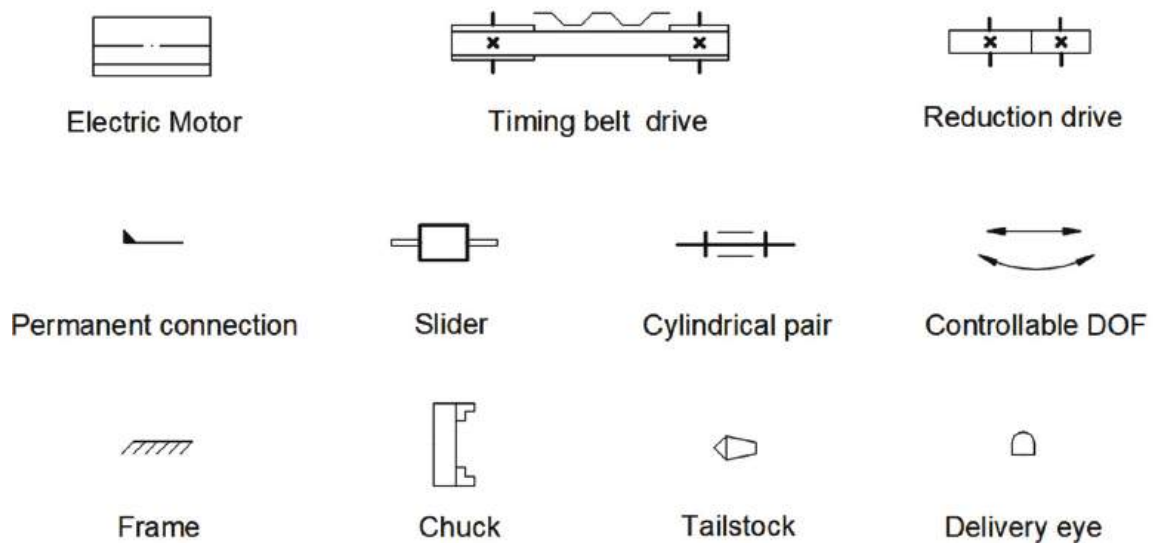
Figure 6. Kinematic diagram of the winder: N·m—unit for torque; NEMA—motor frame size; 1:5 and 1:10—reduction ratios; z—number of teeth.
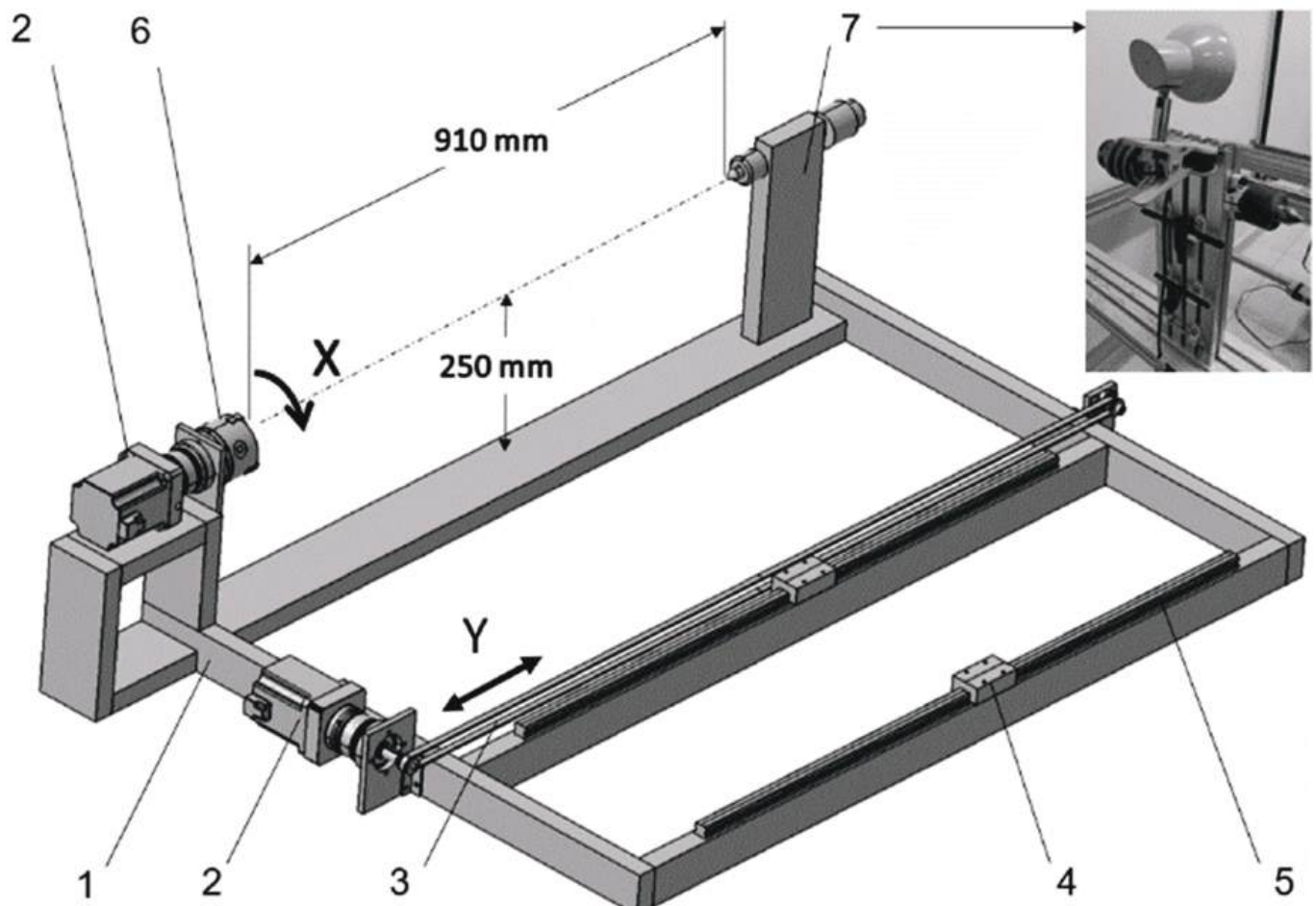
Figure 7. Assembly components of the filament winder frame (sensors are not shown): 1—aluminum V-slot profile; 2—stepper motor with planetary reduction drive; 3—timing belt; 4—slider block; 5—linear guide rail; 6—lathe chuck; 7—tailstock with tool set.

The carriage encompasses three subassemblies (Figure 8): the carriage frame, the impregnator, and the delivery head. The carriage frame is made from a V-slot aluminum profile (Figure 8a). Two braces are installed in a gantry plate between the mini wheels. The timing belt, whose ends are fixed to the extremities of the braces, provides linear translation Z of the braces. The middle portion of the belt is pulled over the GT2 timing pulley, which is driven directly by the stepper motor. The impregnator (Figure 8b) is installed between the carriage braces and consists of a heated resin bath with an impregnation drum, rotating scissor bars with manual adjustment, a couple of guides, and a tension compensator with a torsion spring. The tension compensator works similarly to a rotating scissor bar and the distance between the bars can also be adjusted. The hollowed drum is made from high density polyethylene to facilitate rotation. The guides are made from stainless steel or polyoxymethylene (POM). The delivery head (Figure 8c) is responsible for the fourth controllable DOF and consists of an aluminum tube supported by a set of mini wheels. The tube holds the delivery eye with a couple of rollers made from POM.
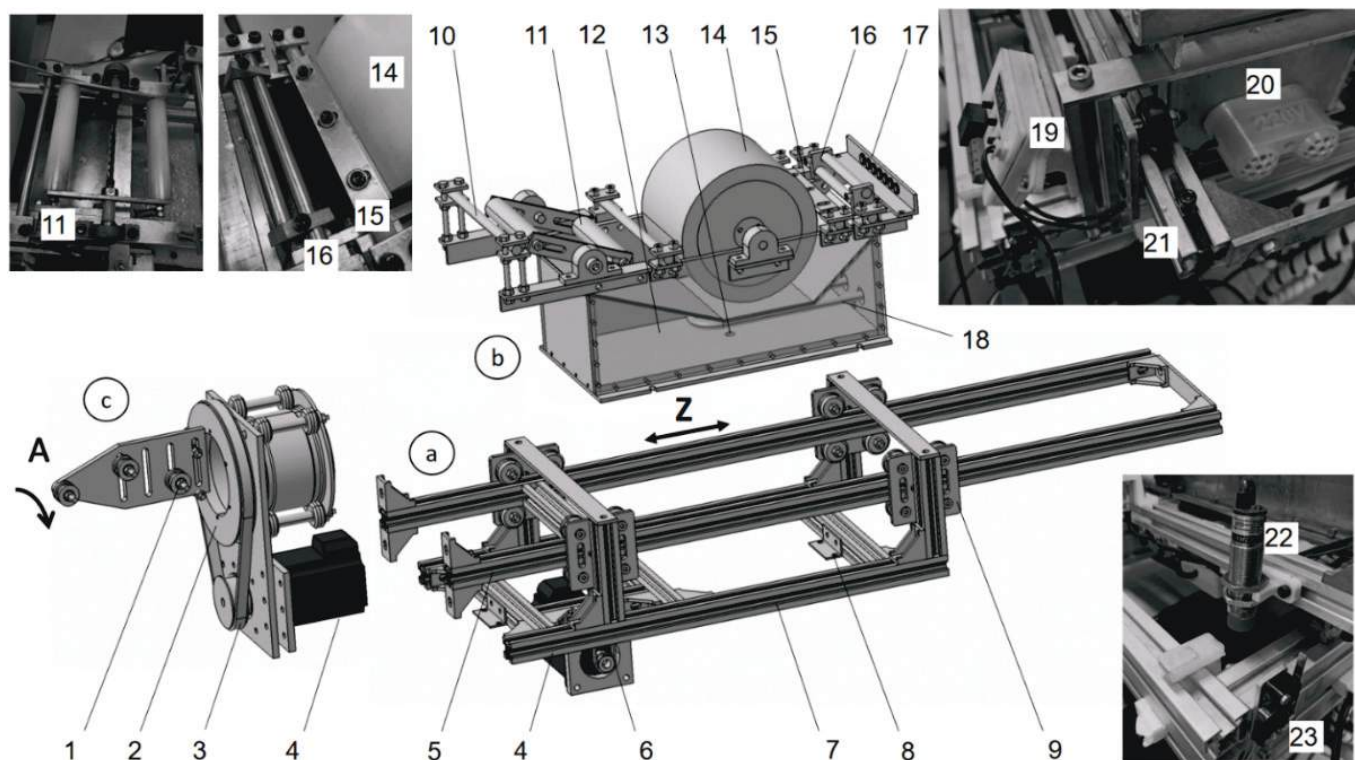
Figure 8. Assembly components of the carriage: (**a**) frame, (**b**) impregnator and (**c**) delivery head; 1—roller; 2—hollow pulley; 3—closed timing belt; 4—stepper motor; 5—brace; 6—timing belt; 7—frame; 8—bracket; 9—gantry plate with mini wheels; 10—static bar; 11—tension compensator; 12—water basin; 13—drain; 14—impregnation drum; 15—doctor blade; 16—rotating scissor bars; 17—guide; 18—heating element; 19—thermostat; 20—terminal for the heating element; 21—fixture of the timing belt at the end of the brace; 22—proximity sensor Z; 23—limit switch Y.

3.1.3. Control System

The control system of the filament winder is based on commercial software ArtSoft Mach3, a widely used solution for custom-made CNC machines [51]. The Mach3 software, in combination with a breakout board, virtually transforms a PC into a CNC machine controller.

The breakout board was incorporated to translate signals from the PC to the winder's components (drivers, switches, and sensors) and vice versa (Figure 9). The low-cost isolating breakout board "Mach3 Interface Board," adopted for the control system, also functions as circuit protection. The requirement of an auxiliary 12–24 V power supply for the switch control can be confirmed as the primary disadvantage of the board.

A low-performance PC (1 GHz processor) with an obsolete version of Microsoft Windows (2000, XP, Vista) can be employed for a direct connection from the PC's motherboard to the "Mach3 Interface Board" through a parallel port [52]. This approach considerably reduces the cost of the control system. The stepper motors with encoders are used to enhance the accuracy of tow deposition. Contact-limit switches are used to prevent the Y and Z linear axes from causing damage to the structure of the winder. The winder is equipped with relocatable proximity sensors, whose primary function is to establish a home position or a reference position (origin of the Y and Z coordinates). The heating control of the impregnation bath is separated from the control system. It is equipped with a simple thermostat that maintains a predetermined temperature of the resin in the impregnation bath.
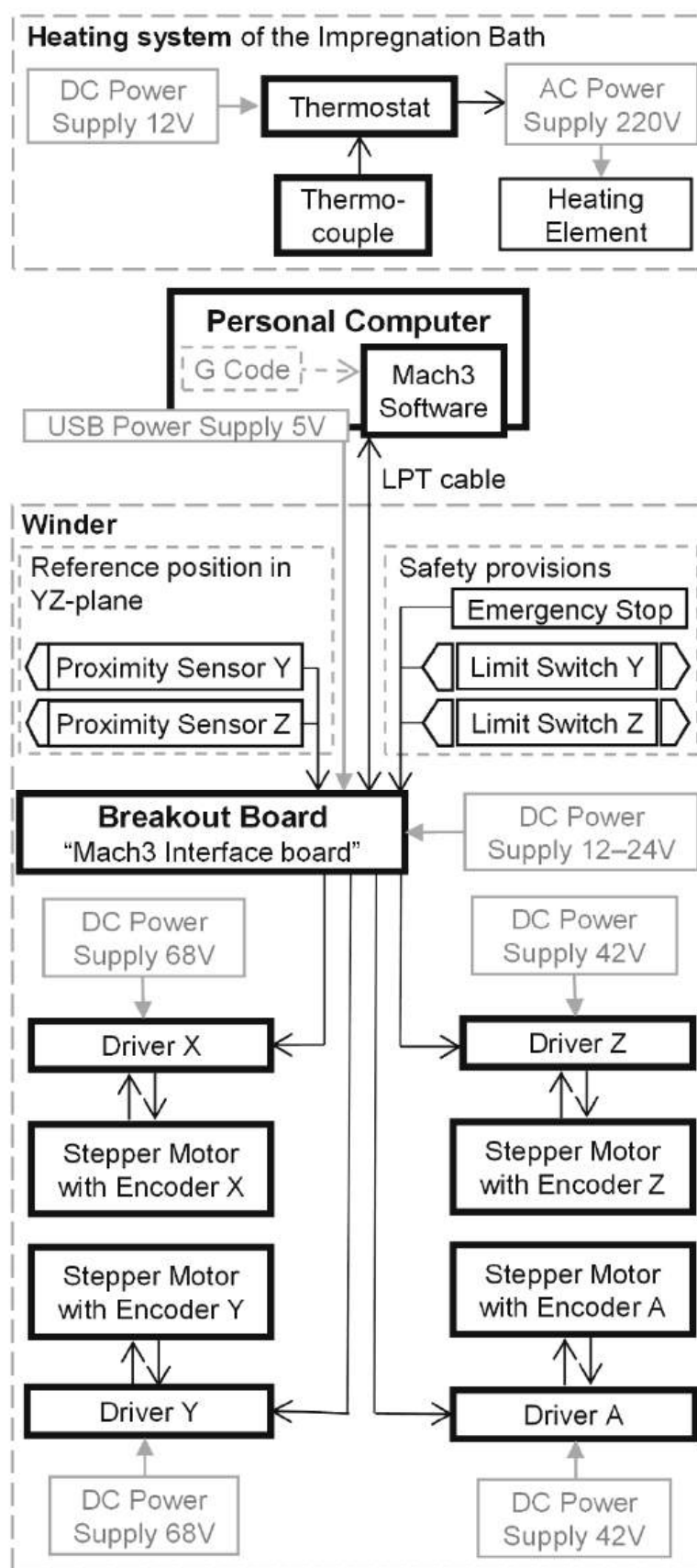
Figure 9. Control system diagram.

3.2. Trajectory of the Delivery Eye

To place the tow along the geodesic path when the distance between the delivery eye and the mandrel surface is not zero, equations for the coordinates of the delivery-eye trajectory are indispensable.

The tow runs over a large circle of the sphere [34], thus the trajectory of the tow is a circle that lies in a plane. The coordinate system of the plane $\overline{xyz}$ is formed by an elemental rotation of the mandrel's coordinate system xyz about axis x by an angle β_c (Figure 10a). For simplicity, it is considered that the trajectory of the delivery eye is also a circle (Figure 10b), and therefore, the distance λ between the delivery eye E and the mandrel surface M is constant.
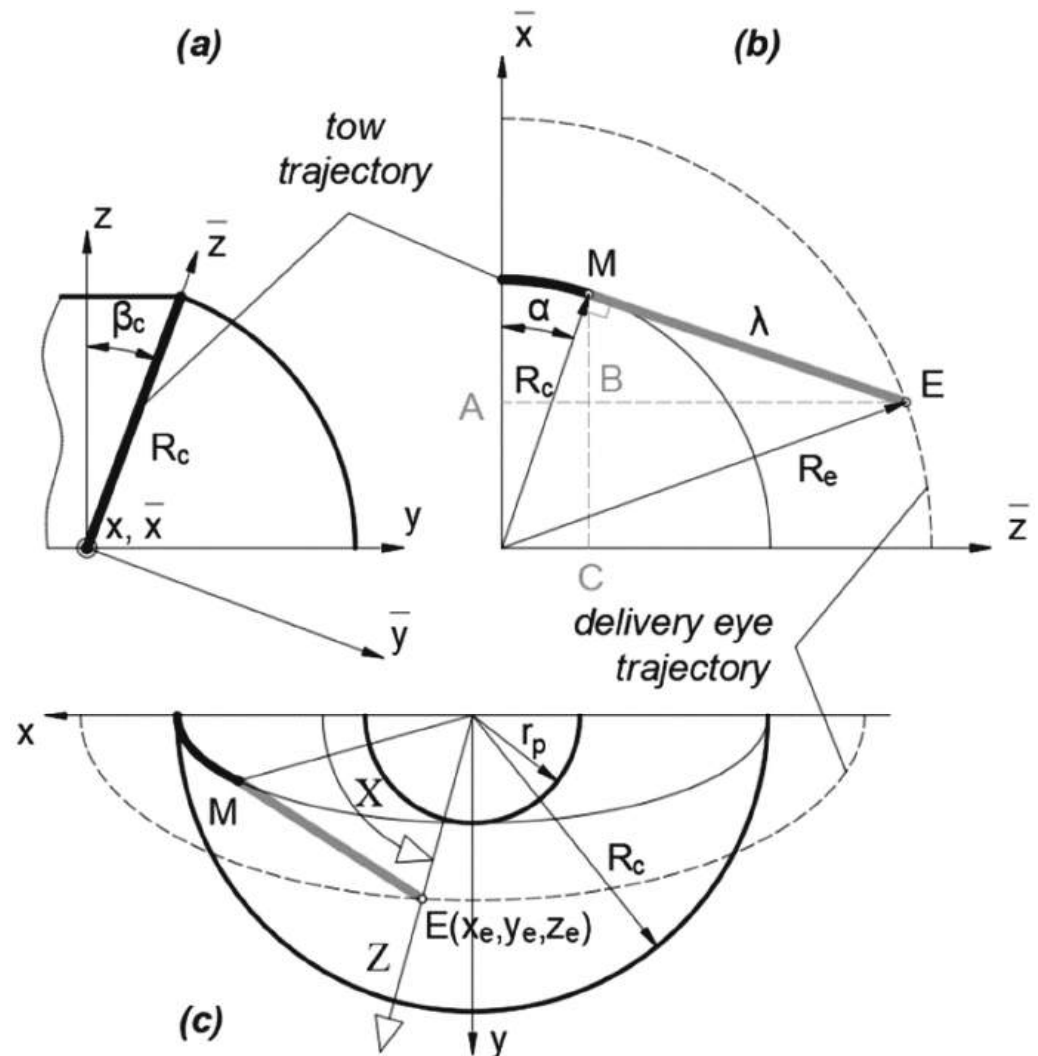
Figure 10. Delivery eye trajectory for the spherical dome: (**a**)—yz-plane; (**b**)—$\overline{xz}$-plane; (**c**)—xy-plane.

The closed-line segment EM must be tangential to the surface of the dome. It is calculated through the radius R_e, defined by the operator:

$$\lambda = \sqrt{R_e^2 - R_c^2}. \tag{12}$$

The coordinates of the delivery eye in the coordinate system $\overline{xyz}$ are defined through the variable angle α depicted in Figure 10b:

$$
\begin{aligned}
\overline{x}_e &= MC - MB = R_c \cos\alpha - \lambda \sin\alpha, \\
\overline{y}_e &= 0, \\
\overline{z}_e &= AB - BE = R_c \sin\alpha - \lambda \cos\alpha.
\end{aligned}
\tag{13}
$$

The coordinates of the delivery eye in the mandrel's coordinate system xyz are defined by the following well-known equations of linear algebra:

$$
\begin{aligned}
x_e &= \overline{x}_e, \\
y_e &= \overline{y}_e \cos\beta_c - \overline{z}_e \sin\beta_c, \\
z_e &= \overline{y}_e \sin\beta_c + \overline{z}_e \cos\beta_c.
\end{aligned}
\tag{14}
$$

Substituting Equations (13) into (14) provides

$$
\begin{aligned}
x_e &= R_c \cos\alpha - \lambda \sin\alpha, \\
y_e &= -\frac{r_p}{R_c}(R_c \sin\alpha + \lambda \cos\alpha), \\
z_e &= \frac{\sqrt{R_c{}^2 - r_p{}^2}}{R_c}(R_c \sin\alpha + \lambda \cos\alpha).
\end{aligned}
\tag{15}
$$

The coordinates of the delivery eye are obtained through controllable DOF (i.e., in the coordinate system of the winder), which are determined from Figure 10c in terms of the coordinates in the mandrel's coordinate system xyz.

$$
\begin{aligned}
X &= \tan^{-1}\frac{y_e}{x_e}, \\
Y &= z_e, \\
Z &= \sqrt{x_e{}^2 + y_e{}^2}.
\end{aligned}
\tag{16}
$$

Finally, substituting Equations (15) into (16) provides the formulas for the delivery eye trajectory as a function of α

$$
\begin{aligned}
X &= \tan^{-1}\left[-\frac{r_p(R_c \sin\alpha + \lambda \cos\alpha)}{R_c(R_c \cos\alpha - \lambda \sin\alpha)}\right], \\
Y &= \frac{\sqrt{R_c{}^2 - r_p{}^2}}{R_c}(R_c \sin\alpha + \lambda \cos\alpha), \\
Z &= \left((R_c \cos\alpha - \lambda \sin\alpha)^2 + \left(\frac{r_p}{R_c}\right)^2(R_c \sin\alpha + \lambda \cos\alpha)^2\right)^{1/2}.
\end{aligned}
\tag{17}
$$

An involute screw surface analytically described in a Cartesian coordinate system [53] provided the coordinates of the delivery eye trajectory for the cylindrical part of the mandrel (Figure 11):

$$
\begin{aligned}
x_i &= R_c \cos\theta + \lambda \sin\beta_c \sin\theta, \\
y_i &= R_c \sin\theta - \lambda \sin\beta_c \cos\theta, \\
z_i &= R_c \theta \cot\beta_c - \lambda \cos\beta_c.
\end{aligned}
\tag{18}
$$

Here, angle θ is a function of the axial coordinate z:

$$
\theta = \frac{z \tan\beta_c}{R_c}.
\tag{19}
$$

The delivery eye trajectory is given through controllable DOF of the winder as follows:

$$
\begin{aligned}
X &= \frac{z \tan\beta_c}{R_c}, \\
Y &= z, \\
Z &= \left((R_c \cos\theta + \lambda \sin\beta_c \sin\theta)^2 + (R_c \sin\theta - \lambda \sin\beta_c \cos\theta)^2\right)^{1/2}
\end{aligned}
\tag{20}
$$
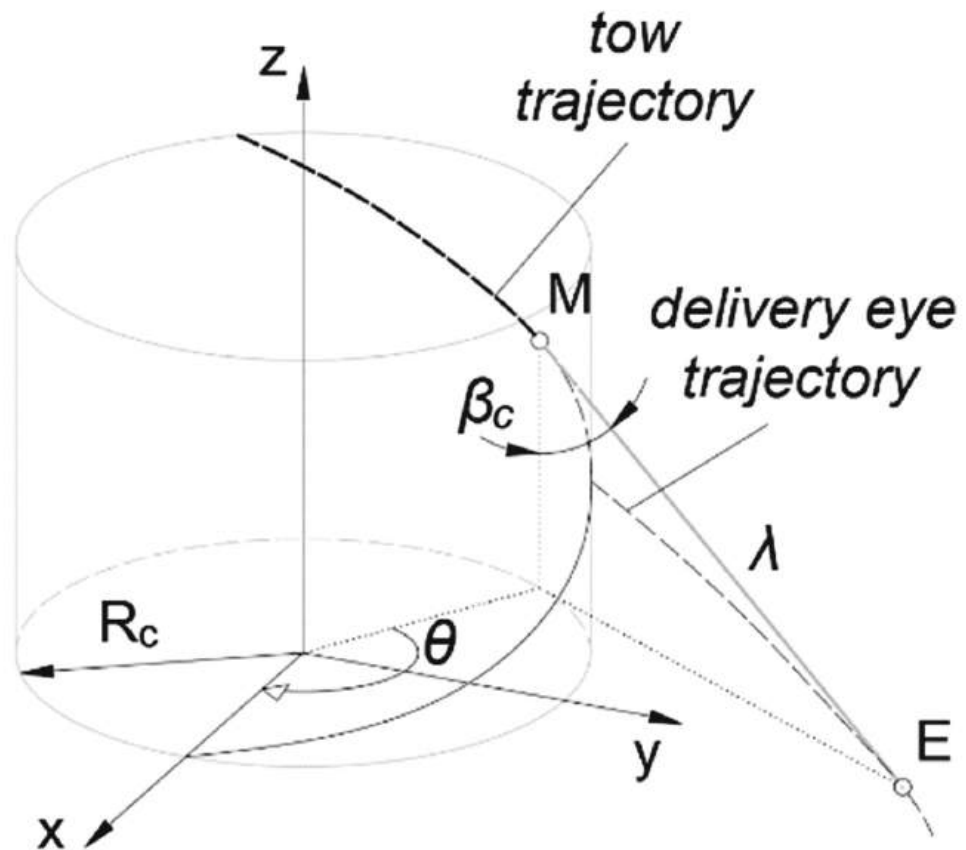
Figure 11. Delivery eye trajectory for the cylinder.

The angle of the eye rotation axis A depends on the winding angle, such that the axis of the roller must be perpendicular to the direction of the tow:

$$A = \frac{\pi}{2} - \beta \tag{21}$$

Here, β is calculated by Equation (3) for the hemispherical dome and by Equation (1) for the cylinder.

3.3. Validation of the Analytical Solution for the Winding Trajectory of the FWM

The length of the cylindrical part of the mandrel L_c = 84.1 mm is chosen in such a manner that the imprinted grooves are continuous along the geodesic path (see Figure 2) and form a closed loop.

The winding parameters (Table 3 and Figure 12) yield the same pattern on the surface of the mandrel for both the tow and the grooves. The trajectories of the delivery eye and the tow calculated for the constant distance λ = 67 mm by Equations (17) and (20) are illustrated in Figure 13. The wound pattern obtained by the calculated trajectories (the generated G-code is given in Appendix A) corresponds to the pattern of the imprinted grooves (Figure 14), which, in turn, substantiates the reliability and effectiveness of the suggested equations.

Table 3. The winding parameters for the mandrel with imprinted geodesic path, in degrees.

β_c	Φ_c	Φ_s	Φ_1	Φ_p	Φ_f	Φ_w
20.5	15	90	420	0	0	15
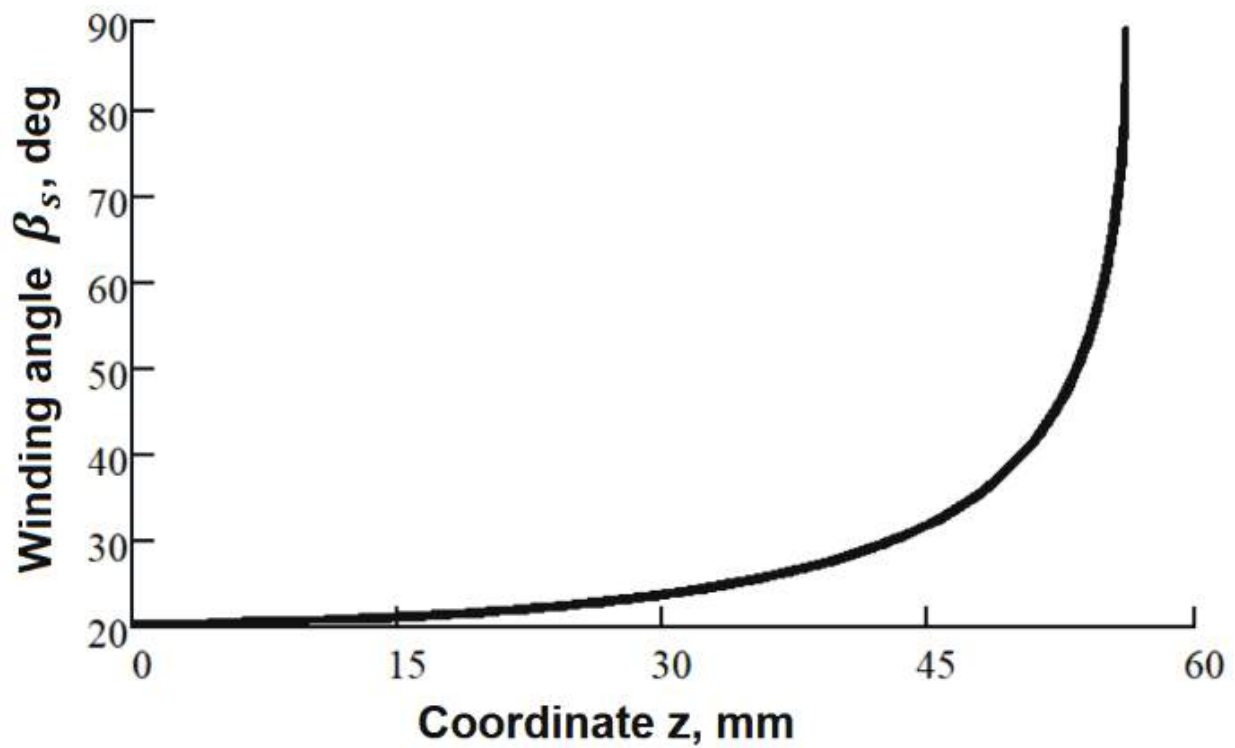
Figure 12. Winding angle on the spherical dome.
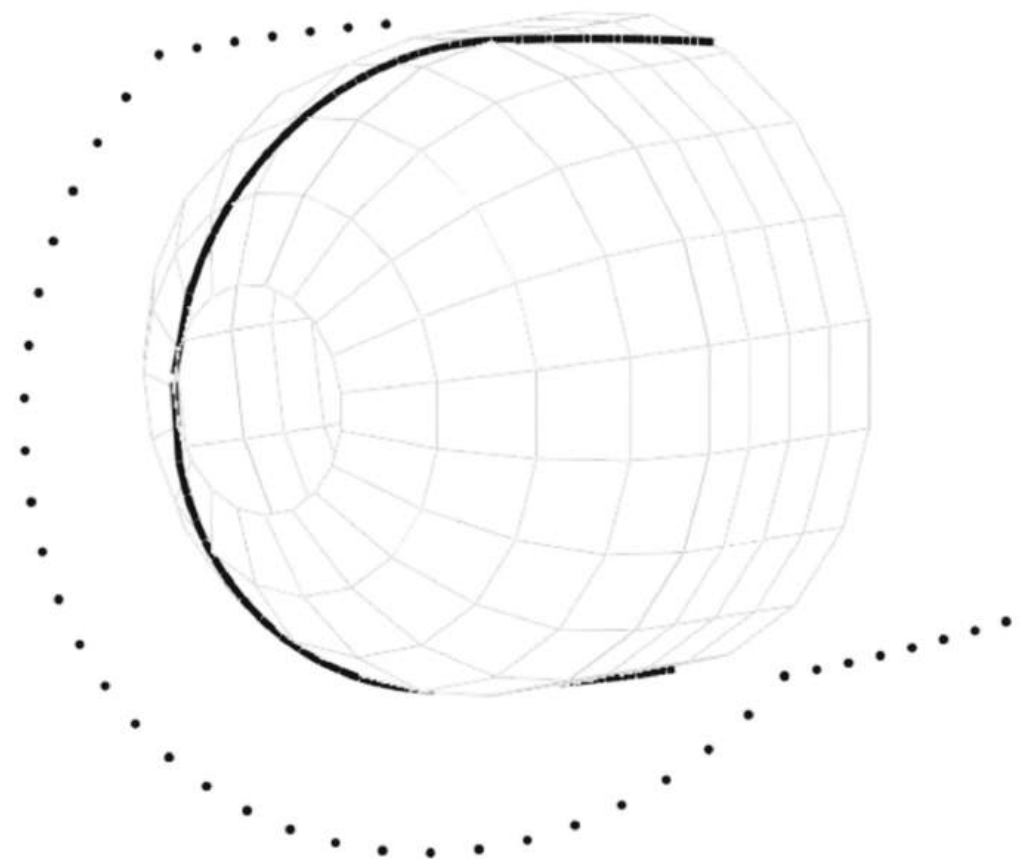
Figure 13. Calculated trajectories of the delivery eye and the tow depicted for half of the mandrel (λ = constant).

Figure 14. Wound pattern on the surface of the mandrel with the imprinted geodesic path.

As the geodesic trajectory has been calculated for a filament with an infinitesimally small width, a strip with a width of 3.5 mm partially covers the surface of the flange. Overlap can be eliminated by decreasing the opening radius in the calculations of the geodesic path or can be regulated with a slight displacement of the initial position of the delivery eye out of the mandrel. However, deviations from the geodesic path are inevitable in the latter case.

3.4. Characterization of the Casings

The winding parameters used for the manufacturing of the casings are the same for all of the double helical plies in the layup (Table 4 and Figure 12). The winding pitch for the 90° ply is 4 mm.

Table 4. The winding parameters for the mandrel with imprinted geodesic path, in degrees.

β_c	Φ_c	Φ_s	Φ_1	Φ_p	Φ_f	Φ_w
20.5	57.1	90	474.2	120	2.91	4.08

Before winding the casings with carbon filament impregnated by two types of the epoxy resin, the calculated trajectory of the delivery eye was already successfully verified for the double angle-ply layer with use of the synthetic strip (Figure 15). The winding of one double angle-ply layer required approximately 16 min at the maximum speed established in the G-code, which is equal to 6000 mm/min for the linear translations (Z and Y axes) and 6000 degrees/min for the rotational motion (X and A axes).
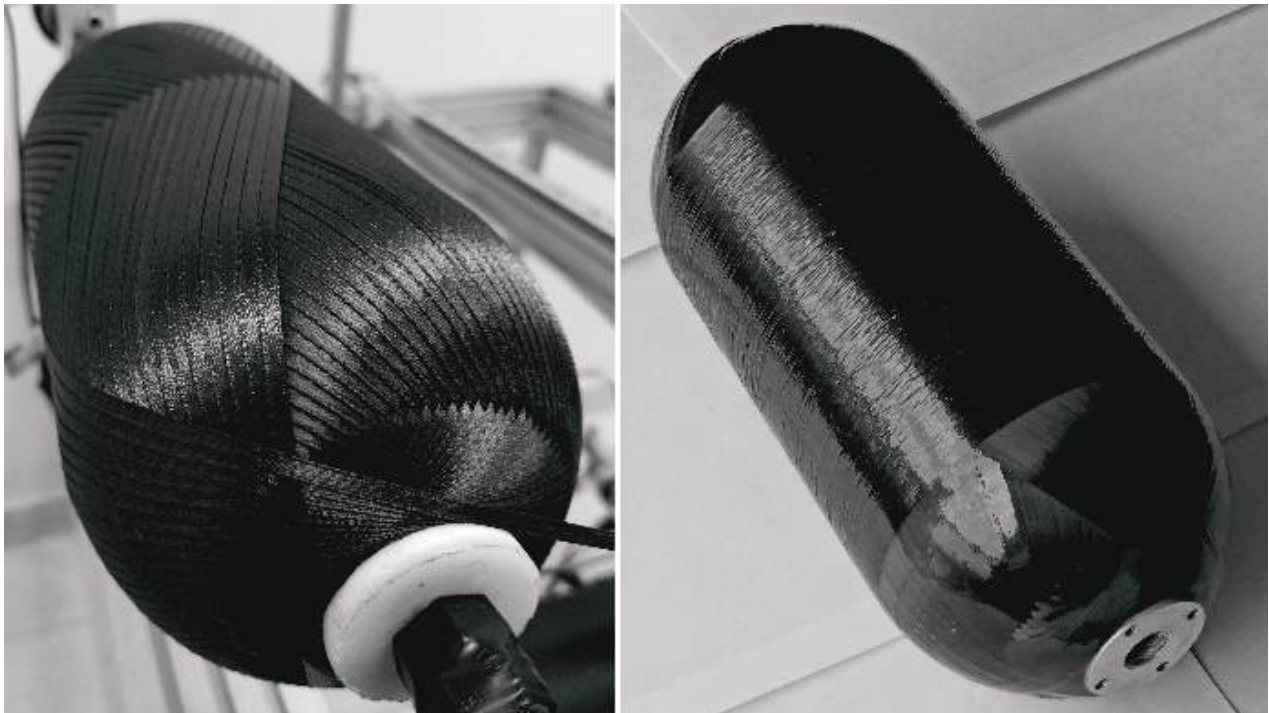
Figure 15. Wound pattern of the double helical layer verified with synthetic strip (**left**) and the carbon/epoxy casing LY5052 [$\pm 20.5_3/90$] after curing (**right**).

The thicknesses measured along the dome wall of the wound casings with different resin compositions and stacking sequences are in good agreement with the distribution predicted by the flat solution, except for the portion near the flange (Figure 16), as a result of the varying compaction performance of the composite material at the dome. Notwithstanding the significant amount of resin drips from the casing surface before the curing is completed, a great volume of resin is trapped inside the layer (Figure 17). At the flange, there is a huge zone covered in resin and there are multiple pores. In the cylindrical part, the trapped resin is between the plies and there are few pores. The most porous casing is made from composition LY1564 (Figure 18). The size and the distribution of voids can be attributed to the absence of an adaptive tensioner of the tow in the developed FWM and excessive resin content inherent to the drum-type bath impregnation system. In the latter case, the voids originate from entrapped air bubbles or from more complex local curing effects described in the literature [54].

The evaluated fiber volume ratio is in the range of 52–55% for the casing LY5052 [$\pm 20.5_3/90$] and in the range of 50–56% for the casing LY1564 [$\pm 20.5_3/90$]. These data are given for the near cylindrical parts of the casing, excluding the layer of the pure resin on the external surface shown in Figure 17.

Although the winder can lay the fiber on the surface of the mandrel straight along the geodesic path (Figure 14), there are compromises to be made in using the low-cost design solutions. For the given setup, the fiber volume ratio decreases by up to 50–52% in the cylindrical casing, depending on the resin type. According to [55], the change in the fiber volume fraction from 50% to 65% improves the strength of the composite by at least 10%.
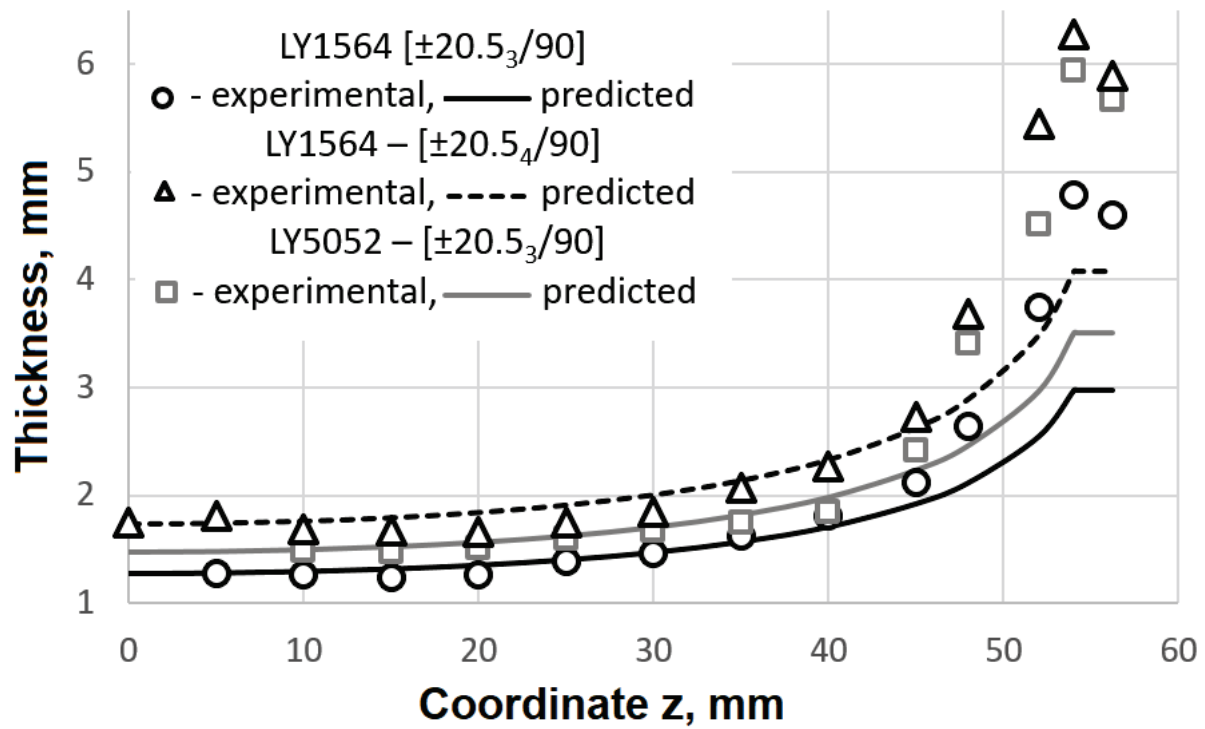
Figure 16. Thickness distribution in the dome of the wound casings.
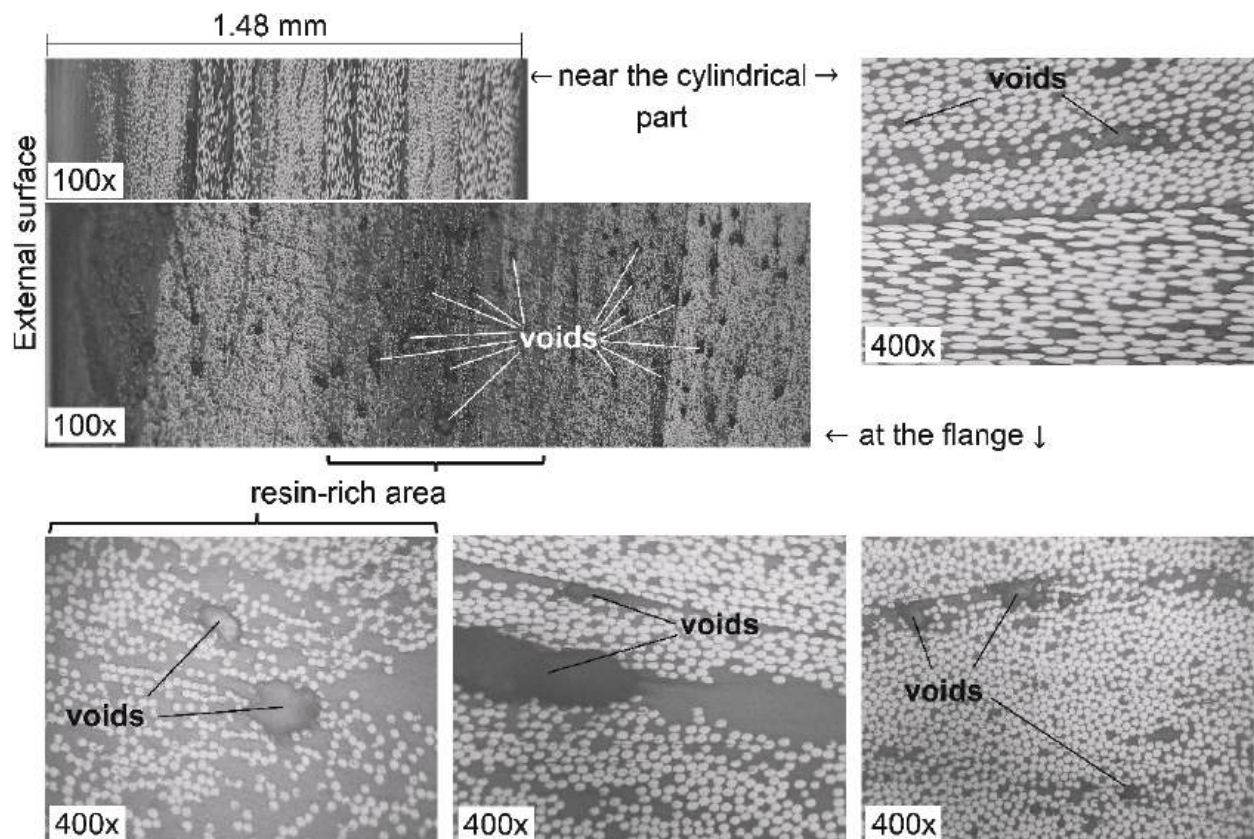
Figure 17. Micrographs at two opposite extremities of the dome of the casing LY5052 [±20.5$_3$/90]: voids.
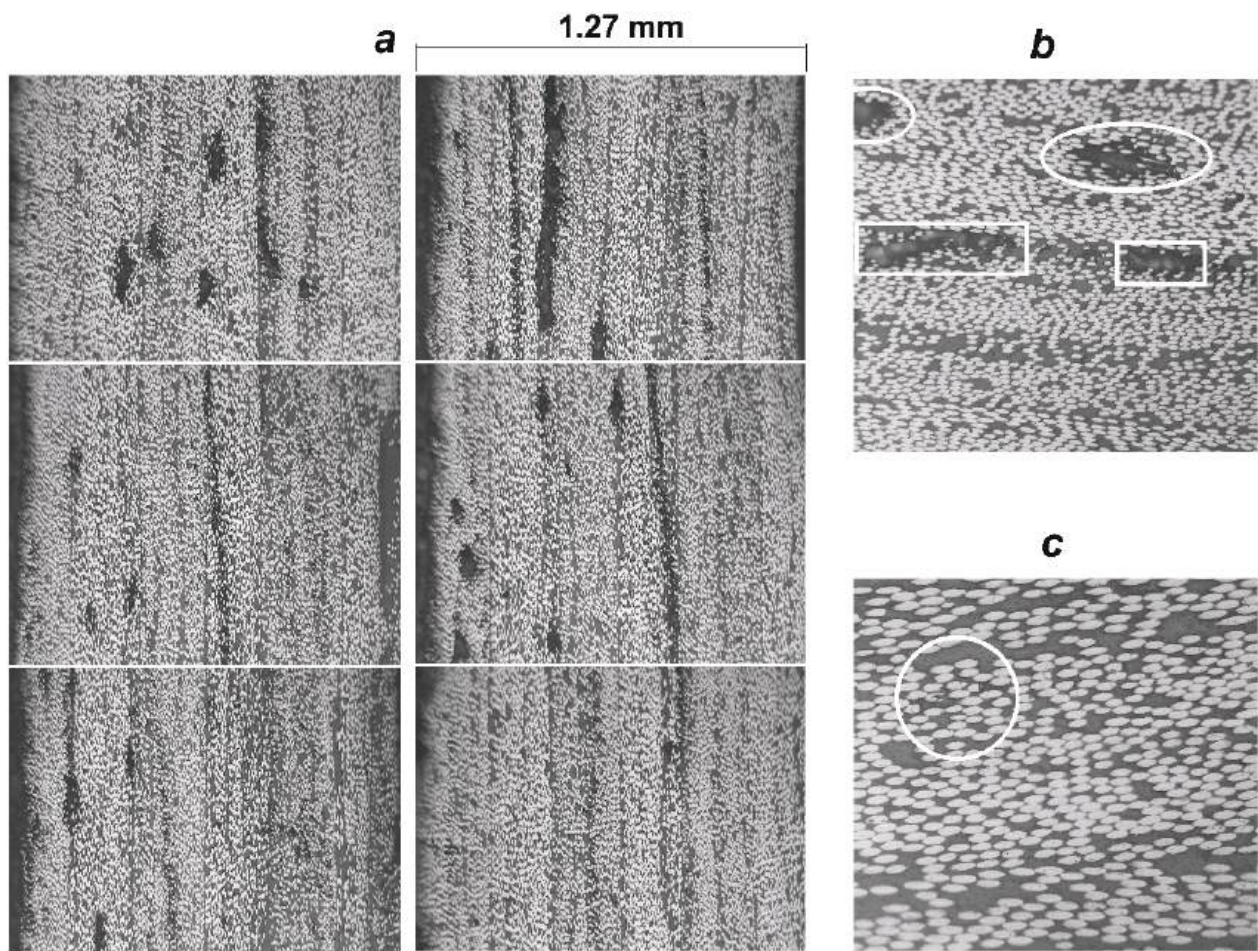
Figure 18. The selected micrographs $100\times$ (**a**) of the dome near the cylindrical part of the casing LY1564 $[\pm 20.5_3/90]$ with different content of the voids: (**b**) inter-ply voids in rectangular marker and intra-ply voids in elliptical marker ($200\times$); (**c**) intra-ply void between broken fibers ($400\times$).

4. Conclusions

The presented work validates the possibility of manufacturing axisymmetric composite structures, such as pressure vessels, with low-cost filament winding equipment. The cost-effective system relies on off-the-shelf components, an obsolete computer, and an affordable control system. The manually generated G-codes using the derived analytical equations for the delivery eye trajectory further reduce the cost of the system. The equations are obtained by referring only to analytic geometry and do not demand additional efforts or specific skills from an FWM operator. The preliminary results of manufacturing trials showed that the winder lays the fiber straight along the geodesic trajectory. Despite this fact, there might be compromises in using low-cost design solutions. Therefore, further works will investigate the performance of wound composite structures and the winding accuracy of other axisymmetric and non-axisymmetric shapes. Consequently, the suggested low-cost equipment provides small research teams with the possibility to carry out their projects, at least in the initial development stages.

Author Contributions: Conceptualization, A.A. and B.T.; methodology, A.A.; validation, A.A. and E.K.T.; formal analysis, A.A. and C.A.G.V.; investigation, A.A.; writing—original draft preparation, A.A.; writing—review and editing, A.A., E.K.T., C.A.G.V. and B.T.; supervision, C.A.G.V.; project administration, A.A.; funding acquisition, A.A. All authors have read and agreed to the published version of the manuscript.

Institutional Review Board Statement: Not applicable.

Informed Consent Statement: Not applicable.

Data Availability Statement: The data presented in this study are available on request from the corresponding author.

Conflicts of Interest: The authors declare no conflict of interest. The funders had no role in the design of the study; in the collection, analyses, or interpretation of data; in the writing of the manuscript, or in the decision to publish the results.

Abbreviations

E	position of the delivery eye on its trajectory;
E_{1f}	tensile modulus of the fiber;
F_{1f}	tensile strength of the fiber;
L_c	length of the cylindrical part;
M	point of tangency of the fiber to the surface of mandrel;
R_c	radius of the cylindrical casing and hemispherical dome;
R_e	radius of the circular trajectory of the delivery eye;
r_p	radius of polar opening;
$t_d(z)$	thickness distribution in the dome (excluding the portion near the opening) as a function of the z-coordinate;
t_{do}	thickness in the dome near the opening;
z_p	z-coordinate of the polar opening;
α	angle between axis $\overline{x}$ and radius vector to the point M in the plane $\overline{xyz}$;
β	winding angle;
β_c	winding angle on the cylindrical part;
$\beta_s(z)$	winding angle on the hemispherical dome as a function of the z-coordinate;
η	initial viscosity, mPa·s
λ	distance between the delivery eye and point of tangency of the fiber to the surface of mandrel;
ρ_f	linear mass density of the fibers;
Φ	turn-around angle (an angle of mandrel rotation to lay the tow along its predetermined trajectory);
Φ_c	turn-around angle for the cylindrical part;
$\Phi_s(z)$	turn-around angle for the hemispherical dome as a function of the z-coordinate;
Φ_1	turn-around angle for one winding cycle;
Φ_p^*	calculated angular pitch of winding;
Φ_p	accepted angular pitch of winding;
Φ_f	turn-around angle per one flange;
Φ_w	turn-around angle for the width of the tow.
CNC	computer numeric control
DOF	degrees of freedom
FWM	filament winding machine
LVDT	linear variable differential transformer
NEMA	National Electrical Manufacturers Association
POM	polyoxymethylene
PC	personal computer

Appendix A

```
O027 (geodesic path with 24 cycles per layer: Y and Z in mm, X and A in deg)
G91 G19 F6000
M98 P001 L4 (# of patterns per one layer)
M30
```

```
O001 (one pattern)
M98 P002 L5 (# of cycles with Φ_f only)
M98 P003 L1 (# of cycles with both Φ_f and Φ_w)
M99
```

```
O002 (one cycle with Φ_w only)
M98  P004  L1 (# of half-cycles forward)
M98  P005  L1 (# of half-cycles backward)
M98  P006  L1 (Φ_w plus the last sector of O004)
M99
```

```
O003 (one cycle with both Φ_f and Φ_w)
M98  P004  L1 (#of half-cycles forward)
M98  P005  L1 (#of half-cycles backward)
M98  P007  L1 (Φ_f and Φ_w plus the last sector of O005)
M99
```

```
O004  (forward stroke)
G91 X 2.283 Y 4.731 Z 3.535 A 11.042
G91 X 2.082 Y 5.005 Z 3.249 A 10.225
G91 X 1.92 Y 5.252 Z 2.931 A 8.9
G91 X 1.793 Y 5.472 Z 2.59 A 7.436
G91 X 1.69 Y 5.662 Z 2.227 A 6.079
G91 X 1.612 Y 5.822 Z 1.844 A 4.93
G91 X 1.55 Y 5.952 Z 1.45 A 3.999
G91 X 1.508 Y 6.048 Z 1.043 A 3.257
G91 X 1.479 Y 6.114 Z 0.629 A 2.667
G91 X 1.466 Y 6.147 Z 0.21 A 2.197
G91 X 1.690 Y 7.082 Z -0.279 A 2.065
G91 X 1.711 Y 7.033 Z -0.835 A 1.666
G91 X 1.755 Y 6.933 Z -1.382 A 1.344
G91 X 1.822 Y 6.783 Z -1.915 A 1.078
G91 X 1.918 Y 6.587 Z -2.430 A 0.856
G91 X 2.045 Y 6.344 Z -2.919 A 0.664
G91 X 2.214 Y 6.056 Z -3.376 A 0.496
G91 X 2.430 Y 5.724 Z -3.793 A 0.343
G91 X 2.711 Y 5.353 Z -4.164 A 0.202
G91 X 3.075 Y 4.944 Z -4.477 A 0.067

G91 X 30.006 Y 84.1 Z 0 A 0 (cylinder)

G91 X 3.047 Y 3.931 Z -4.083 A -0.05
G91 X 3.498 Y 3.575 Z -4.208 A -0.152
G91 X 4.07 Y 3.201 Z -4.264 A -0.256
G91 X 4.797 Y 2.809 Z -4.231 A -0.367
G91 X 5.716 Y 2.403 Z -4.087 A -0.487
G91 X 6.855 Y 1.983 Z -3.797 A -0.619
G91 X 8.203 Y 1.554 Z -3.325 A -0.768
G91 X 9.662 Y 1.116 Z -2.633 A -0.937
G91 X 10.983 Y 0.672 Z -1.708 A -1.134
G91 X 11.798 Y 0.224 Z -0.594 A -1.367
G91 X 13.543 Y -0.298 Z 0.786 A -1.926
G91 X 12.34 Y -0.892 Z 2.232 A -2.393
G91 X 10.493 Y -1.479 Z 3.367 A -2.991
G91 X 8.601 Y -2.057 Z 4.149 A -3.762
G91 X 6.975 Y -2.619 Z 4.623 A -4.769
G91 X 5.687 Y -3.164 Z 4.858 A -6.073
G91 X 4.7 Y -3.685 Z 4.913 A -7.712
G91 X 3.95 Y -4.181 Z 4.833 A -9.613
G91 X 3.382 Y -4.647 Z 4.649 A -11.465
G91 X 2.946 Y -5.08 Z 4.382 A -12.672
M99
```

```
O005 (backward stroke)
G91 X 2.283 Y -4.731 Z 3.535 A -11.042
G91 X 2.082 Y -5.005 Z 3.249 A -10.225
G91 X 1.92 Y -5.252 Z 2.931 A -8.9
G91 X 1.793 Y -5.472 Z 2.59 A -7.436
G91 X 1.69 Y -5.662 Z 2.227 A -6.079
G91 X 1.612 Y -5.822 Z 1.844 A -4.93
G91 X 1.55 Y -5.952 Z 1.45 A -3.999
G91 X 1.508 Y -6.048 Z 1.043 A -3.257
G91 X 1.479 Y -6.114 Z 0.629 A -2.667
G91 X 1.466 Y -6.147 Z 0.21 A -2.197
G91 X 1.690 Y -7.082 Z -0.279 A -2.065
G91 X 1.711 Y -7.033 Z -0.835 A -1.666
G91 X 1.755 Y -6.933 Z -1.382 A -1.344
G91 X 1.822 Y -6.783 Z -1.915 A -1.078
G91 X 1.918 Y -6.587 Z -2.43 A -0.856
G91 X 2.045 Y -6.344 Z -2.919 A -0.664
G91 X 2.214 Y -6.056 Z -3.376 A -0.496
G91 X 2.430 Y -5.724 Z -3.793 A -0.343
G91 X 2.711 Y -5.353 Z -4.164 A -0.202
G91 X 3.075 Y -4.944 Z -4.477 A -0.067

G91 X 30.006 Y -84.1 Z 0 A 0 (cylinder)

G91 X 3.047 Y -3.931 Z -4.083 A 0.05
G91 X 3.498 Y -3.575 Z -4.208 A 0.152
G91 X 4.07 Y -3.201 Z -4.264 A 0.256
G91 X 4.797 Y -2.809 Z -4.231 A 0.367
G91 X 5.716 Y -2.403 Z -4.087 A 0.487
G91 X 6.855 Y -1.983 Z -3.797 A 0.619
G91 X 8.203 Y -1.554 Z -3.325 A 0.768
G91 X 9.662 Y -1.116 Z -2.633 A 0.937
G91 X 10.983 Y -0.672 Z -1.708 A 1.134
G91 X 11.798 Y -0.224 Z -0.594 A 1.367
G91 X 13.543 Y 0.298 Z 0.786 A 1.926
G91 X 12.34 Y 0.892 Z 2.232 A 2.393
G91 X 10.493 Y 1.479 Z 3.367 A 2.991
G91 X 8.601 Y 2.057 Z 4.149 A 3.762
G91 X 6.975 Y 2.619 Z 4.623 A 4.769
G91 X 5.687 Y 3.164 Z 4.858 A 6.073
G91 X 4.7 Y 3.685 Z 4.913 A 7.712
G91 X 3.95 Y 4.181 Z 4.833 A 9.613
G91 X 3.382 Y 4.647 Z 4.649 A 11.465
M99
```

```
O006 (Φ_w plus the last sector of O004)
G91 X 2.946 Y 5.08 Z 4.382 A 12.672
M99
```

```
O007 (Φ_f and Φ_w plus the last sector of O005)
G91 X 17.946 Y 5.08 Z 4.382 A 12.672
M99
```

Figure A1. G-code for the winding trajectory on the mandrel with an imprinted geodesic path (R_c = 60 mm, r_p = 21 mm, and L_c = 84.1 mm).

References

1. Peters, S.T. (Ed.) *Composite Filament Winding*; ASM International: Materials Park, OH, USA, 2011; ISBN 0-61503-722-5.
2. Frketic, J.; Dickens, T.; Ramakrishnan, S. Automated Manufacturing and Processing of Fiber-Reinforced Polymer (FRP) Composites: An Additive Review of Contemporary and Modern Techniques for Advanced Materials Manufacturing. *Addit. Manuf.* **2017**, *14*, 69–86. [CrossRef]
3. Bassler, J. Colorado State University Rocket Team Builds Newly Designed Rocket Fuselage with Filament Winding Equipment Provided by Prodigm, Lattice Composites Resins, and Composites One Carbon Fibers. *Reinf. Plast.* **2020**, *64*, 92–96. [CrossRef]
4. Barros, B.; Oliveira, L.; Nunes, J.P. Development of a laboratorial robotized filament winding equipment. In Proceedings of the PMI 2014-International Conference on Polymers and Moulds Innovations, Guimarães, Portugal, 10–12 September 2014.
5. Ateba, J.A.; Verchery, G.; Aivazzadeh, S. A 5-Axes Filament Winder with Software Control. *Sci. Eng. Compos. Mater.* **2004**, *11*, 259–266. [CrossRef]
6. Tabuchi, D.; Sajima, T.; Doi, T.; Onikura, H.; Ohnishi, O.; Kurokawa, S.; Miura, T. Development of a Filament-Winding Machine Based on Internal Heating by a High-Temperature Fluid for Composite Vessels. *Sens. Mater.* **2011**, *23*, 347–358. [CrossRef]
7. Shotton-Gale, N.; Harris, D.; Pandita, S.D.; Paget, M.A.; Allen, J.A.; Fernando, G.F. Clean and environmentally friendly wet-filament winding. In *Management, Recycling and Reuse of Waste Composites*; Elsevier: Amsterdam, The Netherlands, 2010; pp. 331–368. ISBN 978-1-84569-462-3.
8. Pandita, S.D.; Irfan, M.S.; MacHavaram, V.R.; Shotton-Gale, N.; Mahendran, R.S.; Wait, C.F.; Paget, M.A.; Harris, D.; Leek, C.; Fernando, G.F. Clean Wet-Filament Winding-Part 1: Design Concept and Simulations. *J. Compos. Mater.* **2013**, *47*, 379–390. [CrossRef]
9. Haq, S.A.; Middleton, V.; Owen, M.J. Filament Winding Controller Requirements and B-Spline Solution. *Mater. Manuf. Process.* **1995**, *10*, 65–73. [CrossRef]
10. Sauti, G.; Kim, J.W.; Wincheski, R.A.; Antczak, A.; Campero, J.C.; Luong, H.H.; Shanahan, M.H.; Stelter, C.J.; Siochi, E.J. Structural CNT Composptes Part I: Developing a Carbon Nanotube Filament Winder. In Proceedings of the American Society for Composites-30th Technical Conference, East Lansing, CA, USA, 28–30 September 2015.
11. Hata, T.; Umemura, K.; Yamauchi, H.; Nakayama, A.; Kawai, S.; Sasaki, H. Design and Pilot Production of a "Spiral-Winder" for the Manufacture of Cylindrical Laminated Veneer Lumber. *J. Wood Sci.* **2001**, *47*, 115–123. [CrossRef]
12. Lye, S.W.; Boey, F.Y.C. Development of a Low-Cost Prototype Filament-Winding System for Composite Components. *J. Mater. Process. Technol.* **1995**, *52*, 570–584. [CrossRef]
13. Abdalla, F.H.; Mutasher, S.A.; Khalid, Y.A.; Sapuan, S.M.; Hamouda, A.M.S.; Sahari, B.B.; Hamdan, M.M. Design and Fabrication of Low Cost Filament Winding Machine. *Mater. Des.* **2007**, *28*, 234–239. [CrossRef]
14. Mateen, M.A.; Shankar, D.V.R.; Hussain, M.M. Design and Development of Low Cost Two Axis Filament Winding Machine. *J. Adv. Manuf. Technol.* **2018**, *12*, 117–126.
15. Krishnamurthy, T.N.; Idkan, M. Fabrication of Low Cost Filament Winding Machine. *Int. J. Recent Trends Electr. Electron. Eng.* **2014**, *4*, 30–39.
16. Mutasher, S.; Mir-Nasiri, N.; Lin, L.C. Small-Scale Filament Winding Machine for Producing Fiber Composite Products. *J. Eng. Sci. Technol.* **2012**, *7*, 156–168.
17. Rejab, M.R.M.; Kadirgama, K.; Noor, M.M.; Sani, M.S.M.; Daud, R. Modification and Testing of Four Axes Filament Winding Machine. In Proceedings of the International Conference on Science & Technology: Application in Industry & Education, Singapore, 29 August–2 September 2008; pp. 1505–1509.
18. Uzuner, S.; Akkus, N.; Kaplanoglu, E. Design and Control of Three Axis Fiber Winding Machine Using LabVIEW. In Proceedings of the Ulusal Konya Ereğli Kemal Akman Meslek Yüksekokulu Tebliğ Günleri, Konya, Turkey, 13–14 May 2010. Available online: https://scholar.google.ca/citations?view_op=view_citation&hl=en&user=mHA0yAIAAAAJ&citation_for_view=mHA0yAIAAAAJ:9yKSN-GCB0IC (accessed on 20 January 2022).
19. Quanjin, M.; Rejab, M.R.M.; Idris, M.S.; Bachtiar, B.; Siregar, J.P.; Harith, M.N. Design and Optimize of 3-Axis Filament Winding Machine. In Proceedings of the IOP Conference Series: Materials Science and Engineering, Busan, Korea, 25–27 August 2017.
20. Quanjin, M.; Rejab, M.R.M.; Sahat, I.M.; Amiruddin, M.; Bachtiar, D.; Siregar, J.P.; Ibrahim, M.I. Design of Portable 3-Axis Filament Winding Machine with Inexpensive Control System. *J. Mech. Eng. Sci.* **2018**, *12*, 3479–3493. [CrossRef]
21. Quanjin, M.; Rejab, M.R.M.; Idris, M.S.; Zhang, B.; Merzuki, M.N.M.; Kumar, N.M. Wireless technology applied in 3-axis filament winding machine control system using MIT app inventor. In Proceedings of the IOP Conference Series: Materials Science and Engineering, Kazimierz Dolny, Poland, 21–23 November 2019.
22. Quanjin, M.; Rejab, M.R.M.; Kumar, N.M.; Idris, M.S. Experimental Assessment of the 3-Axis Filament Winding Machine Performance. *Results Eng.* **2019**, *2*, 100017. [CrossRef]
23. Quanjin, M.; Rejab, M.R.M.; Kaige, J.; Idris, M.S.; Harith, M.N. Filament Winding Technique, Experiment and Simulation Analysis on Tubular Structure. In Proceedings of the IOP Conference Series: Materials Science and Engineering, Vladivostok, Russia, 2–4 October 2018.

24. Hunt, C.J.; Wisnom, M.R.; Woods, B.K.S. Design, manufacturing, and testing of an automated winding machine for wraptor composite truss structures. In Proceedings of the ECCM 2018-18th European Conference on Composite Materials, Athens, Greece, 24–28 June 2020.

25. Hunt, C.J.; Wisnom, M.R.; Woods, B.K.S. WrapToR Composite Truss Structures: Improved Process and Structural Efficiency. *Compos. Struct.* **2019**, *230*, 111467. [CrossRef]

26. Lv, Y.; Zhang, W.; Deng, H.; Ding, X. Design of small-scale filament winding placement machine. In Proceedings of the 2018 IEEE International Conference on Robotics and Biomimetics, ROBIO 2018, Kuala Lumpur, Malaysia, 12–15 December 2018.

27. Sofi, T.; Neunkirchen, S.; Schledjewski, R. Path Calculation, Technology and Opportunities in Dry Fiber Winding: A Review. *Adv. Manuf. Polym. Compos. Sci.* **2018**, *4*, 57–72. [CrossRef]

28. Zu, L.; Xu, H.; Jia, X.; Zhang, Q.; Wang, H.; Zhang, B. Winding Path Design Based on Mandrel Profile Updates of Composite Pressure Vessels. *Compos. Struct.* **2020**, *235*, 111766. [CrossRef]

29. Mazumdar, S.K.; Hoa, S.V. Analytical Models for Low Cost Manufacturing of Composite Components by Filament Winding, Part I: Direct Kinematics. *J. Compos. Mater.* **1995**, *29*, 1515–1541. [CrossRef]

30. Koussios, S. *Filament Winding: A Unified Approach*; Delft University Press: Delft, The Netherlands, 2004; ISBN 90-407-2551-9.

31. Abdel-Hady, F. Filament Winding of Revolution Structures. *J. Reinf. Plast. Compos.* **2005**, *24*, 855–868. [CrossRef]

32. Koussios, S.; Bergsma, O.K.; Beukers, A. Filament Winding. Part 2: Generic Kinematic Model and Its Solutions. *Compos. Part A Appl. Sci. Manuf.* **2004**, *35*, 197–212. [CrossRef]

33. Andrianov, A.; Shynkarenko, O.; Bertoldi, A.E.M.; Barcelos, M.N.D.; Veras, C.A.G. Concept and design of the hybrid test-motor for the development of a propulsive decelerator of SARA reentry capsule. In Proceedings of the 51st AIAA/SAE/ASEE Joint Propulsion Conference, Orlando, FL, USA, 27–29 July 2015.

34. Anoshkin, A.N. *Product Forming from Composite Materials by Filament Winding. Part 1: Theoretical Aspects and Formulas*; Perm National Research Polytechnic University: Perm, Russia, 1994.

35. Komkov, M.A.; Tarasov, V.A. *Winding Technology of Composite Structures for Missiles and Weapons*; Bauman Moscow State Technical University: Moscow, Russia, 2011.

36. Minsch, N.; Herrmann, F.H.; Gereke, T.; Nocke, A.; Cherif, C. Analysis of filament winding processes and potential equipment technologies. *Procedia CIRP* **2017**, *66*, 125–130. [CrossRef]

37. *Structural Materials Handbook ECSS-E-HB-32-20—Part 3: Load Transfer and Design of Joints and Design of Structures*; ECSS Secretariat, ESA-ESTEC, Requirements & Standards Division: Noordwijk, The Netherlands, 2011.

38. Munro, M. Review of manufacturing of fiber composite components by filament winding. *Polym. Compos.* **1988**, *9*, 352–359. [CrossRef]

39. Markov, L.; Cheng, R.M.H. Conceptual Design of Robotic Filament Winding Complexes. *Mechatronics* **1996**, *6*, 881–896. [CrossRef]

40. Dionoro, G.; Pilloni, M.T.; Romano, D. Process innovation in composite manufacturing by filament winding: A managerial assessment. In Proceedings of the High Performance Structures and Materials, Lisbon, Portugal, 11–13 July 2022.

41. Romano, D.; Pedone, P. Economic assessment of product-process innovation in filament winding technology. In Proceedings of the 9th QMOD, Liverpool, UK, 8–10 August 2006.

42. Koussios, S.; Beukers, A. Filament Winding: Design, Materials, Structures and Manufacturing Process. In *Wiley Encyclopedia of Composites*; John Wiley & Sons, Inc.: Hoboken, NJ, USA, 2012; pp. 1–16. [CrossRef]

43. Peters, S.T.; Tarnopol'skii, Y.M. Filament winding. In *Composites Engineering Handbook*; Marcel Dekker: New York, NY, USA, 1997; pp. 515–548. ISBN 0-8247-9304-8.

44. Peters, S.T.; Foral, R.F.; Humphrey, W.D. Filament winding. In *Handbook of Composite Reinforcements*; Wiley-VCH: Palo Alto, CA, USA, 1993; pp. 232–247.

45. Koussious, S.; Bergsma, O.K.; Debecker, A. Development of a tumble winder for dedicated products. In Proceedings of the 15th American Society for Composites, College Staton, TX, USA, 26 September 2000.

46. Lossie, M.; Van Brussel, H. Design principles in filament winding. *Compos. Manuf.* **1994**, *5*, 5–13. [CrossRef]

47. Akovali, G. (Ed.) *Handbook of Composite Fabrication*; Rapra Technology Ltd.: Shrewsbury, UK, 2001; ISBN 978-1-85957-263-4.

48. DuVall, F.W. Cost Comparisons of wet filament winding versus prepreg filament winding for type II and type IV CNG cylinders. *SAMPE J.* **2001**, *37*, 38–42.

49. Arrabiyeh, P.A.; May, D.; Eckrich, M.; Dlugaj, A.M. An Overview on Current Manufacturing Technologies: Processing Continuous Rovings Impregnated with Thermoset Resin. *Polym. Compos.* **2021**, *42*, 5630–5655. [CrossRef]

50. Shibley, A.M. Filament winding. In *Handbook of Composites*; Lubin, G., Ed.; Springer: Boston, MA, USA, 1982; pp. 449–478, ISBN 978-1-4615-7141-4.

51. Galantucci, L.M.; Piperi, E.; Lavecchia, F.; Zhavo, A. Semi-automatic low cost 3D laser scanning systems for reverse engineering. *Procedia CIRP* **2015**, *28*, 94–99. [CrossRef]

52. *Mach3 CNC Controller Software Installation and Configuration, Version 3*; Artsoft Software Incorporated: Cluj, Romania, 2008.

53. Radzevich, S.P. *Geometry of Surfaces*, 2nd ed.; Springer Nature: Cham, Switzerland, 2020.

54. Wang, Q.; Li, T.; Wang, B.; Liu, C.; Huang, Q.; Ren, M. Prediction of void growth and fiber volume fraction based on filament winding process mechanics. *Compos. Struct.* **2020**, *246*, 112432. [CrossRef]

55. Cohen, D.; Mantell, S.C.; Zhao, L. The Effect of fiber volume fraction on filament wound composite pressure vessel strength. *Compos. Part B Eng.* **2001**, *32*, 413–429. [CrossRef]

Failure-Mode Shift of Metal/Composite L-Joint with Grooved Structure under Compressive Load

Zhenhang Kang, Zhu Liu, Yongpeng Lei and Jifeng Zhang * [ID]

Key Laboratory of Advanced Ship Materials and Mechanics, College of Aerospace and Civil Engineering, Harbin Engineering University, Harbin 150001, China; kangzhenhang@hrbeu.edu.cn (Z.K.); liuzhu0618@hrbeu.edu.cn (Z.L.); yongpenglei@126.com (Y.L.)
* Correspondence: jfzhang@hrbeu.edu.cn; Tel.: +86-131-9953-2163

Abstract: Bond length and bond interface morphology have a great influence on the performance of metal/composite hybrid joints. In this paper, a metal/composite L-joint with groove structure was designed, and seven groups with different bonding lengths were fabricated using the VARI (Vacuum Assisted Resin Infusion) process to study the effect of different bonding lengths on the performance of the joint. In the simulation analysis of the metal/composite L-joint, the stiffness equivalence method was adopted, and the groove structure was equivalent to a 0-thickness element layer. The applicability of the simulation method was verified by comparing the ultimate load, displacement and failure mode of the test and simulation. Furthermore, the simulation method was used to simulate more compression experiments of metal/composite L-joints with different bonding lengths, and prediction diagrams of failure displacement and failure mode were produced. According to the prediction map, when the bonding length is 100.00 mm, the metal/composite L-joint has better compressive properties.

Keywords: metal/composite; L-joint; bonding length; failure mode; equivalent; RVE

1. Introduction

Fiber-reinforced composite materials are widely used in modern ships for their outstanding performance in strength/weight ratio, design flexibility and electromagnetic resistance [1–3]. Therefore, the connection between metals and composite materials is an inevitable problem. In marine structures, L-shaped joints and similar components are very common, for example, they are easy to find at the intersection between the board edge and the upper deck [4,5]. The design method and performance evaluation of similar steel structures are simple, mature and accurate for engineering. However, for metal/composite structures, due to their many components and complex damage modes, they mostly rely on subjective experience or direct model tests.

As one of the basic structural components of large-scale composite marine structures, the mechanics of L-joints have been studied more in [6–8]. Feih S. and H.R. Shercliff [9,10] predicted the failure behavior of composite L-joint structures under tensile load. The results show that the zone criterion can predict the failure load of joints with different fillet shapes very well, and the damage mechanics method can be used to simulate the crack propagation prediction during failure of the adhesive. In addition, they used ABAQUS to predict the damage and failure of the L-joint. They used a numerical model to evaluate the effects of parameters such as curvature, thickness, stacking order and combined load on the failure mode of the L-joints. Qin Kai and Yan Renjun [11] studied the transition of the failure mode of the sandwich-composite L-shaped joint of the hull structure under tensile load. They manufactured L-joints with transition zone radii (R) of 45 mm, 90 mm and 180 mm, respectively; they then analyzed and summarized the failure modes of the L-joints. Finally, through numerical simulation, the failure mode of L-joints with a radius from 45 mm to

180 mm was predicted. Haiyan Zeng and Renjun Yan [12] studied the failure prediction of sandwich-composite L-shaped joints under bending and established a numerical model to predict the bearing capacity of the joints. The feasibility of the proposed empirical formula was verified through experiments. Many scholars have studied the superstructure of ship structures, focusing on the mechanical behavior of sandwich-composite L-joints. The connection behavior of the composite structure and the hull is mainly a bolted connection and a hybrid connection. In the current paper, a metal/composite bonded L-joint with groove structure is proposed, and its failure behavior is studied. This study may provide a reference for the connection between superstructure and ship structure

The purpose of this paper is to study the compressive damage behavior of metal/composite L-joints and further investigate the effect of bond length for possible design recommendations. In the study, a metal/composite L-joint structure design with groove structure was proposed, and the L-joint was fabricated using the VARI co-curing process. To study the effect of bond length on the compressive properties of metal/composite L-joints, seven bond joints with different lengths were designed, and their failure modes were analyzed in detail. In the simulation analysis of metal/composite L-joints, due to the complexity of the groove structure and the multi-faceted and multi-scale problems, the parameter study of the groove structure required lots of calculations. Therefore, the stiffness equivalence method was adopted, and the groove structure was equivalent to a 0-thickness cohesive layer to facilitate numerical analysis. The parameters of the 0-thickness cohesive element layer were calculated using the RVE method. The feasibility of this method was verified by comparison between the experiment and the simulation.

2. Specimen Manufacturing and Testing

The metal/composite L-joint consisted of a metal corner and two composite laminates. The L-type metal crutch was a right-angled connector, and its size and schematic diagram are shown in Figure 1 (bonding length = 55.00 mm). As shown in Figure 1, the thickness of the corners of the metal parts was 8.00 mm. The bonding area of the metal component was composed of four identical groove structures. The thickness of the groove structure was 3.00 mm, and the distance between adjacent ones was 2.00 mm.
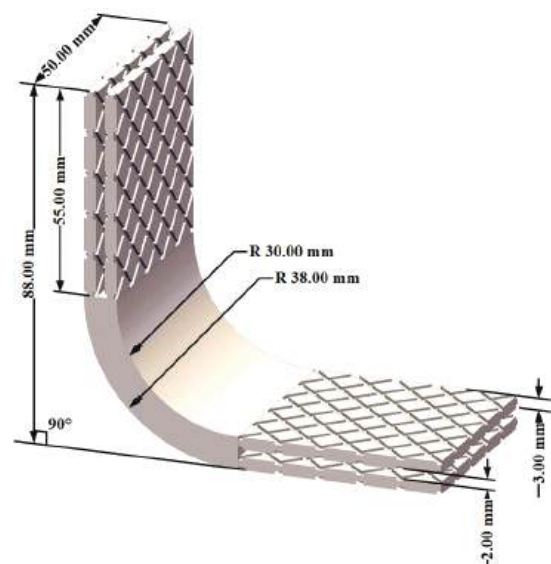
Figure 1. Schematic diagram of L-shaped metal component.

The ±45° groove structure was designed in the L-shaped metal component, as shown in Figure 2. The value of 45° was relative to the boundary of the groove structure. Both sides of the bonding component had groove structure, which can eliminate the warpage caused by the groove structure. The size of the groove was determined based on previous research.

The depth and width of the ±45° groove were 0.75 mm and 1.414 mm, respectively, and the cross-sectional shape of the groove was rectangular. The distance between adjacent grooves was 8.00 mm.
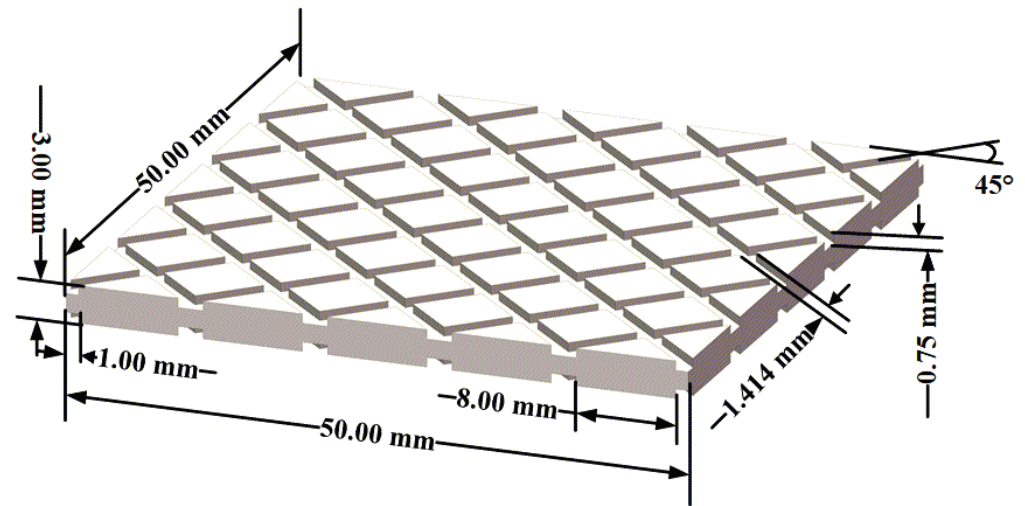
Figure 2. ±45° groove structure (area size: 50 mm × 50 mm).

In addition, to explore the influence of the bonding length on the L-shaped joint, bonding components of other lengths were also designed, as shown in Figure 3. A total of seven metal components with different bonding lengths were designed, and the bonding lengths were 25.00 mm, 40.00 mm, 55.00 mm, 70.00 mm, 85.00 mm, 100.00 mm, and 115.00 mm, respectively.
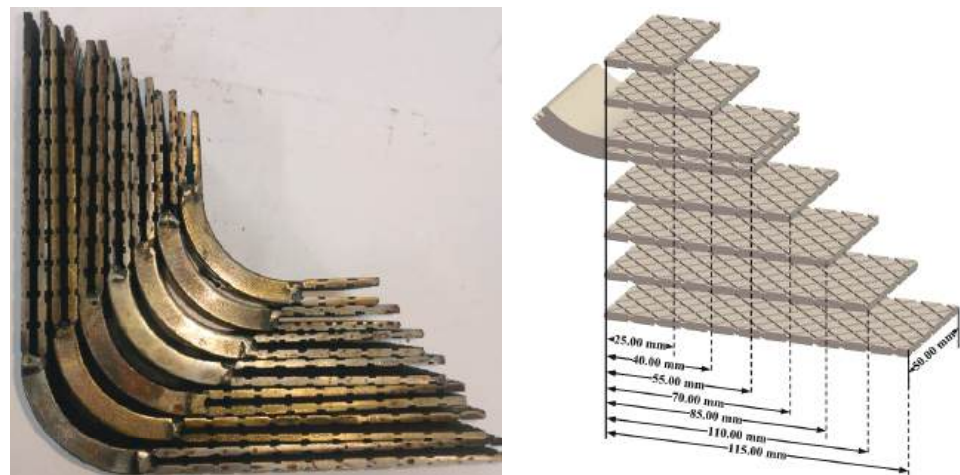
Figure 3. Groove structure with different bonding lengths.

The metal/composite L-joint was made using a vacuum-assisted resin infusion (VARI) process, and there were three specimens for each type of L-joint. The schematic diagram of the finished product is shown in Figure 4. The composite component was composed of two layers of 3.00 mm and three layers of 2.00 mm composite laminates. The composite material was glass-fiber-reinforced plastic (GFRP) (MingRen composite, Harbin, China). The fiber fabric, with a repeating length unit of T = 7.8 mm, was a plain bi-directional woven fabric glass fiber, with a thickness of t = 0.15 mm and a surface density of 600 g/m^2 [13,14]. The performance parameters of the glass fiber reinforced plastic layer were E_{11} = 20 GPa, E_{22} = E_{33} = 6.545 GPa, G_{12} = G_{23} = 3.545 GPa, G_{23} = 1.52 GPa, ν_{12} = ν_{13} = 0.3, ν_{23} = 0.45. In addition, the resin matrix was made of Ashland Derakane™ 411 epoxy vinyl ester resin(Ashland, Catlettsburg, KY, USA), which is used to manufacture glass-fiber-reinforced

composite laminates, and the material parameters of the resin cast body were $E = 2.9$ GPa and $\lambda = 0.3$. The adhesive layer structure was formed during the curing process of the vinyl resin.
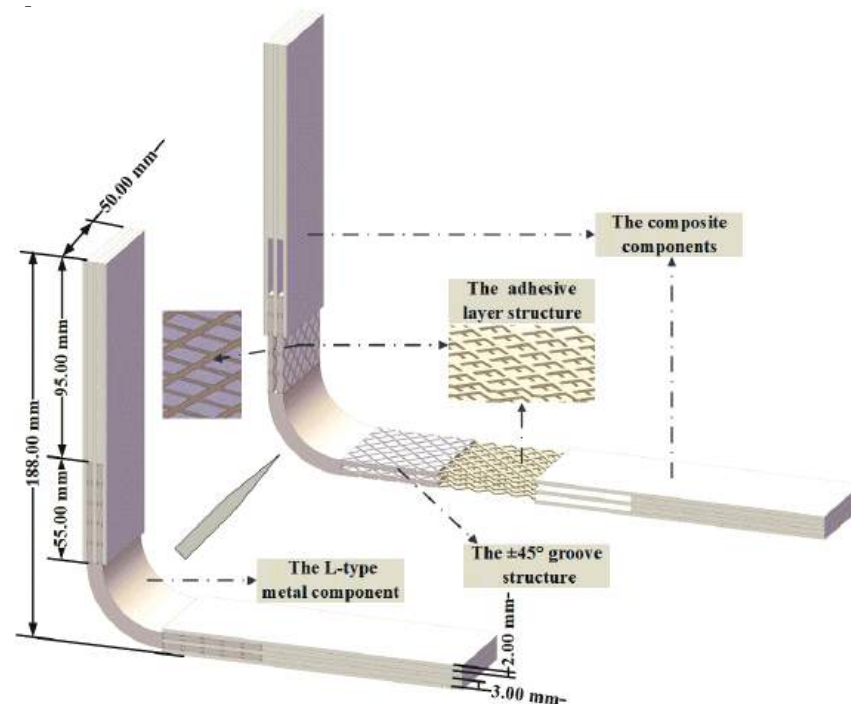
Figure 4. Disassembly schematic diagram of L-joint overall schematic and component.

To verify the ultimate compressive strength of the L-joint, a compression experiment was designed. Experiments on the L-joints were conducted on the Instron 8001 universal testing machine (Instron, Norwood, MA, USA) shown in Figure 5. During the experiments, the two ends of the L-joint were clamped by premade steel fixtures. The lower end was latched onto the test bench, and the upper end was latched onto the actuator. The applied load was controlled through the displacement of the actuator, which was set at a speed of 2.5 mm/min.
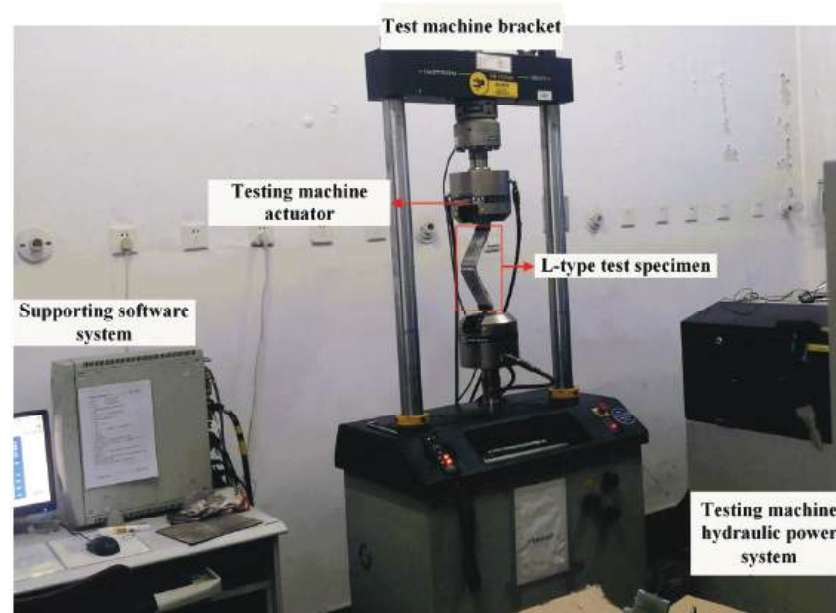
Figure 5. Compression test of metal-composite L-joint and direction of force.

3. Simulation Study

3.1. Establishment of RVE Model

The representative volume element (RVE) of the bonded part was intercepted in the study, as shown in Figure 6. In Figure 6, the established RVE model is a rectangular parallelepiped of 10.00 mm × 10.00 mm × 3.00 mm. The ±45° groove structure was symmetrical diagonally; the depth and width of the groove were 0.75 mm and 1.414 mm, respectively; and the thickness of the adhesive layer was 0.75 mm.
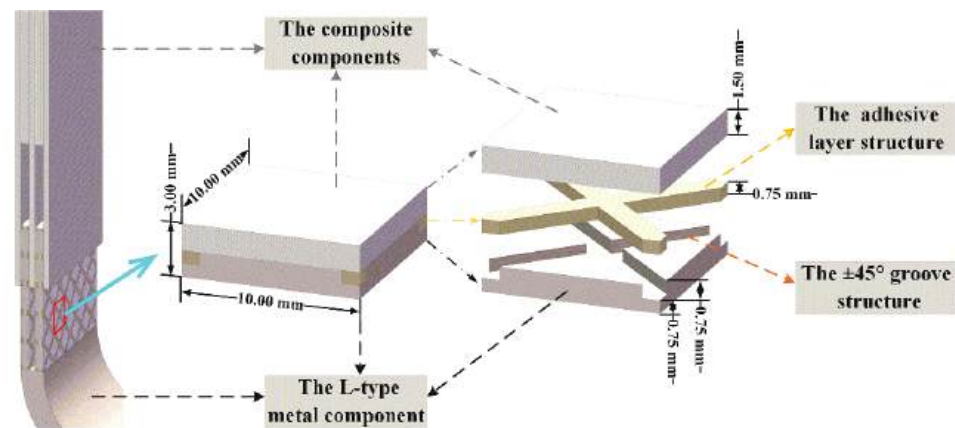
Figure 6. Definition of the RVE.

When using RVE for structural analysis, periodic boundary conditions are usually applied to the elements to achieve deformation control of the numerical model. Periodic boundary conditions can coordinate the deformation of the adjacent contact surfaces of RVE so that the internal deformation of the entire material model has continuity.

The symmetry boundary surface of the RVE must have the same mesh, to ensure that any node on the boundary surface can find its corresponding node on its symmetry surface. Assuming that P_1 is a node on a certain boundary surface of the RVE and P_2 is the node corresponding to it on the symmetry plane, the positions of the node P_1 and P_2 must satisfy the relationship, as follows in Equation (1):

$$\begin{cases} x_i^{P_1} = x_i^{P_2} \\ x_j^{P_1} = x_j^{P_2} \qquad (i,j,k = 1,2,3 \text{ and } i \neq j \neq k) \\ x_k^{P_1} = x_k^{P_2} \pm 1 \end{cases} \tag{1}$$

where $x_i^{P_1}, x_j^{P_1}, x_k^{P_1}$ and $x_i^{P_2}, x_j^{P_2}, x_k^{P_2}$ are the node coordinates of P_1 and P_2, respectively. Assuming finite deformation and applying arbitrary average deformation gradient tensor $\overline{\mathbf{F}}$ to RVE, the periodic boundary condition can be expressed as Equation (2):

$$\begin{aligned} \mathbf{x}(P_1) - \mathbf{x}(P_2) &= \overline{\mathbf{F}}[X(P_1) - X(P_2)] \\ \mathbf{P}(P_1) &= -\mathbf{P}(P_2) \end{aligned} \tag{2}$$

where X and x represent the position vectors of the nodes on the boundary surface before and after deformation, respectively, and **P** represent the load acting on the corresponding nodes.

In Abaqus, the application of periodic boundary conditions of representative volume elements is realized by introducing reference points and establishing parameter constraints. To express the form and application process of periodic boundary conditions more clearly, a representative volume element was established, as illustrated in Figure 7.
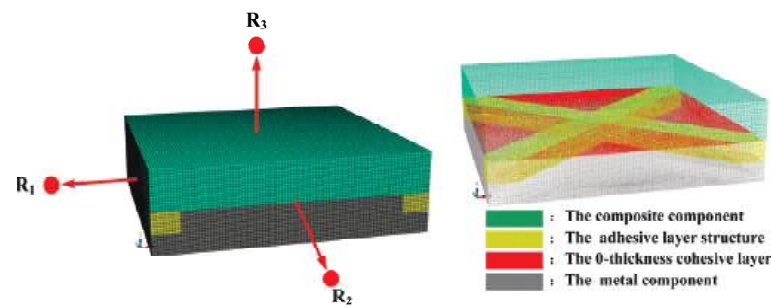
Figure 7. Meshing and components of the RVE.

X_1, X_2, Y_1, Y_2, Z_1 and Z_2 are used to represent the node sets of the front and rear boundary surfaces, left and right interfaces, and upper and lower boundary surfaces of the REV, respectively. R_1, R_2 and R_3 are used to represent the reference points associated with the corresponding boundary surfaces. Then the constraint equation of the periodic boundary condition can be expressed as Equation (3):

$$\left\{ \begin{array}{l} u_1^{X_1} - u_1^{X_2} = u_1^{R_1} \\ u_2^{X_1} - u_2^{X_2} = u_2^{R_1} \\ u_3^{X_1} - u_3^{X_2} = u_3^{R_1} \end{array} \right. , \left\{ \begin{array}{l} u_1^{Y_1} - u_1^{Y_2} = u_1^{R_2} \\ u_2^{Y_1} - u_2^{Y_2} = u_2^{R_2} \\ u_3^{Y_1} - u_3^{Y_2} = u_3^{R_2} \end{array} \right. , \left\{ \begin{array}{l} u_1^{Z_1} - u_1^{Z_2} = u_1^{R_3} \\ u_2^{Z_1} - u_2^{Z_2} = u_2^{R_3} \\ u_3^{Z_1} - u_3^{Z_2} = u_3^{R_3} \end{array} \right. \tag{3}$$

The established RVE numerical model consisted of three parts: the composite component, the adhesive layer structure and the metal component. The whole was a rectangular parallelepiped of 10.00 mm × 10.00 mm × 3.00 mm. These parts consisted of 394,224 C3D8R elements (as shown in Figure 7). In addition, a 0-thickness cohesive layer was defined between the metal component and the adhesive layer structure (red area in Figure 7); a tie constraint was applied between the composite component and the glue layer structure, enabling hard contact between components.

3.2. Material Parameters of the Equivalent Cohesive Layer

To facilitate the analysis of complex contact surfaces, the complex groove structure was made equivalent to a 0-thickness cohesive element layer by a direct equivalent method. The direct equivalent method was used to calculate the equivalent stress and strain directly, based on the average surface or volume of the field, such as stress and strain. It was then used to solve the macro equivalent performance based on the relationship between the macro equivalent stress and the macro equivalent strain [15].

For simple structures, the material mechanics method or elastic mechanics method can be used to directly solve the stress and strain of each component, then average the macro equivalent stress $\overline{\sigma}$; finally, the equivalent stiffness coefficient $\overline{\mathbf{C}}$ of the composite material can be solved according to the definition, as shown in Equation (4):

$$\overline{\sigma} = \overline{\mathbf{C}} : \overline{\varepsilon} \tag{4}$$

where $\overline{\sigma}$ and $\overline{\varepsilon}$ represent the equivalent macroscopic stress and equivalent strain, respectively, and $\overline{\mathbf{C}}$ represents the equivalent macroscopic stiffness tensor. The direct equivalent method is mainly suitable for solving the equivalent stiffness of composite materials with simple structures. Therefore, in practical applications, the direct equivalent method is mainly used for the simple estimation of equivalent stiffness.

To simulate the damage failure of laminated composites in the tensile shear test, the cohesive zone model is considered. In addition to stiffness, the initiation criteria and

energy-based propagation criteria for crack initiation are defined. The criterion for the initiation of interlayer damage is the law of traction separation, as shown in Equation (5):

$$\left(\frac{\sigma_n}{N}\right)^2 + \left(\frac{\sigma_t}{T}\right)^2 + \left(\frac{\sigma_s}{S}\right)^2 = 1 \tag{5}$$

where σ_n, σ_t, are σ_s are, respectively, the tensile stress relative to the normal direction n and shear directions t and s. N, T and S stand for their critical values. The law of exponential damage evolution based on the Power Low energy criterion (Equation (6)), linear softening and mixed-mode is selected.

$$\frac{G_\varepsilon}{G_{\varepsilon C}} = \left(\frac{G_I}{G_{IC}}\right)^{a_m} + \left(\frac{G_{II}}{G_{IIC}}\right)^{a_n} + \left(\frac{G_{III}}{G_{IIIC}}\right)^{a_o} \tag{6}$$

where $G_\varepsilon = G_I + G_{II} + G_{III}$ refers to the total energy release rate, and the value of exponent a_m, a_n and a_o are usually selected to be either 1 or 2. The areas under the traction-relative displacement curves for modes I, II or III are the relative critical energies released at failure G_{IC}, G_{IIC} and G_{IIIC}, as shown in Equations (7) and (8):

$$G_{IC} = \frac{N\delta_I^F}{2} \tag{7}$$

$$G_{IIC} = G_{IIIC} = \frac{T\delta_{II}^F}{2} \tag{8}$$

where δ_I^F and δ_{II}^F are the ultimate opening and tangential displacements, respectively [16]. When the value of the degradation criterion parameter $SDEG = \frac{G_\varepsilon}{G_{\varepsilon C}} = 1$, the 0-thickness cohesive layer completely fails.

In this study, shear and pull-out simulations of the $\pm 45°$ groove structure was carried out, and the load–displacement curve obtained is shown in Figure 8. According to the obtained data and Equations (7) and (8) above, the equivalent zero-layer viscous unit layer parameters are calculated, as shown in Table 1.
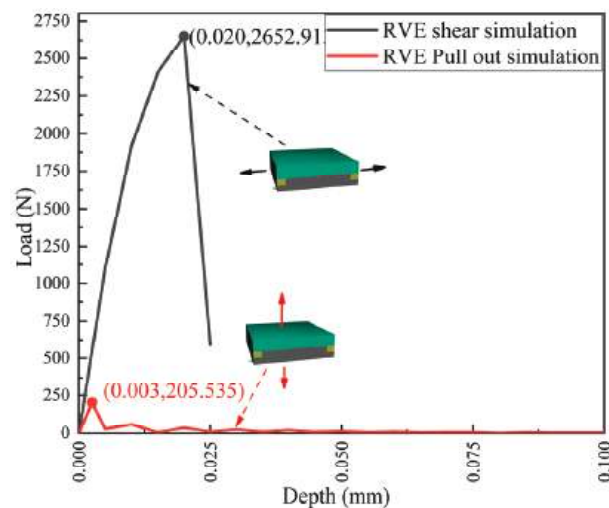
Figure 8. Load–displacement curve of the shear and pull-out tests.

Table 1. Initial stiffness of the interface, damage initiation and propagation parameters.

Initial Stiffness (MPa/mm)			Interlaminar Strength (MPa)			Fracture Toughness (J/mm²)		
Kn	Kt	Ks	N	T	S	G_{IC}	G_{IIC}	G_{IIIC}
5811	5811	5811	2.05	26.53	26.53	0.085	2.65	2.65

3.3. Simulation of Equivalent Metal/GFRP Joints

In this paper, the ABAQUS finite element software was used to numerically analyze the compression experiment of the metal-composite L-joint, and an equal-scale numerical model was established. The loading condition was the same as the experimental condition, which was 2.50 mm/min, as shown in Figure 9. In Figure 9, the boundary conditions of the fixed end were U1 = U2 = U3 = 0, UR1 = UR2 = 0. The boundary conditions of the compressive load loading end were U3 = 0, UR1 = UR2 = 0. The metal-composite L-joint model consisted of metal parts (Figure 9a), GFRP parts (Figure 9b,c) and interfacial cohesive element layers (Figure 9d–f). Metal parts and GFRP parts were divided into 24,675 meshes with element type C3D8R. The metal part (Figure 9a) is composed of two metal groove plates with a thickness of 3.00 mm and a 90° corner with a thickness of 8.00 mm. The failure of the metal structure adopted the ductile damage criterion, and the criterion for the onset of damage, the equivalent plastic strain ($\bar{\varepsilon}_D^{pl}$), η, was a function of the stress triaxiality, $\eta = -p/q$. Stress triaxiality is a parameter that describes the triaxial stress state of a material, such as in pure shear, uniaxial tension (compression), equi-biaxial tension (compression), and equi-triaxial tension (compression) stress states. The values of η were 0, $\pm\frac{1}{3}$, $\pm\frac{2}{3}$ and $\pm\infty$, respectively. The GFRP parts consisted of three layers of 2.00 mm composite board (Figure 9c) and two layers of 3.00 mm composite board (Figure 9b). To predict the progressive damage of GFRP, the 3DHashin failure [17,18] criterion model (used by Puck for matrix failure) was considered. In the process of loading, when some damage was produced, the material properties were adjusted by the corresponding material performance degradation criteria to realize the failure procedure [19,20]. The continuous damage-mechanics constitutive model of GFRP structure was realized by the VUMAT (Vectorized user-material) subroutine in Abaqus. The expression of the 3D Hashin failure criterion is shown in Equations (9)–(14), and the degradation criterion is shown in Table 2.
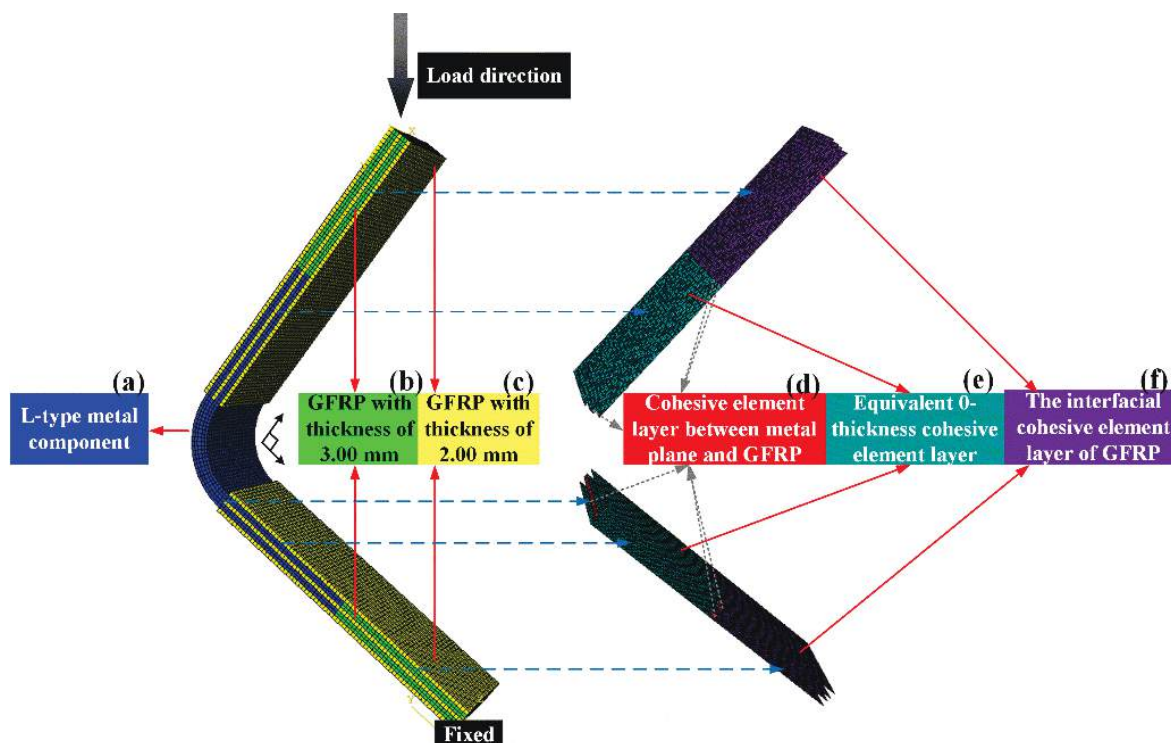
Figure 9. Metal-composite L-joint model mesh and loading conditions: (**a**) L-type metal component; (**b**) GFRP with thickness of 3.00 mm; (**c**) GFRP with thickness of 2.00 mm; (**d**) Cohesive element layer between metal plane and GFRP; (**e**) Equivalent 0-thickness cohesive element layer; (**f**) The interfacial cohesive element layer of GFRP.

Table 2. Degradation rules for the material properties used in the study.

Failure Mode	Failure Criterion	Material Degradation Criterion
Fiber tensile failure	$\sigma_{11} \geq 0$	$E'_{11} = 0.07E_{11};\ G'_{12} = 0.07G_{12};\ G'_{13} = 0.07G_{13}$ $\nu'_{12} = 0.07\nu_{12};\ \nu'_{13} = 0.07\nu_{13}$
Fiber compression failure	$\sigma_{11} < 0$	$E'_{11} = 0.07E_{11};\ G'_{12} = 0.07G_{12};\ G'_{13} = 0.07G_{13}$ $\nu'_{12} = 0.07\nu_{12};\ \nu'_{13} = 0.07\nu_{13}$
Matrix tensile failure	$\sigma_{22} + \sigma_{33} \geq 0$	$E'_{22} = 0.2E_{22};\ G'_{12} = 0.2G_{12};\ G'_{23} = 0.2G_{23}$ $\nu'_{12} = 0.2\nu_{12};\ \nu'_{23} = 0.2\nu_{23}$
Matrix compression failure	$\sigma_{22} + \sigma_{33} < 0$	$E'_{22} = 0.4E_{22};\ G'_{12} = 0.4G_{12};\ G'_{23} = 0.4G_{23}$ $\nu'_{12} = 0.4\nu_{12};\ \nu'_{23} = 0.4\nu_{23}$
Tensile delamination failure	$\sigma_{33} \geq 0$	$E'_{33} = 0.2E_{33};\ G'_{13} = 0.2G_{13};\ G'_{23} = 0.2G_{23}$ $\nu'_{13} = 0.2\nu_{13};\ \nu'_{23} = 0.2\nu_{23}$
Compression delamination failure	$\sigma_{33} < 0$	$E'_{33} = 0.2E_{33};\ G'_{13} = 0.2G_{13};\ G'_{23} = 0.2G_{23}$ $\nu'_{13} = 0.2\nu_{13};\ \nu'_{23} = 0.2\nu_{23}$

Fiber tensile failure ($\sigma_{11} \geqslant 0$):

$$\left(\frac{\sigma_{11}}{X_t}\right)^2 + \left(\frac{\tau_{12}}{S_{12}}\right)^2 + \left(\frac{\tau_{13}}{S_{13}}\right)^2 = 1 \tag{9}$$

Fiber compression failure ($\sigma_{11} < 0$):

$$-\left(\frac{\sigma_{11}}{X_c}\right) = 1 \tag{10}$$

Matrix tensile failure ($\sigma_{22} + \sigma_{33} \geqslant 0$):

$$\left(\frac{\sigma_{22} + \sigma_{33}}{Y_t}\right)^2 + \left(\frac{1}{S_{23}^2}\right)\left(\tau_{23}^2 - \sigma_{22}\sigma_{33}\right) + \left(\frac{\tau_{12}}{S_{12}}\right)^2 + \left(\frac{\tau_{13}}{S_{13}}\right)^2 = 1 \tag{11}$$

Matrix compression failure ($\sigma_{22} + \sigma_{33} < 0$):

$$\frac{1}{Y_c}\left[\left(\frac{Y_c}{2S_c}\right)^2 - 1\right](\sigma_{22} + \sigma_{33}) + \left(\frac{\sigma_{22} + \sigma_{33}}{2S_{12}}\right)^2 + \left(\frac{1}{S_{23}^2}\right)(\tau_{23}^2 - \sigma_{22}\sigma_{33}) + \left(\frac{\tau_{12}}{S_{12}}\right)^2 + \left(\frac{\tau_{13}}{S_{13}}\right)^2 = 1 \tag{12}$$

Tensile delamination failure ($\sigma_{33} \geqslant 0$):

$$\left(\frac{\sigma_{33}}{Z_t}\right)^2 + \left(\frac{\tau_{12}}{S_{13}}\right)^2 + \left(\frac{\tau_{13}}{S_{23}}\right)^2 = 1 \tag{13}$$

Compression delamination failure ($\sigma_{33} < 0$):

$$\left(\frac{\tau_{12}}{S_{13}}\right)^2 + \left(\frac{\tau_{13}}{S_{23}}\right)^2 = 1 \tag{14}$$

where, $\sigma_{11}, \sigma_{22}, \sigma_{33}, \tau_{12}, \tau_{13}$ and τ_{23} are the principal direction stress of the composite, 1 represents the fiber direction, 2 represents the direction perpendicular to the fiber, and 3 represents perpendicularity to the 1 and 2 planes; X_t, Y_t and Z_t are the tensile strength in the main direction of the composite; X_c, Y_c and Z_c are the compressive strengths in the principal direction of the composite; and S_{13}, S_{23} and S_{12} are the shear strengths of the composite.

The interfacial cohesive element layer structure was mainly composed of three different cohesive layers, namely: the interfacial cohesive layer between the metal plane and GFRP (Figure 9d), the equivalent 0-thickness cohesive element layer (Figure 9e), and the interfacial cohesive elemental layer of GFRP (Figure 9f). The purpose of the interfacial cohesive layer between the metal plane and GFRP was to simulate the viscous behavior between the untreated metal surface and GFRP (Figure 9d); and the equivalent 0-thickness

cohesive element layer was to simulate the fracture of the cured adhesive layer resin in the groove structure (Figure 9e); and the interfacial cohesive element layer of GFRP was to simulate the delamination failure of GFRP (Figure 9f). The COH3D8 element format was adopted for the cohesive elements. The bilinear shape law was generally used owing to the analysis time and convergence problem [21–23].

4. Results and Discussion

To facilitate the elaboration and analysis of the failure mode of the metal-composite L-joints, the structure of the L-joint is disassembled and named, respectively, as shown in Figure 10. The composition of the metallic and GFRP components is marked in Figure 10, and the Cohesive structure consists of three different Cohesive elements (refer to Figure 9), defined as C-1, C-2, and C-3. Taking C-1 as an example, it consists of four independent layers of Cohesive elements, defined as C-1-1, C-1-2, C-1-3 and C-1-4, respectively.
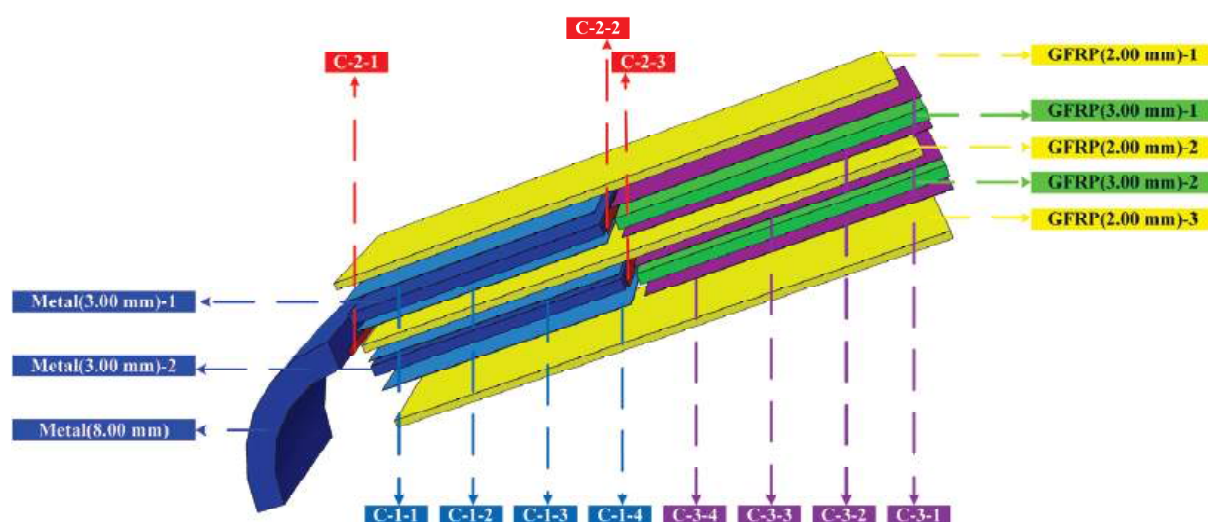
Figure 10. Schematic diagram of disassembly of metal-composite L-joint structure.

4.1. Analysis of Experimental and Simulation Results of L-Joints with Different Bonding Lengths

When the L-joints were damaged and failed, neither the metal structure nor the GFRP structure was significantly damaged, so the failure mode analysis was based on the equivalent 0-thickness cohesion element layer. According to different failure modes, L-joints with different bonding lengths are divided into three groups for discussion.

4.1.1. L-Joint with Bonding Length of 25.00 mm

Figure 11 shows the load–displacement curve for an L-joint with a bond length of 25.00 mm. In Figure 11, the simulated and experimental ultimate loads are approximately 1652.02 N and 1613.74 N, a difference of 2.37%. However, the overall stiffness in the finite element model is higher than in the experiment, and there are two main reasons for the stiffness error. First, due to the unique geometry of the L-joint, after the initial compressive load was applied, small defects were created in the bond area, which can cause a significant drop in stiffness. Second, since the in-plane shear was nonlinear, it mainly existed in the complex ±45° groove structure of the bonding interface, and the nonlinearity became more significant as the load increased. As a combined effect, the displacement results in the experiment are larger than the simulation results. The displacements when the simulation and experiment reach the ultimate load are 4.83 mm and 5.34 mm, respectively, with a difference of 9.6%.
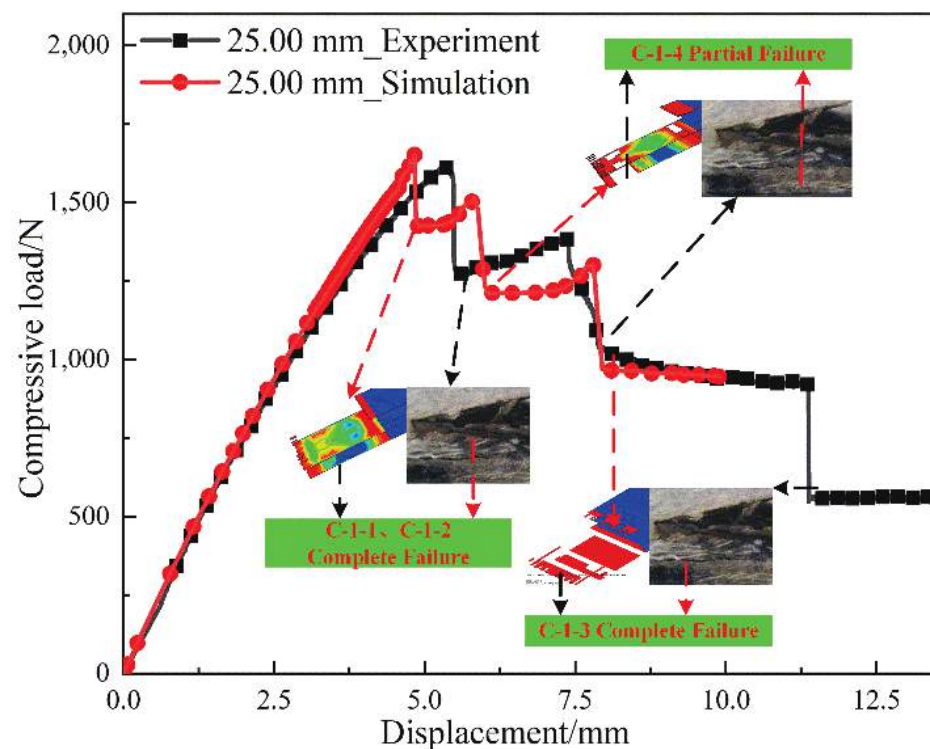
Figure 11. Load–displacement curves for L-joints with a bond length of 25.00 mm.

In Figure 11, the first load dump is due to the complete failure of C-1-1 and C-1-2, resulting in complete separation of the adhesive interface between Metal (3.00 mm)-1, GFRP (2.00 mm)-1 and GFRP (2.00 mm)-2. Obvious separation phenomena can be observed on both the experimental and simulated specimens. With the increase in compressive displacement, C-1-4 partially failed, resulting in incomplete separation of the bonding interface of Metal (3.00 mm)-2 and GFRP (2.00 mm)-3, thus forming the second load mutation. The third load dump was due to the complete failure of C-1-3 and the complete separation of the bonding interface of Metal (3.00 mm)-2 and GFRP (2.00 mm)-2. Obvious cracks were observed on both the experimental and simulated specimens. In the final stage of the experiment and simulation, C-1-4 was still under shear load, and C-3-1 was under peel load, resulting in the plasticity of Metal (3.00 mm)-1 and Metal (3.00 mm)-2; however, the displacement increased and the compressive load remained stable. The simulations agree with the experimental failure modes.

Figure 12 shows the load–displacement curve and its first-order differential curve of the L-joint compression simulation. Observing Figure 11, no matter the experimental or simulated compressive load, there is an obvious plateau before the sudden change. Therefore, the load–displacement curve of the compressive simulation is derived, and its first-order differential curve is obtained. A, B, and C in Figure 12, respectively, frame the stable load region. On the first-order differential curve, at their corresponding displacements, their derivatives are significantly reduced and greater than 0. We analyzed the entire process of the simulation and found that a small plastic deformation occurred in Metal (3.00 mm) before C-1 failed, and we believe that this was the cause of this phenomenon.

4.1.2. L-Joint with Bonding Length of 40.00 mm, 55.00 mm and 70.00 mm

Table 3 shows the comparison of the ultimate loads and corresponding displacements of different L-joint experiments and simulation curves. In Table 3, the deviation ratio between the experimental and simulated ultimate loads and their compressive displacements is within an acceptable range, indicating that the simulation can reflect the experimental results to a certain extent.
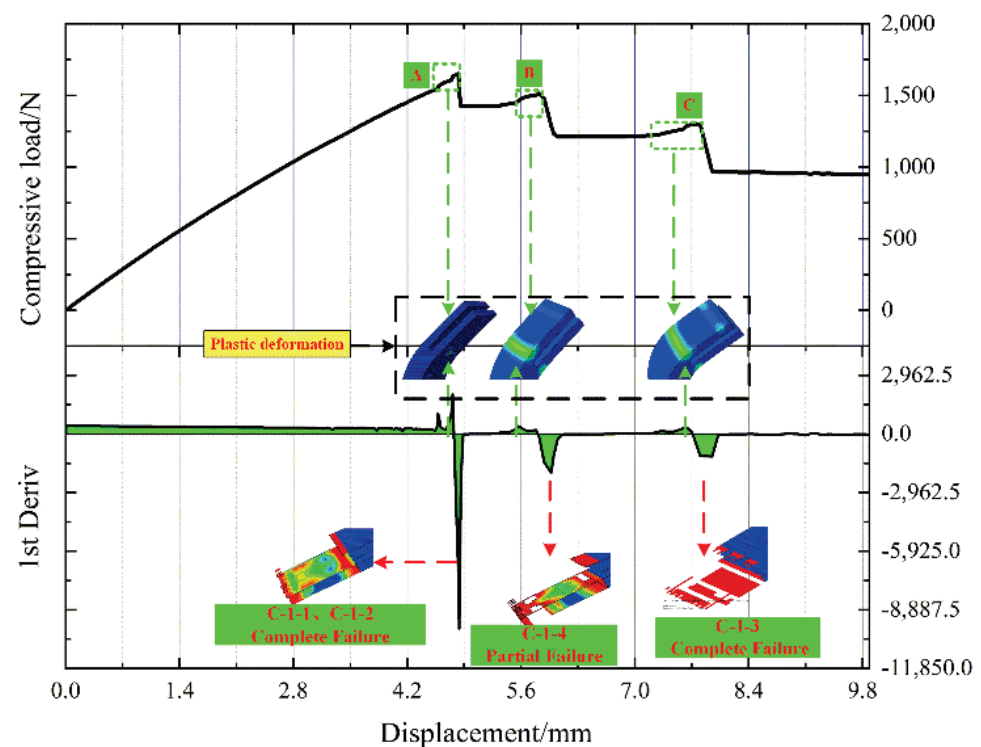
Figure 12. The load–displacement curve and its first derivative curve of the compression simulation of the L-joint, and (**A**) The first load stabilization stage; (**B**) The second load stabilization stage; (**C**) The third load stabilization stage.

Table 3. The comparison of the ultimate loads and corresponding displacements of different L-joint experiments and simulation curves.

Bonding Length	Ultimate Load/N			Displacement Corresponding to Ultimate Load/mm		
	Experiment	Simulation	Deviation Ratio/%	Experiment	Simulation	Deviation Ratio/%
40.00 mm	2166.25	2308.64	6.57	6.95	6.34	8.78
55.00 mm	2075.22	2255.98	8.71	6.41	5.38	16.06
70.00 mm	2071.91	2206.83	6.51	6.42	6.10	4.95

Figure 13 shows load–displacement curves for L-joints with different bonding lengths. In Figure 13, there is a relatively obvious slow growth phase before the first load dump, and the reason for the dump is more complicated than that of the L-joint with a bond length of 25 mm. When the load is abruptly changed, C-1-1, C-1-2 and C-1-3 all partially failed, and the SDEG value of C-1-1 was lower, although the compressive load decreased significantly; however, there was no complete separation of the bonded interface. In Figure 13, C-1-1 has less damage failure in the first load change, and peeling can be observed at the bonding edge of GFRP (2.00 mm)-2 and Metal (3.00 mm)-1. As the failures of C-1-2 and C-1-3 were extended, a second load mutation occurred, at which time, the bonding interface of GFRP (2.00 mm)-2 and Metal (3.00 mm) was completely separated; this can be observed in both experiments and simulations on obvious cracks. When the curve stabilizes, the L-joint enters a stable failure phase. Overall, the experimental and simulated failure modes are about the same.

Figure 13. Load–displacement curves for L-joints with different bonding lengths: (**a**) 40.00 mm, (**b**) 55.00 mm and (**c**) 70.00 mm.

Figure 14 shows the load–displacement curve and its first derivative curve of the compression simulation of the L-joint with different bonding lengths. Observing Figure 13, the loads of the experimental and simulated curves have a relatively gentle change stage, and we analyze the failure mode of the L-joint. In Figure 14, the load changes from A to B, and C-1-1, C-1-2 and C-1-3 both fail; furthermore, the plastic deformation of the metal part is also transferred from the two sides of the Metal (8.00 mm) to the outside and the inside of the Metal (8.00 mm), and finally transferred to the connection area with the metal (3.00 mm). This shows that when C-1-1 does not fail, Metal (8.00 mm) will bear the compressive load; when the load suddenly changes, C-1-1 gradually fails until it is completely deleted, and the plastic deformation of metal parts is also transferred from Metal (8.00 mm) to its connection area. From this, it can be inferred that the stress form of C-1-1 changes from interfacial peeling to interfacial shearing due to the change in the bonding length. Since the interfacial shear strength of C-1 is greater than the interfacial peel strength, C-1-1 is not easy to damage or destroy; conversely, C-1-2 is still in a state of interfacial peeling, so it is easier for it to fail.

4.1.3. L-Joint with Bonding Length of 85.00 mm, 100.00 mm and 115.00 mm

Table 4 shows the comparison of the ultimate loads and corresponding displacements of different L-joint experiments and simulation curves. In Table 4, the difference rate is also suitable, and the ultimate load and compression displacements are larger than those in Table 3, indicating that the mechanical properties of metal-composite L-joints improve with an increase in bonding length.
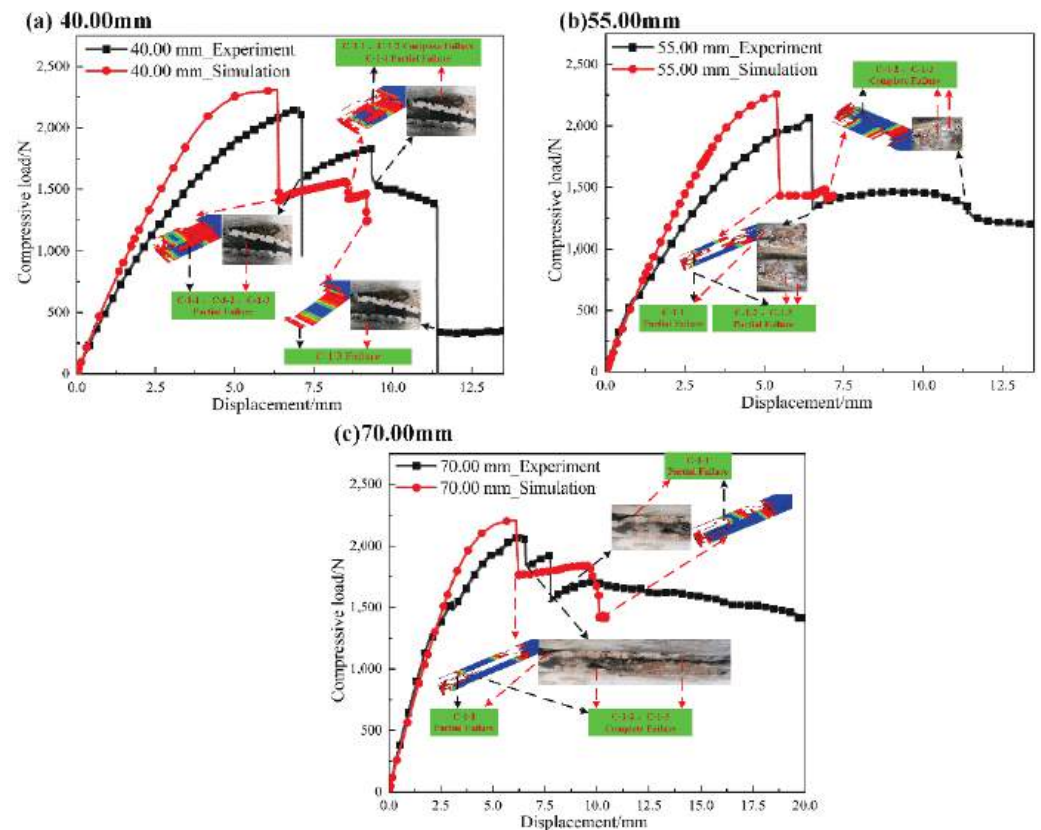
Figure 14. The load–displacement curve and its first derivative curve of the compression simulation of the L-joint with different bonding lengths: (**a**) 40.00 mm, (**b**) 55.00 mm and (**c**) 70.00 mm and (A) The first load stabilization stage; (B) The second load stabilization stage; (C) The third load stabilization stage.

Table 4. The comparison of the ultimate loads and corresponding displacements of different L-joint experiments and simulation curves.

Bonding Length	Ultimate Load/N			Displacement Corresponding to Ultimate Load/mm		
	Experiment	Simulation	Deviation Ratio/%	Experiment	Simulation	Deviation Ratio/%
85.00 mm	2050.47	2232.69	9.89	7.35	6.76	8.03
100.00 mm	2615.07	2677.64	2.39	11.56	10.83	6.31
115.00 mm	2422.13	2547.18	5.16	16.57	14.82	10.56

Figure 15 shows load–displacement curves for L-joints with different bonding lengths. In Figure 15a,b, the load variations of L-joints were mainly caused by the failure of C-1-2 and C-1-3. From the initial partial failure of C-1-1, C-1-2 and C-1-3 to the complete failure of C-1-2 and C-1-3, the damage of the overall structure occurred from partial debonding of GFRP (2.00 mm)-1 with Metal (3.00 mm)-1 to complete failure of GFRP (2.00 mm)-2 with Metal (3.00 mm). Clear cracks can be seen in Figure 15a,b. In Figure 15, partial failure of C-1-1 also occurred in the initial stage, and a clear small-scale peeling phenomenon was found in both experiments and simulations. The incomplete failure of C-1-1 caused the continuous bearing of Metal (8.00 mm); thus, the final stage of the load–displacement curve no longer fluctuates wildly. When the experiments and simulations were over, the metal-composite L-joint had higher residual strength and larger compressive displacement, which were maintained for a longer time.
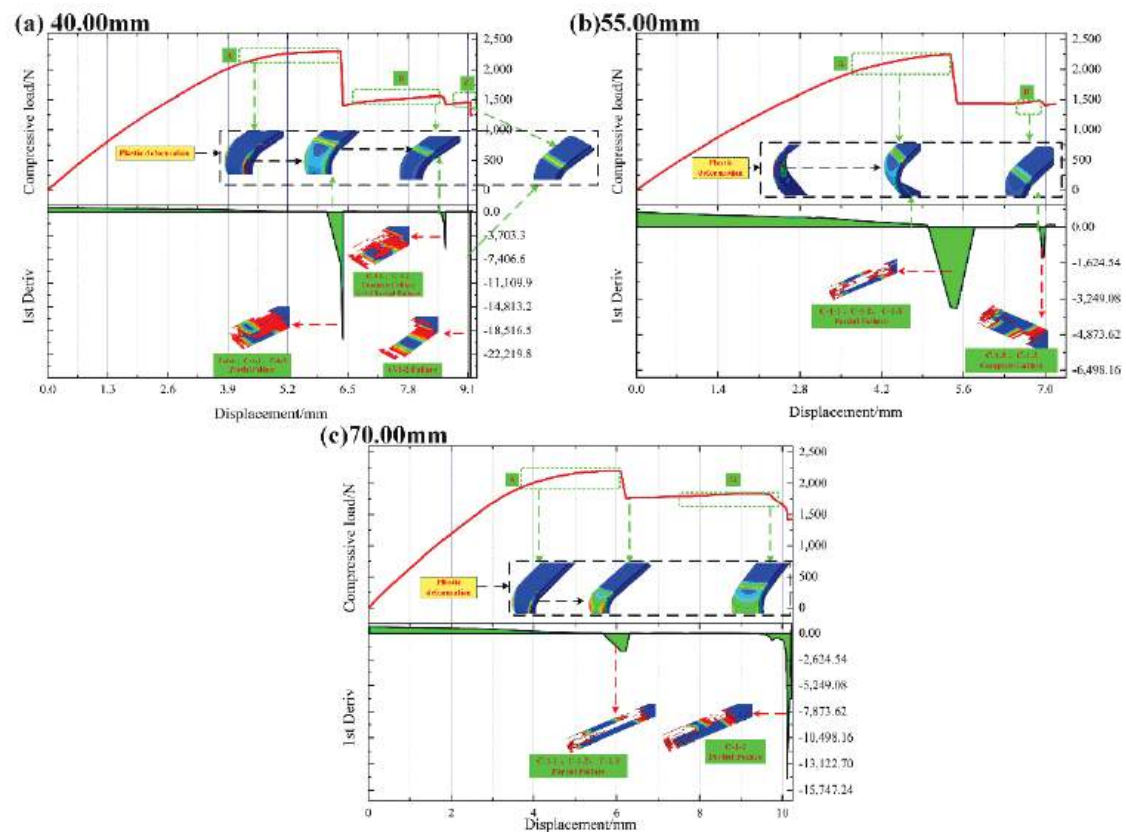
Figure 15. Load–displacement curves for L-joints with different bonding lengths: (**a**) 85.00 mm, (**b**) 100.00 mm and (**c**) 115.00 mm.

Figure 16 shows the load–displacement curve and its first derivative curve of the compression simulation of the L-joint with different bonding lengths. In Figure 16a,b, since C-1-1 did not fail completely, Metal (8.00 mm) was continuously subjected to bending loads and its plastic deformation continued to increase. With the failure of C-1-2 and C-1-3, the plastic deformation at the junction of Metal (3.00 mm) and Metal (8.00 mm) also increased. In Figure 16, the plastic deformation of the metal part continues until the end of the experiment and simulation. This means that in the experiments and simulations, the metal parts undergo severe bending deformation, and the L-joint specimens undergo significant overall inward bending. Therefore, although the metal-composite L-joint did not experience a sudden change in load, we stopped the experiments and simulations and considered the L-joint to have failed.

4.2. Relationship between Failure Mode and Compressive Load for L-Joints

Table 5 shows the different structural failure conditions in the joint, and its corresponding compressive load before the L-joint reaches the ultimate load. In Table 5, when the bonding length is 40.00–100.00 mm, both C-1-1, C-1-2 and C-1-3 have initial failure; when the bonding length is greater than 85.00 mm, the Metal (8.00 mm) has initial failure. The Metal (3.00 mm) did not fail until all L-joints reached their ultimate load.
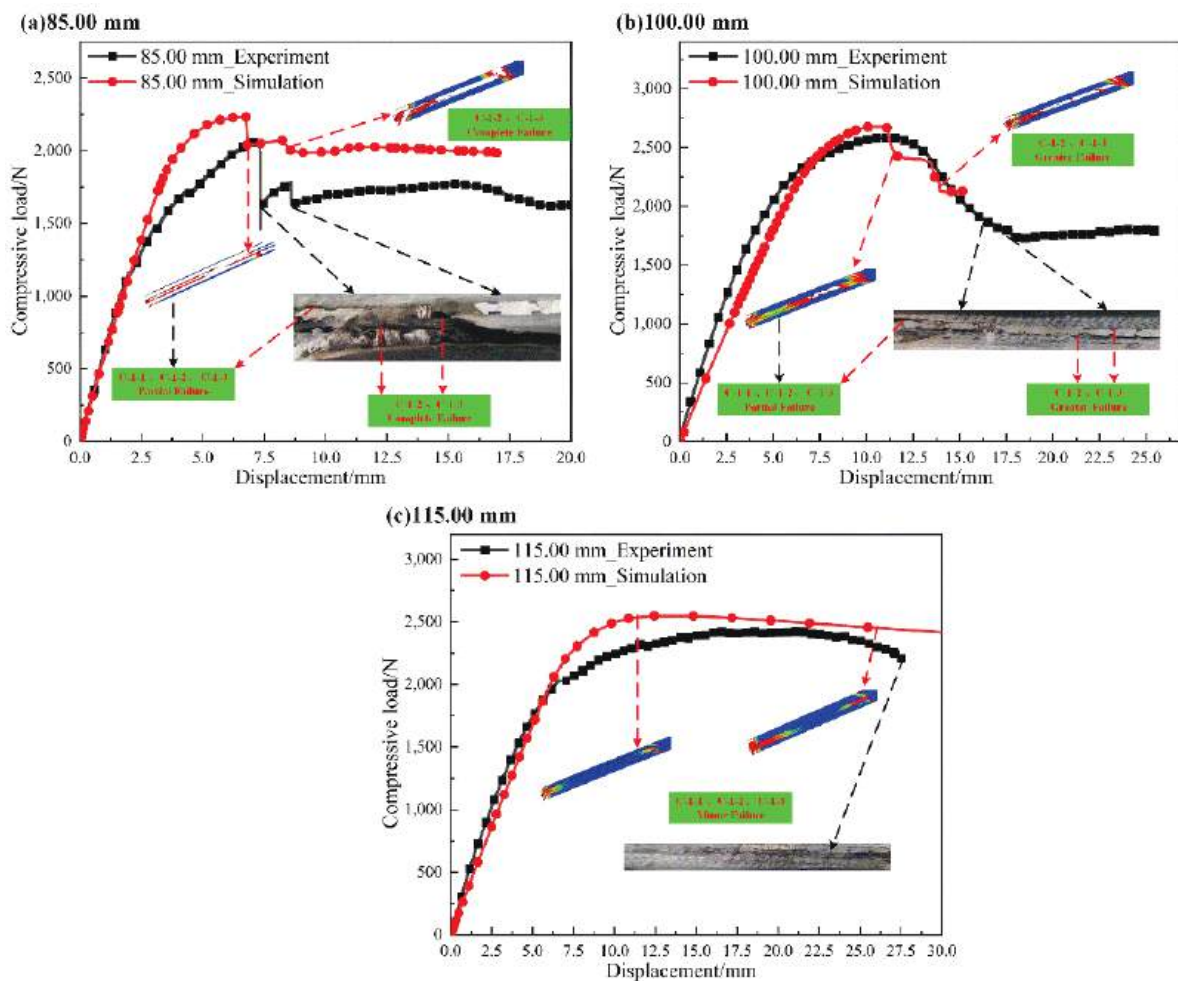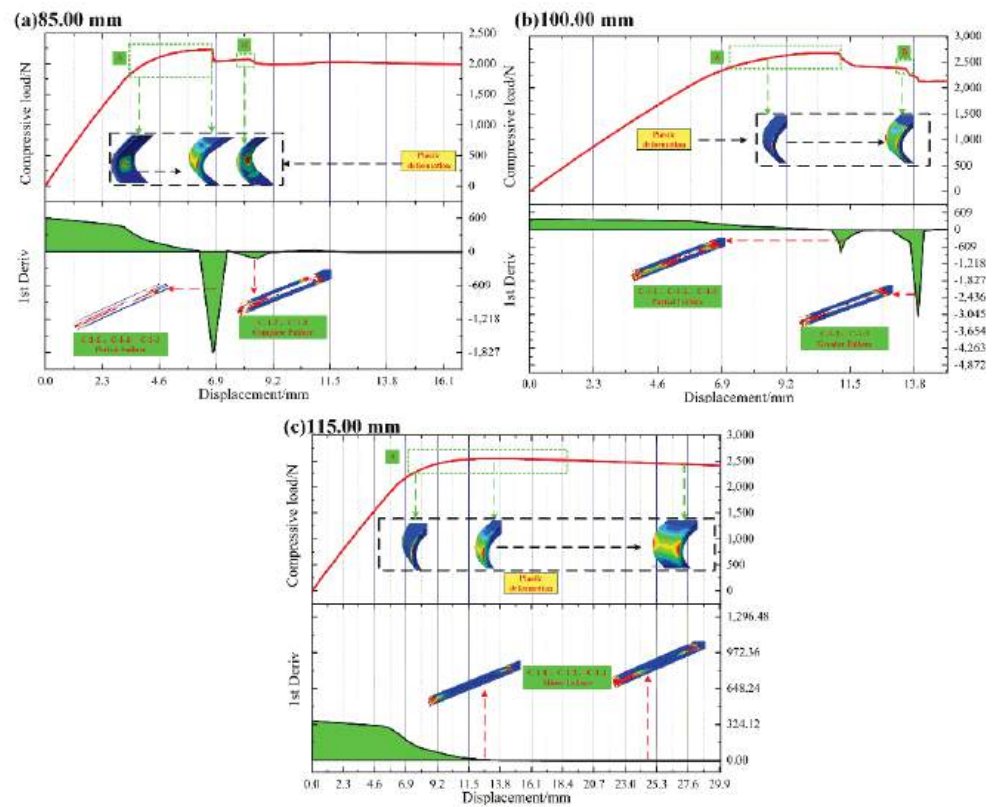
Figure 16. The load–displacement curve and its first derivative curve of the compression simulation of the L-joint with different bonding lengths: (**a**) 85.00 mm, (**b**) 100.00 mm and (**c**) 115.00 mm, and (A) The first load stabilization stage; (B) The second load stabilization stage.

Table 5. Simulated failure mode versus compressive load.

Failure Structure	C-1-1	C-1-2	C-1-3	C-1-4	Metal (8.00 mm)	Ultimate Load
Bonding length 25.00 mm	1058.38 N	1409.94 N				1652.02 N
Bonding length 40.00 mm	1588.23 N	2290.35 N	2300.11 N	2190.23 N		2308.61 N
Bonding length 55.00 mm	1746.51 N	2169.06 N	2224.84 N			2255.95 N
Bonding length 70.00 mm	1796.48 N	2101.12 N	2172.15 N			2206.80 N
Bonding length 85.00 mm	1525.68 N	1725.89 N	1868.06 N		1770.53 N	2232.63 N
Bonding length 100.00 mm	1075.14 N	1444.15 N	1581.67 N		2647.89 N	2679.46 N
Bonding length 115.00 mm					2188.98 N	2548.96 N

The damage and failure processes of metal-composite L-joints with different bond lengths are still questionable. When the bonding length is from 25.00 mm to 115.00 mm, there must be a critical point, which can determine the bonding length when different failure modes are converted. To find the critical point, more bond lengths were designed in the paper; the compression simulation of the L-joint was performed, and the corresponding loads of damage initiation and final failure were recorded, as shown in Figure 17. Figure 17 shows a damage and failure prediction diagram for the metal-composite L-joints. In Figure 17, when the bond length is 40.00 mm and 95.00 mm, the ultimate load of the L-joint changes greatly, and the main failure mode also shifts accordingly. When the bonding length is from 40.00 to 80.00 mm, the initial failure of C-1-3 occurs, and the ultimate load of the L-joint increases and remains stable. When the bond length is from 85.00 to 120.00 mm, the Metal (8.00 mm) has an initial failure; the ultimate load further increases, and finally reaches the maximum at the bond length of 100.00 mm, then remains stable.
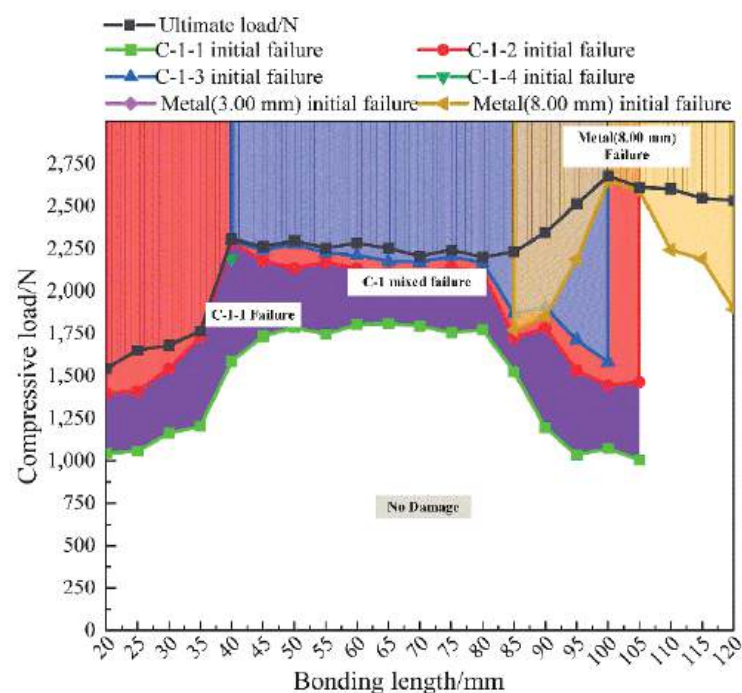
Figure 17. Damage and failure prediction diagram for metal-composite L-joints.

4.3. Relationship between Failure Mode and Compressive Displacement for L-Joints

Combined with the analysis in Section 3.1, it is concluded that different failure modes are closely related to compression displacement, as shown in Table 6. In Table 6, light green indicates partial failure, dark green indicates larger failure, and yellow indicates complete failure. When the metal-composite L-joint is subjected to a compressive load, C-1-1 bears both the interfacial shear load and the peeling load generated by the compressive load moment. However, as the bonding length increases, the moment of the compressive load gradually decreases, and the shear load that C-1-1 can withstand gradually increases. Therefore, when the bonding length increases to a certain extent, C-1-1 does not fail. The failure of C-1-2 and C-1-3 usually occurs after the damage to C-1-1, when the shear component of the compressive load is not on the same plane as the interface of C-1-2 and C-1-3. As a result, C-1-2 and C-1-3 are more prone to peeling. When C-1-2 and C-1-3 failed, Metal (3.00 mm) continued to carry compressive loads, resulting in deformation. When C-1 did not completely fail, the compressive load was transferred to Metal (8.00 mm), which deformed the overall structure.

Table 6. Simulated failure mode versus displacement.

Failure Structure	C-1-1	C-1-2	C-1-3	C-1-4	Metal (3.00 mm)	Metal (8.00 mm)
Bonding length 25.00 mm	2.89 mm 4.48 mm	4.04 mm 4.48 mm	8.03 mm	6.12 mm	8.03 mm	
Bonding length 40.00 mm	6.40 mm 8.61 mm	6.40 mm 8.61 mm	6.40 mm 9.16 mm	6.40 mm	9.16 mm	
Bonding length 55.00 mm	5.79 mm	5.79 mm 7.00 mm	5.79 mm 7.00 mm		7.00 mm	
Bonding length 70.00 mm	6.32 mm 10.21 mm	6.32 mm	6.32 mm		6.32 mm	
Bonding length 85.00 mm	7.35 mm	7.35 mm 9.07 mm	7.35 mm 9.07 mm		9.07 mm	
Bonding length 100.00 mm	12.00 mm	12.00 mm	12.00 mm			14.14 mm
Bonding length 115.00 mm						12.45 mm

Figure 17 can only predict failure modes under compressive loading of metal-composite L-joints of different bond lengths before the ultimate load. The metal-composite L-joint designed in the paper has a large residual strength after reaching the ultimate load. In order to be able to clearly analyze the entire failure process of the L-joint, a prediction diagram between compression displacement and failure mode was also made, as shown in Figure 18.
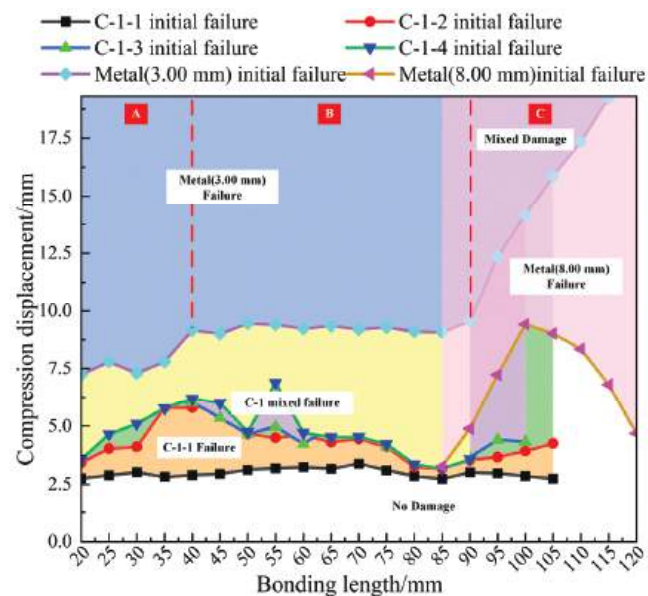
Figure 18. Damage and failure prediction diagram for metal-composite L-joints and Metal (3.00 mm) initial failure displacement fluctuating increasing stage (**A**), stable stage (**B**) and stable increasing stage (**C**).

The solid line in Figure 18 represents the compressive displacement connection line between C-1 and the onset of failure of the metal part. It can be seen from Figure 18 that the initial failure displacement of C-1-1 is relatively stable, and the value is small. After C-1-1 was damaged, C-1-2 and C-1-4 suffered shear damage. Overall, their damage initiation displacement was smaller than that of C-1-3. The initial damage of C-1-2, C-1-3, and C-1-4 in Figure 18 are mixed, and this phenomenon is caused by the different locations of stress concentrations due to different bond lengths.

In Figure 18, Metal (3.00 mm) had an initial failure, indicating that C-1-2 and C-1-3 had completely failed. Metal (3.00 mm) undergoes plastic deformation (plastic deformation exceeding 0.01 is the beginning of damage), and the plastic deformation of Metal (3.00 mm) can be divided into three stages, as shown in A, B and C in Figure 18. The initial damage displacement of Metal (3.00 mm) in stage A was small, and the bearing capacity of the metal-composite L-joint was weak. The initial damage displacement of Metal (3.00 mm) in stage B was relatively stable, and the maximum displacement and residual strength of the metal-composite L-joint were higher. In stage C, the initial damage displacement of Metal (3.00 mm) increased with the increase in the bonding length. The damage in this part was the mixed damage of Metal (3.00 mm) and Metal (8.00 mm). Both the maximum displacement and the residual strength of the metal-composite L-joint were improved due to the involvement of Metal (8.00 mm) in the bearing load.

In Figure 18, Metal (8.00 mm) begins to deform plastically, which indicates that C-1-1 has not completely failed. When Metal (8.00 mm) fails, the overall structure of the metal-composite L-joint is bent, and its included angle is less than 90°. When the bonding length is less than 100.00 mm, the main failure mode of the L-joint changes from Metal (8.00 mm), bending to Metal (3.00 mm), due to the failure of C-1-1; when the bonding length is greater than 100.00 mm (as C-1-1 did not fail) the main failure mode of the L-joint would be the continuous bending of Metal (8.00 mm). The initial displacement of the damage was small, which would result in a large bending of the joint.

Based on the above analysis, we can conclude that the bonding length of 100.00 mm is a better choice. It not only has a larger ultimate load and residual strength, but can also undergo a larger compression displacement. However, if the metal-composite L-joint requires no sudden change in load, the bonding length can be designed to be more than 105.00 mm. If the metal-composite L-joint requires freedom from bending deformation of the structural main body, a bonding length between 40.00 and 90.00 mm can be selected.

5. Conclusions

In the paper, a metal/composite L-joint with a groove structure was designed and seven groups of specimens with different bonding lengths were fabricated, to study the effect of different bonding lengths on the performance of the joint.

(1) In the simulation analysis of metal/composite L-joints, the groove structure is equivalent to a 0-thickness element layer. The applicability of the simulation method is verified by comparing the ultimate load, displacement and failure mode of the test and simulation.

(2) The failure modes of L-joints with different bond lengths are analyzed, and the following conclusions are drawn: When the bonding length is 25.00 mm and 40.00 mm, C-1-1 firstly fails completely, then C-1-2 and C-1-3 fail completely, and most of the structures of metal components and composite components are de-bonded; when the bonding length is 55.00 mm, 70.00 mm and 85.00 mm, C-1-1 fails first but not completely, while C-1-2 and C-1-3 fail completely, and Metal (3.00 mm) continues to carry the compressive load; when the bonding length is 100.00 mm and 115.00 mm, C-1 does not fail completely. At this time, the metal component bears a large bending load, and the overall structure of the metal/composite L-joint is greatly bent.

(3) When the bond length is 25.00–40.00 mm, after the metal/composite L-joint fails, the metal and composite components warp due to excessive compressive displacement. When the bonding length is greater than 100.00 mm, there is no obvious separation of the metal and composite components, and the metal/composite L-joint has obvious overall bending.

(4) Finally, the simulation method is used to simulate the compression of more metal/composite L-joints with different bond lengths, and the prediction graphs of failure displacement and failure mode are produced. According to the failure prediction diagram, designers can select the corresponding bonding length according to their own needs; this provides a reference for the design of metal/composite hybrid L-joints.

References

1. Khosravani, M.; Weinberg, K. Experimental investigations of the environmental effects on stability and integrity of composite sandwich t-joints: Experimentelle untersuchung des umwelteinflusses auf die belastbarkeit von t-stößen in sandwich-platten. *Mater. Und Werkst.* **2017**, *48*, 753–759. [CrossRef]
2. Santiuste, C.; Sánchez-Sáez, S.; Barbero, E. A comparison of progressive-failure criteria in the prediction of the dynamic bending failure of composite laminated beams. *Compos. Struct.* **2010**, *92*, 2406–2414. [CrossRef]
3. Savin-Barcan, M.; Beznea, E.; Chirica, I. *Influence of Fabrication Imperfections on Dynamic Response of a Sandwich Composite Panel of a Ship Deck Structure*; Presented at IOP Conference Series: Materials Science and Engineering; IOP Publishing: Constanta, Romania, 2018; Volume 400, p. 032008.
4. Mouritz, P.A.; Gellert, E.; Burchill, P.; Challis, K. Review of advanced composite structures for naval ships and submarines. *Compos. Struct.* **2001**, *53*, 21–42. [CrossRef]
5. Li, H.; Tu, S.; Liu, Y.; Lu, X.; Zhu, X. Mechanical properties of l-joint with composite sandwich structure. *Compos. Struct.* **2019**, *217*, 165–174. [CrossRef]
6. Khosravani, R.M.; Nasiri, S.; Weinberg, K. Prediction of fracture in sandwich-structured composite joints using case-based reasoning approach. *Procedia Struct. Integr.* **2018**, *13*, 168–173. [CrossRef]
7. Shen, W.; Yan, R.; Luo, B.; Zhu, Y.; Zeng, H. Ultimate strength analysis of composite typical joints for ship structures. *Compos. Struct.* **2017**, *171*, 32–42. [CrossRef]
8. Kim, J.; Park, B.; Han, Y. Evaluation of fatigue characteristics for adhesively-bonded composite stepped lap joint. *Compos. Struct.* **2004**, *66*, 69–75. [CrossRef]
9. Feih, S.; Shercliff, H. Adhesive and composite failure prediction of single-l joint structures under tensile loading. *Int. J. Adhes. Adhes.* **2005**, *25*, 47–59. [CrossRef]
10. Feih, S.; Shercliff, H. Composite failure prediction of single-l joint structures under bending. *Compos. Part A Appl. Sci. Manuf.* **2005**, *36*, 381–395. [CrossRef]
11. Kai, Q.; Renjun, Y.; Mingen, C.; Haiyan, Z. Failure mode shift of sandwich composite l-joint for ship structures under tension load. *Ocean. Eng.* **2020**, *214*, 107863. [CrossRef]
12. Zeng, H.; Yan, R.; Xu, L. Failure prediction of composite sandwich l-joint under bending. *Compos. Struct.* **2018**, *197*, 54–62. [CrossRef]
13. Kinvi-Dossou, G.; Boumbimba, R.M.; Bonfoh, N.; Garzon-Hernandez, S.; Garcia-Gonzalez, D.; Gerard, P.; Arias, A. Innovative acrylic thermoplastic composites versus conventional composites: Improving the impact performances. *Compos. Struct.* **2019**, *217*, 1–13. [CrossRef]
14. Zhang, J.; Xie, Q.; Xie, Y.; Zhou, L.; Wang, Z. Investigation of mechanical performances of composite bolted joints with local reinforcements. *Sci. Eng. Compos. Mater.* **2018**, *25*, 75–83. [CrossRef]
15. Liu, J.Y.; Chen, X. Evaluations of the effective material properties of carbon nanotube-based composites using a nanoscale representative volume element. *Mech. Mater.* **2003**, *35*, 69–81. [CrossRef]
16. Mohammadpour, E.; Awang, M.; Kakooei, S.; Akil, H.M. Modeling the tensile stress–strain response of carbon nanotube/polypropylene nanocomposites using nonlinear representative volume element. *Mater. Des.* **2014**, *58*, 36–42. [CrossRef]
17. Hashin, Z. Fatigue failure criteria for unidirectional fiber composites. *J. Appl. Mech. Dec.* **1981**, *48*, 846–852. [CrossRef]
18. Boufaida, Z.; Boisse, J.; André, S.; Farge, L. Mesoscopic strain field analysis in a woven composite using a spectral solver and 3d-dic measurements. *Compos. Struct.* **2017**, *160*, 604–612. [CrossRef]
19. Tan, S.C. A progressive failure model for composite laminates containing openings. *J. Compos. Mater.* **1991**, *25*, 556–577. [CrossRef]
20. Kang, Z.; Shi, Z.; Lei, Y.; Xie, Q.; Zhang, J. Effect of the surface morphology on the bonding performance of metal/composite hybrid structures. *Int. J. Adhes. Adhes.* **2021**, *111*, 102944. [CrossRef]
21. Truong, -H.V.; Kwak, B.-S.; Roy, R.; Kweon, J.-H. Cohesive zone method for failure analysis of scarf patch-repaired composite laminates under bending load. *Compos. Struct.* **2019**, *222*, 110895. [CrossRef]

22. Truong, -H.V.; Nguyen, K.-H.; Park, S.-S.; Kweon, J.-H. Failure load analysis of c-shaped composite beams using a cohesive zone model. *Compos. Struct.* **2018**, *184*, 581–590. [CrossRef]

23. Nguyen, -H.K.; Ju, H.-W.; Truong, V.-H.; Kweon, J.-H. Delamination analysis of multi-angle composite curved beams using an out-of-autoclave material. *Compos. Struct.* **2018**, *183*, 320–330. [CrossRef]

Article

Effect Mechanism and Simulation of Voids on Hygrothermal Performances of Composites

Zhu Liu, Yongpeng Lei *, Xiangyang Zhang, Zhenhang Kang and Jifeng Zhang *

Key Laboratory of Advanced Ship Materials and Mechanics, College of Aerospace and Civil Engineering, Harbin Engineering University, Harbin 150001, China; liuzhu0618@hrbeu.edu.cn (Z.L.); zxy121382021@163.com (X.Z.); kangzhenhang@hrbeu.edu.cn (Z.K.)

* Correspondence: yongpenglei@126.com (Y.L.); jfzhang@hrbeu.edu.cn (J.Z.); Tel.: +86-132-6362-8085 (Y.L.); +86-131-9953-2163 (J.Z.)

Abstract: Voids are comment defects generated during the manufacturing process and highly sensitive to moisture in the hygrothermal environment, which has deleterious effects on the mechanical performances. However, the combined impact of void content and water-absorbed content on mechanical properties is not clear. Based on the random sequential adsorption algorithm, a microscale unit cell with random distribution of fibers, interfaces and voids was established. The quantitative effects of voids content on strength and modulus under the loading of transverse tension, compression and shear were investigated by introducing a degradation factor dependent on water content into the constitutive model, and the different failure mechanisms before and after hygrothermal aging were revealed. Conclusively, before hygrothermal aging, voids induce the decrease in mechanical properties due to stress concentration, and every 1% increase in the void content results in a 6.4% decrease in transverse tensile strength. However, matrix degradation due to the absorbed water content after hygrothermal aging is the dominant factor, and the corresponding rate is 3.86%.

Keywords: void content; hygrothermal aging; micromechanics; failure mechanism

1. Introduction

Voids are the most common type of defects induced by the residual air during the manufacturing process of composites [1], which significantly affect the hygrothermal aging performances of composites by altering the stress field and moisture field [2,3]. Particularly, void defects are highly sensitive to the moisture under the hygrothermal environment, and they can further decrease the matrix-dominated properties, which can ultimately reduce the service life of composite structures [4,5]. Thus, it is crucial to understand the effect of voids on hygrothermal aging performances and reveal their failure mechanism.

Various characterization techniques were reported for identifying the microscopic void structures and voids content, including densities measurement method [6], optical image analysis [7], infrared thermography [8] and micro X-ray computed tomography [9]. However, these techniques are either unreliable due to inherent testing errors or complex operations at high costs. Thus, many researchers employed the finite element method (FEM) to study the behavior of composites with voids [10–12]. Based on the FEM model and analytical model, a parametric study was conducted by Huang et al. [13] to reveal the effects of voids geometry and distribution on the elastic constants. Nikopour et al. [14] developed a representative volume element (RVE) with the order voids' arrangement to investigate the effect of voids on an estimation of effective transverse properties of composites. Vajari et al. [15] further developed the RVE model with random distribution of fibers and voids, and revealed that the presence of voids significantly reduces the strength of composites. A regression model was presented by Chen et al. [16] to predict the effects of voids on the strength and modulus, based on FEM results. RVE models with different distribution patterns and shapes for voids were established by Wang et al. [17], and

the effects of voids on the transverse tensile strength considering thermal residual stress were analyzed. A combined micro-scale and meso-scale methodology were proposed by Mehdikhani et al. [18] to examine the effect of intra-laminar voids on the evolution of cracks. Hyde et al. [19] vastly discussed the RVE model with a single void and a stress concentration factor was introduced to quantify the effect of void volume fraction, void orientation, shape density and associated void defects to illustrate mechanical properties of the composites. Though voids are highly sensitive to moisture in the hygrothermal environment, only several literatures reported the effects on moisture absorption performances. Gueribiz et al. [20] proposed analytical solutions by solving unit cell problems on RVE to determine the effective diffusivities of composites, including the Porous Matrix model, Four-phase model and Self-consistent model, and investigated the effects of voids on the moisture diffusivities of composites. Bourennane et al. [21] developed an RVE model with an elliptical-shaped void, considering two types of closed and open voids, and investigated the effects of geometric configuration and volume fraction on the moisture diffusion process in the damage polymer matrix.

PA6 matrix can absorb about 10 wt% water [22], and the absorbed water has deleterious effects on the mechanical performances of PA6-based composites [23–25]. It is necessary to understand the combined impact of hygrothermal aging and voids defects on the water absorption properties and mechanical performances for PA6-based composites. Although extensive studies involved the effects of voids on mechanical properties, these studies focused on composite laminates without hygrothermal aging. In fact, the failure mechanism of composite induced by the presence of voids before and after hygrothermal aging is totally different. Thus, to reveal the failure mechanism, the degradation of mechanical properties dependent on the absorbed water content should be introduced into the constitutive model.

2. Computational Model Considering Hygrothermal Aging

2.1. RVE Model with Voids

The presence of void defects has deleterious effects on the service performance of composites. Several manufacturing parameters including molding pressure, curing temperature and resin viscosity can induce the formation of void defects in the matrix, as shown in Figure 1a. In composites, voids are found in different volume fractions, shapes and sizes. In this study, the main purpose is to reveal the effect of voids content on the water absorption behavior and mechanical performances. Thus, the void generation algorithm fulfil the following terms: (1) voids only exist in the matrix, and voids are approximately circular in shape; (2) the void distribution is random, the positions of voids are automatically generated using the random sequential adsorption (RSA)-based algorithm programmed in MATLAB (2018a) [26,27]; (3) as shown in Figure 1b, void size distribution is in accordance with the Weibull distribution, and the values of scale and shape are 15 and 1.5, respectively; (4) there is no intersection between voids and fibers, and void contents of 0%, 1%, 2%, 3%, 4% and 5% are considered in this work, as shown in Figure 1c.
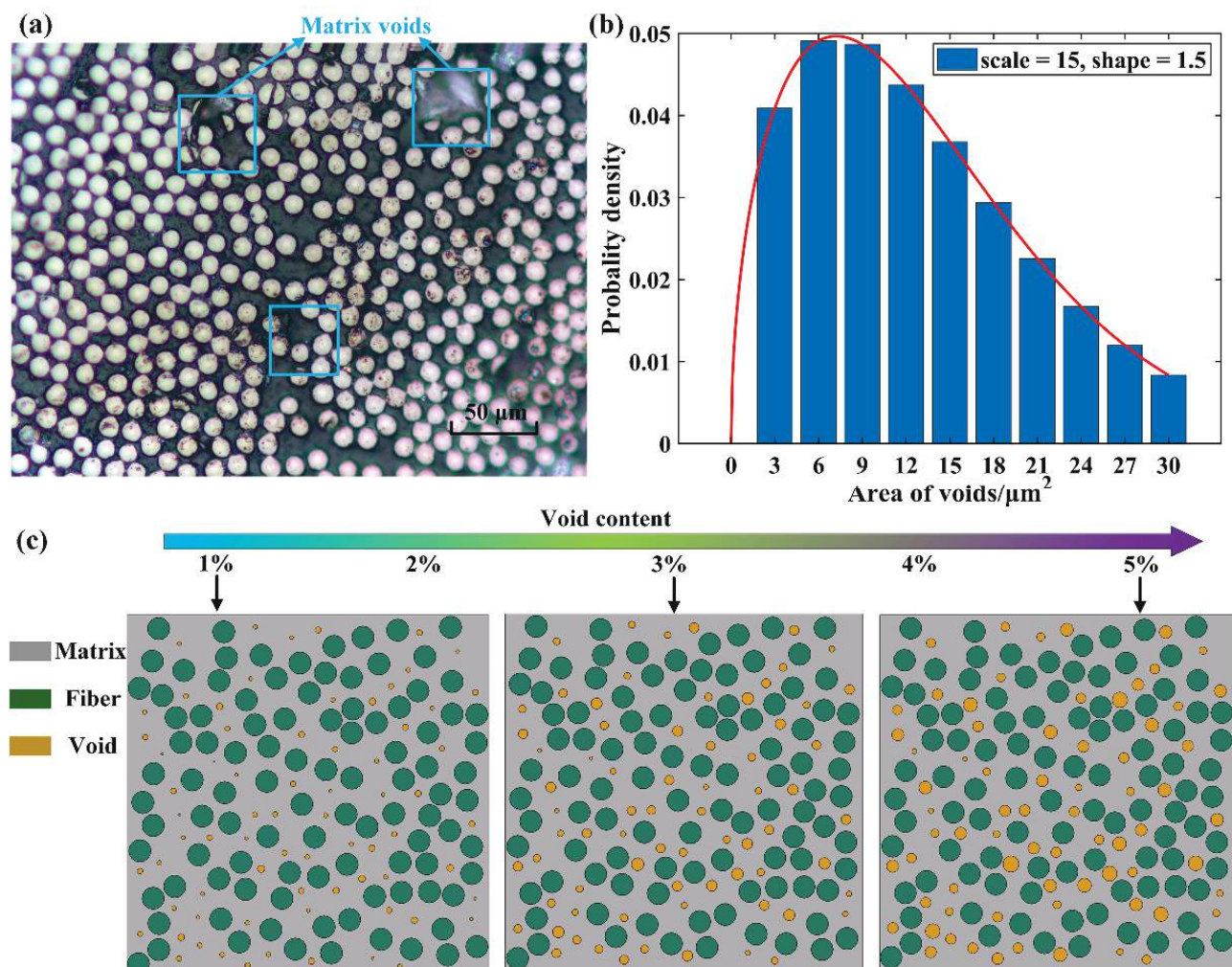
Figure 1. RVE model with different contents of voids. (**a**) metallographic diagram of voids distribution, (**b**) distribution of void size, (**c**) geometric model.

2.2. Constitutive Models in Water Diffusion Process

Moisture absorption testing is conducted to measure the masses of PA6 resin and CF/PA6 composites, according to the standard of ASTM D5229. Water absorption curves are plotted by recording the masses of samples over time. Based on Fick law, the maximum moisture content (M_i) and the diffusivity coefficient (D_i) of component materials can be obtained except for voids. Based on the thermodynamic laws for air, the water content absorbed by voids can be determined by the following equation [21]: $M_v = 0.622 P_V / (P_{atm} - P_V)$, and P_V, P_{atm} are the saturation vapor pressure and the atmospheric pressure, respectively. In this work, it is assumed that the diffusivity of voids is one order of magnitude higher than that of the matrix, due to its faster water absorption rate. More details of water absorption parameters are listed in Table 1.

Table 1. Water absorption parameters for component materials in the CF/PA6 composites immersed at 50 °C water bath.

	Matrix	Carbon Fiber	Voids	Composite
Diffusivity (10^{-6}mm^2/s)	D_m	D_f	D_v	D_{eff}
	4.64	0	46.4	2.16
Water content (%)	M_m	M_f	M_v	M_{eff}
	9.4	0	23.5	5.26

The mechanical properties of the matrix and the interface decrease significantly with the water content increasing under the hygrothermal environment. Thus, an improved traction-separation cohesive law is developed to study the debonding failure under different load conditions, by introducing degradation factors for strength, modulus, and fracture energy. Carbon fibers are modeled as transversally isotropic and linear elastic. The yielding of the PA6 matrix is described by the extended linear Drucker-Prager criterion [28], which considers different yielding strengths in tensile, compression and shear behaviors:

$$\begin{cases} F = t - p \tan \beta - d = 0 \\ t = \frac{1}{2}q \left[1 + \frac{1}{k} - \left(1 - \frac{1}{k}\right)\left(\frac{r}{q}\right)^3 \right] \end{cases} \quad (1)$$

where p is the hydrostatic stress, q is the Mises equivalent stress, r is the third invariant of deviatoric stress, β is the slope of the linear yield surface in the p–t stress plane, d is the cohesion of the material and k is the ratio of the yield stress in triaxial tension to the yield stress in triaxial compression.

Moreover, the ductile criterion is employed to predict damage onset of the PA6 matrix by assuming the equivalent plastic strain as a function of stress triaxially η ($\eta = -p/q$). Here, η takes the value of $1/3$, $-1/3$, 0 under the uniaxial tension, uniaxial compression and pure shear, respectively. Besides the yield criterion, the effect of water content on the mechanical properties is also considered in this work. Experimental hygrothermal aging has quantified the degradation rate of PA6 mechanical properties with respect to the absorbed water content [23], and the retention percentage of strength and modulus can be described as follows:

$$\begin{cases} \sigma_t = 37 + \frac{100 - 37}{1 + \exp[1.08 \times (M_t - 2.76)]} \\ E_t = 15.51 + \frac{100 - 15.51}{1 + \exp[1.66 \times (M_t - 2.81)]} \end{cases} \quad (2)$$

where σ_t and E_t are the retention percentage of tensile strength and elastic modulus after hygrothermal aging, M_t is the water-absorbed content.

The interface behavior is described with the cohesive element model defined in terms of bi-linear traction-separation law. Similarly, the relationship between the mechanical properties and the water content is assumed to be the same as that of PA6 matrix. The cohesive elements between the neighboring matrix and fiber elements are automatically inserted in the Abaqus. All mechanical parameters used in this work are listed in Table 2.

Table 2. Mechanical properties for CF/PA6.

Fiber	E_2^f (GPa)	μ_{23}^f	α^f ($10^{-6}/^\circ$C)	β^f	ρ^f (kg/m^3)
	16.54	0.25	-0.83	0	1810
Matrix	E^m (GPa)	μ^m	σ_{yt} (MPa)	σ_{yc} (MPa)	α^m ($10^{-6}/^\circ$C)
	2.19	0.34	25	50	4
	β^m	ρ^m (kg/m^3)			
	0.1	1080			
Interface	K_n^0 (N/mm^3)	K_s^0 (N/mm^3)	K_t^0 (N/mm^3)	t_n^0 (MPa)	t_s^0 (MPa)
	3.13×10^4	5.0×10^4	5.0×10^4	17.11	40.67
	t_t^0 (MPa)	G_n^c (N/mm)	G_s^c (N/mm)	G_t^c (N/mm)	
	40.67	0.22	0.23	0.23	

3. Experimental Verification

To validate the accuracy of the FEM model, macro-mechanical testing is conducted by comparing the strength, modulus and failure model. Firstly, CF/PA6 prepregs are prepared by a melt impregnation technique, and CF/PA6 composite laminates are fabricated using a high temperature compressing molding technique. The average fiber volume fraction is 30 vol% determined by the ablation method according to ASTM D2584, and the voids content is about 0.13% determined by optical image analysis. Then, the transvers tensile, compression and shear test are also conducted according to the ASTM D3039, D6641 and

D5379, respectively. Five replicated samples are used for mechanical testing, and the corresponding strength and modulus are the average of the five tests. The strength and modulus with standard deviation in the transvers tensile, compression and shear test are listed in Table 3.

Table 3. Mechanical properties of CF/PA6 composites in the transvers tensile, compression and shear test.

	Transverse Tension	Transverse Compression	Transverse Shear
Strength (MPa)	18.10 ± 1.87	52.69 ± 3.25	14.75 ± 1.28
Modulus (GPa)	3.50 ± 0.38	3.59 ± 0.16	7.60 ± 0.23

The stress–strain curves of the RVE model without voids under the transverse tension, transverse compression and transverse shear are shown in Table 2. The blue images in the first row are the equivalent plastic strain (PEEQ) nephogram of the whole RVE model, which indicates the plastic deformation under the three loading modes. The white images in the second row are the stiffness degradation (SDEG) nephogram of cohesive elements, which indicates the damage revolution of the interface during the different load process. The three columns of the images are corresponding to the onset of interface failure ("1"), the peak load ("2") and the end of loading ("3"), respectively. The mechanical performances, including strength and modulus determined by FEM, are also compared with the experimental data to verify the accuracy of numerical simulation.

Under transverse tension, the fiber/matrix is the main reason for the failure process. Figure 2a shows that the initial damage occurs at the fiber poles along the loading direction and gradually evolved to the fiber/matrix debonding. Remarkably, the stress concentration arises in the regions where the clustering degree of fibers is relatively higher, and these regions are susceptible to the interfacial debonding. Then, the matrix at the vicinity of interfacial debonding undergoes plastic deformation and accumulation damaged until ultimate failure. Final interfacial debonding at different locations are linked by matrix cracks, and the final damage cracks of RVE are formed perpendicular to the loading direction. Under transverse compression, the final failure is primarily through the shear bonds of the matrix. As shown in Figure 2b, the initial failure is induced by the interfacial debonding and then a plastic shear band is formed oriented at about 56° with respect to compression direction. The shear bonds further develop along this direction, accompanied by interfacial debonding to jointly final failure of composites. Under transverse shear, the failure mechanism is dominated by interfacial debonding and matrix yielding. The initial fracture is triggered by interfacial debonding, similarly to the transverse compression case. As the matrix holds progressively shear loads, an obvious plastic band is formed and cracks grow until the final failure, as shown in Figure 2c.

The strength and modulus determined from this work agree well with the experimental results, and the relative errors are less than 10% except for the transverse shear modulus. The ultimate damage mode is quite similar to the experimentally observed results [29–31].

Thus, the present computational framework is effective in predicting mechanical properties and failure modes of composites, as well as composites with void defects.
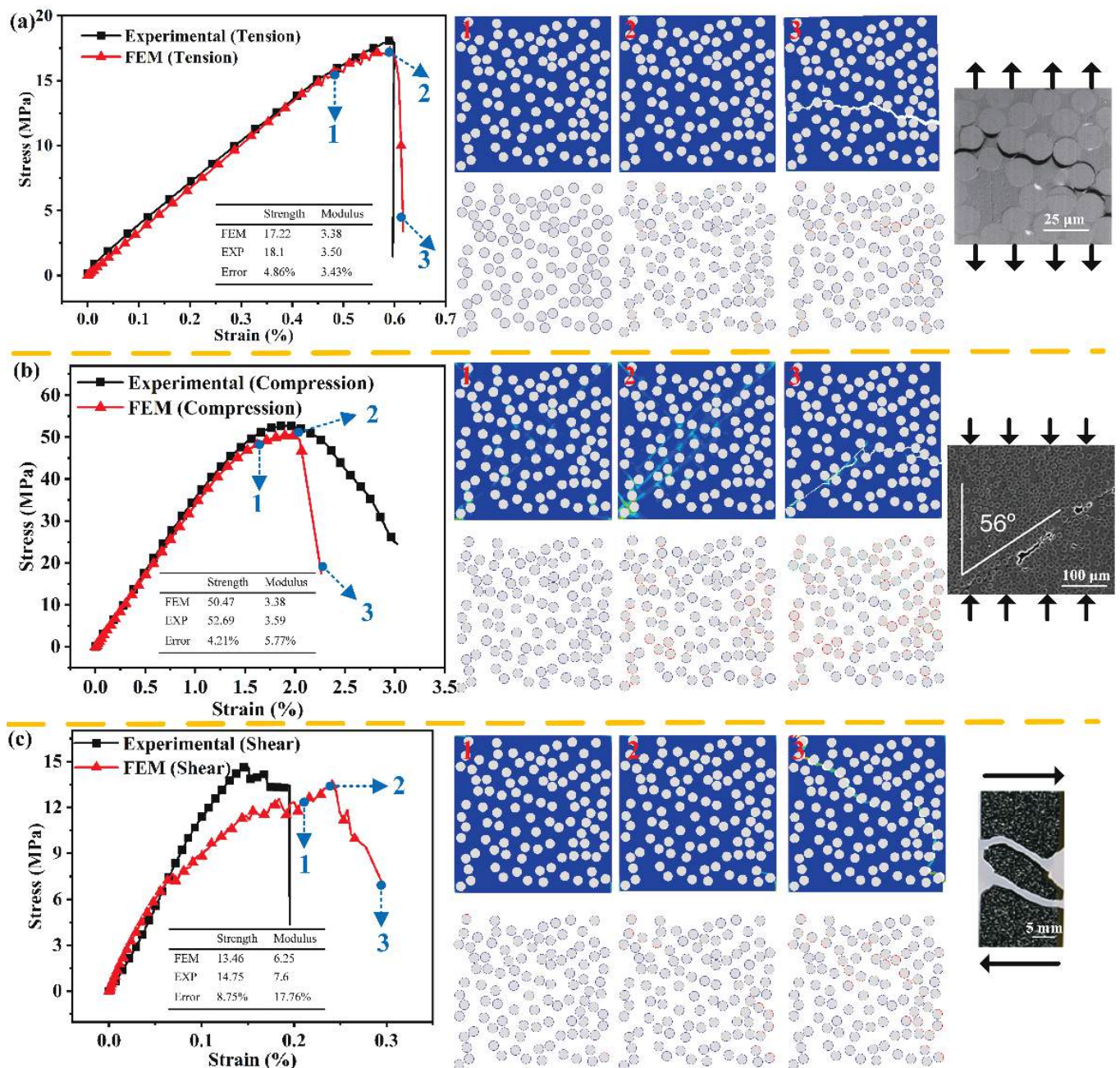
Figure 2. Failure progression in an RVE model under the loading of (**a**) transverse tension, (**b**) transverse compression, (**c**) transverse shearing.

4. Results and Discussion

4.1. Water Absorption Behavior

Several numerical approaches are available for estimating the effective moisture diffusion coefficient of composites with voids defects by solving a unit cell problem on the RVE model. The existing theoretical models are listed in Table 4. The diffusivity ratio between composites and matrix (D_{eff}/D_m) is employed to validate the accuracy of the predicting models. Compared with the experimental value (0.47), the results of the FEM model range from 0.52 to 0.57, which is closer to the experimental data. Thus, the FEM model is accurate and effective, which can be selected as the benchmark to evaluate the accuracy of the other theoretical models. As shown in Figure 3, D_{eff}/D_m calculated from the Four-phase model and the Self-consistent model have apparent discrepancies with the result of FEM. In contrast, the Porous-matrix model agrees well with FEM when the

void content is less than 1%, but the difference increases significantly with the increasing void content.

Table 4. Several theoretical models for calculating the effective diffusion coefficient of composites containing voids [20].

Model	Expression
Porous-matrix model	$\frac{D_{eff}}{D_m} = \left[1 + 2\alpha_{mv} V_v \frac{(D_v/D_m)-1}{(D_v/D_m)+1}\right]\frac{1-V_f}{1+V_f}$ with $\alpha_{mv} = \frac{\rho_{water}}{M_m \rho_m (1-v_{void})}$
Four-phase model	$\frac{D_{eff}}{D_m} = \frac{(1-kV_f)(1+k)+\Phi(1+kV_f)(k-1)}{(1+kV_f)(1+k)+\Phi(1-kV_f)(k-1)}$ with $k = (V_v + V_f)/V_f$, $\Phi = \alpha_{mv}(D_v/D_m)$
Self-consistent model	$\frac{D_{eff}}{D_m} = \frac{1}{2(1+k)}\left(\lambda + \sqrt{4\frac{D_v}{D_m}(k^2-1)+\lambda^2}\right)$ with $\lambda = \frac{D_v}{D_m}(1+k(2V_v-1))+(1+k(1-2V_v))$
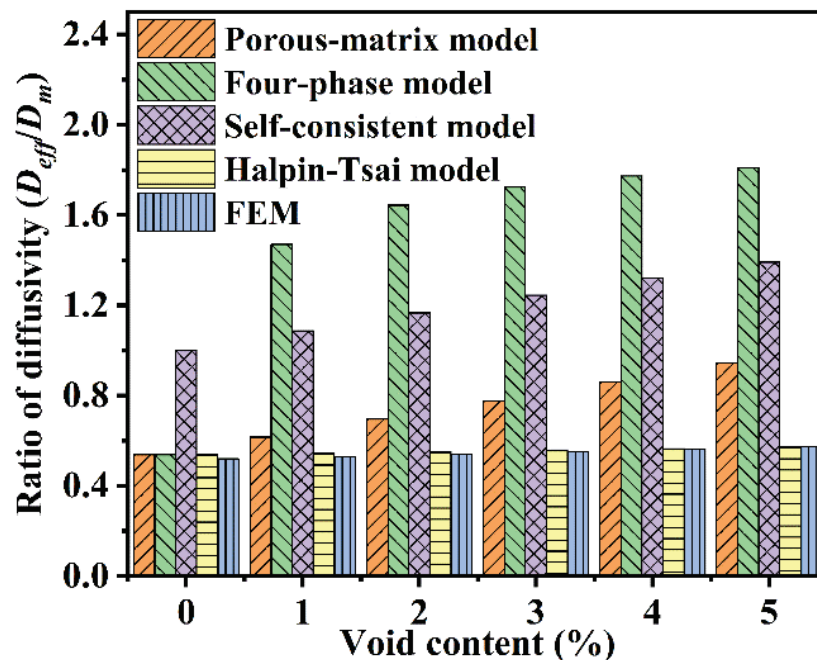
Figure 3. Comparison of prediction models and numerical simulation results.

In this study, a more accurate theoretical model based on the Halpin–Tsai equation is developed to predict the diffusion coefficient of three-component composites containing the carbon fiber, the PA6 matrix and the voids. The classical Halpin–Tsai equation ignores the presence of voids, and it is widely used to predict the transverse water diffusivity of two-component composites [32].

$$\frac{D'_{eff}}{D_m} = \frac{1 - V_f + \psi'\left(1 + V_f\right)}{1 + V_f + \psi'\left(1 - V_f\right)} \tag{3}$$

with

$$\psi' = \alpha' \frac{D_f}{D_m} \tag{4}$$

where D_f, D_m and D'_{eff} are the diffusivity of the fiber, matrix, and composite, respectively, V_f is volume fraction of fibers, α' and ψ' is the moisture concentration and diffusion coefficient gap between the fiber and the matrix, respectively, and α' is defined as follows: $a' = m_f r_f / m_m r_m$

To introduce the water absorption parameters of voids to the Halpin–Tsai equation, the three-phase composite model can be divided into two two-phase composite models (submodel-1 and submodel-2). Submodel-1 comprises the matrix and voids, and voids are embedded in the matrix to form the porous matrix phase. In Submodel-2, the porous matrix phase and the fiber consist of the composite. By substituting the parameters of component materials in submodel-1 and submodel-2 into Equation (3), the transverse diffusivity of three-component composites can be expressed as:

$$\frac{D_{eff}}{D_m} = \frac{1 - V_f}{1 + V_f} \cdot \frac{1 - V_v + \alpha(1 + V_v)D_v/D_m}{1 + V_v + \alpha(1 - V_v)D_v/D_m} \tag{5}$$

where D_v and V_v are the diffusivity and volume fraction of voids, respectively, α is diffusion coefficient gap between voids and the matrix.

As shown in Figure 3, D_{eff}/D_m determined by the Halpin–Tsai model based on Equation (5) agree well with FEM results. Therefore, the Halpin–Tsai model is accurate and effective, which can rapidly predict the transverse diffusivity of composite with different volume fractions of voids.

As shown in Figure 4, the water absorption curves obey the Fick law, and the moisture absorption ability can be obviously enhanced due to the presence of voids. Water absorption parameters increase linearly as the void content increases, and every 1% increase in the void content results in a 1.76% and 3.1% increase in the water diffusion coefficient and water-absorbed content, respectively. The trend of curve for the water-absorbed content versus void content agrees well with that of carbon/epoxy composites [33].
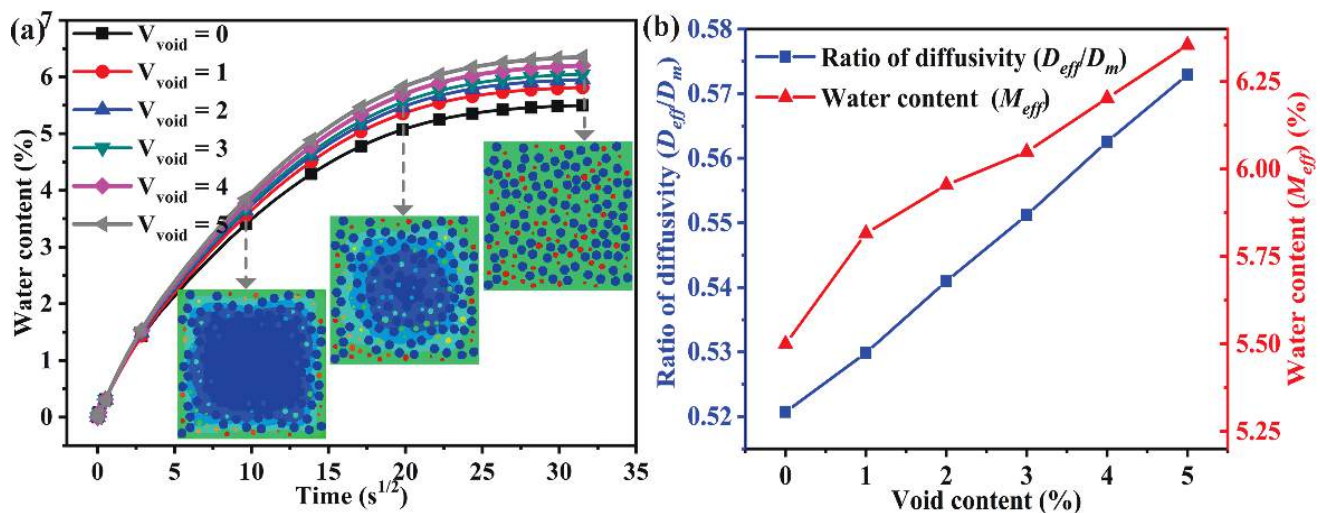
Figure 4. Effect of void content on the water absorption performance, (**a**) water content, (**b**) ratio of diffusivity.

4.2. Residual Stress Evolution

Residual stresses occur in composite structures during the curing process and subsequence service in the hygrothermal environment, which play an important role in composite deformation and mechanical properties. However, the experimental measurement of the residual stresses is often costly and complicated. Alternatively, a numerical simulation method is employed to predict the residual stresses during the process of cooling contraction and hygroscopic expansion, respectively.

As shown in Figure 5a, in the preparation of CF/PA6 laminates by the molding process, the CF/PA6 prepreg is heated to a processing temperature, and subsequently solidified upon cooling from 160 °C to the ambient temperature (about 25 °C). The mismatch in the coefficients of thermal expansion (CET) between the CFs ($-0.83 \times 10^{-6}/°C$) and the PA6 matrix ($4 \times 10^{-6}/°C$) results in a significant difference in deformation behaviors. Figure 5d

describes the changing revolution of residual stress for the matrix and the fiber with the temperature, in the curing process. Through the stress nephogram and the corresponding legend, under the deformation coordination constraint, tensile stress arises in the PA6 matrix, and compressive stress occurs in the CFs. Stress components (S11/S22, S12, Mises stress) increase linearly with the decreasing temperature for the reference points in the CFs and matrix (Figure 5b). In contrast, the average value of stress components for the CFs and matrix is shown in Figure 5c. The average stresses for the CFs and matrix are relatively small after the temperature cooling to 25 °C, with average Mises stress of 1.70 MPa and 1.44 MPa, respectively, which indicates the thermal residual stress is not the main reason for the mechanical damage.

The PA6 matrix is highly sensitive to the moisture under the hygrothermal environment due to the presence of amide groups -CO-NH-, and the absorbed water content can reach 10%. Moreover, the retention rate of mechanical properties for the PA6 matrix decreases exponentially as the water content increases. Thus, water content has deleterious effects on the dimensional stability and mechanical properties in the service environment. The residual stress of hygroscopic expansion in the water absorption process can accelerate mechanical aging.

As shown in Figure 6a, and after CF/PA6 composites' immersion in the distilled water, the volume of the PA6 matrix expands, while the CFs are not affected by the water. Figure 6d describes the changing revolution of residual stress for the matrix and the fiber with the temperature under the hygrothermal environment. Through the stress nephogram and the corresponding legend, under the deformation constraint, compressive stress arises in the PA6 matrix and tensile stress occurs in the CFs. Figure 6b shows the evolution of stress components for the reference points in the CFs and matrix in the water absorption process. The magnitude of residual stress depends on two factors: water content difference and moisture expansion coefficients. The PA6 matrix exhibits tensile stress before hygrothermal aging, and it is the thermal residual stress in the manufacturing process. In the initial water absorption process, the tensile stress increases from 0.58 MPa to 1.65 MPa. It is explained as follows: the reference point is located in the middle area of the RVE model, and the water diffusion front has not arrived. Tensile stress arises in the middle area due to the water content difference between the internal and external area, resulting in an increase in the stress value. As the water diffuses into the middle area and the water content increases, compressive stress occurs in this area, which can reduce the value of the tensile stress and change the stress from the tension (1.65 MPa) to compression (−1.52 MPa). On the contrary, the tension stress arises in the CFs and the stress value increases from −0.46 MPa to 1.15 MPa, though a small fluctuation occurs in the initial process. The average value of stress components for the CFs and matrix in the water absorption is shown in Figure 6c. The shear stress (S12) is almost unchanged, but the normal stress (S22) of the matrix decreases from 0.43 MPa to −1.19 MPa and that of CFs increases from −0.56 MPa to 1.63 MPa. It is worth noting that the transverse tensile strength of CF/PA6 composites is about 9.5 MPa. Compared with the thermal residual stress, the hygrothermal residual stress is closer to the interfacial strength, which can promote initiation and propagation of cracks in the matrix and interfacial debonding.
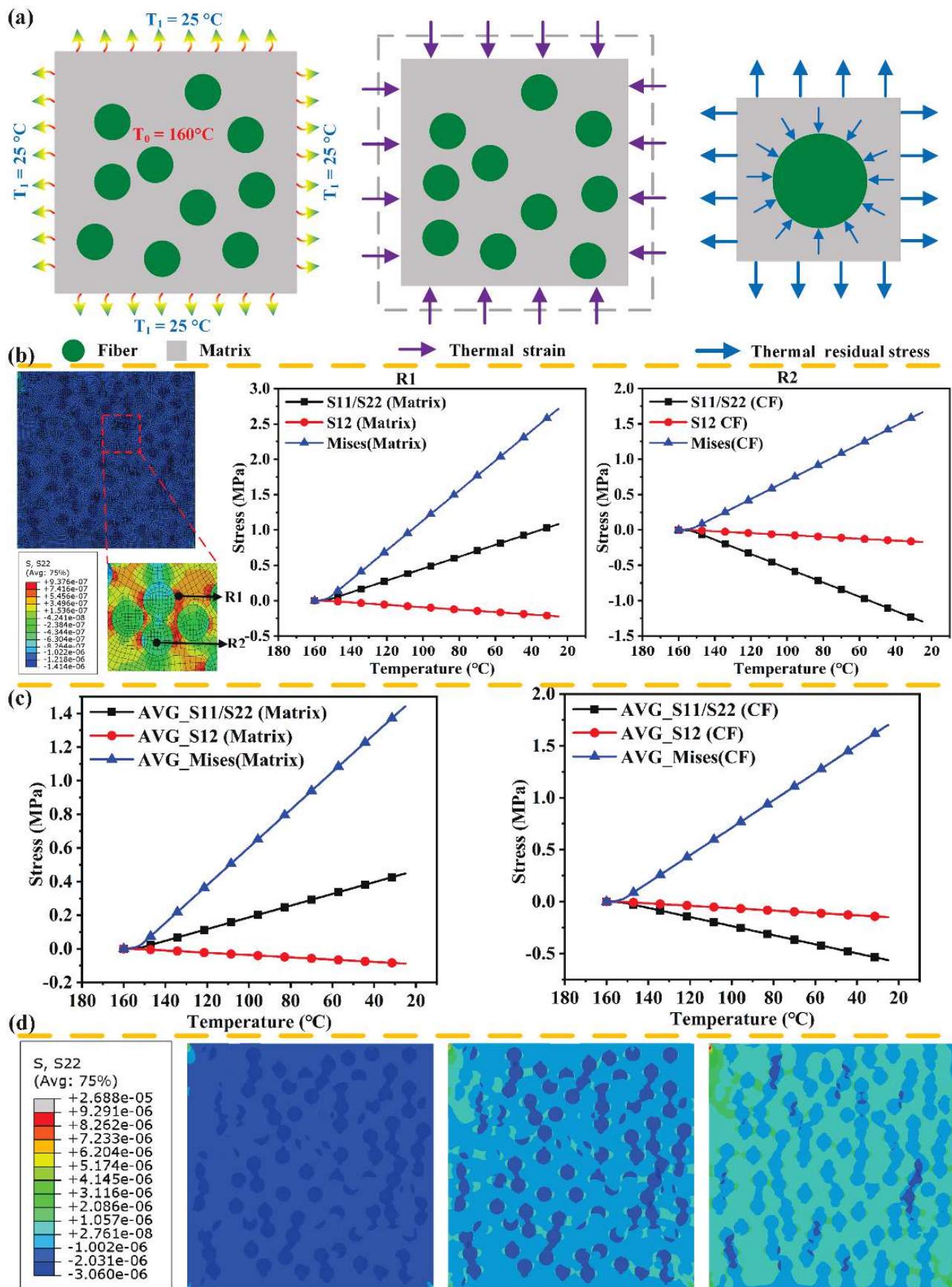
Figure 5. Residual stress of cooling contraction in the molding process, (**a**) schematic diagram, (**b**,**c**) residual stress of component material, (**d**) colored stress patterns.
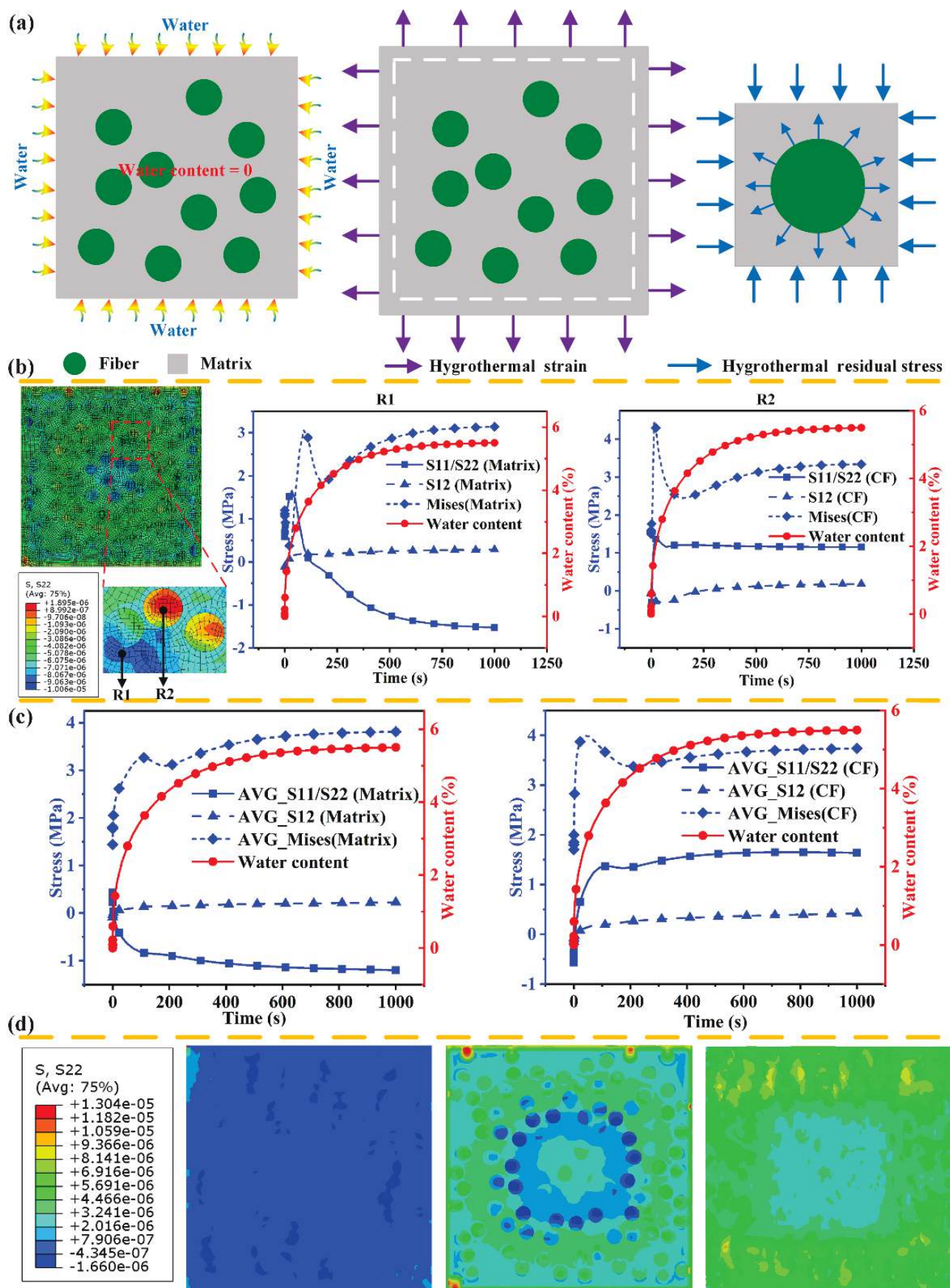
Figure 6. Residual stress of hygroscopic expansion in water absorption process, (**a**) schematic digram, (**b**,**c**) residual stress of component material, (**d**) colored stress patterns.

To study the effects of voids content on the residual stress in the cooling contraction and hygroscopic expansion process, the same material properties and boundary conditions are applied into the RVE models with the different volume fractions of voids.

Moreover, to avoid duplication and redundancy, only the evolution of Mises stress is selected to quantize the effects of voids content. As shown in Figure 7, the Mises stress decreases significantly from 1.5 MPa to 0.47 MPa in the cooling contraction process, and decreases from 3.77 MPa to 2.88 MPa in the hygroscopic expansion process. It is worth noting that the decrease rate is evident with voids content of 1%, but the reduction trend gradually slows down. This indicates that the stress distribution can be obviously changed, and the presence of voids can greatly weaken the residual stress. The increase in the voids content has slight effects on the decrease of residual stress. However, voids have beneficial effects on the relief or decrease the residual stress to some extent. Before and after hygrothermal aging, the effects of voids on the mechanical properties under the different loading conditions will be discussed in the next section.
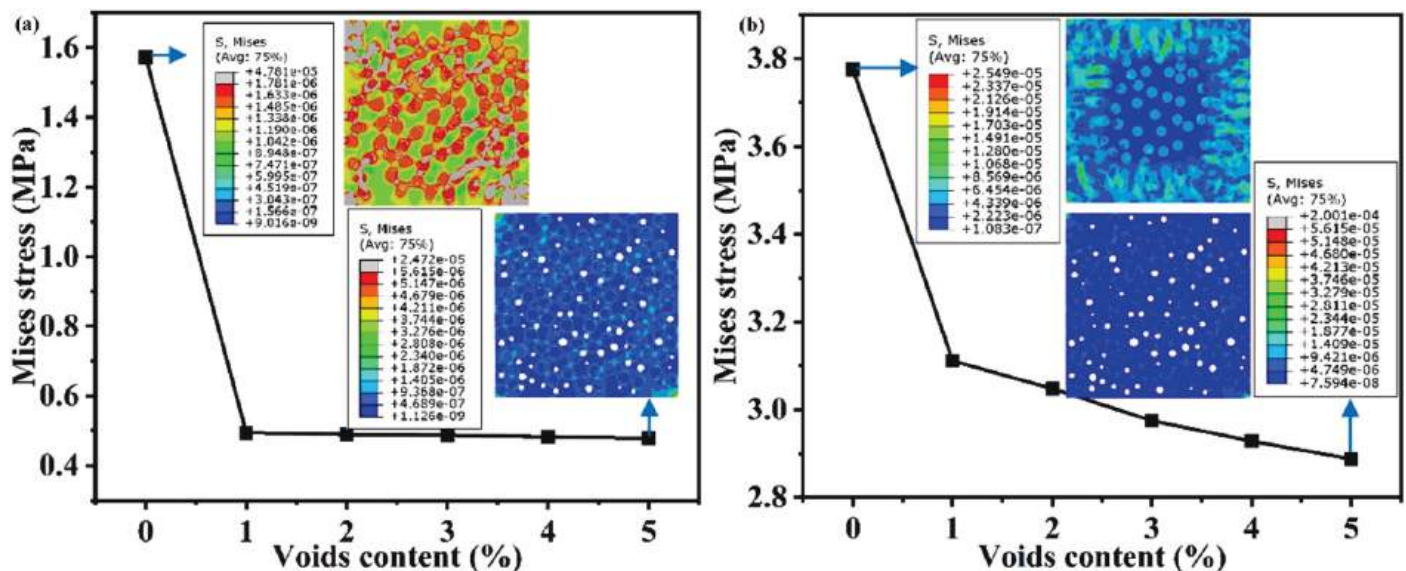
Figure 7. Effect of voids content on the residual stress, (**a**) Mises stress of cooling contraction, (**b**) Mises stress of hygroscopic expansion.

4.3. Mechanical Performance and Failure Analysis

4.3.1. Voids Effects on Mechanical Performances

Figure 8 plots the strength and elastic modulus as a function of voids content without hygrothermal aging for three loading cases, including transverse tension, compression and shear. The voids content has more deleterious effects on the strength than the modulus under different loading, and the reduction of strength is about two times that of modulus. Quantitatively, voids with a volume fraction of 5% decrease the tensile strength by 32.0% and about 16.1% for tensile modulus. In general, the strength in the transverse direction is dominated by the performance of the matrix and the interface. However, the modulus is depended on the modulus and volume fractions of component materials, and it can be estimated using a rule-of-mixture law. It is important to note that the modulus of CFs (16.54 GPa) is one order of magnitude higher than that of the matrix (2.19 GPa). Voids change the stress distribution and lead to the stress concentration in the matrix, but has a slight influence on CFs. Therefore, the strength is more sensitive than the modulus with different voids contents.
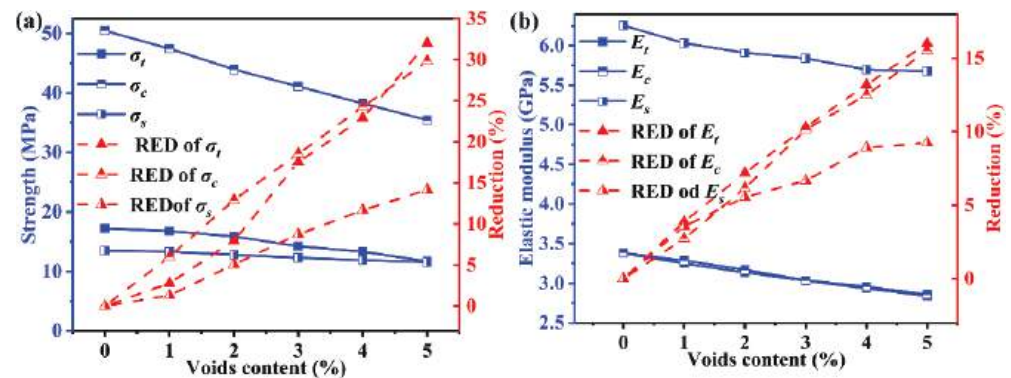
Figure 8. Effect of voids content on the mechanical performance for unaged samples, (**a**) strength, (**b**) elastic modulus.

For the models with 5% voids content before hygrothermal aging, the transverse tensile strength (σ_t) suffers the greatest reduction (32.0%), followed by that of the transverse tensile strength (σ_c) with a reduction (29.8%). In contrast, the reduction of transverse shear strength (σ_s) is minimum (14.15%). The reduction of modulus follows the same order: E_t (16.1%) > E_c (15.5%) > E_s (9.24%). Quantitatively, every 1% increase in the void content results in a 6.4%, 5.96% and 2.83% decrease in σ_t, σ_c and σ_s respectively. Similarly, every 1% increase in voids content results in a 3.22%, 3.1% and 1.85% decrease in E_t, E_c and E_s respectively. This phenomenon can be explained by the angle between crack propagation and loading direction. The angle of crack propagation in the transverse tension, compression and shear is about 90°, 56° and 45°, respectively. This angle is a positive correlation with the reduction rate of mechanical performance.

There is a distinct inflection point in the evolution of strength as shown Figure 9. When voids content is less than 1%, the reduction rate is significantly higher than from 1% to 5%. With the voids content ranging from 1% to 5%, every 1% increase in the void content results in a 3.86%, 2.91% and 2.19% decrease in σ_t', σ_c' and σ_s' respectively. These reductions for the models after hygrothermal aging are lower than those of corresponding unaged models, and the failure mechanism is different. For unaged models, the voids content is the main reason for the mechanical degradation. In contrast, the voids and the water content combined determine the mechanical degradation after the hygrothermal aging. However, the contribution of voids content and water content to the reduction of mechanical performances are different. The decrease in the tensile strength induced by voids content (32.0%) is lower than that of water content (63%), and the negative effects of voids content are diminished. However, the variation trend of modulus is consistent with that of unaged models. After hygrothermal aging, every 1% increase in voids content results in a 3.16%, 2.73% and 2.13% decrease in E_t', E_c' and E_s' respectively.
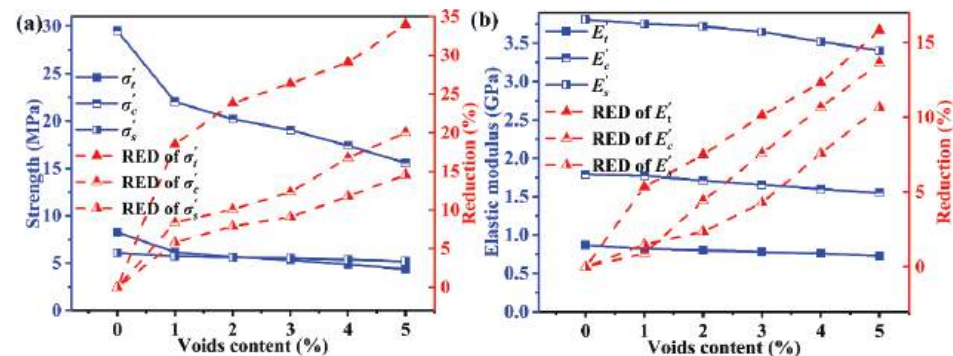
Figure 9. Effect of voids content on the mechanical performance for hygroscopic saturated samples, (**a**) strength, (**b**) elastic modulus.

4.3.2. Progressive Failure Analysis

Figure 10 shows the final damage of RVE models with three different voids content under the transverse tension, compression and shear. It is noted that RVE models have different final damage paths with different voids content. Voids significantly change the stress distribution and cause stress concentration of RVE models. The initial damage is induced around voids and the interface simultaneously, leading to the matrix damage and interfacial debonding, respectively. Then, the cracks propagate to neighbor areas to jointly create the final damage crack.

The final damage patterns of RVE models after hygrothermal aging and mechanical loading are presented in Figure 11. The mechanical properties decrease significantly after hygroscopic saturation, especially for the matrix. The presence of voids can accelerate the matrix damage and interfacial debonding. Therefore, the number and density of cracks increase after hygrothermal aging, compared with unaged RVE models.
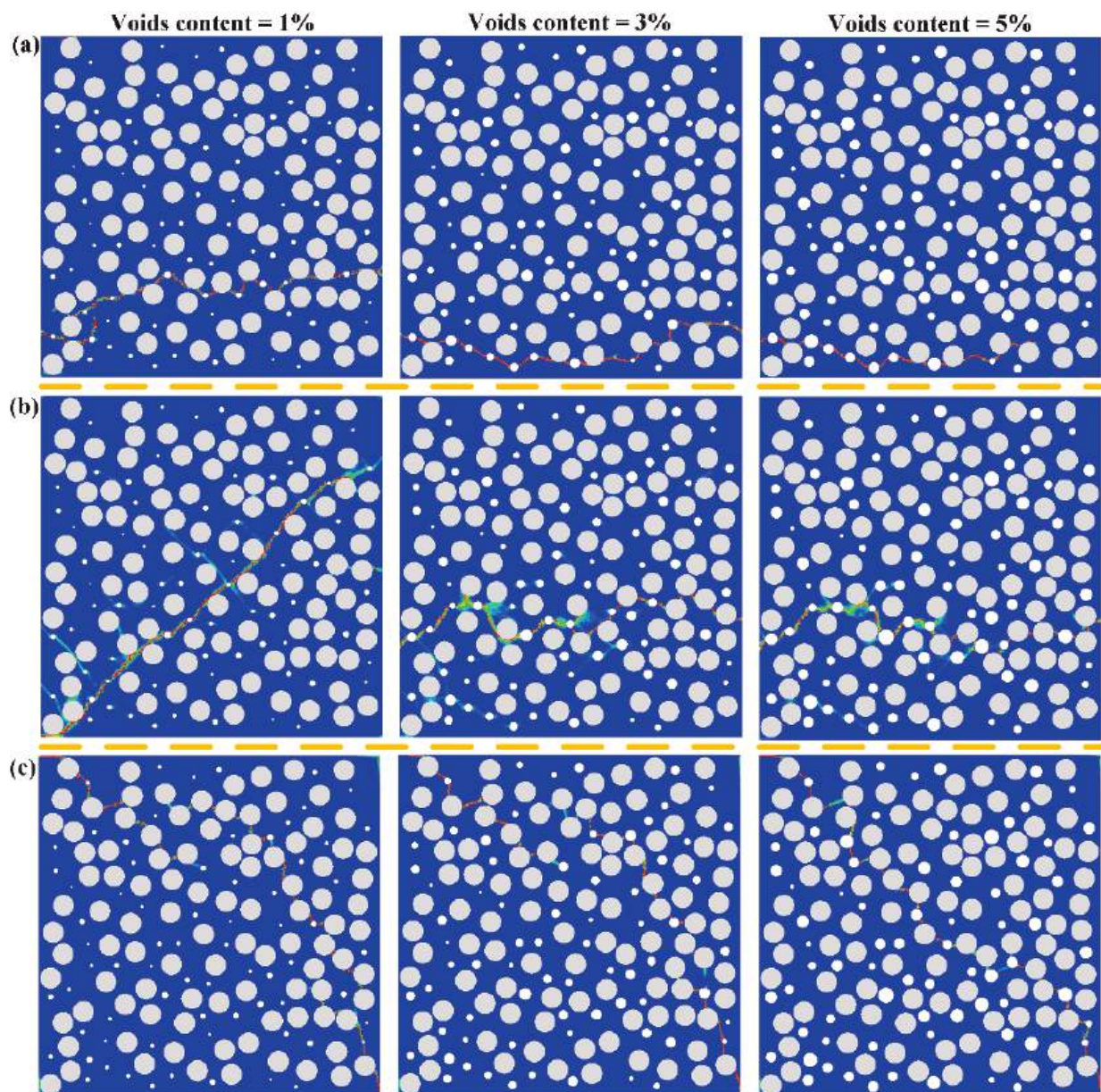
Figure 10. Colored failure patterns of unaged samples in the (**a**) transverse tension, (**b**) transverse compression, (**c**) transverse shear simulation.
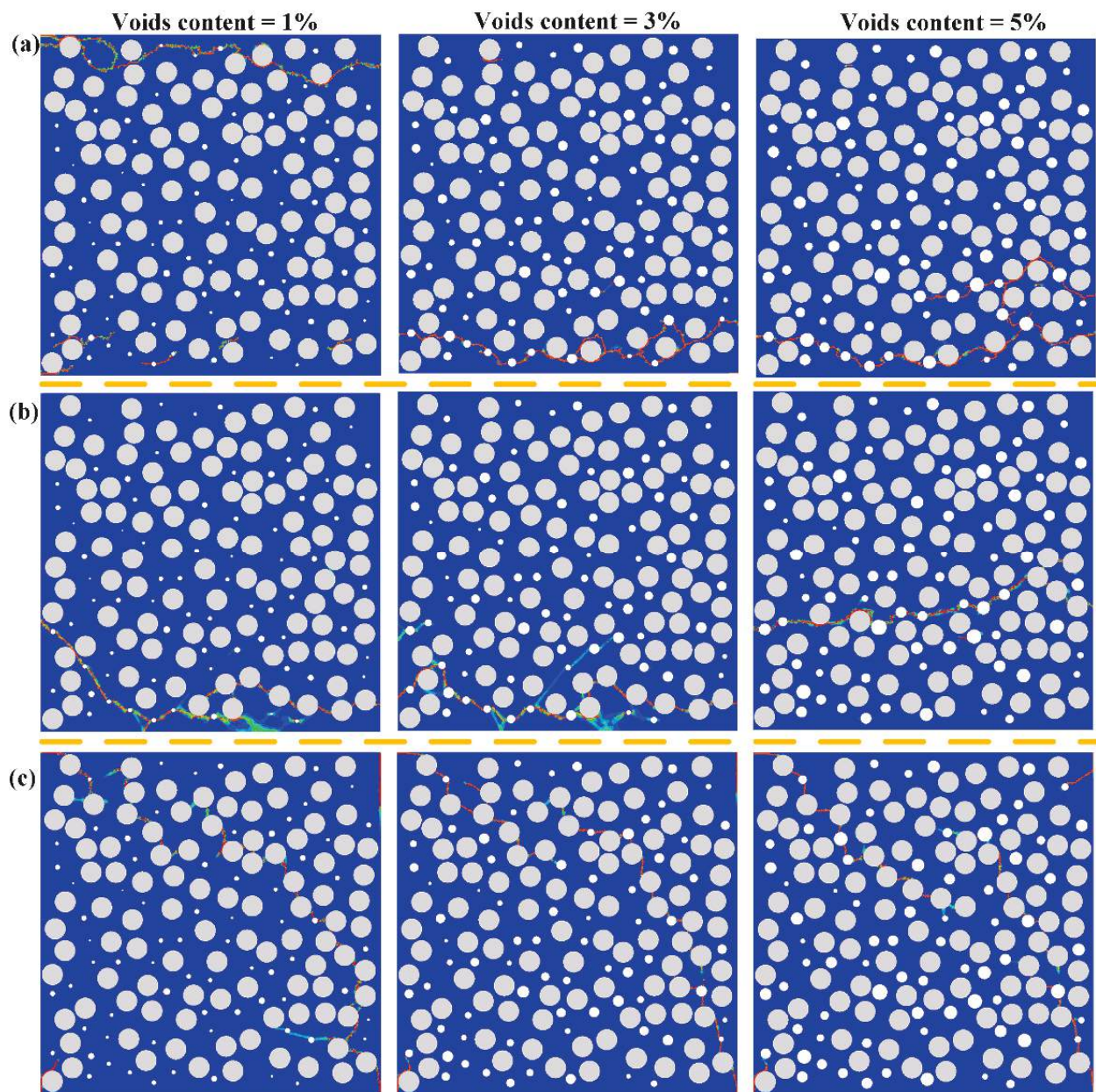
Figure 11. Colored failure patterns of hygroscopic saturated samples in the (**a**) transverse tension, (**b**) transverse compression, (**c**) transverse shear simulation.

5. Conclusions

To reveal the effects of voids content on the moisture absorption performances and mechanical properties under the loading of transverse tension, compression and shear, RVE models with different voids contents are established and analyzed. The following conclusions can be drawn:

(1) Water diffusion is significantly affected by the presence of voids, which significantly accelerate the water absorption rate and increase the water saturation content. Moreover, the modified Halpin–Tsai equation can effectively predict the transverse diffusivity of composite with different volume fractions of voids.

(2) Tensile stress arises for the matrix in the cooling contraction of the molding process, and the stress change from tension to compression after hygrothermal aging. The stress state in CFs is just the opposite of the matrix. Stress distribution can be changed,

and the residual stress can be greatly weakened by the presence of voids. Voids have beneficial effects on the relief or decrease the residual stress to some extent.

(3) For the unaged composites, voids induce the decrease of mechanical properties due to stress concentration, and every 1% increase in the voids content results in a 6.4% decrease of transverse tensile strength. However, matrix degradation due to the absorbed water content after hygrothermal aging is the dominant factor, and the corresponding rate is 3.86%. This indicates that the negative effects of voids content are diminished, and hygrothermal aging is the dominant reason for the failure mechanism.

(4) Compared with the failure images of unaged composites, the number and density of cracks increase after hygrothermal aging, which indicates the presence of voids can accelerate the matrix damage and interfacial debonding.

Author Contributions: Methodology, software, formal analysis, investigation, and writing—original draft, preparation, Z.L. and Y.L.; writing—review and editing, X.Z. and Z.K.; funding acquisition, resources, supervision, writing—review and editing, J.Z. All authors have read and agreed to the published version of the manuscript.

Institutional Review Board Statement: Not applicable.

Informed Consent Statement: Not applicable.

Data Availability Statement: The data presented in this study are available on request from the corresponding author.

Conflicts of Interest: The authors declare no conflict of interest.

References

1. Grunenfelder, L.; Nutt, S. Void formation in composite prepregs—Effect of dissolved moisture. *Compos. Sci. Technol.* **2010**, *70*, 2304–2309. [CrossRef]
2. Mehdikhani, M.; Straumit, I.; Gorbatikh, L.; Lomov, S. Detailed characterization of voids in multidirectional carbon fiber/epoxy composite laminates using X-ray micro-computed tomography. *Compos. Part A: Appl. Sci. Manuf.* **2019**, *125*, 105532. [CrossRef]
3. Luo, L.; Zhang, B.; Lei, Y.; Zhang, G.; Zhang, Z.; Meng, B.; Liu, Z. Identification of voids and interlaminar shear strengths of polymer-matrix composites by optical microscopy experiment and deep learning methodology. *Polym. Adv. Technol.* **2021**, *32*, 1853–1865. [CrossRef]
4. Gagani, A.I.; Echtermeyer, A.T. Influence of delaminations on fluid diffusion in multidirectional composite laminates—Theory and experiments. *Int. J. Solids Struct.* **2019**, *158*, 232–242. [CrossRef]
5. Mehdikhani, M.; Gorbatikh, L.; Verpoest, I.; Lomov, S.V. Voids in fiber-reinforced polymer composites: A review on their formation, characteristics, and effects on mechanical performance. *J. Compos. Mater.* **2018**, *53*, 1579–1669. [CrossRef]
6. Costa, M.L.; de Almeida, S.F.; Rezende, M.C. The influence of porosity on the interlaminar shear strength of carbon/epoxy and carbon/bismaleimide fabric laminates. *Compos. Sci. Technol.* **2001**, *61*, 2101–2108. [CrossRef]
7. Little, J.E.; Yuan, X.; Jones, M.I. Characterisation of voids in fibre reinforced composite materials. *NDT E Int.* **2012**, *46*, 122–127. [CrossRef]
8. Manta, A.; Gresil, M.; Soutis, C. Infrared thermography for void mapping of a graphene/epoxy composite and its full-field thermal simulation. *Fatigue Fract. Eng. Mater. Struct.* **2019**, *42*, 1441–1453. [CrossRef]
9. Tretiak, I.; Smith, R.A. A parametric study of segmentation thresholds for X-ray CT porosity characterisation in composite materials. *Compos. Part A Appl. Sci. Manuf.* **2019**, *123*, 10–24. [CrossRef]
10. Jiang, H.; Ren, Y.; Liu, Z.; Zhang, S. Microscale finite element analysis for predicting effects of air voids on mechanical properties of single fiber bundle in composites. *J. Mater. Sci.* **2018**, *54*, 1363–1381. [CrossRef]
11. Saenz-Castillo, D.; Martín, M.; Calvo, S.; Rodriguez-Lence, F.; Güemes, A. Effect of processing parameters and void content on mechanical properties and NDI of thermoplastic composites. *Compos. Part A Appl. Sci. Manuf.* **2019**, *121*, 308–320. [CrossRef]
12. AbdElmola, F.; Carlsson, L. Water uptake in epoxy matrix with voids: Experiments and modeling. *J. Compos. Mater.* **2018**, *53*, 1049–1065. [CrossRef]
13. Huang, H.; Talreja, R. Effects of void geometry on elastic properties of unidirectional fiber reinforced composites. *Compos. Sci. Technol.* **2005**, *65*, 1964–1981. [CrossRef]
14. Nikopour, H. A virtual frame work for predication of effect of voids on transverse elasticity of a unidirectionally reinforced composite. *Comput. Mater. Sci.* **2013**, *79*, 25–30. [CrossRef]

15. Vajari, D.A.; González, C.; Llorca, J.; Legarth, B.N. A numerical study of the influence of microvoids in the transverse mechanical response of unidirectional composites. *Compos. Sci. Technol.* **2014**, *97*, 46–54. [CrossRef]

16. Dong, C. Effects of Process-Induced Voids on the Properties of Fibre Reinforced Composites. *J. Mater. Sci. Technol.* **2016**, *32*, 597–604. [CrossRef]

17. Wang, M.; Zhang, P.; Fei, Q.; Guo, F. Computational evaluation of the effects of void on the transverse tensile strengths of unidirectional composites considering thermal residual stress. *Compos. Struct.* **2019**, *227*, 111287. [CrossRef]

18. Mehdikhani, M.; Petrov, N.A.; Straumit, I.; Melro, A.R.; Lomov, S.V.; Gorbatikh, L. The effect of voids on matrix cracking in composite laminates as revealed by combined computations at the micro- and meso-scales. *Compos. Part A Appl. Sci. Manuf.* **2019**, *117*, 180–192. [CrossRef]

19. Hyde, A.; He, J.; Cui, X.; Lua, J.; Liu, L. Effects of microvoids on strength of unidirectional fiber-reinforced composite materials. *Compos. Part B Eng.* **2020**, *187*, 107844. [CrossRef]

20. Gueribiz, D.; Rahmani, M.; Jacquemin, F.; Fréour, S.; Guillen, R.; Loucif, K. Homogenization of Moisture Diffusing Behavior of Composite Materials with Impermeable or Permeable Fibers—Application to Porous Composite Materials. *J. Compos. Mater.* **2009**, *43*, 1391–1408. [CrossRef]

21. Bourennane, H.; Gueribiz, D.; Fréour, S.; Jacquemin, F. Modeling the effect of damage on diffusive behavior in a polymeric matrix composite material. *J. Reinf. Plast. Compos.* **2019**, *38*, 717–733. [CrossRef]

22. Lei, Y.; Zhang, J.; Zhang, T.; Li, H. Water diffusion in carbon fiber reinforced polyamide 6 composites: Experimental, theoretical, and numerical approaches. *J. Reinf. Plast. Compos.* **2019**, *38*, 578–587. [CrossRef]

23. Lei, Y.; Zhang, T.; Zhang, J.; Zhang, B. Dimensional stability and mechanical performance evolution of continuous carbon fiber reinforced polyamide 6 composites under hygrothermal environment. *J. Mater. Res. Technol.* **2021**, *13*, 2126–2137. [CrossRef]

24. Pivdiablyk, I.; Rozycki, P.; Jacquemin, F.; Gornet, L.; Auger, S. Experimental analysis of mechanical performance of glass fibre reinforced polyamide 6 under varying environmental conditions. *Compos. Struct.* **2020**, *245*, 112338. [CrossRef]

25. Sang, L.; Wang, C.; Wang, Y.; Hou, W. Effects of hydrothermal aging on moisture absorption and property prediction of short carbon fiber reinforced polyamide 6 composites. *Compos. Part B Eng.* **2018**, *153*, 306–314. [CrossRef]

26. Lin, W.-Q.; Zhang, Y.-X.; Wang, H. Thermal conductivity of unidirectional composites consisting of randomly dispersed glass fibers and temperature-dependent polyethylene matrix. *Sci. Eng. Compos. Mater.* **2019**, *26*, 412–422. [CrossRef]

27. Widom, B. Random Sequential Addition of Hard Spheres to a Volume. *J. Chem. Phys.* **1966**, *44*, 3888–3894. [CrossRef]

28. Yang, L.; Yan, Y.; Liu, Y.; Ran, Z. Microscopic failure mechanisms of fiber-reinforced polymer composites under transverse tension and compression. *Compos. Sci. Technol.* **2012**, *72*, 1818–1825. [CrossRef]

29. Jia, L.; Yu, L.; Zhang, K.; Li, M.; Jia, Y.; Blackman, B.R.K.; Dear, J.P. Combined modelling and experimental studies of failure in thick laminates under out-of-plane shear. *Compos. Part B Eng.* **2016**, *105*, 8–22. [CrossRef]

30. González, C.; Llorca, J. Mechanical behavior of unidirectional fiber-reinforced polymers under transverse compression: Microscopic mechanisms and modeling. *Compos. Sci. Technol.* **2007**, *67*, 2795–2806. [CrossRef]

31. París, F.; Correa, E.; Cañas, J. Micromechanical view of failure of the matrix in fibrous composite materials. *Compos. Sci. Technol.* **2003**, *63*, 1041–1052. [CrossRef]

32. Affdl, J.C.H.; Kardos, J.L. The Halpin-Tsai equations: A review. *Polym. Eng. Sci.* **1976**, *16*, 344–352. [CrossRef]

33. Costa, M.L.; Rezende, M.C.; De Almeida, S.F.M. Effect of Void Content on the Moisture Absorption in Polymeric Composites. *Polym. Technol. Eng.* **2006**, *45*, 691–698. [CrossRef]

Numerical Simulation of Impregnation Process of Reactive Injection Pultrusion for Glass Fiber/PA6 Composites

Xueliang Ding [1,2], Quanguo He [1,2], Qun Yang [3], Suwei Wang [4,*] and Ke Chen [3,*]

1   Chongqing Copolyforce New Materials Co., Ltd., Chongqing 401332, China; dingxxueliang@163.com (X.D.); hequanguo@vip.sina.com (Q.H.)
2   Chongqing Research Institute Co., Ltd. of China Coal Technology & Engineering Group Corporation, Chongqing 400039, China
3   College of Mechanical and Electrical Engineering, Beijing University of Chemical Technology, Beijing 100029, China; honor0612@163.com
4   National Special Superfine Powder Engineering Research Center of China, School of Chemistry and Chemical Engineering, Nanjing University of Science and Technology, Nanjing 210094, China
*   Correspondence: wangsw90@163.com (S.W.); chenke0903@outlook.com (K.C.)

Abstract: Pultrusion of thermoplastic composites has been the hotspot of manufacturing high-performance thermoplastic composites in recent years. The optimization of process parameters in the pultrusion usually needed repeated attempts, which wasted lots of manpower and material resources. A numerical simulation method can accelerate the optimization of process parameters. In this work, the impregnation process of reactive injection pultrusion for glass fiber reinforced nylon 6 (GF/PA6) composites was modeled and numerically simulated by a finite element/controlled volume (Fe/CV) method. Based on Darcy's law, the impregnation process can be regarded as the two-phase flow (liquid resin and air) in porous media (undirectional glass fibers). The distribution of resin flow during the impregnation was explored. The effects of pulling rate and injection pressure on the impregnation time and resin reflux distance were analyzed, and the appropriate range of relevant process parameters was determined. The results showed that increasing the pulling rate can significantly control the reflux distance of resin in the impregnation mold and shorten the impregnation time, but too high a pulling rate would increase the impregnation time. Increasing the injection pressure can greatly shorten the resin impregnation time, but it would significantly increase the resin reflux distance. This work can effectively guide the subsequent optimization of process parameters of reactive injection pultrusion for GF/PA6 composites.

Keywords: thermoplastic composites; reactive injection pultrusion; impregnation; numerical simulation

1. Introduction

Pultrusion is a continuous process of manufacturing composite profiles by impregnating continuous reinforcement fibers or fabrics guided into a die to attain the desired cross-sectional profile followed by heating to achieve curing of the material [1,2]. It has the advantages of controllable fiber content, high raw material utilization, and high production efficiency. The process allows the manufacture of pultruded profiles with virtually unlimited length and higher flexibility and tensile strength compared to those prepared with any other reactive polymer process [3,4]. Pultruded products have the advantages of light weight, high strength, and high corrosion resistance and are widely used in construction, transportation, automotive manufacturing, aircraft, power transmission, and other fields [5–7]. For example, the windshield bracket of the latest BMW I3 is the pultruded continuous carbon fiber reinforced PA6 composites product, which can reduce the mass of the whole vehicle.

During the pultrusion, the impregnation of resin to fiber reinforcement is the key to determine the properties of the final product. The traditional open-bath impregnation method can achieve good impregnation, but the volatile organic compounds (VOC) produced may involve health risks [8]. Closed-injection impregnation was an efficient impregnation strategy in recent years. Once launched, it was favored by many pultrusion manufacturers and was used in the pultrusion of epoxy-based, polyurethane-based composites [9,10]. With closed-injection impregnation technology, high-speed pultrusion can be achieved by optimizing the pulling speed, injection pressure, and structural parameters of the impregnation box, and the maximum production speed can reach 3 m/min by KraussMaffei's iPul technology at K2019 exhibition [11]. Pultrusion involves numerous variables that affect the quality and mechanical properties of the final products [12]. Improper pulling rate or excessive low die temperature would lead to the decline of product performance and even the failure of production. Traditional "trial and error" method consumed too much manpower and material costs, when optimizing the pultrusion process parameters. In recent years, with the rapid development of computer technology, modeling of pultrusion has attracted more and more researchers' interest [13–15]. Numerical simulation can effectively shorten the time of identifying appropriate process parameter. Especially for the impregnation process of closed injection impregnation, it is the most significant target of pultrusion modeling.

Kim et al. [16] were the first to carry out research about impregnation modeling and established a one-dimensional permeability model based on Darcy's law. Kommu et al. [17] used the finite element/control volume (Fe/CV) method to solve the resin flow equation in the two-dimensional calculation domain. Then, Rahatekar et al. [18] also established a two-dimensional resin flow model in the impregnation box. It was found that, in order to ensure the complete impregnation of fiber reinforcement, the injection pressure should be increased when increasing the pultrusion speed, raising fiber volume fraction, or reducing the compression ratio. Srinivasagupta et al. [19] found that the structure parameters of impregnation box had significant influence on the injection pressure required to penetrate the fiber. Liu et al. [20,21] reached the same conclusion when using the finite element/nodal volume (Fe/NV) method to simulate the transient modeling of resin flow front. Jeswani et al. [22] used Fe/CV method to establish a three-dimensional model of resin flow impregnated fiber reinforcement during injection pultrusion, and predicted the flow front of resin in the impregnation box. Masuram et al. [23,24] and Roux et al. [25,26] further considered the influence of compression of fiber reinforcement on resin flow and impregnation effect, so that the numerical simulation of impregnation process of injection pultrusion molding was closer to the reality. These works mainly focused on thermosetting composite systems.

This current work focused on the modeling and numerical simulation of impregnation 3D flow process during thermoplastic injection pultrusion of glass fiber reinforced nylon 6 (GF/PA6) composites. This technology combined PA6 anionic polymerization and injection pultrusion. The infiltration flow of resin to continuous reinforcement during impregnation was numerically simulated by ANSYS CFX 15.0 software. The effects of process parameters such as pultrusion speed and injection pressure on the distribution of resin flow front and backflow distance were analyzed, which provided a theoretical basis for optimizing process parameters of pultrusion.

2. Materials and Methods

2.1. Materials

The pultruded profile with section size of 20×4 mm^2 was investigated in this work. The undirectional reinforcements were E-glass roving (ECT 4301R, 2400 tex, D_f = 17 μm), provided by Chongqing International Composite Materials Co., Ltd., Chongqing, China. Caprolactam (PA6 monomer) was the resin for impregnating reinforcements, which was purchased from BASF Co., Ltd., Shanghai, China. The initiators C10 (2 mol/kg) and activators C20 (2 mol/kg) were kindly provided by Sinopharm Chemical Reagent Co., Ltd.,

Shanghai, China. A C20 concentration of 1.0 mol% and a C10 concentration of 2.0 mol% in caprolactam were optimized by our previous work [27,28] to be optimal formulations for pultrusion.

2.2. Impregnation of Thermoplastic Injection Pultrusion

During the injection pultrusion, the impregnation of unidirectional reinforcement took place in the impregnation box, as showed in Figure 1a. Continuous unidirectional fiber bundles can be regarded as the moving porous media during the pultrusion process. At the initial stage, the pores of the porous media were filled with hot air. The mixed two-component resins were injected into the closed impregnation box, and penetration of the fiber bundles was implemented by the metering pumps of reaction injection molding (RIM) device. This physical process can be regarded as the two-phase transient flow of hot air and liquid resin in moving porous media.
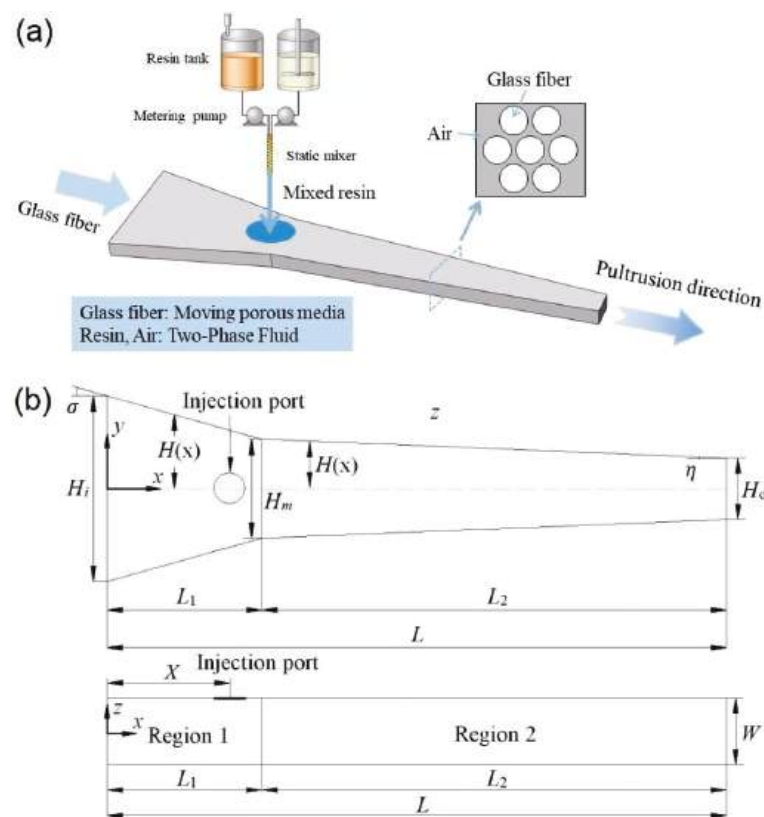
Figure 1. (**a**) Schematic diagram of injection impregnation process; (**b**) geometric parameters of impregnation box cavity.

If the impregnation box was taken as the research object, the coordinate axis was set at the center of the fiber entrance, as shown in Figure 1b. According to the different cone angles, the calculation domain is divided into Region 1 and Region 2. The specific geometric parameters are shown in Table 1.

Table 1. Geometric parameters of impregnation box.

Geometric Parameters	Value
Total length of impregnation box (L)	200 mm
Height (W)	4 mm
Region 1 length (L_1)	50 mm
Region 2 length (L_2)	150 mm
Entrance width (H_i)	60 mm
Region junction width (H_m)	32 mm
Exit width (H_o)	20 mm
Length from injection center to Entrance (X)	40 mm
Region 1 cone angle ($\tan\sigma$)	0.28
Region 2 cone angle ($\tan\eta$)	0.05

The heating temperature of the impregnation box was set as 100 °C; under this condition, the physical parameters of air and liquid resin are present in Table 2.

Table 2. Physical parameters of air and liquid resin.

Materials	Density (kg/m^3)	Viscosity (mPa·s)	Surface Tension Coefficient (N/m)	Contact Angle
Resin (liquid)	950	50	0.034	34°
Air (gas)	0.946	0.0218	—	—

2.3. Modeling of Injection Pultrusion

In order to establish a mathematical model of the pultrusion impregnation process, the following assumptions are made:

(1) Low viscosity resin is incompressible Newtonian fluid;
(2) The flow of resin through the fiber reinforcement (porous medium) complied with Darcy's law [13];
(3) The impregnation process was isothermal, and the viscosity of the resin system was constant;
(4) The initial pressure was atmospheric pressure (101.325 kPa);
(5) The influence of capillary force was neglected.

Darcy formula porous medium model was used to calculate the flow process of resin system in fiber reinforcement. There were gas-liquid two-phase flows (hot air and resin) in porous media; the two continuous phases were completely layered, and the interface was clear. Therefore, it can be assumed that the two continuous phases shared the same velocity field [29]. During the impregnation process, the gas–liquid two-phase flows maintained mass conservation and momentum conservation, so the continuity equation and momentum equation were as follows:

$$\frac{\partial(\rho)}{\partial t} + \nabla \cdot \left(\rho\overline{U}\right) = 0 \tag{1}$$

$$\frac{\partial\left(\rho\overline{U}\right)}{\partial t} + \nabla \cdot \left(\rho \cdot \overline{U} \otimes \overline{U}\right) = -\nabla P \cdot \delta + \nabla \cdot \left(\eta \cdot \left(\nabla\overline{U} + (\nabla\overline{U})^{\mathrm{T}}\right)\right) - \frac{\eta}{K}\overline{U} + S \tag{2}$$

where ρ was the volume fraction weighted average density of liquid resin and air, t was the time, $\overline{U}$ was the apparent velocity, the physical velocity $U = \varphi\overline{U}$, δ was the unit vector, P was the impregnation pressure, η was the weighted average viscosity of volume fraction of liquid resin and air, and K was the permeability (for unidirectional fiber, the permeability takes different values in different directions). S was the momentum source term generated by gravity. In this model, it can be expressed as:

$$S = (\rho - \rho_{\mathrm{ref}}) \cdot g \tag{3}$$

where ρ_{ref} was the reference density.

The gas–liquid two-phase seepage flow between fiber bundle was laminar flow, and the volume fraction method was used to track the interface. The mass conservation equation of liquid resin phase was:

$$\frac{\partial(\alpha_r \rho_r)}{\partial t} + \nabla \cdot (\alpha_r \rho_r \cdot U) = 0 \tag{4}$$

$$\alpha_r + \alpha_{\text{air}} = 1 \tag{5}$$

where the volume fraction of liquid resin was α_r, the volume fraction of air was α_{air}, ρ_r was the density of the liquid resin, ρ_{air} was the density of air, η_r was the viscosity of the liquid resin, and η_{air} was the viscosity of air. Then,

$$\rho = \alpha_r \rho_r + (1 - \alpha_r)\rho_{\text{air}} \tag{6}$$

$$\alpha_r + \alpha_{\text{air}} = 1 \tag{7}$$

The sum of the porosity φ of the porous medium and the fiber volume fraction V_f was 1; thus,

$$\varphi = 1 - V_f \tag{8}$$

For the conical impregnation box, the fiber volume fraction was not constant, but would gradually increase in the X direction according to the gradual reduction in the internal section of the box until the volume fraction V_{f0} of the final product was reached at the outlet of the impregnation box. So, the fiber volume fraction $V_f(x)$ in the X direction can be expressed as:

$$V_f(x) = V_{f0} \frac{H_o}{2H(x)} \tag{9}$$

In Equation (9), *H(x)* was a piecewise function, which was represented in Region 1 and Region 2 of the impregnation box, respectively:

$$H(x) = \frac{(H_m - H_i)}{2L_1}x + \frac{H_i}{2}, 0 \le x \le L_1 \tag{10}$$

$$H(x) = \frac{H_0 - H_m}{2(L - L_1)}(x - L_1) + \frac{H_m}{2}, L_1 < x \le L \tag{11}$$

In the pultrusion process of fiber-reinforced composites, permeability was considered to be the indicator of the difficulty of liquid resin flowing through fiber reinforcement. Pultruded products usually had high fiber content, and the permeability K was related to the structure of the fiber itself. This model adopts the permeability model proposed by Gebart [30]:

$$K_\perp = C_1 \left(\sqrt{\frac{V_{\text{fmax}}}{V_f}} - 1 \right)^{2.5} R_f^2 \tag{12}$$

$$K_\parallel = \frac{8R_f^2}{c} \frac{(1 - V_f)^3}{V_f^2} \tag{13}$$

where $K_\parallel$ was the permeability along the fiber axial direction (X direction), and $K_\perp$ was the permeability along the fiber transverse direction (y direction and z direction). The parameters are shown in Table 3.

Table 3. Permeability model parameters.

Fiber Arrangement	D_f	C_1	V_{fmax}	c
Hexagonal Arrangement	17 μm	0.231	0.907	53

According to Equations (12) and (13) and the parameters in Table 3, when the volume fraction of fiber reinforcement in the final product was 50%, the relationship between the permeability (along the fiber axis and the fiber transverse direction) and the x coordinate is shown in Figure 2.
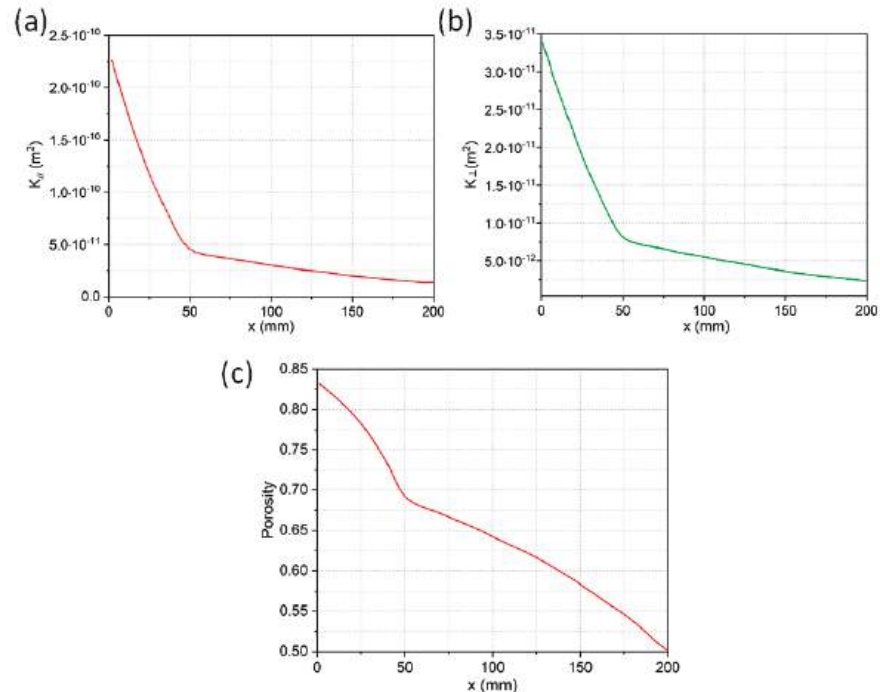
Figure 2. Relationship between fiber permeability, porosity, and *X*-axis coordinate: (**a**) permeability along fiber axis (*X*-axis direction); (**b**) permeability along the fiber radial (*Y*-axis direction); (**c**) porosity along the *X*-axis coordinate.

3. Simulation

3.1. Software Settings

The geometric model of the simulation was drawn in Solidworks 2013 and meshed in ICEM CFD. The maximum size of the grid was set to 0.8 mm. The automatic volume mesh generation method was used to divide geometric model into more than 40,000 meshes dominated by hexahedral mesh, check the mesh quality, and delete the negative mass mesh, as shown in Figure 3.
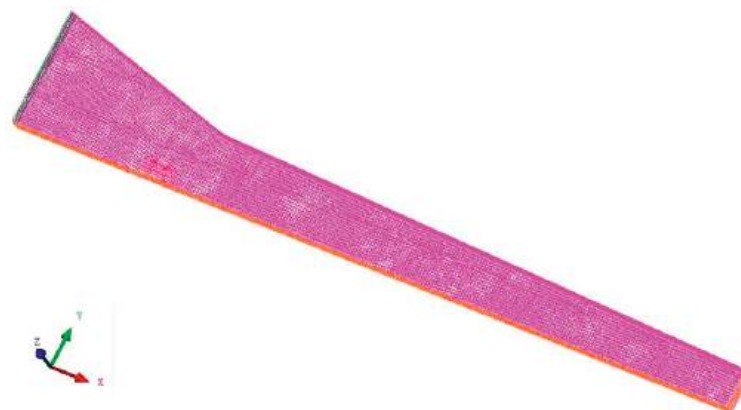
Figure 3. Mesh division of impregnation domain.

The commercial finite element software ANSYS CFX 15.0 was used to simulate the process of resin infiltration into fiber in impregnation box, and the transient solution was

carried out by the finite volume (FV) method. The time step was 0.05 s, and the total simulation time was 10.0 s. The unidirectional fiber area was set as the porous media area, and the buoyancy model was set according to the die inclination of 5°. The fluid phase adopted the homogeneous model, the flow was set as laminar flow, and there was no material transfer between the two continuous phases. The permeability of porous media domain was different along each direction, so it was set as an anisotropic model.

The solution mode adopted a high-order solution mode, which was accurate and reliable, and the transient solutions were set as implicit second-order backward Euler mode. The maximum number of iteration steps was set to 20 times, and the root mean square residual was 10^{-4}, and the accuracy can meet the calculation requirements of this model [31]. Multiphase control adopted a volume fraction coupling method, and the flow front of resin in unidirectional reinforced fiber was tracked by volume fraction (VOF) method. This method defined a fluid volume function that was the ratio of the volume of the target fluid to the grid volume. As long as the value of this function on each grid was known in the flow field, the moving interface could be tracked.

3.2. Boundary Conditions

The impregnation box had axisymmetric geometric structure, and the resin injection port was located on the central axis. Therefore, in order to reduce the simulation computation work, analyzing half of the impregnation box can reflect the process of resin infiltration into the pores between the fiber in the entire impregnation box, and the schematic diagram is shown in Figure 4.
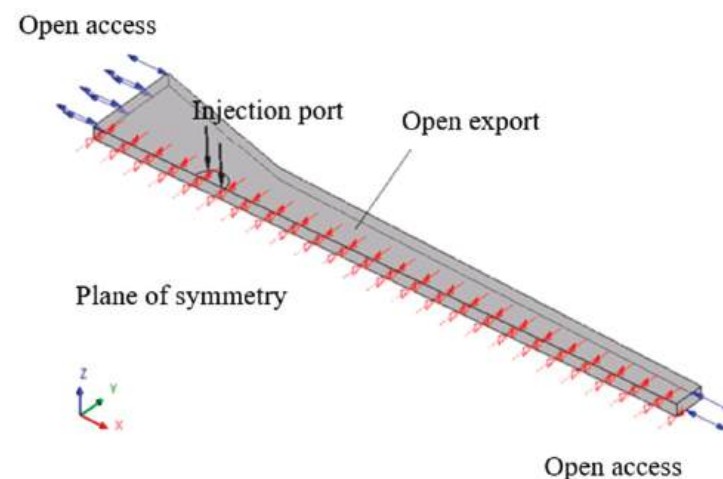
Figure 4. Initial and boundary conditions of impregnation process.

In the initial state, the reference pressure in the computational domain was atmospheric pressure P_{atm}, the porous media were completely filled with air, the liquid phase volume fraction of resin $\alpha_r = 0$, and the initial velocity of the air was 0. In this model, the impregnation box was convergent flow channel, the velocity in the *x*-axis direction of the porous media domain was u_0, that was, the pultrusion velocity of the composite. The velocity V_0 along the *y*-axis direction can be simplified by the cone angle and the pultrusion velocity in the *x*-axis direction, which is expressed as:

$$v_0 = -u_0 \left(\frac{y}{H(x)} \right) tan\theta \tag{14}$$

where $0 \leq X \leq L_1$, $\tan \theta = \tan \sigma$, and $L_1 \leq X \leq L_2$, $\tan \sigma = \tan \eta$.

The boundary conditions were as follows:

(1) Injection port: the injection port was the pressure inlet, the injection pressure was P_i, and the volume fraction of resin was $\alpha_r = 1$;

(2)   Front and rear outlet of impregnation box: at the front and rear channels of the impregnation box, both air and resin may enter and exit, so it was set as an open pressure boundary, and the pressure was atmospheric pressure P_{atm};

(3)   Impregnation box wall: the fluid velocity perpendicular to the inner wall of the impregnation box was 0, and the wall was a no-slip wall.

4. Results and Discussion

4.1. Resin Flow and Impregnation Time in Impregnation Box

The complete impregnation of the resin to the fiber reinforcement in the injection box was the premise of preparing pultruded products with qualified performance. The viscosity of the resin used in this work was as low as 50 mPa·s at 100 °C and can maintain more than 25 min [27], which fully met the residence time requirements of the resin in the impregnation box. Therefore, the injection pressure (P_i) was set to 0.5 bar, and pulling rate was set to 0 cm/min preliminarily to explore the resin flow. The cross section of calculation domain $z = 0$ is intercepted, and the flow distribution state of resin is shown in Figure 5.
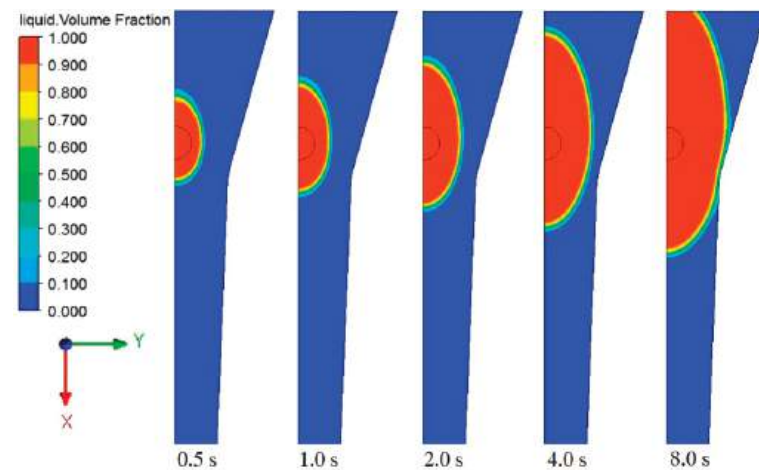
Figure 5. Resin flow distribution in the impregnation box at different times.

It can be obtained from figure that the penetration rate along the *x*-axis direction (fiber axial direction) was obviously faster than that along the *y*-axis direction (fiber radial direction). At the same time, the permeation rate of the resin reflux in the negative direction of the *x*-axis was faster than that in the positive direction of the *x*-axis. This was because the permeability resistance along the *y*-axis was large, as shown in Figure 2b. In the positive *x*-axis direction, due to the compression of the cross-section size, the fiber volume fraction gradually increased, the porosity decreased, and the permeability resistance increased greatly. This can also be illustrated from the variation of porosity along the *x*-axis in Figure 2c.

When $t = 8.0$ s, the resin had overflowed from the entrance of the impregnation box, which would lead to material waste or oxidative deactivation of the reaction mixture. In the process of injection pultrusion, the fiber would move forward along the *x*-axis under the action of the puller. When the pulling speed matched the resin injection flow, the resin reflux can be effectively controlled, but an excessively high pulling rate would shorten the residence time of the reinforcement in the impregnation box, so even the fiber bundle cannot be fully penetrated. Therefore, optimization of process parameters and effective control of resin reflow were also the aims of this work.

Since the impregnation box had only one injection port, the time for the resin to completely penetrate the fiber bundle was the time for the resin to contact the wall of the impregnation box. After that, the complete filling of the resin can be ensured under the compression structure of the box cavity. When $t = 5.60$ s, the resin flow front ($\alpha_r = 0.5$)

reaches the wall of the impregnation box, and the resin flow state distribution is shown in Figure 6.
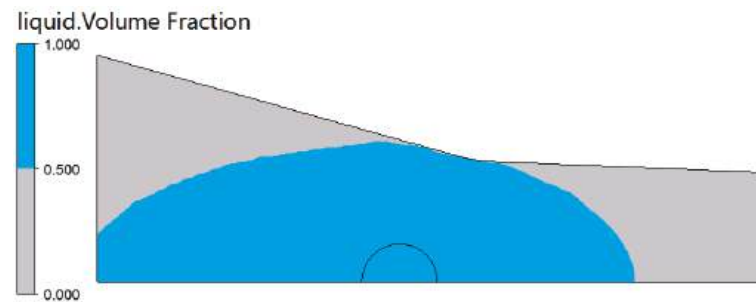
Figure 6. Flow front distribution of resin at t = 5.60 s.

4.2. Effect of the Pulling Rate

Pulling rate was not only an important but also the most easily modified parameter in the pultrusion process [32]. Low pulling rate made it easier to control the forming of composite materials, but it would reduce production efficiency. Although productivity was improved at high pulling rate, the impregnation of fiber bundles was difficult to guarantee. It was necessary to explore a suitable range of pulling rate. The effect of different pulling rates on resin flow was studied when the injection pressure was maintained at 0.5 bar. The distribution of the resin flow at different moments of the z = 0 section is shown in Figure 7.
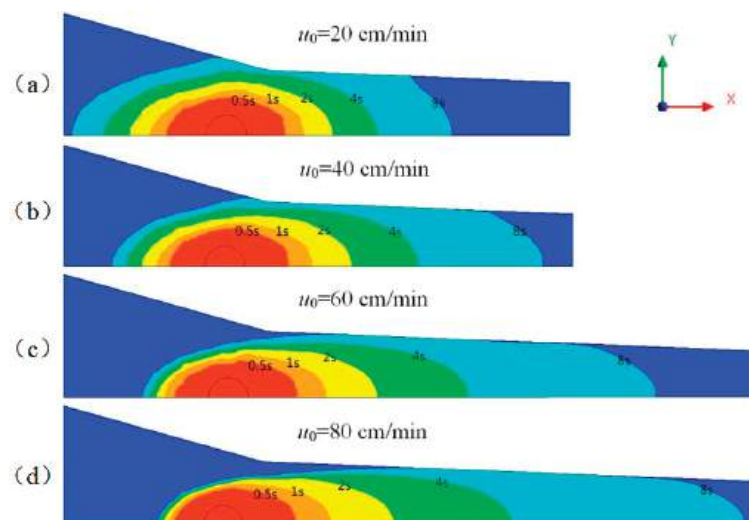
Figure 7. The resin flow front with time under different pulling rates: (**a**) u_0 = 20 cm/min; (**b**) u_0 = 40 cm/min; (**c**) u_0 = 60 cm/min; (**d**) u_0 = 80 cm/min.

As can be seen from the figure, the ultra-low viscosity resin had strong permeability and could fully impregnate the fiber bundle within 8 s. The pulling rate and impregnation time were not completely positively correlated, and the relationship between them is shown in Table 4. In the range of pulling rate 0–20 cm/min, due to the high permeability along the radial direction of the fiber in Region 1, the resin penetrated rapidly, thus shortening the impregnation time. When the pulling rate was further increased, the penetration rate of the resin along the positive x-axis would increase, but the permeability along the radial direction of the fiber would be significantly reduced due to the compression of the box structure, resulting in a severe drop in the resin flow, which required a longer impregnation time.

Table 4. The relationship between pultrusion speed and impregnation time.

Pulling Rate (cm/min)	0	20	40	60	80
Impregnation Time (s)	5.60	5.15	6.25	6.90	7.20

It can also be seen that it was difficult to control the resin reflux at low pultrusion speed. When the pultrusion speed was 20 cm/min, the resin had almost overflowed to the inlet of the impregnation box at 8 s. Pultrusion cannot run stably for long time under this condition. The resin reflux phenomenon was most serious on the line of $y = 0$. The relationship between the reflux distance (x_f) and time under different pulling rates on $y = 0$ line is studied, as shown in Figure 8. When x_f reached 40 mm, it meant that the resin would overflow from the inlet of the impregnation box.
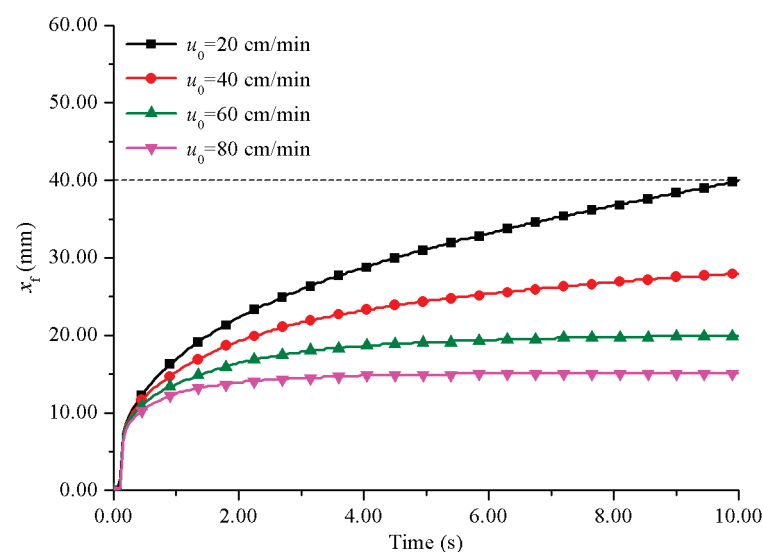
Figure 8. The relationship between resin reflux distance and time at different pulling rates.

Increasing the pulling rate can significantly reduce the reflux distance of resin. When the pulling rate exceeded 60 cm/min, the resin reflux distance increased to a certain value and remained basically unchanged. This was because increasing the pulling rate made the fiber movement and resin reflux reached a dynamic balance so as to maintain the resin flow in a stable state. The resin reflux was effectively controlled. Further increasing the pulling rate would shorten the reflux distance of resin. When the pulling rate was 80 cm/min, the resin reflux distance was only 15.1 mm. It did not mean that the faster the pulling rate, the better. However, when the pulling rate exceeded a certain range, the resin moved too fast along the positive direction of the *x*-axis, resulting in the resin flowing out of the impregnation box before contacting the wall, resulting in defects at the corners of the composite products.

4.3. Effect of the Injection Pressure

Injection pressure was another key process parameter during injection pultrusion process. Figure 9 shows the comparison of resin flow with time at various injection pressures in the section $z = 0$ of the box when the pulling rate was 60 cm/min.
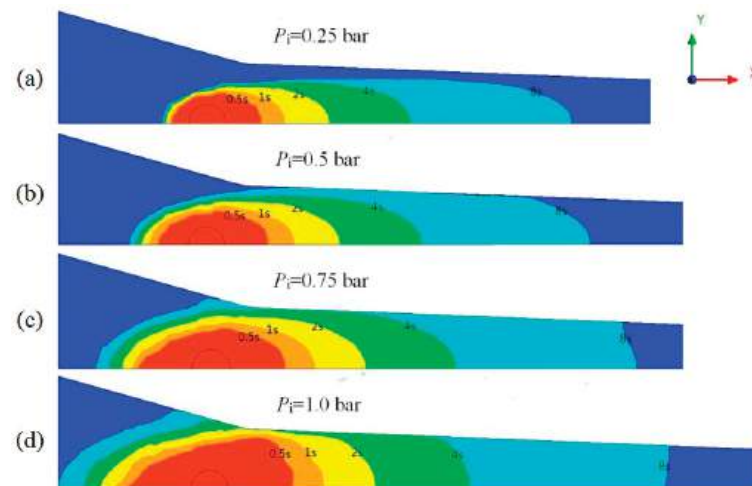
Figure 9. Flow front distribution of resin at different time with different injection pressures: (**a**) P_i = 0.25 bar; (**b**) P_i = 0.5 bar; (**c**) P_i = 0.75 bar; (**d**) P_i = 1.0 bar.

It can be seen from the figure that when the injection pressure was 0.25 bar, the resin failed to flow to the wall of the impregnation box within 8.0 s. With the increase in injection pressure, the resin permeation rate along the fiber radial direction gradually increased and the impregnation time was greatly shortened. The impregnation time under different injection pressures is shown in Table 5.

Table 5. The relationship between injection pressure and impregnation time.

Injection Pressure (bar)	0.25	0.50	0.75	1.00
Impregnation Time (s)	>8.0	5.60	4.05	2.60

With the increase in injection pressure, the reflux distance along the negative direction of *x*-axis also increased, resulting in more serious resin reflux. The relationship between resin reflux distance and time on the line *y* = 0 at different injection pressures is shown in Figure 10.
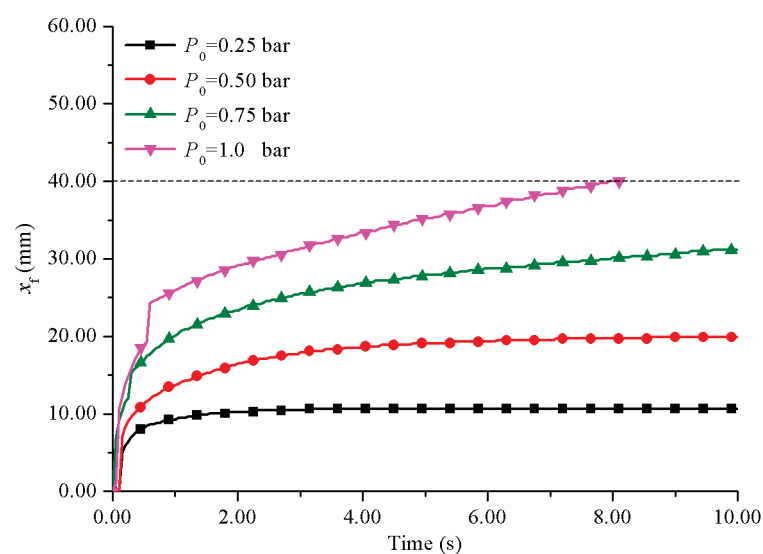
Figure 10. The relationship between resin reflux distance and time at different injection pressures.

The lower the injection pressure, the shorter the reflux distance and the easier it was to control the resin reflux. When the injection pressure was 0.25 bar, the resin reflux distance was only 10.7 mm, which was effectively controlled. When the injection pressure was 0.75 bar or more, the reflux distance was difficult to be controlled within 40 mm. A faster pulling rate was required to match the high injection pressure. Although providing a higher injection pressure can improve production efficiency, the high injection pressure was not recommended. In this study, the porous media model was used to simulate the resistance of fiber reinforcement to resin flow. In fact, the fiber reinforcement was flexible. Under high injection pressure, the resin flow would impact the fiber reinforcement, resulting in fiber compression, resulting in the defect of uneven fiber dispersion in the product [33], which seriously affected the performance of the product. Therefore, the injection pressure should be as low as possible when the impregnation requirements were met. It was more appropriate to set the injection pressure in the range of 0.25–0.5 bar.

5. Conclusions

In this work, modeling and numerical simulation of impregnation in reactive injection pultrusion of GF/PA6 composites were carried out. The process within the impregnation box was regarded as a gas–liquid two-phase seepage flow in a moving porous medium. Considering the influence of air in the reinforcing fibers, the impregnation process was simulated and analyzed by ANSYS CFX 15.0 software. The following conclusions can be obtained:

(1) The caprolactam resin had great permeability; even the injection pressure was only 0.5 bar, and the complete penetration of reinforced fiber can be realized in 0.56 s;

(2) When the injection pressure was 0.5 bar, increasing the pulling rate could shorten the impregnation time in the range of 0–20 cm/min; when the pulling rate was further increased, the impregnation time would increase; increasing the pulling rate can significantly control the reflux distance of resin in the impregnation box. The reflux distance of resin can be controlled to 15.1 mm when the pulling rate was increased to 80 cm/min;

(3) Increasing the injection pressure can greatly shorten the resin impregnation time, but it would significantly increase the resin reflux distance and cause the resin to overflow from the entrance of the impregnation box; a high pulling rate was required to match the high injection pressure; it was more appropriate to set the injection pressure in the range of 0.25–0.5 bar when the impregnation requirements were met.

Author Contributions: Conceptualization, K.C.; formal analysis, Q.Y.; resources, Q.H.; writing—original draft preparation, X.D.; writing—review and editing, X.D. and Q.H.; visualization, X.D.; supervision, K.C. and S.W. All authors have read and agreed to the published version of the manuscript.

Institutional Review Board Statement: Not applicable.

Informed Consent Statement: Not applicable.

Data Availability Statement: The data presented in this study are available on request from the corresponding author.

Conflicts of Interest: The authors declare no conflict of interest.

References

1. Minchenkov, K.; Vedernikov, A.; Safonov, A.; Akhatov, I. Thermoplastic Pultrusion: A Review. *Polymers* **2021**, *13*, 180. [CrossRef]
2. Struzziero, G.; Maistros, G.M.; Hartley, J.; Skordos, A.A. Materials modelling and process simulation of the pultrusion of curved parts. *Compos. Part A-Appl. Sci. Manuf.* **2021**, *144*, 106328. [CrossRef]

3. Fairuz, A.M.; Sapuan, S.M.; Zainudin, E.S.; Jaafar, C.N.A.J. Polymer Composite Manufacturing Using a Pultrusion Process: A Review. *Am. J. Appl. Sci.* **2014**, *11*, 1798–1810. [CrossRef]

4. Safonov, A.A.; Carlone, P.; Akhatov, I. Mathematical simulation of pultrusion processes: A review. *Compos. Struct.* **2017**, *184*, 153–177. [CrossRef]

5. Belingardi, G.; Beyene, A.T.; Koricho, E.G.; Martorana, B. Lightweight solutions for vehicle frontal bumper: Crash Design and Manufacturing Issues. In *Dynamicr Response and Failure of Composite Materials and Structures*, 1st ed.; Valentina, L., Antonio, L., Serge, A., Eds.; Woodhead Publishing: Duxford, UK, 2017; Volume 12, pp. 365–393.

6. Nakada, M.; Miyano, Y.; Morisawa, Y.; Nishida, H.; Hayashi, Y.; Uzawa, K. Prediction of statistical life time for unidirectional CFRTP under creep loading. *J. Reinf. Plast. Compos.* **2019**, *38*, 938–946. [CrossRef]

7. Tinkov, D.V.; Safonov, A.A. Design optimization of truss bridge structures of composite materials. *J. Mach. Manuf. Reliab.* **2017**, *46*, 46–52. [CrossRef]

8. Vedernikov, A.; Safonov, A.; Tucci, F.; Carlone, P.; Akhatov, I. Pultruded materials and structures: A review. *J. Compos. Mater.* **2020**, *54*, 4081–4117. [CrossRef]

9. Faruk, O.; Bledzki, A.K.; Fink, H.P.; Sain, M. Biocomposites reinforced with natural fibers: 2000–2010. *Prog. Polym. Sci.* **2012**, *37*, 1552–1596. [CrossRef]

10. Strauß, S.; Senz, A.; Ellinger, J. Comparison of the Processing of Epoxy Resins in Pultrusion with Open Bath Impregnation and Closed-Injection Pultrusion. *J. Compos. Sci.* **2019**, *3*, 87. [CrossRef]

11. Holmes, M. Composite technologies to the fore at K. *Reinf. Plast.* **2020**, *64*, 261–267. [CrossRef]

12. Yuksel, O.; Sandberg, M.; Hattel, J.H.; Akkerman, R.; Baran, I. Mesoscale Process Modeling of a Thick Pultruded Composite with Variability in Fiber Volume Fraction. *Materials* **2021**, *14*, 3763. [CrossRef] [PubMed]

13. Babeau, A.; Comas-Cardona, S.; Binetruy, C.; Orange, G. Modeling of heat transfer and unsaturated flow in woven fiber reinforcements during direct injection-pultrusion process of thermoplastic composites. *Compos. Part A Appl. Sci. Manuf.* **2015**, *77*, 310–318. [CrossRef]

14. Ngo, S.I.; Lim, Y.-I.; Hahn, M.-H.; Jung, J.; Bang, Y.-H. Multi-scale computational fluid dynamics of impregnation die for thermoplastic carbon fiber prepreg production. *Comput. Chem. Eng.* **2017**, *103*, 58–68. [CrossRef]

15. Kim, D.H.; Lee, W.I.; Friedrich, K. A model for a thermoplastic pultrusion process using commingled yarns. *Compos. Sci. Technol.* **2001**, *61*, 1065–1077. [CrossRef]

16. Kim, Y.; McCarthy, S.; Fanucci, J. Study of resin flow during injection-pultrusion process. In Proceedings of the 49th Annual Technical Conference (ANTEC 1991), Montreal, QC, Canada, 5–9 May 1991; pp. 1966–1969.

17. Kommu, S.; Khomami, B.; Kardos, J.L. Modeling of injected pultrusion processes: A numerical approach. *Polym. Compos.* **1998**, *19*, 335–346. [CrossRef]

18. Rahatekar, S.S.; Roux, J.A. Numerical simulation of pressure variation and resin flow in injection pultrusion. *J. Compos. Mater.* **2003**, *37*, 1067–1082. [CrossRef]

19. Srinivasagupta, D.; Potaraju, S.; Kardos, J.L.; Joseph, B. Steady state and dynamic analysis of a bench-scale injected pultrusion process. *Compos. Part A Appl. Sci. Manuf.* **2003**, *34*, 835–846. [CrossRef]

20. Liu, X.L. Iterative and transient numerical models for flow simulation of injection pultrusion. *Compos. Struct.* **2004**, *66*, 175–180. [CrossRef]

21. Liu, X.L. A finite element/nodal volume technique for flow simulation of injection pultrusion. *Compos. Part A-Appl. Sci. Manuf.* **2003**, *34*, 649–661. [CrossRef]

22. Jeswani, A.L.; Roux, J.A. Numerical modelling of design parameters for manufacturing polyester/glass composites by resin injection pultrusion. *Polym. Polym. Compos.* **2006**, *14*, 651–669. [CrossRef]

23. Masuram, N.B.; Roux, J.A.; Jeswani, A.L. Resin Viscosity Influence on Fiber Compaction in Tapered Resin Injection Pultrusion Manufacturing. *Appl. Compos. Mater.* **2018**, *25*, 485–506. [CrossRef]

24. Masuram, N.B.; Roux, J.A.; Materials, A.L. Fiber Volume Fraction Influence on Fiber Compaction in Tapered Resin Injection Pultrusion Manufacturing. *Appl. Compos. Mater.* **2016**, *23*, 421–442. [CrossRef]

25. Palikhel, D.R.; Roux, J.A.; Jeswani, A.L. Die-Attached Versus Die-Detached Resin Injection Chamber for Pultrusion. *Appl. Compos. Mater.* **2012**, *20*, 55–72. [CrossRef]

26. Shakya, N.; Roux, J.A.; Jeswani, A.L. Effect of Resin Viscosity in Fiber Reinforcement Compaction in Resin Injection Pultrusion Process. *Appl. Compos. Mater.* **2013**, *20*, 1173–1193. [CrossRef]

27. Chen, K.; Jia, M.Y.; Hua, S.; Xue, P. Optimization of initiator and activator for reactive thermoplastic pultrusion. *J. Polym. Res.* **2019**, *26*, 40. [CrossRef]

28. Chen, K.; Jia, M.; Sun, H.; Xue, P. Thermoplastic Reaction Injection Pultrusion for Continuous Glass Fiber-Reinforced Polyamide-6 Composites. *Materials* **2019**, *12*, 463. [CrossRef] [PubMed]

29. Isoldi, L.A.; Oliveira, C.P.; Rocha, L.A.O.; Souza, J.A.; Amico, S.C. Three-Dimensional Numerical Modeling of RTM and LRTM Processes. *J. Braz. Soc. Mech. Sci. Eng.* **2012**, *34*, 105–111. [CrossRef]

30. Gebart, B.R. Permeability of Unidirectional Reinforcements for RTM. *J. Compos. Mater.* **2016**, *26*, 1100–1133. [CrossRef]

31. Baran, I.; Tutum, C.C.; Hattel, J.H.; Akkerman, R. Pultrusion of a vertical axis wind turbine blade part-I: 3D thermo-chemical process simulation. *Int. J. Mater. Form.* **2014**, *8*, 379–389. [CrossRef]

32. Gadam, S.U.K.; Roux, J.A.; McCarty, T.A.; Vaughan, J.G. The impact of pultrusion processing parameters on resin pressure rise inside a tapered cylindrical die for glass-fibre/epoxy composites. *Compos. Sci. Technol.* **2000**, *60*, 945–958. [CrossRef]

33. Epple, S.; Bonten, C. Production of Continuous Fiber Thermoplastic Composites by in-situ Pultrusion. In Proceedings of the PPS-29: The 29th International Conference of the Polymer Processing Society, Nuremberg, Germany, 15–19 July 2013; American Institute of Physics: College Park, MD, USA, 2014; Volume 1593, pp. 454–457.

Article

An Enamel Based Biopolymer Prosthesis for Dental Treatment with the Proper Bond Strength and Hardness and Biosafety

Morakot Piemjai * and **Patcharee Santiwarapan**

Department of Prosthodontics, Faculty of Dentistry, Chulalongkorn University, 34 Henri-Dunant Rd., Pathumwan, Bangkok 10330, Thailand; Anneemapa@gmail.com
* Correspondence: tmorakot@chula.ac.th; Tel.: +66-2-218-8532

Abstract: Although dental prosthesis materials such as metal alloys, ceramics, and cured resin composite have long been utilized to restore teeth, their bond strength and hardness values are not well matched to human enamel. Prosthesis detachment and opposing enamel wear are major concerns in restorative dentistry. An experimental biopolymer, hybridized enamel, was synthesized and utilized as a dental prosthesis to compare hardness and tensile bond strength (TBS) with those of commercial materials. Vickers hardness (VHN) with a 100 g loading for 15 s at eight indentations on each specimen ($n = 20$) was measured. TBSs between prostheses and two types of resin luting agents ($n = 10$), Super-Bond C&B and All-Bond2 + Duo-Link, were tested. Fractured surfaces and the luting resin-prosthesis interface were examined under a stereomicroscope or a scanning electron microscope (SEM). Statistically significant differences in the TBS and hardness were revealed ($p < 0.05$). The experimental biopolymer provided a hardness value comparable with human enamel and the highest TBS for both luting agent types. The SEM micrograph demonstrated a honeycomb-like pattern interface between the experimental biopolymer and luting resin. These results suggest that this experimental biopolymer may be a better restorative material to protect from natural enamel loss from tooth reduction or attrition and prevent prosthesis detachment during mastication.

Keywords: dental prosthesis biopolymer; hardness; tensile bond strength

1. Introduction

There are four main types of materials used for fabricating dental prostheses—ceramics, metal alloys, polymers, and composites. These materials are continually being developed to obtain ideal properties for dental restorative materials. The expected requirements include biological compatibility and permanent attachment to tooth structure with physico-mechanical properties and color esthetics comparable with human enamel. Up until now, none of these materials have achieved these ideal properties [1]. Tooth-colored materials such as ceramics, porcelain fused to metal, and resin composite are widely used to make dental prostheses because of their esthetics. The major problems that contemporary materials encounter are their hardness and reduced ability to adhere to bonding or luting adhesives compared with natural human enamel. These factors affect tooth wear, abrasion or attrition, and prosthesis detachment during function which are still major factors in causing clinical failures and the short-term replacement of dental restorations [2,3].

Abrasion resistance for restorative materials should be similar to the rate of wear of tooth enamel [4]. Vickers hardness values (HV) of base metal alloys (200–395), dental porcelain (380), Lava zirconia (1250), light-cured resin composite (70–124), and human enamel (274.8 ± 18.1) have been reported [1,5–8]. Materials with a higher surface hardness than enamel tend to increase tooth wear while those with lower values are worn more easily than occluding enamel. Even though hybrid resin composites with a high content of high hardness fillers have a lower overall hardness value, they can also lead to antagonist tooth wear as well as the materials themselves [1]. However, it has been proven that wear

resistance relates to hardness which is the most commonly examined mechanical property for prosthetic tooth materials [9,10].

Another important property for dental restorative or prosthesis materials is adhesion to tooth structure via bonding or luting adhesives. Complete hybridization of resin into acid-etched enamel creates a hybrid layer with cohesive failure in resin after tensile testing [11]. The hybrid layer composed of hydroxyl apatite and resin suggests mechanical adhesion is at the monomer molecular level. This high adhesion to dental enamel and less solubility in water makes resin adhesives more popularly used than acid-based cements. However, their intimate attachment, either used as the luting or bonding agent for dental prostheses or intraorally repairing restorations, respectively, mostly fail in adhesion with much less tensile bond strength (TBS) than that of tooth structure [12–16], which can lead to the high failure rates or short-term failure from prosthesis detachment [3]. Because of the low tensile bond strength between resin adhesive and prosthesis, more inner surface area for bonding is needed to provide the prosthesis retention against the masticatory load. Thus, more invasive tooth reduction may be required to increase the prosthesis bonding interface, which reduces the tooth strength itself.

Airborne-particle abrasion with 50 μm aluminum oxide, hydrofluoric acid etching, or chemical primer application are routinely used on the prosthesis surface to improve the bond strength to resin adhesives [13,15–18]. Hydrofluoric acid, a common conditioner to decompose glass ceramics to increase surface roughness and area for higher retention of cemented prosthesis or intraoral ceramic repairing with resin composite, can injure soft tissues after exposure. Incidents of acute and chronic symptoms after hydrofluoric acid exposure such as skin or nail burns, eye injuries, inhalation and ingestion-related symptoms, or fatality have been reviewed [19]. Therefore, it is safer for both patients and clinicians if hydrofluoric acid can be eliminated in dental restorative procedures. Exposure to bisphenol A (BPA), the main molecule of Bis-GMA which is a core for resin matrix in restorative materials or luting adhesives, has an association with the adverse effects in reproductive and developmental, metabolic disease, and other health outcomes of perinatal patients, children, and adults [20]. Thus, materials or products that are BPA-free have been developed to prevent this risk.

There are two main types of resin matrix used to fix the indirect restoration or prosthesis to tooth structure, MMA-based resin or 4-methacryloyloxyethyl trimellitate anhydride in methylmethacrylate initiated by tri-n-butylborane (4-META/MMA-TBB) resin with polymethyl methacrylate (PMMA) powder (Super-Bond C&B, Sun Medical, Shiga, Japan, C&B Metabond, Parkell Inc., Brentwood, NY, USA) and bisphenol A-glycidyl methacrylate (Bis-GMA) based resin. Tensile bond strength is the common indicator used to compare the adhesion between restorative materials and resin luting agents. Although its value depends on the surface treatments and material types, different testing methods also provide different TBS values for the same restorative material or luting resin. Direct tensile testing using mini-dumbbell shaped specimens suggests that dentin bonding via hybrid layer using 4-META/MMA-TBB resin has a significantly higher TBS than those of bonding to prosthetic materials, i.e., base metal alloy, all-ceramic, and light-cured resin composite, which have the with an average of 9–12 MPa [13]. While 4-META/MMA-TBB resin with PMMA powder can provide a very high TBS of 30–40 MPa with the PMMA resin [21].

The hypothesis of this study was that the restorative material for an indirect restoration or a prosthesis developed from biopolymer, which has a human enamel-like composition, could provide the high adhesion to resin adhesives and the proper surface hardness to reduce the tooth loss from occlusal wear or reduction to gain more retention of a prosthesis that is harmless to human health. The study objectives were to compare the microhardness and tensile bond strength of an experimental biopolymer material and the commercial products, either metal alloy, ceramics, or light-cured resin composite, when two different resin luting agents were utilized.

2. Materials and Methods

The research protocol was approved by the Faculty Board Committee, Faculty of Dentistry, Chulalongkorn University, Bangkok, Thailand.

2.1. Prosthesis Fabrication

Four types of materials were selected for testing: three commercial products, metal-based alloy (WILLIAMS, New York, NY, USA), lithium disilicate-based ceramics (IPS Empress 2, Ivoclar, Schaan, Liechtenstein), resin composite (Filtek Z250, 3M ESPE, St. Paul, MN, USA), and one experimental biopolymer. The main composition of these materials is described in Table 1. Each commercial material type, metal alloy or ceramics, was prepared using a lost wax technique in accordance with the manufacturers' recommendations to make a 1 mm thickness inlay-like specimen with 4 mm × 5 mm inner and 5 mm × 6 mm outer surfaces using a standardized silicone mold. Experimental biopolymer specimens were shaped by a single operator. Resin composite was fully filled in the standardized silicone mold and light-cured for 40 s using Elipar Trilight (3M ESPE, USA) and finally polymerized in Labolight LVIII (GC Accord, Tokyo, Japan) for 5 min.

Table 1. Main composition of the tested materials.

Type of Materials	Main Composition
Metal alloy	Ni-Cr-Be-based alloy
Ceramics	Lithium disilicate in glass matrix core ingot, Veneering Layer, Glaze liquid
Resin composite	Bis-GMA (Bisphenol A diglycidyl ether dimethacrylate), UDMA (urethane dimethacrylate), Bis-EMA (Bisphenol A polyethylene glycol diether dimethacrylate), 0.01–3.5 µm silica/zirconia fillers (60% by volume)
Experimental Biopolymer	Etched bovine enamel infiltrated with methylmethacrylate resin

2.2. Microhardness Test

The outer surfaces of resin composite and experimental specimens were abraded with silicon carbide abrasive discs (grit #400, #600, #1000, and #1200) and polished with 0.05 µm alumina paste in wet conditions and then ultrasonically cleaned in water. Hardness measurements ($n = 20$) were conducted on glazed veneering layer of ceramics, polished outer surfaces of resin composite and experimental specimens, using a microhardness tester (Series FM-700e type D, Future-Tech, Kanagawa, Japan). The specimens were embedded in auto-polymerizing acrylic resin (Unifast, GC Dental Products Corp., Tokyo, Japan) and PMMA tubes to form a base for evaluation of the Vickers hardness number. Eight indentations (located at 4 corners with two indentations each and 0.5 mm apart) were measured on each specimen using a Vickers diamond pyramid at a 100 g indentation load for 15 s. For each specimen eight different measurements were recorded, and the results were averaged. The Vickers microhardness measurements of human enamel were made on the lingual inclined plane of lingual cusps of lower molars for a control group.

2.3. Tensile Bond Strength Test

After hardness testing, the ceramic, resin composite, and experimental specimens were removed from the acrylic base to expose the inner surface for tensile testing. All inlay blocks including metal alloy, ceramic, resin composite, and experimental biopolymer were embedded in the self-cured acrylic resin in PMMA tubes with the exposed inner surface. Specimens were randomly divided into two groups of 10 specimens for each type of material to bond with two different luting agents. Top surfaces were wet abraded on silicon carbide abrasive papers (grit #400, #600) to form horizontally parallel flat surfaces. A total of 80 specimens of all groups were air-abraded with 50 µm alumina at 240 kPa pressure for 15 s at 10 mm distance and cleaned in an ultrasonic water bath for 20 min. A circular area of 3.25 mm in diameter was outlined on the prosthesis surface using one-sided adhesive tape and bonded using either 4-META/MMA-TBB or All-Bond2 + DuoLink (Bisco Inc., Schaumburg, IL, USA). resin adhesives with 5 mm diameter PMMA rod vertically

aligned and loaded (10 N) using a surveyor (Figure 1). Surface treatment and bonding procedures for each material were described in Table 2. All specimens were soaked in 37 °C water for 24 h before tensile loading at a crosshead speed of 1 mm/min using a universal testing machine (Instron, Model 8872, Norwood, MA, USA) (Figure 2) following the ISO/TS 11,405 guidance [22]. The maximum forces used to pull the rods off were recorded and calculated into MPa for each group. The mode of failure was examined using a stereomicroscope (Model ML 9300, Canon, Tokyo, Japan) at $20\times$ magnification and scanning electron microscope (SEM) at $500\times$, $2000\times$ magnifications.

Figure 1. A prosthesis bonded to PMMA rod vertically aligned and loaded using a surveyor.

Table 2. Manipulation of prosthesis surface conditioning and adhesive resin.

Procedures	Materials Type	Super Bond C&B	All-Bond2 + Duo-Link
Surface treatment	Experimental biopolymer	Conditioned with 65% H_3PO_4 for 30 s, rinsed off for 10 s, air-dried for 10 s	Conditioned with 32% H_3PO_4 for 15 s, rinsed off for 15 s, air-dried,
Bonding Procedure	Experimental biopolymer, Ceramic, Resin composite	Applied Porcelain liner M with a sponge, air-dried 5 s Applied 4-META/MMA-TBB and PMMA powder using brush-dip technique	Applied primer 5 times, gently air-dried 5 s, applied thin layer of D&E resin, and DuoLink cement, light-cured for 40 s
	Metal alloy	Applied 4-META/MMA-TBB and PMMA powder using brush-dip technique	Applied primer twice, gently air-dried 5 s, applied pre-bond resin, gently air-dried, and applied DuoLink cement, light-cured for 40 s
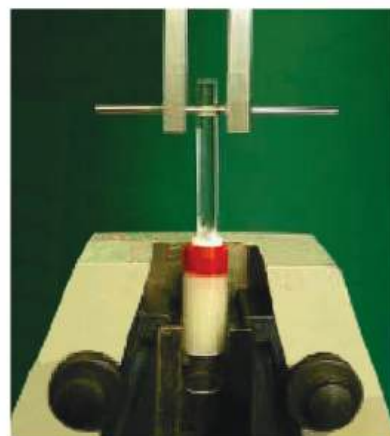
Figure 2. Tensile loading using a universal testing machine.

2.4. Examination of Prosthesis-Luting Resin Interface

After tensile testing, three fractured specimens from each group were randomly selected. Each experimental biopolymer specimen was vertically sectioned into two 5 mm thick specimens using a sectioning machine (IsoMet Isomet 1000 series 15, Buechler, Lake Bluff, IL, USA) for the polished and chemical challenge (soaking in 6 mol/L HCl for 30 s) specimens. The prosthesis-luting resin interface of experimental biopolymer sectioned specimens and the fractured specimens in the other groups were wet abraded with #400, #600, #1000, #1200, and #2000 grit abrasive papers and polished with 0.05 μm alumina paste. After water cleaning in an ultrasonic bath, all specimens were prepared for SEM examination from 35× to 7500× magnifications to visualize the characteristics of the interface.

3. Results

Means and standard deviations (SD) of microhardness values for all materials are shown in Table 3. Levene's test disclosed inhomogeneity of variances among microhardness groups ($p < 0.05$). Brown-Forsythe and Tamhane's multiple comparisons statistics found significant differences between groups ($p < 0.05$). The experimental biopolymer had a microhardness value close to that of enamel when compared with the other materials. A difference in microhardness value of approximately 50 VHN and 226 VHN less than that of human enamel was found in experimental and resin composite groups, respectively. While IPS Empress2 veneering ceramic provided a difference in microhardness value of approximately 214 VHN higher than that of human enamel.

Table 3. Mean ± SD of microhardness value (Vickers hardness number; VHN) for all groups.

Group (*n* = 20)	Vickers Hardness Number
Ceramic	550.02 ± 7.90
Resin composite	109.79 ± 3.31
Experimental biopolymer	287.16 ± 6.42
Enamel	336.12 ± 11.65

Significant differences were found between each group at $p < 0.05$.

The means ± SD tensile bond strength and mode of failure of the resin-prosthesis interface for all groups are summarized in Table 4. Two-way analysis of variance found significant differences in TBS values among different materials and resin adhesives as well as their interactions. Super-Bond C&B provided a significantly higher TBS than All-Bond2 + DuoLink. Brown-Forsythe and Tamhane tests revealed significant differences between groups ($p < 0.05$). The experimental biopolymer provided the highest TBS for both luting agents similar to that of resin composite. Ceramic material had the lowest TBS compared with the others when bonded with the same luting agent.

Table 4. Mean ± SD of tensile bond strength (MPa) and failure modes for all groups (*n* = 10).

Materials	Tensile Bond Strength (Failure Modes)	
	Super-Bond C&B	All-Bond2 + Duo-Link
Experimental biopolymer	20.45 ± 5.21 [a] (R, R/PMMA)	11.95 ± 2.85 [b] (R, A)
Metal alloy	22.00 ± 2.93 [a] (R, R/PMMA)	2.12 ± 0.77 [c] (A)
Ceramic	10.49 ± 1.40 [b] (R, A)	1.38 ± 0.41 [c] (A)
Resin composite	20.38 ± 3.66 [a] (R, R/PMMA)	9.67 ± 2.27 [b] (A)

[a,b,c] Statistically significant differences between groups shown with different superscripts ($p < 0.05$). A = Adhesive failure at prosthesis side interface, R = Cohesive failure in the cured resin, R/PMMA = Adhesive failure at PMMA rod side interface.

The mixed failure of cohesive failure in resin and adhesive failure at PMMA rod side interface (R, R/PMMA) was examined in fractured specimens of experimental biopolymer, metal alloy, and resin composite using Super-Bond C&B groups (Figure 3) with the highest TBS. Adhesive failure on the prosthesis side surface (A) was found in all materials (except

experimental biopolymer) using All-Bond2 + DuoLink (Figure 4) with the lower and least TBS. Mixed failure of cohesive failure in resin and adhesive failure on the prosthesis side interface (R, A) was found in the experimental biopolymer bonded with All-Bond2 + DuoLink and ceramic bonded with Super-Bond groups (Figure 5).
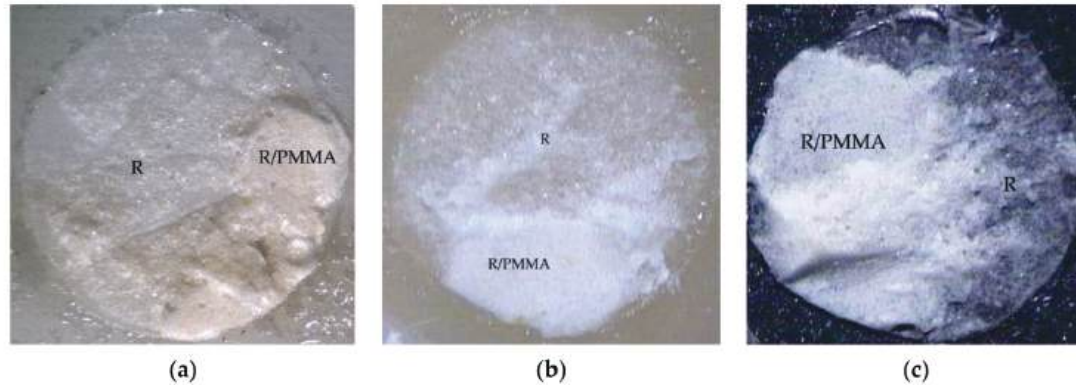
Figure 3. Mixed failure of cohesive in resin (R) and adhesive at resin-PMMA rod interface (R/PMMA) on fractured specimens of (**a**) experimental biopolymer, (**b**) resin composite, and (**c**) metal alloy, using Super-Bond C&B (original 20×).
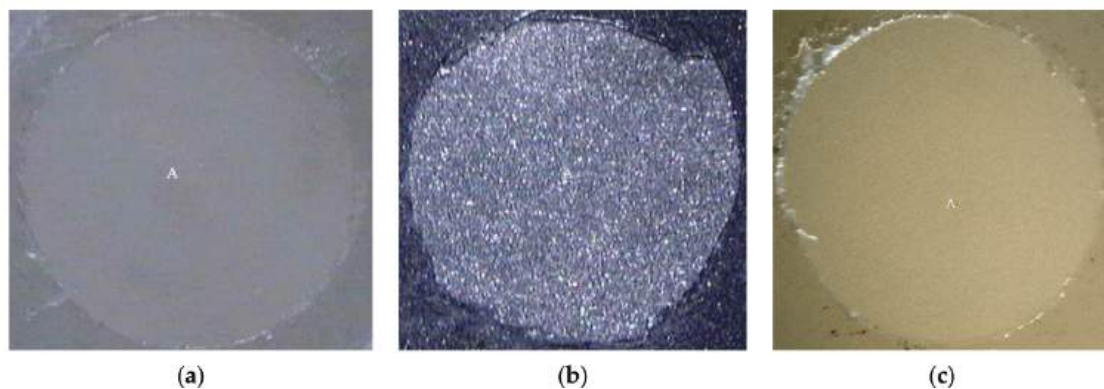
Figure 4. Adhesive failure on the prosthesis side interface (A) on fractured specimens of (**a**) ceramic, (**b**) metal alloy, and (**c**) resin composite using All-Bond2 + DuoLink (original 20×).
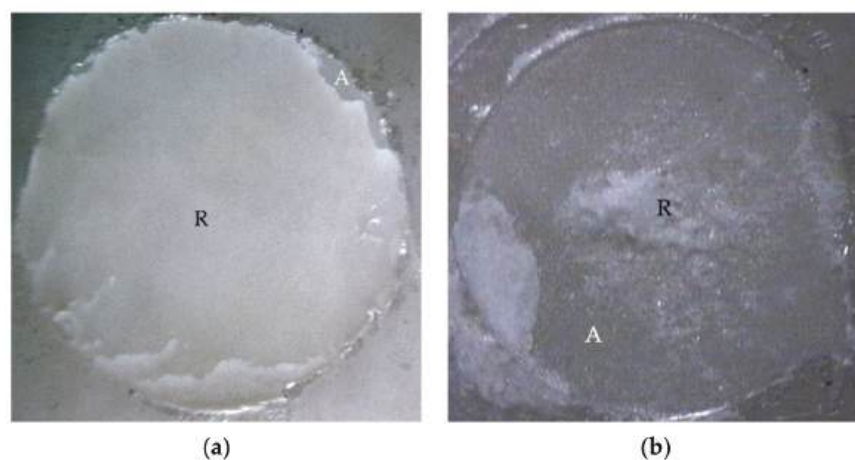
Figure 5. Mixed failure of cohesive failure in resin (R) and adhesive failure on the prosthesis side interface (A) on fractured specimens of (**a**) experimental biopolymer bonded with All-Bond2 + DuoLink and (**b**) ceramic bonded with Super-Bond (original 20×).

The SEM micrographs of experimental biopolymer and Super-Bond interfaces demonstrated the consistent thickness of the hybrid layer in the prosthesis material both before

and after chemical immersion producing a honeycomb-like pattern (Figures 6 and 7). The degradation of the hybrid layer after HCl immersion was found in the experimental biopolymer bonded with All-Bond2 + DuoLink (Figure 8). The interface of metal alloy and resin composite using Super Bond showed well-impregnated resin in the irregular pits and fissures formed by air-abrading with 50 µm alumina (Figure 9), whereas the bonded resin-ceramic interface using Super-Bond showed less irregularity of the ceramic surface with some area of resin detachment (Figure 10).

(**a**)   (**b**)
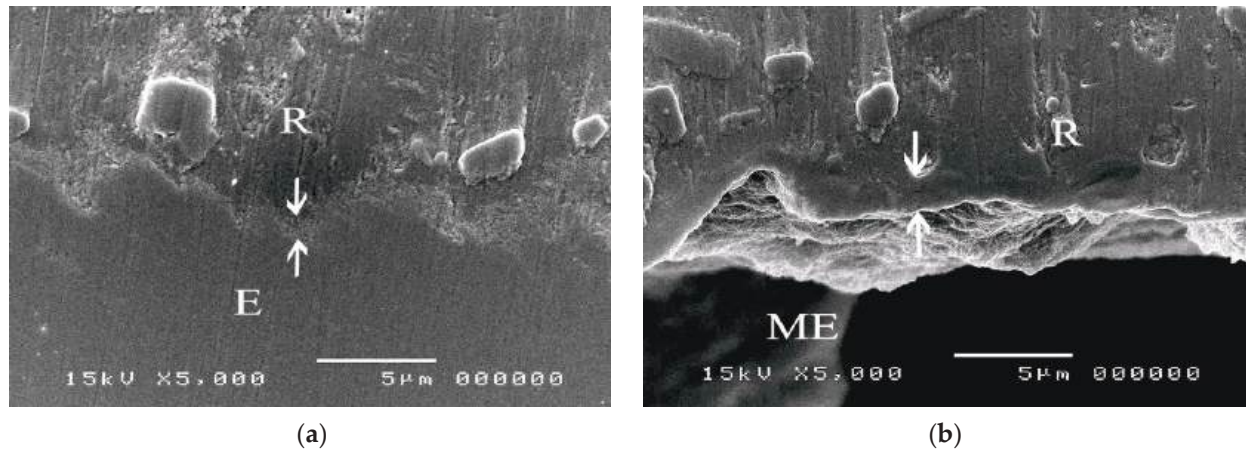
Figure 6. SEM micrographs of fractured experimental biopolymer bonded with Super-Bond demonstrating the consistent thickness of the hybrid layer (arrowed) at the prosthesis-luting resin interface in (**a**) polished and (**b**) chemically challenged specimens (original 5000×, E = experimental biopolymer, R = resin, ME = modified experimental biopolymer).
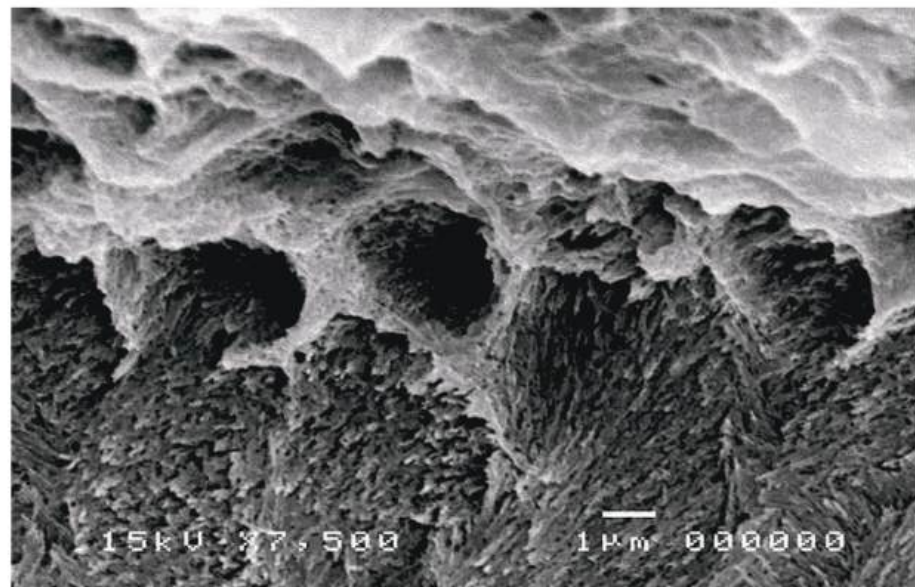
Figure 7. An SEM micrograph of fractured experimental biopolymer bonded with Super-Bond specimen after chemical challenge demonstrating the honeycomb-like pattern at the interfacial area (original 7500×).
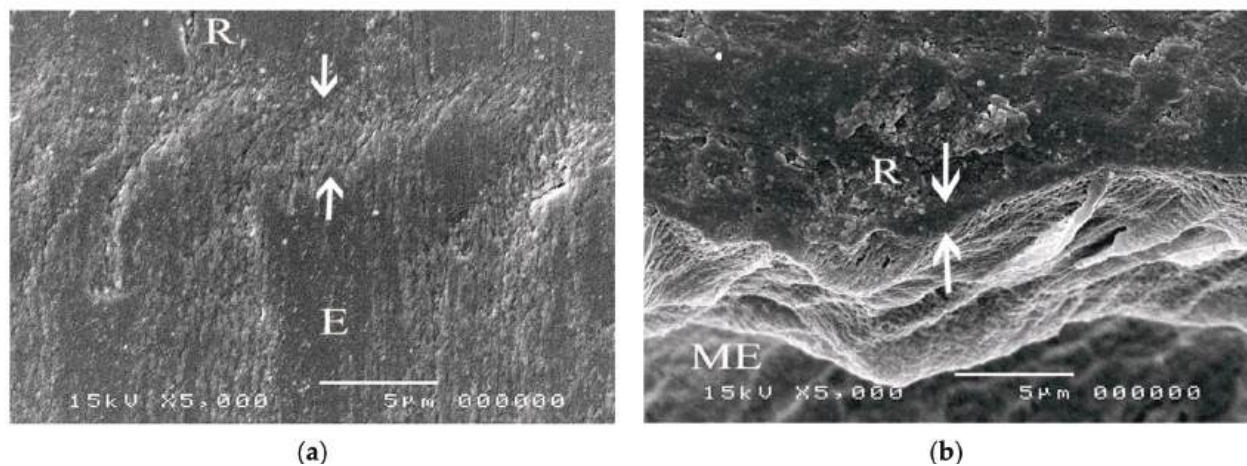
Figure 8. SEM micrographs of fractured ceramic bonded with Super-Bond demonstrating: (**a**) the hybrid layer (arrowed) in a polished specimen and (**b**) the thinner and degradation layer after chemical challenge (original 5000×, E = experimental biopolymer, R = resin, ME = modified experimental biopolymer).
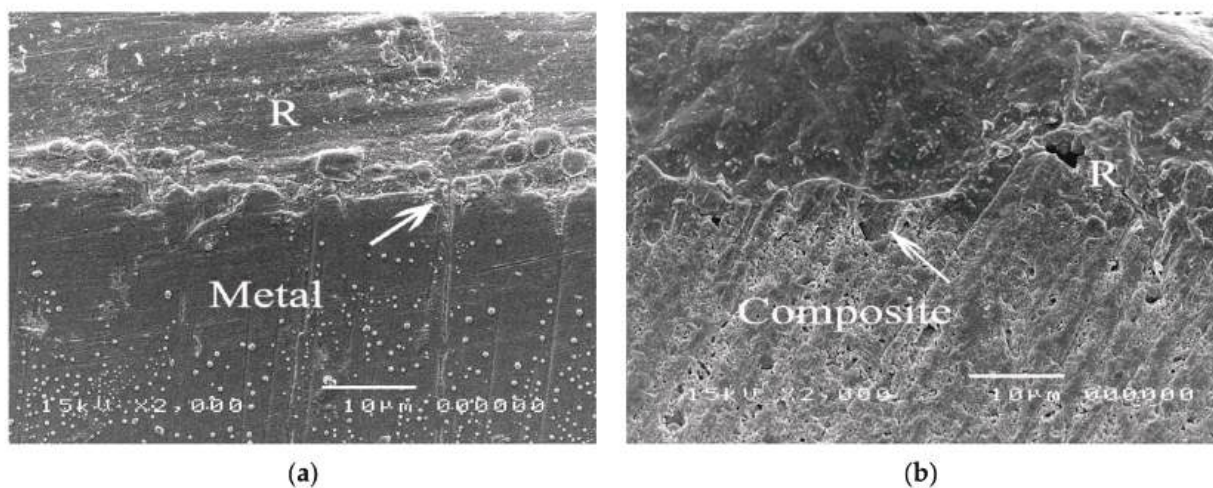
Figure 9. SEM micrographs demonstrating well-impregnated Super-Bond resin into the irregular pits and fissures (arrowed) of the fractured specimens in (**a**) metal alloy and (**b**) resin composite specimens (original 2000×, R = luting resin).
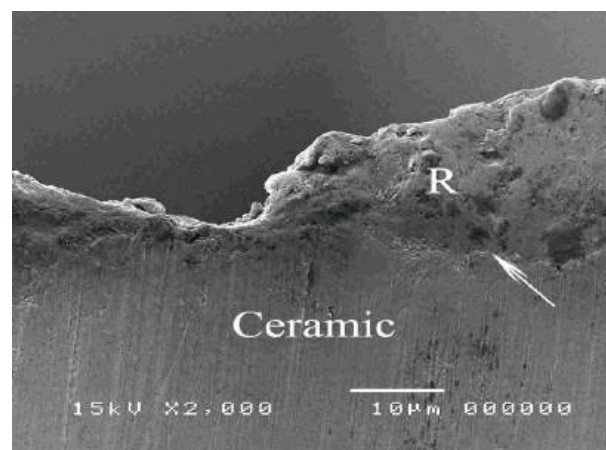
Figure 10. An SEM micrograph of the resin-ceramic interface using Super-Bond demonstrating the shallow irregularity on the ceramic surface of the fractured specimen (original 2000 ×, R = luting resin).

4. Discussion

Vickers hardness is widely used to assess the mechanical properties of dental restorative materials such as resin-based composites and ceramics because it is easier to use compared with other hardness tests. The hardness value has strong correlations with elastic modulus and fracture toughness values [23], which can predict the durability and wear resistance of restorations. In Table 3, the mean VHN of experimental biopolymer (287) is less than the VHN of human enamel (336); this suggests that it is rarely possible for this material to wear the human enamel. The lithium disilicate-based veneering glass ceramic provided the highest VHN (550) suggesting its greatest ability to wear opposing enamel as it has been reported in clinical studies [24,25]. The light-cured microhybrid Z250 resin composite revealed the lowest VHN (110) with 226 VHN lower than that of enamel and hence the higher wear rate reported earlier [26,27]. This may result in shorter-term replacement when occluding with ceramics or based metal alloy. The experimental biopolymer which is composed mainly of bovine enamel, and has 50 VHN less than that of human enamel could be best in terms of preventing antagonist tooth wear, wear resistance, and durability under masticatory load. The least enamel loss occurred when natural enamel occludes against natural enamel [28].

The tensile bond strength test is widely used to compare the adhesive properties of dental restorative materials as well as between tooth and materials. The TBS values between dental restorative materials and luting resin or bonding agents depend on the test methods [29], thus the TBS values can only be reliably compared when using the same standardized method. The results in Table 4 show the statistically significant highest values (20–22 MPa) of metal alloy, resin composite, and experimental biopolymer when bonded with Super-Bond resin. The mode of failure (R, R/PMMA) in these highest TBS groups (Figure 3) suggests that 4-META/MMA-TBB resin can penetrate well and adhere to the micro-roughened prosthesis surface created by being air-abraded with 50 μm alumina either with or without phosphoric acid conditioning better than the tensile strength of cured Super-Bond. The least TBS values (1–2 MPa) were found in metal alloy and ceramic bonded with All-Bond2 + DuoLink resin with adhesive failure (A) (Figure 4a,b). This suggests that there is the least content of Bis-GMA-based resin attached to the air-abraded surface of metal alloy and ceramics after polymerization is initiated. However, this resin could partially infiltrate more into the roughened resin composite surface and micro-porosity surface of alumina-blasted and acid-etched experimental biopolymer resulting in the higher TBS values of 9–11 MPa with adhesive failure (A) (Figure 4c) and mixed failure (R, A) (Figure 5a), respectively. The roughened surface of IPS Empress 2 ingot after air-abrasion with 50 μm alumina and bonding with Super-Bond provided an average TBS of 10 MPa with mixed failure (R, A) (Figure 5b) lower than the other materials, but higher than that bonded with All-Bond2 + DuoLink (1 MPa) with adhesive failure (A) (Figure 4a). These results suggest that type of prosthesis materials and the ability of resin monomers to penetrate micro-spaces are the main factors contributing to the high TBS.

Super-Bond C&B is the MMA-based resin that contains 4-META for a higher penetration rate of MMA and TBB which can initiate a polymerization reaction in the presence of oxygen and water. The molecular weight and viscosity of 4-META/MMA-TBB are much less than those of All-Bond2 + DuoLink, which is mainly composed of Bis-GMA, biphenyl dimethacrylate, and urethane dimethacrylate, therefore, it can effectively penetrate the micro space easier and faster before the polymerization starts. SEM micrographs of the prothesis-luting resin interface of the experimental polymer (Figure 6) demonstrated the consistent thickness of the hybrid layer (2–3 μm) after immersion in HCl solution. This acid-resistant layer with a honeycomb-like pattern at the interfacial area (Figure 7) suggests high permeability of acid-etched biopolymer for the impregnation of 4-META/MMA-TBB resin. In contrast, the degradation of the hybrid layer after soaking in HCl solution (Figure 8) suggests the partial impregnation of All-Bond2 + DuoLink, which leads to the mixed failure (R, A) with a lower TBS (Figure 5a, Table 4).

The prothesis-luting resin interface of fractured metal alloy and resin composite bonded with Super-Bond specimens (Figure 9) suggests the better ability of 4-META/MMA-TBB to penetrate in the deep pits and fissures (4–5 μm) created using air-abrasion with 50 μm alumina resulting in a higher bond strength against the polymerization contraction forces as well as higher tensile strength than that of cured Super-Bond. The interface of ceramic bonded with Super-Bond specimens after tensile loading (Figure 10) demonstrated the shallow irregular surface of ceramic resulting in the lower TBS with mixed failure (R, A) (Table 4, Figure 5b). This result implies that the IPS Empress 2 ingot surface has the highest abrasive resistance against 50 μm alumina blasting compared with the other materials. Therefore, to gain more TBS, the hydrofluoric acid application was recommended to provide micro-undercut spaces on the glass matrix for resin adhesive infiltration [30,31]. For the health concern, experimental biopolymer is composed mainly of natural bovine enamel (90%) and PMMA resin, which is BPA-free and has no need for hydrofluoric acid treatment. The results of this study support the study hypothesis.

5. Conclusions

A dental prosthesis fabricated using a biopolymer provided a microhardness value similar to that of human enamel and the highest TBS for both 4-MATA/MMA-TBB and All-Bond2 + DuoLink resin. With the simple and safe surface treatment, 50 μm alumina blasting and phosphoric acid etching, the experimental biopolymer surface could gain a TBS higher than the tensile strength of cured Super-Bond C&B. According to the best properties compared with the other tooth-colored tested materials, this enamel-based biopolymer may be the first choice for a dental prosthesis fabricated using CAD/CAM (Computer-aided design/Computer-aided manufacturing) technology.

References

1. Anusavice, K. *Phillips Science of Dental Material*, 12th ed.; Elsevier: Amsterdam, The Netherlands, 2013; pp. 680–740.
2. Ferracane, J.L. Resin-based composite performance: Are there some things we can't predict. *Dent. Mater.* **2013**, *29*, 51–58. [CrossRef] [PubMed]
3. Goodacre, C.J.; Bernal, G.; Rungcharassaeng, K. Clinical complications in fixed prosthodontics. *J. Prosthet. Dent.* **2003**, *90*, 31–41. [CrossRef]
4. Lambrechts, P.; Braem, M.; Vuylsteke-Wauters, M.; Vanherle, G. Quantitative in vivo wear of human enamel. *J. Dent. Res.* **1989**, *68*, 1752–1754. [CrossRef] [PubMed]
5. Zafar, M.S.; Amin, F.; Fareed, M.A.; Ghabbani, H.; Riaz, S.; Khurshid, Z.; Kumar, N. Biomimetic Aspects of Restorative Dentistry Biomaterials. *Biomimetics* **2020**, *5*, 34. [CrossRef] [PubMed]
6. Posku, L.T.; Placido, E.; Cardoso, P.E.C. Influence of placement techniques on Vickers and Knoop hardness of class 2 composite resin restorations. *Dent. Mater.* **2004**, *20*, 726–732. [CrossRef]
7. Esmaeili, B.; Safarcherati, H.; Vaezi, A. Hardness Evaluation of Composite Resins Cured with QTH and LED. *J. Dent. Res. Dent. Clin. Dent. Prospect.* **2014**, *8*, 40–44. [CrossRef]

8. Chun, K.J.; Choi, H.H.; Lee, J.Y. Comparison of mechanical property and role between enamel and dentin in the human teeth. *J. Dent. Biomech.* **2014**, *6*, 1758736014520809. [CrossRef]

9. Mandikos, M.N.; McGivney, G.P.; Davis, E.; Bush, P.J.; Carter, J.M. A comparison of the wear resistance and hardness of indirect composite resins. *J. Prosthet. Dent.* **2001**, *85*, 386–395. [CrossRef]

10. Campanha, N.H.; Pavarina, A.C.; Vergani, C.E.; Machado, A.L. Effect of microwave sterilization and water storage on the Vickers hardness of acrylic resin denture teeth. *J. Prosthet. Dent.* **2005**, *93*, 483–487. [CrossRef]

11. Nakabayashi, N.; Pashley, D.H. *Hybridization of Dental Hard Tissue*; Quintessence Publishing, Co.: Tokyo, Japan, 1998; pp. 5–10.

12. Pattaratiwanont, R.; Piemjai, M.; Garcia-Godoy, F. Survival of posterior fixed partial dentures with minimal tooth reduction and improved esthetics: An in vitro study. *J. Prosthet. Dent.* **2020**, *30. in press*. [CrossRef]

13. Piemjai, M.; Nakabayashi, N. Direct Tensile Strength and Characteristics of Dentin Restored with All-Ceramic, Resin-Composite, and Cast Metal Prostheses Cemented with Resin Adhesives. *BioMed Res. Int.* **2015**, *2015*, 656948. [CrossRef]

14. Barkmeire, W.W.; Ericson, R.L. Shear bond strength of composite to enamel and dentin using Scotchbond Multi-purpose. *Am. J. Dent.* **1994**, *7*, 175–179.

15. Parsa, R.Z.; Goldstein, G.R.; Barrack, G.M.; LeGeros, R.Z. An in vitro comparison of tensile bond strengths of noble and base metal alloys to enamel. *J. Prosthet. Dent.* **2003**, *90*, 175–183. [CrossRef]

16. Petrie, C.S.; Eick, D.J.; Williams, K.; Spencer, P.A. Comparison of 3 alloy surface treatments for resin-bonded prostheses. *J. Prosthodont.* **2001**, *10*, 217–223. [CrossRef]

17. Peumans, M.; Valjakova, E.B.; De Munck, J.; Mishevska, C.B.; Van Meerbeek, B. Bonding effectiveness of luting composites to different CAD/CAM materials. *J. Adhes Dent.* **2016**, *18*, 289–302.

18. Piemjai, M.; Adunphichet, N. Impact of hybrid layer formation on the 15-year survival, complications, and failures of full-coverage retainers. *J. Prosthodont. Res.* **2022**, *66*, 131–140. [CrossRef] [PubMed]

19. Özcan, M.; Allahbeickaraghi, A.; Dündar, M. Possible hazardous effects of hydrofluoric acid and recommendations for treatment approach: A review. *Clin. Oral Investig.* **2012**, *16*, 15–23. [CrossRef]

20. Rochester, J.R. Bisphenol A and human health: A review of the literature. *Reprod. Toxicol.* **2013**, *42*, 132–155. [CrossRef]

21. Piemjai, M.; Nakabayashi, N. Effect of dentin conditioners on wet bonding of 4-META/MMA-TBB resin. *J. Adhes. Dent.* **2001**, *3*, 325–331. [PubMed]

22. *ISO/TS 11405*; Dental Materials Guidance on Testing of Adhesion to Tooth Structure, 2nd ed.; ISO: Geneva, Switzerland, 2003.

23. Li, J.; Li, H.; Foka, A.S.L.; Watts, D.C. Multiple correlations of material parameters of light-cured dental composites. *Dent. Mater.* **2009**, *25*, 829–836. [CrossRef]

24. Sorensen, J.A.; Cruz, M.A.; Berge, H.X. In vivo measurement of antagonist tooth wear opposing ceramic bridges. *J. Dent. Res.* **1999**, *78*, 473.

25. Heintze, S.D.; Cavalleri, A.; Forjanic, M.; Zellweger, G.; Rousson, V. Wear of ceramic and antagonist—A Systemic evaluation of influencing factors in vitro. *Dent. Mater.* **2008**, *24*, 433–449. [CrossRef] [PubMed]

26. Heintze, S.D.; Zellweger, G.; Zappini, G. The relationship between physical parameters and wear rates of dental composites. *Wear* **2007**, *263*, 1138–1146. [CrossRef]

27. Say, E.C.; Civelek, A.; Nobecourt, A.; Ersoy, M.; Guleryuz, C. Wear and microhardness of different resin composite materials. *Oper. Dent.* **2003**, *28*, 628–634.

28. Göhring, T.N.; Besek, M.J.; Schmidlin, P.R. Attritional wear and abrasive surface alterations of composite resin materials in vitro. *J. Dent.* **2002**, *30*, 119–127. [CrossRef]

29. Nakabayashi, N. Importance of mini-dumbbell specimen to access tensile strength of restored dentine: Historical background and the future perspective in dentistry. *J. Dent.* **2004**, *32*, 431–442. [CrossRef]

30. Spohr, A.M.; Sobrinho, L.C.; Consani, S.; Sinhoreti, M.A.C.; Knowles, J.C. Influence of surface conditions and silane agent on the bond of resin to IPS Empress 2 ceramic. *Int. J. Prosthodont.* **2003**, *16*, 277–282. [PubMed]

31. Nagai, T.; Kawamoto, Y.; Kakehashi, Y.; Matsumura, H. Adhesive bonding of a lithium disilicate ceramic material with resin-based luting agents. *J. Oral Rehabil.* **2005**, *32*, 598–605. [CrossRef] [PubMed]

Multi-Criteria Decision Approach to Design a Vacuum Infusion Process Layout Providing the Polymeric Composite Part Quality

Sergey Shevtsov [1,*] , Igor Zhilyaev [2], Shun-Hsyung Chang [3] , Jiing-Kae Wu [4] and Natalia Snezhina [5]

1 Laboratory of Composite Materials and Structures, Southern Center of Russian Academy of Science, 344006 Rostov on Don, Russia

2 Institute of Polymer Engineering, University of Applied Sciences Northwestern Switzerland FHNW, CH-5210 Windisch, Switzerland; igor.zhilyaev@fhnw.ch

3 Dept. of Microelectronics, National Kaohsiung University of Science and Technology, Kaohsiung City 82445, Taiwan; shchang@nkust.edu.tw

4 Chen-Wei International Co., Ltd., Kaohsiung City 80764, Taiwan; jiingkae.wu@gmail.com

5 Dept. of Aircraft Engineering, Don State Technical University, 344000 Rostov on Don, Russia; snezhina_nataly@mail.ru

* Correspondence: sergnshevtsov@gmail.com

Abstract: The increasingly widespread use of vacuum assisted technologies in the manufacture of polymer-composite structures does not always provide the required product quality and repeatability. Deterioration of quality most often appears itself in the form of incomplete filling of the preform with resin as a result of the inner and outer dry spot formation, as well as due to premature gelation of the resin and blockage of the vacuum port. As experience shows, these undesirable phenomena are significantly dependent on the location of the resin and vacuum ports. This article presents a method for making a decision on the rational design of a process layout. It is based on early forecasting of its objectives in terms of quality and reliability when simulating its finite element model, on the correlation analysis of the preliminary and final quality assessments, as well as on the study of the cross-correlation of a group of early calculated sub-criteria. The effectiveness of the proposed method is demonstrated by the example of vacuum infusion of a 3D thin-walled structure of complex geometry.

Keywords: polymeric composites; composite technology; vacuum infusion; process modeling and optimization; multi-criteria decision; Pareto frontier

1. Introduction

The processes of vacuum infusion in the production of polymer composite structures have gained significant popularity, especially in the last decade, due to their relative ease of implementation and inexpensive equipment [1–6]. They are increasingly used in aircraft, aerospace, shipbuilding and automotive industries. The implementation of vacuum assisted resin infusion technologies, as a rule, includes the following sequence of actions: laying-up of preform—dry fabric or glass or carbon fiber reinforcement on the mold surface; then covering of the whole preform by the flexible vacuum bag and sealing. The vacuum line connects to the preform through a vent (outlet), while atmospheric pressure acts on the resin inside the vessel, drawing it into the preform through the resin gate (inlet) and onto the vacuum bag, compacting the porous preform. A pressure gradient, which arises in the porous preform, causes the liquid resin to spread and fill the volume of the dry fabric. This process is accompanied by a group of related phenomena that are inherent to the vacuum infusion process. As the preform fills with resin, the average pressure gradient causing it to flow decreases. In addition, gradual resin curing, resulting in an increase in resin viscosity, also slows down the filling rate of the preform, the porosity of which is reduced due to compressive atmospheric pressure [7–9]. When several simultaneously

moving streams occur, which is typical for infused structures of even relatively small complexity or in the presence of accelerating highly permeable (HPM) tissues or tapes, situations are possible when resin streams block empty areas, forming the inner or outer dry spots. Such streams can also block air access to the vacuum vent, stopping the movement of the resin [10–13]. The listed phenomena are extremely undesirable; their consequences are heterogeneity, deterioration of the mechanical properties of the composite in the body of the molded structure, which often leads to the impossibility of its correction and complete unsuitability. In addition, the complexity and high interdependence of the phenomena occurring in the infused structure, their high sensitivity to the process conditions, lead to instability of the achieved quality and bad repeatability of the final results. All most important problems of the vacuum infusion process implementation are discussed in detail in [14–17].

The significant labor intensity and cost of expensive components required to improve the quality indicators of the process by trial and error, gave rise to a large number of works oriented to the development of the computer modeling of the vacuum assisted resin infusion technologies. Most of these works [18–22] use the so-called FE / CV (Finite Element/Control volume) approach, which made it possible to overcome the fundamental difficulty of modeling processes with moving boundaries on which conditions change at each time step. Subsequently, some authors have proposed other approaches. Among them, the approach [23], which is based on the use of a lumped model that considers the vacuum infusion process as a dynamic system and significantly reduces the computational complexity, as well as approaches aimed at increasing the accuracy of reconstruction of the moving resin front using the level set [24] and the phase field equations [25,26]. Due to the fact that the process of vacuum infusion includes several interacting phenomena of different nature, all the numerical modeling methods require many experimental data obtained by independent, rather sophisticated methods, and empirical dependences between the process parameters built on the basis of these data. These are the dependences of the compaction and porosity of the preform on external pressure, its permeability on porosity, the dependence of the degree of cure and resin viscosity on time and temperature, and the dependence of the thermal properties of the preform at various stages of its filling with resin. The experimental technique and the results described in [8,9,27–36] are used in the modified empirical models of this work, whose construction is described in detail in [26,37].

The goal of most of the developed models of the vacuum infusion process is to understand the evolving dynamics of the formation of a resin flow pattern in a porous preform. Only a small part of the developed models was used in algorithms for inverse problems of optimization of quality [38–41] and (or) process productivity [42,43], and also to accept the tradeoff between quality and cost [44,45]. Two classes of parameters are most often used as the design variables: parameters of the process layout (number and location of injection gates and vacuum vents, their throughput) and process modes (temperatures of injected resin and preform heating, pressure in the vacuum line and in the resin injection gate). It depends on the computational complexity of the forward problem simulating the filling the preform with resin and on the number of numerical experiments that need to be carried out to find the region of the global or local optimum, taking into account the existing constraints. Therefore, in the studies on optimization of vacuum infusion processes, very simple geometries of composite preforms are considered.

The aim of the presented work is to significantly reduce the computational costs for solving the inverse problem of optimizing vacuum infusion of a rather complex composite part when varying the parameters of the process layout to obtain their values that provide the best attainable criteria for the quality and reliability. As the quality criterion of infusion is taken the unfilled volume of the preform at the time of the cessation of the resin spreading. To determine the auxiliary criteria that make it possible to predict the results of the process at the early stages of its simulation, an analysis of their correlation with the final values of the quality and reliability criteria is carried out, as well as an analysis of cross-correlation of these sub-criteria. The used approach follows predictive modeling technique, which is

defined as the process of applying a model or mining algorithm to data in order to predict new or future observations [46]. This definition includes temporal prediction, in which observations up to time t are used to predict future values at time t1 > t. A simple statistical analysis of numerous observations to establish a relationship between the current and future state of the system is most relevant when it is impossible to analytically express such a relationship [47,48].

The remainder of this article is organized as follows. The second section contains a brief description of the forward modeling problem formulation with the most important modifications of the empirical dependences of the system parameters. In the third section, an example of computer modeling of a transient process of vacuum infusion of a 3D composite structure is considered, whose geometry is imported from a revised CAD model. As a result of the analysis of the time history of the predictive sub-criteria and the analysis of their correlation with the main quality objective—the relative voids volume V_v in the preform when the resin stops, the combined predictive criterion is determined. The fourth section is focused on an analysis of optimum regions in criteria and design spaces in respect that the studied optimization problem is multi-objective with constraints. The final section is devoted to a discussion of the capabilities of the developed method and software tools, as well as the prospects for its perfectioning to improve the quality and productivity indicators achieved at the post-infusion stage due to controlled exposure to temperature and external pressure.

2. The Forward Modeling Problem Statement

The model under consideration describes the processes in a porous composite preform, which is a relatively thin-walled extended structure with a possible variation in the wall thickness, laid on an open mold. The example presented in the article does not take into account the layered structure, anisotropy of porosity and permeability of the preform. The developed software tool for modeling the forward problem is able to take into account the tensorial nature of the preform permeability, as well as its layered structure. However, the vacuum infusion process is almost never used when molding high loaded composite structures with orthotropic symmetry of the material. In such cases, transversal isotropy is ensured by the corresponding stacking sequence of the unidirectional or fabric layers. As shown in experimental studies [9,11], with a small and almost unchanged wall thickness of the molded composite structure, in-plane permeability plays a decisive role in the infusion process. These considerations justify the assumptions made in the presented work.

An arbitrary number of resin gates and vacuum vents can be attached to any location on the infused preform. The spreading of a liquid resin under the action of the gradient of internal propulsive pressure occurs during its continuous curing and changes in viscosity, while the pressure distribution in the preform depends on its local filling with resin. A local compressive strain of the preform under the action of the difference between external and internal pressure and, as a consequence, its porosity and permeability depend on its state (dry or wet). The evolution of the moving resin state is described by the equation of convection/thermal kinetics/diffusion of the degree of cure. All free surfaces of vacuum bag, which covers the preform, and open mold are exposed to convective action of ambient air at a controlled temperature. The system of the governing equations describes the entire complex of the listed phenomena in the overall system "filling a porous preform-mold" before the start of resin gelation, which prevents its spread. All the assumptions made are described below in the text of the section.

The system of the governing equations of the forward modeling problem is presented in Equations (1a)–(1d).

$$
\begin{cases}
\partial \varphi / \partial t + \mathbf{u} \cdot \nabla \varphi = \nabla \cdot \gamma \nabla G; & (1a) \\
\left(1 - V_f\right) \cdot \dfrac{2}{\pi} \dfrac{\zeta}{1 + (\zeta p_m)^2} \dfrac{\partial p_m}{\partial t} - \nabla \left(\dfrac{[K]}{\mu} \nabla p_m\right) = 0; & (1b) \\
\partial \alpha / \partial t - ([K]/\mu) \cdot \nabla p \cdot \nabla \alpha - \nabla \cdot (c_\alpha \nabla \alpha) = F(\alpha, t, T); & (1c) \\
\rho_{pr} C_{pr} \partial T / \partial T + \nabla \cdot \left(-k_{pr} \nabla T\right) = Q_{exo}; & (1d)
\end{cases}
$$

The dependent variable $\varphi \in [-1; 1]$ in the Cahn-Hilliard phase field Equation (1a) [49], which describes the motion of the boundary between void and filled preform areas defines a local resin filling V_r in accordance with $V_r = (\varphi + 1)/2 \in [0; 1]$. In this equation G is a chemical potential, γ is the phase's mobility, and $\mathbf{u}$ is the superficial resin velocity.

The second Equation (1b) of the coupled problem describing the dynamics of the viscous resin in unsaturated porous medium under pressure p_m is the Richards equation modified by van Genuchten [50], where V_f is a fiber volume fraction, $[K]$ is a permeability tensor, μ is resin viscosity, ζ is the reciprocal of a certain reference pressure, taken equal to atmospheric one $\zeta = 1/p_{atm}$.

The convection/diffusion/kinetic Equation (1c) for the time-space evolution of degree of cure α combines three most important phenomena in the moving epoxy resin—diffusion of α, which depends on the kinetic and rheological state of the resin [51] and its displacement during resin spreading [11]. In this equation c_α is the diffusion coefficient, whereas source term $F(\alpha, t, T)$ describing the time dependence of the evolved α obeys the autocatalytic equation, which solution $\alpha(t)$ allows to determine an intensity of the exothermal heat source Q_{exo}

$$
Q_{exo} = Q_{tot} \rho_r \left(1 - V_f\right) \cdot V_r \cdot \partial \alpha / \partial t, \tag{2}
$$

where Q_{tot} is the total amount of heat released during the curing of the unit mass of the resin and ρ_r is its mass density. The thermal properties of the preform: mass density ρ_{pr}, specific heat capacity C_{pr} and thermal conductivity k_{pr} are determined using mixing rule by using the same thermal properties of resin, dry preform and a local distribution of the resin filling V_r [52]. All the initial and boundary conditions for Equations (1a)–(1d), as well as the dependencies of the fiber volume fraction V_f on the compression pressure $p_{comp}(\mathbf{r}, t) = p_{atm} - p_m(\mathbf{r}, t)$, the permeability K (adopted as isotropic) of the preform on the porosity V_φ, thermal properties of resin and air on the temperature T and pressure p_m, in detail are described in our work [26]. Note, however, that there have been significant changes to some of the system property dependencies.

For the dependence of the viscosity of the resin $\mu(T, \alpha, t)$ on the degree of cure, instead of the Castro-Makosko model [16,29], the model

$$
\mu(T, \alpha, t) = \mu_0(T^{in}) \cdot \exp\left(v_1 \cdot (T(t) - T^{in}) + v_2 \cdot \alpha(T, T^{in}, t)\right) \tag{3}
$$

was proposed. It is devoid of discontinuity at the resin gelation, it contains a directly measurable parameter—the viscosity $\mu_0(T^{in})$ at the initial temperature and only two coefficients v_1, v_2 that are simply determined in the experiment. We use the refined semi-empirical dependence for the diffusion coefficient in Equation (1c), taking into account its decrease with increasing resin viscosity and dependence on the resin filling V_r:

$$
c_\alpha = c_\alpha^0 \cdot \frac{(1 + \tanh((\alpha - 1)/\sigma_\alpha))}{\max(\log 10(\mu), 2) - 1} V_r, \tag{4}
$$

where the values $c_\alpha^0 = 0.001$ and $\sigma_\alpha = 0.15$ were determined on the basis of the compared results of experiments and numerical simulations carried out using a simple 1D system for molding a liquid epoxy resin. The global problem of prediction the dependence of the macroscopic properties of polymers on their properties at the molecular level (variations

in inter- and intramolecular chemical reactivity, diffusivity, segmental compositions, etc.) was studied in [53] on the base of combined kinetic Monte Carlo and molecular dynamics simulations. This work presents a detailed analysis of the difficulties and restrictions encountered by even the sophisticated experimental methods, as well as theoretical methodologies, in particular, the limitations of their adequate description of the time evolution of the concentrations of reagents, intermediates and product concentrations before the onset of gelation. The approach implemented in the presented article is, by definition, phenomenological, i.e., excluding processes at the molecular level from consideration. Therefore, relation (4) should be considered as an empirical one, giving a correct qualitative description, substantiated experimentally, but the quantitative values of its parameters should be refined for each epoxy resin used.

The approach to solving the forward modeling problem formulated here is used in the next section in relation to the process of vacuum infusion of a 3D composite structure in order to identify the most important features of the process and find particular pre-calculated criteria that allow predicting its final indicators. All numerical values of the modeled system parameters are used from the manufacturer, from the reliable results of the referenced studies and own experiments, whose data are published in [25,26,37].

3. Modeled Vacuum Infusion System, Some Simulation Results and Predictive Criteria

The numerical experiments described below were carried out with a model of a composite preform laid on an open mold made of polymerized CFRP (Carbon Fibers Reinforced Plastic) with a thickness of about 5 mm. After eliminating the joints between the patches of the CAD (Computer Aided Design) model surface and attaching an open form to it (see Figure 1), the assembly geometry was imported into the CAE (Computer Aided Engineering) system Comsol Multiphysics 5.5 (Comsol LLC, Burlington, MA, USA) and subjected to finite element (FE) meshing.
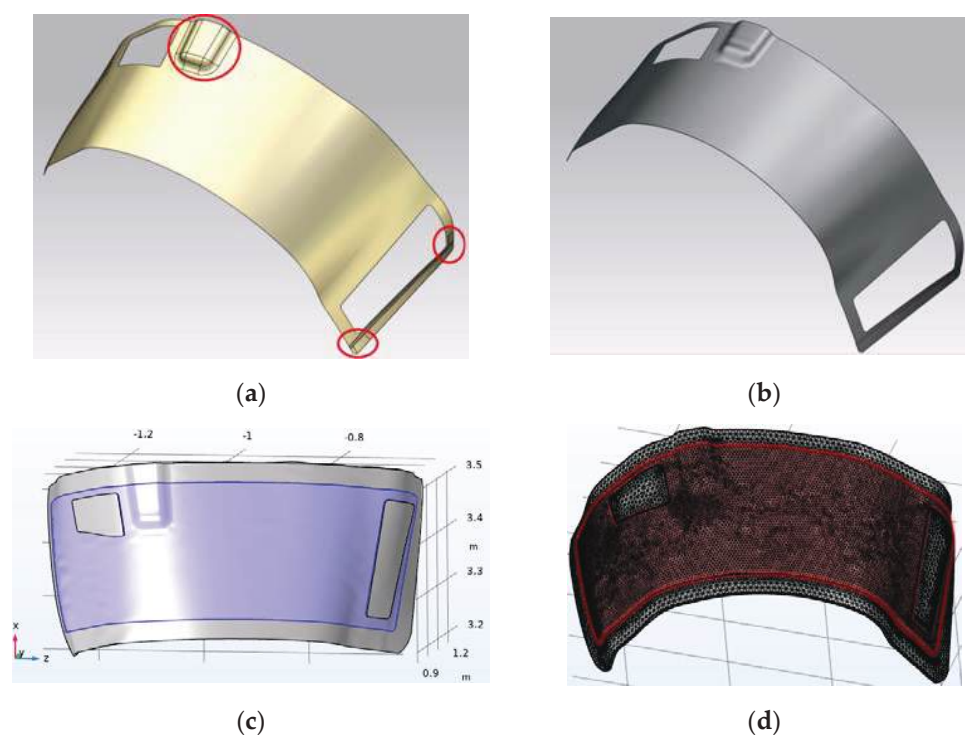
Figure 1. From the CAD model of the molded composite structure to the finite element (FE) model of the system of its vacuum infusion: (**a**) The initial CAD model; (**b**) CAD model of the structure after correction of its surface topology; (**c**) CAD model of assembled open mold with preform laid on it; (**d**) CAE model of the assembly after FE meshing.

A high-permeability (HPM) tape is laid along the perimeter of the preform, which has a gap at the location of the vacuum vent (see Figure 2). Its shift relative to a certain axis of the part and the gap between the edges of the HPM tape can vary.

(a) **(b)**
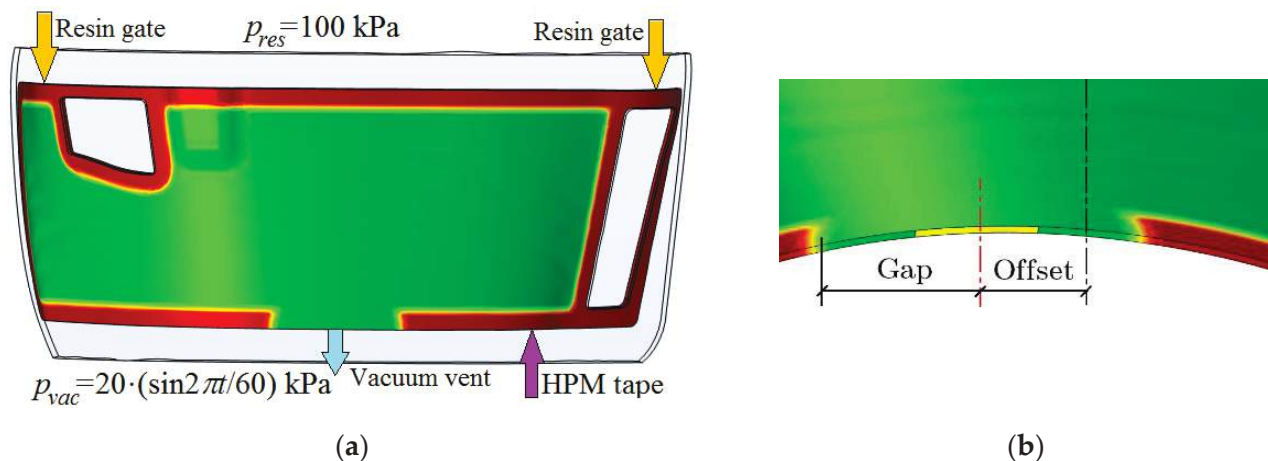
Figure 2. Layout of the vacuum infusion of the composite part: (**a**) HPM, resin injection gates and vacuum vent location on the preform; (**b**) The location of the vacuum vent relative to the axis divides the part into two approximately equal parts, and the distance from the vent to the edges of the HPM tape.

The location of the resin injection gates did not change in the present study. It was accepted on the basis of the results of [26] as the most efficient for the spreading the two resin streams outgoing from them. Toray ER450 resin is introduced into the preform at an initial temperature of 70 °C, then the system is gradually heated for 15 min by convective heat flows and then maintained at an isothermal temperature. Numerical experiments were carried out at holding temperatures T^{hold} of 80, 82 and 84 °C. Numerous simulations were performed at the varying temperatures, vacuum vent offset and vent-HPM gap. The simulated process took 4 h and was always longer than the time until the resin stopped completely. The aim of the study was to understand the patterns of the process, to determine its parameters that can be used to predict at the early stages of modeling its final results—quality, reliability and productivity. Some examples of the evolutions of these process parameters at the fixed vacuum vent offset and gap for three temperatures T^{hold} studied are shown in Figure 3. In these plots the <...> symbol indicates the averaging of a certain value over the preform volume filled with resin by more than 10%.

In addition to the acceleration of processes with an increase in the temperature of isothermal holding, the following important regularities should be noted, which are undesirable for achieving the quality of the process. The graphs in Figure 3c show a sharp increase in viscosity near the vacuum port long before the moment the viscosity is equalized in the entire volume of the preform, which can lead to a slowdown in the resin flow (see Figure 3d) and even to blockage of the outlet. The initial increase in fiber content, caused by the action of the compressive pressure, gradually stabilizes and then decreases below the value before the start of the infusion, which is caused by the increase in the internal pressure in the preform when it is filled with resin (see Figure 3d). This phenomenon is highly undesirable for the strength of the molded structure, which was thoroughly studied in [54], where an improvement of the process using additional external pressure is proposed. However, the modification of the presented modeling method in accordance with this improvement is a task for future research.

Solving the problem of reducing the computation time to the moment when the results of the process can be predicted reliably is very important for using the described process simulation method for this process optimization. This task includes two components: finding the particular criteria that strongly correlate with the final quality indicator and

determining the earliest possible moment in time for such a prediction. Such time instants must satisfy the requirement of being able to be clearly identified in the simulation. As a result of the research, it was found that the requirements for reliability and identification accuracy are satisfied when the maximum relative void volume of the preform becomes less than 0.1, i.e., when the filling level of 0.9 leaves the preform through the vacuum port (see Figure 4). Everywhere below, this time instant is denoted as *t*09.

(a)

(b)

(c)

(d)
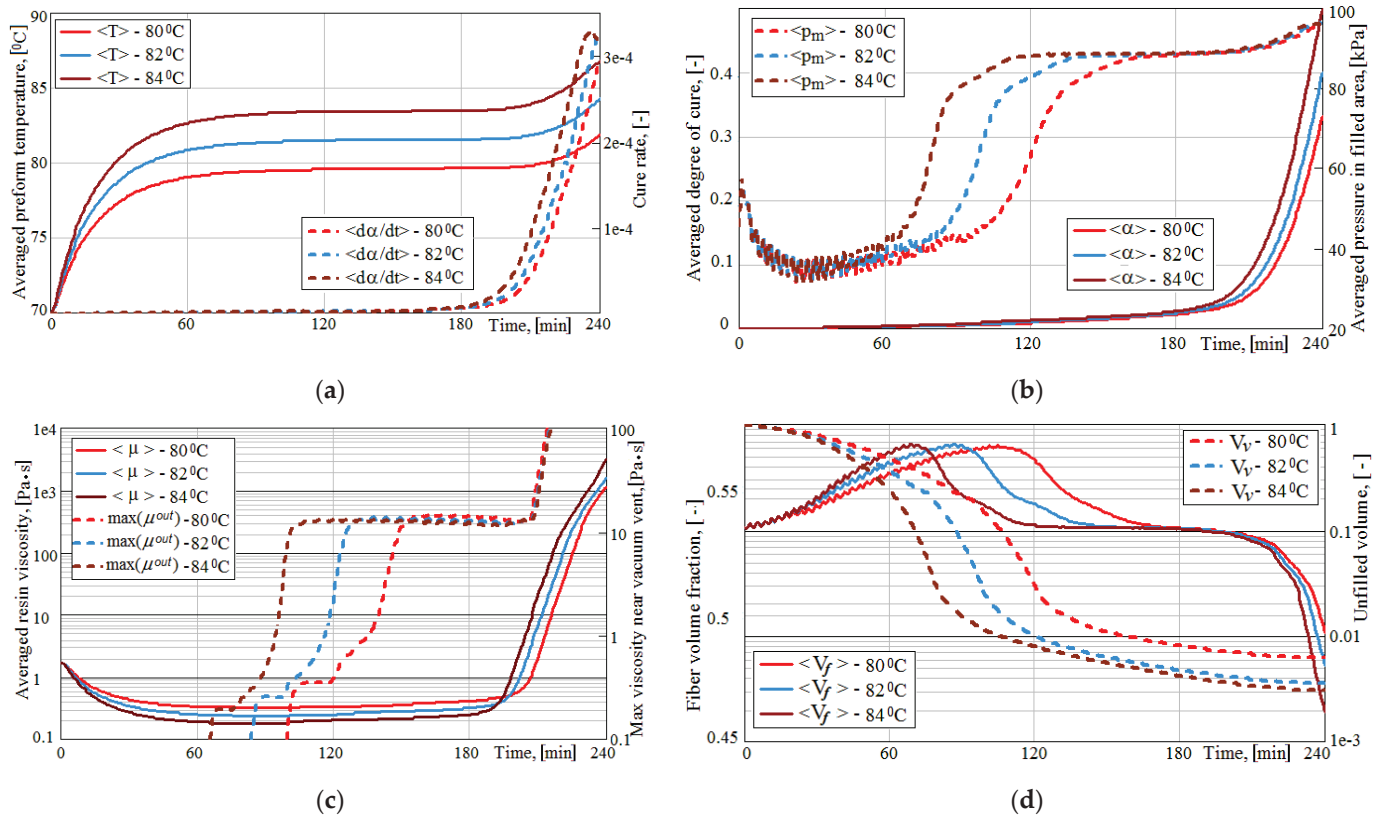
Figure 3. Superimposed time dependences of some process parameters: (**a**) Average temperatures *<T>* and resin cure rate *<dα/dt>*; (**b**) Average pressures *<p_m>* and degree of cure *<α>*; (**c**) Average viscosity *<μ>* and maximum resin viscosity max($μ^{out}$) in the vicinity of the vacuum outlet; (**d**) Average fiber volume fraction *<V_f>* and relative void volume *V_v*.
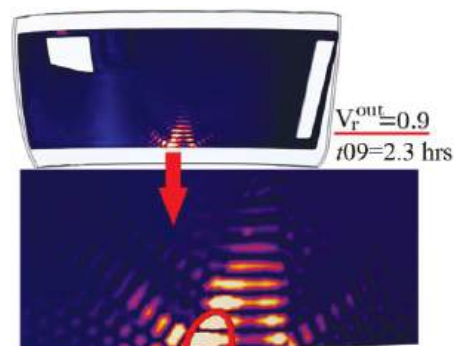
Figure 4. The position of the resin front with the 0.9 filling level just before leaving the outlet at the moment used for the most reliable prediction of the final results of the vacuum infusion process.

It was noted above that some works [42,43] solve the problem of increasing the productivity of the process, i.e., reduce its duration to full completion, which is achieved after the resin is solidified throughout the entire volume of the preform. In this regard, it is

of interest to compare the duration of the process until the moment *t*09 with its duration until the moment of stopping of the resin propagation, denoted hereinafter as *tstop*. The corresponding dependences of these durations on the parameters of the process layout are shown in Figure 5 in the form of stems diagrams. These dependences show that the duration *tstop* is less susceptible to the parameters of the process layout than *t*09. This result confirms the conclusion of the authors of [19,32,55] that believe that the post-infusion stage, which corresponds to the time interval after *tstop* and up to complete consolidation of the preform and determines the total process duration, should be considered separately for optimization of the process performance.
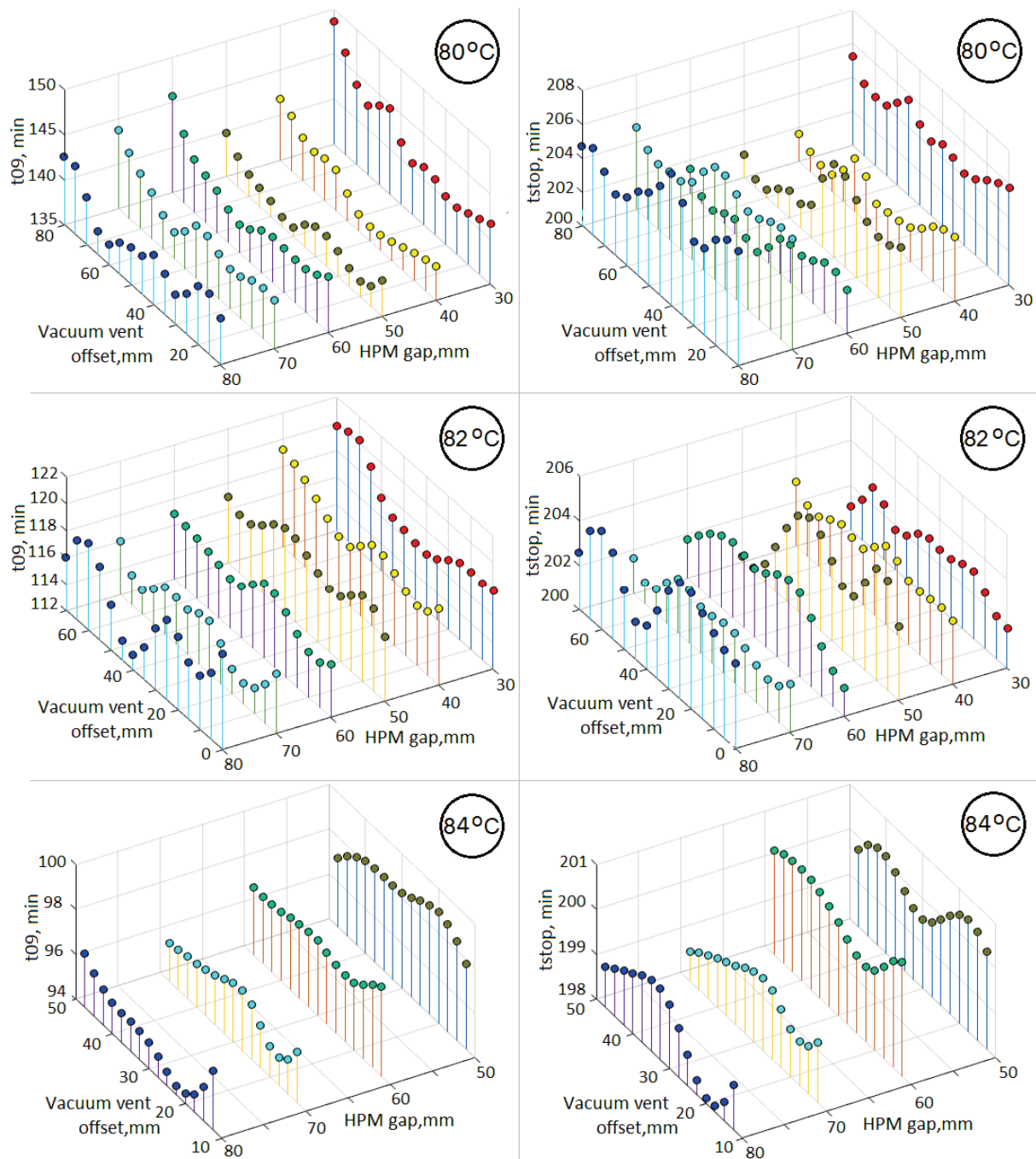
Figure 5. Dependencies of the process duration up to moments *t*09 (**left**) and *tstop* (**right**) at isothermal holding temperatures T^{hold} of 80, 82, and 84 °C on the location of the vacuum vent.

This conclusion, taking into account the capabilities of the formulated forward modeling problem, forces us to restrict ourselves to optimizing the quality criterion $V_v(tstop)$ of the process. To identify particular criteria, the values of which at the moment $t09$ will make it possible to predict the final value of the main quality criterion with the required accuracy and reliability, a comparative analysis of the response functions of these particular sub-criteria and the main criterion was carried out, as well as a correlation analysis of their interdependencies. The values of the main quality criterion and sub-criteria for each investigated temperature were obtained by simulating the process when changing the vacuum port shift and HPM gap with a step of 5 mm. Some of the results of such an analysis for the holding temperature T^{hold} of 84 °C are presented in Figures 6 and 7.
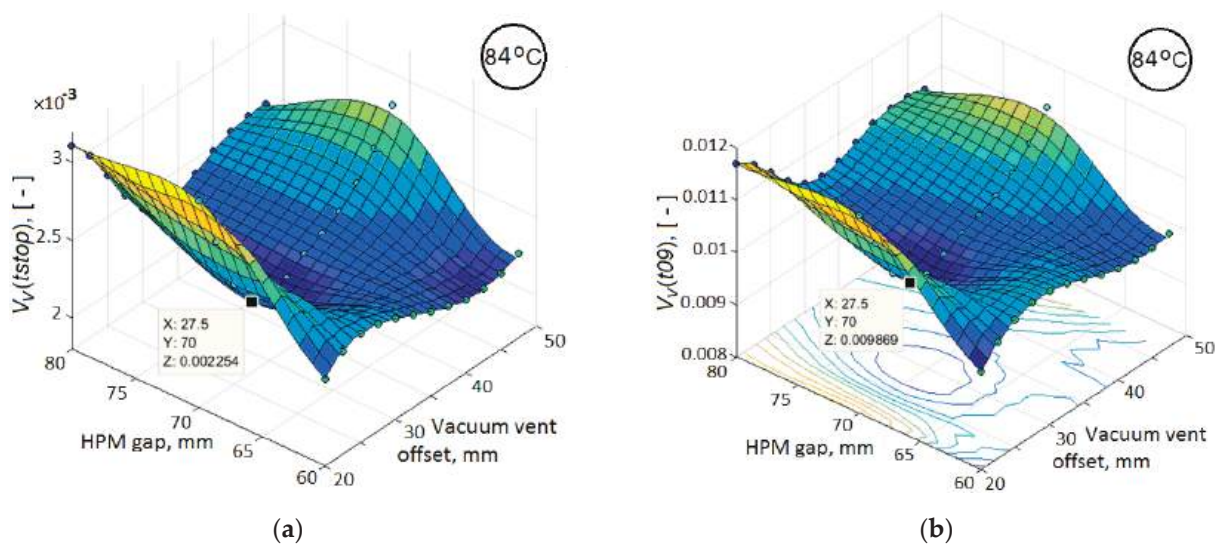
Figure 6. The response functions of the residual void volume V_v in the preform on the parameters of the vacuum vent location: (**a**) at the time instant when motion of the resin stopped; (**b**) at the moment $t09$.

It is important to note that for all three investigated temperatures T^{hold} of isothermal holding, the dependences presented in these figures have the same character, slightly differing in the values of the correlation coefficients. Therefore, here the dependences are given only for a single temperature of 84 °C. The response surfaces in Figure 6 for the residual void volume of the preform have a very similar relief with a clearly manifested minimum, which confirms the necessary sensitivity of the process quality criteria $V_v(tstop)$ and $V_v(t09)$ to its layout. In addition, the graph in Figure 7a shows a very strong correlation between the $V_v(tstop)$ and $V_v(t09)$ values. However, Figure 7b–d show a weak correlation between $V_v(tstop)$ and such preliminary calculated parameters as $< \alpha(t09) >$, $< \mu(t09) >$ and $< p_m(t09) >$. Meanwhile, the smaller values of each of these parameters facilitate a more intensive resin flow at the final phase of vacuum infusion, that is, increase the reliability of the process. This conclusion suggests the advisability of using one or more of the listed parameters together with the $V_v(t09)$ criterion for more reliable achievement of the better results of the process.
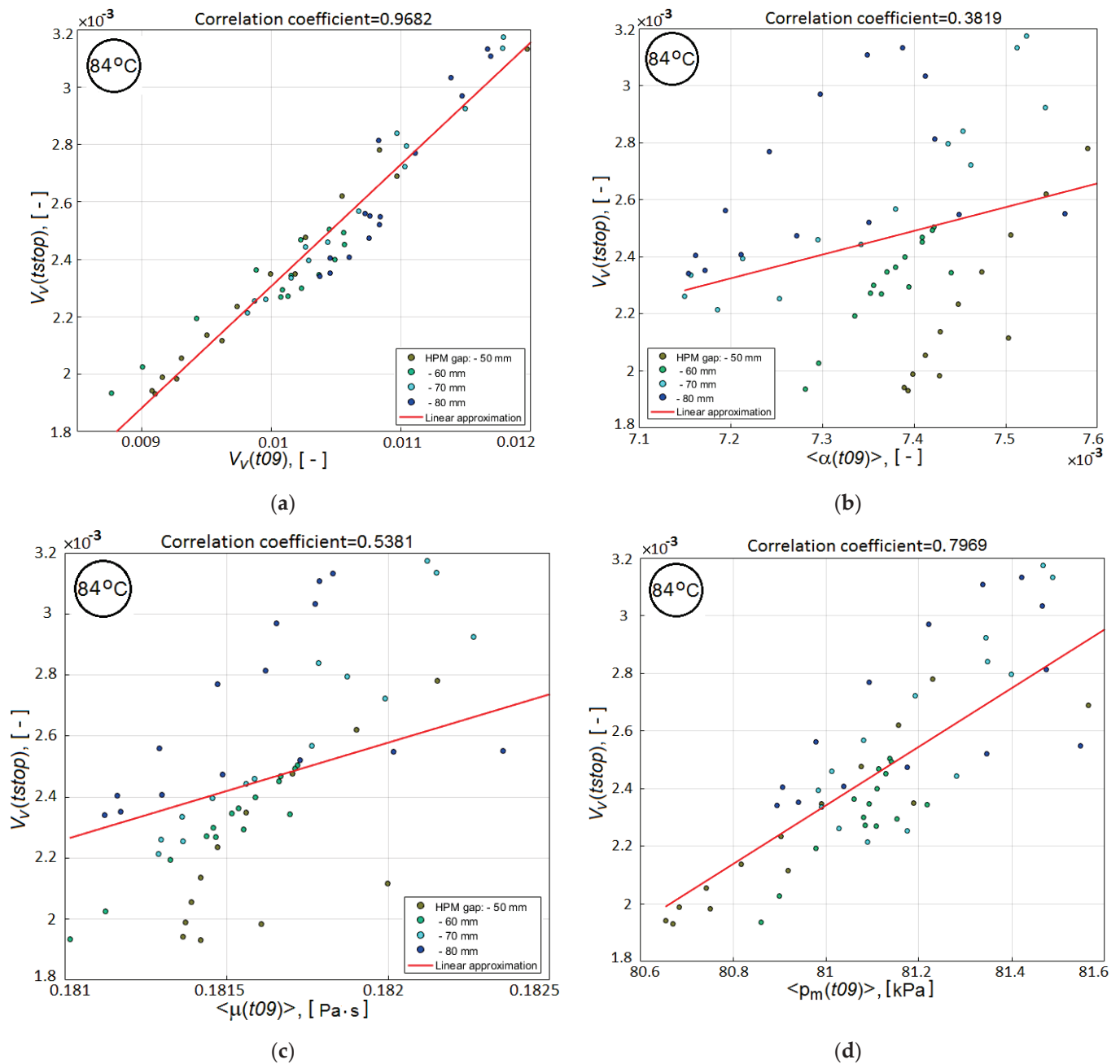
Figure 7. 2D scatter plots showing the correlation between the main quality criterion at the end of the resin infusion and the sub-criteria, which are calculated at time instant *t*09: (**a**) relative void volume $V_v(t09)$; (**b**) averaged degree of cure $<\alpha(t09)>$; (**c**) averaged viscosity $<\mu(t09)>$ and (**d**) averaged pressure $<P_m(t09)>$ in partially filled domain.

This joint use of the two sub-criteria is possible in two ways. The first one involves the formulation of a single objective functional, which includes all sub-criteria with some weights, and the subsequent determination of the global or local optimum of the resulting scalarized functional. Its visualization, especially in the case of two sub-criteria, is very convenient in the coordinates of the design variables. In cases where there is a single optimum of such a combined functional (which, unfortunately, is not often encountered in practice), it is taken as the optimal solution. This approach allows for the constraints on all sub-criteria and design variables to be taken into account. However, this approach is

characterized by arbitrariness in the choice of weights for each sub-criterion, which can distort the real evolution of the optimized process.

The second approach considers two or more sub-criteria as independent, but each in its own way characterizes the efficiency and quality of the developing process. For a non-trivial optimization problem with multiple goals, there is no single solution that simultaneously optimizes each objective. In this situation, it is necessary to make optimal decisions when there are trade-offs between two or more conflicting objectives. Such a compromise decision can be made on the basis of a set of Pareto-optimal solutions, each of which is characterized by the fact that none of the objective functions can be improved in value without degrading some of the other objectives. In the case of bi-objective problems, their solution is visualized by the Pareto frontier, often named the tradeoff curve, which can be drawn at the objective plane. This approach to solving problems of multi-objective optimization, as well as fuzzy logic, simulated annealing and genetic algorithms, is extremely effective in solving problems of optimal synthesis of layouts and parameters of chemical reactions processes, when there are sets of objective criteria and controlled variables of relatively large dimension [56,57]. So, to ensure the minimum curing time and polymeric chain length dispersity in the reversible deactivation radical polymerization process, a variation of the parameters of the temperature cycle and molar amounts of reacting monomer is used [58].

In the presented work, both complementary approaches are used: optimization of the combined scalarized functional and reconstruction of the Pareto frontier.

In the absence of the required experimental information on the relative role of auxiliary sub-criteria in achieving the optimum of the main quality objective $V_v(tstop)$, the resin viscosity $< \mu(t09) >$, determined by averaging over the preform volume at time t09, was chosen as the second candidate for its use in the combined quality-reliability criterion. This choice is due to the close cross-correlation of three predictive sub-criteria (see Figure 8), whose correlation dependences with the main quality criterion $V_v(tstop)$ are presented in Figure 7b–d. The combined quality-reliability criterion is proposed in the form of a product of the normalized partial predictive criteria $V_v(t09)$ and $< \mu(t09) >$:

$$CObj(t09) = \frac{V_v(t09)}{mean(V_v(t09))} \cdot \frac{< \mu(t09) >}{mean(< \mu(t09) >)}, \tag{5}$$

where the mean(...) operation is a simple averaging over a set of performed test numerical experiments.

Based on the analysis, some of the results of which are presented above, the following conclusions can be drawn. The layout of the process (localization of the vacuum port) and the temperature of isothermal holding T^{hold} significantly affect the filling, the preform with resin, changing the relief of the response function of the main quality criterion $V_v(tstop)$, the location and value of its optimum. The strong correlation of the criterion $V_v(t09)$ with the main criterion $V_v(tstop)$ allows it to be used together with the $< \mu(t09) >$ criterion for predictive process optimization. As follows from the analysis of the properties of the used resin, studied in detail in [26], its viscosity during isothermal heating begins to increase sharply when it reaches a value of 2 Pa*s, which may be the reason for stopping the advance of the resin along the preform. This fact can be used as a constraint when choosing options for rational process design. Multiple numerical experiments have shown that the use of predictive criteria of a process to obtain reliable estimates of its final results reduces the computation time from 25% to 45%, which makes the use of predictive criteria preferable in the process optimization system.
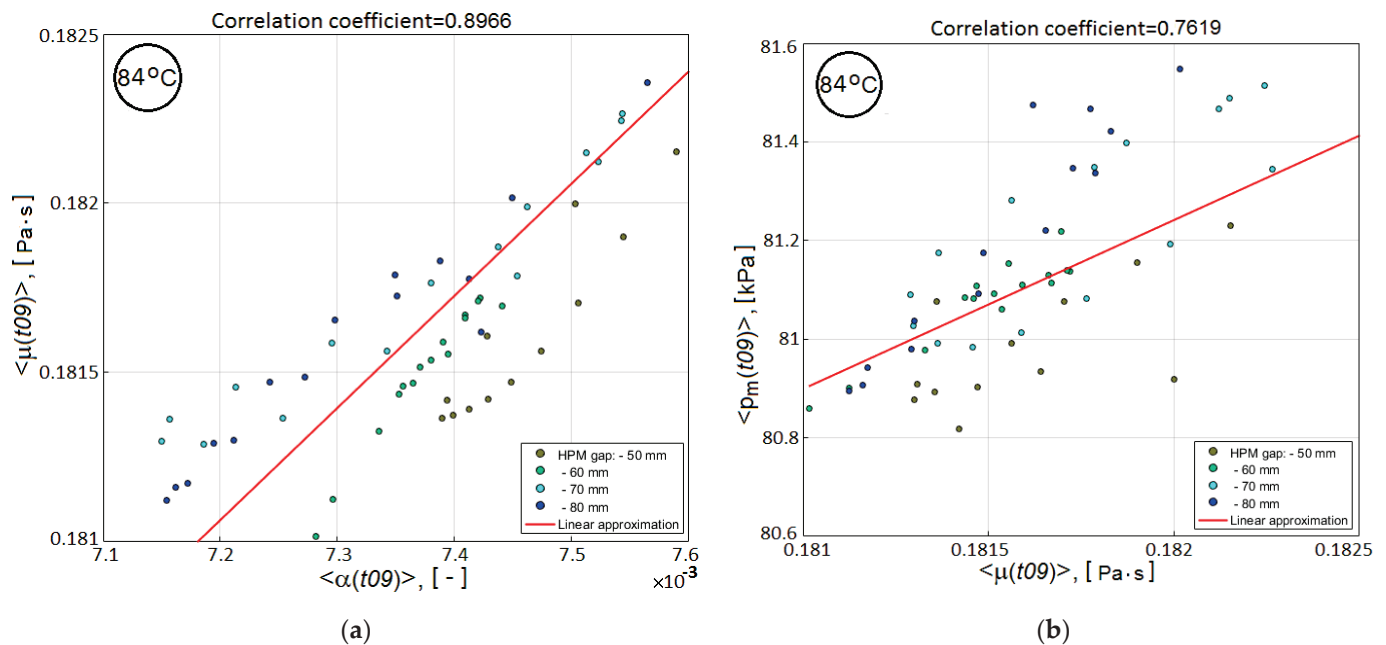
Figure 8. 2D scatter plots showing the cross-correlation between the predictive sub-criteria: (**a**) <$\mu(t09)$> and <$\alpha(t09)$>; (**b**) <$P_m(t09)$> and <$\mu(t09)$>.

In the next section, a combined procedure for improving the vacuum infusion process is considered at the stage of modeling the spread of resin in a preform before its gelation. This procedure includes bi-objective optimization using a combined criterion (5) and making the decision on the rational design of the process layout based on the analysis of the Pareto set.

4. Finding a Quasi-Optimal Design for the Vacuum Infusion Process Layout

To present in the most demonstrative form the method and results of solving this multi-objective problem, the localization and throughputs of the resin injection gates are taken to be fixed, found in our previous work [26]. The variable design parameters will be the position of the vacuum port relative to the preform and the gap between it and the edges of the HPM tape. All illustrative materials are given for isothermal holding at a temperature of 82 °C. For each variant of the variable design parameters, upon completion of the forward problem solution, the values of the predictive criteria $V_v(t09)$, $< \mu(t09) >$, $CObj(t09)$ were generated, as well as the maximum resin viscosity in the vicinity of the vacuum vent $\max(\mu^{out}(t09))$. To implement automatic simulation stop, a stop condition $\min_{\Omega}(V_r) < 0.1$ is defined in the Component Couplings of the FE model, and this stop condition has been added to the Time Dependent Solver setting. The sequential loading of the specified parameter combinations included in the list of the model input parameters is carried out by the solver in the Parametric Sweep mode with the input data and results being saved in a text file for further processing. With such a multiple sequential call of the forward modeling problem, it is very important to achieve the experimental objectives in the simplest manner with the minimum number of measurements and the least expense. The chosen strategy consists in carrying out the first numerical experiments at the extreme values (maximum and minimum setting) of the range of controlled variables with subsequent narrowing and displacement of the center of the numerical experiment plan (see Figure 9). The values $mean(V_v(t09))$ and $mean(< \mu(t09) >)$ obtained as a result of averaging the sub-criteria, calculated at 9 points of the first plan, are used in the future when calculating the combined criterion $CObj(t09)$ for all the following results of numerical experiments.
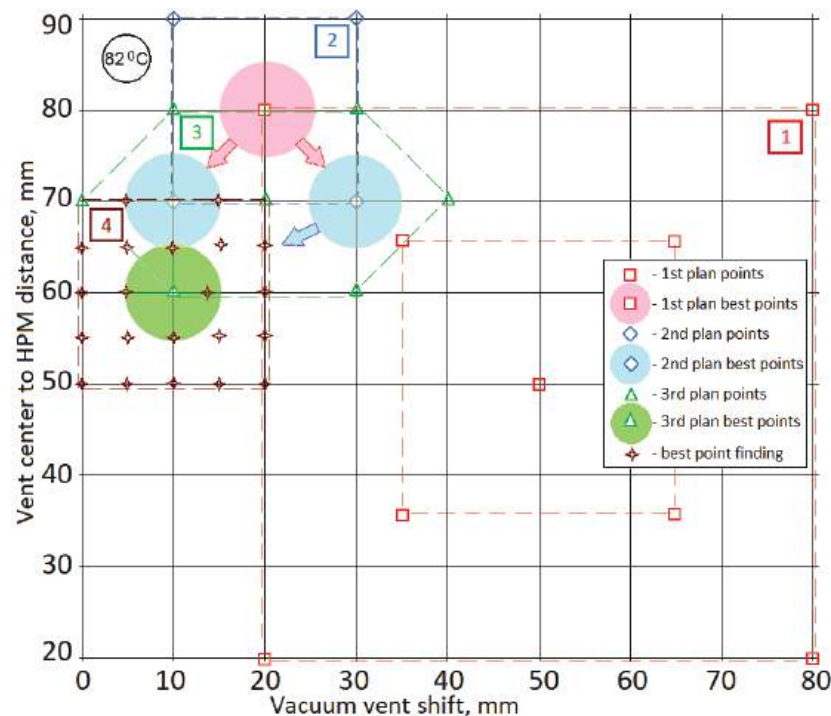
Figure 9. A sequence of plans for the performed numerical experiments to optimize the vacuum infusion process layout.

To obtain the results of bi-objective optimization in the most understandable form and to make a decision on the choice of a process layout, the simulation results of a limited number of variants were smoothed by third-order splines and presented in the form of 3D response surfaces and level line maps (see Figures 10 and 11). Dependences of predictive criteria $V_v(t09)$ and $< \mu(t09) >$, shown in Figures 10 and 11, after normalization were used to build the dependence of the combined quality-reliability criterion $CObj(t09)$ (see Figure 12).

As noted above, when the local viscosity reaches 2 Pa*s, a sharp increase in viscosity begins in the adjacent area. Such a situation near the vacuum port is likely to lead to its blockage, which is unacceptable and must be prevented by introducing an appropriate constraint. For the calculated variants, the smoothed response function $\max(\mu^{out}(t09))$ is shown in Figure 13.

Outwardly the response functions $< \mu(t09) >$ and $\max(\mu^{out}(t09))$ shown in Figures 11 and 13 are similar, but the ranges of their variation are not comparable. The relationship between these sub-criteria, plotted using the tabulated values of their smoothed response functions, is shown in Figure 14. It shows that critical vacuum port blocking situations can occur even with a relatively low average resin viscosity, which is denoted as $< \mu(t09) >_{block}$ in the plot. The sharp influence of sub-criterion $\max(\mu^{out}(t09))$ on the dynamics of the vacuum infusion process forces to use this parameter as a constraint.
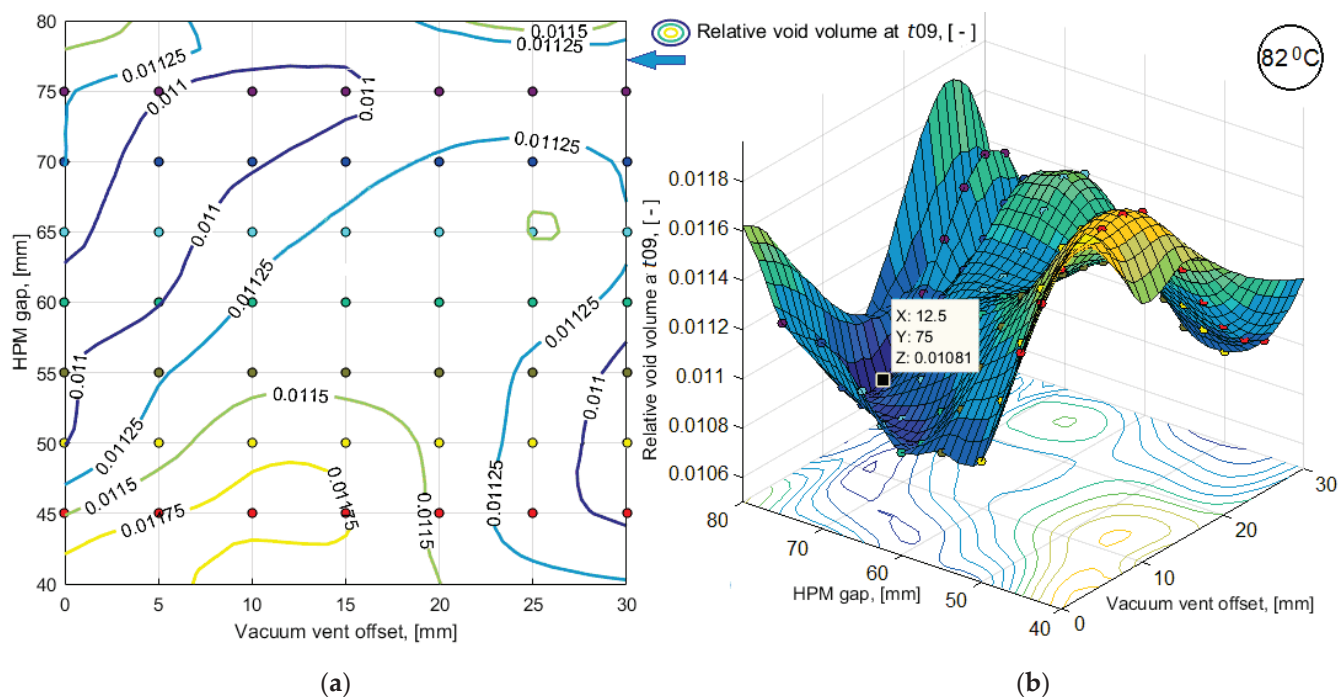
Figure 10. Results of simulation of the predictive sub-criterion $V_v(t09)$ response in the form of: (**a**) map of level lines; (**b**) smoothed 3D function.
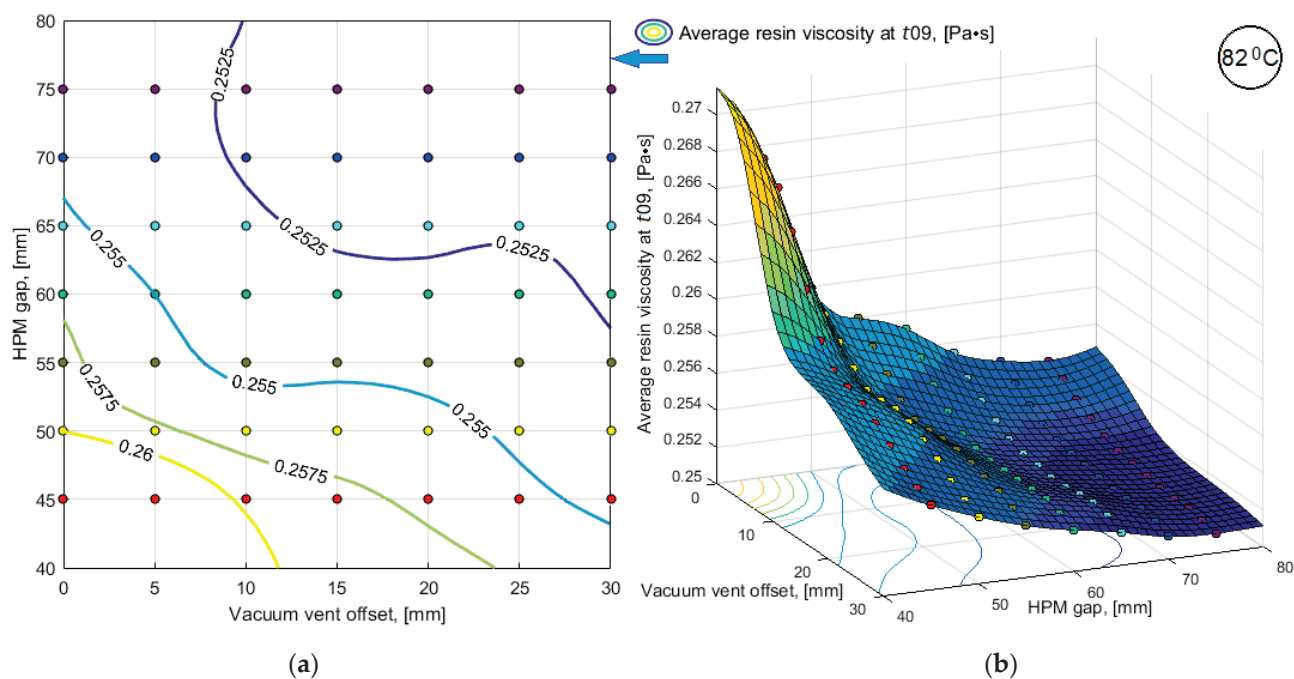
Figure 11. Results of simulation of the predictive sub-criterion $<\mu(t09)>$ response in the form of: (**a**) map of level lines; (**b**) smoothed 3D function.
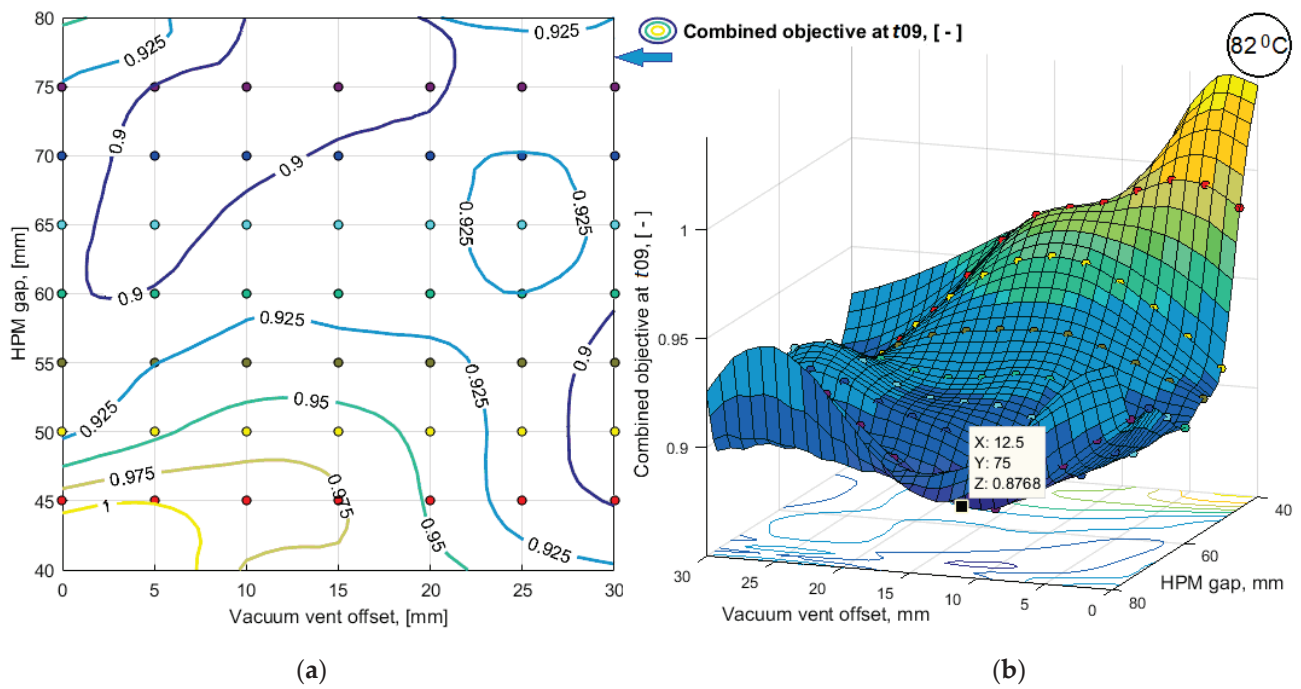
Figure 12. The response function of the predictive combined quality-reliability criterion *CObj*(*t*09) in the form of: (**a**) map of level lines; (**b**) smoothed 3D function.
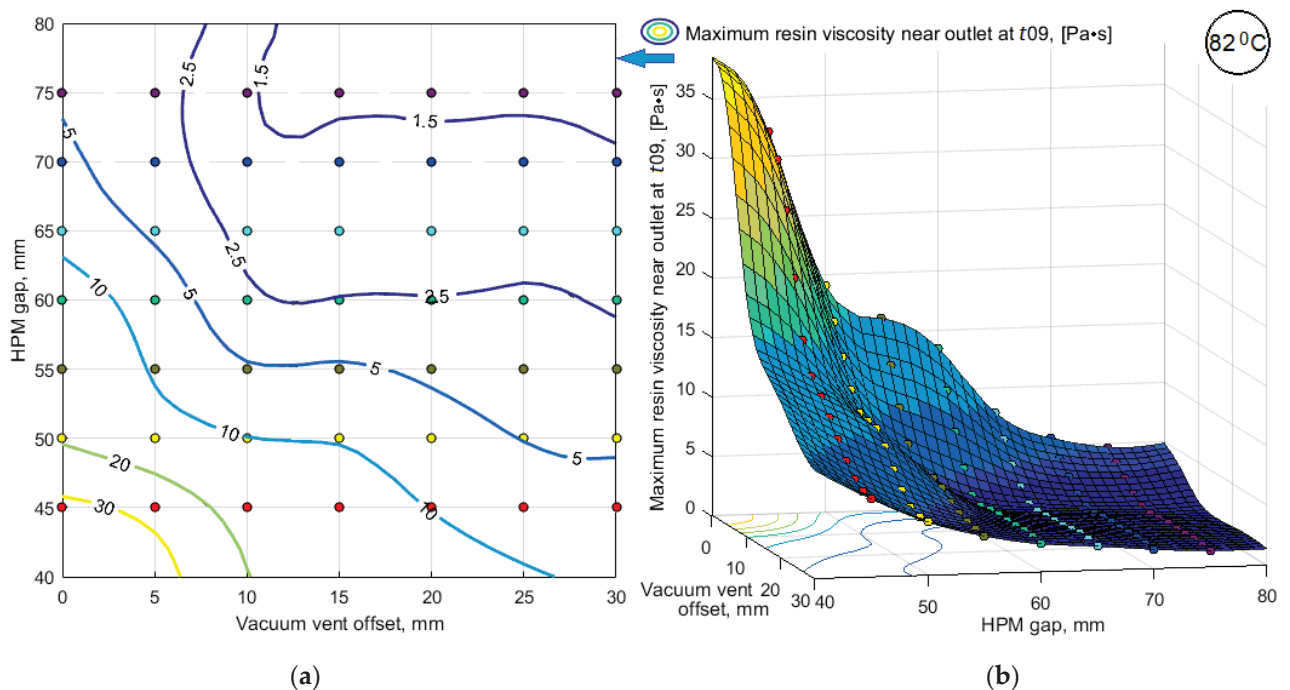
Figure 13. The response function of the predicted maximum resin viscosity in the vicinity of the vacuum vent max(μ^{out}(*t*09)) in the form of: (**a**) map of level lines; (**b**) smoothed 3D function.
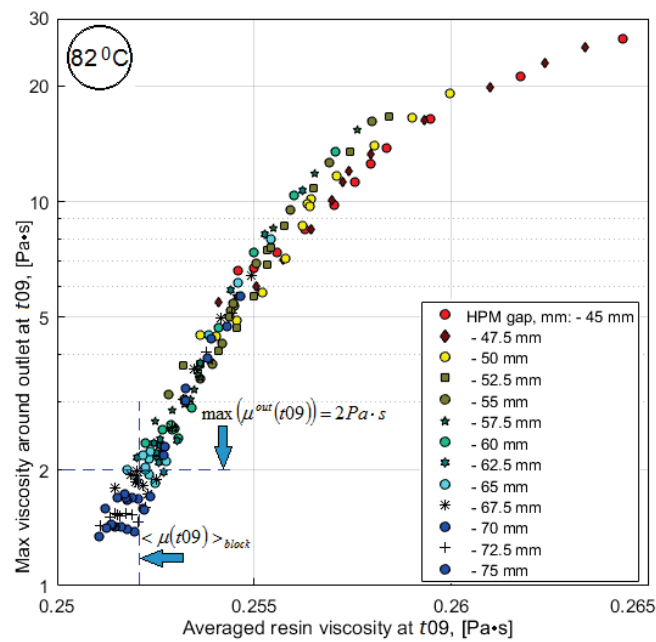
Figure 14. Interdependence between the averaged within the preform and maximum in the vicinity of the vacuum vent resin viscosities.

The results of the problem solved are represented in the decision space and in the quality-reliability criteria space in Figures 15 and 16, respectively.
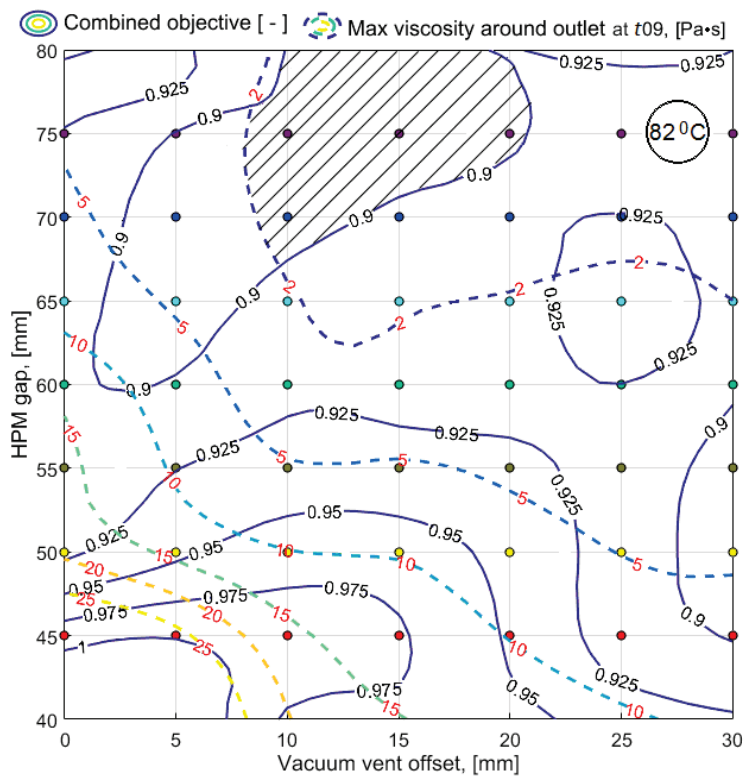
Figure 15. Map of the level lines of the combined quality-reliability criterion $CObj(t09)$ (solid lines), superimposed with the lines of the constraint levels $\max(\mu^{out}(t09))$ (dashed lines). The area of rational choice of the process layout parameters is highlighted by shading.
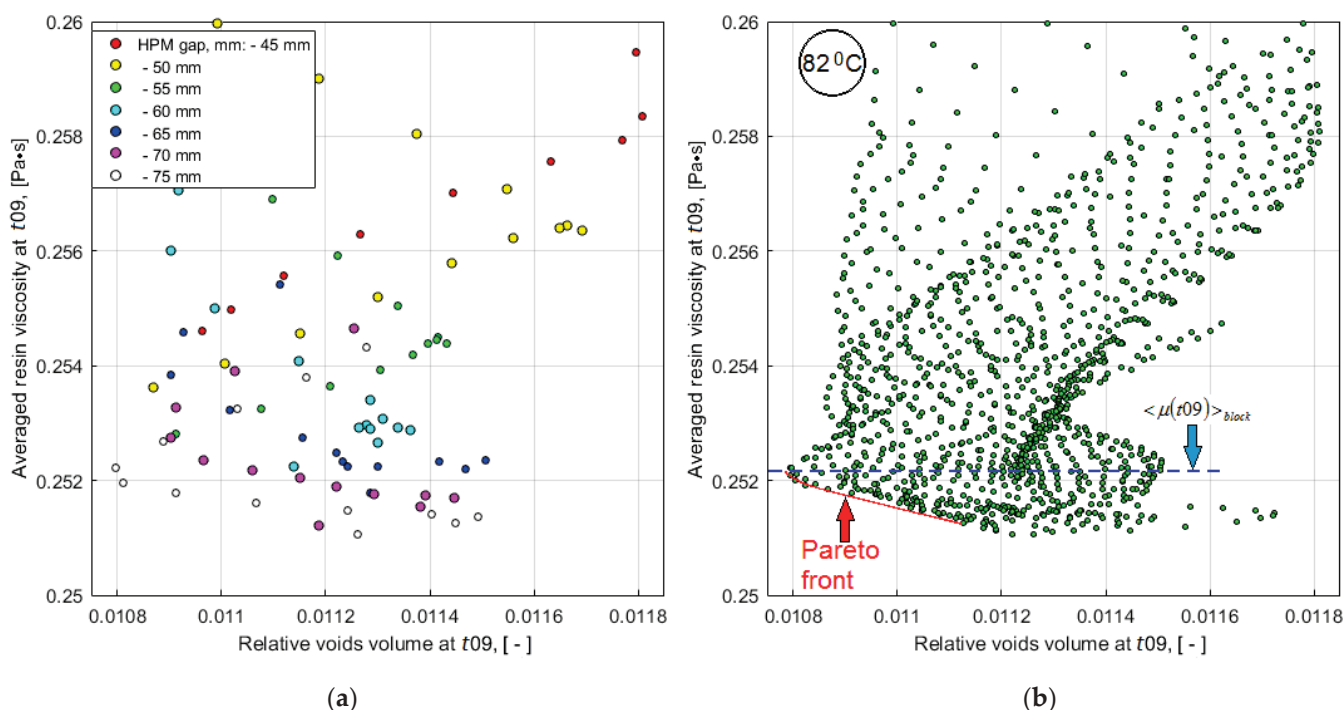
Figure 16. The scatter plots of the evaluating predictive criteria $V_v(t09)$ and $<\mu(t09)>$: (**a**) The results of numerical experiments carried out according to the plans shown in Figure 9; (**b**) Results of tabulation of the smoothed response functions of each criterion with a step of 1 mm in both directions for the reconstruction of the Pareto front (solid red line).

5. Discussion

The results of solving the problem, presented in two forms (see Figures 15 and 16), show that such a problem cannot be an ideal optimization problem with a single optimal solution that is the best for all criteria without exception. The designer always has the freedom to make decisions. At the same time, the nature of the considered restrictions can be very different, and their composition is quite wide. Even in a simple problem statement presented in this article, when the objective sets include only two parameters, and only two design variables are taken into account, solving the problem of making the optimal decision is rather laborious. To reduce the computational complexity, it required the use of predictive criteria, whose effectiveness must be proven in a series of preliminary numerical and real experiments. The scope of the presented model is limited to the stage of infusion of the liquid resin, before its gelation, solidification and the achievement of the final mechanical properties. However, this stage is very important, since it is during its course that such quality indicators as the absence of dry spots and the minimum void volume of the porous preform are achieved. A useful feature of the developed modeling/optimization technology is the ability to analyze and reasonably select one of several Pareto-optimal solutions, which is illustrated in Figure 17, where screenshots of the distributions of viscosity and fiber volume fraction at times $t09$ and $tstop$ of the solution corresponding to vacuum vent offset = 15 mm, HPM gap = 75 mm and T^{hold} = 82 °C are shown. At these time instants the relative void volumes in the preform are $V_v(t09)$ = 0.0107 and $V_v(tstop)$ = 0.0044, that is very satisfactory result. Reducing the volume of voids by more than 2 times became possible due to the low viscosity, which provided the necessary flowing of the resin. However, it can be seen that the resin front at the stopping of the flow has shifted relative to the vacuum port surrounded by the high viscosity resin, which prevents a removing of the remaining air from the preform. This was due to the earlier arrival of the resin flow moving from the right to the vacuum vent. The deficiency can be eliminated by shifting the vent a short distance to the left.
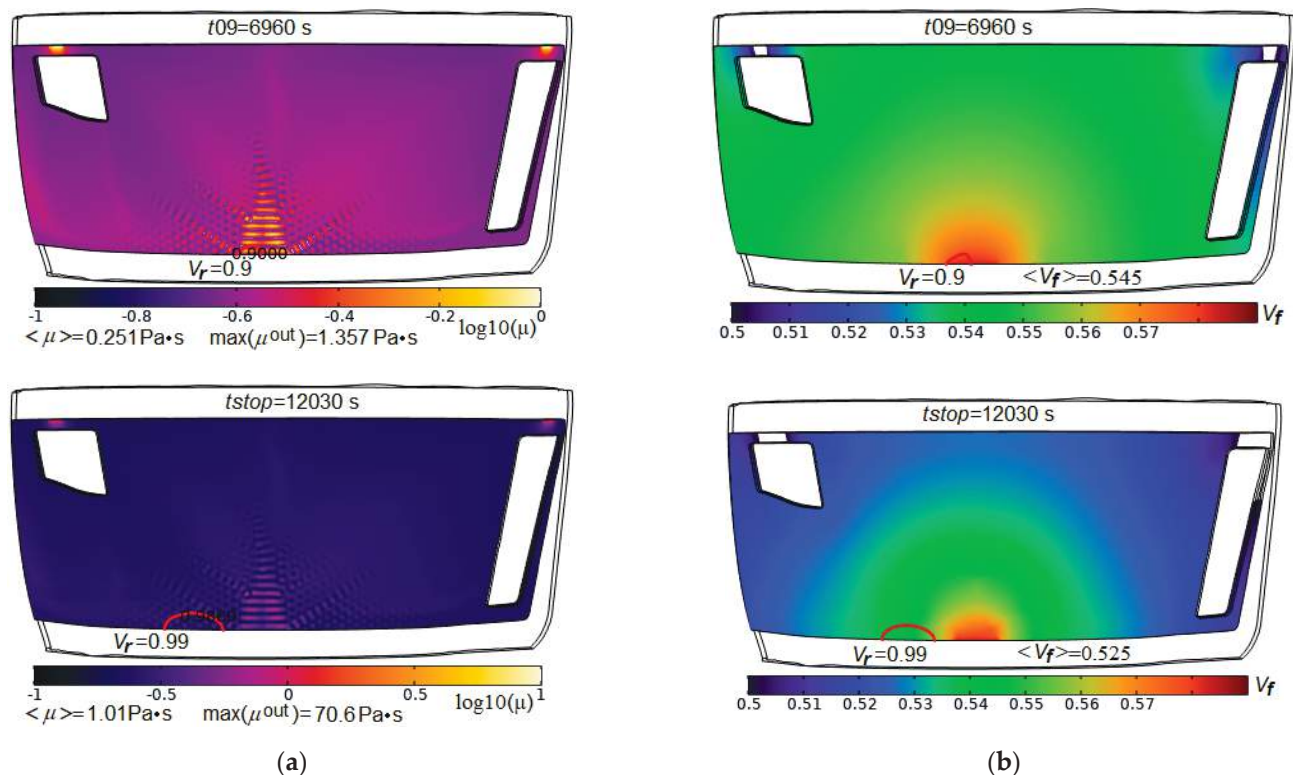
Figure 17. Screenshots of the spatial distributions for the logarithm of local resin viscosity (**a**) and fiber volume fraction (**b**) in partially filled domain at the time instants *t*09 and *tstop*. Red solid lines indicate the resin front positions with filling $V_r = 0.9$ (upper pictures) and $V_r = 0.99$ (lower pictures), respectively.

A significant decrease in the fiber volume fraction, which is shown in Figure 17b, can also be eliminated only at the stage preceding the second stage of resin cure. Apparently, the best solution to this problem is the external controlled pressure technology proposed in [54]. Another important problem is related to the provision of the required thermal schedule during the implementation of the process by the out-autoclave method, when infrared irradiation of the preform can be effectively used [59]. The method requires thorough development for use in the technology of manufacturing composite structures of complex shape.

The above considerations substantiate the place and role of the proposed methods and approaches in the development of promising areas of modeling and practical implementation of varieties of vacuum infusion processes in the production of responsible polymeric composite structures. However, effective application of this technology is impossible in the absence of a large number of reliable experimental data on the properties of the used reinforcements and resins.

6. Conclusions

The article presents the formulation, methodology and results of solving the problem of making a reasonable decision about the parameters of the layout of vacuum infusion of a composite structure of complex shape. The proposed method for solving the forward modeling problem is based on the use of coupled equations of the phase field, Richards, convection/diffusion of the degree of cure of a moving liquid resin in a porous preform, heat transfer, taking into account the refined relations for the evolution of the rheological state of the resin and all system's thermophysical properties during entire stage of filling the preform. The inherent accuracy of the model description of the front of a moving and continuously curing resin in a preform with varying porosity and permeability provides

an effective reconstruction of the process dynamics and identification of such defects as non-impregnated dry spots, possible blockage of the vacuum vent, which result in a violation of the quality of the produced composite parts. These abilities are illustrated in the article using a simplified example of a homogeneous preform with quasi-isotropic permeability, depending on its local porosity, compressibility and resin filling. In order to use the developed method for solving the forward problem in process optimization systems by reducing the computation time, a group of predictive sub-criteria is proposed that are assessed long before the resin stops moving and provide a reasonable prediction of the final quality (residual unfilled volume of the preform) and process reliability at the end of the infusion stage. The result of solving the inverse problem is presented in two forms: in the decision space, allowing identifying the area of rational change in the design parameters of the process layout, considering the constraints, and as the Pareto set in the objectives space, identifying the best achievable results for each of the objectives. The strategy used to search for the region of the best of acceptable constrained decisions, which involves carrying out the first numerical experiments at the extreme values (maximum and minimum) of the range of controlled design variables, followed by narrowing and shifting the center of the numerical experiments plan, made it possible to obtain effective results after about 30 calls of the forward problem.

Author Contributions: Conceptualization, S.S.; methodology, S.S.; software, I.Z.; validation, S.S., I.Z. and N.S.; formal analysis, S.S.; investigation, J.-K.W.; resources, I.Z.; data curation, S.-H.C.; writing—original draft preparation, S.S.; writing—review and editing, J.-K.W.; visualization, N.S.; supervision, S.-H.C.; project administration, S.-H.C.; funding acquisition, S.S. All authors have read and agreed to the published version of the manuscript.

Institutional Review Board Statement: Not applicable.

Informed Consent Statement: Not applicable.

Data Availability Statement: Detailed information about the data confirming the results obtained in the course of the study can be requested from the authors of the article by e-mail.

Conflicts of Interest: The authors declare no conflict of interest.

References

1. Lunn, P. Cost-effective resin infusion. *Reinf. Plast.* **2009**, *53*, 38–39. [CrossRef]
2. Heider, D.; Gillespie, J.W. VARTM Variability and Substantiation. The Joint Advanced Materials and Structures Center of Excellence. 2010. Available online: https://pdfs.semanticscholar.org/3ddc/79c6cf459936fb8a069b27437c5596b220bd.pdf (accessed on 27 November 2021).
3. Hsiao, K.-T.; Heider, D. Vacuum assisted resin transfer molding (VARTM) in polymer matrix composites. In *Manufacturing Techniques for Polymer Matrix Composites (PMCs)*; Woodhead Publishing: Sawston, UK, 2012; pp. 310–347. [CrossRef]
4. Khan, L.A.; Mehmood, A.H. Cost-effective composites manufacturing processes for automotive applications. In *Lightweight Composite Structures in Transport: Design, Manufacturing, Analysis and Performance*; Njuguna, J., Ed.; Woodhead Publishing: Amsterdam, The Netherlands, 2016; pp. 93–119.
5. González, C.; Vilatela, J.; Molina-Aldareguía, J.; Lopes, C.; Llorca, J. Structural composites for multifunctional applications: Current challenges and future trends. *Prog. Mater. Sci.* **2017**, *89*, 194–251. [CrossRef]
6. Popham, N. Resin infusion for the manufacture of large composite structures. In *Marine Composites: Design and Performance*; Pemberton, R., Summerscales, J., Graham-Jones, J., Eds.; Woodhead Publishing: Amsterdam, The Netherlands, 2019; pp. 227–268. [CrossRef]
7. Correia, N.; Robitaille, F.; Long, A.; Rudd, C.; Šimáček, P.; Advani, S. Analysis of the vacuum infusion moulding process: I. Analytical formulation. *Compos. Part A Appl. Sci. Manuf.* **2005**, *36*, 1645–1656. [CrossRef]
8. Govignon, Q.; Bickerton, S.; Kelly, P.A. Simulation of the reinforcement compaction and resin flow during the complete resin infusion process. *Compos. Part A-Appl. Sci.* **2010**, *41*, 45–57. [CrossRef]

9.   Geng, Y.; Jiang, J.; Lin, F.; Shao, H.; Zhang, C.; Chen, N. Study of Compaction Properties and Permeability Prediction of Multilayered Quadriaxial Non-Crimp Fabric in Liquid Composite Molding Process. *Polymers* **2020**, *12*, 1525. [CrossRef] [PubMed]

10. Han, K.; Lee, L.J. Dry spot formation and changes in liquid composite molding: I—Experimental. *J. Compos. Mater.* **1996**, *30*, 1458–1474. [CrossRef]

11. Wei, B.-J.; Chuang, Y.-C.; Wang, K.-H.; Yao, Y. Model-Assisted Control of Flow Front in Resin Transfer Molding Based on Real-Time Estimation of Permeability/Porosity Ratio. *Polymers* **2016**, *8*, 337. [CrossRef] [PubMed]

12. Mehdikhani, M.; Gorbatikh, L.; Verpoest, I.; Lomov, S.V. Voids in fiber-reinforced polymer composites: A review on their formation, characteristics, and effects on mechanical performance. *J. Compos. Mater.* **2019**, *53*, 1579–1669. [CrossRef]

13. Hu, W.; Centea, T.; Nutt, S. Effects of material and process parameters on void evolution in unidirectional prepreg during vacuum bag-only cure. *J. Compos. Mater.* **2020**, *54*, 633–645. [CrossRef]

14. Rydarowski, H.; Koziol, M. Repeatability of glass fiber reinforced polymer laminate panels manufactured by hand lay-up and vacuum-assisted resin infusion. *J. Compos. Mater.* **2015**, *49*, 573–586. [CrossRef]

15. Seong, D.G.; Kim, S.; Lee, D.; Yi, J.W.; Kim, S.W.; Kim, S.Y. Prediction of Defect Formation during Resin Impregnation Process through a Multi-Layered Fiber Preform in Resin Transfer Molding by a Proposed Analytical Model. *Materials* **2018**, *11*, 2055. [CrossRef]

16. Matveev, M.; Belnoue, J.-H.; Nixon-Pearson, O.; Ivanov, D.; Long, A.; Hallett, S.; Jones, I. A numerical study of variability in the manufacturing process of thick composite parts. *Compos. Struct.* **2019**, *208*, 23–32. [CrossRef]

17. Schechter, S.G.; Centea, T.; Nutt, S. Effects of resin distribution patterns on through-thickness air removal in vacuum-bag-only prepregs. *Compos. Part A-Appl. Sci.* **2020**, *130*, 105723. [CrossRef]

18. Bruschke, M.V.; Advani, S.G. A numerical approach to model non-isothermal viscous flow through fibrous media with free surfaces. *Int. J. Numer. Meth. Fl.* **1994**, *19*, 575–603. [CrossRef]

19. Caba, A.C.; Rattazzi, D.; Batra, R.; Loos, A.C. Verification of a simulation model for resin film infusion of complex shaped composite structures. *J. Reinf. Plast. Comp.* **1999**, *18*, 1465–1478. [CrossRef]

20. Dong, C. Injection gate definition for improving the accuracy of liquid composite molding process simulation. *J. Compos. Mater.* **2007**, *41*, 1851–1870. [CrossRef]

21. Francucci, G.; Rodríguez, E.S.; Morán, J. Novel approach for mold filling simulation of the processing of natural fiber reinforced composites by resin transfer molding. *J. Compos. Mater.* **2014**, *48*, 191–200. [CrossRef]

22. Pierce, R.S.; Falzon, B.G. Simulating resin infusion through textile reinforcement materials for the manufacture of complex composite structures. *Engineering* **2017**, *3*, 596–607. [CrossRef]

23. Fracassi, F.T.; Donadon, M.V. Simulation of vacuum assisted resin transfer molding process through dynamic system analysis. *J. Compos. Mater.* **2018**, *52*, 3759–3771. [CrossRef]

24. Adhikari, D.; Gururaja, S.; Hemchandra, S. Resin infusion in porous preform in the presence of HPM during VARTM: Flow simulation using level set and experimental validation. *Compos. Part. A-Appl. Sci.* **2021**, *151*, 106641. [CrossRef]

25. Shevtsov, S.; Zhilyaev, I.; Chang, S.-H.; Wu, J.-K.; Huang, J.-P.; Snezhina, N. Experimental and Numerical Study of Vacuum Resin Infusion for Thin-Walled Composite Parts. *Appl. Sci.* **2020**, *10*, 1485. [CrossRef]

26. Shevtsov, S.; Zhilyaev, I.; Chang, S.-H.; Wu, J.-K.; Snezhina, N.; Huang, J.-P. Two-stage numerical approach for reliable recognition of dry spots at the VAP infusion of large composite parts of complex shape. *Compos. Struct.* **2021**, *259*, 11343. [CrossRef]

27. Grimsley, B.W.; Cano, R.J.; Hubert, P.; Loos, A.C.; Kellen, C.B.; Jensen, B.J. Preform Characterization in VARTM Process Model Development. In Proceedings of the 36th International SAMPE Technical Conference, San Diego, CA, USA, 15 November 2004.

28. Kessels, J.F.; Jonker, A.S.; Akkerman, R. Fully 2 1/2D flow modeling of resin infusion under flexible tooling using unstructured meshes and wet and dry compaction properties. *Compos. Part A-Appl. Sci.* **2007**, *38*, 51–60. [CrossRef]

29. Lionetto, F.; Moscatello, A.; Totaro, G.; Raffone, M.; Maffezzoli, A. Experimental and Numerical Study of Vacuum Resin Infusion of Stiffened Carbon Fiber Reinforced Panels. *Materials* **2020**, *13*, 4800. [CrossRef]

30. Bang, K.G.; Kwon, J.W.; Lee, D.G.; Lee, J.W. Measurement of the Degree of Cure of Glass fiber-epoxy composites using Dielectrometry. *J. Mater. Process. Tech.* **2001**, *113*, 209–214. [CrossRef]

31. Garschke, C.; Parlevliet, P.P.; Weimer, C.; Fox, B.L. Cure kinetics and viscosity modelling of a high-performance epoxy resin film. *Polym. Test* **2013**, *32*, 150–157. [CrossRef]

32. Hwang, S.S.; Park, S.Y.; Kwon, G.C.; Choi, W.J. Cure kinetics and viscosity modeling for the optimization of cure cycles in a vacuum-bag-only prepreg process. *Int. J. Adv. Manuf. Tech.* **2018**, *99*, 2743–2753. [CrossRef]

33. Geissberger, R.; Maldonado, J.; Bahamonde, N.; Keller, A.; Dransfeld, C.; Masania, K. Rheological modelling of thermoset composite processing. *Compos. Part B Eng.* **2017**, *124*, 182–189. [CrossRef]

34. Joven, R.; Das, R.; Ahmed, A.; Roozbehjavan, P.; Minaie, B. Thermal properties of carbon fiber-epoxy composites with different fabric weaves. In Proceedings of the SAMPE International Symposium Proceedings, Charleston, SC, USA, 22–25 October 2012.

35. Aadmi, M.; Karkri, M.; Ibos, L.; Hammouti, M.E. Effective thermal conductivity of random two-phase composites. *J. Reinf. Plast. Comp.* **2014**, *33*, 69–80. [CrossRef]

36. El-Hage, Y.; Hind, S.; Robitaille, F. Thermal conductivity of textile reinforcements for composites. *J. Text. Fibrous Mater.* **2018**, *1*, 2515221117751154. [CrossRef]

37. Huang, J.-P.; Zhilyaev, I.; Snezhina, N.; Shevtsov, S. Evaluation of the vacuum infusion process objectives at the early stages of computer simulation. *J. Phys. Conf. Ser.* **2021**, *2090*, 012004. [CrossRef]

38. Gokce, A.; Advani, S.G. Simultaneous gate and vent location optimization in liquid composite molding processes. *Compos. Part A-Appl. Sci.* **2004**, *35*, 1419–1432. [CrossRef]

39. Hsiao, K.T.; Devillard, M.; Advani, S.G. Simulation based flow distribution network optimization for vacuum assisted resin transfer moulding process. *Model Simul. Mater. Sci.* **2004**, *12*, S175. [CrossRef]

40. Balvers, J.M.; Bersee, H.E.N.; Beukers, A.; Jansen, K.M.B. Determination of Cure Dependent Properties for Curing Simulation of Thick-Walled Composites. In Proceedings of the 49th AIAA/ASME/ASCE/AHS/ASC Structural Dynamics, and Materials Conference, Schaumburg, IL, USA, 7–10 April 2008. [CrossRef]

41. Chai, B.; Eisenbart, B.; Nikzad, M.; Fox, B.; Blythe, A.; Blanchard, P.; Dahl, J. Simulation-based optimisation for injection configuration design of liquid composite moulding processes: A review. *Compos. Part A Appl. Sci. Manuf.* **2021**, *149*, 106540. [CrossRef]

42. Ruiz, E.; Trochu, F. Multi-criteria thermal optimization in liquid composite molding to reduce processing stresses and cycle time. *Compos. Part A-Appl. Sci.* **2006**, *37*, 913–924. [CrossRef]

43. Saad, A.; Echchelh, A.; Hattabi, M.; El Ganaoui, M. Optimization of the cycle time in resin transfer molding process by numerical simulation. *J. Reinf. Plast. Comp.* **2012**, *31*, 1388–1399. [CrossRef]

44. Kaufmann, M.; Zenkert, D.; Åkermo, M. Material selection for a curved c-spar based on cost optimization. *J. Aircraft* **2011**, *48*, 797–804. [CrossRef]

45. Struzziero, G.; Skordos, A.A. Multi-objective optimization of Resin Infusion. *Adv. Manuf. Polym. Compos. Sci.* **2019**, *5*, 17–28. [CrossRef]

46. Shmueli, G. To Explain or to Predict? *Statist. Sci.* **2010**, *25*, 289–310. [CrossRef]

47. Yu, L.; Yang, Z.; Tang, L. Prediction-Based Multi-Objective Optimization for Oil Purchasing and Distribution with the NSGA-II Algorithm. *Int. J. Inf. Tech. Decis.* **2016**, *15*, 423–451. [CrossRef]

48. Balcıoğlu, H.E.; Seçkin, A.Ç. Comparison of machine learning methods and finite element analysis on the fracture behavior of polymer composites. *Arch. Appl. Mech.* **2020**, *91*, 223–239. [CrossRef]

49. Cahn, J.W.; Hilliard, J.E. Free Energy of a Nonuniform System. I. Interfacial Free Energy. *J. Chem. Phys.* **1958**, *28*, 258–267. [CrossRef]

50. van Genuchten, M.T. A Closed-form Equation for Predicting the Hydraulic Conductivity of Unsaturated Soils. *Soil. Sci. Soc. Am.* **1980**, *44*, 892–898. [CrossRef]

51. Khoun, L.; Centea, T.; Hubert, P. Characterization methodology of thermoset resins for the processing of composite materials—Case study: CYCOM 890RTM epoxy resin. *J. Compos. Mater.* **2010**, *44*, 1397–1415. [CrossRef]

52. Dong, C. A modified rule of mixture for the vacuum-assisted resin transfer moulding process simulation. *Compos. Sci. Technol.* **2008**, *68*, 2125–2133. [CrossRef]

53. De Keer, L.; Kilic, K.I.; Van Steenberge, P.H.M.; Daelemans, L.; Kodura, D.; Frisch, H.; De Clerck, K.; Reyniers, M.-F.; Barner-Kowollik, C.; Dauskardt, R.H.; et al. Computational prediction of the molecular configuration of three-dimensional network polymers. *Nat. Mater.* **2021**, *20*, 1422–1430. [CrossRef]

54. Yalcinkaya, M.A.; Sozer, E.M.; Altan, M.C. Dynamic pressure control in VARTM: Rapid fabrication of laminates with high fiber volume fraction and improved dimensional uniformity. *Polym. Compos.* **2019**, *40*, 2482–2494. [CrossRef]

55. Garschke, C.; Parlevliet, P.P.; Weimer, C.; Fox, B.L. Out-of-autoclave cure cycle study of a resin film infusion process using in situ process monitoring. *Compos. Part A-Appl. Sci.* **2012**, *43*, 935–944. [CrossRef]

56. Massebeuf, S.; Fonteix, C.; Hoppe, S.; Pla, F. Development of new concepts for the control of polymerization processes: Multiobjective optimization and decision engineering. I. Application to emulsion homopolymerization of styrene. *J. Appl. Polym. Sci.* **2003**, *87*, 2383–2396. [CrossRef]

57. Mitra, K.; Majumdar, S.; Raha, S. Multiobjective dynamic optimization of a semi-batch epoxy polymerization process. *Comput. Chem. Eng.* **2004**, *28*, 2583–2594. [CrossRef]

58. Fierens, S.K.; D'Hooge, D.R.; Van Steenberge, P.H.M.; Reyniers, M.-F.; Marin, G.B. Exploring the Full Potential of Reversible Deactivation Radical Polymerization Using Pareto-Optimal Fronts. *Polymers* **2015**, *7*, 655–679. [CrossRef]

59. Zhilyaev, I.; Brauner, C.; Queloz, S.; Jordi, H.; Lüscher, R.; Conti, S.; Conway, R. Controlled curing of thermoset composite components using infrared radiation and mathematical modelling. *Compos. Struct.* **2021**, *259*, 113224. [CrossRef]

A Flexible Sandwich Structure Carbon Fiber Cloth with Resin Coating Composite Improves Electromagnetic Wave Absorption Performance at Low Frequency

Yuanjun Liu [1,2,3], Qianqian Lu [1] , Jing Wang [1] and Xiaoming Zhao [1,2,3],*

[1] School of Textile Science and Engineering, Tiangong University, Tianjin 300387, China; liuyuanjunsd@163.com (Y.L.); luqianqian1998@163.com (Q.L.); wjwjwjtg@163.com (J.W.)
[2] Tianjin Key Laboratory of Advanced Textile Composites, Tiangong University, Tianjin 300387, China
[3] Tianjin Municipal Key Laboratory of Advanced Fiber and Energy Storage, Tiangong University, Tianjin 300387, China
* Correspondence: texzhao@163.com; Tel.: +86-135-1284-2601

Abstract: In order to improve the electromagnetic wave absorbing performance of carbon fiber cloth at low frequency and reduce the secondary pollution caused by the shielding mechanism, a flexible sandwich composite was designed by a physical mixing coating process. This was composed of a graphene layer that absorbed waves, a carbon fiber cloth layer that reflected waves, and a graphite layer that absorbed transmitted waves. The influence of the content of graphene was studied by a control variable method on the electromatic and mechanical properties. The structures of defect polarization relaxation and dipole polarization relaxation of graphene, the interfacial polarization and electron polarization of graphite, the conductive network formed in the carbon fiber cloth, and the interfacial polarization of each part, combined together to improve the impedance matching and wave multiple reflections of the material. The study found that the sample with 40% graphene had the most outstanding absorbing performance. The minimum reflection loss value was −18.62 dB, while the frequency was 2.15 GHz and the minimum reflection loss value compared to the sample with no graphene increased 76%. The composites can be mainly applied in the field of flexible electromagnetic protection, such as the preparation of stealth tent, protective covers of electronic boxes, helmet materials for high-speed train drivers, etc.

Keywords: resins; carbon fiber cloth; sandwich structure; graphene; absorbing performance; mechanical property

1. Introduction

With the wide application of various types of electronic equipment and with the communication facilities in many aspects of industrial production and daily life, the problem of electromagnetic pollution is of wide public concern [1,2]. Harmful electromagnetic waves can cause information leakage, interfere with the operation of electronic equipment, threaten human health, and shorten the survivability of weapons on the battlefield [3–5]. Preparation of electromagnetic protective materials has become a research focus. Compared with the wave absorbing materials, the shielding materials can cause secondary pollution, thus researchers need to prepare materials with a more absorbing mechanism [6,7]. In the past few decades, a lot of research has focused on wave absorbing materials but has been mainly concentrated in the Super High Frequency, the studies of wave absorbing materials below the Super High Frequency have been fewer or not ideal. However, a large number of electronic devices have been used in these lower frequency bands [8], so that the research at the lower frequency bands of wave absorption materials has become very significant.

In recent years, researchers have studied many absorbing materials. Magnetic loss type metal materials belong to the major categories. They are characterized by high density,

unstable chemical properties, small specific surface areas, and a weak absorbing performance at low frequency [9]. Magnetic metal materials often need to be compounded with other materials to improve the absorbing performance. For example, Liu et al. [10] prepared $TiO_2/Ti_3C_2Tx/Fe_3O_4$ composites in different proportions by a simple hydrothermal reaction route. By adjusting the ratio, the two-dimensional materials showed a good microwave absorbing performance in terms of maximum RL value and absorber thickness. Carbon-based absorbing materials have the advantages of variety, thin thickness, low cost, light weight, good corrosion resistance, and wide use, while having a certain absorbing performance in the low frequency band [9,11]. Carbon fiber has the characteristics of low density, good flexibility, high hardness, high temperature resistance, corrosion resistance, good electrical conductivity, etc. [12]. For example, Jin et al. [13] proposed a multi-plate composite radar absorption structure, in which short carbon fiber layers with controllable dielectric constants are evenly and randomly dispersed and inserted between glass fabrics. By measuring the complex dielectric constant, the area density of the short carbon fiber layer is controlled, which can absorb electromagnetic waves in the target frequency band. Carbon fiber cloth made by a textile process is widely used in the aerospace, industry, construction, medical and other fields with the requirement of wave absorption [14]. Due to the overlap between carbon fibers in the carbon fiber cloth, the formed three dimensional continuous conductive network gives carbon fiber cloth an excellent shielding performance, and a weak absorbing property [15]. Preparation of the absorbing layer can effectively improve the absorbing performance of the carbon fiber cloth. Graphene and graphite are widely used as two kinds of absorbing functional particles, with the electromagnetic waves then being attenuated by dielectric loss [16]. Graphene has the advantages of a high specific surface area, thin thickness, light weight, and stable chemical properties [17]. For example, Liu et al. [18] prepared a series of cobalt-doped ferrite/graphene nanocomposites with different graphene contents by a simple one-pot method. The cobalt-doped ferrite particles are uniformly loaded on the surface of graphene nanosheets, which gives the composite good absorbing properties. By adjusting the content of graphene, the dielectric properties and magnetic properties of the nanocomposites can be improved and optimized at the same time, further enhancing the impedance matching and attenuation ability. Graphite was one of the earliest applied wave-absorbing materials, and has many advantages, such as the wide source of raw materials, light weight, and low price.

To improve the absorbing performance of carbon fiber cloth, this paper designed a kind of flexible sandwich structure carbon fiber composite by a coating process with a physical mixing method, composed of a graphene layer, a carbon fiber cloth layer, and a graphite layer. The graphene layer improves the impedance matching and absorbs the wave, the carbon fiber cloth as the support structure reflects the electromagnetic wave into the graphene layer to be re-absorbed, and the graphite layer can re-absorb the electromagnetic wave that is transmitted through the carbon fiber layer, as the transmitted wave is less; the use of graphite reduces the cost significantly. Each layer is bonded by a scraper coating process which has the advantages of a simple process, a controllable process, low cost, and mass production, etc. The adhesive used was PU2540 type polyurethane which is flexible, environmentally friendly, non-toxic, and cheap [19,20]. In the previous study, we found that the composites prepared with 30% (weight percentage) graphite in polyurethane on the surface of carbon fiber cloth had the best absorbing effect. In this paper, the control variable method was used to study the influence of the content of graphene particles in the graphene layer, which play a major role in absorbing the wave, on the shielding performance, and the absorbing performance at a frequency of 0.02–3.00 GHz, the dielectric properties at a frequency of 0.02–1.00 GHz, the electrical conductivity, and mechanical properties of the composites.

2. Materials and Methods

2.1. Materials

The main experimental material was plain carbon fiber cloth, provided by Weiduowei Technology Co., Ltd., Tianjin, China. Other chemicals included graphite powders, graphene, polyurethane, thickener, and defoaming agent. The graphite powders (≥98.0%, Q/HG3991-88) were purchased from Tianjin Fengchuan Chemical Reagent Technology Co., Ltd, Tianjin, China. Graphene (of fineness 5–15 μm, and purity larger than 95%) from Tianjin Kairuisi Fine Chemical Co., Ltd, Tianjin, China. Polyurethane (PU-2540) from Guangzhou Yuheng Environmental Protection Materials Co., Ltd, Guangzhou, China. Thickener (7011) from Guangzhou Dian Wood Composite Material Business Department, Guangzhou, China. And defoaming agent (1502) from Wuxi Redwood New Material Technology Co., Ltd., Wuxi, China.

2.2. Preparation of Materials

Preparation of the carbon fiber cloth: The plain carbon fiber cloth was cut into samples of 50 × 25 cm and fixed on the needle plate of a blade coating machine (produced by Werner Mathis, a Swiss company, LTE-S87609 type), requiring that the base cloth be in a state of tension and with a smooth surface without wrinkles; a uniform tension should be applied on the carbon fiber each time.

Preparation of the coatings: The schematic preparation of the coating is included in Figure 1. First, the polyurethane and the functional particle materials (graphene or graphite) were weighed; next the weighed polyurethane was placed in an agitator, and one of the functional particle materials was added to the polyurethane at a low speed of 600 RPM, after all functional material particles had been added to the polyurethane, the speed of the agitator was uniformly raised to 2000 RPM, and the solution was stirred for 5 min. Next thickener (1–2% of the total weight) and defoaming agent (1–3% of the total weight) were added and the solution was stirred for 35 min, and a well-mixed coating was obtained; The viscosity of the dope was measured with the No. 4 rotor of the Digital Viscometer (produced by Shanghai Hengping Instrument Factory, SNB-2 type) with a rotating speed of 6 RPM and a viscosity range between 30,000 and 40,000 mPa·s.
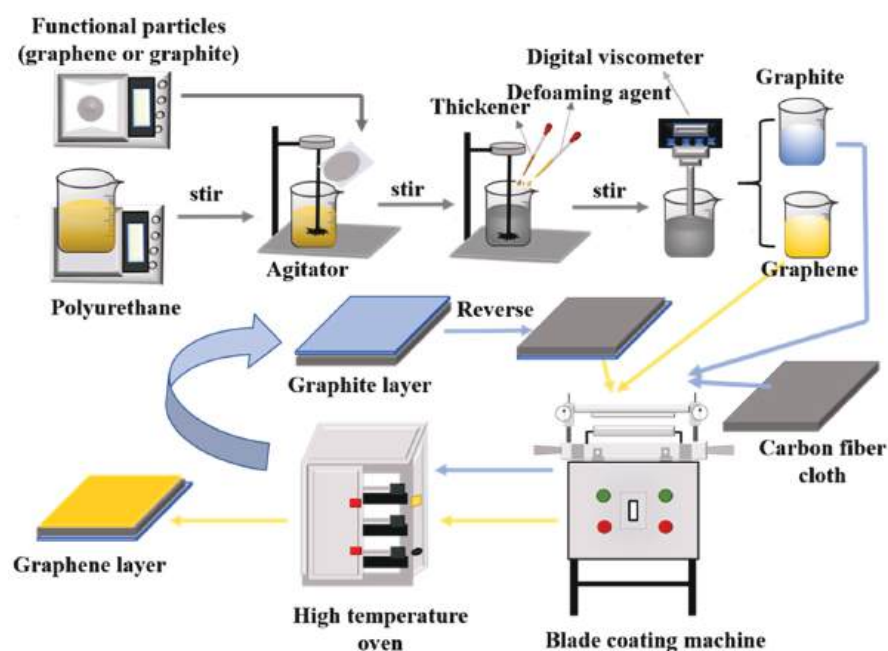
Figure 1. The simple methods for preparing the flexible sandwich structure of carbon fiber cloth.

Preparation of the graphene and graphite layers: The preparation of the sandwich structure can be seen in Figure 1. First, the prepared carbon fiber cloth was placed on the

blade coating machine, and its scraper was fixed, then the thickness (thickness = graphite layer thickness + thickness of the base cloth) was adjusted; Next the speed and coating distance of the blade coating machine were adjusted, and an appropriate coating was made on the surface of the carbon fiber cloth. The scraper was removed after the coating process and then the obtained coated fabric was placed in an oven and dried at 80 °C under vacuum for 10 min. After drying, the preparation of the graphite layer was finished, the thickness of the coated material obtained was measured, and the material was reversed. Finally, the scraper was re-fixed and the thickness (thickness = thickness of the graphite layer + the thickness of graphene layer) was adjusted, and the graphene layer was prepared in the same way. Each layer area needed to be no less than 30 × 22 cm.

2.3. Test Indicators and Methods

Test for the viscosity: An SNB-2 digital viscometer (made by Shanghai Hengping Instrument Factory, Shanghai, China) was used to measure the viscosity of prepared coatings, and the appropriate rotors and rotation speed were selected according to the range table.

Test for the thickness: A YG141D digital fabric thickness meter (made by Laizhou Electronic Instrument Co., Ltd., Laizhou, China) was used to measure the coating thickness. Multiple measurements were made at different locations on the coating materials, the measured data was recorded, and the mean thickness was calculated to reduce the measurement error.

Test for the shielding effectiveness: A ZNB40 vector network analyzer (made by Rohde & Schwarz, Munich, Germany) was used to measure the shielding effectiveness of the samples. According to the standard of GJB 6190-2008—"measuring methods for shielding effectiveness of electromagnetic shielding materials"—the test frequency range was 0.01–3.00 GHz and the sizes of the samples were 13 cm in diameter [19–22].

Test for the reflection loss: A ZNB40 vector network analyzer (made by Rohde & Schwarz, Munich, Germany) was used to measure the reflection loss of samples. The test frequency range was 0.02–3.00 GHz, the sample size was a circle with an outer diameter of 7.6 cm and an inner diameter of 3.35 cm [19–22].

Test for the dielectric properties: The dielectric properties of materials were measured with a BDS50 dielectric spectrometer (made by Novocontrol Gmbh, Frankfurt, Germany) according to the standard of SJ20512-1995—"Test methods for permitivity and permeability of microwave high loss solid materials".The size of the sample was 2 × 2 cm and the test range was 0.02–1.00 GHz [19–22].

Test for the surface resistance: The ohmic range of a F8808A desktop digital multimeter (made by Fluke Testing Instrument Co., Ltd., Everett, WA, USA) was used to measure the surface resistance of each sample. The surface resistance of samples per unit length (1 cm) on the samples' surface was measured, and 20 different locations were continuously selected to carry out the test after the maximum and minimum data had been removed. The average value was taken to reduce the error [19–22].

Test for the tensile strength: A 3369 INSTRON universal strength machine (made by the American INSTRON Company, Boston, MA, USA) was used to measure the tensile strength of the samples according to the testing method for the tensile properties of the GB1447283 standard, and the size of the samples was 15 × 5 cm.

3. Results and Discussion

To improve the wave absorbing performance of carbon fiber cloth at low frequency, a flexible sandwich structure of carbon fiber cloth composite was designed with a physical mixing coating method; the structure is shown in Figure 2d. The composite was composed of a graphene layer absorbing the wave on the surface, a carbon fiber cloth layer reflecting the wave in the middle and a graphite layer re-absorbing the transmitting wave at the bottom. To meet the requirement of a thin absorbing material, the thickness of the graphene and graphite layer was set at 1 mm in the experiment. In the previous experiment, we found

that only when the graphite absorbing layer was prepared on the surface of the carbon fiber cloth, had the composite with 30% graphite in polyurethane a better electromagnetic absorbing effect, while the content of the graphene in the layer had a great influence on the absorbing performance of the composite. Therefore, five kinds of composites with different graphene contents were prepared by the control variable method for the experiment. The specific technological parameters are shown in Table 1. First, the influence of the content of graphene on shielding and absorbing performance was investigated at a frequency of 0.02–3.00 GHz, and the conductivity performance was observed. The experiments showed that graphene content has a little influence on the shielding properties between the frequency of 0–1 GHz, and the wave absorbing performance was enhanced significantly. To study the absorbing mechanism of this frequency, the dielectric properties of composites in the frequency range of 0.02–1.00 GHz were studied. With the excellent mechanical properties of the carbon fiber cloth, the effects of the content of graphene on the mechanical properties were investigated.
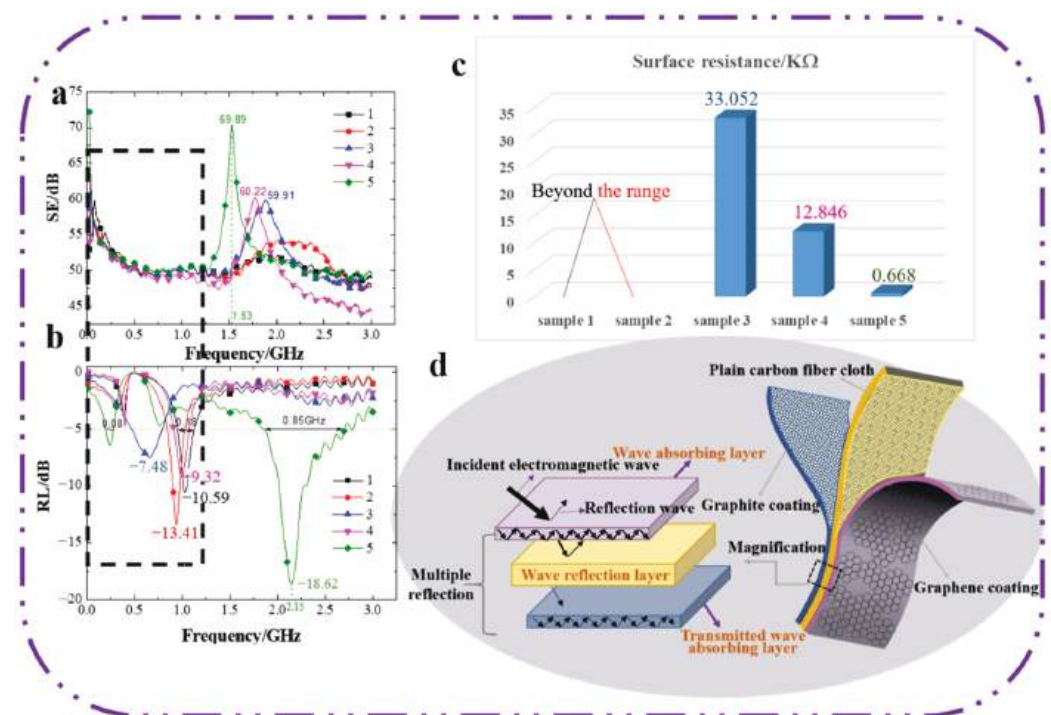
Figure 2. (**a**) The shielding properties of the composites. (**b**) The absorbing properties of the composites. (**c**) The conductive properties of the composites, (**d**) The structure model.

Table 1. Table for technological parameters.

Sample	Content of Graphene on Wave Absorbing Layer (%)	Content of Graphite on Re-Absorbing Transmitted Wave Layer (%)	Thickness of Each Absorbing Layer (mm)
1	0	30	1.0
2	10	30	1.0
3	20	30	1.0
4	30	30	1.0
5	40	30	1.0

Note: the content of functional particles refers to a percentage of the weight content of functional particles relative to that of polyurethane; the viscosity of each layer of coating was 37,000 mPa·s.

3.1. The Influence of the Content of Graphene on the Shielding, Absorbing, and Conductive Properties of the Composites

There are two main parameters of electromagnetic properties of electromagnetic protection materials, namely shielding efficiency (SE) and reflection loss (RL) value. The former represents the shielding performance of the composite to electromagnetic waves and its value is positive; the larger the value, the better the shielding performance will be. The latter represents the absorbing performance to electromagnetic waves and its value is negative; the smaller the value, the better the absorbing performance will be. Both are very important for the sandwich structure carbon fiber cloth composite that was designed to improve the absorbing performance in this paper. The conductive property has a certain auxiliary role in the study of the electromagnetic properties of the material.

3.1.1. The Shielding Performance

As can be seen from Figure 2a, within a frequency range of 0.05–3.00 GHz, the values of the shielding effectiveness of samples 1, 2, 3, 4, and 5 showed first decreasing, next increasing, and then a decreasing trend. It may be the result of carbon fibers overlapping with each other to form a conductive network for the flow of carriers, the flowing carriers then interacting with the electromagnetic field to shield electromagnetic waves [23]. The absorbing performances of graphite and graphene were limited at this frequency wave band and the shielding performance of the materials was excellent. As the frequency increased, the shielding ability of the material to electromagnetic waves was gradually enhanced, the frequency continued to increase, the amount of incident electromagnetic waves gradually increased, and the amount of electromagnetic waves that could be shielded was gradually saturated until the maximum was reached. However, with further increasing frequencies, the electromagnetic waves that could not be shielded transmitted the composite, and thus the shielding ability showed a gradually weakening trend. The growth of the content of graphene led to an increase of the amounts of electrons, ions, and inherent dipoles, and the probability of graphene particles contacting with each other became larger, the conductive network inside the material was denser, and the conductivity was better. Thus, with the increase of electromagnetic wave frequency, samples with more graphene content tended to have a peak earlier and a higher peak. The shielding efficiency peak of sample 5 with the highest graphene content was 69.89 dB when the wave frequency was 1.53 GHz. In a word, compared with control sample 1, samples 2, 3, 4, and 5 showed improved shielding efficiency in the narrow band range, but it was decreased in others.

3.1.2. Absorbing Performance

As can be seen from Figure 2b, the reflection loss values of all samples fluctuated with the increase of electromagnetic wave frequency in the range of 0.02–1.25 GHz. Compared with sample 1, the absorbing ability of the other samples in this frequency range improved, corresponding with the shielding efficiency diagram in Figure 2a, The shielding ability was being reduced while the absorbing performance was being improved, and the electromagnetic wave was transformed into other energy, mainly heat energy. In the range of 1.25–3.00 GHz, the absorbing performance of samples 1, 2, 3, and 4 tended to be stable, the absorbing performance of samples 3 and 4 were slightly improved compared with sample 1, and the minimum reflection loss values of sample 5 were greatly improved. Sample 5 had the best absorbing performance, and the value was improved of about 76% compared to that of sample 1. The reflection loss value of less than −5 dB almost took up 1/3 of the whole test range which was 0.75 GHz more than sample 1. Graphene has a unique wave absorbing property due to the phenomena of electronic dipole polarization–relaxation and structural defective polarization-relaxation [24,25]. Graphite is one type of electrical loss absorbing agent with a large dielectric loss tangent value, which can absorb electromagnetic waves according to interface polarization attenuation or electronic polarization of the mediums [26,27]. Carbon fiber cloth has almost no wave-absorbing property, and thus the ability to absorb electromagnetic waves is weaker; while the two absorbing particles

compound with carbon fibers respectively to form the layer interface. The weak wave absorbing ability of carbon fiber cloth can be enhanced due to excellent impedance matching between the carbon fibers and graphite or graphene. Among them, graphite, graphene and polyurethane, as well as between them and the carbon fiber, all have heterogeneous interfaces. Under the action of an electric field, charge accumulates at the interface of the two heterogeneous materials and the resulting interface polarization loss has a significant attenuation effect on the electromagnetic wave energy [28]. With the increasing content of graphene, the minimum value of the reflection loss became smaller, and the frequency range corresponding to an excellent wave absorbing property became wider. It may be that the increase of the content of graphene led to an increase in the amount of graphene particles in the layer per unit volume. The amounts of electrons, ions, and inherent dipoles were also growing, the impedance matching between carbon fibers and graphene became enhanced, and the ability to absorb electromagnetic waves was improved accordingly.

3.1.3. Conductive Performance

To verify the change of the conductive property of the composites, we measured the surface resistance on a unit length (1 cm) of the graphene layer surface and the test results are shown in Figure 2c. The values of the surface resistance of sample 1 and 2 were extremely large, which exceeded the measuring range of the testing instrument. It may be that the coating of sample 1 was a layer of polyurethane, which is one type of polymer with a stable structure that cannot carry out an electronic transmission. For sample 2, because the content of graphene relative to that of polyurethane was lower, the polyurethane negated the excellent conductivity of graphene. Then, with the increasing contents of graphene, the value of the surface resistance decreased gradually, and the conductivity of the composite also was enhanced gradually. The resistance was still very large, which helped to enhance the absorbing property of the composite.

3.2. The Influence of the Content of Graphene on the Dielectric Properties of the Composites

The dielectric properties test is very important for carbon-based wave absorbing materials, as it is an indirect indicator which shows the electromagnetic properties of materials. The dielectric properties test mainly includes the real part of the dielectric constant, the imaginary part of the dielectric constant, and the loss tangent value. The real part of the dielectric constant represents the polarization ability of the electromagnetic wave, the imaginary part represents the loss ability, and the loss tangent value represents the attenuation ability. In this paper, the real part and the imaginary part of the dielectric constant, and the loss tangent value of the sample were tested in the frequency range of 0.02–1.00 GHz, as shown in Figure 3a–c, Figure 3d is an enlarged figure of Figure 3c,e showing the action mechanism of each part of the composite to electromagnetic waves.

It can be seen from Figure 3 that the dielectric properties of sample 1 were not affected by the electromagnetic wave frequency while the other samples were changed. The content of graphene was the main reason for the changes in the polarization, loss, and attenuation capacity of the materials to electromagnetic waves and this may be related to the interfacial polarization between graphene, polyurethane, and carbon fiber. Due to the lower content of graphene in sample 2, each part of the dielectric constant had a small amount of improvement compared with that in sample 1. The values of the other samples with a relatively high content of graphene varied greatly with the change in the electromagnetic wave frequency.
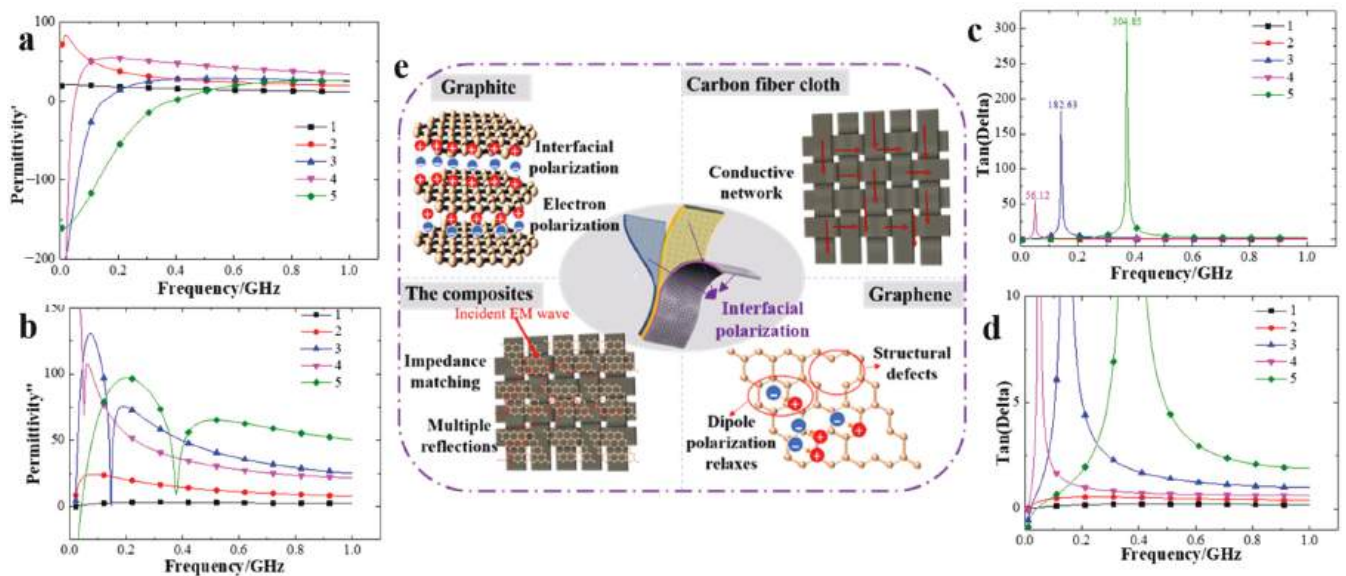
Figure 3. The influence of the content of graphene on dielectric properties of composites. (**a**) The real part of the dielectric constant. (**b**) The imaginary part of the dielectric constant. (**c**) The loss tangent value. (**d**) An enlargement of the loss tangent value. (**e**) The action mechanism of each part of the composite to electromagnetic waves.

3.2.1. The Real Part of the Dielectric Constant

It can be seen from Figure 3a that compared with sample 1, the real part of the dielectric constant of the other samples increased rapidly at first and then slowly decreased to a steady trend with the increase of electromagnetic wave frequency. This may be the result of an interaction of graphite, graphene, and carbon fibers. The impedance matching of electrons, ions, and inherent dipoles in the composite and the impedance matching of their interfaces were both good, which led to an enhancement of the ability to store charges [29–31]. However, with the increasing frequencies of the incident electric field, the effects of the internal structure and impedance matching both reached the upper limit, and the polarization ability to electromagnetic waves reached the upper limit accordingly. As the frequency further increased, the amount of incident electromagnetic waves gradually increased, but the amount of electromagnetic waves that could be polarized was limited, and thus the ability for storing charges weakened gradually. The value of the real part of the dielectric constant of the samples with higher graphene content was larger when the real part of the sample tended to be stable. It may be that the probability of graphene particles contacting with each other became larger with the increasing content of graphene, the gap between particles was smaller, the conductive network inside the material was denser, and the conductivity was better. The impedance matching between carbon fibers and graphene was enhanced, and the polarization ability to electromagnetic waves was also enhanced.

3.2.2. The Imaginary Part of the Dielectric Constant

It can be seen from Figure 3b that compared with sample 1, the value of the imaginary part of the dielectric constant of sample 2 had a trend of first increasing and then slowly decreasing to a stable state, while the value of the other samples fluctuated greatly at a relatively stable state in the measured frequency range. This may be the result of the enhancement of the electronic polarization–attenuation ability of the graphite layer and the electronic dipole polarization–relaxation ability of the graphene layer, and thus the loss of ability to electromagnetic waves was enhanced gradually [32,33]. However, with the increasing frequencies of the incident electric field, the eddy current loss caused by an increase of current gradually dominated, and the positive and negative charges heading off from the original equilibrium position in the layer had to return to the original equilibrium

position, but could not keep up with the changing frequencies, and thus the loss ability to electromagnetic waves showed a gradually weakening trend [34,35]. The higher the content of graphene of the samples, the stronger was the loss ability of the electromagnetic wave in this test frequency range. That is because with the increase of graphene content, the eddy current loss inside the material was stronger, and the loss capacity to electromagnetic waves was stronger. Moreover, the impedance match of the sample with 20% graphene content was stronger than that of the sample with 30% graphene.

3.2.3. The Loss Tangent Value

It can be seen from Figure 3c,d that compared with sample 1, the loss tangent value of sample 2 increased somewhat while the loss tangent values of sample 3, 4, and 5 showed a trend of rapid increase at first and then rapid decrease to a steady state. It may be that carbon fibers can be seen as one type of semiconductor material with an excellent conductivity. Internal fibers can overlap with each other to form a conductive network, a component perpendicular to the incident electric field of the carbon fibers and the structure of each absorbing layer can be produced to attenuate electromagnetic waves. As the frequency of the applied electric field increased, the amount of attenuated electromagnetic waves increased gradually [36]. Due to the conductivity of the carbon fibers, the electronic polarization–attenuation ability of the graphite, and the electronic dipole polarization–relaxation ability of graphene, the attenuation ability of the composite to electromagnetic waves within a specific frequency range was greatly enhanced, and attenuated the majority of incident electromagnetic waves inside the material. As the incident frequency increased, the attenuation ability to electromagnetic waves gradually weakened until there remained a stable state. The higher the content of graphene, the greater was the tangent loss value. Sample 5 with the highest graphene content has the best attenuation ability for the electromagnetic wave, and its loss tangent value reaches 304.85. With the increase of graphene content, the number of electrons, ions, and intrinsic dipoles, and the attenuation ability of the electromagnetic waves became enhanced [37,38]. The attenuation ability of sample 3 to electromagnetic waves was better than that of sample 4, which was similar to Figure 3b. It is possible that the impedance matching characteristic of sample 3 was better than that of sample 4.

3.3. The Influence of the Content of Graphene on the Graphene Layer of the Composite on Mechanical Properties

The mechanical properties of the testing samples are shown in Table 2, the strength test machine is shown in Figure 4a and the displacement–load curve is shown in Figure 4b. As can be seen from Table 2 and Figure 4b, the content of graphene had little effect on the tensile strength, which indicates that the prepared composites can improve their absorbing properties while having no deterioration in their tensile properties. Samples 1 to 5 basically met the trend in that the maximum load increased with increasing contents of graphene. The content of graphene became the main factor affecting the tensile property of the composite, because graphene has a single-layer carbon atom structure with all atoms in the same plane, thus it has good toughness, excellent strength, and a unique deformation mechanism. This unique deformation mechanism can cause the hexagonal structure of graphene in the layer to be destroyed during the stretching process, and eventually lead to a tensile fracture of the coated material [39]. However, as the content of graphene particles gradually increased, the distribution of graphene particles became more uniform in the composite. Moreover, the higher the content of graphene, the stronger the elastic force and anti-pressure ability of the composite, and thus the maximum load increased with the increasing contents of graphene. The excellent mechanical properties of the material benefit from the joint action of carbon fiber, graphite, and graphene, as well as the special plain woven structure of the carbon fiber.

Table 2. Parameters of mechanical properties of composites with different contents of graphene.

Sample	Maximum Load (kN)	Maximum Load Displacement (mm)	Maximum Load Tensile Stress (kMPa)	Modulus of Elasticity (kMPa)
1	5.54	3.04	3.79	146.04
2	5.71	3.39	3.56	141.51
3	5.84	2.83	3.64	147.54
4	5.83	3.98	3.63	126.99
5	6.22	3.29	3.62	149.73
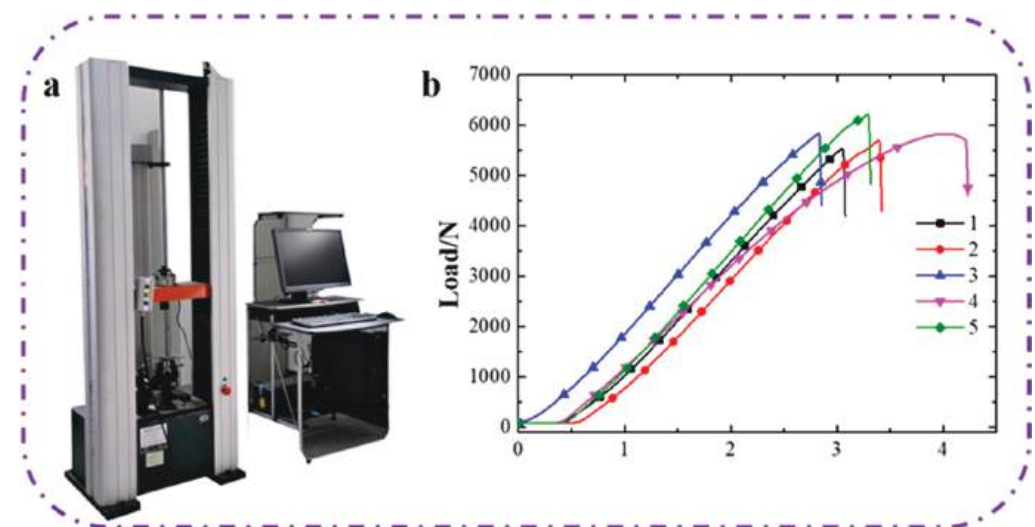
Figure 4. (**a**) A 3369 INSTRON universal strength machine. (**b**) The influence of the content of graphene on the mechanical properties.

4. Conclusions

In this paper, sandwich structure carbon fiber cloth composites prepared by a coating technology can effectively improve wave absorbing performance at low frequency. The electromagnetic parameters of the composites varied greatly in the different test ranges. The sample with a content of 40% graphene in the polyurethane had the most outstanding absorbing performance; the reflection loss value was −18.62 dB when the electromagnetic wave frequency was 2.15 GHz. The absorbing performance is mainly due to its excellent attenuation and loss ability to electromagnetic waves, and conductivity performance. The design of the sandwich structure did not deteriorate the tensile properties of the composites. The design of the absorbing material has the advantages of a simple process, environmental protection, and low price, while being suitable for industrial production. At low frequency, it has the advantages of thin thickness, light weight, good strength, and flexibility.

References

1. Lai, W.W.; Wang, Y.; He, J.K. Effects of carbonyl iron powder (CIP) content on the electromagnetic wave absorption and mechanical properties of CIP/ABS composites. *Polymers* **2020**, *12*, 1694. [CrossRef] [PubMed]
2. Zhang, F.; Cui, W.; Wang, B.B.; Xu, B.H.; Liu, X.H.; Liu, X.H.; Jia, Z.R.; Wu, G.L. Morphology-control synthesis of polyaniline decorative porous carbon with remarkable electromagnetic wave absorption capabilities. *Compos. Part B Eng.* **2021**, *204*, 108491. [CrossRef]
3. Majcher, K.; Musial, M.; Pakos, W.; Rozanski, A.; Sobotka, M.; Trapko, T. Methods of protecting buildings against HPM radiation—A review of materials absorbing the energy of electromagnetic waves. *Materials* **2020**, *13*, 5509. [CrossRef]
4. Ayub, S.; Guan, B.H.; Ahmad, F.; Oluwatobi, Y.A.; Nisa, Z.U.; Javed, M.F.; Mosavi, A. Graphene and iron reinforced polymer composite electromagnetic shielding applications: A review. *Polymers* **2021**, *13*, 2580. [CrossRef] [PubMed]
5. Liu, Q.Z.; He, X.W.; Yi, C.; Sun, D.M.; Chen, J.H.; Wang, D.; Liu, K.; Li, M.F. Fabrication of ultra-light nickel/graphene composite foam with 3D interpenetrating network for high-performance electromagnetic interference shielding. *Compos. Part B Eng.* **2020**, *182*, 107614. [CrossRef]
6. Jiang, S.; Qian, K.; Yu, K.J.; Zhou, H.F.; Weng, Y.X.; Zhang, Z.W. Controllable synthesis and microwave absorption properties of Fe$_3$O$_4$@f-GNPs nanocomposites. *Compos. Commun.* **2020**, *20*, 100363. [CrossRef]
7. Li, Y.; Yang, H.J.; Hao, X.H.; Sun, N.N.; Du, J.H.; Cao, M.S. Enhanced electromagnetic interference shielding with low reflection induced by heterogeneous double-layer structure in BiFeO$_3$/BaFe$_7$(MnTi)$_{(2.5)}$O$_{19}$ composite. *J. Alloys Compd.* **2019**, *772*, 99–104. [CrossRef]
8. Sahu, K.R.; De, U. Polymer composites for flexible electromagnetic shields. *Macromol. Symp.* **2018**, *381*, 1800097. [CrossRef]
9. Zhong, B.; Liu, W.; Yu, Y.L.; Xia, L.; Zhang, J.L.; Chai, Z.F.; Wen, G.W. Enhanced microwave absorption properties of graphite nanoflakes by coating hexagonal boron nitride nanocrystals. *Appl. Surf. Sci.* **2017**, *420*, 858–867. [CrossRef]
10. Liu, P.J.; Yao, Z.J.; Ng, V.M.H.; Zhou, J.T.; Kong, L.B.; Yue, K. Facile synthesis of ultrasmall Fe$_3$O$_4$ nanoparticles on MXenes for high microwave absorption performance. *Compos. Part A-Appl. S* **2018**, *115*, 371–382. [CrossRef]
11. Wang, X.X.; Sun, C.M.; Wen, F.B.; Jiang, S.Y.; Cao, M.S. Strong mechanics and broadened microwave absorption of graphene-based sandwich structures and surface-patterned structures. *J. Mater. Sci. Mater. Electron.* **2018**, *29*, 9683–9691. [CrossRef]
12. Zhang, H.T.; Guo, Y.; Zhang, X.; Wang, X.Q.; Wang, H.; Shi, C.S.; He, F. Enhanced shielding performance of layered carbon fiber composites filled with carbonyl iron and carbon nanotubes in the koch curve fractal method. *Molecules* **2020**, *25*, 969. [CrossRef] [PubMed]
13. Jin, D.H.; Jang, M.S.; Choi, J.H.; Jang, W.H.; Choi, W.H.; Kim, C.G. Multi-slab hybrid radar absorbing structure containing short carbon fiber layer with controllable permittivity. *Compos. Struct.* **2021**, *273*, 114279. [CrossRef]
14. Zhao, K.; Gupta, S.; Chang, C.; Wei, J.Q.; Tai, N.H. Layered composites composed of multi-walled carbon nanotubes/manganese dioxide/carbon fiber cloth for microwave absorption in the X-band. *RSC Adv.* **2019**, *9*, 19217–19225. [CrossRef]
15. Zhang, K.L.; Li, Y.J.; Zhou, H.; Nie, M.; Wang, Q.; Hua, Z.K. Polyurethane carbon fiber composite tubular electrode featuring three-dimensional interpenetrating conductive network. *Carbon* **2018**, *139*, 999–1009. [CrossRef]
16. Wang, C.; Han, X.J.; Xu, P.; Zhang, X.L.; Du, Y.C.; Hu, S.R.; Wang, J.Y.; Wang, X.H. The electromagnetic property of chemically reduced graphene oxide and its application as microwave absorbing material. *Appl. Phys. Lett.* **2011**, *98*, 072906. [CrossRef]
17. Yuan, H.R.; Yan, F.; Li, C.Y.; Zhu, C.L.; Zhang, X.T.; Chen, Y.J. Nickel nanoparticle encapsulated in few-layer nitrogen-doped graphene supported by nitrogen-doped graphite sheets as High-Performance electromagnetic wave absorbing material. *ACS Appl. Mater. Interfaces.* **2018**, *10*, 1399–1407. [CrossRef] [PubMed]
18. Liu, P.J.; Yao, Z.J.; Zhou, J.T.; Yang, Z.H.; Kong, L.B. Small magnetic Co-doped NiZn ferrite/graphene nanocomposites and their dual-region microwave absorption performance. *J. Mater. Chem. C* **2016**, *4*, 9738–9749. [CrossRef]
19. Liu, Y.J.; Yu, Y.T.; Zhao, X.M. Research on the electromagnetic property of the single-layer graphene-coated fabrics. *J. Text. Inst.* **2021**, *112*, 255–263. [CrossRef]
20. Liu, Y.J.; Zhao, X.M. The preparation and performance of a polyaniline/graphene composite coated fabric. *J. Text. Inst.* **2021**, *112*, 1258–1265. [CrossRef]
21. Liu, Y.J.; Wang, H.H.; Zhang, Y.Q.; Wang, X.C.; Yin, G.; Han, X.H.; Niu, J.R. Study on the electromagnetic and mechanical properties of coated composites. *Fibres Text. East. Eur.* **2020**, *28*, 89–97.
22. Liu, Y.J.; Zhao, X.M.; Xiao, T. Study of graphite/silicon carbide coating of plain woven fabric for electrical megawatt absorbing properties. *J. Text. Inst.* **2017**, *108*, 483–488. [CrossRef]
23. Guo, Z.Z.; Ren, P.G.; Zhang, Z.P.; Dai, Z.; Hui, K.D.; Yan, H.H.; Jin, Y.L.; Gao, J.F.; Ren, F. Simultaneous realization of highly efficient electromagnetic interference shielding and human motion detection in carbon fiber felt decorated with silver nanowires and thermoplastic polyurethane. *J. Mater. Chem. C* **2021**, *9*, 6894–6903. [CrossRef]
24. Liu, Y.; Wu, Y.X.; Li, K.X.; Wang, J.; Zhang, G.L.; Ji, J.L.; Wang, W.J. Amorphous SnS nanosheets/graphene oxide hybrid with efficient dielectric loss to improve the high-frequency electromagnetic wave absorption properties. *Appl. Surf. Sci.* **2019**, *486*, 344–353. [CrossRef]
25. Soleimani, M.; Jalili, S.; Mahfouzi, F. Structural defects influence on the conductance of strained zigzag graphene nanoribbon. *Phys. E* **2017**, *93*, 216–223. [CrossRef]
26. Yao, Y.Y.; Jin, S.H.; Sun, J.; Li, L.J.; Zou, H.M.; Wen, P.; Lv, G.; Lv, X.J.; Shu, Q.H. Sandwich-like sulfur-free expanded graphite/CoNi hybrids and their synergistic enhancement of microwave absorption. *J. Alloys Compd.* **2021**, *862*, 158005. [CrossRef]

27. Su, X.G.; Wang, J.; Zhang, X.X.; Liu, Z.J.; Dai, W.; Chen, W.; Zhang, B. Construction of sandwich-like NiCo$_2$O$_4$/Graphite nanosheets/NiCo$_2$O$_4$ heterostructures for a tunable microwave absorber. *Ceram. Int.* **2020**, *46*, 19293–19301. [CrossRef]

28. Chen, J.B.; Zheng, J.; Huang, Q.Q.; Wang, F.; Ji, G.B. Enhanced microwave absorbing ability of carbon fibers with embedded FeCo/CoFe$_2$O$_4$ nanoparticles. *ACS Appl. Mater. Interfaces* **2021**, *13*, 36182–36189. [CrossRef] [PubMed]

29. Li, Y.X.; Duan, Y.G.; Kang, X.Q. Multi-scale integrated design and fabrication of ultrathin broadband microwave absorption utilizing carbon fiber/Prussian blue/Fe$_3$O$_4$-based lossy lattice metamaterial. *J. Mater. Chem. C* **2021**, *9*, 6316–6323. [CrossRef]

30. Pang, L.; Wang, J.J.; Chen, S.A.; Luo, H.; Fan, X.M.; Li, Y.; Zhou, W.; Xiao, P. Multiple dielectric behavior of C-f-SiCNFs/Si$_3$N$_4$ ceramic composite at high temperatures. *Ceram. Int.* **2021**, *47*, 4127–4134. [CrossRef]

31. Zuo, Y.X.; Su, X.R.; Li, X.W.; Yao, Z.J.; Yu, T.T.; Zhou, J.T.; Li, J.; Lu, J.; Ding, J. Multimaterial 3D-printing of graphene/Li$_{0.35}$Zn$_{0.3}$Fe$_{2.35}$O$_4$ and graphene/carbonyl iron composites with superior microwave absorption properties and adjustable bandwidth. *Carbon* **2020**, *167*, 62–74. [CrossRef]

32. Liang, X.H.; Quan, B.; Sun, B.W.; Man, Z.M.; Xu, X.; Ji, G.B. Extended effective frequency of three-dimensional graphene with sustainable energy attenuation. *ACS Sustain. Chem. Eng.* **2019**, *7*, 10477–10483. [CrossRef]

33. Cheng, Y.H.; Hu, P.; Zhou, S.B.; Yan, L.W.; Sun, B.Q.; Zhang, X.H.; Han, W.B. Achieving tunability of effective electromagnetic wave absorption between the whole X-band and Ku-band via adjusting PPy loading in SiC nanowires/graphene hybrid foam. *Carbon* **2018**, *132*, 430–443. [CrossRef]

34. Yin, P.F.; Zhang, L.M.; Tang, Y.T.; Liu, J.C. Earthworm-like (Co/CoO)@C composite derived from MOF for solving the problem of low-frequency microwave radiation. *J. Alloys Compd.* **2021**, *881*, 160556. [CrossRef]

35. Shao, X.L.; Wang, T.H.; Gan, Z.Y.; Hu, R.; Gong, Y.; Li, X.X.; Zhang, X.; Tian, X.Y. Tailoring of N-doped graphite coated cobalt nanoparticles via arc discharge enables high microwave absorption. *Carbon* **2021**, *177*, 171–180. [CrossRef]

36. Vilatela, J.J.; Marcilla, R. Tough electrodes: Carbon nanotube fibers as the ultimate current collectors/active material for energy management devices. *Chem. Mater.* **2015**, *27*, 6901–6917. [CrossRef]

37. Liu, X.D.; Huang, Y.; Ding, L.; Zhao, X.X.; Liu, P.B.; Li, T.H. Synthesis of covalently bonded reduced graphene oxide-Fe$_3$O$_4$ nanocomposites for efficient electromagnetic wave absorption. *J. Mater. Sci. Technol.* **2021**, *72*, 93–103. [CrossRef]

38. Prasad, J.; Singh, A.K.; Haldar, K.K.; Tomar, M.; Gupta, V.; Singh, K. CoFe$_2$O$_4$ nanoparticles decorated MoS$_2$-reduced graphene oxide nanocomposite for improved microwave absorption and shielding performance. *RSC Adv.* **2019**, *9*, 21881–21892. [CrossRef]

39. Gao, H.; Xu, J.A.; Liu, S.; Song, Z.Q.; Zhou, M.; Liu, S.W.; Li, F.; Li, F.H.; Wang, X.D.; Wang, Z.X. Stretchable, self-healable integrated conductor based on mechanical reinforced graphene/polyurethane composites. *J. Colloid Interface Sci.* **2021**, *597*, 393–400. [CrossRef]

PLA Biocomposites: Evaluation of Resistance to Mold

Piotr Borysiuk [1,*], Krzysztof Krajewski [1], Alicja Auriga [2], Radosław Auriga [1], Izabela Betlej [1], Katarzyna Rybak [3], Małgorzata Nowacka [3] and Piotr Boruszewski [1]

1   Institute of Wood Sciences and Furniture, Warsaw University of Life Sciences—SGGW,
    ul. Nowoursynowska 159, 02-776 Warsaw, Poland; krzysztof_krajewski@sggw.edu.pl (K.K.);
    radoslaw_auriga@sggw.edu.pl (R.A.); izabela_betlej@sggw.edu.pl (I.B.);
    piotr_boruszewski@sggw.edu.pl (P.B.)
2   Faculty of Biotechnology and Animal Husbandry, West Pomeranian University of Technology Szczecin,
    Janickiego 33, 71-270 Szczecin, Poland; alicja.auriga@tlen.pl
3   Department of Food Engineering and Process Management, Institute of Food Sciences, Warsaw University of
    Life Sciences—SGGW, 159C Nowoursynowska St., 02-776 Warsaw, Poland;
    katarzyna_rybak@sggw.edu.pl (K.R.); malgorzata_nowacka@sggw.edu.pl (M.N.)
*   Correspondence: piotr_borysiuk@sggw.edu.pl

Abstract: Due to the content of lignocellulosic particles, wood plastic composites (WPC) composites can be attacked by both domestic and mold fungi. Household fungi reduce the mechanical properties of composites, while mold fungi reduce the aesthetics of products by changing their color and surface decomposition of the wood substance. As part of this study, the impact of lignocellulosic fillers in the form of sawdust and bark in poly (lactic acid) (PLA)-based biocomposites on their susceptibility to mold growth was determined. The evaluation of the samples fouled with mold fungi was performed by computer analysis of the image. For comparison, tests were carried out on analogous high-density polyethylene (HDPE) composites. Three levels of composites' filling were used with two degrees of comminution of lignocellulosic fillers and the addition of bonding aids to selected variants. The composites were produced in two stages employing extrusion and flat pressing. The research revealed that PLA composites were characterized by a higher fouling rate by Aspergillus niger Tiegh fungi compared to HDPE composites. In the case of HDPE composites. The type of filler (bark, sawdust) affected this process much more in the case of HDPE composites than for PLA composites. In addition, the use of filler with smaller particles enhanced the fouling process.

Keywords: PLA; HDPE; biocomposites; mold; bark

1. Introduction

The rapidly developing industry of wood-plastic composites (WPC) focuses on the introduction of new material solutions for matrix and fillers. In both cases, the biodegradability of applied raw materials is crucial. Nowadays most WPC composites are produced from polyethylene PE, polypropene PP, or polyvinyl chloride PVC [1]. However, as an alternative can also be used biodegradable poly (lactic acid) PLA or polyhydroxyalkanoate PHA. PHA when exposed to anaerobic conditions slowly decomposes under the influence of bacteria present in the soil, sewage, or silt into water and carbon dioxide. For this reason, it can be applied to manufacture packaging and components with short durability. In turn, PLA does not biodegrade under ordinary conditions of use, so it can be applied in production of components with a long mean life. Furthermore, PLA can be easily disposed of by composting with no harm to the natural environment [2]. Given its features, PLA is used in medicine and industry, replacing conventional petrochemical polymers [3]. However, due to its downsides, such as sensitivity to moisture, susceptibility to aging, limited impact strength, and high rigidity [4], PLA is modified in many ways.

One of the directions of PLA modification is introduction lignocellulosic fillers, such as: wood fibers [5–7], wood flour [8–10], cork [8], bamboo fiber [11], abaca fibers [12], rubber

wood sawdust [13], and bark [14]. The authors generally indicate an improvement in the mechanical properties of PLA composites filled with wood fibers with a filler content of up to 20% [5,7] or 30% [6]. Andrzejewski et al. [8] reported the beneficial effect of cork filler (up to 30%) on the dimensional stability of PLA composites exposed to moisture. The use of wood flour or bark as a filler, on the other hand, deteriorates the resistance of PLA composites to moisture [10,14].

Due to the content of lignocellulosic particles and changing conditions of use WPC composites can be biodegradable [15–23]. They are susceptible to domestic and mold fungi attack. Domestic fungi cause changes in the structure and chemical composition of the lignocellulosic particles in the composites. The degradation effect depends on the weight fraction of lignocellulosic particles, their size and type of wood, as well as the possible application of other additives [24]. The degradation of wood particles is reflected in the decrease in the strength of WPC composites [20,23,25,26], and to a large extent this decrease is also caused by changes caused by the moistening and drying of these particles [27]. Mold fungi, in turn, reduce the aesthetics of the products by changing their color and the surface distribution of the wood substance [28]. Fungi have a detrimental effect on the health of humans and animals living in the vicinity of objects attacked by them [29,30]. Schirp et al. [31], Kartal et al. [32], Feng et al. [33] reported that WPC with a higher content and larger sizes of wood particles are more susceptible to mold fungi. The susceptibility also depends on the type of wood used as the filler [34].

This study determines the impact of lignocellulosic fillers (sawdust and bark) in PLA biocomposites on their susceptibility to mold growth. Schirp et al. [31] reported that the influence of coloring and mold fungi on WPC was measured only by the visual method of assessment of microorganisms fouling the material. As part of the research, the mold growth on the samples was assessment using computer analysis of the image [14]. The tests were carried out on analogous WPC composites made of high-density polyethylene (HDPE). Three levels of filling were used with two degrees of granularity of lignocellulosic fillers and the addition of joining additives to selected variants. The composites were produced in two stages process consisting of extrusion and flat pressing.

2. Materials and Methods

In this study 36 variants of WPC composite panels were produced based on two types of polymer matrices: polylactic acid—PLA (Ingeo™ Biopolymer 2003D, NatureWorks LLC, Minnetonka, MN, USA) and high-density polyethylene—HDPE (Hostalen GD 7255, Basell Orlen Polyolefins Sp. Z.o.o., Płock, Poland) (Tables 1 and 2). Two types of lignocellulosic material were used as a filler: coniferous sawdust and conifer bark. Additives used in selected variants were: calcium oxide CaO (Avantor Performance Materials Poland S. A., Gliwice, Poland) in the case of PLA composites, and polyethylene-graft-maleic anhydride MAHPE (SCONA TSPE 2102 GAHD, BYK-Chemie GmbH, Wesel, Germany) in HDPE composites.

The lignocellulosic material obtained from the sawmill was dried to a humidity of 5% and then mechanically ground and sorted into two size variants:

(1) Particles passing through a 2 mm sieve (approx. 10 mesh) and remaining on a 0.49 mm sieve (approx. 35 mesh);
(2) Particles passing 0.49 mm sieve (greater than 35 mesh).

The composites were produced in a two stage process:

(1) First, WPC granules with an appropriate formulation were produced (Tables 1 and 2) using an extruder (Leistritz Extrusionstechnik GmbH, Nürnberg, Germany) (temperatures in individual sections of the extruder were 170–180 °C), the obtained continuous composite band was then ground in a hammer mill.
(2) Secondly, the obtained granulate was used to produce plates with nominal dimensions $300 \times 300 \times 2.5$ mm^3. The process consisted of flat pressing in a mold, using a one-shelf press (AB AK Eriksson, Mariannelund, Sweden) at a temperature of 200 °C and

a maximum unit pressing pressure pmax = 1.25 MPa (the pressure during pressing, along with the plasticization of the material, was gradually increased from 0 to pmax). The pressing time was 6 min. After hot pressing, the plates were cooled in the mold for 6 min in the cold press.

The manufactured plates were conditioned for 7 days at 20 ± 2 °C and 65 ± 5% humidity.

Table 1. Composition of individual variants PLA composites.

| Variant | Matrix | Share of the Matix (%) | Additvies (CaO) (%) | Share of the Filler [%] | |
				Small Particles >35 Mesh	Large Particles 10–35 Mesh
1P	PLA	60			40 s
2P	PLA	60			40 b
3P	PLA	60		40 b	
4P	PLA	60		40 s	
5P	PLA	50			50 s
6P	PLA	50			50 b
7P	PLA	50		50 b	
8P	PLA	50		50 s	
9P	PLA	40			60 s
10P	PLA	40			60 b
11P	PLA	40		60 b	
12P	PLA	40		60 s	
13P	PLA	57	3		40 s
14P	PLA	57	3	40 b	
15P	PLA	47	3		50 s
16P	PLA	47	3	50 b	
17P	PLA	37	3		60 s
18P	PLA	37	3	60 b	

s—sawdust, b—bark.

Table 2. Composition of individual variants HDPE composites.

| Variant | Matrix | Share of the Matix (%) | Additvies (MAHPE) (%) | Share of the Filler [%] | |
				Small Particles >35 Mesh	Large Particles 10–35 Mesh
1H	HDPE	60			40 s
2H	HDPE	60			40 b
3H	HDPE	60		40 b	
4H	HDPE	60		40 s	
5H	HDPE	50			50 s
6H	HDPE	50			50 b
7H	HDPE	50		50 b	
8H	HDPE	50		50 s	
9H	HDPE	40			60 s
10H	HDPE	40			60 b
11H	HDPE	40		60 b	
12H	HDPE	40		60 s	
13H	HDPE	57	3		40 s
14H	HDPE	57	3	40 b	
15H	HDPE	47	3		50 s
16H	HDPE	47	3	50 b	
17H	HDPE	37	3		60 s
18H	HDPE	37	3	60 b	

s—sawdust, b—bark.

2.1. Resistance to Moulds

The resistance of materials to molds was performed using the test specimens of dimensions $50 \times 50 \times 2.5$ mm^3. Test samples were superficially sterilized by spraying all surfaces with 70% alcohol and then placed separately in sterile glass vessels for 24 h at a temperature of 65 °C. After cooling the samples for the next 24 h, test specimens were exposed to pure cultures of Aspergillus niger Tiegh (ATCC:16888) fungus, growing on a 2% MEA nutrient medium (OXOID Ltd., Basingstoke, UK).

The specimens were placed directly into Petri dishes (diameter of 100 mm) on a nutrient agar medium to ensure their good moisture saturation. Inoculation with the fungus was carried out by placing four inoculums, each, approximately 10 mm from every edge of the specimen. Growth of fungus was conducted in incubators chamber—model Thermolyne Type 42000 (ThermoFisher Scientific, Waltham, MA, USA) for 22 days at temperature of 26 °C. Periodically the mold growth on samples was determined by taking high resolution pictures in laboratory photo making cabinet station for documentation purposes. In accordance with the author's own concept of assessing the degree of contamination (p) of the tested materials by *A. niger*, two parameters of attack by the fungus were determined for each sample. The first parameter of infestation (p_1) was the percentage of mycelium coverage of the sample surface, calculated in relation to the total area of the sample. The second parameter of infestation (p_2) determined the percentage of cover of the sample surface by conidial sporangia of the fungus, calculated in relation to the total area of the sample. The final result of the specimen contamination by the fungus (p), was assumed as the value of the sum of the parameters p_1 and p_2, calculated according to the equation $p = 0.7p_1 + 0.3p_2$. The numerical factors 0.7 and 0.3, respectively for the parameters p_1 and p_2, were adopted on the basis of our own observations and considered as suitable for the parametric determination of the degree of contamination of materials by *A. niger*. The results of the contamination of samples by the fungus was the arithmetic mean value of the results obtained for four replications of each material variant.

The percentage overgrowth of samples was determined with an accuracy of up to 5% with the support of image analysis software ImageJ2 (Fiji v1.52i) [35,36].

2.2. Porosity

The porosity and the pore volume in the samples was determined by using the X-ray micro-CT measurements SkyScan 1272 system (Bruker microCT, Kontich, Belgium). To capture high quality imaging pixel resolution of 25.0 µm, 40 keV source voltage, 193 µA current was used. A stack of approximately 1500 flat projection images (1008×1008 pixels) was obtained after a 180° rotation with 0.4° steps, which averaged 4 frames for each step.

3. Results

At the initial stage (first 3 days) mold growth on PLA composites was significantly influenced by the size of the filler particles (PS) and the interaction between the share of the filler and its particles size (FCxPS), the share of the filler and its type (FCXF), and the proportion of the filler, the particles size of the filler and the type of filler (FCxPSxF). In each of the cases, the influence of factors was significant (the influence percentage of factors ranged from 16.27% to 27.55%). In turn, further growth of mold was to a lesser extent determined by the size of the filler particles, although this effect was still significant (Table 3). In the final stage of fouling the PLA samples, the greatest influence percentage had the share of the filler (FC) and the type of filler (F) as well as the interaction between these factors (FCxF).

In the case of HDPE composites (Table 4), the filler particles size (PS) had the greatest effect on the mold growth over the first 7 days. On the other hand, the further growth was also determined by the share of the filler (FC) and the type of filler (F) as well as the interaction between these factors (FCxF).

Table 3. The influence percentage of individual factors and their interactions affecting the mold growth on PLA composites.

Day	Factors			Interaction between Factors				Error
	FC	PS	F	FCxPS	FCxF	PSxF	FCxPSxF	
2	8.83 [S]	20.11 [S]	0.09 [N]	19.18 [S]	27.46 [S]	0.39 [S]	22.87 [S]	1.04
3	10.44 [S]	18.54 [S]	0.08 [N]	18.48 [S]	27.55 [S]	4.61 [S]	16.27 [S]	4.33
4	8.37 [S]	4.51 [S]	5.72 [S]	16.56 [S]	19.16 [S]	34.84 [S]	6.63 [S]	4.19
5	5.71 [S]	8.41 [S]	6.35 [S]	14.61 [S]	12.28 [S]	22.35 [S]	5.61 [S]	24.66
7	15.12 [S]	9.96 [S]	3.55 [N]	5.52 [N]	16.68 [S]	0.39 [N]	0.82 [N]	47.96
9	14.67 [S]	9.51 [S]	9.29 [S]	6.34 [N]	18.78 [S]	1.06 [N]	2.09 [N]	38.25
12	14.13 [S]	2.35 [N]	21.18 [S]	4.71 [N]	14.13 [S]	2.35 [N]	4.71 [N]	36.43
15	24.65 [S]	0.00 [S]	12.33 [S]	0.00 [S]	24.65 [S]	0.00 [S]	0.00 [S]	38.37

FC—filler content; PS—particle size; F—filler; [N]—no statistical significance ($p > 0.05$); [S]—statistically significant ($p < 0.05$).

Table 4. The influence percentage of individual factors and their interactions affecting the mold growth on HDPE composites.

Day	Factors			Interaction between Factors				Error
	FC	PS	F	FCxPS	FCxF	PSxF	FSxPSxF	
2	2.78 [S]	24.00 [S]	10.07 [S]	13.19 [S]	11.73 [S]	0.05 [N]	31.92 [S]	6.26
3	24.91 [S]	35.85 [S]	0.02 [N]	9.37 [S]	9.53 [S]	1.08 [S]	13.33 [S]	5.91
4	16.37 [S]	51.02 [S]	1.01 [S]	10.34 [S]	14.89 [S]	0.10 [N]	1.13 [S]	5.13
5	9.38 [S]	43.31 [S]	8.90 [S]	4.39 [S]	24.15 [S]	0.62 [N]	0.71 [N]	8.54
7	11.65 [S]	29.56 [S]	15.37 [S]	4.56 [S]	23.52 [S]	1.78 [S]	4.67 [S]	8.88
9	13.41 [S]	18.52 [S]	24.54 [S]	2.72 [S]	17.78 [S]	6.14 [S]	5.06 [S]	11.74
12	21.75 [S]	16.20 [S]	26.19 [S]	1.93 [S]	12.38 [S]	9.57 [S]	3.59 [S]	8.40
15	23.22 [S]	15.48 [S]	25.99 [S]	1.46 [S]	12.95 [S]	8.66 [N]	3.00 [S]	9.24

FC—filler content; PS—particle size; F—filler; [N]—no statistical significance ($p > 0.05$); [S]—statistically significant ($p < 0.05$).

The effect of addition the additive and its interaction with the filler was significant in the first five days of exposure to fungi in case of PLA composites (Table 5). For HDPE composites this effect was generally significant throughout the impact of mold fungi (Table 6). Referring to these analyzes, it is worth noting that, except for HDPE composites filled with large sawdust, in the remaining cases, after four days of fouling, the influence of factors not included in this study started to play an important role (error > 20%).

Table 5. Percentage of the compatibilizer influence, filler fraction and their interactions influencing the mold growth on PLA composites.

Day	Bark Large Particles				Bark Small Particles			
	K	FC	KxFC	Error	K	FC	KxFC	Error
2	31.80 [S]	9.47 [S]	56.19 [S]	2.54	0.03 [N]	33.62 [S]	62.90 [S]	3.45
3	26.35 [S]	58.06 [S]	11.96 [S]	3.64	41.85 [S]	3.39 [S]	50.32 [S]	4.45
4	29.96 [S]	49.03 [S]	18.69 [S]	2.31	50.31 [S]	0.53 [N]	40.44 [S]	8.71
5	11.96 [S]	44.63 [S]	22.90 [S]	20.52	20.91 [S]	2.34 [N]	45.62 [S]	31.13
7	0.26 [N]	46.93 [S]	10.98 [N]	41.83	0.00 [N]	14.96 [N]	14.86 [N]	70.19
9	9.28 [N]	32.64 [S]	4.73 [N]	53.34	14.04 [S]	28.08 [S]	28.08 [S]	29.80
12	4.54 [N]	26.77 [S]	8.99 [N]	59.70				
15	4.54 [N]	26.77 [S]	8.99 [N]	59.70				

K—additives; FC—filler content; [N]—no statistical significance ($p > 0.05$); [S]—statistically significant ($p < 0.05$).

Table 6. Percentage of the compatibilizer influence, filler fraction and their interactions influencing the mold growth on HDPE composites.

Day	Sawdust large Particles				Bark Small Particles			
	K	FC	KxFC	Error	K	FC	KxFC	Error
2	72.87 [S]	11.21 [S]	11.21 [S]	4.70	19.79 [S]	44.51 [S]	26.57 [S]	9.14
3	15.73 [S]	60.40 [S]	16.16 [S]	7.71	28.03 [S]	31.70 [S]	37.52 [S]	2.75
4	44.68 [S]	29.95 [S]	22.92 [S]	2.45	32.75 [S]	26.81 [S]	29.88 [S]	10.56
5	39.23 [S]	47.53 [S]	10.07 [S]	3.18	51.77 [S]	6.35 [N]	10.60 [N]	31.28
7	18.20 [S]	58.94 [S]	20.14 [S]	2.71	15.44 [N]	4.65 [N]	4.64 [N]	75.27
9	15.77 [S]	61.44 [S]	19.86 [S]	2.93	1.92 [N]	3.78 [N]	3.80 [N]	90.51
12	12.85 [S]	65.79 [S]	17.79 [S]	3.57	18.45 [S]	4.11 [N]	12.23 [N]	65.21
15	11.78 [S]	68.75 [S]	16.03 [S]	3.44	18.45 [S]	4.11 [N]	12.23 [N]	65.21

K—additives; FC—filler content; [N]—no statistical significance ($p > 0.05$); [S]—statistically significant ($p < 0.05$).

Regardless the type of filler, PLA composites were more susceptible to mold growth than analogous HDPE composites. After 7 days, 90% of PLA composites surface was covered by mold irrespectively of the composition of the specimens (Figure 1). In the case of HDPE composites, 100% surface coverage of the samples was not achieved even after 15 days of exposure (Figure 2). Exemplary images of samples covered by mold fungi are presented in Figures 3–6. Composites made on the basis of PLA were characterized by a generally higher porosity of the internal structure compared to analogous materials made on the basis of HDPE (Figure 7).

Application of the additives had a significant effect on the mold growth on both, PLA and HDPE composites (Figures 1a,d, 2a,d, 8 and 9). Irrespectively to the type of filler, the additives increased the rate of mold growth. It is worth adding here that the porosity of the composites in most cases (except for the composite based on polyethylene filled with small bark) generally decreased (Figure 10).
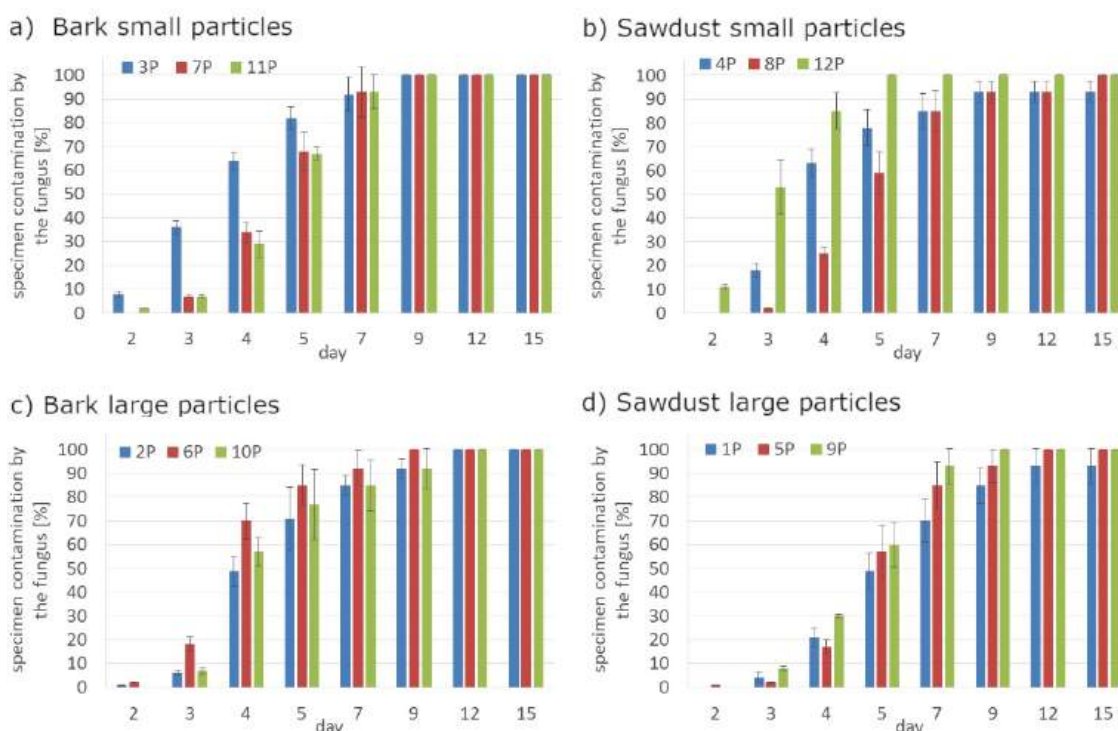
Figure 1. The rate of surface fouling by *Aspergillus niger* Tiegh fungi on PLA composites for: (**a**) bark small particles; (**b**) sawdust particles; (**c**) bark large particles; (**d**) sawdust large particles.
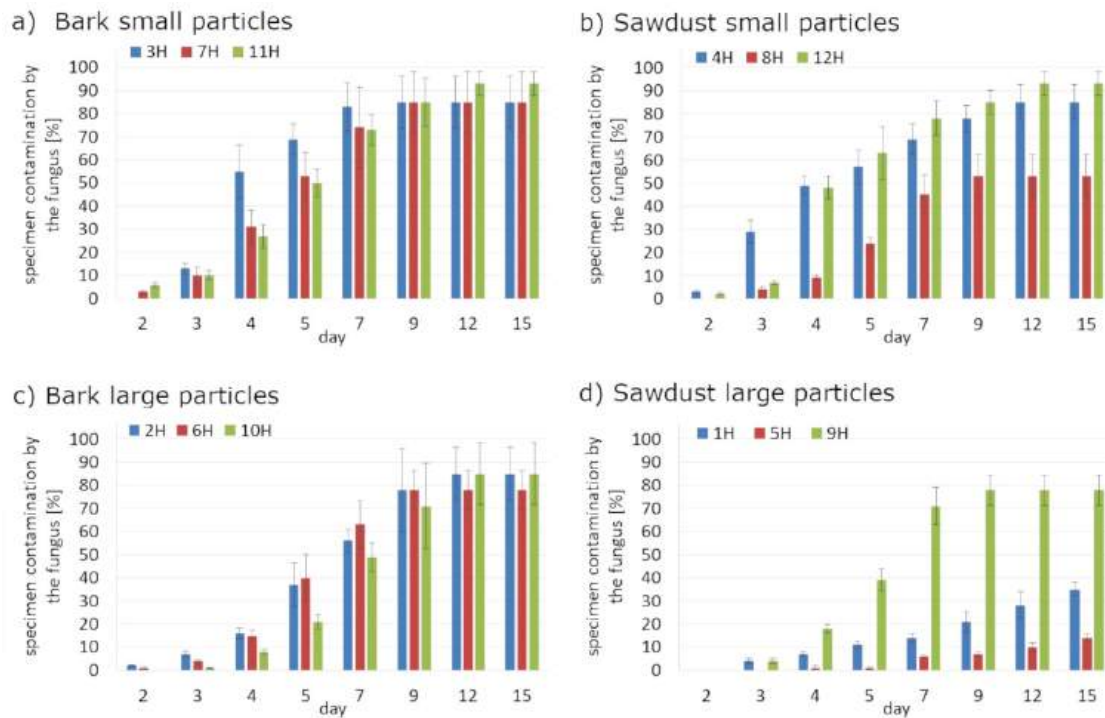
Figure 2. The rate of surface fouling by *Aspergillus niger* Tiegh fungi on HDPE composites for: (**a**) bark small particles; (**b**) sawdust particles; (**c**) bark large particles; (**d**) sawdust large particles.
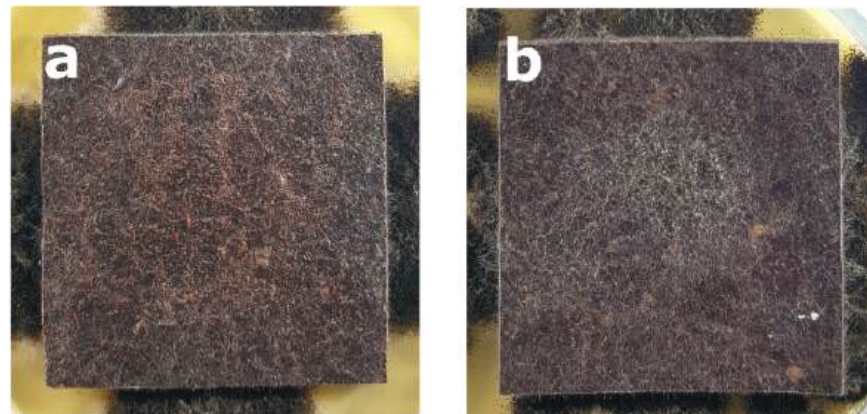
Figure 3. Example of mold growth (*Aspergillus niger* Tiegh) after 7 days of exposure of composite samples with large particle bark filler of 60%, based on a matrix: (**a**) HDPE; (**b**) PLA.
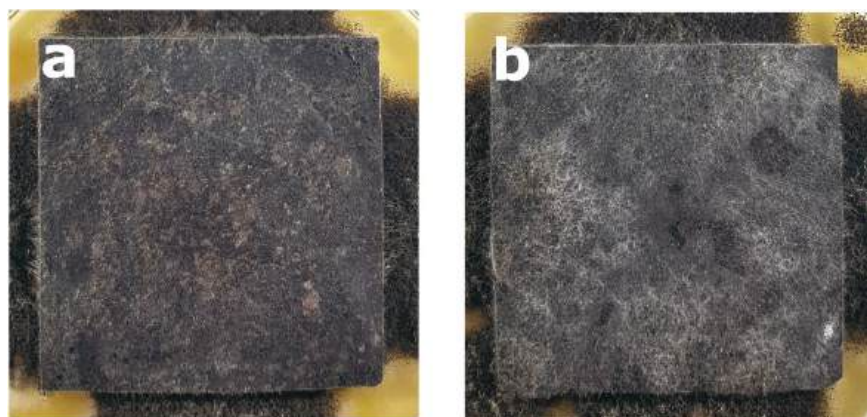
Figure 4. Example of mold growth (*Aspergillus niger* Tiegh) after 7 days of exposure of composite samples with small particle bark filler of 60%, based on a matrix: (**a**) HDPE; (**b**) PLA.
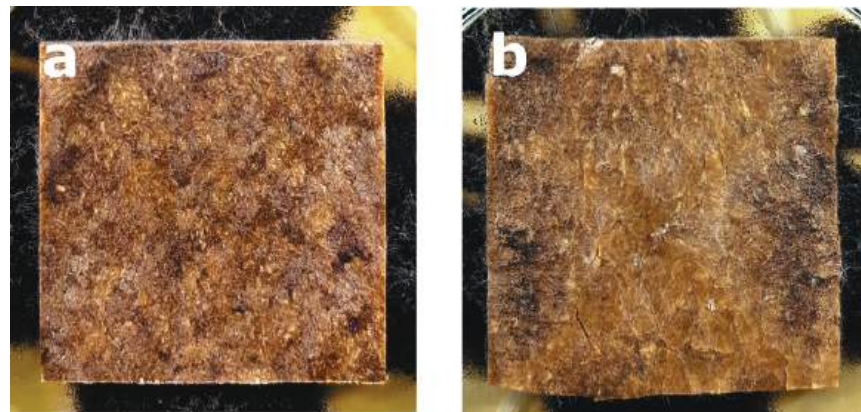
Figure 5. Example of mold growth (*Aspergillus niger* Tiegh) after 7 days of exposure of composite samples with large particle sawdust filler of 60%, based on a matrix: (**a**) HDPE; (**b**) PLA.
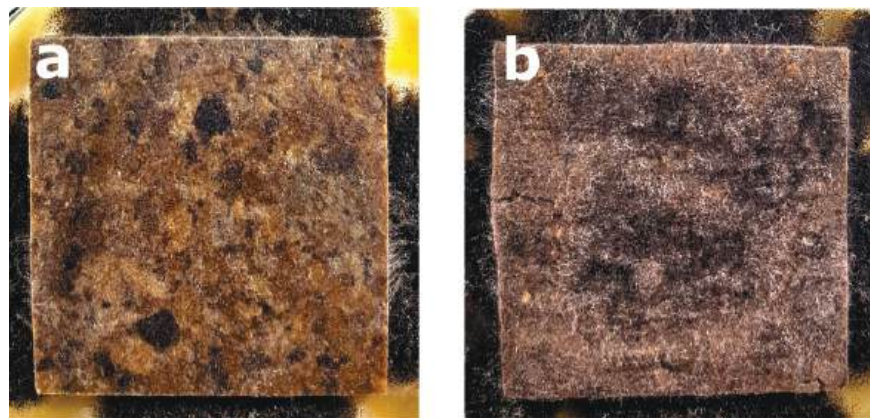
Figure 6. Example of mold growth (*Aspergillus niger* Tiegh) after 7 days of exposure of composite samples with small particle sawdust filler of 60%, based on a matrix: (**a**) HDPE; (**b**) PLA.
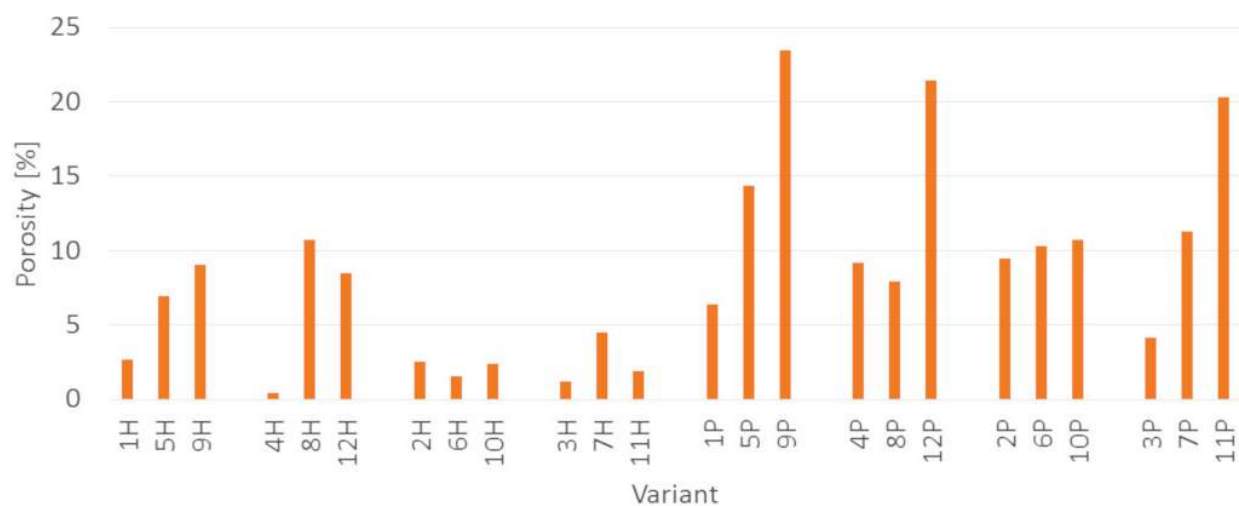
Figure 7. Porosity of the tested PLA and HDPE composites.
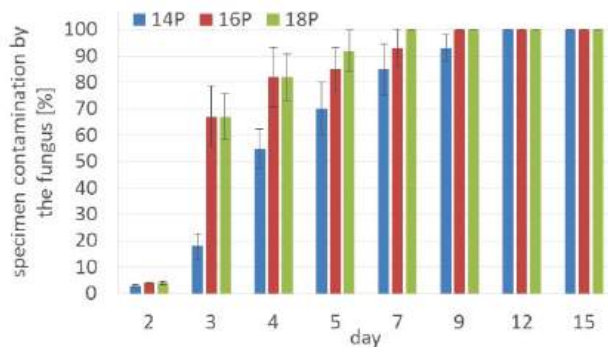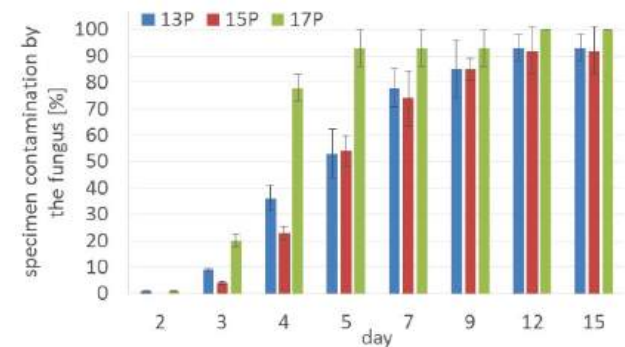
Figure 8. The rate of surface fouling by fungi *Aspergillus niger* Tiegh of PLA composites with CaO addition; (**a**) bark small particles; (**b**) sawdust large particles.
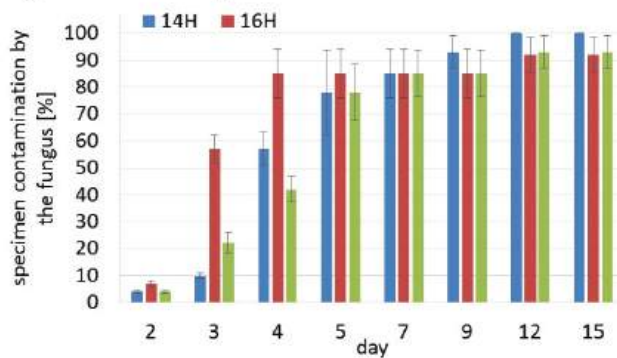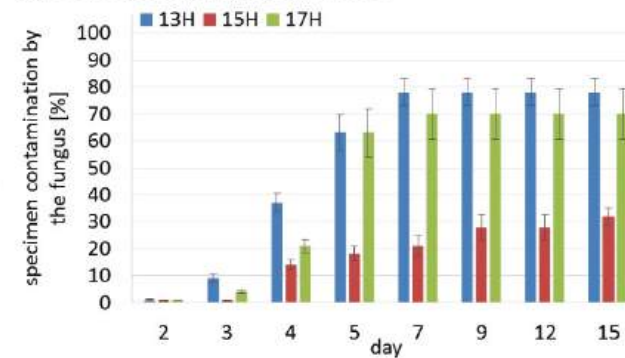
Figure 9. The rate of surface fouling by fungi *Aspergillus niger* Tiegh of HDPE composites with MAHPE addition; (**a**) bark small particles; (**b**) sawdust large particles.
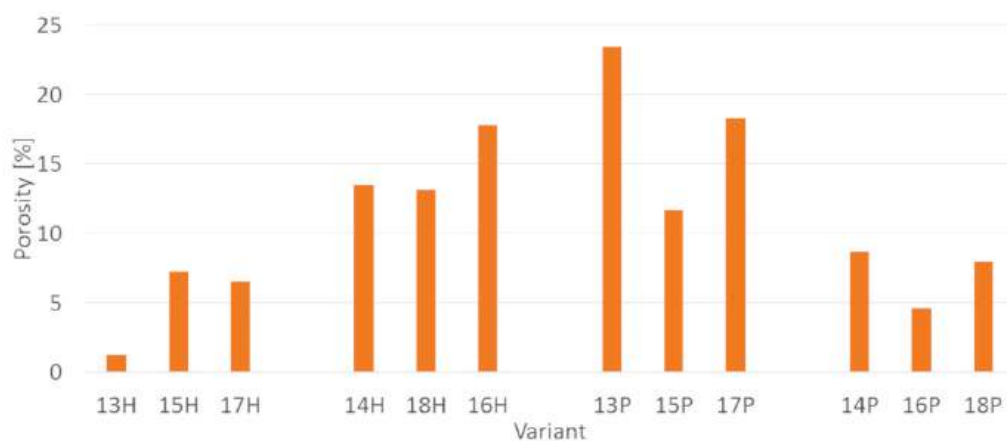
Figure 10. The porosity of the tested PLA and HDPE composites containing additives.

4. Discussion

The higher susceptibility to mold of PLA composites compared to HDPE composites is consistent with existing scientific literature. Zimmermann [37] reports that aliphatic polyesters, including PLA, are more susceptible to microbial degradation than non-hydrolyzable synthetic polymers, such as, inter alia, PE. Maeda et al. [38] showed that fungi of the genus Aspergillus had a hydrolyzing effect on PLA. Porosity, in turn, increases the availability of composite components for microbiological agents and thus increases their susceptibility to degradation [28].

In the case of WPC composites, the addition of additional substances (e.g., a compatibilizer) has a significant impact on their physical and mechanical properties [28]. Yeh et al. [39] revealed that the addition of a compatibilizer has a positive effect on reducing the degradation of WPC composites by fungi throughout improving the reduction of moisture penetration. In the present study, CaO was introduced as an additive—a moisture absorbing and biocidal agent to PLA composites [40], and the MAHPE was applied in HDPE composites [28].

Factors such as type of filler, its contribution and size of particles affected the mold growth regardless the type of matrix PLA or HDPE (Tables 3 and 4). The interaction between these factors is being significant. It is worth noting that this impact varies depending on the duration of the exposure to the mold. Schirp et al. [31], Kartal et al. [32], Feng et al. [33] reported that WPC with a higher content of larger size wood particles are more susceptible to the influence of mold fungi. Ref. [41] found that an increase in the thermoplastic content in the outer layers from 40% to 50% in particle-polymer boards elongates mold growth (Trichoderma virens) about 3.5 times.

Regardless of the matrix type (PLA or HDPE), bark-filled composites were more susceptible to mold. In relation to the tested materials, it is particularly visible in composites filled with large particles (10–35 mesh). This is probably due to the greater availability of large particles for microorganisms, while smaller particles (less than 10 mesh) are better surrounded by the polymer matrix and thus less accessible to fungi. The influence of the type of filler on WPC susceptibility to mold was also demonstrated by Xu et al. [42], Feng et al. [34] and Feng et al. [43], Valentín et al. [44] stated that pine bark can be an excellent source of nutrients for fungi. So et al. [45], in the study of litter, revealed that bark particles are more susceptible to mold growth than coniferous chips used under the same conditions. It is worth noting that the bark contains more extractives, and Hosseinaei et al. [46] found that reducing their content limits the susceptibility of WPC to mold growth.

Nevertheless of the growth rate results, it should be enhanced that mold fungi reduce the aesthetics of WPC products by changing their color and the surface decomposition of the wood substance [28]. Additionally, objects attacked by fungi have a detrimental effect on the health of humans and animals living in their vicinity [29,30].

5. Conclusions

1. PLA composites are characterized by a higher growth rate by *Aspergillus niger* Tiegh mold fungi compared to HDPE composites.
2. The type of filler (bark, sawdust) had a greater impact on fouling by mold fungi in the case of HDPE composites.
3. Composites filled with bark were characterized by a higher growth rate of mold fungi compared to composites filled with sawdust.
4. In the case of sawdust filler, composites filled with small particles revealed a higher fouling rate.
5. In the case of bark filler, PLA composites displayed a higher fouling rate when filled with large particles, while HDPE composites revealed higher fouling rate when filled with small particles.
6. The introduction of additional substances (CaO in PLA composites and MAHPE in HDPE composites) generally increased the rate of mold growth on the composites.

Institutional Review Board Statement: Not applicable.

Informed Consent Statement: Not applicable.

Data Availability Statement: The data presented in this study are available on request from the corresponding author.

Conflicts of Interest: The authors declare no conflict of interest.

References

1. Partanen, A.; Carus, M. Biocomposites, find the real alternative to plastic—An examination of biocomposites in the market. *Reinf. Plast.* **2019**, *63*, 317–321. [CrossRef]
2. Markarian, J. Biopolymers present new market opportunities for additives in packaging. *Plast. Addit. Compd.* **2008**, *10*, 22–25. [CrossRef]
3. Farah, S.; Anderson, D.G.; Langer, R. Physical and mechanical properties of PLA, and their functions in widespread applications—A comprehensive review. *Adv. Drug. Deliv. Rev.* **2016**, *107*, 367–392. [CrossRef] [PubMed]
4. Auras, R.; Harte, B.; Selke, S. An Overview of Polylactides as Packaging Materials. *Macromol. Biosci.* **2004**, *4*, 835–864. [CrossRef]
5. Pilla, S.; Gong, S.; O'Neill, E.; Yang, L.; Rowell, R.M. Polylactide-recycled wood fiber composites. *J. Appl. Polym. Sci.* **2009**, *111*, 37–47. [CrossRef]
6. Peltola, H.; Pääkkönen, E.; Jetsu, P.; Heinemann, S. Wood based PLA and PP composites: Effect of fibre type and matrix polymer on fibre morphology, dispersion and composite properties. *Compos. A Appl. Sci. Manuf.* **2014**, *61*, 13–22. [CrossRef]
7. Georgiopoulos, P.; Kontou, E.; Christopoulos, A. Short-term creep behavior of a biodegradable polymer reinforced with wood-fibers. *Compos. B Eng.* **2015**, *80*, 134–144. [CrossRef]
8. Andrzejewski, J.; Szostak, M.; Barczewski, M.; Łuczak, P. Cork-wood hybrid filler system for polypropylene and poly(lactic acid) based injection molded composites. Structure evaluation and mechanical performance. *Compos. B Eng.* **2019**, *163*, 655–668. [CrossRef]
9. Dalu, M.; Temiz, A.; Altuntaş, E.; Demirel, G.K.; Aslan, M. Characterization of tanalith E treated wood flour filled polylactic acid composites. *Polym. Test.* **2019**, *76*, 376–384. [CrossRef]
10. Kamau-Devers, K.; Kortum, Z.; Miller, S.A. Hydrothermal aging of bio-based poly (lactic acid) (PLA) wood polymer composites: Studies on sorption behavior, morphology, and heat conductance. *Constr. Build. Mater.* **2019**, *214*, 290–302. [CrossRef]
11. Ying-Chen, Z.; Hong-Yan, W.; Yi-Ping, Q. Morphology and properties of hybrid composites based on polypropylene/polylactic acid blend and bamboo fiber. *Bioresour. Technol.* **2010**, *101*, 7944–7950. [CrossRef]
12. Bledzki, A.K.; Jaszkiewicz, A.; Scherzer, D. Mechanical properties of PLA composites with man-made cellulose and abaca fibres. *Compos. A Appl. Sci. Manuf.* **2009**, *40*, 404–412. [CrossRef]
13. Petchwattana, N.; Covavisaruch, S. Mechanical and Morphological Properties of Wood Plastic Biocomposites Prepared from Toughened Poly(lactic acid) and Rubber Wood Sawdust (Hevea brasiliensis). *J. Bionic Eng.* **2014**, *11*, 630–637. [CrossRef]
14. Borysiuk, P.; Boruszewski, P.; Auriga, R.; Danecki, L.; Auriga, A.; Rybak, K.; Nowacka, M. Influence of a bark-filler on the properties of PLA biocomposites. *J. Mater. Sci.* **2021**, *56*, 9196–9208. [CrossRef]
15. Khavkine, M.; Kazayawoko, M.; Law, S.; Balatinecz, J.J. Durability of Wood Flour-Thermoplastic Composites under Extreme Environmental Conditions and Fungal Exposure. *Int. J. Polym. Mater.* **2000**, *46*, 255–269. [CrossRef]
16. Laks, P.E.; Richter, D.L.; Larkin, G.M. Biological deterioration of wood-base composite panels. *Wood Des. Focus* **2000**, *11*, 7–11.
17. Mankowski, M.; Morrell, J.J. Patterns of fungal attack in wood-plastic composites following exposure in a soil block test. *Wood Fiber Sci.* **2000**, *32*, 340–345.
18. Verhey, S.; Laks, P.; Richter, D. Laboratory decay resistance of woodfiber/thermoplastic composites. *Prod. J.* **2001**, *51*, 44–49.
19. Verhey, S.A.; Laks, P.E.; Richter, D.L.; Keranen, E.D.; Larkin, G.M. Use of field stakes to evaluate the decay resistance of woodfiber-thermoplastic composites. *Prod. J.* **2003**, *53*, 67–74.
20. Clemons, C.M.; Ibach, R.E. Application of laboratory fungal resistance tests to solid wood and wood-plastic composite. *Plast. Build. Constr.* **2002**, *27*, 7–14.
21. Pendleton, D.E.; Hoffard, T.A.; Adcock, T.; Woodward, B.; Wolcott, M.P. Durability of an extruded HDPE/wood composite. *Prod. J.* **2002**, *52*, 21–27.

22. Lopez, J.L.; Cooper, P.A.; Sain, M. Evaluation of Proposed Standard Test Method to Determine Decay Resistance of Natural Fiber Plastic Composites. *Prod. J.* **2005**, *55*, 95–99.
23. Schirp, A.; Wolcott, M.P. Influence of fungal decay and moisture absorption on mechanical properties of extruded wood-plastic composites. *Wood Fiber Sci.* **2005**, *37*, 643–652.
24. Verhey, S.A.; Laks, P.E. Wood particle size affects the decay resistance of woodfiber/thermoplastic composites. *Prod. J.* **2002**, *52*, 78–81.
25. Stark, N. Influence of moisture absorption on mechanical properties of wood flour-polypropylene composites. *J. Compos. Mater.* **2001**, *14*, 421–432. [CrossRef]
26. Clemons, C.M.; Ibach, R.E. Effects of processing method and moisture history on laboratory fungal resistance of wood-HDPE composites. *Prod. J.* **2004**, *54*, 50–57.
27. Wang, W.; Morrell, J.J. Water sorption characteristics of two wood-plastic composites. *For. Prod. J.* **2004**, *54*, 209–212.
28. Klysov, A.A. *Wood-Plastic Composites*; Wiley-Interscience: Hoboken, NJ, USA, 2007.
29. Jaakkola, M.S.; Quansah, R.; Hugg, T.T.; Heikkinen, S.A.; Jaakkola, J.J. Association of indoor dampness and molds with rhinitis risk: A systematic review and meta-analysis. *J. Allergy Clin. Immunol.* **2013**, *132*, 1099–1110.e18. [CrossRef] [PubMed]
30. Hernberg, S.; Sripaiboonkij, P.; Quansah, R.; Jaakkola, J.J.; Jaakkola, M.S. Indoor molds and lung function in healthy adults. *Respir. Med.* **2014**, *108*, 677–684. [CrossRef]
31. Schirp, A.; Ibach, R.E.; Pendleton, D.E.; Wolcott, M.P. Biological degradation of Wood-Plastic Composites (WPC) and strategies for improving the resistance of WPC against biological decay. In *Development of Commercial Wood Preservatives*; ACS Symposium Series; American Chemical Society: Washington, DC, USA, 2008; Volume 982, pp. 480–507.
32. Kartal, S.N.; Aysal, S.; Terzi, E.; Yilgör, N.; Yoshimura, T.; Tsunoda, K. Wood and Bamboo-PP Composites: Fungal and Termite Resistance, Water Absorption, and FT-IR Analyses. *BioResources* **2013**, *8*, 1222–1244. [CrossRef]
33. Feng, J.; Shi, Q.; Chen, Y.; Huang, X. Mold Resistance and Water Absorption of Wood/HDPE and Bamboo/HDPE Composites. *J. Appl. Sci.* **2014**, *14*, 776–783. [CrossRef]
34. Feng, J.; Zhang, H.; He, H.; Huang, X.; Shi, Q. Effects of fungicides on mold resistance and mechanical properties of wood and bamboo flour/high-density polyethylene composites. *BioResources* **2016**, *11*, 4069–4085. [CrossRef]
35. Schindelin, J.; Arganda-Carreras, I.; Frise, E.; Kaynig, V.; Longair, M.; Pietzsch, T.; Preibisch, S.; Rueden, C.; Saalfeld, S.; Schmid, B.; et al. Fiji: An open-source platform for biological-image analysis. *Nat. Methods* **2012**, *9*, 676–682. [CrossRef]
36. Tinevez, J.Y.; Perry, N.; Schindelin, J.; Hoopes, G.M.; Reynolds, G.D.; Laplantine, E.; Bednarek, S.Y.; Shorte, S.L.; Eliceiri, K.W. TrackMate: An open and extensible platform for single-particle tracking. *Methods* **2017**, *115*, 80–90. [CrossRef] [PubMed]
37. Zimmermann, W. Degradation of Plastics by Fungi. In *Encyclopedia of Mycology*; Elsevier: Amsterdam, The Netherlands, 2021; pp. 650–661.
38. Maeda, H.; Yamagata, Y.; Abe, K.; Hasegawa, F.; Machida, M.; Ishioka, R.; Gomi, K.; Nakajima, T. Purification and characterization of a biodegradable plastic-degrading enzyme from Aspergillus oryzae. *Appl. Microbiol. Biotechnol.* **2005**, *67*, 778–788. [CrossRef] [PubMed]
39. Yeh, S.-K.; Hu, C.-R.; Rizkiana, M.B.; Kuo, C.-H. Effect of fiber size, cyclic moisture absorption and fungal decay on the durability of natural fiber composites. *Constr. Build. Mater.* **2021**, *286*, 122819. [CrossRef]
40. European Commission (EC). Commission Delegated Regulation (EU) No 1062/2014 of 4 August 2014 on the Work Programme for the Systematic Examination of All Existing Active Substances Contained in Biocidal Products Referred to in Regulation (EU) No 528/2012 of the European Parliament and of the Council Text. *Off. J. Eur. Union* **2014**, *294*, 20–30.
41. Borysiuk, P.; Wikowski, J.; Krajewski, K.; Auriga, R.; Skomorucha, A.; Auriga, A. Selected properties of flat-pressed wood-polymer composites for high humidity conditions. *BioResources* **2020**, *15*, 5141–5155. [CrossRef]
42. Xu, K.; Feng, J.; Zhong, T.; Zheng, Z.; Chen, T. Effects of volatile chemical components of wood species on mould growth susceptibility and termite attack resistance of wood plastic composites. *Int. Biodeterior. Biodegrad.* **2015**, *100*, 106–115. [CrossRef]
43. Feng, J.; Dong, P.; Li, R.; Li, C.; Xie, X.; Shi, Q. Effects of wood fiber properties on mold resistance of wood polypropylene composites. *Int. Biodeterior. Biodegrad.* **2019**, *140*, 152–159. [CrossRef]
44. Valentín, L.; Kluczek-Turpeinen, B.; Willför, S.; Hemming, J.; Hatakka, A.; Steffen, K.; Tuomela, M. Scots pine (Pinus sylvestris) bark composition and degradation by fungi: Potential substrate for bioremediation. *Bioresour. Technol.* **2010**, *101*, 2203–2209. [CrossRef] [PubMed]
45. So, D.T.; Dick, J.W.; Holleman, K.A.; Labosky, P. Mold Spore Populations in Bark Residues Used as Broiler Litter. *Poult. Sci.* **1978**, *57*, 870–874. [CrossRef]
46. Hosseinaei, O.; Wang, S.; Taylor, A.M.; Kim, J.-W. Effect of hemicellulose extraction on water absorption and mold susceptibility of wood–plastic composites. *Int. Biodeterior. Biodegrad.* **2012**, *71*, 29–35. [CrossRef]

Assessment of Extremely Cold Subarctic Climate Environment Destruction of the Basalt Fiber Reinforced Epoxy (BFRE) Rebar Using Its Moisture Uptake Kinetics

Anatoly K. Kychkin [1],*[iD]**, Anna A. Gavrilieva** [1][iD]**, Alina A. Vasilieva** [2]**, Aisen A. Kychkin** [2][iD]**, Mikhail P. Lebedev** [2]
and Anastasia V. Sivtseva [1]

1 V.P. Larionov Institute of Physical and Technical Problems of the North Siberian Branch Russian Academy of Sciences, 1 Oktyabrskaya Street, Yakutsk 677980, Russia; gav-ann@yandex.ru (A.A.G.); sianva@yandex.ru (A.V.S.)
2 Federal Research Center, The Yakut Scientific Centre of the Siberian Branch of the Russian Academy of Sciences, 2 Petrovskogo Str., Yakutsk 677000, Russia; kiir@mail.ru (A.A.V.); icen.kychkin@mail.ru (A.A.K.); m.p.lebedev@mail.ru (M.P.L.)
* Correspondence: kychkinplasma@mail.ru

Abstract: A quite simple method is proposed for the assessment of extremely cold subarctic climate environment destruction of the basalt fiber reinforced epoxy (BFRE) rebar. The method involves the comparison of experimentally obtained long-term moisture uptake kinetic curves of unexposed and exposed BFRP rebars. A moisture uptake test was carried out at the temperature of 60 °C and relative humidity of 98 ± 2% for 306 days. The plasticization can be neglected because of low-level moisture saturation (<0.41% wt.); the swelling and structural relaxation of the polymer network can be neglected due to the high fiber content of BFRP rebar; moisture diffusion into the basalt fibers can be neglected since it is a much lesser amount than in the epoxy binder. These assumptions made it possible to build a three-stage diffusion model. It is observed that an increase in the density of defects with an increase in the diameter of the BFRP rebar is the result of the technology of manufacturing a periodic profile. The diffusion coefficient of the BFRP rebar with a 6, 10, or 18 mm diameter increased at an average of 82.7%, 56.7%, and 30%, respectively, after exposure to the climate of Yakutsk during 28 months, whereas it was known that the strength indicators had been increased.

Keywords: destruction; cold climate; epoxy binder; basalt fiber; BFRP; rebar; moisture uptake; diffusion coefficient; Fick's diffusion; PCM

1. Introduction

The subject of the study is inextricably linked with the actual problem of ensuring high resistance of the strength properties of polymer composites to aggressive environments [1–10], including the forceful impacts of subarctic climate on the composites [10–12]. In this area, examples have been identified [2,13,14], showing that some mechanical indicators of polymer composite materials after an open-air exposure in cold and extremely cold subarctic climate deteriorated comparably or even more significantly than in warm-summer humid continental climate. In [12], it is shown that the indicators' strength of basalt fiber reinforced polymer (BFRP) rebar, which has been under the influence of destructive processes of extremely cold subarctic climate for several years, has improved. Thus, it is necessary to find and confirm more sensitive indicators to the initial destruction of the BFRP rebar.

It was found that for carbon fiber reinforced plastic, fiberglass, and other plastics with an epoxy binder, one of such promising indicators is the diffusion coefficient during desorption of moisture [15–17]. In this case, desorption was carried out after the first equilibrium moisture content of the plastic. Moreover, only the binder's abnormal effects of moisture absorption (plasticization, swelling, hydrolysis, additional hardening, structural

relaxation, pore formation, microcracking) were taken into account. However, usually the initial free volume content is unknown; polymer composite materials (PCM) can contain defects and capillaries in the interface fiber/binder, depending on the initial composition, reinforcement design, manufacturing technology, and environmental conditions. This type of free volume can be the generating part of the moisture content of the PCM [18–21]. For a unidirectional PCM, the moisture uptake by capillaries can be distinguished by considering the moisture uptake by the samples of different heights. Thus, for an adequate quantitative evaluation of the free volume in unidirectional PCM, it is necessary that the samples with different heights were exposed to moisture for a long time.

Thus, this work proposes a quite simple method for evaluating extremely cold subarctic climate environment destructive processes of a basalt fiber reinforced polymer rebar. The way compares the experimentally obtained long-term moisture uptake kinetic of unexposed BFRP rebar with the kinetic of open-air exposed BFRP rebar. A constructive comparison should be achieved by introducing the minimum number of parameters needed to approximate the BFRP rebar moisture uptake. It should be noted that the quantitative control of free volume in a BFRP rebar forms the basis for reliable prediction of the rebar mechanical properties in the long term [19,22].

2. Materials and Methods

2.1. Raw Materials

The reinforcing member was RBN 13-2400-4S basalt roving manufactured by "TBM" LLC (Yakutsk, Russia) in Yakutsk (fiber diameter of 13 microns). The nominal linear density of roving was 2400 tex. Breaking load of roving was not less than 320 mN/tex. The binder was an epoxy resin (ED-22) (Kukdo chemical Co.LTD, Seoul, Korea), which was "hot" cured with a suitable amount of hardener in the presence of accelerator. The hardener isomethyltetrahydrophthalic anhydride (iso-MTHPA) (JSC Sterlitamak Petrochemical Plant, Sterlitamak, Russia) was chosen because the systems cured with it have high mechanical properties, excellent waterproof, good electrical properties, and resistance to climatic impact. 2,4,6-tris(dimethylaminomethyl)phenol (UP 606/2) accelerator was chosen due to its high catalytic activity.

2.2. Manufacture of Composite and Specimen Preparation

The BFRP rebar was manufactured following Technical Specifications 2296-001-86166796-2013 "Non-metallic composite armature made from basalt plastic." BFRP rebars were prepared using the pultrusion molding process. Continuous basalt rovings are impregnated with an epoxy binder; some of the impregnated rovings were pulled through the central spinneret molding an inner rod, then this rod was cured (8 kgF); the remainder of the impregnated rovings are pulled through the peripheral spinneret molding an outer layer and fixed to the cured inner rod. Finally, the outer layer is wrapped by polyamide thread, molding a periodic profile of the rebar.

The profile and key of the size of rebar components are shown in Figure 1. The rebar with a diameter of d means that a diameter of the inner rod is d, above which a step of l wavy protrusions of length n rise, forming the outer diameter of d1 and the polyamide thread with a length of d (Table 1). The object of research is the BFRP rebar with diameters of 6, 10, and 18 mm. Test specimens of 5, 10, 30, 50, 70, and 100 mm height were cut, and cross-sections were polished from each BFRP rebar.
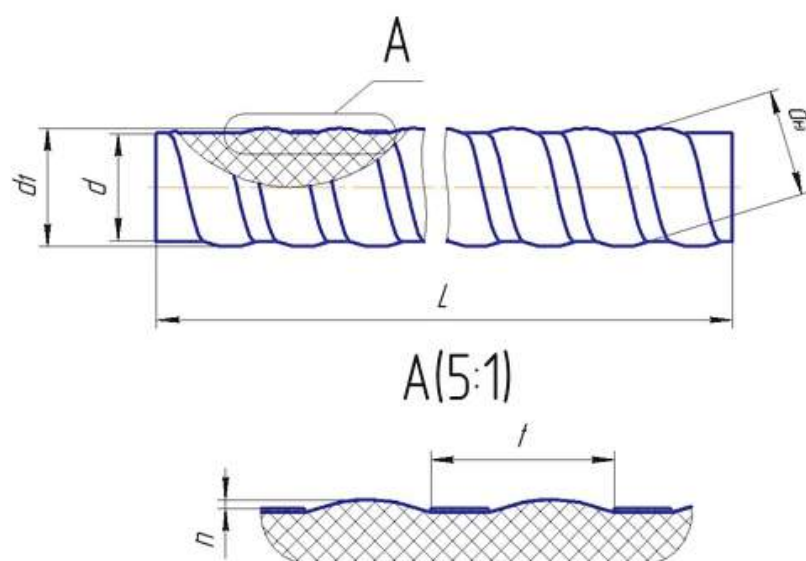
Figure 1. The keys of periodic rebar profile.

Table 1. Technological modes of forming a periodic profile of rebar.

d (mm)	d1 (mm)	d(mm)	n (mm)	l (mm)	Fibres Mass Share (%)
6	7	6.5	0.5	5–7	77
10	12	10.5	1	7–9	78
18	23	18.4	1.5	8–12	70

2.3. Climatic Aging of BFRP Rebar

The FBRP rebars were exposed to the extremely cold subarctic climate in Yakutsk for 28 months (Figure 2). The minimum temperature was registered as minus 64.4 °C. Per year the maximum temperature difference reaches 100 °C, average wind speed is 1.8 m/s, average relative humidity is 68%, 237 mm of precipitation falls, the solar radiation is 3680 MJ/m^2.
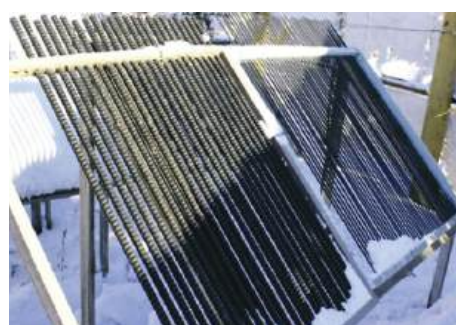
(**a**) (**b**)

Figure 2. Open stands with BFRP rebar in Yakutsk in winter (**a**), and in summer (**b**).

2.4. Moister Absorption Tests and Kinetic Moisture Uptake Profile

The test method for moisture absorption of BFRP rebar was constituted with the recommendations of ASTM [23]. The test and preconditioning chamber was a Binder ED53 oven (Germany) over silica gel(BINDER GmbH, Tuttlingen, Germany). Preconditioning of the sample was for 14 days prior to its constant weight. The test relative humidity was 98 ± 2%. The samples were placed over distilled water in a desiccator 2-240 TY 25.11.1024-88 (JSC "Khimreaktivsnab", UFA, Russia). The measurement time interval was one day.

The test balance was an Ohaus analytical balance (Ohaus, NJ, USA) with measurement error 0.1 mg and range 0.01–210 g, accuracy class I. The percent change in mass determined the kinetic moisture uptake profile of the sample

$$M_t(\%) = \frac{M_t}{M_0} \cdot 100\% = \frac{M - M_0}{M_0} \cdot 100\%, \tag{1}$$

where $M_t(\%)$ was the weight gain, M_t was the amount of diffusing substance that got into the cylinder on time t, M was the weight of sample at time t, and M_0 was the initial sample weight after drying at $t = 0$. Three samples were tested for each rebar mass, and the average moisture uptake data with standard deviation were reported.

2.5. Fickian Diffusion Model for a Long Cylinder

For a homogeneous continuous cylinder with radius R, in which diffusion through the butts can be neglected, the diffusion is described by the Fick equation [24]

$$\frac{\partial C}{\partial t} = \frac{1}{r}\frac{\partial}{\partial r}\left(rD\frac{\partial C}{\partial r}\right),$$

where C is a moisture concentration, r is a radial coordinate and D is the diffusion coefficient. Let the constant concentration be adhered to the cylinder boundary $C(R, t) = \text{const}$. There is no penetrator in the sample at the initial time $C(R, 0) = 0$ $(0 < r < R)$. If M_∞ is the corresponding quantity after the infinite time (saturated or equilibrium), then according to [25]

$$M_t = M_\infty\left(1 - \frac{4}{R^2}\right)\sum_{n=1}^{\infty}\frac{\exp\left(-\alpha_n^2 Dt\right)}{\alpha_n^2}, \tag{2}$$

provided the α_n are roots of $J_0(R\alpha_n) = 0$, where $J_0(r)$ is the Bessel function of the first kind of order zero.

2.6. Macroanalysis of Material Structure

Macroanalysis of samples was done using Nikon Eclips LV100 (Nilon, Tokyo, Japan) at magnifications of 30; 50; 100; and 500.

3. Results and Discussions
3.1. Experimental Moisture Uptake Kinetics (a Three-Stage Diffusion)

Moisture uptake kinetics were calculated as the percent change in mass (1). The moisture uptake kinetics are presented in Figure 3 for the rebars were stored in the warehouse (unexposed rebars). The kinetics are sorted by the diameter of the rebar. The results show differences in moisture uptake behavior between the rebar with a diameter of 6 mm and the rebar with a 10, 18 mm diameter. In contrast to the kinetics of moisture uptake in the rebars with a diameter of 6 mm, the kinetics of moisture uptake in the rebars with a 10, 18 mm diameter during the period of moisture exposure represents the circumstance of three-stage diffusion (see Figure 3c,d). At the first stage, there is a quasi-equilibrium $(M_{1\infty}, t_1)$; at the second stage $(M_{2\infty}, t_2)$, there is a linear increase in moisture absorption, and at the third stage, there is a sharp jump in sample mass or the unchanging of the sample mass. This observation of three-stage diffusion indicates that a time-variable diffusion model is most suitable for describing moisture diffusion of unexposed BFRP rebars with a 10 or 18 mm diameter [26]. However, this time-variable character is not suitable for a quick and adequate comparison of kinetic curves.
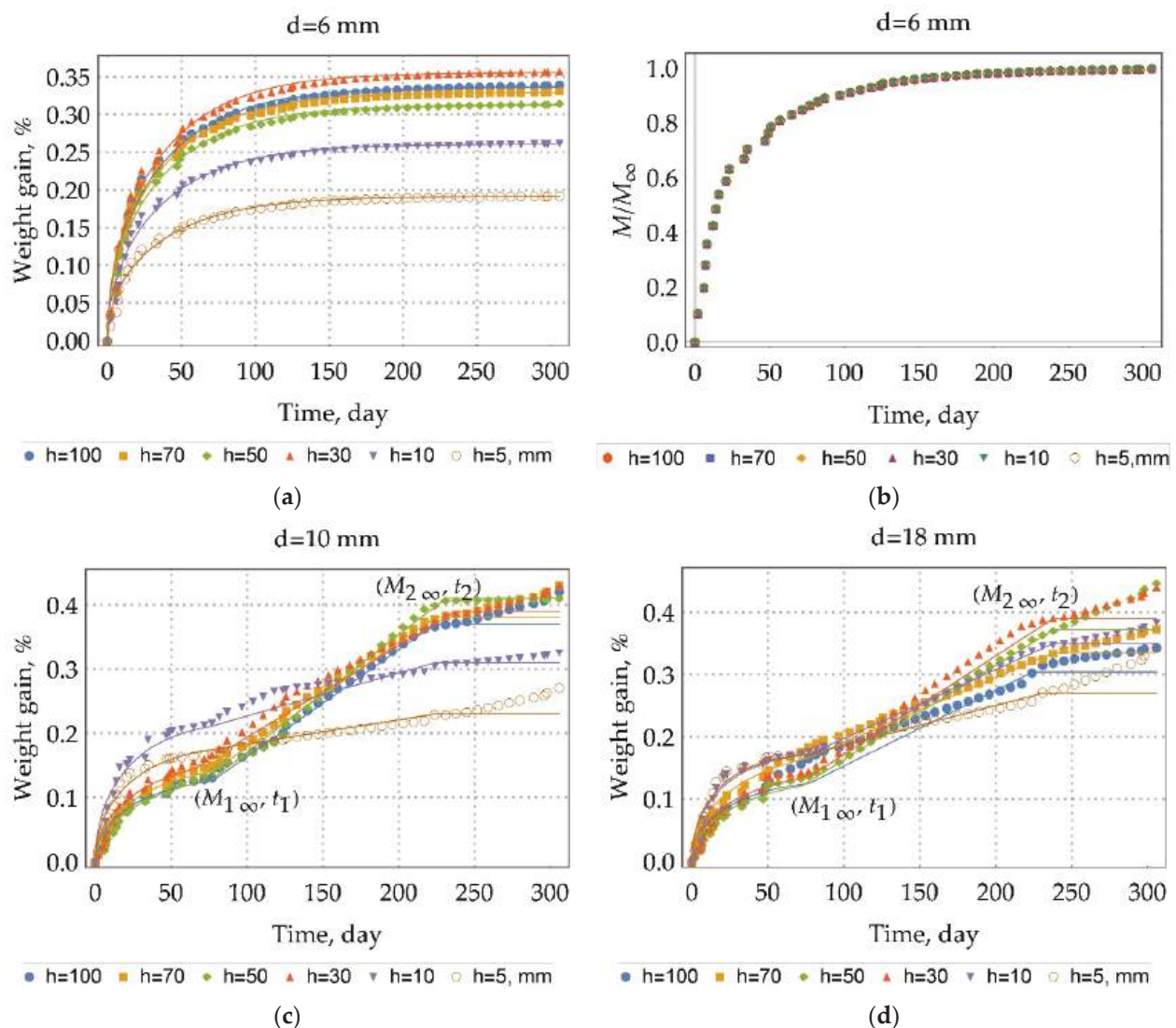
Figure 3. Moisture uptake kinetics (60 °C/98%RH) for the samples of unexposed BFRP rebars with a height (h, mm) and:
(**a**) with a diameter of 6 mm and; (**b**) with a diameter of 6 mm related to M_∞; (**c**) with a diameter of 10 mm; (**d**) with a
diameter of 18 mm. The periodic profile of the rebars is a cause of the first and second stages of diffusion.

The moisture uptake kinetics are presented in Figures 4–6 for the samples of the
DFRP rebars that were exposed in an extremely cold subarctic climate of Yakutsk for
28 months. It can also be seen from these curves of kinetics that there is three-stage
diffusion. At the first stage, there is a quasi-equilibrium; at the second stage, there is a
linear increase in moisture absorption; and at the third stage, there is a linear decrease in
mass. Additionally, this observation of three-stage diffusion indicates that a time-variable
diffusion model is the most fitted for describing moisture diffusion in these exposed
rebars [26]. However, this time-variable character is not suitable for a quick and adequate
comparison of kinetic curves.
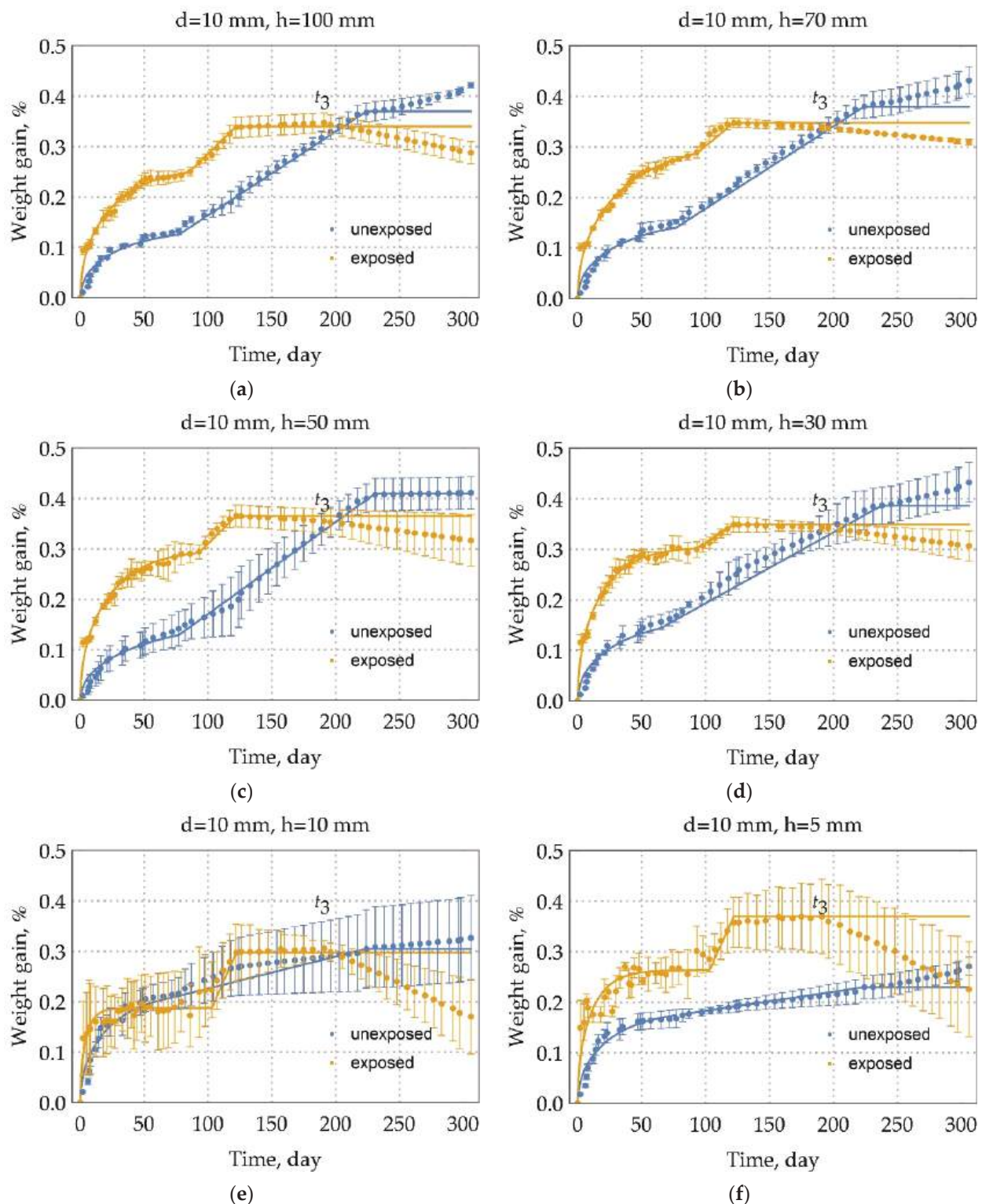
Figure 4. Moisture uptake kinetics (60 °C/98%RH) for the samples of unexposed BFRP rebars and the samples of exposed BFRP rebars in an extremely cold subarctic climate of Yakutsk for 28 months with height (h, mm) and with the diameter of 10 mm. (**a**) 100 mm height sample; (**b**) 70 mm height sample; (**c**) 50 mm height sample; (**d**) 30 mm height sample; (**e**) 10 mm height sample; (**f**) 5 mm height sample. Moisture uptake of the exposed rebars is the three-stage diffusion.
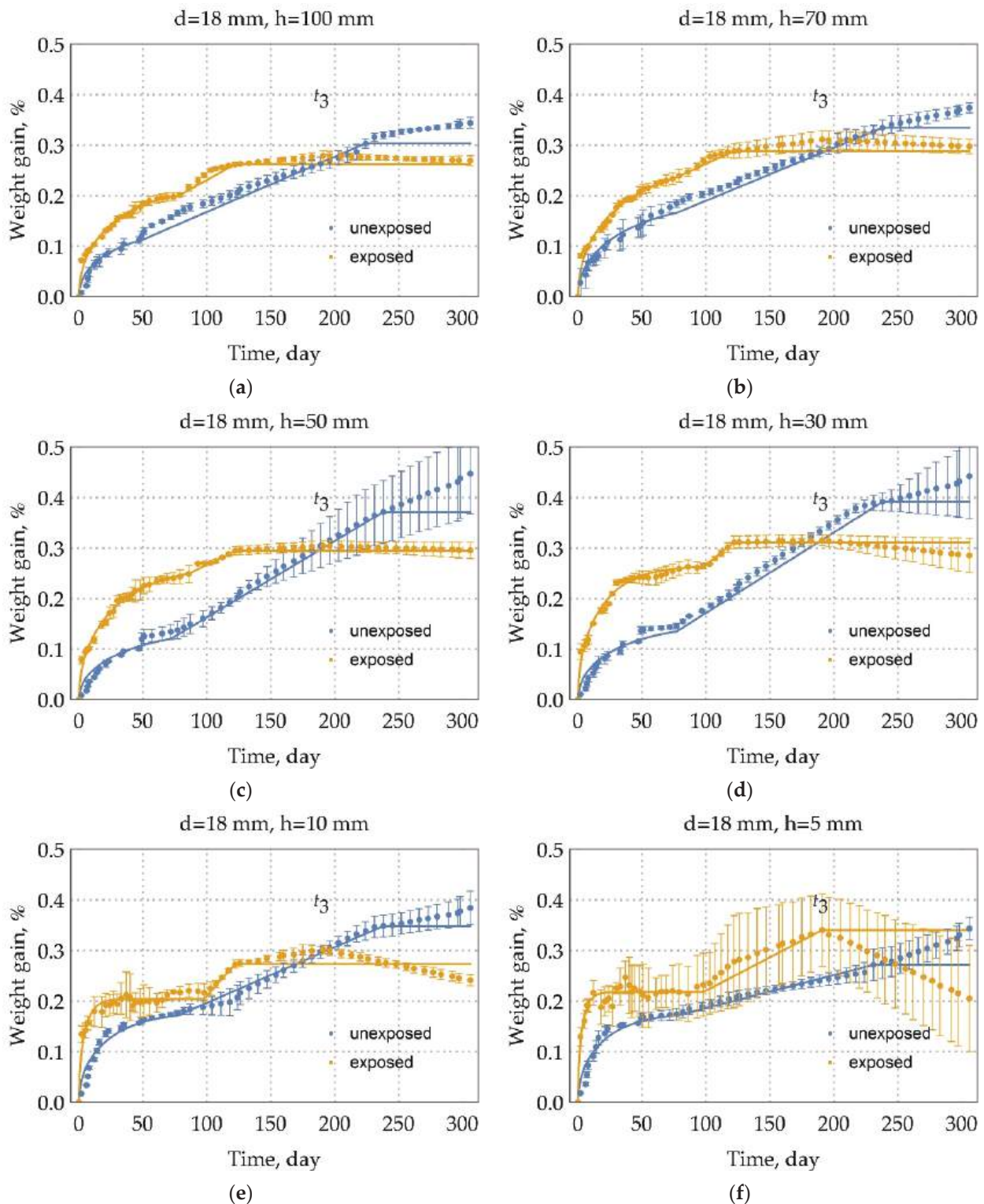
Figure 5. Moisture uptake kinetics (60 °C/98%RH) for the samples of unexposed BFRP rebars and the samples of exposed BFRP rebars in an extremely cold subarctic climate of Yakutsk for 28 months with height (h, mm) and with the diameter of 18 mm. (**a**) 100 mm height sample; (**b**) 70 mm height sample; (**c**) 50 mm height sample; (**d**) 30 mm height sample; (**e**) 10 mm height sample; (**f**) 5 mm height sample. Moisture uptake of the exposed rebars is the three-stage diffusion.
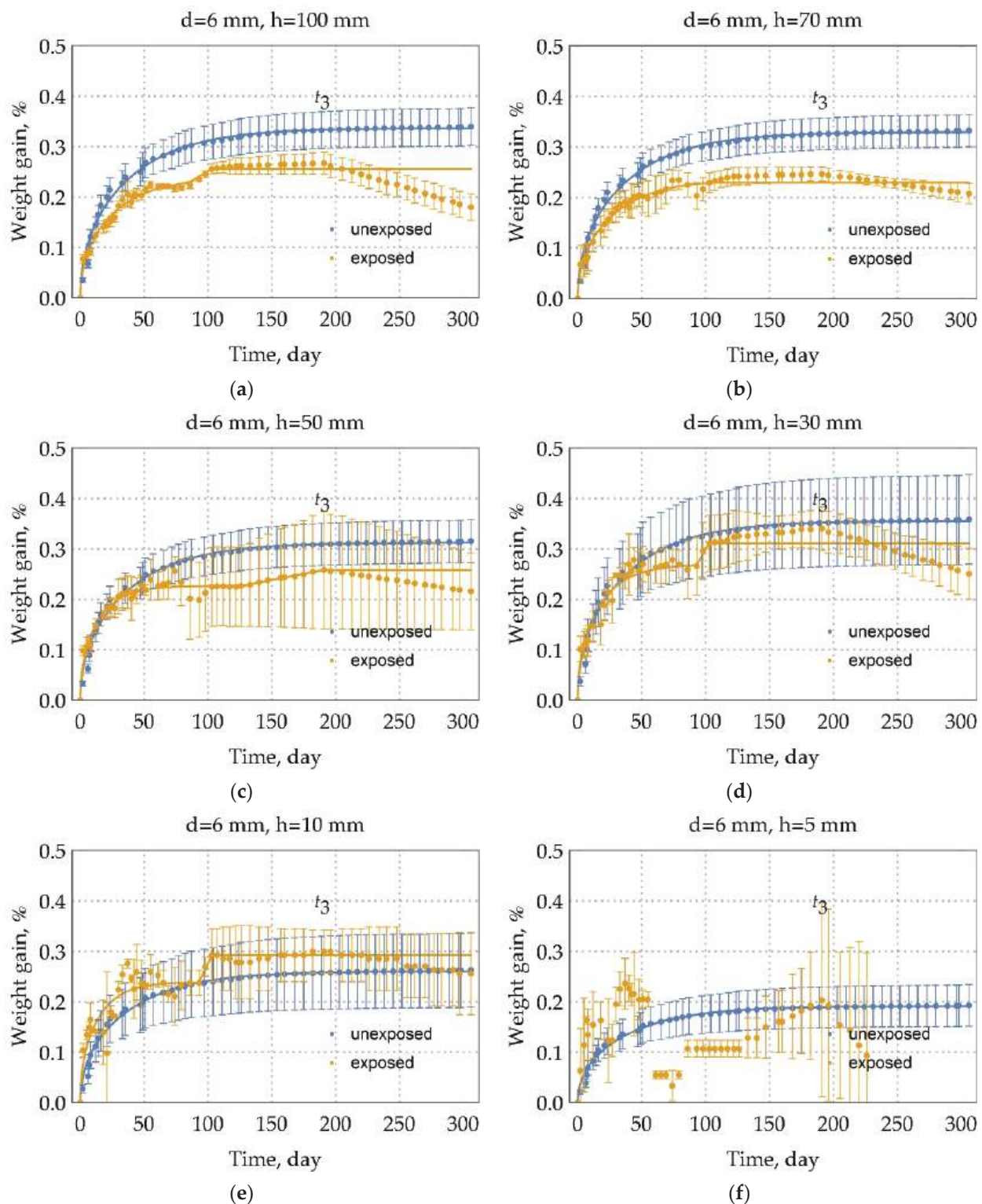
Figure 6. Moisture uptake kinetics (60 °C/98%RH) for the samples of unexposed BFRP rebars and the samples of exposed BFRP rebars in extremely cold subarctic climate of Yakutsk for 28 months with height (h, mm) and with the diameter of 6 mm. (**a**) 100 mm height sample; (**b**) 70 mm height sample; (**c**) 50 mm height sample; (**d**) 30 mm height sample; (**e**) 10 mm height sample; (**f**) 5 mm height sample Moisture uptake of the exposed rebars is the three-stage diffusion.

3.2. Approximation of Moisture Uptake Kinetics

As one could see from Figure 3b value M/M_∞ does not depend on the height of the sample, so the Fickian model could predict the experimental behavior of the test unexposed d6 rebars within the test period very well. To determine approximation parameters: the diffusion coefficient D and the equilibrium moisture uptake M_∞, the least-squares fitting technique was implemented. In this technique, the sum of the square of the offsets of the experimental weight gain from the calculated one

$$(\Delta M)^2 \equiv \sum_{n=1}^{N} \left(M_{t,n}^{\exp}(\%) - M_{t,n}^{cal}(\%) \right)^2 \to \min,$$

was minimized by approximation parameters were varied, using for Fickian model, $M_{t,n}^{\exp}$ was the nth experimental data of the weight gain at the time t, $M_{t,n}^{cal}(\%)$ was determined by Equation (2). Here, N is the aggregate number of the experimental points. The approximated D and $M_\infty(\%)$ are taken as the diffusion coefficient and the saturated moisture content (%) of a sample and listed in Table 2. Additionally, listed in Table 2 are the coefficient of determination ($R2$) values:

$$R2 = 1 - \frac{(\Delta M)^2}{\sum\limits_{n=1}^{N} \left(M_{t,n}^{\exp} \right)^2 - \sum\limits_{n=1}^{N} M_{t,n}^{\exp}/N}, \tag{3}$$

Table 2. Adequacy and parameters of the three-stage diffusion model of unexposed BFRP rebar.

A Diameter	A Height, mm	$M_{1\infty}(\%)$	$D\cdot10^6$, cm^2/Day	$\frac{D}{R^2}\cdot10^3$, 1/Day	t_1, Day	t_2, day	$M_{2\infty}(\%)$	t_3, day	R2 from Equation (3)
	100	0.34	3.49	3.88	-	-	-	-	0.94
	70	0.33	3.49	3.88	-	-	-	-	0.94
6 mm	50	0.31	3.49	3.88	-	-	-	-	0.94
	30	0.36	3.49	3.88	-	-	-	-	0.93
	10	0.26	3.49	3.88	-	-	-	-	0.95
	5	0.19	3.49	3.88	-	-	-	-	0.96
	100	0.14	11.87	4.75	77	224	0.37	224	0.95
	70	0.16	9.84	3.94	77	224	0.38	224	0.94
10 mm	50	0.16	7.20	2.88	77	231	0.41	231	0.95
	30	0.17	10.35	4.14	65	238	0.39	238	0.94
	10	0.22	14.47	5.79	72	224	0.31	224	0.93
	5	0.19	13.79	5.52	77	224	0.23	224	0.94
	100	0.13	40.66	5.02	65	224	0.30	224	0.95
	70	0.19	29.73	3.67	77	238	0.33	238	0.95
18 mm	50	0.14	30.12	3.72	77	238	0.37	238	0.94
	30	0.15	34.39	4.25	77	238	0.39	238	0.94
	10	0.18	50.08	6.18	77	238	0.35	238	0.94
	5	0.18	57.05	7.04	77	231	0.27	231	0.94

From Equation (3), we assess the proportion of the experimental data described by the approximation. If $R2 = 1$ in Equation (3), the model is a complete description of the experimental data. The values D, $M_\infty(\%)$ and $R2$ were calculated using Wolfram Cloud Basic (Wolfram Research, Illinois, United States). The calculated values of the coefficient of determination (in Table 2) confirm our suggestion that the Fick model describes moisture diffusion in the unexposed BFRP rebars with a diameter of 6 mm quite well conditions.

Furthermore, an analysis of the rebar structure showed that rovings are distributed evenly over its cross section, and the degree of fiber filling is high, about 79% wt. (see Table 1), as illustrated in Figure 7. An increase in sample volume due to swelling and structural relaxation of the polymer network can be neglected due to high fiber content, since the resilience of thin basalt fibers is included in counteracting the swelling and structural relaxation. Thus, the first two stages of uptake are not explained by the typical

two-stage Flory [27], Bagley and Long [28], and Newns [29] for glassy polymer systems and other theories arising from them. Moreover, this is not observed in the rebar with a diameter of 6 mm (see Figure 3a). The moisture uptake by a basalt fiber can be neglected since the moisture saturation content of the basalt fiber is much less than the moisture saturation content of the epoxy binder.
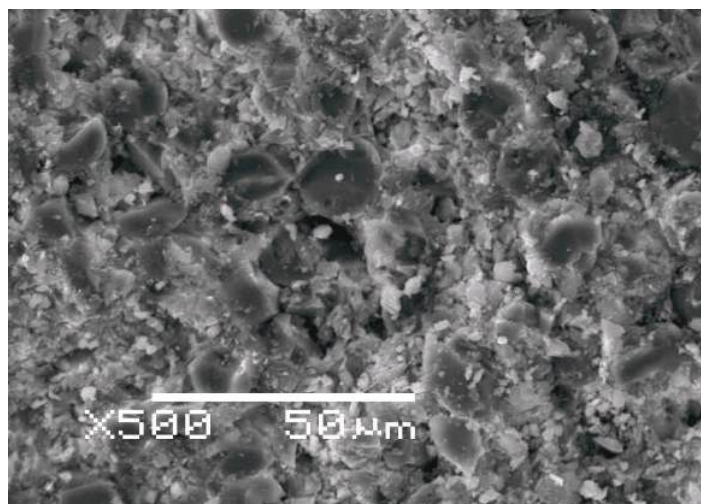
Figure 7. The cross-section of the BFRP rebar. A high degree of fiber filling can be observed.

The mechanism of the second stage can be clearly distinguished by considering the change in the kinetic curves with a height and a diameter in Figure 3c,d. It is known that microchannels occur mainly at fiber/matrix interfaces. The outer layer of the rebar is adjusted to the inner one to create a periodic profile (see Section 2.2. Composite specimen preparation and characterization), creating defects and microchannels. Clearly, with an increase in height, the volume and density of such defects and microchannels increase. In Figure 3c there is the increase of gain $(M_{2\infty} - M_{1\infty})$ with a height increase. The pre-existing quasi-equilibrium suggests that there is some barrier. After overcoming the barrier, the second stage begins. The second stage is linear. The second stage for h = 50 mm sample ends with a complete stop of weight gain. Figure 3d shows the same behavior, but the second stage is slightly smeared because, with an increase in diameter, the volume and density of defects increase according to a periodic profile's manufacture (Figure 8). All this fact suggests that, at first, the rebar's mesopores, micropores, and microchannels are filled by a simple diffusion mechanism through polymer nanopores (the first stage), and then they are filled by capillary condensation of moisture (the second stage). The simple diffusion mechanism of the first stage suggests that the Fick model can be applied (2). Moreover, according to the current view [30], for all fiber-reinforced polymer composites, the first phase of moisture uptake proceeds by simple diffusion according to the Fickian model.

The mechanism of the third stage can be explained by hydrolysis of the epoxy binder. The moisture breaks a polymeric chain under long-term exposure to thermal and humidity. Two phenomena happen simultaneously: (a) the weight gain due to water uptake in the voids constructed by this degradation and cracking of the binder, and (b) the weight loss due to hydrolysis and subsequent binder spalling [31,32]. The different rates of weight gain and weight jump in the third stage suggest the predominance of the mechanism (a) for the unexposed BFRP rebar with a diameter of 10, 18 mm (Figure 3b,c).

(a)   **(b)**
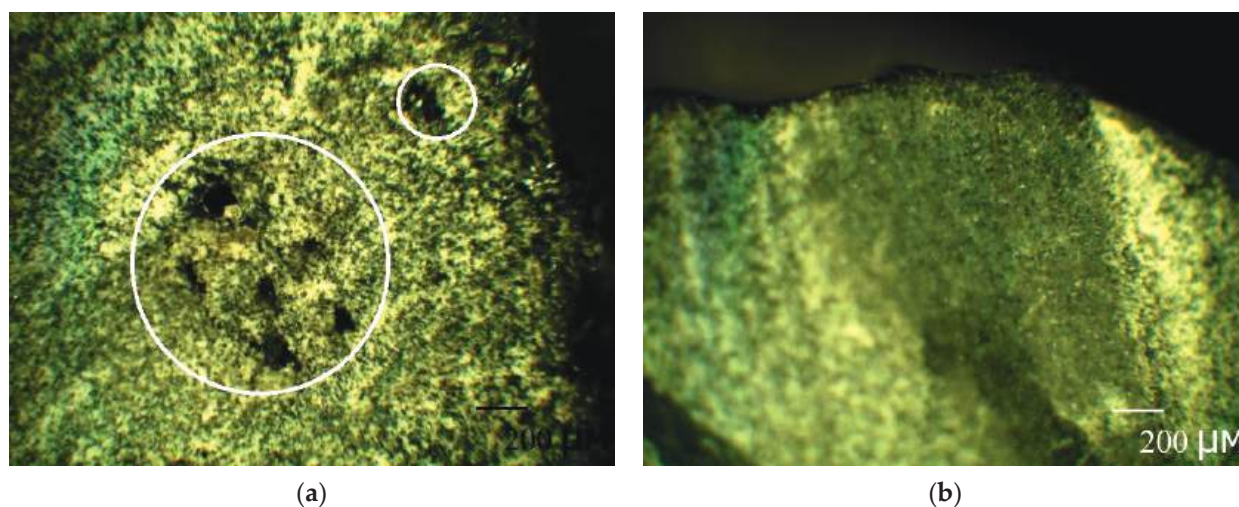
Figure 8. Pictures of the cross-section of unexposed BFRP rebar with a diameter: (**a**) 18 mm and (**b**) 8 mm exposed sample. With an increase in the rebar diameter defects can be observed.

Thus, we approximate the first stage by the Fick model $(M_{1\infty}(\%), D)$ (2), the second stage by linear growth from point $(M_{1\infty}(\%), t_1)$ to point $(M_{2\infty}(\%), t_2)$. The value $M_{2\infty}$ will be considered as the moisture saturation content, which is responsible for the free volume in the rebar, since the third stage describes the degradation of rebar because of exposure to moisture. The modulated parameters and the adequacy of the three-stage diffusion model of the unexposed BFRP rebar are shown in Table 2.

In Figure 3, the approximation of the experimental data by three-stage diffusion (Table 2) is indicated by solid lines. The analysis of Table 2 shows that the model we constructed adequately describes moisture absorption by the unexposed BFRP rebar; the value of a coefficient of determination (3) is not less than 0.93. It takes 77 days to start the second stage. The maximum moisture content is 0.41%. The low value of the moisture content indicates that the plasticization can be neglected. The average weight gain of long (h = 30, 50, 70, 100 mm) rebar with a 10 mm diameter is 0.23%, with an 18 mm diameter is 0.20% at the second stage. Moreover, the second stage with a 6 mm diameter is absent. According to the mechanism of the second stage, it can be suggested that the unexposed BFRP rebar with a 6 mm diameter has an excellent adhesion between the fiber and the binder, the density of the microchannels is higher in the unexposed BFRP rebar with a 10 mm diameter than in unexposed BFRP rebar with an 18 mm diameter (see Figure 3). An increase in the quasi-equilibrium content of moisture with a decrease of height for rebar with a 10 mm diameter from 0.14% to 0.22%, for rebar with an 18 mm diameter from 0.13% to 0.18%, and a decrease in the quasi-equilibrium content of moisture from 0.34% to 0.19% for a 6 mm diameter rebar can be explained by the predominance of one of the following phenomena: (a) with a decrease in the sample height, the density of defects in rebar fabrication decreases, and (b) with an increase in the diameter of the rebar, it is a more significant fracture when cutting the specimen.

3.3. Evaluation of the BFRP Rebar Destruction

The modulated parameters by three-stage diffusion and the assessment of model adequacy for BFRP rebar (see subparagraph 3.2), exposed in an extremely cold subarctic climate during 28 months, are shown in Table 3. In Figures 4–6, there are solid lines that correspond to this approximation. The three-stage diffusion adequately describes moisture absorption by the unexposed BFRP rebar; the value of a coefficient of determination (3) is not less than 0.91 for a long sample.

Table 3. Adequacy and parameters of the three-stage diffusion model of exposed BFRP rebar.

A Diameter	A Height, mm	M_∞(%) from Equation (2)	$\frac{D}{R^2} \cdot 10^3$, 1/Day	$D \cdot 10^6$, cm²/Day	t_1, Day	t_2, Day	$M_{2\infty}$(%)	t_3, Day	R2 from Equation (3)
6 mm	100	0.24	5.72	5.15	85	103	0.26	191	0.95
	70	0.24	5.27	4.74	93	103	0.23	191	0.93
	50	0.23	10.27	9.24	126	191	0.26	191	0.94
	30	0.27	8.38	7.54	93	103	0.31	191	0.91
	10	0.24	10.31	9.28	93	103	0.29	182	0.85
	5	-	-	-	-	-	-	0	-
10 mm	100	0.26	5.74	14.35	85	122	0.34	191	0.96
	70	0.31	4.15	10.38	93	122	0.34	191	0.95
	50	0.30	6.21	15.53	93	122	0.37	191	0.95
	30	0.31	7.65	19.12	93	122	0.35	191	0.95
	10	0.19	29.87	74.68	103	122	0.30	191	0.91
	5	0.26	12.72	31.80	103	122	0.37	191	0.86
18 mm	100	0.22	4.98	40.35	49	122	0.26	191	0.97
	70	0.27	4.07	32.97	75	122	0.29	191	0.96
	50	0.27	4.90	39.72	86	122	0.29	-	0.97
	30	0.26	7.63	61.82	98	122	0.31	191	0.95
	10	0.20	28.69	232.35	98	122	0.27	191	0.94
	5	0.22	38.91	315.21	98	122	0.28	191	0.94

The study [33] dealt with the destruction of an epoxy binder on the surface of basalt textolite under the influence of the same cold climate for two years: in the form of cracking up to 1 micron in-depth, bare fibers and single depressions no more than 30 microns. Similar destruction can be observed for the studied case of the BFRP rebar in Figure 9.

(**a**)　　　　　　　　(**b**)
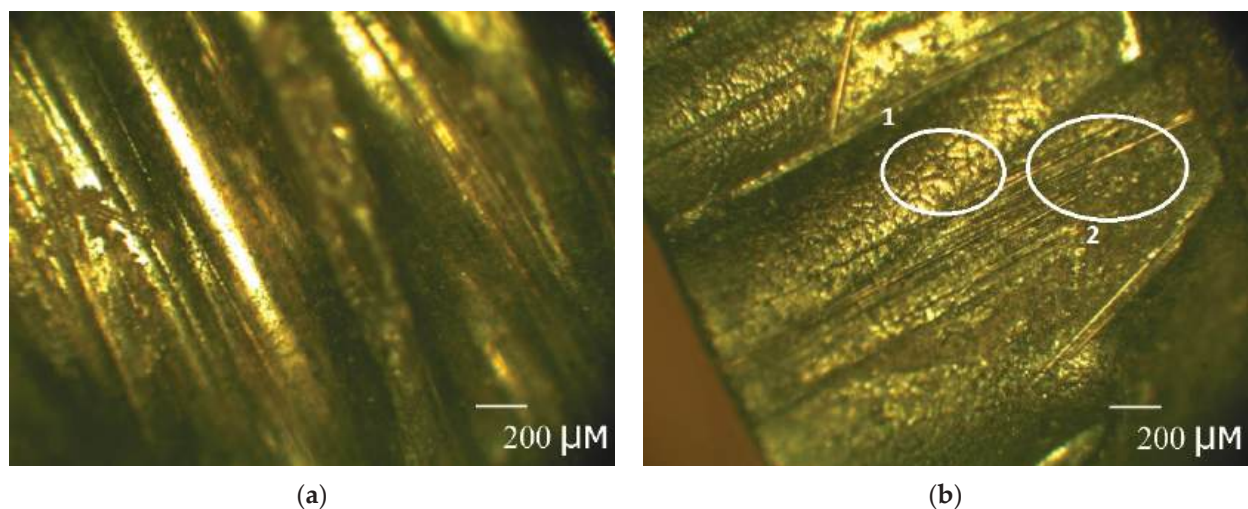
Figure 9. Pictures of the surface of the BFRP rebar: (**a**) unexposed sample, and (**b**) exposed sample. 1—the cracking of the epoxy binder and 2—the fiber denudation can be observed.

It is expected that such cracking of the epoxy binder on the surface of the exposed rebar will increase the surface area of moisture penetration; thus, moisture saturation of the exposed sample will occur faster than the unexposed sample. Indeed, this can be seen in Figures 5 and 6. The diffusion coefficient of the long sample of exposed rebar with a 6, 10, and 18 mm diameter increased at an average of 82.7%, 56.7%, and 30%, respectively (See Table 3). It is clear that this difference is explained by the same thickness of the surface destruction. The change in the diffusion coefficients of samples with a height of 10 and 5 mm was not taken into account, since here the influence of the edge of sample prevails.

The first stage of studying exposed rebar ran mainly 93 days. As can be seen from Figures 4–6 and the analysis of Table 3, the moisture saturation content of the exposed samples is less than that of the unexposed samples by a maximum of 20 percent. The

average weight increase at the second stage of long rebar with a 10 mm diameter is 0.06%, 18 mm diameter is 0.04%, and 6 mm diameter is 0.02%. The existence of a linear second stage of diffusion in exposed rebar with 6 mm diameter, in contrast to diffusion in unexposed rebar with 6 mm diameter, suggests that microchannels occur in the BFRP rebar due to the influence of the climate of Yakutsk.

Analysis of Table 3 and the kinetics of moisture absorption in Figures 4–6 show that after exposure to the climate of Yakutsk for two years, the kinetics of moisture uptake is almost independent of the diameter of the sample. Thus, the difference in the kinetics of moisture uptake for unexposed rebar can be explained by the initial structural nonequilibrium. Structural disequilibrium depends on the mode of reinforcement formation and relaxes at the early stage of climatic aging [34].

As seen from Figures 4–6 and Figure 10, the third stage of the unexposed rebar begins after 191 days and suggests the mechanism's predominance (b) weight loss due to hydrolysis and subsequent binder spalling.

(**a**) (**b**)
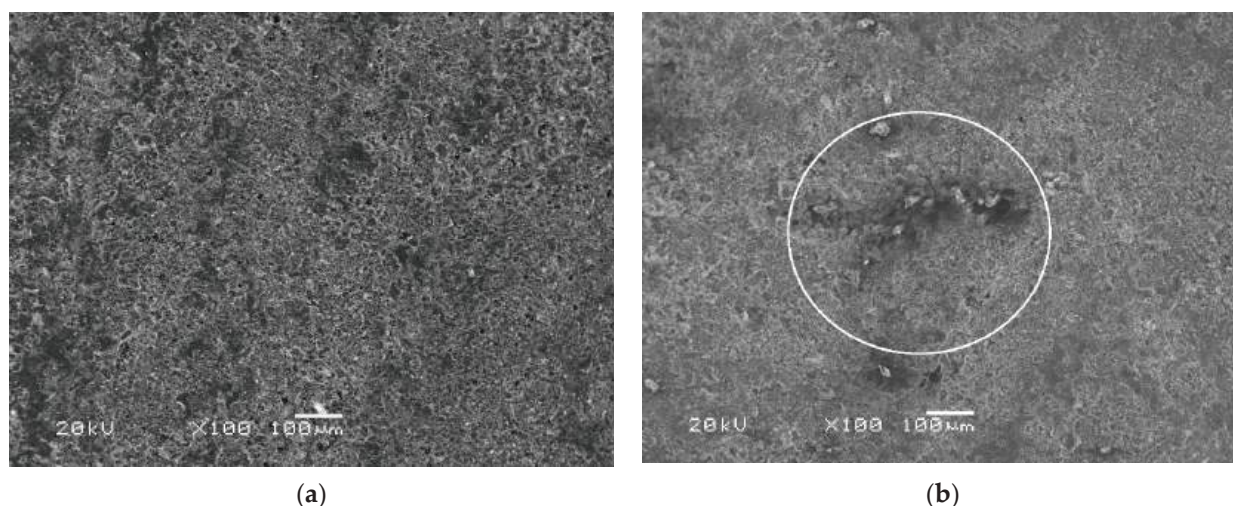
Figure 10. Pictures of the cross-section of the BFRP rebar: (**a**) unexposed, and (**b**) exposed sample. The subsequent epoxy binder spalling can be observed.

4. Conclusions

Water saturation of PCM in comparison with moisture saturation has been extensively studied. It seems that water saturation is a well-known two-stage diffusion, while moisture saturation is three-stage diffusion. Until now, the mechanism of the second stage of moisture diffusion in PCM has no clear explanation. Apparently, in PCM with a high density of fiber filling, the first stage of moisture diffusion corresponds to Fick's diffusion, the second stage is responsible for the capillary filling of defects and/or microchannels, and at the third stage of diffusion, the binder is hydrolyzed. According to this mechanism, it is possible to draw conclusions about the distribution of free volume in the composite by a quite simple but long-term method of moisture saturation of the composite without destroying its integrity. Thus, the change in the diffusion coefficients at the first stage will indeed reflect the degree of surface destruction of PCM with a high density of fiber filling, and the absence of the second stage of moisture saturation will reflect good adhesion between the fiber and the binder.

Moisture uptake test was carried out at the temperature of 60 °C and relative humidity of 98 ± 2% during 306 days. The three-stage diffusion model adequately describes moisture absorption by the BFRE rebar; a coefficient of determination is not less than 0.93. It takes 77 days to start the second stage. The three-stage diffusion model adequately describes moisture absorption by the BFRE rebar after exposure to an extremely cold subarctic climate of Yakutsk for 28 months; a coefficient of determination is not less than 0.85. It takes 93 days

to start the second stage and 191 days to start the third stage. The formation of a periodic profile of the BFRP rebar leads to the fact that as the rebar's diameter increases, there are defects in the periphery of the rebar, as well as microchannels in the fiber/binder interface. The maximum value of the moisture saturation content is 0.41%. The moisture saturation content of the exposed samples is less than that of the unexposed samples by a maximum of 20%. The diffusion coefficient of the long sample of the BFRP rebar with a 6, 10, and 18 mm diameter increased at an average of 82.7%, 56.7%, and 30%, respectively, after exposure to an extremely cold subarctic climate of Yakutsk for 28 months. A future research direction is to validity the second stage of diffusion in BFRP rebar.

References

1. Dexter, H.B. Long-Term Environmental Effects and Flight Service Evaluation of Composite Materials. 1987. Available online: https://ntrs.nasa.gov/citations/19870008425 (accessed on 5 December 2021).
2. Baker, D.J. Ten-Year Ground Exposure of Composite Materials Used on the Bell Model 206L Helicopter Flight Service Program. 1994. Available online: https://ntrs.nasa.gov/citations/19950005944 (accessed on 5 December 2021).
3. Hoffman, D.J.; Bielawski, W.J. Environmental Exposure Effects on Composite Materials for Commercial Aircraft. 1990. Available online: https://archive.org/details/NASA_NTRS_Archive_19910015045 (accessed on 5 December 2021).
4. Vodicka, R. *Environmental Exposure of Boron-Epoxy Composite Material*; Defence Science and Technology Organisation Melbourne: Melbourn, Australia, 2000.
5. Martin, R. *Ageing of Composites*; Martin, R., Ed.; Woodhead Publishing: Cambridge, UK, 2008.
6. Nishizaki, I.; Sakurada, H.; Tomiyama, T. Durability of pultruded GFRP through ten-year outdoor exposure test. *Polymers* **2015**, *7*, 2494–2503. [CrossRef]
7. Bhide, S.J.; Zurale, M.M. Durability aspects of fibre reinforced composites. In *Durability of Building Materials and Components 8*; Lacasse, M.A., Vanier, D.J., Eds.; Institute for Research in Construction: Ottawa, ON, Canada, 1999; pp. 1382–1391.
8. Kablov, E.N.; Startsev, V.O. Klimaticheskoe starenie polimernyh kompozicionnyh materialov aviacionnogo naznacheniya. 1. Ocenka vliyaniya znachimyh faktorov vozdejstviya. *Deform. Razrushenie Mater.* **2019**, *12*, 7–16. [CrossRef]
9. Kablov, E.N.; Startsev, V.O. Klimaticheskoe starenie polimernyh kompozicionnyh materialov aviacionnogo naznacheniya. 2. Razvitie metodov issledovaniya rannih stadij stareniya. *Deform. Razrushenie Mater.* **2020**, *1*, 15–21. [CrossRef]
10. Kablov, E.N.; Startsev, V.O. Sistemnyj analiz vliyaniya klimata na mekhanicheskie svojstva polimernyh kompo-zicionnyh materialov po dannym otechestvennyh i zarubezhnyh istochnikov. *Aviac. Mater. Tekhnologii* **2018**, *2*, 47–58. Available online: https://cyberleninka.ru/article/n/sistemnyy-analiz-vliyaniya-klimata-na-mehanicheskie-svoystva-polimernyh-kompozitsionnyh-materialov-po-dannym-otechestvennyh-i/viewer (accessed on 5 December 2021).
11. Starcev, V.O. Klimaticheskaya Stojkost' Polimernyh Kompozicionnyh Materialov i Zashchitnyh Pokrytij v Umerenno-Teplom Climate. Ph.D. Thesis, Degree-Granting University, Moscow, Russia, 2018.
12. Startsev, V.O.; Lebedev, M.P.; Kychkin, A.K. Influence of moderately warm and extremely cold climate on properties of basalt plastic rebars. *Heliyon* **2018**, *4*, e01060. [CrossRef]

13. Aviacionnye Materialy. Spravochnik v 13 tomah. Tom 13. Klimaticheskaya i Mikrobiologicheskaya Stojkost' Nemetallicheskih Materialov. 2015. Available online: https://viam.ru/sites/default/files/uploads/news/2019/6435/6435_tom_13_soderzhanie.pdf (accessed on 5 December 2021).

14. Nikolaev, E.V.; Barbot'ko, S.L.; Andreeva, N.P.; Pavlov, M.R.; Grashchenkov, D.V. Kompleksnoe issledovanie vozdejstviya klimaticheskih i ekspluatacionnyh faktorov na novoe pokolenie epoksidnogo svyazuyushchego i polimernyh kompozicionnyh materialov na ego osnove. Chast' 4. Naturnye klimaticheskie ispytaniya polimernyh kompozicionnyh materialov na osnove epoksidnoj matricy. *Trudy VIAM* **2016**, *6*, 93–108. Available online: http://viam-works.ru/ru/articles?art_id=975 (accessed on 8 December 2021).

15. Panin, S.V.; Starcev, O.V.; Krotov, A.S. Diagnostika nachal'noj stadia klimaticheskogo stareniya PKM po izmeneniyu koefficienta diffuzii vlagi. *Trudy VIAM* **2014**, *7*, e9. Available online: http://viam-works.ru/ru/articles?art_id=688 (accessed on 5 December 2021).

16. Starcev, O.V.; Kuznecov, A.A.; Krotov, A.S.; Anihovskaja, L.I.; Senatorova, O.G. Modelirovanie vlagoperenosa v sloistyh plastikah i stekloplastikah. *Fiz. Mezomeh.* **2002**, *5*, 109–114.

17. Starcev, O.V.; Krotov, A.S. Sorbciya i diffuziya vlagi v stekloplastikovyh sterzhnyah kruglogo secheniya. *Materialovedenie* **2012**, *6*, 24–28.

18. Alessi, S.; Pitarresi, G.; Spadaro, G. Effect of hydrothermal ageing on the thermal and delamination fracture behaviour of CFRP composites. *Compos. Part B Eng.* **2014**, *67*, 145–153. [CrossRef]

19. Zhang, A.Y.; Li, D.H.; Zhang, D.X.; Lu, H.B.; Xiao, H.Y.; Jia, J. Qualitative separation of the effect of voids on the static mechanical properties of hygrothermally conditioned carbon/epoxy composites. *Express Polym. Lett.* **2011**, *5*, 708–716. [CrossRef]

20. Janas, V.F.; McCullough, R.L. Moisture absorption in unfilled and glass-filled, cross-linked polyester. *Compos. Sci. Technol.* **1987**, *29*, 293–315. [CrossRef]

21. Hodzica, A.; Kim, J.K.; Lowe, A.E.; Stachurski, Z.H. The effects of water aging on the interphase region and interlaminar fracture toughness in polymer–glass composites. *Compos. Sci. Technol.* **2004**, *64*, 2185–2195. [CrossRef]

22. Costa, M.L. Strength of hygrothermally conditioned polymer composites with voids. *J. Compos. Mater.* **2005**, *39*, 1943–1961. [CrossRef]

23. ASTM. *Standard Test. Method for Moisture Absorption Properties and Equilibrium Conditioning of Polymer Matrix Composite Materials*; ASTM D5229; ASTM International: West Conshohocken, PA, USA, 2014.

24. Fick, A. Ueber diffusion. *Ann. Phys. Chem.* **1855**, *170*, 59–86. [CrossRef]

25. Crank, J. *The Mathematics of Diffusion*, 2nd ed.; Glarendon Press: Oxford, UK, 1975.

26. Glaskova, T.I.; Guedes, R.M.; Morais, J.J.; Aniskevich, A.N. A comparative analysis of moisture transport models as applied to an epoxy binder. *Mech. Compos. Mater.* **2007**, *43*, 377–388. [CrossRef]

27. Flory, P.J. *Principles of Polymer Chemistry*; Cornell University Press: Ithaca, NY, USA, 1953.

28. Bagley, E.; Long, F.A. Two-stage sorption and desorption of organic vapors in cellulose acetate. *J. Am. Chem. Soc.* **1955**, *77*, 2172–2178. [CrossRef]

29. Newns, A.C. The sorption and desorption kinetics of water in a re-generated cellulose. *Trans. Faraday Soc.* **1956**, *52*, 1533–1545. [CrossRef]

30. Aniskevich, A.; Glaskova-Kuzmina, T. Effect of moisture on elastic and viscoelastic properties of fiber reinforced plastics: Retrospective and current trends. In *Creep and Fatigue in Polymer Matrix Composites*; Woodhead Publishing: Sawston, UK, 2019; pp. 83–120. [CrossRef]

31. Varelidis, P.C.; Kominos, N.P.; Papaspyrides, C.D. Polyamide coated glass fabric in polyester resin: Interlaminar shear strength versus moisture absorption studies. *Compos. Part A* **1998**, *29*, 1489–1499. [CrossRef]

32. Pothan, L.A.; Thomas, S. Effect of hybridization and chemical modification on the water-absorption behavior of banana fiber–reinforced polyester composites. *J. Appl. Polym. Sci.* **2004**, *91*, 3856–3865. [CrossRef]

33. Lukachevskaya, I.G.; Gavrilieva, A.A.; Kychkin, A.K.; Kychkin, A.A.; Struchkov, N.F.; Diakonov, A.A. Estimate of the early stage of climatic aging of basalt- and glass-fiber reinforced plastics. *Arct. Subarct. Nat. Resour.* **2021**, *26*, 159–169. [CrossRef]

34. Kablov, E.N.; Startsev, O.V.; Krotov, A.S.; Kirillov, V.N. Klimaticheskoe starenie kompozicionny'x materialov aviacionnogo naznacheniya. 2. Relaksaciya isxodnoj strukturnoj neravnoesnosti i gradient svojstv po tolshhine. *Deform. Razrushenie Mater.* **2010**, *12*. Available online: https://viam.ru/sites/default/files/scipub/2010/2010-205598.pdf (accessed on 5 December 2021).

Article

Effect of Low Nanodiamond Concentrations and Polymerization Techniques on Physical Properties and Antifungal Activities of Denture Base Resin

Shaimaa M. Fouda [1,*], **Mohammed M. Gad** [1] , **Passent Ellakany** [1] , **Maram A. Al Ghamdi** [1], **Soban Q. Khan** [2], **Sultan Akhtar** [3] , **Doaa M. Al Eraky** [4] **and Fahad A. Al-Harbi** [1]

[1] Department of Substitutive Dental Sciences, College of Dentistry, Imam Abdulrahman Bin Faisal University, P.O. Box 1982, Dammam 31441, Saudi Arabia; mmjad@iau.edu.sa (M.M.G.); pellakany@iau.edu.sa (P.E.); maalghamdi@iau.edu.sa (M.A.A.G.); falharbi@iau.edu.sa (F.A.A.-H.)

[2] Department of Dental Education, College of Dentistry, Imam Abdulrahman Bin Faisal University, P.O. Box 1982, Dammam 31441, Saudi Arabia; sqkhan@iau.edu.sa

[3] Department of Biophysics, Institute for Research and Medical Consultations, Imam Abdulrahman Bin Faisal University, P.O. Box 1982, Dammam 31441, Saudi Arabia; suakhtar@iau.edu.sa

[4] Department of Biomedical Dental Sciences, College of Dentistry, Imam Abdulrahman Bin Faisal University, P.O. Box 1982, Dammam 31441, Saudi Arabia; dmaleraky@iau.edu.sa

* Correspondence: smfouda@iau.edu.sa

Abstract: Background: Denture base resin has some drawbacks. This study investigated the impact of nanodiamonds (ND) and autoclave polymerization on the surface characteristics, translucency, and *Candida albicans* adherence in polymethyl methacrylate (PMMA) denture base resin after thermocycling. Methods: Heat-polymerized PMMA discs (15×2 mm) with a total sample size $n = 160$ were studied. Specimens were categorized into two main groups ($N = 80$): conventional water-bath-polymerized PMMA (CP/PMMA) and autoclave-polymerized PMMA (AP/PMMA). Each group was subdivided according to the ND concentration into four groups ($n = 20$): unmodified PMMA as a control, and 0.1%, 0.25%, and 0.5% ND–PMMA. Scanning electron microscopy (SEM) was used to inspect the morphology of the ND and the ND–PMMA mixtures before heat polymerization. The specimens were exposed to thermal cycling (5000 cycles at 5 and 55 °C), then surface roughness was measured with a non-contact optical interferometric profilometer, contact angle with an automated goniometer, and translucency using a spectrophotometer. Colony-forming units (CFU) were used to determine the adherence of *Candida albicans* cells to the specimens. ANOVA and Tukey post hoc tests for pairwise comparison were utilized for the statistical analysis ($\alpha = 0.05$). Results: Surface roughness was significantly reduced with ND addition to CP/PMMA ($p < 0.001$), while the reduction was not statistically significant in AP/PMMA ($p = 0.831$). The addition of ND significantly reduced the contact angle, translucency, and *Candida albicans* count of CP/PMMA and AP/PMMA ($p < 0.001$). The incorporation of ND in conjunction with autoclave polymerization of PMMA showed significant reduction in all tested properties (surface roughness, contact angle and *Candida albicans* adherence) except translucency ($p = 0.726$). Conclusions: ND addition to PMMA and autoclave polymerization improved the surface properties with respect to antifungal activities, while the translucency was adversely affected.

Keywords: acrylic resin; candidiasis; nanodiamonds; surface properties; polymerization

1. Introduction

Polymethyl methacrylate (PMMA) is recommended in the manufacture of several dental appliances as it is characterized by being cost-effective, easy to process, and repairable, and has acceptable shade matching [1]. Nevertheless, the limited physical properties of PMMA make it less than ideal [2]. Moreover, the exposure of denture base resin to temperature changes adversely affects the resin properties [3]. To overcome these limitations,

different methods have been suggested to improve the performance of PMMA, such as structural modifications by additives (chemicals, fillers, and nanofillers) and/or a different polymerization method [4].

A denture base material possessing hydrophilic properties and low surface roughness could reduce *Candida albicans* adhesion [5]. Coating the denture base was suggested to improve the surface properties of PMMA and reduce *Candida albicans* adhesion [6,7]. However, the durability of these coatings was doubtful [8]. The addition of antimicrobial agents to PMMA was also investigated, to increase denture resistance to microbial adhesion and consequently improve the oral health of denture wearers [8].

In addition, incorporation of reinforcing/antifungal agents and a different polymerization technique were used to enhance the mechanical characteristics of PMMA [4,9,10]. Recently, nanofillers have been used as a reinforcing agent in PMMA. Nanofillers have large active surfaces due to their small size; therefore, they could result in considerable changes in the properties of PMMA at low concentrations [8]. In addition, some nanofillers, such as nanodiamonds (ND), enhanced the antimicrobial activity of PMMA [11,12]. The antimicrobial activity of the ND might have arisen from oxygen-derived groups on their surface that interact with the components of bacterial cells, causing their death [13]. In addition, ND are biocompatible, have high strength, and are chemically stable [14]. They also link to PMMA through their reactive groups (NH_2, OH) which enhance bonding with PMMA [15]. Al Harbi et al. [16] reported significant enhancement of the flexural strength and surface roughness of PMMA with the addition of 0.5% ND compared to higher concentrations (1% and 1.5% ND), while impact strength was reduced. The *Candida albicans* count was also decreased with ND addition, with the lowest count found at 1% for the ND/PMMA composite [12]. However, the observed color change of ND/PMMA, particularly at high ND concentrations, is considered a drawback [12].

PMMA is most commonly polymerized by being processed in a water bath, which is an uncomplicated conventional technique but requires long processing time [17]. However, other methods are also used for polymerization of PMMA, such as visible light, and autoclave and microwave methods, to speed up the polymerization of PMMA without causing any deterioration in the material composition and properties [9,10]. Polymerization of PMMA by autoclave is easier and can be done in less time than when using the conventional water-bath method [18]. Moreover, studies showed improved properties of the PMMA including improved flexural strength and surface hardness when the material was processed by autoclave, compared to the water-bath method [9,19,20]. Autoclave polymerization depends on the application of steam under high pressure and at higher temperatures. This procedure results in improvement of the PMMA properties by reducing the residual monomer content [21].

The effect of ND addition and autoclave polymerization on PMMA combined with thermal cycling has not been tested previously. The aim of the present study was to detect the effects of low levels of ND addition and autoclave polymerization on the surface properties and translucency of PMMA, as well as on *Candida albicans* adhesion after thermocycling. The first null hypothesis of the study states that addition of low amounts of ND would not change the tested properties of PMMA or the *Candida albicans* adhesion. The second null hypothesis of the study states that the properties of PMMA would be unchanged under the combined effect of ND addition and autoclave polymerization.

2. Materials and Methods

For the sample size calculation, the power was set at 80%, the level of significance was set at 5%, and the confidence interval was taken as 95%. Hence, the calculated sample size revealed that 160 disc-shaped specimens (15 × 2 mm) of heat-polymerized PMMA were required to carry out the study. The specimens were arranged in two main groups according to polymerization technique: conventional water-bath-polymerized PMMA (CP/PMMA) ($N = 80$) and autoclave-polymerized PMMA (AC/PMMA) ($N = 80$). Each group was subdivided according to the ND concentration into four groups ($n = 20$): unmodified as the

control, and 0.1% ND–PMMA, 0.25% ND–PMMA, and 0.5% ND–PMMA. The materials used in the present study are shown in Table 1.

Table 1. Materials used.

Materials	Brand/Supplier
Heat-polymerized PMMA	Major base 20, Major Prodotti Dentari Spa, Moncalieri, Italy
Nanodiamond	Shanghai Richem International Co., Ltd., Shanghai, China
Base plate wax	Set-up Wax; Cavex, Haarlem, The Netherlands
Dental stone	Fujirock EP; GC, Leuven, Belgium
Separating medium	Isol Major; Major Prodotti Dentari Spa, Moncalieri, Italy

Heat treatment of the ND particles was performed at 450 °C for 120 min in air to release superficial functional groups [22]. An electronic balance (S-234; Denver Instrument GmbH, Göttingen, Germany) was employed to weigh the ND in concentrations of 0.1 wt.%, 0.25 wt.%, and 0.5 wt.% in acrylic resin powder. The ND particles were added to the acrylic resin powder and blended manually in a glass mortar and pestle with gentle hand pressure. Then, the samples mixed in an electric mixer at 400 rpm for 30 min at room temperature.

Specimen Preparation and Processing

Wax specimens were prepared using metal molds, then invested and flasked (61B Two Flask Compress; Handler Manufacturing, Westfild, NJ, USA). Mold spaces and all surfaces were painted with a separating medium after wax elimination. Heat-polymerized PMMA was prepared following the manufacturer's instructions. Packing and polymerization were achieved using either the conventional water-bath method or by the autoclave polymerization method. Group 1 (CP) samples were conventionally heat-polymerized using the water-bath method, i.e., by inserting the flasks into a curing unit (KaVo Elektrotechnisches Werk GmbH, Leutkirch, Germany) for 8 h at 74 °C, and then raising the temperature to 100 °C for 60 min. Group 2 (AP) samples were autoclave polymerized by placing the flasks in an autoclave (Ritter M11 UltraClave; Midmark Corporation, Ohio, USA at 210 kPa (kilopascals) pressure and a temperature of 60 °C for 30 min, and then raising the temperature to 130 °C for 20 min [9,18].

After de-flasking, the excess resin was removed from the specimens with a tungsten carbide bur (HM251FX-040-HP; Meisinger, Centennial, CO, USA), followed by polishing with a mechanical polisher (MetaServ 250 grinder–polisher; Buehler, Lake Bluff, IL, USA) at 100 rpm for 120 s in wet conditions. The specimens were then placed in distilled water for 2 days at 37 °C.

Prior to examining the specimens, they were exposed to thermocycling (Thermocycler THE-1100, SD Mechatronik GmbH, Feldkirchen-Westerham, Germany) for 5000 cycles at 5 and 55 °C, with 5 s of transfer time and 30 s of dwell time, to simulate 6 months of actual use intraorally [23].

The surface roughness was evaluated with a non-contact optical interferometric profilometer with 0.01 mm resolution (Contour GT; Bruker Nano GmbH, Berlin, Germany). The specimens were placed horizontally below a standard camera at $20\times$ magnification and the surface of each specimen was scanned across an area approximately 0.43×0.58 mm at five locations to obtain the average surface roughness value. Subsequently, the resulting images were visualized via a software package (Vision64; Bruker Nano, Coventry, UK) to detect pit features [24].

The contact angle was measured with an automated goniometer (DM-501; Kyowa Interface Science Co., Niiza, Japan) using the sessile drop method. After smoothly air-drying the specimen surface, a droplet of distilled water (2 μL) was placed on the surface using an auto-pipette. The average contact angle for each specimen was calculated by determining the tangent angle in relation to the water droplet surface at four distinct locations/specimen. FAMAS software (Kyowa Interface Science Co., Kyowa, Japan) was used to analyze the images [25].

The specimens' reflectance values were detected using a spectrophotometer (Color-Eye 7000A spectrophotometer, X-Rite, Grand Rapids, MI, USA) after performing a calibration following the manufacturer's recommendations. Specimens were kept against the port and supported by white or black backgrounds. A small-aperture viewing area was selected with dimensions of 10×7.5 mm. Four measurements were recorded/specimen to calculate the mean values of L*, a*, and b*. The Commission Internationale de l'Eclairage (CIE) system of L*, a*, and b* coordinates was used in the disc color measurements. CIE was used on the discs against each background. The translucency (TR) was analyzed utilizing the equation TR = $[(\text{L* white} - \text{L* black})^2 + (\text{a* white} - \text{a* black})^2 + (\text{b* white} - \text{b* black})^2]^{1/2}$ [26].

The initial adhesion of *Candida albicans* to a specimen surface was performed to assess the first step of biofilm formation. The number of adhered cells was detected using colony-forming units (CFUs) as follows:

A *Candida albicans* reference strain (ATCC 10231) from a glycerol stock was streaked onto Sabouraud dextrose agar (SDA) plates two days prior to the assay, and plates were incubated at 30 °C for 48 h. A single colony was inoculated into 25 mL SDA broth medium to grow at 30 °C overnight and the yeast suspension was adjusted to 0.5 McFarland (approximately equivalent to 1×10^7 cells/mL).

Transparent sterile 12-well microplates were used, and each specimen was sterilized using 70% isopropyl alcohol (IPA), then placed in a well with 1 mL of the fungal suspension and incubated at 37 °C for 90 min.

After incubation, 200 μL of phosphate buffer saline (PBS) was applied to the discs twice, to remove non-adhered fungal cells, then transferred to a new sterile Petri dish. To dislodge the adhered cells, 200 μL of PBS was added, scraping the surface with a pipette tip and homogenizing the solution by pipetting. Serial dilution was performed and 100 μL from the dilution tube was plated on SDA agar plates. The plates were incubated at 30 °C for 24–72 h, and colonies were counted twice, after 24 h and between 48 and 72 h, to ensure adequate growth and to distinguish colonies. The tests were conducted in three replicates. Positive and negative controls were carried out for each incubation time.

Statistical analysis was performed using SPSS v.23 software. The normality of the data for the tested samples was investigated using a Shapiro–Wilk test. Insignificant results from the test showed that the data were normally distributed; hence, parametric statistical tests were used for the data analysis. In the descriptive analysis, mean and standard deviations were computed. In the inferential statistics, one-way ANOVA was used to test the effect of variation in the concentration of nanodiamonds on the tested properties of heat-polymerized and autoclave-polymerized denture base material, followed by Tukey's post hoc test for pairwise comparison. Additionally, a two-way ANOVA was employed to test the merged effect of the concentration levels and the polymerization method used. In the tests, *p*-values less than 0.05 were considered statistically significant.

3. Results

Figures 1 and 2 show the structures of pure ND and PMMA, and the distribution of ND in the PMMA (ND/PMMA mixture) under scanning electron microscopy (SEM). In addition, the detailed features and the configuration of ND particles were visualized at high resolution in the ND powder by transmission electron microscopy (TEM).
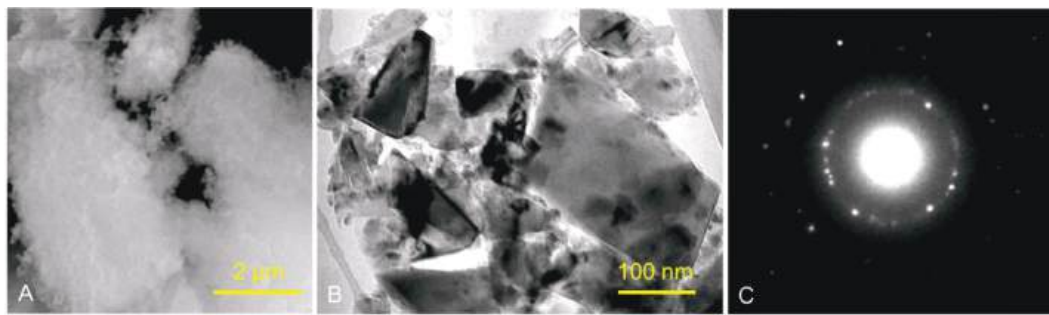
Figure 1. (**A**) SEM micrograph of ND powder, (**B**) TEM image of ND powder, and (**C**) corresponding selected-area electron diffraction (SAED) pattern of ND crystalline particles.
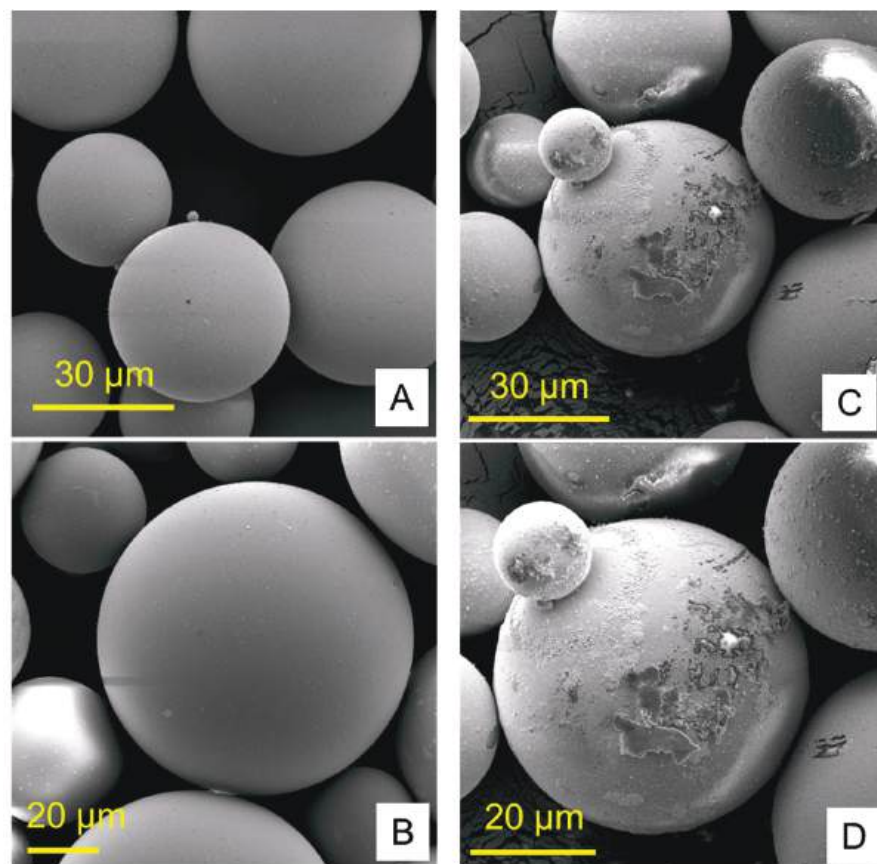
Figure 2. Scanning electron micrographs of (**A**,**B**) pure PMMA and (**C**,**D**) PMMA/ND mixture at two magnifications.

Table 2 shows the mean and standard deviation values of the surface roughness, contact angle, translucency, and *Candida albicans* count. The surface roughness, contact angle, and *Candida albicans* count of conventionally polymerized PMMA (CP) were found to be highest in the control group, while the lowest values of *Candida albicans* and contact angle were found at 0.5% ND–PMMA. The lowest surface roughness value was found at 0.25% ND–PMMA. The translucency of conventionally polymerized and autoclave-polymerized PMMA was found to be highest in the control and lowest at 0.5% ND–PMMA (Table 2).

Table 2. Average and standard deviation values of tested properties.

Groups	Concentration	Surface Roughness (μm)	*C. albicans* (cfu/mL)	Contact Angle (°)	Translucency
CP	Control	0.165 (0.02)	16,220 (4973.4)	88.4 (1.6)	13.7 (1.1)
	0.1%	0.132 (0.01)	15,240 (5474.2)	74.4 (1.7)	9.1 (0.7)
	0.25%	0.129 (0.02)	9160 (1487.9)	74.3 (1.1)	6.3 (0.6)
	0.5%	0.135 (0.02)	6980 (831.1)	70.3 (1.4)	2.8 (0.4)
AP	0%	0.121 (0.02)	15,100 (3177.7)	82.8 (3.1)	13.4 (0.7)
	0.1%	0.115 (0.01)	16,820 (4683.6)	73.5 (2.3)	9.3 (0.72)
	0.25%	0.121 (0.01)	7460 (1780.9)	68.2 (3.3)	6.0 (0.73)
	0.5%	0.118 (0.02)	1930 (583.2)	67.4 (2.7)	2.8 (0.39)

In the autoclave-polymerized group (AP), the average surface roughness was highest for 0% and 0.25% ND–PMMA and lowest for 0.1% ND–PMMA. Similarly, the maximum value for *Candida albicans* was obtained at 0.1% ND–PMMA and the minimum value at 0.5% ND–PMMA. The contact angle value was at a maximum in the control group and its minimum value was found at 0.5% ND–PMMA (Table 2). Furthermore, the one-way ANOVA results revealed a significant association ($p < 0.001$) between concentration levels of nanodiamond and the tested properties in conventionally polymerized PMMA. However, in the autoclave group, concentration levels were insignificantly associated ($p = 0.831$) with surface roughness but significantly associated ($p < 0.001$) with contact angle, translucency, and *Candida albicans* count (Table S1).

One-way ANOVA results were obtained after combining the groups (CP and AP) together. Hence, there were eight different concentrations (as factors for ANOVA) which were analyzed with the tested properties. The effect of concentration levels appeared to be statistically significant ($p < 0.001$) over all the tested properties (Table S2). The Tukey post hoc test was applied for pairwise comparison. Figures 3–6 present the post hoc test results.
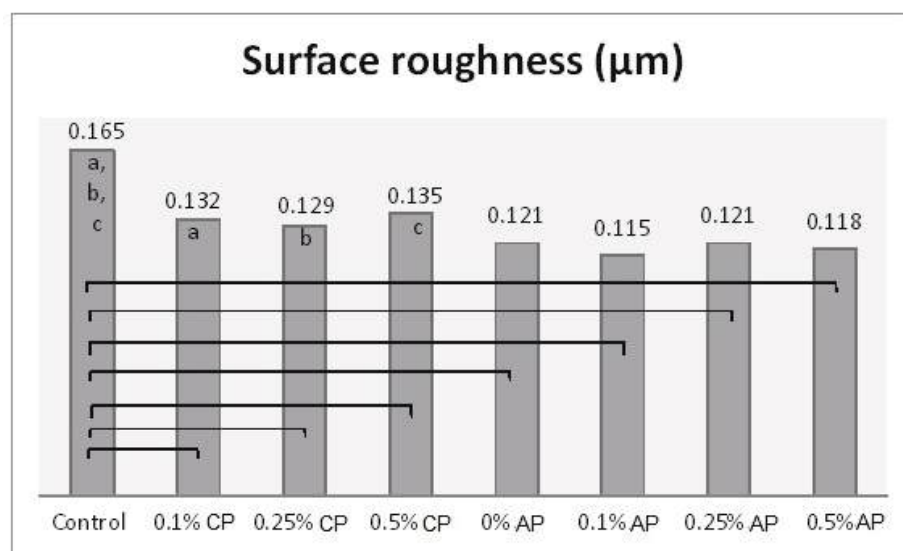
Figure 3. Mean of surface roughness (μm) and significances between groups for ND concentrations and polymerization techniques. Same lower-case letters a, b, c show significant differences in mean within CP group. Lines show the significant differences between all groups comparing polymerization techniques.
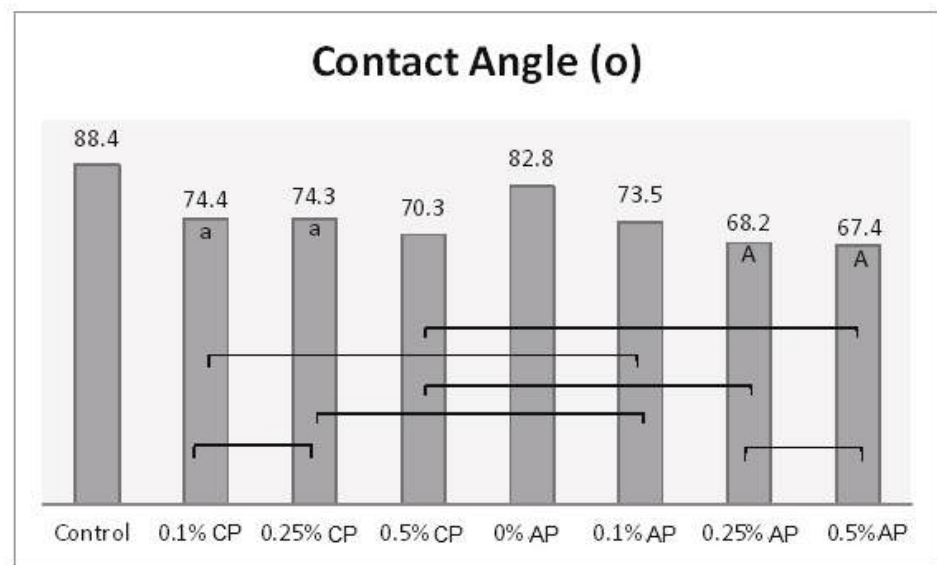
Figure 4. Mean of contact angle (°) and significances between groups for ND concentrations and polymerization techniques. Same lower-case letters a show insignificant differences in means within CP group. Same capital letters A show insignificant differences in means within AP group. Lines show the insignificant differences between all groups comparing polymerization techniques.
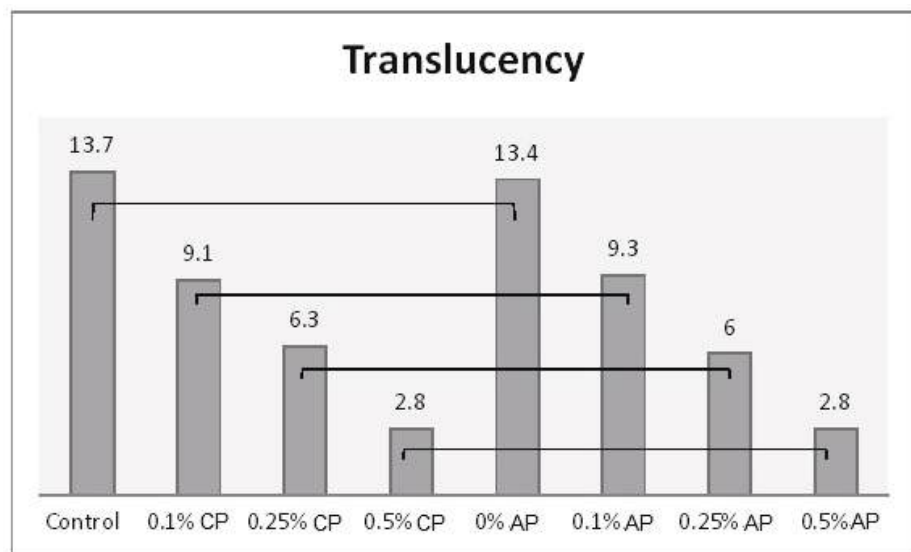
Figure 5. Mean of translucency and significances between groups for ND concentrations and polymerization techniques. Lines show statistically insignificant differences in means comparing polymerization techniques.
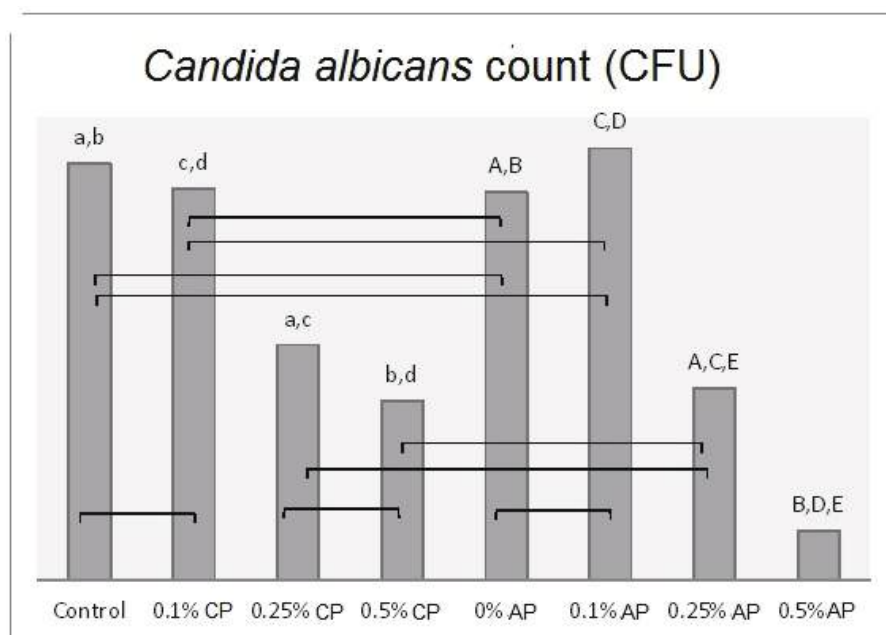
Figure 6. Mean of *Candida albicans* (CFU/mL) count and significances between groups for ND concentrations and polymerization techniques. Same lower-case letters a, b, c, d show significant differences between the means in CP group. Same upper-case letters A, B, C, D, E show significant differences between the means in AP group. Lines show the insignificant differences comparing polymerization techniques.

The combined effects of ND concentration and polymerization method showed **a** significant effect on all tested properties except translucency, as revealed by the two-way ANOVA test (Table 3). Figures 7 and 8A–D show Candida albicans colonies in CP and AP for pure PMMA and 0.1, 0.25, and 0.5% ND, respectively. The fewest Candida albicans colonies can be observed in Figure 8D, while Figure 7A shows the highest number of colonies. Figure 9 shows the contact angles in CP and AP groups.

Table 3. Combined effect of ND concentration and polymerization methods using two-way ANOVA.

Property	Source	Type III Sum of Squares	*df*	Mean Square	*F*	*p*
Surface roughness	concentration	0.005	3	0.002	5.179	0.003 *
	type	0.009	1	0.009	29.017	<0.0001 *
	concentration * type	0.004	3	0.001	3.813	0.014 *
	Error	0.023	72	0.000		
	Total	1.382	80			
C. albicans	concentration	1,940,757,375.000	3	646,919,125.000	55.557	<0.0001 *
	type	49,455,125.000	1	49,455,125.000	4.247	0.043 *
	concentration * type	111,261,375.000	3	37,087,125.000	3.185	0.029 *
	Error	838,381,000.000	72	11,644,180.556		
	Total	12,821,090,000.000	80			
Contact Angle	concentration	3309.149	3	1103.050	210.601	<0.0001 *
	type	299.538	1	299.538	57.190	<0.0001 *
	concentration * type	89.465	3	29.822	5.694	0.001 *
	Error	377.110	72	5.238		
	Total	453,055.840	80			
Translucency	concentration	1259.733	3	419.911	875.552	<0.0001 *
	type	0.277	1	0.277	0.578	0.450
	concentration * type	0.631	3	0.210	0.439	0.726
	Error	34.531	72	0.480		
	Total	6323.585	80			

* Statistically significant at 0.05 level.
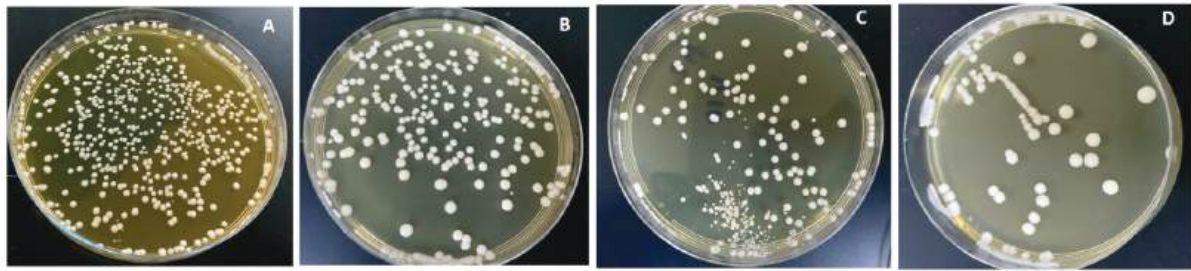
Figure 7. Cultures of *Candida albicans* colonies in CP/PMMA in (**A**) pure PMMA, (**B**) 0.1%, (**C**) 0.25%, and (**D**) 0.5% ND.
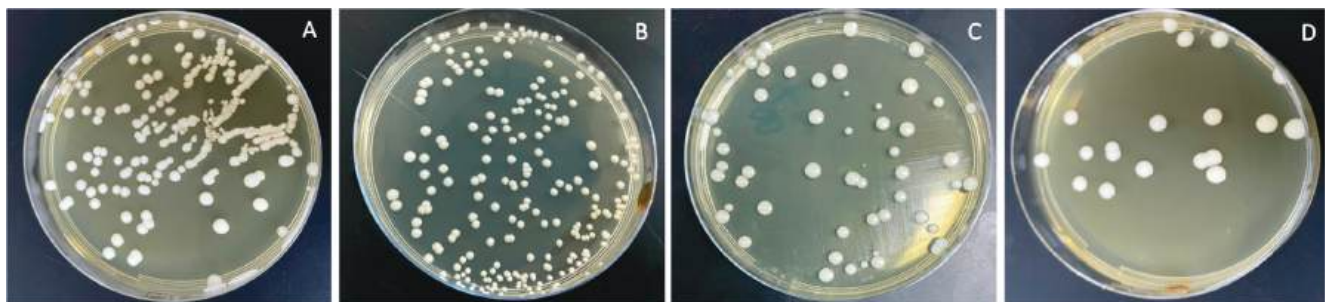
Figure 8. Cultures of *Candida albicans* colonies in AP/PMMA in (**A**) pure PMMA, (**B**) 0.1%, (**C**) 0.25%, and (**D**) 0.5% ND.
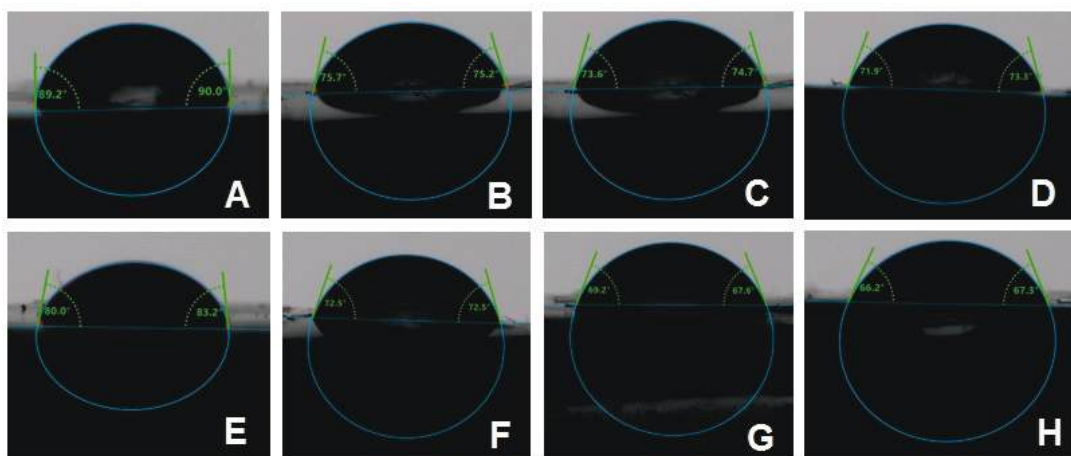
Figure 9. Representative contact angle images of CP groups: (**A**) unmodified, (**B**) 0.1% ND, (**C**) 0.25% ND, (**D**) 0.5% ND; and AP groups: (**E**) unmodified, (**F**) 0.1% ND, (**G**) 0.25% ND, (**H**) 0.5% ND.

4. Discussion

The first null hypothesis was rejected because the addition of ND improved the surface properties of PMMA and also reduced the adhesion of *Candida albicans*, but translucency was adversely affected. The second null hypothesis was also rejected. The addition of ND and autoclave polymerization resulted in a reduction in surface roughness, contact angle, *Candida albicans* adherence to PMMA, and translucency.

It is essential to investigate the properties of PMMA under conditions mimicking actual use intraorally. Therefore, the specimens in this study were exposed to thermal cycling simulating 6 months of actual use, in order to imitate the thermal changes occurring intraorally as a result of food and drinks [23]. This adds to the credibility of the study; however, longer exposure to thermal changes is required to assess the long-term effect of thermal cycling on ND-reinforced PMMA.

Denture base material must have a smooth surface to reduce microbial adhesion [27]. The results showed a significant reduction in surface roughness as a result of ND addition in conventionally polymerized PMMA (CP/PMMA). Previous studies [12,16] found a reduction in surface roughness with ND addition to PMMA at 0.5%, which agrees with the findings of the present study. The addition of nanoparticles fills the pores of the polymer, thus reducing the surface roughness. However, at high concentrations agglomeration of the nanoparticles could cause an opposite effect [16]. Although ND concentration did not significantly change the surface roughness for autoclave-polymerized PMMA (AP/PMMA) subgroups, the surface roughness of AP/PMMA was inferior to that of CP/PMMA. Moreover, the combined effect of ND addition and autoclave polymerization resulted in a significant reduction in the surface roughness of PMMA in the present study. However, Gad et al. [9] reported an insignificant difference in surface roughness between conventionally polymerized and autoclave-polymerized PMMA. The difference in results may be due to the addition of ND to autoclave-polymerized PMMA in the present study and/or the exposure of specimens to thermal cycling.

The findings of the present study showed a significant reduction in contact angle of ND/PMMA in both groups with different polymerization methods. Moreover, autoclave polymerization was associated with lower contact angle values compared to conventional polymerization. This decrease may be attributed to the impact of added nanoparticles on the surface characteristics of PMMA and the reduction of surface tension [25]. Similarly, previous studies found a reduction in the contact angle of PMMA after the addition of various nanoparticles, including silicon oxide, titanium oxide, and zirconium oxide nanoparticles [25,28,29]. However, a previous study showed an insignificant difference in contact angle between pure PMMA and PMMA reinforced with ND at 0.5, 1, and 1.5% [12]. The variation in results might be due to different methods employed in the polymerization, different ND concentrations, or the exposure of the specimens to thermal cycling.

Translucency provides a natural appearance to denture base materials by allowing the passage of light through denture resin, thus reflecting the shade of normal healthy soft tissue. Variations in the denture resin composition and surface roughness reduce light refraction, which in consequence reduces translucency [26]. The findings of the current study showed low translucency for the 0.5% ND conventionally polymerized and autoclave-polymerized PMMA. This is in agreement with previous studies which reported a reduction in the translucency of PMMA denture base resins incorporating fillers or nanofillers such as nano-ZrO_2 particles [26], zirconium oxide, silicon oxide and aluminum oxides, particularly at high filler concentrations [30]. The decrease in translucency might be related to the presence of different filler types possessing dissimilar optical properties [30]. In addition, the increase in filler concentration could result in the formation of clusters that prevent light diffusion through the resin. Moreover, ND possess a higher refractive index (2.11) than PMMA (1.48) [26,31]. Thus, the difference in the refractive indices of ND and PMMA resin explains the reduction in translucency of PMMA denture resin and its opaquer appearance [32]. In a recent study, Gad et al. [33] demonstrated a reduction in PMMA translucency with the addition of different nanofillers at concentrations between 0.5–2.5%, including ND, which showed the lowest translucency amongst the tested nanoparticles. This could be due to the gray color of ND and its sheet-like morphology, which might have reduced light transmission [33].

Significant reduction of *Candida albicans* adherence with ND addition was reported in this study. In addition, autoclave polymerization with ND addition significantly reduced *Candida albicans* adhesion. The lowest count of *Candida albicans* was found with the addition of 0.5% ND in AC/PMMA followed by CP/PMMA. Previous studies reported a reduction in *Candida albicans* adhesion with the addition of ND to heat-polymerized and autopolymerized PMMA, which agrees with the present findings [12,34]. The reason could be the antimicrobial effect of ND, which has been reported in several studies [13,14,35,36]. The antimicrobial effect of ND might result from interaction between its surface oxygen-derived groups and bacterial cells or might be due to its antiadhesive characteristics [13,37,38].

In addition, the impact of ND on the surface characteristics of PMMA was reported in the present study, including the reduction in the surface roughness and contact angle of conventionally polymerized or autoclave-polymerized ND/PMMA. The decrease in surface roughness reduces the area available for microbial adhesion [5]. Therefore, a reduction in surface roughness could reduce colonization of *Candida albicans*, the causative microorganism of denture stomatitis. Moreover, some studies noted a link between low contact angle and decreased fungal adhesion [39,40]. It was mentioned that hydrophilic surfaces reduce fungal adhesion compared to hydrophobic surfaces, which form strong hydrophobic bonds with microbes [41]. In line with the results of the present study, the smallest *Candida albicans* count was found in the AP/PMMA group with 0.5% ND, which had the lowest contact angle value among all the tested groups.

Clinically, the oral health of denture wearers could be enhanced by increasing denture resistance to *Candida albicans* adhesion and improving the surface properties through ND addition and autoclave polymerization, even after exposure to thermal stress. Therefore, low levels of ND addition to PMMA denture base materials in combination with autoclave polymerization could be recommended for denture base fabrication.

Although the specimens in this study were exposed to thermal stress before testing, they were not subjected to all intraoral conditions, such as variation in pH values, exposure to saliva, food, and beverages, and denture cleaning routines. Therefore, in vivo studies are needed to test the effects of these factors and the durability of the ND effect on PMMA. It is also recommended that ND be added to PMMA at the fitting surface or in non-esthetic areas, to avoid the disadvantages of the significant reduction of PMMA's translucency, as was suggested in a previous study [42].

5. Conclusions

The surface roughness, contact angle, and *Candida albicans* adherence were reduced by ND addition and autoclave polymerization. Translucency was adversely affected by ND addition but showed an insignificant difference with regard to the polymerization method.

References

1. El Bahra, S.; Ludwig, K.; Samran, A.; Freitag-Wolf, S.; Kern, M. Linear and volumetric dimensional changes of injection-molded PMMA denture base resins. *Dent. Mater.* **2013**, *29*, 1091–1097. [CrossRef]

2. Darvell, B.W. *Materials Science for Dentistry*, 10th ed.; Woodhead Publishing Series in Biomaterials; Elsevier: Cambridge, UK, 2018; ISBN 978-0-08-101032-7.

3. Ayaz, E.A.; Bagis, B.; Turgut, S. Effects of Thermal Cycling on Surface Roughness, Hardness and Flexural Strength of Polymethyl-methacrylate and Polyamide Denture Base Resins. *J. Appl. Biomater. Funct. Mater.* **2015**, *13*, 280–286. [CrossRef]

4. Gad, M.M.; Fouda, S.M.; Al-Harbi, F.A.; Näpänkangas, R.; Raustia, A. PMMA denture base material enhancement: A review of fiber, filler, and nanofiller addition. *Int. J. Nanomed.* **2017**, *12*, 3801–3812. [CrossRef]

5. Morgan, T.D.; Wilson, M. The effects of surface roughness and type of denture acrylic on biofilm formation by Streptococcus oralis in a constant depth film fermentor. *J. Appl. Microbiol.* **2001**, *91*, 47–53. [CrossRef]

6. Ali, A.A.; Al-Harbi, F.; Suresh, C. Effectiveness of Coating Acrylic Resin Dentures on Preventing Candida Adhesion. *J. Prosthodont.* **2013**, *22*, 445–450. [CrossRef] [PubMed]

7. Lazarin, A.A.; Zamperini, C.A.; Vergani, C.E.; Wady, A.F.; Giampaolo, E.T.; Machado, A.L. *C andida* albicans adherence to an acrylic resin modified by experimental photopolymerised coatings: An in vitro study. *Gerodontology* **2014**, *31*, 25–33. [CrossRef]

8. Gad, M.M.; Fouda, S.M. Current perspectives and the future of Candida albicans-associated denture stomatitis treatment. *Dent. Med. Probl.* **2020**, *57*, 95–102. [CrossRef] [PubMed]

9. Gad, M.; Fouda, S.M.; ArRejaie, A.S.; Al-Thobity, A.M. Comparative Effect of Different Polymerization Techniques on the Flexural and Surface Properties of Acrylic Denture Bases. *J. Prosthodont.* **2017**, *28*, 458–465. [CrossRef]

10. Ayaz, E.A.; Durkan, R.; Koroglu, A.; Bagis, B. Comparative Effect of different Polymerization Techniques on Residual Monomer and Hardness Properties of PMMA-based Denture Resins. *J. Appl. Biomater. Funct. Mater.* **2014**, *12*, 228–233. [CrossRef]

11. Kamonkhantikul, K.; Arksornnukit, M.; Takahashi, H. Antifungal, optical, and mechanical properties of polymethylmethacrylate material incorporated with silanized zinc oxide nanoparticles. *Int. J. Nanomed.* **2017**, *12*, 2353–2360. [CrossRef]

12. Fouda, S.M.; Gad, M.M.; Ellakany, P.; Al-Thobity, A.M.; Al-Harbi, F.A.; Virtanen, J.I.; Raustia, A. The effect of nanodiamonds on candida albicans adhesion and surface character-istics of PMMA denture base material—An in vitro study. *J. Appl. Oral Sci.* **2019**, *27*, e20180779. [CrossRef] [PubMed]

13. Szunerits, S.; Barras, A.; Boukherroub, R. Antibacterial Applications of Nanodiamonds. *Int. J. Environ. Res. Public Health* **2016**, *13*, 413. [CrossRef]

14. Mochalin, V.N.; Shenderova, O.; Ho, D.; Gogotsi, Y. The properties and applications of nanodiamonds. *Nat. Nanotechnol.* **2012**, *7*, 11–23. [CrossRef]

15. Maitra, U.; Prasad, K.E.; Ramamurty, U.; Rao, C.N.R. Mechanical properties of nanodiamond-reinforced polymer-matrix composites. *Solid State Commun.* **2009**, *149*, 1693–1697. [CrossRef]

16. Al-Harbi, F.A.; Abdel-Halim, M.S.; Gad, M.M.; Fouda, S.M.; Baba, N.Z.; AlRumaih, H.S.; Akhtar, S. Effect of Nanodiamond Addition on Flexural Strength, Impact Strength, and Surface Roughness of PMMA Denture Base. *J. Prosthodont.* **2018**, *28*, e417–e425. [CrossRef]

17. Banerjee, R.; Banerjee, S.; Prabhudesai, P.; Bhide, S. Influence of the processing technique on the flexural fatigue strength of denture base resins: An in vitro investigation. *Indian J. Dent. Res.* **2010**, *21*, 391–395. [CrossRef]

18. Abdulwahhab, S.S. High-impact strength acrylic denture base material processed by autoclave. *J. Prosthodont. Res.* **2013**, *57*, 288–293. [CrossRef] [PubMed]

19. Ali, I.L.; Yunus, N.; Abu-Hassan, M.I. Hardness, Flexural Strength, and Flexural Modulus Comparisons of Three Differently Cured Denture Base Systems. *J. Prosthodont.* **2008**, *17*, 545–549. [CrossRef]

20. Durkan, R.; Özel, M.B.; Bagis, B.; Usanmaz, A. In vitro comparison of autoclave polymerization on the transverse strength of denture base resins. *Dent. Mater. J.* **2008**, *27*, 640–642. [CrossRef]

21. Gungor, H.; Gundogdu, M.; Alkurt, M.; Duymus, Z.Y. Effect of polymerization cycles on flexural strengths and microhardness of different denture base materials. *Dent. Mater. J.* **2017**, *36*, 168–173. [CrossRef] [PubMed]

22. Avazkonandeh-Gharavol, M.; Sajjadi, S.; Zebarjad, S.M.; Mohammadtaheri, M.; Abbasi, M.H.; Alimardani, M.; Mossaddegh, K. Effect of heat treatment of nanodiamonds on the scratch behavior of polyacrylic/nanodiamond nanocomposite clear coats. *Prog. Org. Coatings* **2013**, *76*, 1258–1264. [CrossRef]

23. Gale, M.; Darvell, B. Thermal cycling procedures for laboratory testing of dental restorations. *J. Dent.* **1999**, *27*, 89–99. [CrossRef]

24. Gad, M.M.; Al-Thobity, A.M.; Fouda, S.M.; Näpänkangas, R.; Raustia, A. Flexural and Surface Properties of PMMA Denture Base Material Modified with Thymoquinone as an Antifungal Agent. *J. Prosthodont.* **2020**, *29*, 243–250. [CrossRef]

25. Alzayyat, S.T.; Almutiri, G.A.; Aljandan, J.K.; Algarzai, R.M.; Khan, S.Q.; Akhtar, S.; Matin, A.; Gad, M.M. Antifungal Efficacy and Physical Properties of Poly (methylmethacrylate) Denture Base Material Reinforced with SiO_2 Nanoparticles. *J. Prosthodont.* **2021**, *30*, 500–508. [CrossRef]

26. Gad, M.M.; Abualsaud, R.; Rahoma, A.; Al-Thobity, A.M.; Al-Abidi, K.S.; Akhtar, S. Effect of zirconium oxide nanoparticles addition on the optical and tensile properties of polymethyl methacrylate denture base material. *Int. J. Nanomed.* **2018**, *ume 13*, 283–292. [CrossRef]

27. Murat, S.; Alp, G.; Alatalı, C.; Uzun, M. In Vitro Evaluation of Adhesion of Candida albicans on CAD/CAM PMMA-Based Polymers. *J. Prosthodont.* **2019**, *28*, 873–879. [CrossRef] [PubMed]

28. Hashem, M.; Rez, M.F.A.L.; Fouad, H.; Elsarnagawy, T.; Elsharawy, M.A.; Umar, A.; Assery, M.; Ansari, S.G. Influence of titanium oxide nanoparticles on the physical and thermomechanical behavior of Poly Methyl Methacrylate (PMMA): A denture base resin. *Sci. Adv. Mater.* **2017**, *9*, 938–944. [CrossRef]

29. Hamid, S.K.; Alghamdi, L.A.; Alshahrani, F.A.; Khan, S.Q.; Matin, A.; Gad, M.M. In Vitro Assessment of Artificial Aging on the Antifungal Activity of PMMA Denture Base Material Modified with ZrO_2 Nanoparticles. *Int. J. Dent.* **2021**, *2021*, 5560443. [CrossRef] [PubMed]

30. Aszrin, F.N.; Takarini, V.; Hasratiningsih, Z.; Purwasasmita, B.S. Translucency Evaluation of Polymethyl Methacrylate (PMMA) Reinforced with ZrO_2-Al_2O_3-SiO_2 Filler System in Fabricating Indirect Restoration. *UI Proc. Health Med.* **2017**, *1*, 48–52. [CrossRef]

31. Tsugawa, K.; Ishihara, M.; Kim, J.; Hasegawa, M.; Koga, Y. Large-area and low-temperature nanodiamond coating by microwave plasma chemical vapor deposition. *New Diam. Front. Carbon Technol* **2006**, *16*, 337–346.

32. Nakajima, M.; Arimoto, A.; Prasansuttiporn, T.; Thanatvarakorn, O.; Foxton, R.M.; Tagami, J. Light transmission characteristics of dentine and resin composites with different thickness. *J. Dent.* **2012**, *40*, e77–e82. [CrossRef] [PubMed]

33. Gad, M.M.; Abualsaud, R.; Alqarawi, F.K.; Emam, A.-N.M.; Khan, S.Q.; Akhtar, S.; Mahrous, A.A.; Al-Harbi, F.A. Translucency of nanoparticle-reinforced PMMA denture base material: An in-vitro comparative study. *Dent. Mater. J.* **2021**, *40*, 972–978. [CrossRef]

34. Mangal, U.; Kim, J.Y.; Seo, J.Y.; Kwon, J.S.; Choi, S.H. Novel Poly (Methyl Methacrylate) Containing Nanodiamond to Improve the Mechanical Properties and Fungal Resistance. *Materials* **2019**, *12*, 3438. [CrossRef] [PubMed]

35. Lee, D.-K.; Kim, S.V.; Limansubroto, A.N.; Yen, A.; Soundia, A.; Wang, C.-Y.; Shi, W.; Hong, C.; Tetradis, S.; Kim, Y.; et al. Nanodiamond—Gutta Percha Composite Biomaterials for Root Canal Therapy. *ACS Nano* **2015**, *9*, 11490–11501. [CrossRef]

36. Najeeb, S.; Khurshid, Z.; Agwan, A.S.; Zafar, M.S.; Alrahabi, M.; Bin Qasim, S.; Sefat, F. Dental Applications of Nanodiamonds. *Sci. Adv. Mater.* **2016**, *8*, 2064–2070. [CrossRef]

37. Lee, J.-H.; Jo, J.-K.; Kim, D.-A.; Patel, K.D.; Kim, H.-W.; Lee, H.-H. Nano-graphene oxide incorporated into PMMA resin to prevent microbial adhesion. *Dent. Mater.* **2018**, *34*, e63–e72. [CrossRef] [PubMed]

38. Wehling, J.; Dringen, R.; Zare, R.N.; Maas, M.; Rezwan, K. Bactericidal Activity of Partially Oxidized Nanodiamonds. *ACS Nano* **2014**, *8*, 6475–6483. [CrossRef] [PubMed]

39. Pereira-Cenci, T.; Pereira, T.; Cury, A.D.B.; Cenci, M.S.; Rodrigues-Garcia, R.C.M. In vitro Candida colonization on acrylic resins and denture liners: Influence of surface free energy, roughness, saliva, and adhering bacteria. *Int. J. Prosthodont.* **2007**, *20*, 308–310.

40. Sipahi, C.; Anil, N.; Bayramli, E. The effect of acquired salivary pellicle on the surface free energy and wettability of different denture base materials. *J. Dent.* **2001**, *29*, 197–204. [CrossRef]

41. Lazarin, A.A.; Machado, A.L.; Zamperini, C.A.; Wady, A.F.; Spolidorio, D.M.P.; Vergani, C.E. Effect of experimental photopolymerized coatings on the hydrophobicity of a denture base acrylic resin and on Candida albicans adhesion. *Arch. Oral Biol.* **2013**, *58*, 1–9. [CrossRef]

42. Gad, M.M.; Abualsaud, R.; Rahoma, A.; Al-Thobity, A.M.; Akhtar, S.; Fouda, S.M. Double-layered acrylic resin denture base with nanoparticle additions: An in vitro study. *J. Prosthet. Dent.* **2020**. [CrossRef] [PubMed]

Article

Evaluation of the Sensitivity of Various Reinforcement Patterns for Structural Carbon Fibers to Open Holes during Tensile Tests

Elena Strungar *, Dmitrii Lobanov and Valery Wildemann

Center of Experimental Mechanics, Perm National Research Polytechnic University, 614990 Perm, Russia; cem.lobanov@gmail.com (D.L.); wildemann@pstu.ru (V.W.)
* Correspondence: cem.spaskova@mail.ru; Tel.: +7-95-0454-6321

Abstract: This paper is devoted to the experimental study of polymeric composite specimens, with various types of reinforcement, in order to evaluate the breaking strength of specimens with open holes when undergoing uniaxial compression and tensile tests. Four types of interlaced 3D woven preforms were considered (orthogonal, orthogonal combined, with pairwise inter-layer reinforcement, and with pairwise inter-layer reinforcement and a longitudinal layer), with a layered preform used for comparison. Tensile tests of solid specimens without a hole, under ASTM D 3039, and of specimens with an open hole, under ASTM D 5766, were carried out using the Instron 5989 universal electromechanical testing system. Movements and strains on the specimen surface were recorded using a Vic-3D contactless optical video system and the digital images correlation method (DIC). For all the series of carbon fiber tension specimens, strain and stress diagrams, mechanical characteristics, and statistical processing for 10 specimens were obtained. The paper evaluated deformation fields for certain points in time; the obtained fields showed an irregular distribution of deformation and dependency on types of reinforcing fibers. A coefficient of strength variation is introduced, which is defined as a ratio of the ultimate stress limits obtained on solid samples with and without open holes. Within the framework of ASTM D 5766, when calculating the ultimate stress, the hole is not taken into account, and the paper shows that for certain structures a hole cannot be excluded. The hole size must not be neglected when calculating the ultimate stress.

Keywords: carbon-fiber composite; 3D reinforced composite; digital image correlation

1. Introduction

An obvious disadvantage of conventional polymeric composite materials, in the form of fabric-based laminates, is their relatively low inter-layer strength. Nowadays, spatial-reinforced fillers or 3D fabrics are proposed to prevent this. Multi-layered carbon fabrics of various weavings are used as reinforcement materials for carbon fibers, operating under complex conditions of high-speed aerodynamic flows, vibrations, and high temperatures. Three-dimensional woven composites, developed using conventional weaving technology, have better characteristics of thickness and a higher impact strength as compared with conventional layered composites [1–4].

Researchers have achieved great success in studying the mechanical properties of composite laminates with an open hole and have recently started to study 3D textile composites [5–7]. The work [2] studies the failure mechanisms of 3D orthogonal woven composites made of E-glass and epoxy resin with drilled and molded holes using X-ray technology. The authors of [3,4] analyzed the fatigue durability of 2.5D woven composites with a central hole at room and elevated temperatures, and these papers also studied plates with open holes of various diameters during tensile tests.

Composites are used for complex structures where various elements are bolted or riveted. Thus, understanding and predicting the mechanical behavior of composite elements of structures with holes have become necessary in order to design complex irregular

structures. Stress concentration may lead to failure and significantly reduced strength. The analysis of the effects of stress concentration on the behavior of composite materials is an important topic; they are believed to cause a relatively high strength reduction as compared with composite objects without holes [8]. When structural parts are subjected to various loads during operation, high-stress concentration may appear near the hole and cause a reduction in mechanical characteristics. The studies [9–12] clearly show that the sensitivity of the composites in the presence of holes corresponds to an increase in damage within the composite until final failure. Mechanisms forming the damage zone in composites include many interacting types of damage: matrix fractures, laminations, fractures of transverse layers, etc. Averbukh and Madakur [13] gave an overview of the types of damage, which depend on placement, material properties, and geometry. Lamination is one of the primary defects that occur when drilling holes in composite objects and can be an important limiting factor in using composite materials since the drilling process causes micro-fractures that are a concentrated source of high stress.

Due to the very complex damages to composite structures with holes, all failure models contain approximated solutions or suggestions that have been more or less confirmed by experimental observations [14–19]. Therefore, experimental methods are required to improve models and confirm their results. Various experimental methods are available to detect localized damages caused by mechanical loading in composites with holes [11,20–23].

When measuring mechanical characteristics, devices are generally applied to detect movements using two points. Such measurements do not provide complete information on the distribution of the deformations. This information can be obtained when using optical methods for measuring deformation. One such method, which is widely used in connection with the development of computer-based imaging techniques, is the correlation of digital images. This method is based on analyzing the area of interest using a couple of digital photos made before and after specimen deformation [24]. Deformation measured by a strain gauge reflects strain changes in a specific point in the material, while deformation measured by DIC pays more attention to strain changes across a complete field. The strain-gauge method is more accurate in detecting some sensitive areas, while the DIC method is most suitable for the overall monitoring of deformation along the entire surface of the composite specimen. When the material fails, the strain gauge can be most accurate in finding the failure moment, while it is harder to find it using DIC [4]. Taking into account that the behavior of composite structures may differ in various types of tests, the work [25] carried out an experimental study of shear properties in spatial-reinforced composites using the Iosipescu ASTM D5379. Recommendations were made to obtain and mathematically model experimental data using a contactless optical video system.

The paper [25] shows the features of using the Iosipescu ASTM D5379 for a composite with layer-to-layer reinforcement.

This work is a continuation of a comprehensive study of 3D woven carbon fiber-reinforced plastics under different types of loading. Previously, the authors in works investigated a total of eight structures (orthogonal, orthogonal conjoined, with layer-to-layer reinforcement, with layer-to-layer reinforcement and a longitudinal layer, with layer-to-layer conjoint reinforcement, and with through layer-to-layer reinforcement) [6–8]. In the considered work, five configurations were selected, one type from each pair. Such reinforcement schemes were studied as model ones for studying the implementation of mechanical properties and subsequent transfer (transition) to the modeling, design, and manufacture of high-load and medium-load structural elements for critical purposes. Through the analysis of the mechanical strength of fabric-based composites, the performance advantages of 3D reinforced composites are further derived [26,27].

The main aim of this article is an evaluation of the sensitivity of various reinforcement patterns for structural carbon fibers to open holes during tensile tests. This study is required to understand the role of composite damage mechanisms, compare the performance of various reinforcement types, and evaluate the sensitivity to open holes. Damages occurring around the holes, and the nature of their distribution along the entire surface, were studied

using the Vic-3D contactless optical video system and the DIC method of correlating digital images.

2. Materials, Experiments and Methods

2.1. Material

A spatially reinforced carbon fiber composite, based on T26 epoxy resin and AKSA A-49 carbon fiber, was used as the material for this study. A number of mechanical tests were carried out for the uniaxial compression of composite specimens with a round concentrator in the form of a hole along the symmetry axis in the specimen (as per the specimen in Figure 1b, W1 = W2 = 15 mm and L1 = L2 = 147 mm). Preforms of stripe specimens were made using 3D weaving by various weaving methods (Types 1–4), as well as layered preforms (Type 5). Four weaving patterns of 3D woven preforms were considered: orthogonal (Type 1); orthogonal combined (Type 2); with pairwise inter-layer reinforcement (Type 3); and with pairwise inter-layer reinforcement and a longitudinal layer (Type 4). In the central part of the rectangular specimens, which were $300 \times 36 \times 4$ mm in size ($L \times W \times h$) (under ASTM D 5766), there was a concentrator shaped as a single open hole, 6 mm in diameter, and specimens without a concentrator were $250 \times 25 \times 4$ mm ($L \times W \times h$) in size (ASTM D 3039). Since holes were made in the specimens by drilling, defects could form around the holes. Using the Carl Zeiss SteREO Discovery V12 stereo microscope, it was found that damages represented by small shears of the binder were located on outer surfaces around the edge of the holes. The overall extent of plate damage was on average less than 1% of the working volume.

Testing schemes (a) and sketches of specimens (b) without and with an open hole are given in Figure 1. Ten specimens in each group were tested.

2.2. Equipment

Experimental studies were carried out using the large-scale research facilities «Complex of testing and diagnostic equipment for studying properties of structural and functional materials under complex thermomechanical loading» at the PNRPU.

The tests were carried out at the Center of Experimental Mechanics of the Perm National Research Polytechnic University in the city of Perm, Russia.

Tensile tests were carried out using the Instron 5989 ($\pm$ 600 kN) and Instron 5982 ($\pm$ 100 kN) universal electromechanical testing systems with a movable grip speed of 2 mm/min (Figure 1). The loading was recorded by a load cell up to 100 kN and 600 kN. The loading measurement accuracy is 0.5% of the measured value within 0.2–1% of the nominal capacity of the load cell.

Movements and strains on the specimen surface were recorded using a Vic-3D contactless optical video system and the digital images correlation (DIC) method. Video recording of the deformation process was done using Limess 2,0/28/0901 lenses. The filming speed was 15 frames per second with an installed camera resolution of 4.0 MPa. Using a contactless optical video system requires the synchronization of experimental data with the loading process.

The testing system controller was connected to a 16-bit high-speed NI USB-6251 ADC unit supplied with a signal for traverse loading and movement (according to the integrated sensor). The Vic-3D video system was connected to the ADC unit.

2.3. Study Methods

Tensile tests of solid specimens without a hole were carried out under ASTM D 3039 using Instron 5982 ($\pm$ 100 kN), and tensile tests of specimens with an open hole were carried out under ASTM D 5766 using Instron 5989 ($\pm$ 600 kN).

The tensile testing results of specimens with an open hole, and without a hole, were used to find the respective mechanical characteristics. The comparison was based on the maximum stresses.
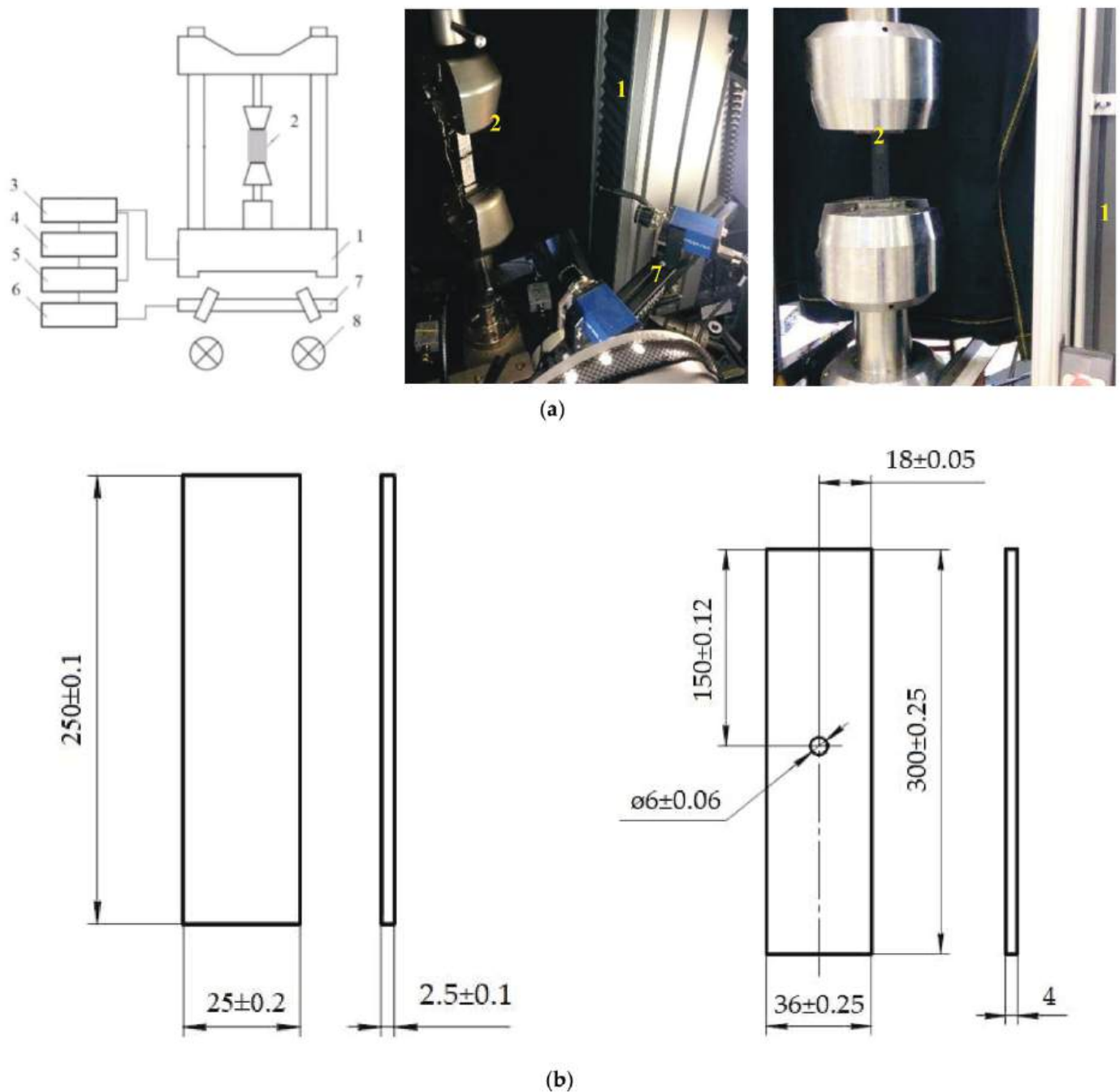
Figure 1. Principled testing scheme for the uniaxial tension of specimens (**a**): 1—test machines, 2—sample installed in the grips, 3—test system controller, 4—PC from which the machine is controlled, 5—synchronization block, 6—PC from which the video system is controlled, 7—cameras installed on tripod, 8—backlight system. Scheme of specimens without an open hole and with an open hole (**b**).

Before testing and before loading, a fine coating must be applied to the surface. The latter ensures an accurate determination of movements and increases the contrast of the surface. A number of black and white points were applied to the surface of the specimen using spray paint. In the DIC method, a zero-mean normalized sum of squared difference criterion was selected since it is the least sensitive to illumination changes during tests. During post-processing by the Vic-3D system, the strain components were calculated using the finite strain tensor in the Lagrange representation $\varepsilon_{ij} = \frac{1}{2}\left(u_{i,j} + u_{j,i} + u_{k,i}u_{k,j}\right)$. The Oy axis is directed along the specimen (along the elongation axis), and the Ox axis is

perpendicular to the loading axis in the specimen plane. When building loading diagrams, an additional software module of the virtual extensometer video system was used to track a mutual shift between two points on the surface of the specimen in relation to the applied force.

The contactless optical system's accuracy is determined by the technical characteristics of lenses and digital cameras, namely the matrix sensitivity, resolution, and permissible frame frequency. The accuracy of obtained experimental data is also influenced by the surface of the specimen and the configuration and calibration of cameras [24]. Upon test results given in [6], a conclusion was drawn that by using the Vic-3D digital optical system, it is possible to determine the strain on a fixed base with an accuracy comparable to the data on a suspended longitudinal strain sensor whose maximum possible deviation from the measured value is 0.15%.

2.4. The Method of Using Contactless 3D Digital Optical Systems

When processing digital photos, vector shifts are not calculated in each individual point of the image (in pixels), but rather sampling is done in the area of study in small local sub-areas or, in other words, subsets (correlation areas) X × X in size [24]. The subset size has a significant effect on the accuracy of the correlation analysis and the detail of movement fields and strains along the surface of the studied object, as well as the size of the zone occurring at the edge or near stress concentrators (holes, inclusions, fractures, defects). The step defines the distance in pixels between points (central pixels of the subset) that are analyzed during mathematical processing [24].

The sub-area size (X) and increment (ΔX) were selected as per the filing conditions, calibration results of the stereo system, as well as the dependency on geometric parameters of the study object and structural specifics of the specimen materials.

This paper takes into account structural features occurring on the surface of a composite material, which were used to select increment ΔX. The value of increment ΔX depends on the size of the structural element of the material (δ) that was found from a photo made using the Carl Zeiss SteREO Discovery V12 stereomicroscope (Figure 2).
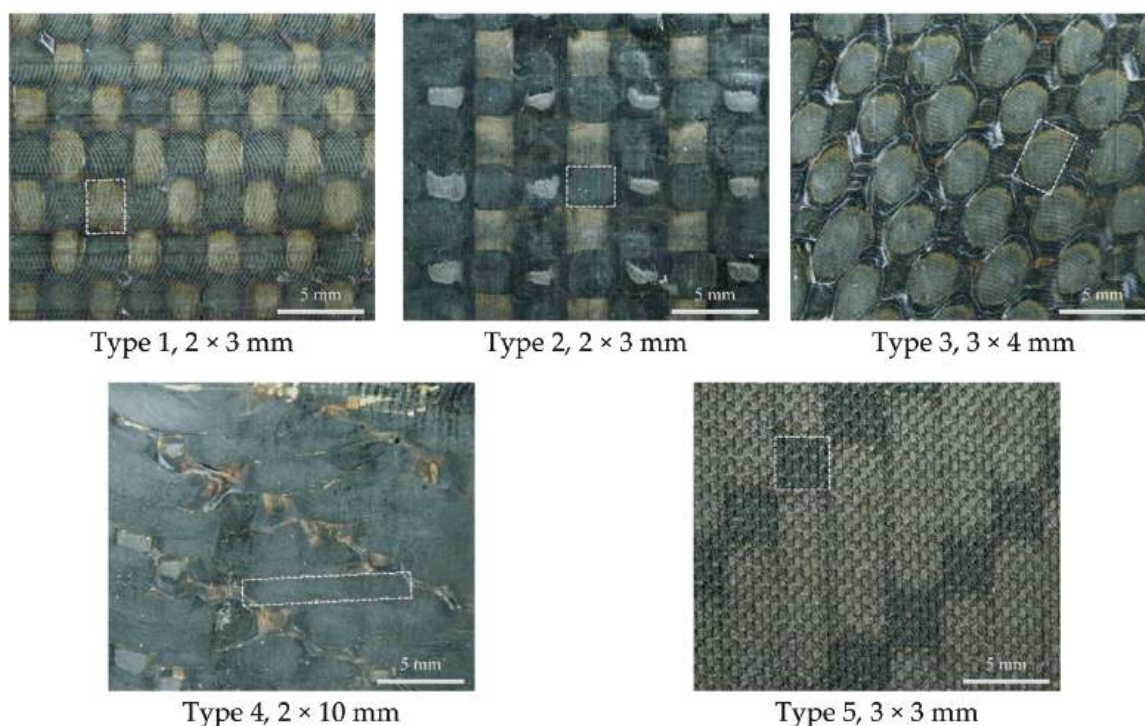
Figure 2. Photo of the surface of samples of three-dimensional-reinforced composites of various weaving patterns with a highlighted structural element (δ).

Since the numerical image processing parameters have a significant influence on the results of movement fields and strains, the presentation of results obtained by the digital image correlation method must include the subset size (X), increment (ΔX), number of points (N) for the area under study, size of the composite material structural element (δ), and pixel size (s) [28–30] (Table 1).

Table 1. Correlation analysis parameters for polymeric composite specimens with various reinforcement types.

Reinforcement Types	X, Pixel	ΔX, Pixel	N	δ, mm	s, mm
Type 1	43	3	20,383	2 × 3	0.083
Type 2	47	3	21,985	2 × 3	0.076
Type 3	55	5	13,650	3 × 4	0.076
Type 4	51	5	19,529	2 × 10	0.084
Type 5	55	3	18,500	3 × 3	0.081

It should be noted that the selection of the parameters of the correlation analysis was done taking into account the material's structural irregularity, which may affect the recording scale of the strains. To change structural strains, a smaller increment must be set that takes into account the structure of the material [28–30].

The studies show that parameters should be selected taking into account the size of the material's structural irregularity. Since the parameters of numerical image processing have a substantial effect on the results, the conclusion was drawn that when presenting these data, the following parameters must be indicated: subset size, increment, number of points for the area under study, size of the composite material structural element, and pixel size.

3. Test Results and Discussion

For all the series of carbon fiber tension specimens tested under ASTM D 3039, strain and stress diagrams (Figure 3), the ultimate strength, and statistical processing for 10 specimens (Table 2) were obtained.

Table 2. Mean ultimate strength (ASTM D 3039) and ultimate stresses (ASTM D 5766) for carbon fiber specimens of the studied reinforcement types.

Reinforcement Types	σ_b, MPa	CV, %	F^{OHTu}, MPa	CV, %
Type 1	940 ± 65	6.91	929 ± 50	5.38
Type 2	922 ± 119	12.91	1129 ± 51	4.52
Type 3	599 ± 39	6.51	419 ± 22	5.25
Type 4	758 ± 60	7.92	649 ± 38	5.85
Type 5	317 ± 54	17.03	358 ± 11	3.07

According to the test results, it can be noted that in accordance with the classification of failure types according to ASTM D 3039, all tested samples were analyzed using a three-part failure mode code (the first character means Failure Type; the second character means Failure Area; and the third character means Failure Location).

Type 1 and Type 2 CFRP samples were destroyed by the LAT (L, Lateral; A, At grip/tab; T, Top) and LGM (L, Lateral; G, Gauge; M, Middle) mechanisms. The Type 3 samples were destroyed by the LGM mechanism. Samples of Type 4 were destroyed by the LGM and AGM (A, Angled; G, Gauge; M, Middle) mechanisms. Samples of Type 5 were destroyed by the DGM (D, edge Delamination; G, Gauge; M, Middle) mechanism.

Analyzing the deformation diagrams for samples of Type 5, it can be observed that when 65–70% of the ultimate strength was reached, the slope of the curves changed.

The authors attribute this phenomenon to the appearance of local damage in the specimen in the form of inter-layer delamination, which subsequently developed to the macrolevel and led to the complete destruction of the specimen.
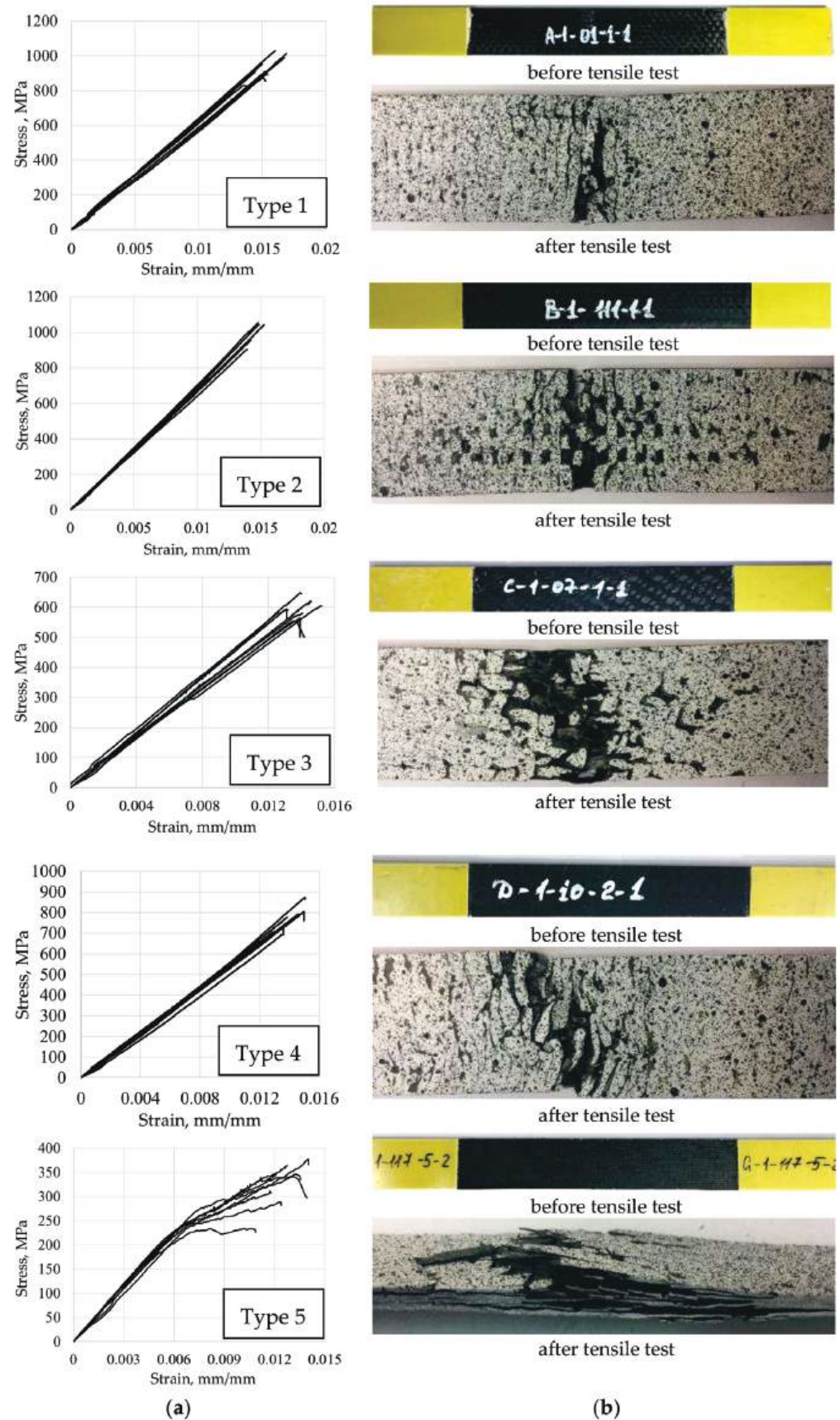
Figure 3. Deformation diagrams (**a**) and view of CFRP specimens of various reinforcement schemes before and after (**b**) the uniaxial tensile test (according to ASTM D 3039).

Figure 4 presents loading diagrams for specimens with an open hole tested under ASTM D 5766, which are characteristic of each reinforcement type. The tensile and specimen tests, with an open hole, show that polymeric composite specimens with orthogonal (Type 1) and orthogonal-combined (Type 2) interweaving schemes have a high ultimate load as compared with specimens with inter-layer reinforcement (Type 3, Type 4) and layered specimens (Type 5). For all carbon fiber specimens with different reinforcement types, the loading diagrams show breaks related to structural failure. Figure 5 gives photos of failed specimens of all reinforcement types with characteristic damages in the area of the hole. In general, almost all curves on the loading diagram (Figure 4) are linear. In some cases, at a later loading stage, the curves show obvious breaks caused by permanent local damages and the reduced bearing capacity of the structure (Types 1, 2, and 3). By analyzing the failure damage of carbon fiber specimens with a hole, it can be noted that Type 1 specimens under the ASTM D 5766 (analog ASTM D 3039) classification failed predominantly under the LGM mechanism. Type 2 specimens failed under various mechanisms: half of them failed under the LGM mechanism, while others failed under the OGM (O, Other; G, Gauge; M, Middle), OMV (O, Other; V, Various; M, Middle), SGM (S, long. Splitting; G, Gauge; M, Middle), and OUU (O, Other; U, Unknown; U, Unknown) mechanisms. For Type 3 specimens, the LGM and AGM mechanisms prevailed, while the MGM (M, Multi-mode; G, Gauge; M, Middle) and AGM mechanisms prevailed for Type 4 specimens. The Type 5 specimens failed under a single mechanism (MGM) (Figure 5). The destruction mechanism (Type 5) can be classified as multiple inter-layer delamination in the area of an open hole (concentrator) with a subsequent detachment of the surface layers.
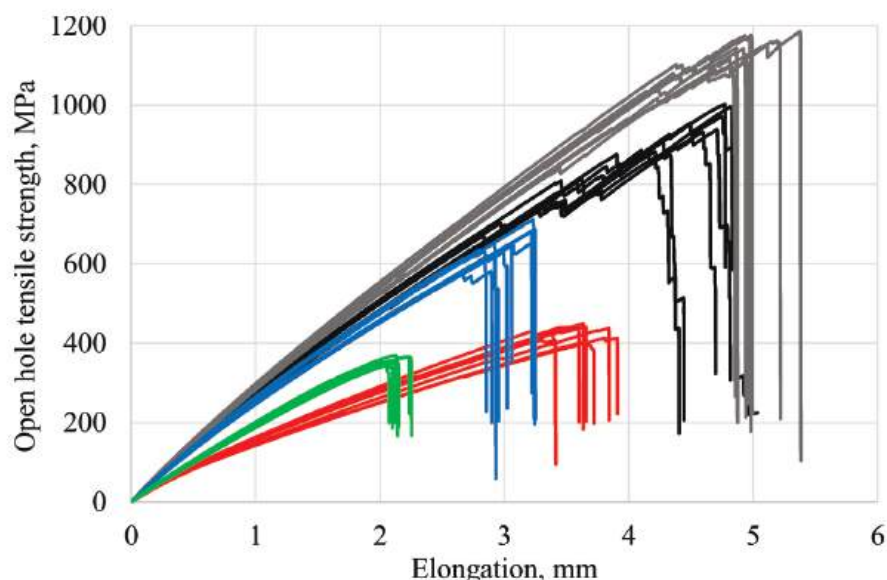
Figure 4. Loading diagrams of CFRP specimens with an open hole in tension (according to ASTM D 5766) with different reinforcement schemes: Type 1—black curves; Type 2—grey curves; Type 3—red curves; Type 4—blue curves; Type 5—green curves.

Analyzing the deformation diagrams, it can be observed that specimens of Type 1 and Type 2 are characterized by disruptions in the loading diagram in the ascending section. For Type 1 samples, breakdowns in the ascending section of the diagram were recorded when reaching from 60 to 70% of the F^{OHTu} values; for Type 2 samples, breakdowns were recorded when the F^{OHTu} reached 70 to 80%.

The authors attribute these phenomena to the fact that the reinforcement system rotates in the direction of load application, which leads to local fractures in the matrix–fiber system, followed by redistribution of the load to neighboring nodes, and so on until the next local failure or complete destruction of the sample. It is also worth noting that the Type1 and Type 2 specimens have the largest deformation margin.
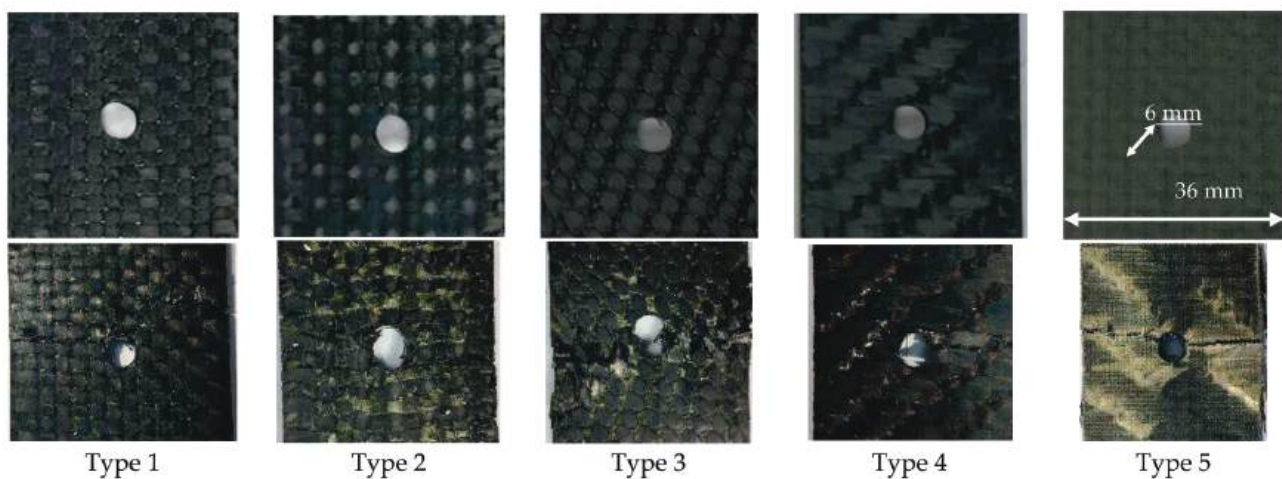
Figure 5. Photographs of CFRP samples in the vicinity of the concentrator before and after tensile tests.

Test results for each group of specimens gave the mechanical characteristics presented in Table 2, mean values (x), mean-square deviations (S), and variation coefficients (V).

It should be noted that ultimate open hole tensile strength F^{OHTu} refers to the ratio between the maximum loading and the initial cross-sectional area of the tested specimen (excluding the hole). The maximum load P_{max} refers to the maximum load prior to failure (Formula (1)).

$$F^{OHTu} = \frac{P_{max}}{hw'} \tag{1}$$

To evaluate irregular strain fields obtained using the video system, specimens with reinforcement types 2, 4, and 5 were considered, which have the highest (Type 2), medium (Type 4), and minimal (Type 5) ultimate loading (Figure 6). The Oy axis is directed along the specimen (along the elongation axis), while the Ox axis is perpendicular to the loading axis in the specimen plane.

The obtained data show that the concentration of stress on the edge of the specimen hole was gradually becoming prominent as the loading developed. The areas of maximum and minimal strain in the specimens appeared on the left/right side and upper/lower side of the holes, respectively, which resulted in a symmetric distribution of the strain field around the edge of the hole. However, at the early stage of loading, strains were not symmetrical. Strains in the upper right part of the specimens were much larger than in other parts, but this phenomenon disappeared at a later loading stage.

For a more detailed analysis, the distribution of longitudinal stress ε_{yy} was evaluated on the specimen surface (Figure 7d) along line L drawn from the hole to the plate edge (12 mm away). Strain diagrams were built at specific stress levels of 10% (Figure 7a), 40% (Figure 7b), and 70% (Figure 7c) of the ultimate stress F^{OHTu}.

The results show that the behavior of specimens with an open hole, with reinforcement types 1, 4, and 5, remained linear-elastic until failure. For reinforcement types 2 and 3 for higher tensile loads, the maximum strain shifted to the plate edge some distance from the hole. The schematic distribution of the strain ε_{yy} from the hole to the plate edge along line L is shown in Figure 7e. Similar experimental results were obtained by researchers in [16,31,32].

Table 3 shows the correspondence between the maximum longitudinal strains ($\varepsilon_{yy, max}$) and the distance from the hole (l), depending on the material structure. The higher the applied load, the higher the maximum strain. The maximum longitudinal strain $\varepsilon_{yy, max}$ = 1.20% was measured for the structure of specimen Type 2.
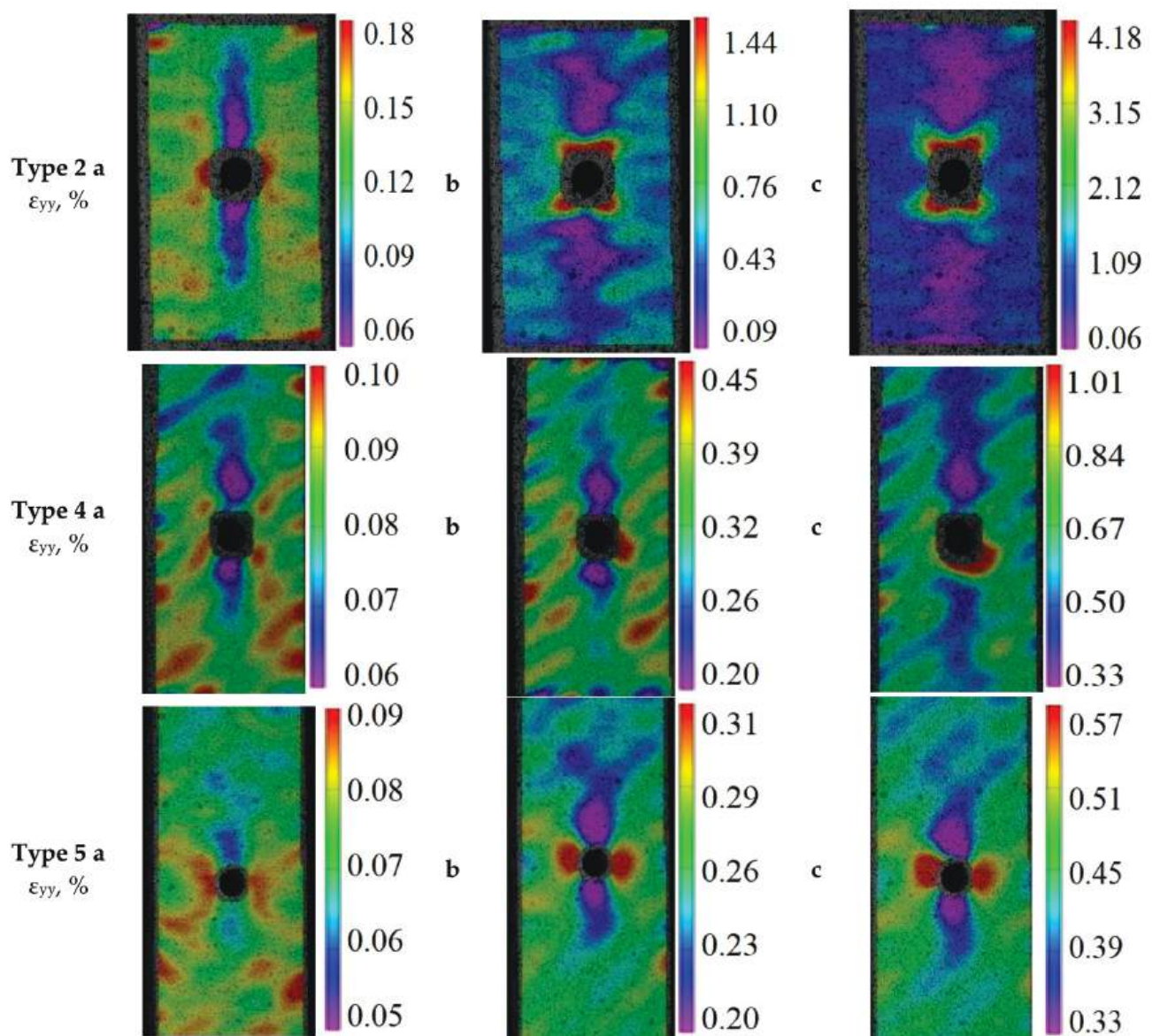
Figure 6. Fields of longitudinal strains ε_{yy} of the surface of specimens of reinforcement types 2, 4, and 5 for a loading of 10% (**a**), 40% (**b**), and 70% (**c**) of the maximum value F^{OHTu}.

Table 3. The correspondence of longitudinal strains to the distance from the hole (l), depending on the material structure.

Reinforcement Types	$\varepsilon_{yy, max}$, %	l, mm
Type 2	1.20	4.13
Type 3	0.95	2.97

It was observed that the higher the applied loading, the higher the maximum strain and the wider the distribution. At a distance from the hole, the distribution of longitudinal strains ($\varepsilon_{yy, max}$) became similar to linear-elastic. It can be suggested that there is a link between the structural element size (δ) and the pixel size ($s \leq 0.080$) (see Table 1) for various reinforcement types and hole sizes (d). Since the hole of the same size (d = 6 mm) includes a number of structural elements that depend on the reinforcement pattern, the strain processes may behave differently, especially when the hole size (d) is comparable to the size of the structural element (δ).
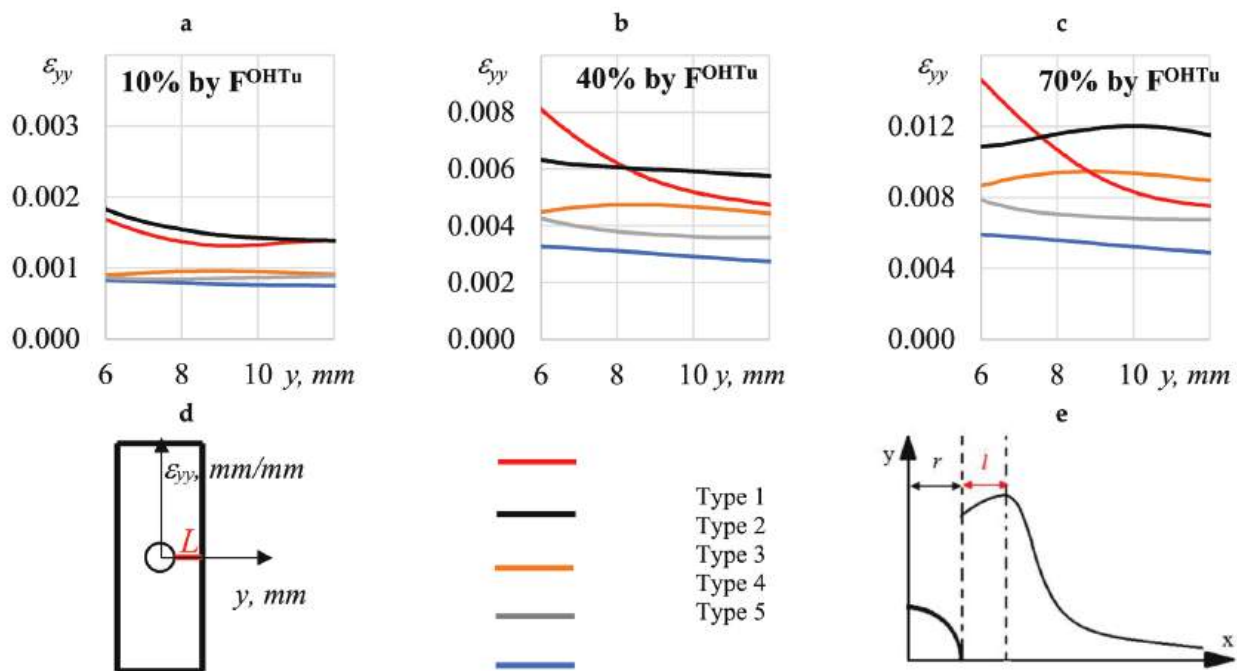
Figure 7. Profiles (ε_{yy}) on the sample surface at specific stress levels of 10% (**a**), 40% (**b**), and 70% (**c**) of the ultimate stress F^{OHTu}. Profiles (ε_{yy}) on the sample surface (**d**). The schematic distribution of the strain (ε_{yy}) (**e**).

In objects with a hole, there is an obvious decrease in the strength (bearing capacity) of the composite in comparison with the same objects without a hole. To evaluate the sensitivity of a reinforcement scheme to a hole, the authors introduced a strength variant coefficient K (Formula (2)), which is defined as a ratio between the ultimate stresses of specimens with the concentrator (F'^{OHTu}) and the ultimate strength of a solid specimen (σ_b).

It should be noted that the ultimate loading F'^{OHTu} refers to the ratio between the maximum loading and the initial cross-sectional area of the tested specimen (given the hole, and a specimen width of 30 mm) (Formula (3)).

$$K = \frac{F'^{OHTu}}{\sigma_b} \tag{2}$$

$$F'^{OHTu} = \frac{P_{max}}{hw} \tag{3}$$

where P_{max} is the maximum load; h is the specimen thickness; and w is the specimen width given the hole (30 mm).

Within the framework of ASTM D 5766, the calculation of the ultimate stress of a specimen with a concentrator (F^{OHTu}) was carried out without taking into account the hole, as per Formula 2, on the assumption that a hole 6 mm in diameter, with the total specimen width of 36 mm, does not affect the bearing capacity. In this case, the strength variance coefficient (K') will be calculated as per Formula (4).

$$K' = \frac{F^{OHTu}}{\sigma_b} \tag{4}$$

where w' is the specimen width without taking into account a hole (36 mm).

In this manner, to compare the obtained results, Table 4 gives mean values with the scattered tensile strength (σ_b) and ultimate stresses in tensile tests of specimens with a hole, taking it into account (F'^{OHTu}), and without a hole, taking it into account (F^{OHTu}), as well as the strength variant coefficients K and K' (under ASTM) for each type of specimen and

reinforcement type. Figure 8 shows the relationship between the ultimate strength and the type of reinforcement in the composite specimens.

Table 4. Test results on the strength variance coefficient for carbon fiber specimens with holes and without holes.

Reinforcement Types	σ_b, MPa	F^{OHTu}, MPa (by ASTM)	F'^{OHTu}, MPa	K	K' (by ASTM)
Type 1	940 ± 65	929 ± 50	1108 ± 60	1.18	0.99
Type 2	922 ± 119	1129 ± 51	1349 ± 60	1.46	1.22
Type 3	599 ± 39	419 ± 22	500 ± 25	0.83	0.70
Type 4	758 ± 60	649 ± 38	777 ± 42	1.02	0.86
Type 5	317 ± 54	358 ± 11	427 ± 12	1.35	1.13
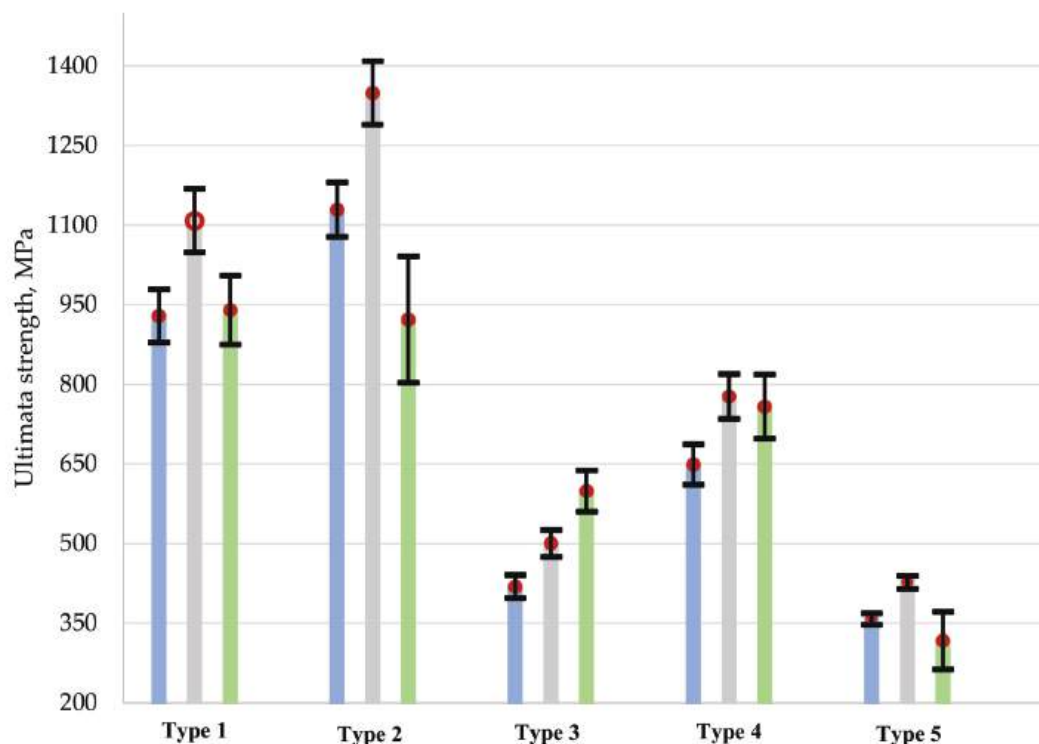
Figure 8. The relationship between the ultimate strength and the reinforcement type in composite specimens. The open hole tensile ultimate stress under ASTM D 5766 F^{OHTu}—blue line; the open hole tensile ultimate strength of specimens with the concentrator F'^{OHTu}—grey line; ultimate stress of solid specimen σ_b—green line.

A comparison of stress concentration coefficients showed that Type 3 reinforcement has the most sensitive effect on the hole. For reinforcement types 1, 2, 4, and 5, the hole did not lead to a significant change in the ultimate stresses, which is related to the material structure and stress re-distribution occurring in the specimen. It can be also observed that the calculation of the ultimate stress F^{OHTu} under ASTM differs from the ultimate stresses F'^{OHTu}.

4. Conclusions

This work included a series of experimental studies of strength in structural carbon fibers with various reinforcement types in tension tests with and without an open hole. The obtained results were analyzed, and the effects of concentrators on the mechanical behavior of carbon fiber specimens were evaluated based on various spatial reinforcement frames. For all series of carbon fiber specimens tested for tension, stress and strain diagrams were obtained. Photos of failed specimens are presented for all reinforcement types with characteristic damages in the area of the open hole. The test results for each group of

specimens gave mechanical characteristics, mean values (x), mean-square deviations (S), and variation coefficients (V).

Using a digital optical video system and the digital image correlation method, strain fields for solid specimens and specimens with an open hole were obtained during the entire loading process. For open-hole specimens, strain distribution diagrams were built in the area of the smallest cross-section and the longitudinal strain distribution on the specimen surface was evaluated. Reinforcement types having the lowest sensitivity in the presence of concentrators were identified.

Within the framework of ASTM D 5766, when calculating the ultimate stress, the hole is not taken into account; nevertheless, the paper shows that, for certain structures, a hole cannot be excluded. Therefore, it can be concluded that the hole size must not be neglected when calculating the ultimate stress.

References

1. Khosravani, M.R.; Zolfagharian, A. Fracture and load-carrying capacity of 3D-printed cracked components. *Extrem. Mech. Lett.* **2020**, *37*, 100692. [CrossRef]
2. Nasser, J.; Zhang, L.; Sodano, H. Sodano Laser induced graphene interlaminar reinforcement for tough carbon fiber/epoxy composites. *Compos. Sci. Technol.* **2021**, *201*, 108493. [CrossRef]
3. Song, J.; Wen, W.; Cui, H.; Wang, Y.; Lu, Y.; Long, W.; Li, L. Warp direction fatigue behavior and damage mechanisms of centrally notched 2.5D woven composites at room and elevated temperatures. *Compos. Sci. Technol.* **2019**, *182*, 107769. [CrossRef]
4. Zhang, Y.; Guo, Q.; Chen, X.; Xie, J.; Chen, L. Effect of apertures on tensile property of warp-reinforced 2.5D woven composites notched plates. *Compos. Struct.* **2020**, *252*, 112693. [CrossRef]
5. Strungar, E.M.; Feklistova, E.V.; Babushkin, A.V.; Lobanov, D.S. Experimental studies of 3D woven composites interweaving types effect on the mechanical properties of a polymer composite material. *Procedia Struct. Integr.* **2019**, *17*, 965–970. [CrossRef]
6. Hilov, P.A.; Babushkin, A.V.; Wildemann, V.E.; Lobanov, D.S.; Staroverov, O.A.; Strungar, E.M.; Krupennikov, V.A. Influence of the reinforcement scheme on mechanical properties of 2d, 3d polymer composites. *IOP Conf. Ser. Mater. Sci. Eng.* **2020**, *953*, 012095. [CrossRef]
7. Strungar, E.M.; Lobanov, D.S.; Zubova, E.M.; Babushkin, A.V. Analysis of the mechanical behavior of spatially reinforced composites with open holes. *IOP Conf. Ser. Mater. Sci. Eng.* **2020**, *953*, 012094. [CrossRef]
8. Pierron, F.; Green, B.; Wisnom, M.R.; Hallett, S.R. Full-field assessment of the damage process of laminated composite open-hole tensile specimens. Part I: Methodology. *Compos. Part A Appl. Sci. Manuf.* **2007**, *38*, 2307–2320. [CrossRef]
9. Touchard-Lagattu, F.B.A.E.; Lafarie-Frenot, M.C. Damage and inelastic deformation mechanisms in notched thermoset and thermoplastic laminates. *Compos. Sci. Technol.* **1996**, *56*, 557–568. [CrossRef]
10. Wu, X.; Fuller, J.D.; Longana, M.L.; Wisnom, M.R. Wisnom Reduced notch sensitivity in pseudo-ductile CFRP thin ply angle-ply laminates with central $0°$ plies. *Compos. Part A Appl. Sci. Manuf.* **2018**, *111*, 62–72. [CrossRef]
11. Dai, S.; Cunningham, P.R.; Marshall, S.; Silva, C. Open hole quasi-static and fatigue characterisation of 3D woven composites. *Compos. Struct.* **2015**, *131*, 765–774. [CrossRef]
12. Czél, G.; Jalalvand, M.; Fotouhi, M.; Longana, M.L.; Nixon-Pearson, O.J.; Wisnom, M.R. Wisnom Pseudo-ductility and reduced notch sensitivity in multi-directional all-carbon/epoxy thin-ply hybrid composites. *Compos. Part A Appl. Sci. Manuf.* **2018**, *104*, 151–164. [CrossRef]

13. Awerbuch, J.; Madhukar, M.S. Notched Strength of Composite Laminates: Predictions and Experiments—A Review. *J. Reinf. Plast. Compos.* **1985**, *4*, 3–159. [CrossRef]

14. Chen, P.; Shen, Z.; Wang, J.Y. Prediction of the strength of notched fiber-dominated composite laminates. *Compos. Sci. Technol.* **2001**, *61*, 1311–1321. [CrossRef]

15. Nuismer, R.J.; Whitney, J.M. Uniaxial failure of composite laminates containing stress concentrations. In *Fracture Mechanics of Composites*; American Society for Testing and Materials: Philadelphia, PA, USA, 1975; pp. 117–142.

16. Lagattu, F.; Lafarie-Frenot, M.C.; Lam, T.Q.; Brillaud, J. Experimental characterization of overstress accommodation in notched CFRP composite laminates. *Compos. Struct.* **2005**, *67*, 347–357. [CrossRef]

17. Bao, H.; Liu, G. Progressive failure analysis on scaled open-hole tensile composite laminates. *Compos. Struct.* **2016**, *150*, 173–180. [CrossRef]

18. Tashkinov, M.A. Modelling of fracture processes in laminate composite plates with embedded delamination. *Frat. Integr. Strutt.* **2016**, *11*, 248–262. [CrossRef]

19. Shi, J.; Tong, M.; Zhou, C.; Ye, C.; Wang, X. Progressive Failure Analysis in Open-Hole Tensile Composite Laminates of Airplane Stringers Based on Tests and Simulations. *Appl. Sci.* **2020**, *11*, 185. [CrossRef]

20. Sket, F.; Enfedaque, A.; López, C.D.; González, C.; Molina-Aldareguía, J.; LLorca, J. X-ray computed tomography analysis of damage evolution in open hole carbon fiber-reinforced laminates subjected to in-plane shear. *Compos. Sci. Technol.* **2016**, *133*, 40–50. [CrossRef]

21. Gao, X.; Yu, G.; Xue, J.; Song, Y. Failure analysis of C/SiC composites plate with a hole by the PFA and DIC method. *Ceram. Int.* **2017**, *43*, 5255–5266. [CrossRef]

22. Caminero, M.A.; Lopez-Pedrosa, M.; Pinna, C.; Soutis, C. Damage monitoring and analysis of composite laminates with an open hole and adhesively bonded repairs using digital image correlation. *Compos. Part B Eng.* **2013**, *53*, 76–91. [CrossRef]

23. Mohammadi, R.; Najafabadi, M.A.; Saeedifar, M.; Yousefi, J.; Minak, G. Correlation of acoustic emission with finite element predicted damages in open-hole tensile laminated composites. *Compos. Part B Eng.* **2017**, *108*, 427–435. [CrossRef]

24. Schreier, H.; Orteu, J.J.; Sutton, M.A. *Image Correlation for Shape, Motion and Deformation Measurements*; University of South Carolina: Columbia, SC, USA, 2009; 364p.

25. Strungar, E.M.; Yankin, A.; Zubova, E.; Babushkin, A.V.; Dushko, A.N. Experimental study of shear properties of 3D woven composite using digital image correlation and acoustic emission. *Acta Mech. Sin.* **2019**, *36*, 448–459. [CrossRef]

26. Xian, G.; Guo, R.; Li, C.; Hong, B. Effects of rod size and fiber hybrid mode on the interface shear strength of carbon/glass fiber composite rods exposed to freezing-thawing and outdoor environments. *J. Mater. Res. Technol.* **2021**, *14*, 2812–2831. [CrossRef]

27. Gui-Hong, X.; Dong, F.; Zhen-Nan, L. Fatigue performance of composite concrete structure specimen (CCS) in flexure. *Mech. Adv. Mater. Struct.* **2019**, *27*, 539–550. [CrossRef]

28. Lobanov, D.S.; Strungar, E.M.; Zubova, E.M.; Wildemann, V.E. Studying the Development of a Technological Defect in Complex Stressed Construction CFRP Using Digital Image Correlation and Acoustic Emission Methods. *Russ. J. Nondestruct. Test.* **2019**, *55*, 631–638. [CrossRef]

29. Tretyakova, T.V.; Dushko, A.N.; Strungar, E.M.; Zubova, E.M.; Lobanov, D.S. Comprehensive analysis of mechanical behavior and fracture processes of specimens of three-dimensional reinforced carbon fiber in tensile tests. *PNRPU Mech. Bull.* **2019**, 175–185. [CrossRef]

30. Lobanov, D.; Strungar, E. Mathematical data processing according to digital image correlation method for polymer composites. *Frat. Integr. Strutt.* **2020**, *14*, 56–65. [CrossRef]

31. Guo, R.; Xian, G.; Li, C.; Huang, X.; Xin, M. Effect of fiber hybridization types on the mechanical properties of carbon/glass fiber reinforced polymer composite rod. *Mech. Adv. Mater. Struct.* **2021**, 1–13. [CrossRef]

32. Strungar, E.; Wildemann, V. Inelastic deformation and destruction of fiber-laminated polymer composites in stress concentration zones. *Frat. Integr. Strutt.* **2020**, *14*, 406–416. [CrossRef]

Antibacterial and UV Protection Properties of Modified Cotton Fabric Using a Curcumin/TiO$_2$ Nanocomposite for Medical Textile Applications

M. M. Abd El-Hady [1,2], **A. Farouk** [1,3], **S. El-Sayed Saeed** [4,*], **and S. Zaghloul** [1]

1   National Research Centre, Institute of Textile Research and Technology, 33 El-Behoth Street, Dokki, P.O. Box 12622, Giza 11311, Egypt; m.aish@qu.edu.sa or Marwa_abdalhady@yahoo.com (M.M.A.E.-H.); asmaa.saleh2015@yahoo.com (A.F.); drsaad_nrc2010@yahoo.com (S.Z.)
2   Department of Physics, College of Science and Arts in Al-Asyah, Qassim University, Buraidah 51452, Saudi Arabia
3   Department of Chemistry, Faculty of Science, King Khalid University, P.O. Box 9004, Abha 62217, Saudi Arabia
4   Department of Chemistry, College of Science, Qassim University, Buraidah 51452, Saudi Arabia
*   Correspondence: s.saeed@qu.edu.sa or saiedelsayed2@yahoo.com

Abstract: Medical textiles are one of the most rapidly growing parts of the technical textiles sector in the textile industry. This work aims to investigate the medical applications of a curcumin/TiO$_2$ nanocomposite fabricated on the surface of cotton fabric. The cotton fabric was pretreated with three crosslinking agents, namely citric acid, 3-Chloro-2-hydroxypropyl trimethyl ammonium chloride (Quat 188) and 3-glycidyloxypropyltrimethoxysilane (GPTMS), by applying the nanocomposite to the modified cotton fabric using the pad-dry-cure method. The chemistry and morphology of the modified fabrics were examined by Fourier transform infrared spectroscopy, energy-dispersive X-ray spectroscopy, and scanning electron microscopy. In addition, the chemical mechanism for the nanocomposite-modified fabric was reported. UV protection (UPF) and antibacterial properties against Gram-positive *S. aureus* and Gram-negative *E. coli* bacterial strains were investigated. The durability of the fabrics to 20 washing cycles was also examined. Results demonstrated that the nanocomposite-modified cotton fabric exhibited superior antibacterial activity against Gram-negative bacteria than Gram-positive bacteria and excellent UV protection properties. Moreover, a good durability was obtained, which was possibly due to the effect of the crosslinker used. Among the three pre-modifications of the cotton fabric, Quat 188 modified fabric revealed the highest antibacterial activity compared with citric acid or GPTMS modified fabrics. This outcome suggested that the curcumin/TiO$_2$ nanocomposite Quat 188-modified cotton fabric could be used as a biomedical textile due to its antibacterial properties.

Keywords: cotton fabric; TiO$_2$ nanoparticles; citric acid; Quat 188; curcumin; antibacterial; UV blocking; durability

1. Introduction

Nowadays, one of the most promising fields of new textile materials is the manufacturing of antimicrobial-acting medical textiles. In fact, extensive work is being put into improving substances and procedures that could provide safe and adequate protection against various microorganisms. For example, chemical materials such as phenols, nitro compounds, and formaldehyde derivatives, have been extensively used in the manufacturing of antibacterial medical textiles [1–4]. However, most of these compounds have serious drawbacks in terms of toxicity and poor biodegradability, which make their use quite limited. In order to avoid these issues, the textile industry has been utilizing natural, nontoxic active substances that have no side effects on people or the environment [5–8].

Fabric modification with nanomaterials designed for enhancing textile properties, such as antibacterial properties [7,9], UV protection [10] wound healing, self-cleaning and military application [11,12], is widely used. In this process, nanoparticles may be incorporated into fabrics for medical applications without affecting their textile properties. In particular, incorporation of antimicrobial agents in the form of nanoparticles can exhibit high levels of antimicrobial activity as well as excellent durability (both in usage and by repetitive laundering cycles), which is much more superior to metal salts or adsorbed quaternary ammonium compounds that operate by leaching from the treated fabrics and are often reduced by laundering [13,14].

Curcumin is a natural material that is used in medicinal textiles. It is a polyphenolic compound and a yellow pigment derived from the ground rhizomes of the Curcuma longa Linn plant, which has a wide variety of beneficial properties. It has a wide range of pharmacological properties, including anti-inflammatory, antioxidative and anti-cancer properties [15,16]. Curcumin contains two phenolic hydroxyl groups and two carbonyl groups in the center, which can form keto-enol tautomers in solution. When it comes to curcumin modifications, the phenolic group is the most important functional group. It is capable of a wide range of reactions, including nucleophilic substitution with organic acids, epoxide and their derivatives [17]. Several experimental studies have indicated that these two groups exist primarily in the enolic form at room temperature [18]. Unfortunately, pure curcumin has a low solubility, which limits its use in medical and clinical applications [19]. In order to overcome this problem, curcumin is used as a complex with other materials in order to enhance its bioavailability [20,21]. Curcumin's therapeutic effectiveness is limited because of its low solubility, absorption, metabolism, and bioavailability [22]. In this regard, curcumin research has recently focused on the production of possible delivery systems to improve its aqueous solubility, stability, bioavailability and its controlled delivery at specific sites. In order to achieve this, curcumin is incorporated into titanium dioxide nanoparticles. In addition, for enhanced antibacterial activity, we chose hydrophilic titanium dioxide nanoparticles to conjugate with hydrophobic curcumin. Titanium dioxide nanoparticles are used in a wide range of consumer products, including sunscreens, cosmetics, pharmaceutical additives, and food coloring agents. They are biodegradable [22] and have good biocompatibility with little or no toxicity in vitro and in vivo. As a result, titanium dioxide nanoparticles may be one of the most promising nanoparticles for a broad variety of medical and pharmaceutical applications. Nano titanium dioxide can be used in biomedical and bioengineering applications due to its special properties and high reactivity [23]. Curcumin was recently used to sensitize TiO_2 for improved photodegradation of dyes [24] and photodegradation of phenols [25]. In addition, a complex of titanium dioxide nanoparticles with curcumin was developed as a wound dressing material using chitosan and polypropylene fabric [26]. The incorporation of positively charged sites, such as cationization, allows for the creation of an electrostatic attraction between the fiber and negatively charged molecules. Cotton cationization yielded new cotton cellulose, which could lead to new uses in cotton pre-treatment and chemical finishing. Previous reports illustrate that cationization of cotton surfaces has been shown to improve silver nanoparticle adsorption [27,28] and dye uptake [29,30].

In the current work, we aimed to develop cellulose-based materials that confer better and more durable antibacterial applications. To achieve this, we prepared a curcumin/TiO_2 nanocomposite for fabrication on the surface of cotton fabric using the pad-dry-cure method. Titanium dioxide nanoparticles in the composite were used to enhance the stability of the curcumin as well as its fabric finishing capacity. To improve the attraction forces between the nanocomposite and the cotton fabric, we used three different crosslinkers, namely 3-Chloro-2-hydroxypropyl trimethyl ammonium chloride (Quat 188), (3 glycidyloxy) propyltrimethoxysilane (GPTMS) and citric acid. This crosslinking process stabilized the curcumin/TiO_2 nanocomposite. Finally, the mechanism of action of the modified fabric was reported and its durability and mechanical properties were investigated under different crosslinking schemes.

2. Experimental

2.1. Materials

Mill bleached pure 100% cotton fabric (138 g/m^2) was supplied by Misr Company for Spinning and Weaving, Mehalla El-Kobra, Egypt.

2.2. Chemicals

3-Chloro-2-hydroxypropyl trimethyl ammonium chloride (69%) of technical grade chemicals (known as Quat 188) was purchased under the commercial name CR-2000 from Aldrich. Titanium dioxide P25 powder was provided by Degussa 3- glycidyloxypropyl-ltrimethoxysilane (GPTMS, 95%) was purchased from ABCR (Karlsruhe, Germany). Curcumin powder (99.8% pure and anhydrous) was purchased from Sigma-Aldrich (Taufkirchen, Germany). Sodium hydroxide, acetic acid, hydrochloric acid and sodium hypophosphite were purchased from Loba Chemie (Mumbai, India). Ethanol was purchased from Fisher chemical (Loughborough, UK)

2.3. Preparation of GPTMS Sol

GPTMS sol was prepared by mixing GPTMS (10 mL) with isopropanol water (20/80 mL) and stirred at 25 °C for 20 min, 1.22 mL of 0.01 M hydrochloric acid solution was then added dropwise to the GPTMS solution and stirred for 1 h at room temperature to obtain the silica sol form [31].

2.4. Preparation of Curcumin: TiO$_2$ Nanocomposites

The solution of 0.5% (w/v) TiO$_2$ nanoparticles was resuspended in 50 mL of isopropyl alcohol. Then, 5% (w/v) curcumin powder in isopropyl alcohol was prepared with stirring. A measurement of 0.5 mL of this solution was then added dropwise to solution of TiO$_2$ with continuous stirring for 3–4 h.

2.5. Cationization of Cotton Fabric

Chemical modification of the cotton fabric through cationization was carried out using the pad-dry-cure method. The experimental procedures adopted were as follows. 3-Chloro-2-hydroxypropyl trimethyl ammonium chloride (Quat 188) was mixed with sodium hydroxide solution at a NaOH/Quat 188 M ratio of 2:1. The cotton fabric was padded in 100 mL of the prepared mixture in two dips and two nips and then squeezed to a wet pick up of about 100%. The fabric was dried at 40 °C for 10 min and cured at 120 °C for 3 min. Finally the cotton fabric was washed with cold water and 1% acetic acid, followed by several washing cycles and dried under the normal laboratory conditions.

2.6. Coating of Cationized Cotton Fabric with TiO$_2$/Curcumin Nanocomposite

Cationized cotton fabrics were padded in 100 mL of the 0.5% (w/v) solution of the TiO$_2$/curcumin nanocomposite prepared solution in two dips and two nips and then squeezed to a wet pick up of 100%. Padded fabrics were dried at 80 °C for 5 min and then cured at 180 °C for 3 min. Treated fabrics were rinsed with hot water, then with cold water, and finally dried at room temperature.

2.7. Coating of Cotton Fabric with GPTMS/Curcumin/TiO$_2$ Nanocomposite

Solution of 2% (w/v) GPTMS sol was added to 0.5% (w/v) solution of the TiO$_2$/curcumin nanocomposite with continuous stirring under sonication for 2 h the cotton fabrics were padded in the 100 mL of the previously prepared solution in two dips and two nips and then squeezed to a wet pick up of 100%. Padded fabrics were dried at 80 °C for 5 min and then cured at 180 °C for 3 min. Treated fabrics were rinsed with hot water, then with cold water, and finally dried at room temperature.

2.8. Coating of Cotton Fabric with Citric Acid/Curcumin/TiO$_2$ Nanocomposite

Aqueous solution of citric acid (30 g/L) with sodium hypophosphite (6% w/w) was added to the 0.5% (w/v) solution of TiO$_2$/curcumin nanocomposite. The cotton fabrics were padded in 100 mL of the previously prepared solution in two dips and two nips and then squeezed to a wet pick up of 100%. The padded fabrics were dried at 80 °C for 5 min and then cured at 180 °C for 3 min. Treated fabrics were rinsed with hot water, then with cold water, and finally dried at room temperature.

3. Characterization

3.1. Fourier Transform Infrared Spectroscopy (FT-IR)

FTIR spectroscopy has been extensively used in cellulose research since it presents a relatively easy method of obtaining direct information on chemical changes that occur during various chemical treatments. ATR-FTIR instrument (JASCO, Model IR 4700, Tokyo, Japan) was used to scan from 4000 to 400 cm^{-1} in ATR mode using KBr as supporting material.

3.2. Scanning Electron Micrograph SEM/EDX Analysis

SEM/EDX Analysis were carried out by using Tescan scanning electron microscope which contains an energy dispersive X-ray (EDX) spectroscopy system (Model vega3, Brono, Czech Republic).

3.3. Antibacterial Test

The antibacterial activity of the treated samples against *Staphylococcus aureus*, (Gram-positive) and *Escherichia coli* (Gram−negative) bacteria were determined using an agar plate. The antibacterial activity of the fabric samples was evaluated by using the disk diffusion method. A mixture of nutrient broth and nutrient agar in 1 L distilled water at pH 7.2, as well as the empty Petri plates, was autoclaved. The agar medium was then cast into the Petri plates and cooled in laminar airflow. Approximately 105 colony-forming units of bacteria were inoculated on the plates and 292 cm^2 of each fabric sample was planted onto the agar plates. All the plates were incubated at 37 °C for 24 h and examined to ascertain whether a zone of inhibition was produced around the samples.

3.4. UV Protection Factor

The ultraviolet protection factor (UPF) was measured using a UV Shimadzu 3101 Spectrophotometer (Shimadzu, Kyoto, Japan). UV Protection and classification according to AS/NZS 4399:1996 were evaluated with a scan range of 200–600 nm.

3.5. The Add-On (%) loading

The add-on (%) loading was calculated as follows:

$$Add - on(\%) = \frac{W_2 - W_1}{W_1} \times 100 \tag{1}$$

where W_1 and W_2 were the weights of the fabric specimens before and after treatment respectively.

3.6. Durability Test

The treated fabric samples were subjected to 20 laundering cycles according the ASTM standard test method (D 737-109 96) to determine the antibacterial durability to washing.

3.7. Tensile Strength

The tensile strength of the fabric samples was determined by the ASTM Test Method D-1682-94 (1994). Two specimens for each treated fabric were tested in the warp direction and the average value was recorded to represent the fabric-breaking load (Lb).

3.8. Statistical Analysis

Results were expressed as a mean value with its standard deviation (mean $\pm$ S.D.) for each sample that was repeated three times (n = 3). Statistical analysis was performed using a Student's t-test and the differences were considered as significant at p-values below 0.05.

4. Results and Discussion

4.1. Mechanism of Deposition of the Curcumin/TiO$_2$ Nanocomposite on the Surface of Cotton Fabric

Figure 1 illustrates the schematic mechanism of formation and fixation of curcumin/TiO$_2$ on the surface of the cotton fabric. At the first stage of this process, formation of the curcumin/TiO$_2$ nanocomposite takes place upon addition of the curcumin solution to the TiO$_2$ nanoparticle solution, which suggested that the curcumin particles dispersed on the surface of the titanium nanoparticles (Figure 1a). This could be attributed to the high metal chelating potential of the diketone functional group located at the center of the curcumin molecule where the diketone group effectively chelates the TiO$_2$ nanoparticles through charge transfer complex formation [24]. Figure 1b illustrates fixation of the curcumin/TiO$_2$ nanocomposite on the fabrics modified with citric acid in the presence of sodium hypophosphite, which allows for formation of ester carbonyl linkages [32] with the fiber. After treatment with citric acid modified fabric with curcumin/TiO$_2$ nanocomposite, the -OH groups of curcumin in nanocomposite get attached to the functionalized carboxylic group of citric acid on the modified fabric. This resulted in a strong electrostatic interaction of opposite charges between the particles [33]. Interestingly, the negative surface charges induced by the existence of carboxylic acid moieties improved the adsorption affinity of the curcumin/TiO$_2$ nanocomposite [34]. In fact, the TiO$_2$ nanoparticles exhibited a strong binding to the carboxylic groups of the citric acid-modified fabric through a number of different forms of binding, including weak anion-cation type attractions, hydrogen bonding and coordination-type interaction [35]. The fabrication of the curcumin/TiO$_2$ nanocomposite on fabrics modified with Quat 188 is presented in Figure 1c. Clearly, development of an ether linkage between Quat 188 and cellulose resulted from the reaction of Quat 188 with the cotton fabrics [36]. Deposition of curcumin/TiO$_2$ nanocomposite on Quat 188-modified fabric was due to strong ionic and van der Waals forces between the –OH groups of the curcumin molecule and the quaternary ammonium modified cotton fabric. Figure 1d illustrates the final treatment of GPTMS-modified cotton fabric using the curcumin/TiO$_2$ nanocomposite. GPTMS was pre-hydrolyzed for conversion of the alkyl oxygen groups (-OCH$_3$) to hydroxyl groups (-OH). The fabric was modified by GPTMS through ether crosslinking within the cotton fabric via the reaction of epoxy groups of GPTMS with hydroxyl groups of cellulose structure [31]. This allowed for hydrogen bond formation between the GPTMS-modified cotton fabric and the hydroxyl groups of the curcumin molecule [37].

4.2. FTIR Analysis

Existence of functional groups on the treated cotton fabric was investigated by fourier transform infrared spectroscopy. Figure 2 illustrates the FTIR spectrum for the untreated cotton fabric (a), curcumin/TiO$_2$–citric-modified cotton fabric (b), curcumin/TiO$_2$–Quat 188-modified cotton fabric (c), curcumin/TiO$_2$–GPTMS-modified cotton fabric (d), and curcumin powder (e). In the untreated cotton fabric, spectrum (a), a band appears in the range of 3200–3500 cm^{-1}, which is attributed to O–H stretching. The presence of C–H, O–H, C–O, and C–O–C vibrations caused the characteristic bands in the range of 1500–800 cm^{-1} [38]. On the other hand, the absorption band at 3310 cm^{-1}, which corresponded to the stretching vibration of phenolic O–H, was indicated in spectrum (e) for pure curcumin. Moreover, sharp absorption bands appear in the range from 1430 to 1630 cm^{-1}. These bands belong to the –OH, C=O, and C=C groups, respectively (enol). Other bands are observed in the region between 1000 cm^{-1} and 1300 cm^{-1}. All bands could be ascribed to the configuration of the symmetric and asymmetric C–O–C groups [39].

Interestingly, spectra (b), (c), and (d) look similar to untreated cotton fabric and curcumin patterns with few significant changes. This could be attributed to the partial interaction of the nanocomposite with the modified cotton fabric. Strong bands in the region 400–600 cm^{-1} were, however, noticeable in spectra (b–d), which corresponded to the Ti–O stretching vibration [24]. This confirmed the deposition of curcumin/TiO$_2$ nanocomposite on the surface of the modified fabric. Importantly, spectrum (b) showed a well-developed band at 1720 cm^{-1} that could be assigned to a carbonyl group stretching, implying that cellulose was successfully crosslinked with citric acid via the formation of ester carbonyl linkages [40]. It is obvious from spectrum (c) that a new peak emerged at 1570 cm^{-1}, which could be attributed to the quaternary ammonium groups. Clearly, spectrum (d) revealed two new bands at 2905 cm^{-1} and 2860 cm^{-1}, which could be aligned with the stretching of the methylene groups from the GPTMS molecules.

Structure a: Curcumine /TiO$_2$ nanoparticles

(a)

Strucure b: curcumin/TiO$_2$ citric acid modified cotton fabric

(b)

Structure c: curcumin/TiO$_2$ Quatt -188 modified cotton fabric

(c)

Strucutre d :curcumine /TiO$_2$ nanocomposite GPTMS modified cotton fabric

(d)
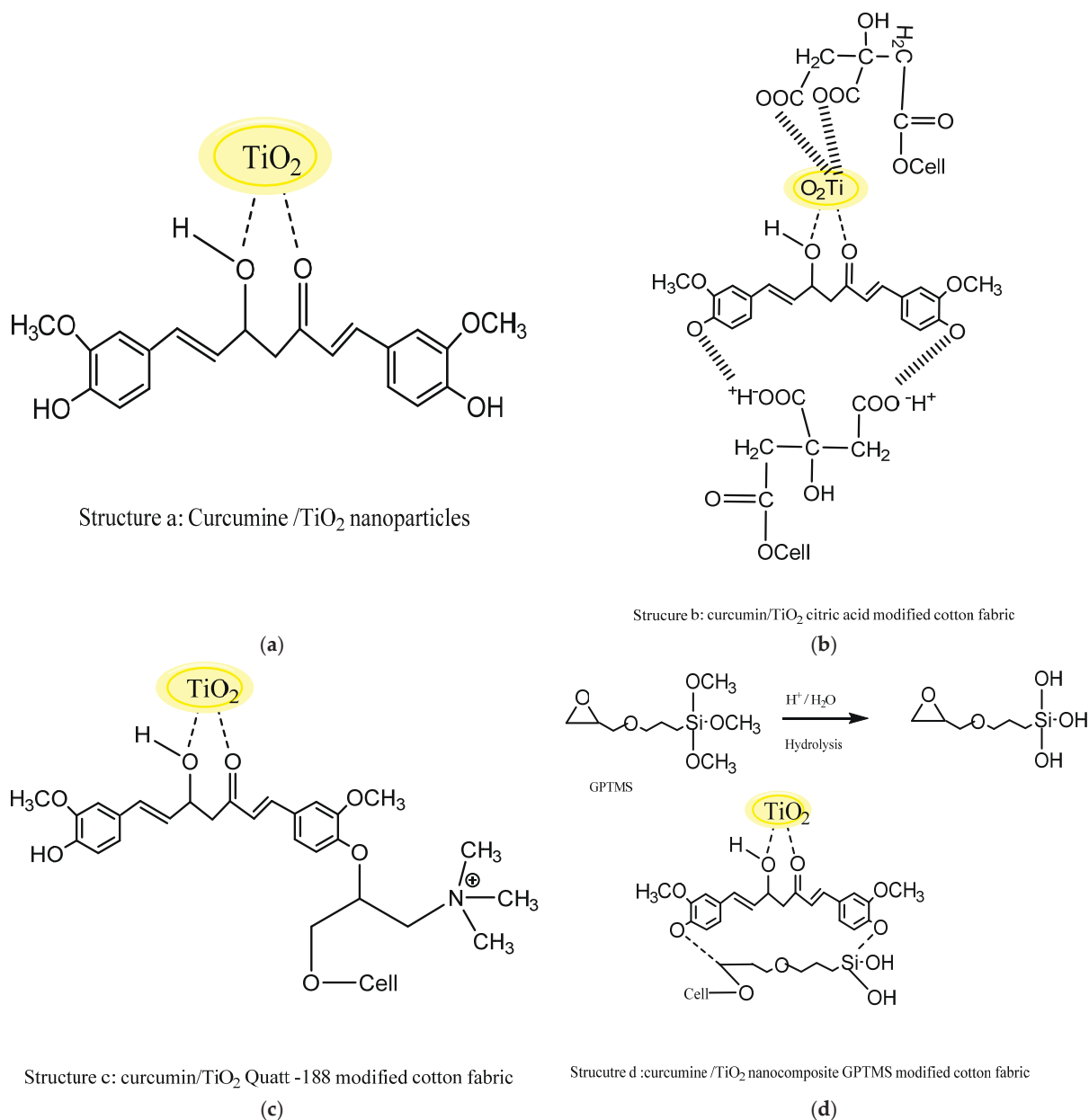
Figure 1. Schematic of the mechanism for the deposition of the curcumin/TiO$_2$ nanocomposite on cotton fabrics. (**a**) Structure a: curcumine/TiO$_2$ nanoparticles; (**b**) Structure b: curcumin TiO$_2$: citric acid modified cotton fabric; (**c**) Structure c: curcumin/TiO$_2$, Quatt-188 modified cotton fabric; (**d**) Structure d: curcumine/TiO$_2$, nanocomposite GPTMS modified cotton fabric.
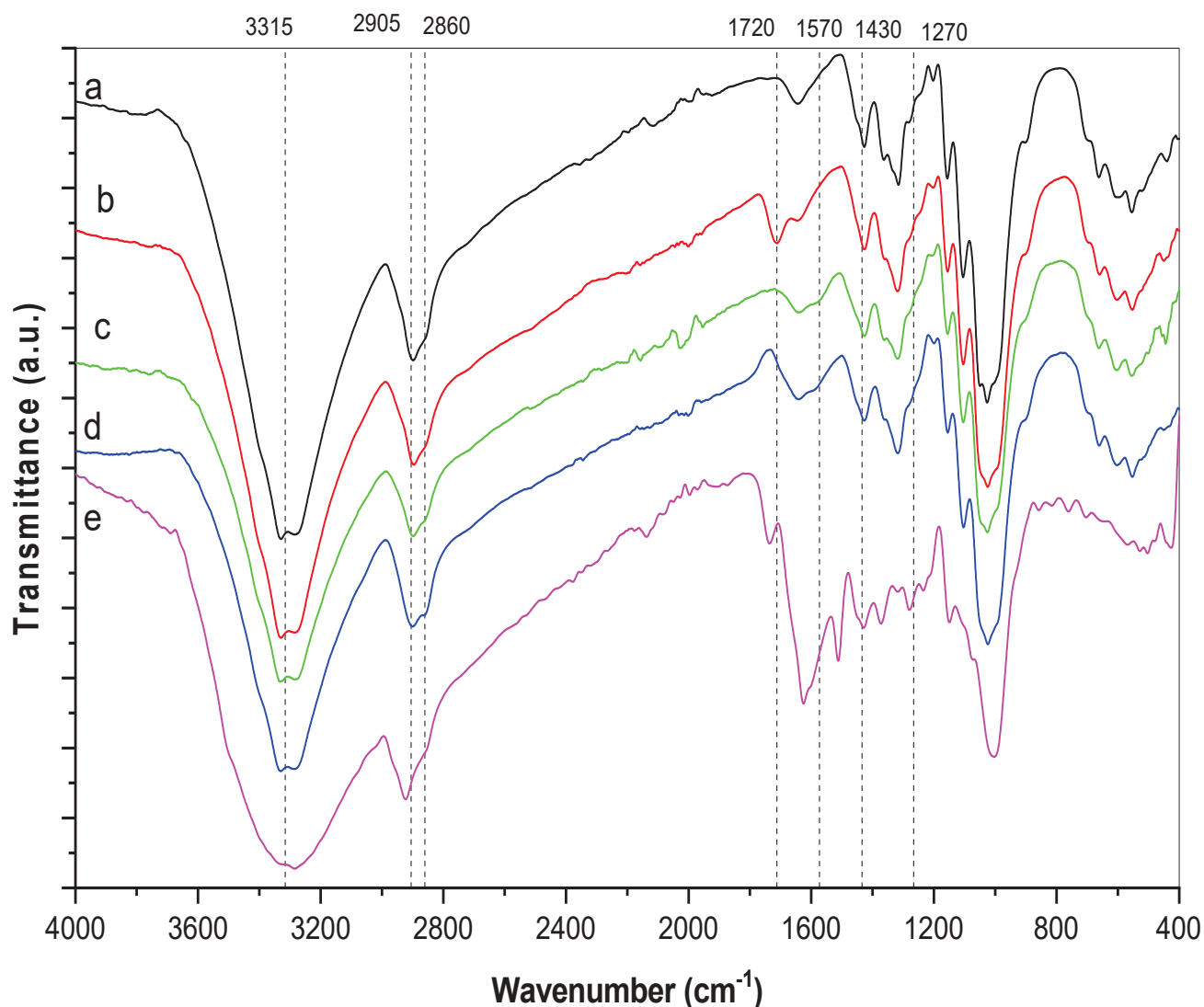
Figure 2. FTIR spectrum of untreated cotton fabric (**a**), curcumin/TiO$_2$–citric-modified cotton fabric (**b**), curcumin/TiO$_2$–Quat 188-modified cotton fabric (**c**), curcumin/TiO$_2$–GPTMS-modified cotton fabric (**d**), and curcumin powder (**e**).

4.3. Surface Morphology of the Cotton Fabrics

SEM images are used to study the morphology of the fabric surface [41]. Figure 3 displays the variations in unmodified and modified cotton fabric morphology. Figure 3a shows that the unmodified cotton fabric formed a fiber with a smooth surface. Figure 3b–d illustrates the effect of deposition of different modifications of cotton fabric. All modified samples show homogenous distribution of the curcumin/TiO$_2$ nanocomposite with less agglomeration in some points. In addition, there were no bridges between cotton adjacent fibers, which is desirable as air and vapor permeability is required for their potential application as wound dressings and medical materials. Figure 3b shows that the curcumin/TiO$_2$ nanocomposite with citric acid-modified cotton fabric formed cracked fibers, which could be attributed to the effect of crosslinking with citric acid. On the other hand, Figure 3c shows a higher dense layer in the curcumin/TiO–Quat 188-modified cotton fabric compared with the curcumin/TiO$_2$–GPTMS-modified cotton fabric. This may be due to the cationic modification of cellulosic fibers bearing a positive charge, resulting in higher deposition of curcumin/TiO$_2$ nanocomposite on their surfaces [42].
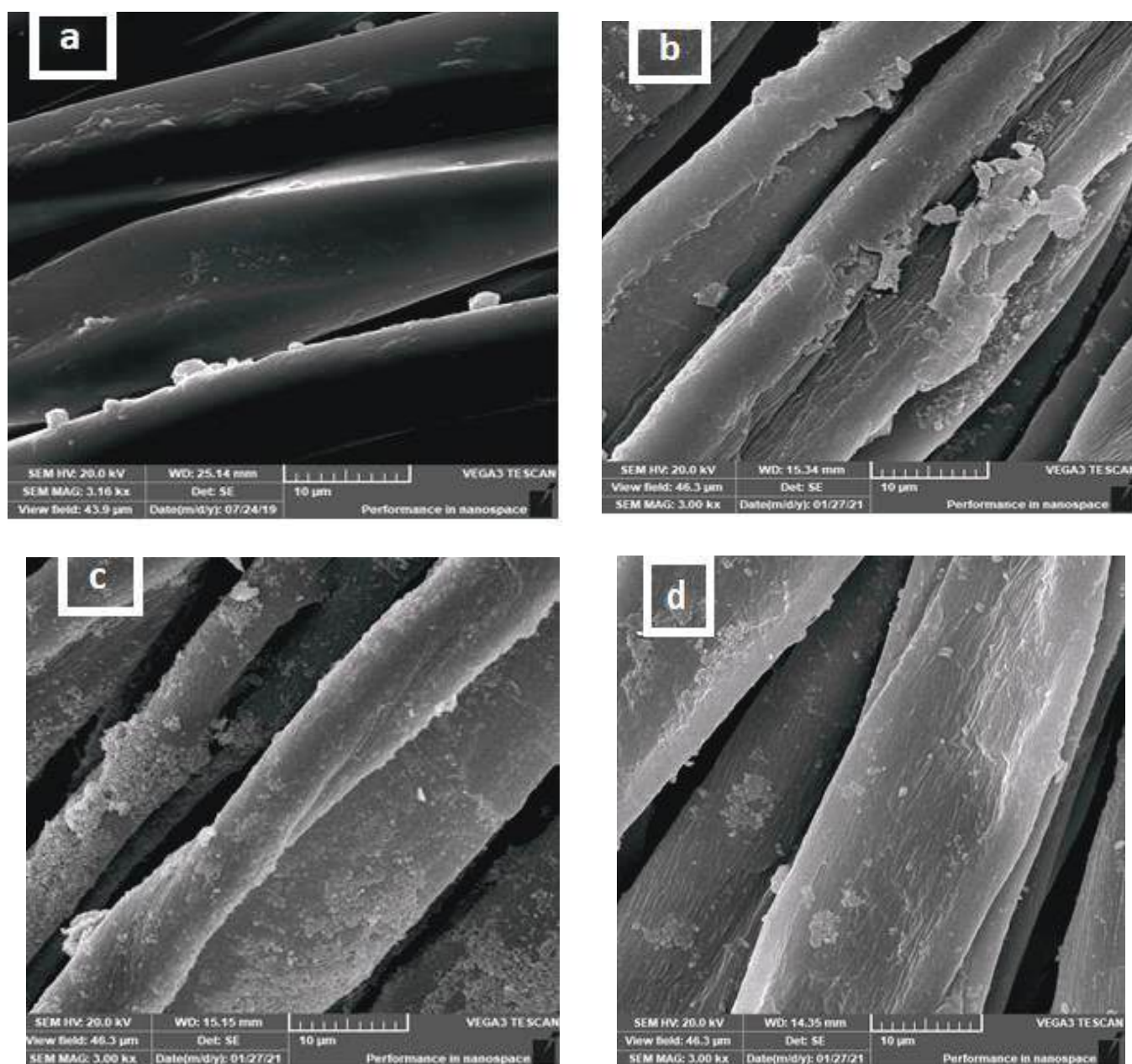
Figure 3. SEM images of control cotton fabric (**a**), curcumin/TiO$_2$–citric-modified cotton fabric (**b**), curcumin/TiO$_2$–Quat 188-modified cotton fabric (**c**), curcumin/TiO$_2$–GPTMS-modified cotton fabric (**d**).

4.4. EDX Analysis

Elemental analysis of the cotton fabric after modification was determined using the EDX spectrum. Figure 4 (blank cotton fabric) shows that the atomic percentage of carbon was 56.86% and oxygen was 43.14%. Interestingly, Figure 4a shows the atomic percentage of carbon as 57.30% and oxygen as 40.61% along with the titanium element as 1.41% for curcumin/TiO$_2$–citric-modified cotton fabric. Moreover, Figure 4b shows that the cotton fabric modified by curcumin/TiO$_2$–Quat 188 had the atomic percentage of carbon at 55.97, oxygen at 36.76%, titanium at 2.42% and a new peak for nitrogen at 4.84%. Such variation was due to the etherification reaction involved in the cationization process on the cotton fabric surface. On the other hand, the cotton fabric that was modified using curcumin/TiO$_2$–GPTMS, Figure 4c, had the atomic percentage of carbon as 65.91%, oxygen as 28.55%, titanium 0.66%, and a new peak for silicon at 4.04%. On the basis of these results,

the higher peaks observed for the titanium element in Figure 4b can be related to the higher content of the curcumin/TiO$_2$ nanocomposite deposited on the Quat 188-modified cotton fabric.
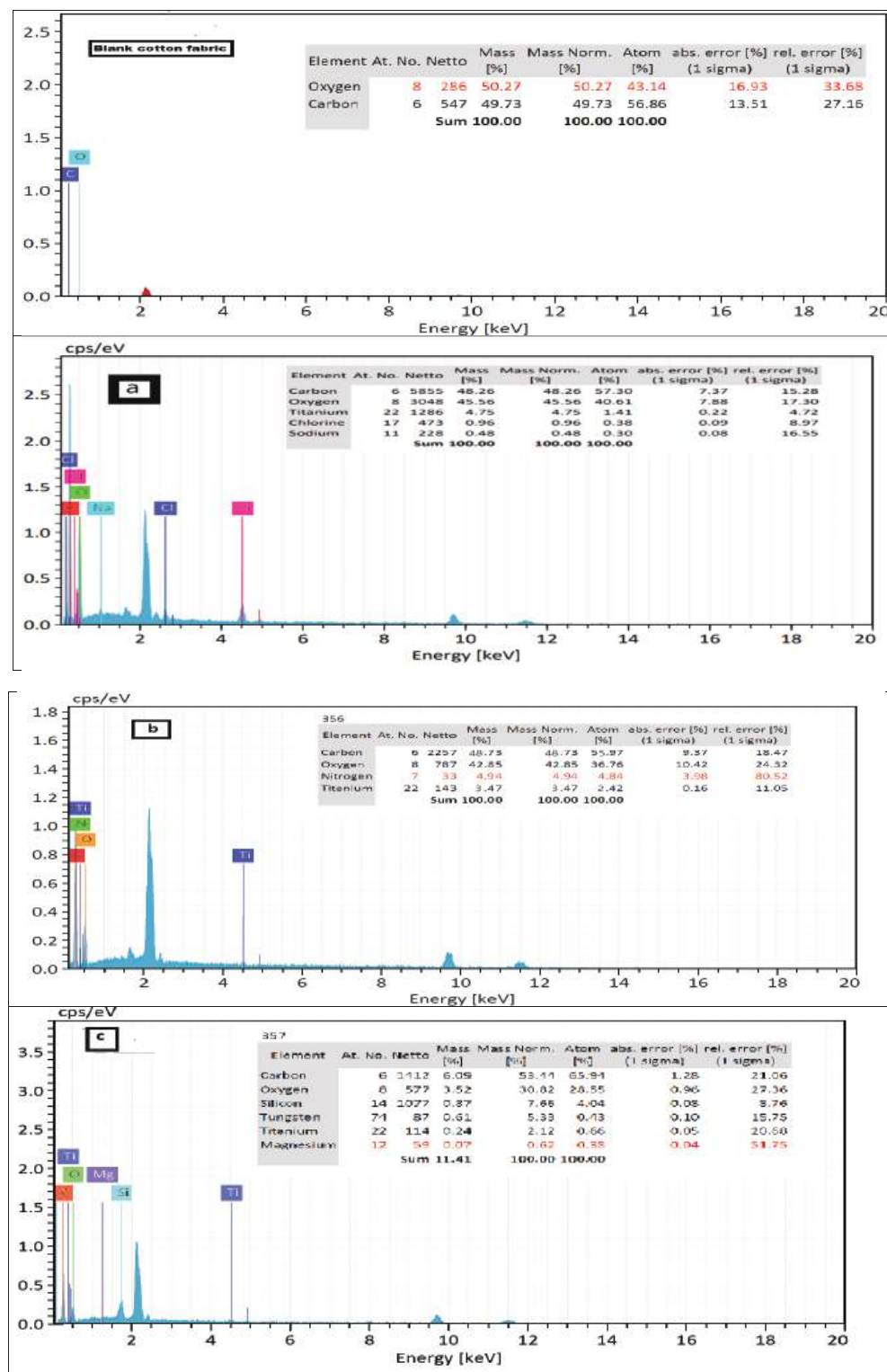
Figure 4. EDX analysis of blank cotton fabric, (**a**) curcumin/TiO$_2$–citric-modified cotton fabric, (**b**) curcumin/TiO$_2$–Quat 188-modified cotton fabric, and (**c**) curcumin/TiO$_2$–GPTMS-modified cotton fabric.

4.5. Antibacterial Activity

The antibacterial activity of curcumin/TiO$_2$-modified cotton fabric with various treatments was analyzed against representative microorganisms of open interest, both Gram-positive (*S. aureus*) and Gram-negative (*E. coli*) strains using the agar diffusion method were used. The antibacterial effect for all treatments ranged from 10 mm to 20 mm of clear zone of inhibition. Results mentioned in Table 1 indicated that *Escherichia coli* had a higher response than *Staphylococcus Aureus,* which could be due to variations in bacterial cell wall organization structure. Gram-positive bacteria had a thicker layer cell than Gram-negative bacteria, which served as a barrier to the spread of active ingredient into the cytoplasm, thereby protecting the cell wall [43]. On the other hand, TiO$_2$ nanoparticles that coated the modified cotton fabric showed higher antimicrobial activity. This could be attributed to the effect of a metal ion that may cause cytoplasmic leakage, protein denaturation, and enzyme malfunctions. Reactive oxygen species (ROSs) are generated by photoactive metal oxides, which can cause oxidative stress, cell content leakage, and DNA damage [26,44]. Since microbes are inhibited, these ROSs can oxidize lipids and lipopolysaccharides. In addition, the curcumin molecule in the cotton fabric modified with the curcumin/TiO$_2$ nanocomposite resulted in higher antibacterial activity. As reported before, curcumin, being a lipophilic molecule, can intercalate into the lipopolysaccharide-containing cell membrane and, thereby, increase the permeability of Gram-negative bacteria. Furthermore, it has been reported that the key mechanism involved in the killing action of curcumin is through the disordering of 1,2-dipalmitoyl- sn-glycero-3-phosphocholine (DPPC) membranes found in both *S. aureus* and *E. coli* [45]. Since curcumin can easily form a complex with titania, it may have been able to break through the bacteria's cell wall and enter the cell. This could have disrupted cell organelles and induced lysis, that killed bacteria [26]. In addition, cotton fabric modified with Quat 188 showed better antibacterial properties compared with fabric modified by either citric acid or GPTMS. From the above results, hindrance against pathogenic strains was accomplished in the following order: curcumin/TiO$_2$ nanocomposite-modified, Quat 188-cationized fabric > curcumin/TiO$_2$ nanocomposite-modified, crosslinked fabric with citric acid/SHP > curcumin/TiO$_2$ nanocomposite-modified fabric with GPTMS.

Table 1. Antibacterial activity and durability properties.

Table	Inhibition Zone (mm/1 cm Sample)			
	G− *Escherichia coli*		G+ *Staphylococcus aureus*	
No. of washing cycles	1	20	1	20
Untreated cotton fabric	0	0	0	0
TiO$_2$-coated, crosslinked fabric with citric acid/SHP	17	16	15	14
Curcumin/TiO$_2$ nanocomposite-modified, crosslinked fabric with citric acid/SHP	18	16	16	14
TiO$_2$-coated, Quat 188-cationized fabric	19	17	14	13
Curcumin/TiO$_2$ nanocomposite-modified, Quat 188- cationized fabric	22	19	16	14
TiO$_2$-coated, pretreated fabric with GPTMS	12	10	11	10
Curcumin/TiO$_2$ nanocomposite-modified fabric with GPTMS	14	13	12	10

Durability to washing cycles is shown in Table 1. Clearly, raising the number of washing cycles to 20 caused a small decrease in the antibacterial properties of the washed treated fabrics. This could be attributed to the effect of the crosslinkers used (citric acid, Quat 188 and GPTMS) [46]. Crosslinkers were used in order to enhance bonding between the curcumin/TiO$_2$ nanocomposite and the cellulosic chains of cotton fabric. Thus, favorable washing durability was obtained.

4.6. UV Blocking

UPF values were measured to determine the UV-radiation protection characteristics of untreated cotton fabrics and nanocomposite-modified fabrics and the results are shown in Table 2. Textiles can be classified into three protection groups according to BS EN

13758-2:2003 [47]: good (UPF range 20–29), very good (UPF range 30–40), and excellent (UPF range > 40).

Table 2. UPF values of cotton fabric treated with different conditions.

Treatment	UPF Value	UV-A	UV-B	UV Protection
Untreated cotton fabric	4.5	26	18.8	Non-ratable
TiO$_2$-coated cotton fabric	20	15.29	13.69	Good
TiO$_2$-coated, crosslinked cotton fabric with citric acid/SHP	27	7.74	6.11	Good
Curcumin/TiO$_2$ nanocomposite-modified, crosslinked cotton fabric with citric acid/SHP	50	3.5	3.1	Excellent
TiO$_2$-coated, Quat 188-cationized cotton fabric	30	5.24	5.23	Very good
Curcumin/TiO$_2$ nanocomposite-modified, Quat 188-cationized fabric	55	2.7	2.5	Excellent
TiO$_2$-coated, pretreated cotton fabric with GPTMS	23	14.1	12.2	Good
Curcumin/TiO$_2$ nanocomposite-modified cotton fabric with GPTMS	38	6.1	4.5	Very good

The calculated UPF value of untreated cotton fabric is 4.5. The UPF of coated cotton fabric varies from 20 to 55, which is higher than the untreated fabric. In addition, the results in Table 2 indicate that curcumin/TiO$_2$-modified cotton fabric increases the UPF values. Inspection of Table 2 revealed that the UPF value of TiO$_2$-coated cotton fabric was 20. The increased UPF could be attributed to the semi-conductive properties of the TiO$_2$ nanoparticles, which can absorb ultraviolet photons [32]. On the other hand, there was a significant increase in UPF values for TiO$_2$-modified cotton fabric. The values varied from 23 to 30 due to the effect othef different treatments according to the following order:

TiO$_2$-coated, cationized cotton fabric > TiO$_2$-coated, crosslinked fabric with citric acid/SHP > TiO$_2$-coated, pretreated cotton fabric with GPTMS.

Moreover, the results in Table 2 indicate that curcumin/TiO$_2$-modified cotton fabric increased the UPF values, which varied from 38 to 55 and were graded from very good to excellent protection. This could be a result of the effectivity of the curcumin molecule in increasing the ultraviolet protection of cotton fabric. It can be concluded that the unmodified cotton fabrics exhibited a rather poor UV protection value due to the inability of the cellulose in UV absorption. In contrast, all the nanocomposite-modified fabrics showed better UV blocking properties than the unmodified fabric. The increasing UPF values ofthe curcumin/TiO$_2$-modified cotton followed the order:

Curcumin/TiO$_2$ nanocomposite-modified, Quat 188-cationized fabric > TiO$_2$-coated, crosslinked cotton fabric with citric acid/SHP > curcumin/TiO$_2$ nanocomposite-modified cotton fabric with GPTMS.

4.7. Add-on and Tensile Strength Measurements

Table 3 shows the percentage of values for add-on measurements and mechanical properties of chemically modified cotton fabric. The amount of chemicals deposited on the cotton fabric during modification was indicated by the add-on values. The results showed that for GPTMS-modified cotton fabric, the add-on values were between 8.45% and 12.57%, whereas the modification of samples with citric acid and cationized agent caused a significant increase in the add-on ranging between 8.65% and 18.87%, and 9.55% and 15.45% respectively.

Table 3. Add-on measurements and tensile strength with standard deviations of treated cotton fabric.

Treatment	Add on (%)	Tensile Strength (Kg f)
Untreated cotton fabric	0	55 ± 1.04
TiO$_2$-coated, crosslinked fabric with citric acid/SHP	9.55 ± 0.1	48 ± 1.3
Curcumin/TiO$_2$ nanocomposite-modified, crosslinked fabric with citric acid/SHP	15.45 ± 0.06	45 ± 1.8
TiO$_2$-coated, Quat 188-cationized fabric	8.65 ± 0.05	47 ± 1.7
Curcumin/TiO$_2$ nanocomposite-modified, Quat 188-cationized fabric	18.87 ± 0.12	44 ± 1
TiO$_2$-coated, pretreated fabric with GPTMS	8.45 ± 0.1	51 ± 0.5
Curcumin/TiO$_2$ nanocomposite-modified fabric with GPTMS	12.57 ± 0.4	47 ± 1.1

On the other hand, Table 1 showed significant decreases in values of tensile strength. This may be attributed to the effect of different modifications and crosslinking agents, resulting in damaged cellulose chains.

5. Conclusions

In this work, we developed materials based on the fabrication of curcumin/TiO$_2$ nanocomposite on the surface of cotton fabric via the pad-dry-cure method. To achieve this goal, cotton fabric was modified with different crosslinkeres, namely citric acid, Quat 188 and GPTMS. Crosslinkers were used to improve the adhesion between cotton fabrics and the prepared curcumin/TiO$_2$ nanocomposite. The prepared nanocomposite-modified fabrics were confirmed using FTIR, SEM and EDX. It has been concluded that curcumin/TiO$_2$ nanocomposite-modified, Quat 188-cationized fabric showed the highest antibacterial activity compared with either curcumin/TiO$_2$ nanocomposite-modified, crosslinked fabric with citric acid/SHP or curcumin/TiO$_2$ nanocomposite-modified fabric with GPTMS. Moreover, the curcumin/TiO$_2$ nanocomposite-modified, Quat 188-cationized fabric exhibited higher efficiency against Gram-negative bacteria than Gram-positive ones. The durability of curcumin/TiO$_2$ nanocomposite-modified cotton fabric showed negligible reduction in antibacterial activity as a result of the crosslinker used. These results are promising for the treatment of fabrics for medical applications. Cationic modification can be used for the modification of cotton fabric to increase curcumin/TiO$_2$ nanocomposite adsorption on the surfaces and produce stronger antibacterial activity. The results of UV protection also revealed that curcumin/TiO$_2$ nanocomposite-modified, Quat 188-cationized fabric acquired UPF values higher than 50, which indicated excellent UV protection properties.

References

1. Edwards, J.V.; Buschle-Diller, G.; Goheen, S.C. *Modified Fibers with Medical and Specialty Applications*; Springer: Berlin/Heidelberg, Germany, 2006.
2. Gert, E.; Torgashov, V.; Zubets, O.; Kaputskii, F. Combination of oxidative and hydrolytic functions of nitric acid in production of enterosorbents based on carboxylated microcrystalline cellulose. *Russ. J. Appl. Chem.* **2006**, *79*, 1896–1901. [CrossRef]
3. Czaja, W.; Krystynowicz, A.; Bielecki, S.; Brown, R.M., Jr. Microbial cellulose—The natural power to heal wounds. *Biomaterials* **2006**, *27*, 145–151. [CrossRef] [PubMed]
4. Hoenich, N.A. Cellulose for medical applications: Past, present, and future. *BioResources* **2006**, *1*, 270–280. [CrossRef]
5. Zemljič, L.F.; Volmajer, J.; Ristić, T.; Bracic, M.; Sauperl, O.; Kreže, T. Antimicrobial and antioxidant functionalization of viscose fabric using chitosan–curcumin formulations. *Text. Res. J.* **2014**, *84*, 819–830. [CrossRef]
6. Ibrahim, H.M.; Zaghloul, S.; Hashem, M.; El-Shafei, A. A green approach to improve the antibacterial properties of cellulose based fabrics using Moringa oleifera extract in presence of silver nanoparticles. *Cellulose* **2021**, *28*, 549–564. [CrossRef]
7. Hashem, M.; Abdalla, A.E.M.; Raouf, E.R.A.; El-Shafei, A.; Zaghloul, S.; El-Bisi, M. Moringa oleifera-silver nanohybrid as green antimicrobial finishing for cotton fabrics. *Egypt J. Chem.* **2016**, *59*, 509–522.
8. Zaghloul, S.; El-shafie, A.; El-bisi, M.; Refaie, R. Herbal Textile Finishes–Natural Antibacterial Finishes for Cotton Fabric. *Egypt J. Chem.* **2017**, *60*, 161–180. [CrossRef]

9. Hebeish, A.; Higazy, A.; AbdelHady, M.; Sharaf, S. Novel route for antibacterial finishing of cotton fabric based on Ag loaded cyclodextrin–PAN copolymers. *Egypt J. Chem.* **2016**, *59*, 887–910.

10. Abd El-Hady, M.; Sharaf, S.; Farouk, A. Highly hydrophobic and UV protective properties of cotton fabric using layer by layer self-assembly technique. *Cellulose* **2020**, *27*, 1099–1110. [CrossRef]

11. Montaser, A.; Rehan, M.; El-Senousy, W.; Zaghloul, S. Designing strategy for coating cotton gauze fabrics and its application in wound healing. *Carbohydr. Polym.* **2020**, *244*, 116479. [CrossRef]

12. Sharaf, S.; Farouk, A.; El-Hady, M. Novel conductive textile fabric based on polyaniline and CuO nanoparticles. *Int. J. Pharm. Tech. Res.* **2016**, *9*, 461–472.

13. Morris, H.; Murray, R. Medical textiles. *Text. Prog.* **2020**, *52*, 1–127. [CrossRef]

14. El-Shafei, A.; Sharaf, S.; Zaghloul, S.; Hashem, M. Development of softener containing metal nano-particle for multipurpose textile finishing. *Int. J. PharmTech Res.* **2015**, *8*, 123–138.

15. Bhawana, B.R.; Buttar, H.S.; Jain, V.; Jain, N. Curcumin nanoparticles: Preparation, characterization, and antimicrobial study. *J. Agric. Food Chem.* **2011**, *59*, 2056–2061. [CrossRef] [PubMed]

16. Jaisamut, P.; Wiwattanawongsa, K.; Graidist, P.; Sangsen, Y.; Wiwattanapatapee, R. Enhanced oral bioavailability of curcumin using a supersaturatable self-microemulsifying system incorporating a hydrophilic polymer; in vitro and in vivo investigations. *Aaps. Pharmscitech.* **2018**, *19*, 730–740. [CrossRef]

17. Bigand, V.; Pinel, C.; Perez, D.D.S.; Rataboul, F.; Huber, P.; Petit-Conil, M. Cationisation of galactomannan and xylan hemicelluloses. *Carbohydr. Polym.* **2011**, *85*, 138–148. [CrossRef]

18. Singh, U.; Verma, S.; Ghosh, H.; Rath, M.; Priyadarsini, K.; Sharma, A.; Pushpa, K.; Sarkar, S.; Mukherjee, T. Photo-degradation of curcumin in the presence of TiO2 nanoparticles: Fundamentals and application. *J. Mol. Catal. A Chem.* **2010**, *318*, 106–111. [CrossRef]

19. Jain, N.; Bhawana, R.; Basniwal, H. Buttar and VK Jain. *J. Agric. Food Chem.* **2011**, *59*, 2056.

20. Kuthati, Y.; Kankala, R.K.; Busa, P.; Lin, S.-X.; Deng, J.-P.; Mou, C.-Y.; Lee, C.-H. Phototherapeutic spectrum expansion through synergistic effect of mesoporous silica trio-nanohybrids against antibiotic-resistant gram-negative bacterium. *J. Photochem. Photobiol. B Biol.* **2017**, *169*, 124–133. [CrossRef]

21. Anand, P.; Kunnumakkara, A.B.; Newman, R.A.; Aggarwal, B.B. Bioavailability of curcumin: Problems and promises. *Mol. Pharm.* **2007**, *4*, 807–818. [CrossRef]

22. Musial, J.; Krakowiak, R.; Mlynarczyk, D.T.; Goslinski, T.; Stanisz, B.J. Titanium dioxide nanoparticles in food and personal care products—What do we know about their safety? *Nanomaterials* **2020**, *10*, 1110. [CrossRef] [PubMed]

23. Sherin, S.; Sheeja, S.; Devi, R.S.; Balachandran, S.; Soumya, R.S.; Abraham, A. In vitro and in vivo pharmacokinetics and toxicity evaluation of curcumin incorporated titanium dioxide nanoparticles for biomedical applications. *Chem.-Biol. Interact.* **2017**, *275*, 35–46. [CrossRef]

24. Buddee, S.; Wongnawa, S.; Sriprang, P.; Sriwong, C. Curcumin-sensitized TiO$_2$ for enhanced photodegradation of dyes under visible light. *J. Nanoparticle Res.* **2014**, *16*, 1–21. [CrossRef]

25. Haghighatzadeh, A. Comparative analysis on optical and photocatalytic properties of chlorophyll/curcumin-sensitized TiO$_2$ nanoparticles for phenol degradation. *Bull. Mater. Sci.* **2020**, *43*, 1–15. [CrossRef]

26. Marulasiddeshwara, R.; Jyothi, M.; Soontarapa, K.; Keri, R.S.; Velmurugan, R. Nonwoven fabric supported, chitosan membrane anchored with curcumin/TiO$_2$ complex: Scaffolds for MRSA infected wound skin reconstruction. *Int. J. Biol. Macromol.* **2020**, *144*, 85–93. [CrossRef]

27. Khalil-Abad, M.S.; Yazdanshenas, M.E.; Nateghi, M.R. Effect of cationization on adsorption of silver nanoparticles on cotton surfaces and its antibacterial activity. *Cellulose* **2009**, *16*, 1147–1157. [CrossRef]

28. Refaie, R.; Zaghloul, S.; Elbisi, M.; Shaaban, H. Bioactive Cotton for Packaging and Storage of Grains using Aromatic Components. *Int. Res. J. Appl. Sci.* **2020**, *2*, 40–49.

29. Acharya, S.; Abidi, N.; Rajbhandari, R.; Meulewaeter, F. Chemical cationization of cotton fabric for improved dye uptake. *Cellulose* **2014**, *21*, 4693–4706. [CrossRef]

30. Grancarić, A.M.; Tarbuk, A.; Sutlović, A.; Castellano, A.; Colleoni, C.; Rosace, G.; Plutino, M.R. Enhancement of acid dyestuff salt-free fixation by a cationizing sol-gel based coating for cotton fabric. *Colloids Surf. A Physicochem. Eng. Asp.* **2021**, *612*, 125984. [CrossRef]

31. Shang, S.-M.; Li, Z.; Xing, Y.; Xin, J.H.; Tao, X.-M. Preparation of durable hydrophobic cellulose fabric from water glass and mixed organosilanes. *Appl. Surf. Sci.* **2010**, *257*, 1495–1499. [CrossRef]

32. Al Sarhan, T.M.; Salem, A. Turmeric dyeing and chitosan/titanium dioxide nanoparticle colloid finishing of cotton fabric. *Indian J. Fibre Text. Res.* **2018**, *43*, 464–473.

33. Wani, K.D.; Kitture, R.; Ahmed, A.; Choudhari, A.S.; Koppikar, S.J.; Kale, S.N.; Kaul-Ghanekar, R. Synthesis, characterization and in vitro study of Curcumin-functionalized Citric acid-Capped Magnetic (CCF) Nanoparticles as drug delivery agents in cancer. *J. Bionanosci.* **2011**, *5*, 59–65. [CrossRef]

34. Lee, W.-H.; Loo, C.-Y.; Rohanizadeh, R. Functionalizing the surface of hydroxyapatite drug carrier with carboxylic acid groups to modulate the loading and release of curcumin nanoparticles. *Mater. Sci. Eng. C* **2019**, *99*, 929–939. [CrossRef]

35. Wijesena, R.N.; Tissera, N.D.; Perera, R.; de Silva, K.N.; Amaratunga, G.A. Slightly carbomethylated cotton supported TiO$_2$ nanoparticles as self-cleaning fabrics. *J. Mol. Catal. A Chem.* **2015**, *398*, 107–114. [CrossRef]

36. Farouk, A.; Sharaf, S.; Abd El-Hady, M. Preparation of multifunctional cationized cotton fabric based on TiO$_2$ nanomaterials. *Int. J. Biol. Macromol.* **2013**, *61*, 230–237. [CrossRef]

37. Ahmadi Nasab, N.; Hassani Kumleh, H.; Beygzadeh, M.; Teimourian, S.; Kazemzad, M. Delivery of curcumin by a pH-responsive chitosan mesoporous silica nanoparticles for cancer treatment. *Artif. Cells Nanomed. Biotechnol.* **2018**, *46*, 75–81. [CrossRef]

38. Farouk, A.; Saeed, S.E.-S.; Sharaf, S.; Abd El-Hady, M. Photocatalytic activity and antibacterial properties of linen fabric using reduced graphene oxide/silver nanocomposite. *RSC Adv.* **2020**, *10*, 41600–41611. [CrossRef]

39. El-Hady, A.; Saeed, S. Antibacterial Properties and pH Sensitive Swelling of Insitu Formed Silver-Curcumin Nanocomposite Based Chitosan Hydrogel. *Polymers* **2020**, *12*, 2451. [CrossRef]

40. Boonroeng, S.; Srikulkit, K.; Xin, J.H.; He, L. Preparation of a novel cationic curcumin and its properties evaluation on cotton fabric. *Fibers Polym.* **2015**, *16*, 2426–2431. [CrossRef]

41. Gashti, M.P.; Alimohammadi, F.; Song, G.; Kiumarsi, A. Characterization of nanocomposite coatings on textiles: A brief review on microscopic technology. *Curr. Microsc. Contrib. Adv. Sci. Technol.* **2012**, *2*, 1424–1437.

42. Cheng, D.; He, M.; Cai, G.; Wang, X.; Ran, J.; Wu, J. Durable UV-protective cotton fabric by deposition of multilayer TiO$_2$ nanoparticles films on the surface. *J. Coat. Technol. Res.* **2018**, *15*, 603–610. [CrossRef]

43. Kim, J.S.; Kuk, E.; Yu, K.N.; Kim, J.-H.; Park, S.J.; Lee, H.J.; Kim, S.H.; Park, Y.K.; Park, Y.H.; Hwang, C.-Y. Antimicrobial effects of silver nanoparticles. *Nanomed. Nanotechnol. Biol. Med.* **2007**, *3*, 95–101. [CrossRef] [PubMed]

44. Behnam, M.A.; Emami, F.; Sobhani, Z.; Dehghanian, A.R. The application of titanium dioxide (TiO$_2$) nanoparticles in the photo-thermal therapy of melanoma cancer model. *Iran. J. Basic Med Sci.* **2018**, *21*, 1133. [PubMed]

45. Saha, S.; Pramanik, K.; Biswas, A. Antibacterial activity and biocompatibility of curcumin/TiO$_2$ nanotube array system on Ti6Al4V bone implants. *Mater. Technol.* **2021**, *36*, 221–232. [CrossRef]

46. Hao, L.; An, Q.; Xu, W. Facile fabrication of superhydrophobic cotton fabric from stearyl methacrylate modified polysiloxane/silica nanocomposite. *Fibers Polym.* **2012**, *13*, 1145–1153. [CrossRef]

47. EN, C. *13758-2: Fabrics–Solar UV Protective Properties–Classification and Marking of Apparel*; European Committee for Standardization: Brussels, Belgium, 2003.

Article

Effect of Fibre Surface Treatment and Nanofiller Addition on the Mechanical Properties of Flax/PLA Fibre Reinforced Epoxy Hybrid Nanocomposite

Adnan Amjad [1], M. Shukur Zainol Abidin [1], Hassan Alshahrani [2] and Aslina Anjang Ab Rahman [1,*]

[1] School of Aerospace Engineering, Universiti Sains Malaysia, George Town 14300, Malaysia; a.adiamondstar@gmail.com (A.A.); aeshukur@usm.my (M.S.Z.A.)
[2] Department of Mechanical Engineering, Najran University, King Abdulaziz Road, P.O. Box 1988, Najran 61441, Saudi Arabia; haalshahrani@nu.edu.sa
* Correspondence: aeaslina@usm.my

Abstract: Natural fibre-based materials are gaining popularity in the composites industry, particularly for automotive structural and semi-structural applications, considering the growing interest and awareness towards sustainable product design. Surface treatment and nanofiller addition have become one of the most important aspects of improving natural fibre reinforced polymer composite performance. The novelty of this work is to examine the combined effect of fibre surface treatment with Alumina (Al_2O_3) and Magnesia (MgO) nanofillers on the mechanical (tensile, flexural, and impact) behaviour of biotex flax/PLA fibre reinforced epoxy hybrid nanocomposites. Al_2O_3 and MgO with a particle size of 50 nm were added in various weight proportions to the epoxy and flax/PLA fibre, and the composite laminates were formed using the vacuum bagging technique. The surface treatment of one set of fibres with a 5% NaOH solution was investigated for its effect on mechanical performance. The results indicate that the surface-treated reinforcement showed superior tensile, flexural, and impact properties compared to the untreated reinforcement. The addition of 3 wt. % nanofiller resulted in the best mechanical properties. SEM morphological images demonstrate various defects, including interfacial behaviour, fibre breakage, fibre pullout, voids, cracks, and agglomeration.

Keywords: flax/PLA; polymer-matrix composites; hybrid; particle-reinforcement; mechanical properties; electron microscopy; surface treatments

1. Introduction

Composite materials are a versatile class of materials with excellent properties and applications. They are made up of two or more chemically distinct constituents, namely the matrix and reinforcement. Typically, the reinforcement is more rigid and superior to the matrix, while the matrix holds the reinforcement and provides a homogenous structure [1]. Although synthetic fibres are the most frequently used reinforcement in polymer composites, growing environmental concerns have recently encouraged the use of renewable resources. Biodegradable reinforcing materials such as natural fibres are the best substitute for synthetic fibres in the composite industry due to their technological and ecological advantages [2]. The mechanical properties and chemical composition of commonly used natural fibres are found in the literature [3,4]. For several applications, including automobiles, construction, and the aerospace industry, research and development (R&D) has proven that natural fibres are advantageous due to their low cost, low density, low CO_2 emission, nonabrasive nature, low energy consumption, lack of skin irritation, and low health risk [5–8]. Additionally, natural fibre reinforced polymer composite (NFRPCs) are less expensive, more substantial, and environmentally-friendly [9].

Along with their numerous benefits, natural fibres have a few disadvantages, including incompatibility between the fibre and the matrix, low resistance to moisture, dimensional instability, and a tendency to aggregate during processing [10]. The weak interfacial bond between water-loving natural fibres and a water-repellent polymer matrix results in a decrease in the properties of the polymer composite, which is detrimental for industrial and structural applications [11]. However, numerous schemes and approaches overcome these shortcomings, including chemical treatment of reinforced fibre, hybridization, and filler application [12,13]. Natural fibres chemical composition, surface morphology, and topography are altered when processed with different chemicals. The existing surface treatment methods are alkali, silane, acetylation, benzoylation, peroxide, permanganate, and sodium chlorite [11,14–18]. Alkaline treatment, also known as mercerization, is one of the most widely used and simplest methods for improving the adhesion properties of the fibre matrix. This method modifies the cellulosic structure of natural fibres with sodium hydroxide (NaOH), resulting in increased fibre fragmentation and disaggregation speed. The alkaline treatment removes oil, wax, lignin, and pectin from fibres, resulting in a clean, uniform surface.

Another technique for enhancing the mechanical properties of composite materials is hybridization. Hybrid composites typically contain two or more distinct fibre types within the same matrix, but they also contain a blend of two or more polymers reinforced with the same fibre type. The primary goal of hybridization is to overcome a material's limitations by supporting it with another material with similar or superior properties to the first [19,20]. Hybridization can create hybrid nanocomposite materials at the nanoscale by combining multiple types of nanofiller or nanomaterial in the same matrix [21]. Due to the unique properties of hybrid nanocomposite materials, they have been used in various applications due to their lower cost than conventional composite materials [22].

The incorporation of nanofillers via advanced manufacturing techniques has improved fibre-reinforced composite materials by modifying the fibre and matrix interaction [23,24]. Nanofillers have a tremendous potential to enhance the mechanical performance of composites, thereby expanding their applications in a myriad of fields. Homogeneous and uniform nanofiller mixing accelerates the composite's mechanical, thermal, and tribological properties [25–27]. Nanofillers are typically inorganic and occasionally organic; the most common inorganic nanofillers are alumina, magnesia, silica, zinc oxide, titanium dioxide, and calcium carbonate; naturally organic nanofillers include synthetic clay, carbon black, and cellulosic fibres [28–30]. The optimal quantity of nanofillers varies according to the filler, matrix, and fibre type [31–40]. By adding the filler, the available free spaces may be reduced, thereby increasing the stiffness of the laminates. The filler can bridge the matrix and the fibre, resulting in increased interaction between them. Once the load is applied, the stress is easily transferred from the polymer matrix to the reinforcing fibre, thus significantly improving their mechanical performance [41]. The addition of nanofillers affects the epoxy matrix's curing process; this effect depends on the size and concentration of the nanofillers in the matrix. Increased filler content and smaller nanofiller size decrease the curing speed of the epoxy matrix, which may be due to the limited movement space for the polymer chain and monomer in nano filled epoxy composites [42–45].

Synthetic fibres are toxic, non-disposable, abrasive and involve a complex manufacturing process, while natural fibres are robust, low-cost, and eco-friendly [46,47]. Increasing environmental concerns have lead to a swift change in the research pace from synthetic to natural fibre composite materials [48]. Many previous researchers have reported using natural fibres; however, their results indicate comparatively inferior properties and poor compatibility compared with synthetic composites, which necessitates modification in the fabrication technique [49–51]. Nanofiller addition and fibre surface enhancement can be considered effective methods to improve NFRPCs performance [52,53]. However, a notable lack of research exists on this topic. In this study, the combined effect of the fibre surface treatment and the addition of nanofillers was investigated in terms of the mechanical properties of the hybrid nanocomposite. The polymeric composite was manufactured

using alkali-treated flax/PLA 2D woven fabric, and nano Al_2O_3 and MgO reinforced epoxy composites using the vacuum bagging technique. The effect of surface treatment and nanofiller addition was investigated for tensile, bending and impact properties, and morphology was observed using electron microscopy scanning (SEM).

2. Materials and Methods

2.1. Materials

The biotex flax/PLA (100% bioderived commingled fabric in which the flax fibre is about 40% and the remaining 60% is PLA) with 2/2 twill weave and 400 g/m^2 fabric weight with a density of 1.33 g/cm^3 was obtained from Composite Evolution Limited, Chesterfield, United Kingdom. Infusion epoxy (Pro-set INF-114/INF-213) with a density of 1.14 g/cm^3 was purchased from Castmech Technologies Sdn. Bhd., Perak, Malaysia. Al_2O_3 and MgO nanofillers were supplied by Richest Group Limited, Shanghai, China. The specifications of Al_2O_3 and MgO nanofillers are presented in Table 1. Sodium hydroxide (NaOH), Sodium dodecyl sulfate (SDS) as a wetting agent, and Ethylene-diamine-tetra-acetic acid (EDTA) as a sequestering agent were obtained from a local supplier in Malaysia.

Table 1. Specifications of Al_2O_3 and MgO nanofillers.

Properties	Al_2O_3	MgO
Size (nm)	50 nm	50 nm
Shape	Spherical	Spherical
Colour	White	White
Purity (%)	99%	99%
Density (g/cm^3)	3.95 g/cm^3	3.58 g/cm^3

2.2. Methodology

The factors and their associated levels that were considered in this study are shown in Table 2. The design of experiment (DOE) was generated using the full factorial design technique in the Minitab-19 statistical tool. Thus, a total of eighteen (18) combinations without repetition were formed, nine for each type of reinforcement, treated or untreated.

Table 2. Factors and levels.

Factors	Levels				
Reinforcement	Treated flax/PLA			Untreated flax/PLA	
Nanofiller Type	Al_2O_3			MgO	
Nanofillers Concentration (wt. %)	0	1	2	3	4

2.2.1. Alkaline Treatment of 2D Woven Biotex Flax/PLA Fabric

The biotex flax/PLA fabric was pre-treated with a 5% sodium hydroxide (NaOH) solution as in Equation (1) [54–56], containing ppm concentrations of sodium dodecyl sulphate (SDS) as a wetting agent that lowers the surface tension of water, allowing drops to spread onto a surface, thereby increasing a liquid's spreading ability and ethylene-diamine-tetra-acetic acid (EDTA) as a sequestering agent that binds the undesirable metal ions together to form a stable structure. The fabric was then heated to 100 °C for 60 min. After 60 min, the fabric was rinsed with hot water and then with cold water. After washing, the fabric was allowed to air dry for 24 h before being oven-dried for 60 min at 80 °C. After that, treated and untreated biotex flax/PLA fabric was cut into a dimension of (300 mm × 300 mm) to be used as reinforcement.

$$\frac{Flax}{PLA}Fibre - O^-H^+ + Na^+ - OH^- \rightarrow \frac{Flax}{PLA}Fibre - O^-Na^+ + H_2O \qquad (1)$$
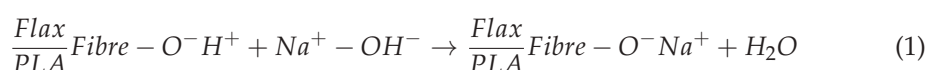
2.2.2. Fabrication of Hybrid Composite

The tri-layer hybrid composite with dimensions of 300 mm × 300 mm and a stacking sequence of [0/90/0] was manufactured by vacuum bagging technique using infusion epoxy as the matrix. The three reinforcement layers in all composite samples were of the same type. The mass ratio of fibres to the matrix was 1:2.5. Prior to applying the epoxy, the nanofillers were added in weight percentages (0–4 wt. %) to the epoxy according to DOE, followed by mechanical stirring at a speed of 3000 rpm for 60 min to disperse the nanofillers. After mixing the nanofiller, the mixture was degassed for ten minutes. Then, in a ratio of 100:27.4, the hardener was added to the epoxy. After composite plate fabrication, samples were removed from vacuum bagging after 24 h and placed in an oven for 120 min at a temperature of 80 °C for post-curing of the composite plates.

2.2.3. Characterization

Tensile tests were conducted under the ASTM D3039 standard using the universal testing machine, Instron 3367, equipped with a load cell with a capacity of 30 kN. The gauge was set to a length of 120 mm, and the speed was 2 mm/min. Flexural tests were conducted as per ASTM D7264 standards using a universal testing machine, Testometric M500-50CT, equipped with a 50 kN load cell. The span length was set to 95 mm, and the crosshead speed was 2 mm/min. Impact tests were conducted using the Zwick/Roell® pendulum impact tester following the ISO 179/180 standard. The Charpy method was applied to unnotched samples of each composite type with a hammer impact energy of 7 J. Using a QUANTA FEG 450 scanning electron microscope, the uncoated tensile fracture morphologies of biotex flax/PLA tri-layer hybrid composites were analyzed. The samples were cut into tiny pieces before scanning with a 5 kV accelerating voltage and high vacuum mode. The surface of interest was mounted upright on double-sided electrically conducting carbon adhesive tapes to prevent the specimens from accumulating surface charge during exposure to the electron beam.

3. Results

3.1. Tensile Properties

The tensile strength and modulus of the treated and untreated biotex flax/PLA fibre reinforced hybrid nanocomposite with nano Al_2O_3 and MgO are depicted in Figure 1. It is revealed that the addition of nano Al_2O_3 and MgO to the treated and untreated flax/PLA fibre reinforced hybrid composites increases tensile strength and modulus by transmitting and distributing the applied load. Adding the filler may reduce the available free spaces and hence increase the stiffness of the laminates. The filler can link the matrix and the fibre, leading to enhanced interaction between the fibre and the matrix. Once the load has been applied, the stress can easily be transferred from the polymer matrix to the reinforcing fibre, thus improving the tensile strength and modulus of the hybrid composite [31,52,57].

Additionally, the Al_2O_3 and MgO nanofiller in the biotex flax/PLA epoxy hybrid nanocomposites exhibit similar tensile strength and modulus behaviour. Biotex flax/PLA reinforcement that has been treated outperforms the untreated version because the sodium hydroxide (NaOH) modifies the flax/PLA cellulosic structure, which increases fibre fragmentation and disaggregation. The alkaline treatment removed the oil, wax, lignin, and pectin from fibres. The surface becomes clean and free from dirt and impurities with functional moieties, helping improve the interfacial bonding between fibres and matrix [11,18]. As illustrated in Figure 1a,c, the tensile strength of the treated biotex flax/PLA in the presence of nano-Al_2O_3 (1–3%) increased by approximately 16%, 26% and 38% as compared to untreated, which has 14%, 22% and 35%, respectively. The modulus of the treated reinforcement was increased by 24%, 44% and 56% compared to untreated, which has 20%, 39% and 52%, respectively, concerning the sample with 0% of nano-Al_2O_3. Further increase in the nanofiller concentration to 4% had reduced the tensile strength by 24% (treated) and 23% (untreated), and modulus by 19% (treated) and 17% (untreated), respectively, when compared to the sample with 3% of nano-Al_2O_3. The decrease is primarily due to a poor

fibre-matrix interface; rather than uniformly dispersing, the nanofillers agglomerate, reducing the surface area and bonding between fibre and matrix, both of which contribute to the crack initiation [1,52,58]. The acquired results are also in agreement with other reported research involving short nylon fibre/nanoclay [59], coir, wood fibre/nanoclay/PP [60], and carbon/graphene/epoxy [61].
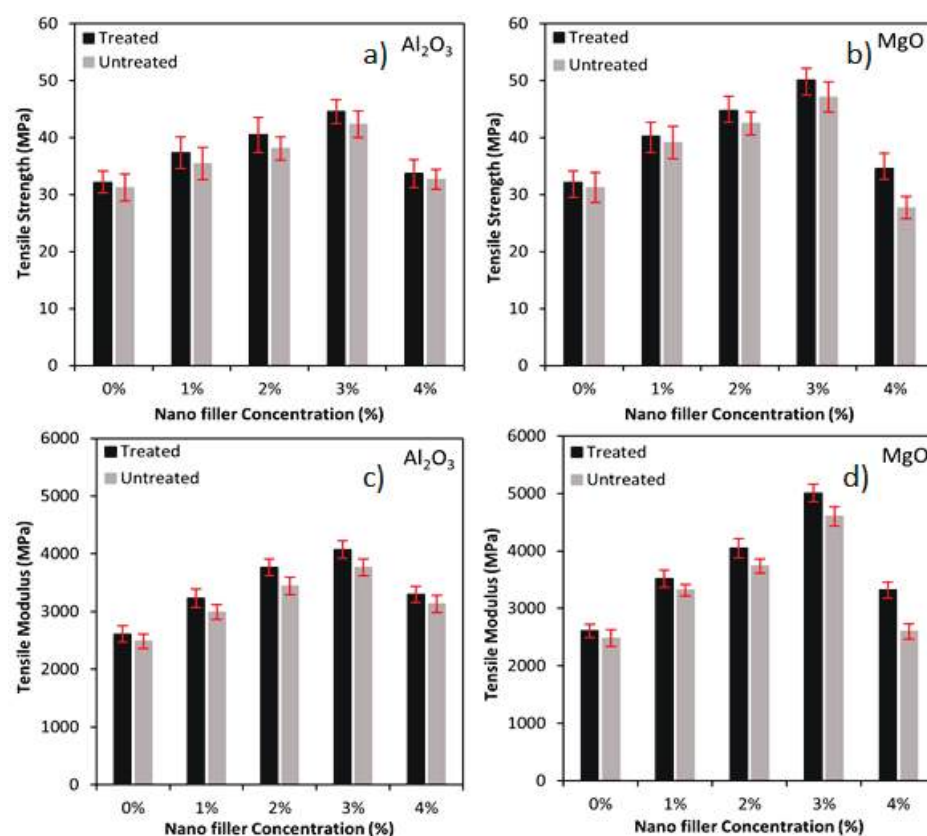
Figure 1. (**a**) Tensile strength of nano Al2O3, (**b**) Tensile strength of MgO, (**c**) Tensile modulus of nano Al2O3, (**d**) Tensile modulus of MgO incorporated flax/PLA epoxy hybrid composites.

In the case of nano-MgO, the tensile strength and modulus of the treated biotex flax/PLA in the presence of nano-MgO (1–3%) increased by approximately 25%, 39% and 56% as compared to untreated, which has 25%, 36% and 51%, respectively, while the modulus of the treated reinforcement increased by 35%, 55% and 92% as compared to untreated which has 34%, 50% and 85%, respectively, when compared to the unfilled sample (0% of nano-MgO). Further increase in the nanofiller concentration to 4% reduced the tensile strength by 31% (treated) and 41% (untreated) and the modulus by 34% (treated) and 44% (untreated), respectively, when compared to the sample with 3% of nano-MgO as shown in Figure 1b,d. The tensile strength and modulus of Al_2O_3-filled hybrid nanocomposite are higher than those of MgO-filled nanocomposite. This could be due to the higher molecular weight and higher topological polar surface area of Al_2O_3 nanofillers. A similar conclusion was reported in luffa/PbO/epoxy [52], short nylon fiber/nanoclay [59], coir, wood fiber/nanoclay/PP [60], and carbon/graphene/epoxy [61].

The tensile stress–strain curves of treated and untreated biotex flax/PLA epoxy hybrid nanocomposite with nanofiller Al_2O_3 and MgO are shown in Figure 2. Tensile stress–strain curves demonstrate that as the nanofiller concentration increases from 1% to 4%, the strain percentage decreases gradually, which indicates that the brittleness of the composite increases. This decrease in strain can be attributed to restriction of the movement of molecular chains by the nanofillers resulting in improved tensile properties [13]. Additionally, it noted that none of the samples failed abruptly, but exhibited pseudo-plastic behaviour before reaching the ultimate tensile stress value.
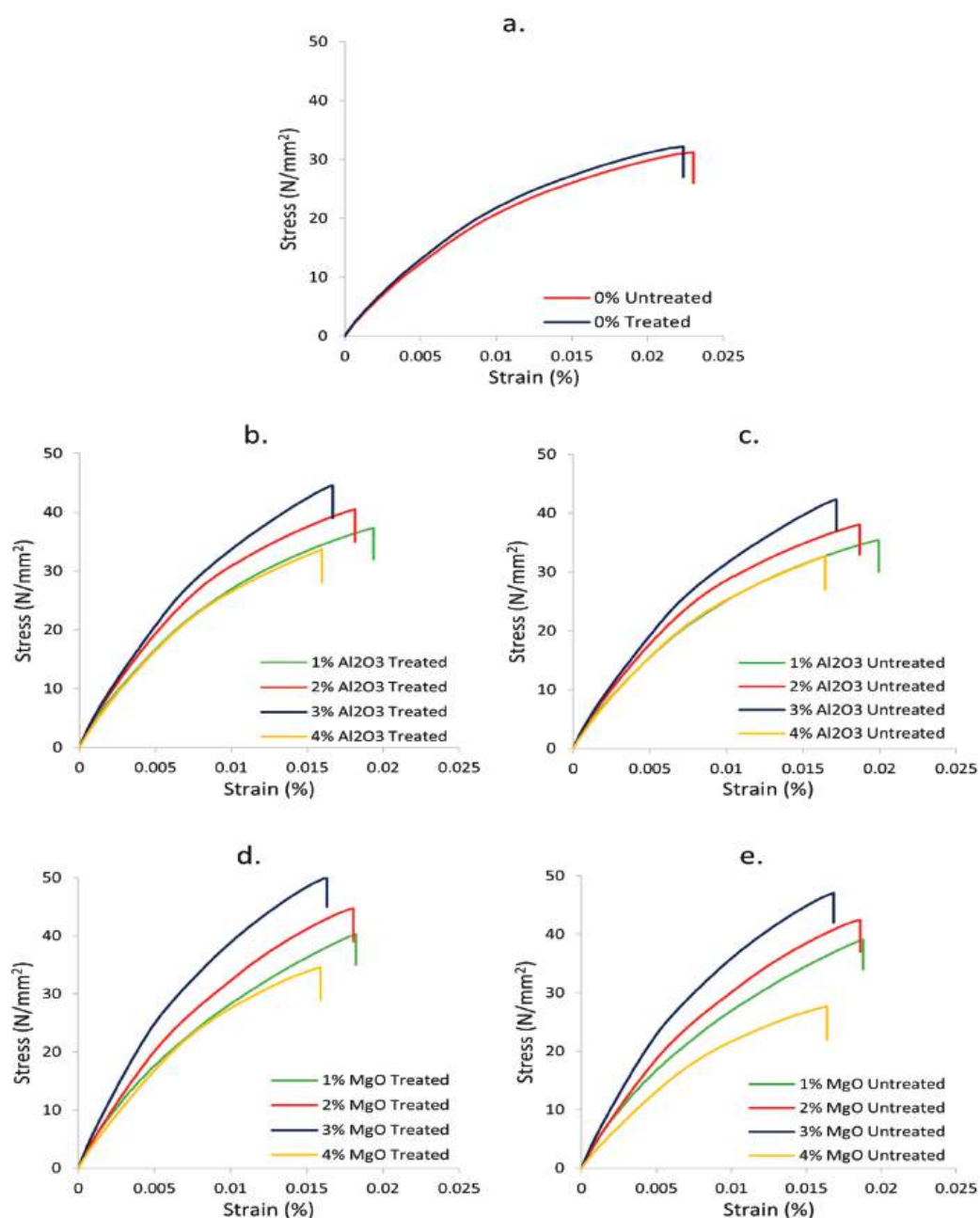
Figure 2. Tensile stress–strain curves of (**a**) neat composite, (**b**) Al_2O_3—treated, (**c**) Al_2O_3—untreated, (**d**) MgO—treated, and (**e**) MgO—untreated flax/PLA epoxy hybrid composites.

The increasing trend in tensile strength and modulus can be explained by the large surface area of the nanofillers, which act as a link between the biotex flax/PLA fibre and epoxy matrix, resulting in improved bonding. Thus, the applied load can be easily transferred from matrix to fibre, resulting in delayed crack initiation. Therefore, it can be concluded that the incorporation of nanofillers increases interfacial adhesion, resulting in an increase in tensile properties, which is also reported in previous studies [1,52,58].

3.2. Flexural Properties

The flexural strength and modulus of the treated and untreated biotex flax/PLA fibre reinforced hybrid nanocomposite with Al_2O_3 and MgO nanofiller are illustrated in Figure 3. It can be seen that the addition of Al_2O_3 and MgO nanofillers to treated and untreated flax/PLA fibre reinforced composites increase flexural strength and modulus via interfacial

adhesion between the nanofillers and epoxy matrix. The surface energy and rigidity of the nanofillers dictate the extent to which they interact with the matrix. Nanofillers such as Al_2O_3 and MgO have higher surface energy and rigidity, which results in a more robust interaction and thus a higher flexural strength and modulus of the filled composite, at the expense of ductility [58].
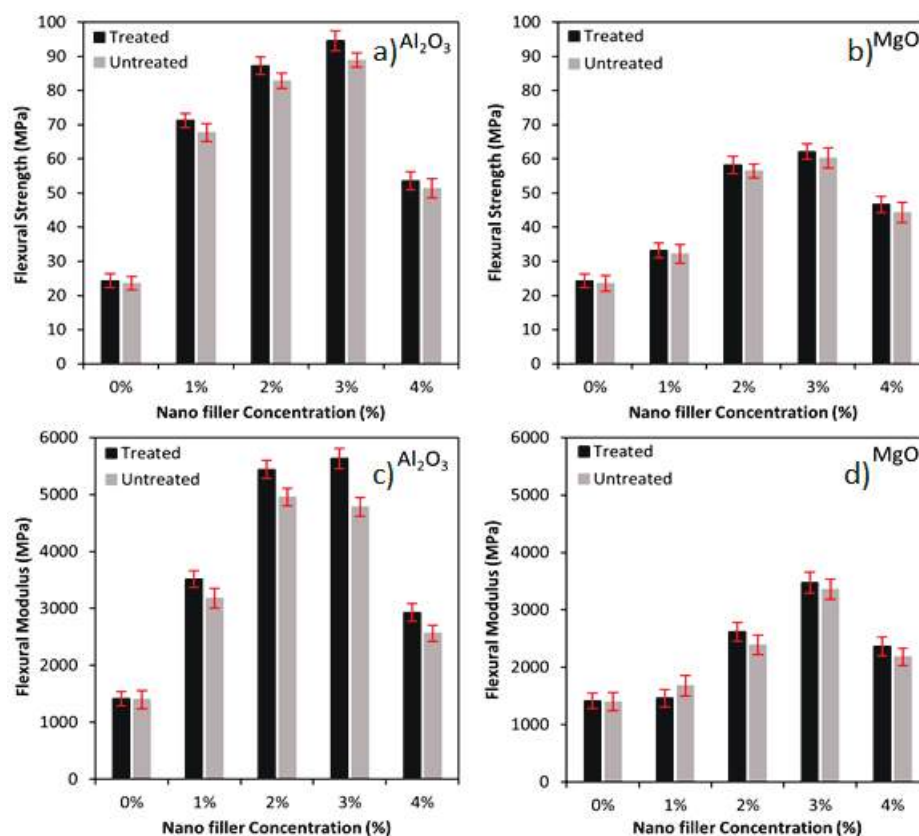
Figure 3. (**a**) Flexural strength of nano Al_2O_3, (**b**) Flexural strength of MgO, (**c**) Flexural modulus of nano Al_2O_3, (**d**) Flexural modulus of MgO incorporated flax/PLA epoxy hybrid composites.

Additionally, the Al_2O_3 and MgO nanofiller in the biotex flax/PLA epoxy hybrid nanocomposites exhibit similar flexural strength and modulus behaviour. Biotex flax/PLA reinforcement that has been treated outperforms untreated one. As illustrated in Figure 3a,c, the flexural strength of the treated biotex flax/PLA in the presence of nano-Al_2O_3 (1–3%) increased by approximately 193%, 259% and 289% as compared to untreated, which has 187%, 252% and 277%, respectively. In contrast, the modulus of the treated reinforcement was increased by 148%, 285% and 298% compared to untreated, which has 227%, 254% and 242%, respectively, when compared with unfilled samples (0% of nano-Al_2O_3). Further increase in the nanofiller concentration to 4% reduced the flexural strength by 43% (treated) and 42% (untreated) and the modulus by 48% (treated) and 46% (untreated), respectively when compared with the sample with 3% of nano-Al_2O_3. This lowering is due to nano-Al_2O_3 aggregation, detrimental to the fabricated nanocomposites' physical and mechanical properties. The greater decrease in flexural strength and modulus for treated samples was due to better fibre fragmentation and disaggregation by alkali treatment, which produces more active sites on the fibre surface where the nanofillers have higher attraction. Similar results are reported in glass/SiO_2/epoxy [31] and luffa/PbO/epoxy [52].

In the case of nano-MgO, the flexural strength and modulus of the treated biotex flax/PLA in the presence of nano-MgO (1–3%) increased by approximately 36%, 140% and 156% as compared to untreated, which has 36%, 140% and 156%, respectively. The modulus of the treated reinforcement was increased by 3%, 85% and 146% as compared to

untreated, which has 20%, 71% and 140%, respectively compared to the neat sample (0% of nano-MgO). Further increase in the nanofiller concentration to 4% reduced the flexural strength by 25% (treated) and 26% (untreated), and the modulus by 32% (treated) and 35% (untreated), respectively when compared with the sample with 3% of nano-MgO, as shown in Figure 3b,d. This decrease is due to nano-MgO aggregation, which negatively impacts the mechanical and physical properties of the fabricated nanocomposites, with similar results reported in glass/SiO_2/epoxy [31] and luffa/PbO/epoxy [52].

The flexural stress–strain curves of treated and untreated biotex flax/PLA epoxy hybrid nanocomposite with nano Al_2O_3 and MgO are shown in Figure 4. Flexural stress–strain curves demonstrate that as the nanofiller concentration increases from 1% to 4%, the strain percentage decreases gradually, which indicates that the ductility of the composite decreases. This is associated with less chain mobility and deformability of the matrix due to the presence of additional rigid nanofillers, which disturb the deformation of the crystalline region in the matrix, resulting in improved bending properties [13,62]. Additionally, it is noted that none of the samples failed abruptly, but exhibited pseudo-plastic behaviour before reaching the ultimate flexural stress value. Flexural strength follows a similar trend to tensile strength, although it varies less between formulations than tensile strength [36].

In Figure 4, there is a slight change in the stress–strain values of the treated and untreated fibre reinforced composite, similar to the tensile stress and strain. The flax/PLA is 100% bioderived commingled fabric in which the percentage of flax fibre is 40% and the remaining 60% is PLA; thus, the alkali treatment only alters the surface properties of the natural fibres, which is responsible for the reduced difference between the treated and untreated reinforcement.

3.3. Impact Properties

The unnotched impact strength of biotex flax/PLA fibre (treated and untreated) and nanofiller reinforced epoxy composite is illustrated in Figure 5. Charpy impact strength (calculated by dividing the absorbed energy with sample width and thickness) is related to the material's toughness, and the fibre-matrix interface and bonding between the lamina indicated the nanocomposite's fracture toughness. Nanofillers such as Al_2O_3 and MgO improved the bonding between the filler and matrix, and their rigidity increased energy absorption. Energy absorption in polymer nanocomposites occurs due to debonding at the fibre–matrix interface, the fracturing of the reinforcing material, and matrix plastic deformation [4,58].

Additionally, the Al_2O_3 and MgO nanofiller in biotex flax/PLA epoxy hybrid nanocomposite exhibit similar impact properties as tensile and flexural properties. Treated biotex flax/PLA reinforcement outperformed as compared to the untreated. The impact strength of the treated biotex flax/PLA in the presence of nano-Al_2O_3 (1–3%) increased approximately by 10%, 15% and 22% as compared to untreated, which has 9%, 12% and 17%, respectively, as compared to unfilled sample (0% of nano-Al_2O_3). Further increase in the nanofiller concentration to 4% reduced the impact strength by 16% (treated) and 18% (untreated) in the sample with 3% of nano-Al_2O_3. Similar results are observed for a research study on bagasse/nanoclay/PP [63].

In the case of nano-MgO, the impact strength of the treated biotex flax/PLA in the presence of nano-MgO (1–3%) increased by approximately 15%, 24% and 28% as compared to untreated, which has 14%, 21% and 23%, respectively, as compared to the neat sample (0% of nano-MgO). Furthermore, an increase in the nanofiller concentration to 4% decreased the impact strength by 11% (treated) and 13% (untreated), concerning the sample having 3% nano-MgO. The presence of Al_2O_3 and MgO nanofiller in the epoxy matrix generates matrix discontinuity, which provides sites for crack initiation, resulting in decreased impact strength at 4% nanofillers; similar results are reported in bagasse/SiO_2/PE [37] and PLA/nanoclay/LLDE [64].
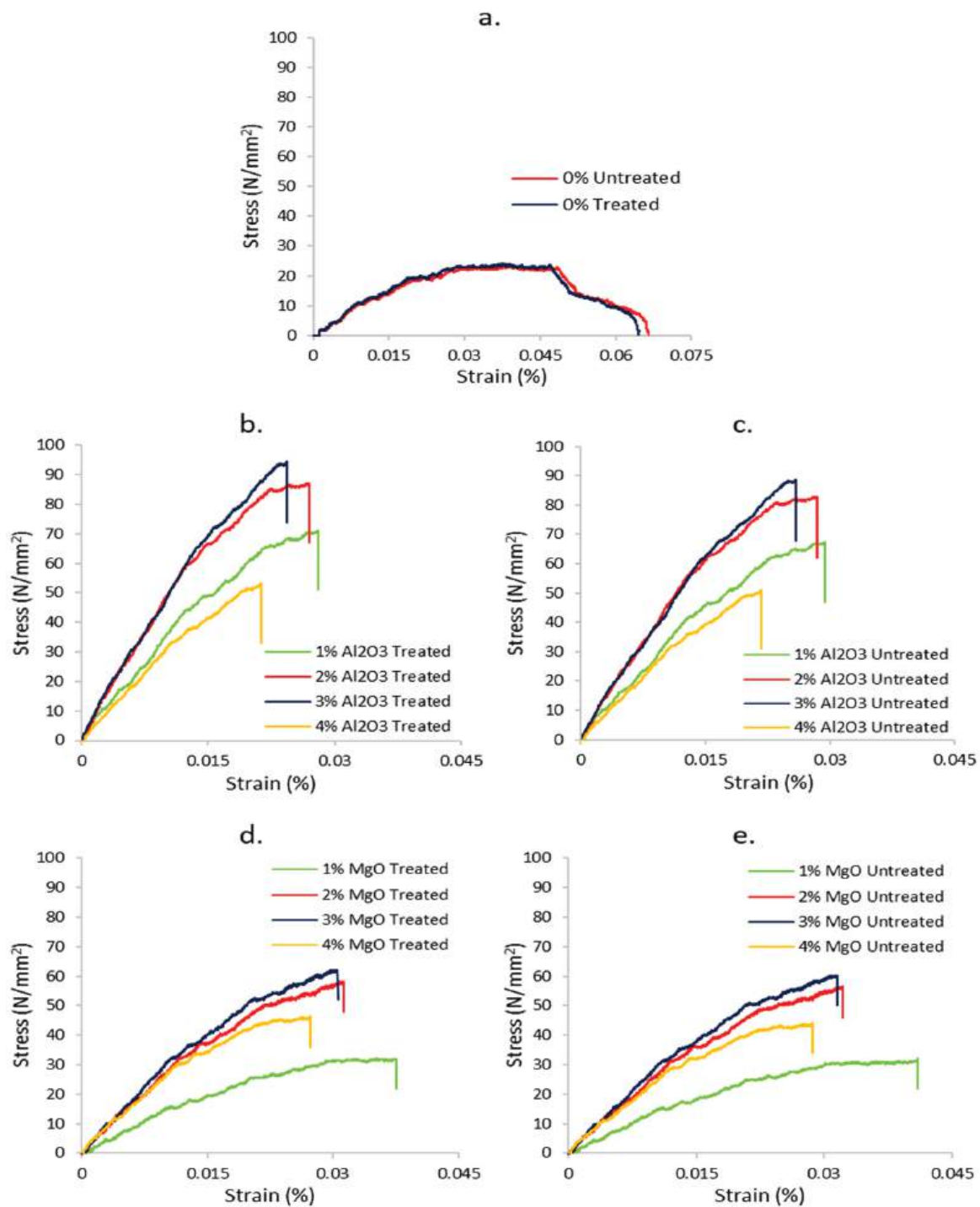
Figure 4. Flexural stress–strain curves of (**a**) neat composite, (**b**) Al_2O_3—treated, (**c**) Al_2O_3—untreated, (**d**) MgO—treated, and (**e**) MgO—untreated flax/PLA epoxy hybrid composites.
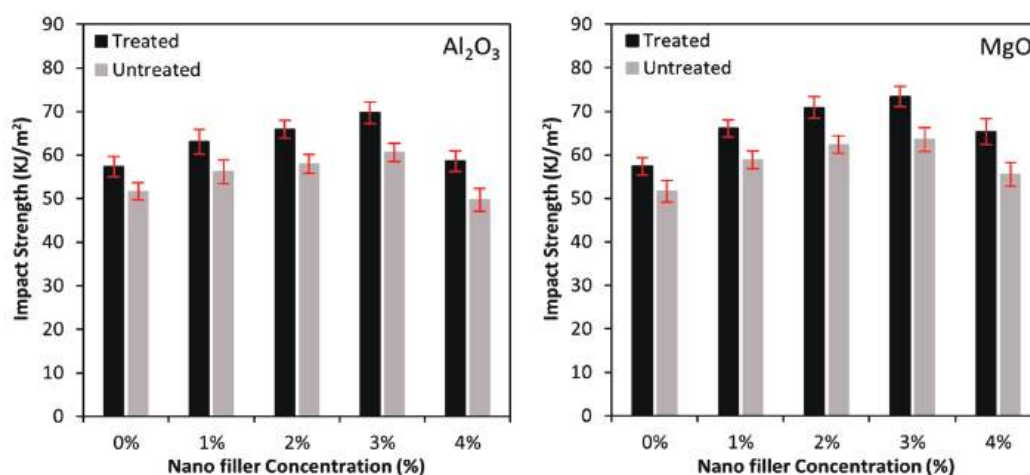
Figure 5. Impact strength of nano Al_2O_3 and MgO incorporated biotex flax/PLA epoxy hybrid composites.

3.4. Scanning Electron Microscope (SEM) Failure Analysis

SEM analysis was used to characterize the surface characteristics of the tensile broken composite material utilized in this investigation. The SEM micrographs of treated and untreated biotex flax/PLA reinforced epoxy composites without nanofillers are shown in Figure 6 at $500\times$ magnification. The literature shows that the alkaline treatment of natural fibre removed the hemicellulose layer from the surface of fibres [19,52]. In Fourier transform infrared spectroscopy (FTIR) analysis, the disappearance of the C=O stretching vibration of hemicellulose at 1750 cm^{-1} indicates the removal of hemicellulose that strengthens the fibre matrix interface, and results in improved mechanical properties of composites [53,65]. This finding is further validated by Figure 6, which shows that the alkali treatments removed impurities from the fibre surface, such as hemicelluloses and lignin. This uneven topography aided mechanical interlocking. It also improved fibre–matrix adhesion, which improved mechanical qualities. In the same way, a corresponding result was accomplished with jute/epoxy composite [65–67].
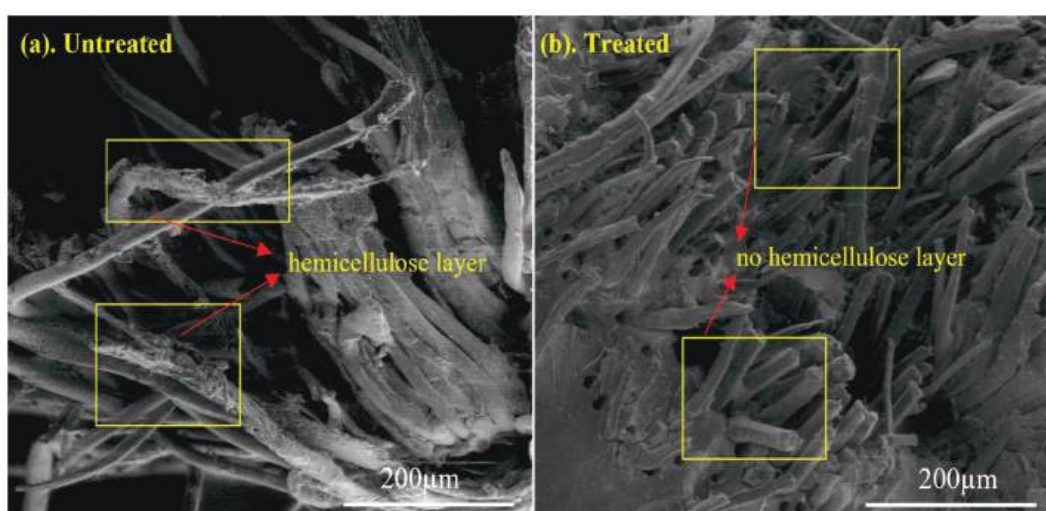
Figure 6. SEM images of tensile fractured (**a**) Untreated (**b**) alkali-treated biotex Flax/PLA reinforced epoxy composite.

Figures 7 and 8 show SEM micrographs of biotex flax/PLA reinforced epoxy hybrid nanocomposites with Al_2O_3 and MgO nanofiller. The fractured surface of the tensile samples was analyzed to determine fibre failure and matrix–fibre interfacial bonding. Micrograph images of treated biotex flax/PLA reinforced epoxy composites with nanofiller Al_2O_3 and MgO at concentrations ranging from 1% to 4% are shown in Figure 7. The

micrograph images indicate that the strength of the polymer composite is highly dependent on the fibre–matrix interface bonding. The fibre–matrix interface of the composite with 1% filler exhibits severe fibre pullout, fibre breakage, cracks, and air bubbles, resulting in poor bonding, low strength, and a poor fibre–matrix interface.
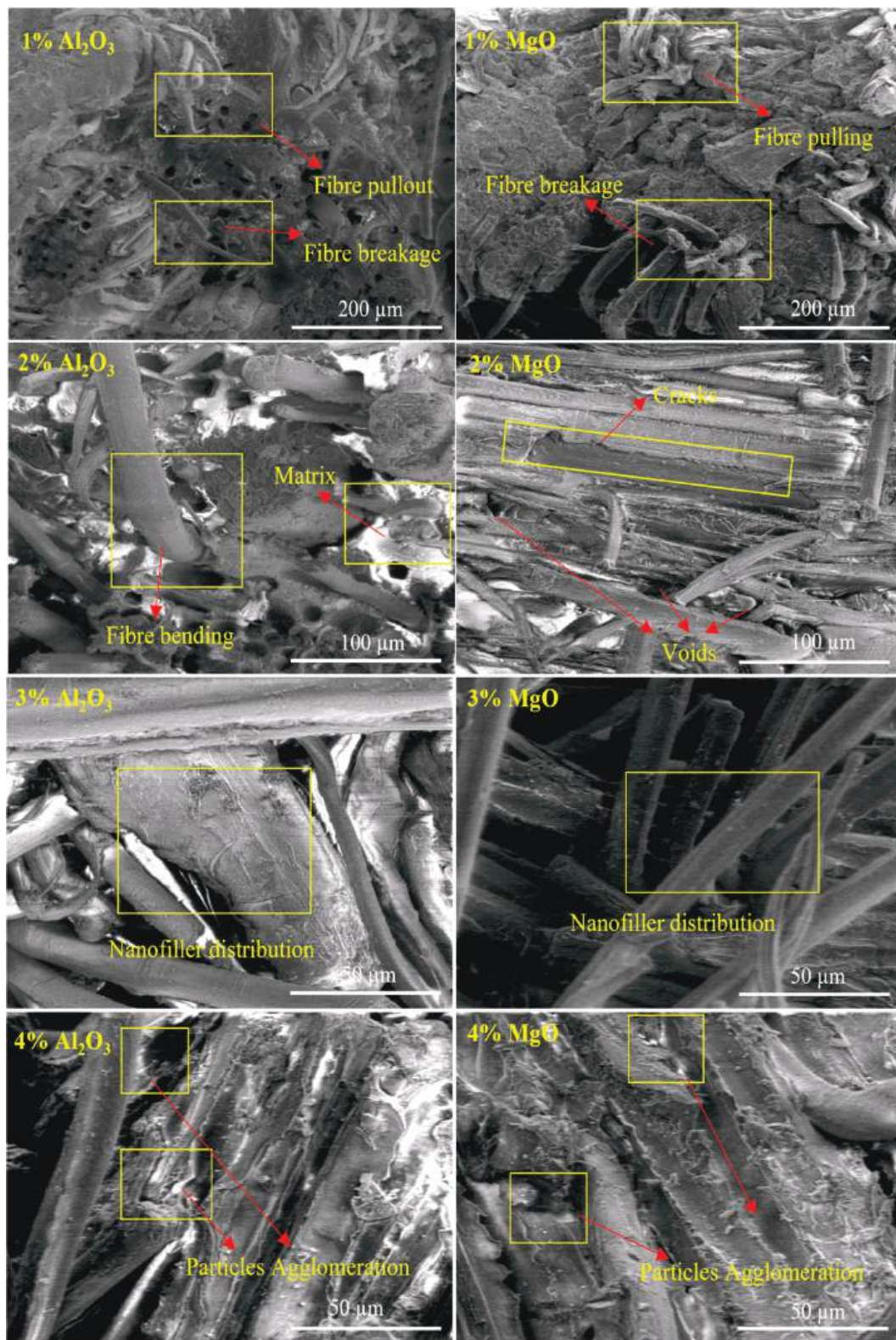
Figure 7. SEM images of alkali-treated biotex flax/PLA reinforced epoxy composite at different percentage of nano-Al$_2$O$_3$ and nano-MgO.
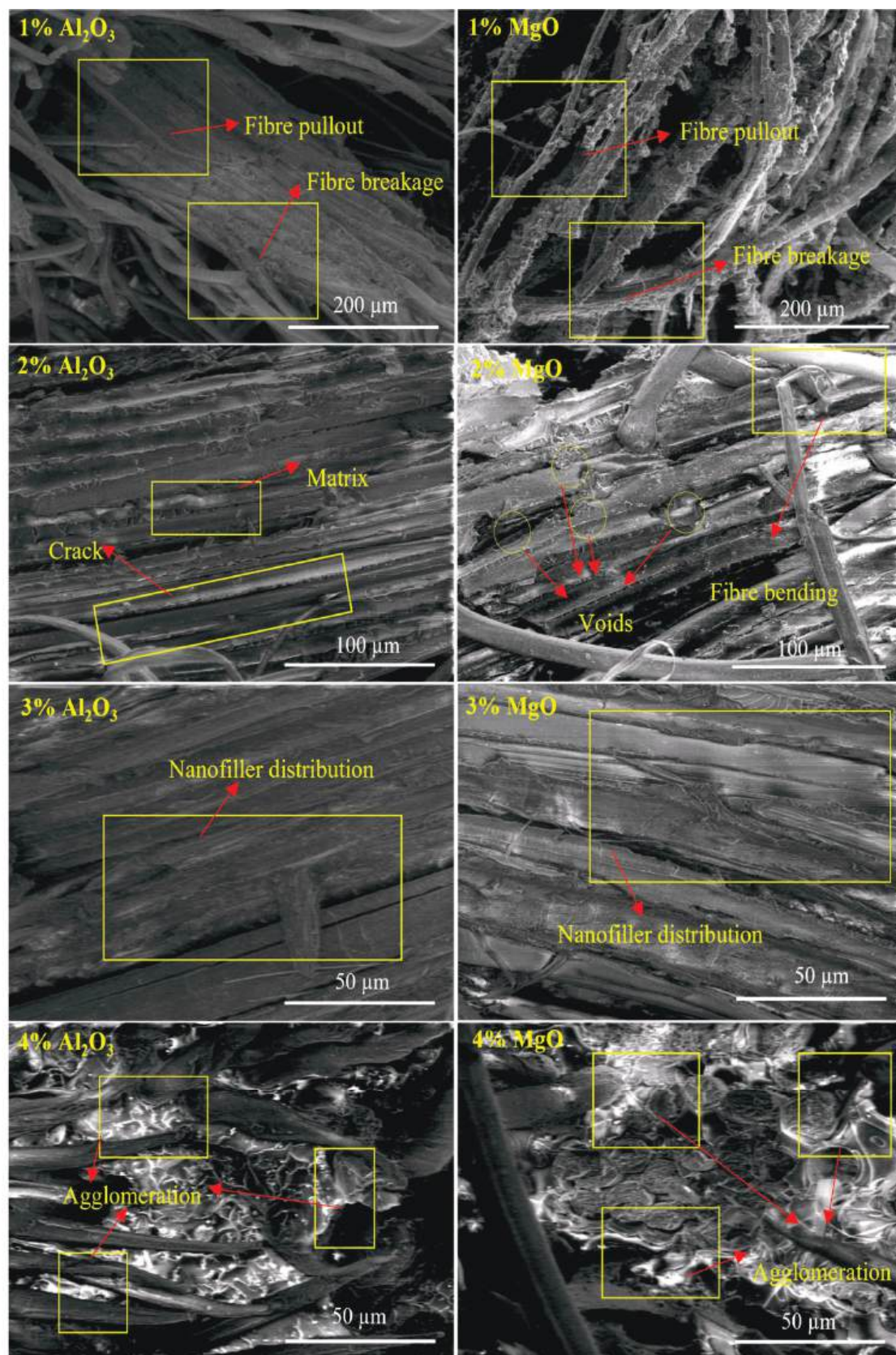
Figure 8. SEM images of untreated biotex flax/PLA reinforced epoxy composite at different percentages of nano-Al_2O_3 and nano-MgO.

However, this interface is better than that of the neat composite. As the amount of nanofiller in the matrix increases, the fibre–matrix interface improves. Better fibre–matrix bonding was observed when the matrix contained 2% and 3% nanofiller. Minimum fibre pullout indicates improved fibre–matrix interfacial adhesion; this aids in transferring load from the matrix to the fibre, thereby increasing its strength. The decrease in mechanical properties caused by the aggregation of nanofiller at 4% is also justified by the micrograph images, which restrict the interaction of the nanofiller with the matrix, resulting in the laminates' poor mechanical properties. The same trend was observed in micrograph images (as shown in Figure 8) of untreated biotex flax/PLA reinforced epoxy composites with nanofiller Al_2O_3 and MgO at concentrations ranging from 1% to 4%. Similar SEM images are also analyzed for oil palm nanofiller/kenaf fibre/epoxy hybrid nanocomposites [1] and lead oxide nanofiller/luffa fibre/epoxy hybrid nanocomposites [52].

4. Conclusions

The purpose of this study was to develop a novel hybrid nanocomposite by incorporating nano-Al_2O_3 and nano-MgO as reinforcing fillers into biotex flax/PLA fibre mat reinforced epoxy composites. The results of this study are encouraging, as the hybrid nanocomposites fabricated using Al_2O_3 and MgO nanofiller and flax/PLA fibres exhibit improved mechanical properties. The addition of nanofiller in the alkali-treated biotex flax/PLA/epoxy composites significantly enhances the mechanical strength in tensile, bending, and impact strength compared to the untreated biotex flax/PLA reinforced epoxy composites, by hindering the crack initiation or propagation paths. Morphological analysis using SEM demonstrated that adding 3% nano-Al_2O_3 and 3% nano-MgO filler to flax/PLA/epoxy composites reduces void contents, fibre pull out, fibre protrusion, and tearing on the fractured surface by simply fracturing or breaking/bending the fibre due to the fibre's improved adhesion and interfacial bonding with the matrix. The enhanced mechanical and morphological properties of the nano-(Al_2O_3 & MgO)/(flax/PLA)/epoxy hybrid nanocomposites indicate a high potential for construction and structural applications requiring renewable resources high performance. As a result of their superior morphological and mechanical properties, the developed hybrid nanocomposites will serve as a low-cost, lightweight, and environmentally friendly composite material for use as a building material. This research could be expanded in the near future by varying types, sizes, and concentrations of nanofillers and different natural fibres and chemical treatment methods.

Author Contributions: Conceptualization, A.A. and A.A.A.R.; methodology, A.A., A.A.A.R. and M.S.Z.A.; software, A.A.; validation, A.A., A.A.A.R., H.A. and M.S.Z.A.; formal analysis, A.A.; investigation, A.A.A.R. and M.S.Z.A.; resources, M.S.Z.A., H.A. and A.A.A.R.; data curation, A.A.; writing—original draft preparation, A.A.; writing—review and editing, A.A., A.A.A.R., M.S.Z.A. and H.A.; visualization, A.A.A.R., M.S.Z.A. and H.A.; supervision, A.A.A.R.; project administration, A.A.A.R.; funding acquisition, A.A.A.R. and H.A. All authors have read and agreed to the published version of the manuscript.

Institutional Review Board Statement: Not applicable.

Informed Consent Statement: Not applicable.

Data Availability Statement: The data presented in this study are available on request from the corresponding author. The data are not publicly available due to privacy of this research.

Conflicts of Interest: The authors declare no conflict of interest.

References

1. Saba, N.; Paridah, M.T.; Abdan, K.; Ibrahim, N.A. Effect of Oil Palm Nano Filler on Mechanical and Morphological Properties of Kenaf Reinforced Epoxy Composites. *Constr. Build. Mater.* **2016**, *123*, 15–26. [CrossRef]
2. Awais, H.; Nawab, Y.; Anjang, A.; Akil, H.M.; Zainol Abidin, M.S. Effect of Fabric Architecture on the Shear and Impact Properties of Natural Fibre Reinforced Composites. *Compos. Part B Eng.* **2020**, *195*, 108069. [CrossRef]
3. Majeed, K.; Jawaid, M.; Hassan, A.; Abu Bakar, A.; Abdul Khalil, H.P.S.; Salema, A.A.; Inuwa, I. Potential Materials for Food Packaging from Nanoclay/Natural Fibres Filled Hybrid Composites. *Mater. Des.* **2013**, *46*, 391–410. [CrossRef]
4. Ibrahim, I.D.; Jamiru, T.; Sadiku, E.R.; Kupolati, W.K.; Agwuncha, S.C. Impact of Surface Modification and Nanoparticle on Sisal Fiber Reinforced Polypropylene Nanocomposites. *J. Nanotechnol.* **2016**, *2016*, 4235975. [CrossRef]
5. Hanan, F.; Jawaid, M.; Md Tahir, P. Mechanical Performance of Oil Palm/Kenaf Fiber-Reinforced Epoxy-Based Bilayer Hybrid Composites. *J. Nat. Fibers* **2020**, *17*, 155–167. [CrossRef]
6. Awais, H.; Nawab, Y.; Amjad, A.; Anjang, A.; Md Akil, H.; Zainol Abidin, M.S.S. Effect of Comingling Techniques on Mechanical Properties of Natural Fibre Reinforced Cross-Ply Thermoplastic Composites. *Compos. Part B Eng.* **2019**, *177*, 107279. [CrossRef]
7. Zakriya, M.; Ramakrishnan, G.; Gobi, N.; Palaniswamy, N.K.; Srinivasan, J. Jute-Reinforced Non-Woven Composites as a Thermal Insulator and Sound Absorber—A Review. *J. Reinf. Plast. Compos.* **2017**, *36*, 206–213. [CrossRef]
8. Xiong, X.; Shen, S.Z.; Hua, L.; Liu, J.Z.; Li, X.; Wan, X.; Miao, M. Finite Element Models of Natural Fibers and Their Composites: A Review. *J. Reinf. Plast. Compos.* **2018**, *37*, 617–635. [CrossRef]
9. Chung, D. *Carbon Composites: Composites with Carbon Fibers, Nanofibers, and Nanotubes*; Elsevier: Amsterdam, The Netherlands, 2016.
10. Amjad, A.; Awais, H.; Ali, M.Z.; Abidin, M.S.Z.; Anjang, A.; Zainol Abidin, M.S.; Anjang, A. Effect of Alumina Nanofiller on the Mechanical Properties of 2D Woven Biotex Flax/PLA Fiber-Reinforced Nanocomposite. In *Lecture Notes in Mechanical Engineering*; Springer: Singapore, 2020; pp. 383–391. [CrossRef]
11. Gholampour, A.; Ozbakkaloglu, T. A Review of Natural Fiber Composites: Properties, Modification and Processing Techniques, Characterization, Applications. *J. Mater. Sci.* **2020**, *55*, 829–892. [CrossRef]
12. Yang, J.; Guo, Y.; Yao, L.; Ni, Q.; Qiu, Y. Effects of Kevlar Volume Fraction and Fabric Structures on the Mechanical Properties of 3D Orthogonal Woven Ramie/Kevlar Reinforced Poly (Lactic Acid) Composites. *J. Ind. Text.* **2018**, *47*, 2074–2091. [CrossRef]
13. Awais, H.; Nawab, Y.; Amjad, A.; Anjang, A.; Abidin, M.S.Z. Mechanical Properties of Hollow Glass Microspheres Filled Jute Woven Comingled Composites. *Key Eng. Mater.* **2020**, *858*, 41–46. [CrossRef]
14. Godara, M.S.S. Effect of Chemical Modification of Fiber Surface on Natural Fiber Composites: A Review. *Mater. Today Proc.* **2019**, *18*, 3428–3434. [CrossRef]
15. Bledzki, A.K.; Mamun, A.A.; Gutowski, V.S. The Effects of Acetylation on Properties of Flax Fibre and Its Polypropylene Composites. *Express Polym. Lett.* **2008**, *2*, 413–422. [CrossRef]
16. Ferreira, D.P.; Cruz, J.; Fangueiro, R. *Surface Modification of Natural Fibers in Polymer Composites*; Elsevier: Amsterdam, The Netherlands, 2019. [CrossRef]
17. Vinayagamoorthy, R. Influence of Fiber Surface Modifications on the Mechanical Behavior of *Vetiveria Zizanioides* Reinforced Polymer Composites. *J. Nat. Fibers* **2019**, *16*, 163–174. [CrossRef]
18. Khan, J.; Mariatti, M. The Influence of Substrate Functionalization for Enhancing the Interfacial Bonding between Graphene Oxide and Nonwoven Polyester. *Fibers Polym.* **2021**, 1–11. [CrossRef]
19. De Araujo Alves Lima, R.; Kawasaki Cavalcanti, D.; de Souza e Silva Neto, J.; Meneses da Costa, H.; Banea, M.D. Effect of Surface Treatments on Interfacial Properties of Natural Intralaminar Hybrid Composites. *Polym. Compos.* **2020**, *41*, 314–325. [CrossRef]
20. Pereira, A.L.; Banea, M.D.; Neto, J.S.S.; Cavalcanti, D.K.K. Mechanical and Thermal Characterization of Natural Intralaminar Hybrid Composites Based on Sisal. *Polymers* **2020**, *12*, 866. [CrossRef] [PubMed]
21. Abdellaoui, H.; Raji, M.; Essabir, H.; Bouhfid, R.; Qaiss, A.E.K. Mechanical Behavior of Carbon/Natural Fiber-Based Hybrid Composites. In *Mechanical and Physical Testing of Biocomposites, Fibre-Reinforced Composites and Hybrid Composites*; Elsevier: Amsterdam, The Netherlands, 2018; pp. 103–122. [CrossRef]
22. Mochane, M.J.; Mokhena, T.C.; Mokhothu, T.H.; Mtibe, A.; Sadiku, E.R.; Ray, S.S.; Ibrahim, I.D.; Daramola, O.O. Recent Progress on Natural Fiber Hybrid Composites for Advanced Applications: A Review. *Express Polym. Lett.* **2019**, *13*, 159–198. [CrossRef]
23. Stankovich, S.; Dikin, D.A.; Dommett, G.H.B.B.; Kohlhaas, K.M.; Zimney, E.J.; Stach, E.A.; Piner, R.D.; Nguyen, S.B.T.; Ruoff, R.S. Graphene-Based Composite Materials. *Nature* **2006**, *442*, 282–286. [CrossRef] [PubMed]
24. Eichhorn, S.J.; Dufresne, A.; Aranguren, M.; Marcovich, N.E.; Capadona, J.R.; Rowan, S.J.; Weder, C.; Thielemans, W.; Roman, M.; Renneckar, S.; et al. Review: Current International Research into Cellulose Nanofibres and Nanocomposites. *J. Mater. Sci.* **2010**, *45*, 1–33. [CrossRef]
25. Hasan, K.M.F.; Horváth, P.G.; Alpár, T. Potential Natural Fiber Polymeric Nanobiocomposites: A Review. *Polymers* **2020**, *12*, 1072. [CrossRef]
26. Awais, H.; Nawab, Y.; Amjad, A.; Anjang, A.; Zainol Abidin, M.S.S. Fabrication and Characterization of Lightweight Engineered Polypropylene Composites Using Silica Particles and Flax Woven Comingled Structure. In *Lecture Notes in Mechanical Engineering*; Springer: Berlin/Heidelberg, Germany, 2020; pp. 403–410. [CrossRef]
27. Khan, J.; Momin, S.A.; Mariatti, M. *A Review on Advanced Carbon-Based Thermal Interface Materials for Electronic Devices*; Elsevier: Amsterdam, The Netherlands, 2020; Volume 168, pp. 65–112. [CrossRef]

28. Bhattacharya, M. Polymer Nanocomposites-A Comparison between Carbon Nanotubes, Graphene, and Clay as Nanofillers. *Materials* **2016**, *9*, 262. [CrossRef]

29. Marquis, D.M.; Guillaume, É.; Chivas-Joly, C.; Damien, M.M.; Eric, G.; Carine, C.-J. *Properties of Nanofillers in Polymer*; Intech Open: London, UK, 2015; Volume 2, p. 64. [CrossRef]

30. Saba, N.; Tahir, P.M.; Jawaid, M. A Review on Potentiality of Nano Filler/Natural Fiber Filled Polymer Hybrid Composites. *Polymers* **2014**, *6*, 2247–2273. [CrossRef]

31. Manjunath, M.; Renukappa, N.M.; Suresha, B. Influence of Micro and Nanofillers on Mechanical Properties of Pultruded Unidirectional Glass Fiber Reinforced Epoxy Composite Systems. *J. Compos. Mater.* **2016**, *50*, 1109–1121. [CrossRef]

32. Foruzanmehr, M.; Vuillaume, P.Y.; Elkoun, S.; Robert, M. Physical and Mechanical Properties of PLA Composites Reinforced by TiO2 Grafted Flax Fibers. *Mater. Des.* **2016**, *106*, 295–304. [CrossRef]

33. Samariha, A.; Hemmasi, A.H.; Ghasemi, I.; Bazyar, B.; Nemati, M. Effect of Nanoclay Contents on Properties, of Bagasse Flour/Reprocessed High Density Polyethylene/Nanoclay Composites. *Maderas Cienc. Tecnol.* **2015**, *17*, 637–646. [CrossRef]

34. Li, Y.; Chen, C.; Xu, J.; Zhang, Z.; Yuan, B.; Huang, X. Improved Mechanical Properties of Carbon Nanotubes-Coated Flax Fiber Reinforced Composites. *J. Mater. Sci.* **2015**, *50*, 1117–1128. [CrossRef]

35. Kushwaha, P.K.; Pandey, C.N.; Kumar, R. Study on the Effect of Carbon Nanotubes on Plastic Composite Reinforced with Natural Fiber. *J. Indian Acad. Wood Sci.* **2014**, *11*, 82–86. [CrossRef]

36. Chaharmahali, M.; Hamzeh, Y.; Ebrahimi, G.; Ashori, A.; Ghasemi, I. Effects of Nano-Graphene on the Physico-Mechanical Properties of Bagasse/Polypropylene Composites. *Polym. Bull.* **2014**, *71*, 337–349. [CrossRef]

37. Hosseini, S.B.; Hedjazi, S.; Jamalirad, L.; Sukhtesaraie, A. Effect of Nano-SiO$_2$ on Physical and Mechanical Properties of Fiber Reinforced Composites (FRCs). *J. Indian Acad. Wood Sci.* **2014**, *11*, 116–121. [CrossRef]

38. Gowthami, A.; Ramanaiah, K.; Ratna Prasad, A.V.; Hema Chandra Reddy, K.; Mohana Rao, K.; Sridhar Babu, G. Effect of Silica on Thermal and Mechanical Properties of Sisal Fiber Reinforced Polyester Composites. *J. Mater. Environ. Sci.* **2013**, *4*, 199–204.

39. Han, S.O.; Karevan, M.; Bhuiyan, M.A.; Park, J.H.; Kalaitzidou, K.; Bhuiyan, M.A.; Karevan, M.; Han, S.O.; Park, J.H. Effect of Exfoliated Graphite Nanoplatelets on the Mechanical and Viscoelastic Properties of Poly(Lactic Acid) Biocomposites Reinforced with Kenaf Fibers. *J. Mater. Sci.* **2012**, *47*, 3535–3543. [CrossRef]

40. Hapuarachchi, T.D.; Peijs, T. Multiwalled Carbon Nanotubes and Sepiolite Nanoclays as Flame Retardants for Polylactide and Its Natural Fibre Reinforced Composites. *Compos. Part A Appl. Sci. Manuf.* **2010**, *41*, 954–963. [CrossRef]

41. Harito, C.; Bavykin, D.V.; Yuliarto, B.; Dipojono, H.K.; Walsh, F.C. Polymer Nanocomposites Having a High Filler Content: Synthesis, Structures, Properties, and Applications. *Nanoscale* **2019**, *11*, 4653–4682. [CrossRef] [PubMed]

42. Tian, J.; Yang, C.; Yang, J.; Hao, S. The Correlated Effects of Filler Loading on the Curing Reaction and Mechanical Properties of Graphene Oxide Reinforced Epoxy Nanocomposites. *J. Mater. Sci.* **2021**, *56*, 3723–3737. [CrossRef]

43. Zhao, Y.; Drummer, D. Influence of Filler Content and Filler Size on the Curing Kinetics of an Epoxy Resin. *Polymers* **2019**, *11*, 1797. [CrossRef]

44. Harsch, M.; Karger-Kocsis, J.; Holst, M. Influence of Fillers and Additives on the Cure Kinetics of an Epoxy/Anhydride Resin. *Eur. Polym. J.* **2007**, *43*, 1168–1178. [CrossRef]

45. Judawisastra, H.; Harito, C.; Anindyajati, D.; Purnama, H.; Abdullah, A.H.D. Mechanical Properties of Carbon Nanotubes/Epoxy Nanocomposites: Pre-Curing, Curing Temperature, and Cooling Rate. *High Perform. Polym.* **2021**, *33*, 741–750. [CrossRef]

46. Pickering, K.L.; Efendy, M.G.A.; Le, T.M. A Review of Recent Developments in Natural Fibre Composites and Their Mechanical Performance. *Compos. Part A Appl. Sci. Manuf.* **2016**, *83*, 98–112. [CrossRef]

47. Gupta, M.; Srivastava, R.; Bisaria, H. Potential of Jute Fibre Reinforced Polymer Composites: A Review. *Int. J. Fiber Text. Res.* **2015**, *5*, 30–38.

48. Wong, D.; Anwar, M.; Debnath, S.; Hamid, A.; Izman, S. A Review: Recent Development of Natural Fiber-Reinforced Polymer Nanocomposites. *Jom* **2021**, *73*, 2504–2515. [CrossRef]

49. Alsubari, S.; Zuhri, M.Y.M.; Sapuan, S.M.; Ishak, M.R.; Ilyas, R.A.; Asyraf, M.R.M. Potential of Natural Fiber Reinforced Polymer Composites in Sandwich Structures: A Review on Its Mechanical Properties. *Polymers* **2021**, *13*, 423. [CrossRef]

50. Wang, H.; Memon, H.; Hassan, E.A.M.; Miah, M.S.; Ali, M.A. Effect of Jute Fiber Modification on Mechanical Properties of Jute Fiber Composite. *Materials* **2019**, *12*, 1226. [CrossRef]

51. Chaudhary, V.; Bajpai, P.K.; Maheshwari, S. Effect of Moisture Absorption on the Mechanical Performance of Natural Fiber Reinforced Woven Hybrid Bio-Composites. *J. Nat. Fibers* **2020**, *17*, 84–100. [CrossRef]

52. Ashok, K.G.; Kalaichelvan, K.; Damodaran, A. Effect of Nano Fillers on Mechanical Properties of Luffa Fiber Epoxy Composites. *J. Nat. Fibers* **2020**, 1–18. [CrossRef]

53. Burrola-Núñez, H.; Herrera-Franco, P.J.; Rodríguez-Félix, D.E.; Soto-Valdez, H.; Madera-Santana, T.J. Surface Modification and Performance of Jute Fibers as Reinforcement on Polymer Matrix: An Overview. *J. Nat. Fibers* **2019**, *16*, 944–960. [CrossRef]

54. Cai, M.; Takagi, H.; Nakagaito, A.N.; Li, Y.; Waterhouse, G.I.N. Effect of Alkali Treatment on Interfacial Bonding in Abaca Fiber-Reinforced Composites. *Compos. Part A Appl. Sci. Manuf.* **2016**, *90*, 589–597. [CrossRef]

55. Yan, L.; Chouw, N.; Huang, L.; Kasal, B. Effect of Alkali Treatment on Microstructure and Mechanical Properties of Coir Fibres, Coir Fibre Reinforced-Polymer Composites and Reinforced-Cementitious. *Constr. Build. Mater.* **2016**, *112*, 168–182. [CrossRef]

56. Naveen, E.; Venkatachalam, N.; Maheswaran, N. Alkalichemical Treatment on the Surface of Natural Fiber. *Int. J. Innov. Res. Sci. Eng. Technol.* **2015**, *4*, 172–178.

57. Hosseini, S.B. A Review: Nanomaterials as a Filler in Natural Fiber Reinforced Composites. *J. Nat. Fibers* **2017**, *14*, 311–325. [CrossRef]

58. Prasob, P.A.; Sasikumar, M. Static and Dynamic Behavior of Jute/Epoxy Composites with ZnO and TiO_2 Fillers at Different Temperature Conditions. *Polym. Test.* **2018**, *69*, 52–62. [CrossRef]

59. Andideh, M.; Naderi, G.; Ghoreishy, M.H.R.; Soltani, S. Effects of Nanoclay and Short Nylon Fiber on Morphology and Mechanical Properties of Nanocomposites Based on NR/SBR. *Fibers Polym.* **2014**, *15*, 814–822. [CrossRef]

60. Islam, M.S.; Ahmad, M.B.; Hasan, M.; Aziz, S.A.; Jawaid, M.; Mohamad Haafiz, M.K.; Zakaria, S.A.H. Natural Fiber-Reinforced Hybrid Polymer Nanocomposites: Effect of Fiber Mixing and Nanoclay on Physical, Mechanical, and Biodegradable Properties. *BioResources* **2015**, *10*, 1394–1407. [CrossRef]

61. Zhang, R.L.; Gao, B.; Du, W.T.; Zhang, J.; Cui, H.Z.; Liu, L.; Ma, Q.H.; Wang, C.G.; Li, F.H. Enhanced Mechanical Properties of Multiscale Carbon Fiber/Epoxy Composites by Fiber Surface Treatment with Graphene Oxide/Polyhedral Oligomeric Silsesquioxane. *Compos. Part A Appl. Sci. Manuf.* **2016**, *84*, 455–463. [CrossRef]

62. Belgacemi, R.; Derradji, M.; Trache, D.; Mouloud, A.; Zegaoui, A.; Mehelli, O.; Khiari, K. Effects of Silane Surface Modified Alumina Nanoparticles on the Mechanical, Thermomechanical, and Ballistic Impact Performances of Epoxy/Oxidized UHMWPE Composites. *Polym. Compos.* **2020**, *41*, 4526–4537. [CrossRef]

63. Nourbakhsh, A.; Ashori, A. Influence of Nanoclay and Coupling Agent on the Physical and Mechanical Properties of Polypropylene/Bagasse Nanocomposite. *J. Appl. Polym. Sci.* **2009**, *112*, 1386–1390. [CrossRef]

64. Balakrishnan, H.; Hassan, A.; Wahit, M.U.; Yussuf, A.A.; Razak, S.B.A. Novel Toughened Polylactic Acid Nanocomposite: Mechanical, Thermal and Morphological Properties. *Mater. Des.* **2010**, *31*, 3289–3298. [CrossRef]

65. Singh, J.I.P.; Singh, S.; Dhawan, V. Effect of Alkali Treatment on Mechanical Properties of Jute Fiber-Reinforced Partially Biodegradable Green Composites Using Epoxy Resin Matrix. *Polym. Polym. Compos.* **2019**, *28*, 388–397. [CrossRef]

66. Nam, T.H.; Ogihara, S.; Nakatani, H.; Kobayashi, S.; Song, J.I. Mechanical and Thermal Properties and Water Absorption of Jute Fiber Reinforced Poly(Butylene Succinate) Biodegradable Composites. *Adv. Compos. Mater.* **2012**, *21*, 241–258. [CrossRef]

67. Gogoi, R.; Tyagi, A.K. Surface Modification of Jute Fabric by Treating with Silane Coupling Agent for Reducing Its Moisture Regain Characteristics. *J. Nat. Fibers* **2019**, *18*, 803–812. [CrossRef]

Article

Influence of Curing Time on the Microbiological Behavior of Bulk-Fill Nanohybrid Resin Composites

Andrei C. Ionescu [1,*], Allegra Comba [2,3], Eugenio Brambilla [1], Nicoleta Ilie [4], Lorenzo Breschi [3], Milena Cadenaro [5,6] and Nicola Scotti [2]

1 Oral Microbiology and Biomaterials Laboratory, Department of Biomedical, Surgical and Dental Sciences, Università degli Studi di Milano, via Pascal, 36, 20133 Milano, Italy; eugenio.brambilla@unimi.it

2 Department of Surgical Sciences, University of Turin, via Nizza, 230, 10126 Torino, Italy; alle_comba@yahoo.it (A.C.); nicola.scotti@unito.it (N.S.)

3 Department of Biomedical and Neuromotor Sciences, DIBINEM, University of Bologna, Alma Mater Studiorum, Via San Vitale 59, 40125 Bologna, Italy; lorenzo.breschi@unibo.it

4 Department of Conservative Dentistry and Periodontology, University Hospital, Ludwig-Maximilians-University, Goethestr. 70, 80336 Munich, Germany; nilie@dent.med.uni-muenchen.de

5 Department of Medical Sciences, University of Trieste, 34125 Trieste, Italy; mcadenaro@units.it

6 Institute for Maternal and Child Health IRCCS "Burlo Garofolo", via dell'Istria 65/1, 34137 Trieste, Italy

* Correspondence: andrei.ionescu@unimi.it; Tel.: +39-0250315106

Abstract: This in vitro study aimed to evaluate the influence of curing time on surface characteristics and microbiological behavior of three bulk-fill resin-based composites (RBCs). Materials were light-cured for either 10 s or 80 s, then finished using a standard clinical procedure. They were characterized by surface morphology (SEM), surface elemental composition (EDS), surface roughness (SR), and surface free energy (SFE). Microbiological behavior was assessed as *S. mutans* adherence (2 h) and biofilm formation (24 h) using a continuous-flow bioreactor. Statistical analysis included a two-way ANOVA and Tukey's test ($p < 0.05$). Materials differed substantially as filler shape, dimension, elemental composition and resin matrix composition. Significant differences between materials were found for SR, SFE, and microbiological behavior. Such differences were less pronounced or disappeared after prolonged photocuring. The latter yielded significantly lower adherence and biofilm formation on all tested materials, similar to conventional RBCs. Improved photoinitiators and UDMA-based resin matrix composition may explain these results. No correlation between surface characteristics and microbiological behavior can explain the similar microbiological behavior of bulk-fill materials after prolonged photocuring. This different performance of bulk-fill materials compared with conventional RBCs, where surface characteristics, especially surface chemistry, influence microbiological behavior, may have important implications for secondary caries occurrence and restoration longevity.

Keywords: bulk fill; composite resin; restorative materials; surface characterization; energy-dispersive X-ray spectroscopy; scanning electron microscopy; microbial adherence; bioreactor; bacterial biofilm; *Streptococcus mutans*

1. Introduction

Bulk-fill resin-based composites (RBCs) have been introduced in the last decade to simplify restoration procedures, allowing for a higher depth of cure of a single increment (they can be placed in ≥4 mm thick bulks instead of the conventional incremental placement of 2 mm-thick layers) [1–6]. This goal was reached by modifying the composition of an RBC, for instance, by lowering the filler content by volume in low-viscosity bulk fills and increasing the dimensions of filler particles (>20 microns); thus, decreasing their specific surface areas. It was shown that these modifications improved light transmission, while lower filler content decreases hardness with no change in the suggested curing time [5,6].

Improving the depth of cure of these polymeric materials was obtained by allowing more light generated by the curing unit to penetrate. This improvement was also made possible by equalizing refractive indices of resin monomers and fillers in the unpolymerized material and incorporating highly reactive photoinitiators. Furthermore, the polymerization shrinkage and the consequent stress on the interfaces were reduced using high-molecular-weight monomers to improve marginal adaptation [7,8]. Bulk-fill RBCs are, in fact, a family of materials that differ from conventional RBCs in many ways, ranging from strategies adopted to enhance its translucency, such as a reduction in the content of the pigment and the use of larger filler particles, to significant changes in the chemical composition such as the use of high-molecular-weight monomers and stress-relieving monomers [5,9–11].

Additionally, their degree of conversion, that is, the amount of monomers that react forming the polymeric chains may be enhanced by adding highly reactive photoinitiators [3,5,12]. As shown by several studies, both characteristics can significantly impact the biological behavior of the polymeric material, especially biofilm formation [13–15]. In fact, the clinical behavior of bulk-fill materials seems to be just similar to conventional RBCs [1,5], and the influence of the dental healthcare provider's experience on the clinical outcome when placing polymer-based restorations may be non-neglectable [16].

An essential factor in caries development is bacterial colonization, which leads to biofilm formation on all oral surfaces, both natural and artificial. Full-grown biofilm consists of several bacterial species forming an ecological unit, which are not necessarily involved in dental caries; depending on its composition, a biofilm can be detrimental, neutral, or even beneficial [17–19]. In particular, cariogenic biofilm shows a high prevalence of acidogenic and acid-resistant species, such as streptococci and lactobacilli. The prevalence of cariogenic microorganisms in the biofilm community is an imbalance representing the first stage of both the primary and secondary caries formation [17,20]. Furthermore, mutans streptococci adherence and colonization of the surfaces of restorative materials are essential elements in secondary caries development [19]. From this point of view, the surface characteristics of restorative materials are particularly interesting as they influence how materials interact with the oral environment throughout their lifespan, posing critical challenges to their longevity [21].

Lastly, it was shown that light-curing characteristics significantly influence the degree of conversion of an RBC [22,23], affecting biofilm formation [24]. However, literature data on the influence of surface properties on microbial colonization of bulk-fill RBCs is limited and not systematically addressed [13,25–28]. Therefore, this in vitro study aimed to evaluate the adherence and biofilm formation by *Streptococcus mutans* on the surfaces of three bulk-fill RBCs. The null hypotheses were that (i) there is no difference in bacterial adherence or biofilm formation between the tested bulk-fill materials and (ii) there is no influence of the curing time on the microbiological behavior of the tested bulk-fill materials.

2. Materials and Methods

2.1. Specimen Preparation

Three different bulk-fill materials were tested, differing in type (one low-viscosity and two high-viscosity) and chemical composition. A flowable RBC with a higher viscosity than a conventional flowable was chosen as a control, having a similar resin/filler ratio to the tested bulk-fill materials (Table 1).

A total of 48 disks with 6 mm diameter and 2 mm thickness were prepared for each tested RBC [28,29]. For the preparation of each disk, a PTFE template was employed. The template was separated from the bench with a glass plate; another glass plate was placed on top to prevent the formation of an oxygen-inhibited layer. Disks from each group were randomly divided into two sub-groups ($n = 24$ each) and light-cured (Celalux 2, Voco, Cuxhaven, Germany) at 1000 mW/cm^2 for 10 s or 80 s, respectively. Once cured, the disks were stored at 37 °C for 24 h. After that, surfaces were polished with sandpapers of increasing grit size until reaching #1200 (SiC waterproof abrasive sheet, 3M, St Paul,

MN, USA). The specimens were then sonicated for two hours in distilled water to remove debris from the finishing procedures and stored separately under light-proof conditions at 37 °C in artificial saliva for six days to minimize the impact of residual monomer leakage or initial fluoride burst on the bacterial cells' viability. The artificial saliva used in the present study reproduced the average electrolytic composition of whole human saliva and was prepared by mixing 100 mL of 150 mM $KHCO_3$, 100 mL of 100 mM NaCl, 100 mL of 25 mM K_2HPO_4, 100 mL of 24 mM Na_2HPO_4, 100 mL of 15 mM $CaCl_2$, 100 mL of 1.5 mM $MgCl_2$, and 6 mL of 25 mM citric acid. The volume was prepared up to 1 L, and the pH was adjusted to 7.0 by pipetting NaOH 4 M or HCl 4 M solutions under vigorous stirring [29].

Table 1. Codename, manufacturer, and composition of the resin-based materials tested in the present study.

Codename	Material	Manufacturer	Organic Matrix	Filler (wt%, vol%)
S	SDR Surefil	Dentsply Sirona, York, PA, USA	UDMA, TEGDMA, EBPDMA	Ba-Al-F-Si glass, Sr-Al-F-Si glass 68 wt%, 45 vol%
F	Filtek Bulk Fill Posterior	3M, St Paul, MN, USA	AUDMA, UDMA, DDMA	Nanofillers and clusters of SiO_2; ZrO; YbF_3 64.5 wt%, 50.4 vol%
V	Admira Fusion X-tra	VOCO GmbH, Cuxhaven, Germany	ORMOCER	Ba-Al-Si glass; SiO_2 84 wt%, 65 vol%
G (Control)	G-aenial Universal Flow	GC Corp. Europe, Leuven, Belgium	UDMA, TEGDMA, Co-monomer dimethacrylates.	SiO_2 (16 nm), Sr glass (200 nm), LaF_3 69 wt%, 50 vol%

Abbreviations: Bis-GMA: bisphenol A glycol dimethacrylate; ethoxylated bis-GMA: EBPDMA; TEGDMA: triethylene glycol dimethacrylate; UDMA: urethane dimethacrylate; aromatic urethane dimethacrylate: AUDMA; 1, 12 dodecane-DMA: DDMA; urethane-based organically modified silicic acid: ORMOCER.

2.2. Analysis of Specimen Morphology and Elemental Surface Distribution by Scanning Electron Microscopy (Sem) and Energy-Dispersive X-ray Spectroscopy (Eds)

SEM/EDS analyses were performed on four specimens for each group using a tabletop scanning electron microscope (TM4000Plus, Hitachi, Schaumburg, IL, USA) equipped with an EDS probe (Quantax 75 with XFlash 630H Detector, Bruker Nano GmbH, Berlin, Germany). Dry specimens were mounted on stubs using conductive tape and were analyzed without sputter-coating, using a backscattered electron (BE) detector and an accelerating voltage of 15 kV in a surface-charge reduction mode. This method was used to display the surface morphology of the specimens and, in particular, the distribution of filler particles, their shape, and dimensions.

Three randomly selected fields were acquired for each specimen ($500\times$, $2000\times$, $5000\times$) for morphological observation of the surface and with the EDS probe (300 μm $\times$ 300 μm fields) in full-frame mode at 150 s acquisition time. The data acquired by EDS were averaged for each specimen and element, the wt% in the $\approx$1 μm superficial layer was displayed. These data were statistically analyzed to assess significant differences in surface chemical composition among the tested materials. Elemental distribution at the surface level was visually obtained in map mode ($5000\times$) using an acquisition time of 600 s.

2.3. Surface Roughness (SR) Analysis

Surface roughness was determined on each disk (*n* = 12) at four randomly selected spots on the surface of each specimen using a profilometric surface contact measurement device (RTP 80-TL90, LTF SpA-Borletti, Antegnate, Italy). A Gaussian filter and a cut-off level of 0.25 were used. A 1.75 mm-long path was measured in one single scan, perpendicular to the expected grinding grooves, using a standard diamond tip (tip radius = 2 μm, tip angle = 90°). The arithmetic mean deviation of the surface roughness profile (Ra), the root mean square average of the profile heights over the evaluation length (Rq), the maximum

height of the profile (Rt), and the average maximum height of the profile on five sampling lengths within the evaluation length (RzDIN) were calculated.

2.4. Surface Free Energy (SFE) Analysis

A 5 μL drop of ultrapure, HPLC-grade water was placed on each of the seven randomly selected specimens for each material (Figure 1). Then, the drop of water was photographed with a reflex camera (EOS-90D equipped with 100 mm macro lens and controlling a Speedlite 600 EX flash with 40 cm bouncer for background illumination, all from Canon, Tokyo, Japan) that was stabilized on a tripod to obtain an orthogonal image. Contact angles were determined using the sessile drop method and a computer-aided contact angle measurement software (Rasband, W.S., ImageJ, U.S. National Institutes of Health, Bethesda, MD, USA). Left and right contact angles were averaged (θ), and the surface free energy (γ_{sv}) was calculated according to the formula:

$$\cos \theta = -1 + 2 \left(\frac{\gamma_{sv}}{\gamma_{lv}} \right) \tag{1}$$

considering that the total surface free energy of water (γ_{lv}) at the temperature at which the experiments were performed (20 °C) is 72.8 mJ/m^2.

2.5. Microbiological Procedures

Culture media were obtained from Becton-Dickinson (BD Diagnostics-Difco, Franklin Lakes, NJ, USA), and reagents were obtained from Sigma-Aldrich (Sigma-Aldrich, St. Louis, MO, USA). Mitis salivarius bacitracin agar (MSB agar) plates were inoculated with *Streptococcus mutans* (ATCC 35668) and incubated in a 5% CO_2-supplemented environment at 37 °C for 48 h. A pure culture of the microorganism in the brain-heart infusion broth (BHI) was obtained from these plates after incubation in a 5% CO_2-supplemented environment at 37 °C for 12 h. Cells were harvested by centrifugation (2200 rpm, 19 °C, 5 min), washed twice with sterile phosphate-buffered saline (PBS), and resuspended in the same buffer. The cell suspension was subsequently subjected to sonication (sonifier model B-150; Branson, Danbury, CT, USA; operating at 7W energy output for 30 s) to disperse bacterial chains. Finally, the suspension was adjusted to 1.0 optical density on the McFarland scale, corresponding to a concentration of approximately 6.0×10^8 cells/mL.

According to a previously published protocol, paraffin-stimulated whole saliva was obtained from five healthy donors [30]. The Institutional Review Board of the University of Milan approved the use of saliva (protocol codename SALTiBO-2017), and written informed consent was obtained from the donors. They refrained from oral hygiene for 24 h, had no active dental disease, and did not use antibiotics for at least three months. Saliva was collected before the beginning of the COVID-19 pandemic, and the donors were not subjected to additional tests regarding their infective status with SARS-CoV-2. Chilled test tubes were used for saliva collection. Saliva was pooled, heated to 60 °C for 30 min and centrifuged (12,000× *g* at 4 °C for 15 min). After that, the supernatant was collected into sterile tubes and stored at −20 °C, to be thawed at 37 °C for 1 h before use.

2.6. Bacterial Adherence

Twelve disks for each RBC and curing group were positioned on the bottom of 48-well microplates to evaluate *S. mutans'* adherence to the surfaces of the tested materials. Disks were sterilized using a hydrogen peroxide gas-plasma chemiclave (Sterrad, ASP, Irvine, CA, USA) operating at a low temperature (42 °C) to reduce modifications of the specimen surfaces. Salivary pellicle formation was simulated by covering sterile disks with 300 μL of thawed sterile saliva for 24 h. Then, excess saliva was discarded by aspiration; a total of 500 μL of sterile BHI supplemented with 3 wt% sucrose and 500 μL of *S. mutans* suspension were inoculated into each well. The plates were incubated in a 5% CO_2-supplemented atmosphere at 37 °C for 2 h. Subsequently, viable biomass adherent to the surface of the disks was assessed as follows.
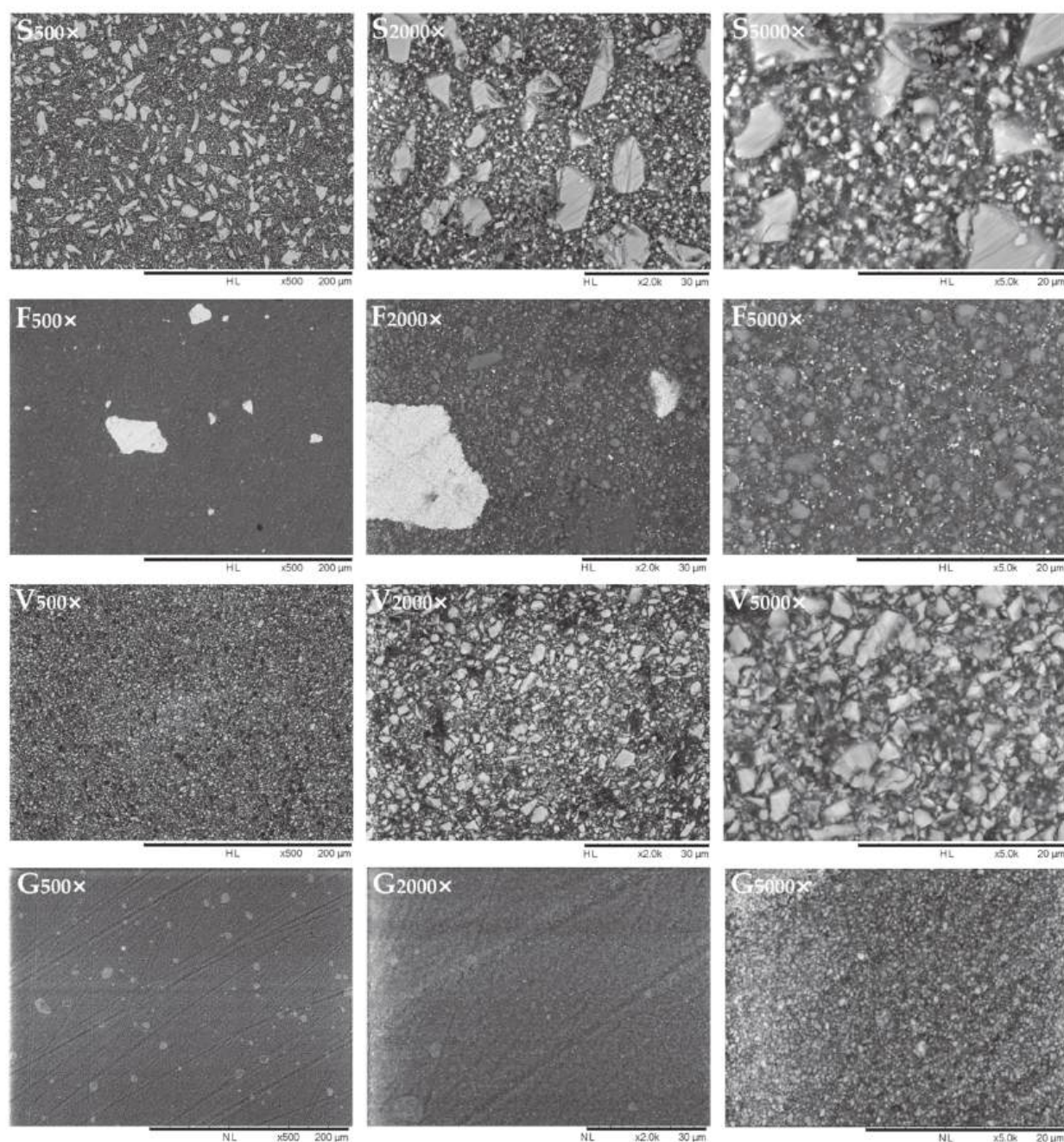
Figure 1. Representative SEM micrographs (500×, 2000× and 5000×) of the tested polymeric materials' surfaces acquired in backscattered mode. Under such electron detection conditions, elements with relatively high atomic number (Sr, Zr, and especially Ba and Yb) reflect electrons more than elements with lower atomic number (C). In this way, they are depicted as white-ish while the organic resin matrix is black. Elements such as F, Al, and Si provide intermediate gray-scale values. This observation allows to better highlight filler size and shape and provides a preliminary qualitative insight on fillers' composition.

2.7. Viable Biomass Assessment

The viable biomass assessment was performed as previously described [30]. Briefly, two stock solutions were prepared by dissolving 5 mg/mL of 3-(4,5)-dimethylthiazol-2-yl-2,5-diphenyltetrazolium bromide (MTT) and 0.3 mg/mL of N-methylphenazonium methyl sulphate (PMS) in sterile PBS. The solutions were stored at 2 °C in light-proof vials until the day of the experiment when a test solution (TS) was prepared by mixing MTT stock solution, PMS stock solution, and sterile PBS in a 1:1:8 ratio. A lysing solution (LS) was

prepared by dissolving 10 vol% sodium dodecyl sulfate and 50 vol% dimethylformamide in distilled water. TS and LS were brought to 37 °C before use. After 2 h of incubation, disks were transferred into new 48-well plates containing 300 μL of TS in each well.

The plates were incubated at 37 °C under light-proof conditions. During incubation, electron transport across the microbial plasma membrane and, to a lesser extent, microbial redox systems converted the yellow salt to insoluble purple formazan crystals. The conversion at the cell membrane level was facilitated by the intermediate electron acceptor (PMS). After one hour, the TS solution was carefully removed, and 300 μL of LS was added to each well. The plates were then stored under light-proof conditions for one additional hour (room temperature) to allow dispersion of the formazan crystals into the surrounding solution. Subsequently, 100 μL of the supernatant was transferred to a 96-well plate, and the absorbance was measured at a wavelength of 550 nm using a spectrophotometer (Genesys 10-S, Thermo Spectronic, Rochester, NY, USA). Results were expressed as relative absorbance in optical density (OD) units corresponding to adherent, viable, and metabolically active biomass.

2.8. Bioreactor Procedures

Biofilm formation was simulated under continuous flow conditions using a modified commercially available drip-flow bioreactor (MDFR; DFR 110, BioSurface Technologies, Bozeman, MT, USA). The modified design allowed the placement of customized polytetrafluoroethylene (PTFE) trays containing 27 holes, in which each specimen was tightly fixed on the bottom of the flow cell, exposing its surface to the surrounding medium. Before the experiments, all tubing and specimen-containing trays of the MDFR were sterilized using the chemiclave (Sterrad). The whole apparatus was then assembled inside a sterile hood [31].

A total of 10 mL of thawed sterile saliva was placed into each flow cell to allow the formation of a salivary pellicle on the surface of the tested disks (n = 12 for each material and curing group). Then, the MDFR was incubated at 37 °C for 24 h. After incubation, saliva was removed by gentle aspiration. A total of 10 mL of the previously prepared *S. mutans* suspension was then placed into each flow cell, and the MDFR was incubated at 37 °C for 4 h to allow bacterial adherence. Then, a constant flow of sterile modified artificial saliva medium [31] including 2.5 g/L mucin (type II, porcine gastric), 2.0 g/L bacteriological peptone, 2.0 g/L tryptone, 1.0 g/L yeast extract, 0.35 g/L NaCl, 0.2 g/L KCl, 0.2 g/L $CaCl_2$, 0.1 g/L cysteine HCl, 0.001 g/L hemin, and 0.0002 g/L vitamin K_1 was provided by a peristaltic pump at a flow rate of 9.6 mL/h. The MDFR was operated for 24 h to allow the development of a multilayer biofilm on the specimens' surfaces. At the end of the incubation, the flow was stopped, and the trays were extracted from the flow cells. The specimens were carefully removed from the trays using a pair of sterile tweezers and gently rinsed with sterile phosphate-buffered saline (PBS) at 37 °C to remove non-adherent cells. The specimens were then placed into sterile 48-well plates, and the adherent, viable biomass was assessed as previously specified.

2.9. Statistical Analysis

Statistical analyses were performed using the JMP 10.0 software (SAS Institute, Cary, NC, USA). Normal distribution of data was checked using the Shapiro–Wilk test, and homogeneity of variances was verified using Levène's test. Means, standard deviations, and standard errors were calculated from the raw data. A two-way analysis of variance (ANOVA) was used to analyze the surface roughness, SFE, EDS, and biomass datasets, considering the material type and the curing time as fixed factors. Tukey's HSD test was employed for post-hoc analysis ($p < 0.05$).

3. Results

3.1. Surface Characterization

SEM-EDS observation showed that SDR surfaces exposed filler with different dimensions, in the range of 5–10 μm (macro), about 1 μm (micro), as well as nanofillers (Figure 1).

EDS mapping (Figure 2) partly confirmed the manufacturer's specification, identifying macro fillers fabricated of fluoro aluminosilicate glass with Sr and smaller filler particles in the range of about 1μm fabricated by barium glass. This material showed a filler shape and composition similar to that of a resin-modified glass-ionomer [32], to which micronized Ba glass was added. Filtek Bulk Fill exposed zirconia and silica nanofillers and nanoclusters, as expected. Interestingly, both clusters and finely dispersed nanoparticles of the ionic compound YbF_3 were identifiable, having an inhomogeneous distribution. Due to the high atomic number of ytterbium, such particles were highly electron-reflective in backscattered mode and easily identifiable. The other two materials showed a very homogeneous filler distribution. Admira Fusion X-tra displayed barium aluminosilicate glass particles in the 1–5 μm range (microhybrid), whereas Universal Flo showed sub-micron filler particles made of Si, Al, Sr, and F (nanofilled).
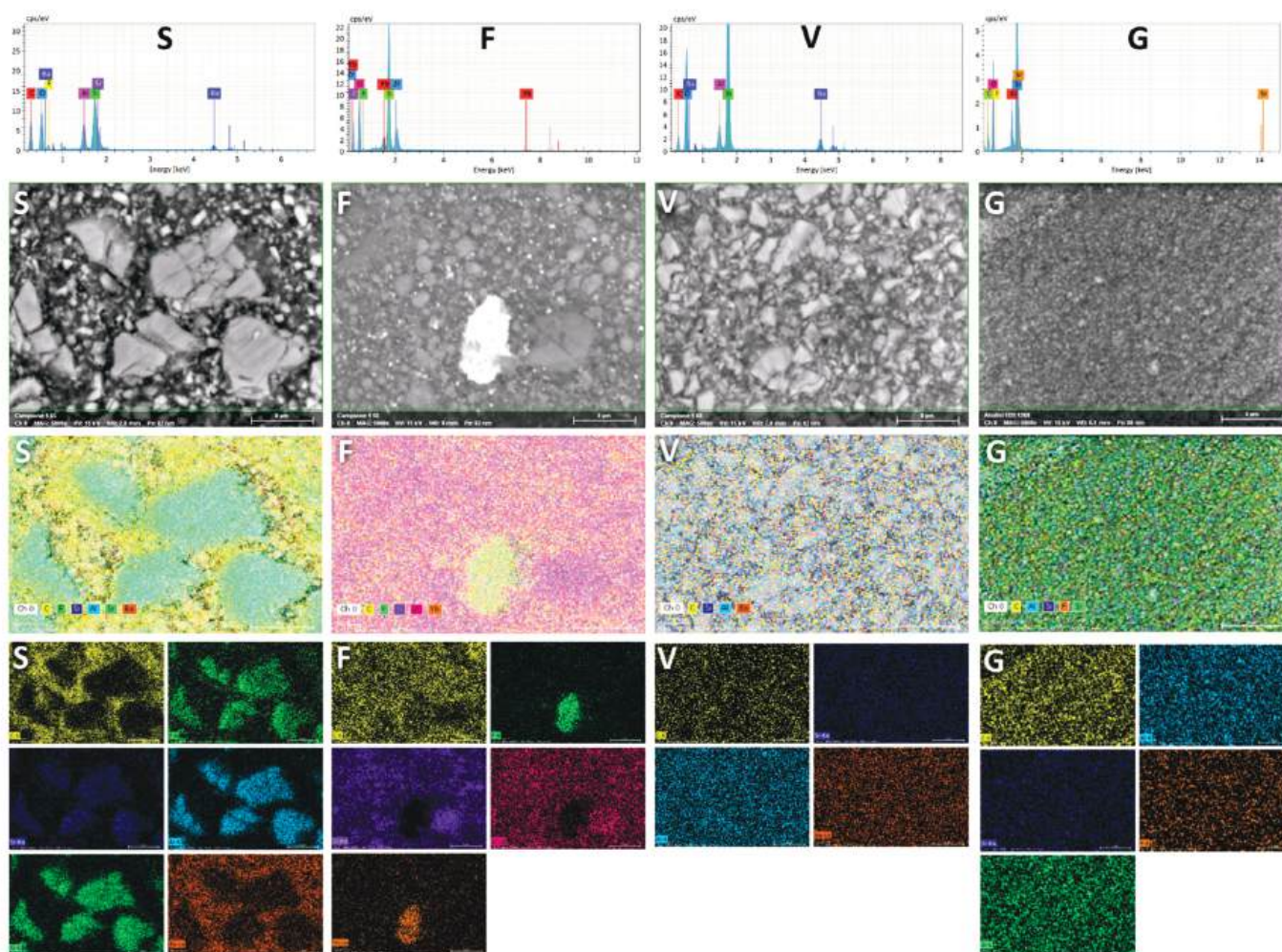
Figure 2. EDS analysis. For each tested polymeric material, from top to bottom are shown a typical spectrum of the surface showing elemental detection, an SEM backscattered micrograph at 5000×, the superimposed false-color image showing elemental detection and smaller pictures depicting each acquired channel. It can be clearly seen that the fillers of the SDR material (**S**) appear very similar in shape, dimension and composition to a resin-based glass ionomer material (F-Al-Si-Sr glass) to which micronized barium glass was added. Filtek Bulk Fill (**F**) shows nanoparticles and clusters of YbF_3 embedded in silica and zirconia nanoparticles and nanoclusters. The composition of Admira Fusion X-tra (**V**) and Universal Flo (**G**) is extremely homogeneous, with the first belonging to the micro-hybrid resin composite class (microfillers+nanofillers) while the second one is nanofilled.

Considering the control material, Al presence was found that can be related to strontium glass. Indeed, strontium cannot stand alone, and strontium oxide needs to be included

as a network-modifier in a SiO_2-Al_2O_3 glass, which is why the Al signal was detected [33]. Fluoride was contained in the control material as the ionic compound LaF_3; yet, the lanthanum signal was not identified, likely being below the instrument's detection limit.

The quantitative analysis of the tested materials' surface is shown in Table 2. The statistical analysis showed that the curing time did not influence the materials' surface elemental composition, and no significant interaction was demonstrated between the tested factors. Therefore, results were grouped by the material.

Table 2. Energy-dispersive X-ray spectroscopy (EDS) compositional analysis of specimens' surface layer after finishing and before microbiological challenges. Means ($\pm$1 SD) are displayed. Inorganic fraction is depicted as the sum of all elements constituting the fillers, as opposed to the organic matrix evidenced by the carbon content. Two-way ANOVA showed that material, not curing time factor, was highly significant ($p < 0.0001$); therefore, results are provided as the average composition for each material. Different superscript letters indicate significant differences between materials (Tukey's test, $p < 0.05$) for a given element.

wt%	S	F	V	G (Control)
C	40.05 (2.74) [a]	33.34 (3.92) [b]	22.59 (4.51) [c]	24.72 (3.29) [c]
O	30.20 (0.62) [c]	32.34 (1.43) [b]	39.82 (1.65) [a]	41.11 (0.89) [a]
F	3.81 (0.66) [a]	1.39 (0.27) [b]	0.00 (0.00) [c]	0.99 (0.19) [b]
Al	4.23 (0.25) [a]	0.00 (0.00) [c]	3.10 (0.34) [b]	4.47 (0.30) [a]
Si	10.33 (0.42) [c]	18.66 (1.36) [b]	22.76 (1.99) [a]	18.22 (1.43) [b]
Sr	5.01 (0.56) [b]	0.00 (0.00) [c]	0.00 (0.00) [c]	10.49 (0.69) [a]
Zr	0.00 (0.00) [b]	10.80 (1.35) [a]	0.00 (0.00) [b]	0.00 (0.00) [b]
Ba	6.37 (1.04) [b]	0.00 (0.00) [c]	11.78 (1.14) [a]	0.00 (0.00) [c]
Yb	0.00 (0.00) [b]	3.47 (0.38) [a]	0.00 (0.00) [b]	0.00 (0.00) [b]
Inorganic fraction	29.75 (2.39) [b]	34.33 (2.51) [a]	37.64 (3.36) [a]	34.18 (2.41) [a,b]

Surface roughness datasets were not normally distributed; therefore, each dataset was log-transformed before statistical analysis to approach a normal distribution. Material and curing time significantly influenced all surface roughness parameters calculated in the present study ($p < 0.001$). A significant interaction was highlighted between the considered factors on all parameters. Rq and Ra showed a similar trend. After 10 s curing time, V showed significantly higher Ra values compared with G and F, and S showed higher Ra compared with F (Figure 3A). After 80 s, S showed significantly higher Ra than V and G. Then again, all materials showed very similar Ra values after 80 s curing, around 0.2 μm. Rt and Rz showed a similar trend. After 10 s of curing time, S and V showed significantly higher Rz values than F and G (Figure 3B). After 80 s, S showed significantly higher Rz values compared with all other materials.

Surface free energy assessment (Figure 3C) showed that G (control) had a significantly higher SFE than the tested bulk-fill materials after 10 s of curing time. After 80 s of curing, both G and S showed significantly higher SFE than F, but differences were less pronounced than after 10 s of curing.

3.2. Microbiological Evaluation

No significant influence of the considered factors on bacterial adherence was highlighted. The post-hoc test showed significantly lower F surfaces adherence than V and G ($p = 0.044$ and $p = 0.0265$, respectively, Figure 4A).

Curing time significantly influenced biofilm formation ($p < 0.0001$), while no significant influence of the material, and no significant interaction between the considered factors were detected ($p = 0.0772$, and $p = 0.341$, respectively). A post-hoc test showed significantly higher biofilm formation on G (control) surfaces compared with S and F ($p = 0.0236$ and $p = 0.0299$, respectively, Figure 4B).
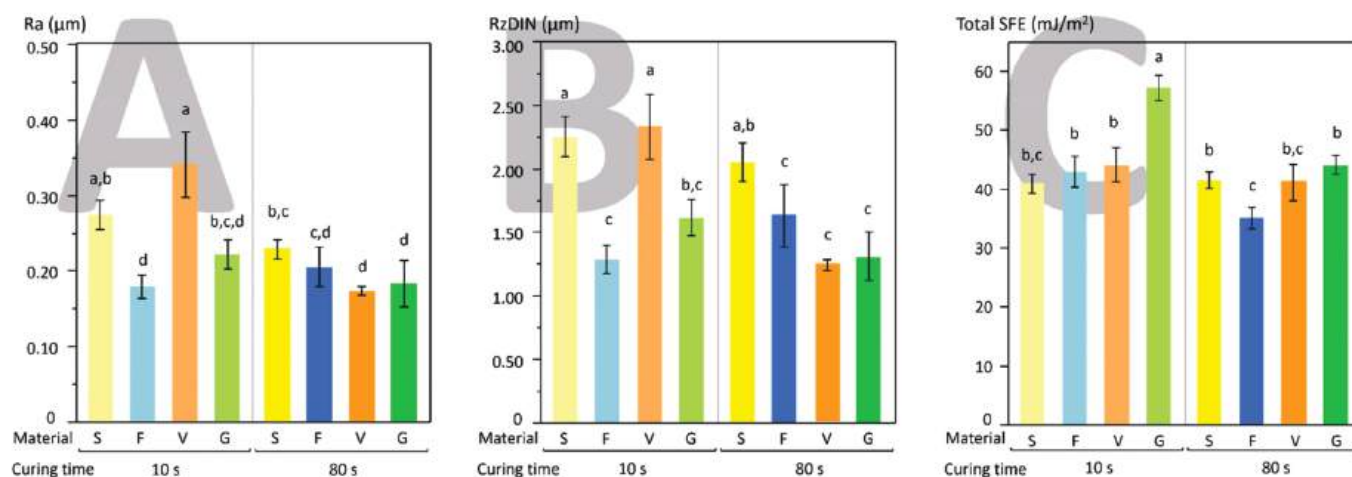
Figure 3. Graphs depicting the results of surface characterization in terms of surface roughness (**A**) Ra parameter and (**B**) RzDIN parameter and surface free energy (**C**). Curing time had a huge impact on both surface roughness and SFE, with differences between tested polymeric materials being significantly reduced after extended curing (80 s). Different superscript letters indicate significant differences between materials (Tukey's test, $p < 0.05$) for a given element.
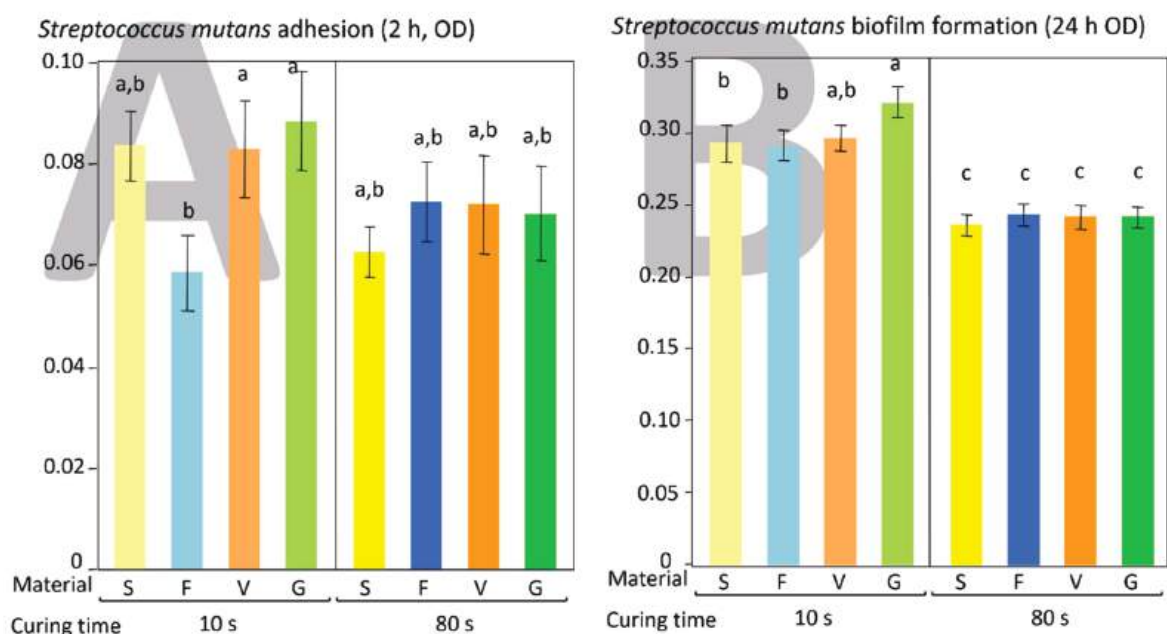
Figure 4. Results of the microbiological behavior of the tested materials in terms of bacterial adherence (**A**) and biofilm formation (**B**) by *S. mutans*. A highly significant decrease in both adherence and biofilm formation can be observed on materials cured for an extended time (80 s). Interestingly, differences in adherence and biofilm formation between materials disappeared after extended curing time (80 s). Different superscript letters indicate significant differences between materials (Tukey's test, $p < 0.05$) for a given element.

4. Discussion

The mutual interactions between the surfaces of polymeric dental materials and overlying biofilms are complex and far from being fully understood. The conventional wisdom is that surface roughness is the main parameter influencing microbial adherence and biofilm formation, with other parameters, such as surface free energy and chemical composition playing a minor role [21]. The purpose of this study was to evaluate the influence of light-curing time on the adherence and biofilm formation by *Streptococcus mutans* on three bulk-fill composites and to put into relation such data with the surface characteristics. The first null hypothesis that there is no difference in bacterial adherence or

biofilm formation between the tested polymeric materials must be rejected in parts. Indeed, after 10 s of polymerization time, significant differences were found between materials both for bacterial adherence and biofilm formation, whereas no significant differences were found after 80 s curing. The second null hypothesis must be entirely rejected since all tested materials showed lower biofilm formation after an extended curing time (80 s).

Our results showed that a reduced curing time produced higher surface roughness on SDR and Admira Fusion X-tra, while the extended curing time generally produced similar lower values. Surface roughness is considered a crucial parameter in influencing all phases of microbial colonization [34,35]. High surface roughness values are believed to improve microbial adherence by providing attachment sites and reducing the shear force of the flow on bacterial cells and microcolonies [36]. However, the present study showed a poor correlation between roughness data and microbiological behavior of materials, both in terms of bacterial adherence and biofilm formation. In particular, adherence and biofilm formation were similar for all tested materials when cured for an extended time (80 s), and the only factor influencing the microbiological behavior was the curing time.

There is, unfortunately, no consensus on the influence of surface roughness on the microbiological behavior of resin-based materials in the literature. The same issue can be found when considering bulk-fill materials. Two studies suggest that surface roughness significantly affects bacterial adherence and biofilm formation [27,37], while most show no effect of this parameter on microbial colonization [13,25,26,28,38]. In particular, Somacal et al. in 2020 evaluated the effect of pH cycling and simulated toothbrushing on the surface roughness and 24 h-biofilm formation (not adherence) of some bulk-fill materials [25]. One of the tested materials (Filtek Bulk Fill) was also tested in the present study. They did not find any correlation between roughness values and biofilm formation, agreeing with the present study's data. In the same year, Park et al. studied the influence of surface roughness on microbial adherence after applying finishing procedures to some polymeric materials, among which was a bulk fill [26]. They only found a weak correlation between surface roughness and *S. mutans* adherence to the specimens. Bilgili et al. evaluated *Streptococcus mutans* and *Streptococcus mitis* 24 h-biofilm formation (not adherence) to bulk-fill resin composites in relation to their surface characteristics [13]. In particular, they evaluated two of the materials tested in the present study (Filtek Bulk Fill and Admira Fusion X-tra). They concluded that the surface roughness did not affect biofilm formation. Cazzaniga et al. evaluated the influence of surface roughness of microhybrid, nanohybrid, nanofill, and bulk-fill composites finished with several finishing/polishing systems on *S. mutans* biofilm formation [28]. The polishing systems significantly influenced surface roughness, yet surface roughness was not found to influence biofilm formation. Several other studies demonstrated no correlation between surface roughness and *S. mutans* colonization of polymeric surfaces [29,30,39].

On the other hand, Soliman et al. in 2019 evaluated the influence of surface roughness on *S. mutans* adherence to bulk-fill materials treated using different polishing systems [37]. One of the materials, Filtek Bulk Fill, was also tested in the present study. Contrarily to our results, they found a significant association between surface roughness and bacterial adherence to the tested surfaces. One of the surface treatments in Soliman's experiment was curing the materials against a mylar strip, which is acknowledged to produce a smooth surface, similar to the protocol adopted in the present study, that involved curing against glass plates.

It is known that other characteristics such as surface free energy can significantly influence bacterial adherence both in vivo and in vitro [21,36]. This influence is reduced over time as the biofilm formation phase progresses [40]. However, previous studies found no significant relationship between the hydrophobicity of polymer-based composites and bacterial adherence [29,41–43]. Our results showed that the control material (Universal Flo) displayed a significantly higher SFE than the tested bulk-fill materials when light-cured for 10 s, while these differences were much less pronounced after 80 s. Microbiological data of biofilm formation showed a similar trend, with the control material showing the highest

biofilm development when light-cured for 10 s, while no differences between groups were seen after 80 s of curing time. While it is generally accepted that higher surface free energy values correlate with higher *S. mutans* adherence [29], only Bilgili et al. [13] evaluated the influence of this parameter on the microbiological performances of bulk-fill surfaces. They tested four different bulk-fill materials and found no significant influence of SFE on *S. mutans* biofilm formation (24 h). Such outcome agrees with the present study results, where a higher SFE, correlating with higher biofilm formation, was only found for the control material.

These experimental findings suggest that biofilm formation is mainly influenced by the surface chemical composition of the material, including filler size, shape, distribution, and matrix composition. The surface microanalysis and elemental composition (SEM-EDS) provided data on the composition of the external $\approx$1 μm layer of the tested materials. A previous study [43] on several conventional RBCs showed that their filler to resin matrix ratio could influence biofilm formation. Indeed, a higher amount of inorganic filler presence on the surface is related to reduced bacterial colonization. SDR showed the lowest filler presence in the present study, whereas Admira Fusion X-tra showed the highest. However, this characteristic did not influence bacterial adherence or biofilm formation. However, it must be noted that the tested bulk-fill materials generally have much lower filler content than conventional RBCs. This feature, along with filler shape and dimensions, is usually selected for bulk-fill composition to improve the depth of cure of the polymeric materials [3,4,7]. In the present study, a nanofill flow composite was used as a control since it had characteristics, such as a filler/matrix ratio similar to the tested bulk-fill materials. Therefore, a relatively low filler to resin matrix ratio may explain the lack of correlation between this characteristic and the microbiological performance of the tested materials.

Furthermore, it was found that SDR, Filtek Bulk Fill, and Universal Flo contained fluoride in their composition, as fluoro aluminosilicate glass, YbF_3, or LaF_3, respectively. Nevertheless, despite its proven antimicrobial and bacteriostatic effect even at low concentrations, no influence of fluoride on microbial adherence or biofilm formation was found. A possible explanation may be that fluoride is firmly incorporated into the material and resin matrix without expressing significant release once polymerized. Literature data on other fluoride-containing conventional and bulk-fill polymeric materials tested under similar biofilm formation conditions, including forming a salivary pellicle, agrees with the present findings [28,30]. Further studies may evaluate the fluoride release capacity of such materials under biofilm formation conditions.

Finally, other factors can contribute to bacterial adherence, such as the resin matrix composition [15,44] and the amount of leaching of residual unpolymerized monomers [45]. In the present study, all materials were extensively rinsed using a standard protocol [31,43] to minimize the impact of possible unpolymerized monomer release or fluoride burst on the microbiological behavior. In agreement with the present study's data, progressively reduced biofilm formation was found on the surfaces of conventional RBCs with increasing curing time [24]. This behavior was explained by increasing the degree of conversion at the RBC surface and decreasing the amount of leachates. Despite incorporating different and supposedly more efficient photoinitiator systems in bulk-fill polymeric materials [9,12], they seem to behave similarly to their conventional counterparts, at least from the point of view of the influence of the curing time on their microbiological behavior. For instance, Alshali et al. [46] showed that elution of residual monomers from SDR did not differ from conventional resin composites. Then again, bacteria and especially *S. mutans* can be deeply influenced by urethane-containing monomers, notably UDMA. With urethane-based derivatives, the latter is currently being used to replace BisGMA to avoid drawbacks such as high viscosity, toxicity, and estrogen-like effects on the human body. Kim et al. in a very recent paper [47], demonstrated that UDMA could contribute to the development of secondary caries around UDMA-containing polymeric materials by prompting *S. mutans* biofilm formation, enhancing its oxidative tolerance, and enabling it to shift its carbon flow toward the ATP generation required for persistence and cariogenicity. The tested

materials all contained UDMA or its derivatives, including Admira Fusion X-tra based on ORMOCER technology incorporating multifunctional urethane and thioether (-meth) acrylate alkoxysilanes as sol-gel precursors [48]. This consideration may explain why all materials had similar microbiological behavior after curing for 80 s. In addition to that, Filtek Bulk Fill was the only material that did not contain TEGDMA in its composition. Together with an improved photoinitiator system, this consideration may explain its significantly lower microbial adherence after only 10 s of curing.

Some choices were made for the experimental design of the present study based on a reductionistic approach. Only 10 s and 80 s of light-curing time were tested, which may be too low or exceed the curing times suggested by the manufacturers, ranging from 20 s (SDR Surefil, Admira Fusion X-tra, Universal Flo) to 40 s (Filtek Bulk Fill). Based on the results of a previous study performed with conventional composites [24], the time categories of the present study were chosen to see best if the microbiological behavior of the tested materials was influenced by the curing time similarly to the conventional composites, despite differences in composition and photoinitiators. Furthermore, *S. mutans* monospecies biofilm is an oversimplistic microbiological model compared with a fully-grown artificial oral microcosm. The bacterium, however, allows the development of a cariogenic biofilm resembling its' in vivo counterparts, thus providing the best comparability of the gathered results with the literature. Future studies on this topic should include artificial oral microcosms based on bioreactor-grown mixed plaque inocula [49].

5. Conclusions

Like conventional RBCs, prolonged curing time (80 s) reduced bacterial adherence and biofilm formation on all tested bulk-fill polymeric materials. Improved photoinitiator systems, providing optimally cured materials after 80 s, and resin matrix composition (UDMA promoting adherence and biofilm formation) may explain these results.

Surprisingly, when bulk-fill composites were extensively cured, no difference in bacterial adherence or biofilm formation could be seen comparing the different materials. Furthermore, no correlation between surface characteristics (surface roughness, surface free energy, elemental composition, fluoride presence, filler/resin ratio) and microbiological data could explain such behavior. Compared with conventional RBCs where surface characteristics, especially surface chemistry, influences microbiological behavior, the different performance of bulk-fill polymeric materials may have important implications in secondary caries occurrence and restoration longevity. Comparative clinical studies are needed in the long term to assess this possibility.

Author Contributions: Conceptualization, A.C.I., E.B. and N.S.; methodology, A.C.I., N.I. and E.B.; software, A.C., L.B. and M.C.; validation, A.C., N.I., L.B. and M.C.; formal analysis, A.C.I., N.I. and E.B.; investigation, A.C.I. and E.B.; resources, E.B., L.B., M.C. and N.S.; data curation, A.C., A.C.I. and E.B.; writing—original draft preparation, A.C.I., E.B. and N.S.; writing—review and editing, A.C., N.I., L.B. and M.C.; supervision, E.B. and N.S. All authors have read and agreed to the published version of the manuscript.

References

1. Arbildo-Vega, H.; Lapinska, B.; Panda, S.; Lamas-Lara, C.; Khan, A.; Lukomska-Szymanska, M. Clinical Effectiveness of Bulk-Fill and Conventional Resin Composite Restorations: Systematic Review and Meta-Analysis. *Polymers* **2020**, *12*, 1786. [CrossRef]
2. El-Banna, A.; Sherief, D.; Fawzy, A.S. Resin-based dental composites for tooth filling. In *Advanced Dental Biomaterials*; Woodhead Publishing: Cambridge, UK, 2019; pp. 127–173. [CrossRef]
3. Reis, A.F.; Vestphal, M.; Amaral, R.C.D.; Rodrigues, J.; Roulet, J.-F.; Roscoe, M.G. Efficiency of polymerization of bulk-fill composite resins: A systematic review. *Braz. Oral Res.* **2017**, *31*, e59. [CrossRef] [PubMed]
4. Czasch, P.; Ilie, N. In vitro comparison of mechanical properties and degree of cure of bulk fill composites. *Clin. Oral Investig.* **2012**, *17*, 227–235. [CrossRef] [PubMed]
5. Haugen, H.J.; Marovic, D.; Par, M.; Le Thieu, M.K.; Reseland, J.E.; Johnsen, G.F. Bulk Fill Composites Have Similar Performance to Conventional Dental Composites. *Int. J. Mol. Sci.* **2020**, *21*, 5136. [CrossRef]
6. Lima, R.B.W.; Troconis, C.C.M.; Moreno, M.B.P.; Murillo-Gómez, F.; De Goes, M.F. Depth of cure of bulk fill resin compo-sites: A systematic review. *J. Esthet. Restor. Dent.* **2018**, *30*, 492–501. [CrossRef]
7. Dikova, T.; Maximov, J.; Todorov, V.; Georgiev, G.; Panov, V. Optimization of Photopolymerization Process of Dental Composites. *Processes* **2021**, *9*, 779. [CrossRef]
8. Fronza, B.M.; Ayres, A.P.; Pacheco, R.R.; Rueggeberg, F.; Dias, C.; Giannini, M. Characterization of Inorganic Filler Content, Mechanical Properties, and Light Transmission of Bulk-fill Resin Composites. *Oper. Dent.* **2017**, *42*, 445–455. [CrossRef] [PubMed]
9. Ilie, N. Impact of light transmittance mode on polymerization kinetics in bulk-fill resin-based composites. *J. Dent.* **2017**, *63*, 51–59. [CrossRef] [PubMed]
10. Ilie, N. Sufficiency of curing in high-viscosity bulk-fill resin composites with enhanced opacity. *Clin. Oral Investig.* **2019**, *23*, 747–755. [CrossRef]
11. Abuelenain, D.A.; Abou Neel, E.A.; Al-Dharrab, A. Surface characterization and mechanical behavior of bulk fill versus in-cremental dental composites. *Tanta Dent. J.* **2017**, *14*, 56. [CrossRef]
12. Ilie, N.; Stark, K. Curing behaviour of high-viscosity bulk-fill composites. *J. Dent.* **2014**, *42*, 977–985. [CrossRef] [PubMed]
13. Bilgili, D.; Dündar, A.; Barutçugil, Ç.; Tayfun, D.; Özyurt, Ö.K. Surface properties and bacterial adhesion of bulk-fill compo-site resins. *J. Dent.* **2018**, *95*, 103317. [CrossRef]
14. Silva, R.A.B.; Nelson-Filho, P.; De-Oliveira, K.M.H.; Romualdo, P.C.; Gatón-Hernandez, P.; Aires, C.; Silva, L.A.B. Adhesion and Initial Colonization of Streptococcus mutans is Influenced by Time and Composition of Different Composites. *Int. J. Odontostomatol.* **2018**, *12*, 395–400. [CrossRef]
15. Hao, Y.; Huang, X.; Zhou, X.; Li, M.; Ren, B.; Peng, X.; Cheng, L. Influence of dental prosthesis and restorative materials in-terface on oral biofilms. *Int. J. Mol. Sci.* **2018**, *19*, 3157. [CrossRef] [PubMed]
16. Scotti, N.; Comba, A.; Gambino, A.; Manzon, E.; Breschi, L.; Paolino, D.; Pasqualini, D.; Berutti, E. Influence of operator ex-perience on non-carious cervical lesion restorations: Clinical evaluation with different adhesive systems. *Am. J. Dent.* **2016**, *29*, 33–38.
17. Marsh, P.D.; Zaura, E. Dental biofilm: Ecological interactions in health and disease. *J. Clin. Periodontol.* **2017**, *44*, S12–S22. [CrossRef]
18. Peterson, S.N.; Meißner, T.; Su, A.I.; Snesrud, E.; Ong, A.C.; Schork, N.J.; Bretz, W.A. Functional expression of dental plaque microbiota. *Front. Cell. Infect. Microbiol.* **2014**, *4*, 108. [CrossRef] [PubMed]
19. Senneby, A.; Davies, J.R.; Svensäter, G.; Neilands, J. Acid tolerance properties of dental biofilms in vivo. *BMC Microbiol.* **2017**, *17*, 1–8. [CrossRef] [PubMed]
20. Brambilla, E.; Ionescu, A.C. Oral Biofilms and Secondary Caries Formation. In *Oral Biofilms and Modern Dental Materials: Ad-vances Toward Bioactivity*; Ionescu, A.C., Hahnel, S., Eds.; Springer Nature: Basingstoke, UK, 2021; p. 19.
21. Günther, E.; Fuchs, F.; Hahnel, S. Complex Polymeric Materials and Their Interaction with Microorganisms. In *Oral Biofilms and Modern Dental Materials: Advances Toward Bioactivity*; Ionescu, A.C., Hahnel, S., Eds.; Springer Nature: Basingstoke, UK, 2021; p. 71.
22. Scotti, N.; Comba, A.; Cadenaro, M.; Fontanive, L.; Breschi, L.; Monaco, C.; Scotti, R. Effect of Lithium Disilicate Veneers of Different Thickness on the Degree of Conversion and Microhardness of a Light-Curing and a Dual-Curing Cement. *Int. J. Prosthodont.* **2016**, *29*, 384–388. [CrossRef]
23. Scotti, N.; Venturello, A.; Migliaretti, G.; Pera, F.; Pasqualini, D.; Geobaldo, F.; Berutti, E. New-generation curing units and short irradiation time: The degree of conversion of microhybrid composite resin. *Quintessence Int.* **2011**, *42*, e89–e95.
24. Brambilla, E.; Gagliani, M.; Ionescu, A.; Fadini, L.; García-Godoy, F. The influence of light-curing time on the bacterial colo-nization of resin composite surfaces. *Dent. Mater.* **2009**, *25*, 1067–1072. [CrossRef]
25. Somacal, D.C.; Manfroi, F.B.; Monteiro, M.S.G.; Oliveira, S.D.; Bittencourt, H.R.; Borges, G.A.; Spohr, A.M. Effect of pH cy-cling followed by simulated toothbrushing on the surface roughness and bacterial adhesion of bulk-fill composite resins. *Oper. Dent.* **2020**, *45*, 209–218. [CrossRef]
26. Park, C.; Park, H.; Lee, J.; Seo, H.; Lee, S. Surface Roughness and Microbial Adhesion After Finishing of Alkasite Restorative Material. *J. Korean Acad. PEDTATRIC Dent.* **2020**, *47*, 188–195. [CrossRef]
27. Eren, M.M.; Ozan, G.; Erdemir, U.; Vatansever, C. Streptococcus Mutans adhesion to dental restorative materials after pol-ishing with various systems: A Confocal Microscopy study. *Acta Microsc.* **2021**, *30*, 102–113.

28. Cazzaniga, G.; Ottobelli, M.; Ionescu, A.C.; Paolone, G.; Gherlone, E.; Ferracane, J.L.; Brambilla, E. In vitro biofilm for-mation on resin-based composites after different finishing and polishing procedures. *J. Dent.* **2017**, *67*, 43–52. [CrossRef]

29. Hahnel, S.; Ionescu, A.; Cazzaniga, G.; Ottobelli, M.; Brambilla, E. Biofilm formation and release of fluoride from dental restorative materials in relation to their surface properties. *J. Dent.* **2017**, *60*, 14–24. [CrossRef]

30. Ionescu, A.C.; Cazzaniga, G.; Ottobelli, M.; Ferracane, J.L.; Paolone, G.; Brambilla, E. In vitro biofilm formation on res-in-based composites cured under different surface conditions. *J. Dent.* **2018**, *77*, 78–86. [CrossRef]

31. Ionescu, A.C.; Cazzaniga, G.; Ottobelli, M.; Garcia-Godoy, F.; Brambilla, E. Substituted Nano-Hydroxyapatite Toothpastes Reduce Biofilm Formation on Enamel and Resin-Based Composite Surfaces. *J. Funct. Biomater.* **2020**, *11*, 36. [CrossRef]

32. Ionescu, A.; Brambilla, E.; Hahnel, S. Does recharging dental restorative materials with fluoride influence biofilm for-mation? *Dent. Mater.* **2019**, *35*, 1450–1463. [CrossRef] [PubMed]

33. Charpentier, T.; Okhotnikov, K.; Novikov, A.N.; Hennet, L.; Fischer, H.E.; Neuville, D.R.; Florian, P. Structure of stronti-um aluminosilicate glasses from molecular dynamics simulation, neutron diffraction, and nuclear magnetic resonance studies. *J. Phys. Chem. B* **2018**, *122*, 9567–9583. [CrossRef] [PubMed]

34. Yuan, C.; Wang, X.; Gao, X.; Chen, F.; Liang, X.; Li, D. Effects of surface properties of polymer-based restorative materi-als on early adhesion of Streptococcus mutans in vitro. *J. Dent.* **2016**, *54*, 33–40. [CrossRef]

35. Schmalz, G.; Cieplik, F. Biofilms on Restorative Materials. *Monogr. Oral Sci.* **2021**, *29*, 155–194. [CrossRef] [PubMed]

36. Renner, L.D.; Weibel, D.B. Physicochemical regulation of biofilm formation. *MRS Bull.* **2011**, *36*, 347–355. [CrossRef] [PubMed]

37. Soliman, W.E.; Ali, A.I.; Elkhatib, W.F. Evaluation of surface roughness and Streptococcus mutans adhesion to bulk-fill res-in composites polished with different systems. *Adv. Microbiol.* **2019**, *9*, 87–101. [CrossRef]

38. Ionescu, A.C.; Hahnel, S.; König, A.; Brambilla, E. Resin composite blocks for dental CAD/CAM applications reduce biofilm formation in vitro. *Dent. Mater.* **2020**, *36*, 603–616. [CrossRef] [PubMed]

39. An, J.S.; Kim, K.; Cho, S.; Lim, B.S.; Ahn, S.J. Compositional differences in multi-species biofilms formed on various ortho-dontic adhesives. *Eur. J. Orthod.* **2017**, *39*, 528–533. [CrossRef] [PubMed]

40. Busscher, H.J.; Rinastiti, M.; Siswomihardjo, W.; Van Der Mei, H.C. Biofilm Formation on Dental Restorative and Implant Materials. *J. Dent. Res.* **2010**, *89*, 657–665. [CrossRef]

41. Tang, H.; Wang, A.; Liang, X.; Cao, T.; Salley, S.O.; McAllister, J.P., III.; Ng, K.S. Effect of surface proteins on Staphylococcus epidermidis adhesion and colonization on silicone. *Colloids Surf. B Biointerfaces* **2006**, *51*, 16–24. [CrossRef]

42. Gyo, M.; Nikaido, T.; Okada, K.; Yamauchi, J.; Tagami, J.; Matin, K. Surface Response of Fluorine Polymer-Incorporated Resin Composites to Cariogenic Biofilm Adherence. *Appl. Environ. Microbiol.* **2008**, *74*, 1428–1435. [CrossRef]

43. Ionescu, A.; Wutscher, E.; Brambilla, E.; Schneider-Feyrer, S.; Giessibl, F.J.; Hahnel, S. Influence of surface properties of res-in-based composites on in vitro Streptococcus mutans biofilm development. *Eur. J. Oral Sci.* **2012**, *120*, 458–465. [CrossRef]

44. Hahnel, S.; Rosentritt, M.; Bürgers, R.; Handel, G. Surface properties and in vitro Streptococcus mutans adhesion to dental resin polymers. *J. Mater. Sci. Mater. Electron.* **2008**, *19*, 2619–2627. [CrossRef] [PubMed]

45. Ikeda, M.; Matin, K.; Nikaido, T.; Foxton, R.M.; Tagami, J. Effect of Surface Characteristics on Adherence of S. mutans Biofilms to Indirect Resin Composites. *Dent. Mater. J.* **2007**, *26*, 915–923. [CrossRef] [PubMed]

46. Alshali, R.Z.; Salim, N.; Sung, R.; Satterthwaite, J.D.; Silikas, N. Analysis of long-term monomer elution from bulk-fill and conventional resin-composites using high performance liquid chromatography. *Dent. Mater.* **2015**, *31*, 1587–1598. [CrossRef] [PubMed]

47. Kim, K.; Kim, J.N.; Lim, B.S.; Ahn, S.J. Urethane Dimethacrylate Influences the Cariogenic Properties of Streptococcus Mu-tans. *Materials* **2021**, *14*, 1015. [CrossRef] [PubMed]

48. Hamama, H.H. Recent advances in posterior resin composite restorations. In *Applications of Nanocomposite Materials in Dentistry*; Woodhead Publishing Series in Biomaterials; Woodhead Publishing: Sawston, UK, 2019; Volume 19, pp. 319–336.

49. Ionescu, A.C.; Brambilla, E. Bioreactors: How to Study Biofilms In Vitro. In *Oral Biofilms and Modern Dental Materials: Advances Toward Bioactivity*; Ionescu, A.C., Hahnel, S., Eds.; Springer Nature: Basingstoke, UK, 2021; p. 37.

Article

3D Printed Hollow Off-Axis Profiles Based on Carbon Fiber-Reinforced Polymers: Mechanical Testing and Finite Element Method Analysis

Martina Kalova [1,*]**, Sona Rusnakova** [2]**, David Krzikalla** [3]**, Jakub Mesicek** [3]**, Radek Tomasek** [1]**, Adela Podeprelova** [1]**, Jiri Rosicky** [4] **and Marek Pagac** [3,*]

[1] Center for Advanced Innovation Technologies, VSB-TU Ostrava, 17. Listopadu 2172/15, 708 00 Ostrava-Poruba, Czech Republic; radek.tomasek@vsb.cz (R.T.); adela.podeprelova@vsb.cz (A.P.)

[2] Department of Production Engineering, Faculty of Technology, Tomas Bata University in Zlin, Vavreckova 275, 760 01 Zlin, Czech Republic; rusnakova@utb.cz

[3] Center of 3D Printing Protolab, Department of Machining, Assembly and Engineering Technology, Faculty of Mechanical Engineering, VSB-TU Ostrava, 17. Listopadu 2172/15, 708 00 Ostrava-Poruba, Czech Republic; david.krzikalla@vsb.cz (D.K.); jakub.mesicek@vsb.cz (J.M.)

[4] Orthopedic Prosthetics Frydek-Mistek, Dr. Janskeho 3238, 738 01 Frydek-Mistek, Czech Republic; jiri.rosicky@inventmedical.cz

* Correspondence: martina.kalova@vsb.cz or kaloma13@seznam.cz (M.K.); marek.pagac@vsb.cz (M.P.)

Abstract: The aim of the paper is to design, manufacture, and test an off-axis composite profile of circular cross-section. Composite profile based on continuous carbon fibers reinforcing the onyx matrix, i.e., a matrix that consists of nylon and micro carbon fibers, was produced by fused deposition modeling (FDM) method. A buckling test of the six printed composite specimens was performed on a tensile test machine. The values of the experiment were compared with the values of the computational simulation using the Finite Element Method (FEM) analysis. The mean value of the experimentally determined critical force at which the composite profile failed was 3102 N, while the value of the critical force by FEM analysis was calculated to be 2879 N. Thus, reliability of the simulation to determine the critical force differed from the experimental procedure by only 7%. FEM analysis revealed that the primary failure of 3D printed composite parts was not due to loss of stability, but due to material failure. With great accuracy, the results of the comparison show that it is possible to predict the mechanical properties of 3D printed composite laminates on the basis of a theoretical model.

Keywords: composite polymer materials; carbon fibers; hollow profile; 3D printing; fused deposition modeling; FEM analysis; SEM analysis

1. Introduction

Due to their excellent mechanical properties, such as high specific stiffness and strength, fiber-reinforced polymer composites (FRP) are used in structural applications, mainly in the automotive industry (luxury bodies, intake manifolds, interior and safety elements, and axles), aerospace industry (refractory parts, internal elements, and rotor blades), or for the things in everyday life (skis, tennis rackets, safety helmets, musical instruments, or outdoor items) [1–3]. In the field of medicine, FRPs appear mainly as a structural part of rehabilitation aids, where they replace traditional materials such as dural. The use of composite materials meets the requirements for lightening, increasing the stability of the structural element, load-bearing capacity, and design [4]. A major disadvantage of conventional carbon fiber-reinforced composite (CFRP) production methods is the high acquisition costs, such as pultrusion lines or a winding machine. It is more suitable for large-series production and products with a constant cross-section [5,6]. Therefore, there is a growing interest in new processes based on additive production. 3D printing enables the

production of complex geometries, faster production times, and the production of accurate and reproducible parts without the need to produce expensive molds [7,8]. The prints are light, durable, geometrically accurate, and, thanks to minimal material waste, 3D printing technology is also environmentally friendly [9].

Fused Deposition Modeling (FDM), one of methods of 3D printing, is based on heating and subsequent melting of a thermoplastic fiber to a temperature higher than the glass transition temperature. This is followed by controlled extrusion of the plastic through a heated nozzle onto the printing surface [10,11]. During the printing process, no pressure is exerted during the laying of the polymer layer. This creates unfilled gaps, pores, or cavities in the material. The high pore content results in much lower stiffness and strength of the material compared to traditionally produced FRP composites. When printing a curved part, there is also a risk of twisting or breaking the fiber bundle [9,12]. However, in addition to temperature and material selection, the productivity of the 3D printing process and the quality of the final parts depend on other factors, including the geometric complexity of the part, fill density, layer thickness, print speed, or fiber orientation [13–15]. As with hand-lay-up composites, there is a strong dependence of the properties of the laminate material on the orientation of both short and continuous fibers. The strength and stiffness of the laminate are maximized when the fiber orientation is parallel to the direction of loading [16,17]. Due to the limited mechanical properties of polymer-based 3D prints, FDM-printed parts are only used as prototypes, not as functional components. The mechanical properties of polymer prints can be improved by adding high-strength fibers (short, continuous) to the polymer matrix during the FDM process. The design of composite printed parts is thus freer in contrast to conventional techniques for the production of composite materials [18–20].

There are a number of FDM 3D printers on the market that are capable of producing composite parts. For example, Markforged, USA, has developed the Mark One/Two printer, which can produce composites with continuous fiber reinforcement. The Mark Two printer is supported by Eiger's own specialized software [21]. This printer uses two extruders and two printheads to separately extrude the die and fibers in the desired positions. The design of the 3D printer allows the placement of continuous fiber reinforcement as needed through the layer-by-layer application process [9,21]. Another commercially available printer is the Markforged X7, which is capable of printing continuous fibers only on the inside of printed parts, and the continuous fiber material contains additives that facilitate the FDM printing process. This causes a reduction in longitudinal and flexural strength compared to raw carbon fibers [22,23].

Increasingly, scientists are evaluating the mechanical properties (tensile and compressive, bending, impact, fatigue, or creep) of 3D printed composites. The tensile and flexural properties of 3D printed fiber-reinforced polymer composites have been discussed, for example, by Justo et al. [24], Korkees et al. [25], Mohammadizadeh et al. [26], and Pertuz et al. [27]. In many cases, such as in the article by Yasa et al. [28], it has been found that adding reinforcement to the thermoplastic matrix increases the tensile strength, but only to a certain extent. The problem with the FDM method is that pores are formed in the structure, which degrade the mechanical properties. The mechanical properties of CFRP based on onyx matrix, the influence of fiber orientation and of defects on the properties of printed structures by Wickramasinghe et al. [29] were studied. Although the tensile strength of the composite (CF/nylon) was increased by the fibers, the addition of additional layers of fibers increased the cavity content, causing poor tensile modulus. The addition of continuous fibers to the thermoplastic increased the tensile and flexural strength, but the compressive strength was reduced, again due to defects caused by printing.

Components in industries often contain structural holes. Holes are places of stress concentration which affect the strength and reliability of the product. Pollen et al. [30] and Sanei et al. [31] investigated the effect of stress concentration on 3D printed parts using tensile samples around the open hole area. Prajapati et al. [32] investigated the effect of HSHT continuous glass fiber reinforcement on the open hole tensile strength of 3D

printed parts. Onyx was used as a polymer matrix material. It has been found that the fiber reinforcement in the onyx matrix increases the open hole tensile strength, but it also increases the specimen weight and printing time of the final part. Ekoi et al. [33] compared the mechanical properties (tensile, flexural, and fatigue) of woven continuous carbon fiber composites printed using FDM and nonwoven printed composites (unidirectional and multidirectional fibers), along with woven composites, and also composites reinforced with chopped carbon fibers (onyx). The maximum tensile strength (714 MPa) achieved for composites was highest for unidirectional nonwoven composites. The lowest tensile value was achieved at the multidirectional nonwoven composite (248 MPa). The maximum flexural strength of unidirectional (nonwoven) composites was 407 MPa, and for woven composites, the flexural strength was 251 MPa. Woven carbon fiber composites achieved the best fatigue strength. Therefore, these materials have great potential for more demanding applications (medical and sports devices). Saghir et al. [34] investigated the effects of constituent materials (particle reinforcement, cut glass, glass fiber, and resin) on the axial tensile and the hoop tensile strength of particulate FRP composite pipes. Three specimens for each type of reinforcement and two types of tests (axial tensile test and hoop tensile test) were selected. Saghir showed that the inclusion of a higher proportion of particulate fillers/reinforcements, such as sand or other components, can reduce production costs, but also causes a reduction in both axial and hoop strength. Research has shown that the ratios of material components have a measurable impact on pipe performance.

An interesting conclusion was reached by the research of Saharudin et al. [35]. Both FDM and CFF (Continuous Filament Fabrication) 3D printing technologies were compared, and it was shown that the addition of carbon fibers alone is not a factor determining the high mechanical properties, the method of fiber supply depending on the 3D printing method is also important.

Latest studies on the mechanical properties of 3D composites with printed continuous fiber have been summarized by Zhuo et al. [36]. The addition of continuous fiber reinforcement improves mechanical properties, but at the cost of increased complexity and cost. The fiber volume fraction must be high enough and the defect content low enough for printed products to be used in real engineering structures. To improve the mechanical properties of printed composites, it is necessary to understand the relationships between the AM (Additive Manufacturing) process, the structure of printed parts and their mechanical performance [37].

From the research to date, it can be stated that the problem with composites is to determine their static and dynamic mechanical properties in advance. To obtain more detailed information on mechanical values, composite materials must be tested during their production, or even on the finished product. This is, of course, time consuming and expensive. This manufacturing process can be facilitated by unique software for advanced modeling and simulation of the structures and properties of a given material. Currently, only a small percentage of people are involved in modeling composite structures using software. However, a number of publications are available on the numerical prediction of the mechanical properties of different types of composite materials [38]. Gao et al. dealt with the numerical prediction of mechanical properties of rubber composites reinforced with short aramid fibers at large deformation. Samples with two different fiber lengths and three different fiber volume fractions were subjected to mechanical testing. To predict the mechanical response of the rubber composite, Gao proposed a computational model based on the finite element method. The results obtained by experiment and by numerical simulation in Digimat-FE software (Finite Element—describing the behavior of the material from a microview based on FEM) were compared to verify the reliability of the FE-model. The results were almost identical. It was thus concluded that, with this method, it is possible to obtain a model with randomly dispersed fibers with a high-volume fraction of fibers, and that with the numerical method, it is possible to obtain the mechanical properties of a rubber composite under high deformation [39]. Gohari et al. [40] dealt with the analysis of the failure location of internally pressurized laminated ellipsoidal

woven composite domes (CFRP). The experimental and numerical results confirmed the analysis that the deformation occurs locally rather than uniform. Potluri et al. [41], for a change, used modeling to predict the mechanical properties of a natural fiber-reinforced composite. He dealt with the prognosis of the value of the Young's modulus of elasticity in tension and the modulus of elasticity in shear of a given material. He compared the results obtained analytically, numerically, and experimentally. He wanted to determine which model can accurately predict the values of elastic and shear properties of composite materials reinforced with natural fibers. By comparing the analyses, Potluri showed that all models show a very good correlation for the modulus of elasticity in tension and shear. FE models were further implemented in ANSYS software. Furthermore, Elmarakbi et al. [42] studied the modeling in Digimat, which was used in modeling hybrid glass profiles with a polyamide matrix (PA6) reinforced with graphene plates. In his work, he investigated the impact resistance of this material in a hierarchical modeling of a hybrid composite material consisting of short matrix-reinforced glass fibers and graphite plates. The multistep method uses both the medium homogenization method and the finite element FE technique.

The main contribution of our paper lies in the expansion of knowledge about the behavior of composite off-axis profiles of carbon fibers produced by an unconventional method of 3D printing. In many applications, due to low-series production, it is not worth investing in expensive equipment, such as pultrusion lines or winding machines, and therefore the results experimentally obtained and verified by FEM are a valuable source of information.

The computational method helps us to understand the mechanisms of continuous printing in terms of local stress distribution. The absence of literature on the production of hollow off-axis composite profiles was a challenge for this paper. After considering the available variants, we chose a technology suitable for low-series production and also economically available for the production of profiles.

2. Materials and Methods

2.1. Design and Manufacture of an Off-Axis CFRP Profiles

The geometry of the sample was designed as a hollow off-axis profile of a circular cross-section using the commercial 3D modeling software SolidWorks 2020 (Dassault Systèmes, Vélizy-Villacoublay, France). This shape element is found, for example, in medical supplies and aids (sticks and crutches), as part of the body structure. This shaped element helps to better transfer compressive loads to the base of the aids and dampens vibrations. The dimensions of the composite profile were given both from an economic point of view, as well as the possibilities of printing itself and the minimum printable thicknesses, so that the walls of the hollow circular profile did not collapse. With a sample diameter of 18 mm, a wall thickness of at least 3.5 mm was required. At this wall thickness, a sufficient coating of the reinforcing fibers with an onyx matrix was achieved. Figure 1 presents a schema of the design of composite profile.
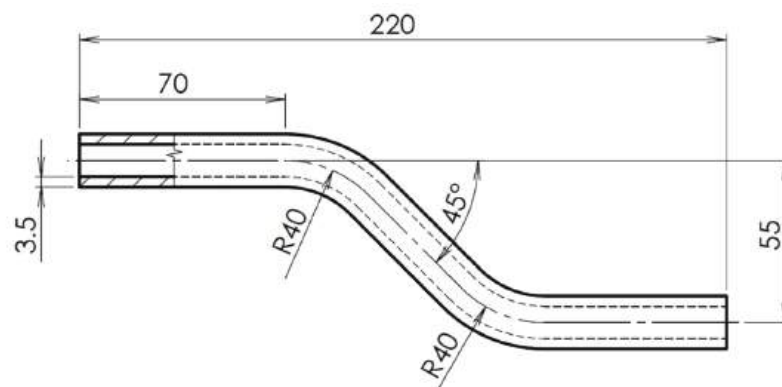
Figure 1. Design of an off-axis hollow CFRP profile.

The Markforged X7 3D printer (Markforget, Watertown, MA, USA) is designed from the ground up to print composite continuous fiber parts. It contains a reinforced two-nozzle system that supports the printing of the matrix, and at the same time continuous carbon or other reinforcing fibers. The laser scans the part during printing to ensure maximum dimensional accuracy [43]. A tough onyx matrix (basic material) reinforced with carbon fiber was chosen for printing composite prototypes using the FDM/FFF method on a 3D printer. The 2D design with matrix and reinforcement layout was performed in the Eiger software (Figure 2), which is an accessory of the 3D printer.
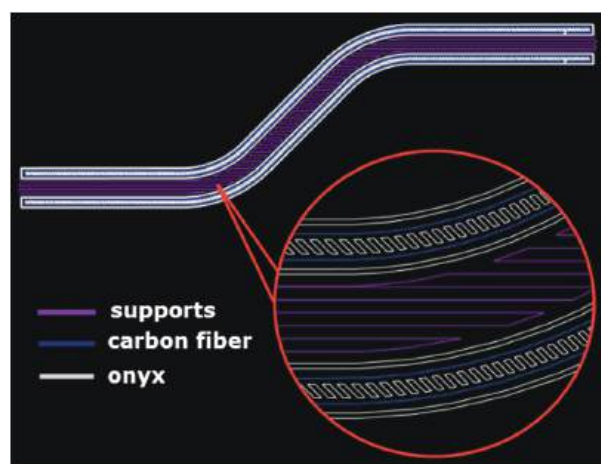
Figure 2. Layout of matrix and reinforcement for 3D printing of CFRP profiles.

Onyx is a thermoplastic that is up to $1.4\times$ stronger than ABS. The strength of the onyx can be further increased by reinforcement in the form of continuous fibers. Onyx is chemically and thermally resistant, but must be stored in a dry box for protection against moisture to prevent deterioration [44]. Onyx fibers with a diameter of 1.75 mm and carbon fibers with a diameter of 0.34–0.38 mm were supplied by Markforged. The mechanical properties (from datasheet) of the material used (onyx/CF) for 3D printing are given in Table 1.

Table 1. Mechanical properties of materials for CF/onyx profiles [43,44].

Composite Base (Matrix)	Test (ASTM)	Onyx
Tensile modulus (Gpa)	D638	1.4
Tensile Stress at Yield (MPa)	D638	40
Tensile Stress at Break (MPa)	D638	37
Tensile Strain at Break (%)	D638	58
Flexural Strength (MPa)	D790 [1]	81
Flexural Modulus (GPa)	D790 [1]	3.6
Heat Deflection Temp (°C)	D648 B	145
Izod Impact-notched (J/m)	D256-10 A	330
Density (g/cm^3)	-	1.2
Continuous Fiber	**Test (ASTM)**	**Carbon**
Tensile Strength (MPa)	D3039	800
Tensile Modulus (GPa)	D3039	60
Tensile Strain at Break (%)	D3039	1.5
Flexural Strength (MPa)	D790 [1]	540
Flexural Modulus (GPa)	D790 [1]	51
Flexural Strain at Break (%)	D790 [1]	1.2
Compressive Strength (MPa)	D6641	420
Compressive Modulus (MPa)	D6641	62
Compressive Strain at Break (%)	D6641	0.7
Heat Deflection Temp (°C)	D648 B	105
Izod Impact-notched (J/m)	D256-10 A	960
Density (g/cm^3)	-	1.2

[1] Measured by a method similar to ASTM D790. Composite Base—only parts do not break before end of flexural test.

The print parameters were also set in the Eiger Markforged software. The print layer height was set to 0.125 mm. The number of layers was then determined to a total of 144. The time required for the preparation and printing of the 6 composite profiles was calculated to be about 63 h. An overview of the printing parameters for one sample is given in Table 2.

Table 2. 3D printing parameters of CF/onyx profiles.

Dimensions	220 mm × 73 mm × 18 mm
Printing Temperature (onyx)	274 °C
Printing Temperature (CF)	252 °C
Layer height	0.125 mm
Number of layers	144
Fiber Fill Type	Isotropic Fiber
Fill Pattern	Triangular Fill
Fill Density	55%
Roof and Floor layers	2
Wall Layers	2
Print time	10 h 22 m
Plastic Volume	27.16 cm^3
Fiber Volume	20.48 cm^3
Final Part Mass	51.14 g
Plastic Angles	90° (not set one angle)
Fiber Angles	0°
Material cost	67.45 USD

2.2. Testing of an Off-Axis CFRP Profile

The composite CFRP profile (six specimens) buckling test was performed on a Zwick/ Roell Z150 universal tensile test machine (ZwickRoell, Ulm, Germany) [45]. This testing machine is fully automated and uses a hydraulic control mechanism to transmit the gradual separation of the jaws at a constant speed. Load-cell of the tensile test machine is calibrated regularly every two years. The mechanical properties of this composite materials class have not been comprehensively studied to date. In this case, it is more precisely a modified buckling test as, due to the shape of the test part, both buckling and the bending occur during loading. For testing off-axis prototypes, it was necessary to tailor-make a jig to attach the composite profile to the upper and lower jaws grips of the tensile test machine. At the top of the machine, the specimens were slid onto a steel mandrel with a sleeve. A steel bench was placed in the lower jaw with holes for accommodating composite rods provided with a steel ring against slipping in the bench. The sample was then set up on the tester to ensure adequate alignment. The load cell was zeroed with each new measurement. Tests were carried out at a deformation speed of 5 mm/min. Load was applied to the samples until the maximum failure force could be evaluated. The modification of the test set-up is shown in Figure 3. By comparing Figure 3b (before loading) and Figure 3c (after loading), it can be seen how the specimen bends downwards towards the steel bench after loading.
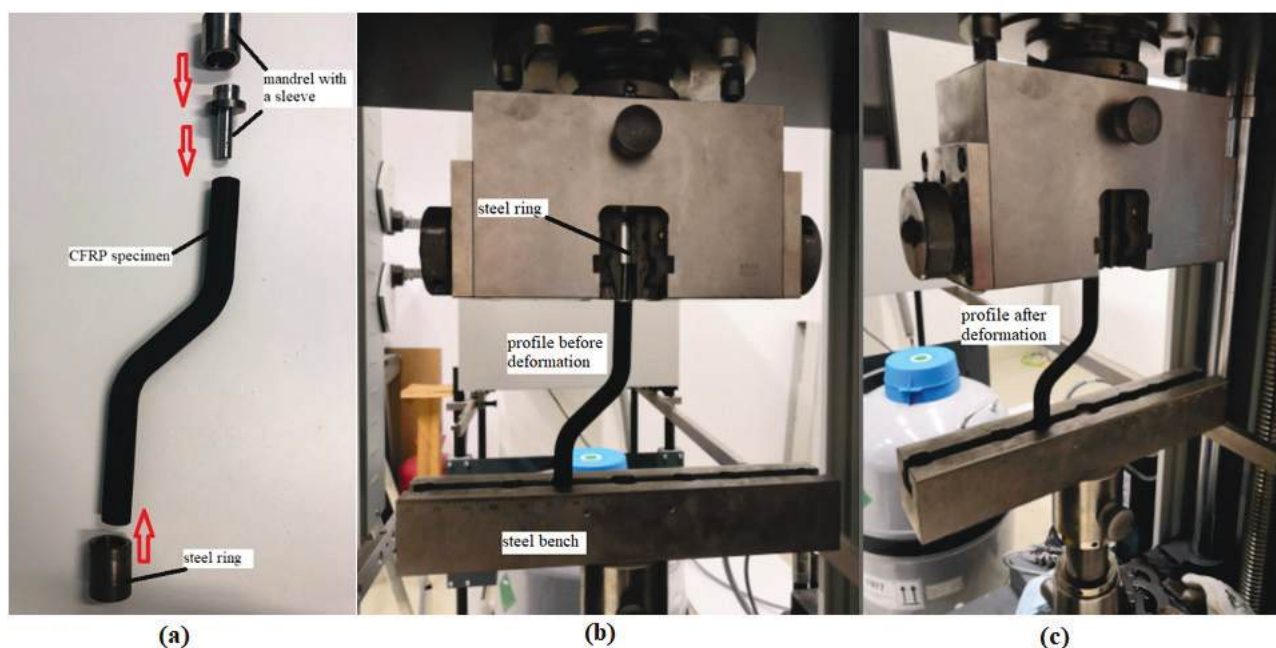
Figure 3. Mechanical testing of an off-axis hollow CFRP profile; (**a**) "tailor-make" a jig to attach the composite profile to the upper and lower jaws grips, (**b**) CF profile before mechanical testing, (**c**) CF profile after mechanical testing.

3. Results and Discussion

There are no uniform test conditions for polymer composites due to their variable morphology and chemical composition; they are regulated only in a framework by the standard. Therefore, the specific method of a particular material is governed by professional discretion, taking into account how the future product will be stressed during its use [46].

In some structures, it is possible to find cases where the load-bearing capacity is not critical in terms of material strength, but in terms of stability. The issue of loss of stability, which most often occurs under pressure, bending, torsion, or a combination thereof, deals with the stability of structures. Stability is most often solved for open and closed profiles or for thin-walled beams. One of the basic cases of stability, which is solved most often, is the so-called buckling. The buckling occurs when the slender member is loaded by a compressive axial force. The pressure acts on the reinforced layer in the direction of the fiber axes until it breaks due to the loss of stability of these fibers. The degree of fiber resistance depends on the fiber crimp and the level of interfacial cohesion. With good adhesion of the fiber-matrix interface, fracture occurs due to shear (coordinated deflection of the fibers after exceeding the critical value of the load), and with poor adhesion due to delamination. Under compressive loading, it is difficult to maintain a uniform tension throughout the test specimen throughout the test. Changing the wall thickness of the sample leads to differences in resistance to loss of stability [47,48]. A combination of pressure and bending is used to calculate the critical force of off-axis hollow sections, so-called geometrically imperfect rods. The buckling test is one of the commonly used mechanical tests, which are based on the deformation of a test specimen by pressure to determine the critical force of stability failure. The test specimen is clamped in the jaws of the tensile testing machine, where it is loaded with a constant force, usually until failure (collapse of the structure) [48].

3.1. Buckling Test of Hollow Composite Profiles

3.1.1. Graphic Evaluation of the Buckling Test of Hollow Composite Profiles

The result of the buckling test was a stress–strain diagram of the material, which is a curve of the dependence of the load force on the profile displacement. The data were plotted in MATLAB R2019b. Two types of graphs were used for graphical evaluation in Figure 4. A line graph (Figure 4a) showing the dependence of load force on the displacement (compression) of the test profile. The second bar graph (Figure 4b) shows the values of maximum failure

strength for each profile. As the hollow sections do not have the shape of a straight bar, they have been subjected to both buckling and bending forces. During testing, the profiles were subjected to compressive forces, but graphs are plotted in absolute values.

(**a**)

(**b**)
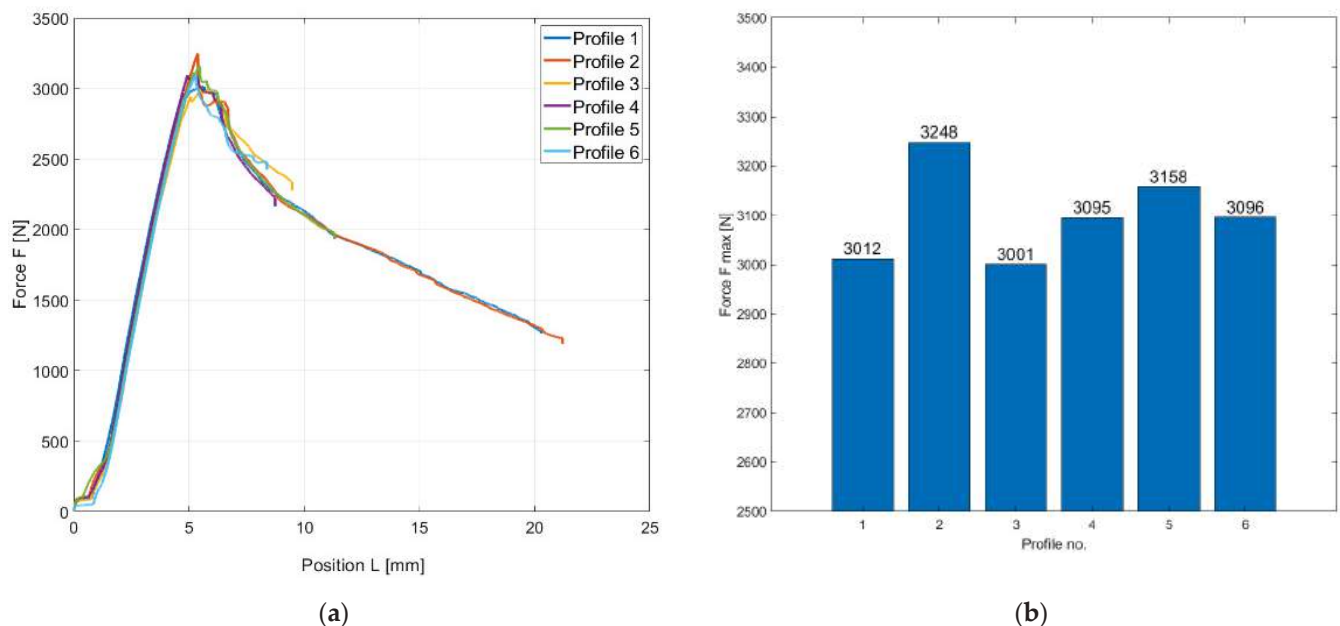
Figure 4. Graphical evaluation buckling test of CFRP profiles produced using 3D printing; (**a**) a line graph of the dependence of the maximum force on the deformation shift, (**b**) a bar graph of the achieved maximum forces for individual profiles.

From both graphs, it is evident that both the course of the test and the resulting values of the maximum forces of the individual composite profiles are very balanced with one another. This is due to the 3D printing technology, which guarantees the accuracy and reproducibility of parts while achieving repeatable values of mechanical properties. The maximum force for the 3D printed composite profiles was approximately in the range of 3000–3250 N at a displacement (deformation by compressive force) of approximately 5 mm.

During loading, the specimens bent at the area of their curvature. At these points, there was a visible deformation of the structure (surface failure of the material), as indicated in Figure 5. Here, it can be assumed that there was not a failure of stability, but failure of strength. After unloading, the profiles partially returned to their original state as were before the load.
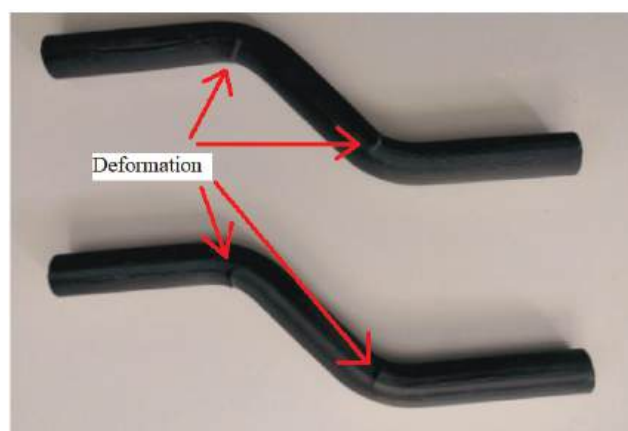
Figure 5. CFRP profiles deformation after buckling test.

3.1.2. Statistical Evaluation of the Buckling Test of Hollow Composite Profiles

Composite materials show a greater scatter of material characteristics than is the case with conventional materials. Therefore, statistical analysis is an essential part of their evaluation.

Table 3 shows the results of experimental testing of 3D composite profiles on buckling with evaluation of the maximum force (critical force) at which the stability of the samples is disturbed. The table is supplemented by statistical characteristics (arithmetic mean, standard deviation, and coefficient of variation).

Table 3. Results comparison of the maximum load force on the buckling test of hollow composite profiles.

n = 6	F_{max} (N)
Profile 1	3012
Profile 2	3248
Profile 3	3001
Profile 4	3095
Profile 5	3158
Profile 6	3096
Arithmetic mean	3102
Standard deviation	93
Coefficient of variation (%)	3

3.2. Analysis of Composite Profiles Using FEM

FEM analysis of the prototypes printed on a 3D printer were performed in Ansys ADPL 18.2 software. The structure of unidirectionally reinforced composite elements with bends was more complex for modeling and analysis. Software designed specifically for this application is still being developed. Onyx wall was considered as an isotropic material with constants according to the Markforged material sheet [44]. The composite part was considered as a transversely isotropic material. The core elements coordinate system was set to respect fiber direction in real tube thus the material model longitudinal direction respects the fiber direction. An overview of material properties is given in Table 4.

Table 4. Static analysis—material properties [44,49].

Onyx Wall	Young's Modulus, E (MPa)	1400
	Poisson's Ratio, μ	0.4
CF composite core	Matrix Young's modulus, E_m (MPa)	1400
	Poisson's ratio, μ_m	0.4
	Fiber Young's modulus, E_f (Mpa)	60,000
	Poisson's ratio, μ_f	0.33
	Fiber volumetric content, v_f	0.77

Analytical Relationships for Long Fiber Unidirectional Composites

The material model constants were determined by analytical relationships for long fiber unidirectional composites. Here, μ_f is Poisson´s ratio of fiber, μ_m is Poisson´s ratio of matrix, E_f is fiber Young's modulus, E_m is matrix Young's modulus and v_f is fiber volumetric content.

- Longitudinal Young's modulus: 46,522 MPa

The ROM approach (Rule of Mixture) for the calculation assumes an idealized state of the composite—continuous reinforcing fibers of the equal diameter, perfect bonding of the fibers and the matrix or the equal strain of the composite in the longitudinal direction (Equation (1)) [50].

$$E_L = v_f \cdot E_f + v_m \cdot E_m \tag{1}$$

- Poisson's ratio: 0.35

The simplicity and accuracy of the ROM was confirmed by several studies comparing the ROM results of analytical and experimental findings (Equation (2)) [51].

$$\mu_{LT} = v_f \cdot \mu_f + v_m \cdot \mu_m \tag{2}$$

- Transversal Young's modulus: 5646 MPa

The relevant Halpin–Tsai model was utilized for the transversal elastic constants of composites. Equations (3) and (4) is a control formula of the H–T model, ksi = 1 [41].

$$E_T = \frac{1 + \xi \cdot \eta \cdot v_f}{1 - \eta \cdot v_f} \cdot E_m \tag{3}$$

$$\eta = \frac{\frac{E_f}{E_m} - 1}{\frac{E_f}{E_m} + \xi} \tag{4}$$

- Transversal Poisson's ratio: 0.59

The Clyne model (Equations (5)–(7)) allows a simple calculation. The accuracy of this model is affected by the input variable Et [52].

$$\mu_{TT'} = 1 - \mu_{TL} - \frac{E_T}{3 \cdot K} \tag{5}$$

$$\mu_{TL} = \mu_{LT} \cdot \frac{E_T}{E_L} \tag{6}$$

$$K = \left(\frac{v_f}{K_f} + \frac{v_m}{K_m} \right)^{-1} \tag{7}$$

- Shear modulus: 2024 Mpa

Inverse rule of mixture (parallel Reuss model in Equation (8)) gives the lowest estimation [53].

$$G_{LT} = \left(\frac{v_f}{K_f} + \frac{v_m}{K_m} \right)^{-1} \tag{8}$$

The component was modeled (Figure 6) as consisting of two parts, an onyx wall and a homogenized composite "core". The mesh (Figure 6a) shown is for illustration only. The final mesh on which the calculation was performed is shown in Figure 6b.
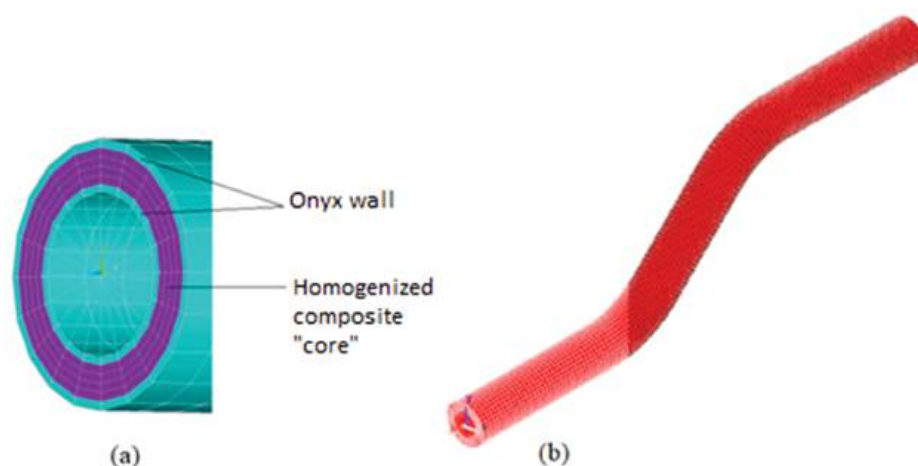
Figure 6. (**a**) The cross-section of the 3D printed prototype model; Onyx walls (blue), composite "core" (purple); (**b**) Final mesh of composite profile.

Volumetric linear solid elements (Solid 185 in ANSYS library) were used in the modeling. Some boundary conditions also required the use of Multi-Point Constraint (MPC) elements, specifically MPC 184. The elementary coordinate systems of the composite part were rotated with respect the direction of the fibers. The boundary conditions were set to be as close as possible to the real situation during testing, as well as for the profiles produced by manual methods. In Figure 7, the bottom part of the tube (the portion in the clamps) was fixed in all directions. Then, the top end of the tube was fixed in lateral directions and a compressive force was also applied.
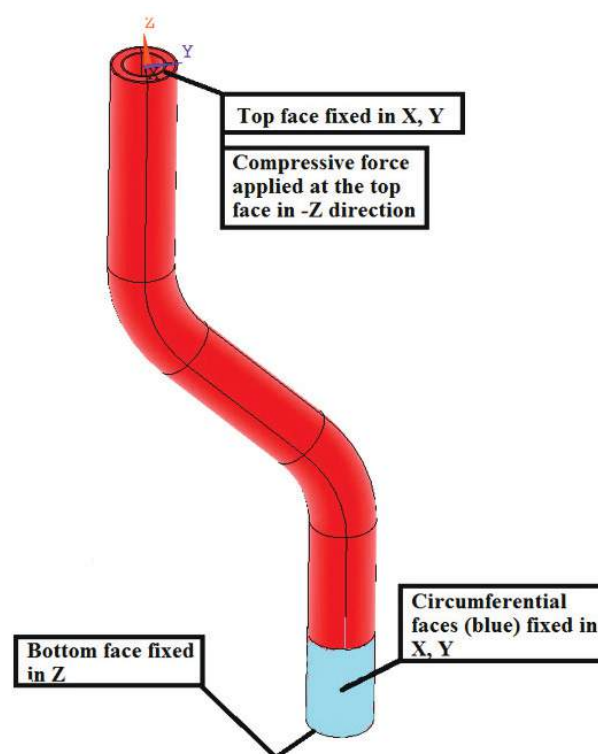
Figure 7. FEM analysis—boundary conditions.

The sufficient mesh density was obtained and checked by a sensitivity analysis. The final mesh consisted of 28,512 elements and 43,020 nodes. Doubled element count led to marginal (0.1%) change in results, hence the depicted mesh was considered as sufficient.

First, a Linear Buckling (LB) or Linear Bifurcation Analysis (LBA) was performed. In LBA, the structure is considered ideal, without any imperfections and material or geometric nonlinearities. The result are the eigenvalues corresponding to the multipliers of the applied force when the loss of stability is reached, and the shapes of the individual modes of loss of stability (MLS). It is important to realize that MLS only shows the displacement ratios of the structure, and does not represent the real deformation of the structure under loss of stability. The MLS serves only to illustrate the expected deformation of the structure at the edge of stability. From the above, it is clear that LBA overestimates the capacity of structures. In general, a minimum overestimation of 15% is reported. The degree of overestimation, however, depends on the geometry and simplifications of the structure.

The lowest calculated critical force was 18,513 N, which is about 500% higher than the critical force determined from the experiment. Considering the above, it follows that the primary failure of the structure was not achieved due to the loss of stability, but rather the failure of the material. Therefore, a static analysis was subsequently performed.

For evaluating the static analysis, the limit states at which the failure occurs were determined for the walls and the composite part. For the given states, the stress limit values were analytically determined on the basis of the material sheets, and the force required to reach the individual limit states was determined by means of static analyses (see Table 5).

Table 5. Static analysis—limit states.

Wall	1	Material Failure	Exceed of Strength Limit	36	3867
	2	Tensile strength along the fibers	Fiber breakage	622	13,705
CF composite core	3	Compressive strength along the fibers	Buckling of micro-fiber, Lo–Chim model	594	6309
	4	Tensile strength transverse to the fibers	Matrix failure in tension	36	2603
	5	Compressive strength transverse to the fibers	Matrix failure in shear	36	2168

It can be seen from Table 5 that, for states 4 and 5, the limit state (LS) is reached at a lower force than determined experimentally. To achieve LS 1, the force required is 25% greater than that obtained by the experiment. LS 2 and LS 3 are unlikely to occur, as they require relatively more force than the experiment, and other LS will fail much sooner. The critical force was determined from this static analysis.

LS 1, 4, and 5 were considered to be realistically achievable limit states. Subsequently, the average value of force (F_p) to achieve them was calculated. The value of the average force was 2879 N. Next, the difference F_p and the critical force F_{krit} were calculated from the experimental part (3102 N) to determine the reliability of the method. The difference between the forces obtained by the experimental and numerical methods was 7%. This difference was assessed as acceptable.

The stress distributions from the static analysis for the load force 3100 N are shown in Figure 8a,b.
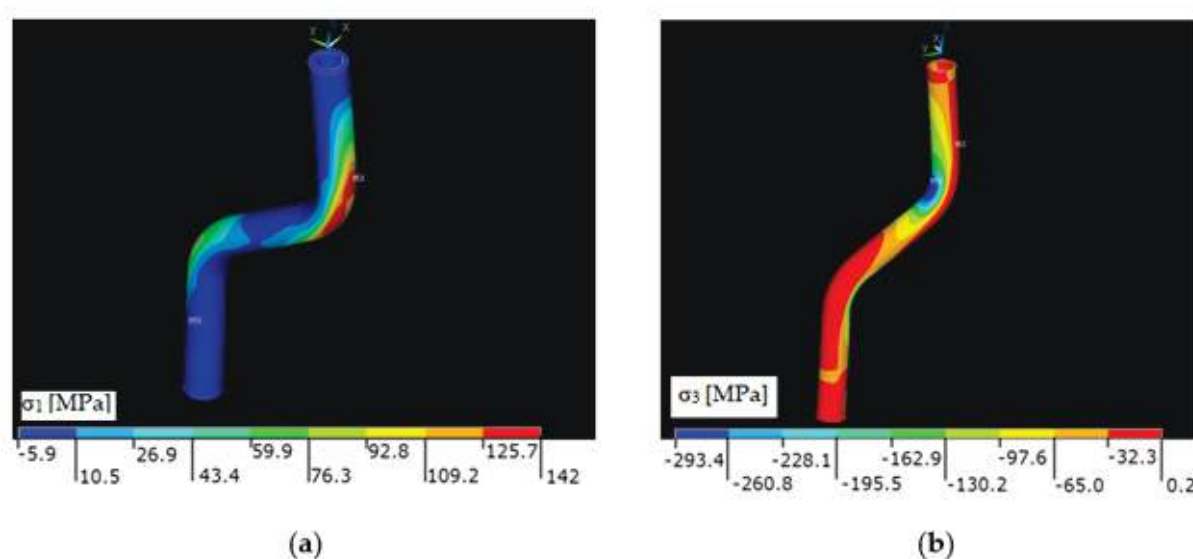
Figure 8. (**a**) Distribution of the first principal stress σ_1 on the composite part in (MPa), (**b**) DistribuTable 3. on the composite part in (MPa).

The greatest stresses occurred in the areas of bends, both for the walls and for the composite part of the profile. The first principal stress expresses the greatest stresses, and the third principal stress shows the lowest stresses, i.e., the stress without shear elements (normal stress). In this way, places with significant tensile or compressive stress can be detected, which can affect local strength, stability, or fatigue. Equivalent stress can mask these areas.

3.3. Microstructure

3.3.1. Microstructure of Composite Profiles Using Optical Microscopy

Images of the microstructure of the observed CF/onyx material were taken using an Olympus GX51 optical microscope with Image-Pro Premium 9.2 software for metallographic analysis.

Samples for metallographic analysis were taken from the composite profile perpendicular to the direction of the fibers. The sample for analysis is thus formed only by the cross-section of the fibers, as the printed profiles are reinforced with fibers in one direction. The carbon fibers coated with an onyx matrix are very strong in the longitudinal direction, especially in tension. The microstructure of the cut on the left is made of a straight part of the profile (Figure 9 (left)). On the right (Figure 9 (right)), is a picture of the microstructure of the sample taken from the bend of the profile, where a visible deformation occurred after the buckling test. Comparing the two figures, it is clear that the deformation caused waviness at the edges of the sample, where there is only a layer of onyx without reinforcing fibers. The middle layer of the onyx matrix is overlap by a deformed layer of carbon reinforcement.
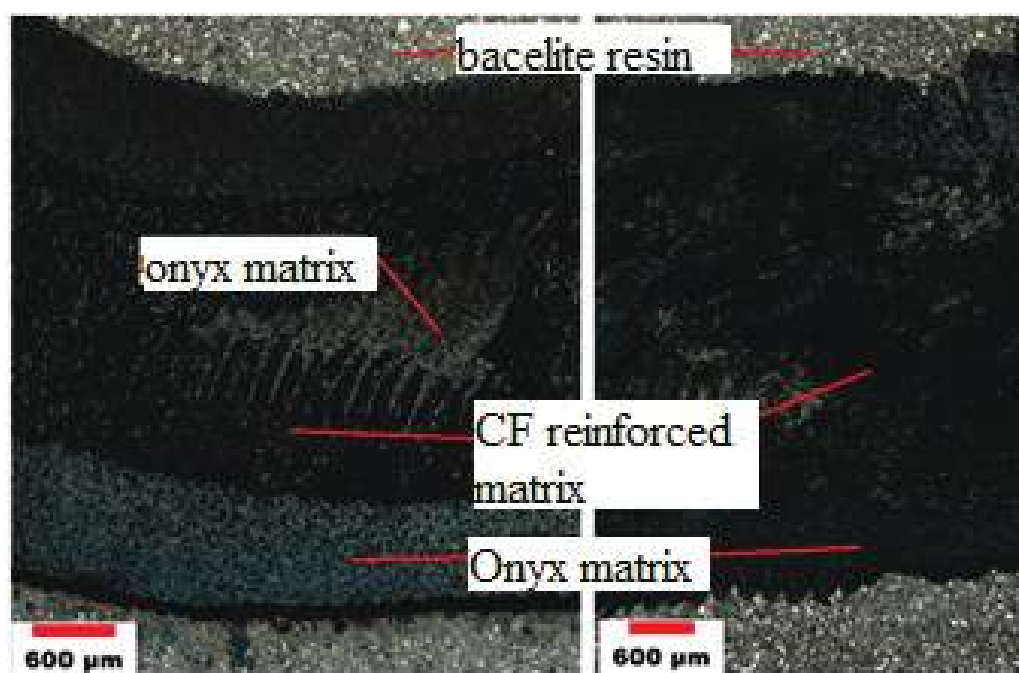
Figure 9. Optical microscopy; microstructure of CFRP/onyx produced by 3D printing. Undeformed sample (**left**), deformed sample (**right**).

3.3.2. Microstructure of Composite Profiles Using SEM Analysis

For observation with SEM (Secondary Electron Microscope), Explorer 4 ThermoFisher Scientific with an accelerating voltage of 15 keV, the transverse surface of the samples had to be sprayed with Au-Pd conductive powder.

Figure 9 shows the microstructure of CFRP profiles made by 3D printing, where carbon fibers are printed into an onyx matrix. There is only a cross-section of the fibers in the microstructure, due to the one-way reinforcement along the length of the composite part. Figure 10 (left) shows the microstructure of a sample taken from an undeformed profile. Figure 10 (right) then shows the microstructure of the 3D printed profile after deformation. While in Figure 10 (left) there are places with missing reinforcement, after deformation, the surrounding composite material was compressed and accumulated in the originally unreinforced places (right).
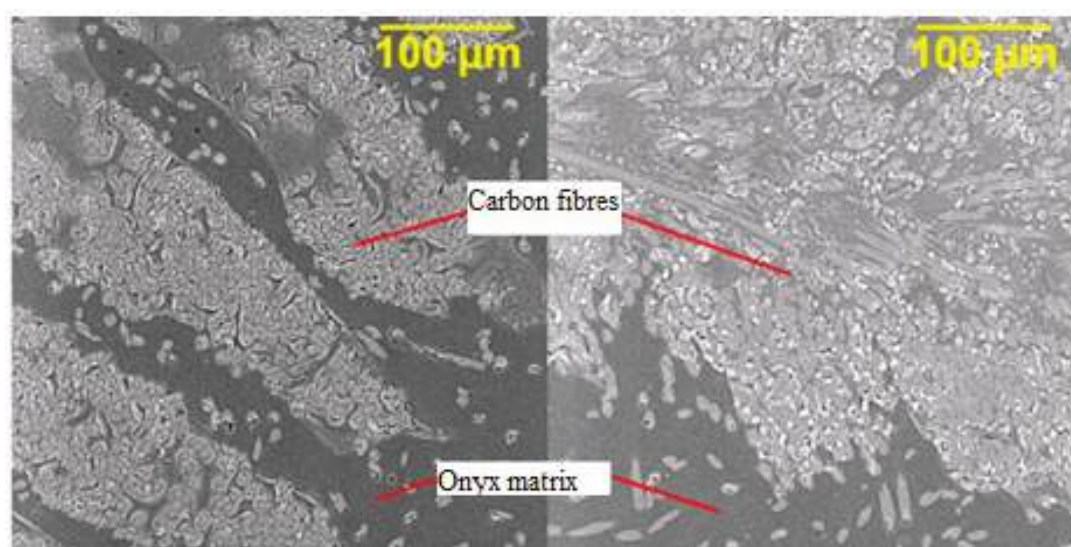
Figure 10. SEM analysis; microstructure of CFRP/onyx produced by 3D printing. Undeformed sample (**left**), deformed sample (**right**).

4. Conclusions

This paper deals with the design and modeling of composite structures. The aim was to design, manufacture, and test an off-axis composite profile of circular cross-section. For 3D printed samples, FEM analysis revealed that the primary failure was not due to a loss of stability, but most likely to material failure. The stress limits for the limit state (LS) were calculated by static analysis, and the force required to achieve the LS was determined for these individual LS. The force value was calculated to be 2879 N. Under loading, several LS are expected to interact at once. Therefore, a procedure was proposed to determine the critical force from the simulation, the reliability of which differs only by 7% from the result of the experiment, 3102 N. In addition, it is on the safe side. The highest stresses were found in the same areas of the profiles where the material was significantly deformed during the experiment, in the place of hollow profiles. The failure was due to high stresses at the bends of the profiles and the interactions of several LS. The material failed, followed by a loss of stability due to the plastic joint.

The analyses created from FEM modeling can be used for approximate prediction of the critical force, especially for the buckling (and other mechanical properties) of composite profiles with respect to the properties of the fibers and resin used. The obtained results from the microstructure provide information on the quality of the final composite parts, especially porosity, insufficient fiber saturation, and corrugation. The connection between the occurrence of such defects in individual processing technologies makes it possible to set up the production process so that their occurrence is eliminated as much as possible. It is concluded from this article that the production of composite profiles using FDM method is geometrically accurate, production-repeatable, and these profiles are highly resistant to compressive deformations. Proposed investigations in the future include the development of experimental and numerical methods for the fatigue failure of an off-axis printed CFRP composite.

Author Contributions: Conceptualization, M.K. and S.R.; methodology, M.K., D.K. and J.M.; software, M.P. and D.K.; formal analysis, M.K.; investigation, M.K.; data curation, R.T., A.P., J.R. and D.K.; writing—review and editing, M.K., D.K., J.M. and R.T. All authors have read and agreed to the published version of the manuscript.

References

1. Yang, C.; Kim, Y.; Ryu, S.; Gu, G.X. Prediction of composite microstructure stress-strain curves using convolutional neural networks. *Mater. Des.* **2020**, *189*, 108509. [CrossRef]
2. Prabhakar, M.M.; Rajini, N.; Ayrilmis, N.; Mayandi, K.; Siengchin, S.; Senthilkumar, K.; Karthikeyan, S.; Ismail, S.O. An overview of burst, buckling, durability and corrosion analysis of lightweight FRP composite pipes and their applicability. *Compos. Struct.* **2019**, *230*, 114419. [CrossRef]
3. Sreejith, M.; Rajeev, R.S. Fiber reinforced composites for aerospace and sports applications. In *Fiber Reinforced Composites*; Elsevier: Amsterdam, The Netherlands, 2021; pp. 821–859.
4. UK Composites. Medical Application for Cmposite Materials. Available online: https://compositesuk.co.uk/composite-materials/applications/medical (accessed on 5 July 2021).
5. Hebei Maple Fiberglass. FRP Machining. Available online: http://www.frpmachining.com/faqs/frpgrp-pipe-filament-winding-machine (accessed on 3 May 2021).
6. Alnex. Composites. Available online: https://www.allnex.com/en/technologies/composites (accessed on 13 May 2021).
7. Chen, A.Y.; Baehr, S.; Turner, A.; Zhang, Z.; Gu, G.X. Carbon-fiber reinforced polymer composites: A comparison of manufacturing methods on mechanical properties. *Int. J. Lightweight Mater. Manuf.* **2021**, *4*, 468–479.
8. Tian, X.; Liu, T.; Yang, C.; Wang, Q.; Li, D. Interface and performance of 3D printed continuous carbon fiber reinforced PLA composites. *Compos. Part A Appl. Sci. Manuf.* **2016**, *88*, 198–205. [CrossRef]
9. Touchard, F.; Chocinski-Arnault, L.; Fournier, T.; Magro, C.; Lafitte, A.; Caradec, A. Interfacial adhesion quality in 3D printed continuous CF/PA6 composites at filament/matrix and interlaminar scales. *Compos. Part B Eng.* **2021**, *218*, 108891. [CrossRef]
10. Dizon, J.R.C.; Espera, A.H.; Chen, Q.; Advincula, R.C. Mechanical characterization of 3D-printed polymers. *Addit. Manuf.* **2018**, *20*, 44–67. [CrossRef]
11. Popescu, D.; Zapciu, A.; Amza, C.; Baciu, F.; Marinescu, R. FDM process parameters influence over the mechanical properties of polymer specimens: A review. *Polym. Test.* **2018**, *69*, 157–166. [CrossRef]
12. Zhang, H.; Chen, J.; Yang, D. Fibre misalignment and breakage in 3D printing of continuous carbon fibre reinforced thermoplastic composites. *Addit. Manuf.* **2021**, *38*, 101775.
13. Wang, K.; Li, S.; Rao, Y.; Wu, Y.; Peng, Y.; Yao, S.; Zhang, H.; Ahzi, S. Flexure Behaviors of ABS-Based Composites Containing Carbon and Kevlar Fibers by Material Extrusion 3D Printing. *Polymers* **2019**, *11*, 1878. [CrossRef]
14. Guessasma, S.; Belhabib, S.; Nouri, H. Microstructure and Mechanical Performance of 3D Printed Wood-PLA/PHA Using Fused Deposition Modelling: Effect of Printing Temperature. *Polymers* **2019**, *11*, 1778. [CrossRef]
15. Zhang, Z.; Demir, K.G.; Gu, G.X. Developments in 4D-printing: A review on current smart materials, technologies, and applications. *Int. J. Smart Nano Mater.* **2019**, *10*, 205–224. [CrossRef]
16. Badini, C.; Padovano, E.; De Camillis, R.; Lambertini, V.G.; Pietroluongo, M. Preferred orientation of chopped fibers in polymer-based composites processed by selective laser sintering and fused deposition modeling: Effects on mechanical properties. *J. Appl. Polym. Sci.* **2020**, *137*, 49152. [CrossRef]
17. Spoerk, M.; Savandaiah, C.; Arbeiter, F.; Traxler, G.; Cardon, L.; Holzer, C.; Sapkota, J. Anisotropic properties of oriented short carbon fibre filled polypropylene parts fabricated by extrusion-based additive manufacturing. *Compos. Part A Appl. Sci. Manuf.* **2018**, *113*, 95–104. [CrossRef]
18. Prajapati, A.R.; Harshit, K.; Dave, H.K.; Raval, H.K. Effect of fiber reinforcement on the open hole tensile strength of 3D printed composites. *Mater. Today Proc.* **2021**, *46*, 8629–8633. [CrossRef]
19. Dickson, A.N.; Abourayana, H.M.; Dowling, D.P. 3D Printing of Fibre-Reinforced Thermoplastic Composites Using Fused Filament Fabrication—A Review. *Polymers* **2020**, *12*, 2188. [CrossRef]
20. Wang, P.; Zou, B.; Ding, S.; Huang, C.; Shi, Z.; Ma, Y.; Yao, P. Preparation of short CF/GF reinforced PEEK composite filaments and their comprehensive properties evaluation for FDM-3D printing. *Compos. Part B Eng.* **2020**, *198*, 108175. [CrossRef]
21. Kabir, S.M.F.; Mathur, K.; Seyam, A.F.M. A critical review on 3D printed continuous fiber-reinforced composites: History, mechanism, materials and properties. *Compos. Struct.* **2020**, *232*, 111476. [CrossRef]

22. Al Rashid, A.; Ko , M. Creep and Recovery Behavior of Continuous Fiber-Reinforced 3DP Composites. *Polymers* **2021**, *13*, 1644. [CrossRef] [PubMed]

23. Markforged. Available online: https://markforged.com/3d-printers/x7 (accessed on 13 May 2021).

24. Justo, J.; Távara, L.; Garzía-Guzmán, L.; París, F. Characterization of 3D printed long fibre reinforced composites. *Compos. Struct.* **2018**, *185*, 537–548. [CrossRef]

25. Korkees, F.; Allenby, J.; Dorrington, P. 3D printing of composites: Design parameters and flexural performance. *Rapid Prototyp. J.* **2020**, *26*, 699–706. [CrossRef]

26. Mohammadizadeh, M.; Imeri, A.; Fidan, I.; Elkelany, M. 3D printed fiber reinforced polymer composites—Structural analysis. *Compos. Part B Eng.* **2019**, *175*, 107112. [CrossRef]

27. Pertuz, A.D.; Díaz-Cardona, S.; González-Estrada, O.A. Static and fatigue behaviour of continuous fibre reinforced thermoplastic composites manufactured by fused deposition modelling technique. *Int. J. Fatigue* **2020**, *130*, 105275. [CrossRef]

28. Yasa, E.; Ersoy, K. Dimensional Accuracy and Mechanical Properties of Chopped Carbon Reinforced Polymers Produced by Material Extrusion Additive Manufacturing. *Materials* **2019**, *12*, 3885. [CrossRef] [PubMed]

29. Wickramasinghe, S.; Do, T.; Tran, P. FDM-Based 3D Printing of Polymer and Associated Composite: A Review on Mechanical Properties, Defects and Treatments. *Polymers* **2020**, *12*, 1529. [CrossRef] [PubMed]

30. Pyl, L.; Kalteremidou, K.A.; Hemelrijck, D.V. Exploration of the design freedom of 3D printed continuous fibre-reinforced polymers in open-hole tensile strength tests. *Compos. Sci. Technol.* **2019**, *171*, 135–151. [CrossRef]

31. Sanei, S.H.R.; Arndt, A.; Doles, R. Open hole tensile testing of 3D printedcontinuous carbon fiber reinforced composites. *J. Compos. Mater.* **2020**, *54*, 2687–2695. [CrossRef]

32. Prajapati, A.R.; Dave, H.K.; Raval, H.K. Influence of fiber rings on impact strengthof 3d printed fiber reinforced polymer composite. *Manuf. Technol.* **2020**, *12*, 157–163.

33. Ekoi, E.J.; Dickson, A.N.; Dowling, D.P. Dowling. Investigating the fatigue and mechanical behaviour of 3D printed woven and nonwoven continuous carbon fibre reinforced polymer (CFRP) composites. *Compos. Part B Eng.* **2021**, *212*, 108704. [CrossRef]

34. Saghir, F.; Gohari, S.; Mozafari, F.; Moslemi, N.; Burvill, C.; Smith, A.; Lucas, S. Mechanical characterization of particulated FRP composite pipes: A comprehensive experimental study. *Polym. Test.* **2021**, *93*, 107001. [CrossRef]

35. Saharudin, M.S.; Hajnys, J.; Kozior, T.; Gogolewski, D.; Zmarzły, P. Quality of Surface Texture and Mechanical Properties of PLA and PA-Based Material Reinforced with Carbon Fibers Manufactured by FDM and CFF 3D Printing Technologies. *Polymers* **2021**, *13*, 1671. [CrossRef]

36. Zhuo, P.; Li, S.; Ashcroft, I.A.; Jones, A.I. Material extrusion additive manufacturing of continuous fibre reinforced polymer matrix composites: A review and outlook. *Compos. Part B Eng.* **2021**, *224*, 109143. [CrossRef]

37. Van de Werken, N.; Tekinalp, H.; Khanbolouki, P.; Ozcan, S.; Williams, A.; Tehrani, M. Additively manufactured carbon fiber-reinforced composites: State of the art and perspective. *Addit. Manuf.* **2020**, *31*, 100962. [CrossRef]

38. Naveen, J.; Mohammad Jawaid, M.; Vasanthanathan, A.; Chandrasekar, M. Finite element analysis of natural fiber-reinforced polymer composites. In *Modelling of Damage Processes in Biocomposites, Fibre-Reinforced Composites and Hybrid Composites*; Elsevier: Amsterdam, The Netherlands, 2019; pp. 153–170.

39. Gao, J.; Yang, X.; Huang, L.; Suo, Y. Experimental study on mechanical properties of aramid fibres reinforced natural rubber/SBR composite for large deformation—Quasi-Static mechanical properties. *Plast. Rubber Compos.* **2018**, *47*, 381–390. [CrossRef]

40. Gohari, S.; Sharifi, S.; Burvill, C.; Mouloodi, S.; Izadifar, M.; Thissen, P. Localized failure analysis of internally pressurized laminated ellipsoidal woven GFRP composite domes: Analytical, numerical, and experimental studies. *Arch. Civ. Mech. Eng.* **2019**, *19*, 1235–1250. [CrossRef]

41. Potluri, R.; Diwakar, V.; Venkatesh, K.; Reddy, S.B. Analytical Model Application for Prediction of Mechanical Properties of Natural Fiber Reinforced Composites. *Mater. Today Proc.* **2018**, *5*, 5809–5818. [CrossRef]

42. Elmarakbi, A.; Azoti, W.; Serry, M. Multiscale modelling of hybrid glass fibres reinforced graphene platelets polyamide PA6 matrix composites for crashworthiness applications. *Appl. Mater. Today* **2017**, *6*, 1–8. [CrossRef]

43. Markforged. Available online: https://markforged.com/ (accessed on 1 April 2021).

44. Markforged. Available online: https://support.markforged.com/portal/s/article/Onyx/ (accessed on 6 July 2021).

45. ZwickRoell. Available online: https://www.zwickroell.com/ (accessed on 5 July 2021).

46. Callister, W.D.; Rethwish, D.G. *Materials Science and Engineering: An Introduction*, 8th ed.; Wiley: Hoboken, NJ, USA, 2010; ISBN 978-0-470-41997-7.

47. Ehrenstein, G.W. *Polymerni Kompozitni Materialy*, 1st ed.; Scientia: Prague, Czech Republic, 2009; pp. 133–194.

48. Partskhaladze, G.; Mshvenieradze, I.; Medzmariashvili, E.; Chavleshvili, G.; Yepes, V.; Alcala, J. Buckling Analysis and Stability of Compressed Low-Carbon Steel Rods in the Elastoplastic Region of Materials. *Adv. Civ. Eng.* **2019**, *2019*, 7601260. [CrossRef]

49. Strong, A.B. *Fundamentals of Composites Manufacturing*, 2nd ed.; Society of Manufacturing Engineers: Southfield, MI, USA, 2008; pp. 463–485.

50. Sanei, S.H.R.; Popescu, D. 3D-Printed Carbon Fiber Reinforced Polymer Composites: A Systematic Review. *J. Compos. Sci.* **2020**, *4*, 98. [CrossRef]

51. Fedotov, A.F. Hybrid model of homogenization of engineering elastic moduli of composites reinforced with ellipsoid particles. *Compos. Part B Eng.* **2020**, *182*, 107585. [CrossRef]

52. Clyne, T.W.; Hull, D. *An Introduction to Composite Materials*, 3rd ed.; Cambridge University Press: New York, NY, USA, 2019.
53. Adeniyi, A.G.; Adeoye, S.A.; Onifade, D.V.; Ighalo, J.O. Multi-scale finite element analysis of effective elastic property of sisal fiber-reinforced polystyrene composites. *Mech. Adv. Mater. Struct.* **2021**, *28*, 1245–1253. [CrossRef]

Polyaniline: Doping and Functionalization with Single Walled Carbon Nanotubes for Photovoltaic and Photocatalytic Application

Mariem Saoudi [1], Boubaker Zaidi [2,3,*], Abdullah A. Alotaibi [4], M.G. Althobaiti [5], Eid M. Alosime [6] and Ridha Ajjel [1]

1. Laboratory of Energies and Materials (LabEM), Higher School of Sciences and Technology of Hammam Sousse, Sousse University, Sousse 4011, Tunisia; mariem_saoudi@yahoo.fr (M.S.); ajjelridha@gmail.com (R.A.)
2. Laboratoire Physico-Chimie des Matériaux, Département de Physique, Faculté des Sciences de Monastir, Université de Monastir, Monastir 5000, Tunisia
3. Department of Physics, Faculty of Science, Shaqra University, Dawadmi 11911, Saudi Arabia
4. Department of Chemistry, Faculty of Science, Shaqra University, Dawadmi 11911, Saudi Arabia; aaalotaibi@su.edu.sa
5. Department of Physics, Faculty of Science, Taif University, Taif 888, Saudi Arabia; m.althobaiti@tu.edu.sa
6. King Abdulaziz City for Science and Technology (KACST), P.O. Box 6086, Riyadh 11442, Saudi Arabia; alosimi@kacst.edu.sa
* Correspondence: boubaker_zaidi@yahoo.fr

Abstract: Polyaniline (PANI) was chemically doped and functionalized with single walled carbon nanotubes (SWCNTs). Various characterization methods were employed to study the structure and optical properties of PANI/SWCNTs nanocomposite, such as Fourier transform infrared (FTIR), differential scanning calorimetry (DSC), scanning electron microscopy (SEM), optical absorption, and stationary photoluminescence. Additionally, a theoretical study using density functional theory calculations was also carried out. It has been demonstrated that the doping process may reduce the band gap without affecting the molecular structure, leading to a better compatibility with the solar spectrum. Moreover, the functionalization process with SWCNTs was able to significantly improve the properties of the resulting nanocomposite. The final interpenetrating network of PANI/SWCNTs exhibited an optical gap of nearly 2.28 eV, from which localized states induced by the charge transfer were created at nearly 1.70 eV. In addition, the resulting donor–acceptor network leads to a separation of electron holes pairs rather than their recombination, which can be used as an active layer in photovoltaic applications and a photocatalyst for advanced oxidation processes.

Keywords: doping; carbon nanotubes; functionalization; optical characterization; DFT; solar cells

1. Introduction

A significant number of works have been focused on exploiting the properties of nanoparticles [1]. New nano-structured materials with improved properties can be elaborated by inserting nanoparticles into the organic matrix [2,3]. Since the 1990s, considerable efforts have been devoted for carbon nanotubes (CNTs), due to their form factor and their unique and reproducible properties. The electronics industry is currently developed around organic materials [4–6] in an attempt to replace silicon technology with lower cost and easier processing. Polymer materials are widely studied as active layers for electronic devices where the majority of handicaps are related to their fragility and their limited operation lifetime. The addition of the small quantities of CNTs permits not only the improvement of their mechanical properties [7], but also offers a higher operating life time [8]. Particularly, the good dispersion of CNTs in the polymer matrix leads to charge transfer and good transport properties due to their high electron and hole mobilities [9]. Physically, charge transfer is created by nano-junctions imposed by interpenetration of the donor and acceptor domains [10]. In addition, the resulting interpenetrating network may improve the electron–hole pairs after photo-excitation, leading to a good collection

process. The obtained bulk hetero-nano-junctions lead to high photovoltaic conversion efficiency [11,12]. Among the conducting polymers, PANI is the most studied due to its physical and chemical properties that can be easily modified [13,14]. Particularly, PANI exhibits better environmental stability and easy synthesis [15,16]. In this context, a simple treatment of PANI results in a new degree of oxidation where its conductivity can be reversibly switched from the insulating to the conductive state [17]. Recently, it has been demonstrated that PANI/SWCNTs composites gave enhanced field emission characteristics due to π–π interaction between the quinoid rings of PANI and the π bond of the SWCNTs lattice [18]. Moreover, the nanocomposite exhibits significant enhancement in both electrical and thermoelectric properties [19]. On the other hand, the modified PANI/SWCNTs nanocomposite was used for the electrochemical determination of some metals with good selectivity and sensitivity [20]. As the leucomeraldine base form is generally an insulator, it will be useful to carry out a doping process before its functionalization with the CNTs [21]. The procedure of acid doping [22,23] is the easiest method and leads to switching between its oxidized forms.

In order to establish a good structure property correlation, experimental conclusions are often supported by theoretical methods [24,25]. Quantum calculations based on functional density theory (DFT) are the most appropriate tools to describe organic materials' properties [26,27]. Using these calculations, we can predict properties of materials and their corresponding application field [27,28]. Due to the development of computational processors, it is currently possible to carry out calculations using higher degrees of freedom with a higher basis set of computation [26,27].

In this paper, we are primarily interested in establishing a structure–property correlation by means of experimental and theoretical characterization techniques of both doped and pure PANI states. We also investigate and describe the functionalization of PANI with SWCNTs, particularly the nature of the resulting nano-junctions at the molecular scale. Fourier transform infrared (FTIR), differential scanning calorimetry (DSC) and scanning electron microscopy (SEM) techniques are used to evidence changes in vibrational and structural properties. However, changes in the optical properties are evaluated by means of optical absorption and photoluminescence spectroscopies. The obtained results are correlated with those obtained theoretically using the DFT.

2. Materials and Methods

PANI and SWCNTs were produced by Sigma Aldrich (St. Quentin Fallavier, Cedex France). At 300 K, the black colored PANI powder was characterized by a purity of 99.99%, an average macromolecular mass Mn > 15,000, a refractive index of 1.85, a melting temperature above 600 K, and a density of 1.36 g/mL. SWCNTs were obtained by the electric arc technique where the diameter of the individual tube varied from 1.0 to 1.2 nm, while they exhibited a typical length of 500 nm [26,29]. The PANI doping process was similar to the classical method reported by A. G. MacDiarmid et al. [23]. The process was accomplished in a solution where the PANI was placed for two hours in a mixture of 20% sulfonic acid (R-SO$_3$H) and 80% dimethyl formamide (DMF). After evaporation of the solvent and drying, the obtained product was washed three times with DMF to remove residual acid particles. The functionalization process of SWCNTs with PANI is a purely mechanical method [30]. SWCNTs' are dispersed in the appropriate solvent (DMF) in order to isolate bundled tubes, using the velocity of 8000 rpm for three hours. The obtained composite is then introduced into an ultrasonic bath and submitted to centrifugal forces for 30 min in order to homogenize SWCNTs' distribution and orientation in the PANI matrix [31–33]. The viscous obtained solutions were deposited with nearly uniform thickness on glass slides for FTIR and photoluminescence measurements and on silica slides for optical absorption measurements. All substrates were already cleaned with deionized water and ethanol in an ultrasonic bath. FTIR measurements were conducted using a Bruker Vertex 80 V interferometer (Bruker Optics, Ettlingen, Germany) with a resolution of 4 cm^{-1}. The DSC measurements were recorded on a Perkin Elmer DSC

8500 analyzer (Perkin Elmer, Inc. Shelton, CT, USA). All samples in the powder state had nearly the same weight of 2.6 mg. During measurements, the temperature was scanned from 323 K to 600 K, at the heating rate of 10 K/min, under nitrogen atmosphere, for which the Gas Switch to nitrogen was 20 mL/min. The optical absorption spectra were recorded using a UV1800 spectrophotometer (Shimadzu Scientific istruments, Inc. Colombia, MD, USA) working in the absorption mode with the wavelength varying from 200 nm (6.2 eV) to 2000 nm (0.62 eV). The SEM micrographs were carried out using the JEOL 7600 F microscope (JOEL, Inc, Peabody, MA, USA) which was equipped with a source delivering field effect, operating with the voltage of 10 KV, making it possible to obtain electron beams of a very large smoothness, reaching a space resolution of a few tens of nanometers. For photoluminescence (University of Monastir, Tunisia), in order to cover the entire emission spectrum, two excitation wavelengths were used (325 nm and 540 nm). Theoretical data were obtained from quantum calculations based on density functional theory (DFT), the most appropriate tool to describe the organic materials' properties [27,34]. The modeling structure has been fully optimized using the most popular three-parameter hybrid function, Becke's B3 [35], with the basis set 6-31-G (d). Calculations applied to the modeling structure were conducted with the non-local correlation of Lee–Yang–Parr, LYP, abbreviated as the B3LYP method [36], without constraint, which was often used in in our previous calculations [37]. Optical absorption spectra were calculated using the time-dependent density functional theory (TD-DFT) method with the 6-31G (d) basis set and were fitted into Gaussian curves within the Swizard program [27,37].

3. Results and Discussion

Figure 1 shows the infrared absorption spectra of the PANI in both the pure and acid-doped states. Band positions and their assignments are summarized in Table 1 [30,38].
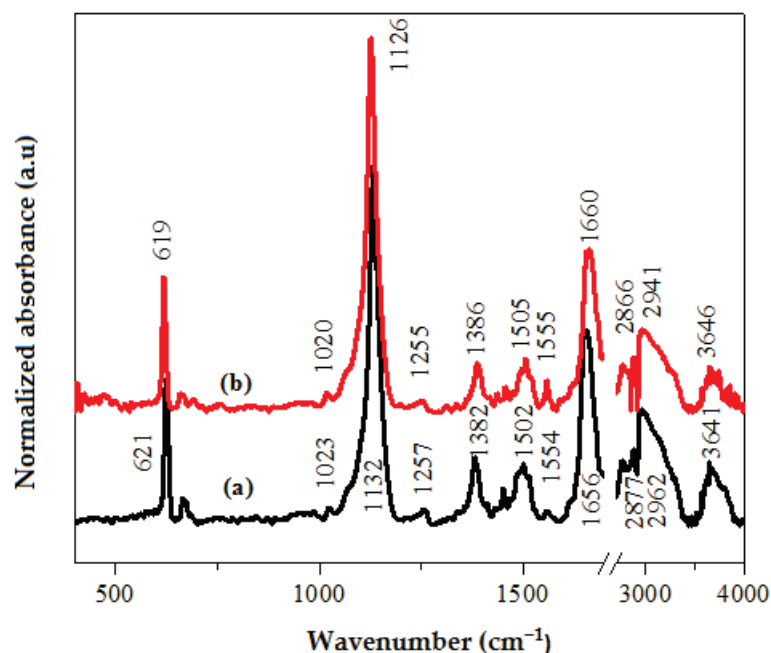
Figure 1. FTIR spectrum of pure (**a**) and acid-doped (**b**) PANI.

The spectra of Figure 1 have been normalized by referring to the band situated at 1132 (1126) cm^{-1}, attributed to the benzene ring deformation. Spectra show that the same bands are found after doping but the band intensity and positions are changed (Table 1), demonstrating that the material skeleton is conserved. The intensity increase/decrease and the slight frequency shift are the consequences of the geometrical relaxation after doping. Particularly, the band at 1554 cm^{-1}, attributed to the C=C vibration of the quinoid form, has been greatly intensified. At the same time, the band at 1656 cm^{-1}, attributed to the

same group but relative to the aromatic form, is decreased. This demonstrates that the undoped leucomeraldine form is partially transformed into its oxidized form, inducing the appearance of a local charge (Scheme 1). This local charge formation is the consequence of hydrogen departure, leading to a new oxidation degree [23].

Table 1. FTIR vibrational modes of PANI in both pure and doped states.

Frequency (cm^{-1})		Intensity Ratio (I_{doped}/I_{pure})	Assignment
Neutralpure	Doped		
621	619	0.98	Torsion C-N outside the plane
1023	1020	1.02	C-H deformation
1132	1126	1.00	Benzene ring vibration
1257	1255	0.65	C-N of the benzene ring vibration
1382	1386	0.70	CH in the plane switching
1502	1505	1.09	Ring deformation
1554	1555	3.76	Quinoid aromatic C=C vibration
1656	1660	0.78	Benzene aromatic C=C vibration
2877	2866	0.81	Symmetric C-H stretching
2962	2941	0.91	N-H deformation
3643	3646	0.83	N-H stretching
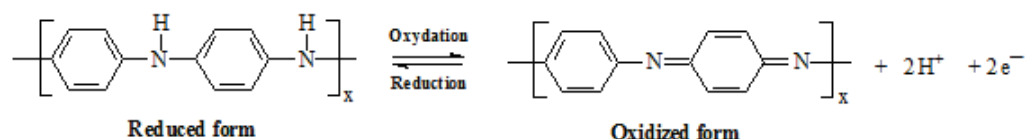
Scheme 1. Mechanism of acid doping of the leucomeraldine base form: transformation to the oxidized form (EB).

Figure 2 shows SEM pictures of PANI in both the pure and doped states. It is clearly seen that the structure of undoped PANI is constituted by agglomerations with sizes of a few tens of microns (20 to 30 microns). These agglomerations are composed of granular features with 1–2 µm diameters, comparable to those commonly found in the literature [39–41]. We also note that after doping, the PANI structure still remains granular where the grain size has been decreased (ranging from 0.5 to 1 µm). We believe that the doping species, which is a strong acid, leads to the increase in the solubility of PANI and, consequently, the decrease in grain size.

Figure 3 shows the changes in the optical absorption spectrum after the PANI sulfonic acid doping. It should be noted that the absorption spectrum of pure PANI exhibits four absorption bands situated at 207 nm, 219 nm, 252 nm and 286 nm. According to the literature [42], these bands are, respectively, attributed to σ–σ*, σ–π *, π–σ* and π–π* transitions. After acid doping, the absorption spectrum is strongly affected. Principally, we show the creation of a new absorption band at 387 nm, supporting the optical gap reduction. This broad band is the consequence of the transformation of PANI from leucomeraldine form to the emeraldine salt/base forms [43], which agrees well with FTIR results. Therefore, the newly created optical transition is the consequence of a new energetic level in the PANI band gap [44]. A similar effect has been already observed for HCl-doped PANI [45].
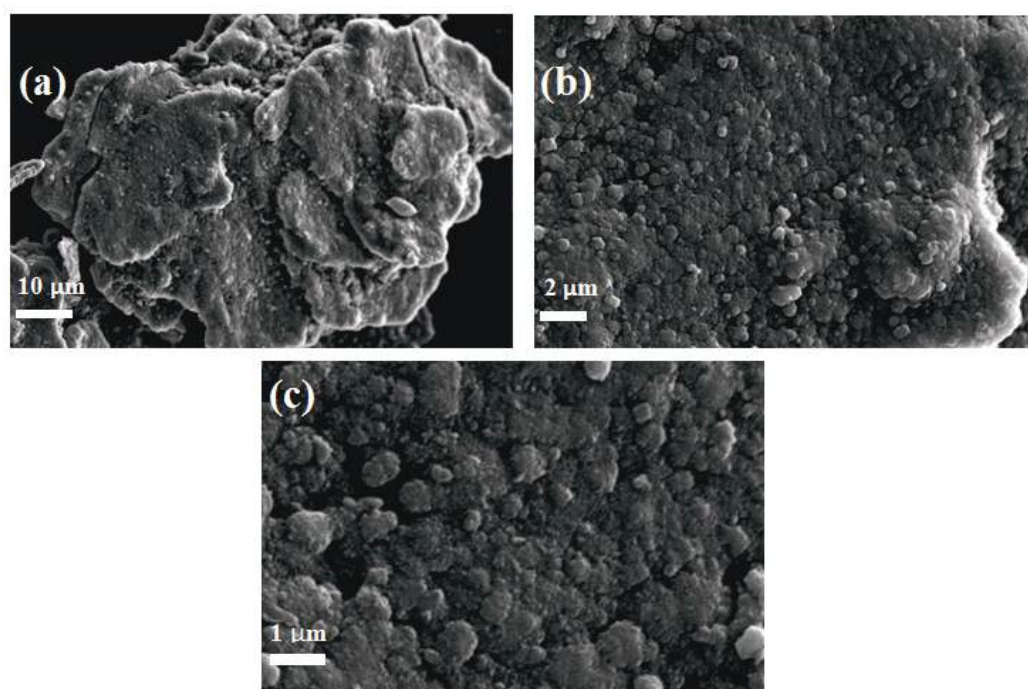
Figure 2. SEM images of (**a**,**b**) PANI and (**c**) sulfonic acid-doped PANI.
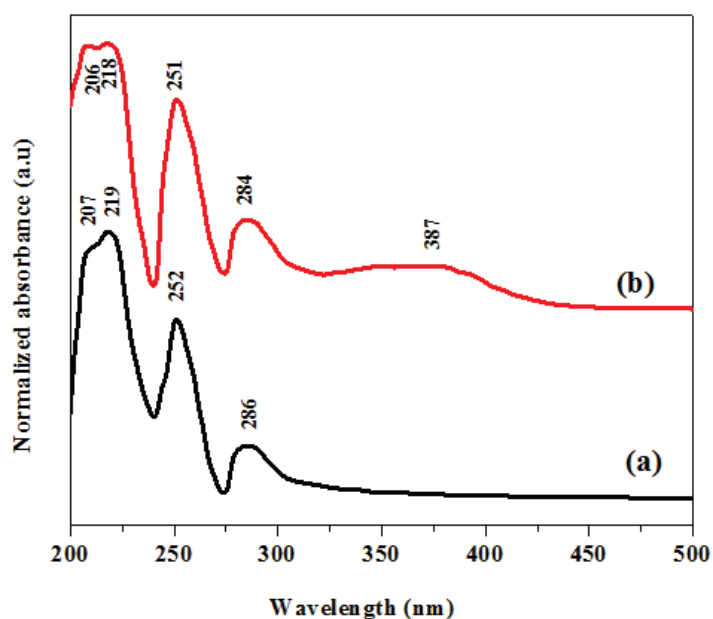
Figure 3. Optical absorption spectra of PANI in the pure (**a**) and doped (**b**) states.

Photoluminescence spectra of Figure 4 show that the PANI emits in the spectral range from 340 nm to 480 nm, similar to the previously reported results [46]. The decomposition of PL spectrum shows three lines separated by the same amount of energy (in the order of 215 meV). As this energy corresponds approximately to the most intense band observed on the FTIR spectrum, at approximately 1660 cm^{-1} [47], we believe that these lines are derived from 0–0, 0–1 and 0–2 phonon emission. The acid doping is accompanied by a PL quenching effect, indicating that quinoidal fragments are created, representing inter-channel energy dissipation [48]. On the other hand, the spectrum has been red shifted by nearly 14 nm, showing that there is a sufficient decrease in the optical gap.
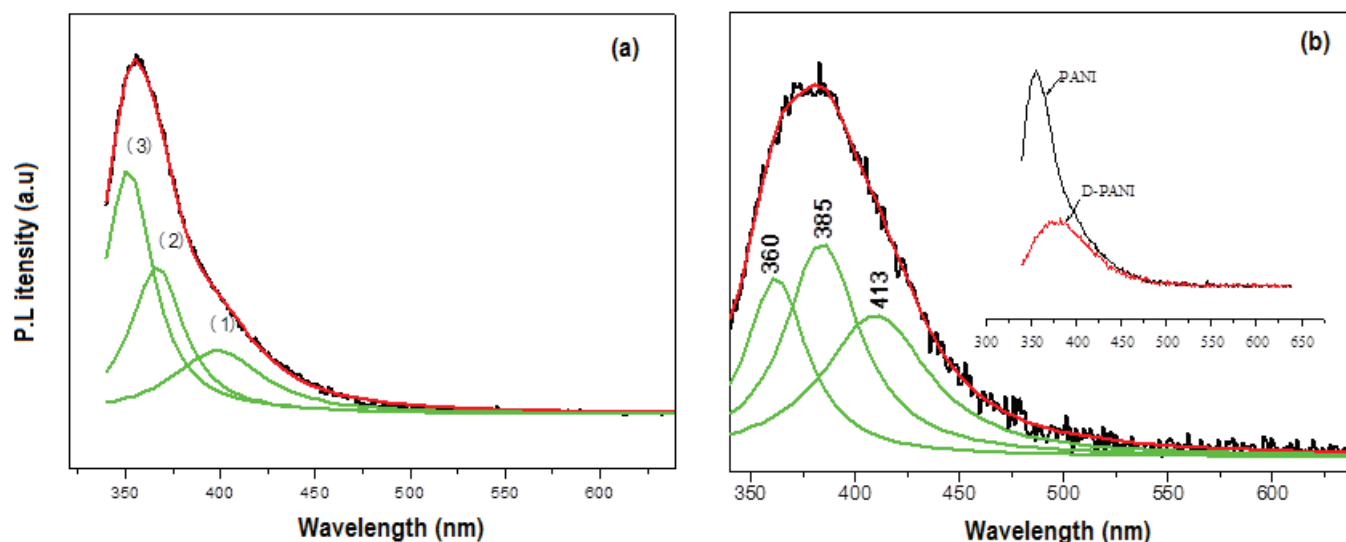
Figure 4. Photoluminescence spectra of pure (**a**) and sulfonic acid-doped (**b**) PANI. Black line: experimental; red line: Gaussian fit; green line: Gaussian components. The inset shows the PL intensity decrease from pure to doped PANI.

As it is often generalized, the optical gap can be elucidated from the variation of the absorption coefficient as a function of energy, according to the Tauc equation of [49], as shown in Equation (1) below:

$$\alpha h\nu = B(h\nu - Eg)^n \qquad (1)$$

In this expression, α represents the absorption coefficient, B is a band tail parameter, Eg is the band gap of the material and n is an index representing the transition probability, taken equal to 2 for indirect transitions in amorphous materials [45,50]. The variation of $(\alpha h\nu)^{1/n}$ as a function of $h\nu$ (Figure 5) makes it possible to give the value of the gap, which is estimated by extrapolation of the linear part occurring in the absorption threshold [45,51]. The band gap relative to the pure PANI evaluated to 3.75 eV decreases, reaching 2.63 eV after doping. These values are comparable to those previously published for both the pure and doped PANI forms [45]. In fact, for low photon energy, the spectral dependence of the absorption coefficient (α) as a function of energy ($h\nu$) is known as Urbach's empirical law, in accordance with Equation (2) [52]:

$$\alpha = \alpha_0 \exp(\frac{h\nu}{E_U}) \qquad (2)$$
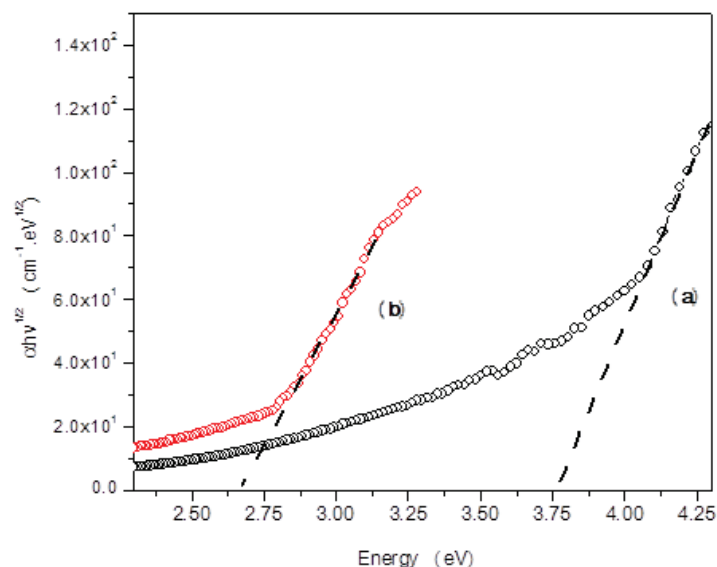
Figure 5. Variation of $(\alpha h\nu)^{1/2}$ versus $h\nu$ for pure (**a**) and sulfonic acid-doped (**b**) PANI.

In this expression, α_0 is a constant and E_U is the band-tail energy that is commonly referred to as Urbach energy [52]. Generally, this energy is weakly temperature dependent and is often interpreted as the width of localized states, created within the optical gap. These states are associated with disorder for amorphous and low crystalline materials [52,53]. Therefore, the variation of Ln (α) as a function of the photon energy presents linearity behavior in the concerned spectral range. In this case, the Urbach energy e (E_U) can be obtained from the slope shown in Figure 6.

$$Ln\ (\alpha) = Ln\ (\alpha_0) + \frac{h\nu}{E_U} \tag{3}$$
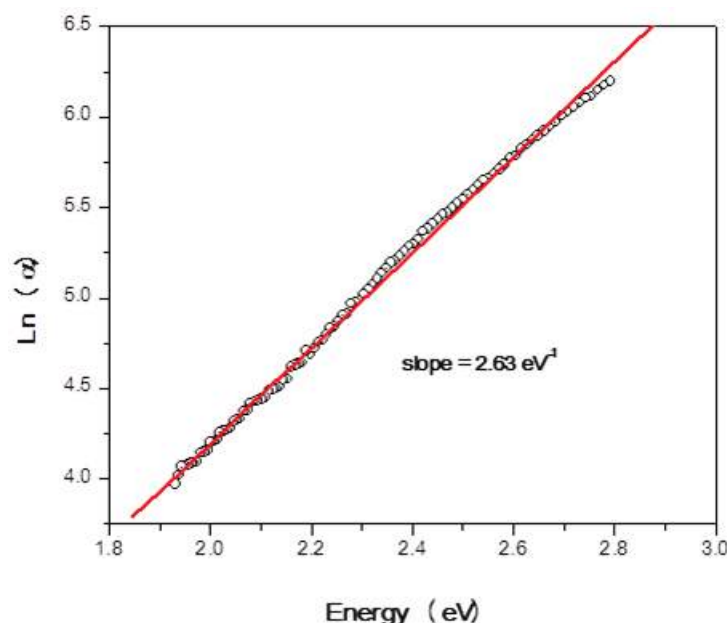
Figure 6. Variation of Ln (α) as a function of the photon energy in the case of doped PANI. (o) Experimental, (—) linear fit.

From Figure 6, we estimate the E_U in the order of 380 meV involved by the broad absorption band created within the PANI band gap. According to the literature, if the doping rate is high, the doped materials exhibit a continuum of individual levels [54]. Their recovery leads to a large band, as is observed in our case. This result agrees well with prior studies for which the doping procedure was carried out at saturation (higher doping level) [55].

To evidence changes on the molecular structure after SWCNTs' functionalization process, the obtained composite was studied by FTIR spectroscopy. In Figure 7, we represent the FTIR spectrum of the 2.10% SWCNTs weight concentration nano-composite with those of the PANI in both the pure and doped states.

The decision to use this relatively lower weight concentration for SWCNTs was principally made with the aim of reaching a good dispersion process. Compared to the doped PANI, the spectrum shows the creation of new intense absorption bands at 1256, 1412 and 1438 cm^{-1}. These new bands clearly represent the interaction between both components of the composite. The functionalization process is governed by a grafting reaction between PANI and carbon nanotubes. In this context, the new vibrational frequencies reflect vibration modes of SWCNTs and/or those relative to the linking between both constituents of the composite in the new chemical environment [10,56]. The modes of some frequencies, such as 664 cm^{-1} and 1126 cm^{-1}, are shifted. This shift reflects new molecular arrangement due to the insertion of SWCNTs on the organic matrix. Similar effects were observed for other CNT-based composites [57].
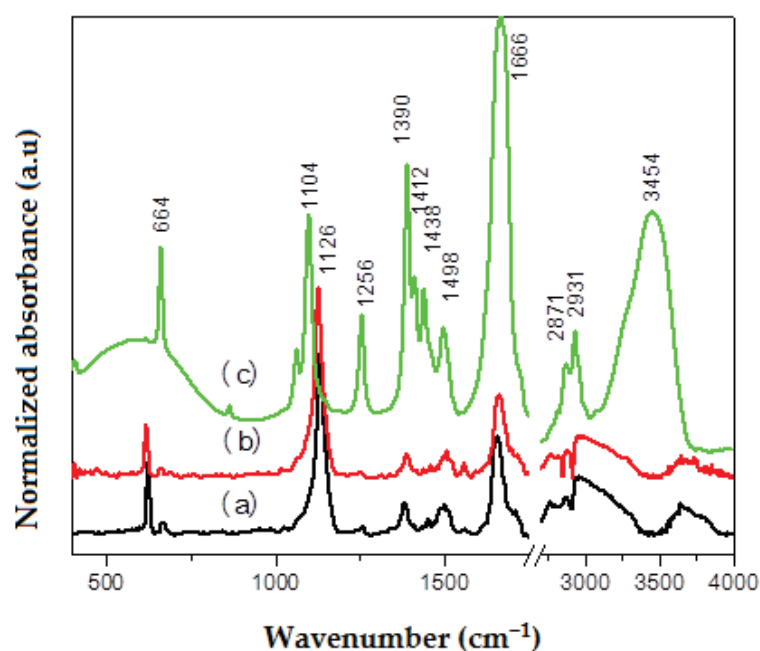
Figure 7. FTIR spectra of PANI (**a**), doped PANI (**b**) and Doped PANI/SWCNTs (**c**).

To provide additional information on the functionalization process between D-PANI and SWCNTs, we present, in Figure 8, DSC thermograms of either doped PANI, SWCNTs or the resulting nano-composite.
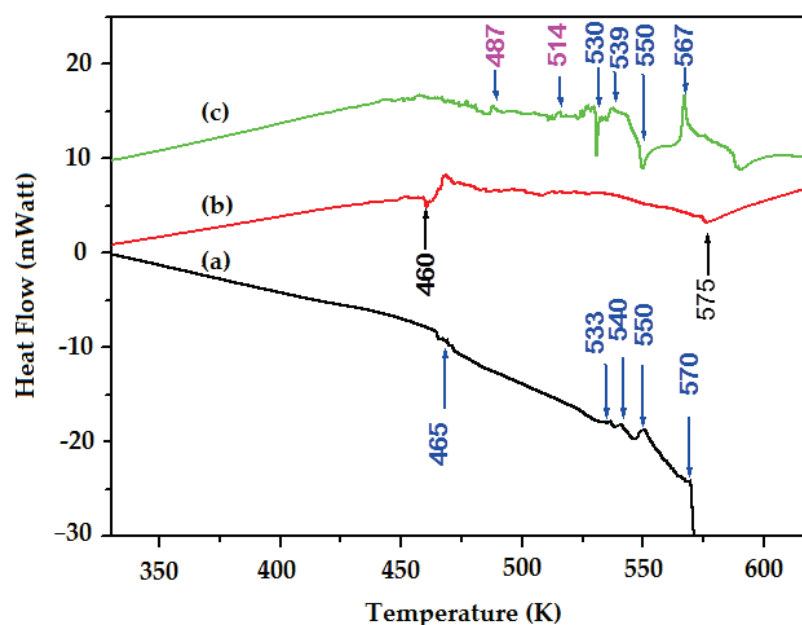
Figure 8. DSC thermograms of D-PANI (**a**), of SWCNTs (**b**) and of D-PANI/SWCNTs composite (**c**).

Compared to the PANI with thermal stability for temperatures lower than 465 K, the nano-composite results in much higher thermal stability, as is reported for other PANI-based nano-composites [58]. As a result, if there is no interaction between both components, the final structure will be a mixture of non-interacting compounds and the corresponding DSC thermogram will certainly be the superposition of individual thermograms. This hypothesis is not the case of Figure 8c, since the nano-composite exhibits additional thermal transitions in comparison to the D-PANI. These additional thermal transitions peaked at 487 K and 514 K, and are also not found in the case of SWCNTs. We think, therefore, that

these latter transitions are the consequence of new structural modifications, mainly the de-grafting process between both components. For SWCNTs, the first thermal stage is observed in the temperature range of 460–470 K, for which there are two apparent thermal transitions. We think that these transitions are a consequence of the tube defect departure; they are not envisaged in the case of the nano-composite, proving that these defects are removed under the functionalization process. The browed peak starting from 575 K has been attributed to the wall degradation, typically the breaking of the SWCNTs' C-C bond. For the PANI, added to the melting point at temperatures higher than 570 K, the DSC thermogram shows four principal thermal transitions centered, respectively, at 465 K, at 533 K, at 540 K and at 550 K. According to the previously published results [59], the first and the fourth ones are, respectively, related to the defect in D-PANI (residual doping agents) and the beginning of PANI degradation. However, both narrow intermediate peaks are, in our opinion, attributed to the ring opening and chain scission resulting from the already cross-linked chains under temperature elevation, as suggested in the case of PANI polymers [60,61]. The same behavior has been also evidenced in our previous work for annealed PANI/SWCNTs composite [62].

The inserting of SWCNTs on the PANI matrix generally results in the creation of a charge transfer [63]. If there is compatibility between the junction size and the diffusion length, the created photo-excitation in the polymer matrix can reach the carbon nanotubes after the diffusion process [64,65]. In this context, the changes of optical absorption spectra after the insertion of the SWCNTs in the doped PANI are already published in our previous work [29]. The spectrum shows that the SWCNTs' functionalization process is accompanied by a broadening effect of the already created band caused by doping, and a new absorption band appears at around 572 nm. The observed feature at lower energy is due to the creation of localized states [45]. To elucidate the quantitative aspect of these effects, we present, in Figure 9, the optical gap variation and localized states' characteristics using, respectively, Tauc and Urbach relations [49,52] (Equations (1) and (2)).
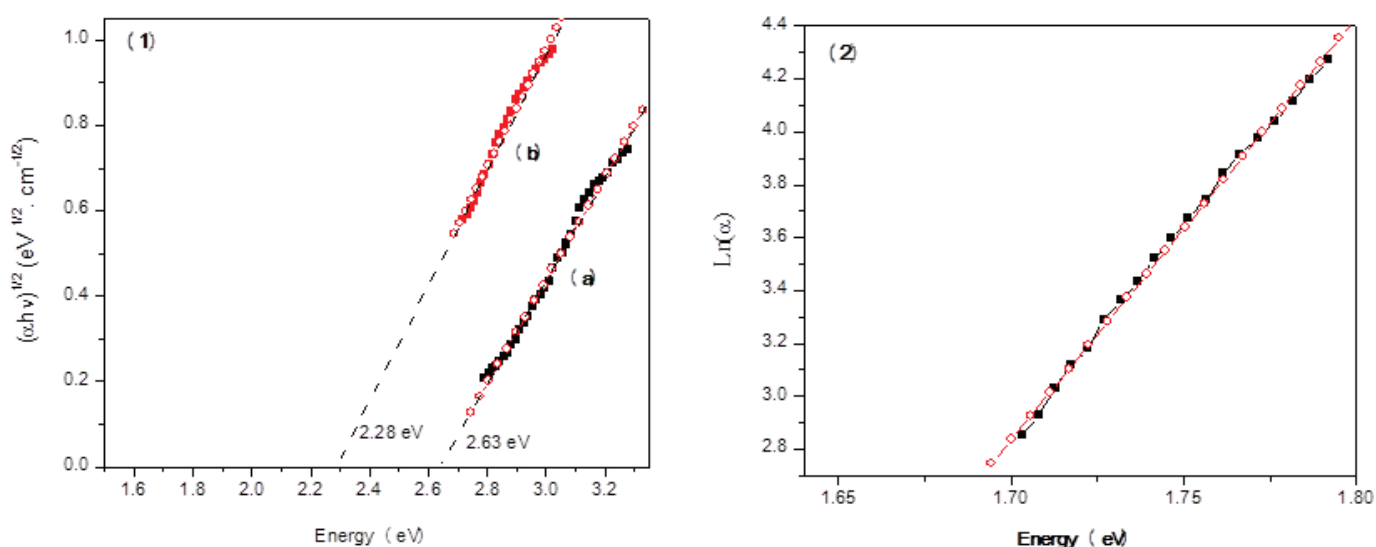
Figure 9. (**1**): Variation of the optical gap (a) sulfonic acid-doped PANI and doped PANI functionalized with SWCNTs (**2**): Evaluation of the localized states' parameters (■): experimental. (o): linear fit.

The optical gap after doped PANI is reduced to 2.63 eV, showing energy levels creation within the band gap. These levels are associated with polaronic and/or bipolaronic species [42]. However, after adding SWCNTs, the latter is more decreased, reaching the value of 2.28 eV. Moreover, new localized states are also created at 1.62 eV, with an Urbach energy (E_U) of 80 meV. These states often originate from the charge transfer between PANI and SWCNTs.

The effect of the addition of SWCNTs is also evidenced by photoluminescence spectrum variation (Figure 10). The spectra show that, independently of the PANI state, (pure, doped or functionalized with SWCNTs), there is emission in the spectral domain ranging from 350 to 500 nm. Then, it is clearly seen that the insertion of SWCNTs on the doped PANI leads to quenching effects. This effect is often envisaged for CNT-based polymer composites and also in the case of the acid doping process [66,67]. Otherwise, the spectrum shows a slight shift towards the red region and a new narrow feature at approximately 550 nm. This weak luminescent center corresponds to the already created localized state due to the charge transfer. The weak intensity of this peak implies that a separation process has occurred rather than a recombination process for these transferred charges. As the PANI/SWCNTs composite absorbance exhibits a good compatibility with the solar spectrum, it can serve as an active layer for organic photovoltaic solar cells and a photocatalyst for advanced oxidation processes under solar irradiation.
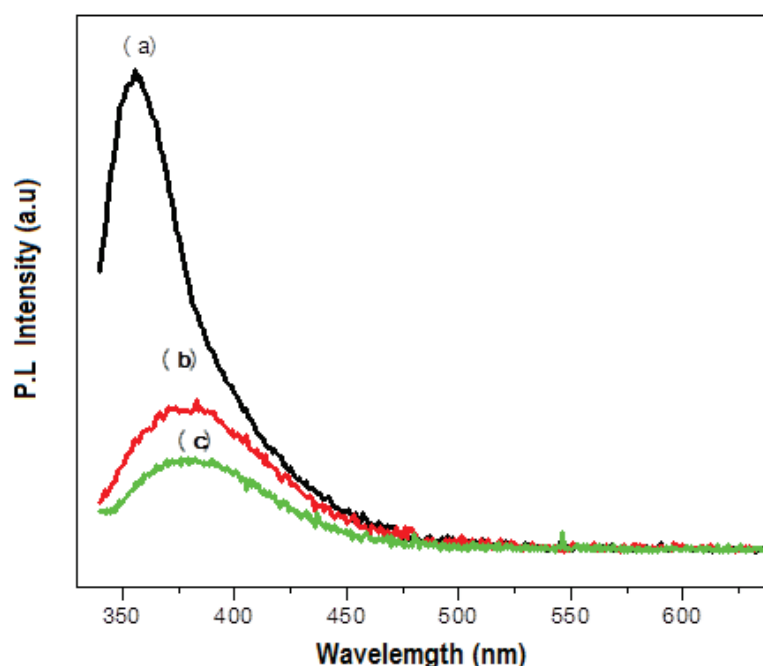
Figure 10. Photoluminescence spectra of (**a**) PANI, (**b**) doped PANI and doped-PANI/SWCNTs composite at 2.1% concentration (**c**).

To theoretically support the modifications that occur after doping and the insertion of SWCNTs, we use the already proposed modeling structures (Scheme 2) [29]. In fact, for the PANI, justifications are based on DFT calculations of the HOMO-LUMO energy difference in both the pure and doped states as a function of the chain length (n: monomer number). The properties of the polymer with infinite chain length are obtained by extrapolation ($1/n \rightarrow 0$) [68]. Principally, it has been found that these energetic levels at the infinite length take the values of 3.62 eV and 2.29 eV, which are close to the experimental results.

The modeling structure of the nano-composite is, however, evidenced via the selection of PANI reactive sites based on atomic charge modification, spin density variation and theoretical infrared spectra. The results demonstrate that reactive sites for the grafting of SWCNTs are located around nitrogen atoms. A similar result has already been found in a systematic SERS and FTIR experimental study, but, in that case, the study was conducted with pure PANI [69]. It is important to note that fragments resulting from non-covalent bonding may also be present on the final structure. The preponderance of non-covalent or covalent interacting fragments is strictly dependent on the strength of the SWCNTs' cohesive Van der Waals force, which inhibits the homogeneous dispersion of carbon nanotubes [70,71].

(a)

(b)
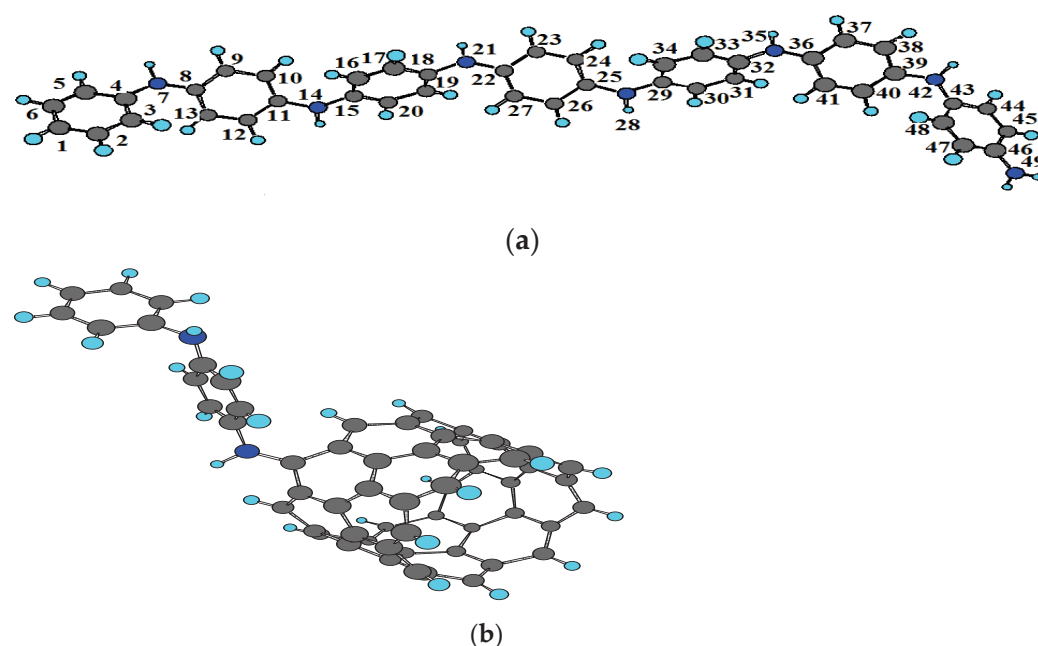
Scheme 2. Modeling structure of PANI (**a**), and of the D-PAN/SWCNT composite (**b**).

The above-presented modeling structures are used to calculate the optical absorption spectra of both PANI to PANI/SWCNTs composite, as presented in Figure 11.
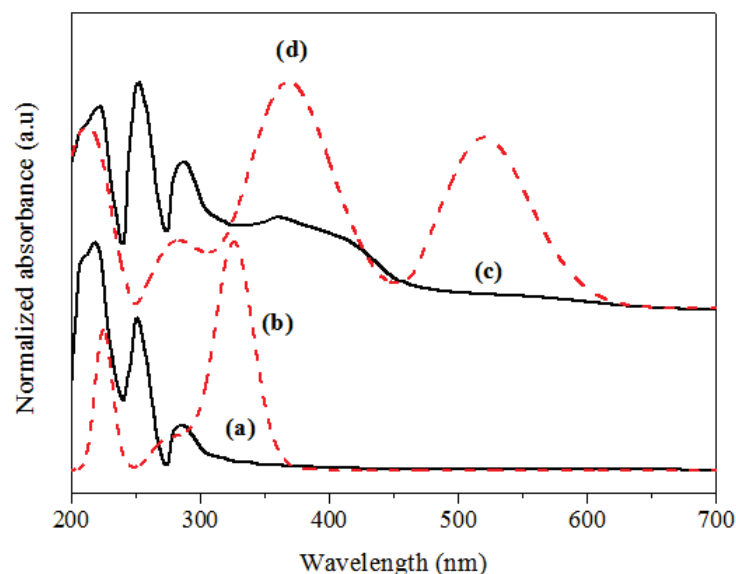
Figure 11. Optical absorption spectra of PANI—(**a**): experimental; (**b**): theoretical and those of doped-Pani/SWCNTs nano-composite; (**c**): experimental; (**d**): theoretical.

Referring to the experimental results, the same optical transitions are found and there is a decrease in the optical band gap after doping and after adding SWCNTs. It is suggested that theoretical band intensities are more pronounced than those obtained experimentally, due to the fact that calculations are carried out on a modeling structure with a higher concentration of SWCNTs than the real sample. In addition, the real sample presents additional interchain interactions, since calculations are expected to be performed with isolated fragments. When SWCNTs are added, the theoretical optical absorption spectrum is considerably affected. Particularly, new absorption band appears at λmax = 535 nm, giving rise to an absorption edge of 1.7 eV. It is believed that this new band is attributed to charge transfer creation [57]. If there is compatibility between the diffusion length and the nano-

junction size, the created electron–hole pairs after photo-excitation can be easily transferred to SWCNTs, as already reported for other polymer/SWCNT nano-composites [72]. This charge transfer is the major parameter leading to improved photovoltaic characteristics [73]. Based on the PL results, the band created in the absorption regime after the insertion of SWCNTs is not luminescent. From these findings, it was concluded that after photo-exciton, the separation process is favored rather than the recombination via the electric field created by the resulting hetero-nano-junctions.

4. Conclusions

The correlation between both the experimental and theoretical results makes it possible to conclude that the PANI doping process with the sulfonic acid has been successfully conducted. The easy doping process permits the advantageous modification of the properties of the pure PANI. The band gap of PANI was reduced from 3.75 eV to reach 2.63 eV. Moreover, the localized states had a bandwidth of nearly 380 meV, and these were created with an energy level of 1.62 eV. On the other hand, the functionalization process of the doped PANI with SWCNTs involves grafting between the nitrogen atoms and the side wall. The resulting interpenetrating network presents an optical gap in the range of 2.28 eV. The nano-hetero-junctions give rise to the formation of localized states that result from the charge transfer with an Urbach energy of 80 meV. The stationary photoluminescence measurements make it possible to affirm that these localized states do not provide radiative recombination processes. The luminescence is strongly quenched after either doping or the insertion of SWCNTs. The correlations found in the experimental results provide evidence that the created nano-junction leads to the charge transfer, where SWCNTs play the role of dissociation sites of the exciton constituents. Due to the good compatibility with the solar spectrum in the absorption process, the resulting interpenetrating network can be used as an active layer for photovoltaic solar cells and a photocatalyst for advanced oxidation processes.

References

1. Wang, J.; David, Y.H.P. Dispersion and filtration of carbon nanotubes (CNTs) and measurement of nanoparticle agglomerates in diesel exhaust. *Chem. Eng. Sci.* **2013**, *85*, 69–76. [CrossRef]
2. Spitalsky, Z.; Dimitrios, T.; Konstantinos, P.; Costas, G. Carbon nanotube–polymer composites, Chemistry, processing, mechanical and electrical properties. *Prog. Polym. Sci.* **2010**, *35*, 357–401. [CrossRef]
3. Chang, W.-M.; Wang, C.-C.; Chen, C.-Y. Plasma-Induced Polyaniline Grafted on Carbon Nanotube-embedded Carbon Nanofibers for High-Performance Supercapacitors. *Electrochim. Acta.* **2016**, *212*, 130–140. [CrossRef]
4. Lizin, S.; Passel, S.V.; Schepper, E.D.; Vranken, L. The future of organic photovoltaic solar cells as a direct power source for consumer electronics.Sol. *Energy Mater. Sol. Cells* **2012**, *103*, 1–10. [CrossRef]

5.   Deng, P.; Lei, Y.; Zheng, X.; Li, S.; Wu, J.; Zhu, F.; Ong, B.S.; Zhang, Q. Polymer based on benzothiadiazole-bridged bis-isoindigo for organic field-effect transistor applications. *Dye. Pigment.* **2016**, *125*, 407–413. [CrossRef]

6.   Tehrani, Z.; Korochkina, T.; Govindarajan, S.; Thomas, D.J.; Mahony, J.O.; Kettle, J.; Claypole, T.C.; Gethin, D.T. Ultra-thin flexible screen printed rechargeable polymer battery for wearable electronic applications. *Org. Electron.* **2015**, *26*, 386–394. [CrossRef]

7.   Moaseri, E.; Karimi, M.; Baniadam, M.; Maghreb, M. Improvements in mechanical properties of multi-walled carbon nanotube-reinforced epoxy composites through novel magnetic-assisted method for alignment of carbon nanotubes. *Compos. Part. A Appl. Sci. Manuf.* **2014**, *64*, 228–233. [CrossRef]

8.   Mulligan, C.J.; Bilen, C.; Zhou, X.; Belcher, W.J.; Dastoor, P.C. Levelised cost of electricity for organic photovoltaics. *Sol. Energy Mater. Sol.* **2015**, *133*, 26–31. [CrossRef]

9.   Zhu, H.; Wei, J.; Wang, K.; Wu, D. Applications of carbon materials in photovoltaic solar cells. *Sol. Energy Mater. Sol.* **2009**, *93*, 1461–1470. [CrossRef]

10.   Zaidi, B.; Bouzayen, N.; Wéry, J.; Alimi, K. Grafting of oligo-N-vinyl carbazole on single walled carbon nanotubes. *J. Mol. Struct.* **2010**, *971*, 71–80. [CrossRef]

11.   Ferguson, A.J.; Blackburn, J.L.; Kopidaki, N. Fullerene and carbon nanotubes as acceptor materials in organic photovoltaic. *Mater. Lett.* **2013**, *90*, 115–125. [CrossRef]

12.   Janssen, R.A.J.; Hummelen, J.C.; Sariciftci, N.S. Polymer–Fullerene Bulk Heterojunction Solar Cells. *MRS Bull.* **2005**, *30*, 33–36. [CrossRef]

13.   MacDiarmid, A.G. Polyaniline and polypyrrole: Where are we headed. *Synth. Met.* **1997**, *84*, 27–34. [CrossRef]

14.   Hundley, M.F.; Adams, P.N.; Mattes, B.R. The influence of 2-acrylamido-2-methyl-1-propanesulfonic acid (AMPSA) additive concentration and stretch orientation on electronic transport in AMPSA-modified polyaniline films prepared from an acid solvent mixture. *Synth. Met.* **2002**, *129*, 291–297. [CrossRef]

15.   Pinto, N.J.; Johnson, A.T.J.; MacDiarmid, A.G.; Mueller, C.H.; Theofylaktos, N.; Robinson, D.C.; Miranda, F.A. Electrospun polyaniline/polythethylene oxide nanofiber field-effect transistor. *Appl. Phys. Lett.* **2003**, *83*, 4244–4246. [CrossRef]

16.   Zhou, Y.; Freitag, M.; Hone, J.; Staii, C.; Johnson, A.T.J.; Pinto, N.J.; MacDiarmid, A.G. Fabrication and electrical characterization of polyaniline-based nanofibers with diameter below 30 nm. *Appl. Phys. Lett.* **2003**, *83*, 3800–3802. [CrossRef]

17.   Bejbouji, H.; Vignau, L.; Miane, J.L.; Dang, M.T.; ElMostafa, O.; Harmouchi, M.; Mouhsen, A. Polyaniline as a hole injection layer on organic photovoltaic cells. *Sol. Energy Mater. Sol.* **2010**, *94*, 176–181. [CrossRef]

18.   Ansari, N.; Shumaila; Lone, M.Y.; Ali, J.; Husain, M.; Husain, S. Single-walled carbon nanotubes–polyaniline composites: Synthesis and field-emission analysis. *J. Mater. Compos.* **2018**, 1–13. [CrossRef]

19.   Mukulika, J.C.; Dipali, B.; Krishanu, C. Composite of single walled carbon nanotube and sulfosalicylic acid doped polyaniline: A thermoelectric material. *Mater. Res. Express* **2016**, *3*, 85009. [CrossRef]

20.   Megha, A.D.; Raimonda, C.; Almira, R.; Mahendra, D.S.; Arunas, R. EDTA_PANI/SWCNTs nanocomposite modified electrode for electrochemical determination of copper (II), lead (II) and mercury (II) ions. *Electrochim. Acta* **2018**, *259*, 930–938. [CrossRef]

21.   Mehmet, C.; Bayram, G. Change of optoelectronic parameters of the boric acid-doped polyaniline conducting polymer with concentration. *Colloids Surf. A* **2017**, *532*, 263–269. [CrossRef]

22.   Daikh, S.Z.; Zeggai, F.; Bellil, A.; Benyoucef, A. Chemical polymerization, characterization and electrochemical studies of PANI/ZnO doped with hydrochloric acid and/or zinc chloride: Differences between the synthesized nanocomposites. *J. Phys. Chem. Solids* **2018**, *121*, 78–84. [CrossRef]

23.   Chiang, J.C.; MacDiarmid, A.G. Polyaniline: Protonic acid doping of the emeraldine form to the metallic regime. *Synth. Met.* **1986**, *13*, 193–205. [CrossRef]

24.   Ayachi, S.; Alimi, K.; Bouachrine, M.; Hamidi, M.; Mevellec, J.Y.; Porte, J.P.L. Spectroscopic investigations of copolymers incorporating various thiophene and phenylene monomers. *Synth. Met.* **2006**, *156*, 318–326. [CrossRef]

25.   Zou, L.Y.; Ren, A.M.; Feng, J.K.; Ran, X.Q.; Liu, Y.L.; Sun, C.C. Structural, electronic, and optical properties of phenol-pyridyl boron complexes for light-emitting diodes. *Int. J. Quantum Chem.* **2009**, *109*, 1419–1429. [CrossRef]

26.   Khoshkholgh, M.J.; Marsusi, F.; Abolhassani, M.R. Density functional theory investigation of opto-electronic properties of Functional thieno [3,4-b] thiophene and benzodithiophenepolymer and derivatives and their applications in solar cell. *Spectrochim. Acta A* **2015**, *136*, 373–380. [CrossRef]

27.   Mbarek, M.; Zaidi, B.; Wéry, J.; Alimi, K. Structure–properties correlation of copolymers derived from poly (phenylene vinylene) (PPV). *Synth. Met.* **2012**, *162*, 1762–1768. [CrossRef]

28.   Ayachi, S.; Ghomrasni, S.; Alimi, K. A combined experimental and theoretical study on vibrational and optical properties of copolymer incorporationg thienylene-dioctyloxyphenylene and bipyridine units. *J. Appl. Polym. Sci.* **2012**, *123*, 2684. [CrossRef]

29.   Saoudi, M.; Ajjel, R.; Zaidi, B. Experimental and theoretical study on the charge transfer between polyaniline and single walled carbon nanotubes. *J. Mater. Environ. Sci.* **2016**, *7*, 4435–4447.

30.   Shivani, D. Cost effective synthesis of MWCNT/PANI composite. *Mater. Res. Express* **2016**, *3*, 105002. [CrossRef]

31.   Omidi, M.J.; Mehr, M.S. Improving the dispersion of SWNT in epoxy resin through a simple Multi-Stage method. *J. King Saud Univ. Sci.* **2019**, *31*, 202–208. [CrossRef]

32.   Liu, J.; Liu, T.; Kum, S. Effect of solvent solubility parameter on SWNT dispersion in PMMA. *Polymer* **2005**, *46*, 3419–3424. [CrossRef]

33. Hopkins, A.R.; Kruk, N.A.; Lipeles, R.A. Macroscopic alignment of single-walled carbon nanotubes (SWNTs). *J. Coat. Technol. Res.* **2007**, *202*, 1282–1286. [CrossRef]

34. Ben Khalifa, I.; Bargaoui, S.; Haj Said, A.; Ayachi, S.; Zaidi, B.; Wéry, J.; Alimi, K. About some properties of electro-synthesized short Oligo(Para-Fluoro-Anisole) (OPFA): A combined experimental and theoretical study. *J. Mol. Struct.* **2011**, *997*, 37–45. [CrossRef]

35. Becke, A.D. Density-functional thermochemistry. III. The role of exact exchange. *J. Chem. Phys.* **1993**, *98*, 5648–5652. [CrossRef]

36. Lee, C.; Yang, W.; Parr, R.G. Development of the Colle-Savletti correlation-energy formula into a functional of the electron density. *Phys. Rev.* **1988**, *37*, 785–789. [CrossRef] [PubMed]

37. Mbarek, M.; Zaidi, B.; Alimi, K. Theoretical study of the alkoxyls groups effect on PPV-ether excited states, a relationship with femtosecond decay. *Spectrochim. Acta* **2012**, *88*, 23–30. [CrossRef] [PubMed]

38. Jamadade, V.S.; Dhawale, D.S.; Lokhande, C.D. Studies on electrosynthesized leucoemeraldine, emeraldine and pernigraniline forms of polyaniline films and their supercapacitive behavior. *Synth. Met.* **2010**, *160*, 955–960. [CrossRef]

39. Mello, H.J.N.P.D.; Mulat, M. Effect of aniline monomer concentration on PANI electropolymerization process and its influence for applications in chemical sensors. *Synth. Met.* **2018**, *239*, 66–70. [CrossRef]

40. Lobotka, P.; Kunzo, P.; Kovacova, E.; Vavra, I.; Krizanova, Z.; Smatko, V.; Stejskal, J.; Konyushenko, E.N.; Omastova, M.; Spitalsky, Z. Thin polyaniline and polyaniline/carbon nanocomposite films for gas sensing. *Thin Solid Film.* **2011**, *519*, 4123–4127. [CrossRef]

41. Mahudeswaran, A.; Vivekanandan, J.; Jeeva, A.; Chandrasekaran, J.; Vijayanand, P.S. Synthesis, characterization, optical and electrical properties of nanostructured poly(aniline-co-o-bromoaniline) prepared by in-situ polymerization method. *Optik* **2016**, *127*, 3984–3988. [CrossRef]

42. Scotto, J.; Florit, M.I.; Posadas, D. About the species formed during the electrochemical half oxidation of polyaniline: Polaron-bipolaron equilibrium. *Electrochim. Acta* **2018**, *268*, 187–194. [CrossRef]

43. Nguyen, H.D.; Nguyen, T.H.; Hoang, N.V.; Le, N.N.; Nguyen, T.N.N.; Doan, D.C.T.; Dang, M.C. pH sensitivity of emeraldine salt polyaniline and poly(vinyl butyral) blend. *Adv. Nat. Sci. Nanosci. Nanotechnol.* **2014**, *5*, 045001–045005. [CrossRef]

44. Pocas, L.C.; Travain, S.A.; Duarte, J.L.; Silva, R.A.; Giacometti, J.A.; Marletta, A. Annealing effects on conductivity and optical properties of the PAni layer in ITO/PAni/PPV+DBS/Al polymer light-emitting diodes. *J. Phys. Condens. Matter* **2007**, *19*, 436221–4362230. [CrossRef]

45. Banerjee, S.; Kumar, A. Swift heavy ion irradiation induced modifications in the optical band gap and Urbach's tail in polyaniline nanofibers. *Nucl. Instrum. Methods Phys. Res. Sect. B* **2011**, *269*, 2798–2806. [CrossRef]

46. Baibarac, M.; Matea, A.; Daescu, M.; Mercioniu, I.; Quillard, S.; Mevellec, J.Y.; Lefrant, S. Polyaniline photoluminescence quenching induced by single-walled carbon nanotubes enriched in metallic and semiconducting tubes. *Sci. Rep.* **2018**, *8*, 9518. [CrossRef]

47. Nascimento, G.M.; Temperini, M.L.A. Studies on the resonance Raman spectra of polyaniline obtained with near-IR excitation. *J. Raman Spectrosc.* **2008**, *39*, 772–778. [CrossRef]

48. Shimano, J.Y.; MacDiarmid, A.G. Polyaniline, a dynamic block copolymer: Key to attaining its intrinsic conductivity. *Synth. Met.* **2001**, *123*, 251–262. [CrossRef]

49. Tauc, J. *Amorphous and Liquid Semiconductors*; Springer: Plenum, NY, USA, 1974.

50. Kabir, H.; Rahman, M.M.; Uddin, K.M.; Bhuiya, A.H. Structural, Morphological, Compositional and Optical Studies of Plasma Polymerized 2-Furaldehyde Amorphous Thin Films. *Appl. Surf. Sci.* **2017**, *423*, 983–994. [CrossRef]

51. Chithra, L.P.; Subramanian, E.; Padiyan, D.P. Electrodeposition of polyaniline thin films doped with dodeca tungstophosphoric acid: Effect on annealing and vapor sensing. *Sens. Actuators B Chem.* **2007**, *122*, 274–281. [CrossRef]

52. Urbach, F. The Long-Wavelength Edge of Photographic Sensitivity and of the Electronic Absorption of Solids. *Phys. Rev. B* **1953**, *92*, 1324. [CrossRef]

53. Kazmersky, L.L. *Polycrystalline and Amorphous Thin Films and Devices*; Academic Press: New York, NY, USA, 1980; p. 135, ISBN 9780323156042.

54. Fernandes, M.R.; Garcia, J.R.; Schultz, M.S.; Nart, F.C. Polaron and bipolaron transitions in doped poly(p-phenylene vinylene) films. *Thin Solid Film.* **2005**, *474*, 279–284. [CrossRef]

55. Smita, S.K.; Pramod, S.P. Secondary electrochemical doping level effects on polaron and bipolaron bands evolution and interband transition energy from absorbance spectra of PEDOT: PSS thin films. *Synth. Met.* **2016**, *220*, 661–666. [CrossRef]

56. Oueiny, C.; Berlioz, S.; Perrin, F.X. Carbon nanotube–polyaniline composites. *Prog. Polym. Sci.* **2014**, *39*, 707–748. [CrossRef]

57. Zaidi, B.; Bouzayen, N.; Wéry, J.; Alimi, K. Annealing treatment and carbon nanotubes concentration effects on the optical and vibrational properties of single walled carbon nanotubes functionalized with short oligo-N-vinyl carbazole. *Mater. Chem. Phys.* **2011**, *126*, 417–423. [CrossRef]

58. Naqash, W.; Majid, K. Synthesis, characterisation and study of thermal, electrical and photocatalytic activity of nanocomposite of PANI with [Co(NH3)4 (C12H8N2)] Cl3_5H2O photoadduct. *Chem. Phys.* **2016**, *478*, 118–125. [CrossRef]

59. Baltog, I.; Baibarac, M.; Smarand, I.; Matea, A.; Ilie, M.; Mevellec, J.Y.S.; Lefrant, S. Optical properties of single-walled carbon nanotubes functionalized with copolymer poly(3,4-ethylenedioxythiophene-co-pyrene). *Opt. Mater.* **2016**, *62*, 604–611. [CrossRef]

60. Rozlivkova, Z.; Trchova, M.; Exnerova, M.; Stejska, J. The carbonization of granular polyaniline to produce nitrogen-containing carbon. *Synth. Met.* **2011**, *161*, 1122–1129. [CrossRef]

61. Liu, D.; Wang, H.; Du, P.; Liu, P. Independently double-crosslinked carbon nanotubes/polyaniline composite films as flexible and robust free-standing electrodes for high-performance supercapacitors. *Carbon* **2017**, *122*, 761–774. [CrossRef]

62. Saoudi, M.; Zaidi, B.; Ajjel, R. Correlation between microstructures and optical properties of polyaniline/single walled carbon nanotubes composites. *Polym. Compos.* **2019**, *40*, E821–E831. [CrossRef]

63. Cui, L.; Yu, J.; Lv, Y.; Li, G.; Zhou, S. Doped polyaniline/multiwalled carbon nanotube composites: Preparation and characterization. *Polym. Compos.* **2013**, *34*, 1119–1125. [CrossRef]

64. AbdulAlmohsin, S.; Li, Z.; Mohammed, M.; Wu, K.; Cui, J. Electrodeposited polyaniline/multi-walled carbon nanotube composites for solar cell applications. *Synth. Met.* **2012**, *162*, 931–935. [CrossRef]

65. Zaidi, B.; Bouzayen, N.; Znaidia, S.; Mbarek, M.; Massuyeau, F.; Faulques, E.; Gautron, E.; Wery, J.; Duvail, J.L.; Ghedira, M.; et al. Dynamic properties of the excited states of oligo-N-vinylcarbazole functionalized with single walled carbon nanotubes. *J. Mol. Struct.* **2013**, *1039*, 46–50. [CrossRef]

66. Mulazzi, E.; Perogo Aarab, H.; Mihut, L.; Faulques, E.; Lefrant, S.; Wery, J. Optical properties of carbon nanotube-PPV composites: Influence of the PPV conversion temperature and nanotube concentration. *Synt. Met.* **2005**, *154*, 221–224. [CrossRef]

67. Remyamol, T.; Gopinath, P.; Honey, J. Core-shell nanostructures of covalently grafted polyaniline multi-walled carbonnanotube hybrids for improved optical limiting. *Opt. Lett.* **2015**, *40*, 21–24. [CrossRef]

68. Arı, H.; Buyukmumcu, Z. Comparison of DFT functionals for prediction of band gap of conjugated polymers and effect of HF exchange term percentage and basis set on the performance. *Comput. Mater. Sci.* **2017**, *138*, 70–76. [CrossRef]

69. Baibarac, M.; Baltog, I.; Lefrant, S.; Mevellec, J.Y.; Chauvet, O. Polyaniline and Carbon Nanotubes Based Composites Containing Whole Units and Fragments of Nanotubes. *Chem. Mater.* **2003**, *15*, 4149–4156. [CrossRef]

70. Byron, P.R.; Hubert, P.; Salvetat, J.P.; Zalamea, L. Flexural deflection as a measure of van der Waals interaction forces in the CNT array. Compos. *Sci. Technol.* **2006**, *66*, 1125–1131. [CrossRef]

71. Schroder, E.; Hyldgaard, P. Van der Waals interactions of parallel and concentric nanotubes. *Mater. Sci. Eng. C* **2003**, *23*, 721–725. [CrossRef]

72. Jeong, D.C.; Song, S.G.; Satheeshkumar, C.; Lee, Y.; Kim, K.S.; Song, C. Enhanced photo-induced electron transfer by multi-walled carbon nanotubes in self-assembled terpyridine polymer networks. *Polymer* **2015**, *69*, 39–44. [CrossRef]

73. He, B.; Tang, Q.; Luo, J.; Li, Q.; Chen, X.; Cai, H.J. Rapid charge-transfer in polypyrrole–single wall carbon nanotube complex counter electrodes: Improved photovoltaic performances of dye-sensitized solar cells. *J. Power Sources* **2014**, *256*, 170–177. [CrossRef]

EVA Films Loaded with Layered Double Hydroxide (LDH) Modified with Methacrylic Anion: Effect of the Nanohybrid Filler on the Photodegradation Phenomena

Giuliana Gorrasi [1] , Gianluca Viscusi [1] , Giusy Curcuruto [2], Maria Cantarella [3] , Alessandro Di Mauro [3], Paola Bernardo [4] , Gabriele Clarizia [4] , Andrea A. Scamporrino [2,*] and Sabrina Carroccio [2]

1   Dipartimento di Ingegneria Industriale, Università degli Studi di Salerno, Via Giovanni Paolo II, 132, 84084 Fisciano, SA, Italy; ggorrasi@unisa.it (G.G.); gviscusi@unisa.it (G.V.)
2   Consiglio Nazionale delle Ricerche, CNR-IPCB s.s Catania, Via P. Gaifami 18, 95126 Catania, CT, Italy; giusy.curcuruto@cnr.it (G.C.); sabrinacarola.carroccio@cnr.it (S.C.)
3   Consiglio Nazionale delle Ricerche, CNR-IMM s.s Catania (Università), via Santa Sofia 64, 95123 Catania, CT, Italy; maria.cantarella@ct.infn.it (M.C.); alessandro.dimauro@ct.infn.it (A.D.)
4   Consiglio Nazionale delle Ricerche, CNR-ITM, via P. Bucci 17/c, 87036 Rende, CS, Italy; p.bernardo@itm.cnr.it (P.B.); g.clarizia@itm.cnr.it (G.C.)
*   Correspondence: andreaantonio.scamporrino@cnr.it

Abstract: The photo-oxidative studies of ethylene vinyl acetate copolymer (EVA) matrix, filled with Layered Double Hydroxide (LDH) modified with methacrylic anion (MA), were herein reported, together with gas permeation tests. The formulation of nano-hybrid LDHs was characterized using X-ray diffractometry (XRD) and thermogravimetric analysis (TGA), demonstrating the partial intercalation of the 30% of MA anion between the LDH's galleries. The as-modified filler was introduced into an EVA matrix by mechanical milling, producing free-standing films subjected to accelerated aging. Fourier transform infrared spectroscopy (FT-IR) results suggested that the nanohybrid presence determined a stabilizing effect up to 45 days of UV irradiation, especially if compared to the EVA/LDH references for all formulated EVA hybrid nanocomposites. Conversely, the presence of nanohybrid in the matrix did not significantly change the thermal stability of EVA samples. The dispersion of modified MA-LDH in the EVA matrix produces defect-free samples in the whole range of investigated loadings. The samples show a slight decrease in gas permeability, coupled with a substantial stabilization of the original CO_2/O_2 selectivity, which also proves the integrity of the films after 30 days of UV irradiation.

Keywords: ethylene vinyl acetate copolymer; EVA nanocomposite; Layered Double Hydroxide (LDH); photo-oxidation; degradation; gas permeation; ball milling

1. Introduction

The primary worldwide source of energy mainly derives from fossil fuels, whose reservations are constantly decreasing. In addition, the large consumption of fossil fuels is harmful for the environment, and a great effort is needed to move from non-renewable to sustainable energy sources. Among the reliable approaches to satisfy criteria for a new green deal, the use of solar energy, being the most abundant renewable energy resource, is considered the winning strategy in different fields of application. Specifically, photovoltaics (PV) is currently the fastest growing technology, reaching the most competitive prices compared to other technologies [1]. To be a cost-effective technology, photovoltaic modules are expected to operate reliably for about 25–30 years under the interactive conditions in which they are installed [2]. It is known that photovoltaic modules work in non-controlled field conditions, that greatly influence their efficiency during the aforementioned working period. In light of this, the understanding of aging processes involved during outdoor exposure for each component of the photovoltaic module becomes of

outstanding importance [2–5]. One of these elements comprises the ethylene vinyl acetate copolymer (EVA) as an encapsulation agent. The latter possesses several peculiar features, such as high transmittance, good adhesion to glass and relative weather and UV resistance, although degradation phenomena can occur for prolonged light exposure times [6–9]. Degradation of EVA involves complex chemical and physical phenomena that mainly depend on temperature, UV radiation and moisture. In this regard, since the identification of structural and physico-chemical changes involved during EVA aging can provide useful information to slow down the process, several studies have been devoted to the comprehension of polymer degradation and its stabilization. Among them, the addition of fillers by using different formulation technologies was reported as a valuable solution to extend the material lifetime in terms of light resistance and mechanical and gas barrier properties [8,10–15]. However, the selection of nanoparticles to improve the performance of polymer nanocomposites can be a difficult task. Indeed, by adding a specific filler to a specific matrix, great benefits in terms of mechanical properties can be obtained, and vice versa, the same filler can determine a depletion of UV durability. This phenomenon can be tuned, depending on the chemical composition of the nanofiller, its UV and thermal stability, its morphology and the possible interactions and/or reactions that may occur between the matrix and nanofiller [16]. In this context, Layered Double Hydroxides (LDHs) are receiving increasing interest as fillers for polymeric matrices, owing to their unique versatility. Particularly, their anion exchange capability allows to design a great variety of nano-fillers, simply by varying the intercalated species. Despite that several papers have reported the photo-oxidative behavior of polymer nanocomposites filled with LDHs [17–21], related studies on EVA filled with LDHs are missing in the literature. This work reports as a novelty the preparation and characterization of LDHs modified with methacrylic acid and their formulation with the EVA matrix by using a mechanical milling procedure. As stated, LDHs are able to boost the mechanical and thermal properties of several polymer matrices, although their introduction can cause serious concerns about the polymer durability. In this regard, the unusual choice to use MA as an intercalating species was made assuming that its polymerization, triggered by UV exposure, might assist in "repairing" the macromolecular structure that is subjected to unrelenting chains' scission. Herein, the influence of the filler on degrading or stabilizing the nanocomposite materials was reported and discussed, also comparing results obtained by loading different filler concentrations and related references. Finally, transport properties versus O_2 and CO_2 were also evaluated, tracking the response to photo-oxidation.

2. Materials and Methods

2.1. Materials

$MgCl_2 \times 6H_2O$, $AlCl_3 \times 6H_2O$, NaOH and methacrylic acid (MA) were purchased from Sigma-Aldrich (Italy). Ethylene vinyl acetate (EVA) Green Flex® ML 40 (14% of vinyl acetate content, Melt Flow Rate (190 °C/2.16 kg) 2.5 g/10 min) was kindly supplied by Versalis. Carbon dioxide (CO_2) and oxygen (O_2), used in the permeation tests, had a purity of 99.99% and were purchased from SAPIO (Italy). LDH in carbonate form (cas number: 11097-59-9) was purchased from Sigma-Aldrich (Saint Louis, MO, USA).

2.2. MgAl-Methacrylate (LDH-MA) Preparation by Coprecipitation Method

Fifty mL of an aqueous solution of $MgCl_2 * 6H_2O$ (16.8 g, 82.8 mmol) and $AlCl_3 * 6H_2O$ (10 g, 41.4 mmol) was added to fifty mL of a methacrylic sodium salt solution (5.8 g, 66.7 mmol) under stirring and nitrogen flow. The pH slowly reached the value of 9 by adding 1M NaOH. At the end, the precipitate was washed with distilled water and left in an oven at 50 °C for 24 h, under vacuum [22]. The chemical formula obtained from the elemental analysis was the following: $[Mg_{0.65}Al_{0.35}(OH)_2] (C_4O_2H_5)_{0.35} * 0.7 H_2O$, with the value of the molar fraction x = MIII/(MIII + MII) of 0.35 and molecular weight of 101.59 g/mol. The amount of methacrylic anion intercalated in MgAl-MA (LDH-MA) is 30 wt% of the total weight.

2.3. Preparation of EVA/LDH-MA Composites

Composites based on EVA and 3, 5 and 10 wt% of LDH-MA nano-hybrid were prepared by milling LDH-methacrylate and EVA powders at room temperature in a Retsch (Germany) planetarium ball mill (model PM 100), using a cylindrical steel jar of 50 cm^3 with 5 steel balls of 10 mm in diameter. The rotation speed used was 580 rpm and the milling time was 3 h. Films of EVA and composites, having the same thickness $\cong$ 100 μm, were obtained by compression molding at 150 °C, using a Carver Laboratory press, and cooled at room temperature. Films of EVA and unmodified LDH were produced using the same experimental conditions.

2.4. Methods

X-ray diffraction (XRD) patterns were obtained in reflection with an automatic Bruker diffractometer D8 (Karlsruhe, Germany), using nickel-filtered Cu *Kα* radiation (Kα = 1.54050 Å) and operating at 40 kV and 40 mA, with a step scan of 0.05° of 2θ and 3 s of counting time.

The photo-oxidative degradation of neat EVA and composite films was carried out on a QUV PANEL apparatus at 60 °C, with continued exposure to UV radiation up to 60 days, in the absence of water. At least two separate films were analyzed at each exposure time. The irradiance (0.68 W/m^2) of the UV lamps has a broad band with a maximum at 340 nm (UVA 340 lamps) [23].

The thermogravimetric analyses (TGA) of LDHs were carried out from 30 to 800 °C at a heating rate of 10 °C/min under air flow using a TA Instrument Q500 (TA Instruments, New Castle, DE, US). The same measurements on the films submitted to photodegradation were performed under a nitrogen atmosphere at 10 °C/min, from 50 to 600 °C. Sample weights were approximately 3–6 mg. The weight loss percent and its derivate (DTG) were recorded as a function of temperature.

Fourier transform infrared (FT-IR) characterization in ATR mode was performed by a JASCO FT/IR-4700 spectrometer (average of 10 scans, at a resolution of 4 cm^{-1}).

The permeation rates of O_2 and CO_2 were measured at a feed pressure of 1 bar and 25 °C in a fixed volume/pressure increase apparatus (Elektro & Elektronik Service Reuter, Germany) [24]. The instrument has a high vacuum system (turbo molecular pump after a backing pump) in order to evacuate the membrane samples. A pressure transducer monitors the pressure increase due to the gas permeation in the permeate side, where the volume is calibrated. The gas permeability (*P*) is obtained from the slope of the pressure curve at steady-state conditions. In addition, the diffusion coefficient [*D*, Equation (1)] of each gas is evaluated from the gas time-lag (*θ*) [25] that is obtained by extrapolating the linear portion of the curve on the abscissa. The solubility coefficient [*S*, Equation (2)] was indirectly obtained according to the "solution-diffusion" transport model that describes the permeation of permanent gases at low pressure in dense polymeric films [26].

$$D = l^2/6\theta \tag{1}$$

$$S = P/D \tag{2}$$

The ideal selectivity was calculated as the ratio of the permeability values for two gases. The film thickness was calculated as the average of multiple point measurements taken with a digital micrometer (Mitutoyo).

Quantitative determination of metal ions in solution after the sequestration procedure was performed by an Inductively Coupled PlasmapMass Spectrometry (ICP/MS) Nexion 300X (Perkin Elmer Inc., Waltham, MA, USA), using the kinetic energy discrimination mode (KED) for interference suppression. Each determination was performed three times. The accuracy of the analytical procedure was confirmed by measuring a standard reference material, Nist 1640a trace element in natural water, without observing an appreciable difference. Results obtained for LDH and LDH-MA were 18.80 and 20.21 ppm, respectively.

Film transparency was determined through an ultraviolet-visible (UV-Vis) spectropho-tometer UV-2401 PC Shimadzu (Kyoto, Japan). Light transmission in UV-Vis ranges (200–800 nm) was determined. A film sample (4×1 cm^2) was placed into the cell of the spectrophotometer, and the transmission value at a wavelength of 600 nm was recorded. The transparency of the films was then evaluated according to Equation (3):

$$\text{Transparency (\%Tr)} = \frac{\log(T_{600})}{x} \tag{3}$$

where T_{600} is the % transmittance taken at 600 nm and x is the film thickness (mm). According to this equation, the lower the transparency index value is, the higher the film transparency [27–29].

3. Results

3.1. Materials

The as-prepared LDH-MA nanohybrid was characterized by XRD and TGA measure-ments. Figure 1 reports the XRD of the pristine LDH with chloride anion (A) and the LDH modified with MA (B). The pristine LDH shows the peak at $2\theta \cong 11.8°$ corresponding to the basal reflection (003) and to an interlayer distance of 0.376 nm. The XRD of LDH-MA shows that part of MA is intercalated into the pristine LDH, as evidenced by the peak at lower $2\theta \cong 5.8°$, while part of LDH resulted as not intercalated, because of the co-presence of the peak at $2\theta \cong 11.8°$.
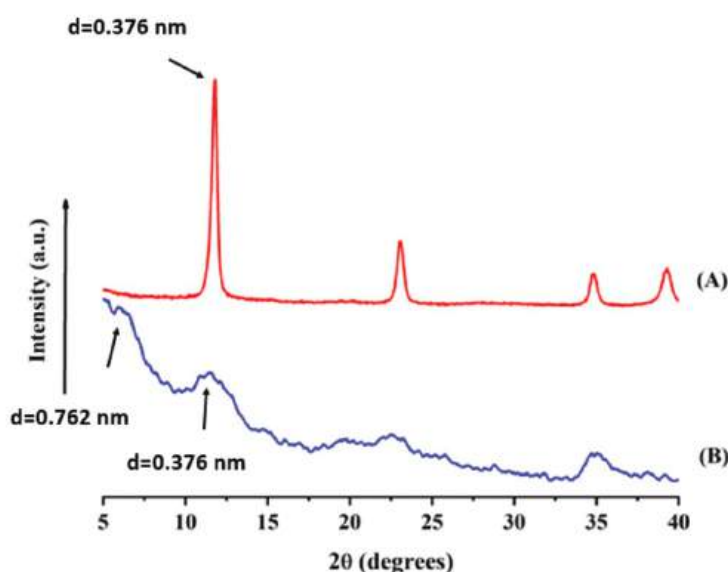
Figure 1. XRD of the pristine LDH with chloride anion (**A**) and the LDH modified with MA (**B**).

Figure 2 reports the TGA thermograms of the pristine LDH with chloride anion (A), the LDH modified with MA (B) and the MA (C). The first weight loss, between 100 and 140 °C, is due in both cases to the loss of intercalated water. The second weight loss, as temperature increases from 300 to 500 °C, is due to the dehydroxylation of the octahedral layers as well as the decomposition of the interlayer anion [30]. In the case of LDH-MA, the second degradation step resulted as anticipated for the presence of the intercalated MA. The methacrylic acid (MA) has a degradation temperature at about 75 °C. It is evident that the intercalation into the LDH results in a significant improvement in MA's thermal stability, with the main thermal decomposition of the hybrid at around 350 °C. The hydroxide framework is transformed into the corresponding oxide by dehydroxylation above 400 °C. Such behavior, already found for several organic molecules intercalated into LDH layers [31], confirms that the LDH hosts constitute an interesting protection of the

organic molecule, providing the possibility to incorporate thermolabile molecules even in polymers with high melting points.
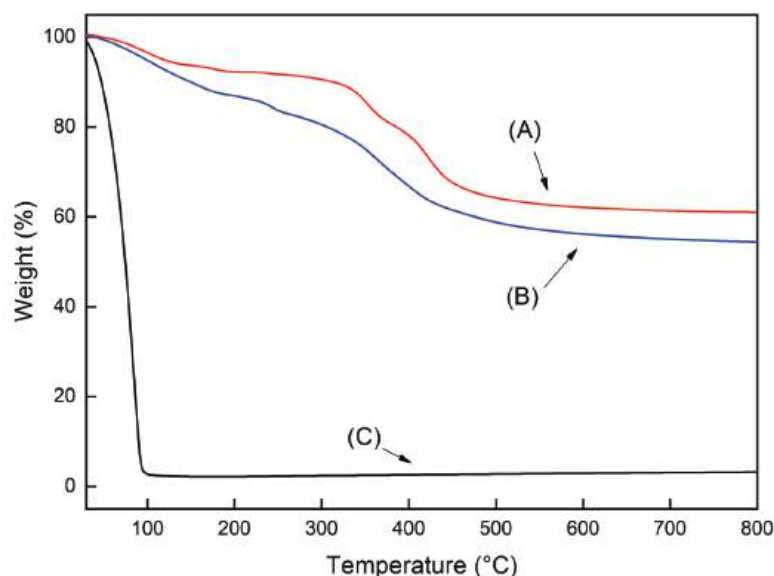
Figure 2. TGA of the pristine LDH with chloride anion (A), LDH modified with MA (B) and MA (C).

3.2. Photodegradation of EVA and Composites

Samples of neat EVA, EVA + LDH and EVA + LDH−MA were subjected to accelerated aging by using a UV lamp at 340 nm for up to 60 days. To appreciate variations in chemical structure during the aging, samples were collected at different irradiation times and analyzed by TGA and FT-IR spectroscopy. Degradation of the EVA sample became detectable after 15 days; indeed, at lower exposure times, the characteristic signals remain almost unmodified (see Supplementary Figure S1). Specifically, at 30 days of photo-exposure, the EVA sample registered an increase of carbonyl signals at 1775 cm^{-1} (Figure 3a) due to the formation of lactone groups derived from UV exposure at 60 °C (Scheme 1). At longer exposure times, this peak continued to increase, confirming data reported in the literature [32–35]. By increasing the exposure time, oxidation of aliphatic groups bearing to alcohol, acid and ketone groups occurred alongside, as confirmed by the appearance of the peaks at 3484 cm^{-1} assigned to alcoholic species (Supplementary Figure S2).
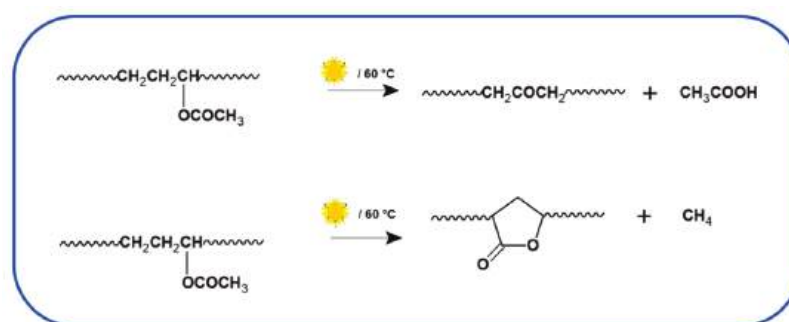
Scheme 1. Photo-oxidative degradation with formation of acidic acid and lactone via back-biting process.
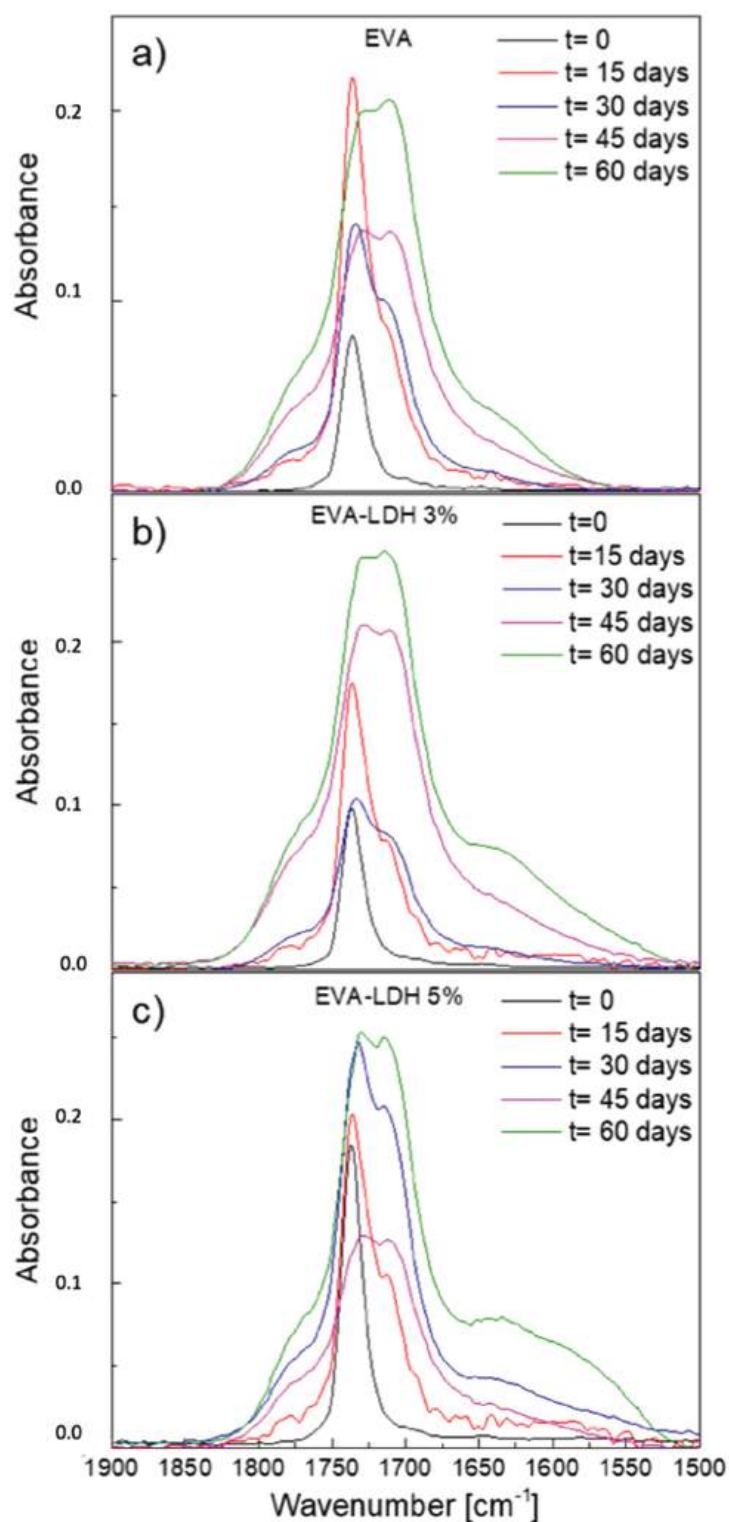
Figure 3. FT-IR spectra in the carbonyl region for EVA (**a**), EVA-LDH 3% (**b**) and EVA-LDH 5% (**c**) samples at different exposure times.

The latter species were formed by hydrogen abstraction as well as Norrish reactions occurring in polyethylene (PE) parts (Scheme 2), and reasonably contributed to the formation of lactone, acid and ester bands. Due to the change of chemical surrounding as a function of irradiation time, the peak at 1735 cm^{-1} was shifted at lower wavelengths, whereas a shoulder at 1710 cm^{-1} assigned to the formation of acetic groups concomitantly

appeared, becoming the predominant species (Schemes 1–3). The carbonyl band related to C=O stretching is sensitive to the environment and its blueshift can be related to a strong H-bonding [36].
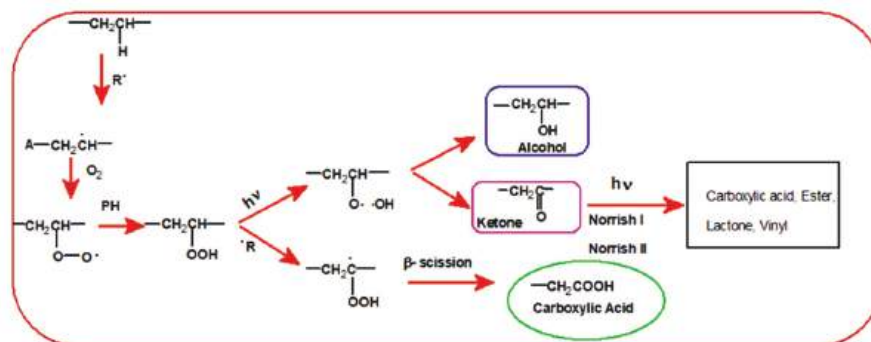
Scheme 2. Mechanisms of photo-oxidation of PE moieties in the EVA copolymer [36].
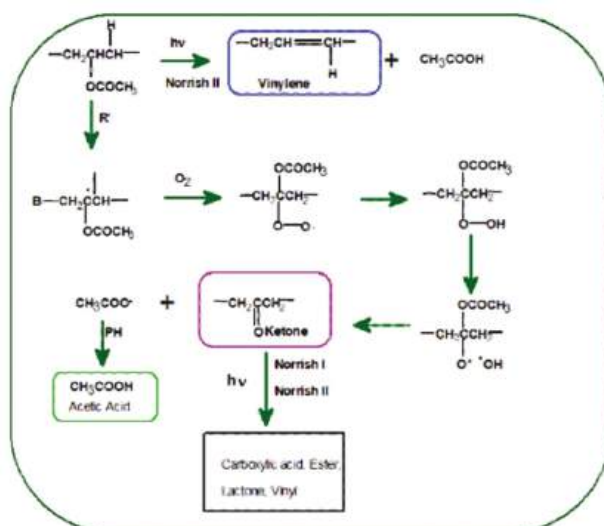
Scheme 3. Mechanisms of photo-oxidation of VA moieties in the EVA copolymer [36].

It is worth noticing that at higher stages of degradation, photoproducts that originated from different mechanisms were observable [36]. Particularly, photo-processes (Scheme 1) occurred in the polymer bulk where the permeation of air is restricted, whereas the exposed material surface is involved in photo-oxidative reaction pathways (Schemes 2 and 3).

As stated in the literature, polymeric matrices filled with nano-clays suffer light exposure [16,37,38]. Hence, it is not surprising that EVA filled with 5% of LDH showed an acceleration of photodegradation reactions as a function of exposure time, leading to the formation of carboxylic groups already evident for low irradiation periods (Figure 3c). As reported by Bocchini et al., LDH nanofillers can adsorb the antioxidant molecules, preventing their migration at the polymer surface and thus reducing the oxidative induction time [18].

From the inspection of samples filled with the LDH-MA at 3%, 5% and 10%, it appears evident that the presence of LDH-MA nanohybrids changes the fate of the materials during the exposure (Figure 4). A comparison of these spectra with those recorded for the samples loaded with the not modified LDH shows a reduced incidence of the photoproducts in the films loaded with the LDH-MA nanohybrids.
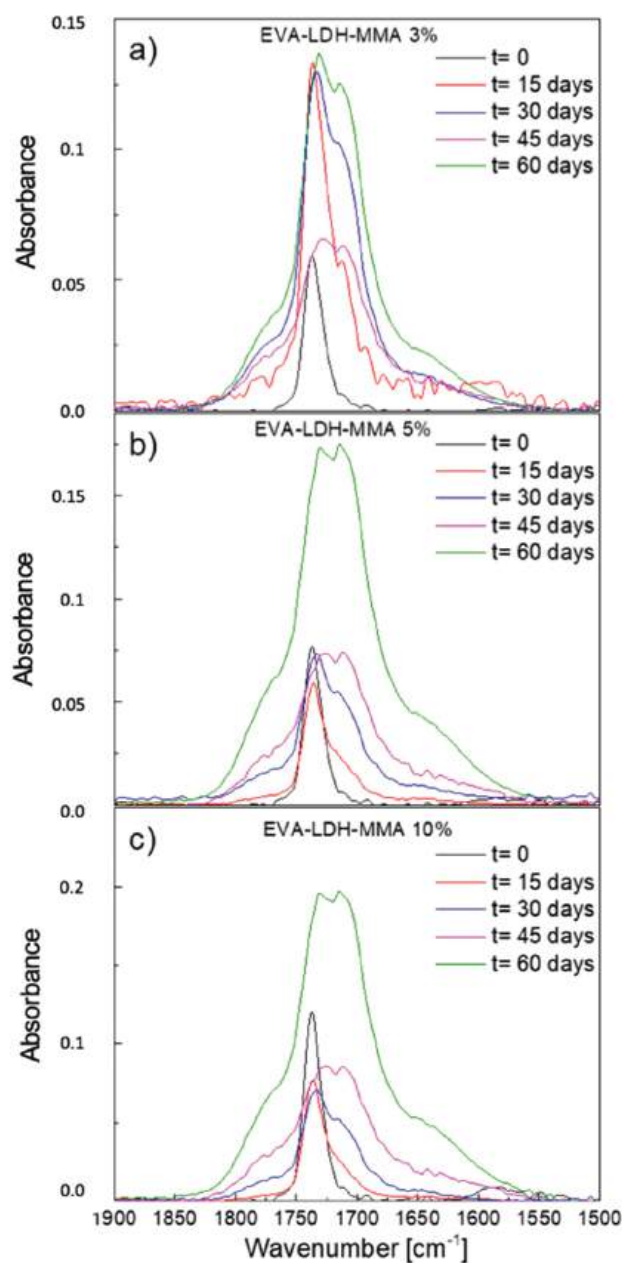
Figure 4. FT-IR spectra in the carbonyl region for EVA + LDH-MA 3% (**a**), EVA + LDH-MA 5% (**b**) and EVA + LDH-MA 10% (**c**) samples at different exposure times.

Figure 5 reports the absorbance values registered for acetic acid (Figure 5a) and lactone (Figure 5b) signals as a function of the irradiation time, collected for all LDH-MA-filled samples. As observed, a stabilizing effect induced by the presence of LDH-MA over this time was shown.
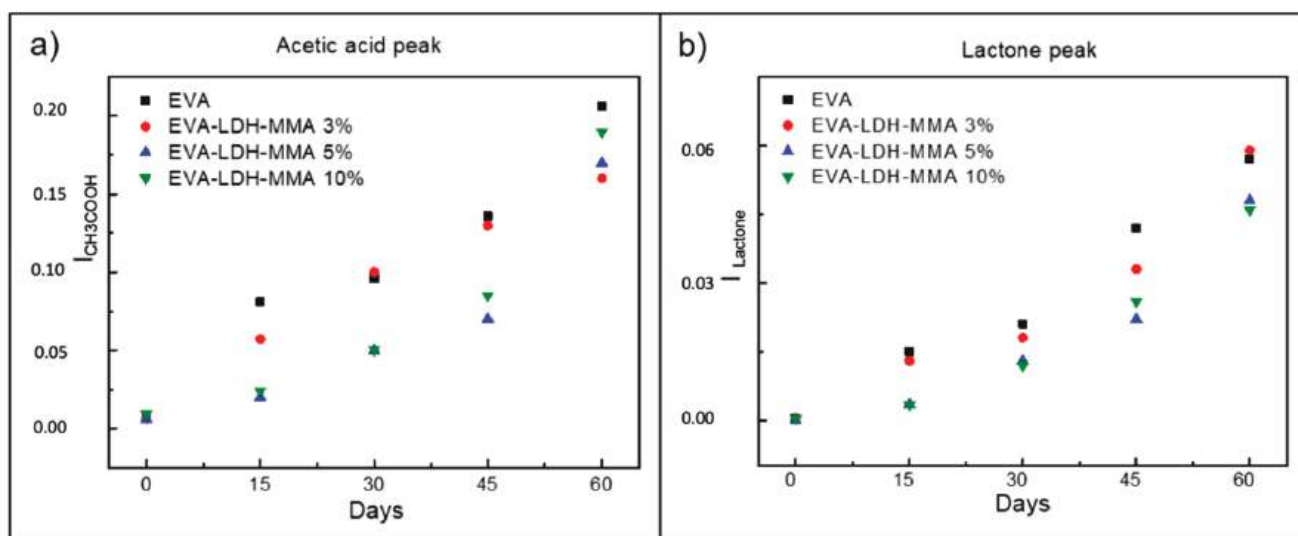
Figure 5. Absorbance values in FT-IR registered at different exposure times for (**a**) acetic acid and (**b**) lactone groups with the EVA samples and the samples of EVA + LDH-MA at different percentages.

Specifically, formation of lactone and acetic acid groups derived principally from the photodegradation process (Scheme 1) were drastically reduced by the presence of 5% and 10% of LDH-MA in the EVA matrix up to 45 days of exposure.

If compared with both LDH-filled and EVA original samples, the results suggested an improved UV stabilizing effect due to the presence of nanohybrids in the matrix. It is reasonable to suppose at least two possible explanations for this experimental evidence: A different content of impurities, such as transition metal, responsible for the increase of photo-oxidation rate [18], and alternately, the embedded MA can act as sacrificial molecules by blocking radicals responsible for UV degradation and employing them in MA polymerization. To discern between the two scenarios, ICP-MS analysis of LDHs and LDH-MA were performed. As expected, a similar content of Fe ions for both samples (see Section 2.4 Methods) was obtained. In light of this, the MA polymerization seems to play a key role in preventing the photo-oxidative reactions in the EVA matrix.

As a consequence, an increment of stabilization activity by adding more LDH-MA nanohybrid to the EVA is also expected. Samples containing 10% of nanohybrid exhibited a controversy in terms of mechanical properties. Specifically, after 45 days of photo-irradiation, the sample was extremely fragile, indicating that chain scission processes were prevalent and mostly extended for these irradiation times. Since the addition of such hybrid nano-clays can notably accomplish the photostability of the EVA matrix, suggesting its application for PV or agriculture purposes, transparency measurements were also performed. In Figure 6, the film transparency calculated by UV-Vis spectroscopy (see Section 2) revealed that such a peculiar feature, strictly required for application as an encapsulation agent or greenhouse film, was not significantly affected by the introduction of the modified LDH filler. In particular, the optical transparency was decreased by only 0.4%, 1.2% and 1.7%, with an LDH-MA content of 3%, 5% and 10% respectively, if compared to a neat EVA sample.
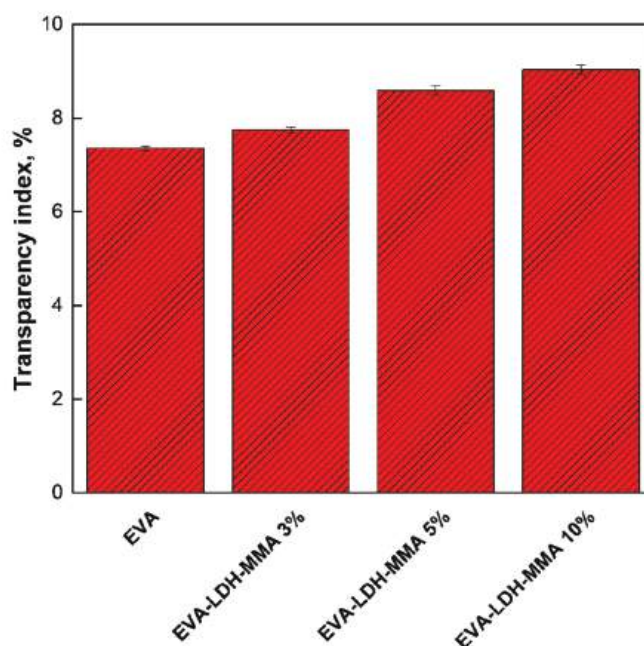
Figure 6. Transparency index (%) of neat EVA and EVA + LDH/MA films.

TGA measurements of EVA, EVA + LDH and EVA + LDH−MA films were performed to appreciate the variation of their thermal stability as a function of UV exposure time. Tables 1–3 report onset temperature of degradation (a), temperatures at maximum rate of decomposition (TMD) (b) and residual masses (c) for films based on EVA or on EVA loaded with 5% of filler. As expected, the addition of LDH fillers (Table 2, Supplementary Figure S5) increased the thermal stability of the EVA polymer for all formulations if compared to a neat EVA sample, although values underwent to a slight decrement as a function of exposure times (Supplementary Figures S4–S6, Tables S3 and S4). It is worth noting that higher LHD content triggered the formation of insoluble residue for prolonged photo-oxidation times, indicating the occurrence of crosslinking phenomena (Table 2, Supplementary Figures S4–S6, Tables S3 and S4). A different trend in thermal stability was registered for the samples containing nanohybrid at 5% (Table 3). Although LHD is added, the presence of the 30% of MA into the clay determines an inferior effect in terms of final thermal stability, resulting quite similar to that exhibited by the EVA film (Table 1). Light irradiation also induced gel formation, even if the amounts measured along the exposure time are reasonably inferior if compared with the EVA samples filled with only LHD. Similar results were obtained by analyzing EVA filled with 3% of nanohybrid.

Table 1. Onset temperatures of degradation, temperatures at maximum rate of decomposition and residual masses of EVA at 0, 45 and 60 days of exposure.

EVA	T_{95} (°C) [a]	T_{peak} (°C) [b]	Residue [c]
t = 0	336	471	-
t = 45	326	471	-
t = 60	323	472	-

[a] Temperature at 5 wt% of weight loss; [b] Temperature at the maximum derivate of weight loss; [c] % of residue at 600 °C.

Table 2. Onset temperatures of degradation, temperatures at maximum rate of decomposition and residual masses of EVA + LDH 5% at 0, 45 and 60 days of exposure.

EVA	T_{95} (°C) [a]	T_{peak} (°C) [b]	Residue [c]
t = 0	337	476	0.5
t = 45	332	473	1.6
t = 60	328	479	5.3

[a] Temperature at 5 wt% of weight loss; [b] Temperature at the maximum derivate of weight loss; [c] % of residue at 600 °C.

Table 3. Onset temperatures of degradation, temperatures at maximum rate of decomposition and residual masses of EVA + LDH-MA 5% at 0, 45 and 60 days of exposure.

EVA	T_{95} (°C) [a]	T_{peak} (°C) [b]	Residue [c]
t = 0	336	470	1.5
t = 45	327	438	3.4
t = 60	327	465	3.3

[a] Temperature at 5 wt% of weight loss; [b] Temperature at the maximum derivate of weight loss; [c] % of residue at 600 °C.

3.3. Gas Permeation Tests

The prepared films were tested as-prepared and after the prolonged photo-oxidation treatment. The neat EVA membranes presented a CO_2 permeability higher than O_2. Indeed, the polar acetate group (O=C-O-) in the EVA copolymers has a preferential affinity for the polar CO_2. The measured data on the neat EVA films are in agreement with those reported by Mousavi et al. for EVA membranes prepared by a thermal-wet-phase separation method using THF as a solvent (referred to as "EVA-28") [39]. Interestingly, the present values are higher than those reported for membranes prepared using the thermal-phase inversion method [38]. The UV exposure reduces the gas permeability in neat EVA samples (Figure 7) and an accelerated physical aging of the films is evident at treatment times larger than 15 days.

Figure 7. CO_2 permeability (**a**) and CO_2/O_2 selectivity (**b**) for the films based on EVA with increasing loadings of LDH-MA. Film conditions: "as-prepared" (0 days) and photo-exposed (15 and 30 days). 1 Barrer = 10–10 cm^3 (STP) cm cm^{-2} cmHg^{-1} s^{-1}.

A substantially constant permeability was observed for both gases as LDH content increased (Supplementary Figure S10). The permeability decay observed in the neat polymer was also evident in the LDH-filled films upon photo-oxidation (Supplementary Figure S10). It is coupled to a progressive decrease of CO_2/N_2 selectivity (Supplementary

Figure S10) when the treatment time is prolonged. At higher filler content, the selectivity is further depressed, probably due to the formation of nano-defects at the polymer-filler interface resulting from the densification of the membrane matrix upon photo-oxidation.

The gas permeation data measured in LDH-MA-loaded films evidenced the stabilizing role exerted by the modified fillers. The increase in the LDH-MA loading produced a systematically larger permeability (Figure 7) for both gases that can be attributed to the channels in the LDHs or to structural changes caused by the exfoliated lamellae within the polymer matrix. This phenomenon is coupled to a negligible change in CO_2/N_2 selectivity, proving the integrity of the tested films (Figure 7). The evaluation of diffusion and solubility coefficients provided more information on the nanocomposites (Figure 8). In particular, the incorporation of the modified lamellar LDHs within the EVA matrix resulted in a reduction in the diffusion coefficient owing to an increased tortuosity for the diffusion pathways. On the other hand, the calculated solubility coefficient of CO_2 increased in the presence of the fillers, indicating a preferential affinity of the additives. However, the solubility contribution was predominant.
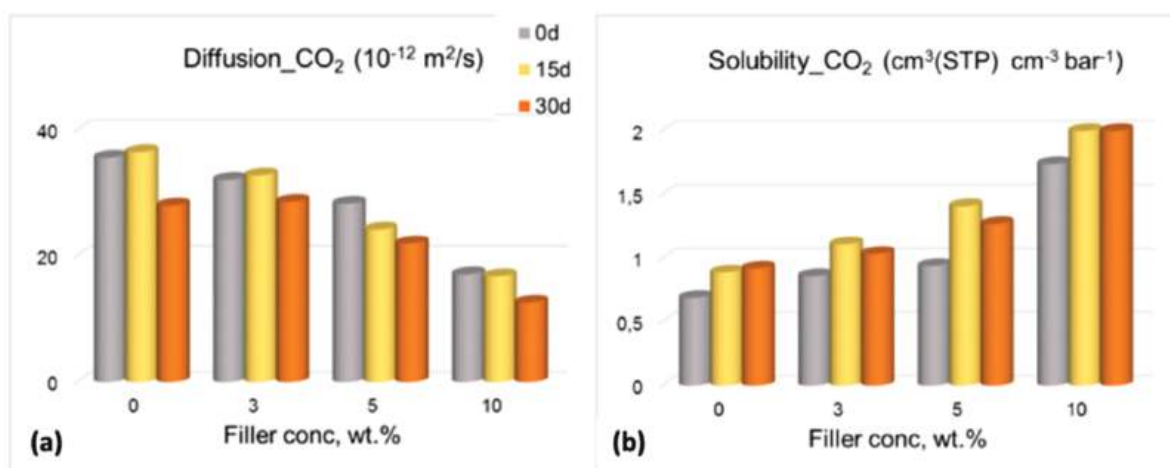
Figure 8. CO_2 diffusion (**a**) and solubility (**b**) coefficients for the films based on EVA with increasing loadings of LDH-MA. Film conditions: "as-prepared" (0 days) and photo-exposed (15 and 30 days).

As already observed on the neat polymer, the photo-oxidative stress reduced the gas permeability of the films with respect to the "as-prepared" samples. Small differences were detected after a photo-exposition of 15 days, while a more pronounced permeability reduction was registered after the prolonged photo-oxidative treatment (30 days). The films remained defect-free after their photo-oxidation for irradiation times up to 30 days, and reached a similar permeability, independent of the filler amount. Indeed, the CO_2/O_2 selectivity remained nearly constant (ca. 5.5). A deeper analysis of the CO_2 transport terms on the photo-oxidized films revealed, in analogy to what was observed in the as-prepared samples, a reduced gas diffusion coefficient coupled with a larger solubility upon the increase in the photo-oxidation exposure time (Figure 8). This behavior could be ascribed to crosslinking phenomena occurring on the films during the oxidation, as suggested by TGA data (Tables 2 and 3). Song et al. demonstrated the creation of surface-densified layers for highly permeable PIM-1 membranes upon photo-oxidation treatment [40].

4. Conclusions

In order to take advantage of the great potential of Layered Double Hydroxides (LDHs) in formulating EVA nanocomposites without sacrificing their light durability, in this study, they were intercalated with methacrylic anion (MA) and mixed with the polymer matrix using the sustainable ball-milling process. It was demonstrated that up to 10% of loading, EVA nanohybrids maintained transparency, while their characteristic photo-oxidative processes triggered by UV irradiation were postponed at longer exposure

times, allowing an increase of polymer durability. The presence of MA, that reasonably underwent to polymerization upon UV exposure, seems to play a key role in mitigating the photodegradation also triggered by the loading of nano-clays into the EVA matrix. Furthermore, the addition of LDH-MA is more effective in providing enhanced resistance to UV radiation, also noticeable in terms of gas transport properties. Indeed, their selectivity remained almost unchanged up to 30 days of exposure, whereas a slight permeability decay was observed in both neat EVA and LDH-filled samples. In general, the EVA/LDH-MA nanocomposite films demonstrated a good structural stability, since the post-treatment had no detrimental impact on their gas selectivity.

Supplementary Materials: The following are available online at https://www.mdpi.com/article/10.3390/polym13152525/s1, Figure S1: ATR infrared spectrum of EVA at different exposure time, Figure S2: ATR infrared spectra of EVA (a), EVA-LDH 3% (b) and EVA-LDH-MMA 3% (c) as prepared, and after 45 days of exposure time, Figure S3: TGA profiles of EVA TQ as prepared, and after 45 and 60 days of exposure time, Figure S4: TGA profiles of EVA + LDH 3% as prepared, and after 45 and 60 days of exposure time, Figure S5: TGA profiles of EVA + LDH 5% as prepared, and after 45 and 60 days of exposure time, Figure S6: TGA profiles of EVA + LDH 10% as prepared, and after 45 and 60 days of exposure time, Figure S7: TGA profiles of EVA + LDH +MMA 3% as prepared, and after 45 and 60 days of exposure time, Figure S8: TGA profiles of EVA + LDH +MMA 5% as prepared, and after 45 and 60 days of exposure time, Figure S9: TGA profiles of EVA + LDH +MMA 3, 5 and 10%, Figure S10: CO_2 Permeability and CO_2/O_2 selectivity for the films based on EVA with in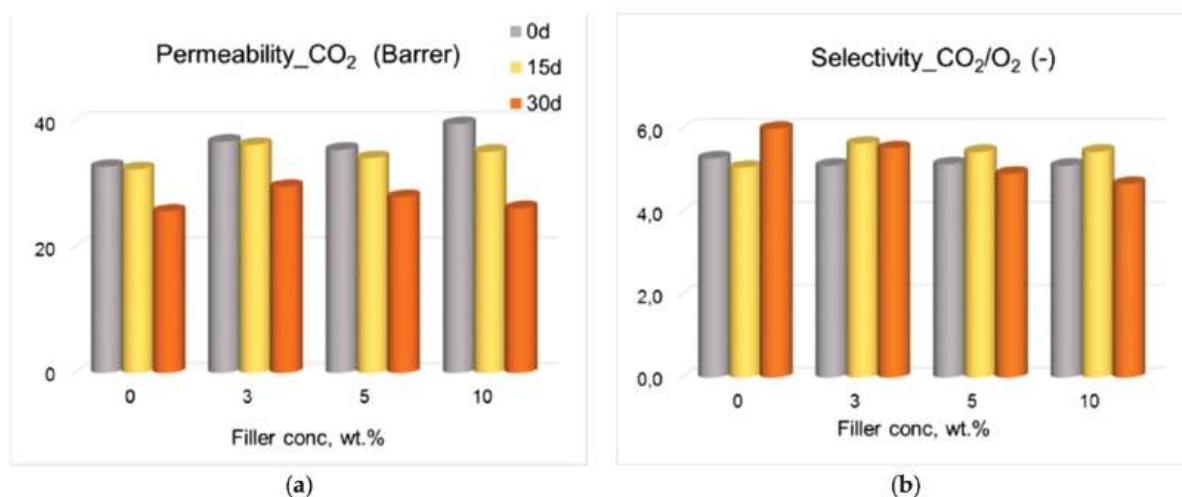creasing loadings of LDH and photo-exposed (15 d, 30 d and 45 d). Table S1: Onset temperature of degradation, temperature at maximum rate of decomposition and residual masses of EVA+LDH+MMA 3% at 0, 45 and 60 days of exposure, Table S2: Onset temperature of degradation, temperature at maximum rate of decomposition and residual masses of EVA+LDH+MMA 10% at 0, 45 and 60 days of exposure, Table S3: Onset temperature of degradation, temperature at maximum rate of decomposition and residual masses of EVA+LDH 3% at 0, 45 and 60 days of exposure, Table S4: Onset temperature of degradation, temperature at maximum rate of decomposition and residual masses of EVA+LDH 10% at 0, 45 and 60 days of exposure, Table S5: CO_2 Diffusion coefficient extracted from values in Figure S8.

References

1. Sharma, V.; Chandel, S.S. Performance and degradation analysis for long term reliability of solar photovoltaic systems: A review. *Renew. Sustain. Energy Rev.* **2013**, *27*, 753–767. [CrossRef]
2. Ottersböck, B.; Oreski, G.; Pinter, G. Comparison of different microclimate effects on the aging behavior of encapsulation materials used in photovoltaic modules. *Polym. Degrad. Stab.* **2017**, *138*, 182–191. [CrossRef]

3. Makrides, G.; Zinsser, B.; Norton, M.; Georghiou, G.E.; Schubert, M.; Werner, J.H. Potential of photovoltaic systems in countries with high solar irradiation. *Renew. Sustain. Energy Rev.* **2010**, *14*, 754–762. [CrossRef]

4. Ndiaye, A.; Charki, A.; Kobi, A.; Kébé, C.M.F.; Ndiaye, P.A.; Sambou, V. Degradations of silicon photovoltaic modules: A literature review. *Sol. Energy* **2013**, *96*, 140–151. [CrossRef]

5. Charki, A. Accelerated degradation testing of a photovoltaic module. *J. Photonics Energy* **2013**, *3*, 033099. [CrossRef]

6. Jiang, S.; Wang, K.; Zhang, H.; Ding, Y.; Yu, Q. Encapsulation of PV Modules Using Ethylene Vinyl Acetate Copolymer as the Encapsulant. *Macromol. React. Eng.* **2015**, *9*, 522–529. [CrossRef]

7. Schneller, E.J.; Brooker, R.P.; Shiradkar, N.S.; Rodgers, M.P.; Dhere, N.G.; Davis, K.O.; Seigneur, H.P.; Mohajeri, N.; Wohlgemuth, J.; Scardera, G.; et al. Manufacturing metrology for c-Si module reliability and durability Part III: Module manufacturing. *Renew. Sustain. Energy Rev.* **2016**, *59*, 992–1016. [CrossRef]

8. De Oliveira, M.C.C.; Diniz Cardoso, A.S.A.; Viana, M.M.; de Lins, V.F.C. The causes and effects of degradation of encapsulant ethylene vinyl acetate copolymer (EVA) in crystalline silicon photovoltaic modules: A review. *Renew. Sustain. Energy Rev.* **2018**, *81*, 2299–2317. [CrossRef]

9. Pern, J. *Module Encapsulation Materials, Processing and Testing (Presentation)*; National Renewable Energy Lab.(NREL): Golden, CO, USA, 2008.

10. Soheilmoghaddam, M.; Adelnia, H.; Bidsorkhi, H.C.; Sharifzadeh, G.; Wahit, M.U.; Akos, N.I.; Yussuf, A.A. Development of Ethylene-Vinyl Acetate Composites Reinforced with Graphene Platelets. *Macromol. Mater. Eng.* **2017**, *302*, 1600260–1600268. [CrossRef]

11. Ayutthaya, S.I.N.; Wootthikanokkhan, J. Investigation of the photodegradation behaviors of an ethylene/vinyl acetate copolymer solar cell encapsulant and effects of antioxidants on the photostability of the material. *J. Appl. Polym. Sci.* **2008**, *107*, 3853–3863. [CrossRef]

12. Bahmanyar, M.; Sedaghat, S.; Ramazani, S.A.A.; Baniasadi, H. Preparation of Ethylene Vinyl Acetate Copolymer/Graphene Oxide Nanocomposite Films via Solution Casting Method and Determination of the Mechanical Properties. *Polym. Plast. Technol. Eng.* **2015**, *54*, 218–222. [CrossRef]

13. Gorrasi, G.; Sorrentino, A. Photo-oxidative stabilization of carbon nanotubes on polylactic acid. *Polym. Degrad. Stab.* **2013**, *98*, 963–971. [CrossRef]

14. Xue, H.; Xu, Z.; Zhang, M.; Wang, J.; Ruan, W. Ethylene vinyl acetate films filled with ytterbium containing rare earth particles (Y$_2$SiO$_5$: Ce^{3+}, Yb^{3+}) which have optical down-conversion capabilities and useful for encapsulating solar cells. *J. Plast. Film Sheeting* **2015**, *31*, 233–247. [CrossRef]

15. Jin, J.; Chen, S.; Zhang, J. UV aging behaviour of ethylene-vinyl acetate copolymers (EVA) with different vinyl acetate contents. *Polym. Degrad. Stab.* **2010**, *95*, 725–732. [CrossRef]

16. Rosu, D.; Visakh, P.M. *Photochemical Behavior of Multicomponent Polymeric-Based Materials*; Rosu, D., Visakh, P.M., Eds.; Advanced Structured Materials; Springer International Publishing: Cham, Switzerland, 2016; Volume 26, ISBN 978-3-319-25194-3.

17. Leroux, F.; Meddar, L.; Mailhot, B.; Morlat-Thérias, S.; Gardette, J.L. Characterization and photooxidative behaviour of nanocomposites formed with polystyrene and LDHs organo-modified by monomer surfactant. *Polymer* **2005**, *46*, 3571–3578. [CrossRef]

18. Bocchini, S.; Morlat-Therias, S.; Gardette, J.L.; Camino, G. Influence of nanodispersed hydrotalcite on polypropylene photooxidation. *Eur. Polym. J.* **2008**, *44*, 3473–3481. [CrossRef]

19. Magagula, B.; Nhlapo, N.; Focke, W.W. Mn2Al-LDH- and Co2Al-LDH-stearate as photodegradants for LDPE film. *Polym. Degrad. Stab.* **2009**, *94*, 947–954. [CrossRef]

20. Lonkar, S.P.; Therias, S.; Caperaa, N.; Leroux, F.; Gardette, J.L. Photooxidation of polypropylene/layered double hydroxide nanocomposites: Influence of intralamellar cations. *Eur. Polym. J.* **2010**, *46*, 1456–1464. [CrossRef]

21. Kovanda, F.; Jindová, E.; Lang, K.; Kubát, P.; Sedláková, Z. Preparation of layered double hydroxides intercalated with organic anions and their application in LDH/poly(butyl methacrylate) nanocomposites. *Appl. Clay Sci.* **2010**, *48*, 260–270. [CrossRef]

22. Frunza, M.; Lisa, G.; Popa, M.I.; Miron, N.D.; Nistor, D.I. Thermogravimetric analysis of layered double hydroxides with chloramphenicol and salicylate in the interlayer space. *J. Therm. Anal. Calorim.* **2008**, *93*, 373–379. [CrossRef]

23. Carroccio, S.; Puglisi, C.; Montaudo, G. Photo-oxidation products of polyetherimide ULTEM determined by MALDI-TOF-MS. Kinetics and mechanisms. *Polym. Degrad. Stab.* **2003**, *80*, 459–476. [CrossRef]

24. Clarizia, G.; Bernardo, P.; Gorrasi, G.; Zampino, D.; Carroccio, S. Influence of the Preparation Method and Photo-Oxidation Treatment on the Thermal and Gas Transport Properties of Dense Films Based on a Poly(ether-block-amide) Copolymer. *Materials* **2018**, *11*, 1326. [CrossRef]

25. Crank, J. *The Mathematics of Diffusion*, 2nd ed.; Clarendon Press: Oxford, UK, 1979; ISBN 3804204422.

26. Wijmans, J.G.; Baker, R.W. The solution-diffusion model: A review. *J. Memb. Sci.* **1995**, *107*, 1–21. [CrossRef]

27. Pattarasiriroj, K.; Kaewprachu, P.; Rawdkuen, S. Properties of rice flour-gelatine-nanoclay film with catechin-lysozyme and its use for pork belly wrapping. *Food Hydrocoll.* **2020**, *107*, 105951–105960. [CrossRef]

28. Han, J.H.; Floros, J.D. Casting antimicrobial packaging films and measuring their physical properties and antimicrobial activity. *J. Plast. Film Sheeting* **1997**, *13*, 287–298. [CrossRef]

29. Pérez-Mateos, M.; Montero, P.; Gómez-Guillén, M.C. Formulation and stability of biodegradable films made from cod gelatin and sunflower oil blends. *Food Hydrocoll.* **2009**, *23*, 53–61. [CrossRef]

30. Miyata, S. Physico-Chemical Properties of Synthetic Hydrotalcites in Relation to Composition. *Clays Clay Miner.* **1980**, *28*, 50–56. [CrossRef]

31. Gorrasi, G.; Bugatti, V. Mechanical dispersion of layered double hydroxides hosting active molecules in polyethylene: Analysis of structure and physical properties. *Appl. Clay Sci.* **2016**, *132–133*, 2–6. [CrossRef]

32. Helfand, M.A.; Mazzanti, J.B.; Fone, M.; Reamey, R.H.; Lindley, P.M. Effect of acetate distribution on surface segregation in poly(vinyl alcohol-co-vinyl acetate) copolymer films. *Langmuir* **1996**, *12*, 1296–1302. [CrossRef]

33. McEvoy, R.L.; Krause, S.; Peter, W. Surface characterization of ethylene-vinyl acetate (EVA) and ethylene-acrylic acid (EAA) co-polymers using XPS and AFM. *Polymer (Guildf)* **1998**, *39*, 5223–5239. [CrossRef]

34. Rabek, J.F. *Photodegradation of Polymers*; Springer: Berlin/Heidelberg, Germany, 1996.

35. Morlat-Therias, S.; Fanton, E.; Gardette, J.L.; Peeterbroeck, S.; Alexandre, M.; Dubois, P. Polymer/carbon nanotube nanocomposites: Influence of carbon nanotubes on EVA photodegradation. *Polym. Degrad. Stab.* **2007**, *92*, 1873–1882. [CrossRef]

36. Nie, B.; Stutzman, J.; Xie, A. A vibrational spectral maker for probing the hydrogen-bonding status of protonated Asp and Glu residues. *Biophys. J.* **2005**, *88*, 2833–2847. [CrossRef] [PubMed]

37. Ussia, M.; Curcuruto, G.; Zampino, D.; Dintcheva, N.T.; Filippone, G.; Mendichi, R.; Carroccio, S.C. Role of organo-modifier and metal impurities of commercial nanoclays in the photo-and thermo-oxidation of polyamide 11 nanocomposites. *Polymers* **2020**, *12*, 1034–1045. [CrossRef] [PubMed]

38. Gorrasi, G.; Bugatti, V.; Ussia, M.; Mendichi, R.; Zampino, D.; Puglisi, C.; Carroccio, S.C. Halloysite nanotubes and thymol as photo protectors of biobased polyamide 11. *Polym. Degrad. Stab.* **2018**, *152*, 43–51. [CrossRef]

39. Mousavi, S.A.; Sadeghi, M.; Motamed-Hashemi, M.M.Y.; Pourafshari Chenar, M.; Roosta-Azad, R.; Sadeghi, M. Study of gas separation properties of ethylene vinyl acetate (EVA) copolymer membranes prepared via phase inversion method. *Sep. Purif. Technol.* **2008**, *62*, 642–647. [CrossRef]

40. Song, Q.; Cao, S.; Zavala-Rivera, P.; Ping Lu, L.; Li, W.; Ji, Y.; Al-Muhtaseb, S.A.; Cheetham, A.K.; Sivaniah, E. Photo-oxidative enhancement of polymeric molecular sieve membranes. *Nat. Commun.* **2013**, *4*, 1918. [CrossRef]

Comprehensive Review of the Properties and Modifications of Carbon Fiber-Reinforced Thermoplastic Composites

Basheer A. Alshammari [1,*], **Mohammed S. Alsuhybani** [2], **Alaa M. Almushaikeh** [2], **Bander M. Alotaibi** [3], **Asma M. Alenad** [4], **Naif B. Alqahtani** [1] **and Abdullah G. Alharbi** [5]

1   Material Science Research Institute, King Abdulaziz City for Science and Technology, Riyadh 11442, Saudi Arabia; nqahtani@kacst.edu.sa
2   Nuclear Science Research Institute, King Abdulaziz City for Science and Technology, Riyadh 11442, Saudi Arabia; sohybani@kacst.edu.sa (M.S.A.); aalmushaigeh@kacst.edu.sa (A.M.A.)
3   Energy and Water Research Institute, King Abdulaziz City for Science and Technology, Riyadh 11442, Saudi Arabia; bmalotaibi@kacst.edu.sa
4   Chemistry Department, College of Science, Jouf University, Sakaka 2014, Saudi Arabia; amenad@ju.edu.sa
5   Electrical Engineering Department, Faculty of Engineering, Jouf University, Sakaka 2014, Saudi Arabia; agalharbi@ju.edu.sa
*   Correspondence: bshammari@kacst.edu.sa; Tel.: +966-11-481-3707

Abstract: Carbon fiber-reinforced polymers are considered a promising composite for many industrial applications including in the automation, renewable energy, and aerospace industries. They exhibit exceptional properties such as a high strength-to-weight ratio and high wear resistance and stiffness, which give them an advantage over other conventional materials such as metals. Various polymers can be used as matrices such as thermosetting, thermoplastic, and elastomers polymers. This comprehensive review focuses on carbon fiber-reinforced thermoplastic polymers due to the advantages of thermoplastic compared to thermosetting and elastomer polymers. These advantages include recyclability, ease of processability, flexibility, and shorter production time. The related properties such as strength, modulus, thermal conductivity, and stability, as well as electrical conductivity, are discussed in depth. Additionally, the modification techniques of the surface of carbon fiber, including the chemical and physical methods, are thoroughly explored. Overall, this review represents and summarizes the future prospective and research developments carried out on carbon fiber-reinforced thermoplastic polymers.

Keywords: carbon fibers; polymer-matrix composites (PMCs); thermoplastic resin; surface treatment

1. Introduction

In an ever-evolving world, developing new sustainable materials with excellent properties while ensuring they fall into the category of circular economy materials is essential to meet industrial demands and prevent environmental pollution. New materials must overcome existing challenges such as high cost, recyclability, reliability, and energy consumption. For example, such materials for high-performance products need to be lightweight and strong to take diverse loading conditions, such as turbine blades in wind energy applications. They also must not create new problems regarding safety, availability, and processability. One of the main challenges of developing a new product is reducing the weight and increasing load-bearing capability at the same time [1–4]. One of the promising lightweight materials is carbon fiber (CF), characterized by high-strength, high-temperature resistance, and good chemical resistance. CF is non-toxic, low-density, has high wear resistance, and is a non-corrosive, recyclable material with an outstanding strength-to-weight ratio. Overall, it has exceptional thermal, mechanical, and electrical properties. CF is made when source materials such as synthetic polymers (polyacrylonitrile, pitch resin, or rayan spun) are carbonized through oxidation and thermal treatments (hydrolysis) at high temperatures while applying tension with final CF products' appropriate controlled properties.

It is well known that higher carbonization temperatures (up to 2500 °C) can achieve a high carbon content in CF. Today, CF-reinforced polymer matrix composite products are widely used in various applications due to their excellent mechanical, thermal, electrical, structural, and tribological properties. These applications include use in wind energy, aerospace, automobile, infrastructure, marine, and building and construction industries, as well as in sporting goods [4–7].

The global CF-reinforced polymer matrix composites demand is shown in Figure 1. This figure shows significant CF use in several industrial applications. CF can be classified into several categories depending on the properties, precursor materials, and final heat treatment temperatures. They can also be classified based on length or orientation within a matrix as long, short, continuous, and discontinuous fibers. Consequently, the various architectures of CF enable different applications. For example, discontinuous fiber composites are used in high-volume applications where nearly isotropic mechanical properties are desirable. Continuous fiber (CCF) composites are best used in low-volume applications that require maximum mechanical properties in one or two directions, such as impact panels, support beams, and containment vessels. Several studies reported the effect of CF's orientation on the properties of polymer composites [8–18].

Figure 1. Global CFRP consumption in 2018 is categorized by (**a**) application, (**b**) sales, (**c**) region, and (**d**) manufacturing techniques. Global CF consumption in 2020 (**e**) by application and (**f**) estimated worldwide CFRP waste in 2050 from the aeronautical sector by region [6].

Carbon fiber reinforced polymers (CFRP) have been widely investigated. Many types of research have focused on using CF-reinforced thermosetting polymers such as epoxy and polyester resins. Many published reviews have explored state-of-the-art CF-reinforced thermosetting polymers. Moreover, manufactured thermoset composites are unrecyclable due to thermosetting polymers' characteristics. Hence, in large-scale production aspects, they exemplify environmental and economic issues [19]. A recent review by Hegde et al. [17], who reviewed CFRP materials and their mechanical performance, stated that such materials' prices considerably dropped in the 1990s. Subsequently, these materials were utilized in sports equipment. Additionally, between 1998 and 2006, the utilization of CFRP doubled

in the world market. The compound annual growth rate for the utilization of CFRP in 2018 was predicted to be 12.5%.

On the other hand, another class of promising lightweight materials is thermoplastic polymers. They are also called thermosoftening plastics that become modulable at certain temperatures and solid upon cooling. Most thermoplastic polymers are recyclable and easily shaped to the desired requirements. Thermoplastic polymers can be combined with unidirectional CF, discontinuous (short and long CF), or CCF to achieve composite materials with improved mechanical, thermal, and electrical properties in one or multiple directions. Thermoplastic polymers can further be classified as the following: (1) commodity or general plastics such as polyethylene (PE), polypropylene (PP), polystyrene (PS), and acrylonitrile butadiene styrene (ABS) resin. (2) High performance or engineering plastics including polyamide (PA), polyethylene terephthalate (PET), polycarbonate (PC), polyetheretherketone (PEEK), polyetherimide (PEI), polyethersulfone (PES), and polyphenylene sulfide (PPS) [1,4,7]. Table 1 shows some thermoplastic polymers, chemical formulas, and related applications. Therefore, thermoplastic polymers have received vital consideration as a matrix due to the lack of prerequisites in curing stages and less dangerous chemical compositions, and better recycling suitability and mass production capability compared to thermosetting polymers. These characteristics give thermoplastic polymers an advantage over thermosetting polymers. Furthermore, the final composite products have enhanced properties compared to the individual components, i.e., thermoplastic and CF. Carbon fiber-reinforced thermoplastic polymers (CFRTP) offer weight reductions of about 50% compared to steel and 20% compared to aluminum [5,20,21].

Table 1. Types of thermoplastics include commodity and high-performance engineering plastics.

Thermoplastic Polymers					
Commodity Plastics			High Performance Engineering Plastics		
PE	PP	PS	PA	PEEK	PET
$(C_2H_4)n$ Electrical high voltage applications in cables and water storage applications such as pipes and tanks.	$(C_3H_6)n$ Manufacturing parts of automobiles, refrigerators, medical use, clothing, washing machines.	$(C_8H_8)n$ Electrical and thermal insulation applications. Used frequently in the building and construction.	$(CO\text{-}NH)n$ Used in manufacturing fibers and yarns as well as bearings, valves, and gears plus packaging industry.	$(C_{19}O_3)n$ Used in manufacturing parts in automobiles and airplanes including gears, valves.	$(C_{10}H_8O_4)n$ Mostly used in food packaging, bottles, cloth, fibers, tapes, thermal and electrical insulations.

CFRTPs are frequently manufactured using conventional molding approaches, such as injection, rotational, extrusion, vacuum, and compression moldings. Although CFRTP has attracted many researchers recently due to its excellent mechanical and thermal properties, recyclability, flexibility, less production time, and environment-friendly manufacturing, it is still in the development stages for some applications, and there are existing issues with high manufacturing costs to be overcome [1,7,19].

It is well known that synthesized CF materials have a smooth, natural surface with chemical inertness and are non-polar, while the polymer is generally polar. Due to this different polarity, the reinforcing process must be preceded by treating the CF's surface. The treatment is conducted by creating functional groups on the surface of CF to ensure good interfacial adhesion between the polymer (matrix) and the CF (reinforcement), which is required to achieve high-performance composite materials; this is essential to their practical application. Many researchers have noticed the importance of strong bonding between the reinforcement and the matrix for high-performance composites [21–25].

Moreover, during the manufacturing process, many aspects must be taken into account to ensure a high quality of the final product while maintaining an efficient manufacturing process. For instance, the manufactured CF must be wear resistant, handle loads without cracking, and function successfully in a wide range of conditions such as high temperatures

and humidity. Additionally, during the manufacturing process, energy consumption, cost of equipment and labor, environmental sustainability, and large-scale production ease are essential factors that must also be taken into account [4,25–27]. To improve the composites' potential in the mentioned sectors and others, it is important to make a strategic road-mapping activity. Europe has a competitive composites industry. However, many challenges are still to be addressed. A roadmap for the challenges and the industrial uptake of CF and advanced high-performance composites' supply chain in Europe has been published recently by Koumoulos et al. [25].

In this review, we explore the state-of-the-art of CF-reinforced thermoplastic polymers and their future, focusing on the modification methods for CF reinforcement. These possible modification processes are needed to improve the interfacial adhesion between the matrix and the CF. In conclusion, this review offers a comprehensive overview of the CFRTP properties necessary for scientists and decision makers to decide if CFRTP is a suitable material for their objectives and how this composite material could be utilized to achieve a more sustainable and circular economy of the materials for several high-performance applications including in the automotive aerospace industries and in turbine blades used in wind energy.

2. Properties of CFRTP

Researchers and developers have shown a great deal of interest in CFRTP composite due to its tremendous and wide range of properties and the potential of utilizing it in many industrial applications. Moreover, these properties can be altered or enhanced by determining which materials and methods to use. For example, what is the length of the fibers? In which direction are they aligned in the matrix? Was the surface of CF treated or not? Every choice made during the process will affect the composite properties; hence, it will either limit or expand the possibility of utilizing the material in specific industries. Some of these properties are crucial in every thinkable application, such as the mechanical strength of CFRTP.

Meanwhile, enhancing the electrical conductivity needed in specific industrial sectors such as electronics, energy storage, or in the automotive industry, when it is being used as a multifunctional part in addition to electromagnetic shielding effectiveness (EMI shielding effectiveness), is crucial when the composite is meant to be used in an application that requires an electromagnetic attenuation material, for example, when it is used in the wings of airplanes to protect them from lightning strikes. The following sections will explore CF surface modification and CFRTP's properties as reported in the previous literature. It is essential to keep in mind that certain properties were enhanced for specific applications. Therefore, what seems like an excellent result for a particular application might be viewed as an obstacle in another sector, as shown in Figure 2.

2.1. CF Surface Modification: A Primary Factor Affecting the Performance of CFRTP

The interfacial property is a primary factor because when the bond is strong, the load is transferred successfully from the matrix to the CF without causing any damages to the product. The interfacial bond between the CF and the thermoplastic matrix is seemingly weak due to their unidentical polarities. Thermoplastics are mostly polar, while CF is not. Several CF surface treatment methods have been investigated to solve this issue, including both chemicals and physical treatment approaches [7,12,21,22,24,28–37]. It has been reported that the adsorption of some polymeric particles using the electrophoresis process could be used for controlling the interfacial properties and adhesion between carbon fibers and thermoplastic resins through the control surface adhesion between CF and polymer matrix [38]. Figure 3 displays a schematic diagram showing bad and excellent interfacial adhesion between the polymer matrix and CF. Figure 4 shows the most common treatment methods of CF surfaces used in this field.
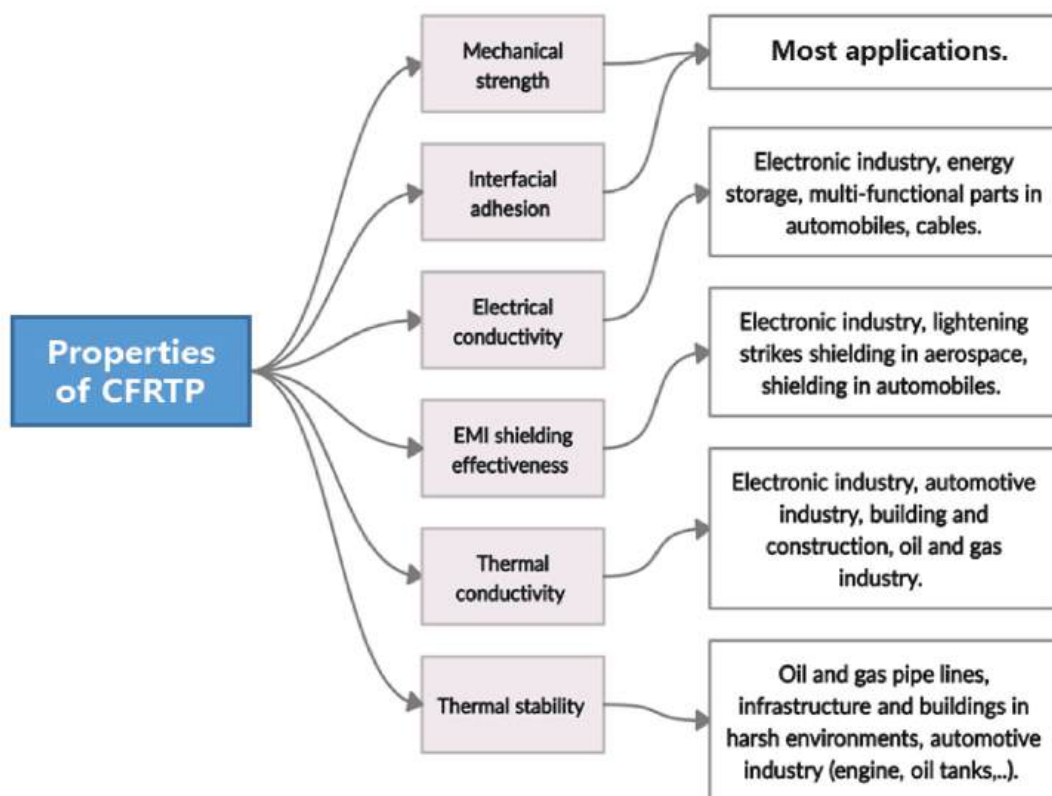
Figure 2. Properties and their connections to different industrial sectors.
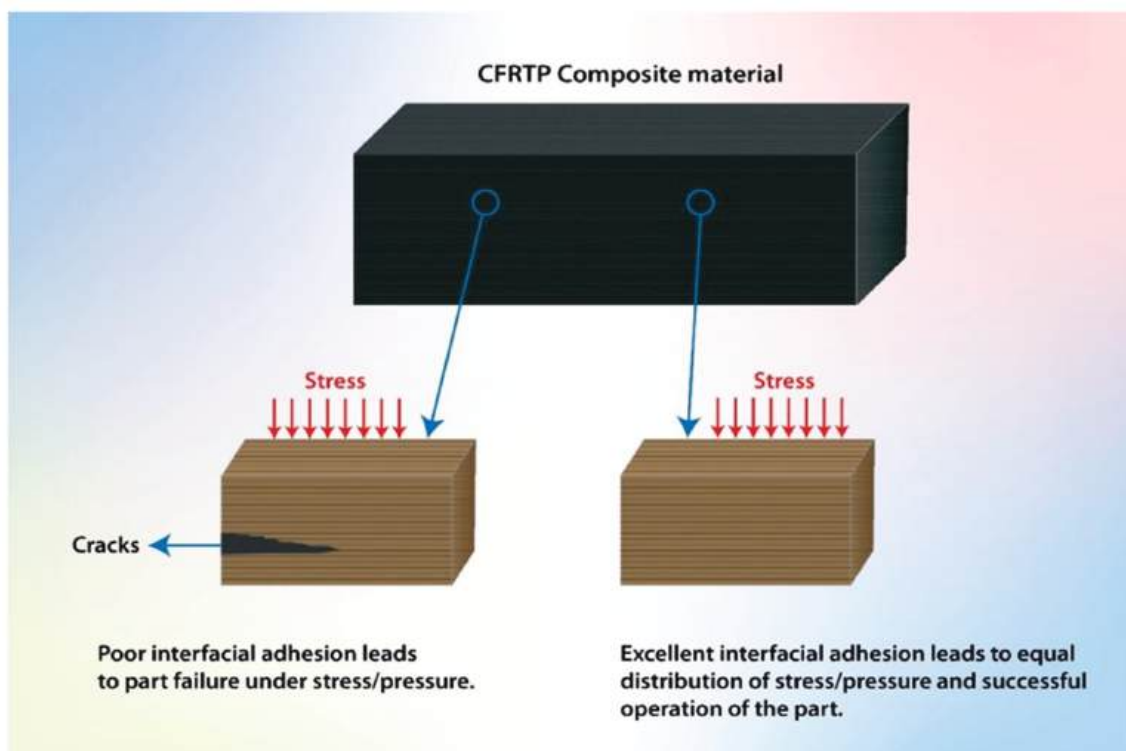
Figure 3. Schematic diagram of poor and excellent interfacial adhesion between the polymer matrix and the reinforcement.
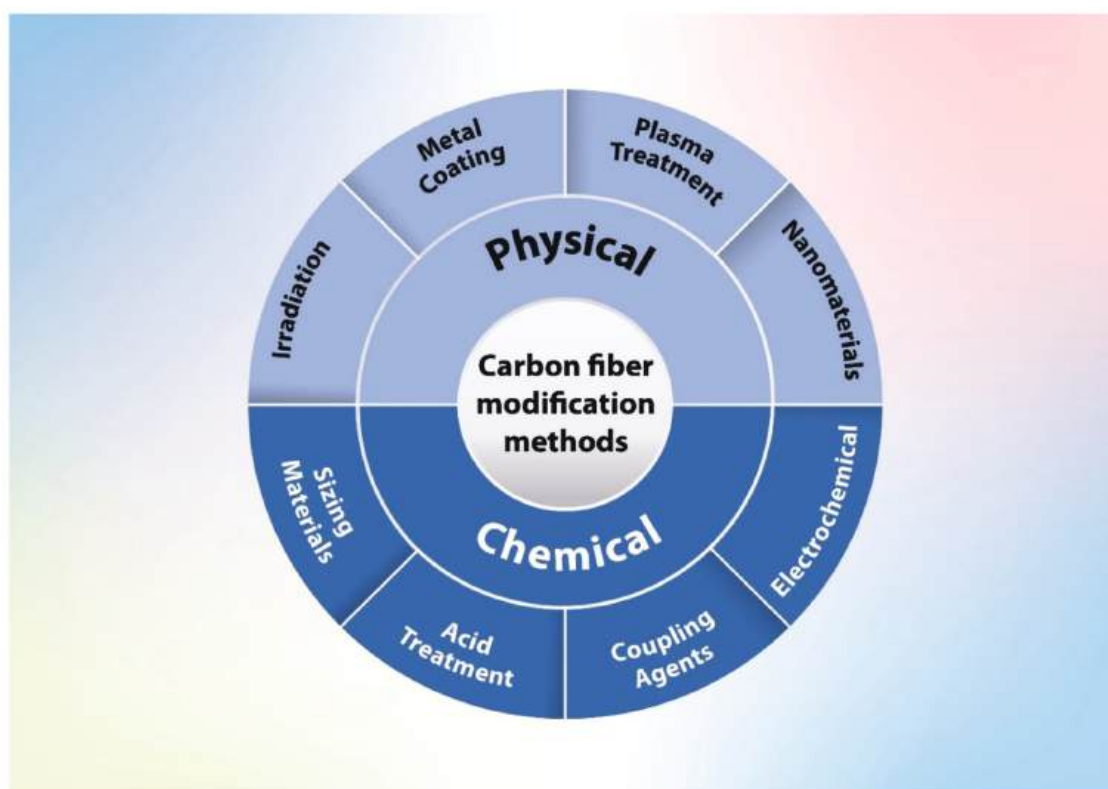
Figure 4. The standard treatment methods of CF surfaces.

2.1.1. Chemical Treatments

Coupling agents and compatibilizers improve the adhesion characteristics in bonds between the reinforcement and matrix in composite materials. For instance, the addition of three types of maleic anhydride grafted polypropylene (MAPP) as coupling agents with different molecular weights and maleic anhydride contents were investigated by Wong et al. [28]. They studied their effects on the interfacial adhesion of recycled carbon fiber (RCF)-reinforced PP composites. They concluded that the compatibility was strongly dependent on the molecular weight and anhydride groups in the coupling agent. Various coupling agents also have been investigated by Han et al. [39], who used a silane coupling agent for CF-reinforced PP composites. The authors concluded that treating the CF surface using coupling agents significantly impacts the CF-PP matrix interaction and composite materials' performance. A similar study has been carried out by Unterweger and his colleagues [35], who evaluated the influence of short carbon fiber (SCF) surface properties and the amount of modified homo PP (MAPP) as a coupling agent. Strong adhesion between CF and PP matrix has been reported by Cho et al. [40], who used a bi-functional group grafted as a coupling agent to modify long carbon fiber (LCF) to enhance PP/LCF composites' mechanical strength. An aminated polyphenylene sulfide (PPS-NH2) as a compatibilizer agent has been investigated by Zhang et al. [41], who studied PPS/CF composites. The results showed that such amination chemical treatments improved the compatibility between the CF and PPS matrix, which enhanced the adhesion at their interface. Additionally, three different PE copolymers as compatibilizers have been used by Savas et al. [42], who fabricated a CF-reinforced high-density polyethylene (HDPE) matrix. It was found that interfacial adhesion depended on the type of copolymers. However, all compatibilizers' addition improved interfacial properties of the investigated composites compared with the composites without any compatibilizers. Park et al. [43] investigated PC/CF composites' interfacial properties using two coupling agents, including tetrahydrofuran-soluble graft copolymers and a water-dispersible coupling agent. His results indicated that both copolymers caused an enhancement in the interfacial shear strength (ILSS) due to chemical

bonding at the interface between the functional group at the surface of CF and the groups in the copolymers. Liu et al. [44] stated that an enhancement of surface energy between CF and PVDF had been achieved after using a novel maleic anhydride grafted PVDF as a coupling agent. In a similar study, three different modification techniques were combined by Tran et al. [45], who fabricated PVDF/CF composites. The PVDF was modified by a maleic anhydride grafted PVDF, and the surface of CF was treated by electrochemical oxidation and/or epoxy sizing materials. The sizing materials are a coupling agent coating coated over a CF surface to improve CF's binding capacity to the polymers. The term sizing is frequently used to remove the confusion between the coupling agent's size and the size relating dimension [36].

Consequently, sizing materials have been applied to modify the surface of CF. The properties of CF-reinforced polyamide 6 (PA6) Composites have been evaluated by Karsli et al. [46], who used different sizing materials including polyurethane (PU), PA, poly-imide (PI), phenoxy, and epoxy/phenoxy. The results obtained in this study confirmed that the selection of sizing materials had a critical effect on the final properties of CF-reinforced polyamide 6,6 (PA6,6) composites. As a result, PA and PU were determined to be suitable CF sizing materials for the PA6,6 matrix compared with phenoxy and epoxy/phenoxy. In an attempt to produce high-quality PA6 incorporated with long CF (LCF) composites, Luo et al. [47] used an isocyanate modified epoxy emulsion and silane coupling agent as sizing treatment of CF first to achieve the desirable interfacial bonding between CF and PA6. Another set of sizing material, i.e., epoxy/phenoxy, PI, and phenoxy and their effect on the mechanical properties of CF-reinforced PC composites, has been investigated by Ozkan et al. [48], who concluded that these sizing materials protected CF during the processing leading to better interactions between sized CF and PC matrix. In another study, PC polymer was used as a sizing agent for PA6/CF composites by Zhang et al. [49]. It was concluded that the sizing alters the chemical composition of the CF surface, including the (oxygen/carbon) O/C ratio, and the percentage of activated carbon atoms gradually increases as the sizing concentration increases. The interfacial strength between CF and PA6 matrix improved remarkably. Considering the composites' interfacial strength, the most effective sizing concentration is determined to be 1.0–1.2%. The transverse fiber bundle test was completed to determine the interfacial adhesion between CF and PA6 matrix. Liu et al. [50] prepared poly (phthalazinone ether ketone) (PPEK)/CF composites, and they used PPEK as a sizing material for CF with three different concentrations: 0.1, 0.5, and 1 wt%. They studied the compatibility between sized CF and PPEK resin using contact angle and found that the uniformly sized CF was more compatible with PPEK resin than unsized CF. A similar result was observed by Wen Bo et al. [51], who investigated the interfacial properties of CF-reinforced PPEK composites. In contrast, Yu et al. [52] reported weak interfacial adhesion between the PC matrix and CF reinforcement after coating its surface by PET following by coupling agent treatment. A similar observation was noted for CF-reinforced PP composites by Unterweger and his colleagues [35]. It has been reported that, due to the complexity of the CF's surface, sizing material composition, and differences in chemistry, a more comprehensive investigation into a cross-section of sizing materials should be conducted in future research [53].

Acid treatments have also been utilized to improve the interfacial properties of CFRTP composites. For example, the chemical interaction of HDPE with CF without using any coupling agent has been reported by Khan et al. [54]. They concluded that significantly proliferated fracture strain, flexural modulus, and flexural strength increased the CF layers in composites up to 20 layers. However, Shengbo et al. [55] reported that treated CF (with nitric acid) is more compatible with the HDPE matrix than the untreated one. They explained that the hydrophilic carboxylic group of benzoic acid reacted with a hydroxyl group of treated CF, which improved their compatibility with the PE matrix. Additionally, Chunzheng et al. [56] reported an enhancement of the interfacial interaction between ultra-high-molecular-weight polyethylene (UHMWPE) and CF after acid treatments. The CF was exposed to nitric acid oxidation treatments and introduced into polyoxymethylene

composites (POM/CF) in an experiment conducted by Zhang et al. [57]. They concluded that the introduction of reactive functional groups, the surface's roughness, and increased disordered carbon on the surface of nitric acid-treated fiber were proved. The nitric acid treatment altered the fiber's surface roughness in a way that significantly enhanced the flexural strength and modulus relative to virgin POM for POM/CF composites. Liang et al. [58] used chloroform as a solvent for treating the surface of SCF.

Two methods of improving the interfacial interaction between CF and PS were investigated by Li et al. [59]. They used the modification of the PS matrix by adding the compatibilizing agent maleic anhydride grafted PS and functionalization of the CF surface with nitric acid. As expected with the surface treatment of carbon fiber, the authors concluded that the surface oxygen and nitrogen content increased, leading to a rise in the overall surface energy of the fibers, which resulted in an excellent interfacial interaction between CF and PS matrix. Both physical and chemical techniques (oxidation and coating) were used by Yan et al. [60], who modified the surface of CF with the oxidation method and coated it with a layer of PA12. The results showed improvements in dispersion and interfacial bonding between CF and thermoplastic matrix after these treatments. Qiujun et al. [61] manufactured UHMWPE/CF composite materials; they used acid-treated carbon nanotubes (CNTs) to enhance the resin, and CF's interfacial adhesion is a combination of physical and chemical treatment methods. CF was immersed in CNTs solution. The results showed a significant improvement in interfacial interaction. This enhancement was attributed to CNTs interlock, which improved the compatibility between the UHMWPE matrix and CF reinforcement.

The electrochemical method was used to modify the CF's surface by Shengbo et al. [55], in which packs of CF were connected to positive electrodes and immersed in nitric acid (HNO_3). Their results indicated an enhancement in the interfacial strength due to CF's functionalized surface. Li et al. [62] found that HNO_3 treatment efficiently improved the CF-reinforced ABS composites' interfacial adhesion. Additionally, ozone treatment was found to increase the oxygen concentration on the CF surface, which improved the interfacial adhesion with the matrix, by Fu et al. [63]. They reported no changes in the other properties, such as the tensile strength of the fibers themselves. Ozone modification and air-oxidation modification were used to improve the interfacial adhesion of CF-reinforced PI composites by Li et al. [64]. They found that ozone treatment effectively improved the interfacial adhesion between CF and PI. The strong interfacial adhesion of the composite made CF not easily detachable from the PI matrix and prevented the rubbing-off of PI, which, accordingly, improved the friction and wear properties of the composite. Similar observations were reported by Li et al. [65] for PA6/CF composites.

2.1.2. Physical Treatments

Furthermore, **plasma treatment** for treating CF surfaces was reported by Montes et al. [66], who studied its effect on the interfacial properties of CF-reinforced PC composites. The authors concluded that the interfacial adhesion between CF and PC increased due to increased functional groups after the plasma treatment. A plasma treatment (oxygen and helium) at atmospheric pressure for different time treatments was conducted by Xie et al. [67]. The researchers found an improvement in the PA6/CF composite systems' interfacial properties due to the increase in oxygen concertation in the surface of CF, roughening, and its energy surface. Additionally, microwave plasma treatments on CF have been reported by Lee et al. [34]; they reported an improvement in the interfacial properties of CFRTP composites due to the enhancement in the mechanical interlocking between the modified CF and cyclic butylene terephthalate (CBT) matrix. Lee et al. [68] investigated the effects of RCF plasma treatment at dry air and CO_2 plasma conditions. They reported that the gas types and exposure time are the main factors for the modification's efficiency for improving the adhesion properties. Recently, the effect of the atmospheric plasma treatment of RCF-reinforced PP composites at different plasma powers was investigated by Altay et al. [69]. Similarly, Han et al. [39] concluded that the hydroxyl group's density

was the highest among the specimens with 1 min of plasma treatment, but it reduced the plasma treatment time (at 3 min). Moreover, it has been reported that low-pressure plasma treatment was found to increase the amount of oxygen on the CF's surface [67,69].

Additionally, the irradiation method is to enhance the adhesion performance of CFRTP composites. For example, an irradiated PP was used by Karsli et al. [70] as a compatibilizer for fabricating PP/CF composites. Their results concluded that the irradiated PP as a compatibilizer enhanced the interfacial adhesion between the CF and PP matrix, leading to improved mechanical properties. A similar achievement for adhesion has been reported by Mao et al. [71]. They used amino-functionalized CF using an electron beam irradiation technique, which gave a better surface and interfacial properties of their composites. An overview of new oxidation methods for PAN-based CF conducted by Shin et al. [24] selected PAN precursor fibers as the subject of focus and studied three major categories of radiation-induced polymer stabilization processes: electron beam, γ-radiation, ultraviolet, and plasma treatment. Therefore, it is concluded that further development of these radiation-based oxidation processes can significantly improve the speed of CF production and reduce its environmental impact. Additional recent studies by Jung et al. investigated the radiation effect on CF-reinforced HDPE composites [72], who concluded that the adhesion between CF and HDPE was improved, and the surface properties of CF HDPE were changed by irradiation. It was also supposed that irradiation provided two main effects on CFRTP. One was cross-linking of thermoplastic resin for efficient load transfer from resin to CF and the formation of surface functional groups and attractive interaction of these functional groups at the fiber and matrix interface.

Materials coating is also one of the methods that have been used to improve interfacial adhesion. For instance, metal coating with Ni-plated CF improves the desirable properties and the interfacial adhesion reported by Lu et al. [73], who manufactured different commodity plastics and reinforced CF composites, respectively. Still, this is not a favorable choice due to increased possibilities of corrosion occurrence. This degradative process is attributed to the electrically conductive nature of CF and its surface chemistry. The Ni-plated CF was used as a tracer to investigate the CF orientation in thermoplastic/CF composites by Nagura et al. [10]. Ofoegbu et al. [33] carried out a recent review that highlighted the potential corrosion challenges in multi-material combinations containing CFRP, the surface chemistry of carbon, its plausible effects on the electrochemical activity of carbon, and, consequently, the degradation processes on CFRP.

Furthermore, there are examples of grafting nanoparticles to the surface of CF to enhance the interfacial adhesion between CF and thermoplastic matrices. For instance, excellent interfacial adhesion has been reported by Li et al. [74], who investigated the performance of PES/SCF composites. They coated CF's surface with graphene oxide (GO) and reported a remarkable improvement in the interfacial adhesion properties. Similar results were observed by Wang et al. [75], who investigated the effect of GO coating on PP/SCF composites' properties. These improvements were attributed to the excellent progress in the chemical and mechanical interaction (interlocking) between GO on the surface of CF and the PP matrix as superior interfacial bonding. Yongqiang et al. [76] deposited CNTs and GO on CF. They reported an enhancement in the interfacial adhesion, roughness, and wettability of the CF surface to increase adhesion between the PI matrix and the CF due to hydrogen bonding and mechanical interlocking.

Ma et al. [77] prepared PA6/CF, and to enhance compatibility between CF and PA6, they modified the surface of CF by grafting GO on its surface using a coupling agent. The results showed an enhancement in the interfacial properties compared to untreated specimens. Li et al. [78] coated SCF with GO to enhance the PES/CF composite's interfacial properties. They found an enhancement in the composite's interfacial and mechanical properties compared to uncoated SCF with 0.5 wt% as the highest concentration of GO to enhance the composite properties. Irisawa et al. [79] studied the effect of nanofiber for CF-reinforced PA6 and concluded that nanofiber's addition increased the bending properties of such composites. These results showed that nanomaterials are a promising

candidate for improving interfacial adhesion between thermoplastic and CF to achieve maximum mechanical properties. A better interfacial adhesion for CF-reinforced vinyl ester composites was observed by Li et al. [80]. They concluded that better interfacial adhesion between CF and PEEK matrix was noticed after adding/grafting CNTs to the CF-reinforced composites' surface. An article that reviews interfacial bonding techniques used to increase the fiber-matrix interfacial bond strength of CF-reinforced polyaryl ether ketones (PAEK) polymer has been published by Veazey et al. [81].

2.2. Mechanical Strength and Modulus of CFRTP

Due to excellent mechanical properties, the use of CF has grown remarkably. The CF-reinforced thermoplastic composites enhanced mechanical properties of final composites, including tensile strength, tensile modulus, flexural modulus, flexural strength, creep resistance, wear resistance, and toughness alongside other properties such as thermal and electrical conductivity. In the automotive, aerospace, and many other manufacturing industries, the usage of CF-reinforced polymers has rapidly improved in the last ten years due to the features mentioned above. However, the CF-reinforced composites have low wettability with most polymers because of their nonpolar surface characteristics. The low-interfacial bonding strength between the fibers and polymer matrices results in inadequate mechanical performance in composites [17,35,56,63,69]. The apparent ILSS of the composite is usually used to characterize adhesion quality between the fiber and matrix [39,51,56]. Likewise, a transverse fiber bundle test technique has been proposed to assess the fiber/matrix interfacial adhesion without making composite materials [48,82].

The ILSS increased by 300% for PP/SCF composites prepared with the addition of CNTs and MAPP as a coupling agent, as reported by Arao et al. [83]. Additionally, an increase of 115.4% and a 27% increase in impact toughness have been reported after grafting CNTs on CF as hybrid fibers for a CF-reinforced PPEK composite by Liu et al. [84]. Wen Bo et al. [51] reported that about 80% of the apparent ILSS in the PPEK/CF composite system was attributed to residual radial compressive stress at the fiber/matrix interface. A similar conclusion has been reported by Qiujun et al. [61], who studied the mechanical properties of CF-reinforced UHMWPE composites and stated that a 70% increase in ILSS was observed. Ma et al. [77] found that the ILSS increased by 40.2% of PA6/CF composites when GO was grafted onto CF's surface compared with unmodified composites. Li et al. [78] investigated the mechanical properties of PPS/SCF composites. The maximum improvement was 12.1% and 31.7% for the tensile strength and Young's modulus, and the maximum gains were 12.4% and 17.3% for the flexural strength and flexural modulus, respectively. These improvements were attributed to existing of GO in the composites. Khan et al. [54] reported that flexural properties of HDPE increased significantly upon increasing the layer of CF in the composites. Wang et al. [75] found that all flexural, tensile, and impact strength of PP increased by about 43% upon addition of 10 wt%.

Han et al. [39] reported an increase of up to 47.8% in ILSS in treated composites using coupling agents followed by plasma treatments compared with the untreated composites. Other mechanical properties were also enhanced after the treatment. A study was carried out by Tran et al. [45] in which they concluded that the ILSS increased by 184% due to the enhancement in the interfacial bonding for CF-reinforced poly (vinylidene fluoride) (PVDF) composites. Liu et al. [50] reported that CF improved the ILSS after coating its surface with PPEK. The authors also stated that the value of ILSS for sized CF was about 51.50 MPa, higher than the unsized CF, which was around 39.50 MPa.

Moreover, the enhancement of surface energy and mechanical interlocking between CF and PVDF has been investigated by Liu et al. [44]. The authors noticed that the surface of CF roughness and H-bonding improved and wettability of the treated CF-reinforced PVDF matrix. Additionally, they found that the flexural strength and modulus of the composites containing modified CF were also improved by 47% and 74%, respectively, compared to unmodified CF did. Connor et al. [85] found an increase in ILSS of 33% for the CF-reinforced nylon composites. Park et al. [43] reported an improvement of ILSS

up to 70% for PC/CF composites. These variations in ILSS values could be attributed to several factors including interfacial area properties, matrix type, CF type, CF loading, and surface treatments.

Li et al. [86] studied the tensile properties of a treated CF-reinforced ABS matrix and reported that when the oxidized SCF content increased in the ABS matrix from 10 to 30 wt%, the tensile strength and tensile modulus improved significantly. However, these properties enhanced dramatically when PA6 was blended with ABS. Similar observations were reported by Li et al. [62] for an ABS/AP6 blend composites reinforced SCF system. A similar observation was noted by Anish et al. [87], who found that CF enhanced ABS's hardness and compression strength in different wt%. However, ABS/CF in 30 wt% exhibited the best mechanical results. These improvements were due to better enhancements in the surface properties of CF reinforcement.

A different blend of polymers was fabricated by Zhou et al. [88], who studied the effect of CF reinforcement (5, 10, and 15 wt%) on the mechanical properties of PA6/PPS blend composites. This study's mechanical results showed that the strength, modulus, wear resistance, and hardness of the composites improved significantly, although the strain values at break and impact strength were slightly decreased. A similar study was carried out by Luo et al. [89], who studied the effect of SCF on composites based on a PPS/polytetrafluoroethylene (PTFE) blend as a polymer matrix. They concluded that the strength, modulus, hardness and wear resistance, the elongation at break, and hardness of the PPS/PTFE composites were improved by introducing 15 vol.% of CF compared with the unreinforced blend matrix. Different composites based on polymer blends have been carried out by Zheng et al. [90], who prepared a blend of PEI/PES thermoplastics and introduced them into poly(phthalazinone ether sulfone ketone) (PPESK) polymers as a matrix and CCF as the reinforcement of PPESK/CF composites. They investigated both PPESK/PEI/CF and PPESK/PES/CF composites' mechanical properties. The results indicated that the mechanical properties were enhanced. The improvement was attributed to good interfacial adhesion and low porosity resulting from PEI and PES's addition into the PPESK matrix. This also improved the rheological properties of the PPESK matrix and gave enough impregnation during the preparation process of the composite materials.

Sharma et al. [15] studied the effect of the CCF orientation on PEI/CF composites' mechanical properties with a loading of 80 vol.% CF, and the orientation angles were (0°, 30°, 45°, 60°, and 90°). Their results indicated that CF orientation influenced mechanical properties remarkably, including Young's modulus, toughness, Poisson's ratio, and percentage strain with respect to the loading direction. For instance, composites having CF in a direction parallel to loading (0°) proved most beneficial, while fibers beyond 45° deteriorated in performance excessively. Fibers at 75° were shown to have the poorest strength properties, followed by those at 90°. In conclusion, the aligning of fibers in a proper direction leads to better mechanical properties.

Luo et al. [47] prepared LCF-reinforced PA6 composites. The authors concluded that the tensile strength of PA6 composites containing LCF was much higher than the tensile strength of other composites having SCF by 24%. These enhancements were attributed to the excellent adhesion properties between PA6 and CF and the high aspect ratio of such LCF. The optimal loading of CF and sizing was 20 and 22 wt%, respectively, which exhibited the highest flexural and tensile strengths of PA6/LCF composites.

The tensile properties of poly(trimethylene terephthalate) (PTT)/CF composites have also been investigated by Vivekanandhan and colleagues [91], who reported an enhancement in mechanical properties as the concentration of CF increased. The addition of 30 wt% of CF into PTT resulted in significant tensile enhancement up to 120% and flexural strength up to 30% compared to neat PTT.

Yan et al. [60] fabricated PA12/CF composites to investigate their mechanical properties upon the addition of CF loading. They concluded that the incorporation of 50 wt% CF greatly enhanced both flexural strength and modulus of the investigated PA12/CF composites by 114% and 243.4%, respectively. Yan et al. [92] reported the flexural properties

of PA6/CF composites. They stated that the addition of 30 wt% CF significantly enhanced flexural strength and modulus by 208% and 438%, respectively. These improvements in the flexural properties were attributed to good interfacial bonding, filler dispersion, and surface CF chemistry after surface treatment of CF.

Ma et al. [93] prepared a higher performance unidirectional CF-reinforced PA6 thermoplastic composite and investigated its mechanical properties. The results indicated that excellent tensile properties, including tensile modulus and strength of PA6/CF composites and uniform CF distribution, have been proved. Similar results have been reported for CF-reinforced nylon composites by Hassan and colleagues [94] and Dickson et al. [16].

A comparison between the mechanical behavior of PA6/CF and PA66/CF composites was carried out by Botelho et al. [95]. They concluded that both matrices showed slight mechanical behavior improvements, including tensile, compressive, and ILSS behavior when reinforced by both fabric and unidirectional CF. The microscopic damage progress in both composites was observed through optical and scanning electron microscope techniques. It was shown that shear failure at the/PA/CF interface was mostly responsible for damage development, initiated at relatively low stress.

The performance of plastic gear made of CF-reinforced PA12 was investigated and compared with PA6/CF, PA66/CF, and PA46/CF composites by Kurokawa and colleagues [96]. The authors reported that the PA12/CF composites having grease showed an excellent load-bearing characteristic among all investigated PA composites, and this load increased by increasing the molecular weight of PA12.

Wu and coworkers [97] reported that the interlaminar fracture toughness and transverse properties enhanced the PES matrix's molecular weight. Their results also concluded that the CF distribution was uniform and with reasonably good wetting with the investigated matrix. This resulted in a higher longitudinal flexural modulus and PES/CF composites' strength compared with the pure PES matrix.

Numerous studies have focused on the relationship between fiber length and the mechanical performance of CFRP. For instance, Karsli et al. [98] studied the effect of both loading and size of CF-reinforced PA6 on the tensile properties of resultant composites. Their results showed that increasing the CF loading led to improvements in tensile strength, modulus, and hardness, but reduced strain at the break values of composites. Meanwhile, the investigated length ranges of CF (0 to 50 μm) had no effect on these mechanical properties except that strain at break was improved. Kim et al. [99] analyzed the impact of CF length, CF loading, and processing speed on PU/CF composites' mechanical properties. They concluded that these parameters have a substantial effect on the mechanical properties of the composites. It was noticed that the CF length decreased from 163 to 148 μm after the extrusion process. This indicates that the manufacturing process impacts the final properties of the prepared composites. Li et al. [82] stated some details about interfacial parameters between such materials, which may be useful for further simulation studies for optimizing all related parameters that affect mechanical properties such as CF length, loading and processing conditions, annealing temperature, and cooling rate. They used a transverse fiber bundle test which was proposed to assess the fiber/matrix interfacial adhesion without manufacturing composite materials. Furthermore, fiber length distributions have been reported to depend on the processing conditions by Fu et al. [100]. They investigated the fracture resistance of PP/CF composites under Charpy impact load. They concluded that the composite impact resistance was shown to depend on the CF's length and hence on processing. The notched Charpy impact energy of the PP/CF composites increased with decreased CF loading in the PP matrix. Similar observations have been reported by Rezaei et al. [101], who studied the effect of fiber length on the thermomechanical properties of SCF-reinforced PP composites. Similarly, Unterweger et al. [102] evaluated the effect of fiber length distributions and content on SCF-reinforced PP polymer's mechanical properties. They concluded that tensile strength, tensile modulus, and impact strength were improved upon the increasing amount of SCF despite reducing fiber length, tensile strength, tensile modulus, and impact strength. The longest CF in the final composites

was reported in their study. This result seems to contrast with the result obtained by Kim et al. [99], who noticed that the tensile strength of the PC/CF composites decreased. This reduction was attributed to the decrease in the CF length after the fabrication process.

Ozkan et al. [48] considered the effect of SCF on tensile strength and modulus of the PU matrix. They found that the unseized CF improved the tensile strength and modulus of composites by 105% and 450%, respectively. In comparison, sized CF improved the tensile strength and modulus of composites by 150% and 540%, respectively, compared to the simple PU matrix.

Different thermoplastic composites were synthesized by Hwang [103], who investigated the effect of CF loading on the tensile strength of foamed and solid polybutylene terephthalate (PBT) composites. The author stated that the addition of 8 wt% loadings of CF to PBT resulted in improved tensile strength; however, further addition of CF led to a reduction in such property. This reduction is attributed to agglomeration/aggregation of CF into the PBT matrix and a reduction in the foams' cell size.

Gabrion et al. [104], who fabricated CF-reinforced PI composites, investigated the influence of temperature on the tensile properties. The authors concluded that the tensile strength was higher than 1200 MPa in the fiber direction at a temperature range varying from -50 to 250 °C but with low ILSS at high temperatures. The material also had outstanding fatigue strength under tension in this material direction.

Yu et al. [52] reported that the strength and modulus of shopped CF-reinforced PET composites continuously increased along with a clear ductile–brittle transition by increasing the amount of CF with different length and aspect ratios. They stated that the tensile strength and modulus of PET/CF composites increased with an increasing aspect ratio of CF (under the same loading of CF); this increase accompanied the decreased impact strength and elongation at break 20 wt% of the CF. Hamilton et al. [105] reported that 20 wt% of CF could increase thermoplastic composites' wear resistance based on the PEEK matrix. Similar observations have been noted by Karsli and Aytac [106], who reported an enhancement of wear properties by incorporating CF into PEEK composites.

Kada et al. [107], who investigated the effect of tensile properties of SCF-reinforced PP composites, reported that a 30 wt% SCF content in the PP matrix improved the tensile strength and modulus of composites by 455% and 168%, respectively, when a MAPP was used as coupling agent during the preparation process. However, without MAPP, although the tensile modulus increased, the tensile strength decreased due to poor adhesion between inert hydrophobic CF and the hydrophobic PP matrix. The MAPP treatment had a direct influence on the mechanical properties of the composite. Do et al. [108] investigated the effect of PP on PA6/CF composites' mechanical properties. Their results showed that the investigated mechanical properties, including ultimate tensile strength, elastic modulus, and elongation at break, were exceptional for the composites containing PP compared to those composites without PP as a coupling agent. The composite with 30% PP had the lowest ratio of tensile strength and elastic modulus reduction by 18% and 15%, respectively, compared with the composites with 0% PP loading.

Cho et al. [40] analyzed the tensile and flexural strengths of PP/LCF thermoplastic composites by increasing the adhesion between the PP and CF matrix. The mechanical strength of the resulting composite was significantly enhanced. These improvements can indicate better interfacial bonding between fiber and matrix as discussed earlier in Section 2.1.

Cho et al. [109] investigated the mechanical properties of polyketone (PK)/CF novel composites, and they found an enhancement in Young's modulus of 520% and tensile strength by 189% at 30 wt% CF content. In contrast, a significant decrease in the elongation at break was observed in the PK/CF composites even at very low loading (5 wt%) of CF.

The tensile strength of the as-received and plasma-treated CF-reinforced CBT composites was enhanced by ~362.5% and 436.3%, respectively, compared with that of the pure CBT matrix as reported by Lee et al. [34]. They incorporated 70 vol.% of CF into CBT without any defects and pores in the final composites. However, Tobias et al. [110] reported a 60% increase in the strength of the CF-reinforced CBT matrix when the latter

was chemically modified with a small number of chain extenders. They stated that the composites samples show poor ILSS, and cracks were observed.

Different PC/vapor-grown carbon fiber (VGCF) composites prepared by Choi et al. [111] were investigated for their mechanical properties before and after the CF rolling process. Their results indicated that the mechanical properties improved significantly due to CF's orientation within the PC matrix. In contrast, Carneiro and colleagues [112] found that the tensile properties improved after adding VGCF into the PC matrix, but the impact resistance property was reduced significantly. They suggested that the rolling process could be used for further improvements in mechanical properties. Recently, Maqsood et al. [113] characterized both CCF and SCF's influence on the tensile strength of CF-reinforced poly-lactic acid (PLA). They concluded that the tensile strength and flexural stress increased by 460% and 121%, respectively, for composites containing CCF compared to those having SCF.

Li et al. [114] reviewed the analysis of the properties of the CF and the tensile and dynamic mechanical properties of the UHMWPE hybrid composites (charcoal wood and CF in the matrix). Young's modulus with tensile strength was significantly augmented with increasing loading of CF. They increased by 415% and 46% correspondingly. However, the elongation/strain at break decreased substantially by 95%. There is no doubt that whenever we increase CF concentration, it always increases the storage modulus. The storage modulus reached ~20 GPa for the samples containing 8 wt% CF compared to ~2 GPa for unreinforced UHMWPE/charcoal samples at room temperature.

Unterweger et al. [115] provided a good overview of the mechanical and physical properties, cost, and reinforcement effectiveness of synthetic and thermoplastic fibers and their characterization. Most materials are affected in some manner by environmental effects such as temperature and humidity. The properties and characteristics may change, and the material could be degraded. Research has explored this aspect, and it has shown several outcomes [93,116–121]. Table 2 summarizes the variety of composite materials, modification techniques, and the obtained mechanical properties of CFRTP over the last decade.

Table 2. The type of thermoplastic polymer and CF, modification techniques for CF, and mechanical properties of a variety of CFRTP composites.

Composite Material	CF Modification Method	Mechanical Properties	[Reference No.] (Publication Year)
PEI/CCF	Not mentioned	Young's modulus, toughness, and % strain with respect to the loading direction were increased remarkably.	[15] (2010)
PP/RCF	Coupling agents followed by plasma treatments	An increase of up to 47.8% in ILSS.	[28] (2012)
CBT/CF	Microwave plasma treatments	Tensile strength enhanced by ~436.3%.	[34] (2014)
PP/SCF	Sizing materials followed by plasma treatment. A coupling agent was added to all samples	An increase of up to 47.8% in ILS.	[39] (2014)
PP/LCF	Coupling agent	The mechanical strength of the resulting composite was significantly enhanced.	[40] (2014)
PVDF/CF	Coupling agent	Flexural strength and modulus improved by 47% and 74%, respectively.	[44] (2016)
PA6/CF	Coupling agent and sizing treatment	The tensile strength of composites containing LCF was much higher than other composites having SCF by 24%.	[47] (2014)
PC/CF	Sizing materials	The tensile strength and modulus improved by 150% and 540%, respectively.	[48] (2014)
PPEK/CF	Sizing materials	The value of ILSS of sized CF is about 51.50 MPa, higher than the unsized CF, which was around 39.50 MPa.	[50] (2013)

Table 2. *Cont*.

Composite Material	CF Modification Method	Mechanical Properties	[Reference No.] (Publication Year)
PPEK/CF	Sizing materials	About 80% of the ILSS in PPEK/CF composite system was attributed to residual radial compressive stress at the fiber/matrix interface.	[51] (2013)
PC/shopped CF	Material coating followed by coupling agent treatment.	The strength and modulus of composites continuously increased along with a clear ductile-brittle transition by increasing the amount of CF.	[52] (2018)
HDPE/CF	Without using any coupling agent	Flexural properties increased significantly upon increasing the layer of CF in the composites.	[54] (2016)
POM/CF	Oxidation treatments	The flexural strength and modulus were enhanced remarkably.	[57] (2015)
PA12/CF	Oxidation method followed by coating with a layer of PA12	The flexural strength and modulus improved by 114% and 243.4%, respectively.	[60] (2011)
UHMWPE/CF	Acid treatment	A 70% increase in ILSS was observed.	[61] (2017)
PA6/ABS/SCF	Acid treatment	The tensile strength and tensile modulus improved significantly. However, these properties were enhanced dramatically when PA6 was blended with ABS.	[62] (2011)
PI/CF	Ozone modification and air-oxidation modification.	Improved friction and wear properties of the composite.	[64] (2010)
PP/RCF	Different plasma powers treatment	The tensile and flexural strength values of composites increased considerably by 17% and 11%, respectively, at 100 W.	[69] 2019
PP/CF	Irradiated PP as compatibilizer agent.	The tensile strength improved by 30%.	[70] (2013)
PP/SCF	Material coating	All flexural, tensile, and impact strength increased by about 43%.	[75] (2018)
PA6/CF	Material coating	ILSS increased by 40.2%.	[77] (2018)
PES/CF	Material coating	The maximum improvement was 12.1%, 31.7%, 12.4%, and 17.3% for the tensile strength, Young's modulus, flexural strength, and flexural modulus, respectively.	[78] (2015)
PP/CF	Material coating	The ILSS increased by 300%.	[83] (2013)
PEEK/CF	Material coating	An increase of 115.4% and a 27% increase in impact toughness.	[84] (2017)
Nylon/CF	Not mentioned	An increase in ILSS of 33%.	[85] (2019)
ABS/CF	Not mentioned	An enhancement in hardness and compression strength was reported.	[87] (2014)
PPS/CF	Not mentioned	The strength, modulus, wear resistance, and hardness were improved significantly, although the strain values at break and impact strength were slightly decreased.	[88] (2013)
PTFE/CF & PPS/CF	Sizing materials	The strength, modulus, hardness and wear resistance, the elongation at break, and hardness were improved.	[89] (2016)
PTT/CF	Sizing materials	A significant tensile enhancement of up to 120% and flexural strength up to 30% were observed.	[91] (2012)

Table 2. *Cont*.

Composite Material	CF Modification Method	Mechanical Properties	[Reference No.] (Publication Year)
PA6/CF	Not mentioned	The addition of CF significantly enhanced flexural strength and modulus by 208% and 438%, respectively.	[92] (2014)
PA6/CF	Not mentioned	The results indicated that excellent tensile properties, including tensile modulus and strength and uniform CF distribution, have been proved.	[93] (2018)
PA6/CF	Not mentioned	An increasing CF loading led to improvements in tensile strength, modulus, and hardness, but reduced strain at break values of composites. Meanwhile, the investigated length ranges of CF (0 to 50 μm) had no effect on these mechanical properties except that strain at break was improved.	[98] (2013)
PP/SCF	Sizing materials	Tensile strength, tensile modulus, and impact strength were improved upon the increasing amount of SCF despite reducing fiber length, tensile strength, tensile modulus, and impact strength.	[102] (2020)
PBT/CF	Not mentioned	Improvements in tensile strength up to a certain amount of CF; however, further addition of CF led to a reduction in such property.	[103] (2016)
PI/CF	Not mentioned	The tensile strength was higher than 1200 MPa in the fiber direction on a temperature range varying from −50 to 250 °C but with low ILSS at high temperatures.	[104] (2016)
PEEK/CF	Not mentioned	Improvements in wear resistance were reported.	[105] (2019)
PEEK/CF	Coupling agent	The tensile strength and modulus increased by 455% and 168%, respectively.	[107] (2018)
PA6/CF	Coupling agent	The ultimate tensile strength, elastic modulus, and elongation at break values were exceptional.	[108] (2016)
PK/CF	Not mentioned	An enhancement in Young's modulus of 520% and in tensile strength by 189%. In contrast, a significant decrease in the elongation at break was observed in the PK/CF composites even at very low loading.	[109] (2019)
PLA/SCF&CCF	Not mentioned	The tensile strength and flexural stress increased by 460% and 121%, respectively.	[113] (2021)
UHMWPE/CF	Not mentioned	Young's modulus with the tensile strength significantly increased by 415% and 46%, correspondingly. However, the elongation/strain at break decreased substantially by 95%.	[114] (2014)

2.3. Electrical Conductivity and Electromagnetic Shielding Effectiveness of CFRTP

Besides the great mechanical properties of CF, it can be used for other tasks based on its multifunctional properties, including electrical conductivity and electromagnetic interference shielding. These properties of CF used as reinforcement in composite structures are the basis for several multifunctional applications. The significance of carbon is the extremely stable hexagonal plane grid and the planes' delocalized electron cloud. The

deformation and separation of the hexagonal carbon rings require high energy, which provides the CF's strength at the macro level. The free electrons in the electron cloud make it an excellent electrical conductor. The electrical resistance of CFRTP depends mostly on the type of material used (precursors), the manufacturing conditions, the crystalline structure of polymer matrices, and treatments [2,3].

Lu et al. [73] studied the preparation of CF-filled ABS composites and investigated their electromagnetic interference (EMI) shielding effectiveness (SE) and electrical conductivity with and without metal coating (thickness of the layer was 0.2–0.5 μm). With the increase in the CF content, the composites' resistivity with the nickel-coated CF decreased. The further decrease in the composites' resistivity with the same nickel-coated CF was higher than that with the uncoated CF. They reported a resistivity of around 10–4 Ωcm, an order of magnitude less than that for the uncoated fibers. The composites' EMI SE with 10 vol.% content of the CF coated with nickel was found to be 50 dB.

Similarly, Huang et al. [122] reported an enhancement in PC/ABS/nickel-coated CF composites' EMI shielding. The best EMI shielding effectiveness was about 47 dB. The same group also reported some promising results in enhancing the EMI shielding of a Ni-coated ABS/CF composite. The best **EMI shielding effectiveness** was 44 dB [123]. A similar composite was prepared by Nishikawa et al. [124], who reported the electrical properties with different CF loadings. The composites' electrical resistivity decreased with an increase in the CF-reinforced ABS plastic content, and the critical volume fraction (percolation threshold value) was found to be 0.11 vol.%. The EMI SE was not as expected due to the composites' low conductivity in the out-of-plane direction.

Rahaman et al. [125] reported the EMI SE of SCF-reinforced ethylene-vinyl acetate (EVA) and acrylonitrile butadiene copolymer and their blend composites. They reported a marginal increase in EMI SE with the increase in electromagnetic radiation frequency, but a sharp increase was observed with an increase in the SCF contents of 20 phr. Das et al. [126] reported an SE of 34.1 dB at a similar fiber loading (30 phr) in NR- and EVA-based composites. The authors stated that the composites having a CF loading of ≥ 20 phr could be used for EMI shielding applications.

Zhang et al. [127] aimed to improve the blend composite's electrical properties by using an electric conductive reinforcement, VGCF. They used HDPE and isotactic polypropylene (iPP) (50/50) as a matrix. They reported an enhancement in the electrical conductivity and lower percolation threshold of CFRTP when the CF loading was 1.25 parts per hundred parts resin (phr), compared with the neat polymers. To explain the results, SEM was used, and they attributed the improvements to the particular locations of CF; in other words, the dispersion of the filler within the matrix plays a role in enhancing the composite's properties. A similar VGCF was utilized by Choi et al. [111], who reported the electrical conducting properties of PC composite sheets reinforced with VGCF reinforcement. The composites' resistivity was found to be 10 and 0.5 Ωcm at a VGCF content of 10 and 25 wt%, respectively. The dispersion of the VGCF in the polymer matrix was found to be homogeneous, and the electrical conductivities of the composites increased. Simultaneously, percolation threshold values decreased with an increase in the loading of the VGCF, leading to better conduction networks.

An ultra-low percolation threshold value was observed by Zhao et al. [128], who studied the effect of CF with a large aspect ratio of carbon black on the conductive properties of the PP composites. The addition of 0.155 vol.% CF resulted in a significant decrease in the percolation threshold value. The reduction in the percolation threshold observed in the scanning electron microscope was ascribed to the increase in interparticle contacts, resulting in developing a shish–calabash-like conductive network. A similar morphology observation was reported by Cipriano et al. [129], who investigated the influence of carbon nanofibers on the electrical properties of PS composites. They found that the unfilled PS matrix's electrical conductivity was around 10–8 S/cm, which increased to about 10^{-2} S/cm for the composites filled with 15 wt% carbon nanofibers. The authors also reported that annealing processes could improve the electrical conductivities of composites

at high temperatures. Similarly, Thongruang et al. [130] studied the effect of graphite filler on the HDPE/CF composites system. They demonstrated that the addition of graphite to the composites increased the conductivity compared to the composites without graphite. The conductivity increased from ~0.1 (Ωcm) to 5 (Ωcm) for a composite having 10 wt% CF compared to HDPE matrix; however, it jumped to 18 (Ωcm) for a composite containing 10 wt% CF and 50 wt% graphite. Microscopic analysis of the composites showed that the CF depicted favored alignment according to their length compared to the composite film's thickness.

Liang et al. [58] reported composites' resistivity prepared by incorporating SCF in ABS resin matrix. The ABS composites with an SCF loading of up to 2 vol.% showed no improvement in the conductivity of the composites. However, above 2 vol.%, the composites' resistivity showed a steep decline in resistivity from 10^{13} to 8.83 Ωcm and 10^{14} to 884 Ωcm for the 6 mm and 3 mm length of SCF, respectively, thereby providing good electrical conductivity to the resultant composites. The ABS composites rapidly changed from the inductor phase to conductor at a critical percolation threshold value between 1 and 2 vol.%. Another study was carried out by Tzeng et al. [131], who reported the EMI SE of on ABS/CF composites coated with nickel and copper metals. The electroless nickel-coated CF-reinforced ABS composites demonstrated higher electrical conductivity. Hence, the better EMI SE ability compared to the copper-coated CF was due to the excellent bonding between the nickel coating and CF surfaces. It has been reported that double-layer metals covering CF increased the EMI SE of composites effectively [132]. Ozkan et al. [48] reported the electrical properties of SCF-reinforced PC composites. These composites' highest electrical conductivity containing 30 wt% CF was around 0.0035 S/cm compared to about 0.0005 S/cm for a pure PI matrix. Additionally, Hong et al. [133] reported an EMI SE of 30 wt% for CF-reinforced PP composites with the addition of 1 wt% of carbon nanotubes. A decrease in volume resistivity and an increase in the PP/CF composites' EMI SE were observed. Increasing the CF length from 200 to 250 μm in the PP composites showed the best results; moreover, a long blending time and high speed can lead to good CF dispersion in principle, but there was an optimal saturation point in this composites system. A similar study was conducted by Unterweger et al. [102], who evaluated the impact of CF length and content on PP/CF composites' electrical conductivity. They concluded that electrical conductivity showed a strong dependence on the fiber length and showed a linear correlation with the weight and average fiber length in the investigated range of 100–350 μm. When the CF content was raised from 5 to 10 vol.%, more than two orders of magnitude were in the electrical conductivity. However, a further growth to 15 vol.% CF only had a minor impact on the conductivity.

Xi et al. [134] studied the electrical properties of SCF-reinforced PEs including both UHMWPE and low-molecular-weight polyethylene composites. An excellent positive temperature coefficient was achieved. The conductivity increased with an increase in the heat treatment time due to the formation of better reconnection of SCF networks in the polymer matrix. A similar study was conducted by Shen et al. [135]. They investigated the combined effects of carbon black and CF on composites' electrical properties based on PE or a PE/PP blend. The volume resistivity of the HDPE/carbon black/CF and HDPE/PP/carbon black/CF with 2 wt% CF decreased by around 3.0 and 11.2 orders of magnitude, respectively compared to that of the HDPE/carbon black and HDPE/PP/carbon black composites. The intensity of the positive temperature coefficient and the temperature coefficient of resistivity of the HDPE/carbon black/CF and HDPE/PP/carbon black/CF composites increased significantly with increasing CF loading.

The negative temperature coefficients were neglected because CF is not as easily agglomerated as other reinforcement such as carbon black and graphite. Another study was carried out by Ameli et al. [136], who investigated EMI SE and the electrical conductivity of a CF-reinforced PP composite containing carbon black in two forms, i.e., solid and foams. At 5 vol.% CF content, both composite samples' conductivity decreased proportionally with frequency in the whole range. However, the electrical percolation threshold was

8.75 and 7 vol.% for solid and foams composites, respectively. The dielectric permittivity improved, and the through-plane electrical conductivity increased by up to six orders of magnitude, resulting in an increase of 65% in these foamed composites' specific EMI SE. These results indicate that processing and matrix form could affect the electrical properties of the final composite materials. Hwang [103] reported the EMI SE property of solid and microcellular (foamed)-injected PBT/CF composites with various fiber contents and aspect ratios. He found that the microcellular composites showed better electrical conductivity for any particular CF content than those of the solid ones. The foaming process distorts the CF's orientation, increasing the end-to-end fiber contacts, thereby increasing the electrical conductivity. The composites showed almost no EMI SE at 13 wt% CF content; however, at 30 wt%, it improved significantly to around 10 and 11.16 dB for solid and foamed composites, respectively. This result indicated the advantages of foamed composites over solid one to enhance the final composites' electrical conductivity.

Saleem et al. [137] reported CF-reinforced composites of PEEK and PES as polymer matrices. They observed that the percolation threshold for the PES/CF and the PEEK/CF composites occurred at a CF loading of 10 wt% and 35 wt%, respectively. The higher percolation threshold for the PEEK was because the PEEK is a highly crystalline polymer compared to PES. Hence, the formation of the conducting pathways is not as easy in PES. At the percolation threshold, the measured electrical resistivity for both the composites was around 10^6 Ωcm. The authors observed that the heat treatment of CF at a higher temperature improved the graphitic structure, resulting in the CF's better electrical conductivity. This observation is in good agreement with previous results reported by Xi et al. [134]. It has been reported that the electrical resistivity of the CF treated around 2000 °C showed a resistivity of around five orders of magnitude lower compared to the untreated ones [138]. Table 3 summarizes the variety of composite materials, modification techniques, and the obtained electrical properties of CFRTP over the last decade.

Table 3. The type of thermoplastic polymer and CF, modification techniques of CF, and electrical properties of a variety of CFRTP composites.

Composite Material	CF Modification Method	Electrical Properties	[Reference No.] (Publication Year)
PC/CF	Sizing materials	The highest electrical conductivity was around 0.0035 S/cm compared to about 0.0005 S/cm.	[48] (2014)
PP/SCF	Sizing materials	The electrical conductivity showed a strong dependence on the CF length. Two orders of magnitude in the electrical conductivity were reported.	[102] (2020)
PBT/CF	Not mentioned	The EMI SE improved significantly to around 10 and 11.16 dB for solid and foamed composites, respectively.	[103] (2016)
ABS/EVA/SCF	Coupling agent	A marginal increase in EMI SE with an increase in electromagnetic radiation frequency, but a sharp increase was observed with an increase in the SCF contents.	[125] (2011)
PP/CF	Not mentioned	The addition of CF resulted in a significant decrease in the percolation threshold value.	[128] (2014)
PP/CF with the addition of 1 wt% of CNTs	Material coating	A decrease in volume resistivity with an increase in the EMI SE was observed.	[133] (2014)
PP/CF	Not mentioned	The electrical percolation threshold was 8.75 and 7 vol.% for solid and foam composites, respectively. The dielectric permittivity improved, and the through-plane electrical conductivity increased by up to 6 orders of magnitude, resulting in an increase of 65% in these foamed composites' specific EMI SE.	[136] (2013)

2.4. Thermal Stability and Thermal Conductivity of CFRTP

The primary thermal properties of CFRTP are thermal stability, thermal conductivity, melting temperature (T_m), and glass transition temperature (T_g). Researchers have investigated these properties extensively in an attempt to enhance them. The T_g of polymer composites normally depends on several factors such as the chemical structure and conformation of the polymers, degree of crystallinity, fiber dispersion, and interactions between the fiber and the polymer. Several studies have confirmed that the addition of fillers affects the T_g and the breadth of the transition due to changes in the mobility of the polymeric chains in the host matrix. By improving thermal properties, CFRTP becomes more suitable for fulfilling the already existing demands in various high-temperature sectors such as the aerospace, oil, and gas industries.

Kada et al. [107] reported the thermal properties of PP composites reinforced with varying quantities of SCF (9, 15, 20, 25, and 30 wt%). The results showed that the PP matrix and their CF composites exhibit a single-step decomposition. The PP molecular degradation started at around 408 °C, and the decomposition maxima occurred at 468 °C, and the maximum rate of degradation was 2.3%/min. An improvement in the initial degradation temperature was observed on the incorporation of the SCF into the PP matrix. Compared to the neat PP, the composites with 9% and 30% SCF content showed an increase of 10 °C and 20 °C in initial degradation temperature, respectively, which was attributed to the higher heat absorption capacity of the CF and the delayed decomposition temperature results from the reduced heat release rate of the CF. The enhancement in the composites' thermal conductivity with an increasing volume fraction of the CF was due to the CF's higher thermal conductivity than that of the PP matrix.

On the other hand, Yilmaz et al. [139] reported that the melting behavior of CF-reinforced PP composite was considerably influenced by the thermal history rather than the CF's presence. Their results show melting over a wide range of temperatures, with two peaks appearing for the samples with no thermal treatment and those annealed at lower temperatures irrespective of the CF's presence. Wang et al. [75] reported PP/SCF composite's thermal properties containing 10 wt% of SCF. Their results exhibited that the composite exhibited improvement in thermal stability and crystallization temperature. Cho et al. [109] studied the thermal properties of the PK/CF composite and reported an enhancement of thermal conductivity up to 300% with an increase in CF content up to 30 wt% in the PK matrix. It has been reported that thermal stability increased in EVA, acrylonitrile butadiene copolymer, and their blend composites due to the restraint of their chain motion into the polymer composites generated by adding CF [125].

Khan et al. [54] reported the thermal properties of multi-layered laminated composite panels of CF-reinforced HDPE. The thermal degradation of the neat HDPE and the HDPE/CF composite showed a single continuous decline in the residual weight mainly due to the HDPE chains' unsystematic scission. The composites' thermal degradation temperature started at around 30 °C higher than that of the neat HDPE. Similarly, the maximum decomposition temperature for the composites was about 15 °C higher compared to pure HDPE. The multi-layered laminated composite panels' thermal stability also improved by 41%, making these composites suitable for applications at higher temperatures.

In contrast, Thongruang et al. [130] found that SCF does not significantly affect the HDPE matrix's thermal properties. They stated that the effect of long CF was more pronounced at high temperatures on the thermal properties. Additionally, Liu et al. [50] concluded that the CF coated by thermoplastic resin was more stable than untreated CF and had increased surface energy and wetting performance.

Rezaei et al. [101] used SCF of five different length sizes (10, 5, 2, 1, and 0.5 mm) as a reinforcing fiber (10 wt%) in PP as a matrix. They reported that compared to the shorter CF, the longer CF showed better thermo-mechanical properties as fillers in the matrix. The thermogravimetric analysis results showed that increasing the incorporated CF's length led to an increase in the composites' thermal stability. The glass transition temperature (T_g) of composites combined with 10 mm length CF increased by 19.5% compared to that of the

unfilled PP. Overall, the thermal degradation of the PP/SCF composites was improved for all investigated lengths compared to plain PP.

Gabrion et al. [104] studied two types of composite structures (plates and tubes) of a unidirectional CF-reinforced PI composite. The authors reported a longitudinal and transversal coefficient of thermal expansion of $1.7 \times 10^{-6}/°C$ and $30 \times 10^{-6}/°C$, respectively, clearly depicting the materials' high anisotropy. They reported that above 200 °C, the expansion with an increase in temperature was non-linear. Two transitions were observed at approximately 235 °C and 385 °C, attributed to T_g and T_m of the polymeric material, respectively. They reported that the weight loss depended strongly on the environmental conditions. The weight loss in the inert atmosphere due to degradation was significant above 500 °C; however, the degradation started at a lower temperature (~400 °C) in an oxidizing atmosphere. A similar study was carried out by Karsli et al. [52], who examined the performance of CF-reinforced PA6,6 composites. The initial decomposition temperature and the decomposition temperature at the maximum rate of the composite material were determined. It was found that the lowest decomposition temperature was about 270 °C, and the highest temperature at which no further weight loss was observed was approximately 500 °C for all composite samples used in their study.

Samyn et al. [140] reported the thermal properties of PI/CF composite materials. PI filled with 30 wt% CF showed an improvement in the heat distortion temperature or heat distortion temperature value by 10 °C. T_g and melting points showed no considerable change in the values with the incorporation of the CF. The thermal conductivity improved from 0.17 W/(mK) for the neat PI to 0.49 W/(mK) in the molding direction and 0.22 W/(mK) in the transverse direction for the composites. In a similar composite, Dong et al. [141] reported PI/CF composites' thermal properties. The T_g value obtained showed an increase in the T_g values with the increase in CF content in the composites. At 5 vol.% CF contents, a slight decrease in T_g was reported but was found to increase to 241 °C and 244 °C at a CF content of 20 and 30 vol.%, respectively, compared to that of the neat PI value of 231 °C. The number of these confined chains increased with an increase in the CF content. The segmental motion and relaxations can occur only at higher temperatures and over a broad range of temperatures leading to an enhancement in T_g values. Similar observations have been reported by Vivekanandhan et al. [91], who fabricated PTT/CF composites. They reported that PTT composites containing 30 wt% exhibited an increase of more than 150 °C in the heat deflection temperature, and no significant changes in the melt temperature were observed. Additionally, Karsli et al. [98] investigated the effect of SCF content and its length on the thermal properties of CF-reinforced PA6 composites. The results showed no change in the values T_g and T_m for the composites even with the CF loading increase. However, the heat of fusion and the degree of crystallinity of the composites decreased with the rise in the composites' CF loading. The higher fiber content restricts the mobility of polymer chains in the matrix and obstructs the crystal growth. On the other hand, CF length at the studied range did not significantly affect the thermal properties.

Yan et al. [92] studied PA6 composite with 30 wt% CF with a length of 7 mm and a diameter of 7 μm. The thermal conductivity of PA6 annealed at 80 °C and was 0.21 W/mK, and increased by about 24% when the annealing temperature was increased to 190 °C. The thermal conductivity of PA6/CF composites increased to 0.32 W/mK and improved by 13% in the annealing process. The heat deflection temperature value for PA6 lies between 64 °C to 77 °C based on its annealing temperature; however, for the PA6/CF composites, it was around 214 °C with a negligible effect for thermal annealing. The results also showed that the T_g of PA6 increased from 60 °C to 78 °C with the incorporation of the CF and thermal annealing, which led to an improved T_g for both the PA6 and the PA6/CF composites.

A variation in T_g reported by Munirathnamma et al. [142] characterized the PBT and PES polymer composites reinforced by CF. Their result showed a T_g of 44 °C for neat PBT, whereas the PBT composites containing 30 and 40 wt% CF showed a T_g of 46 and 44 °C, respectively. The incorporation of 30 wt% CF in the PBT matrix led to a nominal increase in T_g, suggesting a restriction on the matrix's segmental chain mobility due to the

CF's presence. However, a T_g of 218 °C for pure PES decreased to 212 °C for composites containing 30 and 40 wt% CF. This reduction in T_g suggests compact molecular packing due to interface development. Connor et al. [85] reported the thermal properties of CCF incorporated in nylon. Filaments were used to fabricate composite layers by printing with a CF content of around 35 to 41 vol.%. The nylon filament composites showed no melting peak attributed to the addition of CF in the thermal processing history of this polymer.

Yu et al. [46] reported PC composites' thermal conductivity with different loadings of chopped CF coated with PET and treated using 3-aminopropyl triethoxy silane. The results revealed that incorporating the chopped CF enhanced the thermal stability of composites by restricting the pyrolytic degradation of the polymer matrix. They reported an increase in the composites' in-plane and through-thickness thermal conductivities with the increase in chopped CF content. The in-plane and through-thickness thermal conductivity for a 50% fiber content was 2.45 W/mK and 0.59 W/mK, compared to that of 0.20 W/mK for the neat matrix. Sun et al. [13] reported the thermal conductivity of a polysulfone/CF composite. The thermal conductivity was 1.82 W/mK at a CF loading of 26 vol.%. Similar results have been reported by Yoo et al. [143]. They stated a significant difference (up to 25 times) between the in-plane and the through-plane thermal conductivities of PA6 composites reinforced by CF. Saleem et al. [137] investigated the thermal conductivity of CF-reinforced PEEK and PES matrices. They stated that the thermal conductivity of the matrices improved upon the incorporation of 20 wt% CF. The further addition of CF resulted in a slight improvement in the conductivities. They also concluded that composites containing PES had better thermal conductivity due to the deficiency of crystallinity. Table 4 summarizes the variety of composite materials, modification techniques, and the obtained thermal properties of CFRTP over the last decade.

Table 4. The type of thermoplastic polymer and CF, modification techniques of CF, and thermal properties of different CFRTP composites.

Composite Material	CF Modification Method	Thermal Properties	[Reference No.] (Publication Year)
Polysulfone/CF	Not mentioned	The thermal conductivity was 1.82 W/mK at a CF loading of 26 vol.%.	[13] (2017)
PA6/LCF	Sizing materials	The in-plane and through-thickness thermal conductivity were 2.45 W/mK and 0.59 W/mK, respectively.	[46] (2013)
PEEK/CF	Sizing materials	Sized CF was more stable than untreated CF with an increase in surface energy and wetting performance.	[50] (2013)
PC/CF	Material coating followed by coupling agents	It was found that the lowest decomposition temperature was about 270 °C, and the highest temperature at which no further weight loss was observed was approximately 500 °C.	[52] (2018)
HDPE/CF	Without using any coupling agent	The thermal degradation temperature started at around 30 °C higher than that of the neat HDPE. Similarly, the maximum decomposition temperature was about 15 °C higher compared to pure HDPE. The multi-layered laminated composite panels' thermal stability also improved by 41%.	[54] (2020)
PP/CF	Material coating	An improvement in thermal stability and crystallization temperature was reported.	[75] (2018)
nylon/CCF	Not mentioned	The nylon filament composites showed no melting peak attributed to the addition of CF to the thermal processing history of this polymer.	[85] (2019)
PTT/CF	Sizing materials	PTT composites containing CF exhibited an increase of more than 150 °C in the heat deflection temperature, and no significant changes in the melt temperature were observed.	[91] (2012)

<div align="center">

Table 4. *Cont.*

</div>

Composite Material	CF Modification Method	Thermal Properties	[Reference No.] (Publication Year)
PA6/CF	Not mentioned	The thermal conductivity at 80 °C was 0.21 W/mK, and increased by about 24% when the annealing temperature was increased to 190 °C. The thermal conductivity of composites increased to 0.32 W/mK and improved by 13% in the annealing process. The heat deflection temperature value for PA6 lies between 64 °C to 77 °C based on its annealing temperature; however, for the composites, it was around 214 °C with a negligible effect for thermal annealing. The results also showed that the T_g of PA6 increased from 60 °C to 78 °C with the incorporation of the CF.	[92] (2014)
PA6/CF	Not mentioned	The effect of SCF content and its length on the thermal properties of CF-reinforced PA6 composites. The results showed no change in the values T_g and T_m for the composites even with the CF loading increase. However, the heat of fusion and the degree of crystallinity of the composites decreased with the rise in the composites' CF loading.	[98] (2013)
PI/CF	Not mentioned	The authors reported a longitudinal and transversal coefficient of thermal expansion of $1.7 \times 10^{-6}/$°C and $30 \times 10^{-6}/$°C, respectively, clearly depicting the materials' high anisotropy. They reported that above 200 °C, the expansion with an increase in temperature was non-linear. Two transitions were observed at approximately 235 °C and 385 °C, attributed to Tg and Tm of the polymeric material, respectively.	[104] (2016)
PEEK/CF	Coupling agent	The degradation started at around 408 °C, and the decomposition maxima occurred at 468 °C, and the maximum rate of degradation was 2.3%/min. Improvement by 20 °C in the initial degradation temperature was observed.	[107] (2018)
PK/CF	Not mentioned	An enhancement of thermal conductivity up to 300%.	[109] (2019)
CBT/SCF	Sizing materials	The T_g increased by 19.5%. Overall, thermal degradation of improved for all investigated composites compared to plain PP.	[110] (2016)
ABS/EVA/SCF	Coupling agent	An enhancement in thermal stability was reported.	[125] (2011)
PP/CF	Not mentioned	No change in the melting behavior was reported.	[139] (2012)
PI/CF	Not mentioned	An improvement in the heat distortion temperature by 10 °C. T_g and T_m showed no considerable changes. The thermal conductivity improved from 0.17 W/(mK) to 0.49 W/(mK) in the molding direction and 0.22 W/(mK) in the transverse direction.	[140] (2010)
PI/CF	Not mentioned	The T_g value obtained showed an increase to 241 °C and 244 °C.	[141] (2018)
PBT/PES/CF	Oxidation treatment followed by material coating	Their result showed improvement in T_g from 44 °C to 46 °C for composites containing PBT. However, the T_g of composites containing PES decreased from 218 °C to 212 °C.	[142] (2019)

3. Future Prospects

In the future, CFRTP research and development activities will be focused on manufacturing techniques, recycling methods, cost reduction, and improving properties. These materials are attractive characteristics for various industrial applications as many types of thermoplastic polymers can be utilized as matrices for CFRTP composites. Ongoing developments in the processability and engaging CFRTP in terms of a cost-effective viewpoint and synergies between industrial sectors will pave the way to high-volume production that industries need to meet progressive demands. Advancements are also required for

the preparation of efficient, cost-effective, and facile CFRTP materials. The progressive ideas are likewise vital for the high production rate of such materials. The overall growth of polymer composite materials having embedded functionality is anticipated to exceed five kilotons by 2029 [144]. CFRTP are lightweight polymer composite materials that show excellent properties and great potential for low-cost manufacturing when compared to thermosetting composite materials. As for CF, the worldwide industry manufacturing CF is set to grow enormously over the next ten years. This tremendous growth will be led by various factors, such as high demand for low-weight materials and creative design that needs solutions related to composite technology [145]. The future perspectives of CF are undoubtedly on a positive track. However, the integration of CF into huge markets and several common utilizations mainly depends on the capabilities of the manufacturers. CFRTP will achieve a wide potential if both polymer and CF manufacturers [146] continue to observe new applications and develop creative and low-cost technologies. The major CFRTP consumption sectors include the aerospace, defense, automotive, renewable energies, sports equipment, and construction industries [147]. For instance, aircraft makers have also been focusing on reducing the overall weight of aircraft so as to increase the efficiency of the product. The use of CFRTP helps in drastically lowering the overall weight. Rising demand for CFRTP as an alternative to metals such as steel and aluminum is expected to stimulate growth in such applications [148]. Similarly, the use of CFRTP-based parts is increasing compared with the use of metallic-based parts in airplanes and automobiles, which could decrease weight, greenhouse gas emissions, and consumption of energy. For example, CFRTP manufacturing processes have been recognized for automotive body panel applications including structural and non–structural components such as seat structures, bumpers, hoods, and fuel tanks [5,6,149]. In general, the strength and stiffness of a CFRTP material remain very much a function of the reinforcing material, but its mechanical natures are determined not only by the CF alone but by a synergetic influence between the CF and the polymer matrix. Particularly, the mechanical testing results of CFRTP materials can provide a 40–50 percent saving in weight for an equivalent bending stiffness in comparison with steel panels [150–153]. In terms of cost, CFRTP composite materials offer the cheapest processing technologies, as stated by Friedrich et al. [154] who suggested CFRTP composites as a future possibility in automotive applications. Another possible application for CFRTP is in pipelines in the oil and gas industries. The progress of reinforced thermoplastic polymer pipes for oil and gas applications have been reviewed by Morozov et al. [155], who stated that reinforced thermoplastic polymer pipes have been gradually recognized as a significant alternative to metallic pipes due to their diverse advantages such as a higher stiffness-to-weight ratio, enhanced fatigue resistance, and improved corrosion resistance. Venkatesan et al. [156] studied the mechanical properties of CF-reinforced composites in the deep sea. Their results showed that the investigated mechanical properties were not affected by the sea environment, and corrosion or degradation and bio-film formation was not observed. Therefore, CFRTPs are increasingly being utilized in oil and pipeline applications, especially those in deep water, as they can maintain their mechanical properties in seawater and provide additional cost savings in terms of strength-to-weight ratio in comparison with steel [157–159], which has a direct impact on lowering the consumption of energy. Extensive research on developing such materials is underway to improve the properties and performance of CFRTP for many industrial sectors to reduce corrosion effects, energy consumption, and overall manufacturing costs. Furthermore, CFRTP can be an alternative to other composite materials in blade production for wind energy applications. Prabhakaran et al. [146] and Mishnaevsky et al. [160] discussed the suitability of CFRTP and thermoplastic resin for future turbine blades and associated challenges for producing large blade structures from such materials. Additionally, the aerospace industry has recognized that CFRTP composite materials provide outstanding cost savings compared to traditional materials such as thermosetting composite materials and metal [25].

Despite these promising advantages of CFRTP, there are some drawbacks and challenges. One of the challenges is the high cost of virgin CF; although the cost dropped

considerably in the past few years. Thus, the manufacturing cost of CFRTP is relatively high, however; it costs less than CF reinforced thermosetting polymers since it consumes less energy. These are some of the challenges that face the incorporation of the composite as a highly demanded material in many industries. Researchers have focused on developing recycling methods of CF and CFRTP composites, which are expected to lower the cost by 50% [161]. This will make using CFRTP material composites more economically sound in terms of the life cycle of the composites. Meanwhile, one of the main challenges in manufacturing CFRTP is that CF is non-polar while thermoplastics are polar materials. This disagreement in polarity results in poor interfacial adhesion of the manufactured composite unless the surface of CF was treated prior to the manufacturing process. Although the treatment process increases the manufacturing time and the cost of the end product, it is essential to ensure compatibility between CF and the polymer. In addition, polymers cannot withstand high temperatures and oxidation, unlike CF which must be taken into consideration when choosing a manufacturing process [22–25]. CFRTP are favorable composite materials due to their high strength-to-weight ratio compared to other conventional materials; however, it is rather difficult to estimate the fatigue of CFRTP, unlike metals. The lack of the fatigue (endurance) limit of CFRTP makes it challenging for engineers and designers to predict the exact fatigue failure properties of CFRTP. Also, CFRTP composites are hard, tough, and extremely abrasive which makes machining CFRTP a challenge. Without tools designed to withstand the damage CFRTP can cause, tool life can be very short when machining CFRTP composites. These challenges attracted many researchers into building trusted models that can accurately predict fatigue failure of the composite and achieve an ideal machining process [117,155,162].

Overall, CFRTP composite materials have become a progressively used class of lightweight materials. The research and development activities carried out to investigate the relationships between processing, structure, and properties of CFRTP have resulted in a better fundamental understanding of these materials and led to an enhancement of their properties, offering more flexibility in the design for several possibilities applications. Therefore, CFRTP is a promising candidate in a variety of industrial applications. The properties of CFRTP composite materials such as high strength, low weight, and good thermal and electrical properties make it a preferred composite material compared to neat polymers, CFRPs, and even other metallic materials. However, the polymer matrix and the treatment method of CF prior to the manufacturing process is crucial and will affect the composite properties; hence, it will also affect the applications of the composite material. Thus, the large-volume market applications of CFRTP are still to be discovered. Nevertheless, with the huge demand of emerging industries, the opportunities for improvements, and the support of developing standardizations for testing and using CFRTP composite, more high-efficiency CFRTP products will be developed.

4. Conclusions

In this comprehensive review, developments in the research on carbon fiber-reinforced polymers thermoplastic (CFRTP) have been explored extensively with a focus on the properties of the composite, such as the mechanical, electrical, and thermal properties. The outstanding properties exhibited by CFRTP are the primary motivation for further research and development. For example, these properties improved significantly with the addition of carbon fiber (CF) as a reinforcement compared to the neat polymer properties, which paves the way for CFRTP products in many industrial sectors. Furthermore, the modification of the CF's surface is essential to improve the interfacial bond between the CF and the thermoplastic matrices. Either a chemical or physical modification technique will increase the oxygen concentration on the CF's surface. Increasing oxygen makes the surface of CF more similar to the thermoplastic matrix in terms of polarity. Moreover, modifications have improved the filler/matrix bond and have had excellent positive effects on the mechanical properties of the composite compared to the untreated thermoplastic

polymer/CF composites. A variety of modifying techniques for the surface of CF prior to the manufacturing process were discussed.

In general, the properties of various thermoplastic composites improved significantly with the addition of CF as a reinforcement compared to the neat thermoplastic properties. However, there is a variety in such improvements. This could be attributed to several factors, including manufacturing technique, processing parameters, thermoplastic type, CF type and orientation, loading, dimension, and surface treatment techniques, leading to interfacial adhesion and dispersion statues. All such aspects are essential to attain the anticipated properties, particularly mechanical properties, and to understand the relationships of the modification methods and mechanical properties of the final CFRTP composites. Therefore, this review provides the required stepping-stone to fully exploit the potential of CFRTPs in the manufacturing industry.

Abbreviations

ABS	Acrylonitrile butadiene styrene
CBT	Cyclic butylene terephthalate
HDPE	High density polyethylene
PA	Polyamide
PA6	Polyamide 6
PA6,6	Polyamide 6,6
PA12	Polyamide 12
PAEK	Polyaryl ether ketone
PBT	Poly butylene terephthalate
PC	Polycarbonate
PE	Polyethylene
PEEK	Polyetheretherketone
PEI	Polyetherimide
PES	Polyether sulfone
PET	Polyethylene terephthalate
PI	Polyimide
PLA	Polylactic acid
POM	Polyoxymethylene
PP	Polypropylene
PPEK	Polyphthalazinone ether ketone
PPESK	Phthalazinone ether sulfone ketone
PPS	Polyphenylene sulfide
PS	Polystyrene
PES	Polyethersulfone

PTFE	Polytetrafluoroethylene
PTT	Polytrimethylene terephthalate
PU	Polyurethane
PVDF	Poly vinylidene fluoride
UHMWPE	Ultra-high-molecular-weight polyethylene
PK	Polyketone
CF	Carbon fiber
CCF	Continuous carbon fiber
SCF	Short carbon fiber
LCF	Long carbon fiber
VGCF	Vapor-grown carbon fiber
RCF	Recycled carbon fiber

References

1. Park, S.-J.; Heo, G.-Y. Precursors and Manufacturing of Carbon Fibers. In *Superconductivity*; Springer Series in Materials Science and Business Media; Springer: Dordrecht, The Netherlands, 2014; Volume 210, pp. 31–66.
2. Qin, X.; Lu, Y.; Xiao, H.; Wen, Y.; Yu, T. A comparison of the effect of graphitization on microstructures and properties of polyacrylonitrile and mesophase pitch-based carbon fibers. *Carbon* **2012**, *50*, 4459–4469. [CrossRef]
3. Forintos, N.; Czigany, T. Multifunctional application of carbon fiber reinforced polymer composites: Electrical properties of the reinforcing carbon fibers—A short review. *Compos. Part B Eng.* **2019**, *162*, 331–343. [CrossRef]
4. Rajak, D.K.; Pagar, D.D.; Menezes, P.L.; Linul, E. Fiber-Reinforced Polymer Composites: Manufacturing, Properties, and Applications. *Polymers* **2019**, *11*, 1667. [CrossRef] [PubMed]
5. Ishikawa, T.; Amaoka, K.; Masubuchi, Y.; Yamamoto, T.; Yamanaka, A.; Arai, M.; Takahashi, J. Overview of automotive structural composites technology developments in Japan. *Compos. Sci. Technol.* **2018**, *155*, 221–246. [CrossRef]
6. Zhang, J.; Chevali, V.S.; Wang, H.; Wang, C.-H. Current status of carbon fibre and carbon fibre composites recycling. *Compos. Part B Eng.* **2020**, *193*, 108053. [CrossRef]
7. Yao, S.-S.; Jin, F.-L.; Rhee, K.Y.; Hui, D.; Park, S.-J. Recent advances in carbon-fiber-reinforced thermoplastic composites: A review. *Compos. Part B Eng.* **2018**, *142*, 241–250. [CrossRef]
8. Yu, G.-C.; Wu, L.-Z.; Feng, L.-J.; Yang, W. Thermal and mechanical properties of carbon fiber polymer-matrix composites with a 3D thermal conductive pathway. *Compos. Struct.* **2016**, *149*, 213–219. [CrossRef]
9. Tatsuno, D.; Yoneyama, T.; Kawamoto, K.; Okamoto, M. Production system to form, cut, and join by using a press machine for continuous carbon fiber-reinforced thermoplastic sheets. *Polym. Compos.* **2016**, *39*, 2571–2586. [CrossRef]
10. Nagura, A.; Okamoto, K.; Itoh, K.; Imai, Y.; Shimamoto, D.; Hotta, Y. The Ni-plated carbon fiber as a tracer for observation of the fiber orientation in the carbon fiber reinforced plastic with X-ray CT. *Compos. Part B Eng.* **2015**, *76*, 38–43. [CrossRef]
11. Almajid, A.; Friedrich, K.; Floeck, J.; Burkhart, T. Surface Damage Characteristics and Specific Wear Rates of a New Continuous Carbon Fiber (CF)/Polyetheretherketone (PEEK) Composite under Sliding and Rolling Contact Conditions. *Appl. Compos. Mater.* **2011**, *18*, 211–230. [CrossRef]
12. Alarifi, I.; Alharbi, A.; Khan, W.S.; Rahman, A.; Asmatulu, R. Mechanical and Thermal Properties of Carbonized PAN Nanofibers Cohesively Attached to Surface of Carbon Fiber Reinforced Composites. *Macromol. Symp.* **2016**, *365*, 140–150. [CrossRef]
13. Sun, D.; Lin, G.; Sui, G.; Hao, Y.; Yang, R.; Zhang, K. Multi-gating injection molding to enhance the thermal conductivity of carbon fiber/polysulfone composite. *Polym. Compos.* **2015**, *38*, 185–191. [CrossRef]
14. Tseng, H.-C.; Chang, R.-Y.; Hsu, C.-H. Numerical prediction of fiber orientation and mechanical performance for short/long glass and carbon fiber-reinforced composites. *Compos. Sci. Technol.* **2017**, *144*, 51–56. [CrossRef]
15. Sharma, M.; Rao, I.M.; Bijwe, J. Influence of fiber orientation on abrasive wear of unidirectionally reinforced carbon fiber-polyetherimide composites. *Tribol. Int.* **2010**, *43*, 959–964. [CrossRef]
16. Dickson, A.; Barry, J.N.; McDonnell, K.A.; Dowling, D. Fabrication of continuous carbon, glass and Kevlar fibre reinforced polymer composites using additive manufacturing. *Addit. Manuf.* **2017**, *16*, 146–152. [CrossRef]
17. Hegde, S.; Shenoy, S.; Chethan, K. Review on carbon fiber reinforced polymer (CFRP) and their mechanical performance. *Mater. Today Proc.* **2019**, *19*, 658–662. [CrossRef]
18. Suresh, A.; Harsha, A.; Ghosh, M. Solid particle erosion of unidirectional fibre reinforced thermoplastic composites. *Wear* **2009**, *267*, 1516–1524. [CrossRef]
19. Jin, F.-L.; Lee, S.-Y.; Park, S.-J. Polymer matrices for carbon fiber-reinforced polymer composites. *Carbon Lett.* **2013**, *14*, 76–88. [CrossRef]
20. Othman, R.; Ismail, N.I.; Pahmi, M.A.A.H.; Basri, M.H.M.; Sharudin, H. Hemdi Application of carbon fiber reinforced plastics in automotive industry: A review. *J. Mech. Manuf.* **2018**, *1*, 144–154.
21. Kishi, H.; Nakao, N.; Kuwashiro, S.; Matsuda, S. Carbon fiber reinforced thermoplastic composites from acrylic polymer matrices: Interfacial adhesion and physical properties. *Express Polym. Lett.* **2017**, *11*, 334–342. [CrossRef]
22. Park, S.-J.; Seo, M.-K. Carbon Fiber-Reinforced Polymer Composites: Preparation, Properties, and Applications. *Polym. Compos.* **2012**, *135*, 135–183. [CrossRef]

23. Xie, S.; Liu, S.; Cheng, F.; Lu, X. Recent Advances toward Achieving High-Performance Carbon-Fiber Materials for Supercapacitors. *ChemElectroChem* **2018**, *5*, 571–582. [CrossRef]

24. Shin, H.K.; Park, M.; Kim, H.-Y.; Park, S.-J. An overview of new oxidation methods for polyacrylonitrile-based carbon fibers. *Carbon Lett.* **2015**, *16*, 11–18. [CrossRef]

25. Koumoulos, E.P.; Trompeta, A.-F.; Santos, R.-M.; Martins, M.; Dos Santos, C.M.; Iglesias, V.; Böhm, R.; Gong, G.; Chiminelli, A.; Verpoest, I.; et al. Research and Development in Carbon Fibers and Advanced High-Performance Composites Supply Chain in Europe: A Roadmap for Challenges and the Industrial Uptake. *J. Compos. Sci.* **2019**, *3*, 86. [CrossRef]

26. Huang, X. Fabrication and Properties of Carbon Fibers. *Materials* **2009**, *2*, 2369–2403. [CrossRef]

27. Baker, D.A.; Rials, T.G. Recent advances in low-cost carbon fiber manufacture from lignin. *J. Appl. Polym. Sci.* **2013**, *130*, 713–728. [CrossRef]

28. Wong, K.; Mohammed, D.S.; Pickering, S.; Brooks, R. Effect of coupling agents on reinforcing potential of recycled carbon fibre for polypropylene composite. *Compos. Sci. Technol.* **2012**, *72*, 835–844. [CrossRef]

29. Hung, P.-Y.; Lau, K.-T.; Fox, B.; Hameed, N.; Lee, J.H.; Hui, D. Surface modification of carbon fibre using graphene-related materials for multifunctional composites. *Compos. Part B Eng.* **2018**, *133*, 240–257. [CrossRef]

30. Jin, F.-L.; Park, S.-J. Preparation and characterization of carbon fiber-reinforced thermosetting composites: A review. *Carbon Lett.* **2015**, *16*, 67–77. [CrossRef]

31. Zhang, G.; Sun, S.; Yang, D.; Dodelet, J.-P.; Sacher, E. The surface analytical characterization of carbon fibers functionalized by H2SO4/HNO3 treatment. *Carbon* **2008**, *46*, 196–205. [CrossRef]

32. Park, S.-J.; Donnet, J.-B. Anodic Surface Treatment on Carbon Fibers: Determination of Acid-Base Interaction Parameter between Two Unidentical Solid Surfaces in a Composite System. *J. Colloid Interface Sci.* **1998**, *206*, 29–32. [CrossRef] [PubMed]

33. Ofoegbu, S.U.; Ferreira, M.G.; Zheludkevich, M.L. Galvanically Stimulated Degradation of Carbon-Fiber Reinforced Polymer Composites: A Critical Review. *Materials* **2019**, *12*, 651. [CrossRef] [PubMed]

34. Lee, H.S.; Kim, S.-Y.; Noh, Y.J.; Kim, S.Y. Design of microwave plasma and enhanced mechanical properties of thermoplastic composites reinforced with microwave plasma-treated carbon fiber fabric. *Compos. Part B Eng.* **2014**, *60*, 621–626. [CrossRef]

35. Unterweger, C.; Duchoslav, J.; Stifter, D.; Fuerst, C. Characterization of carbon fiber surfaces and their impact on the mechanical properties of short carbon fiber reinforced polypropylene composites. *Compos. Sci. Technol.* **2015**, *108*, 41–47. [CrossRef]

36. Agrawal, M. Effect of fiber sizing on Mechanical properties of carbon reinforced composites: A Review. *Org. Polym. Mater. Res.* **2020**, *1*. [CrossRef]

37. Park, S.-J.; Seo, M.-K.; Lee, Y.-S. Surface characteristics of fluorine-modified PAN-based carbon fibers. *Carbon* **2003**, *41*, 723–730. [CrossRef]

38. Yamamoto, T.; Uematsu, K.; Irisawa, T.; Tanabe, Y. Controlling of the interfacial shear strength between thermoplastic resin and carbon fiber by adsorbing polymer particles on carbon fiber using electrophoresis. *Compos. Part A Appl. Sci. Manuf.* **2016**, *88*, 75–78. [CrossRef]

39. Han, S.H.; Oh, H.J.; Kim, S.S. Evaluation of fiber surface treatment on the interfacial behavior of carbon fiber-reinforced polypropylene composites. *Compos. Part B Eng.* **2014**, *60*, 98–105. [CrossRef]

40. Cho, S.M.; Jung, H.-T. Highly enhanced mechanical properties of polypropylene-long carbon fiber composites by a combined method of coupling agent and surface modification of long carbon fiber. *Macromol. Res.* **2014**, *22*, 1066–1073. [CrossRef]

41. Zhang, K.; Zhang, G.; Liu, B.; Wang, X.; Long, S.; Yang, J. Effect of aminated polyphenylene sulfide on the mechanical properties of short carbon fiber reinforced polyphenylene sulfide composites. *Compos. Sci. Technol.* **2014**, *98*, 57–63. [CrossRef]

42. Savas, L.A.; Tayfun, U.; Dogan, M. The use of polyethylene copolymers as compatibilizers in carbon fiber reinforced high density polyethylene composites. *Compos. Part B Eng.* **2016**, *99*, 188–195. [CrossRef]

43. Park, J.-M. Interfacial Properties of Two-Carbon Fiber Reinforced Polycarbonate Composites Using Two-Synthesized Graft Copolymers as Coupling Agents. *J. Colloid Interface Sci.* **2000**, *225*, 384–393. [CrossRef] [PubMed]

44. Liu, P.; Zhang, S.; Lu, C.; Yuan, H. Increased interfacial adhesion between carbon fiber and poly(vinylidene fluoride) by an aqueous sizing agent. *Surf. Interface Anal.* **2016**, *48*, 1410–1417. [CrossRef]

45. Tran, M.Q.; Ho, K.K.; Kalinka, G.; Shaffer, M.S.; Bismarck, A. Carbon fibre reinforced poly(vinylidene fluoride): Impact of matrix modification on fibre/polymer adhesion. *Compos. Sci. Technol.* **2008**, *68*, 1766–1776. [CrossRef]

46. Karsli, N.G.; Ozkan, C.; Aytac, A.; Deniz, V. Effects of sizing materials on the properties of carbon fiber-reinforced polyamide 6,6 composites. *Polym. Compos.* **2013**, *34*, 1583–1590. [CrossRef]

47. Luo, H.; Xiong, G.; Ma, C.; Li, D.; Wan, Y. Preparation and performance of long carbon fiber reinforced polyamide 6 composites injection-molded from core/shell structured pellets. *Mater. Des.* **2014**, *64*, 294–300. [CrossRef]

48. Ozkan, C.; Karsli, N.G.; Aytac, A.; Deniz, V. Short carbon fiber reinforced polycarbonate composites: Effects of different sizing materials. *Compos. Part B Eng.* **2014**, *62*, 230–235. [CrossRef]

49. Zhang, T.; Zhao, Y.; Li, H.; Zhang, B. Effect of polyurethane sizing on carbon fibers surface and interfacial adhesion of fiber/polyamide 6 composites. *J. Appl. Polym. Sci.* **2018**, *135*. [CrossRef]

50. Liu, W.; Zhang, S.; Hao, L.F.; Jiao, W.C.; Yang, F.; Li, X.F.; Wang, R.G. Properties of carbon fiber sized with poly(phthalazinone ether ketone) resin. *J. Appl. Polym. Sci.* **2013**, *128*, 3702–3709. [CrossRef]

51. Wenbo, L.; Shu, Z.; Lifeng, H.; Weicheng, J.; Fan, Y.; Xiaofei, L.; Rongguo, W. Interfacial shear strength in carbon fiber-reinforced poly(phthalazinone ether ketone) composites. *Polym. Compos.* **2013**, *34*, 1921–1926. [CrossRef]

52. Yu, Z.; Bai, Y.; Li, Y.; Wang, X.; Wang, W.; Liu, J. Fiber length distribution and thermal, mechanical and morphological properties of thermally conductive polycarbonate/chopped carbon fiber composites. *Polym. Int.* **2018**, *67*, 1137–1144. [CrossRef]

53. Hendlmeier, A.; Simon, Ž.; Chutani, A.; Henderson, L.C. Generating short carbon fiber polyamide-6 composites from continuous carbon fiber—A preliminary examination of surface treatment and sizing effects. *Compos. Part A Appl. Sci. Manuf.* **2020**, *138*, 106058. [CrossRef]

54. Khan, S.M.; Gull, N.; Munawar, A.; Islam, A.; Zia, S.; Shafiq, M.; Sabir, A.; Awais, S.M.; Butt, M.A.; Jamil, T. 2D Carbon Fiber Reinforced High Density Polyethylene Multi-Layered Laminated Composite Panels: Structural, Mechanical, Thermal, and Morphological Profile. *J. Mater. Sci. Technol.* **2016**, *32*, 1077–1082. [CrossRef]

55. Shengbo, Z.; Qingling, D. The surface modification of carbon fiber for thermoplastic HDPE composites. *Surf. Interface Anal.* **2018**, *51*, 184–189. [CrossRef]

56. Chunzheng, P. Improved interfacial properties of carbon fiber/UHMWPE composites through surface coating on carbon fiber surface. *Surf. Interface Anal.* **2018**, *50*, 558–563. [CrossRef]

57. Zhang, Y.; Zhu, S.; Liu, Y.; Yang, B.; Wang, X. The mechanical and tribological properties of nitric acid-treated carbon fiber-reinforced polyoxymethylene composites. *J. Appl. Polym. Sci.* **2015**, *132*. [CrossRef]

58. Liang, X.; Ling, L.; Lu, C.; Liu, L. Resistivity of carbon fibers/ABS resin composites. *Mater. Lett.* **2000**, *43*, 144–147. [CrossRef]

59. Li, J.; Sun, F.F. The interfacial feature of thermoplastic polystyrene composite filled with nitric acid oxidized carbon fiber. *Surf. Interface Anal.* **2009**, *41*, 255–258. [CrossRef]

60. Yan, C.; Hao, L.; Xu, L.; Shi, Y. Preparation, characterisation and processing of carbon fibre/polyamide-12 composites for selective laser sintering. *Compos. Sci. Technol.* **2011**, *71*, 1834–1841. [CrossRef]

61. QiuJun, L.; Feng, H.; Ming, Y.; Di, Y. The addition of acid treated carbon nanotube on the interfacial adhesion of carbon fiber reinforced UHMWPE composite. *Surf. Interface Anal.* **2017**, *49*, 717–720. [CrossRef]

62. Li, J.; Cai, C. The carbon fiber surface treatment and addition of PA6 on tensile properties of ABS composites. *Curr. Appl. Phys.* **2011**, *11*, 50–54. [CrossRef]

63. Fu, X.; Lu, W.; Chung, D. Ozone treatment of carbon fiber for reinforcing cement. *Carbon* **1998**, *36*, 1337–1345. [CrossRef]

64. Li, J.; Xu, Z.S. Effect of surface oxidation treatment on the tribological performance of carbon fiber reinforced polyimide composites. *Materwiss Werksttech* **2010**, *41*, 106–110. [CrossRef]

65. Li, J. Interfacial studies on the O_3 modified carbon fiber-reinforced polyamide 6 composites. *Appl. Surf. Sci.* **2008**, *255*, 2822–2824. [CrossRef]

66. Montes-Morán, M.; Martinez-Alonso, A.; Tascon, J.M.D.; Paiva, M.; Bernardo, C. Effects of plasma oxidation on the surface and interfacial properties of carbon fibres/polycarbonate composites. *Carbon* **2001**, *39*, 1057–1068. [CrossRef]

67. Xie, J.; Xin, D.; Cao, H.; Wang, C.; Zhao, Y.; Yao, L.; Ji, F.; Qiu, Y. Improving carbon fiber adhesion to polyimide with atmospheric pressure plasma treatment. *Surf. Coat. Technol.* **2011**, *206*, 191–201. [CrossRef]

68. Lee, H.; Wei, H.; Takahashi, J. The influence of plasma in various atmospheres on the adhesion properties of recycled carbon fiber. *Macromol. Res.* **2015**, *23*, 1026–1033. [CrossRef]

69. Altay, L.; Bozaci, E.; Atagur, M.; Sever, K.; Tantug, G.S.; Sarikanat, M.; Seki, Y. The effect of atmospheric plasma treatment of recycled carbon fiber at different plasma powers on recycled carbon fiber and its polypropylene composites. *J. Appl. Polym. Sci.* **2019**, *136*. [CrossRef]

70. Karsli, N.G.; Aytac, A.; Akbulut, M.; Deniz, V.; Güven, O. Effects of irradiated polypropylene compatibilizer on the properties of short carbon fiber reinforced polypropylene composites. *Radiat. Phys. Chem.* **2013**, *84*, 74–78. [CrossRef]

71. Mao, L.; Wang, Y.; Zang, Z.; Zhu, S.; Zhang, H.; Zhou, H. Amino-functionalization of carbon fibers through electron-beam irradiation technique. *J. Appl. Polym. Sci.* **2013**, *131*. [CrossRef]

72. Jung, S.; Park, S.K.; Ghim, H.-D.; Lee, D.Y.; Yoo, S.H. Synergetic effect of cross-linking and interfacial interaction in carbon fiber reinforced thermoplastic to enhance its tensile strength by electron-beam irradiation. *Carbon Lett.* **2019**, *30*, 165–175. [CrossRef]

73. Lu, G.; Li, X.; Jiang, H. Electrical and shielding properties of ABS resin filled with nickel-coated carbon fibers. *Compos. Sci. Technol.* **1996**, *56*, 193–200. [CrossRef]

74. Li, F.; Hua, Y.; Qu, C.-B.; Xiao, H.-M.; Fu, S.-Y. Greatly enhanced cryogenic mechanical properties of short carbon fiber/polyethersulfone composites by graphene oxide coating. *Compos. Part A Appl. Sci. Manuf.* **2016**, *89*, 47–55. [CrossRef]

75. Wang, C.-C.; Zhao, Y.-Y.; Ge, H.-Y.; Qian, R.-S. Enhanced mechanical and thermal properties of short carbon fiber reinforced polypropylene composites by graphene oxide. *Polym. Compos.* **2016**, *39*, 405–413. [CrossRef]

76. Yongqiang, L.; Chunzheng, P. Improved interfacial properties of PI composites through graphene oxide and carbon nanotubes on carbon fiber surface. *Surf. Interface Anal.* **2018**, *50*, 634–639. [CrossRef]

77. Ma, Y.; Yan, C.; Xu, H.; Liu, D.; Shi, P.; Zhu, Y.; Liu, J. Enhanced interfacial properties of carbon fiber reinforced polyamide 6 composites by grafting graphene oxide onto fiber surface. *Appl. Surf. Sci.* **2018**, *452*, 286–298. [CrossRef]

78. Li, F.; Liu, Y.; Qu, C.-B.; Xiao, H.-M.; Hua, Y.; Sui, G.-X.; Fu, S.-Y. Enhanced mechanical properties of short carbon fiber reinforced polyethersulfone composites by graphene oxide coating. *Polymer* **2015**, *59*, 155–165. [CrossRef]

79. Irisawa, T.; Shibata, M.; Yamamoto, T.; Tanabe, Y. Effects of carbon nanofibers on carbon fiber reinforced thermoplastics made with in situ polymerizable polyamide 6. *Compos. Part A Appl. Sci. Manuf.* **2020**, *138*, 106051. [CrossRef]

80. Li, J.; Zhang, L.Q. The research on the mechanical and tribological properties of carbon fiber and carbon nanotube-filled PEEK composite. *Polym. Compos.* **2009**, *31*, 1315–1320. [CrossRef]

81. Veazey, D.; Hsu, T.; Gomez, E. Next generation high-performance carbon fiber thermoplastic composites based on polyaryletherketones. *J. Appl. Polym. Sci.* **2017**, *134*. [CrossRef]

82. Li, H.; Wang, Y.; Zhang, C.; Zhang, B. Effects of thermal histories on interfacial properties of carbon fiber/polyamide 6 composites: Thickness, modulus, adhesion and shear strength. *Compos. Part A Appl. Sci. Manuf.* **2016**, *85*, 31–39. [CrossRef]

83. Arao, Y.; Yumitori, S.; Suzuki, H.; Tanaka, T.; Tanaka, K.; Katayama, T. Mechanical properties of injection-molded carbon fiber/polypropylene composites hybridized with nanofillers. *Compos. Part A Appl. Sci. Manuf.* **2013**, *55*, 19–26. [CrossRef]

84. Liu, W.; Li, L.; Zhang, S.; Yang, F.; Wang, R. Mechanical properties of carbon nanotube/carbon fiber reinforced thermoplastic polymer composite. *Polym. Compos.* **2015**, *38*, 2001–2008. [CrossRef]

85. O'Connor, H.J.; Dowling, D.P. Low-pressure additive manufacturing of continuous fiber-reinforced polymer composites. *Polym. Compos.* **2019**, *40*, 4329–4339. [CrossRef]

86. Li, J.; Zhang, Y.F. The tensile properties of HNO3-treated carbon fiber reinforced ABS/PA6 composites. *Surf. Interface Anal.* **2009**, *41*, 610–614. [CrossRef]

87. Omar, N.W.Y.; Shuaib, N.A.; Ab Hadi, M.H.J.; Azmi, A.I. Mechanical properties of carbon and glass fibre reinforced composites produced by additive manufacturing: A short review. *IOP Conf. Ser. Mater. Sci. Eng.* **2019**, *670*, 12020. [CrossRef]

88. Zhou, S.; Zhang, Q.; Wu, C.; Huang, J. Effect of carbon fiber reinforcement on the mechanical and tribological properties of polyamide6/polyphenylene sulfide composites. *Mater. Des.* **2013**, *44*, 493–499. [CrossRef]

89. Luo, W.; Liu, Q.; Li, Y.; Zhou, S.; Zou, H.; Liang, M. Enhanced mechanical and tribological properties in polyphenylene sulfide/polytetrafluoroethylene composites reinforced by short carbon fiber. *Compos. Part B Eng.* **2016**, *91*, 579–588. [CrossRef]

90. Zheng, L.; Liao, G.-X.; Gu, T.-S.; Han, Y.-J.; Jian, X.-G. Modified continuous carbon fiber-reinforced poly(phthalazinone ether sulfone ketone) composites by blending polyetherimide and polyethersulfone. *Polym. Compos.* **2008**, *30*, 1842–1847. [CrossRef]

91. Vivekanandhan, S.; Misra, M.; Mohanty, A.K. Thermal, mechanical, and morphological investigation of injection molded poly(trimethylene terephthalate)/carbon fiber composites. *Polym. Compos.* **2012**, *33*, 1933–1940. [CrossRef]

92. Yan, X.; Imai, Y.; Shimamoto, D.; Hotta, Y. Relationship study between crystal structure and thermal/mechanical properties of polyamide 6 reinforced and unreinforced by carbon fiber from macro and local view. *Polymer* **2014**, *55*, 6186–6194. [CrossRef]

93. Masahito, U.; Jin, S.; Ueda, M.; Yokozeki, T.; Yang, Y.; Kobayashi, F.; Kobayashi, H.; Sugahara, T.; Hamada, H. Higher performance carbon fiber reinforced thermoplastic composites from thermoplastic prepreg technique: Heat and moisture effect. *Compos. Part B Eng.* **2018**, *154*, 90–98. [CrossRef]

94. Hassan, A.; Hornsby, P.; Folkes, M. Structure–property relationship of injection-molded carbon fibre-reinforced polyamide 6,6 composites: The effect of compounding routes. *Polym. Test.* **2003**, *22*, 185–189. [CrossRef]

95. Botelho, E.C.; Figiel, Ł.; Rezende, M.C.; Lauke, B. Mechanical behavior of carbon fiber reinforced polyamide composites. *Compos. Sci. Technol.* **2003**, *63*, 1843–1855. [CrossRef]

96. Kurokawa, M.; Uchiyama, Y.; Iwai, T.; Nagai, S. Performance of plastic gear made of carbon fiber reinforced polyamide 12. *Wear* **2003**, *254*, 468–473. [CrossRef]

97. Wu, G.M.; Schultz, J.M. Processing and properties of solution impregnated carbon fiber reinforced polyethersulfone composites. *Polym. Compos.* **2000**, *21*, 223–230. [CrossRef]

98. Karsli, N.G.; Aytac, A. Tensile and thermomechanical properties of short carbon fiber reinforced polyamide 6 composites. *Compos. Part B Eng.* **2013**, *51*, 270–275. [CrossRef]

99. Kim, Y.H.; Yoon, S.H.; Jang, S.H.; Lee, Y.K.; Sung, Y.-T.; Lee, H.S.; Kim, W.N. Effects of Fiber Characteristics on the Rheological and Mechanical Properties of Polycarbonate/Carbon Fiber Composites. *Compos. Interfaces* **2009**, *16*, 477–491. [CrossRef]

100. Fu, S.-Y.; Lauke, B.; Mäder, E.; Hu, X.; Yue, C. Fracture resistance of short-glass-fiber-reinforced and short-carbon-fiber-reinforced polypropylene under Charpy impact load and its dependence on processing. *J. Mater. Process. Technol.* **1999**, *89*, 501–507. [CrossRef]

101. Rezaei, F.; Yunus, R.; Ibrahim, N. Effect of fiber length on thermomechanical properties of short carbon fiber reinforced polypropylene composites. *Mater. Des.* **2009**, *30*, 260–263. [CrossRef]

102. Unterweger, C.; Mayrhofer, T.; Piana, F.; Duchoslav, J.; Stifter, D.; Poitzsch, C.; Fürst, C. Impact of fiber length and fiber content on the mechanical properties and electrical conductivity of short carbon fiber reinforced polypropylene composites. *Compos. Sci. Technol.* **2020**, *188*, 107998. [CrossRef]

103. Hwang, S.-S. Tensile, electrical conductivity and EMI shielding properties of solid and foamed PBT/carbon fiber composites. *Compos. Part B Eng.* **2016**, *98*, 1–8. [CrossRef]

104. Gabrion, X.; Placet, V.; Trivaudey, F.; Boubakar, L. About the thermomechanical behaviour of a carbon fibre reinforced high-temperature thermoplastic composite. *Compos. Part B Eng.* **2016**, *95*, 386–394. [CrossRef]

105. Hamilton, S.; Muñoz-Escalona, P. Enhancement of Wear properties of a polyether ether ketone polymer by incorporation of carbon and glass fibers. *J. Appl. Polym. Sci.* **2019**, *1*. [CrossRef]

106. Karsli, N.G.; Aytac, A. Effects of maleated polypropylene on the morphology, thermal and mechanical properties of short carbon fiber reinforced polypropylene composites. *Mater. Des.* **2011**, *32*, 4069–4073. [CrossRef]

107. Kada, D.; Koubaa, A.; Tabak, G.; Migneault, S.; Garnier, B.; Boudenne, A. Tensile properties, thermal conductivity, and thermal stability of short carbon fiber reinforced polypropylene composites. *Polym. Compos.* **2016**, *39*, E664–E670. [CrossRef]

108. Do, V.-T.; Nguyen-Tran, H.-D.; Chun, D.-M. Effect of polypropylene on the mechanical properties and water absorption of carbon-fiber-reinforced-polyamide-6/polypropylene composite. *Compos. Struct.* **2016**, *150*, 240–245. [CrossRef]

109. Cho, J.; Lee, S.-K.; Eem, S.-H.; Jang, J.G.; Yang, B. Enhanced mechanical and thermal properties of carbon fiber-reinforced thermoplastic polyketone composites. *Compos. Part A Appl. Sci. Manuf.* **2019**, *126*, 105599. [CrossRef]

110. Abt, T.; Karger-Kocsis, J.; Sánchez-Soto, M. Toughened carbon fiber fabric-reinforced pCBT composites. *Polym. Compos.* **2014**, *37*, 1453–1460. [CrossRef]

111. Choi, Y.-K.; Sugimoto, K.-I.; Song, S.-M.; Endo, M. Production and characterization of polycarbonate composite sheets reinforced with vapor grown carbon fiber. *Compos. Part A Appl. Sci. Manuf.* **2006**, *37*, 1944–1951. [CrossRef]

112. Carneiro, O.; Covas, J.; Bernardo, C.; Caldeira, G.; Van Hattum, F.; Ting, J.-M.; Alig, R.; Lake, M. Production and assessment of polycarbonate composites reinforced with vapour-grown carbon fibres. *Compos. Sci. Technol.* **1998**, *58*, 401–407. [CrossRef]

113. Maqsood, N.; Rimašauskas, M. Characterization of carbon fiber reinforced PLA composites manufactured by fused deposition modeling. *Compos. Part C Open Access* **2021**, *4*, 100112. [CrossRef]

114. Li, S.; Li, D. Carbon fiber reinforced highly filled charcoal powder/ultra high molecular weight polyethylene composites. *Mater. Lett.* **2014**, *134*, 99–102. [CrossRef]

115. Unterweger, C.; Brüggemann, O.; Fuerst, C. Synthetic fibers and thermoplastic short-fiber-reinforced polymers: Properties and characterization. *Polym. Compos.* **2014**, *35*, 227–236. [CrossRef]

116. Hasan, M.M.B.; Nocke, A.; Cherif, C. High temperature resistant insulated hybrid yarns for carbon fiber reinforced thermoplastic composites. *J. Appl. Polym. Sci.* **2013**, *130*, 1179–1184. [CrossRef]

117. Alam, P.; Mamalis, D.; Robert, C.; Floreani, C.; Brádaigh, C.Ó. The fatigue of carbon fibre reinforced plastics—A review. *Compos. Part B Eng.* **2019**, *166*, 555–579. [CrossRef]

118. Fang, Y.; Fang, Z.; Jiang, R.; Jiang, Z.; Zhu, D. Effect of temperature on the transverse impact performance of preloaded CFRP wire. *Compos. Struct.* **2020**, *231*, 111464. [CrossRef]

119. Hanchi, J.; Eiss, N. Dry sliding friction and wear of short carbon-fiber-reinforced polyetheretherketone (PEEK) at elevated temperatures. *Wear* **1997**, *203*, 380–386. [CrossRef]

120. Fujihara, K.; Huang, Z.-M.; Ramakrishna, S.; Hamada, H. Influence of processing conditions on bending property of continuous carbon fiber reinforced PEEK composites. *Compos. Sci. Technol.* **2004**, *64*, 2525–2534. [CrossRef]

121. Hou, M.; Friedrich, K. Stamp forming of continuous carbon fibre/polypropylene composites. *Compos. Manuf.* **1991**, *2*, 3–9. [CrossRef]

122. Huang, C.-Y.; Wu, C.-C. The EMI shielding effectiveness of PC/ABS/nickel-coated-carbon-fibre composites. *Eur. Polym. J.* **2000**, *36*, 2729–2737. [CrossRef]

123. Huang, C.-Y.; Pai, J.-F. Optimum conditions of electroless nickel plating on carbon fibres for EMI shielding effectiveness of ENCF/ABS composites. *Eur. Polym. J.* **1998**, *34*, 261–267. [CrossRef]

124. Nishikawa, T.; Ogi, K.; Tanaka, T.; Okano, Y.; Taketa, I. Electrical properties of ABS resin reinforced with recycled CFRP. *Adv. Compos. Mater.* **2007**, *16*, 1–10. [CrossRef]

125. Rahaman, M.; Chaki, T.K.; Khastgir, D. High-performance EMI shielding materials based on short carbon fiber-filled ethylene vinyl acetate copolymer, acrylonitrile butadiene copolymer, and their blends. *Polym. Compos.* **2011**, *32*, 1790–1805. [CrossRef]

126. Das, N.; Khastgir, D.; Chaki, T.; Chakraborty, A. Electromagnetic interference shielding effectiveness of carbon black and carbon fibre filled EVA and NR based composites. *Compos. Part A Appl. Sci. Manuf.* **2000**, *31*, 1069–1081. [CrossRef]

127. Zhang, C.; Yi, X.; Yui, H.; Asai, S.; Sumita, M. Selective location and double percolation of short carbon fiber filled polymer blends: High-density polyethylene/isotactic polypropylene. *Mater. Lett.* **1998**, *36*, 186–190. [CrossRef]

128. Zhao, S.; Zhao, H.; Li, G.; Dai, K.; Zheng, G.; Liu, C.; Shen, C. Synergistic effect of carbon fibers on the conductive properties of a segregated carbon black/polypropylene composite. *Mater. Lett.* **2014**, *129*, 72–75. [CrossRef]

129. Cipriano, B.H.; Kota, A.K.; Gershon, A.L.; Laskowski, C.J.; Kashiwagi, T.; Bruck, H.; Raghavan, S. Conductivity enhancement of carbon nanotube and nanofiber-based polymer nanocomposites by melt annealing. *Polymer* **2008**, *49*, 4846–4851. [CrossRef]

130. Thongruang, W.; Spontak, R.J.; Balik, C. Correlated electrical conductivity and mechanical property analysis of high-density polyethylene filled with graphite and carbon fiber. *Polymer* **2002**, *43*, 2279–2286. [CrossRef]

131. Tzeng, S.-S.; Chang, F.-Y. EMI shielding effectiveness of metal-coated carbon fiber-reinforced ABS composites. *Mater. Sci. Eng. A* **2001**, *302*, 258–267. [CrossRef]

132. Huang, C.-Y.; Mo, W.-W.; Roan, M.-L. Studies on the influence of double-layer electroless metal deposition on the electromagnetic interference shielding effectiveness of carbon fiber/ABS composites. *Surf. Coat. Technol.* **2004**, *184*, 163–169. [CrossRef]

133. Hong, M.-S.; Choi, W.-K.; An, K.-H.; Kang, S.-J.; Park, S.-J.; Lee, Y.S.; Kim, B.-J. Electromagnetic interference shielding behaviors of carbon fibers-reinforced polypropylene matrix composites: II. Effects of filler length control. *J. Ind. Eng. Chem.* **2014**, *20*, 3901–3904. [CrossRef]

134. Xi, Y.; Bin, Y.; Chiang, C.; Matsuo, M. Dielectric effects on positive temperature coefficient composites of polyethylene and short carbon fibers. *Carbon* **2007**, *45*, 1302–1309. [CrossRef]

135. Shen, L.; Wang, F.; Yang, H.; Meng, Q. The combined effects of carbon black and carbon fiber on the electrical properties of composites based on polyethylene or polyethylene/polypropylene blend. *Polym. Test.* **2011**, *30*, 442–448. [CrossRef]

136. Ameli, A.; Jung, P.; Park, C.B. Electrical properties and electromagnetic interference shielding effectiveness of polypropylene/carbon fiber composite foams. *Carbon* **2013**, *60*, 379–391. [CrossRef]

137. Saleem, A.; Frormann, L.; Iqbal, A. High performance thermoplastic composites: Study on the mechanical, thermal, and electrical resistivity properties of carbon fiber-reinforced polyetheretherketone and polyethersulphone. *Polym. Compos.* **2007**, *28*, 785–796. [CrossRef]

138. Yajima, S. Silicon carbide fibres. In *Strong Fibres, Handbook of Composites*; Watt, W., Perov, B.V., Eds.; North-Holland Publishing Company: Amsterdam, The Netherlands, 1985; Volume 1, pp. 201–240.

139. Yılmaz, H.; Imai, Y.; Nagata, K.; Sato, K.; Hotta, Y. Localized thermal analysis of carbon fiber-reinforced polypropylene composites. *Polym. Compos.* **2012**, *33*, 1764–1769. [CrossRef]

140. Samyn, P.; De Baets, P.; Schoukens, G. Role of internal additives in the friction and wear of carbon-fiber-reinforced polyimide. *J. Appl. Polym. Sci.* **2009**, *116*, 1146–1156. [CrossRef]

141. Dong, F.; Hou, G.; Liu, H.; Liu, L.; Cao, F.; Wang, J.; Yan, F. An investigation on the mechanical and tribological properties of carbon fiber/polyimide composites at elevated temperatures. *Polym. Compos.* **2018**, *39*, E869–E882. [CrossRef]

142. Munirathnamma, L.M.; Ravikumar, H.B. Positron lifetime study of PAN-based carbon fiber-reinforced polymer composites. *Polym. Compos.* **2018**, *40*. [CrossRef]

143. Yoo, Y.; Lee, H.L.; Ha, S.M.; Jeon, B.K.; Won, J.C.; Lee, S.-G. Effect of graphite and carbon fiber contents on the morphology and properties of thermally conductive composites based on polyamide 6. *Polym. Int.* **2014**, *63*, 151–157. [CrossRef]

144. Burela, R.G.; Kamineni, J.N.; Harursampath, D. Chapter 8—Multifunctional Polymer Composites for 3D and 4D Printing. In *3D and 4D Printing of Polymer Nanocomposite Materials*; Sadasivuni, K.K., Deshmukh, K., Almaadeed, M.A., Eds.; Elsevier: Amsterdam, The Netherlands, 2020; pp. 231–257.

145. Five Reasons Why Carbon Fibre Is the Future of Design—The Manufacturer. 2021. Available online: https://www.themanufacturer.com/articles/five-reasons-why-carbon-fibre-is-the-future-of-design/ (accessed on 19 February 2021).

146. Prabhakaran, R.T.D. Are Reactive Thermoplastic Polymers Suitable for Future Wind Turbine Composite Materials Blades? *Mech. Adv. Mater. Struct.* **2013**, *21*, 213–221. [CrossRef]

147. Khurshid, M.F.; Hengstermann, M.; Hasan, M.M.B.; Abdkader, A.; Cherif, C. Recent developments in the processing of waste carbon fibre for thermoplastic composites—A review. *J. Compos. Mater.* **2019**, *54*, 1925–1944. [CrossRef]

148. Kim, Y.; Ryu, K.-H.; Na, W.; Yu, J.; Lee, M.W. Origami-inspired reforming method for carbon fiber-reinforced thermoplastics via simple thermal stitching. *Compos. Part B Eng.* **2020**, *193*, 108043. [CrossRef]

149. Ahmed, A.; Wei, L. Introducing CFRP as an alternative material for engine hood to achieve better pedestrian safety using finite element modeling. *Thin-Walled Struct.* **2016**, *99*, 97–108. [CrossRef]

150. Turner, T.; Harper, L.T.; Warrior, N.; Rudd, C.D. Low-cost carbon-fibre-based automotive body panel systems: A performance and manufacturing cost comparison. *Proc. Inst. Mech. Eng. Part D J. Automob. Eng.* **2008**, *222*, 53–63. [CrossRef]

151. Sarfraz, M.S.; Hong, H.; Kim, S.S. Recent developments in the manufacturing technologies of composite components and their cost-effectiveness in the automotive industry: A review study. *Compos. Struct.* **2021**, *266*, 113864. [CrossRef]

152. Todor, M.P.; Kiss, I. Systematic approach on materials selection in the automotive industry for making vehicles lighter, safer and more fuel-efficient. *Appl. Eng. Lett.* **2016**, *1*, 91–97.

153. Ning, H.; Lu, N.; Hassen, A.A.; Chawla, K.; Selim, M.; Pillay, S. A review of long fibre thermoplastic (LFT) composites. *Int. Mater. Rev.* **2020**, *65*, 164–188. [CrossRef]

154. Friedrich, K. Carbon fiber reinforced thermoplastic composites for future automotive applications. *AIP Conf. Proc.* **2016**, *1736*, 20001. [CrossRef]

155. Yu, K.; Morozov, E.V.; Ashraf, M.A.; Shankar, K. A review of the design and analysis of reinforced thermoplastic pipes for offshore applications. *J. Reinf. Plast. Compos.* **2017**, *36*, 1514–1530. [CrossRef]

156. Venkatesan, R.; Dwarakadasa, E.; Ravindran, M. Study on behavior of carbon fiber-reinforced composite for deep sea applications. *All Days* **2002**, *2829*. [CrossRef]

157. Qi, D.; Ding, N.; Cai, X.; Li, H.; Shuhui, Z.; Yan, M. Application and Qualification of Reinforced Thermoplastic Pipes in Chinese Oilfields. *Int. Conf. Pipeline Trenchless Technol.* **2011**, *267*, 267–275. [CrossRef]

158. Song, P.; Yao, D.; Chen, B.; Wang, C. The Development of a New Reinforced Thermoplastic Pipe with Large Diameter for Oil and Gas Transmission Pipeline. *Chin. Mater. Conf.* **2019**, *133*, 133–139. [CrossRef]

159. Osborne, J. Thermoplastic pipes-lighter, more flexible solutions for oil and gas extraction. *Reinf. Plast.* **2013**, *57*, 33–38. [CrossRef]

160. Mishnaevsky, L.; Branner, K.; Petersen, H.N.; Beauson, J.; McGugan, M.; Sørensen, B.F. Materials for Wind Turbine Blades: An Overview. *Materials* **2017**, *10*, 1285. [CrossRef]

161. Giorgini, L.; Benelli, T.; Brancolini, G.; Mazzocchetti, L. Recycling of carbon fiber reinforced composite waste to close their life cycle in a cradle-to-cradle approach. *Curr. Opin. Green Sustain. Chem.* **2020**, *26*, 100368. [CrossRef]

162. Bondy, M.; Rodgers, W.; Altenhof, W. Tensile fatigue characterization of polyamide 66/carbon fiber direct/in-line compounded long fiber thermoplastic composites. *Compos. Part B Eng.* **2019**, *173*, 106984. [CrossRef]

Effects of Particle Size on the Dielectric, Mechanical, and Thermal Properties of Recycled Borosilicate Glass-Filled PTFE Microwave Substrates

Ibrahim Abubakar Alhaji [1,2], Zulkifly Abbas [1,3,*], Mohd Hafiz Mohd Zaid [1,4] and Ahmad Mamoun Khamis [1]

[1] Department of Physics, Faculty of Science, Universiti Putra Malaysia, Serdang 43400, Malaysia; gs54099@student.upm.edu.my (I.A.A.); mhmzaid@upm.edu.my (M.H.M.Z.); akhameis@yahoo.com (A.M.K.)

[2] Department of Physics, Faculty of Science, Federal University of Kashere, Gombe PMB 0182, Gombe State, Nigeria

[3] Institute of Tropical Forestry and Forest Product, Universiti Putra Malaysia, Serdang 43400, Malaysia

[4] Institute of Advanced Technology, Universiti Putra Malaysia, Serdang 43400, Malaysia

* Correspondence: za@upm.edu.my; Tel.: +60-17-330-0429

Abstract: Low dielectric loss and low-cost recycled borosilicate (BRS) glass-reinforced polytetrafluoroethylene (PTFE) composites were fabricated for microwave substrate applications. The composites were prepared through a dry powder processing technique by dispersing different micron sizes (25 μm, 45 μm, 63 μm, 90 μm, and 106 μm) of the recycled BRS filler in the PTFE matrix. The effect of the filler sizes on the composites' thermal, mechanical, and dielectric properties was studied. The dielectric properties of the composites were characterised in the frequency range of 1–12 GHz using an open-ended coaxial probe (OCP) connected to a vector network analyser (VNA). XRD patterns confirmed the phase formation of PTFE and recycled BRS glass. The scanning electron microscope also showed good filler dispersion at larger filler particle sizes. In addition, the composites' coefficient of thermal expansion and tensile strength decreased from 12.93 MPa and 64.86 ppm/°C to 7.12 MPa and 55.77 ppm/°C when the filler size is reduced from 106 μm to 25 μm. However, moisture absorption and density of the composites increased from 0.01% and 2.17 g/cm^3 to 0.04% and 2.21 g/cm^3. The decrement in filler size from 106 μm to 25 μm also increased the mean dielectric constant and loss tangent of the composites from 2.07 and 0.0010 to 2.18 and 0.0011, respectively, while it reduced the mean signal transmission speed from 2.088×10^8 m/s to 2.031×10^8 m/s. The presented results showed that PTFE/recycled BRS composite exhibited comparable characteristics with commercial high-frequency laminates.

Keywords: recycled borosilicate; PTFE; sintering; permittivity; high-frequency; substrates

1. Introduction

The last decade has seen rapid and unprecedented developments in information technology driven by military and consumer markets [1–3]. This change creates demands for high-speed, light and low-cost microwave substrate. A microwave substrate that meets specific criteria supports microwave circuits [4–6]. Microwave substrates are dielectric materials with low permittivity and a low loss tangent at microwave frequencies [5]. The substrate materials should have the following properties: low permittivity and loss tangent for rapid signal propagation, low coefficient of thermal expansion (CTE) for dimensional stability, high thermal conductivity for transporting the heat generated away from the microwave circuit and good mechanical strength for material rigidity [7].

Polymers are employed for substrate applications due to their excellent electrical properties. Polytetrafluoroethylene (PTFE) is the most widely used among polymers because of its low permittivity, dielectric loss, moisture absorption and chemical inertness [8–10]. However, it has a high CTE (~109 ppm/°C) and melting point (~327 °C) that hinder its utilisation [11]. It also lacks rigidity for practical substrate applications. These limitations

can be overcome by adding inorganic and rigid fillers such as glass with lower CTE and moderate dielectric properties. That is possible because the properties of polymers depend on their microstructure and composition [12]. The high melting point of PTFE can also be circumvented by employing a processing technique, such as the powder processing method, that does not require heat treatment to mix PTFE-glass composites [13].

Recently, recycled glass fillers have attracted considerable attention for microwave applications due to their rigidity and moderate dielectric properties [14]. Recycled glass is cheaper and reduces environmental pollution. In this work, the preparation and characterisation of recycled borosilicate glass filled PTFE substrate is reported. Borosilicate (BRS) is an industrial glass with a thermal conductivity ranging from 1–1.3 W/mK. It has a low CTE of 3.2 ppm/°C–4.0 ppm/°C and tensile strength of about 22 MPa–32 MPa. The glass is also an excellent electrical insulator with a dielectric constant and loss factor of 4.65–6.00 and 0.01–0.017 [15,16]. These excellent properties of BRS glass make it a perfect filler when recycled for PTFE-based substrate applications. To the best of our knowledge, no systematic study of the effect of the recycled BRS filler size on PTFE/recycled BRS composites has been reported. Therefore, this work investigated the dielectric, thermal, and mechanical properties of PTFE/recycled BRS. In addition, signal propagation speed across the composites with different filler sizes was calculated and analysed. The PTFE/recycled BRS composite was also compared with commercial high-frequency laminates.

2. Materials and Methods

2.1. Materials

The PTFE of type MF90C with an average particle size of 50–110 μm was obtained from Fujian Sannong New Materials Co., Ltd., Sanming, China. At the same time, BRS glass was acquired from Top Globe Sdn. Bhd. Selangor, Malaysia, in the form of waste moulds.

Glass Powder Preparation

The BRS glass moulds were initially cleaned, washed, and dried at room temperature for 24 h. After that, the moulds were crushed with a hammer into glass pebbles. A Plunger was further used to grind the glass pebbles into coarse glass powder. In addition, the coarse glass powder was transferred to a grinding mill jar with a powder-to-ball ratio of 20:1, which was then milled. The milling was conducted at room temperature for 24 h at 45 rpm using the U.S. Stoneware Jar Mills (U.S. Stoneware, East Palestine, OH, USA). After the milling stage, the recycled BRS powder was sieved to 25 μm, 45 μm, 63 μm, 90 μm, and 106 μm particle sizes. The range of these representative filler particle sizes is given in Table 1.

Table 1. Particle size distribution.

Representative Particle Size (μm)	Range of Particle Size (μm)
25	$X_1 \leq 25$
45	$25 < X_2 \leq 45$
63	$45 < X_2 \leq 63$
90	$63 < X_2 \leq 90$
106	$90 < X_2 \leq 106$

2.2. Preparation of PTFE/Recycled BRS Composites

The PTFE/recycled BRS composites were prepared by mixing 25 μm, 45 μm, 63 μm, 90 μm, and 106 μm of the recycled BRS filler with PTFE through a dry powder processing technique. The mixing was conducted via a Wing dry mixer for 10 min, and filler content in each composite was fixed at 5 wt.%. Then, the compositions were pressed into preforms using a hydraulic press at a pressure of 10 MPa for 5 min. The compacted composites were mechanically weak due to air voids. Hence, sintering is required for the removal of the voids. The samples were sintered from room temperature to 380 °C with a temperature rising time of 3 °C/min and held for 1 h to allow for particles fusion, coalescence and void elimination in the composites. The cooling rate was set at 1 °C/min from 380 °C to room

temperature to complete the sintering cycle. A Drying Oven (Jiangsu Sunkoo Machine Tech Co., Ltd., Changzhou, China) was utilised for the sintering.

2.3. Characterisations

2.3.1. Phase, Morphology and Composition

In this work, XRD was employed to analyse the phase formation of recycled BRS powder and PTFE/recycled BRS composites. The XRD data were collected using an automated Philips X'pert system (Model PW3040/60 MPD) with Cu–Kα radiation operating at a voltage of 40.0 kV and a current of 40.0 mA with a wavelength of 1.5405 Å. The 2-theta range of 10°–70° with a scanning speed of 2.0 °/min was used to record the diffraction patterns. All data were exposed to the Rietveld analysis on X'Pert Highscore Plus v3.0 software (PANalytical B.V., Almelo, The Netherlands). The samples were classified by comparing their diffraction peaks with the Inorganic Crystal Structure Database (ICSD).

The shape, arrangement and dispersion of the recycled BRS particles in the composites were investigated using LEO 1455 Variable Pressure Scanning Electron Microscope (VPSEM, Leo Electron Microscopy Group, Oberkochen, Germany). The elemental composition of the samples was obtained via an Oxford Inca energy dispersive X-ray micro-analyser (EDX, Oxford Instruments, Buckinghamshire, England) attached to the Leo 1455 VPSEM. Five spots on each sample were examined with the EDX for accurate determination of the elemental compositions of the composites qualitatively.

2.3.2. Moisture Absorption

The presence of moisture within a material increases its dielectric properties [17]. This change degrades the performance of the materials. Thus, determining the moisture absorption of materials is essential to identify suitable environmental operating conditions. PTFE/recycled BRS composites were cut into 25.4 mm by 76.2 mm following the ASTM D570 standard. The samples were then immersed in distilled water at 25 °C for 24 h. The percentage of moisture absorption for the composites was calculated according to Equation (1) [18].

$$MA\ (\%) = \frac{w_{f} - w_{i}}{w_{i}} \times 100 \tag{1}$$

where w_f and w_i are the respective wet and dry weights of the samples.

2.3.3. Density

The density of the PTFE/recycled BRS composites was measured at room temperature using the Archimedes principle. An electronic densitometer (Alfa Mirage Co., Osaka, Japan) was utilised for the measurement. Distilled water was then used as the reference liquid. Hence, the density of the sample was calculated using the following equation [19].

$$\rho_c = \frac{W_{air}}{W_{air} - W_{distilled\ water}} \times \rho_{distilled\ water} \tag{2}$$

where ρ_c is the density of the composite, $\rho_{distilled\ water}$ is the density of distilled water, and w_{air} and $w_{distilled\ water}$ are the weights of the sample in air and distilled water, respectively.

2.3.4. Tensile Strength

The dimensions of PTFE/recycled BRS composites were cut according to the ASTM D638 to determine the tensile strength of the composites [20]. The tensile strength test was conducted at room temperature using a Shimadzu AGS-X 100 kN computerised universal testing machine (UTM, Shimadzu, Kyoto, Japan). The UTM stretched the samples at a 5 mm/min stroke rate with a 10 kN load cell.

2.3.5. Coefficient of Thermal Expansion (CTE)

The CTE of the composites was measured in line with ASTM E228-17 [21]. A push-rod dilatometer, Linseis L75 Platinum (Linseis, Selb, Germany), was used. The measurement was done at room temperature, and the heating rate was set at 10 °C/min.

2.3.6. Complex Permittivity

The complex permittivity of PTFE/recycled BRS composites was characterised using the open-ended coaxial probe (OCP) technique in the 1–12 GHz frequency range [22]. The probe was connected to an Agilent N5227A vector network analyser (Agilent Technologies, Santa Clara, CA, USA), as shown in Figure 1. A one-port reflection calibration technique was used. The one-port calibration technique consists of air, a shorting block and distilled water at 25 °C. After complete calibration, the probe was placed flat on the surface of the samples for characterisation to avoid air gaps between the sample and the open probe that may affect measurement accuracy. A standard (unfilled PTFE) material was first characterised to confirm the accuracy of the calibration. In addition, the dimensions of the composites were 6 cm × 3.6 cm × 0.7 cm.
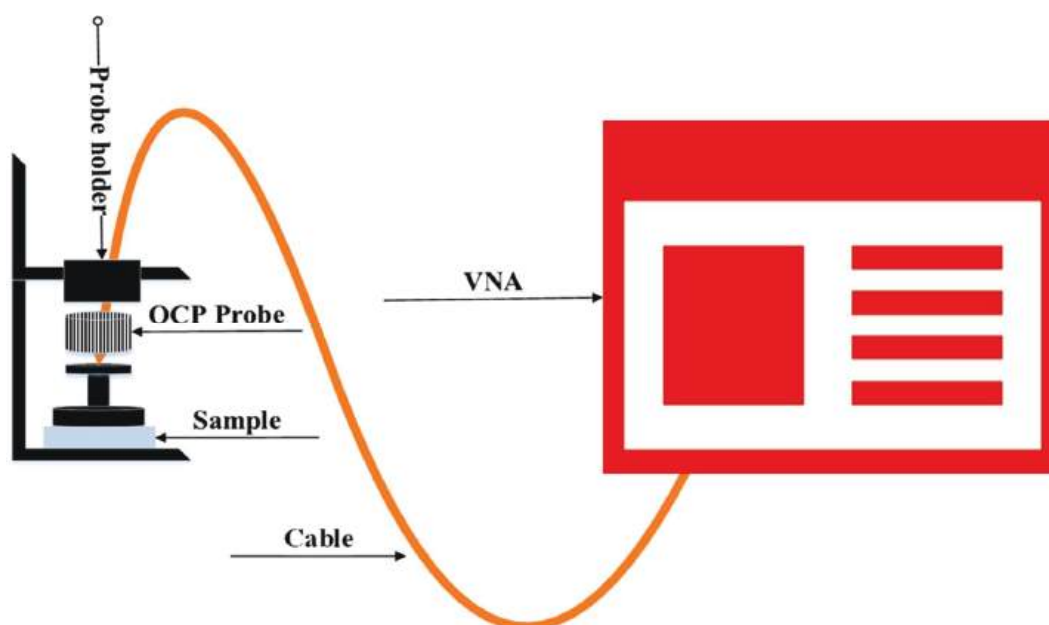
Figure 1. OCP measurement set-up.

The following equation gives the complex permittivity:

$$\varepsilon^* = \varepsilon' - j\varepsilon'' \tag{3}$$

where ε^* is the complex permittivity, ε' is the dielectric constant denoting energy storage, and ε'' is the loss factor, representing energy loss. The loss tangent, being the ratio of loss factor and dielectric constant, is therefore evaluated as follows [23]:

$$tan\delta = \frac{\varepsilon''}{\varepsilon'} \tag{4}$$

2.3.7. Signal Propagation Speed

A fast signal transmission with minor delay is required to transmit high data. Generally, electromagnetic waves are attenuated when passing through a denser medium. Thus, investigating the influence of filler size on the signal propagation speed is critical to the

design of microwave circuits for efficient data transmission. The signal transmission speed can be calculated using the following equation [24].

$$V_s = \frac{c}{\sqrt{\varepsilon' \mu'}}$$

(5)

where V_s is the signal transmission speed, c is the speed of light in vacuum, ε' is the dielectric constant, and μ' is the permeability of the material.

3. Results and Discussion

3.1. Phase, Morphology and Composition

The X-ray diffraction patterns of 63 µm recycled BRS powder and PTFE/recycled composites are shown in Figure 2. In the 63 µm recycled BRS XRD profile, a broad peak at $2\theta = 15° - 30°$ is observed, confirming the amorphous nature of the recycled BRS glass. This pattern is consistent with the work presented [25], which affirms that no impurities were introduced during the glass powder preparation. The same figure depicts the XRD pattern of PTFE. The diffractogram of the PTFE displays a sharp peak and five low-intensity peaks positioned at $2\theta = 18.05°$, $31.53°$, $36.60°$ $37.13°$, $41.18°$, and $49.07°$. These peaks relate to the (100), (110), (200), (107), (108), and (210) planes and are matched with the ICSD index of PTFE (ICSD 00-047-2217) [26,27]. Furthermore, the intensity of the peak located at $2\theta = 18.05°$ can be seen to decrease slightly as different sizes of recycled BRS filler are introduced to the PTFE matrix. In addition, no unwanted peaks in the pattern of the composites indicate that chemical interaction did not occur between the PTFE matrix and recycled BRS particulate.
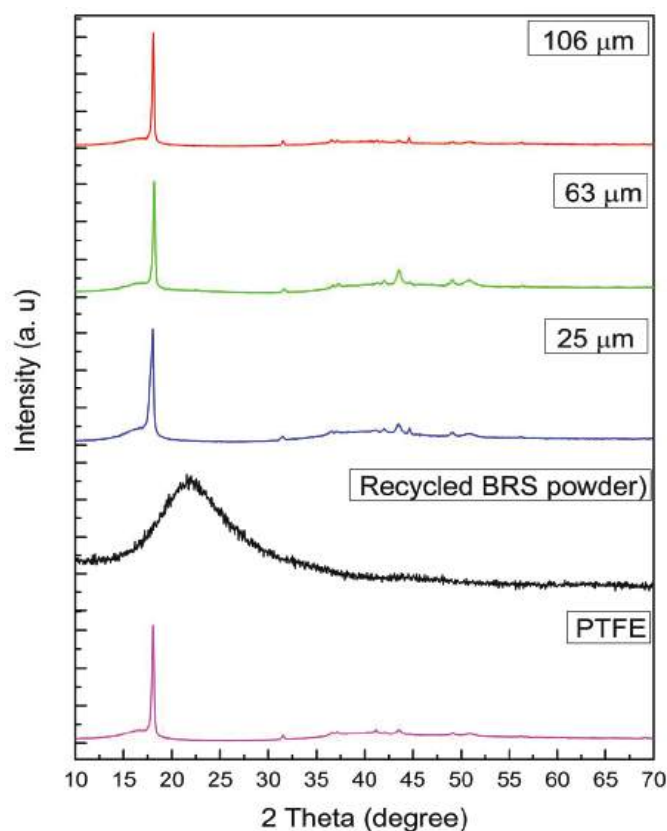
Figure 2. XRD patterns of PTFE, recycled BRS powder and PTFE/recycled BRS composites.

The scanning electron microscope (SEM) images of pure PTFE, 63 µm recycled BRS powder, and PTFE/recycled BRS composites are illustrated in Figure 3. It can be observed that the BRS particles are of arbitrary geometry. The recycled BRS particulates are also more

dispersed in the PTFE matrix at larger filler sizes, indicating a good connection between the PTFE matrix and recycled BRS filler. It is reported that effective dispersion of recycled BRS particulate in the PTFE promotes a homogeneous structure that enhances the properties of the composites [28,29].
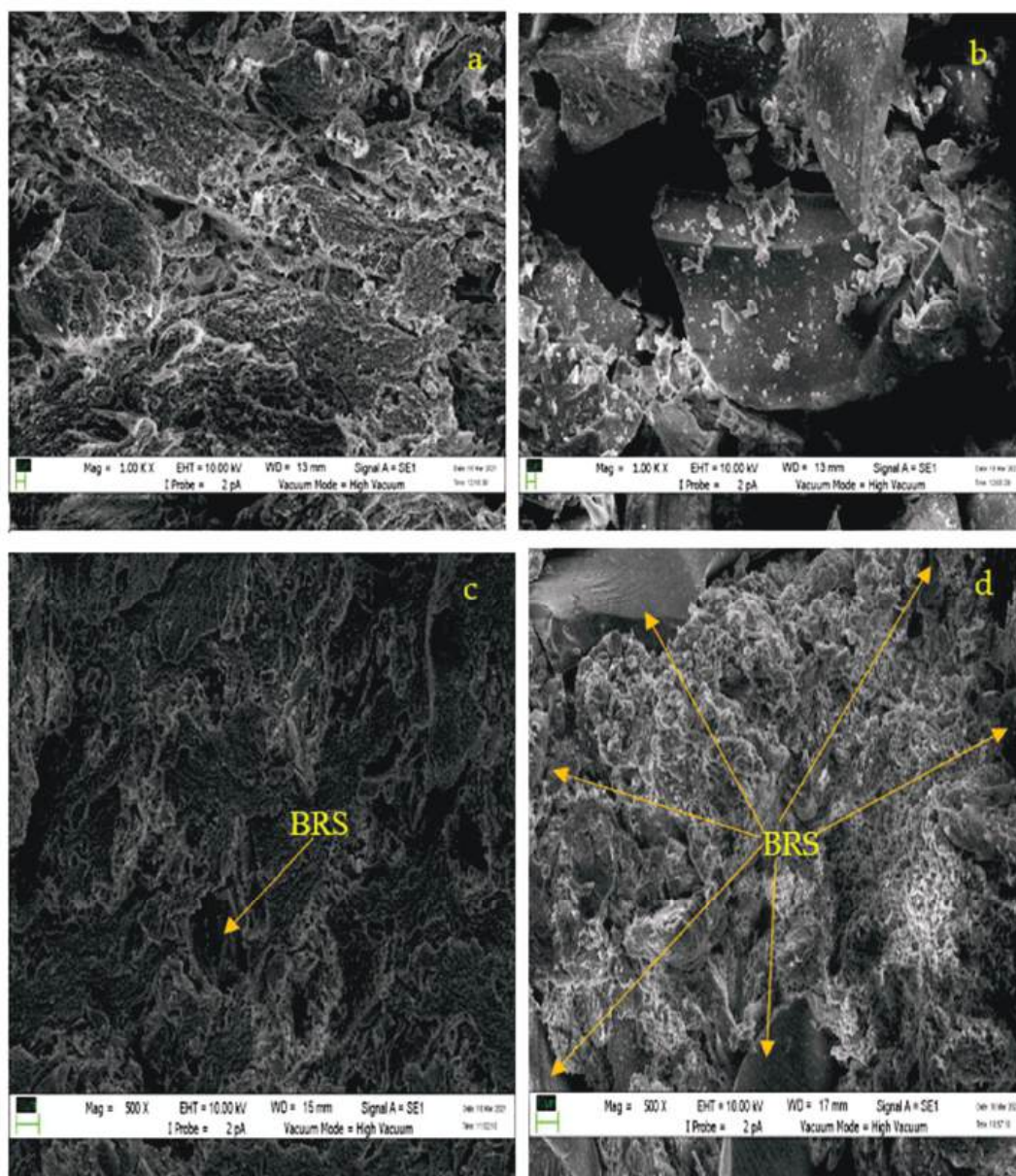
Figure 3. SEM micrographs of (**a**) PTFE, (**b**) recycled BRS powder, (**c**) PTFE/recycled BRS at (at 25 μm BRS) and (**d**) PTFE/recycled BRS composites at (106 μm BRS).

EDX analysis was conducted to determine the elemental composition of PTFE, 63 μm recycled BRS and PTFE/recycled BRS composites qualitatively. In Figure 4, the spectra show that PTFE comprises mainly C at 0.1 keV and F at 0.5 keV. In addition, the same figure reveals that the 63 μm recycled BRS powder consists of B, O, Na, Al and Si, validating the purity of recycled BRS glass [30]. Further analysis shows that PTFE and recycled BRS glass elements were all present in the PTFE/recycled BRS composites except Na and Al at 25 μm and 106 μm recycled BRS filler loadings. This incidence happens when the concentration level of the respective element falls below the detection limit [31]. Thus, the findings attest to the suitability of the dry powder-processing technique for composite fabrication.
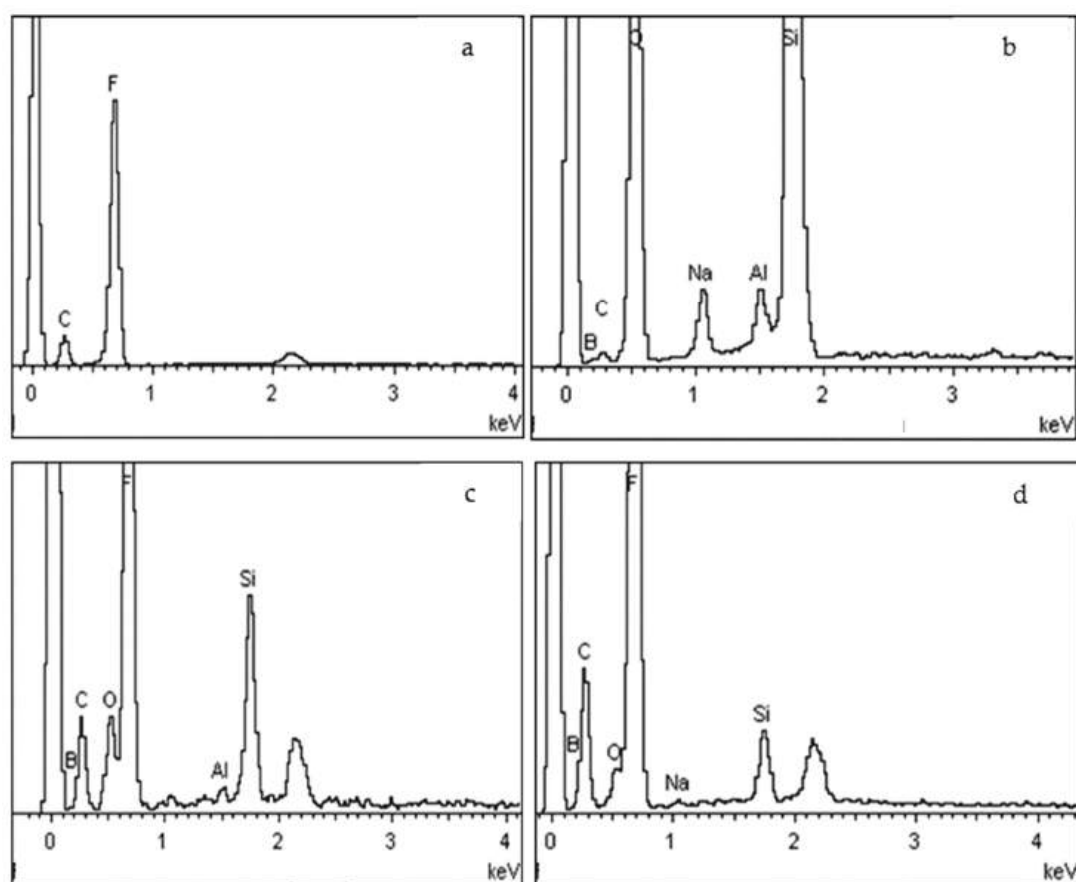
Figure 4. EDX spectra of (**a**) PTFE, (**b**) 63 recycled BRS powder, (**c**) PTFE/recycled BRS at 25 μm BRS and (**d**) PTFE/recycled BRS at 106 μm BRS.

3.2. Moisture Absorption

Moisture absorption significantly affects composite's dielectric properties because water has a high dielectric constant and loss. It is reported that moisture absorption of <0.1% is ideal for electronic packaging applications [6,8,32]. Figure 5 shows the variation in the moisture absorption of PTFE/recycled BRS composites. It can be seen that the moisture absorption increases from 0.011% to 0.040% when the recycled BRS filler size is reduced from 106 μm to 25 μm. It is worth noting that the composite records moisture absorption lower than the ideal value recommended. The increase in moisture absorption is attributed to the higher surface area of the smaller-sized recycled BRS particles [8]. Furthermore, the deterioration of moisture absorption is related to the enhanced porosity and density in the composites [33].

3.3. Density

The effect of recycled BRS filler size on the density of the PTFE matrix is shown in Figure 6. The 106 μm, 90 μm, 63 μm, 45 μm, 25 μm, recycled BRS composites had density values of 2.17, 2.18, 2.19, 2.20, and 2.21 g/cm^3, respectively. Thus, decreasing recycled BRS particle size led to the increase in the density of the composites. A similar result has been reported by Jiang and Yuan [8]. The enhanced density is related to introducing a denser recycled BRS filler than the PTFE matrix [34]. In addition, smaller-sized particles possess more particles per unit volume than larger-sized particles. Therefore, the smaller-sized filler particles occupy less volume, leading to the increased density of the composites. The increase in the density is also due to the higher moisture absorbed by the composites [6,35]. This variation significantly affects the PTFE matrix's CTE, tensile strength and dielectric properties [11].
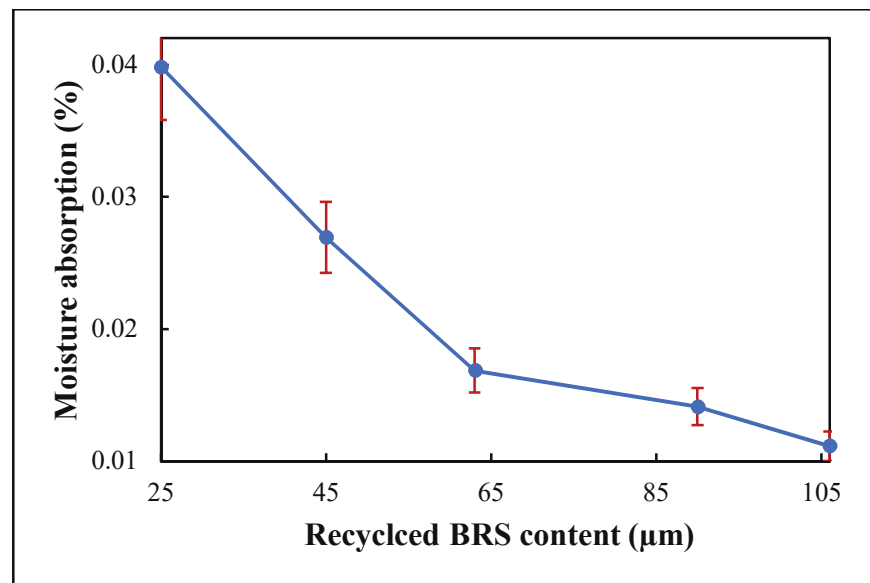
Figure 5. Variation of moisture absorption with filler size.
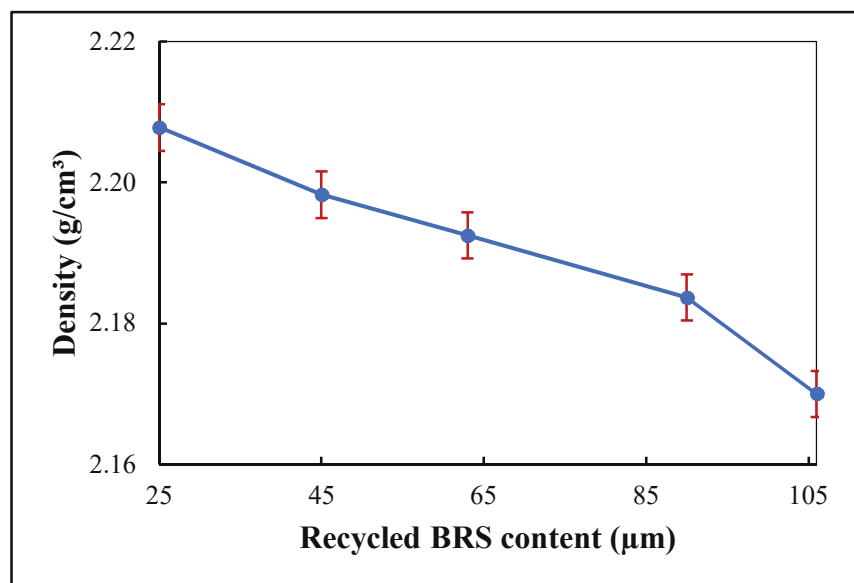
Figure 6. Variation of density with filler size.

3.4. Tensile Strength

The change of tensile strength as a function of recycled BRS particle size is presented in Figure 7. The 106 µm, 90 µm, 63 µm, 45 µm and 25 µm recycled BRS composites had respective tensile strength values of 12.93, 12.93, 12.92, 9.18 and 7.12 MPa. It could be seen that the reduction in particle size corresponded with a decrease in tensile strength consistent with the studies reported [36,37]. Although, the differences in tensile strength at 106 µm, 90 µm and 63 µm BRS sizes are smaller than at 45 µm and 25 µm filler sizes. This reduction in tensile strength is due to poor adhesion between the recycled BRS filler and PTFE matrix [36]. In addition, the smaller-sized particles with a higher surface area tend to absorb more water, which reduced the tensile strength of the PTFE matrix [38,39].
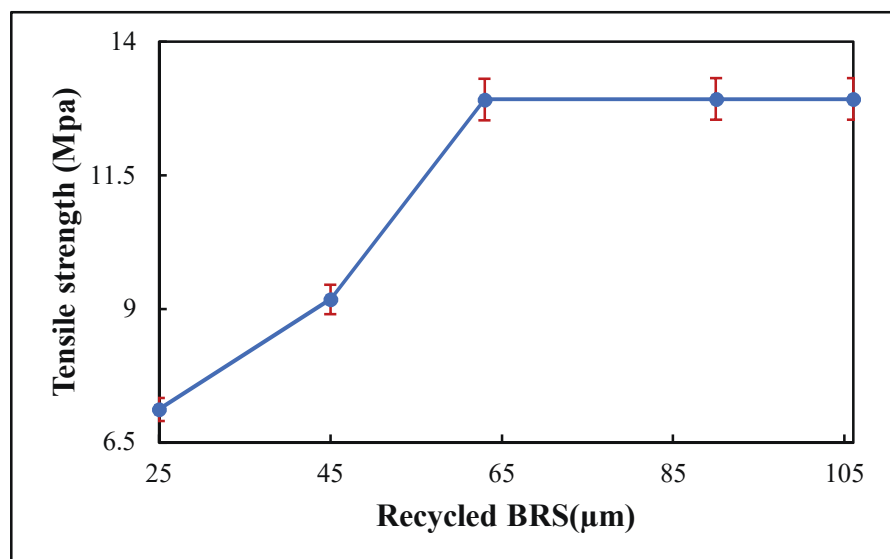
Figure 7. Variation of tensile strength with filler size.

3.5. Coefficient of Thermal Expansion (CTE)

The variation in CTE with recycled BRS particle size is shown in Figure 8. The composites showed a respective CTE of 64.8, 62.33, 60.45, 55.08 and 55.77 ppm/°C at 106 μm, 90 μm, 63 μm, 45 μm and 25 μm filler sizes. It is, therefore, evident that the decrease in filler size matched the drop in the CTE of the composites [8,36]. The variation is first attributed to the mismatch in the CTE of the PTFE matrix (∼109 ppm/°C) and the recycled BRS filler (~4 ppm/°C [40,41]. In addition, smaller-sized filler particles have a larger surface area and higher density. Thus, the matrix volume decreases with smaller-sized particles, restricting the matrix expansion, which further reduces the CTE of the composites [12].
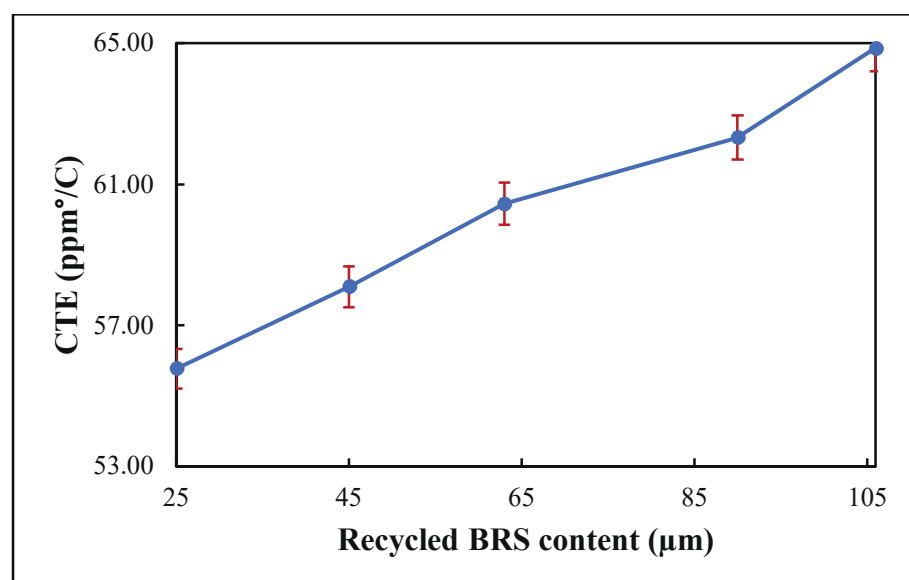
Figure 8. Variation of CTE with filler size.

3.6. Complex Permittivity

The influence of recycled BRS filler size reduction on the dielectric constant and loss factor of PTFE/recycled BRS composites was studied. The variation of ε' and ε'' in the 1–12 GHz range is presented in Figures 9 and 10, while the calculated $tan\delta$ is shown in Figure 11. It can be seen that the ε' and ε'' slightly decreased with the frequency [42–44].

In addition, the ε'' had a similar pattern for all composites, which is attributed to the calibration consistent with the loss factor result presented in [45]. The higher values of the ε' and ε'' at lower frequencies are due to the significant influence of charge relaxation and interfacial polarisation [46]. Generally, as frequency increases, the composite's overall polarisation lags the alternating electric field. Thus, each polarisation process stops contributing, decreasing its dielectric constant and loss factor [47].
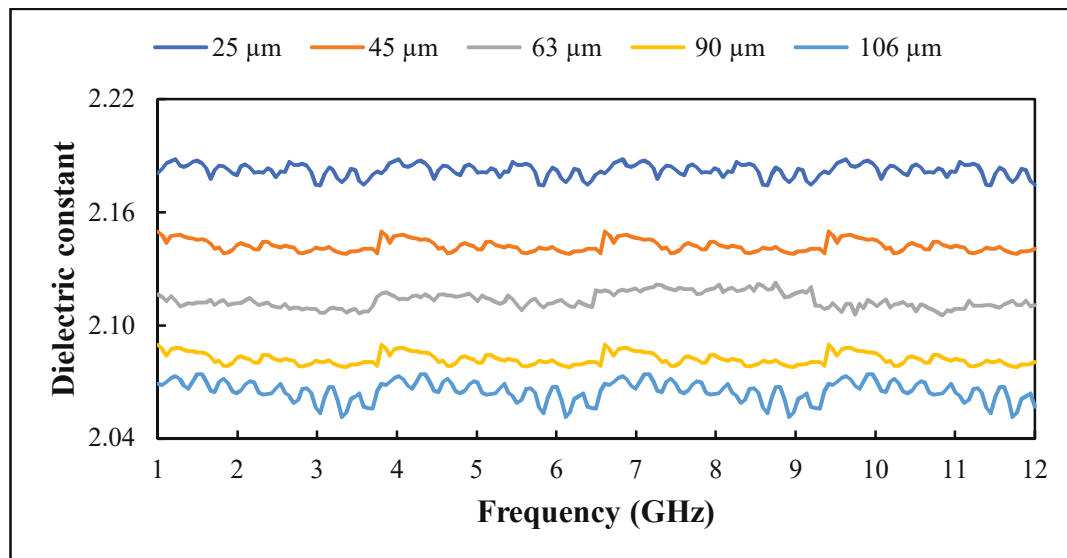
Figure 9. Variation of dielectric constant with filler size.
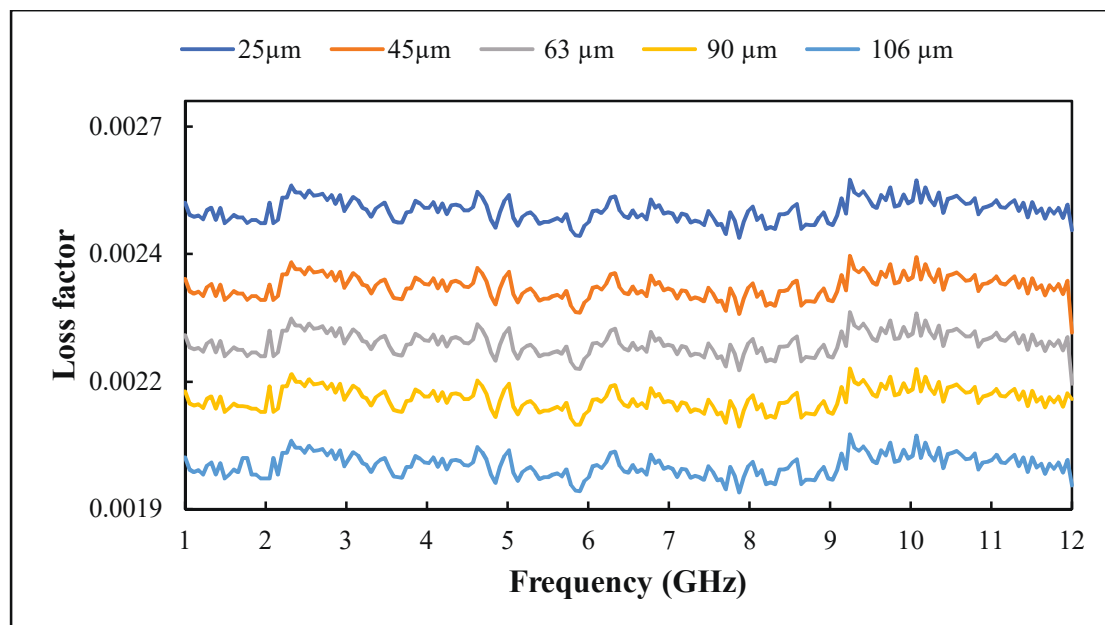
Figure 10. Variation of loss factor with filler size.
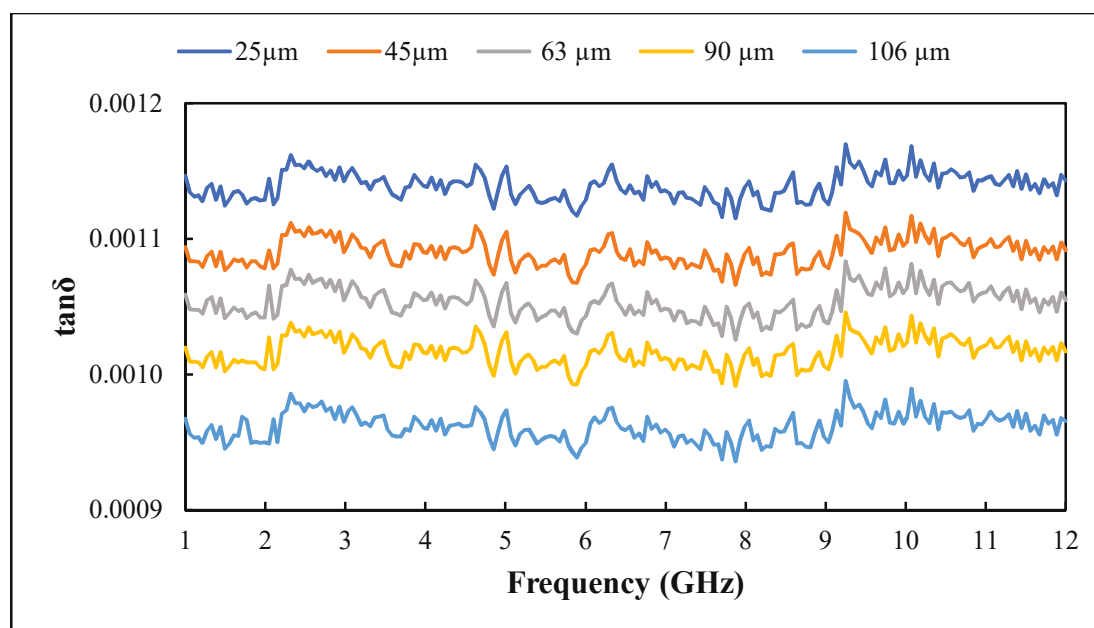
Figure 11. Variation of loss tangent with filler size.

Further analysis showed that the ε' and ε'' of PTFE/recycled BRS composites increased with the reduction in recycled BRS filler size (Table 2), in agreement with previous work [12,36]. This behaviour is attributed to the higher densification and stronger interfacial polarisation [3]. Composites reinforced with smaller grain-sized particles tend to possess a more significant interfacial area, leading to extra interfacial polarisation, which increases the dielectric properties [12,48]. Moreover, at the same filler content, the number of particulates in the smaller-sized filler is higher than that in the bigger-sized filler. This occurrence leads to a denser composite, which increases the ε' and ε'' of the composite [12]. At 1 GHz, the values ε' and *tanδ* increased from 2.07 and 0.0010 to 2.18 and 0.0011 with a decreament of filler size from 106 μm to 25 μm. Additionally, the values of ε' and *tanδ* varied from 2.06 and 0.0010 to 2.17 and 0.0011 at 12 GHz.

Table 2. Mean complex permittivity and loss tangent of PTFE/recycled BRS composites at different filler sizes.

Recycled BRS Size (μm)	ε'	ε''	*tanδ*
25	2.18	0.0026	0.0011
45	2.14	0.0024	0.0011
63	2.11	0.0022	0.0011
90	2.08	0.0021	0.0010
106	2.07	0.0020	0.0010

3.7. Signal Transmission Speed

The variation of signal transmission speed across the PTFE/recycled BRS composites at different recycled BRS sizes and frequencies is depicted in Figure 12. It can be seen that transmission speed decreases with filler size reduction. The higher transmission speed is associated with lower relative permittivity at larger filler sizes. At 1 GHz, PTFE/recycled BRS composites had Vs of 2.032×10^8 m/s, 2.046×10^8 m/s, 2.062×10^8 m/s, 2.075×10^8 m/s and 2.086×10^8 m/s at 25 μm, 45 μm, 63 μm, 90 μm and 106 μm of recycled BRS filler sizes, respectively. The Vs increased to 2.034×10^8 m/s, 2.050×10^8 m/s, 2.065×10^8 m/s, 2.080×10^8 m/s and 2.092×10^8 m/s at 12 GHz for the same filler sizes.
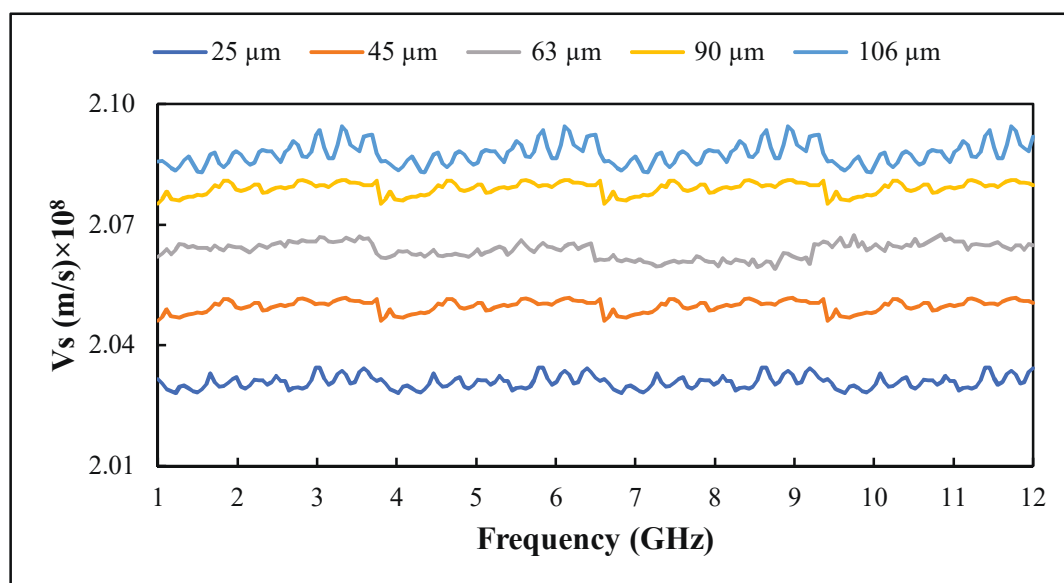
Figure 12. Variation of signal transmission speed with filler size.

The comparison of the PTFE/recycled BRS composite at a filler size of 63 μm with commercial high-frequency laminates is presented in Table 3. The laminates are PTFE-based materials produced by [49,50]. It can be seen that the PTFE/recycled BRS composite shows a lower dielectric constant, loss tangent, moisture absorption and CTE than the laminates. The highest tensile strength is achieved by the TLX-8 laminate, followed by the PTFE/recycled BRS composite. This result proves that recycled BRS glass can reinforce PTFE to produce a low-cost substrate for microwave applications.

Table 3. Comparison between PTFE/recycled BRS composite and commercial high-frequency laminates.

Name	ε'	$tan\delta$	Tensile Strength (MPa)	CTE (ppm/°C)	Moisture Absorption (%)	Reference
	At 10 GHz					
PTFE/recycled BRS composite	2.11 ± 0.05	0.0011 ± 0.00005	12.92 ± 0.005	60.45 ± 0.01	0.02 ± 0.00001	This study
AD250C	2.50	0.0013	6.00	196.00	0.04	[49]
AD255C	2.60	0.0013	8.1	196.00	0.03	[49]
TLX-8	2.55	0.0017	245	215.00	0.02	[50]

4. Conclusions

The PTFE/recycled BRS composites were fabricated through the dry powder processing technique by varying the recycled BRS filler size. XRD profiles of the composites exhibited no unwanted peaks. The scanning electron microscope showed better dispersion of the filler at a larger recycled BRS size. EDX analysis indicated that no foreign element was present in the composites. The complex permittivity of PTFE/recycled BRS composites showed an increasing trend with recycled BRS filler size reduction. The moisture absorption and density of the composites also increased for the same reason. However, the tensile strength, CTE, and signal transmission speed decreased with recycled BRS filler size reduction. At 10 GHz, the 63 μm recycled BRS composite showed suitable dielectric properties ($\varepsilon' = 2.11$ and $tan\delta = 0.0011$), CTE of 60.45 ppm/°C, low moisture absorption of 0.02% and favourable tensile strength of 12.92 MPa, ideal for microwave substrate applications.

References

1. Manu, K.; Ananthakumar, S.; Sebastian, M. Electrical and thermal properties of low permittivity Sr2Al2SiO7 ceramic filled HDPE composites. *Ceram. Int.* **2013**, *39*, 4945–4951. [CrossRef]
2. Manu, K.M.; Soni, S.; Murthy, V.R.K.; Sebastian, M.T. Ba(Zn1/3Ta2/3)O3 ceramics reinforced high density polyethylene for microwave applications. *J. Mater. Sci. Mater. Electron.* **2013**, *24*, 2098–2105. [CrossRef]
3. Xie, C.; Liang, F.; Ma, M.; Chen, X.; Lu, W.; Jia, Y. Microstructure and dielectric properties of PTFE-based composites filled by micron/submicron-blended CCTO. *Crystals* **2017**, *7*, 126. [CrossRef]
4. Murali, K.P.; Rajesh, S.; Nijesh, K.J.; Ratheesh, R. Effect of particle size on the microwave dielectric properties of alumina-filled PTFE substrates. *Int. J. Appl. Ceram. Technol.* **2010**, *7*, 475–481. [CrossRef]
5. Rajesh, S.; Murali, K.; Jantunen, H.; Ratheesh, R. The effect of filler on the temperature coefficient of the relative permittivity of PTFE/ceramic composites. *Phys. B Condens. Matter* **2011**, *406*, 4312–4316. [CrossRef]
6. Varghese, J.; Nair, D.R.; Mohanan, P.; Sebastian, M.T. Dielectric, thermal and mechanical properties of zirconium silicate reinforced high density polyethylene composites for antenna applications. *Phys. Chem. Chem. Phys.* **2015**, *17*, 14943–14950. [CrossRef]
7. Murali, K.; Rajesh, S.; Prakash, O.; Kulkarni, A.; Ratheesh, R. Preparation and properties of silica filled PTFE flexible laminates for microwave circuit applications. *Compos. Part A Appl. Sci. Manuf.* **2009**, *40*, 1179–1185. [CrossRef]
8. Jiang, Z.; Yuan, Y. Effects of particle size distribution of silica on properties of PTFE/SiO2 composites. *Mater. Res. Express* **2018**, *5*, 066306. [CrossRef]
9. Mazur, K.; Gądek-Moszczak, A.; Liber-Kneć, A.; Kuciel, S. Mechanical behavior and morphological study of polytetrafluoroethylene (PTFE) composites under static and cyclic loading condition. *Materials* **2021**, *14*, 1712. [CrossRef]
10. Huang, F.; Yuan, Y.; Jiang, Z.; Tang, B.; Zhang, S. Microstructures and properties of glass fiber reinforced PTFE composite substrates with laminated construction. *Mater. Res. Express* **2019**, *6*, 075305. [CrossRef]
11. Luo, F.; Yuan, Y.; Tang, B.; Yang, J.; Zhang, S. The effects of TiO2 particle size on the properties of PTFE/TiO2 composites. *J. Mater. Sci. Chem. Eng.* **2017**, *05*, 53–60. [CrossRef]
12. Thomas, S.; Kavil, J.; Malayil, A.M. Dielectric properties of PTFE loaded with micro- and nano-Sm2Si2O7 ceramics. *J. Mater. Sci. Mater. Electron.* **2016**, *27*, 9780–9788. [CrossRef]
13. Francis, L.F. *Powder Processes*; Elsevier: Amsterdam, The Netherlands, 2016; pp. 343–414.
14. Meli, A.D.; Abbas, Z.; Zaid, M.H.M.; Ibrahim, N.A. The effects of SLS on structural and complex permittivity of SLS-HDPE composites. *Adv. Polym. Technol.* **2019**, *2019*, 1–7. [CrossRef]
15. Ashby, M.F. Materials and the environment. *Phys. Status Solidi A* **1992**, *131*, 625–638. [CrossRef]
16. Hasanuzzaman, M.; Rafferty, A.; Sajjia, M.; Olabi, A.-G. Properties of glass materials. In *Reference Module in Materials Science and Materials Engineering*; Hashmi, S., Ed.; Elsevier: Amsterdam, The Netherlands, 2016.
17. Kochetov, R.; Tsekmes, I.A.; Morshuis, P.H.F.; Smit, J.J.; Wanner, A.J.; Wiesbrock, F.; Kern, W. Effect of water absorption on dielectric spectrum of nanocomposites. In Proceedings of the 2016 IEEE Electrical Insulation Conference (EIC), Montreal, QC, Canada, 19–22 June 2016; pp. 579–582. [CrossRef]
18. Zou, C.; Fothergill, J.C.; Rowe, S.W. The effect of water absorption on the dielectric properties of epoxy nanocomposites. *IEEE Trans. Dielectr. Electr. Insul.* **2008**, *15*, 106–117. [CrossRef]
19. Ismail, N.Q.A.; Saat, N.K.; Zaid, M.H.M. Effect of soda lime silica glass doping on ZnO varistor ceramics: Dry milling method. *J. Asian Ceram. Soc.* **2020**, *8*, 909–914. [CrossRef]

20. Chaichanawong, J.; Thongchuea, C.; Areerat, S. Effect of moisture on the mechanical properties of glass fiber reinforced polyamide composites. *Adv. Powder Technol.* **2016**, *27*, 898–902. [CrossRef]

21. Vartak, D.; Ghotekar, Y.; Deshpande, N.; Munjal, B.; Bhatt, P.; Satyanarayana, B.; Vyas, K.; Lal, A. New horizons of space qualification of single-walled carbon nano tubes-carbon fibre reinforced polymer composite. *J. Physics Conf. Ser.* **2021**, *1854*, 012001. [CrossRef]

22. Mensah, E.E.; Abbas, Z.; Azis, R.S.; Khamis, A.M. Enhancement of complex permittivity and attenuation properties of recycled hematite (α-Fe2O3) using nanoparticles prepared via ball milling technique. *Materials* **2019**, *12*, 1696. [CrossRef]

23. Khamis, A.M.; Abbas, Z.; Ahmad, A.F.; Azis, R.S.; Abdalhadi, D.M.; Mensah, E.E. Experimental and computational study on epoxy resin reinforced with micro-sized OPEFB using rectangular waveguide and finite element method. *IET Microw. Antennas Propag.* **2020**, *14*, 752–758. [CrossRef]

24. Ratheesh, R.; Sebastian, M. *Polymer-Ceramic Composites for Microwave Applications*; John Wiley & Sons: Hoboken, NJ, USA, 2017; Volume 50, pp. 481–535.

25. Irshidat, M.R.; Al-Saleh, M.H.; Sanad, S. Effect of nanoclay on the expansive potential of cement mortar due to alkali-silica reaction. *ACI Mater. J.* **2015**, *112*. [CrossRef]

26. Yamaguchi, A.; Kido, H.; Ukita, Y.; Kishihara, M.; Utsumi, Y. Anisotropic pyrochemical microetching of poly(tetrafluoroethylene) initiated by synchrotron radiation-induced scission of molecule bonds. *Appl. Phys. Lett.* **2016**, *108*, 51610. [CrossRef]

27. Feng, W.; Yin, L.; Han, Y.; Wang, J.; Xiao, K.; Li, J. Tribological and physical properties of PTFE-NBR self-lubricating composites under water lubrication. *Ind. Lubr. Tribol.* **2021**, *73*, 82–87. [CrossRef]

28. Lago, E.D.; Cagnin, E.; Boaretti, C.; Roso, M.; Lorenzetti, A.; Modesti, M. Influence of different carbon-based fillers on electrical and mechanical properties of a PC/ABS blend. *Polymers* **2019**, *12*, 29. [CrossRef] [PubMed]

29. Das, S.; Chattopadhyay, S.; Dhanania, S.; Bhowmick, A.K. Improved dispersion and physico-mechanical properties of rubber/silica composites through new silane grafting. *Polym. Eng. Sci.* **2020**, *60*, 3115–3134. [CrossRef]

30. Hubert, M.; Faber, A.J. On the structural role of boron in borosilicate glasses. *Phys. Chem. Glas. Eur. J. Glas. Sci. Technol. Part B* **2014**, *55*, 136–158.

31. Nasrazadani, S.; Hassani, S. Modern analytical techniques in failure analysis of aerospace, chemical, and oil and gas industries. In *Handbook of Materials Failure Analysis with Case Studies from the Oil and Gas Industry*; Elsevier: Amsterdam, The Netherlands, 2016; pp. 39–54.

32. Yuan, Y.; Zhang, S.; Zhou, X.; Li, E. MgTiO3 filled PTFE composites for microwave substrate applications. *Mater. Chem. Phys.* **2013**, *141*, 175–179. [CrossRef]

33. Wang, H.; Zhou, F.; Guo, J.; Yang, H.; Tong, J.; Zhang, Q. Modified BCZN particles filled PTFE composites with high dielectric constant and low loss for microwave substrate applications. *Ceram. Int.* **2020**, *46*, 7531–7540. [CrossRef]

34. Hu, Y.; Zhang, Y.; Liu, H.; Zhou, D. Microwave dielectric properties of PTFE/CaTiO3 polymer ceramic composites. *Ceram. Int.* **2011**, *37*, 1609–1613. [CrossRef]

35. Murali, K.P.; Rajesh, S.; Jacob, K.S.; Prakash, O.; Kulkarni, A.R.; Ratheesh, R. Preparation and characterization of cordierite filled PTFE laminates for microwave substrate applications. *J. Mater. Sci. Mater. Electron.* **2010**, *21*, 192–198. [CrossRef]

36. Chen, Y.-C.; Lin, H.-C.; Lee, Y.-D. The effects of filler content and size on the properties of PTFE/SIO2 composites. *J. Polym. Res.* **2003**, *10*, 247–258. [CrossRef]

37. Xu, G.; Yu, Y.; Zhang, Y.; Li, T.; Wang, T. Effect of B4C particle size on the mechanical properties of B4C reinforced aluminum matrix layered composite. *Sci. Eng. Compos. Mater.* **2019**, *26*, 53–61. [CrossRef]

38. Mortazavian, S.; Fatemi, A.; Khosrovaneh, A. Effect of water absorption on tensile and fatigue behaviors of two short glass fiber reinforced thermoplastics. *SAE Int. J. Mater. Manuf.* **2015**, *8*, 435–443. [CrossRef]

39. JA, M.H.; Majid, M.S.A.; Afendi, M.; Marzuki, H.; Hilmi, E.A.; Fahmi, I.; Gibson, A. Effects of water absorption on Napier grass fibre/polyester composites. *Compos. Struct.* **2016**, *144*, 138–146. [CrossRef]

40. Thomas, D.; Sebastian, M.T. HDPE matrix composites filled with Ca4La6(SiO4)4(PO4)2O2 for microwave substrate applications. *J. Electron. Packag.* **2014**, *136*, 031002. [CrossRef]

41. Han, K.; Zhou, J.; Li, Q.; Shen, J.; Qi, Y.; Yao, X.; Chen, W. Effect of filler structure on the dielectric and thermal properties of SiO2/PTFE composites. *J. Mater. Sci. Mater. Electron.* **2020**, *31*, 9196–9202. [CrossRef]

42. Elloumi, I.; Koubaa, A.; Kharrat, W.; Bradai, C.; Elloumi, A. Dielectric properties of wood-polymer composites: Effects of frequency, fiber nature, proportion, and chemical composition. *J. Compos. Sci.* **2021**, *5*, 141. [CrossRef]

43. Rayssi, C.; Kossi, S.E.; Dhahri, J.; Khirouni, K. Frequency and temperature-dependence of dielectric permittivity and electric modulus studies of the solid solution Ca0.85Er0.1Ti1$-$xCo4x/3O3 ($0 \leq x \leq 0.1$). *RSC Adv.* **2018**, *8*, 17139–17150. [CrossRef]

44. Yang, G.; Cui, J.; Ohki, Y.; Wang, D.; Li, Y.; Tao, K. Dielectric and relaxation properties of composites of epoxy resin and hyperbranched-polyester-treated nanosilica. *RSC Adv.* **2018**, *8*, 30669–30677. [CrossRef]

45. Abdalhadi, D.M.; Abbas, Z.; Ahmad, A.F.; Matori, K.A.; Esa, F. Controlling the properties of OPEFB/PLA polymer composite by using Fe2O3 for microwave applications. *Fibers Polym.* **2018**, *19*, 1513–1521. [CrossRef]

46. Frank Gladson, T.S.; Ramesh, R.; Kavitha, C. Experimental investigation of mechanical, tribological and dielectric properties of alumina nano wire-reinforced PEEK/PTFE composites. *Mater. Res. Express* **2019**, *6*, 115327. [CrossRef]

47. Khan, M.S.; Osada, M.; Kim, H.-J.; Ebina, Y.; Sugimoto, W.; Sasaki, T. High-temperature dielectric responses in all-nanosheet capacitors. *Jpn. J. Appl. Phys.* **2017**, *56*, 06GH09. [CrossRef]

48. Todd, M.G.; Shi, F.G. Validation of a novel dielectric constant simulation model and the determination of its physical parameters. *Microelectron. J.* **2002**, *33*, 627–632. [CrossRef]
49. Advanced Connectivity Solution. AD Series®Laminates 2021:1–4. Available online: https://rogerscorp.com/advanced-connectivity-solutions/ad-series-laminates (accessed on 23 January 2021).
50. Microwave & RF Laminates Products. TLX High Volume Fiberglass Reinforced Microwave Substrate 2020. Available online: https://www.agc-multimaterial.com/page/microwave--rf-laminates-66.html (accessed on 5 July 2021).